Critical evaluation and thermodynamic modeling of Mg-RE-X (X = Mn, Si, Sn) systems coupled with experimental investigation

Junghwan Kim

Department of Mining and Materials Engineering

McGill University, Montreal, QC

August 2015

A thesis submitted to McGill University in partial fulfilment of the requirements of the degree of Doctorate of Philosophy.

© Junghwan Kim 2015.

Acknowledgements

First of all, I would like to thank God, the Almighty, for having made everything possible by giving me strength and courage to do this work.

My deepest gratitude to Dr. In-Ho Jung, my supervisor, for his encouragement, financial support, enthusiastic guidance and patience.

Sincere thanks to my family, my lovely wife Eunyoung Jung and adorable daughter Yunha Kim, and my father, mother and my brother, relatives and friends in Korea who all gave me courage and support.

I am grateful to all my group members, Dr. Pierre Hudon for his encouragement and helpful advice in the experimental works, Dr. Manas Paliwal for his collaboration and experimental supports, Dr. Sazol K. Das for his knowledge and encouragement, Mr. Dong-Geun Kim and Sun Yong Kwon for the friendship and meaningful discussions, I also thank to all other members to be a good friend with me in Canada.

I am also deeply indebted to the pastor and friends in Montreal Korean Presbyterian Church, who pray for me.

I acknowledge the financial support during the present study by the National Sciences and Engineering Research Council of Canada (NSERC) Collaborative Research and Development grant and General Motors of Canada.

Abstract

Magnesium (Mg) alloys are considered as excellent structural materials owing to their light weight along with high specific strength. As for searching new and better Mg alloys, the effect of various alloying elements are currently being investigated. As well as conventional alloying elements like Al, Zn, Mn, etc., rare earth (RE) metals are excellent candidates to enhance the mechanical and chemical properties of Mg alloys. The addition of RE in the casting Mg alloys leads to enhanced strength at both ambient and elevated temperatures. High temperature stable RE compounds are often responsible for the improved creep resistance of the Mg alloys. Recently, the RE addition in the wrought Mg alloys is of great interest in automotive applications because the addition of RE results in weaker and more random textures, which can improve the formability of Mg alloys.

The thermodynamic calculations, using thermodynamic database, in the evaluation of existing and potential new Mg alloys are very effective. Accordingly, the development of thermodynamic database of Mg alloys including large amount of alloying species is important to enable the thermodynamic tools to use in many practical applications with regards to Mg alloy development.

In the present study, the thermodynamic database for the Mg alloys with RE metals containing Mn, Si, and Sn was developed with a critical evaluation and the optimization of the Mn-RE (13 binary), Si-RE (13 binary), and Sn-RE (13 binary) systems, and several Mg-RE-X (X = Mn, Si, and Sn) (9 ternary) systems. This is part of the development of a large thermodynamic database for the Mg alloys. In the optimizations, the systematic trends and certain similarities were observed in the phase diagrams and thermodynamic properties through the RE series. The systematics was taken into account to complete the optimizations, in particular by the appropriate predictions of the unknown thermodynamic properties. As a result, discrepancies among existing data were successfully resolved during the optimizations, and reliable thermodynamic functions for all the phases in each system were obtained even with the limited amount of experimental data. In addition, key experiments, including phase diagram determinations by differential scanning calorimetry (DSC), and enthalpy of formation measurements by solution calorimetry, were performed for the Mn-Dy system. These experiments enabled to resolve the discrepancies in

available experimental data and the lack of thermodynamic information in other Mn-heavy RE systems by the systematic analysis. In the expansion to the ternary systems, the phase diagrams of the Mg-Sn-Nd and Mg-Sn-Gd systems at 500 to 700 ºC were determined by the equilibration/quenching method. The existence of the ternary compounds, MgNd(Gd)Sn, $MgNd(Gd)Sn_2$, and $Mg_4Nd_2Sn_3$ was revealed with the respective phase equilibria. These new ternary phase diagram information were used for the optimization for the Mg-Sn-RE systems.

As well as showing the systematics in each binary RE-X system, theoretically, the limitation of the thermodynamic models (Modified quasichemical model vs. Bragg-Williams random mixing model), and the possible reason behind the RE systematics in the enthalpy of formation, the melting temperatures of the RE compounds, etc. were discussed based on the present thermodynamic optimization.

Finally, several case studies for Mg alloy evaluation and design were performed to discuss the potential applications of the present optimized thermodynamic database.

Résumé

Les alliages de magnésium sont considérés comme d'excellents matériaux de structure en raison de leur poids léger de leur résistance spécifique élevée. Afin de trouver de nouveaux et meilleurs alliages de Mg, l'effet de divers éléments d'alliage est actuellement à l'étude. Les éléments d'alliage classiques comme Al, Zn, Mn, etc., et les terres rares (RE) sont d'excellents candidats pour améliorer les propriétés mécaniques et chimiques des alliages de Mg. L'ajout de RE dans les alliages de Mg destinés au moulage conduit à une résistance accrue à températures ambiante et élevées. Les composés de RE stables à haute température sont souvent responsables de la résistance au fluage des alliages de Mg. Récemment, l'ajout de RE dans les alliages de Mg a créé un grand intérêt dans les applications automobiles parce que l'addition de RE a produit des textures plus faibles et plus aléatoires ce qui peut améliorer la formabilité des alliages de Mg.

Les calculs thermodynamiques, à l'aide de bases de données thermodynamiques, sont très efficaces pour évaluer des alliages de Mg existants ou potentiellement nouveaux. Par conséquent, le développement d'une base de données thermodynamiques pour les alliages de Mg contenant une grande quantité d'éléments est essentiel pour l'emploi d'outils thermodynamiques utiles dans le développement d'alliages de Mg.

Dans la présente étude, la base de données thermodynamiques pour les alliages de Mg avec des métaux de RE contenant du Mn, Si et Sn a été développée en réalisant une évaluation critique et une optimisation des systèmes Mn-RE (13 binaires), Si-RE (13 binaires), Sn-RE (13 binaires) et plusieurs systèmes Mg-RE-X (X = Mn, Si, Sn) (9 ternaires). Ceci fait partie de l'élaboration d'une grande base de données thermodynamiques pour les alliages de Mg. Dans les optimisations, les tendances systématiques et certaines similitudes ont été observées dans les diagrammes de phases et propriétés thermodynamiques à travers la série des RE. Cette systématique a été prise en compte pour compléter les optimisations et pour prédire certaines propriétés thermodynamiques inconnues. Par conséquent, les différences observées entre les données existantes ont été résolues avec succès pendant les optimisations et des fonctions thermodynamiques fiables pour toutes les phases de chaque système ont été obtenues même avec une quantité limitée de données

expérimentales. En outre, des expériences clés, y compris des déterminations de diagramme de phase par calorimétrie différentielle à balayage (DSC), et des mesures d'enthalpie de formation, par calorimétrie de solution, ont été réalisées pour le système Mn-Dy. Ces expériences ont permis de résoudre les anomalies dans les données expérimentales disponibles et le manque d'information thermodynamique dans d'autres systèmes de Mn-RE lourds par analyse systématique. Dans le développement des systèmes ternaires, les diagrammes de phase des systèmes Mg-Sn-Nd et Mg-Sn-Gd de 500 à 700 °C ont été déterminées par la méthode d'équilibre et de trempe. L'existence des composés ternaires MgNd(Gd)Sn, MgNd(Gd)Sn_2 et $Mg_4Nd_2Sn_3$ a été révélé avec les équilibres de phases respectifs. Ces nouvelles informations de diagramme de phase ternaire ont été utilisées pour l'optimisation des systèmes Mg-Sn-RE.

En plus de montrer la systématique dans chaque système binaire RE-X, la limitation des modèles thermodynamiques (Modèle quasichimique modifié vs Modèle de mélange aléatoire Bragg-Williams) et la raison possible derrière la systématique des RE dans l'enthalpie de formation, les températures de fusion des composés de RE, etc., ont été théoriquement examinées sur la base de la présente optimisation thermodynamique.

Enfin, plusieurs études de cas pour l'évaluation et le design d'alliages de Mg ont été effectuées pour examiner les applications potentielles de la présente base de données thermodynamiques optimisée.

Table of contents

Acknowledgement ii

Abstract iii

Résumé v

Table of contents vii

List of appendices ix

List of figures x

List of tables xiv

1. Introduction 1

    1.1. General background 1

    1.2. Objectives 4

2. Literature review 9

    2.1. Rare earth (RE) elements and their alloying behavior 9

    2.2. The properties of Mg alloys containing RE 17

    2.3. Computational thermodynamic modeling: Calculation of phase diagram (CALPHAD) method 27

3. Methodology 30

    3.1. Thermodynamic model 30

        3.1.1. Liquid phase 33

3.1.2. Solid solution phase 39

3.1.3. Stoichiometric compound and pure solid 41

3.2. Estimation techniques (Systematics and Miedema Model) 43

3.3. Experiments 46

3.3.1. Differential scanning calorimetry (DSC) 46

3.3.2. Solution calorimetry 47

3.3.3. Equilibration 49

4. Discussion of the optimized Mg-RE-X (X = Mn, Si, Sn) systems 50

4.1. The Mn-RE system 50

4.2. The Si-RE system 57

4.3. The Sn-RE system 64

4.4. The ternary Mg-RE-X (X = Mn, Si, Sn) systems 71

5. Application of the thermodynamic database to Mg alloy development 73

6. Summary and future work 83

7. Contributions to original knowledge 86

8. References 87

List of appendices

Appendix I: Article “Critical systematic evaluation and thermodynamic optimization of the Mn-RE system: RE = La, Ce, Pr, Nd and Sm”

Appendix II: Article “Thermodynamic modeling of the Mn-Y and Mn-Gd systems for the application of RE in Mg alloy development”

Appendix III: Article “Critical systematic evaluation and thermodynamic optimization of the Mn-RE system (RE = Tb, Dy, Ho, Er, Tm and Lu) with key experiments for the Mn-Dy system”

Appendix IV: Article “Critical evaluation and thermodynamic optimization of the Si-RE systems: Part I. Si-RE system (RE = La, Ce, Pr, Nd and Sm)”

Appendix V: Article “Critical evaluation and thermodynamic optimization of the Si-RE systems: Part II. Si-RE system (RE = Gd, Tb, Dy, Ho, Er, Tm, Lu and Y)”

Appendix VI: Article “Critical evaluation and thermodynamic optimization of the Sn-RE systems: part I. Sn-RE system (RE = La, Ce, Pr, Nd and Sm)”

Appendix VII: Article “Critical evaluation and thermodynamic optimization of the Sn-RE systems: part II. Sn-RE system (RE = Gd, Tb, Dy, Ho, Er, Tm, Lu and Y)”

Appendix VIII: Article “The thermodynamic optimizations of the ternary Mg-RE-X (X = Mn, Si, Sn) systems”

List of figures

Fig. 1.1. Collection of the Mg-RE phase diagrams (elements in the red box: light RE, the rest: heavy RE) [12]. 6

Fig. 1.2. Collection of the Al-RE phase diagrams (elements in the red box: light RE, the rest: heavy RE) [15, 16]. 7

Fig. 1.3. Collection of the Zn-RE phase diagrams (elements in the red box: light RE, the rest: heavy RE) [17, 18]. 8

Fig. 2.1. Atomic radius of the rare earth elements and Mg [19]. 12

Fig. 2.2. Maximum solubility of RE in hcp-Mg in the binary Mg-RE systems [21]. 13

Fig. 2.3. Schematic representation of the melting behavior of binary Mg-RE systems [22]. 13

Fig. 2.4. The experimental enthalpies of formation of selected lanthanide compounds [23]. ... 14

Fig. 2.5. Volume contractions of selected lanthanide compounds [23]. 14

Fig. 2.6. Selected properties of $REAl_2$ phases plotted against the atomic number of RE (a) Volume ratio and (b) Enthalpy of formation at 300 K [22]. 15

Fig. 2.7. The relation between the melting temperature of $RE_{11}M_{10}$ ($L + RE_5M_4 \rightarrow RE_{11}M_{10}$), RE_5M_4 ($L + RE_5M_3 \rightarrow RE_5M_4$), RE_5M_3 (congruent), and eutectic temperature ($L \rightarrow RE + RE_5M_3$), (M = Gd, Sn, Pb): 1) Ge, 2) Sn, 3) Pb, 4) experimental data. The black symbols were taken from the data on other types of reaction [46]. 16

Fig. 2.8. Atomic radius of RE and solubility of RE in in solid Mg as a function of the atomic number of RE [47]. 20

Fig. 2.9. Variation of the hardness of solid-solution-hardened binary magnesium alloys in the process of aging at 200°C (a) heavy RE, (b) light RE [47]. 21

Fig. 2.10. Tensile properties of the cast Mg alloys with La, Ce, Pr and Nd at room temperature [19]. 22

Fig. 2.11. Tensile strength properties of the cast Mg alloys with La, Ce and Nd at 260 ºC [19]. 23

Fig. 2.12. Tensile properties of the Mg-RE alloys at room temperature [19]. 23

Fig. 2.13. (a) to (c) Creep curves of selected Mg–RE alloys at 177 ºC and 90 MPa, and (d) variation of the secondary creep rate with the RE content. The solid symbols in (d) represent where the applied stress in creep is above the 0.2% yield strength [48]. 24

Fig. 2.14. Corrosion rate of binary Mg alloys in 3% NaCl aqueous solution [19]. 25

Fig. 2.15. Textures of binary Mg–RE sheets: (a) recalculated (0002)-pole figures of sheets with a low and high alloying content in as-rolled condition and after annealing; (b) maximum (0002)-pole figure intensity in as-rolled condition and (c) after annealing [51]. 26

Fig. 3.1. Some geometric models: symmetric model (a) and (c), and asymmetric model (b) and (d) [95]. 38

Fig. 3.2. Systematic change in the experimental data of enthalpy of mixing for the Mn-RE liquid at 1700 K (See Appendix I to III for the experimental references). 45

Fig. 3.3. Systematic changes in the melting temperatures of Si-RE compounds (Appendix V). 45

Fig. 3.4. DSC curve for the alloy (80.5 at. % Mn and 19.5 at. % Dy) (Appendix III). 46

Fig. 3.5. Fig. 3.5. Solution calorimeter: ① Reaction crucible, ② Thermopile, ③ Tantalum blocks, ④ Alumina layer, ⑤ Alumina rod, ⑥ Charge tube, ⑦ Thermocouple, and ⑧ Stirrer (Appendix III). 49

Fig. 4.1. Collection of the optimized phase diagrams of Mn-RE systems (Appendix III). 53

Fig. 4.2. The Mn-Nd phase diagram with experimental data (Appendix I). 54

Fig. 4.3. The Mn-Gd phase diagram with experimental data (Appendix II). 54

Fig. 4.4. The standard entropy of formation of the Mn-Gd compounds along with experimental data (Appendix II). 55

Fig. 4.5. Optimized standard enthalpy of formation of the Mn-RE system (Appendix III). 55

Fig. 4.6. Optimized standard entropy of formation of the Mn-RE system (Appendix III). 56

Fig. 4.7. Collection of the optimized phase diagrams of Si-RE systems (Appendix V). 60

Fig. 4.8. Phase diagrams of (a) Si-Ce and (b) Si-Pr systems; solid lines: calculated from the present study and dotted lines: proposed by experimental studies (see Appendix IV for the references). 61

Fig. 4.9. Comparison of integral enthalpies of mixing of liquid Si-RE at 2000 K. ((a) Si-light RE and (b) Si-heavy RE) (Appendix V). 62

Fig. 4.10. Comparison of entropies of mixing of liquid Si-RE at 2000 K. ((a) Si-light RE and (b) Si-heavy RE) (Appendix V). 62

Fig. 4.11. Comparison of enthalpies of formation of Si-RE compounds at 298 K (based on one mole of Si-RE system) (Appendix V). 63

Fig. 4.12. Comparison of entropies of formation of Si-RE compounds at 298 K (based on one mole of Si-RE system) from elemental references (Appendix V). 63

Fig. 4.13. Collection of the optimized phase diagrams of the Sn-RE systems. 67

Fig. 4.14. Systematic changes in the melting temperatures of Sn-RE compounds. The melting temperatures estimated in the present study are indicated by the empty squares (Appendix VII). 68

Fig. 4.15. Comparison of integral enthalpies of mixing of liquid Sn-RE at 2000 K ((a) Sn-light RE and (b) Sn-heavy RE) (Appendix VII). 69

Fig. 4.16. Comparison of entropies of mixing of liquid Sn-RE at 2000 K ((a) Sn-light RE and (b) Sn-heavy RE) (Appendix VII). 69

Fig. 4.17. Comparison of enthalpies of formation of Sn-RE compounds at 298 K (based on one mole of Sn-RE system) (Appendix VII). 70

Fig. 4.18. Comparison of entropies of formation of Sn-RE compounds at 298 K (based on one mole of Sn-RE system) from elemental references (Appendix VII). 70

Fig. 5.1. The phase fraction vs. temperature diagrams of the Mg-Gd alloys with the addition of Zr, Mn, and Mn+Sc. 79

Fig. 5.2. (a) Age-hardening response at different temperatures after solution treated at 610 ºC for 24 h [126], and (b) the phase fraction vs. temperature diagrams of the Mg-Gd-Mn-Sc alloy. 80

Fig. 5.3. Calculated Mg-rich corner of the Mg-Si-La system at 400 ºC with an assumption of no ternary phases. 80

Fig. 5.4. Calculated solvus of hcp-Mg at 400 ºC for the Mg-Al-RE system (solid lines; y-axis left side) and Mg-Zn-RE system (dotted lines; y-axis right side) [21]. 81

Fig. 5.5. Calculated phase diagrams (Mg-rich corner) at 400 ºC for the Mg-Mn-Gd and Mg-Sn-Gd systems. 82

List of tables

Table 1.1. Convention for alloy elements designation. 2

Table 2.1. Electronegativity, melting temperature and crystal structure of the RE elements and Mg [19]. 11

Table 4.1. Crystal structures of the Mn-RE compounds. 52

Table 4.2. Crystal structures of the Si-RE compounds. 59

Table 4.3. Crystal structures of the Sn-RE compounds. 66

Table 5.1. Chemical compositions of the investigated alloys (mass%). 78

Table 5.2. The average grain sizes (μm) of the alloys at various states. 78

1. Introduction

1.1. General background

Magnesium (Mg) alloys have attractive properties including low density, high specific strength and specific stiffness, superior damping and electromagnetic shielding capacities etc. [1-3]. In particular, their light weight associated with superior specific mechanical properties has engaged great attention in automotive, aircraft, and electronic applications. For instance, the conventional cast Mg alloy (AZ91D) has about 1.43, 1.54, 2.63 and 3.03 times higher values in relative strength to weight ratio than the conventional other alloys used in automotive parts: steel, cast aluminum (Al), zinc (Zn) and cast iron (Fe), respectively [4, 5]. Therefore, the usage of Mg alloys are constantly increasing due to the weight reduction trends in the transportation fields associated with the energy saving to solve the recent global problems such as environmental pollution, depletion of fossil fuels, and the strengthening of international environmental regulations accordingly. That is to say specifically, every 10 per cent reduction in weight of the vehicle will result in a 6-8 per cent decrease in fuel consumption [5, 6]. Furthermore, according to a conservative estimation, if every new car is fitted with an Mg engine block, one could reduce 825,000,000 tonnes of CO_2 emission in a year [5, 7].

To employ Mg alloys for engineering applications, a wide range of alloying elements are being used to enhance the physical and chemical properties of Mg alloys. One of the most commonly used alloying elements is Al of which the maximum solubility is 11.5 at. % (12.7 wt. %). Alloying Al results in good combination of room temperature strength and ductility as well as good castability. In addition to Al, Zn is another effective alloying element which leads to strengthening as well as grain refining. When Al is present, small amount of manganese (Mn), about 0.2 wt. % is added to improve grain structure. If zirconium (Zr) is added supplementally, the grain refinement effect can be further increased. Most conventional Mg alloys are AZ series (i.e., AZ31, AZ91, and AZ63, etc.), which contain Al, Zn and small amount of Mn, and they are commonly used as cast and wrought alloys. The designation for Mg alloys generally uses two prefix letters which tell main

alloying elements followed by two numerals which indicate approximately respective nominal compositions of main alloying elements by weight. For example, AS41 has 4% aluminum and 1% silicon and AZ81 has 7.5% aluminum and 0.7% zinc. The convention to indicate the main elements in the magnesium alloys is tabulated in table.1.

Table 1.1. Convention for alloy elements designation.

Letter	Alloying elements	Letter	Alloying elements
A	Aluminum (Al)	Q	Silver (Ag)
C	Copper (Cu)	S	Silicon (Si)
E	Rare earths (RE)	T	Tin (Sn)
H	Thorium (Th)	W	Yttrium (Y)
K	Zirconium (Zr)	X	Calcium (Ca)
L	Lithium (Li)	Z	Zinc (Zn)
M	Manganese (Mn)		

For the Mg-Al alloys, it is well known that the creep resistance of the alloys is limited due to the poor thermal stability of the $Mg_{17}Al_{12}$ phase [8]. In addition, the applications of wrought alloys are limited due to the restricted plasticity of magnesium associated with the small number of deformation mechanisms of hcp structure and the preferred strong crystallographic orientation (texture) that develops in wrought alloys. Therefore, various alloying elements such as silicon, tin, silver, calcium, rare earths (RE), etc. are added to overcome such limitations and also to improve the manufacturing process [9]. Briefly stating: the addition of silicon increases the fluidity of molten alloys and the high temperature mechanical properties and creep resistance; small amounts of tin with aluminum serve to improve ductility and reduces the tendency to cracking during forging; silver increases the age hardening response and high temperature properties of thorium or rare earth containing alloys, e.g. QE22 and QE21; calcium improves creep resistance by replacing $Mg_{17}Al_{12}$ with $Al_{12}Ca$ and also increases the rollability; rare earths are added to improve the high temperature strength and creep resistance. The introduction of RE elements and the principal

effects of alloying RE in magnesium are specifically reviewed in the following chapter (2. literature review).

To develop new Mg alloys having enhanced mechanical and chemical properties, the potential candidates for alloying elements and the most optimum alloy compositions should be established. The properties of alloys mostly depend upon the phases and microstructural constituents (eutectics, precipitates, solid solution etc.). The phase constituents in the alloy system with several alloying elements are usually very complex. To understand these complex phase relationships efficiently, it is very useful to develop thermodynamic database which can be used to obtain the amounts and compositions of all phases at any temperature and composition in multicomponent alloys. That is, the database can provide the phase diagrams, equilibrium or non-equilibrium (Scheil-Gulliver) cooling, and heat effects, etc. with the help of Gibbs (free) energy minimization software like FactSage [10]. Such thermodynamic databases are often prepared by critical evaluation and optimization (or assessment). In the optimization process, the adjustable model parameters that describe the Gibbs energy functions of constituent phases can be obtained based on the thermodynamic and phase equilibrium data. It is also often possible to resolve discrepancies in the available data during the optimization process. The databases with the optimized parameters are rendered self-consistent and compliant with thermodynamic principles, and stored in the computer.

In the present study, the thermodynamic database of several Mg-RE-X (X = Mn, Si, Sn) (9 ternary) systems including the Mn-RE (13 binary), Si-RE (13 binary) and Sn-RE (13 binary) systems have been developed (Appendices I to VIII). In addition, several case studies for the Mg alloy evaluation and design are shown to discuss the applicability of the optimized thermodynamic database (Chapter 5).

1.2. Objectives

As introduced, the thermodynamic calculations in the evaluation of existing and potential new Mg alloys is very effective. Developing the thermodynamic database for the Mg alloys including large amount of alloying species is indispensable accordingly. The thermodynamic assessments for Mg alloy systems had already been performed through the effort of several research groups during the international COST-507 project [11]. The project developed the thermodynamic database of the binary and ternary systems including Mg with Al, Zn, Cu, Si, Mn, Y, and Li. On top of that, the database has been extended, in particular including RE elements in considering the importance of alloying RE in Mg alloys, as well as Ca, Sr, Sn, etc. The extension of database toward RE was started from the assessments of the binary Mg-RE systems. The optimizations of the binary Mg-RE systems were previously performed by Kang et al. [12] based on the available experimental data set and predictions considering the systematic trends which were captured in the Mg-RE systems with successive RE atomic number. One thing to be emphasized about RE-containing systems, due to the high chemical reactivity and oxygen affinity of RE metals, it is especially difficult to carry out the experimental investigations of RE-containing systems, so that the experimental data for certain RE-containing systems are often quite scarce or the accuracy of the existing data is often not very reliable compared with other conventional metallic systems. Therefore, a systematic analysis ensuring that the thermodynamic properties do not significantly differ from one system to the other can help to fill out the lack of experimental data or to overcome the inaccuracy of data. Subsequently, the optimizations of the Mg-Al-RE [13, 14] and Mg-Zn-RE (unpublished work) systems have been continued including the complete optimizations of the binary Al-RE [15, 16] and Zn-RE [17, 18] systems using a similar approach for the optimizations of the Mg-RE systems. The systematic analyses were successfully applied to the optimizations of those binary systems. For instance, the collections of the phase diagrams of the Mg-RE, Al-RE and Zn-RE systems with the optimized thermodynamic parameters are shown in Fig. 1.1 to 1.3, respectively. One can clearly see the systematic changes along with the RE species in the melting temperatures of the intermediate phases, and the homogeneity range of the solid solutions, eutectic temperatures, etc.

The main objective of the present study is to develop the thermodynamic database for the Mg alloys with RE metals containing Mn, Si, and Sn as part of the large thermodynamic database for the Mg alloys. That includes the thermodynamic optimizations of the Mn-RE (13 binary), Si-RE (13 binary), and Sn-RE (13 binary) systems, and several Mg-RE-X (X = Mn, Si, and Sn) (9 ternary) systems through critical evaluations of experimental data and systematic analysis approach. Among the RE elements, Pm, Eu, Yb, Sc were not included in the present study due to the radioactivity of Pm and the abnormal properties of Eu, Yb and Sc. In the optimization of the binary Mn-RE, Si-RE, and Sn-RE systems, clear systematic trends and certain similarities in thermodynamic properties and phase diagrams through the RE series were found and discussed. The systematic analysis approach enabled to assess the unexplored phase diagrams and unknown thermodynamic properties. Furthermore, in order to overcome the lack of the experimental data and discrepancies in the available data, the experimental investigations including the phase diagram determination using an equilibrated alloy method and different scanning calorimetry (DSC) were carried out, as well as the measurement of the standard enthalpy of formation of compound using solution calorimetry.

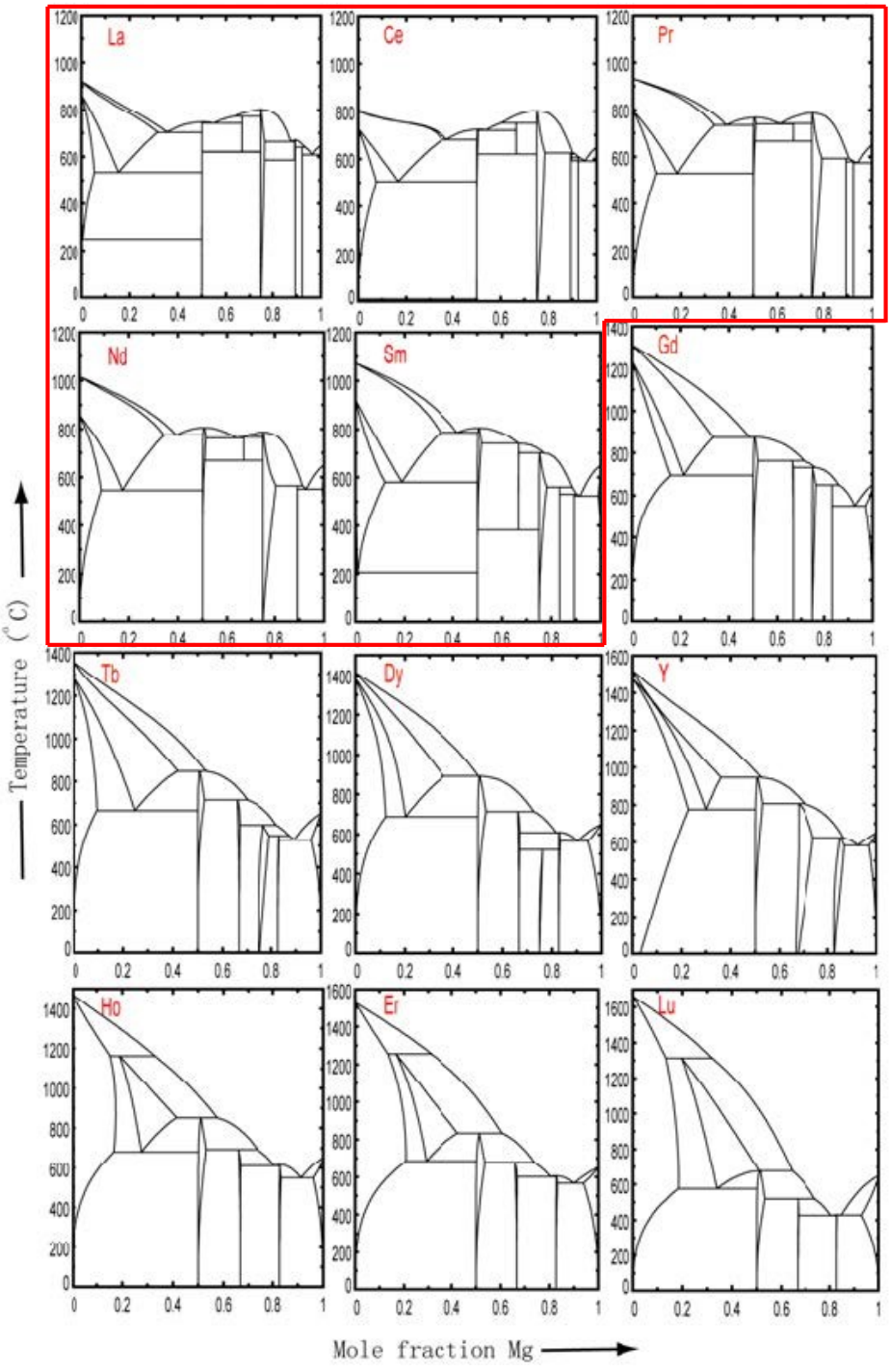


Fig. 1.1. Collection of the Mg-RE phase diagrams (elements in the red box: light RE, the rest: heavy RE) [12].

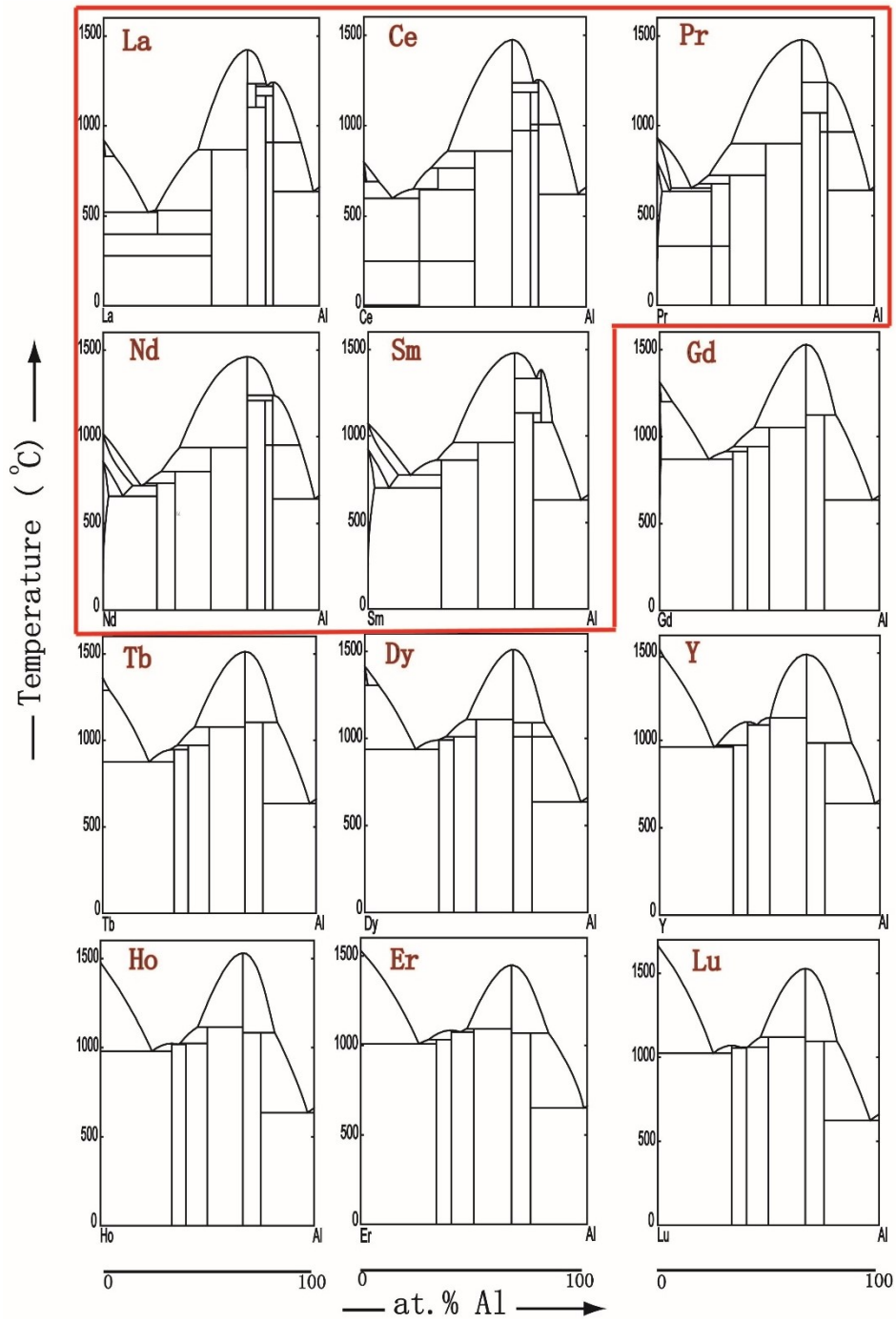


Fig. 1.2. Collection of the Al-RE phase diagrams (elements in the red box: light RE, the rest: heavy RE) [15, 16].

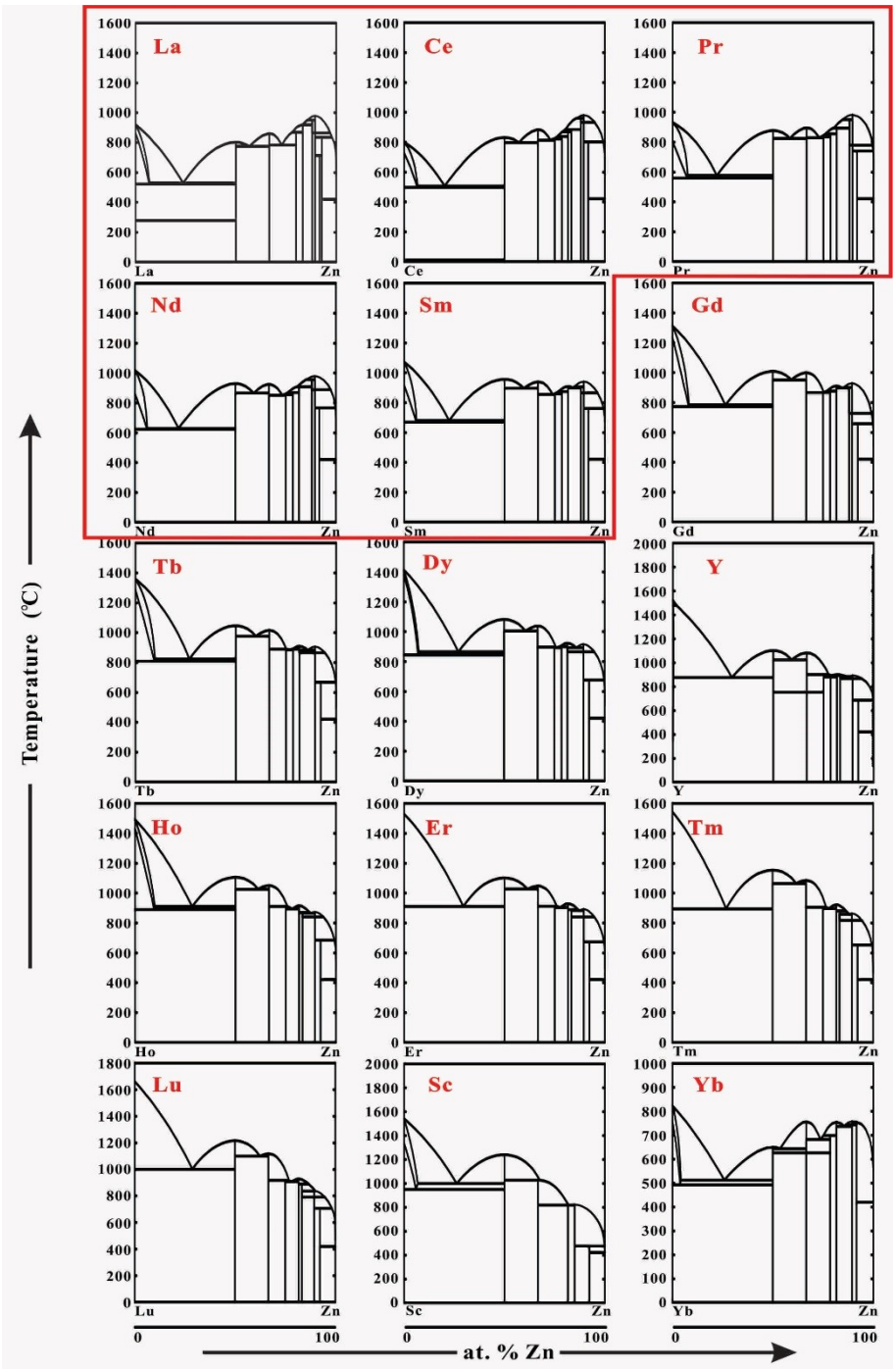


Fig. 1.3. Collection of the Zn-RE phase diagrams (elements in the red box: light RE, the rest: heavy RE) [17, 18].

2. Literature review

2.1. Rare earth (RE) elements and their alloying behavior

Rare earth (RE) elements are large group of elements in IIIA subgroup of the periodic table including those of lanthanide series and also Y and Sc. REs are conventionally categorized into two groups by weight: light RE (La to Eu, also known as Ce subgroup) and heavy RE (Gd to Lu, also known as Y subgroup). Y is lighter than the light RE, but included in the heavy RE because of its chemical and physical similarity with heavy RE. Sc is neither light RE nor heavy RE. RE elements reveal many similar features, especially in chemical properties, and also certain regularities in the change of properties with successive increase of the RE atomic number. For instance, the metallic and ionic radius of RE elements are shown in Fig. 2.1. Besides atomic radius, electronegativity, melting temperature and crystal structure of the RE elements are presented in Table 2.1. For comparison, the properties of Mg are presented together. The electronegativity values are close to each other within the limits 1.17-1.22 for the elements of the lanthanide series, except Eu and Yb, and also for Sc. The decrease of atomic radius with increasing atomic number for the elements of the lanthanum series (from La to Lu) is known as “lanthanide contraction”, which is explained by increase of attraction between electrons in the electron shells and nucleus with increasing nuclear charge due to poor shielding effect of the 4f electrons [19]. The properties of Eu and Yb are clearly distinct from other RE elements due to their divalent behavior, while other REs are trivalent [20]. The small irregularity for Ce is possibly due to the presence of a stable 4+ ions. The melting temperatures of lanthanides successively increase with increasing atomic number except Ce, Eu and Yb. The melting temperatures of Sc and Y are close to those of the heavy RE series. From the viewpoint of the melting temperatures, Y and Sc are placed between Ho and Er, and between Er and Tm, respectively.

Likewise, when a certain metal is alloyed with the RE elements, a systematic variation in the properties such as the shapes of the phase diagrams, the number and type of intermediate phases is observed. That is, the similarity and systematic trend through the RE series can extend to the

phase diagrams of the systems containing RE elements, thermodynamic properties of liquid, and also the physical and chemical properties of RE compounds. For instance, the maximum solubility of RE in hcp-Mg in the binary Mg-RE systems from 227 ºC to eutectic temperatures are shown in Fig. 2.2 [21]. As can be seen, the solubilities of light RE are typically lower than those of heavy RE. The solubilities of Ce and Nd are 0.012 and 0.11 at. % at 400 ºC while the solubilities of Gd and Y are about 1.75 and 1.95 at. %, respectively. The solubility of RE in Mg typically increases with increasing atomic number of RE. For the RE compounds, the systematics are also shown in the characteristics of the lanthanide alloys. For example, the schematic representation of the melting behavior of binary Mg-RE systems is shown in Fig. 2.3 [22]. In another example, Ferro et al. [23] showed the experimental enthalpies of formation and the volume contractions of selected lanthanide intermetallic compounds as seen in Figs. 2.4 and 2.5. Similar to the pure RE elements, the regular smooth trends in the enthalpies of formation and the volume contractions in particular for the compounds with trivalent lanthanides can be seen. There is no question about the fact that the trends are closely related with the properties of constituent RE elements. In many other studies, the systematics of the RE alloys with metals such as Ag [24, 25], Al [26], Au [27], Bi [28], Ga [29], Ge [30], In [31, 32], Mn [33], Pd [34], Pb [28, 35], Sb [28, 36, 37] Sn [38-40], Tl [41], Zn [42] etc., and also critical review [22, 43] were discussed. In addition, the systematics was often used empirically and theoretically to predict the phase diagrams and thermodynamic properties of the alloys containing RE elements. For example, certain correlation of the volume contraction, enthalpy of formation, and the melting temperature of the RE compounds with pure RE metals were found by using convenient normalization principles. According to Gschneidner [44], there is also a correlation between volume change and the enthalpy of formation, simply stated: the greater the volume contraction on forming a compound, the more negative the enthalpy of formation. The correlation can be found in the schematics of volume ratio and enthalpy of formation in Fig. 2.6 [22]. The volume ratio (r_{vol}) (relative to La) is defined between relative degree of the lanthanide contraction and the volume contraction in the compounds by the expression:

$$r_{vol} = \frac{V(RE_{1-x}M_x)}{V(La_{1-x}M_x)} \cdot \frac{V_{La}}{V_{RE}} \tag{2.1}$$

where V is the volume of one mole of the stated compound or element, RE is a rare earth element, and M indicates any other element.

For the melting temperature (in the specific case of RE compounds), reduced melting temperature (r_{vol}) was proposed by Gschneidner [44]:

$$r_{temp} = \frac{T_m(RE_{1-x}M_x)}{T_m(RE)} \tag{2.2}$$

where T_m is the melting temperature expressed in Kelvin.

Using a similar normalization approach, Bulanova et al. [45, 46] showed the correlation of the melting temperatures of certain RE-containing compounds (Si-RE, Ge-RE, Sn-RE and Pb-RE), and also the eutectic temperature ($L \rightarrow RE + RE_5M_3$) with the melting temperature of the pure RE metals in Fig. 2.7. Based on the linear interpolation of the melting temperatures of the same type of the compounds versus the melting temperatures of pure RE metals, the melting temperatures of several RE compounds were estimated.

Table 2.1. Electronegativity, melting temperature and crystal structure of the RE elements and Mg [19].

Atomic number	Element	Electronegativity	Melting temperature, ^oC	Crystal structure at room temp.
12	Mg	1.20	650	hcp
21	Sc	1.27	1541	hcp
39	Y	1.20	1522	hcp
57	La	1.17	918	dhcp
58	Ce	1.21	798	fcc
59	Pr	1.19	931	dhcp
60	Nd	1.19	1021	dhcp

61	Pm	1.2	1042	dhcp
62	Sm	1.18	1074	rhombohedral
63	Eu	0.97	822	bcc
64	Gd	1.2	1313	hcp
65	Tb	1.21	1365	hcp
66	Dy	1.21	1412	hcp
67	Ho	1.21	1474	hcp
68	Er	1.22	1529	hcp
69	Tm	1.22	1545	hcp
70	Yb	0.99	819	hcp
71	Lu	1.22	1663	hcp

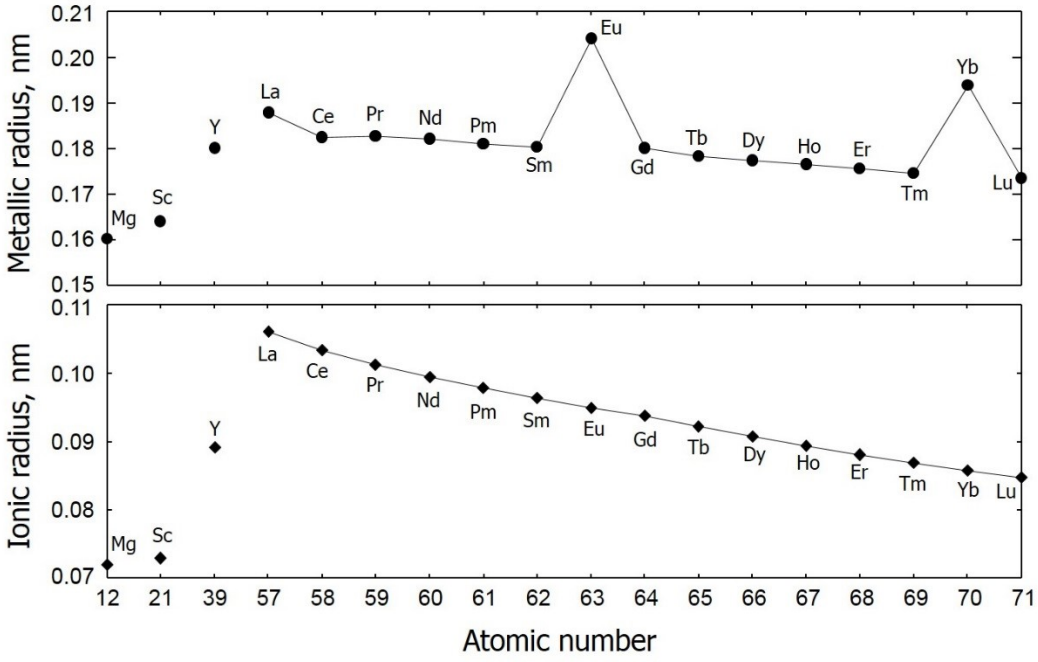


Fig. 2.1. Atomic radius of the rare earth elements and Mg [19].

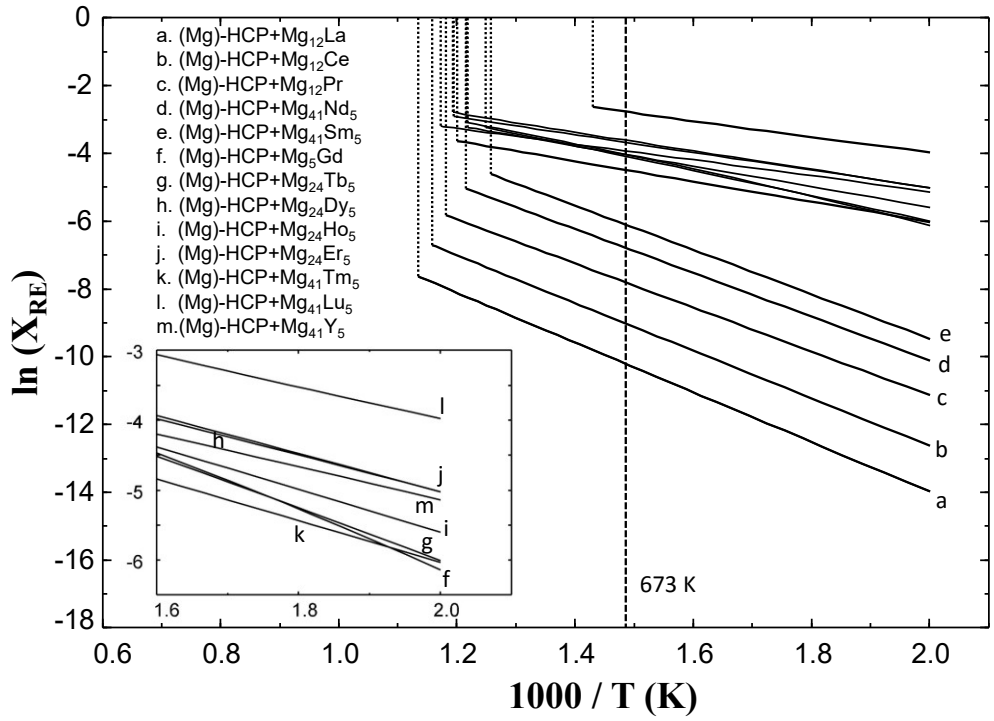


Fig. 2.2. Maximum solubility of RE in hcp-Mg in the binary Mg-RE systems [21].

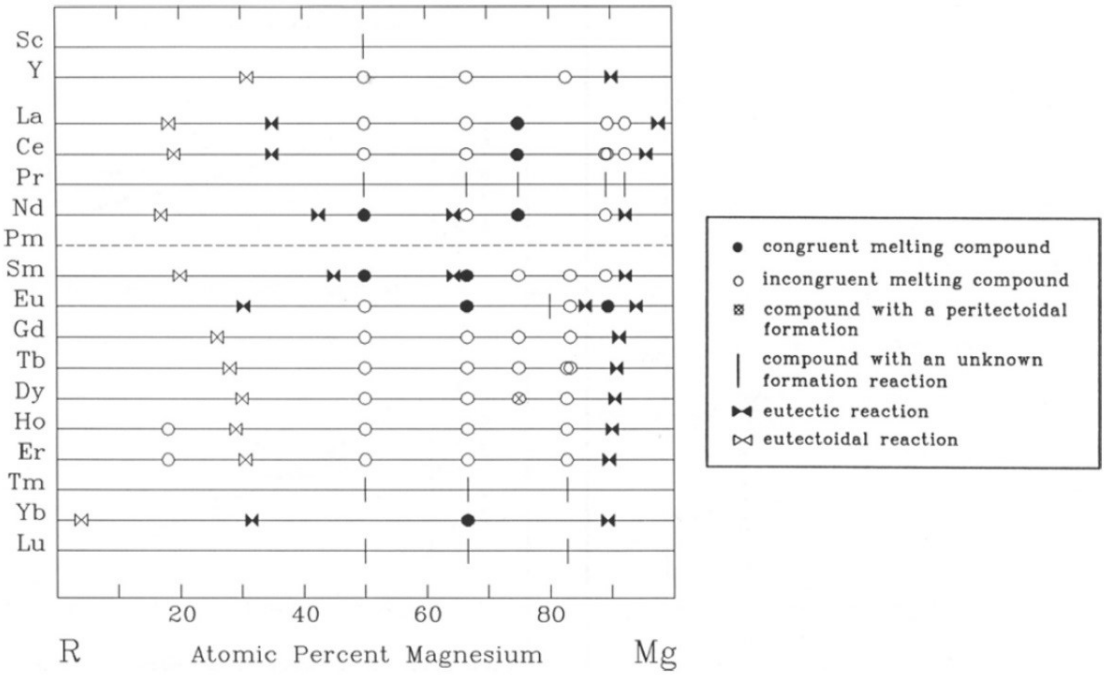


Fig. 2.3. Schematic representation of the melting behavior of binary Mg-RE systems [22].

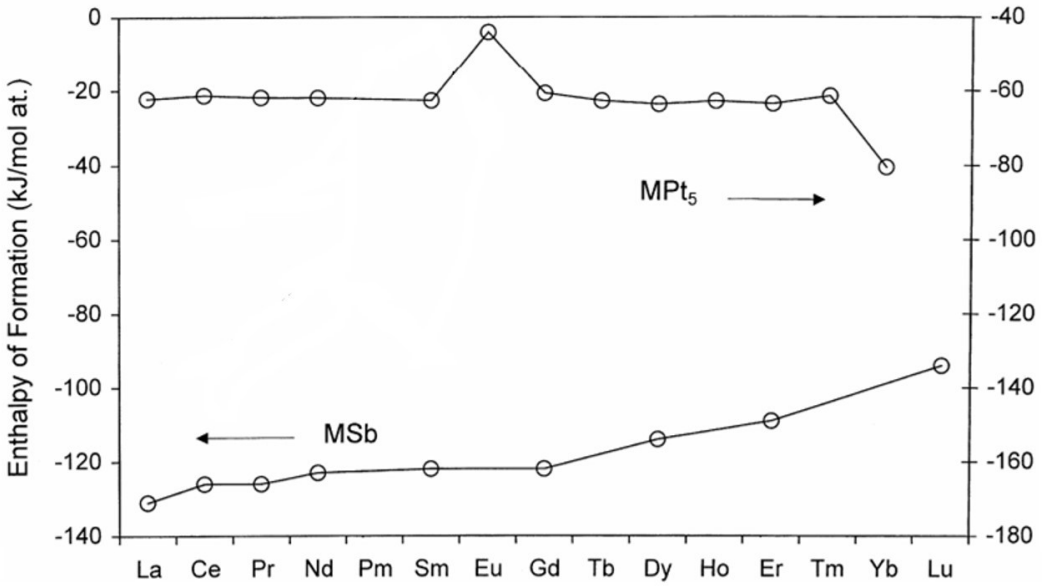


Fig. 2.4. The experimental enthalpies of formation of selected lanthanide compounds [23].

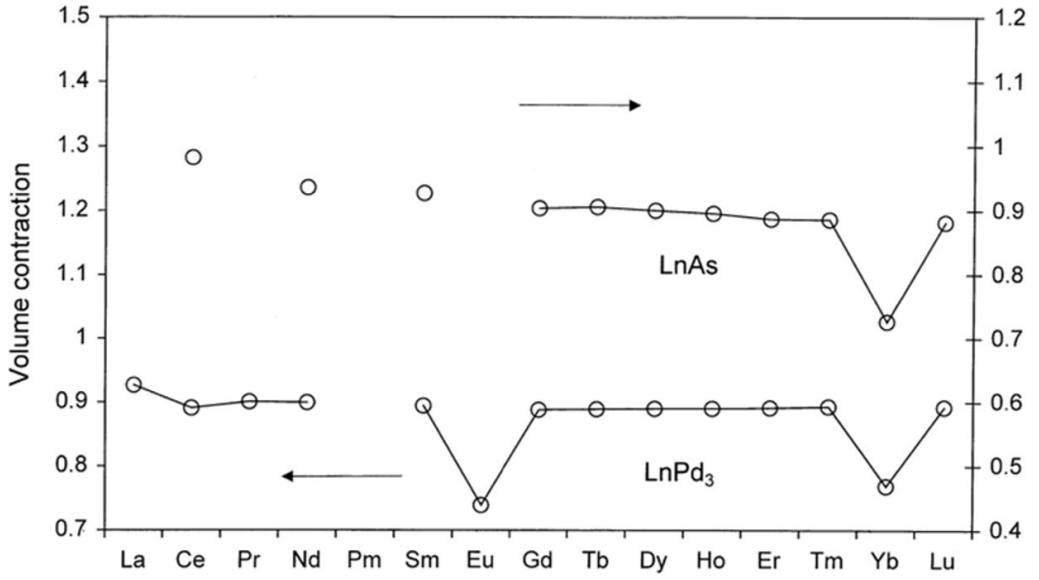


Fig. 2.5. Volume contractions of selected lanthanide compounds [23].

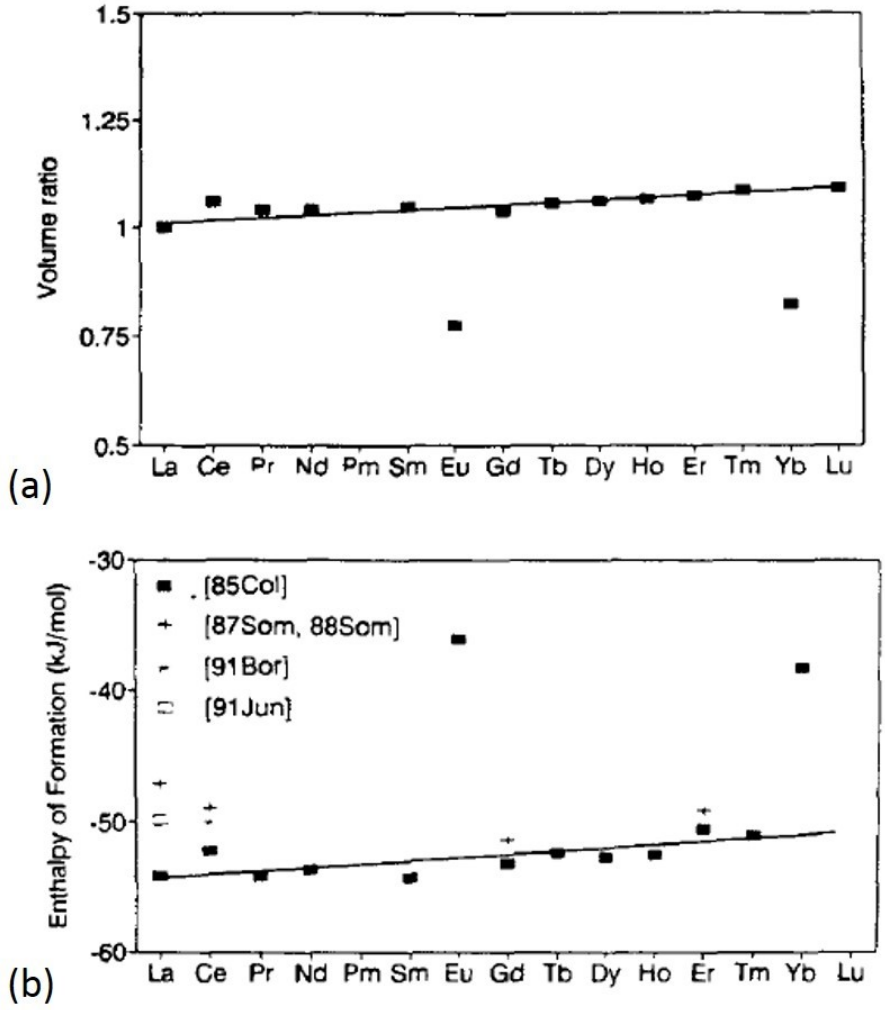


Fig. 2.6. Selected properties of $REAl_2$ phases plotted against the atomic number of RE (a) Volume ratio and (b) Enthalpy of formation at 300 K [22].

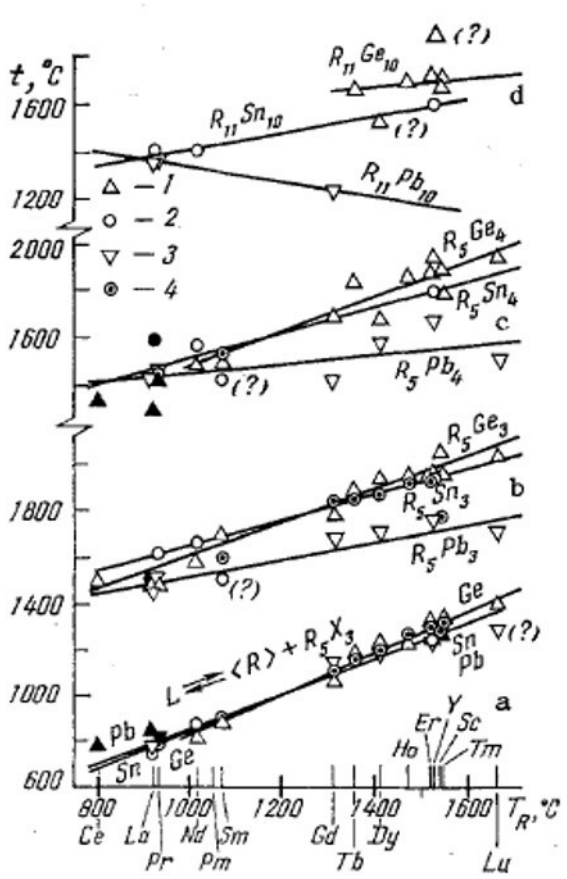


Fig. 2.7. The relation between the melting temperature of $RE_{11}M_{10}$ ($L + RE_5M_4 \rightarrow RE_{11}M_{10}$), RE_5M_4 ($L + RE_5M_3 \rightarrow RE_5M_4$), RE_5M_3 (congruent), and eutectic temperature ($L \rightarrow RE + RE_5M_3$), (M = Gd, Sn, Pb): 1) Ge, 2) Sn, 3) Pb, 4) experimental data. The black symbols were taken from the data on other types of reaction [46].

2.2. The properties of Mg alloys containing RE

It is known that the addition of RE in Mg alloys leads to high strength properties at ambient and elevated temperatures. The mechanical properties of the Mg-RE alloys typically depend on the solubility of RE in Mg. The atomic size of RE is one of the key factors that affect the solubility of RE in Mg. A dependence of the solubility of RE in solid Mg on the atomic size of RE is presented in Fig. 2.8 [47]. It is associated with the change in the atomic radius of RE, which decreases along with increasing in the atomic number and with closing to the atomic radius of Mg. The decrease of the solubility of RE with decrease in the temperature provokes the formation of supersaturated solid solution and its decomposition upon aging. This process is very important for the effect of RE on the mechanical properties of Mg alloys. The decomposition of solid solutions of Mg-RE alloys make the precipitation hardening (aging hardening) and the results are shown in Fig. 2.9 [47]. The hardness of light RE group (except La; The solubility of La in solid Mg is very small) increased with aging time and the effect of aging hardening is intensified with the increase of atomic number of the RE and their solubility in solid Mg. On the other hand, heavy RE group shows that the higher aging hardening effect is observed in the smaller atomic number metals (Gd). Gd has the highest solubility difference between solution treatment temperature and 200°C and high solubility of higher atomic number of heavy RE at low temperature suppress the hardening effect in the aging process. Another peculiarity on ageing process of heavy RE is that the aging hardening curve shows an obvious latent period unlike the curve for light RE. In another investigation [19], the cast alloys with La, Ce, Pr, and Nd (light RE) was heat-treated as solution treatment with subsequent ageing at 204 ºC for 16h for maximum strengthening. The data on mechanical properties of the cast binary alloys with La, Ce, Pr and Nd obtained by tensile tests at room temperature are presented in Fig. 2.10. It shows an increase in tensile strength and tensile yield strength as all the four RE metals along with an expectable decrease in elongation. The alloy of Mg-La shows the lowest level of strength properties and the strength level increased in the order Ce, Pr and Nd with increasing atomic number and their solubility. The RE concentration of alloys at maximum strength properties corresponds approximately to the solubility of the RE in solid Mg at temperatures of solution treatment. Mechanical properties of the alloys with La, Ce, and Nd at 260°C was also obtained in Fig. 2.11. The results shows the similar tendencies as at room

temperature. The character of the plasticity change at elevated temperatures with increasing RE content was mainly the same as at room temperature. However, the absolute values of the tensile properties and plasticity (elongation) were decreased and increased, respectively. The alloy with high content of La shows the highest elongation (10.5 % for 6.7 % La, 3.2 % for 6.73 % Ce and 6.5 % for 6.19 % Nd (wt. %) at 260°C).

For the heavy RE, hot extruded alloys were prepared in direct ageing after hot working (ageing : 200 ºC/12h for Mg-Sm, 200 ºC /100h for Mg-Y, 200 ºC /24h for Mg-Gd, 200 ºC /50h for Mg-Tb, 200 ºC /50h for Mg-Dy, 200 ºC /50h for Mg-Ho and 300 ºC /100h for Mg-Er. The tensile properties of the alloys with heavy RE metals, and also Sm (light RE) is presented in Fig. 2.12. In the case of Mg-Er alloy, the ageing was chosen based on the results of Mg-Y alloys, it was not enough to reach maximum strengthening, which requires 200°C/400h as it was proved afterwards. Except for the alloys with Er, the ageing corresponded to maximum ageing strengthening and achieve significant increase of strength and decrease of plasticity. The tendency of the strength property curves is shifted in the direction of greater contents of alloying elements with increasing atomic number of the RE. The order corresponds to the respective increase of solubility of the RE in Mg. High strength properties in the alloys were achieved with low plasticity. Not only the high temperature strength, but also the improvement of the creep resistance was found in the Mg alloys with La, Ce, and Nd [48]. The results are shown in Fig. 2.13. The mechanism of the improvement is mainly related with the grain boundary reinforcement by the intermetallic phases.

There is also some improvement in the corrosion resistance of the Mg alloys with RE. The corrosion resistance of some binary alloys including Mg-RE were investigated [19]. The alloys were prepared with the main impurity contents in limits Fe < 0.003 %, Ni < 0.0005 %, Cu < 0.003 %, except the systems Mg-Ca, Mg-Sc and Mg-Ce where Fe content was 0.007 %, 0.02 % and 0.008 %, respectively. The alloys were tested in 3 % NaCl aqueous solution. The results are shown in Fig. 2.14. The corrosion rate of the alloys increased with increasing RE contents except Sm. However, the corrosion rate of the alloys with RE is substantially less than that with the detrimental elements, such as Cu, Ag, Bi. The alloys with Mn, Zr and Cd showed less corrosion rate than that of alloys with RE. The corrosion rate of alloys with Al, Zn and Si is close to that of

Mg alloys with RE. The alloy with small content of RE showed less corrosion rates than the initial Mg because of the interaction of RE with impurities in initial Mg. In the Mg-Al-Y alloys, the addition of 8-9 % Y resulted in decrease of corrosion resistance. The decrease of corrosion resistance can be explained by the formation of $Mg_{24}Y_5$ compound which is supposed to be an effective cathode for the solid solution. Although RE metals can damage corrosion resistance of Mg alloys, their corrosion resistant is at the same level as the common commercial Mg alloys with Al or Zn.

Recently, alloying rare earth (RE) elements is of great interest in the applications of wrought magnesium alloys. It is generally recognized that the hexagonal close-packed (hcp) structure of Mg limits the number of active deformation mechanisms. During rolling or hot extrusion which are the essential process for increasing use of Mg alloys in industrial application, the majority of grains are oriented with their basal planes in the sheet plane. This strong texture disposition is responsible for a plastic anisotropy, low elongation and limited formability. Recently, many research have been suggested that the addition of RE results in weaker and more random textures which can improve the formability of Mg alloys [21, 49-55]. For example, Mg alloy sheets with different Ce, Nd and Y as alloying elements were studied for the investigation of the texture weakness [51]. The weakening of the alloys textures with increasing content of Ce, Nd and Y was observed in Fig. 2.15. The reason for this is believed that the addition of RE into Mg can change the staking fault energy (SFE) of hcp Mg and/or enhance the solute drag of grain boundaries and dislocations. The investigations related to the former observed the decrease in the basal SFE which promotes more frequent activity of non-basal slip [55-60]. Regarding the latter, it was found that the RE had a strong tendency to segregate to grain boundaries or any other defect sites to reduce the size misfit energy in the Mg matrix [50, 61-65]. The segregation of RE can slow down the movement of dislocations and grain boundaries which corresponds to the solute drag effect. That is, the RE strongly retards dynamic recrystallization by segregation, leading to drag and pinning. This not only tends to activate other slip systems, but also increases twin activity. Another interesting RE effect in the Mg alloy is the formation of the long period stacking ordered (LPSO) structure which were found in the Mg-Zn-RE [66-72] and Mg-Al-RE alloys [73-75]. The LPSO alloys show superior mechanical properties both at ambient and elevated temperatures. For

instance, the hot extruded LPSO Mg-Zn-Y cast alloys exhibited high yield strength (>350 MPa) and reasonable elongation (>5 %) at room temperature, and high yield strength (>300 MPa) at 473 K [70]. According to Jung et al. [21], the existence of LPSO indicates that, energetically when small amounts of RE and Zn(Al) are dissolved together in hcp-Mg, a short-range-ordering of Mg, Zn and RE atoms may occur to form small clusters dissolved in hcp-Mg. This is possibly one of the factors for texture weakening, explaining by the formation of clusters near grain boundaries or dislocations where the RE is segregated.

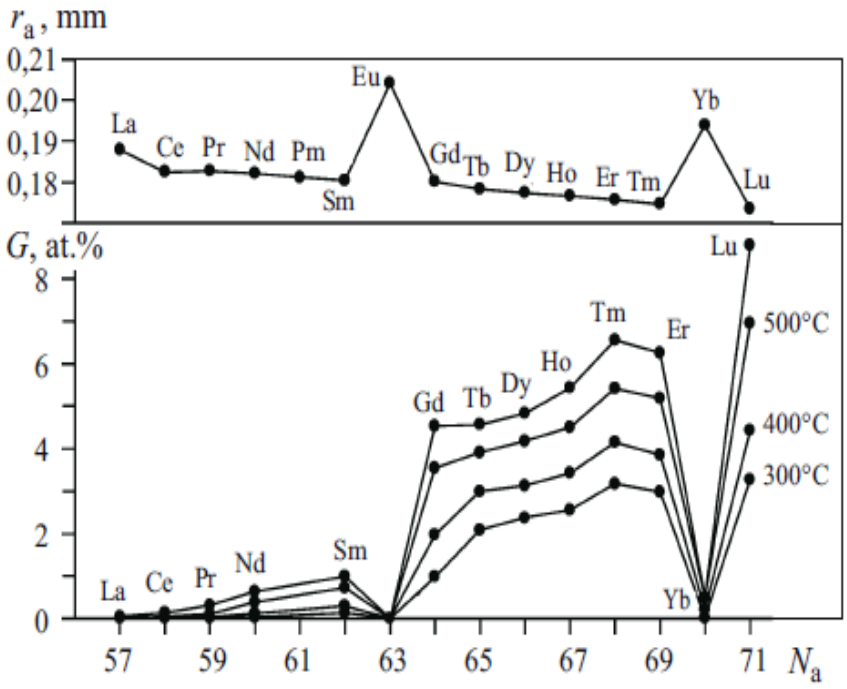


Fig. 2.8. Atomic radius of RE and solubility of RE in in solid Mg as a function of the atomic number of RE [47].

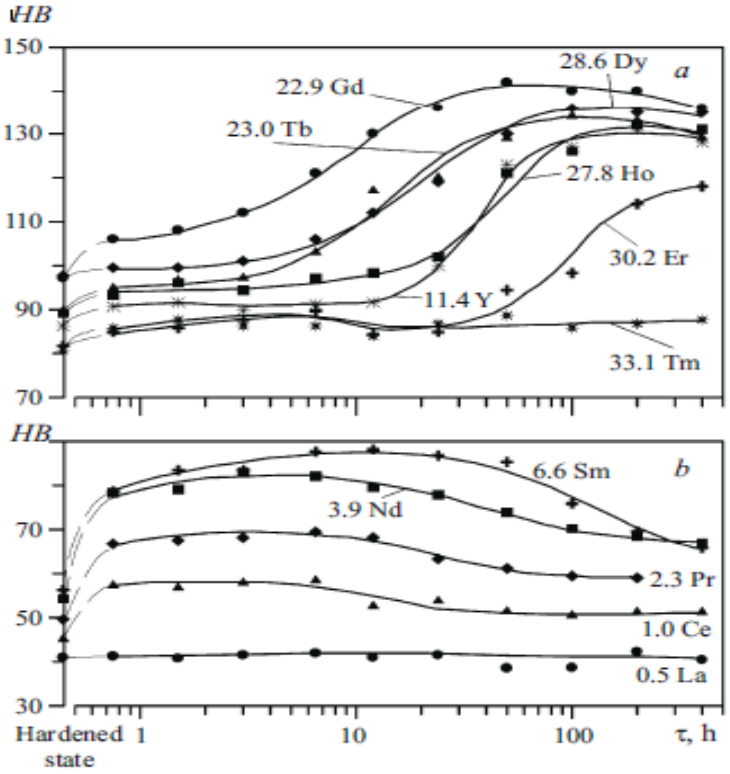


Fig. 2.9. Variation of the hardness of solid-solution-hardened binary magnesium alloys in the process of aging at 200°C (a) heavy RE, (b) light RE [47].

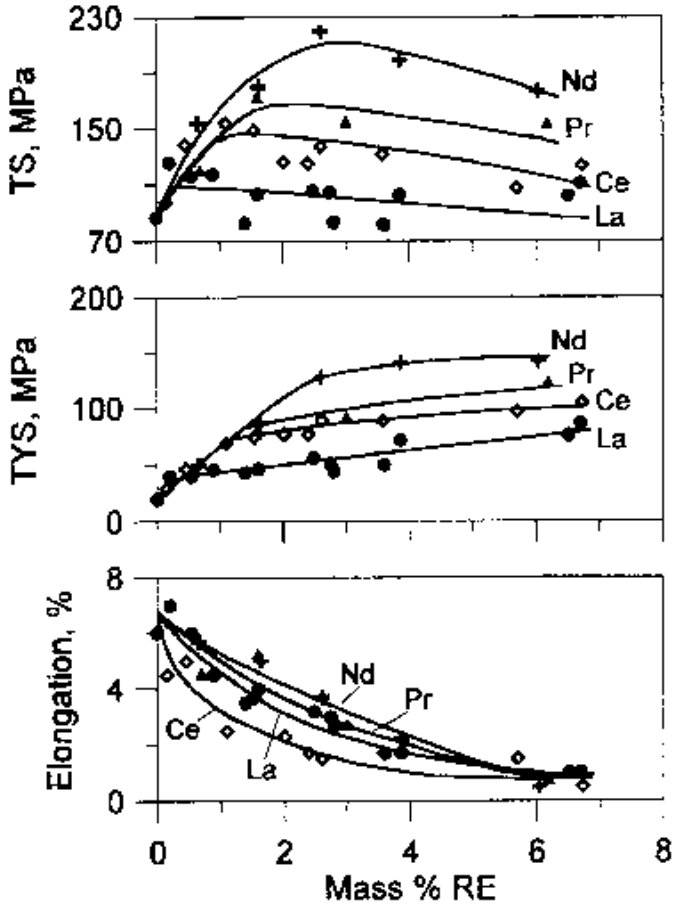


Fig. 2.10. Tensile properties of the cast Mg alloys with La, Ce, Pr and Nd at room temperature [19].

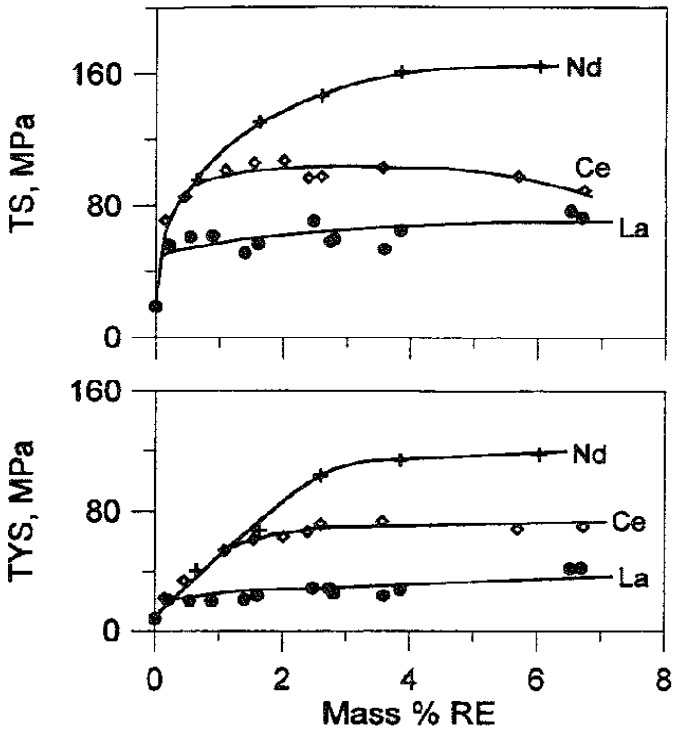


Fig. 2.11. Tensile strength properties of the cast Mg alloys with La, Ce and Nd at 260 ºC [19].

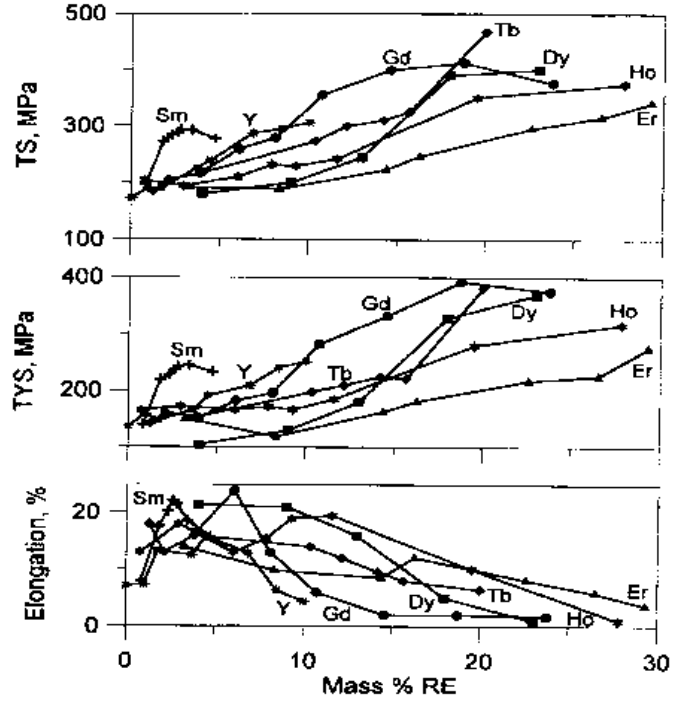


Fig. 2.12. Tensile properties of the Mg-RE alloys at room temperature [19].

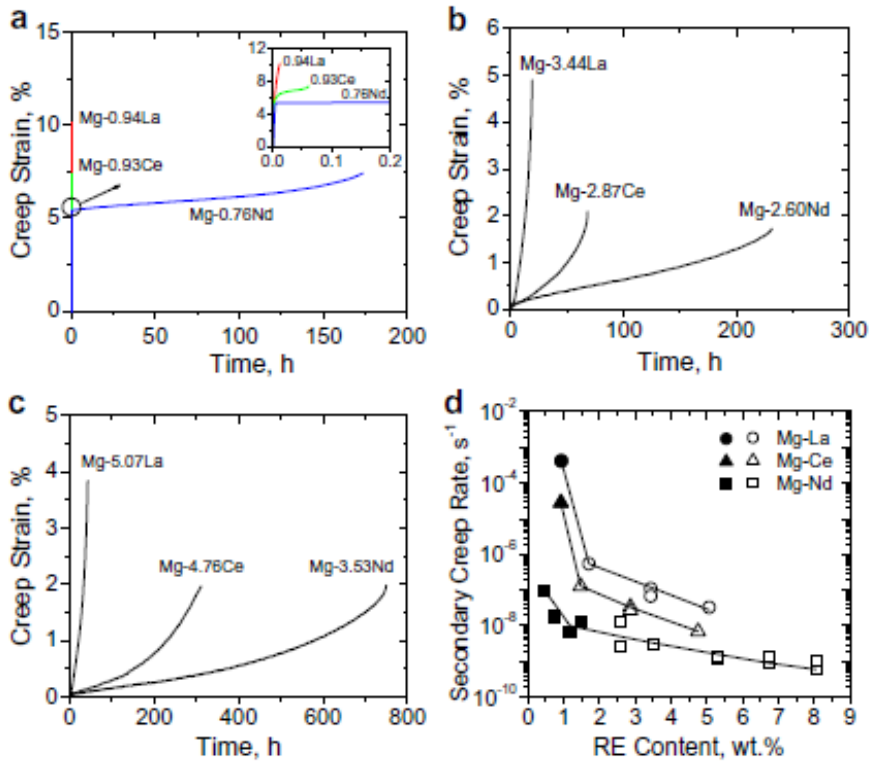


Fig. 2.13. (a) to (c) Creep curves of selected Mg–RE alloys at 177 ºC and 90 MPa, and (d) variation of the secondary creep rate with the RE content. The solid symbols in (d) represent where the applied stress in creep is above the 0.2% yield strength [48].

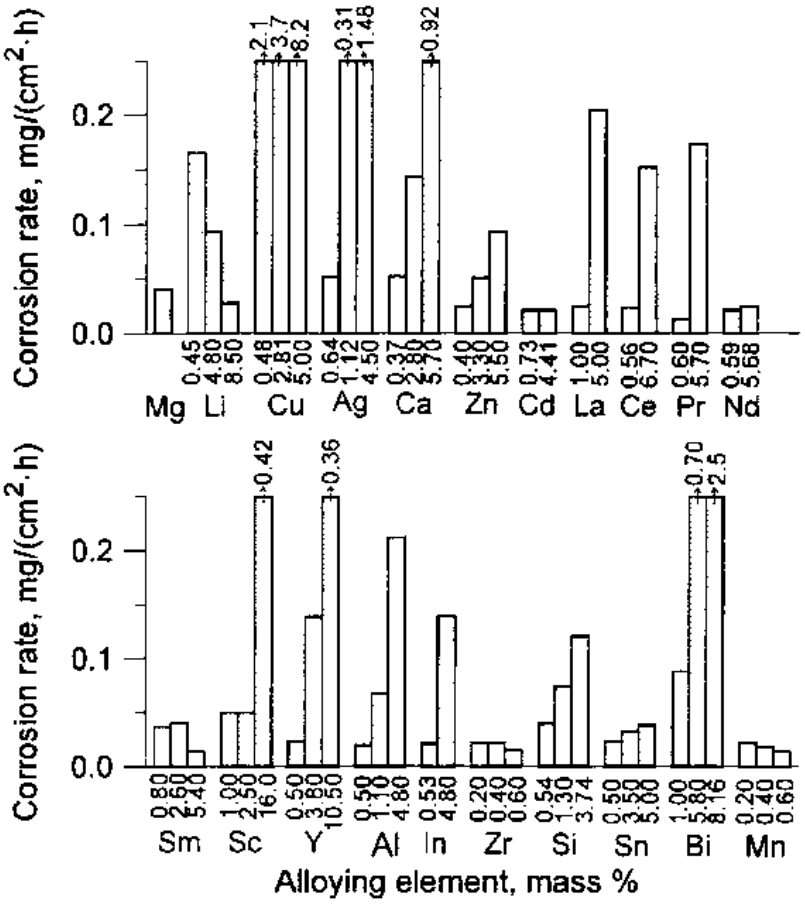


Fig. 2.14. Corrosion rate of binary Mg alloys in 3% NaCl aqueous solution [19].

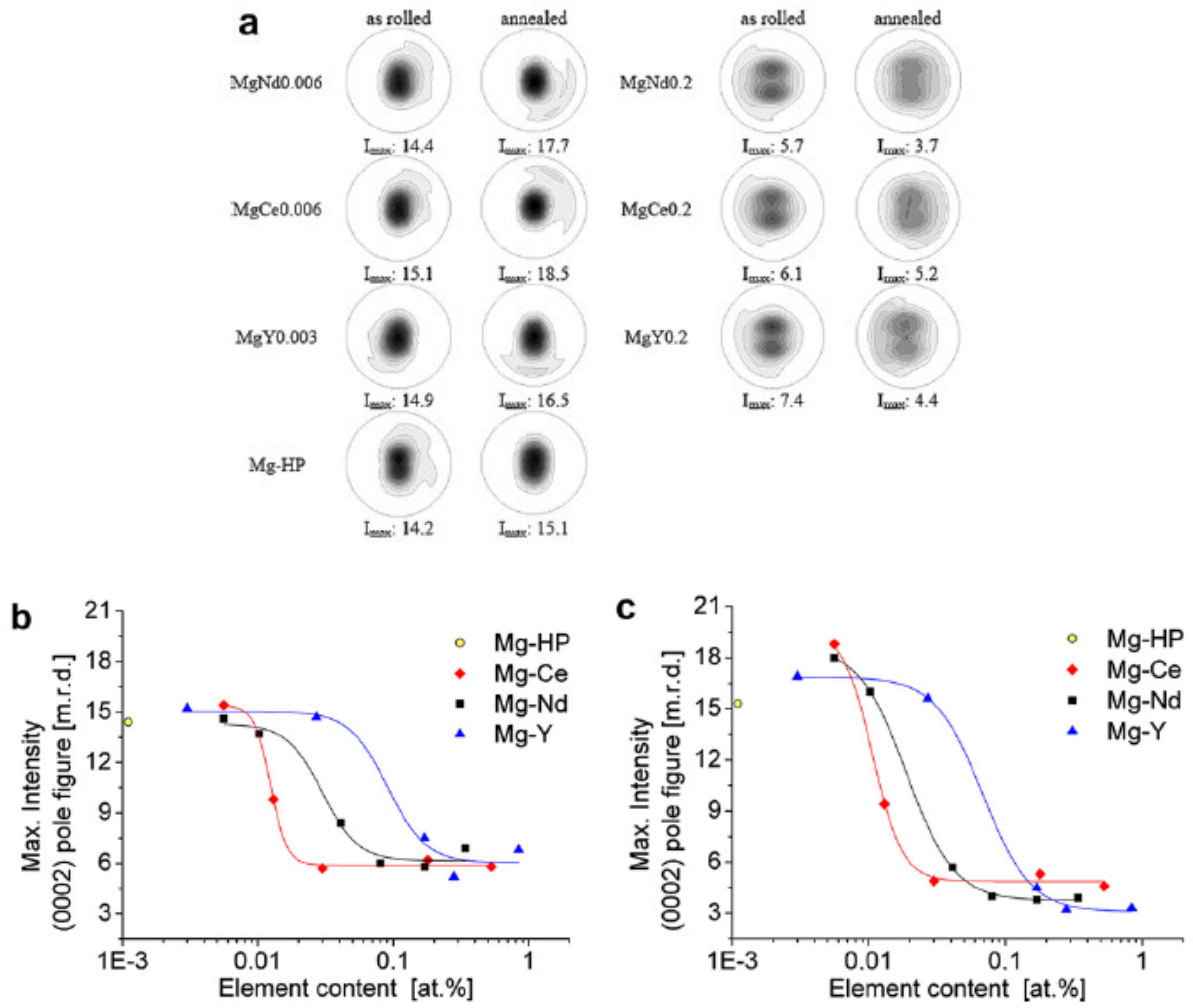


Fig. 2.15. Textures of binary Mg–RE sheets: (a) recalculated (0002)-pole figures of sheets with a low and high alloying content in as-rolled condition and after annealing; (b) maximum (0002)-pole figure intensity in as-rolled condition and (c) after annealing [51].

2.3. Computational thermodynamic modeling: Calculation of phase diagrams (CALPHAD) method

CALPHAD is an abbreviation for the CALculation of Phase Diagrams. It is also described as "The Computer Coupling of Phase Diagrams and Thermochemistry."

Phase diagram is one of the most important fundamental tools to apprehend the phase equilibria. In the metallurgical engineering, the relationship between the chemical compositions and the microstructure under certain processing conditions is important to understand the physical and chemical properties of alloys. The phase diagrams enable one to be capable of understanding this complex relationship graphically. However, the experimental determinations of numerous combinations of alloy materials (especially multicomponent systems) are very limited. With the advance of computing technology, the numerical Gibbs energy minimization technique was successfully applied to calculate the multi-component phase diagrams, and also the all types of thermodynamic data. The Gibbs energy, often combined by the enthalpy and entropy, can be expressed as mathematical functions of temperature and chemical composition. The parameters of the thermodynamic Gibbs energy functions including the enthalpy of formation of compounds, enthalpy of mixing in liquid, heat capacity etc. are stored as databases in the computer. Such thermodynamic databases are often prepared by critical "evaluation" and "optimization" (or assessment) using proper thermodynamic models to construct multicomponent databases. In the optimization process, the adjustable model parameters that describe the Gibbs energy functions of constituent phases can be obtained based on the available thermodynamic and phase equilibrium data. This is called the CALPHAD technique.

The procedure of evaluation and optimization is as follows:

i) Collection of the experimental data: The experimental data include phase equilibria, thermodynamic data (heat capacity, enthalpy of formation, enthalpy of mixing, vapor

pressure, chemical potentials, activities, etc.), structural data, physical properties (magnetism, conductivity, etc.).

ii) Choice of the appropriate thermodynamic model: The appropriate model based on the structure of the phase is critical to construct the accurate multicomponent database because only a decent physical model can yield good predictions of multicomponent solution properties from lower-order (binary and ternary) model parameters.

iii) Evaluation of the experimental data: The critical evaluation of the experimental data is necessary to eliminate contradictory or unreliable data. Often the evaluation is based on the experimental techniques, sample preparation and analytical methods. When it is difficult to evaluate the accuracy of thermodynamic data solely from the literature, the data can be compared with other systems which are chemically similar like the RE metals (systematic analysis), giving regularities in certain properties. Sometimes, the experimental data in lower-order systems can be evaluated from the data in the higher-order systems by extrapolation.

iv) Optimization of model parameters for the system: The model parameters for the Gibbs energy of each phase should be determine to reproduce the reliable experimental data and the appropriate predictions. Afterwards, any type of thermodynamic calculations can be back-calculated.

Several research groups have been performed thermodynamic modeling using the CALPHAD method. For example, the Thermo-Calc group [53, 76] at KTH in Sweden, the THERMODATA group [77] in France, Thermotech Inc. [78] in the UK, and thermochemical group [79] at National Institute of Standards and Technology (NIST) in the USA, the FACT group [10, 80] at Ecole Polytechnique in Canada in collaboration with GTT technology in Germany, the MTDATA group [81, 82] at National Physical laboratory (NPL) in the UK, the CaTCalc group [83] at national institute of Advanced Industrial Science and Technology (AIST) in Japan, the PANDAT group [84] in USA are actively developing the thermodynamic databases. In addition, the Scientific Group Thermodata Europe (SGTE) [85] has been organized as a consortium of research groups to develop the alloy databases.

Not only the computation of multi-component phase equilibria, but also microstructural evolution of the alloys during heat treatment or solidification is possible with the help of computational thermochemistry. One of the kinetic process simulation programs is DICTRA [53, 76], performing the calculation of the multicomponent diffusion in the alloys. However, the accurate thermodynamic database is prerequisite for developing the kinetic modeling.

3. Methodology

3.1. Thermodynamic model

The thermodynamic optimizations and calculations in the present study were performed by using the Gibbs energy minimization software FactSage [80]. The fundamental equations in the thermodynamic models are described below.

The Gibbs energy of a pure *i* component is written as:

$$G_i = H_i - TS_i \tag{3.1}$$

where G_i , H_i and S_i are the Gibbs energy, enthalpy and entropy of *i*, respectively. and *T* is the absolute temperature.

The enthalpy and entropy at certain temperature can be expressed as functions of heat capacity C_p by

$$H(T) = \Delta H^{\circ}_{298} + \int_{298}^{T} C_p dT \tag{3.2}$$

$$S(T) = S^{\circ}_{298} + \int_{298}^{T} \frac{C_p}{T} dT \tag{3.3}$$

For the pure elemental species, ΔH°_{298} is defined as zero, while S°_{298} comes from the integration of C_p at low temperatures from 0 K and 298 K according to the third law of thermodynamics.

When components A and B are mixed to from a solution, the Gibbs energy of solution becomes dependent on interactions between A and B. The Gibbs energy of a solution is described as:

$$G_m = g_A^{\circ} n_A + g_B^{\circ} n_B - T\Delta S^{\text{config}} + G_m^{\text{ex}} \tag{3.4}$$

where G_m is the Gibbs energy of the solution, g_i° is the molar Gibbs energy of component *i*, ΔS^{config} is the molar configurational entropy of solution, and G_m^{ex} is the excess Gibbs energy. For the ideal solution which assumes no interaction between A and B in solution, the G_m^{ex} is zero. The G_m^{ex} is often expanded as a polynomial in the mole fractions:

$$G_m^{\text{ex}} = \sum_{i,j} q_{AB}^{ij} X_A^i X_B^j \tag{3.5}$$

where the excess interaction parameters $q_{AB}^{ij} = a + bT + cT^2 + \cdots$ can be dependent on temperature. There are several other mathematical polynomial expressions from simple to complex form to describe the G_m^{ex}. One of the simple description is "regular solution" when only q_{AB}^{11} is used. The most popular expression is "Redlich-Kister" polynomial as expressed by:

$$G_m^{\text{ex}} = X_A X_B \sum_{i=0}^{n} L_i (X_A - X_B)^i$$

where L_i is the interaction parameter similar to the q_{AB}^{ij}.

When phase equilibrium is established for a given temperature, composition and pressure, the total Gibbs energy of a system should reach minimum. It can be expressed by follows:

$$G = \sum_{\varphi} n^{\varphi} g^{\varphi} = \text{minimum} \tag{3.6}$$

where n^{φ} is number of moles of phase φ, and g^{φ} is molar Gibbs energy functions of phase φ.

The chemical potential of system component *i*, μ_i is defined as:

$$\mu_i = g_i = (\partial G / \partial n_i)_{T,P,n_j} \tag{3.7}$$

where G is the Gibbs energy of a solution, n_i is the number of moles of component *i*, and the derivative is taken at constant temperature, pressure and $n_j (j \neq i)$, and g_i is the partial molar Gibbs energy of component *i*.

When phase equilibrium of a system is reached for given temperature, pressure, and overall composition, the chemical potential of each component *i*, μ_i should be equal in all phases, φ as follow:

$$\mu_i^1 = \mu_i^1 = \cdots = \mu_i^{\varphi} \tag{3.8}$$

Then, the total Gibbs energy at equilibrium in Eq. (3.6) can be written as:

$$G = \sum_i n_i g_i \tag{3.9}$$

At equilibrium, the total G in Eq. (3.9) at constant temperature, pressure, and overall composition is minimized under mass balance constraints. Finally, a set of mole numbers of each phase φ and compositions of each phase can be obtained by the Gibbs energy minimization algorithms.

As for the liquid model, the Bragg Williams random mixing model (BWRMM) with the excess Gibbs energy function using Redlich-Kister polynomial is often limited when the solution is deviated highly negative from ideal behavior like the Si-RE and Sn-RE systems. For example, the

previous optimizations of the Si-RE system used the BWRMM were unsuccessful to reproduce the large negative enthalpy of mixing (about -80 kJ mol^{-1}). In this case, the associate model [86] can be used adopting hypothetical associated species with a fixed stoichiometry which is often equal to the most stable compound in the system. The assumption of associate may give a reasonable description of the Gibbs energy of binary system. However, the assumption of real associate formation in solution can create another problem in configurational entropy. When associate formation energy becomes zero, the entropy cannot become that of ideal binary solution. Very positive formation energy is needed to nearly prevent the formation of associate and then ideal mixing entropy can be achieved. Regarding the limitation of the BWRMM and associate model, the discussion was made more deeply in Appendix IV.

In the present study, the Modified Quasichemical Model (MQM) was used for describing the liquid solution. The details of the MQM is described in following chapter (3.1.1).

3.1.1. Liquid phase

The Modified Quasichemical Model (MQM) [87, 88], which accounts for short-range-ordering of nearest-neighbor atoms, was used to model the liquid solutions because it gives a more realistic thermodynamic description of the liquid phase compared to the conventional simple Bragg Williams random mixing model [87, 88]. The MQM was successfully applied to many liquid metallic solutions [88-90] and ionic solutions [91, 92] exhibiting strong short-range-ordering behavior.

Recently, the energy of nearest-neighbor pair formation in the MQM was expanded as a polynomial in the pair fractions [87, 88] instead of the component fractions [91, 93]. In addition, coordination numbers are now allowed to vary with composition. These modifications provide greater flexibility in reproducing the binary experimental data and in combining optimized binary liquid parameters into a large database for multicomponent solutions [87]. A short description of the model is given below; details can be found in previous studies [87, 88].

In the case of a binary A-B liquid solution, the atoms A and B are distributed over the sites of a quasi-lattice in liquid solution. The following pair exchange reaction can be considered:

$$(\mathrm{A}-\mathrm{A})+(\mathrm{B}-\mathrm{B})=2(\mathrm{A}-\mathrm{B}) \tag{3.10}$$

where (A-B) represents a first-nearest-neighbor pair of A and B. The non-configurational Gibbs energy change for the formation of two moles of (A-B) pairs according to the reaction (3.10) is Δg_{AB}. Then the Gibbs energy of the solution is given by:

$$G=(n_{\mathrm{A}}G_{\mathrm{A}}^{\mathrm{o}}+n_{\mathrm{B}}G_{\mathrm{B}}^{\mathrm{o}})-T\Delta S^{\mathrm{config}}+n_{\mathrm{AB}}(\Delta g_{\mathrm{AB}}/2) \tag{3.11}$$

where $G_{\mathrm{A}}^{\mathrm{o}}$ and $G_{\mathrm{B}}^{\mathrm{o}}$ are the molar Gibbs energies of the pure components A and B, n_{A} and n_{B} are the numbers of moles of A and B atoms, and n_{AB} is the number of moles of (A-B) pairs. $\Delta S^{\mathrm{config}}$ is the configurational entropy of mixing given by a random distribution of the (A-A), (B-B) and (A-B) pairs in the one-dimensional Ising approximation:

$$\begin{aligned}\Delta S^{\mathrm{config}} &= -R(n_{\mathrm{A}}\ln X_{\mathrm{A}}+n_{\mathrm{B}}\ln X_{\mathrm{B}})\\ &\quad -R[n_{\mathrm{AA}}\ln(X_{\mathrm{AA}}/Y_{\mathrm{A}}^2)+n_{\mathrm{BB}}\ln(X_{\mathrm{BB}}/Y_{\mathrm{B}}^2)\\ &\quad +n_{\mathrm{AB}}\ln(X_{\mathrm{AB}}/2Y_{\mathrm{A}}Y_{\mathrm{B}})]\end{aligned} \tag{3.12}$$

where n_{AA}, n_{BB} and n_{AB} are the numbers of moles of each kind of pairs, and the pair fraction (X_{AA}, X_{BB} and X_{AB}) and coordination equivalent fraction (Y_{A} and Y_{B}) can be calculated as:

$$X_{\mathrm{AA}}=n_{\mathrm{AA}}/(n_{\mathrm{AA}}+n_{\mathrm{BB}}+n_{\mathrm{AB}}) \tag{3.13}$$

$$X_{\mathrm{BB}}=n_{\mathrm{BB}}/(n_{\mathrm{AA}}+n_{\mathrm{BB}}+n_{\mathrm{AB}}) \tag{3.14}$$

$$X_{\mathrm{AB}} = n_{\mathrm{AB}} / (n_{\mathrm{AA}} + n_{\mathrm{BB}} + n_{\mathrm{AB}}) \tag{3.15}$$

$$Y_{\mathrm{A}} = X_{\mathrm{AA}} + X_{\mathrm{AB}} / 2 \tag{3.16}$$

$$Y_{\mathrm{B}} = X_{\mathrm{BB}} + X_{\mathrm{AB}} / 2 \tag{3.17}$$

The Δg_{AB} is the model parameter to reproduce the Gibbs energy of liquid phase of the binary A-B system, which is expanded as a polynomial in terms of the pair fractions, as follows:

$$\Delta g_{\mathrm{AB}} = \Delta g^{\circ}_{\mathrm{AB}} + \sum_{i \geq 1} g^{i0}_{\mathrm{AB}} (X_{\mathrm{AA}})^i + \sum_{j \geq 1} g^{0j}_{\mathrm{AB}} (X_{\mathrm{BB}})^j \tag{3.18}$$

where $\Delta g^{\circ}_{\mathrm{AB}}$, g^{i0}_{AB} and g^{0j}_{AB} are the adjustable model parameters which can be functions of temperature.

In the MQM, the coordination numbers of A and B, Z_{A} and Z_{B}, can be varied with composition to reproduce the short-range-ordering as follows:

$$\frac{1}{Z_{\mathrm{A}}} = \frac{1}{Z^{\mathrm{A}}_{\mathrm{AA}}} \left(\frac{2n_{\mathrm{AA}}}{2n_{\mathrm{AA}} + n_{\mathrm{AB}}} \right) + \frac{1}{Z^{\mathrm{A}}_{\mathrm{AB}}} \left(\frac{n_{\mathrm{AB}}}{2n_{\mathrm{AA}} + n_{\mathrm{AB}}} \right) \tag{3.19}$$

$$\frac{1}{Z_{\mathrm{B}}} = \frac{1}{Z^{\mathrm{B}}_{\mathrm{BB}}} \left(\frac{2n_{\mathrm{BB}}}{2n_{\mathrm{BB}} + n_{\mathrm{AB}}} \right) + \frac{1}{Z^{\mathrm{B}}_{\mathrm{BA}}} \left(\frac{n_{\mathrm{AB}}}{2n_{\mathrm{BB}} + n_{\mathrm{AB}}} \right) \tag{3.20}$$

where $Z^{\mathrm{A}}_{\mathrm{AA}}$ is the value of Z_{A} when all nearest neighbors of an A atom are A atoms, and $Z^{\mathrm{A}}_{\mathrm{AB}}$ is the value of Z_{A} when all nearest neighbors are B atoms. $Z^{\mathrm{B}}_{\mathrm{BB}}$ and $Z^{\mathrm{B}}_{\mathrm{BA}}$ are defined in an analogous manner.

In the case of multicomponent solutions, a brief summary of the model equations is given below. For simplicity, the ternary solution is assumed.

The pair exchange reaction between atoms *m* and *n* in a ternary 1-2-3 solution distributed over the sites of a quasi-lattice is:

$$(m\text{-}m) + (n\text{-}n) = 2(m\text{-}n);\ \Delta g_{mn} \tag{3.21}$$

where *m* and *n* = 1, 2, 3; (*m*-*m*), (*n*-*n*), and (*m*-*n*) represent first-nearest-neighbor pairs.

Similar to the binary solutions, the mass balance constrains for the ternary solutions are:

$$Z_m n_m = 2n_{mm} + \sum_{n \neq m} n_{mn} \tag{3.22}$$

where Z_m and n_m are the coordination number of *m* and the number of moles of *m*, respectively. n_{mm} and n_{mn} are the number of moles of (*m*-*m*) and (*m*-*n*) pairs, respectively.

The pair fraction (X_{mm}), overall mole (or site) fraction (X_m) and "coordination-equivalent" fractions (Y_m) are defined as:

$$X_{mn} = n_{mm} / \sum n_{ij} \qquad (i, j = 1, 2, 3) \tag{3.23}$$

$$X_m = n_m / \sum n_i \qquad (i = 1, 2, 3) \tag{3.24}$$

$$Y_m = Z_m n_m / \sum (Z_i n_i) \qquad (i = 1, 2, 3) \tag{3.25}$$

The Gibbs energy of the solution is expressed as:

$$G = \sum n_m g_m^\circ - T\Delta S^{\text{config}} + \sum_{n>m}\sum n_{mn}(\Delta g_{mn}/2) \tag{3.26}$$

where g_m° is the molar Gibbs energy of the pure component *m*, and ΔS^{config} is an approximate configurational entropy of mixing, which can be given by:

$$\Delta S^{\text{config}} = -R\sum(n_m \ln X_m) - R\left(\sum n_{mm}\ln(X_{mm}/Y_m^2) + \sum_{n>m}\sum n_{mn}\ln(X_{mn}/2Y_mY_n)\right) \tag{3.27}$$

In the present study, Δg_{mn} is given by a polynomial in terms of pair fractions. Then, the Δg_{mn} is proposed from the proper geometric model [94] such as symmetric or asymmetric model for estimating ternary thermodynamic properties from the optimized sub-binary systems. Some geometric models are presented in Fig. 3.1.

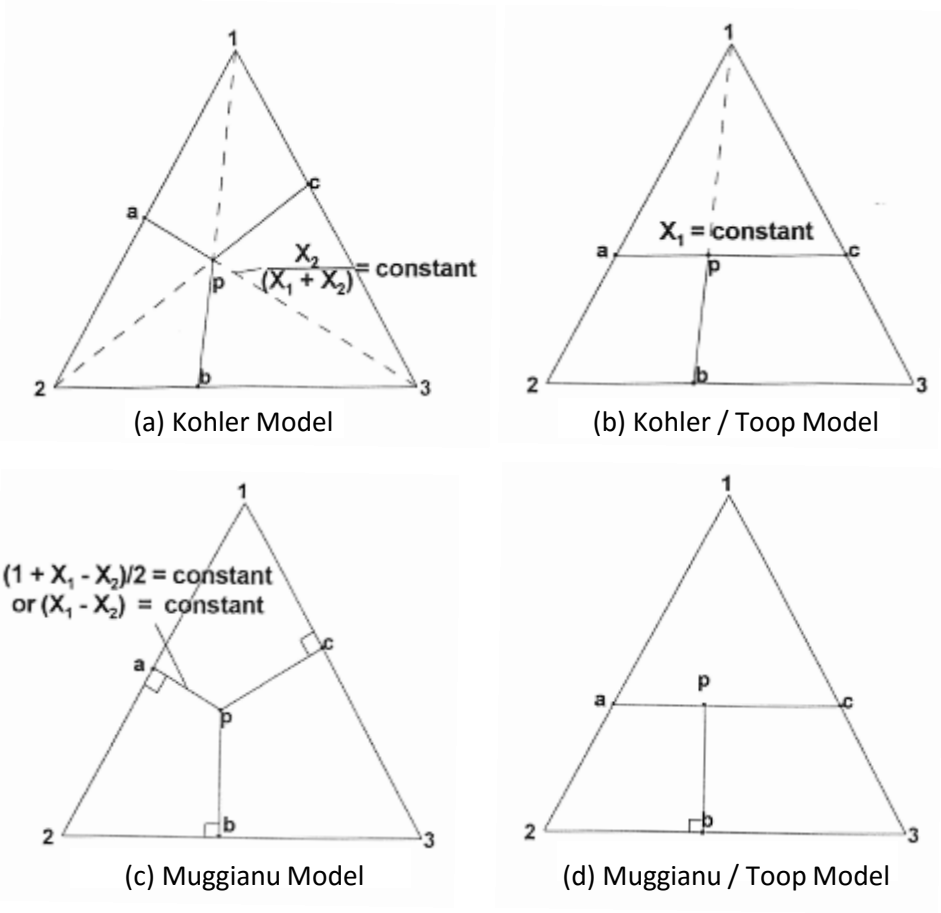


Fig. 3.1. Some geometric models: symmetric model (a) and (c), and asymmetric model (b) and (d) [94].

In a symmetric ternary system, the Kohler-type interpolation is used. The Δg_{mn} is expressed by:

$$\Delta g_{12} = \Delta g_{12}^{\circ} + \sum_{(i+j)\geq 1} g_{12}^{ij} \left(\frac{X_{11}}{X_{11}+X_{22}+X_{12}} \right)^{i} \left(\frac{X_{22}}{X_{11}+X_{22}+X_{12}} \right)^{j} + \sum_{\substack{i\geq 0 \\ j\geq 0 \\ k\geq 0}} g_{12(3)}^{ijk} \left(\frac{X_{11}}{X_{11}+X_{22}+X_{12}} \right)^{i} \left(\frac{X_{22}}{X_{11}+X_{22}+X_{12}} \right)^{j} Y_3^k \tag{3.28}$$

In an asymmetric ternary system, the Kohler-Toop interpolation is used. Let 1 be an asymmetric component for 1-2 system. That is, the energy of forming (1-2) nearest-neighbor pairs is assumed

to be constant as component 2 is replaced by component 3 in the 1-2-3 ternary system. Then, the following equation can be written:

$$\Delta g_{12} = \Delta g_{12}^{\circ} + \sum_{(i+j)\geq 1} g_{12}^{ij} (X_{11})^i (X_{22} + X_{23} + X_{33})^j + \sum_{\substack{i\geq 0 \\ j\geq 0 \\ k\geq 0}} g_{12(3)}^{ijk} (X_{11})^i (X_{22} + X_{23} + X_{33})^j \left(\frac{Y_3}{Y_2 + Y_3} \right)^k \quad (3.29)$$

3.1.2. Solid solution phase

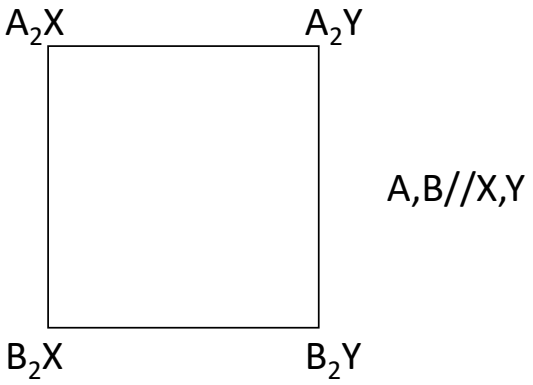
The solid solution phases like bcc and fcc solutions were described by the Compound Energy Formalism (CEF) [95] with a one-sublattice approach for substitutional site. The molar Gibbs energy of the solid solution (A-B) can be expressed as:

$$G = (y_A G_A^o + y_B G_B^o) + RT(y_A \ln y_A + y_B \ln y_B) + {}^a L_{A,B} y_A y_B (y_A - y_B)^a \quad (3.30)$$

where y_A and y_B are the site fractions of A and B elements in the sublattice, and R and T are the gas constant and temperature in Kelvin. G_A^o and G_B^o are the molar Gibbs energies of solid phases of A and B in the respective standard state of solid solution. The binary interaction parameters between A and B in the sublattice, ${}^a L_{A,B}$ where $a \geq 0$, are adjustable model parameters.

In the case of the phase with more than two sublattices like “Laves-C15” phase (two sublattices), the CEF was used to describe the Gibbs energy of solution phases as follows:

Laves-C15 phase, $(A,B)_2(X,Y)_1$



The Gibbs energy of laves-C15 phase is expressed by:

$$
\begin{aligned}
G = {} & y_A y_X G_{A_2X} + y_A y_Y G_{A_2Y} + y_B y_X G_{B_2X} + y_B y_Y G_{B_2Y} \\
& + 2RT(y_A \ln y_A + y_B \ln y_B) + RT(y_X \ln y_X + y_Y \ln y_Y) \\
& + \sum_i {}^i L_{AB/X} (y_A - y_B)^i y_A y_B y_X + \sum_i {}^i L_{AB/Y} (y_A - y_B)^i y_A y_B y_Y \\
& + \sum_i {}^i L_{A/XY} (y_X - y_Y)^i y_A y_X y_Y + \sum_i {}^i L_{B/XY} (y_X - y_Y)^i y_B y_X y_Y \\
& + L_{AB/XY} y_A y_B y_X y_Y
\end{aligned}
\tag{3.31}
$$

where A_2X, B_2X, A_2Y, B_2Y are the end-members.

y_A, y_B are site fractions of component A and B on the first sublattice, where $y_A + y_B = 1$.

y_X, y_Y are site fractions of component A and B on the first sublattice, where $y_X + y_Y = 1$.

$G_{A_2X}, G_{A_2Y}, G_{B_2X}, G_{B_2Y}$ are Gibbs energies of the end-members, A_2X, B_2X, A_2Y, B_2Y, respectively.

$L_{AB/X}$ and $L_{AB/Y}$ are interaction parameters between components A and B on the first sublattice when the second sublattice is only occupied by X or Y, respectively.

$L_{A/XY}$ and $L_{B/XY}$ are interaction parameters between components X and Y on the second sublattice when the first sublattice is only occupied by A or B, respectively.

$L_{AB/XY}$ is the reciprocal interaction parameter when the first sublattice is occupied by A and B, and the second sublattice is occupied by X and Y.

3.1.3 Stoichiometric compound and pure solid

The Gibbs energies of all pure elements were taken from the SGTE database version 5.0 [96]. The Gibbs energies of the stoichiometric compounds were optimized based on available experimental data using the standard Gibbs energy expression based on heat capacity, enthalpy and entropy of formation at 298 K. When the heat capacities of stoichiometric compounds were not available, they were typically estimated using the Neumann-Kopp (NK) rule [97]. Certain intermetallic compounds such as $Mn_{23}Gd_6$, $Mn_{23}Tb_6$ and Gd_5Si_4, etc. exhibit magnetic transitions associated with Néel or Curie temperatures. The magnetic transition below 298 K (typically antiferromagnetic transition with Néel temperature) was taken directly into account in the calculation of S_{298}. The Curie temperature (ferromagnetic transition) occurs typically above 298 K, of which magnetic contribution to the Gibbs energy was considered by an empirical relationship suggested by Inden [98] and modified by Hillert and Jarl [99]. The magnetic contribution to the Gibbs energy is given by:

$$G_{mag} = RT\ln(B_0 + 1)g(\tau) \tag{3.32}$$

where τ is T/T^*, T^* is the critical temperature (the Curie temperature T_C for ferromagnetic materials or the Néel temperature T_N for antiferromagnetic materials) and B_0 is the average magnetic moment per atom. $g(\tau)$ is given by:

$$g(\tau) = 1 - \left[\frac{79\tau^{-1}}{140p} + \frac{474}{497}\left(\frac{1}{p} - 1\right)\left(\frac{\tau^3}{6} + \frac{\tau^9}{135} + \frac{\tau^{15}}{600}\right)\right]/D \qquad \cdots\cdots\cdots\cdots \tau \le 1 \tag{3.33}$$

$$g(\tau) = -\left[\frac{\tau^{-5}}{10} + \frac{\tau^{-15}}{315} + \frac{\tau^{-25}}{1500}\right] / D \qquad \cdots\cdots\cdots\cdots\tau > 1 \qquad (3.34)$$

where $D = \frac{518}{1125} + \frac{11692}{15975}\left(\frac{1}{p} - 1\right)$

The value of p, which can be thought of as the fraction of the magnetic enthalpy absorbed above the critical temperature, depends on the structure. For the simple bcc-A2 phase $p = 0.40$ while for other common phases encountered $p = 0.28$.

3.2. Estimation techniques (Systematics and Miedema Model)

As mentioned in the literature review chapter, regular changes in the phase diagrams and thermodynamic properties can be observed in the RE-containing system. In the present study, the systematic trend was taken advantage of estimating the unknown properties in the Mn-RE, Si-RE, and Sn-RE systems by using simple extrapolation methods. For example, the enthalpy of mixing in Mn-RE liquid at 1700 K shows gradual change from positive (mostly for the Mn-light RE) to negative values (mostly for the Mn-heavy RE) with increasing atomic number of RE as shown in Fig. 3.2. Among the enthalpy of mixing values, the experimentally unknown enthalpy for the Mn-Ho and Mn-Er liquid were assumed to lie proportionally in between the enthalpy of mixing of the Mn-Dy and Mn-Tm liquid where the latter were determined experimentally (see Appendix III). In another example, the unknown melting temperatures of the Si-RE compounds were estimated by the extrapolation as seen in Fig. 3.3 (Appendix V).

As for the Mn-RE system, experimental data for the enthalpy of formation of the Mn-RE compounds were very scarce. The experimental data were only available for the Mn_2Y and $Mn_{23}Y_6$. In order to overcome such limitation, a semi-quantitative model, modified Miedema model [100-102] was used to predict the standard enthalpy of formation (ΔH°_{298}) of all Mn-RE compounds (Appendix III). The modification from the original Miedema model [103] was proposed by adding a pre-factor *S(c)* taking into account the significant effect of the atomic size difference on the contact surface while two dissimilar metals approaching together, then, further developed by statistical approach (ab initio throughput data-mining (HTDM) method). According to the modified Miedema model, the ΔH°_{298} was proposed by the formula as follows:

$$\Delta H_f^{\circ} = f(c) \cdot \frac{S(c) \cdot V_B^{2/3}}{\left(n_{ws}^{-1/3}\right)_{av}} \times \left\{ - P(\Delta\Phi^*)^2 + Q(\Delta n_{ws}^{1/3})^2 \right\} \tag{3.35}$$

where $f(c)$ is a function of alloy composition, which has considered the effect of the chemical short-range-order in an ordered intermetallic compound on the formation enthalpy, and is expressed by:

$$f(c) = c_A^s c_B^s \left[1 + 8(c_A^s c_B^s)^2\right] \tag{3.36}$$

The pre-factor *S(c)* is defined to describe the effect of the atom size difference on the contact interface and the bonding energy, and is expressed as:

$$S(c) = 1 - c_B^s \left| V_A^{2/3} - V_B^{2/3} \right| / (c_A^s V_A^{2/3} + c_B^s V_B^{2/3}) \quad \cdots\cdots \; 0 < S(c) < 1 \tag{3.37}$$

The physical meaning of the other parameters are as follows. n_{ws} is electron density (WS: Wigner-Seitz unit cells), $(n_{ws}^{-1/3})_{av}$ indicates the average value of $n_{ws}^{-1/3}$ which means the expression as a measure of electrostatic screening length, which determines the width of the dipole layer, $\Delta\Phi^*$ is electronegativity difference, and *P* and *Q* are two empirical constants.

First-principles quantum mechanics technique based on density functional theory (DFT) has recently progressed to estimate the thermodynamic properties. First-principles calculations with the knowledge of the atomic species and crystal structure provide the quantities related to the electronic structure and total energy of a given structure. For example, the enthalpies of formation of several magnesium compounds were obtained by the first-principles calculations and compared with the available experimental data [104]. The reasonable agreement was found between the calculated and measured data. However, large discrepancies between first-principles and experimental data were found in the Mg-RE systems. The reason was not completely clear, but it was proposed that the errors in the first-principles calculations involving RE elements were most probably due to the use of an approximate exchange-correlation potential for the tightly bound *f* electrons. In the present study, the first-principles calculations were not taken into account due to the uncertainty of the calculations for the RE-containing systems.

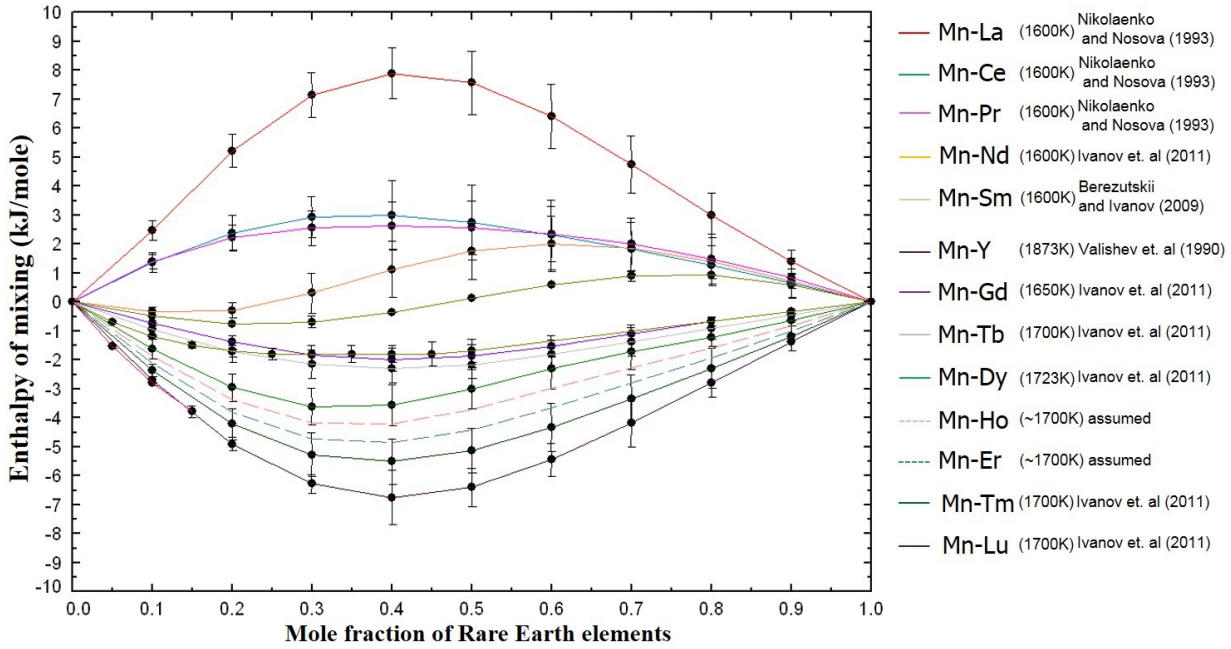


Fig. 3.2. Systematic change in the experimental data of enthalpy of mixing for the Mn-RE liquid at 1700 K (See Appendix I to III for the experimental references).

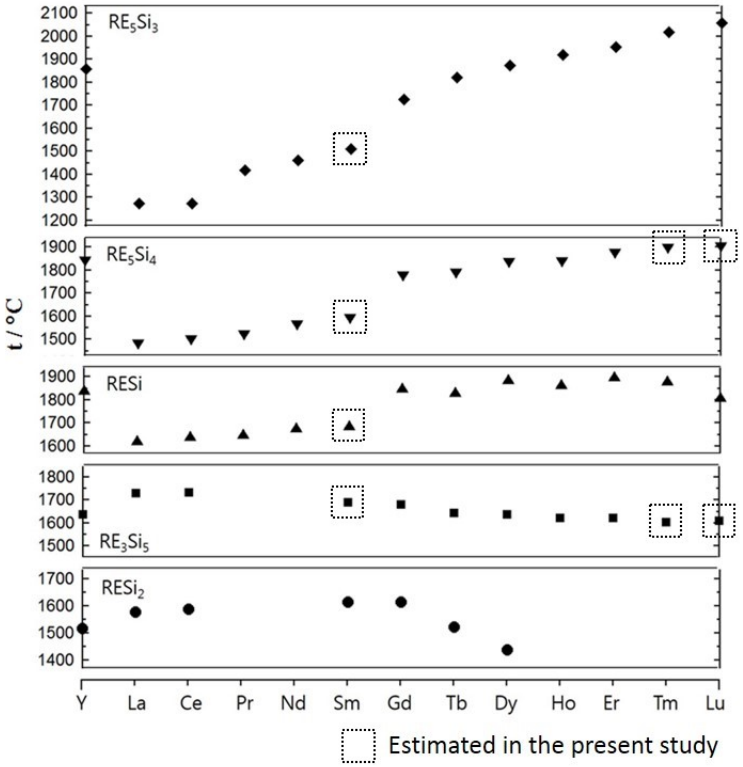


Fig. 3.3. Systematic changes in the melting temperatures of Si-RE compounds (Appendix V).

3.3. Experiments

3.3.1. Differential scanning calorimetry (DSC)

The phase diagram of the Mn-Dy system was investigated by the determination of the phase transformations of the Mn-Dy alloys, which were prepared by the vacuum arc melting, using a differential scanning calorimetry (DSC, a Jupiter STA 449 F3 terminal analyzer (NETZSCH Instruments, Germany)). Due to considerably high oxygen affinity of Dy, a special oxygen trap system, OTS, supplied from NETZSCH was installed in the DSC to minimize the oxidation of Mn and RE, as well as high purity argon (99.999%) atmosphere with a gas flow rate of 40 ml min^{-1}. As a result, the phase transformation temperatures of the alloys were determined from the DSC curves. The example of the DSC curve for the alloy (80.5 at. % Mn and 19.5 at. % Dy) is presented in Fig. 3.4. The experimental details including the sample preparation, DSC, and the analyses methods are described in Appendix III.

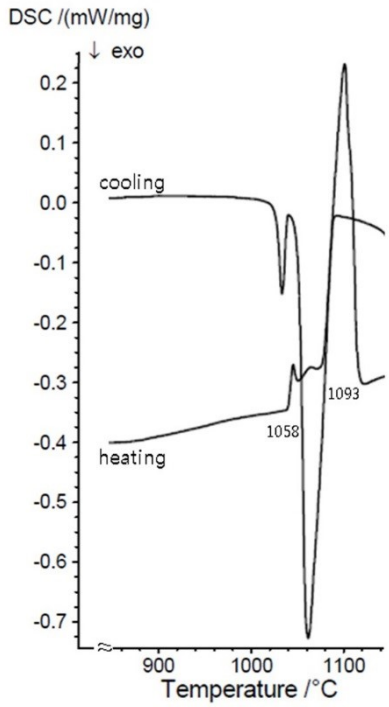


Fig. 3.4. DSC curve for the alloy (80.5 at. % Mn and 19.5 at. % Dy) (Appendix III).

3.3.2. Solution calorimetry

The standard enthalpy of formation (ΔH°_{298}) for the alloy (80.5 at. % Mn and 19.5 at. % Dy) was determined by a solution calorimeter (Ames Lab, USA). High purity Cu (> 99.9999 %) was used as solvent for the solution calorimetry because the reaction of Cu with Mn and Dy is practically small to measure a heat of dissolution of Mn and Dy in liquid Cu. According to the corresponding ratio of the component composition, the heat of dissolution for the component mixture of Mn and Dy was measured using 54.9 mg of Mn and 39.3 mg of Dy. The ΔH°_{298} of the $Mn_{0.805}Dy_{0.195}$ alloy was determined to be -4009.43 J mol-atom^{-1}.

The schematic construction of the solution calorimeter is shown in Fig. 3.5. The calorimeter consists of a center cell and blocks. The cell is composed of a reaction crucible filled with liquid metal ① and a thermopile ②. The thermopile measures the temperature difference between the crucible bottom and the surroundings. The blocks are made of tantalum ③ and their temperature is kept constant during the measurement. Alumina paste is applied to form the alumina layer ④ between the crucible and the tantalum blocks to hold the crucible and to cover the thermopile. Alumina rods ⑤ are used to hang the calorimetric system. Sample addition is carried out through the sample charge tube ⑥ from the sample chamber which is under argon atmosphere. When a measurement is performed, a thermocouple ⑦ measures the temperature of the liquid metal inside the crucible and a stirrer ⑧ agitates the liquid metal.

Solution calorimetry is employed to determine the standard enthalpy of formation of Mn-Dy alloys from the reaction:

$$xMn + yDy = Mn_xDy_y \text{ at } 298 \text{ K} \qquad (3.38)$$

The standard enthalpy of formation of Mn_xDy_y is deduced from the dissolution enthalpy of the alloy (ΔH_2) and that of its component mixture (ΔH_1) in liquid copper using Hess's law.

The enthalpy change of each reaction is given by:

$$\Delta H_1 = x\Delta H_{Mn}^{298\to T} + y\Delta H_{Dy}^{298\to T} + x\Delta H_{Mn}^{diss} + y\Delta H_{Dy}^{diss} \quad (3.39)$$

$$\Delta H_2 = \Delta H_{Mn_xDy_y}^{298\to T} + \Delta H_{Mn_xDy_y}^{diss} \quad (3.40)$$

$$\Delta H_3 = xH_{Mn}^{298} + yH_{Dy}^{298} - H_{Mn_xDy_y}^{298} = -\Delta H_{Mn_xDy_y}^{formation} \quad (3.41)$$

where $\Delta H_{Mn}^{298\to T}$ and ΔH_{Mn}^{diss} are the required enthalpy to heat Mn from 298 K to the temperature of liquid Cu (T) and the dissolution enthalpy of Mn in liquid Cu, respectively. $\Delta H_{Dy}^{298\to T}$, $\Delta H_{Mn_xDy_y}^{298\to T}$, ΔH_{Dy}^{diss} and $\Delta H_{Mn_xDy_y}^{diss}$ are similarly defined.

By Hess's law:

$$\Delta H_2 = \Delta H_1 + \Delta H_3 \quad (3.42)$$

Thus, the standard enthalpy of formation of Mn_xDy_y is:

$$\Delta H_{Mn_xDy_y}^{formation} = \Delta H_1 - \Delta H_2 \quad (3.43)$$

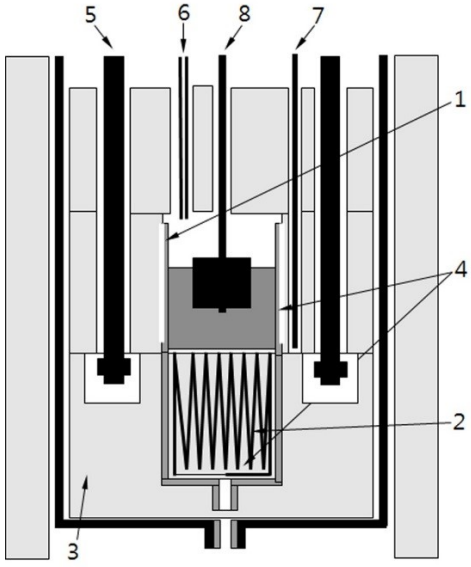


Fig. 3.5. Solution calorimeter: ① Reaction crucible, ② Thermopile, ③ Tantalum blocks, ④ Alumina layer, ⑤ Alumina rod, ⑥ Charge tube, ⑦ Thermocouple, and ⑧ Stirrer (Appendix III).

3.3.3. Equilibration

For the Mg-Sn-Nd and Mg-Sn-Gd ternary systems, the equilibrated alloy method including conventional quenching and microscopic analyses was used to investigate the isothermal phase diagrams. The desired ternary alloys were prepared with the high purity materials, Mg (99.99%), Sn (99.99%), and Mg-40wt.%Nd(Gd) master alloys. All starting alloys were prepared using an induction melting furnace with graphite susceptor under controlled atmosphere with continuously flowing argon gas purified by Mg turnings at 500 ºC. The samples were cut into small pieces (2-3mm) and wrapped with Ta foil and sealed in Mo capsule. Then the samples were annealed in the horizontal tube furnace under high purity argon atmosphere at 500, 600, and 700 ºC for 1 month, 1 week, and 4 hours, respectively. Subsequently, all the samples were rapidly quenched by water. The chemical analysis of each sample was conducted by means of the electron probe microscopy analysis (EPMA –JEOL8600) equipped with wavelength dispersive spectroscopy (WDS). As the ternary compounds were particularly prone to oxidation, the sample preparation for the analysis required special treatment including water free alcohol lubricant for the grinding and polishing. More experimental details can be found in Appendix VIII.

4. Discussion of the optimized Mg-RE-X (X = Mn, Si, Sn) systems

The thermodynamic optimizations of the Mn-RE (13 binary), Si-RE (13 binary), and Sn-RE (13 binary) systems, and several Mg-RE-X (X = Mn, Si, and Sn) (9 ternary) systems were performed through the critical evaluations and systematic analysis approach along with the experimental investigations of the key alloys. In this chapter, as well as the summary of the optimizations including the systematics in the phase diagrams and the thermodynamic properties, some difficulties arose during the optimizations are discussed.

4.1. The Mn-RE system

The thermodynamic optimization of the Mn-RE system is discussed in Appendix I to III. The collection of the optimized phase diagram of Mn-RE system is presented in Fig. 4.1 (Appendix III). The crystal structures of the Mn-RE compounds were summarized in Table 4.1. As expected, the regularity regarding the RE series is observed in the phase diagrams. The stability of the intermetallic phases increases from the light RE to the heavy RE, and the number of stable binary intermetallic phases goes from none (La and Ce) to three (Gd to Tm and Lu). The Pr- and Nd-Mn compounds decompose at lower temperatures while the compounds of the heavier RE are stable down to room temperature except for the Mn_2Y. Among the compounds, Mn_2RE becomes stabilized faster than others, and it melts congruently in Mn-heavy RE systems. Regarding the phase diagram, the limited amount of experimental data and the unreliable phase diagram data of Kirchmayr and Lugscheider [105, 106] made the optimization difficult. Kirchmayr and Lugscheider [105, 106] experimentally investigated the Mn-Nd, -Sm, -Gd, -Tb, -Dy, -Ho, and –Er systems. Among these systems, the Mn-Nd and -Gd systems were revised by other experimental data as seen in Figs. 4.2 and 4.3. In particular the peritectic melting of Mn_2Gd was very difficult to be reproduced along with the experimental S°_{298} of Mn_2Gd as seen in Fig. 4.4. The same was true for the Mn_2Tb in the Mn-Tb system. However, no other experimental data were available for the phase diagrams of the other systems. In the present study, the Mn-Dy system was re-evaluated by conducting phase diagram investigation using DSC and the enthalpy of formation measurements using solution calorimetry. Based on the present experimental findings for the Mn-

Dy system, the Mn_2RE and $Mn_{23}RE_6$ compounds were assumed to melt congruently in the Mn-Tb, -Ho, -Er, -Tm, and –Lu systems unlike the data of Kirchmayr and Lugscheider [105, 106]. Further experimental investigation may be required to verify the proposed phase diagrams of those systems.

As mentioned in the chapter (3.2), the enthalpy of mixing for the Mn-RE liquid shows clear systematic trend that the enthalpy gradually decreases from positive to negative with increasing atomic number of RE. The possible reason of this trend was proposed by the electron density, electronegativity and atomic volume differences between Mn and RE, based on the theoretical model, in Appendix III. Considering the similar systematics as well as the available experimental data, the other thermodynamic properties were determined in the present study. As for the ΔH°_{298} of all Mn-RE compounds, the predicted values from the modified Miedema model are compared with those obtained in the present optimization and calorimetric data. In the present optimization, the ΔH°_{298} of all the compounds were evaluated by the combination of the experimental data and the predicted values. It is worth mentioning that the ΔH°_{298} of Mn_2RE (per atoms) are less negative than that of $Mn_{23}RE_6$ (per atoms) unlike the predicted values except for the compounds in the Mn-Sm and Mn-Lu systems. This is due to the relatively high ΔS°_{298} of Mn_2RE resulting from the previous experimental S°_{298} for Mn_2Gd and Mn_2Tb. The S°_{298} of the Mn-Dy, -Ho, -Er and -Tm compounds were estimated to be similar to those of the Mn-Tb compounds because the sum of S°_{298} of components (NK rule) for those compounds are similar to each other. The optimized enthalpy and entropy of formation for all compounds are shown in Figs. 4.5 and 4.6.

Table 4.1. Crystal structures of the Mn-RE compounds.

Stoichiometry		Y	La	Ce	Pr	Nd	Sm	Gd	Tb	Dy	Ho	Er	Tm	Lu	Structural Types
Mn_2RE	LT	*				+	+	*	*	*	+	+	+	+	+$P6_3/mmc$, $hP12$, $MgZn_2$
	HT										*				*$Fd\bar{3}m$, $cF24$, Cu_2Mg
$Mn_{23}RE_6$		#			#	#	#	#	#	#	#	#	#	#	#$Fm\bar{3}m$, $cF116$, $Mn_{23}Th_6$
$Mn_{12}RE$		@						@	@	@	@	@	@		@$I4/mmm$, $tI26$, $Mn_{12}Th$
Mn_5RE														&	&$P6_3mc$, $hP12$, derivative $MgZn_2$

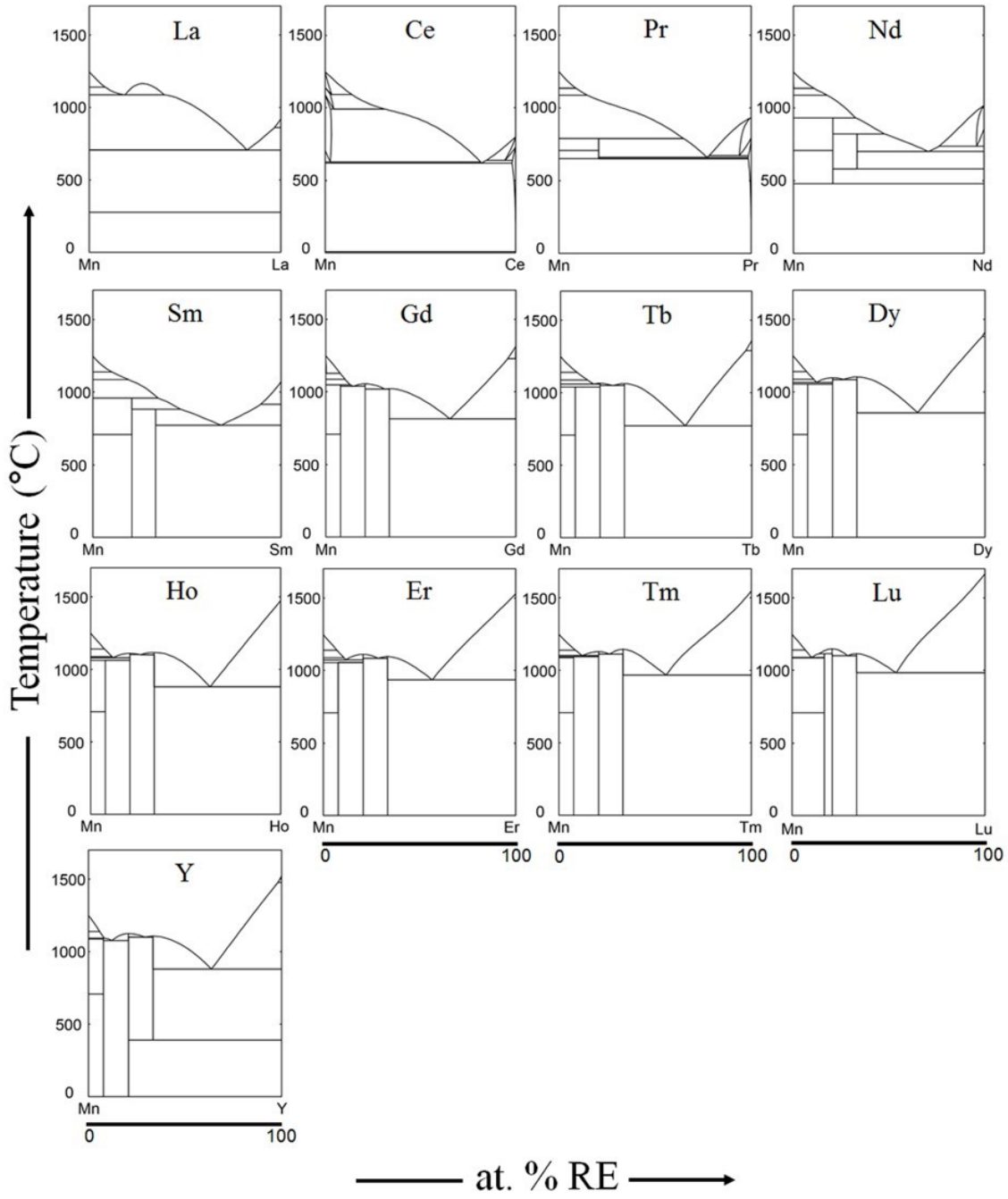


Fig. 4.1. Collection of the optimized phase diagrams of Mn-RE systems (Appendix III).

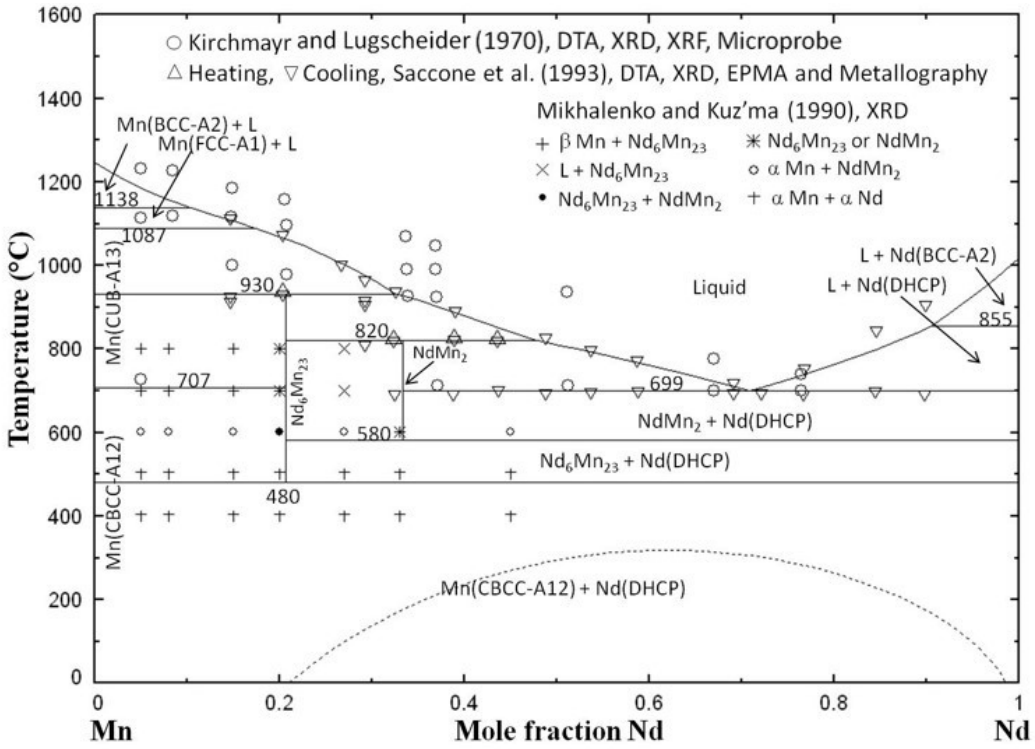


Fig. 4.2. The Mn-Nd phase diagram with experimental data (Appendix I).

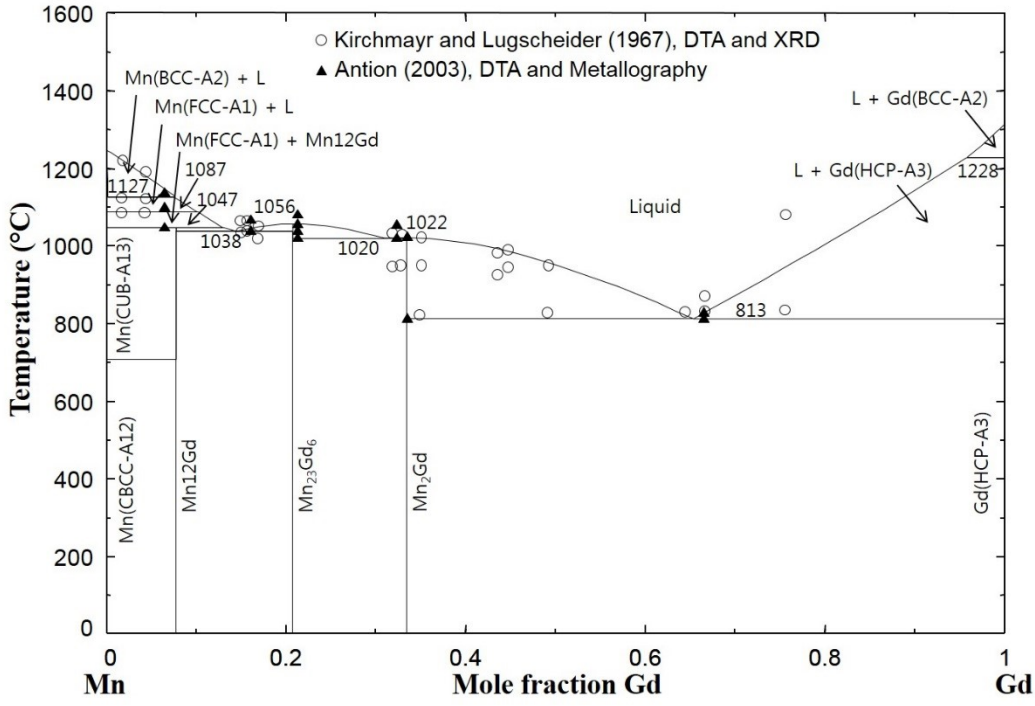


Fig. 4.3. The Mn-Gd phase diagram with experimental data (Appendix II).

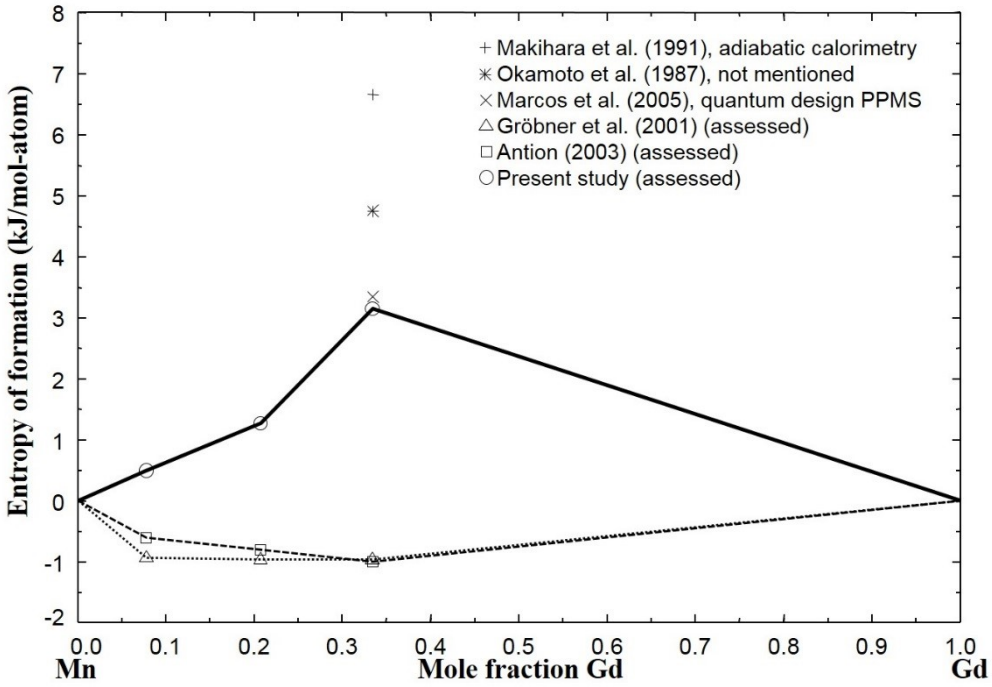


Fig. 4.4. The standard entropy of formation of the Mn-Gd compounds along with experimental data (Appendix II).

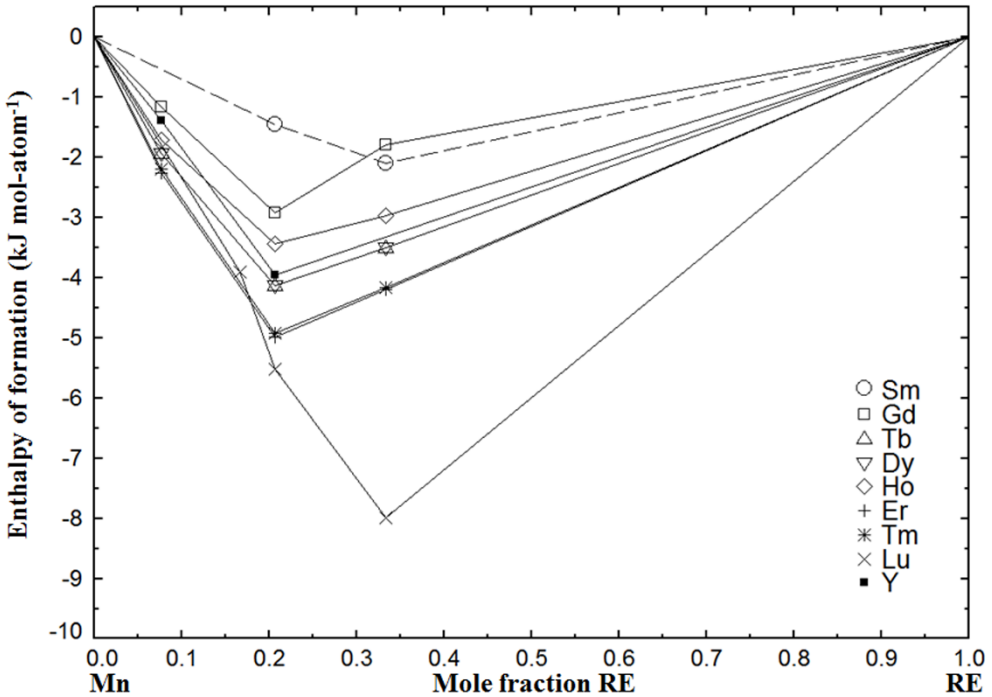


Fig. 4.5. Optimized standard enthalpy of formation of the Mn-RE system (Appendix III).

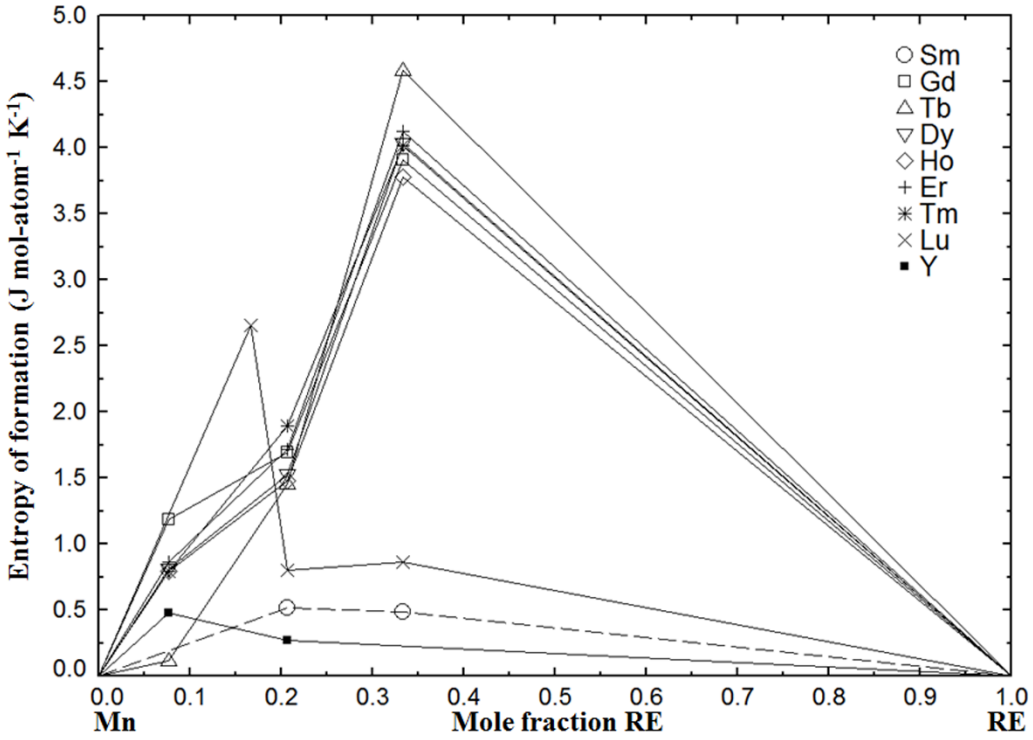


Fig. 4.6. Optimized standard entropy of formation of the Mn-RE system (Appendix III).

4.2. The Si-RE system

The thermodynamic optimization of the Si-RE system is discussed in Appendix IV and V. The collection of the optimized phase diagram of Si-RE system is presented in Fig. 4.7 (Appendix V). The crystal structures of the Si-RE compounds were summarized in Table 4.2. As shown in Fig. 3.3, a clear systematic trend in the melting temperatures of intermetallic compounds was found in the phase diagrams of the Si-RE systems. The compounds which have the highest melting temperature shift from the low RE-containing compounds to the high RE-containing compounds with increasing atomic number of RE. The systematic trends in the phase diagram were successfully used to assess the phase diagrams of the Si-Sm, -Tm and -Lu systems which were rarely known. The predicted melting temperatures by Bulanova et al. [45, 46] using the normalization approach (linear interpolation of the melting temperatures of the compounds versus the melting temperatures of pure RE metals) is only valid for the compounds such as RE_5Si_3 and RE_5Si_4 whose melting temperatures are increasing along with atomic number of RE. Moreover, La and Y turned out to be off from the linear relation for the RE_5Si_3 and RE_5Si_4. The possible reason of such trend was proposed by the relative stability of Si-RE compounds corresponding to the systematic change of the enthalpy of formation in Appendix V. In the present optimization, the experimental eutectic temperatures between La_3Si_5 and LaSi, Ce_3Si_5 and CeSi, Pr_5Si_9 and PrSi, and Nd_5Si_9 and NdSi were difficult to be reproduced. The calculated eutectic temperatures are higher than the experimental data by 50 to 80 ^oC. The liquidus slopes of RE_3Si_5 and RE_5Si_9 should be steeper than current calculations in order to reproduce the eutectic temperatures. However, the experimentally proposed liquidus in the Mn-La, -Ce, -Pr, and –Nd systems seem to be improbable. For example, the calculated phase diagrams of the Ce-Si and Pr-Si systems along with the experimental liquidus of Ce_3Si_5 and Pr_5Si_9 are shown in Fig. 4.8. The experimental liquidus on the Ce-rich side is steeper than the current calculation by more than twice. The same is true for the La-Si system. In order to reproduce such a drastic change of liquidus slope, the temperature dependence of the liquid Gibbs energy (that is, entropy) around Ce_3Si_5 composition should be changed drastically. This is very difficult to be described. In the case of Pr-Si system, the experimental liquidus of Pr_5Si_9 is straight, which is also very difficult to be reproduced. Theoretically, the liquidus slope of the intermetallic compound should be zero at its stoichiometric

composition. Such a sharp liquidus slope can be happened if the enthalpy of liquid at the composition is very negative, and very strong short range ordering in liquid occurs. However, in the present evaluation, we could not find strong evidence to support this.

The thermodynamic properties of the Si-RE liquid and compounds are shown in Figs. 4.9 to 4.12 (Appendix V). The enthalpies of mixing for liquid Si-RE at 2000 K show minimum values in the range of -65 to -75 kJ mol^{-1}. These are much larger in magnitude than those of the Mn-RE systems (8 to -8 kJ mol^{-1}) (Present study), Al-RE systems (-30 to -40 kJ mol^{-1}) [15, 16] and Zn-RE systems (-20 to -32 kJ mol^{-1}) [17, 18], but similar to the Pb-RE systems (-40 to -50 kJ mol^{-1}) [107]. Unfortunately it is hard to find visible trend in the enthalpy of mixing changing with atomic number of RE like Mn-RE system, but still the enthalpy of mixing seems roughly decreasing with increasing atomic number of RE. The positions of minimum enthalpies of mixing are near 0.5 mole fraction of RE or slightly more rich in Si. Corresponding to the large negative enthalpies of mixing at the middle composition range, the entropies of mixing have typical "M" shape, which can be seen in the systems having short range ordering in liquid phase. In general, the entropy of mixing values are negative at 0.5, which means there could be significant non-configuration entropy can be involved in this Si-RE at liquid state possibly associated to the strong short range ordering. Like the liquid enthalpies, the enthalpies of formation of the Si-RE compounds of all Si-RE systems are similar, which show a minimum in the range of about -68 to -88 kJ mol^{-1} (based on one mole of Si-RE system). Most of solid RE silicides show negative entropies of formation from the elemental references.

The limitation of the MQM was previously pointed out by Hillert et al. [108] that the model with coordination number other than '2' can result in negative configurational entropy when the model parameter becomes too negative. In the optimized Si-RE system with coordination number '6', the calculated configurational entropies of mixing for all Si-RE liquid become negative at certain temperature. Although the negative configurational entropy can be only calculated at the composition and temperature where the liquid phase is metastable state, theoretically the negative configurational entropy is unrealistic. When the solution is deviated very negatively from ideal behavior, like the present liquid Si-RE solution, the configurational entropy term is negatively

overestimated from the MQM especially at low temperature, although the total entropy of solution is still correctly calculated. Further discussion including the limitation of the MQM model, the effectiveness of the model parameters, and the comparison with BWRMM are made in Appendix IV.

Table 4.2. Crystal structures of the Si-RE compounds.

Stoichiometry		Y	La	Ce	Pr	Nd	Sm	Gd	Tb	Dy	Ho	Er	Tm	Lu	Structural Types
$RESi_2$	LT	!	+	+			*	*	*	*					+$I4_1/amd$, $tI12$, $ThSi_2$
	HT	+					+	+							*$Imma$, $oI12$, $GdSi_2$
															!$P6/mmm$, $hP3$, AlB_2
RE_5Si_9	LT				*	*					*				+$I4_1/amd$, $tI12$, $ThSi_2$
	HT				+	+									*$Imma$, $oI12$, $GdSi_2$
RE_3Si_5		+	*	*			!	!	!	!	!	!			+$I4_1/amd$, $tI12$, $ThSi_2$
															*$Imma$, $oI12$, $GdSi_2$
															!$P6/mmm$, $hP3$, AlB_2
RE_2Si_3						!									!$P6/mmm$, $hP3$, AlB_2
RESi		♠	§	§	§	§	§	§	§	§	§	§			§$Pnma$, $oP8$, FeB
															♠$Cmcm$, $oC8$, CrB
RE_5Si_4		¤	¢	¢	¢	¢	¤	¤	¤	¤	¤	¤			¢$P4_12_12$, $tP36$, Zr_5Si_4
															¤$Pnma$, $oP36$,Sm_5Ge_4
RE_3Si_2			♦	♦											♦$P4/mbm$, $tP10$, Si_2U_3
RE_5Si_3		♣	♥	♥	♥	♥	♣	♣	♣	♣	♣	♣			♥$I4/mcm$, $tI32$, Cr_5B_3
															♣$P6_3/mcm$, $hP16$, Mn_5Si_3

+distorted $ThSi_2$ for YSi_2 and Y_3Si_5.

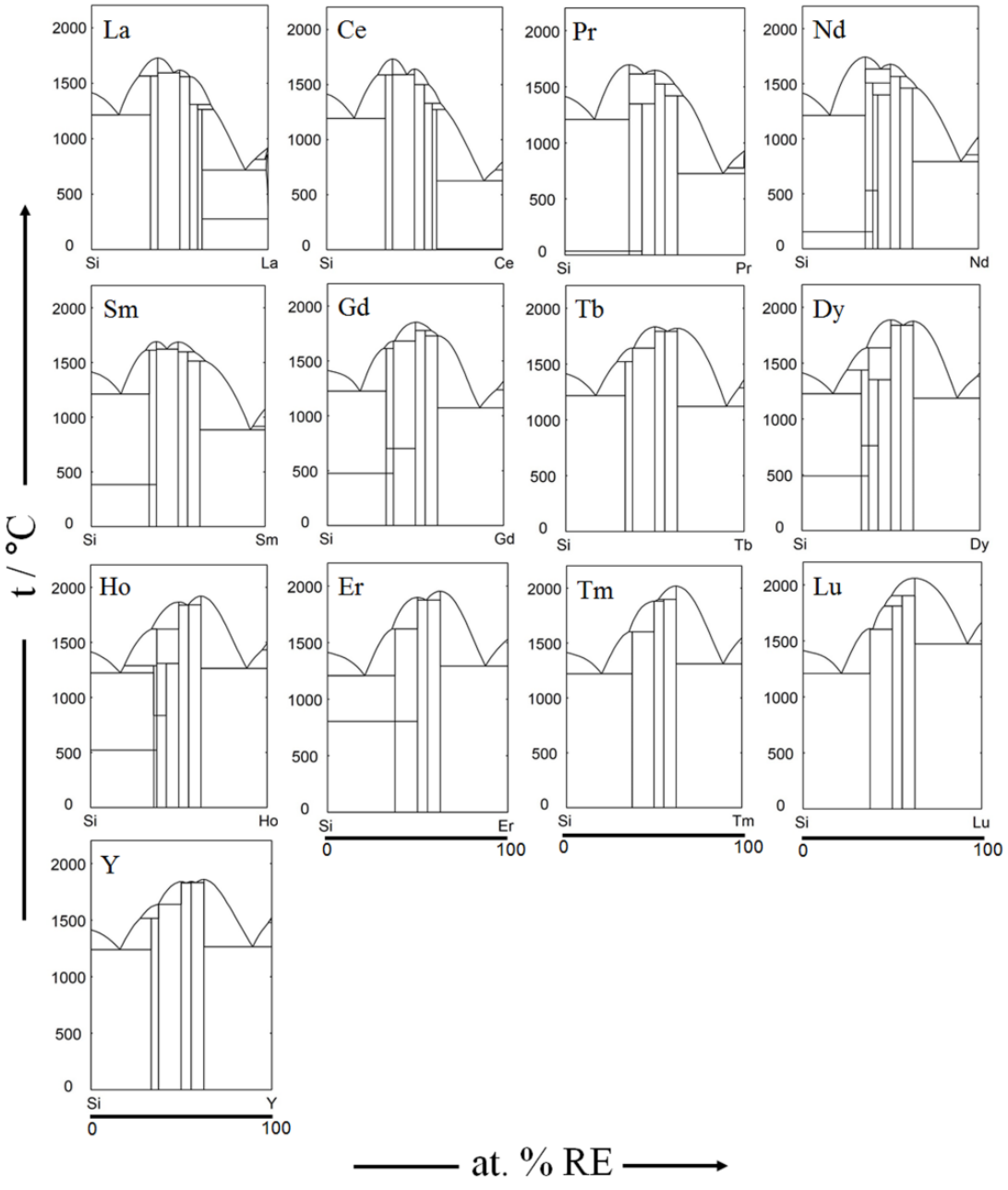


Fig. 4.7. Collection of the optimized phase diagrams of Si-RE systems (Appendix V).

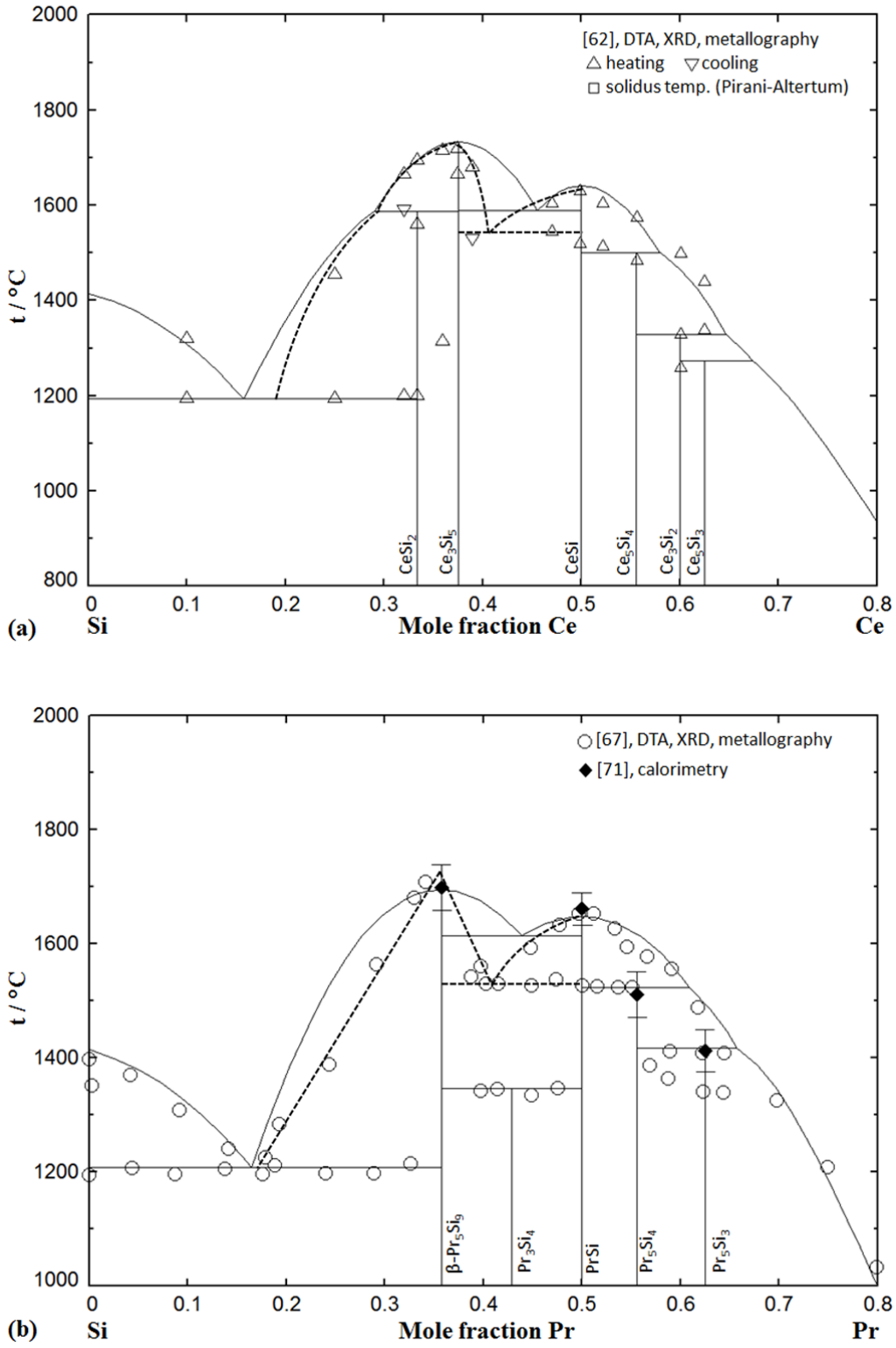


Fig. 4.8. Phase diagrams of (a) Si-Ce and (b) Si-Pr systems; solid lines: calculated from the present study and dotted lines: proposed by experimental studies (see Appendix IV for the references).

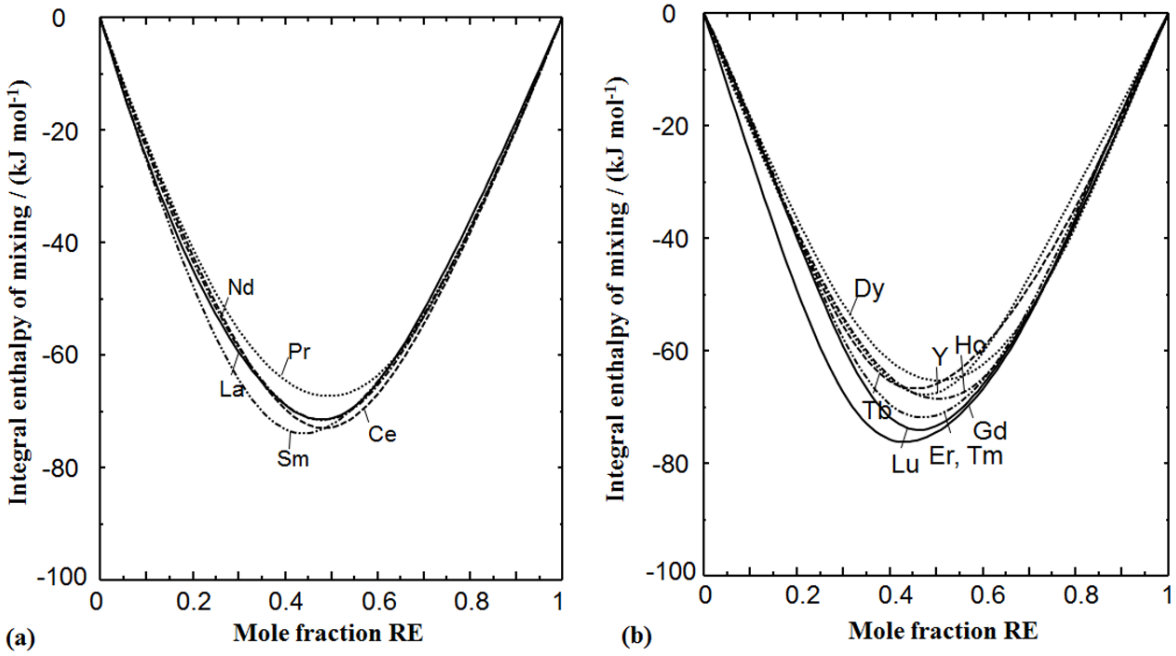


Fig. 4.9. Comparison of integral enthalpies of mixing of liquid Si-RE at 2000 K. ((a) Si-light RE and (b) Si-heavy RE) (Appendix V).

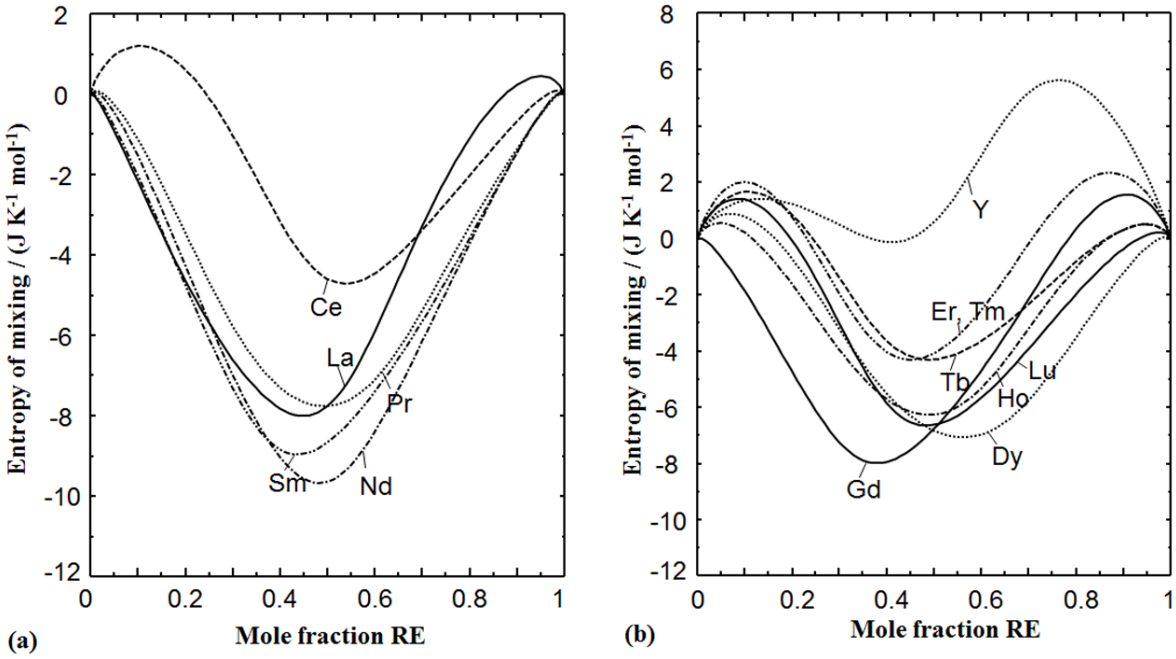


Fig. 4.10. Comparison of entropies of mixing of liquid Si-RE at 2000 K. ((a) Si-light RE and (b) Si-heavy RE) (Appendix V).

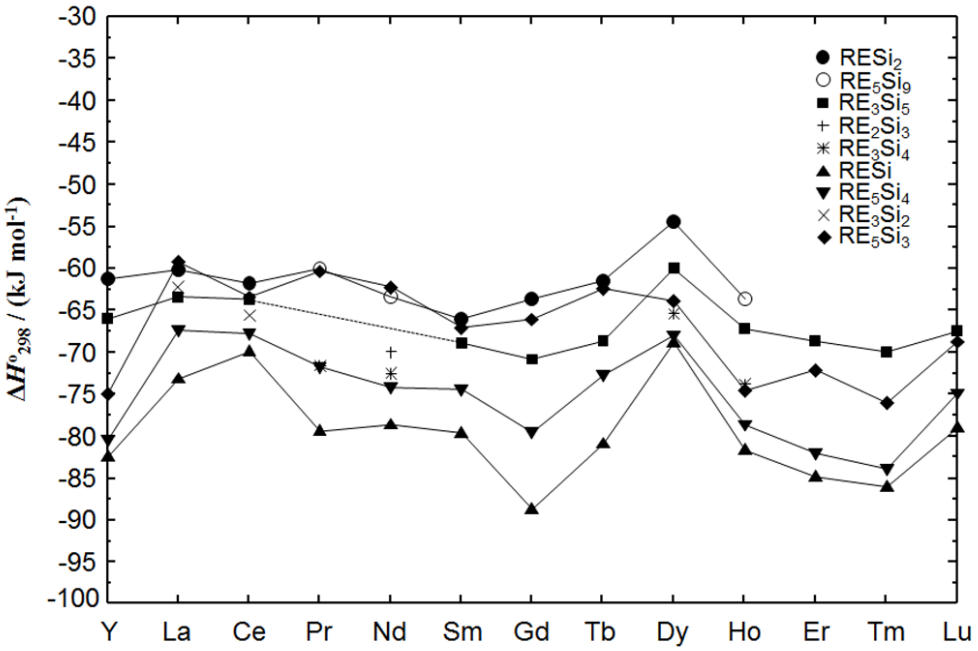


Fig. 4.11. Comparison of enthalpies of formation of Si-RE compounds at 298 K (based on one mole of Si-RE system) (Appendix V).

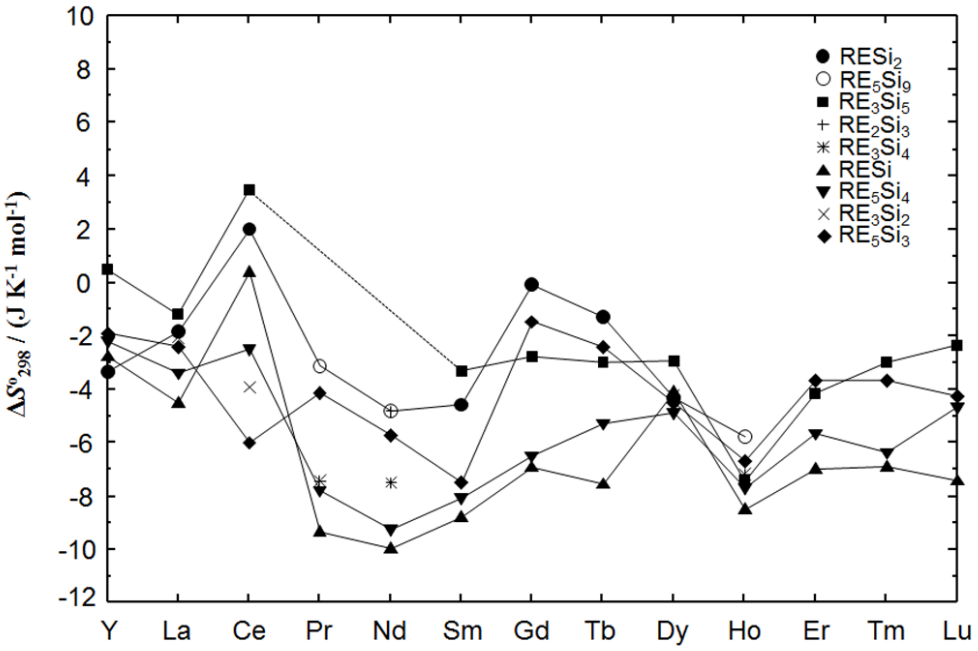


Fig. 4.12. Comparison of entropies of formation of Si-RE compounds at 298 K (based on one mole of Si-RE system) from elemental references (Appendix V).

4.3. The Sn-RE system

The thermodynamic optimization of the Sn-RE system is discussed in Appendix VI and VII. The collection of the optimized phase diagram of Sn-RE system is presented in Fig. 4.13 (Appendix VII). The crystal structures of the Sn-RE compounds were summarized in Table 4.3. A systematic trend in the melting temperatures of Sn-RE compounds were found showing that the melting temperatures of the low RE-containing compounds are decreasing with increasing atomic number of RE, while the melting temperatures of the high RE-containing compounds are increasing with atomic number of RE. The trend is quite similar to that found in the Si-RE systems and it was used to assess the unknown melting temperatures of compounds. The melting temperatures of Sn-RE compounds are shown in the order of atomic number of RE in Fig. 4.14 (Appendix VII). There were some discrepancies in the existence of the certain Sn-RE compounds. For example, although the presence of La_2Sn_5 (Ce_2Sn_5 type), La_3Sn_7 (Ce_3Sn_7 type), and $LaSn_2$ ($NdSn_2$ type) with their respective lattice parameters was reported in the crystallographic study by Weitzer et al. [109], those phases are not found in the phase diagram investigation of Eremenko et al. [110]. Such discrepancies were resolved by looking at the experimental phase diagram investigations of the ternary systems containing RE and Sn. However, further careful experimental investigations may be required to verify the intermetallic compounds, in particular between 0.2 and 0.45 mole fraction of RE like the refinement of Sn-Nd system by Saccone et al. [111]. In the work of Saccone et al. [111], the Nd_2Sn_5, Nd_3Sn_7, and $NdSn_2$ were additionally found with respective melting temperatures, 1135 ^oC, 1145 ^oC, and 1180 ^oC, respectively.

The thermodynamic properties of the Sn-RE liquid and compounds are shown in Figs. 4.15 to 4.18 (Appendix VII). The enthalpies of mixing of all liquid Sn-RE alloys show minimum values in the range of -50 to -65 kJ mol^{-1} near 0.5 mole fraction of RE. These are in-between the Pb-RE system (-40 to -50 kJ mol^{-1}) [107] and Si-RE system (-65 to -75 kJ mol^{-1}) (Present study). This seems to be very reasonable considering the fact that the Sn is in-between Si and Pb in the same group 14 of the periodic table. However, similar to the Si-RE system, it is difficult to find a trend of gradual decrease in the enthalpy of mixing with atomic number of RE which was found in the Mn-RE system. Rather, it seems that the enthalpy of mixing increase with atomic number of RE

particularly for the heavy RE as seen in Fig. 28(b). However, it it is still uncertain because the experimental data for many Sn-RE systems were unavailable or partially available (Sn-rich region). Corresponding to the large negative enthalpies of mixing at the middle composition range, the entropies of mixing have typical "M" shape, which can be seen in the systems having short range ordering in liquid phase. Unlike the entropies of mixing of Si-RE liquid which have negative values at 0.5 mole fraction of RE associated with significant non-configuration entropy, the entropies of mixing have positive values over the whole composition range because only small entropic parameters or none of them were used, explaining that the configuration entropies are dominant factor in total entropy. Based on one mole of Sn-RE system, the minimum value of the enthalpy of formation is associated with the RESn or $RE_{11}Sn_{10}$ (about 0.5 mole fraction of RE) with -75 to -90 kJ mol·atom^{-1} except the Sn-Y system. Exceptionally, the Y_5Sn_3 has the most negative enthalpy of formation among the Y containing stannides. The variation of entropies of formation is within the range of 10 J K^{-1} mol^{-1} with mostly negative values.

Table 4.3. Crystal structures of the Sn-RE compounds.

Stoichiometry		Y	La	Ce	Pr	Nd	Sm	Gd	Tb	Dy	Ho	Er	Tm	Lu	Structural Types
$RESn_3$	LT	*	+	+	+	+	+	*	*	*	*	*	*		+*Pm* $\bar{3}$ *m*, *cP*4, $AuCu_3$
	HT							+							**Cmcm*, *oC*16, $GdSn_3$
RE_2Sn_5		§		!	!	!	!				§	§	§	§	!*Cmmm*, *oC*28, Ce_2Sn_5 §*Pmmm*, *oP*14, Y_2Sn_5
RE_3Sn_7				♠	♠	♠	♠	♦	♦	♦					♠*Cmmm*, *oC*20, Ce_3Sn_7 ♦*Cmmm*, *oC*20, Gd_3Sn_7
$RESn_2$		¤			¢	¢	¢	¤	¤	¤	¤	¤	¤	¤	¢*Cmmm*, *oC*12, $ZrGa_2$ ¤*Cmcm*, *oC*12, $ZrSi_2$
RE_3Sn_5			#	#	#										#*Cmcm*, *oC*32, Pu_3Pd_5
RE_2Sn_3			@		@		@								@*P* $\bar{1}$, *aP*20
RESn			♥												♥*Cmcm*, *oC*8, CrB
$RE_{11}Sn_{10}$		♣	♣	♣		♣	♣	♣	♣	♣	♣	♣	♣	♣	♣*I*4/*mmm*, *tI*84, $Ho_{11}Ge_{10}$
RE_5Sn_4		&	&	&	&	&	&	&	&	&	&	&			&*Pnma*, *oP*36, Sm_5Ge_4
RE_4Sn_3							%								%*I* $\bar{4}$ 3*d*, Th_3P_4
RE_5Sn_3	LT	$	^	^	^	$	$	$	$	$	$	$	$	$	^*I*4/*mcm*, *tI*32, W_5Si_3
	HT		$	$	$										$*P*63/*mcm*, *hP*16, Mn_5Si_3
RE_3Sn				+	+										+*Pm* $\bar{3}$ *m*, *cP*4, $AuCu_3$

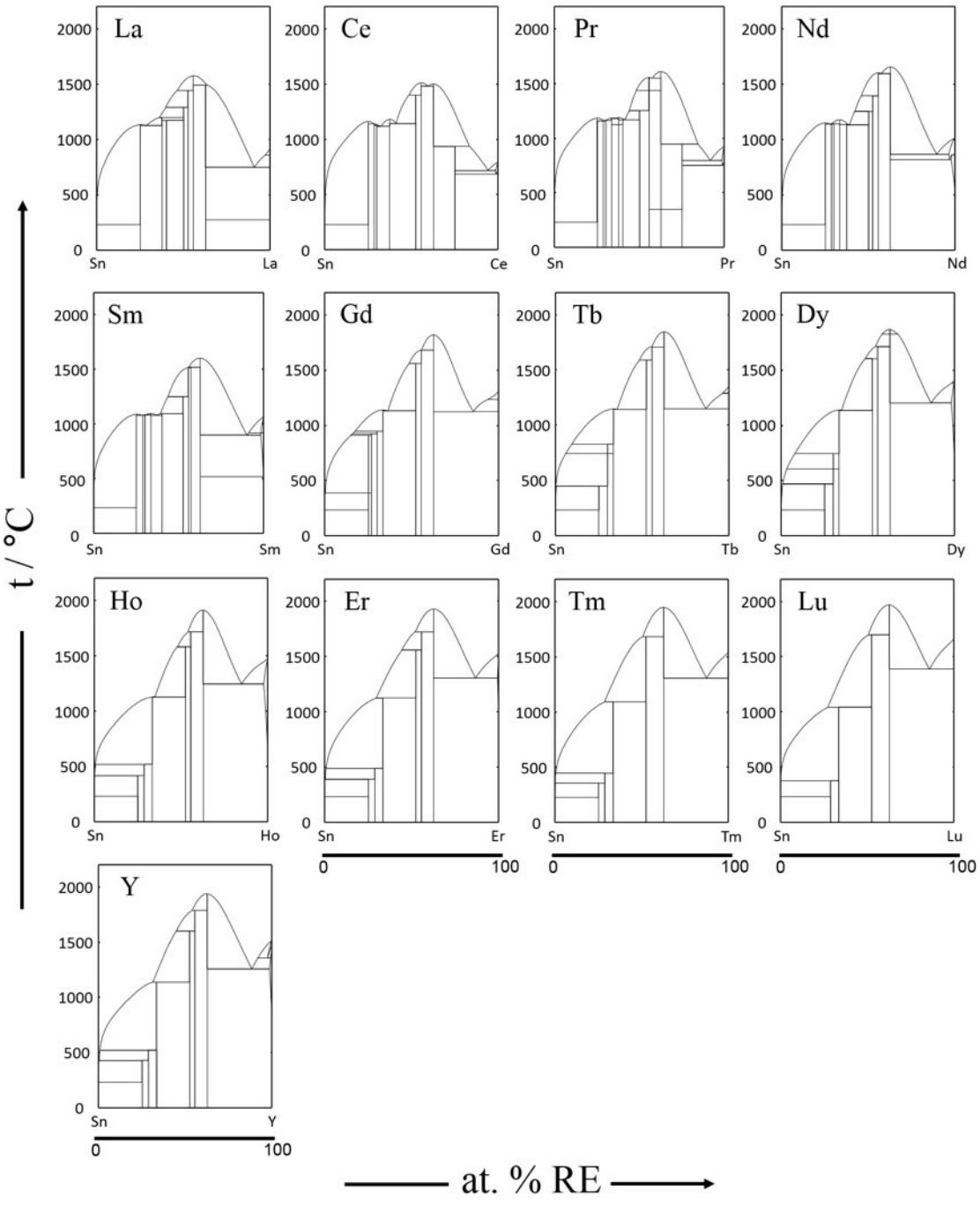


Fig. 4.13. Collection of the optimized phase diagrams of the Sn-RE systems.

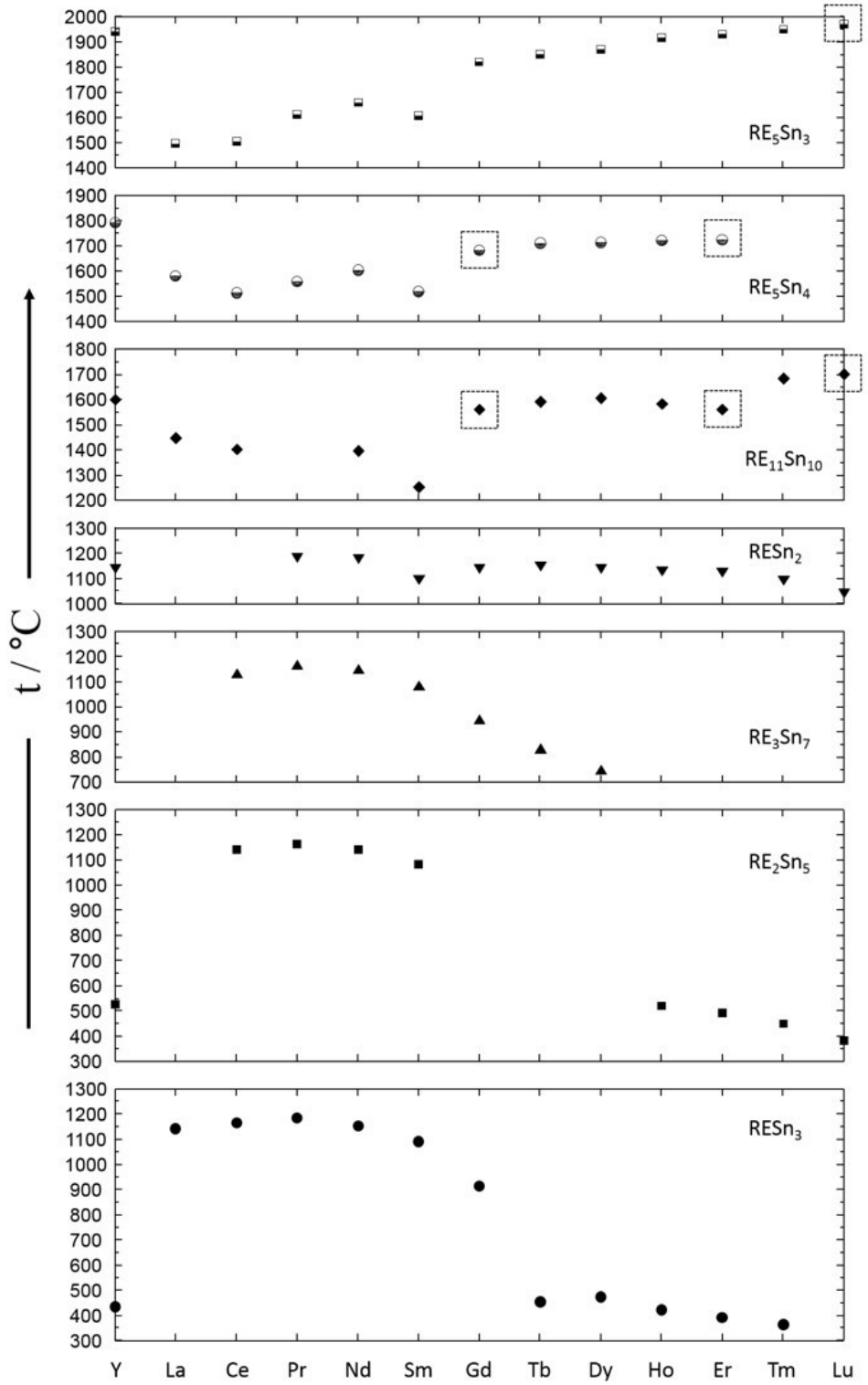


Fig. 4.14. Systematic changes in the melting temperatures of Sn-RE compounds. The melting temperatures estimated in the present study are indicated by the empty squares (Appendix VII).

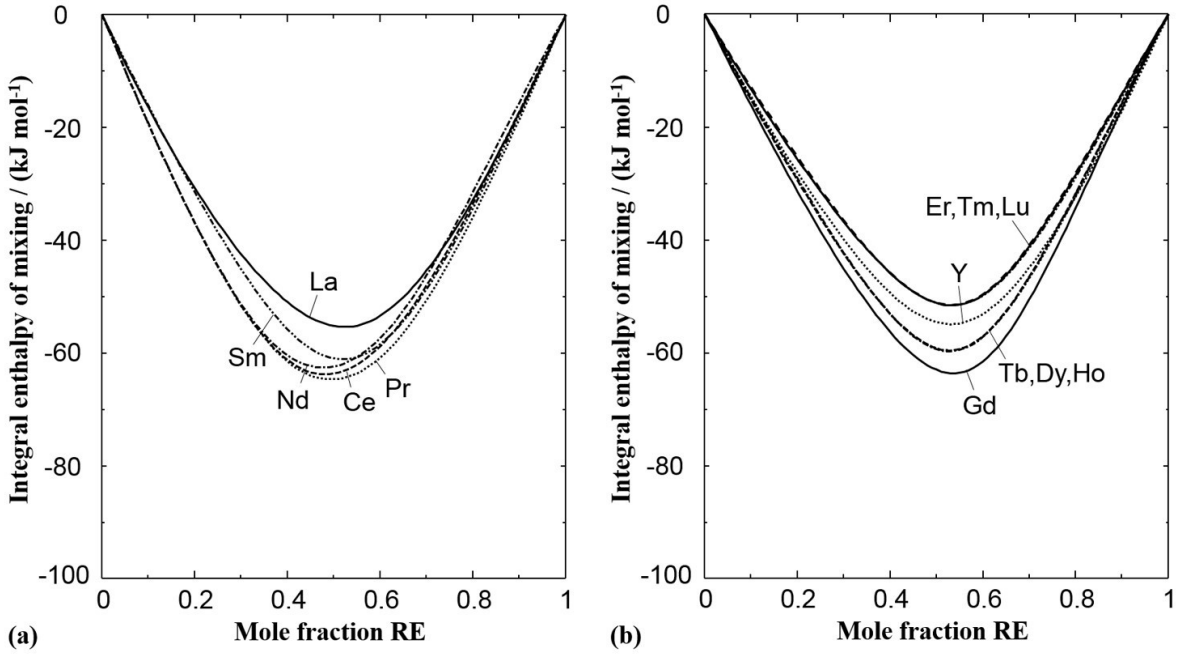


Fig. 4.15. Comparison of integral enthalpies of mixing of liquid Sn-RE at 2000 K ((a) Sn-light RE and (b) Sn-heavy RE) (Appendix VII).

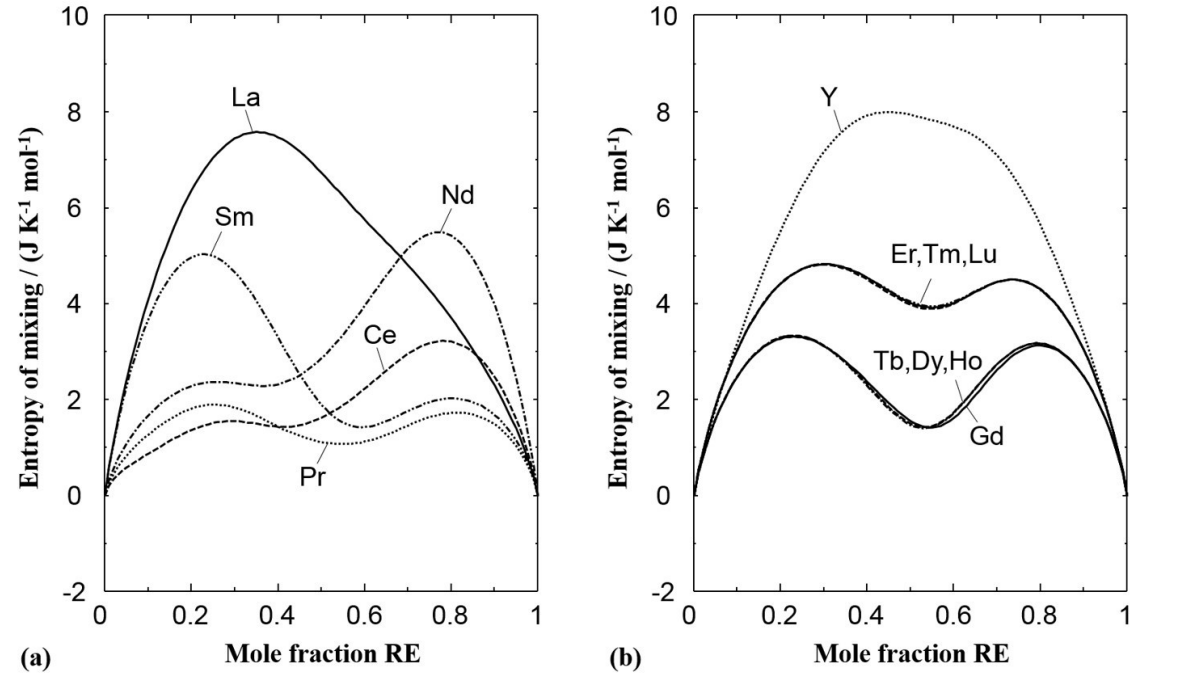


Fig. 4.16. Comparison of entropies of mixing of liquid Sn-RE at 2000 K ((a) Sn-light RE and (b) Sn-heavy RE) (Appendix VII).

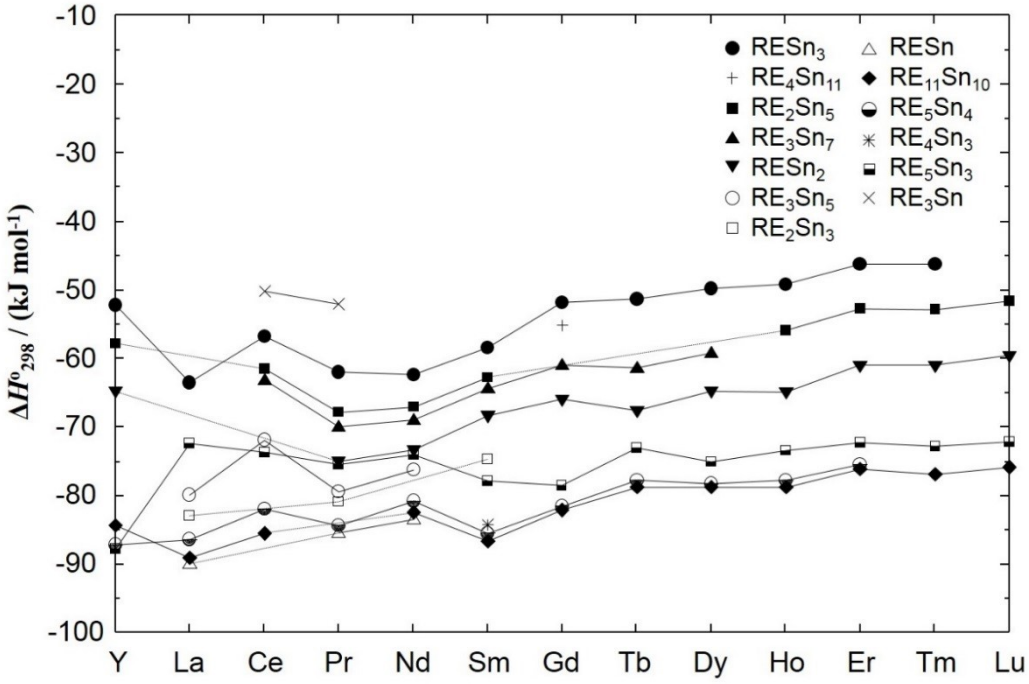


Fig. 4.17. Comparison of enthalpies of formation of Sn-RE compounds at 298 K (based on one mole of Sn-RE system) (Appendix VII).

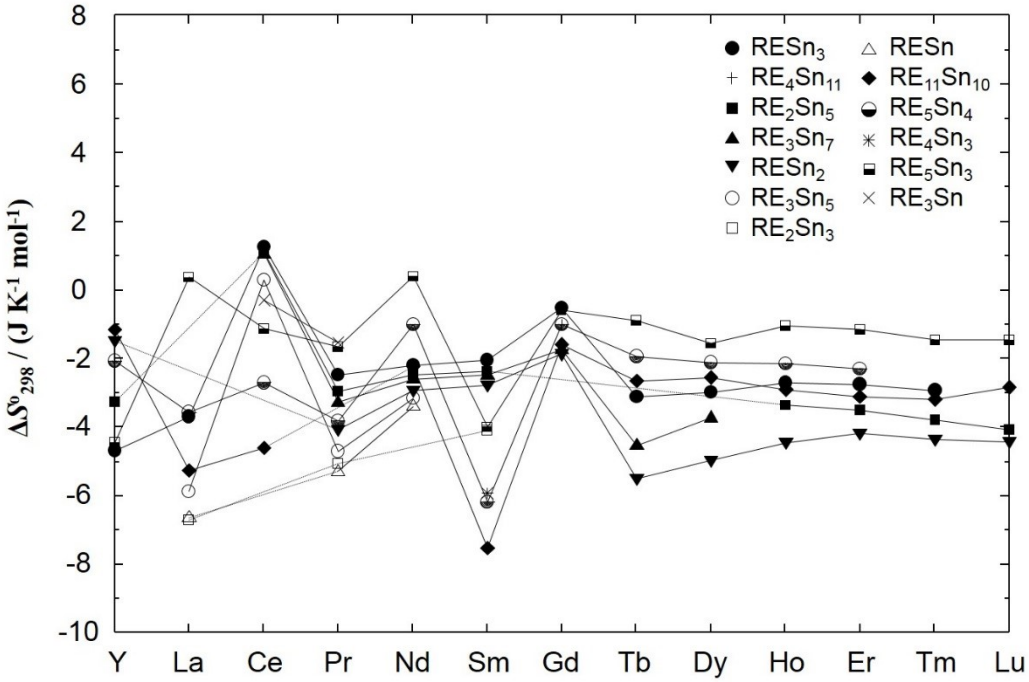


Fig. 4.18. Comparison of entropies of formation of Sn-RE compounds at 298 K (based on one mole of Sn-RE system) from elemental references (Appendix VII).

4.4. The ternary Mg-RE-X (X = Mn, Si, Sn) systems

The thermodynamic optimization of 9 ternary systems among the Mg-X-RE (X = Mn, Si, Sn) is discussed in Appendix VIII, where the systems having no experimental data are excluded.

For the Mg-Mn-RE systems, the Mg-Mn-Ce, Mg-Mn-Nd, Mg-Mn-Gd, and Mg-Mn-Y systems were thermodynamically assessed with the available data [112-115]. According to the experimental studies, no ternary compounds exist in the Mg-Mn-RE systems. The reported homogeneity ranges of the certain phases such as MgRE(bcc-B2), Mg_2RE(laves-C14), etc. in the experimental studies were described with respective sublattice model depending on the crystal structure. The Kohler type of symmetric approximation was generally adopted as the interactions between constituent binary elements for three binary systems do not show significant difference. During the optimization of Mg-Mn-Nd system, the binary Mn-Nd system was re-optimized from the one optimized in Appendix I as new binary phase, $Mn_{17}Nd_2$ was found. The re-optimized Mn-Nd system with the $Mn_{17}Nd_2$ phase was used to build the ternary Mg-Mn-Nd system.

For the Mg-Si-RE systems, the presence of the ternary compounds, $REMgSi_2$ (RE = La, Ce, Pr, Nd), $CeMg_2Si_2$, CeMgSi, $CeMg_3Si$ and Ce_2MgSi_2, were reported in several studies [116-118]. However, the phase equilibria or any thermodynamic properties of the compounds were not available. As the phase equilibria in the Mg-rich corner of the Mg-Si-Y was experimentally determined [119], the comparison between the experimental data and the calculated phase diagrams from the present optimization was only made for the Mg-Si-Y system. The system was optimized by combining three binary systems without ternary liquid parameters. The asymmetric approximation was applied because the Y-Si liquid phase exhibits very negative deviations from ideal solution behavior whereas the Mg-Si and Mg-Y are closer to ideality. However, it is highly possible that certain stable ternary compounds are present in the system. Further investigation regarding the existence of ternary compounds and the solid solubilities would be required to optimize the system.

For the Mg-Sn-RE systems, the Mg-Sn-Nd and Mg-Sn-Gd systems were selected for the experimental investigation to overcome the limited experimental data. The phase equilibria of the Mg-Sn-Nd and Mg-Sn-Gd systems at 500-700 ºC were determined by the equilibrated alloy method. The existence of the ternary compounds, MgNd(Gd)Sn, MgNd(Gd)Sn_2, and $Mg_4Nd_2Sn_3$ was revealed with the respective phase equilibria. Based on the present phase equilibria data, the thermodynamic optimizations of the Mg-Sn-Nd and Mg-Sn-Gd systems were carried out with additional help of the systematic study for the melting temperature of MgRESn (RE = La-Lu and Y) determined by DTA method [120]. The asymmetric approximation was applied with Mg as the asymmetric component, as the Sn-RE liquid exhibits very negative deviations from ideal solution behavior unlike the other two binaries. The thermodynamic properties of the ternary compounds, MgNd(Gd)Sn, MgNd(Gd)Sn_2, and $Mg_4Nd_2Sn_3$ were successfully estimated. Moreover, the experimental data of the phase equilibria in the Mg-Sn-Gd [121], Mg-Sn-Er [122] and Mg-Sn-Y [123, 124] at 300-500 ºC were available in the literature. The thermodynamic optimizations of the Mg-Sn-Er and Mg-Sn-Y systems were similarly performed based on the experimental data.

The calculated phase diagrams along with the experimental data, and the model parameters can be found in Appendix VIII.

5. Application of the thermodynamic database to Mg alloy development

In general, the developed thermodynamic database can be used multiple types of calculations by means of the Gibbs energy minimization software like FactSage, in particular providing the phase diagrams (isothermal, isoplethal, projection, etc.), cooling paths of alloys (equilibrium, Scheil-Gulliver, etc.), thermodynamic properties (heat evolution, activity, etc.), etc. In addition, the database with additional thermophysical properties such as interfacial energy and diffusivity can offer the calculation of diffusion and precipitation kinetics, etc. and can also be coupled to software for phase field modeling and other kinetic modeling.

In this chapter, several examples of the potential applications of the present optimized Mg alloy database are discussed.

The first example is shown for the Mg-Gd, Mg-Gd-Zr, Mg-Gd-Zn, and Mg-Gd-Mn-Sc alloys. These alloys were studied by Fang et al. [125] to investigate the effect of Zr, Mn and Mn + Sc additions on the grain size of Mg-10Gd alloy. The alloys were prepared in the electric resistance furnace under an anti-oxidizing flux. The compositions of the alloys are given in Table 5.1. The alloys were homogenization treated at 520 ºC for 10, 20 and 40 h, respectively, to investigate the trend of grain growth. The samples treated at 520 ºC for 10 h were chosen for extrusion at 400 ºC with an extrusion ratio of 22:1. In their conclusion, the alloy with Zr addition (alloy B) showed a significant grain refinement in the as-cast alloy, but it showed rapid grain coarsening during homogenization treatment and lost the grain refining effect for the extruded alloy. The addition of Mn (alloy C) showed no grain refining effect for the as-cast alloy, but it refined microstructure to some extent during extrusion. The alloy with Mn and Sc (alloy D) showed successful grain refinement in both as-cast and the extruded alloy. The average grain sizes of the alloys at various states are shown in Table 5.2. The main mechanism of the grain refinement was suggested by grain boundary pinning effect by the particles, Zr, Mn, and Mn_2Sc for the alloy B, C, and D, respectively.

In the present study, Scheil-Gulliver cooling calculation and the equilibrium calculation for the phase fraction vs. temperature diagrams are conducted for all four alloys to elucidate the study of Fang et al. [125]. As it is known that Scheil-Gulliver cooling calculations can give reasonable predictions of the as-cast microstructure, the calculations can be compared with the microstructure of the as-cast alloys. According to the calculations, the as-cast alloy A is composed of hcp-Mg dendrites with about 7.8 wt. % Mg_5Gd, the as-cast alloy B is composed of hcp-Mg dendrites with about 5.7 wt. % Mg_3Gd, the as-cast alloy C is composed of hcp-Mg dendrites with about 8.1 wt. % Mg_5Gd plus 0.03 wt. % cbcc-Mn, and the as-cast alloy D is composed of hcp-Mg dendrites with about 8.1 wt. % Mg_5Gd plus 0.04 wt. % $Mn_{23}Sc_6$. The grain refinement of Mg alloys by Zr typically depends on both soluble and total (soluble + undissolved) Zr contents in the melt. As the Mg-Zr master alloys typically show the microstructures, where Zr or Zr-rich particles and particle clusters are embedded in hcp-Mg matrix that contains approximately 0.6 wt. % Zr, such Zr-rich particles and clusters which has a high melting point (T_m of Zr is 1855 ºC) often remain as undissolved particles in the melt, and act as the grain refiner, even though the Zr contents are less than the maximum solubility. However, as it was assumed that the the Scheil-Gulliver cooling calculations start cooling from the 100 % homogeneous liquid in this case that the Zr content is less than the maximum solubility in liquid Mg, it is difficult to explain the grain refinement without knowing the process conditions. The grain refinement in the alloy D may also be attributed to the undissolved particles of Sc or Sc compound (T_m of Sc is 1541 ºC). On the other hand, the phase fraction vs. temperature diagrams shown in Fig. 5.1 can explain the grain refinement by the amount of the precipitates in the homogenization treated alloys and also in the extruded alloys. According to Fang et al. [125], the alloy with Zr (alloy B) showed grain coarsening during homogenization treatment at 520 ºC and lost the grain refining effect for the extruded alloy. That is simply because at 520 ºC there should be no precipitate phases in equilibrium (Fig. 5.1(a)). All the undissolved Zr and Mg_3Gd (from the Scheil-Gulliver cooling calculation) particles in the as-cast alloy B are continuously dissolving during the heat treatment. That's why the grain refining effect was also not found in the extruded alloy. Then, it is possible that the heat treatment below 500 ºC or adding more Zr (higher than the maximum solubility) will result in the grain refinement by the pinning effect of Zr precipitations. As for the alloy C and alloy D, the grain growth was restricted during the heat treatment, and also the growth of recrystallization grains was inhibited during extrusion due to the Mn and the Mn_2Sc particles, respectively. In fact, the Mn_2Sc should be corrected to be $(Mn,Mg)_{23}Sc_6$ in view of the present calculation. Fang et al. [125] assumed the

phase as Mn_2Sc after the composition analysis by EDS, indicating 59.29 at. % Mg (interference by the matrix), 10.29 at. % Sc, and 30.42 at. % Mn. From the present calculation, at equilibrium, the amount of cbcc-Mn in the alloy C and $(Mn,Mg)_{23}Sc_6$ in the alloy D is 0.35 wt. % and 0.65 wt. %, respectively.

In another study of Fang et al. [126], the age-hardening response of Mg-5wt.%Gd-1.1wt.%Mn-0.8wt.%Sc alloy was examined under different solution treatment conditions. One of their result which is the Vickers hardness of the alloy heat treated at 200, 250, 300, and 350 ºC after solution treatment at 610 ºC for 24 h can be compared with the present thermodynamic calculation as shown in Fig. 5.2. The phase fraction vs. temperature diagrams of Mg-5wt.%Gd-1.1wt.%Mn-0.8wt.%Sc alloy was calculated. According to the Fang et al. [126], the tiny Mn_2Sc discs (diameter ~20 nm, thickness ~5nm) and very thin Mg-Gd plates (diameter ~50-150 nm, thickness ~1.5 nm) were observed by transmission electron microscopy (TEM) to be parallel to the hcp-Mg basal plane. The dense precipitation of these phases was considered to be mainly responsible for the greatly improved age-hardening response for the alloy. This is in good agreement with the present thermodynamic calculation. It can be interpreted easily by looking the diagram in Fig. 5.2(b) that the formation of the Mn_2Sc (tiny Mn_2Sc discs) and Mg_5Gd (very thin Mg-Gd plates) increases at lower temperature (maximum at 200 ºC and minimum at 350 ºC).

The next example is shown for the Mg alloys containing Si and RE. Recently, many wrought and casting Mg alloys have been developed. One of the most important aspects considered in the development of wrought Mg alloy is the formability. RE has been known to improve ductility of Mg significantly. But the alloy system is still limited mostly to Mg-Zn based alloys. Si is one of the common impurity elements in Mg to be well controlled. If Si is precipitated as Mg_2Si having Chinese script morphology, it is known that Mg_2Si decreases creep resistance of Mg alloy. So, a certain alloying elements like Sn, Sb, As, P, etc. were added to control the morphology of Mg_2Si and improve the mechanical properties (strength and creep resistance) [127, 128]. As can be seen in the present thermodynamic evaluations, the Si_xRE_y intermetallic phases are thermodynamically much more stable than other usual precipitates such as $Mg_{17}Al_{12}$, $Mg_{51}Zn_{20}$, Mg_2Si, etc., appearing in conventional Mg alloys. This means that Si_xRE_y phase can be easily formed in the Mg alloy

than other intermetallic phases. For example, the iso-thermal phase diagram of the Mg-Si-RE system at 400 ºC is calculated in Fig. 5.3. Because there is no phase diagram study on the ternary Mg-Si-La system, no ternary phases was assumed in this calculation. According to the calculation result, the formation of Mg_2Si can be suppressed when the mass ratio of La/Si > 5. Similar results can be obtained with other RE addition. This means that Mg alloy with Si impurity can be treated with RE (or mischmetal, RE alloys) to prevent Mg_2Si phase and form more thermally stable Si_xRE_y phase potentially improving mechanical properties of Mg casting alloy. In the case of wrought Mg alloy, solute RE in hcp Mg contributes the improvement of ductility. When Si is contained as an impurity element in this Mg alloy, the solubility of RE in hcp Mg can be significant decreased by the formation of Si_xRE_y phase. So, such a loss should be taken into account to adjust overall RE content in wrought Mg-RE alloy.

RE in Mg alloy can induce texture weakening. There were several interpretations about role of RE to texture weakening, but it is generally accepted that RE dissolved in Mg matrix can play a role to texture weakening [21]. As RE elements cost higher than other metallic elements, the main concern of the usage of Mg-RE alloy is the reduction of RE content in Mg alloy. Looking for the potential alloying elements for the wrought Mg alloy with RE, it has been known that Zn is the most well-known element because the addition of Zn can reduce the amount of RE required to have texture weakening of Mg alloy. In the recent review of Jung et al. [21], the critical amounts of RE required for the texture weakening of binary Mg-RE alloys are usually much lower than their maximum solubility limits at binary Mg-RE systems. For example, only 36% Nd, 8% Y, and 3% Gd are required to induce texture weakening during rolling and recrystallization, compared to their solubility limits at 400 ºC. When RE is less than the critical solubility, no significant texture weakening can be observed. Therefore, the Mg-Zn alloy containing small amount of RE can be good candidate for wrought Mg alloy and has been studied actively.

The calculated solvus of the hcp Mg at 400 ºC for the Mg-Al-RE and Mg-Zn-RE systems at the Mg-rich corner are presented in Fig. 5.4. The equilibrium solubility of RE is smaller in the Mg-Al-RE system than in the Mg-Zn-RE system when the same amount of Al and Zn is added in Mg-RE alloy. The texture weakening is often found in the Mg-Zn-RE system [49, 129-135]. According

to Jung et al. [21], this was explained by the formation of the Mg-Zn-RE cluster in Mg matrix which can be very effective for grain boundary and dislocation pinning in Mg matrix during the deformation and recrystallization. However, no noticeable texture weakening has been reported in the Mg-Al-RE alloy system because the dissolved RE in Mg-Al-RE alloys is lower than the critical RE content to induce texture weakening.

In this study, the influence of Sn and Mn to RE solubility in Mg can be calculated and this can be used to evaluate the possibility of Sn and Mn as alloying elements for the Mg-RE wrought alloy. According to the calculated phase diagrams of the Mg-Mn-Gd and Mg-Sn-Gd systems in Fig. 5.5, the addition of Sn continuously decreases the solubility of RE in hcp-Mg by the formation of the ternary compound, MgRESn, and the amount of RE can become nearly zero with high amount of Sn addition. On the other hand, Mn leads to insignificant change in the solubility of RE. This results are closely related to the interaction energy between RE and Sn or Mn. The enthalpy of mixing of liquid is a good index showing the interaction energy. As already mentioned, the enthalpy of mixing value is about 8 to -8 kJ mol^{-1} for the Mn-RE, -20 to -32 kJ mol^{-1} for the Zn-RE, -30 to -40 kJ mol^{-1} for the Al-RE, and -50 to -65 kJ mol^{-1} for the Sn-RE. Therefore, the addition of Al or Sn results in the formation of stable ternary compounds reducing the solubility of RE in hcp-Mg, and no texture weakening can be expected for Mg-Sn-RE alloy like Mg-Al-RE alloy. On the other hand, the decrease of RE solubility is moderate for the Zn addition, and the Mn addition does not change significantly the RE solubility. For the Mg-Mn-RE alloy, however, the formation of the Mg-Mn-RE cluster in Mg matrix like Mg-Zn-RE system cannot be expected due to the low interaction energy (even repulsive energy between Mn and light RE). Either the texture weakening in the Mg-Mn-RE alloy is similar to the Mg-RE alloy or there may be only a slight improvement (or diminishment) of the texture modification by the Mn addition compared to binary Mg-RE alloy. In fact, the texture weakening was found in the Mg-1 wt.% Mn with 0.05 to 1 wt.% Ce alloys compared to the Mg-1 wt.% Mn [136]. On the other hand, basal texture was intensified in the Mg-0.4 wt.% Ce with addition of Mn from 0 to 1.4 wt.% [137]. In summary, the Mg-Mn-RE alloy can be potential wrought Mg alloys with less strong texture, but Mg-Sn-RE and Mg-Si-RE alloys are not recommended.

Table 5.1. Chemical compositions of the investigated alloys (mass%).

Alloys	Gd	Zr	Mn	Sc	Mg
(A)	10.03 (10)	-			Bal.
(B)	10.16 (10)	0.73 (0.8)			Bal.
(C)	9.94 (10)		0.91 (0.8)		Bal.
(D)	9.87 (10)		0.86 (0.8)	0.61 (0.7)	Bal.

*The target compositions are shown inside parentheses.

Table 5.2. The average grain sizes (μm) of the alloys at various states.

Alloys	As-cast	Homogenized 520 ºC / 10 h	Homogenized 520 ºC / 20 h	Homogenized 520 ºC / 40 h	As-extruded
(A)	685	810	938	1025	18
(B)	49	82	147	336	19
(C)	587	603	627	814	11
(D)	166	168	175	173	6

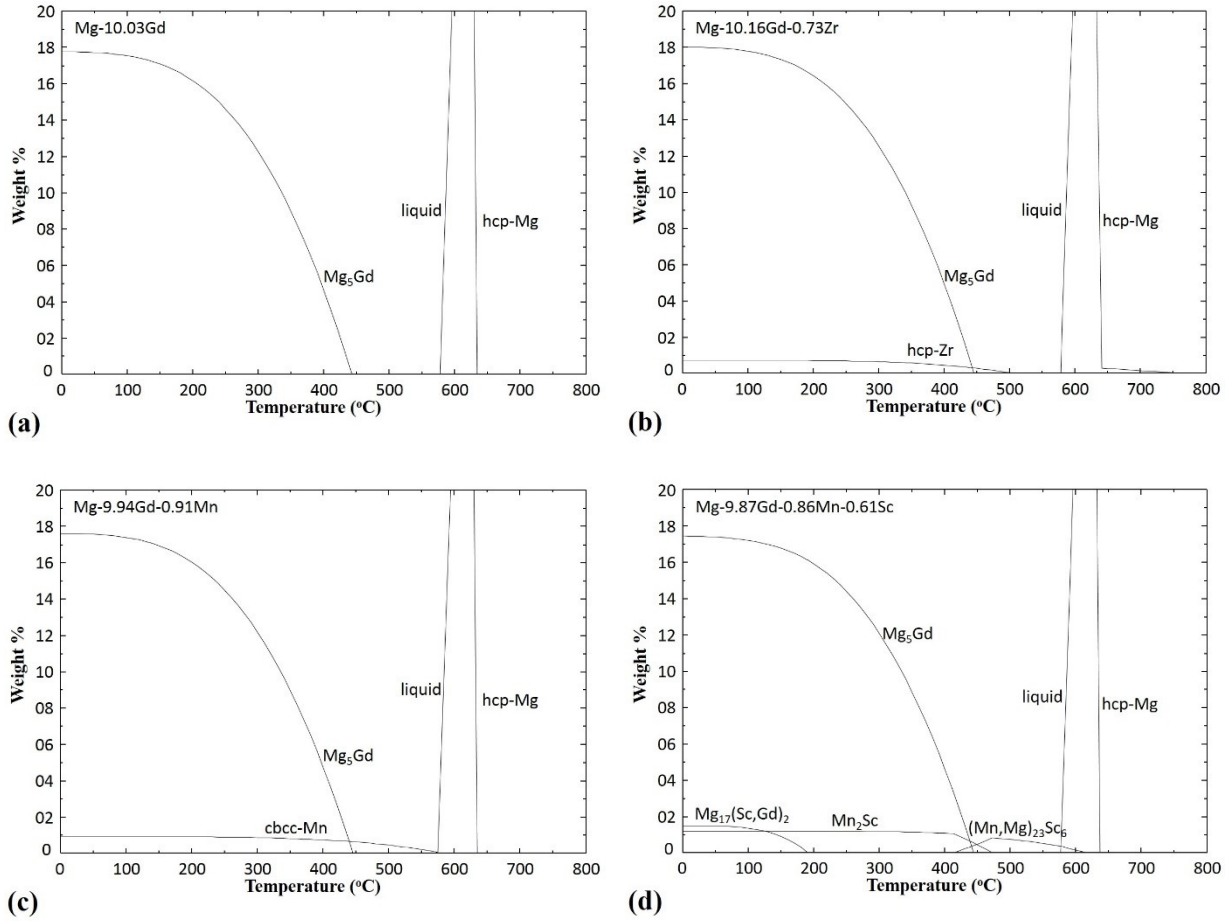


Fig. 5.1. The phase fraction vs. temperature diagrams of the Mg-Gd alloys with the addition of Zr, Mn, and Mn+Sc.

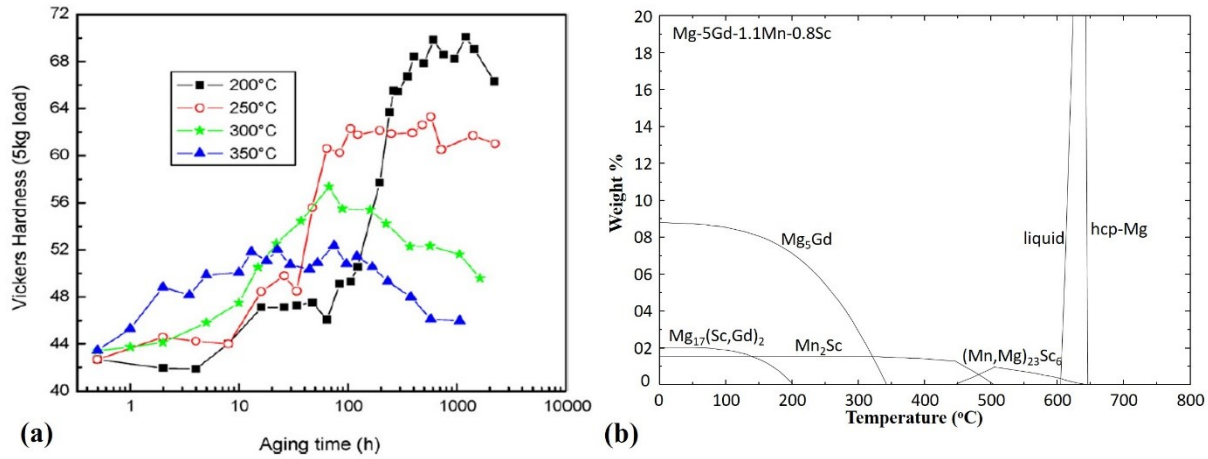


Fig. 5.2. (a) Age-hardening response at different temperatures after solution treated at 610 °C for 24 h [126], and (b) the phase fraction vs. temperature diagrams of the Mg-Gd-Mn-Sc alloy.

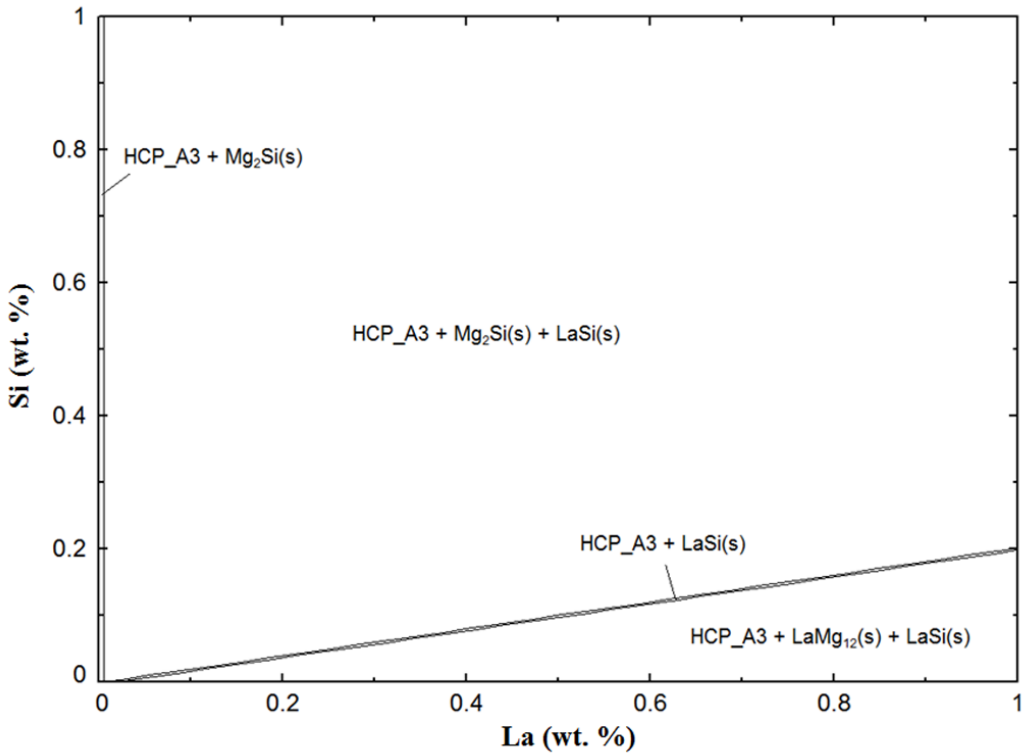


Fig. 5.3. Calculated Mg-rich corner of the Mg-Si-La system at 400 °C with an assumption of no ternary phases.

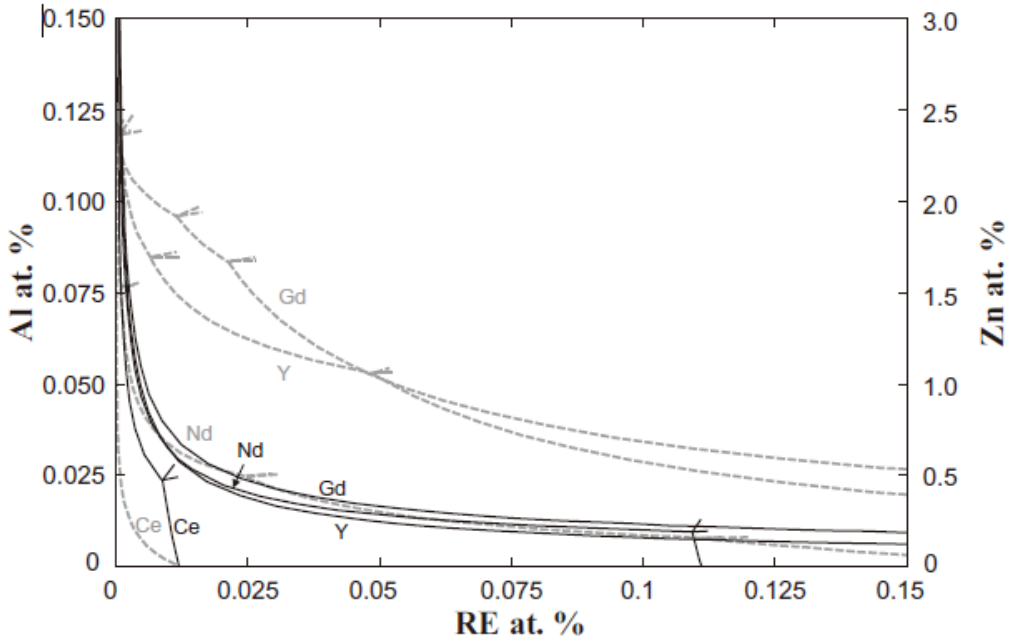
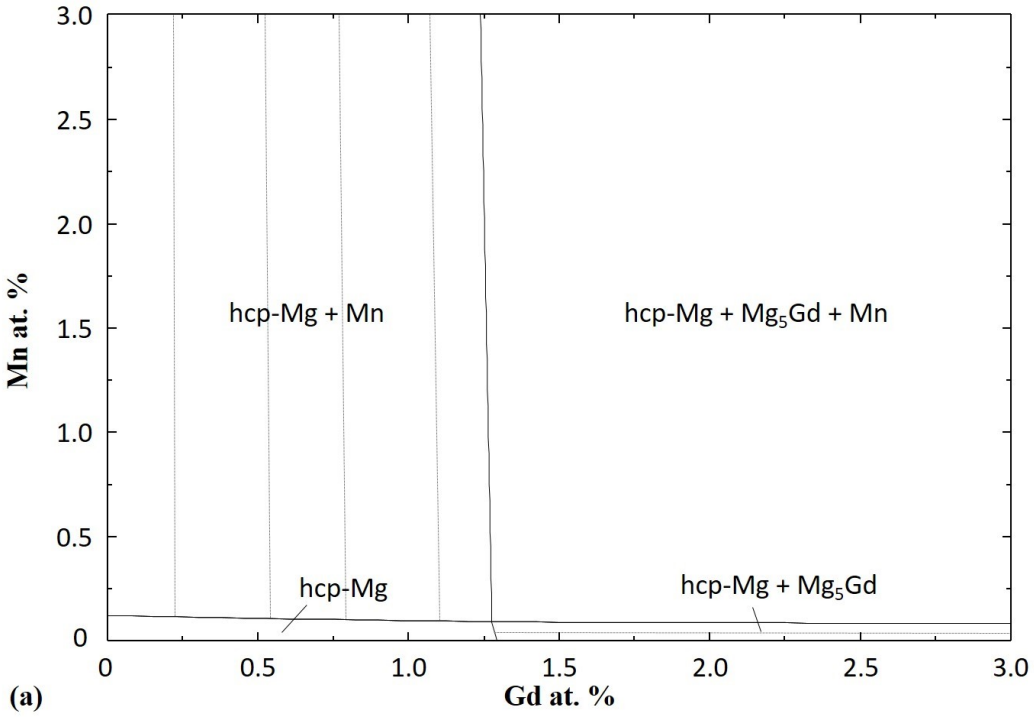


Fig. 5.4. Calculated solvus of hcp-Mg at 400 ºC for the Mg-Al-RE system (solid lines; y-axis left side) and Mg-Zn-RE system (dotted lines; y-axis right side) [21].



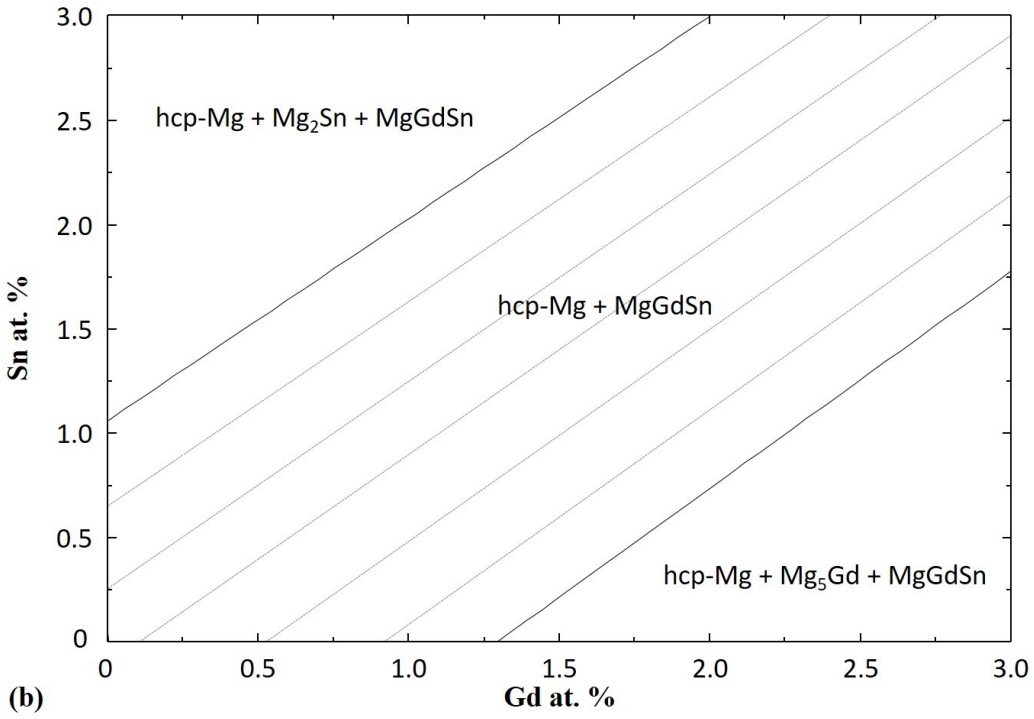


Fig. 5.5. Calculated phase diagrams (Mg-rich corner) at 400 °C for the Mg-Mn-Gd and Mg-Sn-Gd systems.

6. Summary and future work

The thermodynamic optimizations of the Mn-RE (13 binary), Si-RE (13 binary), and Sn-RE (13 binary) systems, and the Mg-RE-X (X = Mn, Si, and Sn) (9 ternary) systems through critical evaluations of experimental data and systematic analysis approach were performed to develop the thermodynamic database for the Mg alloys with RE metals containing Mn, Si, and Sn as part of the large thermodynamic database for the Mg alloys. All the optimizations and the calculations were carried out using the Gibbs energy minimization software, FactSage. The Gibbs energy of liquid phase was described by using the Modified Quasichemical Model and the solid solution phases such as bcc, fcc, dhcp, and laves-C15, etc. were described by adopting the Compound Energy Formalism with appropriate sublattice model. If necessary, the magnetic properties of solid phases were also taken into account to the Gibbs energy functions. In the main body of thesis, the introduction of RE and their alloying behavior as well as the mechanical and chemical properties of Mg alloys containing RE were reviewed from literature. In addition, the CALPHAD approach, which was used in the present works, was concisely described followed by stating the methodology including the thermodynamic model equations and the experimental works. Then, the optimization results are briefly summarized with the key points and some challenges during the work. The details of the optimizations are discussed in Appendices.

In Appendix I, a critical evaluation and optimization of all available phase diagram and thermodynamic data for the Mn-light RE (La, Ce, Pr, Nd and Sm) systems were conducted to obtain reliable thermodynamic functions of all the phases in the system.

In Appendix II, the Mn-Y and Mn-Gd systems as parts of Mn-heavy RE were optimized with the experimental data. At the time, there were difficulties to conduct the optimizations of the systems with the other heavy RE due to the limited experimental data.

In Appendix III, the thermodynamic optimization of the Mn-heavy RE (Tb, Dy, Ho, Er, Tm and Lu) systems was performed. The Mn-Dy system was experimentally re-evaluated by conducting phase diagram measurements using DSC and the enthalpy of formation measurements using

solution calorimetry. The systematic trend and similarity in the phase diagram and the thermodynamic properties across the lanthanide series was taken into account to overcome the shortage of experimental data. This study also proposes the undetermined phase diagram of the Mn-Tm and Mn-Lu systems.

In Appendix IV, the thermodynamic optimization of the Si-light RE (La, Ce, Pr, Nd and Sm) systems was conducted to obtain reliable thermodynamic functions for all the phases in the systems. The systematic analysis was applied to resolve inconsistencies in the experimental data in the present Si-RE systems and to predict the phase diagram of the Si-Sm system.

In Appendix V, a critical evaluation and optimization of all available phase diagrams and thermodynamic data of the Si-heavy RE (Gd, Tb, Dy, Ho, Er, Tm, Lu and Y) systems was conducted to obtain reliable thermodynamic functions for all the phases. The systematic trends were found in phase diagram data and thermodynamic properties through the Si-RE system, which helped to assess the unexplored phase diagrams of the Si-Sm, Si-Tm and Si-Lu systems.

In Appendix VI, a critical evaluation and optimization of all available phase diagram and thermodynamic data for the Sn-light RE (La, Ce, Pr, Nd and Sm) systems were conducted to obtain reliable thermodynamic functions of all the phases in the system.

In Appendix VII, the thermodynamic optimization of the Sn-heavy RE (Gd, Tb, Dy, Ho, Er, Tm, Lu and Y) systems was conducted to obtain reliable thermodynamic functions for all the phases. The systematic trends were found in phase diagram data and thermodynamic properties through the Sn-RE system, which helped to assess the only partially explored phase diagrams of the Sn-Gd, Sn-Er and Si-Lu systems.

In Appendix VIII, the thermodynamic optimization of the Mg-RE-X (X = Mn, Si, Sn) (9 ternary) systems was carried out. The Mg-Sn-Nd and Mg-Sn-Gd systems were selected for the experimental investigation to overcome the limited experimental data. The phase equilibria of the Mg-Sn-Nd and Mg-Sn-Gd systems at 500-700 ºC were determined by the equilibrated alloy

method. The existence of the ternary compounds, MgNd(Gd)Sn, MgNd(Gd)Sn_2, and $Mg_4Nd_2Sn_3$ was revealed with the respective phase equilibria.

Finally, several examples showed to discuss the potential applications of the optimized thermodynamic database along with the thermodynamic calculations. For the Mg-Gd, Mg-Gd-Zr, Mg-Gd-Zn, and Mg-Gd-Mn-Sc alloys, the experimental study of the precipitation behaviors to the grain refinement as well as age-hardening response was in good agreement with the present calculations. In addition, the effect of RE to the restriction of the Mg_2Si phase in wrought Mg alloys was discussed with the phase diagram calculation. The influence of the Mn or Sn addition on the formability of wrought Mg-RE alloy was also discussed.

In the present study, although only 9 ternary systems have been optimized due to the limitation of the experimental information, it may be possible to adopt the reasonable assumption in the phase equilibria and the thermodynamic properties of the other ternary systems based on the systematics through the RE series. However, if possible, it is always welcome to verify the phase equilibria or the thermodynamic properties by performing experiments using key alloys in collaboration with other research groups. In this approach, in future, the database can expand to the complete Mg-RE-X systems as well as the addition of the different types of RE together (misch metal), Mg-X-RE1-RE2-RE3 etc.

7. Contributions to original knowledge

1. The Mn-RE (13 binary), Si-RE (13 binary), Sn-RE (13 binary), and the Mg-RE-X (X = Mn, Si, and Sn) (9 ternary) systems were thermodynamically and systematically assessed for the first time.

2. The systematic analysis and optimization allow the appropriate estimation of the unexplored phase diagrams and unknown thermodynamic properties in the binary Mn-RE, Si-RE, and Sn-RE systems.

2.1. The new phase diagrams of the Mn-Sm, -Tb, -Ho, -Er, -Tm, -Lu, and Si-Sm, -Tm, -Lu, and Sn-Gd, -Er, -Lu systems were proposed by the CALPHAD approach.

2.2. Gibbs energy of liquid and RE compounds along with the heat capacity, enthalpy, and entropy were evaluated and reasonably determined by the CALPHAD approach.

3. Phase diagram of Mn-Dy system was studied using DSC measurement and equilibration/quenching followed by the XRD and EPMA analysis. In addition, the enthalpy of formation of Mn_2Dy was determined by a solution calorimetry. The problem of the previous phase diagram was revised based on new phase diagram measurement.

4. The phase diagrams of the Mg-Sn-Nd and Mg-Sn-Gd systems at 500 to 700 ºC were determined by the equilibration/quenching method using sealed capsule. The ternary compounds, MgNd(Gd)Sn, MgNd(Gd)Sn_2, and $Mg_4Nd_2Sn_3$ were found with the respective phase equilibria. The existence of the MgNd(Gd)Sn_2 and $Mg_4Nd_2Sn_3$ compounds were established for the first time.

8. References

[1] B.L. Mordike, T. Ebert, Mater. Sci. Eng., A, A302 (2001) 37-45.
[2] M. Pekguleryuz, In: Proc. 2013. pp. 152-196.
[3] R.L. Edgar, Global Overview on Demand and Applications for Magnesium Alloys, in: Magnesium Alloys and their Applications, Wiley-VCH Verlag GmbH & Co. KGaA, 2006, pp. 1-8.
[4] M.S. Dargusch, G.L. Dunlop, K. Pettersen, In: Proc. 1998. pp. 277-282.
[5] A. Boby, U.T.S. Pillai, B.C. Pai, Indian Foundry J., 57 (2011) 29-37.
[6] E. Aghion, B. Bronfin, H. Friedrich, Z. Rubinovich, In: Proc. 2004. pp. 167-172.
[7] H. Friedrich, S. Schumann, Materialwiss. Werkstofftech., 32 (2001) 6-12.
[8] B.C. Pai, U.T.S. Pillai, P. Manikandan, A. Srinivasan, Trans. Indian Inst. Met., 65 (2012) 601-606.
[9] B. Mordike, P. Lukáč, Physical Metallurgy, in: Magnesium Technology, Springer Berlin Heidelberg, 2006, pp. 63-107.
[10] C.W. Bale, E. Bélisle, P. Chartrand, S.A. Decterov, G. Eriksson, K. Hack, I.H. Jung, Y.B. Kang, J. Melançon, A.D. Pelton, C. Robelin, S. Petersen, Calphad, 33 (2009) 295-311.
[11] I. Ansara, C.A.o.M.S.C. 507, E. Commission, E.C.i.t.F.o. Scientific, T.R.C. 507, COST 507: Thermochemical Database for Light Metal Alloys, European Commission, Directorate-General XII, Science, Research and Development, 1994.
[12] Y.B. Kang, L.L. Jin, P. Chartrand, A.E. Gheribi, K.W. Bai, P. Wu, Calphad-Computer Coupling of Phase Diagrams and Thermochemistry, 38 (2012) 100-116.
[13] L. Jin, D. Kevorkov, M. Medraj, P. Chartrand, The Journal of Chemical Thermodynamics, 58 (2013) 166-195.
[14] L. Jin, PhD Thesis, Ecole Polytechnique, Montreal, 2012.
[15] L. Jin, Y.-B. Kang, P. Chartrand, C.D. Fuerst, Calphad, 34 (2010) 456-466.
[16] L. Jin, Y.-B. Kang, P. Chartrand, C.D. Fuerst, Calphad, 35 (2011) 30-41.
[17] Z. Zhu, A.D. Pelton, Journal of Alloys and Compounds, 641 (2015) 261-271.
[18] Z. Zhu, A.D. Pelton, Journal of Alloys and Compounds, 641 (2015) 249-260.
[19] L.L. Rokhlin, Magnesium Alloys Containing Rare Earth Metals: Structure and Properties, Taylor & Francis, 2003.
[20] B.J. Beaudry, K.A. Gschneidner Jr, Chapter 2 Preparation and basic properties of the rare earth metals, in: Karl A. Gschneidner, Jr., E. LeRoy (Eds.) Handbook on the Physics and Chemistry of Rare Earths, Elsevier, 1978, pp. 173-232.
[21] I.-H. Jung, M. Sanjari, J. Kim, S. Yue, Scripta Materialia, 102 (2015) 1-6.
[22] R. Ferro, S. Delfino, G. Borzone, A. Saccone, G. Cacciamani, J. Phase Equilib., 14 (1993) 273-279.
[23] R. Ferro, G. Cacciamani, A. Saccone, G. Borzone, Journal of Alloys and Compounds, 320 (2001) 326-340.
[24] R. Ferro, S. Delfino, R. Capelli, A. Borsese, J. Less-Common Met., 42 (1975) 13-18.
[25] R. Ferro, S. Delfino, J. Less-Common Met., 68 (1979) P23-P29.
[26] A. Saccone, G. Cacciamani, D. Maccio, G. Borzone, R. Ferro, Intermetallics, 6 (1997) 201-215.
[27] A. Saccone, D. Maccio, S. Delfino, R. Ferro, Intermetallics, 10 (2002) 903-913.

[28] C. Colinet, A. Pasturel, A. Percheron-Guegan, J.C. Achard, J. Less-Common Met., 102 (1984) 239-249.
[29] S.P. Yatsenko, A.A. Semyannikov, B.G. Semenov, K.A. Chuntonov, J. Less-Common Met., 64 (1979) 185-199.
[30] V.N. Eremenko, I.M. Obushenko, Poroshk. Metall. (Kiev), (1980) 53-61.
[31] S. Delfino, A. Saccone, R. Ferro, J. Less-Common Met., 102 (1984) 289-310.
[32] S.P. Yatsenko, A.A. Semyannikov, H.O. Shakarov, E.G. Fedorova, J. Less-Common Met., 90 (1983) 95-108.
[33] R. Ferro, A. Saccone, S. Delfino, D. Maccio, M. Giovannini, Powder Metall. Met. Ceram., 36 (1997) 117-127.
[34] G. Borzone, G. Cacciamani, R. Ferro, CALPHAD: Comput. Coupling Phase Diagrams Thermochem., 14 (1990) 139-149.
[35] K.A. Gschneidner, Jr., O.D. McMasters, Monatsh. Chem., 102 (1971) 1499-1515.
[36] G. Borzone, A. Borsese, S. Delfino, R. Ferro, Z. Metallkd., 76 (1985) 208-213.
[37] R. Ferro, G. Borzone, G. Cacciamani, Thermochim. Acta, 129 (1988) 99-113.
[38] V.N. Eremenko, M.V. Bulanova, P.S. Martsenyuk, In: Proc. 1990. pp. 70-100.
[39] A. Yassin, R. Castanet, J. Alloys Compd., 307 (2000) 191-198.
[40] C. Colinet, A. Pasturel, A. Percheron-Guegan, J.C. Achard, J. Less-Common Met., 102 (1984) 167-177.
[41] A. Saccone, S. Delfino, R. Ferro, J. Less-Common Met., 143 (1988) 1-23.
[42] G. Borzone, G. Cacciamani, R. Ferro, J. Charles, J. Hertz, J. Less-Common Met., 128 (1987) 297-312.
[43] K.A. Gschneidner, Jr., N.A. Kippenhan, O.D. McMasters, Thermochemistry of the rare earths. I. Rare earth oxides. II. Rare earth oxysulfides. III. Rare earth compounds with boron, tin, lead, phosphorus, arsenic, antimony, bismuth, copper, and silver, in, Iowa State Univ. Sci. Technol., 1973, pp. 67 pp.
[44] K.A. Gschneidner, Jr., J. Less-Common Metals, 17 (1969) 1-12.
[45] M.V. Bulanova, A.N. Mikolenko, K.A. Meleshevich, G. Effenberg, P.A. Saltykov, Z. Metallkd., 90 (1999) 216-222.
[46] M.V. Bulanova, P.S. Martsenyuk, Poroshk. Metall. (Kiev), (1991) 82-85.
[47] L.L. Rokhlin, Met. Sci. Heat Treat., 48 (2006) 487-490.
[48] S.M. Zhu, M.A. Gibson, M.A. Easton, J.F. Nie, Scr. Mater., 63 (2010) 698-703.
[49] M. Sanjari, S.F. Farzadfar, T. Sakai, H. Utsunomiya, E. Essadiqi, I.H. Jung, S. Yue, Mat. Sci. Eng. A, 561 (2012) 191-202.
[50] N. Stanford, M.R. Barnett, Mat. Sci. Eng. A, 496 (2008) 399-408.
[51] K. Hantzsche, J. Bohlen, J. Wendt, K.U. Kainer, S.B. Yi, D. Letzig, Scripta Mater., 63 (2010) 725-730.
[52] T. Al-Samman, X. Li, Mat. Sci. Eng. A, 528 (2011) 3809-3822.
[53] D. Wu, R.S. Chen, E.H. Han, J. Alloy. Compd., 509 (2011) 2856-2863.
[54] J.P. Hadorn, K. Hantzsche, S. Yi, J. Bohlen, D. Letzig, S.R. Agnew, Metall. Mater. Trans. A, 43 (2012) 1363-1375.
[55] S. Sandlöbes, M. Friák, S. Zaefferer, A. Dick, S. Yi, D. Letzig, Z. Pei, L.F. Zhu, J. Neugebauer, D. Raabe, Acta Mater., 60 (2012) 3011-3021.
[56] S. Sandlöbes, S. Zaefferer, I. Schestakow, S. Yi, R. Gonzalez-Martinez, Acta Mater., 59 (2011) 429-439.
[57] S.R. Agnew, M.H. Yoo, C.N. Tomé, Acta Mater., 49 (2001) 4277-4289.

[58] S. Sandlöbes, Z. Pei, M. Friák, L.F. Zhu, F. Wang, S. Zaefferer, D. Raabe, J. Neugebauer, Acta Mater., 70 (2014) 92-104.
[59] W.Y. Wang, S.L. Shang, Y. Wang, Z.-G. Mei, K.A. Darling, L.J. Kecskes, S.N. Mathaudhu, X.D. Hui, Z.-K. Liu, Mater. Res. Lett., 2 (2014) 29-36.
[60] M.H. Yoo, J.R. Morris, K.M. Ho, S.R. Agnew, Metall. Mater. Trans. A, 33 (2002) 813-822.
[61] S.A. Farzadfar, E. Martin, M. Sanjari, E. Essadiqi, S. Yue, J. Mater. Sci., 47 (2012) 5488-5500.
[62] N. Stanford, G. Sha, J.H. Xia, S.P. Ringer, M.R. Barnett, Scripta Mater., 65 (2011) 919-921.
[63] N. Stanford, G. Sha, A. La Fontaine, M.R. Barnett, S.P. Ringer, Metall. Mater. Trans. A, 40 (2009) 2480-2487.
[64] J.D. Robson, Metall. Mater. Trans. A, 45 (2014) 3205-3212.
[65] J. Hadorn, K. Hantzsche, S. Yi, J. Bohlen, D. Letzig, J. Wollmershauser, S. Agnew, Metall. Mater. Trans. A, 43 (2012) 1347-1362.
[66] H. Kawamura, S. Yoshimoto, In: Proc. 2005. pp. 499-502.
[67] S. Huang, J. Wang, F. Hou, Y. Li, F. Pan, Mater. Lett., 137 (2014) 143-146.
[68] J. Kim, Y. Kawamura, In: Proc. 2011. pp. 229-232.
[69] M. Yamasaki, Y. Kawamura, Scr. Mater., 60 (2008) 264-267.
[70] Y. Kawamura, M. Yamasaki, Mater. Trans., 48 (2007) 2986-2992.
[71] F. Lu, A. Ma, J. Jiang, D. Yang, Q. Zhou, Rare Met. (Beijing, China), 31 (2012) 303-310.
[72] A. Inoue, Y. Kawamura, M. Matsushita, K. Hayashi, J. Koike, J. Mater. Res., 16 (2001) 1894-1900.
[73] H. Yokobayashi, K. Kishida, H. Inui, M. Yamasaki, Y. Kawamura, MRS Online Proc. Libr., 1295 (2011) No pp. given.
[74] K. Kishida, A. Inoue, H. Yokobayashi, H. Inui, Scr. Mater., 89 (2014) 25-28.
[75] K. Kishida, H. Yokobayashi, H. Inui, M. Yamasaki, Y. Kawamura, Intermetallics, 31 (2012) 55-64.
[76] J.-O. Andersson, T. Helander, L. Höglund, P. Shi, B. Sundman, Calphad, 26 (2002) 273-312.
[77] J.-H. Park, T.-H. Ahn, H.-S. Choi, J.-M. Chung, D.-I. Kim, K.H. Oh, H.N. Han, Microsc. Microanal., 19 (2013) 21-24.
[78] X. Huang, K. Suzuki, Y. Chino, Mat. Sci. Eng. A, 560 (2013) 232-240.
[79] NIST, 2002. www.nist.gov, Gaithersburg., in.
[80] J.-Y. Lee, Y.-S. Yun, B.-C. Suh, N.-J. Kim, W.-T. Kim, D.-H. Kim, J. Alloy. Compd., 589 (2014) 240-246.
[81] T. Wang, L. Jiang, R.K. Mishra, J.J. Jonas, Metall. Mater. Trans. A, 45 (2014) 4698-4709.
[82] R.H. Davies, A.T. Dinsdale, J.A. Gisby, J.A.J. Robinson, S.M. Martin, CALPHAD: Comput. Coupling Phase Diagrams Thermochem., 26 (2002) 229-271.
[83] K. Shobu, CALPHAD: Comput. Coupling Phase Diagrams Thermochem., 33 (2009) 279-287.
[84] S.L. Chen, S. Daniel, F. Zhang, Y.A. Chang, X.Y. Yan, F.Y. Xie, R. Schmid-Fetzer, W.A. Oates, CALPHAD: Comput. Coupling Phase Diagrams Thermochem., 26 (2002) 175-188.
[85] D.W. Kim, B.C. Suh, M.S. Shim, J.H. Bae, D.H. Kim, N. Kim, Metall. Mater. Trans. A, 44 (2013) 2950-2961.
[86] R. Schmid, Y.A. Chang, Calphad, 9 (1985) 363-382.
[87] A.D. Pelton, S.A. Degterov, G. Eriksson, C. Robelin, Y. Dessureault, Metall. Mater. Trans. B, 31B (2000) 651-659.
[88] A.D. Pelton, P. Chartrand, Metall. Mater. Trans. A, 32A (2001) 1355-1360.

[89] I.-H. Jung, D.-H. Kang, W.-J. Park, N.J. Kim, S. Ahn, Calphad, 31 (2007) 192-200.
[90] D. Nassyrov, I.-H. Jung, Calphad, 33 (2009) 521-529.
[91] A.D. Pelton, M. Blander, Metall. Trans. B, 17B (1986) 805-815.
[92] P. Wu, G. Eriksson, A.D. Pelton, M. Blander, ISIJ Int., 33 (1993) 26-35.
[93] A.D. Pelton, M. Blander, In: Proc. 1984. pp. 281-294.
[94] A.D. Pelton, Calphad, 25 (2001) 319-328.
[95] M. Hillert, B. Jansson, B. Sundman, Z. Metallkd., 79 (1988) 81-87.
[96] A.T. Dinsdale, Calphad, 15 (1991) 317-425.
[97] J. Leitner, P. Vonka, D. Sedmidubsky, P. Svoboda, Thermochim. Acta, 497 (2010) 7-13.
[98] G. Inden, Dusseldorf, Germany, , (1976) 111.
[99] M. Hillert, M. Jarl, Calphad, 2 (1978) 227-238.
[100] R.F. Zhang, B.X. Liu, Appl. Phys. Lett., 81 (2002) 1219-1221.
[101] R.F. Zhang, B.X. Liu, Philos. Mag. Lett., 85 (2005) 283-287.
[102] R.F. Zhang, S.H. Sheng, B.X. Liu, Chem. Phys. Lett., 442 (2007) 511-514.
[103] A.R. Miedema, P.F. De Chatel, F.R. De Boer, Physica B+C (Amsterdam), 100 (1980) 1-28.
[104] H. Zhang, S. Shang, J.E. Saal, A. Saengdeejing, Y. Wang, L.-Q. Chen, Z.-K. Liu, Intermetallics, 17 (2009) 878-885.
[105] H.R. Kirchmayr, W. Lugscheider, Z. Metallkd., 58 (1967) 185-188.
[106] H.R. Kirchmayr, W. Lugscheider, Z. Metallk., 61 (1970) 22-23.
[107] M. Zydzik, M. Smids, M.-A. Van Ende, I.-H. Jung, Calphad, 46 (2014) 1-17.
[108] M. Hillert, M. Selleby, B. Sundman, Acta Mater., 57 (2009) 5237-5244.
[109] F. Weitzer, K. Hiebl, P. Rogl, J. Solid State Chem., 98 (1992) 291-300.
[110] V.N. Eremenko, M.V. Bulanova, P.S. Martsenyuk, V.E. Listovnichii, Poroshk. Metall. (Kiev), (1989) 79-90.
[111] A. Saccone, D. Maccio, R. Ferro, J. Alloys Compd., 201 (1993) L9-L11.
[112] D.A. Petrov, M.S. Mirgalovskaya, I.A. Strel'nikova, E.M. Komova, Tr. Inst. Metall., Akad. Nauk SSSR, (1957) 142-143.
[113] X. Zhang, D. Kevorkov, I.H. Jung, M. Pekguleryuz, J Alloy Compd, 482 (2009) 420-428.
[114] A. Mostafa, M. Medraj, J Alloy Compd, 608 (2014) 247-257.
[115] C. Antion, PhD Thesis, Institut National Polytechnique de Grenoble, 2003.
[116] F. Wrubl, M. Pani, P. Manfrinetti, P. Rogl, J Solid State Chem, 182 (2009) 716-724.
[117] O.F. Zmii, E.I. Gladishevskii, Visnik L'viv. un-tu. Ser. khim., (1974) 24-26.
[118] S.K. Dhar, P. Manfrinetti, A. Palenzona, J. Alloys Compd., 252 (1997) 24-27.
[119] M.E. Drits, E.M. Padezhnova, T.V. Dobatkina, Redk. Metally V Tsvet. Splavakh, (1975) 5-11.
[120] P. Manfrinetti, A. Provino, K.A. Gschneidner, J Alloy Compd, 482 (2009) 81-85.
[121] Y. Guo, PhD Thesis, Northeastern University, Shenyang, 2009.
[122] C. Ma, D. Zhang, Y. Fan, F. Qi, J. Li, J. Phase Equilib. Diffus., 34 (2013) 9-16.
[123] H.D. Zhao, G.W. Qin, Y.P. Ren, W.L. Pei, Y. Guo, J. Alloys Compd., 481 (2009) 140-143.
[124] H.-d. Zhao, Y.-p. Ren, W.-l. Pei, Y. Guo, D. Chen, G.-w. Qin, Zhongguo Youse Jinshu Xuebao, 20 (2010) 177-181.
[125] X.Y. Fang, D.Q. Yi, J.F. Nie, X.J. Zhang, B. Wang, L.R. Xiao, J. Alloys Compd., 470 (2009) 311-316.
[126] X.Y. Fang, D.Q. Yi, J.F. Nie, J. Alloys Compd., 486 (2009) 900-904.
[127] I.-H. Jung, D.H. Kang, W.-J. Park, N.J. Kim, S.H. Ahn, Int. J. Mater. Res., 98 (2007) 807-815.

[128] J.J. Kim, D.H. Kim, K.S. Shin, N.J. Kim, Scripta Mater., 41 (1999) 333-340.
[129] L.W.F. Mackenzie, M.O. Pekguleryuz, Scripta Mater., 59 (2008) 665-668.
[130] P. Dobroň, J. Balík, F. Chmelík, K. Illková, J. Bohlen, D. Letzig, P. Lukáč, J. Alloy. Compd., 588 (2014) 628-632.
[131] Y. Chino, X. Huang, K. Suzuki, K. Sassa, M. Mabuchi, Mat. Sci. Eng. A, 528 (2010) 566-572.
[132] Z.X. Cai, H.T. Jiang, D. Tang, Z. Ma, Q. Kang, Rare Metals, 32 (2013) 441-447.
[133] J. Bohlen, M.R. Nürnberg, J.W. Senn, D. Letzig, S.R. Agnew, Acta Mater., 55 (2007) 2101-2112.
[134] L. Ma, R.K. Mishra, M.P. Balogh, L. Peng, A.A. Luo, A.K. Sachdev, W. Ding, Mat. Sci. Eng. A, 543 (2012) 12-21.
[135] Y. Chino, K. Sassa, M. Mabuchi, Mat. Sci. Eng. A, 513–514 (2009) 394-400.
[136] M. Masoumi, M. Hoseini, M. Pekguleryuz, Mater. Sci. Eng., A, A528 (2011) 3122-3129.
[137] Q. Yang, B. Jiang, W. Jiang, S. Luo, F. Pan, Mater. Sci. Eng., A, 628 (2015) 143-148.

Appendix I

Appendix I

Critical systematic evaluation and thermodynamic optimization of the Mn-RE system: RE = La, Ce, Pr, Nd and Sm

Junghwan Kim and In-Ho Jung

Department of Mining and Materials Engineering, McGill University, 3610 University St., Montreal, Quebec, H3A 2B2, Canada

Corresponding author: In-Ho Jung

Tel : 1-514-398-2608

Fax : 1-514-398-4492

E-mail: in-ho.jung@mcgill.ca

Published in

Journal of Alloys and Compounds 525 (2012) 191-201

Abstract

Critical evaluation and optimization of all available phase diagram and thermodynamic data for the Mn-RE (RE = La, Ce, Pr, Nd and Sm) systems have been conducted to obtain reliable thermodynamic functions of all the phases in the system. In the thermodynamic modeling, it is found that the Mn-RE systems show systematic changes in the phase diagrams and thermodynamic properties such as enthalpy of mixing in liquid state in the order of periodic number in the lanthanide series. This systematic thermodynamic modeling approach for all light RE elements can allow to resolve inconsistencies in the experimental data.

Keywords

Thermodynamic modeling; Phase diagrams; Thermodynamic properties; Modified Quasichemical Model; Compound Energy Formalism.

1. Introduction

Rare Earth (RE) metals are widely used in many industrial fields including permanent magnet, electronic materials and structural materials. As a small addition of RE can enhance magnetic, electronic, optical and mechanical properties of numerous materials, the usage of the RE is still expanding regardless of the strategic control of their supply.

Magnesium alloys are getting great scientific and industrial attention as the lightest structural materials. One of the drawbacks of Mg alloys is their poor formability at room temperature due to the limited slip system with hcp crystal structure. Recently, several studies [1-5] show that the additions of small amounts of RE can considerably enhance the ductility of Mg alloys. Therefore, a lot of research on Mg-RE alloys is undergoing to clarify the role of RE on the enhanced deformation mechanism and to find out the most optimum Mg alloy compositions. In order to respond to the need of Mg-RE alloy development, a large thermodynamic database for Mg alloys containing RE has been developed with critical systematic analysis and optimization of the entire RE series data. This includes the thermodynamic database of the Mg-RE [6], Mg-RE-RE [6], Mg-Al-RE [7, 8], Mg-Zn-RE and Mg-Mn-RE systems.

In the thermodynamic "optimization" of a chemical system, all available thermodynamic and phase equilibrium data are evaluated simultaneously in order to obtain one set of model equations for the Gibbs energies of all phases as functions of temperature and composition. From these equations, all the thermodynamic properties and phase diagrams can be back-calculated. In this way, all the data are rendered self-consistent and consistent with thermodynamic principles. Thermodynamic property data, such as activity data, can aid in the evaluation of the phase diagram, and phase diagram measurements can be used to deduce thermodynamic properties. Discrepancies in the available data can often be resolved, and interpolations and extrapolations can be made in a thermodynamically correct manner.

Recently, the thermodynamic optimizations for several binary Mn-light RE systems have been performed. The Mn-Ce system was optimized by Tang et al. [9] and Kang et al. [10], and the Mn-

Pr and Mn-Sm systems were optimized by Wang et al. [11, 12]. No thermodynamic optimizations have been conducted for the Mn-La and Mn-Nd systems. In addition, new enthalpy of mixing data for liquid Mn-Sm and Mn-Nd systems were determined very recently by Berezutskii and Ivanov [13] and Ivanov et al.[14], respectively, which can be critical to constrain the thermodynamic properties of the systems. The entalapy prediction by the previous optimization by Wang et al.[12] for the Mn-Sm system is completely inconsistent with these new experiemntal data by Berezutskii and Ivanov [13].

Therefore, the primary purpose of the present study is to perform a complete review of all available experimental data and previous optimizations and critical optimization of thermodynamic properties of alloy phases in binary Mn-light RE alloy systems. In particular, the systematic analysis of the whole light RE systems can provide a more accurate evaluation of the thermodynamic properties and phase diagram data of Mn-RE. The Mn-Pm and Mn-Eu systems were not considered in the present study because no thermodynamic and phase diagram data are available in the literature although Pm and Eu are in the light RE class. This study is part of the thermodynamic database development of multicomponent Mg-RE alloy design.

2. Thermodynamic models

2.1. Liquid phase

The Modified Quasichemical Model [15, 16], which accounts for short-range-ordering of nearest-neighbor atoms, was used to model the liquid solutions because it gives a more realistic thermodynamic description of the liquid phase compared with the conventional simple random-mixing Bragg Williams model [15, 16]. The Modified Quasichemical Model was successfully applied to many liquid metallic solutions [16-18] and ionic solutions [19, 20] exhibiting strong short-range-ordering behavior.

Recently, the energy of nearest-neighbor pair formation in the Modified Quasichemical Model is expanded as a polynomial in the pair fractions [15, 16] instead of the component fractions [19, 21]. In addition, the coordination numbers are now allowed to vary with composition. These modifications provide greater flexibility in reproducing the binary experimental data and in combining optimized binary liquid parameters into a large database for multicomponent solutions [15]. A short description of the model is given below; details can be found in previous studies [15, 16].

In the case of a binary A-B liquid solution, the atoms A and B are distributed over the sites of a quasi-lattice in liquid solution. The following pair exchange reaction can be considered:

$$(A-A)+(B-B)=2(A-B) \qquad (1)$$

where (A-B) represents a first-nearest-neighbor pair of A and B. The non-configurational Gibbs energy change for the formation of two moles of (A-B) pairs according to reaction [1] is Δg_{AB}. Then the Gibbs energy of the solution is given by:

$$G = (n_A G_A^{\circ} + n_B G_B^{\circ}) - T\Delta S^{\text{config}} + n_{AB}(\Delta g_{AB}/2) \tag{2}$$

where G_A° and G_B° are the molar Gibbs energies of the pure components A and B, n_A and n_B are the numbers of moles of A and B atoms, and n_{AB} is the number of moles of (A-B) pairs. ΔS^{config} is the configurational entropy of mixing given by a random distribution of the (A-A), (B-B) and (A-B) pairs in the one-dimensional Ising approximation:

$$\begin{aligned}\Delta S^{\text{config}} &= -R(n_A \ln X_A + n_B \ln X_B) \\ &\quad - R[n_{AA} \ln(X_{AA}/Y_A^{\,2}) + n_{BB} \ln(X_{BB}/Y_B^{\,2}) \\ &\quad + n_{AB} \ln(X_{AB}/2Y_AY_B)]\end{aligned} \tag{3}$$

where n_{AA}, n_{BB} and n_{AB} are the numbers of moles of each kind of pairs, and the pair fraction (X_{AA}, X_{BB} and X_{AB}) and coordination equivalent fraction (Y_A and Y_B) can be calculated as:

$$X_{AA} = n_{AA}/(n_{AA} + n_{BB} + n_{AB}) \tag{4}$$

$$X_{BB} = n_{BB}/(n_{AA} + n_{BB} + n_{AB}) \tag{5}$$

$$X_{AB} = n_{AB}/(n_{AA} + n_{BB} + n_{AB}) \tag{6}$$

$$Y_A = X_{AA} + X_{AB}/2 \tag{7}$$

$$Y_B = X_{BB} + X_{AB}/2 \tag{8}$$

The Δg_{AB} is the model parameter to reproduce the Gibbs energy of liquid phase of the binary A-B system, which is expanded as a polynomial in terms of the pair fractions, as follows:

$$\Delta g_{AB} = \Delta g_{AB}^{o} + \sum_{i\geq 1} g_{AB}^{i0}(X_{AA})^i + \sum_{j\geq 1} g_{AB}^{0j}(X_{BB})^j \tag{9}$$

where Δg°_{AB}, g^{i0}_{AB} and g^{0j}_{AB} are the adjustable model parameters which can be functions of temperature.

In the Modified Quasichemical Model, the coordination numbers of A and B, Z_A and Z_B, can be varied with composition to reproduce the short-range-ordering as follows:

$$\frac{1}{Z_A} = \frac{1}{Z^A_{AA}}\left(\frac{2n_{AA}}{2n_{AA}+n_{AB}}\right) + \frac{1}{Z^A_{AB}}\left(\frac{n_{AB}}{2n_{AA}+n_{AB}}\right) \tag{10}$$

$$\frac{1}{Z_B} = \frac{1}{Z^B_{BB}}\left(\frac{2n_{BB}}{2n_{BB}+n_{AB}}\right) + \frac{1}{Z^B_{BA}}\left(\frac{n_{AB}}{2n_{BB}+n_{AB}}\right) \tag{11}$$

where Z^A_{AA} is the value of Z_A when all nearest neighbors of an A atom are A atoms, and Z^A_{AB} is the value of Z_A when all nearest neighbors are B atoms. Z^B_{BB} and Z^B_{BA} are defined in an analogous manner. In the present study, Z^i_{ii} for all elements (i = Mn and RE (La, Ce, Pr, Nd and Sm)) are set to be 6. To reproduce the maximum or minimum enthalpies of Mn-light RE liquid alloys at 0.3 ~ 0.4 mole fraction RE, Z^{Mn}_{MnRE} and Z^{RE}_{MnRE} are set to be 3 and 6, respectively. During the course of the present study, it was found that this set of coordination numbers can reproduce the experimental data more accurately with a small number of model parameters. For example, if the coordination numbers of Mn and RE for all nearest neighbors were set to 6, more model parameters would have been required and the experimental data would have been less accurately reproduced.

2.2. Solid solutions

The solid solution phases were described by the Compound Energy Formalism [22] with a one-sublattice approach (Mn, RE) for substitutional site. The molar Gibbs energy of the solid solution can be expressed as:

$$G = (y_{Mn}G^{\circ}_{Mn} + y_{RE}G^{\circ}_{RE}) + RT(y_{Mn}\ln y_{Mn} + y_{RE}\ln y_{RE}) + {}^{a}L_{Mn,RE}\,y_{Mn}y_{RE}(y_{RE}-y_{Mn})^{a} \tag{12}$$

where y_{Mn} and y_{RE} are the site fractions of Mn and RE elements in the sublattice, and R and T are the gas constant and temperature in Kelvin. G^{o}_{Mn} and G^{o}_{RE} are the molar Gibbs energies of solid phases of Mn and RE. The binary interaction parameters between Mn and RE in the sublattice, ${}^{a}L_{Mn,RE}$ where $a \geq 0$, are adjustable models parameters.

2.3. Stoichiometric compounds and elements

The Gibbs energies of all pure elements are taken from the SGTE database version 5.0 [23]. As the heat capacities of all stoichiometric compounds in Mn-light RE systems were not available, they were estimated using the Neumann-Kopp rule. There is no experimental study for the enthalpy and entropy of formation at 298 K of the intermetallic compounds in Mn-light RE systems. Consequently, the enthalpy and entropy of formation at 298 K were used as adjustable parameters to reproduce the phase diagram of the systems.

BCC (Mn), FCC (Mn) and $Mn_{23}Sm_6$ phases in Mn-light RE systems exhibit magnetic transitions associated with Neel or Curie temperatures. The magnetic transition below 298 K (typically anti-ferromagnetic transition with Neel temperature) was taken directly into account in the calculation of S_{298}. The Curie temperature (ferromagnetic transition) occurs typically above 298 K, of which magnetic contribution to the Gibbs energy was considered by an empirical relationship suggested by Inden [24] and modified by Hillert and Jarl [25].

3. Critical evaluation and thermodynamic optimization

The thermodynamic optimizations of the binary systems were performed based on all available thermodynamic data for the compounds, solid and liquid solutions and on the critically assessed phase diagram data. The optimized values for the model parameters are listed in Table 1. The details of the thermodynamic optimization are explained in the following sections. All the thermodynamic calculations were performed using the FactSage thermodynamic software [26].

Table 1. Optimized model parameters for the all binary systems (J mol^{-1} or J mol^{-1} K^{-1}).

Phase	Thermodynamic parameters
Liquid	Coordination Numbers
	i j Z_{ij}^{i} Z_{ij}^{j}
	Mn La 3 6
	Mn Ce 3 6
	Mn Pr 3 6
	Mn Nd 3 6
	Mn Sm 3 6
	Δg_{MnLa}= 15062.4 - 7.1128T + (-2092.0 + 4.6024T) X_{MnMn} + (-3347.2 + 0.8368T) X_{LaLa} - 3765.6 X_{MnMn}^{2}
	Δg_{MnCe} = 5439.2 - 0.8368T - 1673.6 X_{MnMn}^{2}
	Δg_{MnPr} = 5020.8 - 0.523T - 627.6 X_{PrPr}
	Δg_{MnNd}= 2092 - 1.883T + (-4184 + 6.276T) X_{MnMn} + (4184 + 0.335T) X_{NdNd}
	Δg_{MnSm}= -1673.6 + 2.51T + (-418.4 + 2.51T) X_{MnMn} + (3347.2 - 2.72T) X_{SmSm} + 4184 X_{SmSm}^{2}
FCC-A1 (Mn, Ce)	${}^{0}L_{Mn,Ce}$ = 27519.4, ${}^{1}L_{Mn,Ce}$ = 2173.96
	$T_{C,Mn}^{FCC-A1}$ (Curie temperature) = 540 K,
	$B_{O,Mn}^{FCC-A1}$ (Magnetic moment) = 0.62 $\mu_B mol^{-1}$,
	P factor = 0.28
BCC-A2 (Mn, Ce, Pr, Nd)	${}^{0}L_{Mn,Ce}$ = 22812.24, ${}^{1}L_{Mn,Ce}$ = -1915.28
	${}^{0}L_{Mn,Pr}$ = 41840, ${}^{1}L_{Mn,Pr}$ = -39748 + 4.184T, ${}^{2}L_{Mn,Pr}$ = 50208 - 38.074T

	${}^{0}L_{Mn,Nd}$ = 41840, ${}^{1}L_{Mn,Nd}$ = -34727.2 + 4.184T, ${}^{2}L_{Mn,Nd}$ = 50208 - 38.074T $T_{C,Mn}^{BCC-A2}$ = 580 K, $B_{O,Mn}^{BCC-A2} = 0.27\ \mu_B mol^{-1}$, P factor = 0.4
CUB-A13 (Mn)	$G_{Ce}^{CUB-A13} = G_{Ce}^{FCC-A1} + 2510.4$ ${}^{0}L_{Mn,Ce} = 20920 + 5.02T$
DHCP (Pr)	$G_{Mn}^{DHCP} = G_{Mn}^{CBCC-A12} + 2000$ ${}^{0}L_{Mn,\mathrm{Pr}} = 31380$
$Mn_{23}Pr_6$	$\Delta H_{298}^{o} = 130047.88$, $S_{298}^{o} = 1326.34$ $C_p = 23 \times C_p$ (Mn, CBCC-A12) + $6 \times C_p$ (Pr, DHCP)
$Mn_{23}Nd_6$	$\Delta H_{298}^{o} = 113453.68$, $S_{298}^{o} = 1318.16$ $C_p = 23 \times C_p$ (Mn, CBCC-A12) + $6 \times C_p$ (Nd, DHCP)
Mn_2Nd	$\Delta H_{298}^{o} = 16202.94$, $S_{298}^{o} = 156.05$ $C_p = 2 \times C_p$ (Mn, CBCC-A12) + C_p (Nd, DHCP)
$Mn_{23}Sm_6$	$\Delta H_{298}^{o} = -42000$, $S_{298}^{o} = 1186.09$ $C_p = 23 \times C_p$ (Mn, CBCC-A12) + $6 \times C_p$ (Sm, RHOMB.) T_c = 439 K, $B_0 = 3\ \mu_B mol^{-1}$ [47], P factor = 0.28
Mn_2Sm	$\Delta H_{298}^{o} = -6300$, $S_{298}^{o} = 136.90$ $C_p = 2 \times C_p$ (Mn, CBCC-A12) + C_p (Sm, RHOMB)

3.1. The Mn-La system

The only available experimental phase diagram for this system was investigated by Rolla and Iandelli [27] using thermal analysis (TA) followed by metallography and X-ray diffraction (XRD) in the entire composition range. The alloys were prepared from 99.5 wt. % La and 99.8 wt. % Mn in Pythagoras crucibles under a melt of NaCl + $BaCl_2$ in a Tamann furnace. The monotectic and eutectic reactions were observed at 1081 °C and 701 °C, respectively, using TA. The existence of a liquid miscibility gap was found from a thermal arrest detected at 1081 °C in the composition range of 0.6 to 0.85 mole fraction La. However, the consolute temperature of the binary miscibility gap was not determined. No intermediate phases were found in the system. Using XRD, the authors also proposed no mutual solubility of La and Mn in the solids. The phase diagram data of Rolla and Iandelli [27] are shown in Fig. 1.

Nikolaenko and Nosova [28] determined the partial enthalpy of mixing of La between $0 < X_{La} < 0.63$ and that of Mn between $0.48 < X_{La} < 1.0$ at 1600 K in liquid Mn-La using isoperibolic calorimetry and starting materials made of 99.9 wt. % Mn and 99.86 wt. % La . Then, using the Gibbs-Duhem equation, they suggested smoothed values of both, the partial enthalpies of mixing and the integral enthalpy of mixing, in the whole Mn-La liquid. The experimental data of the partial and integral enthalpies of the liquid are presented in Figs. 2 and 3, respectively. The integral enthalpy of mixing of the Mn-La liquid shows a positive deviation from ideal solution behavior with a maximum at about 8 kJ mol^{-1} near 0.4 mole fraction La.

The system was previously assessed by Palenzona and Cirafici [29] using only the experimental data of Rolla and Iandelli [27], for which the melting temperature of La and the liquidus were modified. In our optimization, the temperature-independent terms of the liquid interaction parameters were firstly adjusted to reproduce the experimental enthalpy data of Figs. 2 and 3. However, the parameters were insufficient to reproduce the phase diagram data of Fig. 1. Consequently, the calculated phase diagram and enthalpies were well reproduced after adding small temperature-dependent model parameters as shown in Figs. 1 to 3. The only remaining discrepancies are observed for the La liquidus though. Its melting temperature reported by Rolla

and Iandelli [27] is already lower than the accepted melting temperature by about 100 °C. The reason of the experimental error cannot be clarified, but it may be associated to the strong oxidation behavior of La. The calculated invariant reactions are listed in Table 2 in comparison with the experimental ones. The calculated consolute temperature of the binary miscibility gap is 1165 °C at 0.28 mole fraction La.

Table 2. Calculated invariant reactions with the experimental data in the Mn-La system.

Type	Reaction	T (°C)	Reference
Monotectic	$L_{(X_{La}=0.187)} \leftrightarrow Mn_{(CUB\text{-}A13,\ X_{La}=0)} + L_{(X_{La}=0.392)}$	1086.2	This work
	$L_{(X_{La}=0.122)} \leftrightarrow Mn_{(CUB\text{-}A13,\ X_{La}=0)} + L_{(X_{La}=0.392)}$	1081.0	[21]
Eutectic	$L_{(X_{La}=0.825)} \leftrightarrow Mn_{(CBCC\text{-}A12,\ X_{La}=0)} + La_{(FCC\text{-}A1,\ X_{La}=1)}$	705.3	This work
	$L_{(X_{La}=0.830)} \leftrightarrow Mn_{(CBCC\text{-}A12,\ X_{La}=0)} + La_{(FCC\text{-}A1,\ X_{La}=1)}$	701.0	[21]

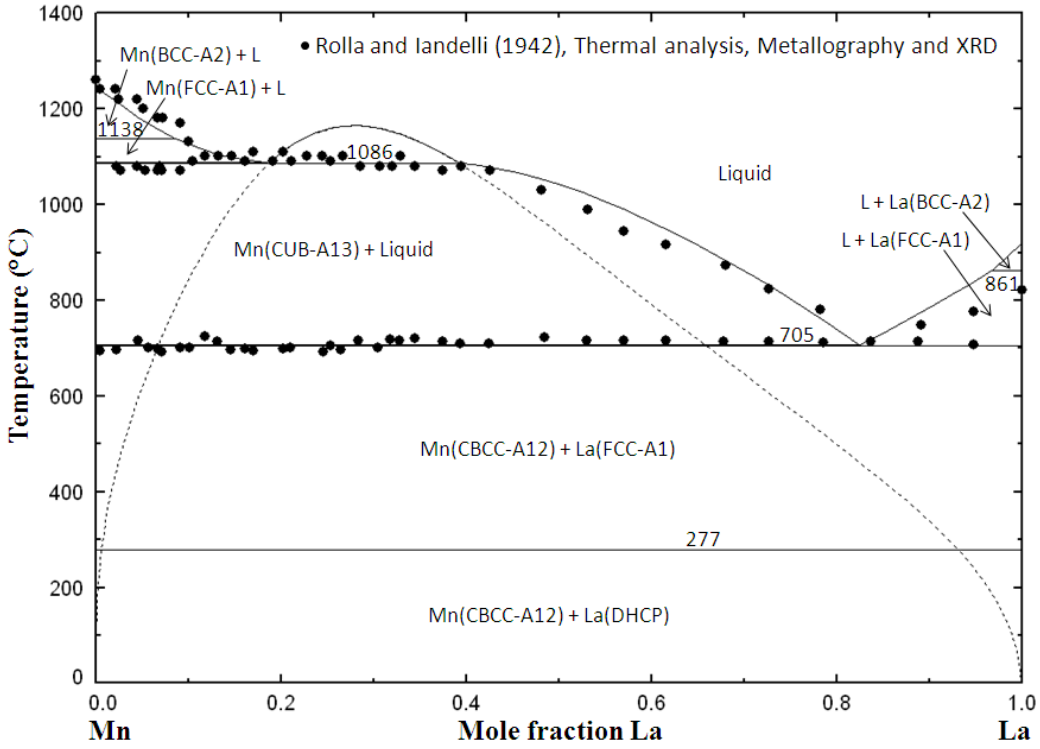


Fig. 1. The optimized phase diagram of the Mn-La system with experimental data [27].

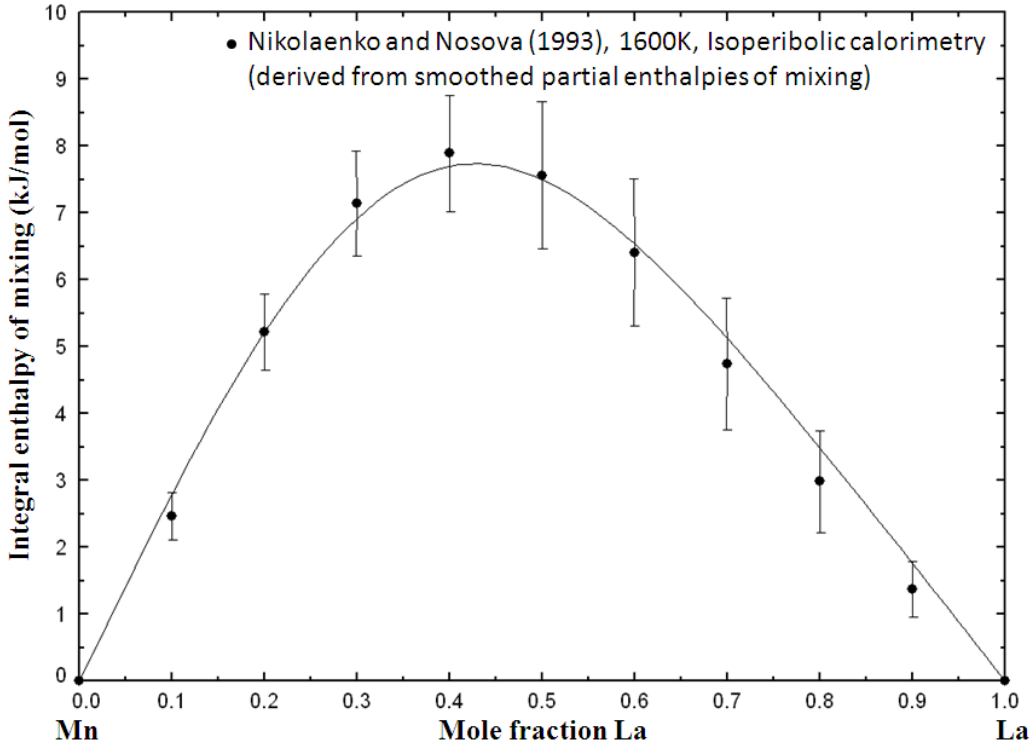


Fig. 2. Integral enthalpy of mixing in Mn-La liquid at 1600 K with experimental data [28].

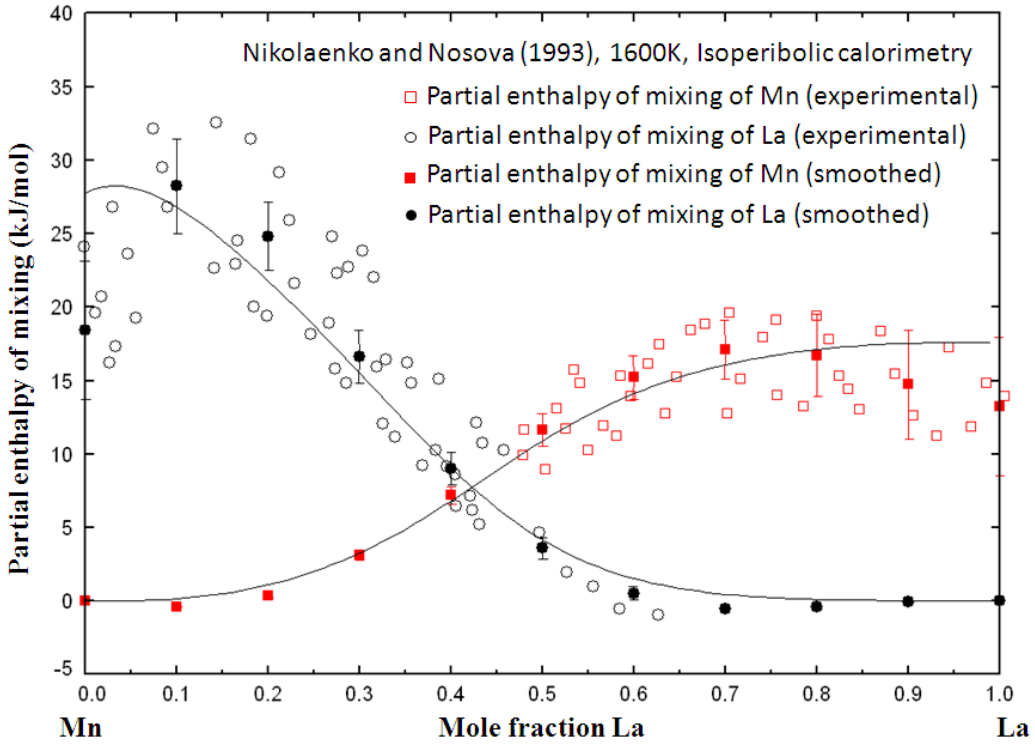


Fig. 3. Partial enthalpies of mixing in Mn-La liquid at 1600 K with experimental data [28].

3.2. The Mn-Ce system

An early investigation of the phase diagram was carried out by Iandelli [30] using TA with alloys made from 99.5 wt. % Ce and 99.8 wt. % Mn. The eutectic reaction was located at 0.85 mole fraction Ce at 612 °C while a possible liquid miscibility gap with a monotectic between 0.18 and 0.324 mole fraction Ce at 998 °C was reported. No intermediate solid phases were detected. Mirgalovskaya and Strel'nikova [31] reinvestigated the system using TA and metallography and agreed reasonably well with the work of Iandelli [30] except for the eutectic temperature at 635 °C. Mirgalovskaya and Strel'nikova assumed that the allotropic transition temperatures of Mn at 998 °C and 1087 °C, which are different from those of pure Mn, were due to some solid solubility of Ce in Mn (BCC and FCC). Thamer [32] determined the phase diagram by DTA, metallography and XRD in the Ce-rich region between 500 and 800 °C with starting materials having a higher purity than those of Iandelli [30]. The eutectic reaction was positioned at 0.84 mole fraction Ce at 622 °C. The solubility of Mn in Ce was determined to be about 5 mol % Mn in Ce (BCC) and about 2 mol % Mn in Ce (FCC) at 638 °C. Later, Tang et al. [33] prepared several alloys in the liquid miscibility gap region assumed by Iandelli [30] and confirmed the non-existence of immiscibility by XRD and scanning electron microscopy (SEM) analysis from the quenched samples. Afterwards, Tang et al. [9] prepared four key alloys by arc melting using 99.9 wt. % Mn and Ce, respectively, for key experiments to support their thermodynamic modeling. Samples were annealed at 600 °C and identified by XRD. Phase transition temperatures were determined by DTA using alumina crucibles under Ar atmosphere. Results agree well with other experimental data, which are depicted in Fig. 4.

Nikolaenko and Nosova [28] measured the partial enthalpy of mixing of Mn in the Ce-rich region and that of Ce in the Mn-rich region of the Mn-Ce liquid at 1600 K using isoperibolic calorimetry and starting materials made of 99.9 wt. % Mn and 99.86 wt. % Ce. Then, based on the Gibbs-Duhem equation, they proposed smoothed values of both, the partial and the integral enthalpies of mixing, for the entire Mn-Ce liquid. Unlike the Mn-La system, they only showed smoothed values without any experimental data. The experimental data of the partial and integral enthalpies of the liquid are presented in Figs. 5 and 6, respectively. The integral enthalpy of mixing of the Mn-Ce

liquid shows positive deviation from ideal solution behavior with a maximum at about 3 kJ mol^{-1} near 0.4 mole fraction Ce, which is less than half of the Mn-La system.

The system was previously assessed by Palenzona and Cirafici [34] based mainly on the work of Iandelli [30], Mirgalovskaya and Strel'nikova [31] and Thamer [32] and reviewed by Okamoto [35]. Recently, thermodynamic optimizations were performed by Tang et al. [9] and Kang et al. [10]. Unfortunately, the optimization of Kang et al. [10] omitted the solubility of Mn in Ce determined by Thamer [32]. In the thermodynamic optimization of Tang et al. [9], the authors adopted the Bragg-Williams random mixing model with the Redlich–Kister expression for the liquid. However, they did not consider the thermodynamic data of the liquid phase determined by Nikolaenko and Nosova [28]. The calculated integral and partial enthalpies of mixing for the liquid phase at 1600 K optimized by Tang et al. [9] are slightly off from the experimental data of Nikolaenko and Nosova [28]; this is shown in Figs. 5 and 6.

In the present thermodynamic modeling, the mutual solubilities of Mn and Ce in both, FCC-A1 and BCC-A2 solid solutions, were reproduced with two temperature-independent Gibbs excess parameters with the assumption of large solid state miscibility gaps. The solubility of Ce in Mn CUB-A13 solid solution was estimated using its liquidus and the transition temperatures of Mn CUB-A13 to Mn FCC-A1 and Mn CBCC-A12 to Mn CUB-A13, respectively. The eutectic temperature determined by Thamer [32] (622 °C) and Tang et al. [9] (621 °C) were considered as the eutectic temperature of L → Ce FCC-Al solid solution + Mn CBCC-A12. The Gibbs energy of Ce in Mn CUB-A13 structure is assessed to be 2.5104 kJ mol^{-1} relative to the stable structure of Ce FCC-A1 since the stable Ce CUB-A13 is not available. No solid solution was considered for the Mn CBCC-A12 phase because no solubility data exist for this phase. For the liquid, a small temperature dependent term was needed to reproduce both, the phase diagram and enthalpy data, of the liquid phase. The computed phase diagram and the partial and integral enthalpies of the liquid are in good agreement with the experimental data, which is shown in Figs. 4 to 6. In the phase diagram of Fig. 4a, the metastable liquid miscibility gap is depicted as a dotted line. The calculated invariant reactions are compared to the experimental ones in Table 3.

Table 3. Calculated invariant reactions with the experimental data in the Mn-Ce system.

Type	Reaction	T (°C)	Reference
Catatectic	$Mn_{(BCC\text{-}A2,\ X_{Ce}=\ 0.033)} \rightarrow Mn_{(FCC\text{-}A1,\ X_{Ce}=\ 0.027)} + L_{(X_{Ce}=\ 0.136)}$	1094.0	This work
	$Mn_{(BCC\text{-}A2,\ X_{Ce}*)} \rightarrow Mn_{(FCC\text{-}A1,\ X_{Ce}*)} + L_{(X_{Ce}=\ 0.130)}$	1087.0	[25]
Catatectic	$Mn_{(FCC\text{-}A1,\ X_{Ce}=\ 0.044)} \rightarrow Mn_{(CUB\text{-}A13,\ X_{Ce}=\ 0.028)} + L_{(X_{Ce}=\ 0.314)}$	989.4	This work
	$Mn_{(FCC\text{-}A1,\ X_{Ce}*)} \rightarrow Mn_{(CUB\text{-}A13,\ X_{Ce}*)} + L_{(X_{Ce}=\ 0.175)}$	998.0	[25]
Catatectic	$Mn_{(CUB\text{-}A13,\ X_{Ce}=\ 0.028)} \rightarrow Mn_{(CBCC\text{-}A12,\ X_{Ce}=\ 0)} + L_{(X_{Ce}=\ 0.815)}$	626.2	This work
	$Mn_{(CUB\text{-}A13,\ X_{Ce}*)} \rightarrow Mn_{(CBCC\text{-}A12,\ X_{Ce}*)} + L_{(X_{Ce}=\ 0.835)}$	625.0	[26]
Catatectic	$Ce_{(BCC\text{-}A2,\ X_{Ce}=\ 0.944)} \rightarrow Ce_{(FCC\text{-}A1,\ X_{Ce}=\ 0.983)} + L_{(X_{Ce}=\ 0.846)}$	637.8	This work
	$Ce_{(BCC\text{-}A2,\ X_{Ce}=\ 0.95)} \rightarrow Ce_{(FCC\text{-}A1,\ X_{Ce}=\ 0.98)} + L_{(X_{Ce}=\ 0.86)}$	638.0	[26]
	$Ce_{(BCC\text{-}A2,\ X_{Ce}*)} \rightarrow Ce_{(FCC\text{-}A1,\ X_{Ce}*)} + L_{(X_{Ce}*)}$	640.0	[28]
Eutectic	$L_{(X_{Ce}=\ 0.821)} \rightarrow Mn_{(CBCC\text{-}A12,\ X_{Ce}=\ 0)} + Ce_{(FCC\text{-}A1,\ X_{Ce}=\ 0.981)}$	618.7	This work
	$L_{(X_{Ce}=\ 0.850)} \rightarrow Mn_{(CBCC\text{-}A12,\ X_{Ce}=\ 0)} + Ce_{(FCC\text{-}A1,\ X_{Ce}=\ 1)}$	612.0	[24]
	$L_{(X_{Ce}=\ 0.878)} \rightarrow Mn_{(CBCC\text{-}A12,\ X_{Ce}=\ 0)} + Ce_{(FCC\text{-}A1,\ X_{Ce}*)}$	635.0	[25]
	$L_{(X_{Ce}=\ 0.839)} \rightarrow Mn_{(CBCC\text{-}A12,\ X_{Ce}=\ 0)} + Ce_{(FCC\text{-}A1,\ X_{Ce}*)}$	622.0	[26]
	$L_{(X_{Ce}=\ *)} \rightarrow Mn_{(CBCC\text{-}A12,\ X_{Ce}*)} + Ce_{(FCC\text{-}A1,\ X_{Ce}=\ *)}$	621.0	[28]

* The exact compositions are not specified in the reference.

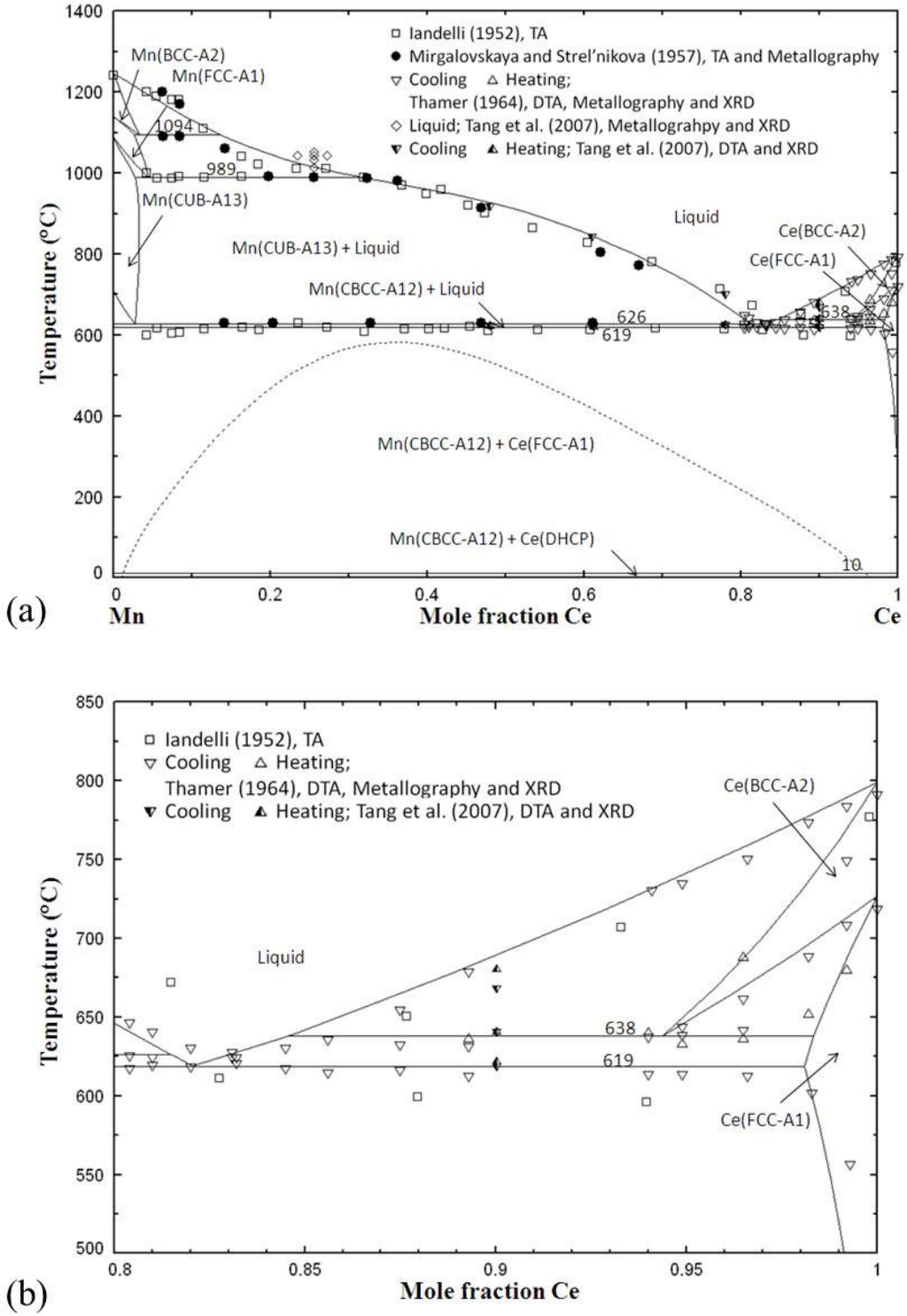


Fig. 4. The optimized phase diagram of the Mn-Ce system in whole composition range (a) and in the range of 0-20 mol % Mn (b) with experimental data [9, 30-33].

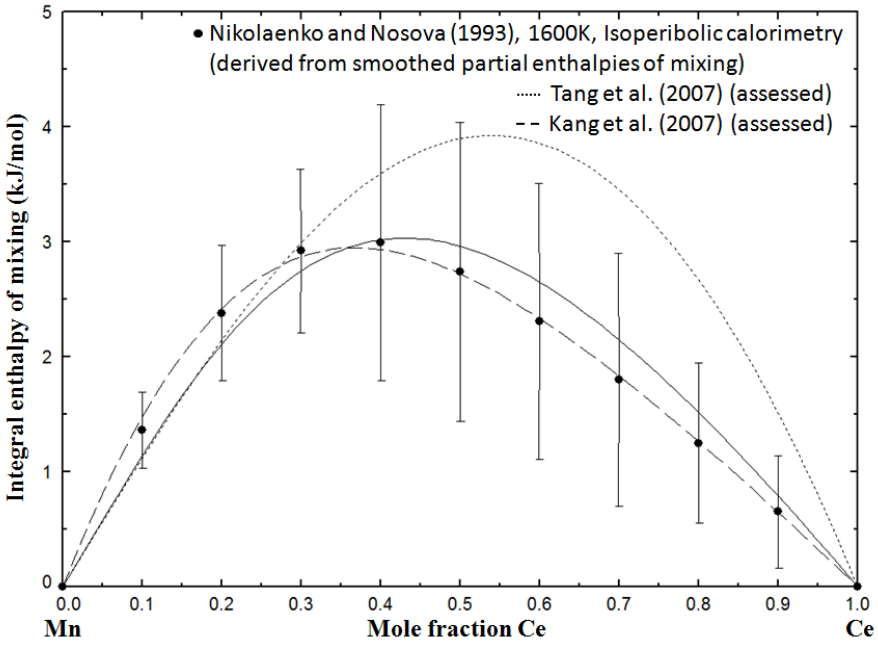


Fig. 5. Integral enthalpy of mixing in Mn-Ce liquid at 1600 K with experimental data [28]. The previous optimizations of Tang et al. [9] and Kang et al. [10] are depicted by the dotted line and dashed line, respectively.

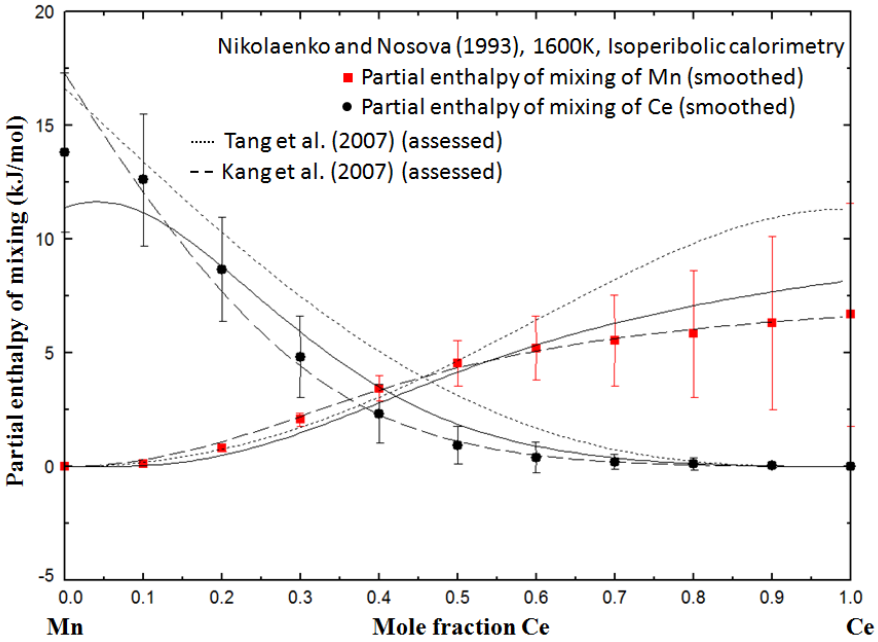


Fig. 6. Partial enthalpies of mixing in Mn-Ce liquid at 1600 K with experimental data [28]. The previous optimizations of Tang et al. [9] and Kang et al. [10] are depicted by the dotted line and dashed line, respectively.

3.3. The Mn-Pr system

Saccone et al. [36] investigated the complete phase diagram using DTA, metallography, XRD and electron probe micro-analysis (EPMA). The alloys were prepared in the induction furnace using starting materials made of 99.9 wt. % Pr and 99.9 wt. % Mn and tantalum or molybdenum crucibles which were sealed by welding to prevent the oxidation and evaporation of sample. The authors reported the existence of the $Mn_{23}Pr_6$ compound, which forms peritectically at 790 °C and decomposes at about 650 °C, after verifying the quenched samples by EPMA and corresponding powders by XRD. They also confirmed that the metastable Laves-type $PrMn_2$ phase forms peritectically at 740 °C and disappears to form Pr_6Mn_{23} after annealing for a few hours at temperatures slightly below 740 °C. Using DTA, it was proposed that the solubilities of Mn in Pr BCC and Pr DHCP at 665 °C are about 6 mol % Mn and 1 ~ 2 mol % Mn, respectively. Moreover, the solubility of Pr in Mn was shown to be negligible based on EPMA results. The phase transformation temperature of Mn CBCC-A12 to Mn CUB-A13 was detected at 600 °C by DTA (cooling path), which is much lower than the accepted allotropic transformation of Mn (707 °C). Apparently, this difference is due to the slow kinetics of the transformation in the solid state and therefore these experimental data were not taken into account in the present optimization. The experimental data of Saccone et al. [36] are presented in Fig. 7.

Nikolaenko and Nosova [28] measured the partial enthalpy of mixing of Mn in the Pr-rich region and that of Pr in the Mn-rich region of Mn-Prliquid at 1600 K using isoperibolic calorimetry and starting materials made of 99.9 wt. % Mn and 99.86 wt. % Pr. Like in the previous two Mn-RE systems, they proposed smoothed values of both, the partial and the integral enthalpies of mixing, for the whole Mn-Ce liquid using the Gibbs-Duhem equation. Unfortunately, they also gave only smoothed values without any experimental data. The enthalpy data are presented in Figs. 8 and 9. The Mn-Pr liquid has a slightly lower positive enthalpy of mixing than the Mn-Ce liquid. The maximum in the integral enthalpy of mixing curve is about 2.5 kJ mol^{-1} near 0.4 mole fraction Pr.

Previous optimization for this system was performed by Wang et al. [11] using a random-mixing model for the liquid phase. Although Wang et al. could reproduce the experimental data of the

phase diagram, the calculated integral and partial enthalpies of mixing of the liquid at 1600 K are slightly dissimilar with the trend from the smoothed values of both, the partial and integral enthalpies of mixing. Moreover, five model parameters including two temperature-dependent parameters were used for the description of the liquid phase. The calculated partial and integral enthalpies of mixing of the liquid phase at 1600 K are shown in Figs. 8 and 9, respectively, together with the ones obtained by Wang et al. [11].

The Mn-Pr system was optimized using the experimental phase diagram of Saccone et al. [36] and the enthalpy data of Nikolaenko and Nosova [28]. First, the liquid model parameters were mostly fixed by the liquidus of Mn and the enthalpy data. Then, the Gibbs energies of the Pr BCC and Pr DHCP solid solutions and of the $Mn_{23}Pr_6$ stoichiometric compound were assessed to fit the phase diagram. The Gibbs energy of Mn in Pr DHCP structure is assessed to be 2 kJ/mole relative to the stable structure of Mn CBCC-A12 since the stable Mn DHCP is not available. As no thermodynamic data for $Mn_{23}Pr_6$ are available, the ΔH_{298} and S_{298} of the compound were determined to reproduce its dissociation temperature after the C_p was evaluated by the Neumann-Kopp rule. As seen in Figs. 7 to 9, the optimized phase diagram and calculated enthalpies are in good agreement with the experimental data. The calculated invariant reactions are compared with the experimental ones in Table 4.

Table 4. Calculated invariant reactions with the experimental data in the Mn-Pr system.

Type	Reaction	T (°C)	Reference
Peritectic	$Mn_{(CUB\text{-}A13,\ X_{Pr}=0)} + L_{(X_{Pr}=0.648)} \rightarrow Mn_{23}Pr_6$	789.9	This work
	$Mn_{(CUB\text{-}A13,\ X_{Pr}=0)} + L_{(X_{Pr}=0.635)} \rightarrow Mn_{23}Pr_6$	790.0	[32]
Catatectic	$Pr_{(BCC\text{-}A2,\ X_{Pr}=0.939)} \rightarrow Pr_{(DHCP,\ X_{Pr}=0.9852)} + L_{(X_{Pr}=0.784)}$	672.4	This work
	$Pr_{(BCC\text{-}A2,\ X_{Pr}=0.94)} \rightarrow Pr_{(DHCP,\ X_{Pr}=0.985)} + L_{(X_{Pr}=0.758)}$	665.0	[32]
Eutectic	$L_{(X_{Pr}=0.770)} \rightarrow Mn_{23}Pr_6 + Pr_{(DHCP,\ X_{Pr}=0.9846)}$	660.5	This work
	$L_{(X_{Pr}=0.750)} \rightarrow Mn_{23}Pr_6 + Pr_{(DHCP,\ X_{Pr}=0.985)}$	665.0	[32]
Eutectoid	$Mn_{23}Pr_6 \rightarrow Mn_{(CBCC\text{-}A12,\ X_{Pr}=0)} + Pr_{(DHCP,\ X_{Pr}=0.9852)}$	649.5	This work
	$Mn_{23}Pr_6 \rightarrow Mn_{(CBCC\text{-}A12,\ X_{Pr}=0)} + Pr_{(DHCP,\ X_{Pr}=0.985)}$	650.0	[32]

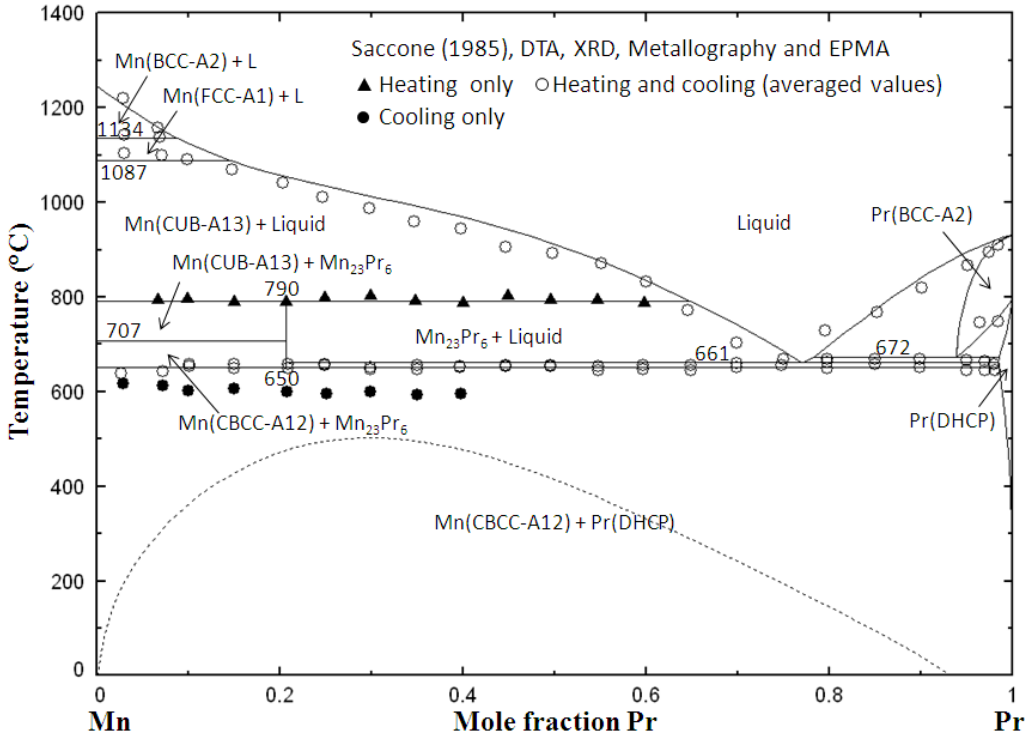


Fig. 7. The optimized phase diagram of the Mn-Pr system with experimental data [36].

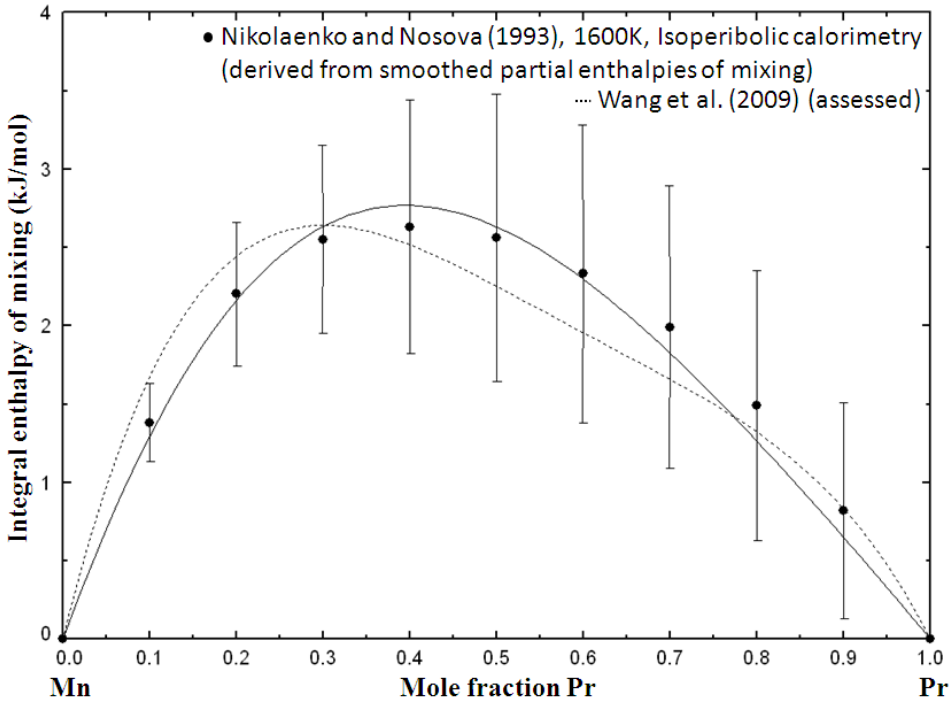


Fig. 8. Integral enthalpy of mixing in Mn-Pr liquid at 1600 K with experimental data [28]. The dotted line shows the previous optimization of Wang et al. [11].

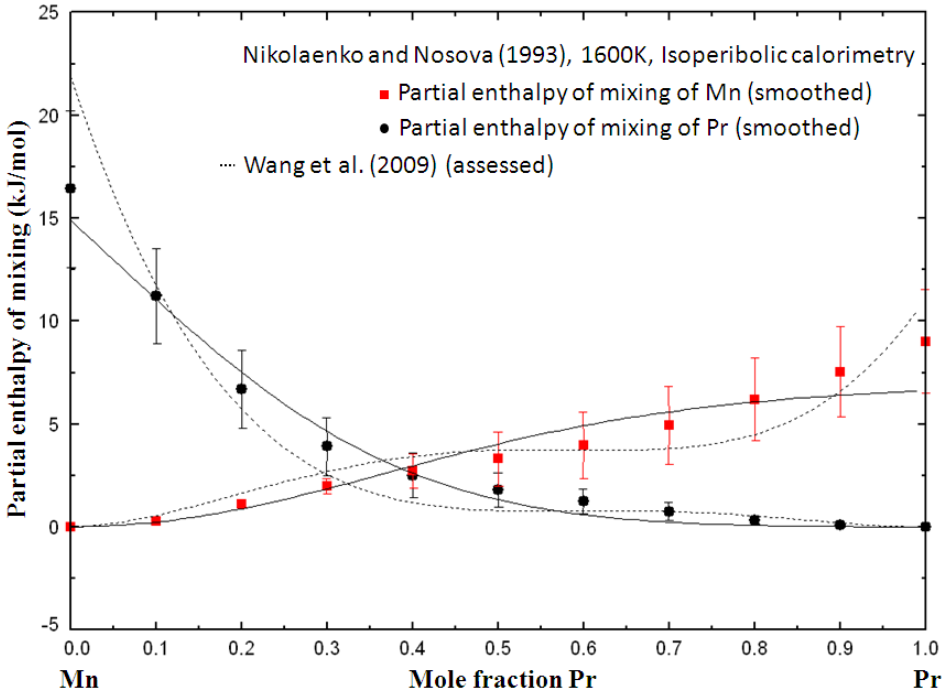


Fig. 9. Partial enthalpies of mixing in Mn-Pr liquid at 1600 K with experimental data [28]. The previous optimization of Wang et al. [11] is depicted by the dotted line.

3.4. The Mn-Nd system

The first phase diagram investigation of this system was carried out by Kirchmayr and Lugscheider [37]. Alloys made of 99.9 wt. % Mn and Nd were prepared by melting in a high frequency induction furnace using alumina crucibles. Three compounds, $Mn_{12}Nd$, $Mn_{23}Nd_6$, and Mn_2Nd were identified by means of DTA and XRD and verified by X-ray fluorescence spectrometry (XRF) and metallography. Mikhalenko and Kuz'ma [38] performed long duration annealing experiments of Mn-rich alloys characterized by XRD to determine the stability of the three compounds observed by Kirchmayr and Lugscheider. They found that $Mn_{12}Nd$ is unstable in the entire temperature range while the $Mn_{23}Nd_6$ and Mn_2Nd are stable in limited temperature ranges. Recently, Saccone et al. [39] reinvestigated the system using DTA, XRD, metallography and EPMA. The alloys were prepared from 99.9 wt. % Nd and Mn in an induction furnace with tantalum crucibles. The authors reported much lower liquidus boundaries than those determined by Kirchmayr and Lugscheider and slightly different peritectic and eutectoid decomposition temperatures for $Mn_{23}Nd_6$ and Mn_2Nd than the ones determined by Makhalenko and Kuz'ma [38]. Saccone et al. [39] proposed that Mn_2Nd and $Mn_{23}Nd_6$ form peritectically at 820 °C and 930 °C, respectively, and decompose at about 580 °C and 480 °C after analyzing the quenched samples by EPMA and corresponding powders by XRD. Preference was given to their results in the present optimization because of the higher resolution of the EPMA technique over the XRD, which was used to identify the phases in the work of Makhalenko and Kuz'ma [38]. No comprehensive study on the homogeneity ranges of Nd and Mn were performed, but Kirchmayr and Lugscheider [37] mentioned that even if they exist, they will be very small from based on their XRD analysis of Mn and Nd samples. The experimental data are shown in the phase diagram of Fig. 10.

Regarding the thermodynamic properties of Mn-Nd liquid, Ivanov et al. [14] measured the partial enthalpy of mixing of Nd between $0 < X_{Nd} < 0.25$ and that of Mn between $0.42 < X_{Nd} < 1.0$ in the Mn-Nd liquid using isoperibolic calorimetry and high purity alloys prepared from 99.95 wt. % Mn and 99.85 wt. % Nd. The partial enthalpy of Nd were measured using alumina crucibles for the alloys having less than 10 mol % Nd and zirconia crucibles for the alloys having up to 28 mol % Nd at 1550 K. The partial enthalpy of Mn were measured using molybdenum crucibles for the

alloys having less than 10 mol % Mn and zirconia crucibles for the alloys having up to 58 mol % Mn at 1600 K. The smoothed values of both, the partial enthalpies of mixing and the integral enthalpy of mixing in the entire Mn-Nd liquid were determined by the same method used by Nikolaenko and Nosova [28] assuming that the change of partial enthalpy is negligible in the temperature range between 1550 K and 1600 K. The experimental data are shown in Figs. 11 and 12. Interestingly, the integral enthalpy of mixing of the Mn-Nd liquid vary from small negative values between 0 and about 0.25 mole fraction Nd to positive values above 0.25 mole fraction Nd. The maximum and minimum in the integral enthalpy curves are about 2 kJ mol^{-1} near 0.6 mole fraction Nd and about -0.3 kJ mol^{-1} near 0.1 mole fraction Nd, respectively. There is no thermodynamic data for the intermediate phases $Mn_{23}Nd_6$ and Mn_2Nd.

The whole system was reviewed by Okamoto [40, 41] based on the phase diagram study of Kirchmayr and Lugscheider [37], Mikhsalenko and Kuz'ma [38] and Saccone et al. [39]. Since then, no thermodynamic modeling was performed on this system.

The experimental Mn liquidus determined by Saccone et al. [39] is thermodynamically more plausible than the one reported by Kirchmayr and Lugscheider [37] from the viewpoint of the limiting slope rule [42]. Moreover, the experimental data of Saccone et al. are more consistent with the stability data of intermetallics reported by Mikhalenko and Kuz'ma [38]. In the thermodynamic optimization, therefore, the phase diagram experimental data of Saccone et al. [39] were preferred over the ones of Kirchmayr and Lugscheider [37]. Although Kirchmayr and Lugscheider [37] mentioned that there is little mutual solubility of Mn and Nd, the solubility of Mn in Nd BCC-A2 is expected due to the similarity of the Mn-Nd system with the Mn-Pr one and the Mn-Nd liquidus measured by Saccone et al. [39]. A solubility of about 4 mol % Mn in Nd BCC-A2 at 736 °C was assumed in the present study. The calculated phase diagram and enthalpy curves are in good agreement with the experimental data as shown in Figs. 10 to 12. The thermodynamic data of the two intermetallic compounds $Mn_{23}Nd_6$ and Mn_2Nd were determined to reproduce the phase diagram data in Fig. 10 after determining their heat capacities using the Neumann-Kopp rule. The low temperature C_p of the Mn_2Nd phase measured by Kim-Ngan et al. [43], using adiabatic calorimetry, was not taken into account in the present optimization because

of the insufficient temperature range (1.2 to 200 K). The invariant reactions of the system are compared with experimental data in Table 5. The predicted metastable liquid miscibility gap shown as a dotted line in Fig. 10 has a consolute point near 0.6 mole fraction Nd.

Table 5. Calculated invariant reactions with the experimental data in the Mn-Nd system.

Type	Reaction	T (°C)	Reference
Peritectic	$Mn_{(CUB\text{-}A13,\ X_{Nd}=0)} + L_{(X_{Nd}=0.327)} \rightarrow Mn_{23}Nd_6$	930.0	This work
	$Mn_{(CUB\text{-}A13,\ X_{Nd}=0)} + L_{(X_{Nd}=0.283)*} \rightarrow Mn_{23}Nd_6$	1100.0	[34]
	$Mn_{(CUB\text{-}A13,\ X_{Nd}=0)} + L_{(X_{Nd}=0.325)} \rightarrow Mn_{23}Nd_6$	930.0	[36]
Peritectic	$Mn_{23}Nd_6 + L_{(X_{Nd}=0.478)} \rightarrow Mn_2Nd$	820.1	This work
	$Mn_{23}Nd_6 + L_{(X_{Nd}=0.448)} \rightarrow Mn_2Nd$	975.0	[34]
	$Mn_{23}Nd_6 + L_{(X_{Nd}=0.488)} \rightarrow Mn_2Nd$	820.0	[36]
Catatectic	$Nd_{(BCC\text{-}A2,\ X_{Nd}=0.96)} \rightarrow Nd_{(DHCP,\ X_{Nd}=1)} + L_{(X_{Nd}=0.763)}$	734.9	This work
Eutectic	$L_{(X_{Nd}=0.708)} \rightarrow Mn_2Nd + Nd_{(DHCP,\ X_{Nd}=1)}$	699.4	This work
	$L_{(X_{Nd}=0.749)} \rightarrow Mn_2Nd + Nd_{(DHCP,\ X_{Nd}=1)}$	700.0	[34]
	$L_{(X_{Nd}=0.730)} \rightarrow Mn_2Nd + Nd_{(DHCP,\ X_{Nd}=1)}$	695.0	[36]
Eutectoid	$Mn_2Nd \rightarrow Mn_{23}Nd_6 + Nd_{(DHCP,\ X_{Nd}=1)}$	580.4	This work
	$Mn_2Nd \rightarrow Mn_{23}Nd_6 + Nd_{(DHCP,\ X_{Nd}=1)}$	580.0	[36]
Eutectoid	$Mn_{23}Nd_6 \rightarrow Mn_{(CBCC\text{-}A12,\ X_{Nd}=0)} + Nd_{(DHCP,\ X_{Nd}=1)}$	480.4	This work
	$Mn_{23}Nd_6 \rightarrow Mn_{(CBCC\text{-}A12,\ X_{Nd}=0)} + Nd_{(DHCP,\ X_{Nd}=1)}$	480.0	[36]

* Note that the liquid composition determined in the experimental study [34] is less reliable (see the text for more details).

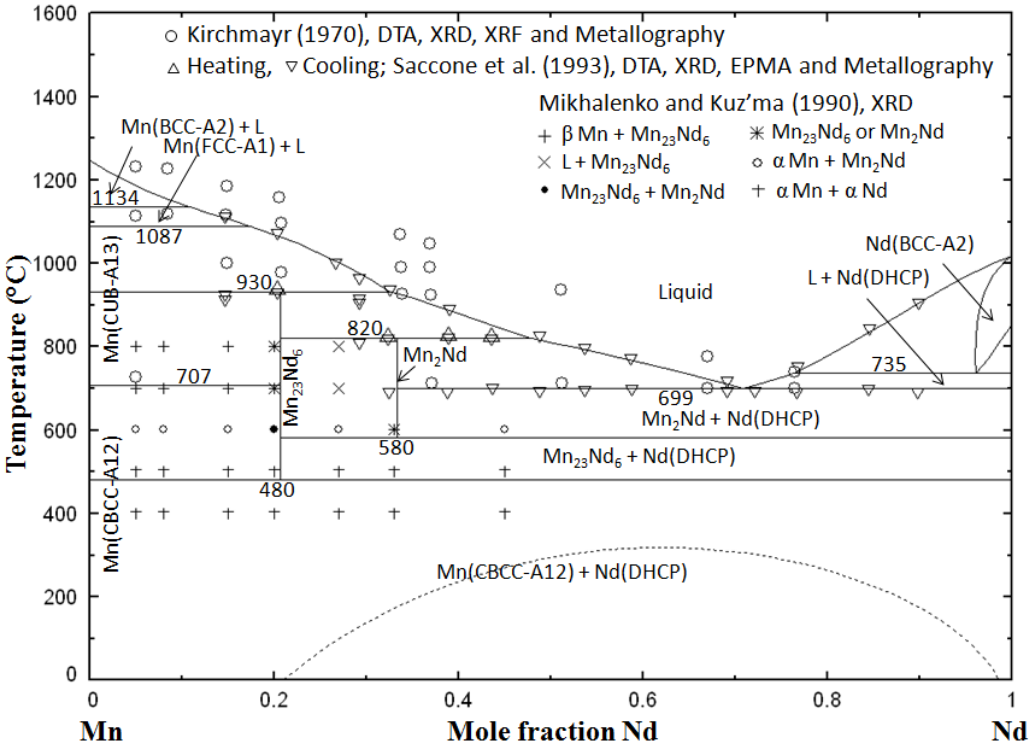


Fig. 10. The optimized phase diagram of the Mn-Nd system with experimental data [37-39].

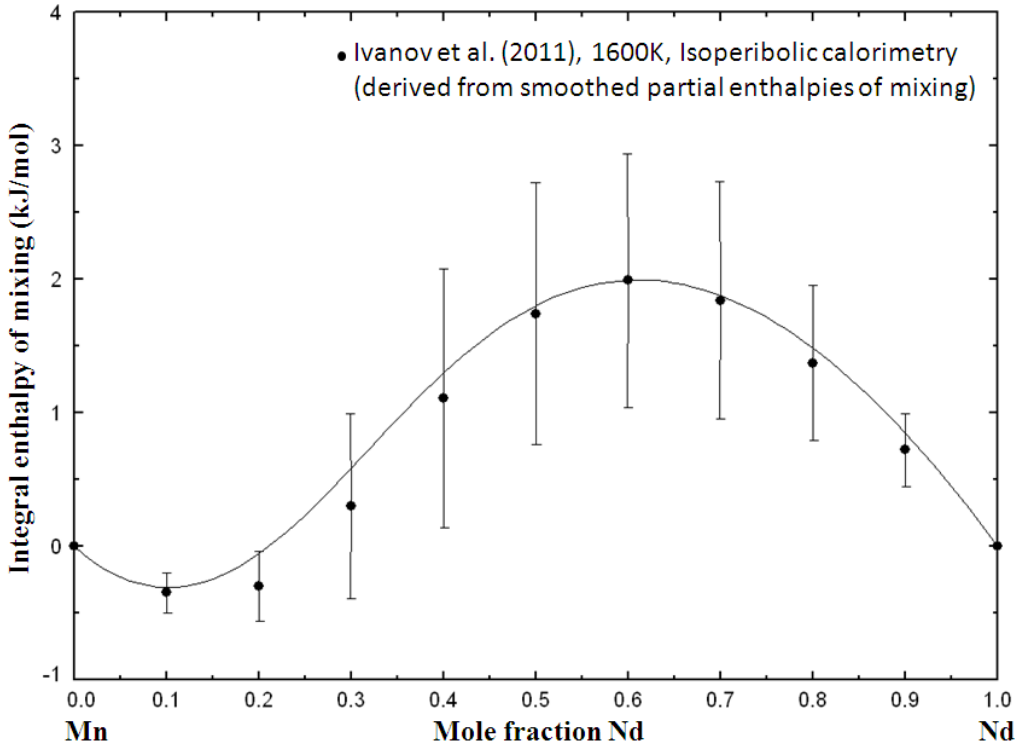


Fig. 11. Integral enthalpy of mixing in Mn-Nd liquid at 1600 K with experimental data [14].

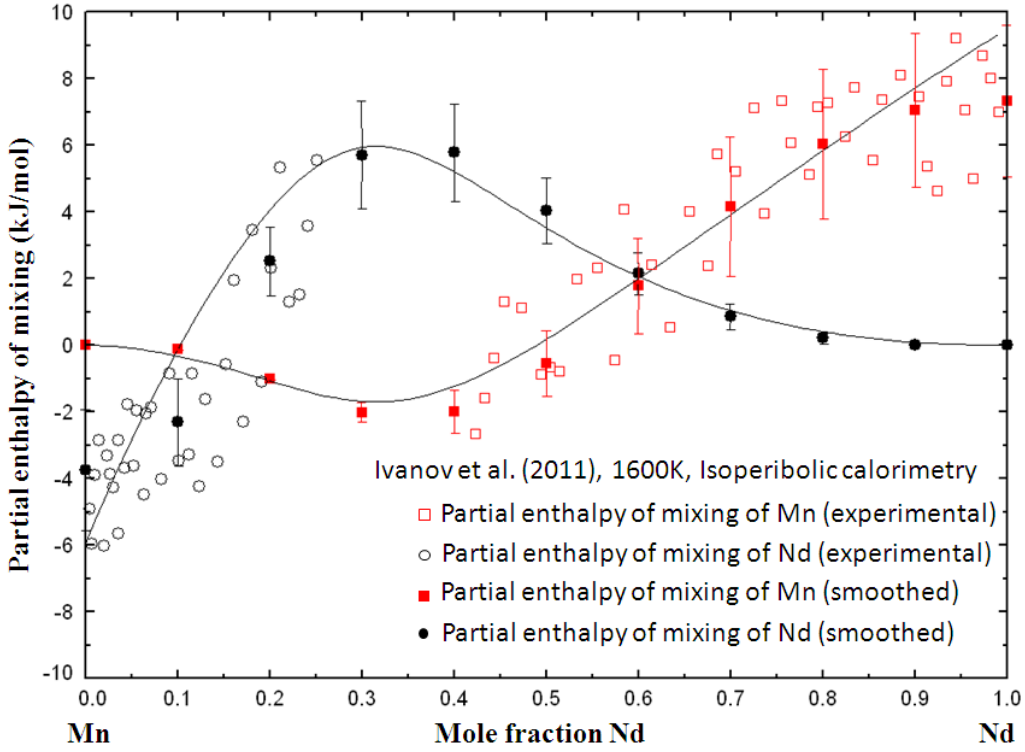


Fig. 12. Partial enthalpies of mixing in Mn-Nd liquid at 1600 K with experimental data [14].

3.5. The Mn-Sm system

Kirchmayr and Lugscheider [37] determined the phase diagram of Mn-Sm system using DTA, XRD and XRF which are the same techniques that they used for determining the Mn-Nd system in the same study. The results are shown in Fig. 13. Two intermetallic compounds, Mn_2Sm and $Mn_{23}Sm_6$, which melt peritectically, were identified. In the solid state, the mutual solubilities of Sm and Mn were proposed to be small based on XRD data. No other phase diagram study has been carried out for this system.

Berezutskii and Ivanov [13] determined the partial and integral enthalpies of mixing of the Mn-Sm liquid using isoperibolic calorimetry. The experimental method and estimation technique used by Berezutskii and Ivanov [13] are the same as the ones used by Nikolaenko and Nosova [28]. Using high purity starting materials prepared from 99.99 wt. % Mn and 99.98 wt. % Sm, the partial enthalpies of mixing were measured at 1400 K between $0.42 < X_{Sm} < 1.0$ in molybdenum crucibles and at 1600 K between $0 < X_{Sm} < 0.28$ in alundum crucibles. Then, the smoothed values of the partial enthalpies of mixing and the integral enthalpy of mixing were determined by the same method used by Nikolaenko and Nosova [28] assuming that the change of partial enthalpy is negligible in the temperature range between 1400 K and 1600 K. The enthalpies of mixing of the liquid are depicted in Figs. 14 and 15. Like the Mn-Nd system, the integral enthalpy of mixing of Mn-Sm liquid vary from negative values between 0 and about 0.5 mole fraction Sm to positive values above 0.5 mole fraction Sm. The enthalpy curves show a maximum of about 1 kJ mol^{-1} near 0.75 mole fraction Sm and a minimum of about -0.8 kJ mol^{-1} near 0.1 mole fraction Sm. Using high-temperature isoperibolic calorimetry, Shilov et al. [44] determined the enthalpy of formation of $Mn_{23}Sm_6$ at 1320 K to be -92 ± 5 kJ mol^{-1}; unfortunately, no data are available for Mn_2Sm.

The system was previously optimized by Wang et al. [12] based on the work of Kirchmayr and Lugscheider [37] using the Bragg-Williams random mixing model with the Redlich-Kister expression for the liquid phase. As shown in Figs. 14 and 15, the integral and partial enthalpies of mixing of the liquid at 1600 K optimized by Wang et al. [12] are significantly off the recent experimental data of Berezutskii and Ivanov [13].

Like for the Mn-Nd system, the Mn liquidus reported by Kirchmayr and Lugscheider [37] is thermodynamically the less reasonable. Consequently in the present optimization, the assessed Mn liquidus was lowered to be thermodynamically more reasonable from the viewpoint of the limiting slope rule [42]. For the phases Mn_2Sm and $Mn_{23}Sm_6$, who melt peritectically, no other data than the ones of Kirchmayr and Lugscheider [37] exist and we had no other choice than to use their data. The enthalpy of mixing of the liquid, determined by Berezutskii and Ivanov [13], was taken into account to determine the model parameters of liquid phase. The enthalpy of formation of $Mn_{23}Sm_6$ measured by Shilov et al. [44] (-92 ± 5 kJ mol^{-1}) was relatively well reproduced in the present optimization (-91.3 kJ mol^{-1}) . The calculated invariant reactions are compared with experimental ones in Table 6. Although the enthalpy data shown in Figs. 14 and 15 are well reproduced in the present optimization, the calculated phase diagram is in less agreement with the experimental data of Kirchmayr and Lugscheider [37] due to the above-mentioned possible error in the experiments. In order to validate the present thermodynamic optimization or obtain a more accurate thermodynamic optimization of the system, new phase diagram experiments are clearly needed.

Table 6. Calculated invariant reactions with the experimental data in the Mn-Sm system.

Type	Reaction	T (°C)	Reference
Peritectic	$Mn_{(CUB\text{-}A13,\ X_{Sm}=0)} + L_{(X_{Sm}=0.289)} \rightarrow Mn_{23}Sm_6$	1025.3	This work
	$Mn_{(CUB\text{-}A13,\ X_{Sm}=0)} + L_{(X_{Sm}=0.411)*} \rightarrow Mn_{23}Sm_6$	1025.0	[34]
Peritectic	$Mn_{23}Sm_6 + L_{(X_{Sm}=0.471)} \rightarrow Mn_2Sm$	930.1	This work
	$Mn_{23}Sm_6 + L_{(X_{Sm}=0.531)} \rightarrow Mn_2Sm$	930.0	[34]
Eutectic	$L_{(X_{Sm}=0.718)} \rightarrow Mn_2Sm + Sm_{(DHCP,\ X_{Sm}=1)}$	792.8	This work
	$L_{(X_{Sm}=0.678)} \rightarrow Mn_2Sm + Sm_{(DHCP,\ X_{Sm}=1)}$	795.0	[34]

* Note that the liquid composition determined in the experimental study [34] is less reliable (see the text for more details).

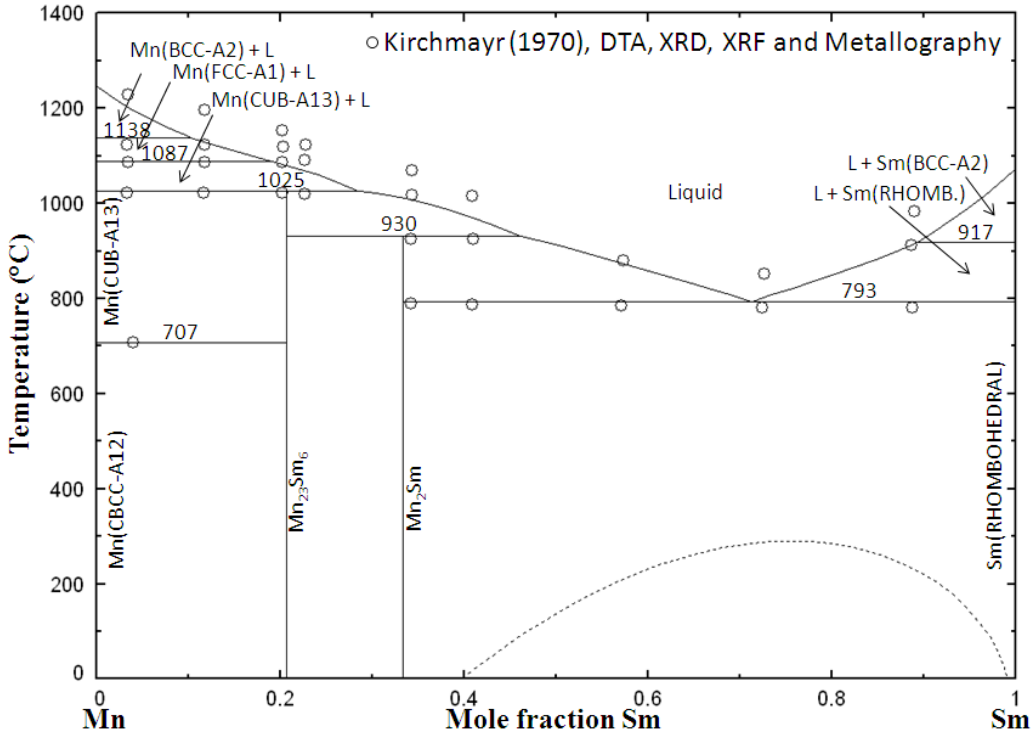


Fig. 13. The optimized phase diagram of the Mn-Sm system with experimental data [37].

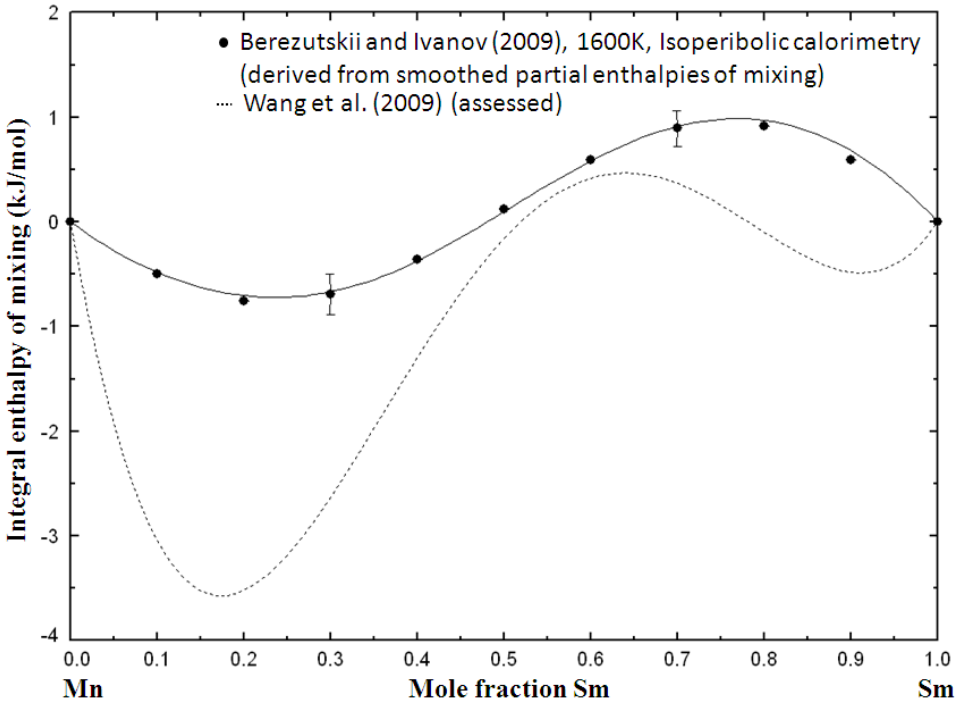


Fig. 14. Integral enthalpy of mixing in liquid Mn-Sm alloys at 1600 K with experimental data [13]. The dotted line is from the previous optimization of Wang et al. [12].

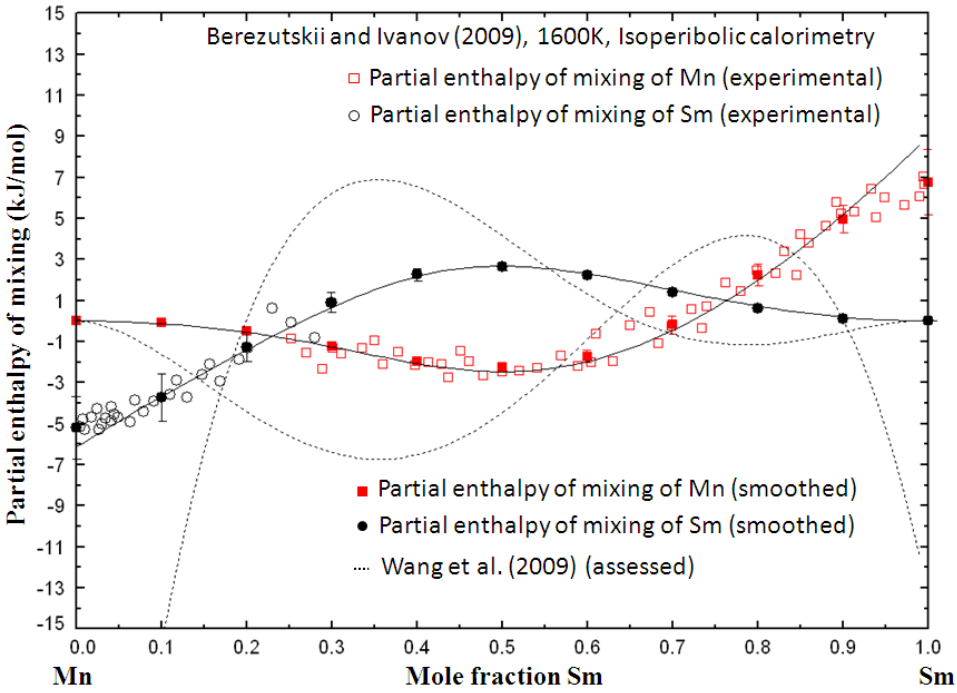


Fig. 15. Partial enthalpies of mixing in Mn-Sm liquid at 1600 K with experimental data [13]. The previous optimization of Wang et al. [12] is shown by the dotted line.

4. Systematic analysis of Mn-light RE systems

It is shown that the available and reliable experimental data of Mn-light RE systems are consistently reproduced by the present optimizations in all the systems. As it is well known, the RE metals across the lanthanide series show regular changes in electronic (electronegativity) and physical properties such as the melting temperature, the atomic radius and the density, with an increase of the atomic number. It is therefore expected that certain trends exist as well in the thermodynamic properties and phase relationships of the Mn-RE binary systems.

In the course of the present study, it is found that the enthalpies of mixing in liquid Mn-RE (RE = La, Ce, Pr, Nd and Sm) follow such trends, as shown in Fig. 16. The calculated and experimental integral enthalpies of mixing of liquid Mn-RE solutions at 1600 K are gradually changed from positive to negative values from La to Sm. The light RE elements, except La, are metallic elements which are characterized by the filling of *f* orbital. By filling the *f* orbital in atomic number order, the attractive interaction between Mn and RE elements seems to become stronger with a minimum between 0.3 and 0.4 mole fraction RE. The asymmetry observed in the enthalpies of mixing curves comes possibly from the size difference between Mn and RE. That is, RE has a larger atomic size (180 pm for Sm ~ 188 pm for La) than Mn (130 pm) [45]. Consequently, the negative interaction between Mn and RE can naturally induce the short range ordering of Mn and RE near the Mn-rich side, which produces the slight negative deviation observed in the Mn-rich region. Likewise, the calculated entropies of mixing in liquid Mn-RE alloys at 1600 K shown in Fig. 17 are also gradually changed from positive to negative deviation from the ideal entropy of mixing (dotted curve). The lesser entropies near 0.3 to 0.4 mole fraction RE support the gradual change of enthalpies with increasing the RE atomic number. These thermodynamic properties are also reflected in the phase diagrams. From the assessed phase diagram of each system (Fig. 1, 4, 7, 10 and 13), it is clearly seen that the stability of solid intermetallic phases in the systems increases with increasing the RE atomic number, especially near 0.3 and 0.4 mole fraction RE. No stable intermetallic compounds appear in the Mn-La and Mn-Ce systems. Stable compounds appear from the Mn-Pr system ($Mn_{23}Pr_6$) and become stable at lower temperature with increasing the atomic number ($Mn_{23}Sm_6$ and Mn_2Sm). The change of hypothetical liquid miscibility gap (dotted curve)

also shows the trend of increasing stability in liquid phases with RE atomic order. These interesting trends and regularities are also successively found in the Mn-heavy RE (Gd, Tb, Dy, Ho, Er, Tm, Lu and Y) systems [46].

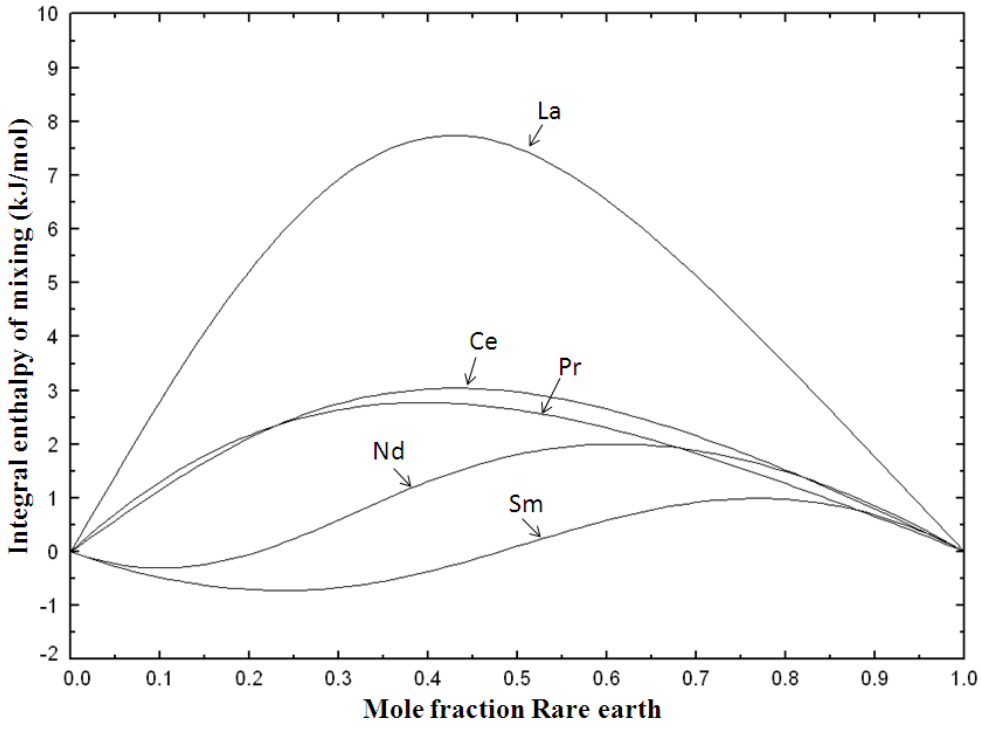


Fig. 16. Calculated enthalpies of mixing in Mn-RE (La, Ce, Pr, Nd and Sm) liquid at 1600 K.

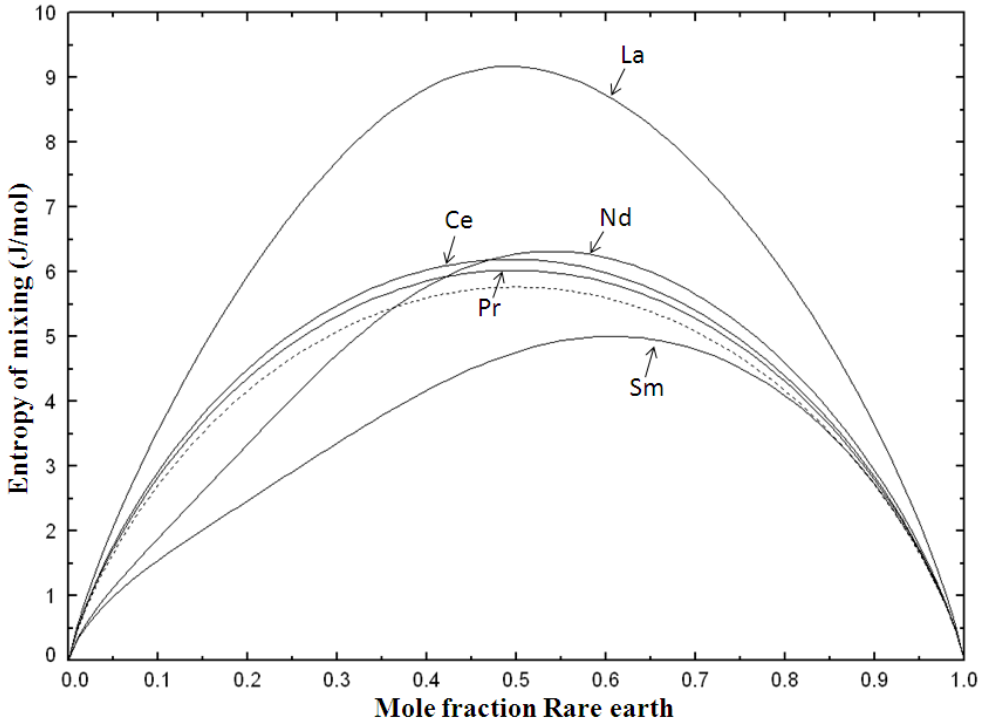


Fig. 17. Calculated entropies of mixing in Mn-RE (La, Ce, Pr, Nd and Sm) liquid at 1600 K. The dotted line represents the ideal entropy of mixing.

5. Summary

Critical evaluation and optimization of all available phase diagram and thermodynamic data for the Mn-RE (RE = La, Ce, Pr, Nd and Sm) systems have been conducted to obtain reliable thermodynamic functions of all the phases in the system. The thermodynamic properties of liquid phase were described using the Modified Quasichemical Model and the solid solution phases such as bcc, fcc, cubic and dhcp were described using the one-sublattice Compound Energy Formalism. The magnetic properties of solid phases were also taken into account.

In the thermodynamic modeling, it is found that the Mn-RE systems show systematic changes in the phase diagrams and thermodynamic properties such as enthalpy of mixing in liquid state in the order of periodic number in the lanthanide series. With increase of periodic number of light RE elements, the interaction between atoms in the liquid becomes more negative and promotes the formation of stable intermetallic compounds. This systematic thermodynamic modeling approach for all light RE elements can also allow to resolve inconsistencies in the experimental data in particular for the Mn-Sm system.

Acknowledgement

This project was supported by the National Sciences and Engineering Research Council of Canada (NSERC) Collaborative Research and Development grant and General Motors of Canada.

6. References

[1] N. Stanford, D. Atwell, A. Beer, C. Davies, M.R. Barnett, Scripta Mater. 59 (2008) 772-775.
[2] N. Stanford, Mater. Sci. Eng. A 527 (2010) 2669-2677.
[3] S. Sandloebes, S. Zaefferer, I. Schestakow, S. Yi, R. Gonzalez-Martinez, Acta Mater. 59 (2010) 429-439.
[4] H. Yan, S.W. Xu, R.S. Chen, S. Kamado, T. Honma, E.H. Han, Scripta Mater. 64 (2010) 141-144.
[5] S.A. Farzadfar, M. Sanjari, I.-H. Jung, E. Essadiqi, S. Yue, Mater. Sci. Eng. A 528 (2011) 6742-6753.
[6] Y.-B. Kang, C. Aliravci, P.J. Spencer, G. Eriksson, C.D. Fuerst, P. Chartrand, A.D. Pelton, JOM 61 (2009) 75-82.
[7] L. Jin, Y.-B. Kang, P. Chartrand, C.D. Fuerst, CALPHAD 34 (2010) 456-466.
[8] L. Jin, Y.-B. Kang, P. Chartrand, C.D. Fuerst, CALPHAD 35 (2011) 30-41.
[9] C. Tang, Y. Du, L. Zhang, H. Xu, Z. Zhu, J. Alloys Compd. 437 (2007) 102-106.
[10] Y.-B. Kang, A.D. Pelton, P. Chartrand, P. Spencer, C.D. Fuerst, J. Phase Equilib. Diff. 28 (2007) 342-354.
[11] C.P. Wang, Z. Lin, X.J. Liu, J. Alloys Compd. 469 (2009) 123-128.
[12] C.P. Wang, H.L. Zhang, S.L. Wang, Z. Lin, X.J. Liu, A.T. Tang, F.S. Pan, J. Alloys Compd. 481 (2009) 291-295.
[13] V.V. Berezutskii, M.I. Ivanov, Powder Metall. Met. Ceram. 48 (2009) 454-461.
[14] M. Ivanov, V. Berezutski, N. Usenko, Int. J. Mater. Res. 102 (2011) 277-281.
[15] A.D. Pelton, S.A. Degterov, G. Eriksson, C. Robelin, Y. Dessureault, Metall. Mater. Trans. B 31 (2000) 651-659.
[16] A.D. Pelton, P. Chartrand, Metall. Mater. Trans. A 32 (2001) 1355-1360.
[17] I.-H. Jung, D.H. Kang, W.J. Park, N.J. Kim, S. Ahn, CALPHAD 31 (2007) 192-200.
[18] D. Nassyrov, I.-H. Jung, CALPHAD 33 (2009) 521-529.
[19] A.D. Pelton, M. Blander, Metall. Trans. B 17 (1986) 805-815.
[20] P. Wu, G. Eriksson, A.D. Pelton, M. Blander, ISIJ Int. 33 (1993) 26-35.
[21] A.D. Pelton, M. Blander, Metall. Soc. AIME, Lake Tahoe, NV, 1984, pp. 281-294.
[22] M. Hillert, B. Jansson, B. Sundman, Z. Metallkd. 79 (1988) 81-87.
[23] A.T. Dinsdale, CALPHAD 15 (1991) 317-425.
[24] G. Inden, in: Project meeting CALPHAD V, Max-Planck-Inst. Eisenforschung, G.m.b.H., Dusseldorf, Germany, 1976, pp. 111.
[25] M. Hillert, M. Jarl, CALPHAD 2 (1978) 227-238.
[26] C.W. Bale, E. Belisle, P. Chartrand, S.A. Decterov, G. Eriksson, K. Hack, I.-H. Jung, Y.-B. Kang, J. Melancon, A.D. Pelton, C. Robelin, S. Petersen, CALPHAD 33 (2009) 295-311.
[27] L. Rolla, A. Iandelli, Ber. Dtsch. Chem. Ges. 75B (1942) 2091-2095.
[28] I.V. Nikolaenko, V.V. Nosova, Rasplavy (1993) 76-79.
[29] A. Palenzona, S. Cirafici, Bull. Alloy Phase Diagrams 11 (1990) 491-493.
[30] A. Iandelli, Atti Accad. Naz. Lin. 13 (1952) 265-268.
[31] M.S. Mirgalovskaya, I.A. Strel'nikova, Tr. Inst. Metall., Akad. Nauk SSSR (1957) 135-138.
[32] B.J. Thamer, J. Less-Common Met. 7 (1964) 341-346.
[33] C. Tang, Y. Du, H. Xu, S. Hao, L. Zhang, J. Min. Metall., Sect. B 43 (2007) 21-28.

[34] A. Palenzona, S. Cirafici, J. Phase Equilib. 17 (1996) 53-56.
[35] H. Okamoto, J. Phase Equilib. Diff. 29 (2008) 381-382.
[36] A. Saccone, S. Delfino, R. Ferro, J. Less-Common Met. 108 (1985) 89-105.
[37] H.R. Kirchmayr, W. Lugscheider, Z. Metallkd. 61 (1970) 22-23.
[38] S.I. Mikhalenko, Y.B. Kuz'ma, Izv. Akad. Nauk SSSR, Neorg. Mater. 26 (1990) 2432-2433.
[39] A. Saccone, S. Delfino, R. Ferro, Z. Metallkd. 84 (1993) 563-568.
[40] H. Okamoto, J. Phase Equilib. 13 (1992) 331-332.
[41] H. Okamoto, J. Phase Equilib. 15 (1994) 568-569.
[42] A.D. Pelton, Ber. Bunsen. Phys. Chem. 84 (1980) 212-218.
[43] N.H. Kim-Ngan, F.F. Bekker, P.E. Brommer, J.J.M. Franse, Physica B 160 (1990) 388-392.
[44] A.L. Shilov, L.N. Padurets, M.E. Kost, Zh. Fiz. Khim. 57 (1983) 555-560.
[45] W.B. Pearson, The crystal chemistry and physics of metals and alloys, Wiley-Interscience, New York, 1972.
[46] J. Kim, I.-H. Jung, Critical systematic evaluation and thermodynamic optimization of the Mn-RE system: RE = Gd, Tb, Dy, Ho, Er, Tm, Lu, Y and Sc, unpublished work.
[47] K.H.J. Buschow, Rep. Prog. Phys. 40 (1977) 1179-1256.

Appendix II

Appendix II

Thermodynamic modeling of the Mn-Y and Mn-Gd systems for the application of RE in Mg alloy development

Junghwan Kim and In-Ho Jung

Department of Mining and Materials Engineering, McGill University, 3610 University St., Montreal, Quebec, H3A 2B2, Canada

Corresponding author: In-Ho Jung

Tel : 1-514-398-2608

Fax : 1-514-398-4492

E-mail: in-ho.jung@mcgill.ca

Published in

Canadian Metallurgical Quarterly 52 (2013) 311-320

Abstract

Mg alloys are extensively used as light structural materials in the modern industry. Mn and RE (rare earth) metals are effectively used as alloying elements to enhance the properties of Mg alloys. Therefore, the thermodynamic database of those alloys is important in the design and processing of Mg alloys. Critical evaluation and optimization of all available literature data for the Mn-Y and Mn-Gd systems were conducted to obtain reliable thermodynamic functions of all solid and liquid phases. Recent experimental data were taken into account and the phase diagram and thermodynamic properties were slightly revised for the Mn-Y system and considerably altered for the Mn-Gd one from previous studies. Both systems have quite similar thermodynamic properties and phase diagrams. The systematic trend observed in RE elements for Mn-RE systems is discussed.

Keywords

Mg-RE (rare earth) alloy, Mn-RE system, Thermodynamic modeling, Phase diagrams, Thermodynamic properties.

1. Introduction

Magnesium alloys are getting great scientific and industrial attention as the lightest structural materials. One of the drawbacks of Mg alloys is their poor formability at room temperature due to the limited slip system with the hcp crystal structure. Recently, several studies [1-5] have shown that the addition of small amounts of RE can considerably enhance the ductility of Mg alloys. This can help to clarify the role of RE on the enhanced deformation mechanism and aid to find out the most optimum Mg alloy compositions. In order to respond to the need of Mg-RE alloy development, a large thermodynamic database for Mg alloys containing RE has been developed with critical systematic analysis and optimization of the entire RE series data. This includes the thermodynamic database of the Mg-RE [6], Mg-RE-RE [6], Mg-Al-RE [7, 8], Mg-Zn-RE and Mg-Mn-RE systems.

In the thermodynamic "optimization" of a chemical system, all available thermodynamic and phase equilibrium data are evaluated simultaneously in order to obtain one set of model equations for the Gibbs energies of all phases as functions of temperature and composition. From these equations, all the thermodynamic properties and phase diagrams can be back-calculated. In this way, all the data are rendered self-consistent and consistent with thermodynamic principles. Thermodynamic property data, such as activity data, can aid in the evaluation of the phase diagram, and phase diagram measurements can be used to deduce thermodynamic properties. Discrepancies in the available data can often be resolved, and interpolations and extrapolations can be made in a thermodynamically correct manner.

The main goal of the present study is to perform a review and critical optimization of the thermodynamic properties of alloy phases in the Mn-Y and Mn-Gd systems as an extension of the previous thermodynamic optimizations of the Mn-light RE systems (light RE = La, Ce, Pr, Nd and Sm) published by the present authors [9]. These successive studies contribute to the systematic trend observed in binary Mn-RE alloys. The lack of experiments and some discrepancies in the data available for the Mn-RE systems may be solved by the systematic analysis of the whole RE series, which can provide a more accurate evaluation of the thermodynamic properties and phase

diagram data of the Mn-RE systems. This study is part of the thermodynamic database development for multicomponent Mg-RE alloy design.

2. Thermodynamic models

2.1. Liquid phase

The Modified Quasichemical Model [10, 11], which accounts for short-range ordering of nearest-neighbor atoms, was used to model the liquid solutions because it gives a more realistic thermodynamic description of the liquid phase compared with the conventional simple random-mixing Bragg Williams model [10, 11]. The Modified Quasichemical Model was successfully applied to many liquid metallic solutions [11-13] and ionic solutions [14, 15] exhibiting strong short-range ordering.

Recently, the energy of nearest-neighbor pair formation in the Modified Quasichemical Model was expanded as a polynomial in the pair fractions [10, 11] instead of the component fractions [14, 16]. In addition, the coordination numbers are now allowed to vary with composition. These modifications provide greater flexibility in reproducing binary experimental data and in combining optimized binary liquid parameters into a large database for multicomponent solutions [10]. A short description of the model is given below; details can be found in previous studies [10, 11].

In the case of a binary *A-B* liquid solution, the atoms *A* and *B* are distributed over the sites of a quasi-lattice in liquid solution. The following pair exchange reaction can be considered:

$$(A-A)+(B-B)=2(A-B) \qquad (1)$$

where *(A – B)* represents a first-nearest-neighbor pair of *A* and *B*. The non-configurational Gibbs energy change for the formation of two moles of *A-B* pairs according to reaction (1) is Δg_{AB}. Then the Gibbs energy of the solution is given by:

$$G = (n_A G_A^{\circ} + n_B G_B^{\circ}) - T\Delta S^{\text{config}} + n_{AB}(\Delta g_{AB}/2) \tag{2}$$

where G_A° and G_B° are the molar Gibbs energies of the pure components *A* and *B*, n_A and n_B are the numbers of moles of *A* and *B* atoms, and n_{AB} is the number of moles of *A*-*B* pairs. ΔS^{config} is the configurational entropy of mixing given by a random distribution of the *A*-*A*, *B*-*B* and *A*-*B* pairs in the one-dimensional Ising approximation:

$$\begin{aligned}\Delta S^{\text{config}} &= -R(n_A \ln X_A + n_B \ln X_B) \\ &\quad - R[n_{AA} \ln(X_{AA}/Y_A^{\,2}) + n_{BB} \ln(X_{BB}/Y_B^{\,2}) \\ &\quad + n_{AB} \ln(X_{AB}/2Y_AY_B)]\end{aligned} \tag{3}$$

where n_{AA}, n_{BB} and n_{AB} are the numbers of moles of each kind of pairs, and the pair fraction (X_{AA}, X_{BB} and X_{AB}) and coordination equivalent fraction (Y_A and Y_B) can be calculated as:

$$X_{AA} = n_{AA}/(n_{AA} + n_{BB} + n_{AB}) \tag{4}$$

$$X_{BB} = n_{BB}/(n_{AA} + n_{BB} + n_{AB}) \tag{5}$$

$$X_{AB} = n_{AB}/(n_{AA} + n_{BB} + n_{AB}) \tag{6}$$

$$Y_A = X_{AA} + X_{AB}/2 \tag{7}$$

$$Y_B = X_{BB} + X_{AB}/2 \tag{8}$$

The Δg_{AB} is the model parameter to reproduce the Gibbs energy of liquid phase of the binary *A*-*B* system, which is expanded as a polynomial in terms of the pair fractions, as follows:

$$\Delta g_{AB} = \Delta g_{AB}^{\circ} + \sum_{i\geq 1} g_{AB}^{io}(X_{AA})^i + \sum_{j\geq 1} g_{AB}^{oj}(X_{BB})^j \tag{9}$$

where Δg°_{AB}, g^{io}_{AB} and g^{oj}_{AB} are the adjustable model parameters which can be functions of temperature.

In the Modified Quasichemical Model, the coordination numbers of *A* and *B*, Z_A and Z_B, can be varied with composition to reproduce the short-range-ordering as follows:

$$\frac{1}{Z_A} = \frac{1}{Z^A_{AA}}\left(\frac{2n_{AA}}{2n_{AA}+n_{AB}}\right) + \frac{1}{Z^A_{AB}}\left(\frac{n_{AB}}{2n_{AA}+n_{AB}}\right) \tag{10}$$

$$\frac{1}{Z_B} = \frac{1}{Z^B_{BB}}\left(\frac{2n_{BB}}{2n_{BB}+n_{AB}}\right) + \frac{1}{Z^B_{BA}}\left(\frac{n_{AB}}{2n_{BB}+n_{AB}}\right) \tag{11}$$

where Z^A_{AA} is the value of Z_A when all nearest neighbors of an *A* atom are *A* atoms, and Z^A_{AB} is the value of Z_A when all nearest neighbors are *B* atoms. Z^B_{BB} and Z^B_{BA} are defined in an analogous manner. In the present study, Z^i_{ii} for all elements (i = Mn and RE) are set to be 6. To reproduce the maximum or minimum enthalpies of the Mn-RE liquid alloys at 0.3 ~ 0.4 mole fraction RE, Z^{Mn}_{MnRE} and Z^{RE}_{MnRE} are set to be 3 and 6, respectively. During the course of the present study, it was found that this set of coordination numbers can reproduce the experimental data more accurately with a small number of model parameters. For example, if the coordination numbers of Mn and RE for all nearest neighbors were set to 6, more model parameters would have been required and the experimental data would have been less accurately reproduced.

2.2. Solid solutions

The solid solution phases were described by the Compound Energy Formalism [17] with a one-sublattice approach (Mn, RE) for substitutional site. The molar Gibbs energy of the solid solution can be expressed as:

$$G = (y_{Mn} G^{\circ}_{Mn} + y_{RE} G^{\circ}_{RE}) + RT(y_{Mn} \ln y_{Mn} + y_{RE} \ln y_{RE}) + {}^{a}L_{Mn,RE} y_{Mn} y_{RE} (y_{RE} - y_{Mn})^{a} \quad (12)$$

where y_{Mn} and y_{RE} are the site fractions of Mn and RE elements in the sublattice, and R and T are the gas constant and temperature in Kelvin, respectively. G°_{Mn} and G°_{RE} are the molar Gibbs energies of solid phases of Mn and RE. The binary interaction parameters between Mn and RE in the sublattice, ${}^{a}L_{Mn,RE}$ where $a \geq 0$, are adjustable model parameters.

2.3. Stoichiometric compounds and elements

The Gibbs energies of all pure elements are taken from the SGTE database version 5.0 [18]. As the heat capacities of all stoichiometric compounds in the Mn-Y and Mn-Gd systems were not available, they were estimated using the Neumann-Kopp (NK) approximation and slightly adjusted to reproduce the low-temperature heat capacity data. When there is no experimental study for the enthalpy and entropy of formation at 298 K of the intermetallic compounds, the enthalpy and entropy of formation at 298 K were used as adjustable parameters to reproduce the phase diagram of the systems.

Mn (BCC-A2), Mn (FCC-A1), Mn_2RE and $Mn_{23}RE_6$ (RE = Gd and Y) phases exhibit magnetic transitions associated with Néel or Curie temperatures. The magnetic transition below 298 K (typically anti-ferromagnetic transition with Néel temperature) was directly taken into account in the calculation of S°_{298}. The Curie temperature (ferromagnetic transition) occurs typically above 298 K, of which magnetic contribution to the Gibbs energy was considered by an empirical relationship suggested by Inden [19] and modified by Hillert and Jarl [20].

3. Critical evaluation and thermodynamic optimization

The thermodynamic optimizations of the Mn-Y and Mn-Gd systems were performed based on all available thermodynamic data for the compounds, solid and liquid solutions and on the critically

assessed phase diagram data. The details of the thermodynamic optimizations are explained in the following sections. The optimized model parameters for the Mn-Y and Mn-Gd systems are listed in Table 1. All the thermodynamic calculations were performed using the FactSage thermodynamic software [21].

Table 1. Optimized model parameters for the binary Mn-Y and Mn-Gd systems (J mol^{-1} or J mol^{-1} K^{-1}).

Phase	Thermodynamic parameters
Liquid	Coordination Numbers
	i j Z_{ij}^{i} Z_{ij}^{j}
	Mn Y 3 6
	Mn Gd 3 6
	Δg_{MnY}= -2301.2 - 2510.4 X_{MnMn}+ (-836.8 - 0.837T) X_{YY}
	+ (-418.4 - 1.255T) X_{MnMn}^{3}
	Δg_{MnGd}= -3640.1 + (836.8 - 1.255 T) X_{MnMn}+ (1589.9 - 1.046 T) X_{GdGd}
BCC-A2	${}^{0}L_{Mn,Y}$ = 35564
	${}^{0}L_{Mn,Gd}$ = 37656
	$T_{c,Mn}^{BCC-A2}$ (Curie temperature) = 580 K,
	$B_{o,Mn}^{BCC-A2}$ (Magnetic moment) = 0.27 μ_B mol^{-1}
FCC-A1	${}^{0}L_{Mn,Y}$ = 33472
	$T_{c,Mn}^{FCC}$ = 540 K, $B_{o,Mn}^{FCC}$ = 0.62 μ_B mol^{-1}
Mn_2Y	ΔH_{298}^{o} = -6500, S_{298}^{o} = 114.507
	C_p = 2 × C_p (Mn,CBCC-A12) + C_p (Y,HCP-A3) + 10 J mol^{-1} K^{-1}
$Mn_{23}Y_6$	ΔH_{298}^{o} = -115000, S_{298}^{o} = 1017.55
	C_p = 23 × C_p (Mn,CBCC-A12) + 6 × C_p (Y,HCP-A3) + 60 J mol^{-1} K^{-1}
	T_c = 486 K, B_o = 13.2 μ_B mol^{-1} [47]
$Mn_{12}Y$	ΔH_{298}^{o} = -18000, S_{298}^{o} = 437.62
	C_p = 12 × C_p (Mn,CBCC-A12) + C_p (Y,HCP-A3) + 19 J mol^{-1} K^{-1}

Mn_2Gd	ΔH^{o}_{298} = -5400, S^{o}_{298} = 144.25 C_p = 2 × C_p (Mn,CBCC-A12) + C_p (Gd,HCP-A3) + 4 J mol^{-1} K^{-1}
$Mn_{23}Gd_6$	ΔH^{o}_{298} = -84700, S^{o}_{298} = 1198.60 C_p = 23 × C_p (Mn,CBCC-A12) + 6 × C_p (Gd,HCP-A3) + 24 J mol^{-1} K^{-1} T_c = 461 K, B_O = 49 μ_B mol^{-1} [47]
$Mn_{12}Gd$	ΔH^{o}_{298} = -15200, S^{o}_{298} = 470.20 C_p = 12 × C_p (Mn,CBCC-A12) + C_p (Gd,HCP-A3) + 4 J mol^{-1} K^{-1}

*The Gibbs energies of all pure solid and liquid elements are taken from the SGTE database version 5.0 [18].

3.1. The Mn-Y system

The first phase diagram investigation of the Mn-Y system was carried out by Hellawell [22] on Mn-rich alloys using thermal analysis (TA) with thoria refractory crucibles followed by metallography and XRD phase analysis. From the three thermal arrests detected at 1133 °C, 1100 °C and 1079 °C, which correspond to the transition temperatures of Mn solid solutions, Hellawell [22] observed nearly no solubility of Y in Mn (CBCC-A12) and Mn (CUB-A13) and a solubility of about 0.5 at. % Y in Mn (FCC-A1) and Mn (BCC-A2). Later, Myklebust and Daane [23] investigated the complete phase diagram using TA, metallography and XRD. The alloys were prepared from starting materials made of 99.9 wt. % Mn and 99.7 wt. % Y in an arc-melting furnace under argon atmosphere and were sealed in tantalum crucibles for TA to prevent oxidation and evaporation of the samples. In order to minimize the reactions between crucibles and high-Mn alloys (higher than 80 at. % Mn), the thermal arrests of the first heating cycles were the only ones used in the determination of the phase diagram. Three intermetallic compounds ($Mn_{12}Y$, Mn_4Y and Mn_2Y) and their invariant reactions were reported. The existence of a miscibility gap associated to the syntectic reaction ($l_1 + l_2 \rightarrow Mn_4Y$) was indicated by TA, metallograhy and XRD at 80.6 at. % Mn, but the composition and temperature of the miscibility gap were not confirmed. The solubility of Mn in solid Y was proposed to be very small based on the transition temperature (1453 °C) between Y (BCC-A2) and Y (HCP-A3), which is close to the transition temperature (1455 °C by TA and 1459 °C by resistivity measurements) reported by Habermann [24]. However, those transition temperatures differ with the transition temperature of pure Y reported in the SGTE database (1478 °C) [18] due to possible impurities in the yttrium starting material. The Mn_4Y phase determined by Myklebust and Daane [23] was corrected to be $Mn_{23}Y_6$ by Kripyakevich and Frankevich [25] based on a crystallographic study. Another solid solubility study was performed by Flandorfer et al. [26] using XRD and EPMA from annealed (at 800 °C in Mo foil) and quenched alloys. The solubilities of Mn in Y (HCP-A3) and Y in Mn (CUB-A13) at 800 °C and the homogeneity range of the Mn_2Y phase were confirmed to be negligible. All the phase diagram experimental data are shown in Figure 1.

Valishev et al. [27] determined the partial and integral enthalpies of mixing of liquid Mn-Y solution using isoperibolic calorimetry. Using starting materials made of high purity alloys prepared from 99.98 wt. % Mn and 99.8 wt. % Y, the partial enthalpies of mixing of the Mn-rich region ($0 < X_{Mn} < 0.52$) were measured at 1873 K in corundum crucibles with helium atmosphere. Then, based on a least-squares analysis and the Gibbs-Duhem equation, the authors suggested smoothed values for both, the partial enthalpies of mixing and the integral enthalpy of mixing, in the composition range up to 50 at. % Y. Unfortunately, the authors give only smoothed values of partial and integral enthalpies of mixing without any experimental data. The integral enthalpy of mixing of liquid Mn-Y shows negative deviation from ideal solution behavior and the minimum seems to be about -2 kJ mol^{-1} between 0.3 to 0.4 mole fraction of Y. The enthalpies of mixing of the liquid solution are both shown in Figure 2.

Some thermodynamic properties of the intermetallic compounds were experimentally determined as well. The low-temperature heat capacities (C_p) of $Mn_{12}Y$ and Mn_2Y, which can be used to determine the entropies of the phases at 298 K (S^{o}_{298}), were measured by Piqué et al. [28] and Okamoto et al. [29], respectively. Piqué et al. [28] measured the heat capacity of $Mn_{12}Y$ between 5 and 350 K using adiabatic calorimetry and the heat pulse method. The calculated S^{o}_{298} from the integration of experimental C_p values is 438.6 J mol^{-1} K^{-1}. Okamoto et al. [29] measured the C_p of Mn_2Y between 4 and 280 K. There is an anomaly (Figure 3(a)) in the C_p of Mn_2Y at about 100 K corresponding to the Néel temperature; by integrating the C_p data, the resulting S^{o}_{298} is 116.5 J mol^{-1} K^{-1}. The delta entropies of formation at 298 K calculated from the experimental data of $Mn_{12}Y$ and Mn_2Y are shown in Figure 3(b). Pisch et al. [30] determined the enthalpies of formation (ΔH^{o}_{298}) of Mn_2Y and $Mn_{23}Y_6$ using drop solution calorimetry with liquid Al. The compounds were prepared by levitation melting from high purity starting materials (99.98 % Mn, 99.9 % Y and > 99.9999 % Al). The measured ΔH^{o}_{298} of Mn_2Y and $Mn_{23}Y_6$ are -2.4 ± 2.5 and -5.3 ± 1.7 kJ mol-atom^{-1}, respectively. Recently, Meschel et al. [31] measured the ΔH^{o}_{298} of Mn_2Y using high-temperature direct synthesis calorimetry at 1373 K. A ΔH^{o}_{298} of -2.8 ± 2.8 kJ mol-atom^{-1} was obtained by the difference in enthalpy change associated with the reaction between Mn_2Y and its corresponding elements. The authors also reported a heat content H_{1373K}-H_{298K} of 29.3 ± 2.6 kJ

mol-atom^{-1} for Mn_2Y. In order to reproduce this data, the C_p of Mn_2Y must be much lower than the one predicted by the NK approximation, which is in conflict with the low temperature C_p data of Mn_2Y measured by Okamoto et al. [29]. Therefore, the heat content data was not taken into account in the present study. Experimental and calculated ΔH^{o}_{298} are compared in Figure 3(c).

The Mn-Y system was previously assessed by Palenzona and Cirafici [32] using mainly the phase diagram investigations of Hellawell [22] and Myklebust and Daane [23] and the system reviewed by Okamoto [33]. Thermodynamic optimizations were performed by Flandorfer et al. [26], Gröbner et al. [34] and Kang et al. [35]. The liquid miscibility gap proposed by Myklebust and Daane [23] was excluded since the syntectic formation of $Mn_{23}Y_6$ seemed to be very unlikely according to Okamoto and Massalski [36]. Flandorfer et al. [26] assessed the system using mostly the data of Myklebust and Daane [23] and their own solubility investigation based on the Bragg-Williams random mixing model and the Redlich–Kister polynomial expression for the liquid phase. However, they did not consider in their optimization the thermodynamic data of the liquid phase determined by Valishev et al. [27] and thermodynamic data of the compounds measured by Okamoto et al. [29]. Unfortunately, the thermodynamic data of the compounds determined by Piqué et al. [28], Pisch et al. [30] and Meschel et al. [31] were not available at the time of their optimization. Gröbner et al. [34] optimized the system using the same liquid model as Flandorfer et al. [26] based on the phase diagram data of Myklebust and Daane [23], the thermodynamic data of the liquid phase determined by Valishev et al. [27], and the ΔH^{o}_{298} of Mn_2Y and $Mn_{23}Y_6$ determined by Pisch et al. [30]. Regrettably, again, the thermodynamic data of Piqué et al. [28] and Meschel et al. [31] were not available for their optimization. In the recent optimization of Kang et al. [35], the solubilities of Y in Mn (CBCC-A12) and Mn (CUB-A13) determined by Hellawell [22] were not taken into account. In the optimization of Flandorfer et al. [26], the calculated integral and partial enthalpies of mixing of the liquid phase at 1873 K are significantly off from the experimental data of Valishev et al. [27] and those from the work of Gröbner et al. [34] are also not very satisfactory. Moreover, in the optimization of Flandorfer et al. [26], the ΔH^{o}_{298} and S^{o}_{298} of the compounds are remarkably different from the experimental data. Although there is no experimental proof, Mn_2Y can be unstable at 298 K as shown in the optimizations of Gröbner et al. [34] and Kang et al. [35] due to its enthalpy of formation. On the other hand, in the

optimization of Flandorfer et al. [26], $Mn_{23}Y_6$ is unstable at 298 K. The calculated integral and partial enthalpies of mixing and the enthalpy and entropy of formation of the compounds from all previous optimizations are compared to the experimental data in Figures 2 and 3, respectively.

In the present thermodynamic modeling, the enthalpy of mixing of the liquid, determined by Valishev et al. [27], was taken into account to determine the model parameters of the liquid phase. The temperature-independent terms of the liquid interaction parameters were firstly adjusted to reproduce the experimental enthalpy data. Then, the Gibbs energies of the BCC-A2 and FCC-A1 solid solutions and of the three stoichiometric compounds were assessed to fit the phase diagram based on the available experimental data. The mutual solubilities of Mn and Y in both FCC-A1 and BCC-A2 solid solutions were reproduced with one temperature-independent Gibbs energy excess parameter with the assumption of large solid state miscibility gaps. The solubilities of Y in Mn (BCC-A2) and Mn (FCC-A1) were estimated using their liquidus and the transition temperatures of Mn (BCC-A2) to Mn (FCC-A1) and Mn (FCC-A1) to Mn (CUB-A13), respectively. The C_p above 298 K for $Mn_{12}Y$, $Mn_{23}Y_6$ and Mn_2Y were increased from the C_p evaluated by the NK approximation to fit the experimental low-temperature C_p data, as shown in Figure 3(a). The C_p increment of $Mn_{23}Y_6$ was applied to be consistent with other compounds ($Mn_{12}Y$ and Mn_2Y). The ΔH^{o}_{298} and S^{o}_{298} of the compounds were optimized to reproduce the experimental thermodynamic properties of compounds and the phase diagram. Finally, a small temperature-dependent model parameter for the liquid phase was needed to reproduce the phase diagram accurately. As seen in Figures 1 to 3, the optimized phase diagram, calculated enthalpies of the liquid phase and enthalpy of formation of compounds are in good agreement with experimental data. The only discrepancies observed are for the Mn and Y liquidus. However, such experimental liquidus data are little plausible from the viewpoint of the limiting slope rule [37].

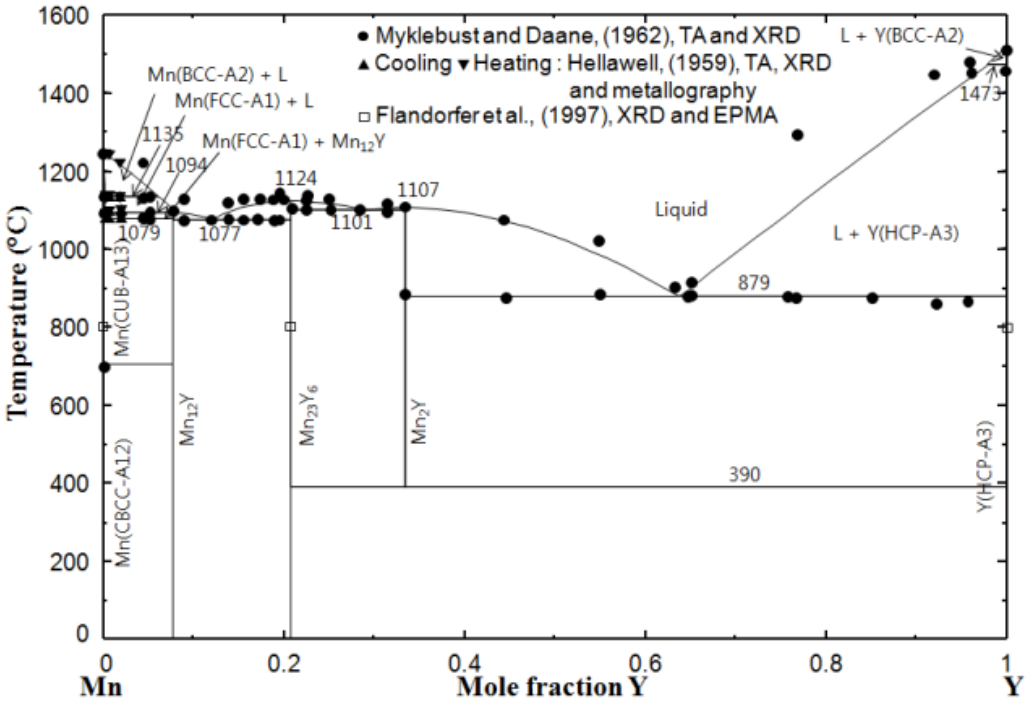


Fig. 1. The optimized Mn-Y phase diagram with experimental data [22, 23, 26].

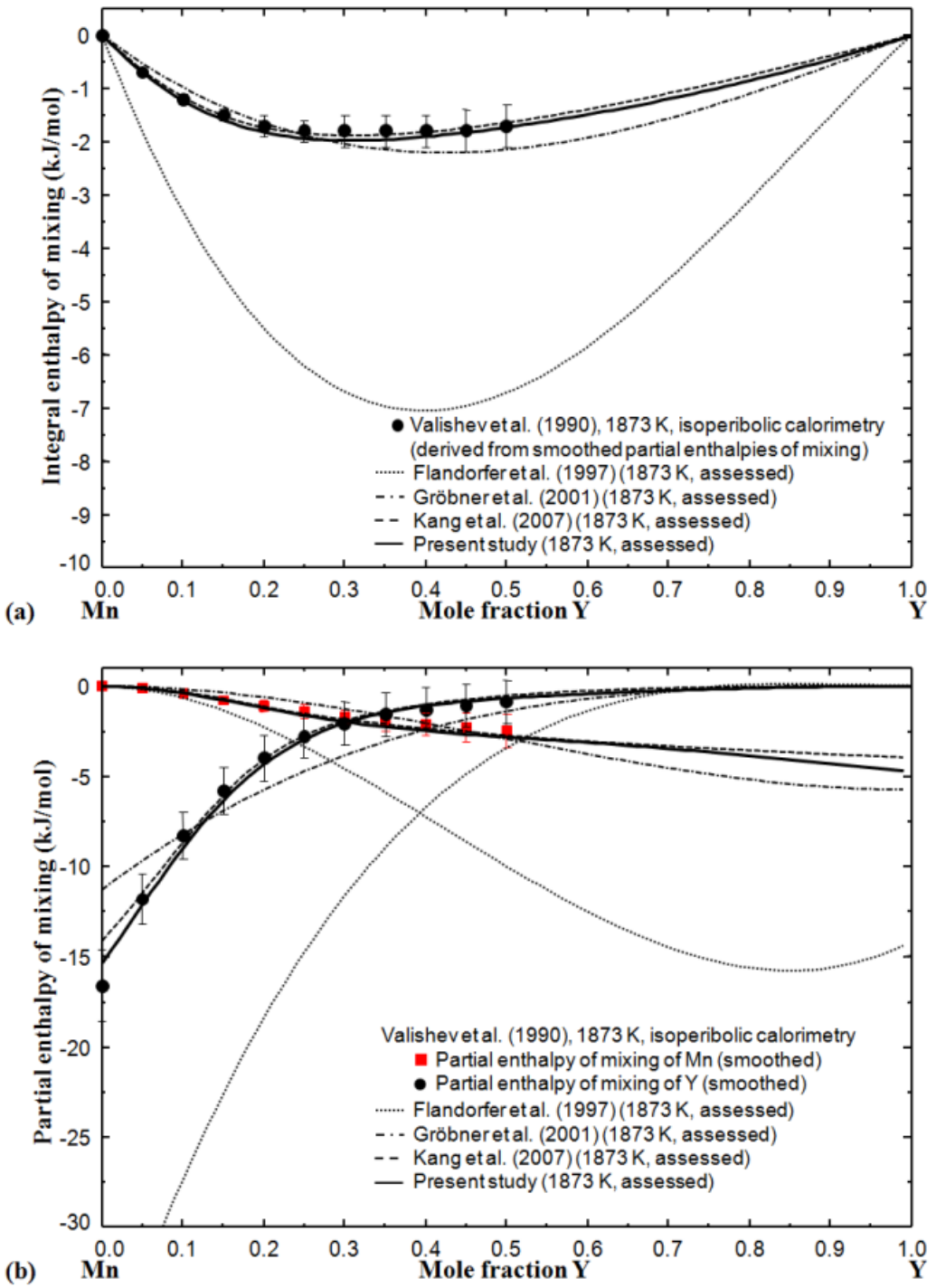
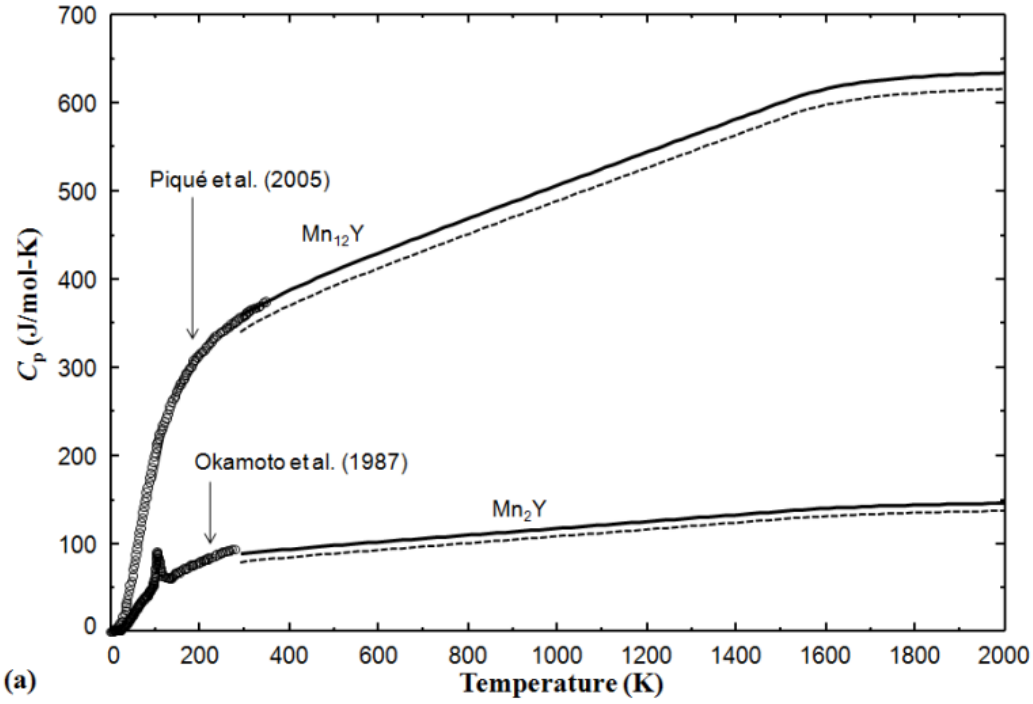
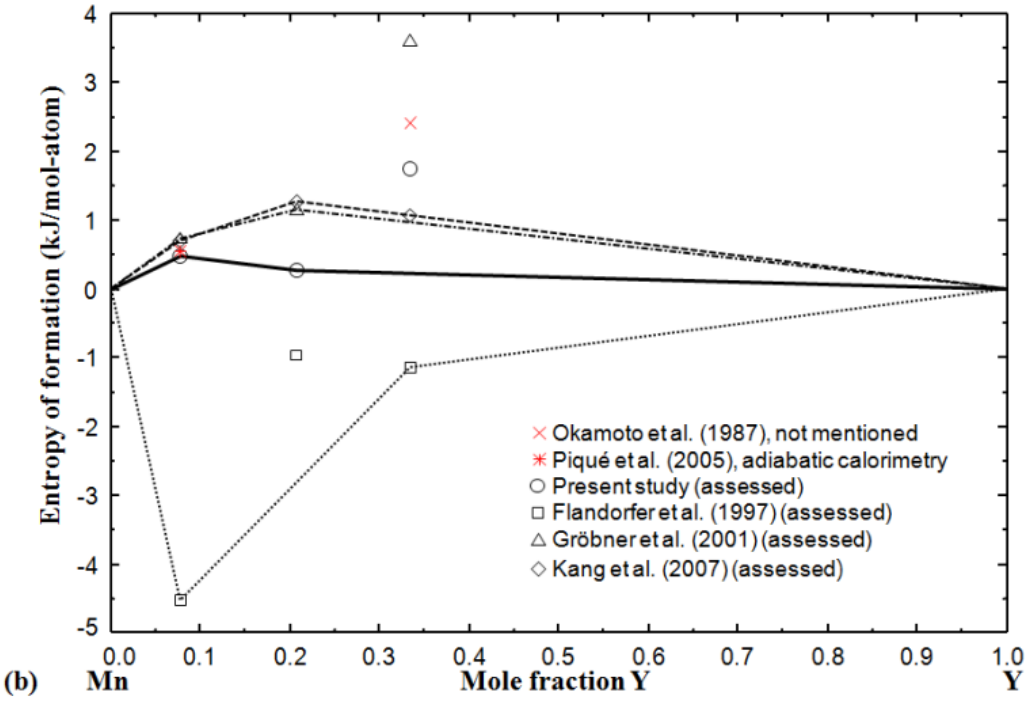


Fig. 2. (a) Integral enthalpy of mixing and (b) partial enthalpies of mixing in Mn-Y liquid at 1873 K with experimental data [27]. The previous optimizations [26, 34, 35] are depicted by lines.


Piqué et al. (2005)
$Mn_{12}Y$
Okamoto et al. (1987)
Mn_2Y
C_p (J/mol-K)
Temperature (K)

(a)


Okamoto et al. (1987), not mentioned
Piqué et al. (2005), adiabatic calorimetry
Present study (assessed)
Flandorfer et al. (1997) (assessed)
Gröbner et al. (2001) (assessed)
Kang et al. (2007) (assessed)
Entropy of formation (kJ/mol-atom)
Mole fraction Y

(b) Mn Y

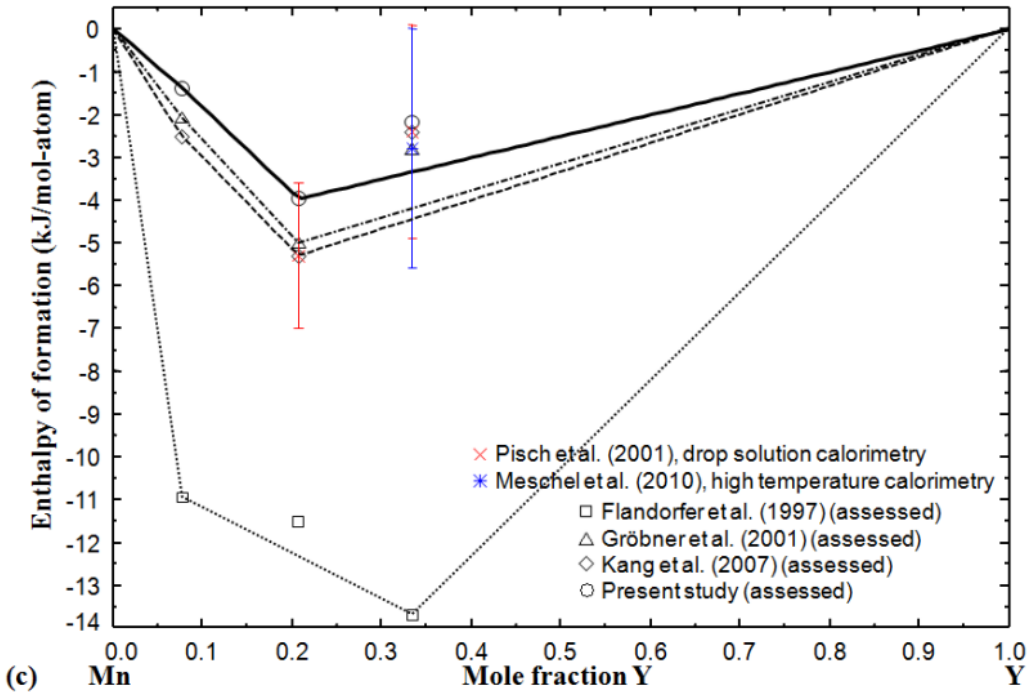


Fig. 3. (a) Heat capacities of $Mn_{12}Y$ and Mn_2Y with experimental data [28, 29]. The C_p, obtained by the NK approximation, is drawn as dashed line. (b) Delta entropy of formation of the compounds at 298 K with experimental data [28, 29] and previous optimizations [26, 34, 35] (c) Enthalpy of formation of the compounds at 298 K with experimental data [30, 31] and previous optimizations [26, 34, 35]. The previous optimizations are depicted by lines except for the unstable compounds at 298 K.

3.2. The Mn-Gd system

The first phase diagram investigation was performed by Kirchmayr and Lugscheider [38] using differential thermal analysis (DTA) and XRD. The RE-Mn alloys were prepared by amalgam process [39] by heating RE-Mn-Hg alloys below the liquidus (900 ~ 1100 °C) to remove Hg by evaporation. The heating rate used was less than 6 °C min^{-1} and tantalum crucibles and purified argon were employed to prevent oxidation and reactions between the samples and the crucibles. Numerous invariant reactions (eutectic and peritectic) and three incongruent melting intermetallic compounds ($Mn_{12}Gd$, $Mn_{23}Gd_6$ and Mn_2Gd) were observed. A eutectic reaction point was detected at 0.65 mole fraction Gd and 830 °C. The solubility of Gd in Mn at 1000 °C reaches about 1 mol % Gd. Recently, Antion [40] reinvestigated the system by DTA (using Ta and alumina crucibles), metallography, and six alloys. Unlike the work of Kirchmayr and Lugscheider [38], Antion [40] suggested that Mn_2Gd melts congruently and a syntectic reaction involving a liquid miscibility gap takes place during the melting of $Mn_{23}Gd_6$. In addition, the eutectic temperature of the reaction liquid → Mn_2Gd + Gd (HCP-A3) was observed at 812 °C, which is rather low. All these experimental data are shown in Figure 4.

Nikolaenko and Nosova [41] measured the partial enthalpy of mixing of Gd between $0 < X_{Gd} < 0.27$ and that of Mn between $0.45 < X_{Gd} < 1.0$ at 1600 K in Mn-Gd liquid using isoperibolic calorimetry. Alundum crucibles and starting materials made of 99.9 % Mn and 99.98 % Gd were used. Experimental data were submitted to least-squares analysis and with the help of the Gibbs-Duhem equation, smoothed values were obtained for both the partial and integral enthalpies of mixing of the entire liquid Mn-Gd solution. The smoothed integral enthalpy of mixing is positive between 0 and about 0.35 mol fraction Gd and negative above 0.35 mol fraction Gd. The enthalpy curves reach a maximum of about 3 kJ mol^{-1} at 0.2 mol fraction Gd and a minimum of about -2.5 kJ mol^{-1} at 0.5 mol fraction Gd. Recently, Ivanov et al. [42] measured the partial enthalpy of mixing of Gd between $0 < X_{Gd} < 0.38$ and that of Mn between $0.45 < X_{Gd} < 1.0$ in the Mn-Gd liquid at 1650 K using isoperibolic calorimetry with high purity alloys prepared from 99.95 wt. % Mn and 99.98 wt. % Gd. The partial enthalpies of Gd were measured with alumina crucibles for the alloys having high Mn contents and zirconia crucibles for the alloys having low Mn contents while the

partial enthalpies of Mn were measured with molybdenum crucibles for the alloys having high Gd contents and zirconia crucibles for the alloys having low Gd contents. The smoothed values of both the partial enthalpies of mixing and the integral enthalpy of mixing in the entire liquid Mn-Gd solution were determined by the same method used by Nikolaenko and Nosova [41]. However, the results of both smoothed partial and integral enthalpies of mixing are considerably different to the ones determined by Nikolaenko and Nosova [41]. The smoothed integral enthalpy of mixing shows negative values in the whole composition range, which has a minimum of about -2 kJ mol^{-1} at 0.4 mol fraction Gd. All the experimentally measured enthalpies of mixing of the Mn-Gd liquid are presented in Figures 5(a) and 5(b).

Some thermodynamic properties of the intermetallic compounds were also determined. Low-temperature C_p data were measured by Okamoto et al. [29], Makihara et al. [43] and Marcos et al. [44] for the Mn_2Gd phase. These C_p data are presented in Figure 6(a). Okamoto et al. [29] measured the C_p between 7 and 274 K but the authors did not explain their experimental procedure. The S^{o}_{298} was calculated from the C_p values measured by Okamoto et al. [29] after extrapolation to 298 K; a value of 148.8 J mol^{-1} K^{-1} was obtained. Makihara et al. [43] measured the C_p between 5 and 250 K using adiabatic calorimetry. The calculated S^{o}_{298} after extrapolation to 298 K is 154.6 J mol^{-1} K^{-1}. Marcos et al. [44] measured the C_p between 1.8 and 300 K by a relaxation method using a Quantum Design PPMS system. The calculated S^{o}_{298} is 144.6 J mol^{-1} K^{-1}. The delta entropies of formation at 298 K calculated from all the experimental data of Mn_2Gd are shown in Figure 6(b). No ΔH^{o}_{298} was available in the literature for the compounds.

The system was reviewed by Okamoto [45] and thermodynamic optimizations were carried out by Gröbner et al. [34] and Antion [40] using the same liquid model than for the Mn-Y system. The experimental phase diagram data of Kirchmayr and Lugscheider [38] were the only data available for the optimization of Gröbner et al. [34]. The experimental data of Nikolaenko and Nosova [41] were excluded because they show a large scattering. Moreover, their calculated integral enthalpy of mixing at 1650 K is slightly more positive than the experimental data of Ivanov et al. [42]. On the other hand, Antion [40] optimized the system using the enthalpy of mixing data of Nikolaenko

and Nosova [41] and his own experimental phase diagram data which was quite different with the one of Kirchmayr and Lugscheider [38]. The congruent melting of Mn_2Gd and the liquid miscibility gap associated to the syntectic reaction that involves $Mn_{23}Gd_6$ were considered in his optimization. Unfortunately in both optimizations, the low-temperature C_p data [29, 43] were not taken into account and the new enthalpy data of the liquid by Ivanov et al. [42] and the low-temperature C_p data of Marcos et al. [44] were not available. The calculated integral and partial enthalpies of mixing at 1650 K from both optimizations are compared to the experimental data in Figure 5 and the calculated entropies and delta enthalpies of formation of the compounds are presented in Figures 6(b) and (c), respectively.

In our optimization, the enthalpy of mixing of the liquid, determined by Ivanov et al. [42], was taken into account to determine the model parameters of the liquid phase because the data of Ivanov et al. [42] are consistent with the enthalpy of mixing of the liquid in the Mn-light RE systems [9]. The integral enthalpies of mixing systematically decrease along the periodic number of RE. The enthalpies of mixing at 1600 K for the Mn-Y, Mn-Gd and Mn-light RE systems are shown in Figure 7. Like the Mn-Y system, the temperature-independent terms of the liquid interaction parameters were firstly evaluated to reproduce the experimental enthalpy data. Then, the Gibbs energies of the BCC-A2 solid solution and the three stoichiometric compounds were assessed to fit the phase diagram using all the available experimental data. The mutual solubility of Mn and Gd in BCC-A2 solid solution was reproduced with one temperature-independent Gibbs energy excess parameter with the assumption of large solid state miscibility gaps. The solubility of Gd in Mn (BCC-A2) was considered and estimated using the liquidus and the transition temperatures of Mn (BCC-A2) to Mn (FCC-A1). The C_p above 298 K of Mn_2Gd was increased from the C_p evaluated by the NK approximation to fit the experimental data as shown in Figure 6(a). A slight increment in the C_p of $Mn_{12}Gd$ and $Mn_{23}Gd_6$ was applied to be consistent with Mn_2Gd. The ΔH^{o}_{298} and S^{o}_{298} of the compounds were assessed to reproduce the experimental data. Considering the enthalpies of mixing of the liquid [42] and S^{o}_{298} of Mn_2Gd, which are calculated from the low-temperature C_p [29, 43, 44], the congruent melting of Mn_2Gd suggested by Antion [40] appears to be more reliable than the incongruent melting suggested by Kirchmayr and Lugscheider [38] because it was unfeasible to reproduce the peritectic reaction of Mn_2Gd, the

enthalpies of mixing of the liquid, and the S^{o}_{298} of Mn_2Gd simultaneously despite of using temperature-dependent parameters for the liquid phase. This result also supports our previous study [9] which shows that the phase diagram investigation of Kirchmayr and Lugscheider [46] was not reliable for the Mn-Nd system. We also proposed a possible phase diagram for the Mn-Sm system rather than the one suggested by Kirchmayr and Lugscheider [46] even though there is no other phase diagram investigation. In addition, the phase diagram and thermodynamic properties of the Mn-Gd system are expected to be quite similar to those of the Mn-Y system in which the $Mn_{23}Y_6$ and Mn_2Y compounds melt congruently, regarding the similarity of Gd and Y in terms of electronic and physical properties (metallic radius: 180 pm for Y and 180 pm for Gd; electronegativity: 1.20 for Y and 1.20 for Gd). However, the liquid miscibility gap proposed by Antion [40] was excluded since the syntectic formation of $Mn_{23}Gd_6$ seemed to be very unlikely due to the same reason discussed for the Mn-Y system. Therefore, the optimization was conducted based mostly on the invariant temperatures of Antion [40] and other thermodynamic properties. The proposed liquidus temperatures by Antion [40] seem not to be correct according to the present optimization. The results are compared to the experimental data and previous thermodynamic optimizations in Figures 4 to 6.

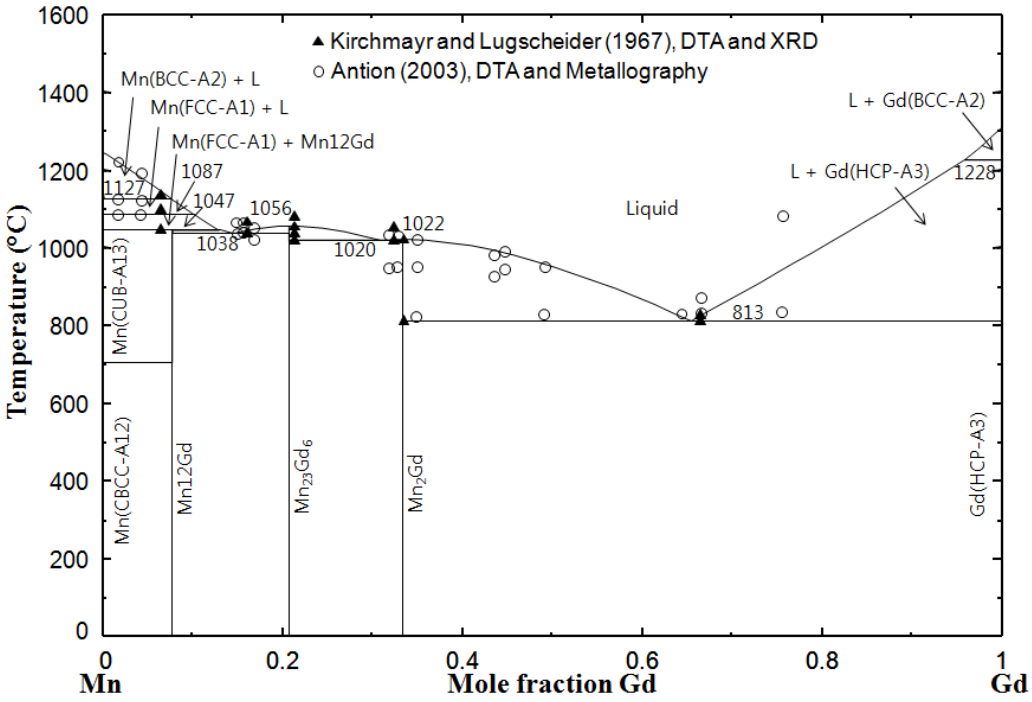


Fig. 4. The optimized Mn-Gd phase diagram with experimental data [38, 40].

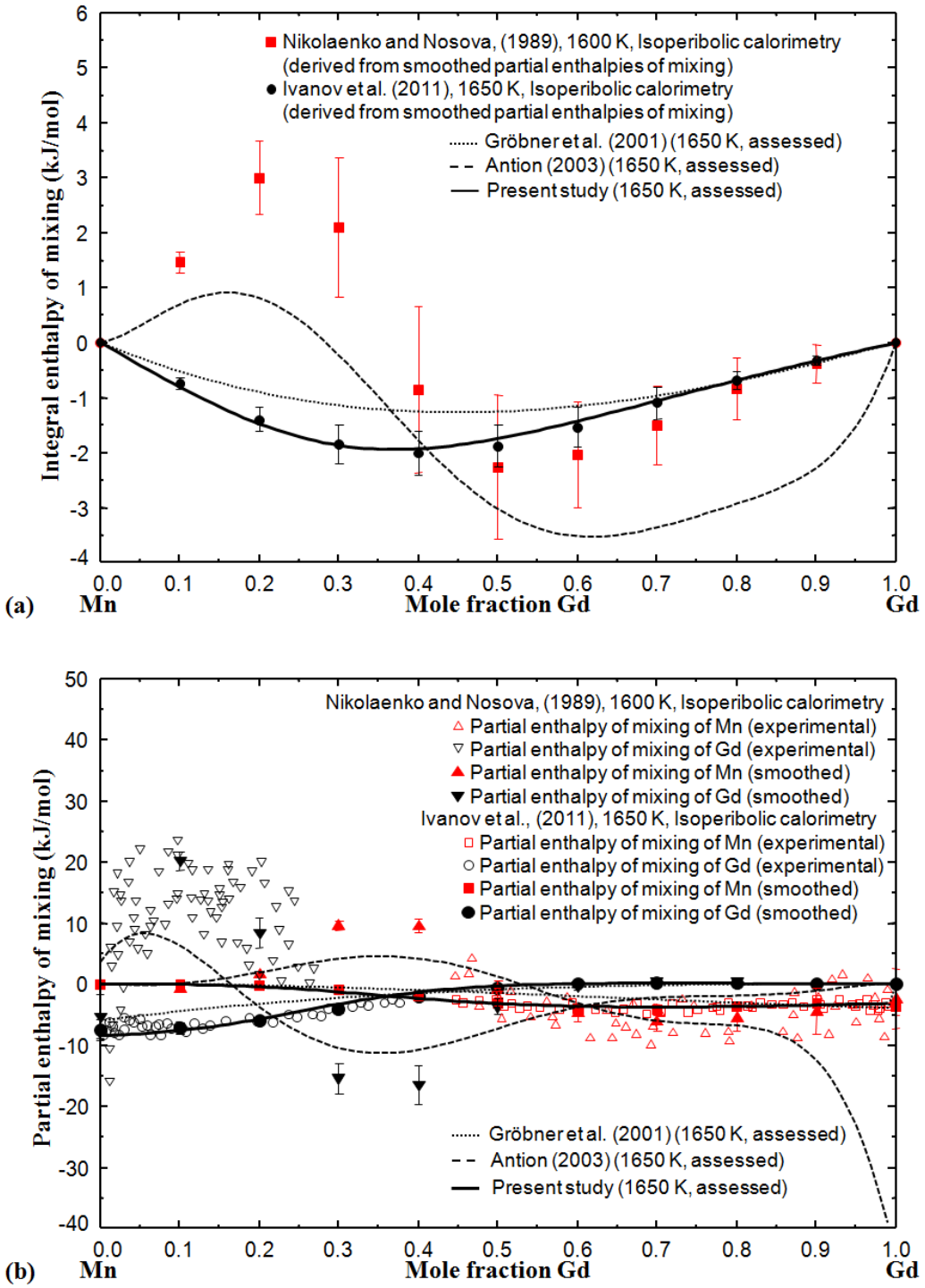
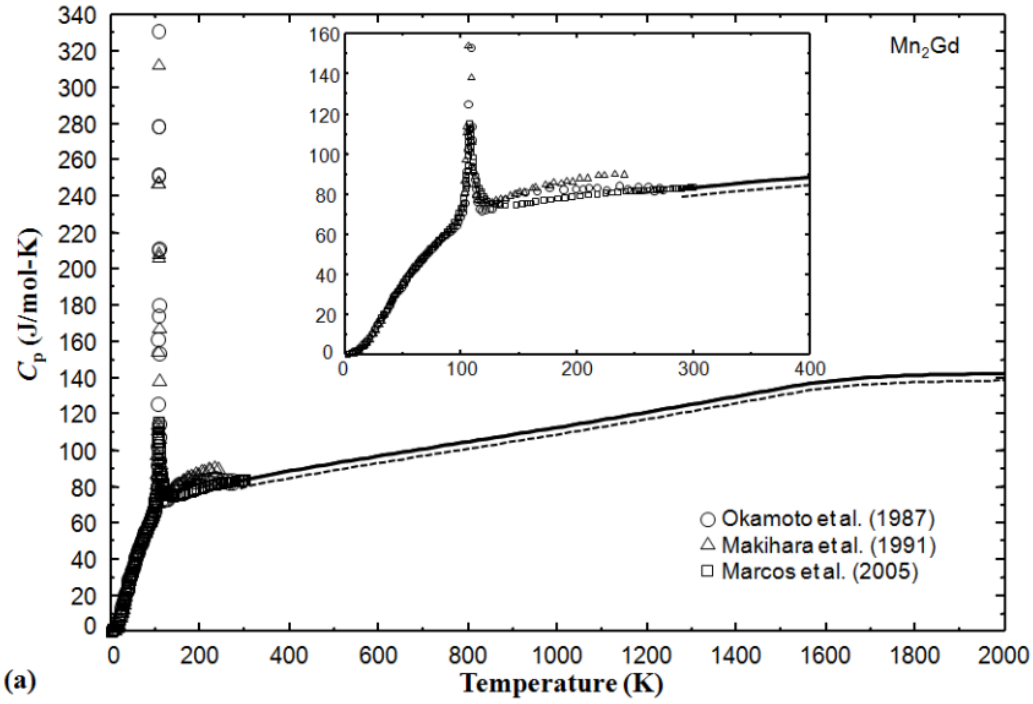
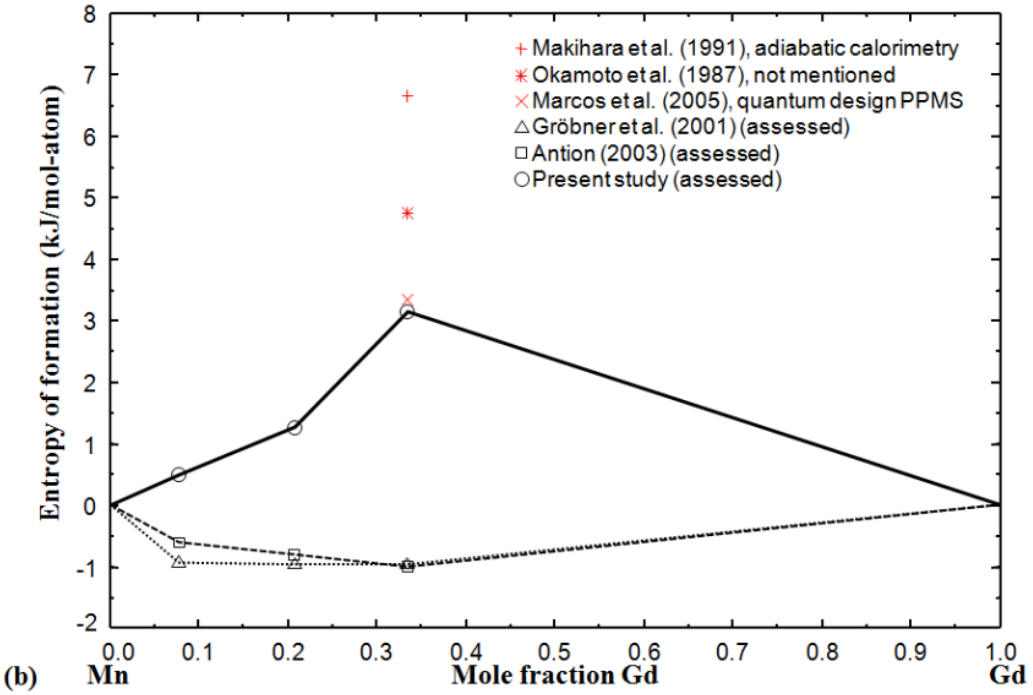


Fig. 5. (a) Integral enthalpy of mixing and (b) partial enthalpies of mixing in Mn-Gd liquid at 1650 K with experimental data [41, 42]. The previous optimizations [34, 40] are depicted by lines.


Mn2Gd
Cp (J/mol-K)
Temperature (K)
Okamoto et al. (1987)
Makihara et al. (1991)
Marcos et al. (2005)

(a)


Makihara et al. (1991), adiabatic calorimetry
Okamoto et al. (1987), not mentioned
Marcos et al. (2005), quantum design PPMS
Gröbner et al. (2001) (assessed)
Antion (2003) (assessed)
Present study (assessed)
Entropy of formation (kJ/mol-atom)
Mole fraction Gd
Mn
Gd

(b)

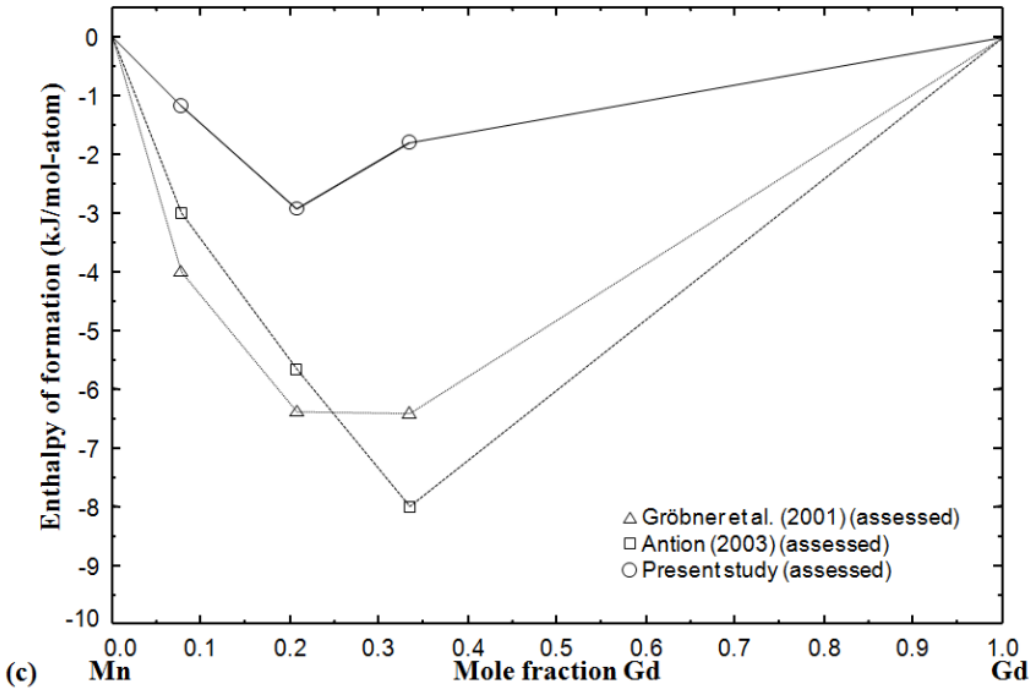


Fig. 6. (a) Heat capacities of Mn_2Gd with experimental data [29, 43, 44]. The C_p, obtained by the NK approximation, is drawn as dashed line. (b) Delta entropy of formation of the compounds at 298 K with experimental data [29, 43, 44] and previous optimizations [34, 40] (c) Enthalpy of formation of the compounds at 298 K with previous optimizations [34, 40]. The previous optimizations are depicted by lines.

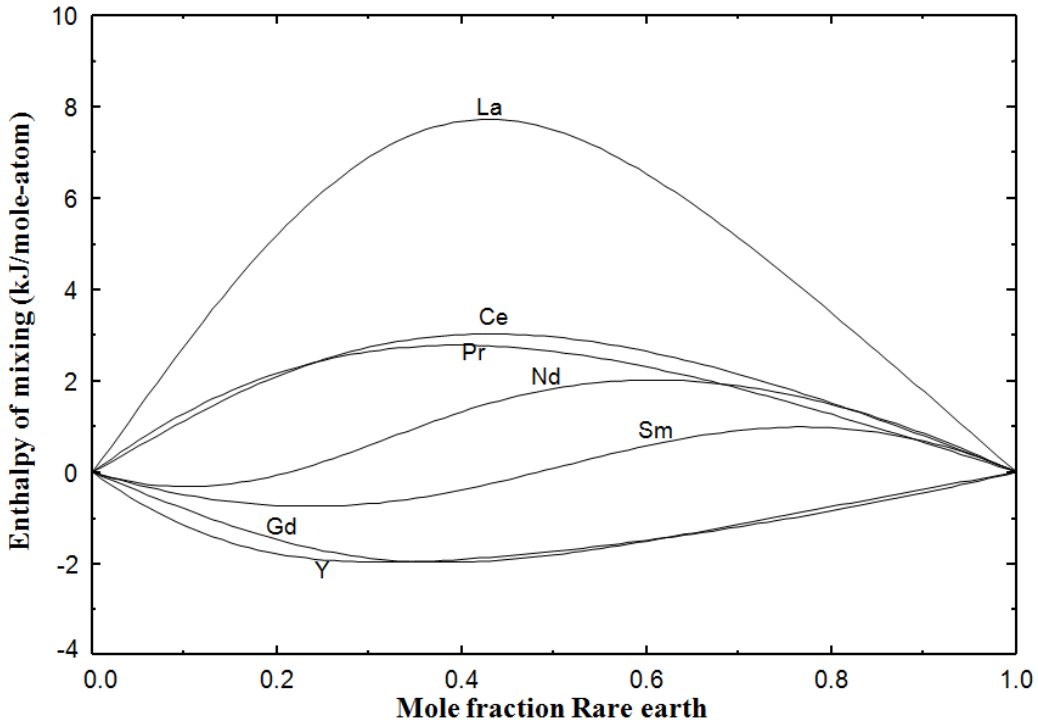


Fig. 7. Calculated enthalpies of mixing in the Mn-Y, Mn-Gd and Mn-light RE liquid at 1600 K.

4. Summary

Critical evaluation and optimization of all available phase diagram and thermodynamic data of the Mn-Y and Mn-Gd systems were conducted to obtain reliable thermodynamic functions of all phases in the systems. Recent experimental data which were not taken into account in previous optimizations such as the standard enthalpy of formation of Mn_2Y [31] and the low-temperature heat capacity data of Mn_2Y [28] for the Mn-Y system and the phase diagram [40] and enthalpy of mixing of liquid [42] for the Mn-Gd system were considered in this study. As a result, the phase diagram and thermodynamic properties were slightly revised for the Mn-Y system and considerably altered for the Mn-Gd system.

Both systems have small negative integral enthalpy of mixing for the liquid in the entire composition range as depicted in Figure 7, which is in accord with the gradual decreasing trend shown in the Mn-light RE systems. It is also exemplified by the three stable intermetallic compounds ($Mn_{12}RE$, $Mn_{23}RE_6$ and Mn_2RE) that the stability of solid intermetallic phases increases with increasing the RE atomic number as discussed in the systematic analysis of our previous study [9]. This systematic approach for all RE elements can overcome the lack of experimental data and inconsistencies in available data. This will be discussed in more details in our next study on the thermodynamic modeling of the remaining Mn-RE systems.

Thermodynamic modeling is being expanded toward the Mg-Mn-RE systems and a similar approach will be also used for other binary and ternary RE systems in order to develop the thermodynamic database of the ternary Mg-RE-X (X = Al, Zn, Mn, Fe, Sn, Si, etc.) and higher order Mg-RE systems for Mg alloy development.

ACKNOWLEDGMENTS

This project was supported by the National Sciences and Engineering Research Council of Canada (NSERC) Collaborative Research and Development grant and General Motors of Canada.

5. References

1. N. Stanford, D. Atwell, A. Beer, C. Davies and M.R. Barnett, "Effect of microalloying with rare-earth elements on the texture of extruded magnesium-based alloys", *Scr. Mater.*, 2008, vol. 59, pp. 772-775.
2. N. Stanford, "Micro-alloying Mg with Y, Ce, Gd and La for texture modification-A comparative study", *Mater. Sci. Eng., A*, 2010, vol. A527, pp. 2669-2677.
3. S. Sandloebes, S. Zaefferer, I. Schestakow, S. Yi and R. Gonzalez-Martinez, "On the role of non-basal deformation mechanisms for the ductility of Mg and Mg-Y alloys", *Acta Mater.*, 2010, vol. 59, pp. 429-439.
4. H. Yan, S.W. Xu, R.S. Chen, S. Kamado, T. Honma and E.H. Han, "Twins, shear bands and recrystallization of a Mg-2.0%Zn-0.8%Gd alloy during rolling", *Scr. Mater.*, 2010, vol. 64, pp. 141-144.
5. S.A. Farzadfar, M. Sanjari, I.H. Jung, E. Essadiqi and S. Yue, "Role of yttrium in the microstructure and texture evolution of Mg", *Mater. Sci. Eng., A*, 2011, vol. 528, pp. 6742-6753.
6. Y.-B. Kang, C. Aliravci, P.J. Spencer, G. Eriksson, C.D. Fuerst, P. Chartrand and A.D. Pelton, "Thermodynamic and volumetric databases and software for magnesium alloys", *JOM*, 2009, vol. 61, pp. 75-82.
7. L. Jin, Y.-B. Kang, P. Chartrand and C.D. Fuerst, "Thermodynamic evaluation and optimization of Al-Gd, Al-Tb, Al-Dy, Al-Ho and Al-Er systems using a Modified Quasichemical Model for the liquid", *CALPHAD*, 2010, vol. 34, pp. 456-466.
8. L.-L. Jin, Y.-B. Kang, P. Chartrand and C.D. Fuerst, "Thermodynamic evaluation and optimization of Al-La, Al-Ce, Al-Pr, Al-Nd and Al-Sm systems using the Modified Quasichemical Model for liquids", *CALPHAD*, 2011, vol. 35, pp. 30-41.
9. J. Kim, I.-H. Jung, "Critical systematic evaluation and thermodynamic optimization of the Mn–RE system: RE = La, Ce, Pr, Nd and Sm", *J. Alloys Compd.*, 2012, vol. 525, pp. 191-201.
10. A.D. Pelton, S.A. Degterov, G. Eriksson, C. Robelin and Y. Dessureault, "The modified quasichemical model I - binary solutions", *Metall. Mater. Trans. B*, 2000, vol. 31B, pp. 651-659.
11. A.D. Pelton and P. Chartrand, "The modified quasi-chemical model: Part II. Multicomponent solutions", *Metall. Mater. Trans. A*, 2001, vol. 32A, pp. 1355-1360.
12. I.-H. Jung, D.-H. Kang, W.-J. Park, N.J. Kim and S. Ahn, "Thermodynamic modeling of the Mg-Si-Sn system", *CALPHAD*, 2007, vol. 31, pp. 192-200.
13. D. Nassyrov and I.-H. Jung, "Thermodynamic modeling of the Mg-Ge-Pb system", *CALPHAD*, 2009, vol. 33, pp. 521-529.
14. A.D. Pelton and M. Blander, "Thermodynamic analysis of ordered liquid solutions by a modified quasichemical approach-application to silicate slags", *Metall. Trans. B*, 1986, vol. 17B, pp. 805-815.
15. P. Wu, G. Eriksson, A.D. Pelton and M. Blander, "Prediction of the thermodynamic properties and phase diagrams of silicate systems - evaluation of the iron(II) oxide-magnesia-silica system", *ISIJ Int.*, 1993, vol. 33, pp. 26-35.
16. A.D. Pelton and M. Blander, "Computer-assisted analysis of the thermodynamic properties and phase diagrams of slags", *Metall. Soc. AIME*, 1984, pp. 281-294.

17. M. Hillert, B. Jansson and B. Sundman, "Application of the compound-energy model to oxide systems", *Z. Metallkd.*, 1988, vol. 79, pp. 81-87.
18. A.T. Dinsdale, "SGTE data for pure elements", *CALPHAD*, 1991, vol. 15, pp. 317-425.
19. G. Inden, *Project meeting CALPHAD V*, Max-Planck-Inst. Eisenforschung, G.m.b.H., Düsseldorf, Germany, 1976, pp. III. 4-1.
20. M. Hillert and M. Jarl, "A model for alloying effects in ferromagnetic metals", *CALPHAD*, 1978, vol. 2, pp. 227-238.
21. C.W. Bale, E. Belisle, P. Chartrand, S.A. Decterov, G. Eriksson, K. Hack, I.H. Jung, Y.B. Kang, J. Melancon, A.D. Pelton, C. Robelin and S. Petersen, "FactSage thermochemical software and databases - recent developments", *CALPHAD*, 2009, vol. 33, pp. 295-311.
22. A. Hellawell, "The constitution of manganese-base alloys with metals of the second transition series", *J. Less-Common Met.*, 1959, vol. 1, pp. 343-347.
23. R.L. Myklebust and A.H. Daane, "The yttrium-manganese system", *Trans. Am. Inst. Min., Metall. Pet. Eng.*, 1962, vol. 224, pp. 354-357.
24. C.E. Habermann, "Purification of yttrium metal by distillation", 1960, M.S. Thesis, Iowa State University, U.S.A.
25. P.I. Kripyakevich and D.P. Frankevich, "New compounds of the lanthanides with Mn and Fe, and their crystalline structures", *Kristallografiya*, 1965, vol. 10, pp. 560.
26. H. Flandorfer, J. Gröbner, A. Stamou, N. Hassiotis, A. Saccone, P. Rogl, R. Wouters, H. Seifert, D. Maccio, R. Ferro, G. Haidemenopoulos, L. Delaey and G. Effenberg, "Experimental investigation and thermodynamic calculation of the ternary system Mn-Y-Zr", *Z. Metallkd.*, 1997, vol. 88, pp. 529-538.
27. M.G. Valishev, O.Y. Sidorov, S.P. Kolesnikov, Y.O. Esin and A.Y. Dubrovskii, "Partial and integral heats of mixing of components in manganese-yttrium molten binary alloys", *Rasplavy*, 1990, pp. 90-91.
28. C. Piqué, E. Abad, J.A. Blanco, R. Burriel and M.T. Fernandez-Diaz, "Interplay between competing exchange interactions and magnetocrystalline anisotropies in YFexMn12-x: The magnetic phase diagram", *Phys. Rev. B: Condens. Matter Mater. Phys.*, 2005, vol. 71, pp. 174422/174421-174422/174410.
29. T. Okamoto, H. Nagata, H. Fujii and Y. Makihara, "Heat capacities of Laves phase compounds RMn2 (R = yttrium, gadolinium and erbium)", *J. Magn. Magn. Mater.*, 1987, vol. 70, pp. 139-141.
30. A. Pisch, F. Hodaj, P. Chaudouet and C. Colinet, "Standard enthalpies of formation of some Mn-Y and Mn-Sc intermetallic compounds", *J. Alloys Compd.*, 2001, vol. 319, pp. 210-213.
31. S.V. Meschel, P. Nash and X.-Q. Chen, "The standard enthalpies of formation of binary intermetallic compounds of some late 4d and 5d transition metals by high temperature direct synthesis calorimetry", *J. Alloys Compd.*, 2010, vol. 492, pp. 105-115.
32. A. Palenzona and S. Cirafici, "The Mn-Y (manganese-yttrium) system", *J. Phase Equilib.*, 1991, vol. 12, pp. 474-478.
33. H. Okamoto, "Mn-Y (manganese-yttrium)", *J. Phase Equilib.*, 2002, vol. 23, pp. 460.
34. J. Gröbner, A. Pisch and R. Schmid-Fetzer, "Thermodynamic optimization of the systems Mn-Gd and Mn-Y using new experimental results", *J. Alloys Compd.*, 2001, vol. 317-318, pp. 433-437.
35. Y.-B. Kang, A.D. Pelton, P. Chartrand, P. Spencer and C.D. Fuerst, "Critical evaluation and thermodynamic optimization of the binary systems in the Mg-Ce-Mn-Y system", *J. Phase Equilib. Diffus.*, 2007, vol. 28, pp. 342-354.

36. H. Okamoto and T.B. Massalski, "Guidelines for binary phase diagram assessment", *J. Phase Equilib.*, 1993, vol. 14, pp. 316-335.
37. A.D. Pelton, "Calculation of a binary solidus from the liquidus and minimal additional thermodynamic information", *Ber. Bunsenges. Phys. Chem.*, 1980, vol. 84, pp. 212-218.
38. H.R. Kirchmayr and W. Lugscheider, "Constitution of binary alloys of gadolinium, dysprosium, holmium, and erbium with manganese", *Z. Metallkd.*, 1967, vol. 58, pp. 185-188.
39. H.R. Kirchmayr, "Preparation of RE-Mn alloys by the "amalgam process." X-ray, differential thermal, and thermomagnetic analyses", *U.S. Dept. Comm. Clearing House Sci. Tech. Inform.*, 1965, vol. AD 627, 225, pp. 77-88.
40. C. Antion, "Etude du système Mg-Mn-Y-Gd et développement d'alliages de magnésium pour des applications structurales à chaud", 2003, Ph.D. Thesis, Institut National Polytechnique de Grenoble, France.
41. I.V. Nikolaenko and V.V. Nosova, "Enthalpy of the mixing of gadolinium with manganese and iron", *Ukr. Khim. Zh. (Russ. Ed.)*, 1989, vol. 55, pp. 1260-1262.
42. M. Ivanov, V. Berezutski and N. Usenko, "Mixing enthalpies in liquid alloys of manganese with the lanthanides", *Int. J. Mater. Res.*, 2011, vol. 102, pp. 277-281.
43. Y. Makihara, H. Fujii, K. Hiraoka, H. Nagata and T. Hihara, "Magnetic phase transitions in the gadolinium-manganese-cobalt ($Gd(Mn_{1-x}Co_x)_2$) system", *J. Magn. Magn. Mater.*, 1991, vol. 96, pp. 305-314.
44. J.S. Marcos, J.R. Fernandez, B. Chevalier, J.L. Bobet and J. Etourneau, "Heat capacity and magnetocaloric effect in polycrystalline and amorphous $GdMn_2$", *J. Magn. Magn. Mater.*, 2004, vol. 272-276, pp. 579-580.
45. H. Okamoto, "Gd-Mn (gadolinium-manganese)", *J. Phase Equilib.*, 2002, vol. 23, pp. 459.
46. H.R. Kirchmayr and W. Lugscheider, "Neodymium-, samarium-, and terbium-manganese phase diagrams", *Z. Metallk.*, 1970, vol. 61, pp. 22-23.
47. K.H.J. Buschow and R.C. Sherwood, "Magnetic properties and hydrogen absorption in rare-earth intermetallics of the type RMn2 and R6Mn23", *J. Appl. Phys.*, 1977, vol. 48, pp. 4643-4648.

Appendix III

Appendix III

Critical systematic evaluation and thermodynamic optimization of the Mn-RE system (RE = Tb, Dy, Ho, Er, Tm and Lu) with key experiments for the Mn-Dy system

Junghwan Kim[a], Manas Paliwal[a], Shihuai Zhou[b], Hanshin Choi[c], and In-Ho Jung[a]

[a]Department of Mining and Materials Engineering, McGill University, 3610 University St., Montreal, Quebec, H3A 2B2, Canada
[b]Materials Sciences and Engineering, Ames Laboratory, US DOE, Ames, IA 50011-3020, USA
[c]Korea Institute of Industrial Technology, Incheon 406-840, South Korea

Corresponding author: In-Ho Jung
Tel : 1-514-398-2608
Fax : 1-514-398-4492
E-mail: in-ho.jung@mcgill.ca

Published in

Journal of Phase Equilibria and Diffusion 35(6) (2014) 670-694

Abstract

Critical evaluation and optimization of all available phase diagrams and thermodynamic data for the Mn-RE (RE = Tb, Dy, Ho, Er, Tm, and Lu) systems has been conducted to obtain reliable thermodynamic functions of all the phases in the systems. Key experiments for the Mn-Dy system were performed using DSC and solution calorimeter. In the thermodynamic modeling, it is found that the Mn-RE systems show systematic changes in the phase diagrams and thermodynamic properties such as enthalpy of mixing in liquid state in the order of periodic number in the lanthanide series. The systematic thermodynamic modeling approach for RE elements allow to resolve inconsistencies in the experimental data and estimate unknown thermodynamic properties and phase equilibria of Mn-RE system.

Keywords

Mg-RE alloy; Mn-RE system; Thermodynamic Modeling; Phase Diagrams; Thermodynamic Properties.

1. Introduction

Rare Earth (RE) metals are extensively used in various industrial fields including permanent magnet, electronic materials and structural materials [1, 2]. It has been investigated that even a small addition of RE elements enhances magnetic, electronic, optical and mechanical properties of various materials. For example, several recent studies [3-7] show that the additions of small amounts of RE can remarkably improve the ductility of Mg alloys. Therefore, many research on Mg-RE alloys is undertaken to elucidate the role of RE on the enhanced deformation mechanism and to find out the most optimum alloy compositions. As a necessity of Mg-RE alloy development, a large thermodynamic database of Mg-RE alloys containing Al, Zn, Mn, Si, Sn, etc. is under development using the CALPHAD type thermodynamic optimization based on a critical and systematic analysis of available thermodynamic and phase diagram data [8-20].

In the thermodynamic optimization (modeling) of a chemical system, all available thermodynamic and phase equilibrium data are evaluated simultaneously to obtain a set of model equations for the Gibbs energies of all phases as functions of temperature and composition. From these equations, all the thermodynamic properties and phase diagrams can be back-calculated. In this way, all the data are rendered self-consistent and consistent with thermodynamic principles. Discrepancies in available experimental data can be resolved during the thermodynamic optimization because different kind of experimental data such as thermodynamic properties data and phase diagram are interconnected in term of Gibbs energy.

The main objective of the present study is to perform a critical review and systematic optimization of thermodynamic data and phase diagrams of the binary Mn-heavy RE alloy systems. The present study is a follow-up to the previous thermodynamic modeling of the Mn-light RE systems (light RE = La, Ce, Pr, Nd and Sm) [17], Mn-Gd and Mn-Y systems [18]. Previously, only the Mn-Gd and Mn-Y systems among the Mn-heavy RE systems were reported because the remaining heavy RE systems suffered from insufficient experimental data for the optimization. In particular, the phase diagrams for the Mn-Tb [21], Mn-Dy [22], Mn-Ho [22] and Mn-Er [22] systems were investigated only by Kichmayr [21, 22] in 1967 and 1970 using DTA and metallography phase

determination. There were even no phase diagram data available for the Mn-Tm and Mn-Lu systems. However, it was found that the experimental phase diagrams of the Mn-Nd and Mn-Gd systems reported by Kichmayr [21, 22] were turn out to be wrong in more recent phase diagram experiments [23-25] and this was also point out in our previous works [17, 18] as shown in Fig. 1. Like the Mn-Nd and Mn-Gd systems, the phase diagrams of the Mn-Tb, Mn-Dy, Mn-Ho and Mn-Er systems reported by Kichmayr [21, 22] were evaluated to be significantly doubtful in our preliminary modeling. The previous thermodynamic assessments of the Mn-Dy and Mn-Ho systems by Wang et al. [26, 27] were based on the phase diagram data by Kirchmayr and Lugscheider [22].

In the present study, the thermodynamic optimization of the Mn-heavy RE systems (heavy RE = Tb, Dy, Ho, Er, Tm and Lu) was performed based on the available experimental data and new key phase diagram experiment for the Mn-Dy system using the DTA and thermodynamic data using a solution calorimeter. The new key phase diagram data will again support that the phase diagrams of the Mn-RE system by Kichmayr are questionable. As thermodynamic data of solid and liquid phases of the Mn-RE system are also scarce, the unknown data were estimated with the assumption of the systematic change of thermochemical properties in lanthanide series.

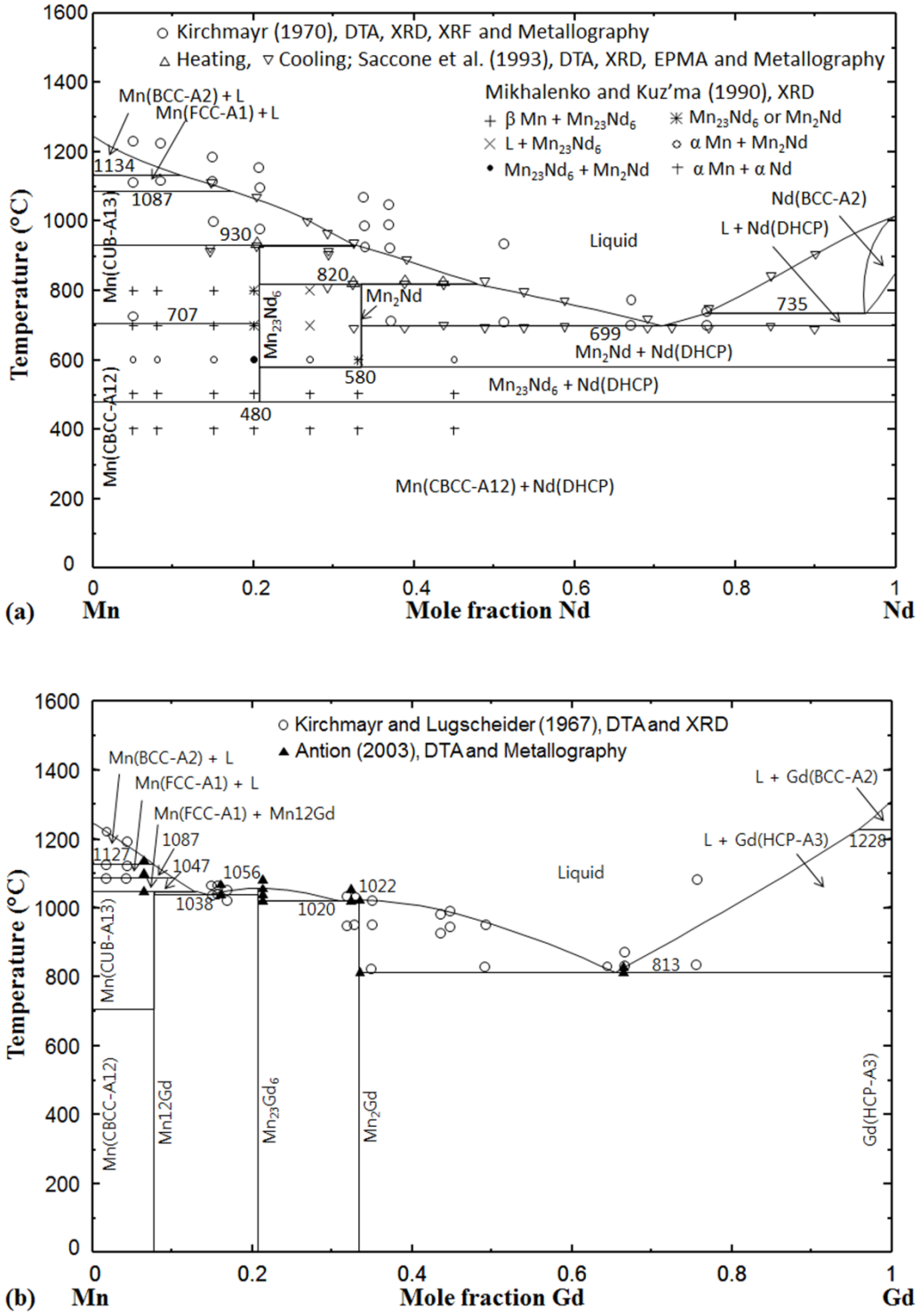


Fig. 1. Previously optimized phase diagrams of (a) Mn-Nd system [17] and (b) Mn-Gd system [18].

2. Thermodynamic models

2.1. Liquid phase

The Modified Quasichemical Model [28, 29], which accounts for short-range-ordering of nearest-neighbor atoms, was used to model the liquid solutions because it gives a more realistic thermodynamic description of the liquid phase compared with the conventional simple random-mixing Bragg Williams model [28, 29]. The Modified Quasichemical Model was successfully applied to many liquid metallic solutions [29-31] and ionic solutions [32, 33] exhibiting strong short-range-ordering behavior.

Recently, the energy of nearest-neighbor pair formation in the Modified Quasichemical Model is expanded as a polynomial in the pair fractions [28, 29] instead of the component fractions [32, 34]. In addition, the coordination numbers are now allowed to vary with composition. These modifications provide greater flexibility in reproducing the binary experimental data and in combining optimized binary liquid parameters into a large database for multicomponent solutions [28]. A short description of the model is given below; details can be found in previous studies [28, 29].

In the case of a binary A-B liquid solution, the atoms A and B are distributed over the sites of a quasi-lattice in liquid solution. The following pair exchange reaction can be considered:

$$(A-A)+(B-B)=2(A-B) \qquad (1)$$

where (A-B) represents a first-nearest-neighbor pair of A and B. The non-configurational Gibbs energy change for the formation of two moles of (A-B) pairs according to reaction (1) is Δg_{AB}. Then the Gibbs energy of the solution is given by:

$$G = (n_A G_A^{\circ} + n_B G_B^{\circ}) - T\Delta S^{\text{config}} + n_{AB}(\Delta g_{AB}/2) \tag{2}$$

where G_A° and G_B° are the molar Gibbs energies of the pure components A and B, n_A and n_B are the numbers of moles of A and B atoms, and n_{AB} is the number of moles of (A-B) pairs. ΔS^{config} is the configurational entropy of mixing given by a random distribution of the (A-A), (B-B) and (A-B) pairs in the one-dimensional Ising approximation:

$$\begin{aligned}\Delta S^{\text{config}} &= -R(n_A \ln X_A + n_B \ln X_B) \\ &\quad - R[n_{AA} \ln(X_{AA}/Y_A^{\,2}) + n_{BB} \ln(X_{BB}/Y_B^{\,2}) \\ &\quad + n_{AB} \ln(X_{AB}/2Y_AY_B)]\end{aligned} \tag{3}$$

where n_{AA}, n_{BB} and n_{AB} are the numbers of moles of each kind of pairs, and the pair fraction (X_{AA}, X_{BB} and X_{AB}) and coordination equivalent fraction (Y_A and Y_B) can be calculated as:

$$X_{AA} = n_{AA}/(n_{AA} + n_{BB} + n_{AB}) \tag{4}$$

$$X_{BB} = n_{BB}/(n_{AA} + n_{BB} + n_{AB}) \tag{5}$$

$$X_{AB} = n_{AB}/(n_{AA} + n_{BB} + n_{AB}) \tag{6}$$

$$Y_A = X_{AA} + X_{AB}/2 \tag{7}$$

$$Y_B = X_{BB} + X_{AB}/2 \tag{8}$$

The Δg_{AB} is the model parameter to reproduce the Gibbs energy of liquid phase of the binary A-B system, which is expanded as a polynomial in terms of the pair fractions, as follows:

$$\Delta g_{AB} = \Delta g_{AB}^{\circ} + \sum_{i\geq 1} g_{AB}^{i0}(X_{AA})^i + \sum_{j\geq 1} g_{AB}^{0j}(X_{BB})^j \tag{9}$$

where Δg°_{AB}, g^{i0}_{AB} and g^{0j}_{AB} are the adjustable model parameters which can be functions of temperature.

In the Modified Quasichemical Model, the coordination numbers of A and B, Z_A and Z_B, can be varied with composition to reproduce the short-range-ordering as follows:

$$\frac{1}{Z_A} = \frac{1}{Z^A_{AA}}\left(\frac{2n_{AA}}{2n_{AA}+n_{AB}}\right) + \frac{1}{Z^A_{AB}}\left(\frac{n_{AB}}{2n_{AA}+n_{AB}}\right) \quad (10)$$

$$\frac{1}{Z_B} = \frac{1}{Z^B_{BB}}\left(\frac{2n_{BB}}{2n_{BB}+n_{AB}}\right) + \frac{1}{Z^B_{BA}}\left(\frac{n_{AB}}{2n_{BB}+n_{AB}}\right) \quad (11)$$

where Z^A_{AA} is the value of Z_A when all nearest neighbors of an A atom are A atoms, and Z^A_{AB} is the value of Z_A when all nearest neighbors are B atoms. Z^B_{BB} and Z^B_{BA} are defined in an analogous manner. In the present study, Z^i_{ii} for all elements (i = Mn and RE) are set to be 6. To reproduce the minimum enthalpies of Mn-RE liquid alloys at 0.3 ~ 0.4 mole fraction RE, Z^{Mn}_{MnRE} and Z^{RE}_{MnRE} are set to be 3 and 6, respectively. This set of coordination numbers can reproduce the experimental data more accurately with a small number of model parameters. For example, if the coordination numbers of Mn and RE for all nearest neighbors were set to 6, more model parameters would have been required and the experimental data would have been less accurately reproduced.

The thermodynamic properties of binary liquid phase having enthalpy of mixing less than -10 kJ mol^{-1} can be well described using the simple Bragg-Williams random mixing model. However, the random mixing model can have difficulty in describing the thermodynamic properties of solution with highly negative enthalpy of mixing. Several RE-containing liquid solutions such as Si-RE (about -65 to -75 kJ mol^{-1}) Al-RE (-30 to -40 kJ mol^{-1}), Zn-RE (-30 kJ mol^{-1}) and Sn-RE (-60 kJ mol^{-1}) have very negative enthalpy of mixing showing a considerable short range ordering. Therefore, in our development of the Mg alloy database, we have used the Modified Quasichemical Model to describe the liquid phase. In order to keep consistency in this development, the present

liquid Mn-RE solutions were also described by the same model. But, strictly speaking, as liquid Mn-RE solutions are not seriously deviated from ideal solution behavior, they can be also described well using the Bragg Williams random mixing model.

2.2. Solid solutions

The solid solution phases were described by the Compound Energy Formalism [35] with a one-sublattice approach (Mn, RE) for substitutional site. The molar Gibbs energy of the solid solution can be expressed as:

$$G = (y_{Mn} G^{o}_{Mn} + y_{RE} G^{o}_{RE}) + RT(y_{Mn} \ln y_{Mn} + y_{RE} \ln y_{RE}) + {}^{a}L_{Mn,RE} y_{Mn} y_{RE} (y_{RE} - y_{Mn})^{a} \qquad (12)$$

where y_{Mn} and y_{RE} are the site fractions of Mn and RE elements in the sublattice, and R and T are the gas constant and temperature in Kelvin. G^{o}_{Mn} and G^{o}_{RE} are the molar Gibbs energies of solid phases of Mn and RE. The binary interaction parameters between Mn and RE in the sublattice, ${}^{a}L_{Mn,RE}$ where $a \geq 0$, are adjustable models parameters.

2.3. Stoichiometric compounds and elements

The Gibbs energies of all pure elements were taken from the SGTE database version 5.0 [36]. The Gibbs energies of the stoichiometric intermetallic compounds were optimized based on available experimental data using the standard Gibbs energy expression based on heat capacity, enthalpy and entropy of formation at 298 K. As the heat capacities of the compounds were not available, they were estimated using a conventional Neumann-Kopp (NK) method [37]. Overall, the experimental data for the intermetallic compounds of the Mn-RE were very scarce. The systematic analysis was applied to evaluate the undetermined thermodynamic properties. In addition, a semi-quantitative model, which was improved by Zhang et al. [38-40] using statistical approach (ab initio throughput data-mining (HTDM) method) from Miedema model, was used to predict the

standard enthalpy of formation (ΔH^{o}_{298}) of all Mn-RE compounds. Mn (bcc-A2), Mn (fcc-A1), Mn_2RE, and $Mn_{23}RE_6$ phases exhibit magnetic transitions associated with Néel or Curie temperatures. The magnetic transition below 298 K (typically anti-ferromagnetic transition with Néel temperature) was directly taken into account in the calculation of S^{o}_{298}. The Curie temperature (ferromagnetic transition) occurs typically above 298 K, of which magnetic contribution to the Gibbs energy was considered by an empirical relationship suggested by Hillert and Jarl [41].

3. Experimental: Mn-Dy system

3.1. Sample preparation

Mn-Dy alloys were prepared from high purity Mn and Dy (> 99.99 wt. %) using a vacuum arc melting. Three alloy buttons of different compositions were cast into a copper mold in a purified argon atmosphere. The alloys were remelted three times to homogenize their composition. Microstructures were investigated by scanning electron microscopy (SEM-Philips-XL300) in the back-scattered electrons (BSE) mode and quantitative analyses were performed by energy-dispersive spectroscopy (EDS). The oxidation of alloys was hardly avoided due to very high oxygen affinity of Dy. An insignificant amount of Dy-rich oxide phases were found in Alloy 1 (Mn-rich sample). Alloy 2 contained slightly more oxide phases. However, a noticeable amount of oxide phases were observed in Alloy 3 (Dy-rich sample). The alloy compositions before (mixing amount of Mn and Dy) and after (EDS analysis) the arc melting are listed in Table 1. The standard deviations of the measurements by EDS were typically less than 2 %. Alloys 1 and 2 were targeted to $Mn_{23}Dy_6$ and Mn_2Dy compositions. The X-ray diffraction (XRD) patterns of as cast Mn-Dy samples were obtained using a Bruker Discover D8 equipped with HiSTAR area detector.

Table 1. Compositions of the Mn-Dy alloys.

Alloy	Compositions (at. %) before arc melting	Compositions (at. %) after arc melting
1	Mn: 79.3 Dy: 20.7	Mn: 80.5 Dy: 19.5
2	Mn: 66.7 Dy: 33.3	Mn: 66.1 Dy: 33.9
3	Mn: 42.5 Dy: 57.5	Mn: 46.3 Dy: 53.7

3.2. Phase diagram experiments: DSC and Annealing

Differential scanning calorimetry (DSC) was performed using a Jupiter STA 449 F3 terminal analyzer (NETZSCH Instruments, Germany). Alumina crucibles with lids were used to carry 50 to 100 mg of sample for each run. The heating and cooling rates were 10 K min^{-1} and high purity argon (99.999%) atmosphere with a gas flow rate of 40 ml min^{-1} was used to minimize oxidation of the alloys. In addition, a special oxygen trap system, OTS, supplied from NETZSCH was installed in the DSC to minimize the oxidation of Mn and RE. Overall, the oxidation of sample during the DSC experiment could be controlled below 1 wt. %. The maximum temperature of heating cycle was 1200 ºC. The strong consistent peaks were observed at the first heating and cooling cycle, which were used for the determination of phase transformation temperatures in the present study. In the preliminary test, several thermal cycles were performed but it was found that the peak temperatures were continuously changed with number of cycles due to the oxidation of samples.

For the better DSC analysis, the sample could be homogenized before DSC experiment. However, because the present alloy samples containing Dy are highly susceptible to oxidation, the samples were not annealed prior to DSC experiment. Instead, alloy samples were held at 700 ºC for 2 hours in the first heating cycle of the present DSC experiment, which could help to homogenize the samples to a certain extent.

Alloy 2 contained in a sealed platinum capsule was annealed at 1000 ºC for 48 hours in a steel tube furnace, subsequently followed by water quenching. During the annealing, high purity Ar gas was continuously flowed into steel tube to reduce oxidation. The quenched sample was polished and analyzed using SEM and XRD method for equilibrium phase analysis.

3.3. Solution Calorimetry

The standard enthalpy of formation for Alloy 1, which contained negligible amount of oxide phase, was measured by a solution calorimeter (Ames Lab, USA). High purity Cu (> 99.9999 %) was used as solvent for the solution calorimetry because the reaction of Cu with Mn and Dy is practically small to measure a heat of dissolution of Mn and Dy in liquid Cu. 32.3 g of Cu was inserted into a zirconia crucible placed inside the chamber of the furnace. The calorimeter was evacuated to a pressure of less than 10^{-4} mbar and then flushed and evacuated three times with argon gas. The calorimeter was afterwards kept at 1170 ºC overnight in the argon atmosphere to stabilize liquid Cu. The calibration factor was determined using 1.56 g of solid Cu and by comparing the measured heat of reaction in liquid copper to the known enthalpy. 103.3 mg of the sample was inserted to measure the heat of dissolution for the alloy. According to the corresponding ratio of the component composition, the heat of dissolution for the component mixture of Mn and Dy was measured using 54.9 mg of Mn and 39.3 mg of Dy.

The schematic construction of the solution calorimeter is shown in Fig. 2. The calorimeter consists of a center cell and blocks. The cell is composed of a reaction crucible filled with liquid metal ① and a thermopile ②. The thermopile measures the temperature difference between the crucible bottom and the surroundings. The blocks are made of tantalum ③ and their temperature is kept constant during the measurement. Alumina paste is applied to form the alumina layer ④ between the crucible and the tantalum blocks to hold the crucible and to cover the thermopile. Alumina rods ⑤ are used to hang the calorimetric system. Sample addition is carried out through the sample charge tube ⑥ from the sample chamber which is under argon atmosphere. When a measurement

is performed, a thermocouple ⑦ measures the temperature of the liquid metal inside the crucible and a stirrer ⑧ agitates the liquid metal.

Solution calorimetry is employed to determine the standard enthalpy of formation of Mn-Dy alloys from the reaction:

$$xMn + yDy = Mn_xDy_y \text{ at 298 K} \quad (13)$$

The standard enthalpy of formation of Mn_xDy_y is deduced from the dissolution enthalpy of the alloy (ΔH_2) and that of its component mixture (ΔH_1) in liquid copper using Hess's law.

The enthalpy change of each reaction is given by:

$$\Delta H_1 = x\Delta H_{Mn}^{298\to T} + y\Delta H_{Dy}^{298\to T} + x\Delta H_{Mn}^{diss} + y\Delta H_{Dy}^{diss} \quad (14)$$

$$\Delta H_2 = \Delta H_{Mn_xDy_y}^{298\to T} + \Delta H_{Mn_xDy_y}^{diss} \quad (15)$$

$$\Delta H_3 = xH_{Mn}^{298} + yH_{Dy}^{298} - H_{Mn_xDy_y}^{298} = -\Delta H_{Mn_xDy_y}^{formation} \quad (16)$$

where $\Delta H_{Mn}^{298\to T}$ and ΔH_{Mn}^{diss} are the required enthalpy to heat Mn from 298 K to the temperature of liquid Cu (T) and the dissolution enthalpy of Mn in liquid Cu, respectively. $\Delta H_{Dy}^{298\to T}$, $\Delta H_{Mn_xDy_y}^{298\to T}$, ΔH_{Dy}^{diss} and $\Delta H_{Mn_xDy_y}^{diss}$ are similarly defined.

By Hess's law:

$$\Delta H_2 = \Delta H_1 + \Delta H_3 \quad (17)$$

Thus, the standard enthalpy of formation of Mn_xDy_y is:

$$\Delta H^{formation}_{Mn_xDy_y} = \Delta H_1 - \Delta H_2 \quad (18)$$

Unfortunately, the solution calorimeter for Alloy 1 was carried out only one time in between other measurements for the Fe-Nd-B system. Therefore it is hard to tell the statistical error of this experiment. From the experience of solution calorimeter, the estimated error of this measurement would be about ± 1 kJ mol-atom^{-1}.

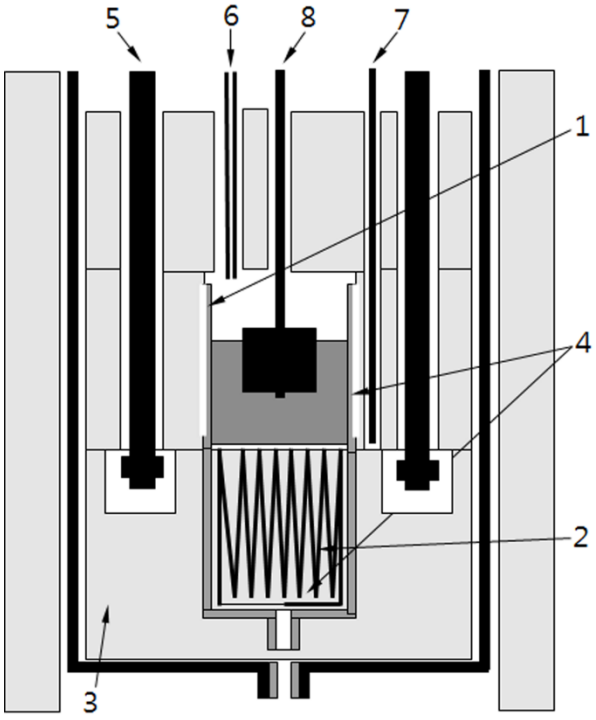


Fig. 2. Solution calorimeter: ① Reaction crucible ② Thermopile ③ Tantalum blocks ④ Alumina layer ⑤ Alumina rod ⑥ Charge tube ⑦ Thermocouple ⑧ Stirrer.

4. Critical evaluation and thermodynamic optimization

The thermodynamic optimization of the Mn-RE (RE = Tb, Dy, Ho, Er, Tm and Lu) systems was performed based on the thermodynamic data and the phase diagrams which were critically assessed in the present study. The optimized values for the model parameters are listed in Table 2. The thermodynamic optimization of Mn-Dy system was performed based on the present experimental data and available data in literature. We found significant inconsistency in the previous phase diagram data by Kirchmayr and Lugscheider [22], in particular on the melting behaviors of $Mn_{23}Dy_6$ and Mn_2Dy. The present investigation reveals that the $Mn_{23}Dy_6$ and Mn_2Dy melt congruently unlike the peritectic melting of those in the study of Kirchmayr and Lugscheider [22]. Similarly the congruent melting of the $Mn_{23}Gd_6$ and Mn_2Gd in the Mn-Gd system were established in our previous study [18] as shown in Fig. 1(b). Considering the similarity of Mn-RE systems, all $Mn_{23}RE_6$ and Mn_2RE compounds were presumed to melt congruently in the present optimization. The details are explained below. All the thermodynamic calculations were performed using FactSage thermodynamic software [42].

Table 2. Optimized model parameters for the all binary systems (J mol^{-1} or J mol^{-1} K^{-1}).

Phase	Thermodynamic parameters			
Liquid	Coordination Numbers			
	Mn	Tb	3	6
	Mn	Dy	3	6
	Mn	Ho	3	6
	Mn	Er	3	6
	Mn	Tm	3	6
	Mn	Lu	3	6

$$\Delta g_{MnTb} = -3765.6 - 2.9288\ T + (-209.2 + 3.7656\ T)\, X_{MnMn} + (418.4 - 1.79912\ T)\, X_{TbTb}$$

$$\Delta g_{MnDy} = -5439.2 + 0.46024\ T + (-1255.2 + 1.2552\ T)\, X_{MnMn} + (1255.2 - 1.38072\ T)\, X_{DyDy}$$

$$\Delta g_{MnHo} = -6694.4 + 2.5104\ T + (-1255.2 + 1.2552\ T)\, X_{MnMn} + (1004.16 - 3.68192)\, X_{HoHo}$$

$$\Delta g_{MnEr} = -7531.2 - 0.4184\ T + (-1255.2 + 2.092\ T)\, X_{MnMn}$$

$$+ (1757.28 - 0.2092\ T)\, X_{ErEr}$$

$$\Delta g_{MnTm} = -9204.8 + 0.4184\ T + (-209.2 + 4.184\ T)\, X_{MnMn} + (1255.2 + 5.0208\ T)\, X_{TmTm}$$

$$\Delta g_{MnLu} = -11296.8 + 1.84096\ T + 836.8\, X_{MnMn} + (1255.2 + 3.138\ T)\, X_{LuLu}$$

BCC-A2 (Mn,Dy)

${}^{0}L_{Mn,Dy} = 28451.2$

$T_{C,Mn}^{BCC}$ (Curie temperature) = 580 K,

$B_{0,Mn}^{BCC}$ (Magnetic moment) = 0.27 μ_B mol^{-1}

FCC-A1 (Mn,Dy)

${}^{0}L_{Mn,Dy} = 37656$

$T_{C,Mn}^{FCC} = 540$ K, $B_{0,Mn}^{FCC} = 0.62\ \mu_B$ mol^{-1}

Mn_2Tb

$\Delta H_{298}^{o} = -10500$, $S_{298}^{o} = 151.5$

$C_p = 2 \times C_p$ (Mn,cbcc-A12) + C_p (Tb,hcp-A3)

$Mn_{23}Tb_6$

$\Delta H_{298}^{o} = -120000$, $S_{298}^{o} = 1223$

$C_p = 23 \times C_p$ (Mn, cbcc-A12) + $6 \times C_p$ (Tb, hcp-A3)

$T_C = 455$ K, $B_0 = 49\ \mu_B$ mol^{-1} [46]

$Mn_{12}Tb$

$\Delta H_{298}^{o} = -25300$, $S_{298}^{o} = 461.5$

$C_p = 12 \times C_p$ (Mn, cbcc-A12) + C_p (Tb, hcp-A3) + 12 J mol^{-1} K^{-1}

Mn_2Dy

$\Delta H_{298}^{o} = -10500$, $S_{298}^{o} = 151.5$

$C_p = 2 \times C_p$ (Mn, cbcc-A12) + C_p (Dy, hcp-A3)

$Mn_{23}Dy_6$

$\Delta H_{298}^{o} = -120000$, $S_{298}^{o} = 1235$

$C_p = 23 \times C_p$ (Mn, cbcc-A12) + $6 \times C_p$ (Dy, hcp-A3)

$T_C = 443$ K, $B_0 = 49.6\ \mu_B$ mol^{-1} [46]

$Mn_{12}Dy$

$\Delta H_{298}^{o} = -25300$, $S_{298}^{o} = 472.15$

$C_p = 12 \times C_p$ (Mn, cbcc-A12) + C_p (Dy, hcp-A3)

Mn_2Ho

$\Delta H_{298}^{o} = -8900$, $S_{298}^{o} = 150.8$

$C_p = 2 \times C_p$ (Mn, cbcc-A12) + C_p (Ho, hcp-A3)

$Mn_{23}Ho_6$

$\Delta H_{298}^{o} = -100000$, $S_{298}^{o} = 1234$

$C_p = 23 \times C_p$ (Mn, cbcc-A12) + $6 \times C_p$ (Ho, hcp-A3)

$T_C = 434$ K, $B_0 = 59.8\ \mu_B$ mol^{-1} [51]

$Mn_{12}Ho$

$\Delta H_{298}^{o} = -22200$, $S_{298}^{o} = 472$

$C_p = 12 \times C_p$ (Mn, cbcc-A12) + C_p (Ho, hcp-A3)

Mn_2Er	$\Delta H^{o}_{298} = -12600,\ S^{o}_{298} = 150$ $C_p = 2 \times C_p$ (Mn, cbcc-A12) + C_p (Er, hcp-A3)
$Mn_{23}Er_6$	$\Delta H^{o}_{298} = -145000,\ S^{o}_{298} = 1230$ $C_p = 23 \times C_p$ (Mn, cbcc-A12) + $6 \times C_p$ (Er, hcp-A3) $T_C = 415$ K, $B_0 = 38\ \mu_B$ mol^{-1} [51]
$Mn_{12}Er$	$\Delta H^{o}_{298} = -29500,\ S^{o}_{298} = 471$ $C_p = 12 \times C_p$ (Mn, cbcc-A12) + C_p (Er, hcp-A3)
Mn_2Tm	$\Delta H^{o}_{298} = -12500,\ S^{o}_{298} = 150.5$ $C_p = 2 \times C_p$ (Mn, cbcc-A12) + C_p (Tm, hcp-A3)
$Mn_{23}Tm_6$	$\Delta H^{o}_{298} = -143000,\ S^{o}_{298} = 1240$ $C_p = 23 \times C_p$ (Mn, cbcc-A12) + $6 \times C_p$ (Tm, hcp-A3)
$Mn_{12}Tm$	$\Delta H^{o}_{298} = -28500,\ S^{o}_{298} = 471$ $C_p = 12 \times C_p$ (Mn, cbcc-A12) + C_p (Tm, hcp-A3)
Mn_2Lu	$\Delta H^{o}_{298} = -24000,\ S^{o}_{298} = 118$ $C_p = 2 \times C_p$ (Mn, cbcc-A12) + C_p (Lu, hcp-A3) + 3 J mol^{-1} K^{-1}
$Mn_{23}Lu_6$	$\Delta H^{o}_{298} = -160000,\ S^{o}_{298} = 1070$ $C_p = 23 \times C_p$ (Mn, cbcc-A12) + $6 \times C_p$ (Lu, hcp-A3) + 53 J mol^{-1} K^{-1} $T_C = 378$ K, $B_0 = 8.9\ \mu_B$ mol^{-1} [59]
Mn_5Lu	$\Delta H^{o}_{298} = -23500,\ S^{o}_{298} = 228$ $C_p = 5 \times C_p$ (Mn, cbcc-A12) + C_p (Lu, hcp-A3)

4.1. The Mn-Dy system

Kirchmayr and Lugscheider [22] firstly investigated the phase diagram of Mn-Dy system using differential thermal analysis (DTA) and XRD. The Mn-RE alloys were prepared by amalgam process [43] by heating Mn-RE-Hg alloys below the liquidus (900 - 1100 ºC) to remove Hg by evaporation. The heating rate was less than 6 ºC min^{-1} and tantalum crucible and purified argon were employed to prevent oxidation and reactions between the samples and the crucibles. The experimental data of Kirchmayr and Lugscheider [22] are presented in Fig. 3. Several invariant reactions which include one eutectic reaction between Dy and Mn_2Dy and three peritectic reactions corresponding to the melting of three incongruent melting compounds ($Mn_{12}Dy$, $Mn_{23}Dy_6$, and Mn_2Dy) were observed. The eutectic reaction was located at 0.713 mole fraction Dy and 855 °C. Although the mutual solubility was not specifically studied, a small solubility of Dy in Mn was proposed by the allotropic transformation temperatures lowered to 1120 °C (bcc-A2 to fcc-A1) and 1075 °C (fcc-A1 to cub-A13).

The present phase diagram experimental results are incoherent with the data of Kirchmayr and Lugscheider [22]. Fig. 4 shows the XRD analysis results for the alloys prepared from vacuum arc melting. In Alloy 1, $Mn_{23}Dy_6$ phase is dominant and small peak of $Mn_{12}Dy$ is also observed. XRD pattern of Alloy 3 shows two phases Dy and Mn_2Dy, and no significant Dy oxide phase peak is detected in Alloy 3. In the case of Alloy 2 having nearly Mn_2Dy composition, only Mn_2Dy phase was identified. If Mn_2Dy melted peritectically as suggested by Kirchmayr and Lugscheider, single Mn_2Dy microstructure cannot be obtained in as-cast state. Therefore, this single Mn_2Dy phase structure in Alloy 2 already tells that Mn_2Dy melts congruently. The heating and cooling curves of three alloys as a result of DSC in the present study are shown in Fig. 5. In spite of the presence of the Dy-rich oxide phases in the alloys, it was believed that the DSC signal with a temperature range up to 1200 ºC was mainly captured from the transformation of the metallic phases because Dy-oxide is stable up to above 1200 ºC. The present experimental data (Fig. 3) were taken from heating curves (onset of transformations) for solidus temperatures and from the cooling curves (onset of transformations) for liquidus temperatures. The eutectic temperature between Mn_2Dy and Dy for Alloys 2 and 3 was determined to be about 860 ºC which is similar to that of Kirchmayr

and Lugscheider (855 ºC) [22]. In case of Alloy 1, the transformation at 1093 ºC in the heating curve of DSC in Fig. 5(a) mainly correspond to the melting of the $Mn_{23}Dy_6$. The high intensities of high temperature transformations in the DSC curves detected in Alloy 1 (1093 ºC) and Alloy 2 (1110 ºC) most likely correspond to the congruent melting of the $Mn_{23}Dy_6$ and Mn_2Dy, respectively. No thermal arrest near 930 ºC reported for the peritectic melting of Mn_2Dy by Kirchmayr and Lugscheider was detected for Alloys 2 and 3. It should be also noted that Alloy 2 was also investigated by NETZSCH Instruments, Germany and the same results as in Fig. 5(b) were obtained. The present experimental results are noticeably inconsistent with the results by Kirchmayr and Lugscheider [22] who reported the incongruent melting of $Mn_{23}Dy_6$ and Mn_2Dy at about 1035 ºC and 930 ºC, respectively. In order to confirm the existence of Mn_2Dy above 1000 ºC, Alloy 2 was annealed at 1000 ºC for 48 hours. Unfortunately, several annealing attempts of Alloy 2 were all suffered from the oxidation of samples even though the samples were contained in sealed Pt capsules. Although it was hard to distinguish Mn_2Dy and $Mn_{23}Dy_6$ phase in SEM (BSE) image, XRD patterns of the annealed Alloy 2 in Fig. 6 shows that there are both intermetallics, $Mn_{23}Dy_6$ and Mn_2Dy, as well as Dy oxide.

The as-cast microstructure of starting Alloy 2 and DSC results of Alloys 2 and 3 supported that Mn_2Dy melts congruently at 1110 ºC, which is completely inconsistent with the peritectic melting of Mn_2Dy at 930 ºC reported by Kirchmayr and Lugscheider [22]. In fact, the same kind of controversy was also found in the Mn-Gd system [18]. The Mn_2Gd and $Mn_{23}Gd_6$ compounds had previously been known to melt peritectically based on the work of Kirchmayr and Lugscheider [22]. However, the DTA experiments of Antion [25] and the thermodynamic modeling [18] suggested that the Mn_2Gd and $Mn_{23}Gd_6$ melt congruently (Fig. 1(b)).

The enthalpy of liquid Mn-Dy solution was determined by Nikolaenko and Nosova [44] and Ivanov et al. [45] as seen in Fig. 7. Nikolaenko and Nosova [44] measured the partial enthalpy of mixing of Dy between $0 < X_{Dy} < 0.4$ at 1600 K in the Mn-Dy liquid using high-temperature isoperibolic calorimetry. Alundum crucibles and starting materials made of 99.9 % Mn and > 99.9 % Dy were used. Experimental data were submitted to least squares analysis and smoothed values were obtained for both partial and integral enthalpies of mixing of liquid Mn-Dy solution with the

help of the Gibbs-Duhem equation. The smoothed curves for the partial enthalpy of mixing of Dy and the integral enthalpy of mixing were proposed. The integral enthalpy of mixing curve varies from small negative value (minimum: -0.5 ± 0.3 kJ mol^{-1} at 0.05 mole fraction Dy) to small positive value (maximum: 0.53 ± 0.6 kJ mol^{-1} at 0.3 mole fraction Dy). However, the original experimental data were not presented. Recently, Ivanov et al. [45] measured the partial enthalpy of mixing of Mn in the Dy-rich region and that of Dy in the Mn-rich region of Mn-Dy liquid at 1723 K using an isoperibolic calorimeter and starting materials made of 99.9 wt. % Mn and 99.96 wt. % Dy. They presented smoothed values of both partial and integral enthalpies of mixing for the whole composition range of Mn-Dy liquid without original data. The integral enthalpy of mixing curve is negative in the whole composition range with minimum about -3.7 kJ mol^{-1} at about 0.35 mole fraction of Dy, which is considerably different from the results by Nikolaenko and Nosova [44].

Prior to the present experimental study, the thermodynamic properties for the intermetallic compounds have not yet been reported. In the present study, the standard enthalpy of formation (ΔH^{o}_{298}) of Alloy 1 (X_{Dy} = 0.195) was measured using a solution calorimeter. Liquid Cu was used as solvent to dissolve Mn and Dy at 1160 ºC. The heat of reactions were 18709.92 J mol-$atom^{-1}$ for the component mixture, and 22719.3 J mol-$atom^{-1}$ for Alloy 1, respectively. As a result, the ΔH^{o}_{298} of the $Mn_{0.805}Dy_{0.195}$ alloy was obtained to be -4009.43 J mol-$atom^{-1}$ and the value is presented in Fig. 8. Pourarian et al. [46] reported the magnetic transformation temperature (T_C = 443 K) and magnetic moment (B_0 = 49.6 μ_B) of the $Mn_{23}Dy_6$ from magnetization measurements.

The thermodynamic optimization of the Mn-Dy system was previously performed by Wang et al. [26] based on the experimental data of Kirchmayr and Lugscheider [22] and Nikolaenko and Nosova [44] using a random-mixing model for Mn-Dy liquid. The present authors, however, believe that the experimental data of Kirchmayr and Lugscheider [22] and Nikolaenko and Nosova [44] are inaccurate according to the present experimental data and the systematic trend in the enthalpy of mixing which will be discussed later. The liquidus at Mn-rich side in the phase diagram suggested by Kirchmayr and Lugscheider [22] are also unlikely to happen from the viewpoint of the limiting slope rule [47]. The enthalpy data of Ivanov et al. [45] were not available at that time.

Consequently, the calculated integral and partial enthalpies of mixing at 1723 K from Wang et al. [26] are notably different from the data of Ivanov et al. [45] as shown in Figs. 7(a) and 7(b).

In the present study, the phase diagram and thermodynamic properties of all phases were optimized based on the newly obtained experimental data and systematic analysis in Mn-RE systems. The optimized phase diagram of the Mn-Dy system is presented and compared with the experimental data in Fig. 3 and the calculated thermodynamic properties with the optimized thermodynamic parameters are compared with the experimental data and the previous optimization in Figs. 7 to 9. The enthalpy of mixing of the liquid, determined by Ivanov et al. [45], was taken into account to determine the thermodynamic parameters of liquid. The measured ΔH°_{298} of the $Mn_{0.805}Dy_{0.195}$ alloy was used to determine the ΔH°_{298} of the $Mn_{23}Dy_6$. Since there were no experimental data for the ΔH°_{298} of the $Mn_{12}Dy$ and Mn_2Dy, they were estimated by considering the systematic similarity of other Mn-heavy RE systems. The standard entropies (S°_{298}) of all intermetallic phases were initially assumed to be similar to those in the Mn-Tb system where the experimental S°_{298} data of the Mn_2Tb and $Mn_{12}Tb$ are available. Then, they were slightly adjusted to reproduce the phase diagram data obtained in the present study. The magnetic properties of $Mn_{23}Dy_6$ measured by Pourarian et al. [46] were also taken into account. As seen in Fig. 3, the solubility of Dy in Mn (bcc) and Mn (fcc) were reproduced to have the allotropic transformation temperatures determined by Kirchmayr and Lugscheider [22] with the assumption of large solid state miscibility gaps for both the bcc-A2 and the fcc-A1 solid solution phases. In the present optimization, the peritectoid transformation of $Mn_{12}Dy$ ($Mn_{23}Dy_6$ + Mn (cub-A13) → $Mn_{12}Dy$) was assumed to occur at about 1053 ºC. Since no specific experimental data are available, additional investigation is necessary with regard to the transformation of $Mn_{12}Dy$. The calculated invariant reactions are tabulated in Table 3 in comparison to the experimental data.

Table 3. Calculated invariant reactions with the experimental data in the Mn-Dy system.

Type	Reaction	T (°C)	Reference
Peritectic	$Mn_{(fcc\text{-}A1,\ X_{Dy}=0.01^*)} + L_{(X_{Dy}=0.158^*)} \rightarrow Mn_{12}Dy$	1075.0	[22]
Peritectic	$Mn_{12}Dy + L_{(X_{Dy}=0.445^*)} \rightarrow Mn_{23}Dy_6$	1035.0	[22]
Peritectic	$Mn_{23}Dy_6 + L_{(X_{Dy}=0.636^*)} \rightarrow Mn_2Dy$	930.0	[22]
Catatectic	$Mn_{(fcc\text{-}A1,\ X_{Dy}=0.002)} \rightarrow Mn_{(cub\text{-}A13,\ X_{Dy}=0)} + L_{(X_{Dy}=0.116)}$	1075.3	This work
Catatectic	$Mn_{(bcc\text{-}A2,\ X_{Dy}=0.003)} \rightarrow Mn_{(fcc\text{-}A1,\ X_{Dy}=0.001)} + L_{(X_{Dy}=0.085)}$	1120.4	This work
Peritectoid	$Mn_{(cub\text{-}A13,\ X_{Dy}=0)} + Mn_{23}Dy_6 \rightarrow Mn_{12}Dy$	1053.3	This work
Eutectic	$L_{(X_{Dy}=0.124)} \rightarrow Mn_{(cub\text{-}A13,\ X_{Dy}=0)} + Mn_{23}Dy_6$	1065.0	This work
Congruent	$L_{(X_{Dy}=0.207)} \leftrightarrow Mn_{23}Dy_6$	1096.7	This work
Eutectic	$L_{(X_{Dy}=0.261)} \rightarrow Mn_{23}Dy_6 + Mn_2Dy$	1085.6	This work
Congruent	$L_{(X_{Dy}=0.333)} \leftrightarrow Mn_2Dy$	1105.7	This work
Eutectic	$L_{(X_{Dy}=0.649)} \rightarrow Mn_2Dy + Dy_{(hcp\text{-}A3,\ X_{Dy}=1)}$	861.3	This work
	$L_{(X_{Dy}=0.720^*)} \rightarrow Mn_2Dy + Dy_{(hcp\text{-}A3,\ X_{Dy}=1)}$	855.0	[22]

* The exact compositions are not specified in the reference.

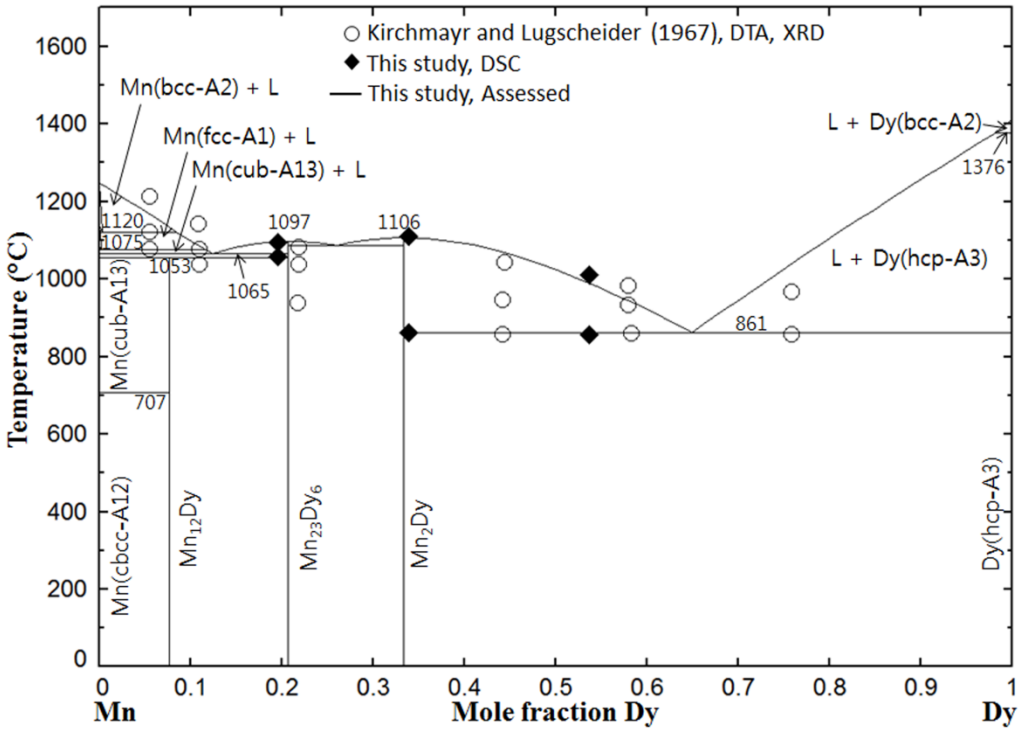


Fig. 3. The optimized phase diagram of the Mn-Dy system with experimental data.

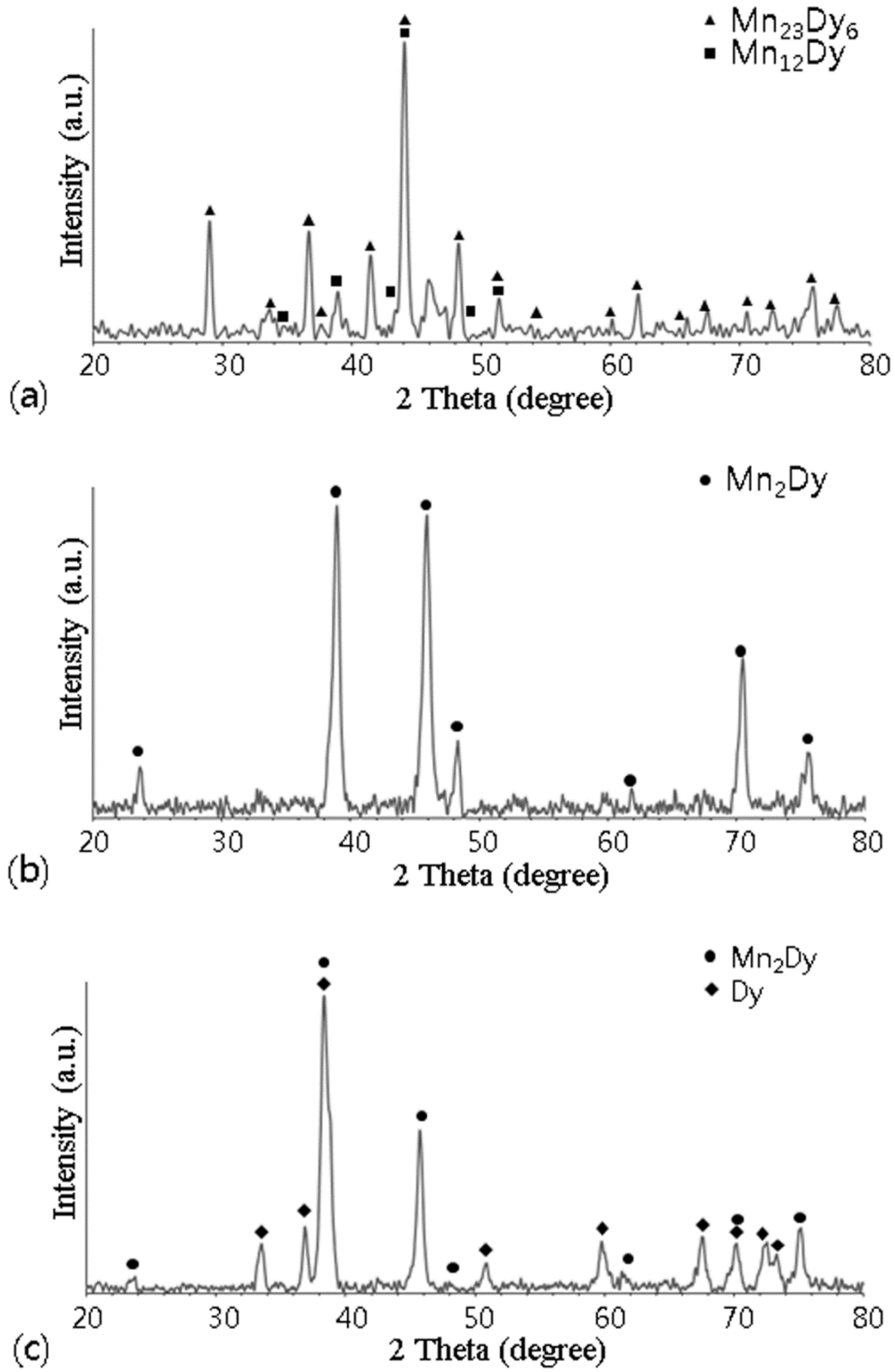


Fig. 4. XRD patterns of (a) Alloy 1, (b) Alloy 2, and (c) Alloy 3.

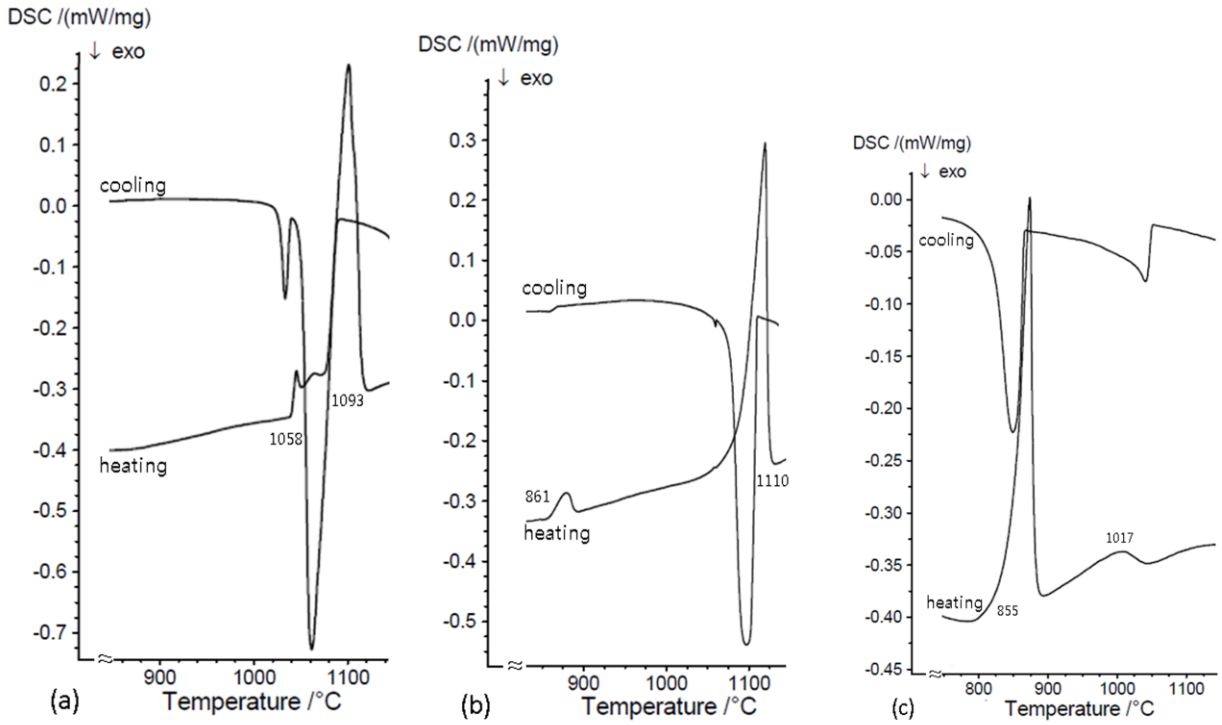


Fig. 5. Heating and cooling curves from DSC for (a) Alloy 1, (b) Alloy 2, and (c) Alloy 3.

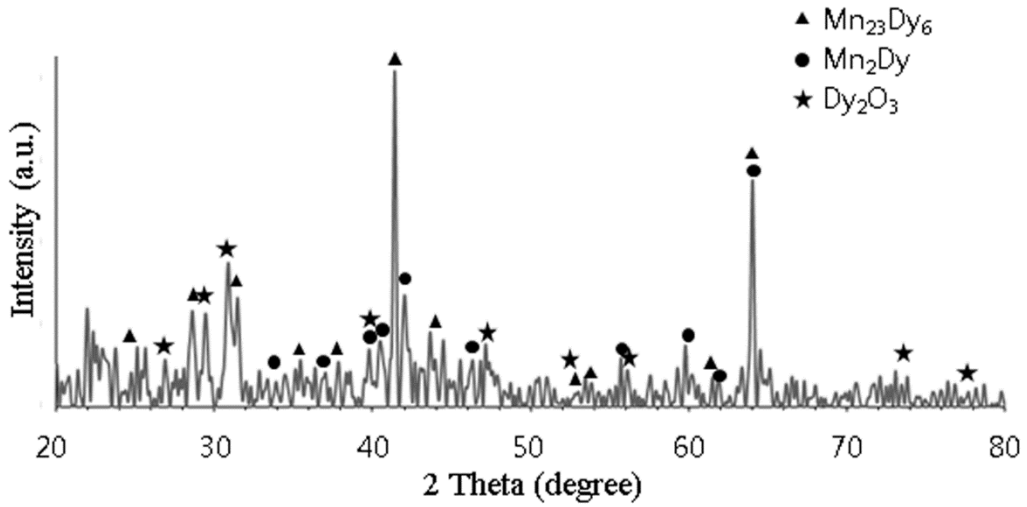


Fig. 6. XRD pattern of Alloy 2 after annealing at 1000 oC for 48 hours.

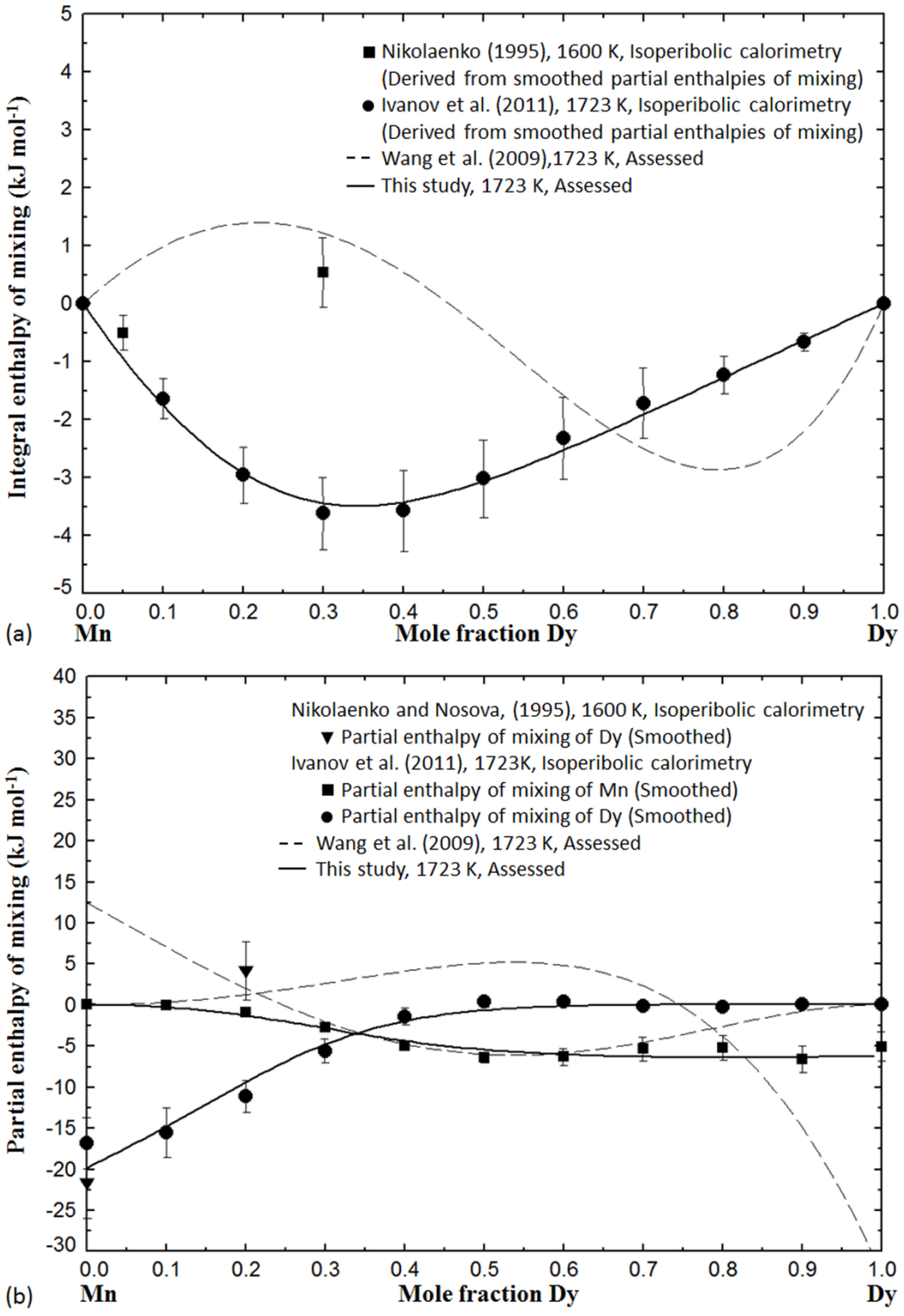


Fig. 7. (a) Integral enthalpy of mixing and (b) partial enthalpies of mixing in Mn-Dy liquid at 1723 K with experimental data and the previous optimization.

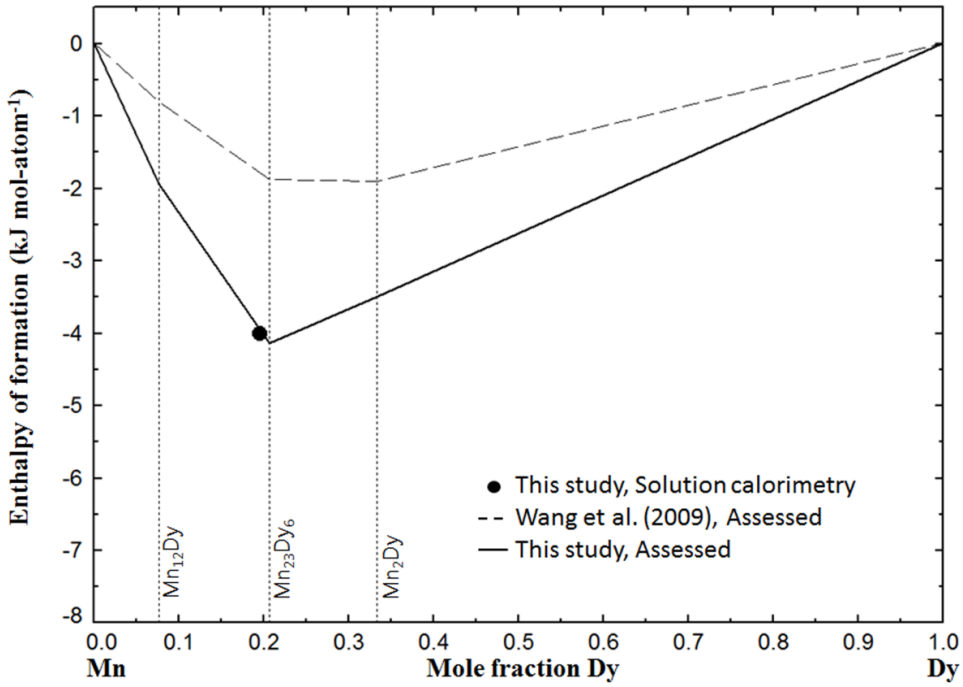


Fig. 8. Enthalpy of formation of the intermetallic compounds with the present experimental data, the previous optimization and the estimated values by the modified Miedema model.

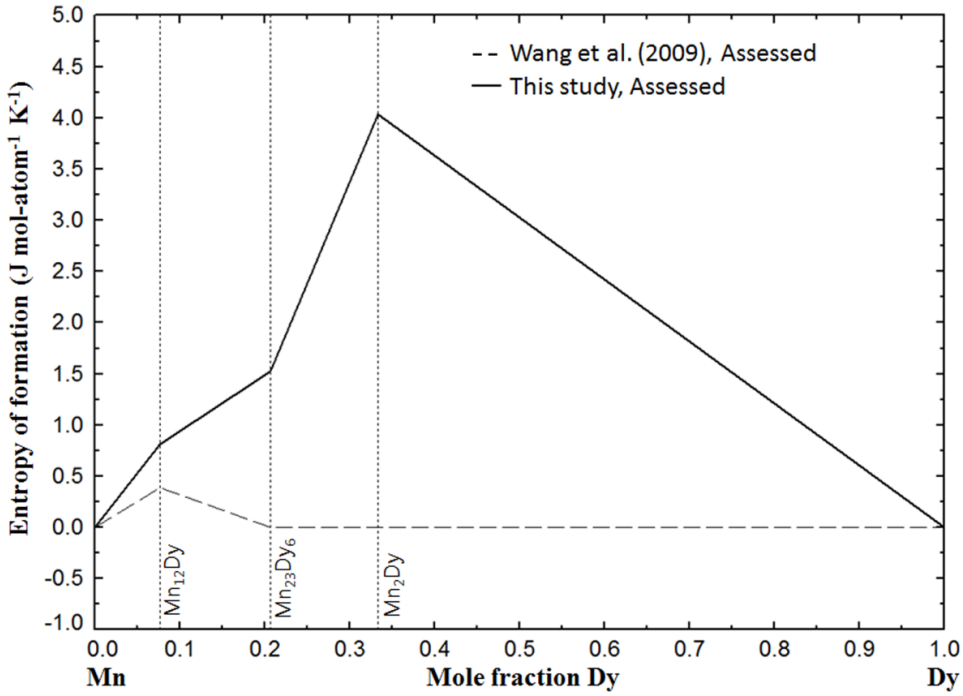


Fig. 9. Entropy of formation of the intermetallic compounds with the previous optimization.

4.2. The Mn-Tb system

Kirchmayr and Lugscheider [21] determined the phase diagram of Mn-Tb system. Alloys made of 99.9 wt. % Mn and Tb were prepared by amalgam process which was similarly used in the investigation of the Mn-Dy system. The results are shown in Fig. 10. Three incongruent melting compounds ($Mn_{12}Tb$, $Mn_{23}Tb_6$, and Mn_2Tb) and invariant reactions (eutectic and peritectic reactions) were identified by means of DTA and XRD and verified by X-ray fluorescence spectrometry (XRF) and metallography. The solubility of Tb in solid Mn and that of Mn in solid Tb were not specifically studied, but the mutual solubility of Tb and Mn were proposed to be very small.

Ivanov et al. [45] measured the partial enthalpy of mixing of Mn in the Tb-rich region and that of Tb in the Mn-rich region of Mn-Tb liquid at 1700 K using an isoperibolic calorimeter and starting materials made of 99.9 wt. % Mn and 99.96 wt. % Tb. Like the Mn-Dy system, they proposed smoothed values of the integral and partial enthalpies of mixing for the Mn-Tb liquid. The authors presented only smoothed values without actual experimental data. The enthalpy data are presented in Figs. 11(a) and 11(b).

Piqué et al. [48] measured the low temperature C_p of the $Mn_{12}Tb$ using an adiabatic calorimeter based on the heat pulse method. In the present study, the S°_{298} of $Mn_{12}Tb$ was calculated by integrating experimental C_p data up to 298 K (461.4 J mol^{-1} K^{-1}). Shiga and Wada [49] measured the C_p of the Mn_2Tb from 1.5 to 300 K using an adiabatic calorimeter. The magnetic transition temperature (T_N : Néel temperature) was reported to be about 45 K. The calculated S°_{298} of Mn_2Tb was 152.9 J mol^{-1} K^{-1}. Kolwicz-Chodak et al. [50] measured the C_p of the Mn_2Tb using two different methods, a quasi-adiabatic method in the temperature range 50 to 320 K and a relaxation method using Quantum Design physical properties measuring system (PPMS) in the temperature range 2 to 350 K. It was reported that a good agreement was obtained for the data from the two different measurements and the T_N was about 47 K. The S°_{298} was calculated from the experimental data (136.8 J mol^{-1} K^{-1}). The experimental C_p data for $Mn_{12}Tb$ and Mn_2Tb are plotted

in Fig. 12, and the entropy of formation (ΔS^{o}_{298}) of $Mn_{12}Tb$ and Mn_2Tb from elements, which were obtained from experimental C_p data, are presented in Fig. 13. The magnetic transformation temperature (T_C = 455 K) and magnetic moment (B_0 = 49 μ_B) for $Mn_{23}Tb_6$ were reported by Pourarian et al. [46].

The optimized phase diagram of the Mn-Tb system in this study is presented in Fig. 10 along with the experimental data. As pointed out in the Mn-Dy system of the present study and also in the Mn-Nd and Mn-Sm systems [17] and the Mn-Gd system [18] of our previous studies, the phase diagram data by Kirchmayr and Lugscheider [21] turned out to be unreliable. Consequently, only the eutectic temperature between Mn_2Tb and Tb was considered to be reliable from the work of Kirchmayr and Lugscheider [21] as seen in the Mn-Dy (this work) and Mn-Gd [18] systems. Furthermore, the Mn_2Tb and $Mn_{23}Tb_6$ were presumed to melt congruently like those of the Mn-Dy and Mn-Gd systems. The peritectoid transformation of the $Mn_{12}Tb$ was assumed to be similar to that of the $Mn_{12}Dy$. Both solid solution of Mn in Tb and Tb in Mn were assumed to be negligible as mentioned by Kirchmayr and Lugscheider [21]. However, further experimental investigation is recommended to verify the proposed phase diagram of the Mn-Tb system. The calculated thermodynamic properties are compared with the experimental data in Figs. 11 to 13. Like the Mn-Dy system, the enthalpy of mixing of the liquid by Ivanov et al. [45] were taken into account to determine the thermodynamic parameters of liquid phase. The temperature-independent terms of the liquid interaction parameters were firstly evaluated to reproduce the experimental enthalpy data. The C_p of the $Mn_{12}Tb$ was increased by 12 J mol^{-1} K^{-1} from the C_p evaluated by the NK rule to be consistent with the experimental low temperature C_p data [48] as shown in Fig. 12. The magnetic properties of $Mn_{23}Tb_6$ measured by Pourarian et al. [46] were used. As seen in Fig. 13, the experimental S^{o}_{298} of the $Mn_{12}Tb$ from Piqué et al. [48] was taken into account, and the S^{o}_{298} of the Mn_2Tb calculated from the low temperature C_p measured by Shiga and Wada [49] was believed to be more reasonable than that from Kolwicz-Chodak et al. [50] because the C_p of Shiga and Wada [49] was coherent with the C_p above 298 K evaluated by NK rule. Moreover, the S^{o}_{298} of the Mn_2Tb calculated from the C_p data of Kolwicz-Chodak et al. [50] was too small to reproduce the congruent melting of Mn_2Tb in the phase diagram. The ΔH^{o}_{298} of the compounds were assumed

to be the same as those in the Mn-Dy system as seen in the predicted enthalpies of formation from the modified Miedema model (See Table 9). Like the Mn-Dy system, three small temperature-dependent parameters for liquid phase were needed to reproduce the proposed phase diagram. It should be also noted that the experimental data [21] in the liquidus of Mn-rich side is less acceptable from the viewpoint of the limiting slope rule [47]. The calculated invariant reactions are tabulated in Table 4 in comparison to the experimental data.

Table 4. Calculated invariant reactions with the experimental data in the Mn-Tb system.

Type	Reaction	T (°C)	Reference
Peritectic	$Mn_{(bcc\text{-}A2,\ X_{Tb}=0)} + L_{(X_{Tb}=0.171^*)} \rightarrow Mn_{12}Tb$	1140.0	[21]
Peritectic	$Mn_{12}Tb + L_{(X_{Tb}=0.310^*)} \rightarrow Mn_{23}Tb_6$	1048.0	[21]
Peritectic	$Mn_{23}Tb_6 + L_{(X_{Tb}=0.504^*)} \rightarrow Mn_2Tb$	912.0	[21]
Peritectoid	$Mn_{(cub\text{-}A13,\ X_{Tb}=0)} + Mn_{23}Tb_6 \rightarrow Mn_{12}Tb$	1038.3	This work
Eutectic	$L_{(X_{Tb}=0.170)} \rightarrow Mn_{(cub\text{-}A13,\ X_{Tb}=0)} + Mn_{23}Tb_6$	1060.1	This work
Congruent	$L_{(X_{Tb}=0.207)} \leftrightarrow Mn_{23}Tb_6$	1063.6	This work
Eutectic	$L_{(X_{Tb}=0.275)} \rightarrow Mn_{23}Tb_6 + Mn_2Tb$	1049.3	This work
Congruent	$L_{(X_{Tb}=0.333)} \leftrightarrow Mn_2Tb$	1061.9	This work
Eutectic	$L_{(X_{Tb}=0.653)} \rightarrow Mn_2Tb + Tb_{(hcp\text{-}A3,\ X_{Tb}=1)}$	768.6	This work
	$L_{(X_{Tb}=0.660^*)} \rightarrow Mn_2Tb + Tb_{(hcp\text{-}A3,\ X_{Tb}=1)}$	768.0	[21]

* The exact compositions are not specified in the reference.

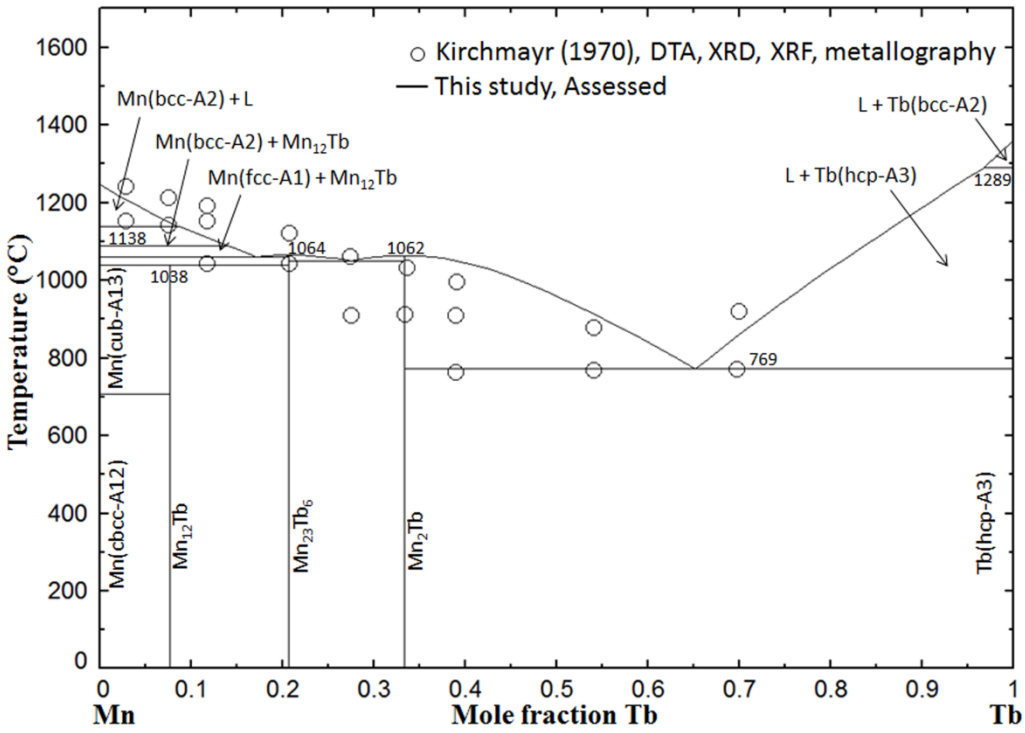


Fig. 10. The optimized phase diagram of the Mn-Tb system with experimental data.

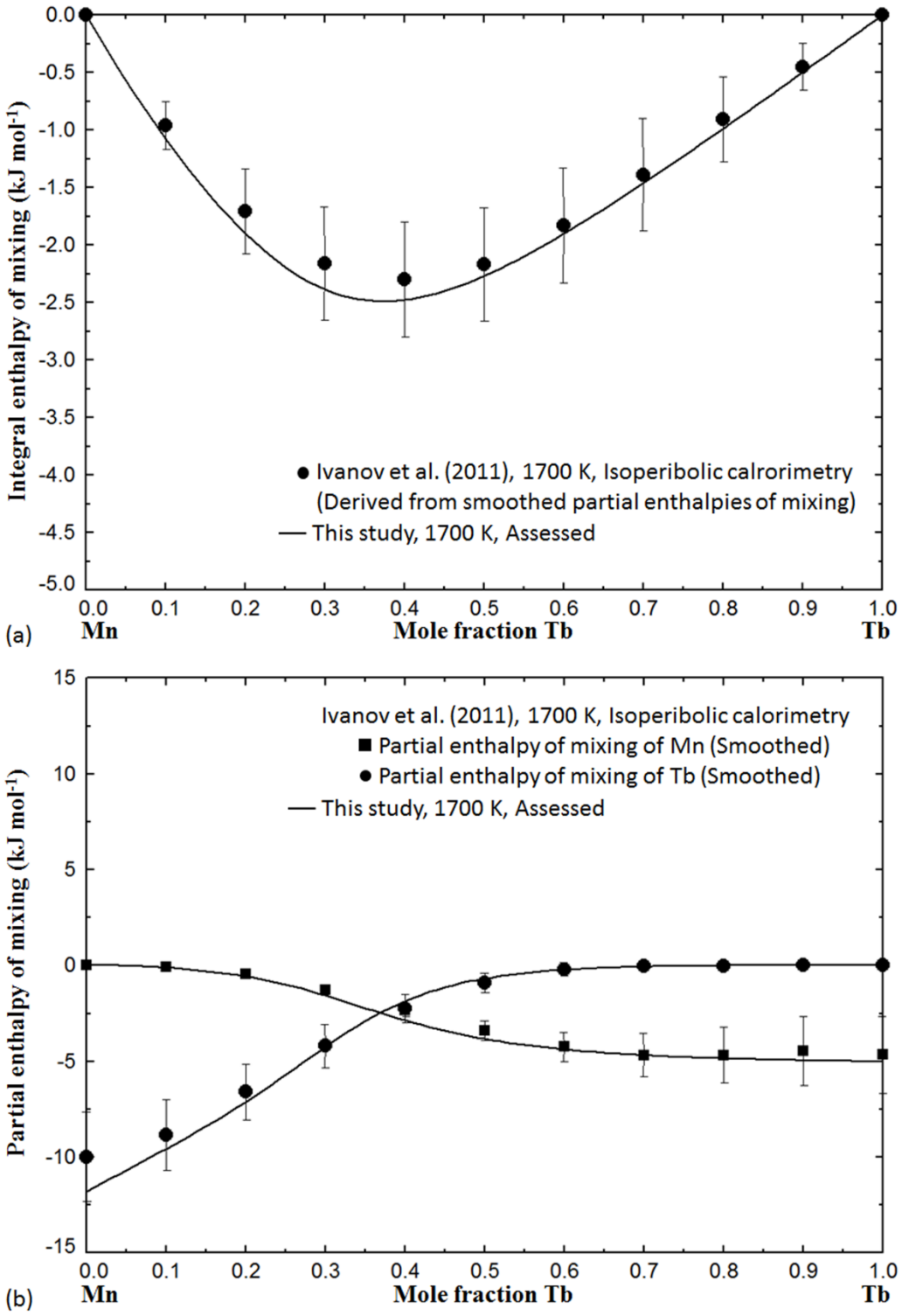


Fig. 11. (a) Integral enthalpy of mixing and (b) partial enthalpies of mixing in Mn-Tb liquid at 1700 K with experimental data.

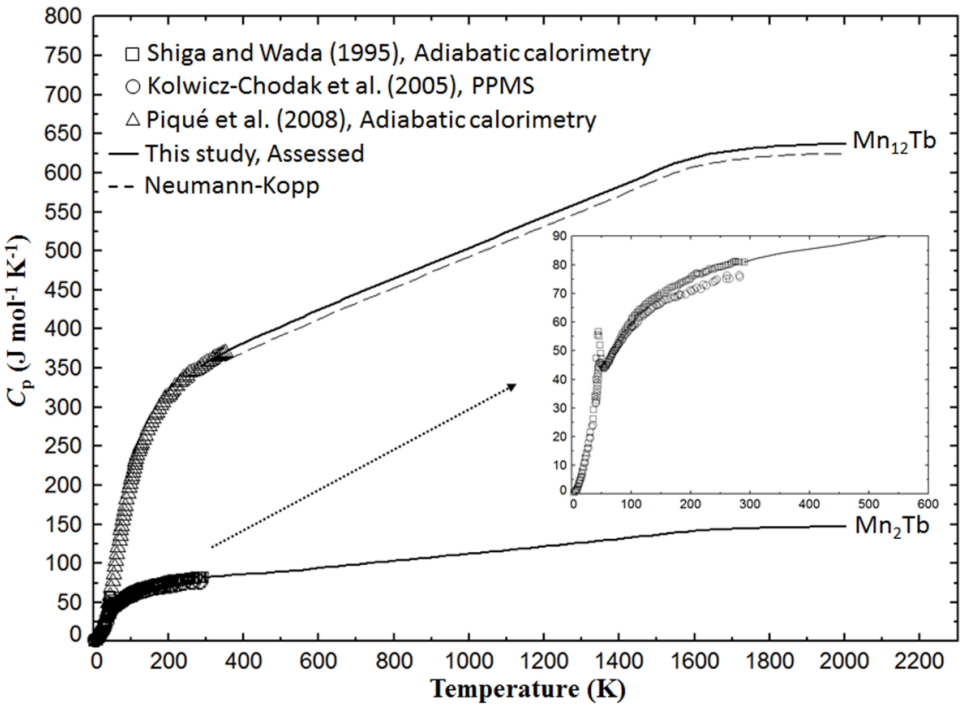


Fig. 12. The heat capacity (Cp) of the compounds for Mn12Tb and for Mn2Tb with experimental data. The Cp, obtained by the Neumann-Kopp rule, is drawn as dashed line.

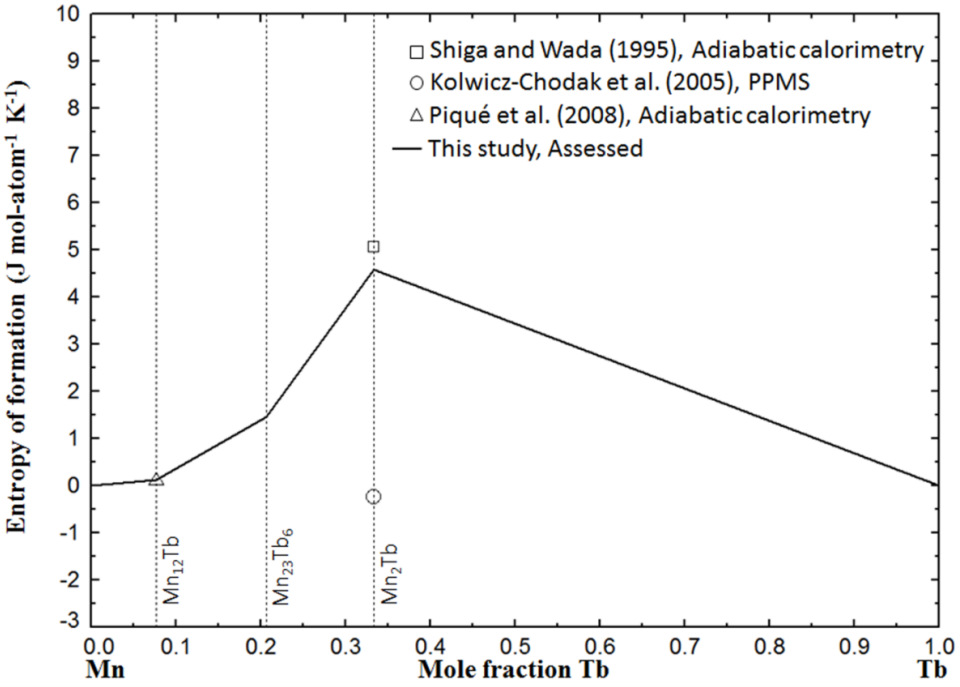


Fig. 13. Entropy of formation of the intermetallic compounds with experimental data.

4.3. The Mn-Ho system

Kirchmayr and Lugscheider [22] investigated the phase diagram of the Mn-Ho system using the same technique that they used for determining the Mn-Dy system. The experimental data are shown in Fig. 14. Three incongruent melting compounds ($Mn_{12}Ho$, $Mn_{23}Ho_6$, and Mn_2Ho) and invariant reactions including eutectic and peritectic reactions were identified. The eutectic reaction was located at 0.73 mole fraction Ho and 875 °C. A small solubility of Ho in Mn was proposed by the allotropic transformation temperature for bcc-A2 to fcc-A1 lowered to 1125 °C.

Nikolaenko and Nosova [44] measured the partial enthalpy of mixing of Ho between $0 < X_{Ho} < 0.4$ at 1600 K in the Mn-Ho liquid using a high-temperature isoperibolic calorimeter. Alundum crucible and starting materials made of 99.9 % Mn and > 99.9 % Ho were used. Using the same method as for the Mn-Dy system, the smoothed curves for the partial enthalpy of mixing of Ho and the integral enthalpy of mixing were suggested. The integral enthalpy of mixing has negative value (-2.3 ± 0.73 kJ mol^{-1} at 0.3 mole fraction Ho). The results are shown in Figs. 15(a) and 15(b). The thermodynamic data for the intermetallic compounds have not yet been investigated.

Wang et al. [27] previously optimized the system based solely on the experimental data of Kirchmayr and Lugscheider [22] using a random-mixing model for the liquid phase. However, the present authors believe that the experimental data of Kirchmayr and Lugscheider [22] are incorrect as seen in the previous systems.

The thermodynamic optimization of the Mn-Ho system was carried out in a similar way which was used in the Mn-Tb and Mn-Dy systems. Simultaneous optimization of the phase diagram and thermodynamic properties of all phases were conducted based on the experimental data and systematic analysis. The calculated phase diagram of the Mn-Ho system is presented in Fig. 14 along with the experimental data. As discussed in the Mn-Tb system, the phase diagram suggested by Kirchmayr and Lugscheider [22] was considered only partially. That is, the eutectic temperature from Kirchmayr and Lugscheider [22] was reproduced and congruent melting was presumed for the intermetallic compounds, Mn_2Ho and $Mn_{23}Ho_6$. It was also assumed that the $Mn_{12}Ho$

peritectoidally decomposes to Mn (cub-A13) and $Mn_{23}Ho_6$ like the $Mn_{12}Dy$. Both solid solution of Mn in Ho and Ho in Mn were not considered as the specific data were not available. Further experimental investigation of the phase diagram of the Mn-Ho system is recommended to verify the proposed phase diagram. The calculated thermodynamic properties using the thermodynamic parameters obtained in this optimization are compared with the experimental data and the previous optimization of Wang et al. [27] in Figs. 15 to 17. From the systematic analysis, the enthalpy data of Nikolaenko and Nosova [44] was considered to be inaccurate. Instead, considering the periodic trend, it was assumed that the enthalpy of mixing of Mn-Ho lies proportionally in between the enthalpy of mixing of Mn-Dy and Mn-Tm where the latter were determined experimentally. The enthalpy of mixing was modeled based on the estimated values. Both the calculated integral enthalpy of mixing and the estimated values are presented in Fig. 15(a). Due to absence of thermodynamic data for the intermetallic compounds, the ΔH°_{298} of the compounds were assessed by the systematic analysis. The S°_{298} of the compounds were modeled to be similar to those of the Mn-Dy system. The magnetic properties of $Mn_{23}Ho_6$ (T_C = 434 K and B_0 = 59.8 μ_B) which were reported by Pourarian et al. [51] were taken into account. Like the previous systems, three small temperature-dependent parameters for liquid phase were applied to reproduce the proposed phase diagram. The calculated invariant reactions are tabulated in Table 5 in comparison to the experimental data.

Table 5. Calculated invariant reactions with the experimental data in the Mn-Ho system.

Type	Reaction	T (°C)	Reference
Peritectic	$Mn_{(fcc\text{-}A1,\ X_{Ho}=0.001^*)} + L_{(X_{Ho}=0.221^*)} \rightarrow Mn_{12}Ho$	1085.0	[22]
Peritectic	$Mn_{12}Ho + L_{(X_{Ho}=0.488^*)} \rightarrow Mn_{23}Ho_6$	1045.0	[22]
Peritectic	$Mn_{23}Ho_6 + L_{(X_{Ho}=0.632^*)} \rightarrow Mn_2Ho$	965.0	[22]
Peritectoid	$Mn_{(cub\text{-}A13,\ X_{Ho}=0)} + Mn_{23}Ho_6 \rightarrow Mn_{12}Ho$	1061.3	This work
Eutectic	$L_{(X_{Ho}=0.119)} \rightarrow Mn_{(cub\text{-}A13,\ X_{Ho}=0)} + Mn_{23}Ho_6$	1079.5	This work
Congruent	$L_{(X_{Ho}=0.207)} \leftrightarrow Mn_{23}Ho_6$	1110.4	This work
Eutectic	$L_{(X_{Ho}=0.265)} \rightarrow Mn_{23}Ho_6 + Mn_2Ho$	1100.7	This work
Congruent	$L_{(X_{Ho}=0.333)} \leftrightarrow Mn_2Ho$	1114.5	This work
Eutectic	$L_{(X_{Ho}=0.628)} \rightarrow Mn_2Ho + Ho_{(hcp\text{-}A3,\ X_{Ho}=1)}$	876.0	This work
	$L_{(X_{Ho}=0.724^*)} \rightarrow Mn_2Ho + Ho_{(hcp\text{-}A3,\ X_{Ho}=1)}$	875.0	[22]

* The exact compositions are not specified in the reference.

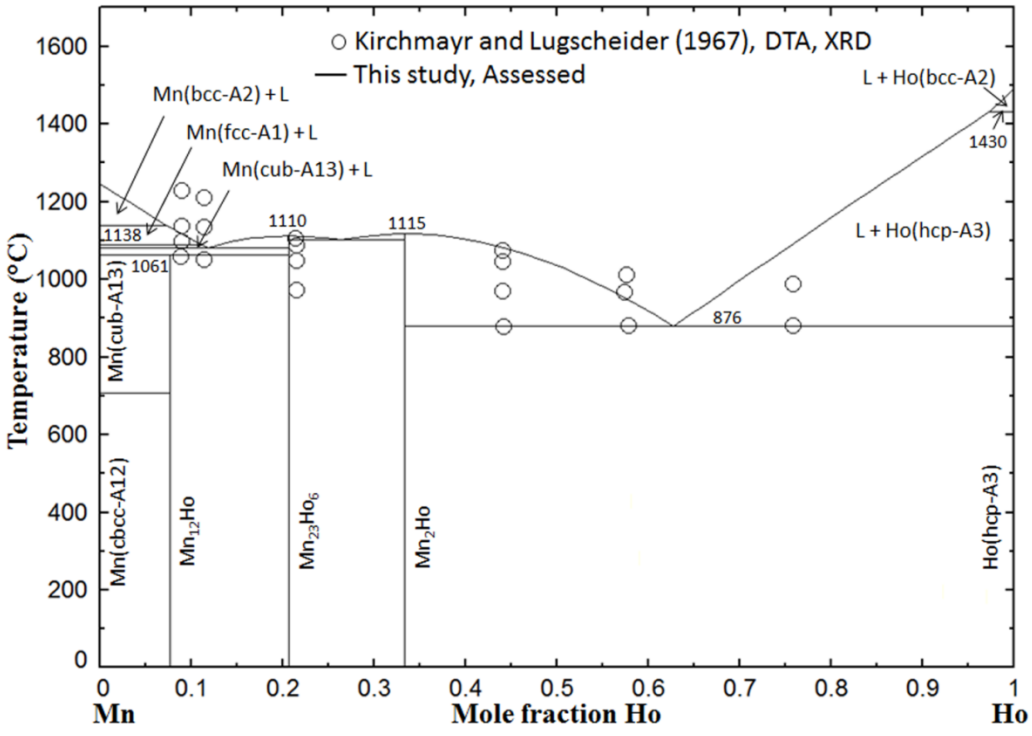


Fig. 14. The optimized phase diagram of the Mn-Ho system with experimental data.

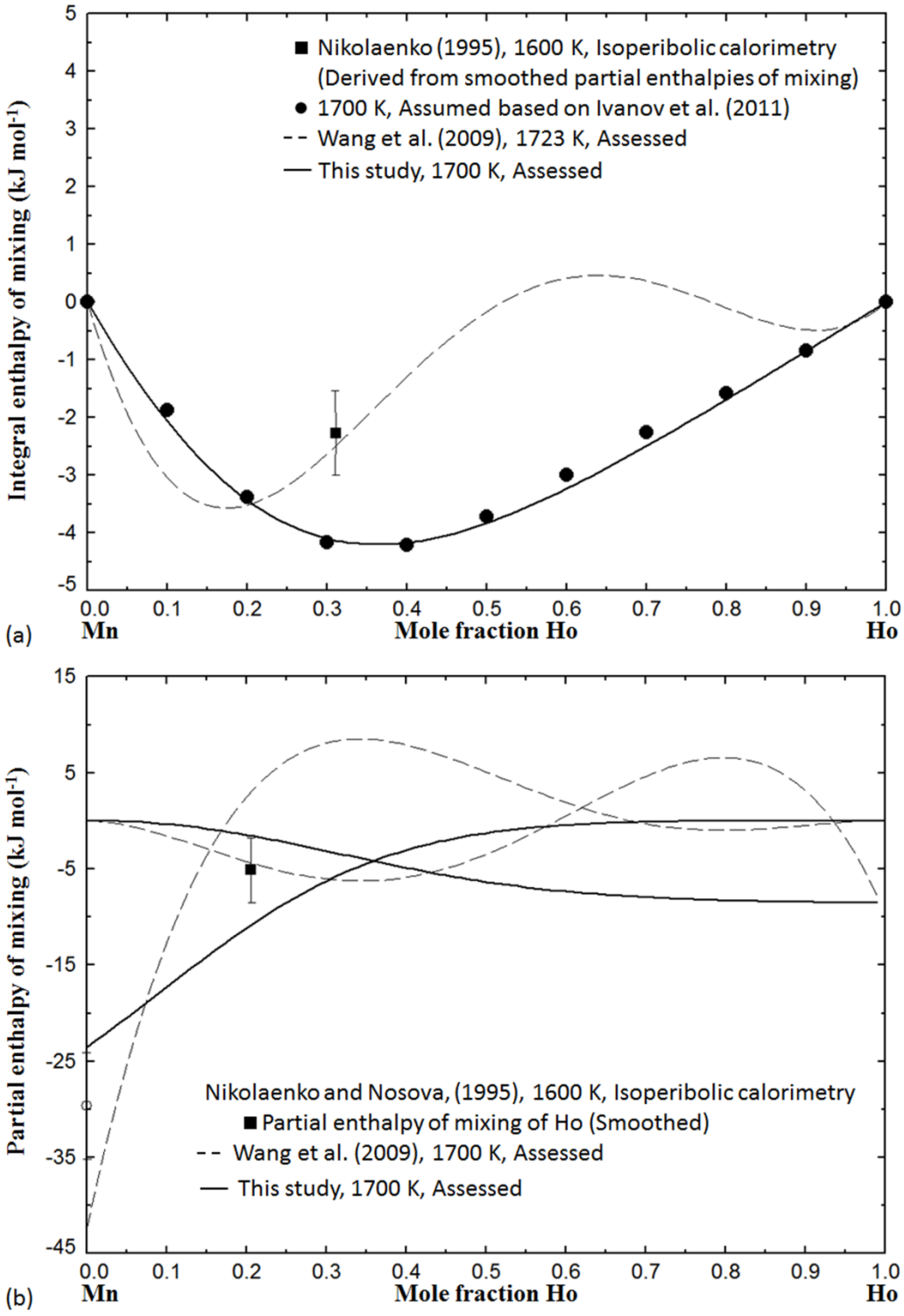


Fig. 15. (a) Integral enthalpy of mixing and (b) partial enthalpies of mixing in Mn-Ho liquid at 1700 K with experimental data and the previous optimization.

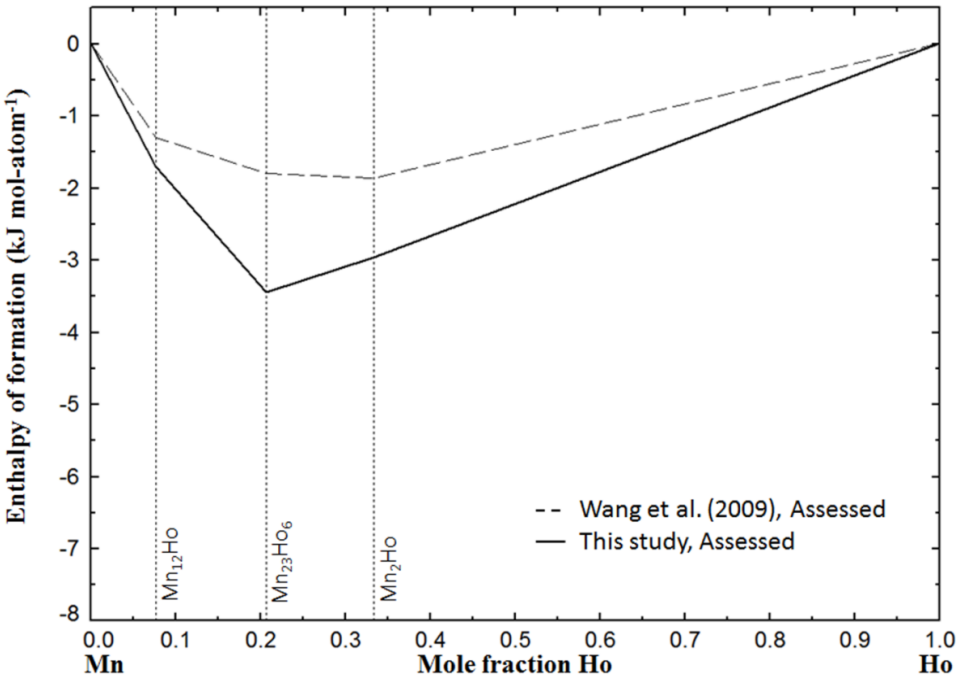


Fig. 16. Enthalpy of formation of the intermetallic compounds with the previous optimization and the estimated values by the modified Miedema model.

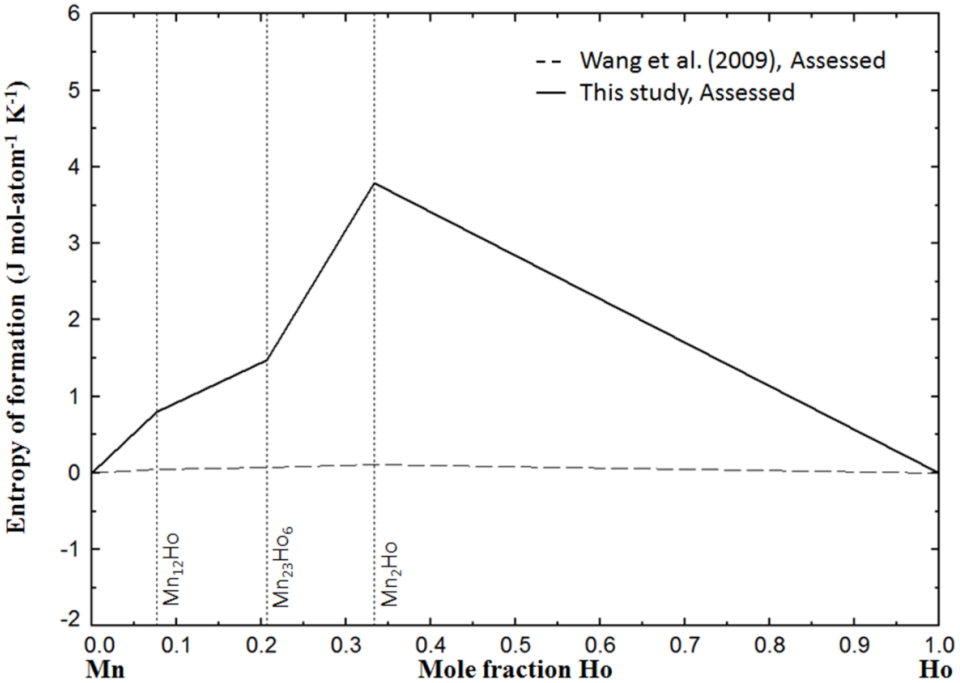


Fig. 17. Entropy of formation of the intermetallic compounds with the previous optimization.

4.4. The Mn-Er system

Kirchmayr and Lugscheider [22] investigated the phase diagram of the Mn-Er system. The experimental data are shown in Fig. 18. Three incongruent melting compounds ($Mn_{12}Er$, $Mn_{23}Er_6$, and Mn_2Er) and invariant reactions including eutectic and peritectic reactions were identified. The eutectic reaction was located at 0.73 mole fraction Ho and at 940 °C.

Nikolaenko and Nosova [44] measured the partial enthalpy of mixing of Er within $0 < X_{Er} < 0.4$ at 1600 K in the Mn-Er liquid using a high-temperature isoperibolic calorimeter. Only the smoothed curves for the partial enthalpy of mixing of Ho and the integral enthalpy of mixing were suggested without original experimental data as shown in Figs. 19(a) and 19(b). The integral enthalpy of mixing for Mn-Er liquid was slightly more negative than that of Mn-Ho liquid (-3.4 ± 1 kJ mol^{-1} at 0.3 mole fraction Er). The thermodynamic data for the intermetallic compounds have not yet been investigated.

Like the previous systems, both the phase diagram and thermodynamic properties for the Mn-Er system were optimized simultaneously based on the experimental data and systematic analysis. The calculated phase diagram of the Mn-Er system is presented along with the experimental data in Fig. 18. As mentioned previously, the phase diagram evaluations reported by Kirchmayr and Lugscheider [22] was considered inaccurate. Contrary to Kirchmayr and Lugscheider [22] the Mn_2Er and $Mn_{23}Er_6$ were considered to melt congruently and only the eutectic temperature was reproduced from their work. Similar to the $Mn_{12}Dy$, the peritectoid transformation was assumed for the $Mn_{12}Er$. Further investigation of the phase diagram of Mn-Er system is recommended to verify the proposed phase diagram. Like the Mn-Ho system, the enthalpy of mixing of Mn-Er system was estimated to lie proportionally in between the enthalpy of mixing of Mn-Dy and Mn-Tm based on their periodic position instead of the enthalpy data of Nikolaenko and Nosova [44]. The enthalpy of mixing was modeled based on the estimated values. Both the calculated integral enthalpy of mixing and the estimated values are presented in Fig. 19(a). The ΔH°_{298} of the compounds were estimated considering systematic trend which was found in the predicted values from the modified Miedema model (See Table 9). The S°_{298} of the compounds were assessed to be

similar to those of the Mn-Ho system. The magnetic properties of $Mn_{23}Er_6$ (T_C = 415 K and B_0 = 38 μ_B) which were reported by Pourarian et al. [51] were used. Additionally, the liquid phase was modeled using three small temperature-dependent parameters to reproduce the proposed phase diagram. The calculated invariant reactions are tabulated in Table 6 in comparison to the experimental data.

Table 6. Calculated invariant reactions with the experimental data in the Mn-Er system.

Type	Reaction	T (°C)	Reference
Peritectic	$Mn_{(fcc\text{-}A1,\ X_{Er}=0.003^*)} + L_{(X_{Er}=0.094^*)} \rightarrow Mn_{12}Er$	1210.0	[22]
Peritectic	$Mn_{12}Er + L_{(X_{Er}=0.244^*)} \rightarrow Mn_{23}Er_6$	1115.0	[22]
Peritectic	$Mn_{23}Er_6 + L_{(X_{Er}=0.610^*)} \rightarrow Mn_2Er$	990.0	[22]
Peritectoid	$Mn_{(cub\text{-}A13,\ X_{Er}=0)} + Mn_{23}Er_6 \rightarrow Mn_{12}Er$	1054.3	This work
Eutectic	$L_{(X_{Er}=0.117)} \rightarrow Mn_{(cub\text{-}A13,\ X_{Er}=0)} + Mn_{23}Er_6$	1072.5	This work
Congruent	$L_{(X_{Er}=0.207)} \leftrightarrow Mn_{23}Er_6$	1111.8	This work
Eutectic	$L_{(X_{Er}=0.283)} \rightarrow Mn_{23}Er_6 + Mn_2Er$	1084.5	This work
Congruent	$L_{(X_{Er}=0.333)} \leftrightarrow Mn_2Er$	1097.1	This work
Eutectic	$L_{(X_{Er}=0.564)} \rightarrow Mn_2Er + Er_{(hcp\text{-}A3,\ X_{Er}=1)}$	939.8	This work
	$L_{(X_{Er}=0.724^*)} \rightarrow Mn_2Er + Er_{(hcp\text{-}A3,\ X_{Er}=1)}$	940.0	[22]

* The exact compositions are not specified in the reference.

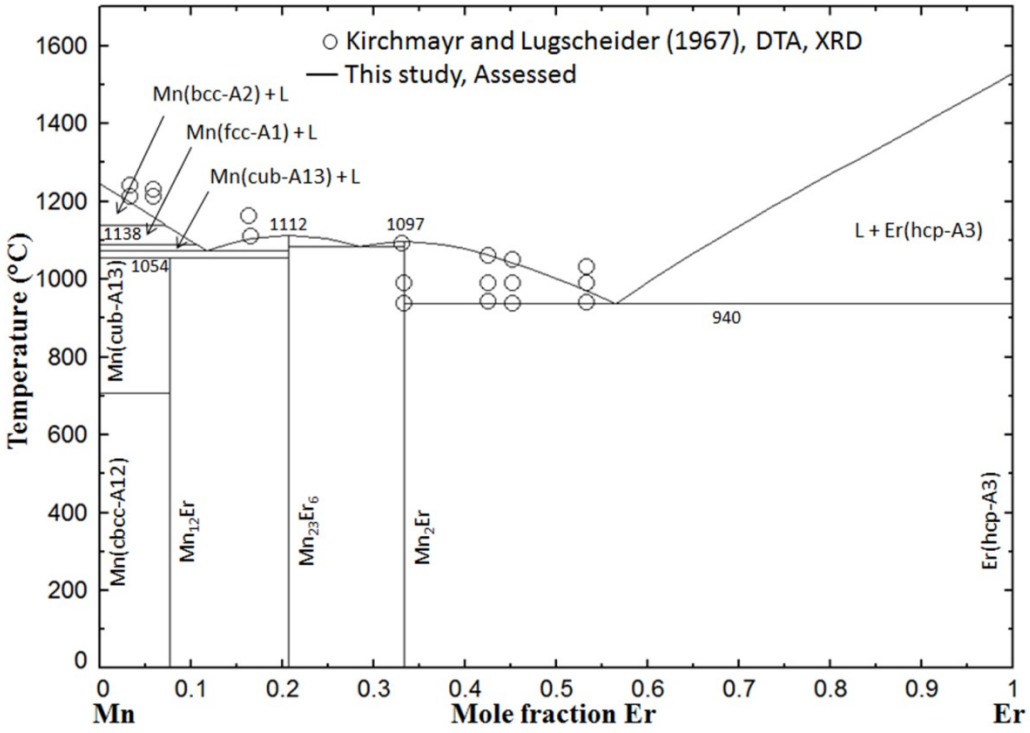


Fig. 18. The optimized phase diagram of the Mn-Er system with experimental data.

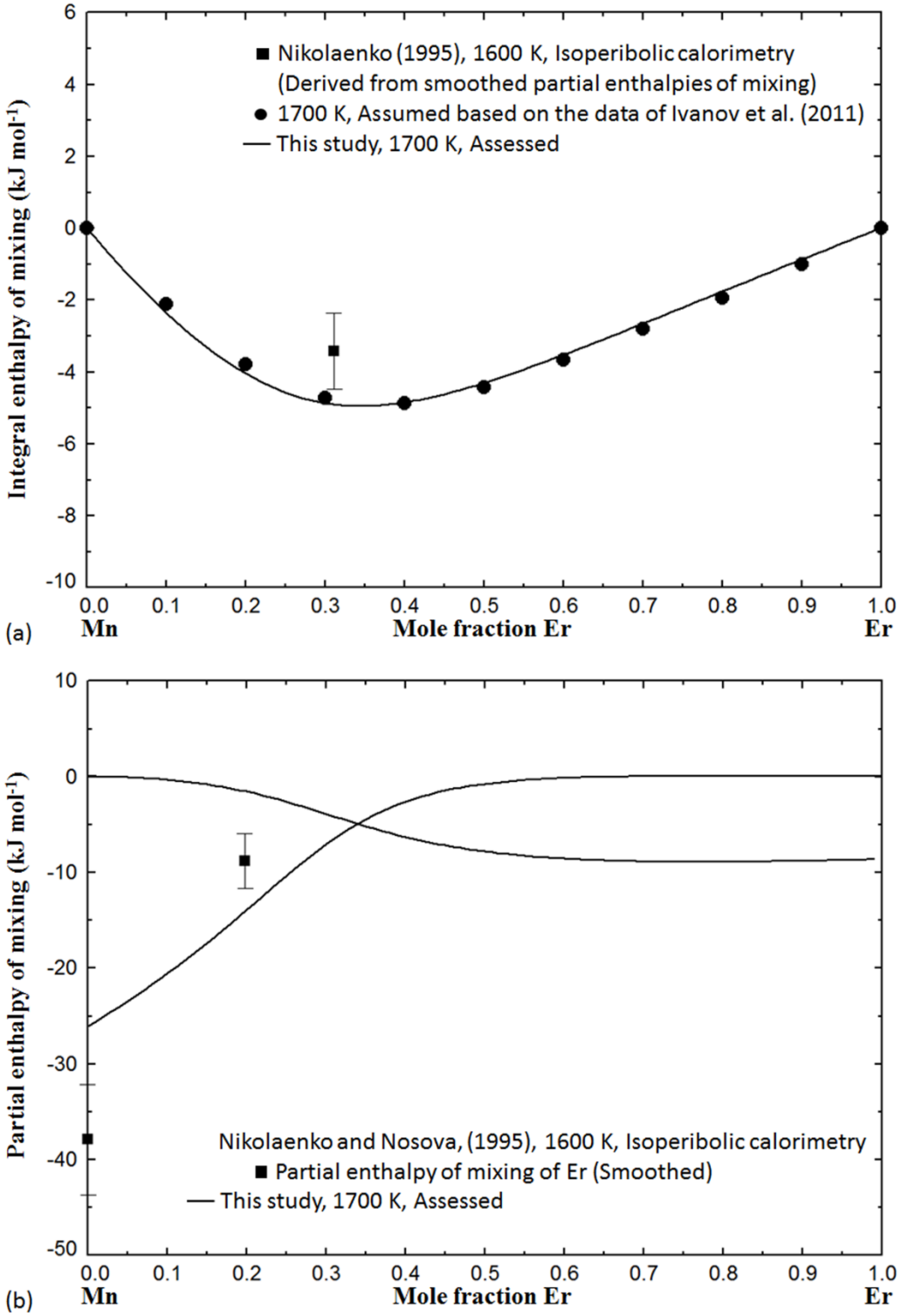


Fig. 19. (a) Integral enthalpy of mixing and (b) partial enthalpies of mixing in Mn-Er liquid at 1700 K with experimental data.

4.5. The Mn-Tm system

The phase diagram of Mn-Tm system has not yet been investigated. Massalski [52] proposed the estimated phase diagram considering the existence of intermediate phases, $Mn_{12}Tm$ [53], $Mn_{23}Tm_6$ [54], and Mn_2Tm [55], and the similarity to the previous systems. In the present study, the phase diagram of the Mn-Tm system was proposed by thermodynamic assessment and systematic analysis of the Mn-RE series in Fig. 20.

The only available experimental data are the enthalpy of mixing of liquid Mn-Tm determined by Ivanov et al. [45] using an isoperibolic calorimeter. The proposed integral and partial enthalpies of mixing of liquid Mn-Tm solution are presented in Figs. 21(a) and 21(b). The enthalpies of mixing in the liquid Mn-Tm alloys were measured within a large composition region (up to 0.7 mole fraction of Tm) at 1700 K. The enthalpy data were not obtained in the Tm-rich composition region due to experimental difficulties (high vapor pressure of Tm). The mixing enthalpy data were evaluated by extrapolation for the composition, $X_{Tm} > 0.8$. The smoothed values were presented at the whole composition range without original data. The integral enthalpy curve show similar shape to that of Mn-Dy system, but more negative having the minimum (-5.52 ± 0.79 kJ mol^{-1}) at 0.4 mole fraction Tm. The thermodynamic data for the intermetallic compounds have not yet been measured.

In the thermodynamic optimization, the enthalpy of mixing of the liquid determined by Ivanov et al. [45] was used to evaluate the model parameters of liquid phase as seen in Fig. 21. Like the previous systems, both the ΔH^{o}_{298} and the S^{o}_{298} of the compounds were assessed to be similar to those of Mn-Er system. As seen in the previous systems, three small temperature-dependent parameters for liquid phase were added. The invariant reactions obtained in the present study are presented in Table 7.

Table 7. Calculated invariant reactions in the Mn-Tm system.

Type	Reaction	T (°C)	Reference
Peritectoid	$Mn_{(fcc\text{-}A1,\ X_{Tm}=0)} + Mn_{23}Tm_6 \rightarrow Mn_{12}Tm$	1094.0	This work
Eutectic	$L_{(X_{Tm}=0.122)} \rightarrow Mn_{(fcc\text{-}A1,\ X_{Tm}=0)} + Mn_{23}Tm_6$	1099.8	This work
Congruent	$L_{(X_{Tm}=0.207)} \leftrightarrow Mn_{23}Tm_6$	1127.0	This work
Eutectic	$L_{(X_{Tm}=0.264)} \rightarrow Mn_{23}Tm_6 + Mn_2Tm$	1110.3	This work
Congruent	$L_{(X_{Tm}=0.333)} \leftrightarrow Mn_2Tm$	1143.8	This work
Eutectic	$L_{(X_{Tm}=0.558)} \rightarrow Mn_2Tm + Tm_{(hcp\text{-}A3,\ X_{Tm}=1)}$	966.4	This work

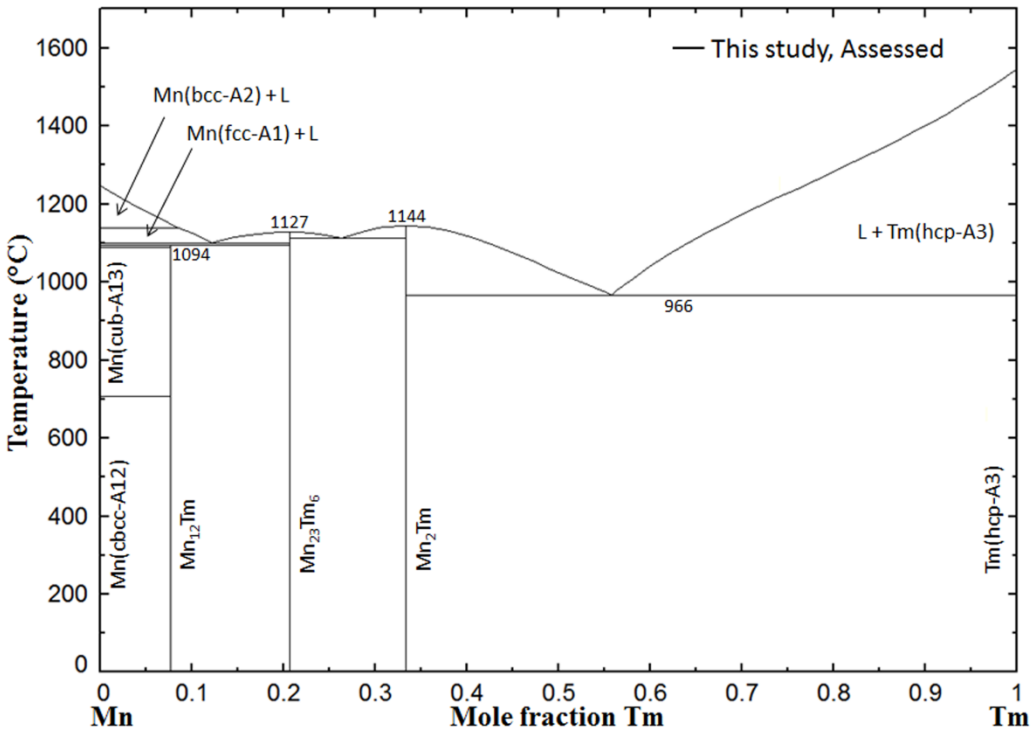


Fig. 20. The optimized phase diagram of the Mn-Tm system.

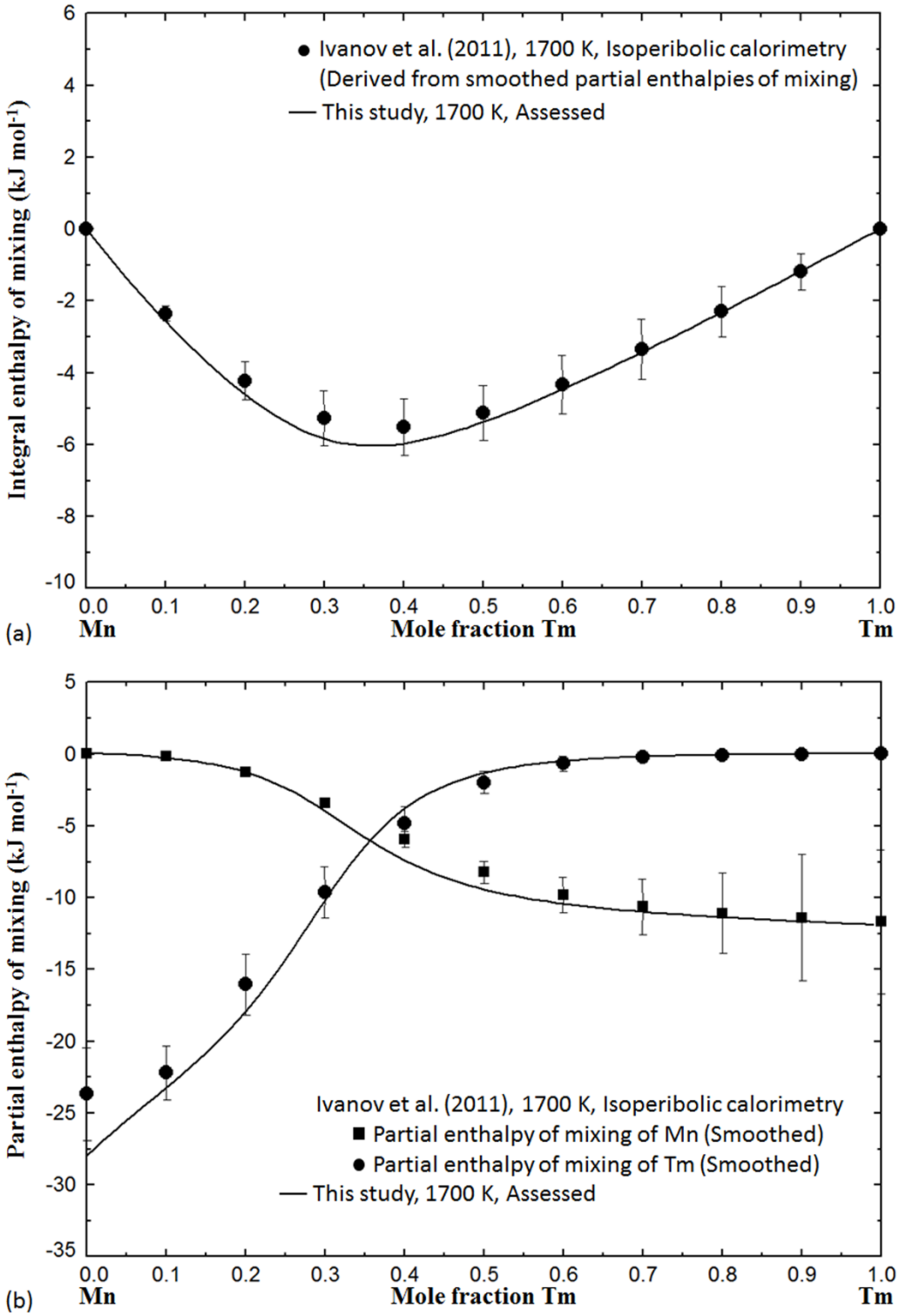


Fig. 21. (a) Integral enthalpy of mixing and (b) partial enthalpies of mixing in Mn-Tm liquid at 1700 K with experimental data.

4.6. The Mn-Lu system

Similar to the Mn-Tm system, there has been no phase diagram investigation for the Mn-Lu system. Massalski [52] proposed a phase diagram based on crystallographic data of intermediate phases (Mn_5Lu [53], $Mn_{23}Lu_6$ [54], and Mn_2Lu [56]) in accordance with the other Mn-RE systems. The system has the Mn_5Lu phase instead of $Mn_{12}Lu$ unlike other Mn-heavy RE systems. In the present study, the phase diagram of the Mn-Lu system was proposed by thermodynamic assessment and systematic analysis. The phases diagram is presented in Fig. 22.

Nikolaenko and Nosova [44] measured the partial enthalpy of mixing of Lu between $0 < X_{Lu} < 0.3$ at 1600 K in the Mn-Lu liquid using the same method as stated in the previous systems, the smoothed curves for the partial enthalpy of mixing of Lu and the integral enthalpy of mixing were presented without original data. Recently, Ivanov et al. [45] measured the enthalpies of mixing in the liquid Mn-Lu alloys within a wide composition region (up to 0.7 mole fraction of Lu) at 1700 K. The enthalpy data was unavailable in the Lu-rich composition region due to experimental difficulties (high melting temperature of Lu). The mixing enthalpy data were extrapolated for the composition, $X_{Lu} > 0.8$. The integral enthalpy curve show similar shape to that of Mn-Tm system, but more negative with the minimum -6.76 ± 0.93 kJ mol^{-1} at 0.4 mole fraction Lu. All the enthalpy data are presented in Figs. 23(a) and 23(b).

The low temperature C_p values for the $Mn_{23}Lu_6$ and Mn_2Lu are presented in Fig. 24. Ohta et al. [57] measured the C_p for the $Mn_{23}Lu_6$ using an adiabatic calorimeter. The magnetic transformation temperature (T_C) for $Mn_{23}Lu_6$ was reported to be about 380 K. The S^{o}_{298} of $Mn_{23}Lu_6$ was calculated from the experimental C_p data (about 1076.8 J mol^{-1} K^{-1}). Kim-Ngan et al. [58] measured the C_p for the Mn_2Lu using an adiabatic calorimeter in the temperature range 1.5 to 300 K. The calculated S^{o}_{298} was about 114.7 J mol^{-1} K^{-1}. The experimental ΔS^{o}_{298} of $Mn_{23}Lu_6$ and Mn_2Lu are presented in Fig. 25. The magnetic properties of $Mn_{23}Lu_6$ (T_C = 378 K and B_0 = 8.9 μ_B) were reported by Buschow and Sherwood [59] from the magnetic measurements adapting Faraday method in the range 1.2 – 600 K.

In the present optimization, the enthalpy of mixing of the liquid determined by Ivanov et al. [45] was used to evaluate the model parameters of liquid phase as seen in Fig. 23. The C_p of all compounds above 298 K were estimated by the NK rule and then, the C_p of the $Mn_{23}Lu_6$ and of the Mn_2Lu were increased by 53 J mol^{-1} K^{-1} and 3 J mol^{-1} K^{-1}, respectively, to reproduce the low temperature C_p data as shown in Fig. 24. The magnetic properties of $Mn_{23}Lu_6$ which were determined by Buschow and Sherwood [59] were used. Both the ΔH^{o}_{298} and the S^{o}_{298} of the compounds were assessed to be similar to those of Mn-Tm compounds. The calculated ΔS^{o}_{298} of the compounds are presented along with the experimental data in Fig. 25. The calculated invariant reactions are listed in Table 8.

Table 8. Calculated invariant reactions in the Mn-Lu system.

Type	Reaction	T (°C)	Reference
Eutectic	$L_{(X_{Lu} = 0.099)} \rightarrow Mn_{(fcc\text{-}A1,\ X_{Lu} = 0)} + Mn_5Lu$	1088.9	This work
Peritectic	$L_{(X_{Lu} = 0.142)} + Mn_{23}Lu_6 \rightarrow Mn_5Lu$	1115.6	This work
Congruent	$L_{(X_{Lu} = 0.207)} \leftrightarrow Mn_{23}Lu_6$	1148.1	This work
Eutectic	$L_{(X_{Lu} = 0.286)} \rightarrow Mn_{23}Lu_6 + Mn_2Lu$	1101.1	This work
Congruent	$L_{(X_{Lu} = 0.333)} \leftrightarrow Mn_2Lu$	1114.8	This work
Eutectic	$L_{(X_{Lu} = 0.540)} \rightarrow Mn_2Lu + Lu_{(hcp\text{-}A3,\ X_{Lu} = 1)}$	982.9	This work

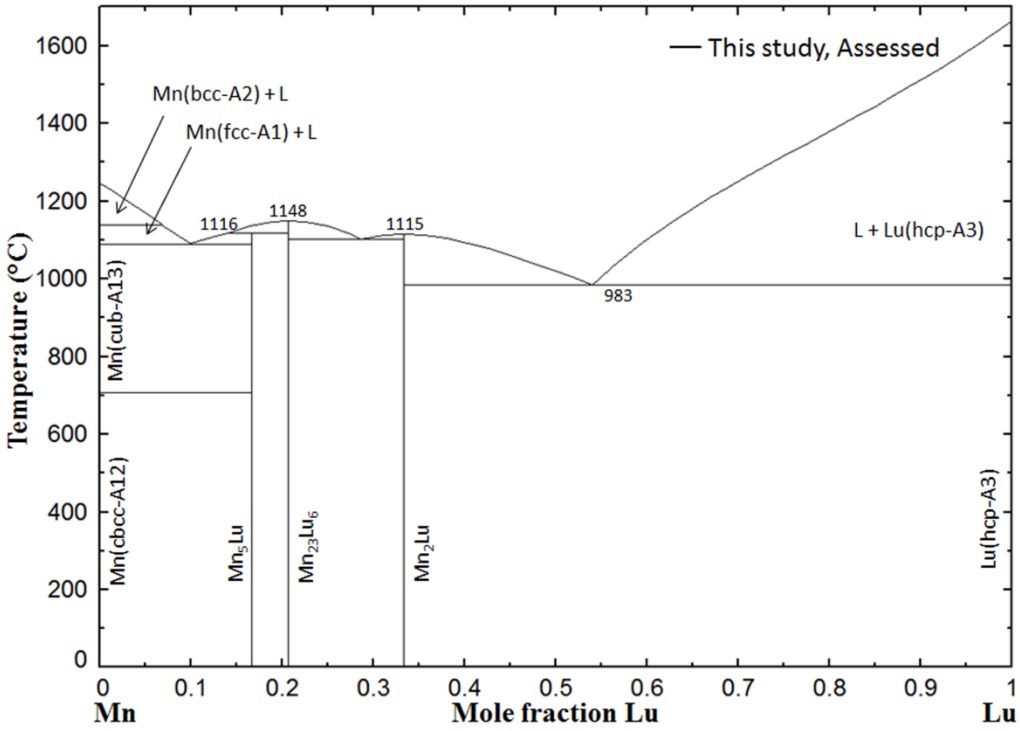


Fig. 22. The optimized phase diagram of the Mn-Lu system.

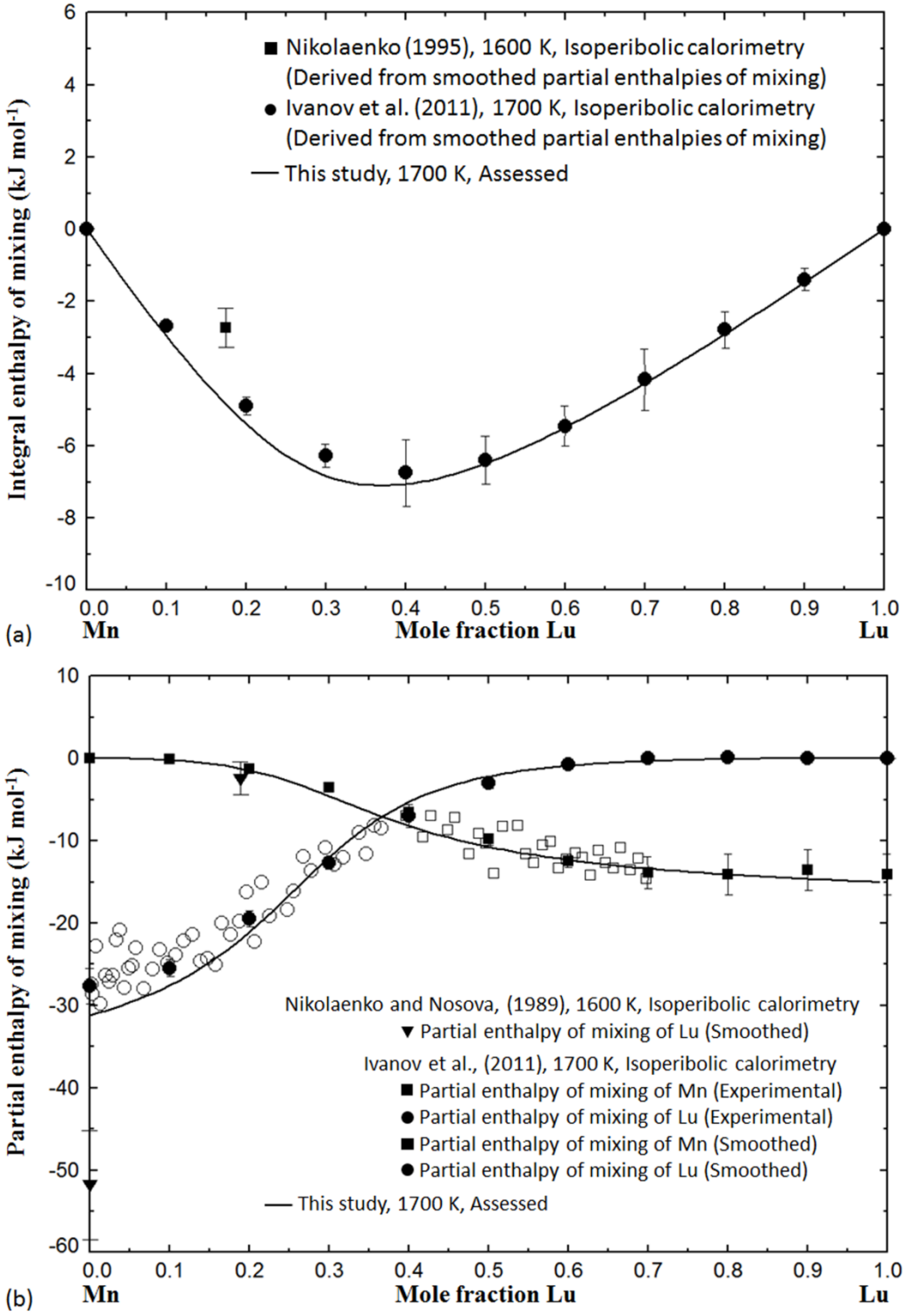


Fig. 23. (a) Integral enthalpy of mixing and (b) partial enthalpies of mixing in Mn-Lu liquid at 1700 K with experimental data.

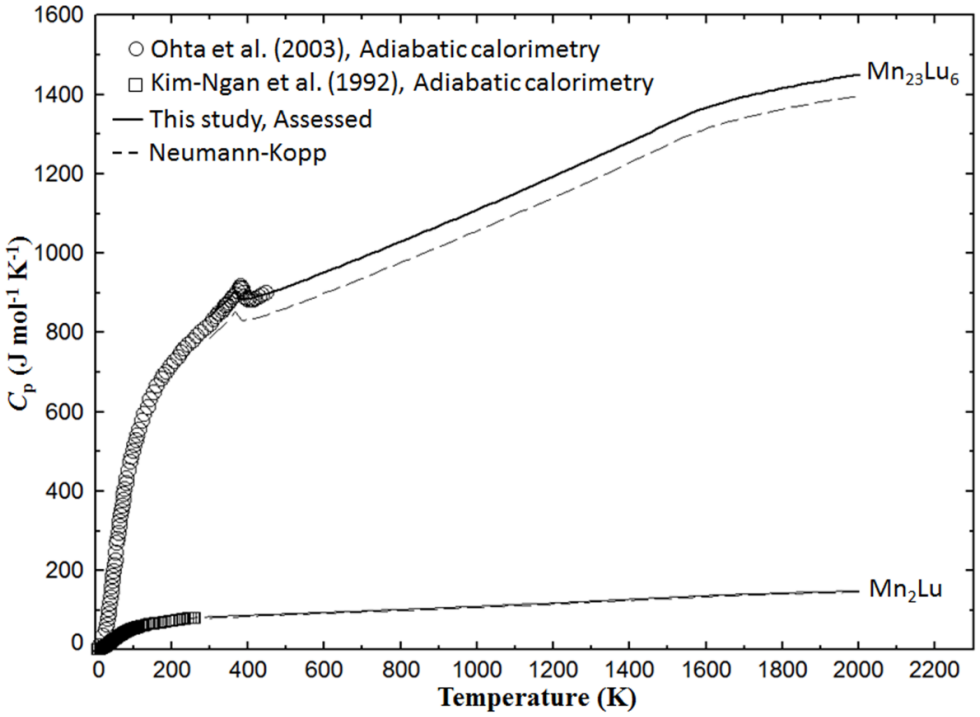


Fig. 24. The heat capacity (C_p) of the compounds above 298 K for $Mn_{23}Lu_6$ and for Mn_2Lu with experimental data. The C_p, obtained by the Neumann-Kopp rule, are drawn as dashed line.

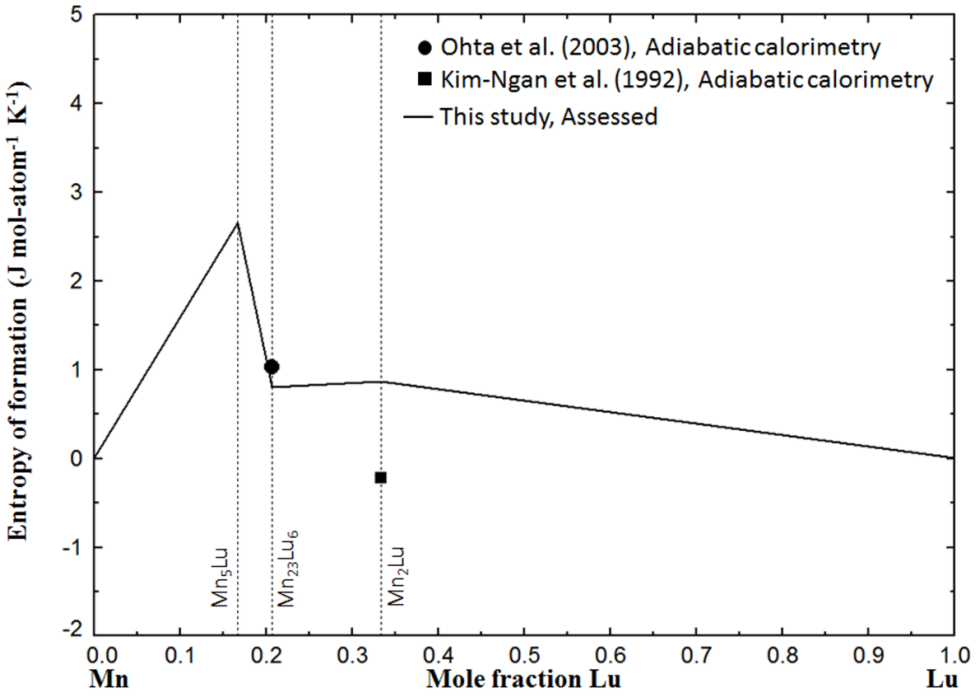


Fig. 25. Entropy of formation of the intermetallic compounds with experimental data.

5. Systematic analysis

We previously discussed the trends and regularities of the thermodynamic properties in the Mn-light RE binary systems [17]. It has been shown that the similarity and regular changes in the physic-chemical properties of RE metals across the lanthanide series lead to certain trends in the thermodynamic properties and phase relationships in the Mn-light RE systems. Similar trend can be seen in the Mn-heavy RE systems as well. The overall systematic trends in the phase diagram and thermodynamic properties of the Mn-RE systems are discussed below, where RE are from La to Sm (light RE) and from Gd to Lu and Y (heavy RE) except the Pm, Eu and Yb.

Figure 26 shows the collection of the 13 optimized phase diagram of all Mn-RE systems from the previous [17, 18] and present study. Regularity in the phase diagram of the Mn-RE systems is clearly observed. The stability of the intermetallic phases increases from the light RE (La to Eu) to the heavy RE (Gd to Lu and Y) and the number of stable binary intermetallic phases goes from none (La and Ce) to three (Gd to Tm and Lu). The Pr- and Nd-Mn phases decompose at lower temperatures while the compounds of the heavier RE are stable down to room temperature except for the Mn_2Y. Among the compounds, Mn_2RE becomes stabilized faster than others, and it melts congruently in Mn-heavy RE systems.

It was also found that the enthalpies of mixing in liquid Mn-RE (1700 K) gradually change from positive (mostly for the Mn-light RE) to negative values (mostly for the Mn-heavy RE) with increasing atomic number of RE as shown in Fig. 27. Previously, Ivanov et al. [45] explained this trend by the formation of hybrid sd-band through the overlap of (3d, 4s)-bands of a transition metal (Mn) with (5d, 6s)-bands of a lanthanide. The strength of this band depends on the Fermi energy, the electronic density of states and the bandwidth of the components. Moreover, according to the theoretical model [40], the important parameters for the enthalpy calculation are the electronegativity difference, the electro-density mismatch, and the atomic size difference. Therefore, most probably the discontinuity of the electron density at the boundaries between the Mn and RE induces positive affect to the enthalpy and then, a certain difference between the Fermi

energies of the components, which is related to the electronegativity (χ_{Mn} = 1.55 and $\chi_{RE} \approx$ 1.1 to 1.27 [60]), brings on the exothermic effect, although the significant atomic volume difference between the Mn and the RE (V^{o}_{Mn} = 7.35 cm^3 mol^{-1}, whereas V^{o}_{La} = 22.39 cm^3 mol^{-1} and V^{o}_{Lu} = 17.78 cm^3 mol^{-1} [61]) makes the exothermic effect small. However, the decrease in the atomic volume difference across the lanthanide series (the lanthanide contraction) leads to the effective band overlapping resulting in higher exothermic interaction between the Mn and heavy RE. Therefore, the attractive interaction between Mn and RE elements become stronger with a minimum between 0.3 and 0.4 mole fraction RE. The asymmetry observed in the enthalpies of mixing curves comes from the size difference between Mn and RE.

Figures 28 and 29 present the optimized enthalpy and entropy of formation of the compounds for the Mn-RE systems. Due to limited experimental data of the compounds, the ΔH^{o}_{298} and S^{o}_{298} of compounds were mostly estimated by considering systematic trend. As for the ΔH^{o}_{298} of all Mn-RE compounds, the predicted values from the modified Miedema model are compared with those obtained in the present optimization and calorimetric data (this work and [62, 63]) in Table 9. In the present optimization, the ΔH^{o}_{298} of all the compounds were evaluated by the combination of the experimental data and the predicted values. The systematic changes in the enthalpy of formation for all compounds are seen in Fig. 28. It is worth mentioning that the ΔH^{o}_{298} of Mn_2RE (per atoms) are less negative than that of $Mn_{23}RE_6$ (per atoms) unlike the predicted values except for the compounds in the Mn-Sm and Mn-Lu systems. This is due to the relatively high ΔS^{o}_{298} of Mn_2RE resulting from the previous experimental S^{o}_{298} for Mn_2Gd and Mn_2Tb. The S^{o}_{298} of the Mn-Dy, -Ho, -Er and -Tm compounds were estimated to be similar to those of the Mn-Tb compounds because the sum of S^{o}_{298} of components (NK rule) for those compounds are similar to each other. The optimized ΔS^{o}_{298} of all compounds are shown in Fig. 29. Interestingly, the ΔH^{o}_{298} of Mn_2Lu (Fig. 28) was estimated to be exceptionally lower than other Mn_2RE compound due to the lower experimental S^{o}_{298} of Mn_2Lu. It is still unclear but possibly linked to the exceptionally low S^{o}_{298} of Lu (50.96 J mol^{-1} K^{-1}) compared to the S^{o}_{298} of other heavy RE (Tb to Er : about 73 to 75 J mol^{-1} K^{-1}).

The entropy of mixing of liquid in the entire Mn-RE systems (1700 K) are shown in Fig. 30. Most of the Mn-RE systems exhibit ideal entropy of mixing with few exceptions that show a higher (La and Tb) or lower (Tm and Lu) deviation from the ideal mixing behavior. The deviations could be due to the non-configurational contribution to the entropy of mixing (vibrational and electronic, etc.).

Table 9. Enthalpy of formation of the Mn-RE compounds in comparison with the prediction and experimental data.

Compound	ΔH^{o}_{298} (kJ mol-atom^{-1})	Method	Reference
$Mn_{23}Sm_6$	-1.27	Semi-quantitative prediction	[38-40]
	-1.45	CALPHAD	[17]
Mn_2Sm	-1.59	Semi-quantitative prediction	[38-40]
	-2.10	CALPHAD	[17]
$Mn_{12}Gd$	-0.53	Semi-quantitative prediction	[38-40]
	-1.17	CALPHAD	[18]
$Mn_{23}Gd_6$	-1.26	Semi-quantitative prediction	[38-40]
	-2.92	CALPHAD	[18]
Mn_2Gd	-1.59	Semi-quantitative prediction	[38-40]
	-1.80	CALPHAD	[18]
$Mn_{12}Tb$	-1.05	Semi-quantitative prediction	[38-40]
	-1.95	CALPHAD	This work
$Mn_{23}Tb_6$	-2.51	Semi-quantitative prediction	[38-40]
	-4.14	CALPHAD	This work
Mn_2Tb	-3.19	Semi-quantitative prediction	[38-40]
	-3.50	CALPHAD	This work
$Mn_{12}Dy$	-1.04	Semi-quantitative prediction	[38-40]
	-1.95	CALPHAD	This work
$Mn_{23}Dy_6$	-2.49	Semi-quantitative prediction	[38-40]
	-4.14	CALPHAD	This work
	-4.01 ($Mn_{0.805}Dy_{0.195}$)	Solution calorimetry	This work
Mn_2Dy	-3.19	Semi-quantitative prediction	[38-40]
	-3.50	CALPHAD	This work
$Mn_{12}Ho$	-0.82	Semi-quantitative prediction	[38-40]
	-1.71	CALPHAD	This work

$Mn_{23}Ho_6$	-1.96	Semi-quantitative prediction	[38-40]
	-3.45	CALPHAD	This work
Mn_2Ho	-2.52	Semi-quantitative prediction	[38-40]
	-2.97	CALPHAD	This work
$Mn_{12}Er$	-1.37	Semi-quantitative prediction	[38-40]
	-2.27	CALPHAD	This work
$Mn_{23}Er_6$	-3.30	Semi-quantitative prediction	[38-40]
	-5.00	CALPHAD	This work
Mn_2Er	-4.26	Semi-quantitative prediction	[38-40]
	-4.20	CALPHAD	This work
$Mn_{12}Tm$	-1.36	Semi-quantitative prediction	[38-40]
	-2.19	CALPHAD	This work
$Mn_{23}Tm_6$	-3.28	Semi-quantitative prediction	[38-40]
	-4.93	CALPHAD	This work
Mn_2Tm	-4.25	Semi-quantitative prediction	[38-40]
	-4.17	CALPHAD	This work
$Mn_{12}Lu$	-4.09	Semi-quantitative prediction	[38-40]
	-3.92	CALPHAD	This work
$Mn_{23}Lu_6$	-4.87	Semi-quantitative prediction	[38-40]
	-5.52	CALPHAD	This work
Mn_2Lu	-6.35	Semi-quantitative prediction	[38-40]
	-8.00	CALPHAD	This work
$Mn_{12}Y$	-0.53	Semi-quantitative prediction	[38-40]
	-1.38	CALPHAD	[18]
$Mn_{23}Y_6$	-1.26	Semi-quantitative prediction	[38-40]
	-3.97	CALPHAD	[18]
	-5.3 ± 1.7	Solution calorimetry	[62]
Mn_2Y	-1.59	Semi-quantitative prediction	[38-40]
	-2.17	CALPHAD	[18]
	-2.4 ± 2.5	Solution calorimetry	[62]
	-2.8 ± 2.8	Direct synthesis calorimetry	[63]

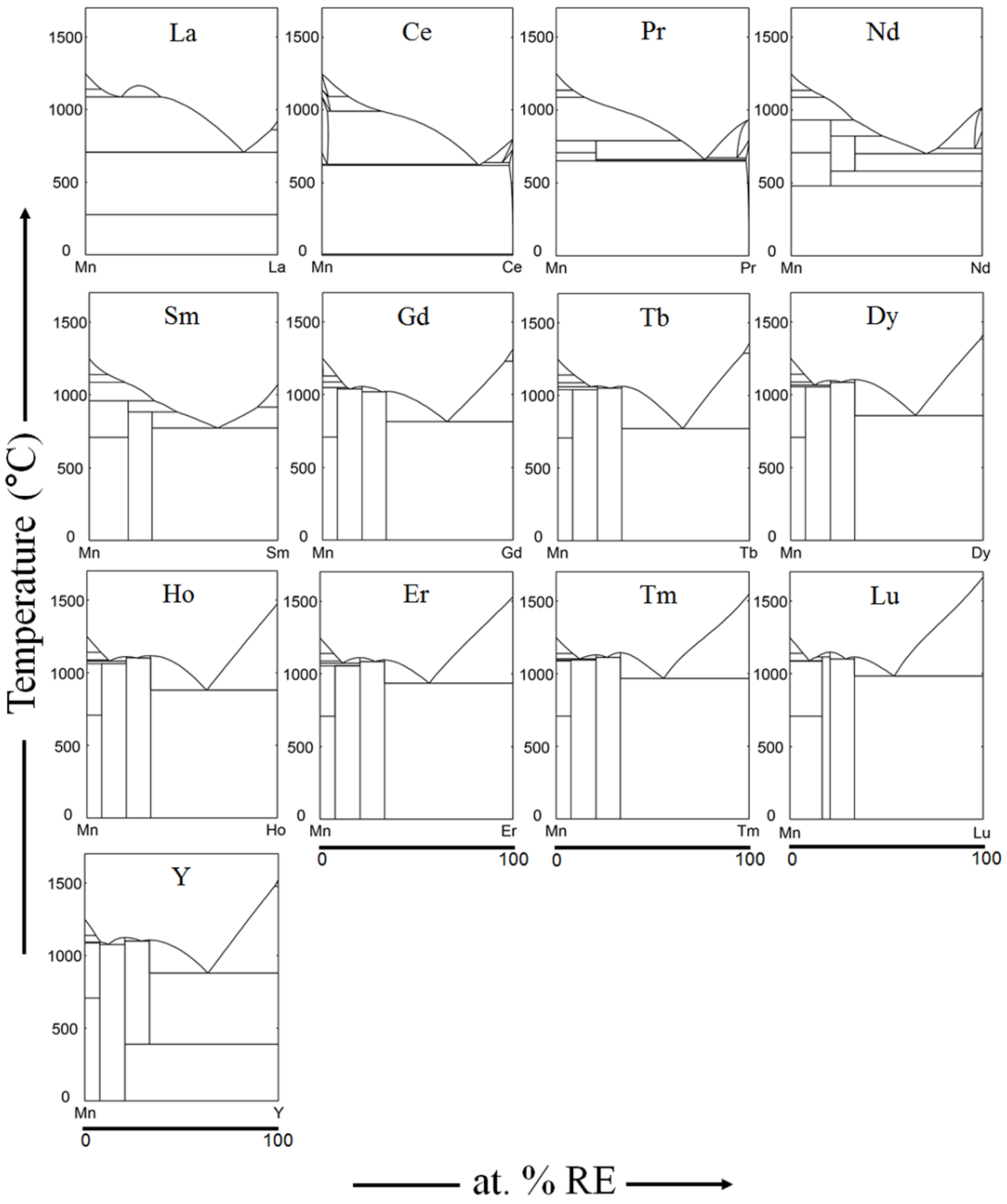


Fig. 26. The collection of the optimized phase diagram of all Mn-RE systems in the present study.

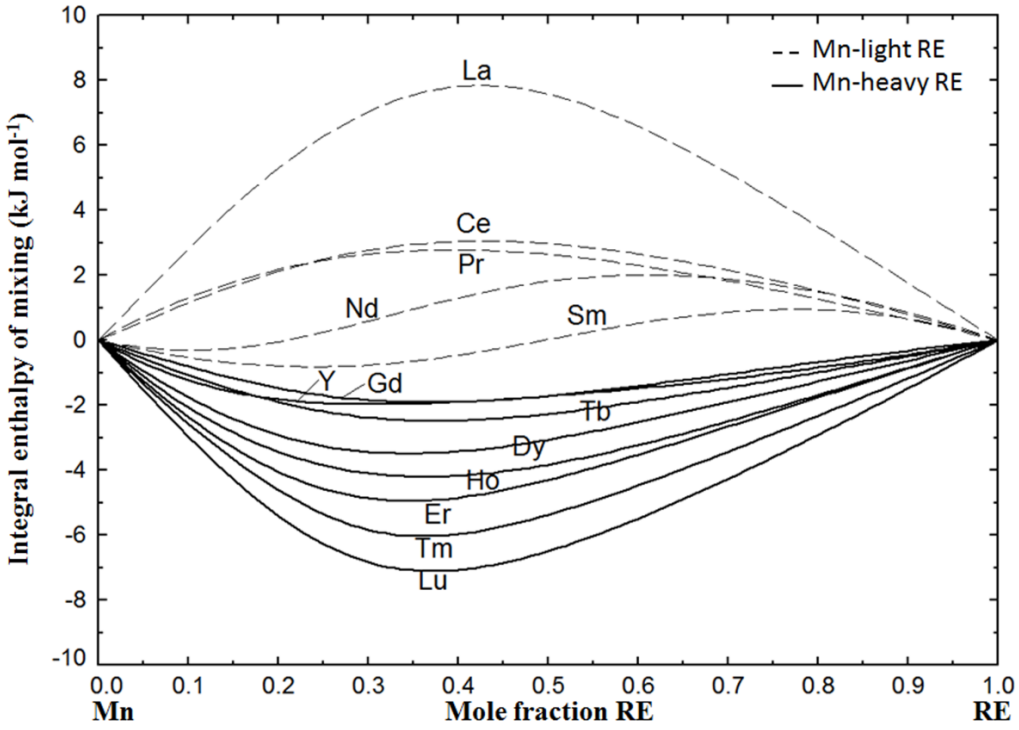


Fig. 27. The collection of the calculated enthalpies of mixing of the Mn-RE liquid at 1700 K.

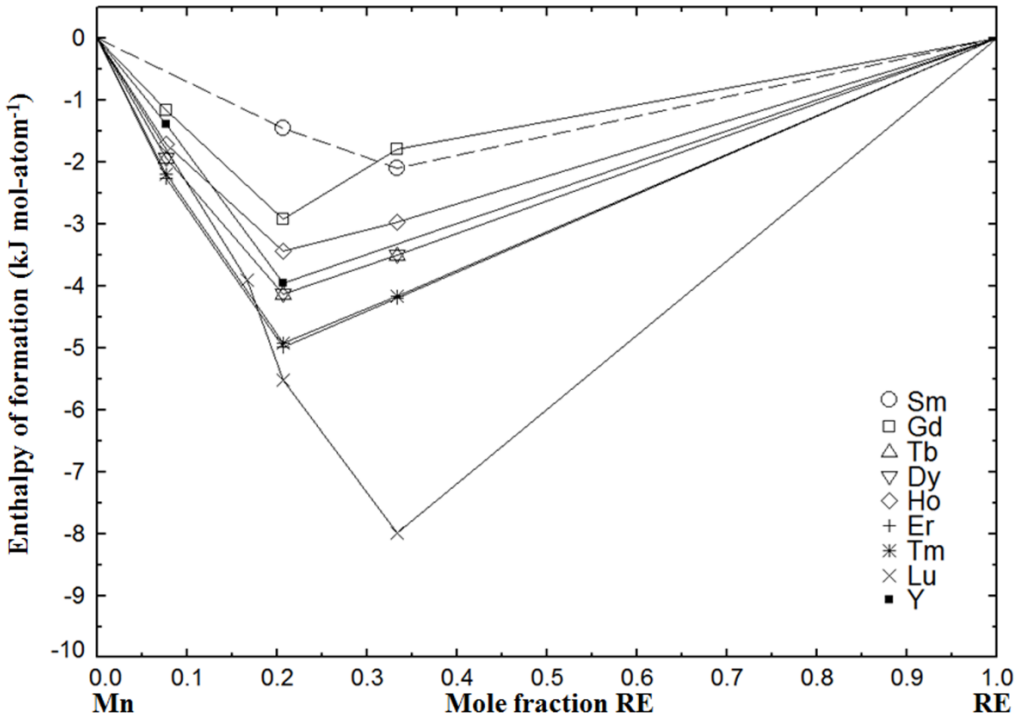


Fig. 28. The collection of the calculated standard enthalpies of formation of the Mn-RE system.

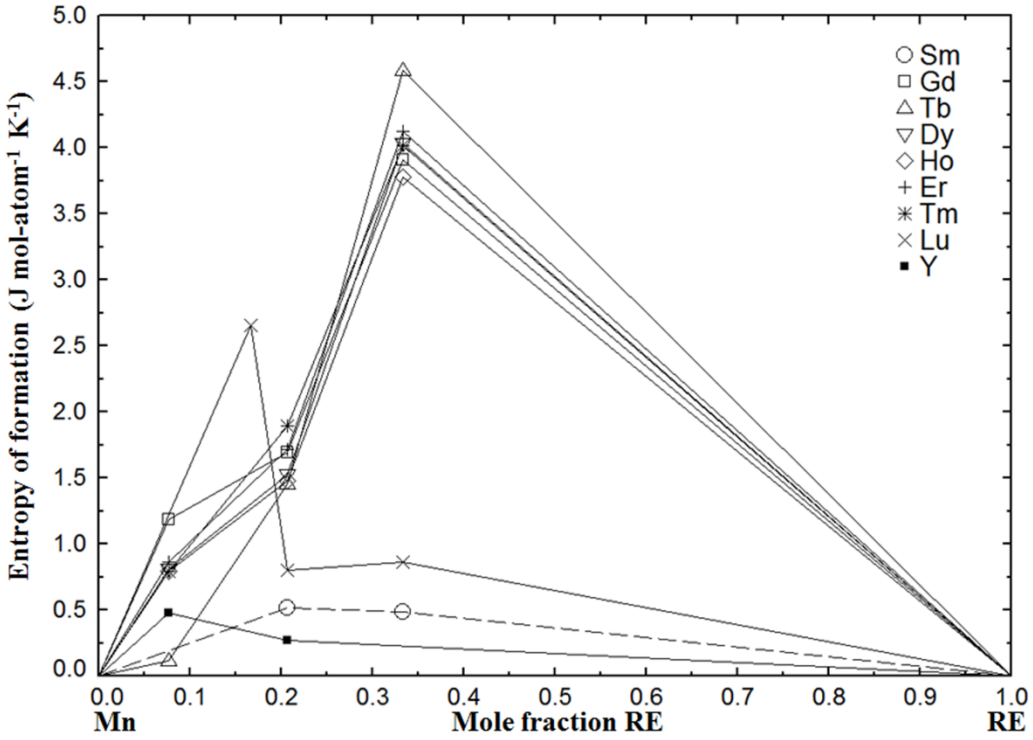


Fig. 29. The collection of the calculated entropy of formation of the Mn-RE system from elements.

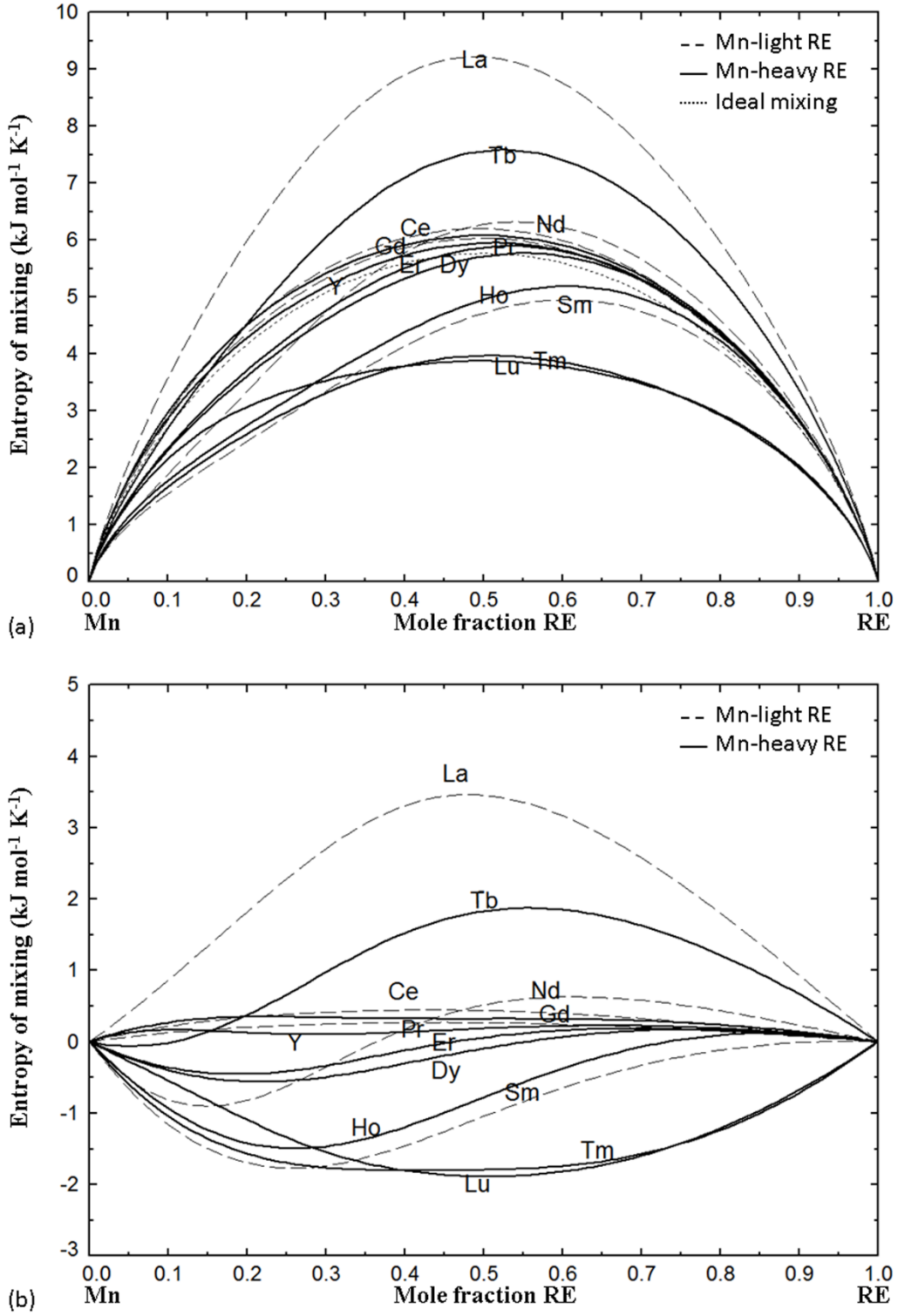


Fig. 30. The collection of the calculated (a) total entropies of mixing and (b) excess entropies of mixing of the Mn-RE liquid at 1700 K.

6. Summary

The thermodynamic optimization of the Mn-heavy RE (Tb, Dy, Ho, Er, Tm and Lu) systems was performed by the systematic analysis and available experimental data on the phase diagram and thermodynamic properties. This work is continuation from the previous study of the thermodynamic optimization of the Mn-light RE (La, Ce, Pr, Nd and Sm) and Mn-heavy RE (Gd and Y) systems. In the present study, difficulties arose from limited amount of experimental data and unreliable phase diagram data. The Mn-Dy system was re-evaluated by conducting phase diagram measurements using DSC and the enthalpy of formation measurements using solution calorimetry. Subsequent thermodynamic modeling with current experimental work helped in resolving inconsistencies with the previous experimental data. The systematic trend and similarity in the phase diagram and the thermodynamic properties across the lanthanide series was taken into account to overcome the shortage of experimental data. This study also proposes the undetermined phase diagram of the Mn-Tm and Mn-Lu systems.

Acknowledgement

This project was supported by the National Sciences and Engineering Research Council of Canada (NSERC) Collaborative Research and Development grant and General Motors of Canada. We would like to thank to Dr. I. Beta and Mr. D. Shepard from Netzsch for DSC experiments.

7. References

[1] B.L. Mordike, T. Ebert, Mater. Sci. Eng., A, A302 (2001) 37-45.
[2] M. Pekguleryuz, In: Proc. CAPLUS AN 2013:747810(Conference; General Review), 2013. pp. 152-196.
[3] R.L. Edgar, Global Overview on Demand and Applications for Magnesium Alloys, in: Magnesium Alloys and their Applications, Wiley-VCH Verlag GmbH & Co. KGaA, 2006, pp. 1-8.
[4] M.S. Dargusch, G.L. Dunlop, K. Pettersen, In: Proc. CAPLUS AN 2000:220343(Conference), 1998. pp. 277-282.
[5] A. Boby, U.T.S. Pillai, B.C. Pai, Indian Foundry J., 57 (2011) 29-37.
[6] E. Aghion, B. Bronfin, H. Friedrich, Z. Rubinovich, In: Proc. CAPLUS AN 2004:534901(Conference; General Review), 2004. pp. 167-172.
[7] H. Friedrich, S. Schumann, Materialwiss. Werkstofftech., 32 (2001) 6-12.
[8] B.C. Pai, U.T.S. Pillai, P. Manikandan, A. Srinivasan, Trans. Indian Inst. Met., 65 (2012) 601-606.
[9] B. Mordike, P. Lukáč, Physical Metallurgy, in: Magnesium Technology, Springer Berlin Heidelberg, 2006, pp. 63-107.
[10] C.W. Bale, E. Bélisle, P. Chartrand, S.A. Decterov, G. Eriksson, K. Hack, I.H. Jung, Y.B. Kang, J. Melançon, A.D. Pelton, C. Robelin, S. Petersen, Calphad, 33 (2009) 295-311.
[11] I. Ansara, C.A.o.M.S.C. 507, E. Commission, E.C.i.t.F.o. Scientific, T.R.C. 507, COST 507: Thermochemical Database for Light Metal Alloys, European Commission, Directorate-General XII, Science, Research and Development, 1994.
[12] Y.B. Kang, L.L. Jin, P. Chartrand, A.E. Gheribi, K.W. Bai, P. Wu, Calphad-Computer Coupling of Phase Diagrams and Thermochemistry, 38 (2012) 100-116.
[13] L. Jin, D. Kevorkov, M. Medraj, P. Chartrand, The Journal of Chemical Thermodynamics, 58 (2013) 166-195.
[14] L. Jin, PhD Thesis, Ecole Polytechnique, Montreal, 2012.
[15] L. Jin, Y.-B. Kang, P. Chartrand, C.D. Fuerst, Calphad, 34 (2010) 456-466.
[16] L. Jin, Y.-B. Kang, P. Chartrand, C.D. Fuerst, Calphad, 35 (2011) 30-41.
[17] Z. Zhu, A.D. Pelton, Journal of Alloys and Compounds, 641 (2015) 261-271.
[18] Z. Zhu, A.D. Pelton, Journal of Alloys and Compounds, 641 (2015) 249-260.
[19] L.L. Rokhlin, Magnesium Alloys Containing Rare Earth Metals: Structure and Properties, Taylor & Francis, 2003.
[20] B.J. Beaudry, K.A. Gschneidner Jr, Chapter 2 Preparation and basic properties of the rare earth metals, in: Karl A. Gschneidner, Jr., E. LeRoy (Eds.) Handbook on the Physics and Chemistry of Rare Earths, Elsevier, 1978, pp. 173-232.
[21] I.-H. Jung, M. Sanjari, J. Kim, S. Yue, Scripta Materialia, 102 (2015) 1-6.
[22] R. Ferro, S. Delfino, G. Borzone, A. Saccone, G. Cacciamani, J. Phase Equilib., 14 (1993) 273-279.
[23] R. Ferro, G. Cacciamani, A. Saccone, G. Borzone, Journal of Alloys and Compounds, 320 (2001) 326-340.
[24] R. Ferro, S. Delfino, R. Capelli, A. Borsese, J. Less-Common Met., 42 (1975) 13-18.
[25] R. Ferro, S. Delfino, J. Less-Common Met., 68 (1979) P23-P29.

[26] A. Saccone, G. Cacciamani, D. Maccio, G. Borzone, R. Ferro, Intermetallics, 6 (1997) 201-215.
[27] A. Saccone, D. Maccio, S. Delfino, R. Ferro, Intermetallics, 10 (2002) 903-913.
[28] C. Colinet, A. Pasturel, A. Percheron-Guegan, J.C. Achard, J. Less-Common Met., 102 (1984) 239-249.
[29] S.P. Yatsenko, A.A. Semyannikov, B.G. Semenov, K.A. Chuntonov, J. Less-Common Met., 64 (1979) 185-199.
[30] V.N. Eremenko, I.M. Obushenko, Poroshk. Metall. (Kiev), (1980) 53-61.
[31] S. Delfino, A. Saccone, R. Ferro, J. Less-Common Met., 102 (1984) 289-310.
[32] S.P. Yatsenko, A.A. Semyannikov, H.O. Shakarov, E.G. Fedorova, J. Less-Common Met., 90 (1983) 95-108.
[33] R. Ferro, A. Saccone, S. Delfino, D. Maccio, M. Giovannini, Powder Metall. Met. Ceram., 36 (1997) 117-127.
[34] G. Borzone, G. Cacciamani, R. Ferro, CALPHAD: Comput. Coupling Phase Diagrams Thermochem., 14 (1990) 139-149.
[35] K.A. Gschneidner, Jr., O.D. McMasters, Monatsh. Chem., 102 (1971) 1499-1515.
[36] G. Borzone, A. Borsese, S. Delfino, R. Ferro, Z. Metallkd., 76 (1985) 208-213.
[37] R. Ferro, G. Borzone, G. Cacciamani, Thermochim. Acta, 129 (1988) 99-113.
[38] V.N. Eremenko, M.V. Bulanova, P.S. Martsenyuk, In: Proc. CAPLUS AN 1991:587749(Conference), 1990. pp. 70-100.
[39] A. Yassin, R. Castanet, J. Alloys Compd., 307 (2000) 191-198.
[40] C. Colinet, A. Pasturel, A. Percheron-Guegan, J.C. Achard, J. Less-Common Met., 102 (1984) 167-177.
[41] A. Saccone, S. Delfino, R. Ferro, J. Less-Common Met., 143 (1988) 1-23.
[42] G. Borzone, G. Cacciamani, R. Ferro, J. Charles, J. Hertz, J. Less-Common Met., 128 (1987) 297-312.
[43] K.A. Gschneidner, Jr., N.A. Kippenhan, O.D. McMasters, Thermochemistry of the rare earths. I. Rare earth oxides. II. Rare earth oxysulfides. III. Rare earth compounds with boron, tin, lead, phosphorus, arsenic, antimony, bismuth, copper, and silver, in, Iowa State Univ. Sci. Technol., 1973, pp. 67 pp.
[44] K.A. Gschneidner, Jr., J. Less-Common Metals, 17 (1969) 1-12.
[45] M.V. Bulanova, A.N. Mikolenko, K.A. Meleshevich, G. Effenberg, P.A. Saltykov, Z. Metallkd., 90 (1999) 216-222.
[46] M.V. Bulanova, P.S. Martsenyuk, Poroshk. Metall. (Kiev), (1991) 82-85.
[47] L.L. Rokhlin, Met. Sci. Heat Treat., 48 (2006) 487-490.
[48] S.M. Zhu, M.A. Gibson, M.A. Easton, J.F. Nie, Scr. Mater., 63 (2010) 698-703.
[49] M. Sanjari, S.F. Farzadfar, T. Sakai, H. Utsunomiya, E. Essadiqi, I.H. Jung, S. Yue, Mat. Sci. Eng. A, 561 (2012) 191-202.
[50] N. Stanford, M.R. Barnett, Mat. Sci. Eng. A, 496 (2008) 399-408.
[51] K. Hantzsche, J. Bohlen, J. Wendt, K.U. Kainer, S.B. Yi, D. Letzig, Scripta Mater., 63 (2010) 725-730.
[52] T. Al-Samman, X. Li, Mat. Sci. Eng. A, 528 (2011) 3809-3822.
[53] D. Wu, R.S. Chen, E.H. Han, J. Alloy. Compd., 509 (2011) 2856-2863.
[54] J.P. Hadorn, K. Hantzsche, S. Yi, J. Bohlen, D. Letzig, S.R. Agnew, Metall. Mater. Trans. A, 43 (2012) 1363-1375.

[55] S. Sandlöbes, M. Friák, S. Zaefferer, A. Dick, S. Yi, D. Letzig, Z. Pei, L.F. Zhu, J. Neugebauer, D. Raabe, Acta Mater., 60 (2012) 3011-3021.
[56] S. Sandlöbes, S. Zaefferer, I. Schestakow, S. Yi, R. Gonzalez-Martinez, Acta Mater., 59 (2011) 429-439.
[57] S.R. Agnew, M.H. Yoo, C.N. Tomé, Acta Mater., 49 (2001) 4277-4289.
[58] S. Sandlöbes, Z. Pei, M. Friák, L.F. Zhu, F. Wang, S. Zaefferer, D. Raabe, J. Neugebauer, Acta Mater., 70 (2014) 92-104.
[59] W.Y. Wang, S.L. Shang, Y. Wang, Z.-G. Mei, K.A. Darling, L.J. Kecskes, S.N. Mathaudhu, X.D. Hui, Z.-K. Liu, Mater. Res. Lett., 2 (2014) 29-36.
[60] M.H. Yoo, J.R. Morris, K.M. Ho, S.R. Agnew, Metall. Mater. Trans. A, 33 (2002) 813-822.
[61] S.A. Farzadfar, E. Martin, M. Sanjari, E. Essadiqi, S. Yue, J. Mater. Sci., 47 (2012) 5488-5500.
[62] N. Stanford, G. Sha, J.H. Xia, S.P. Ringer, M.R. Barnett, Scripta Mater., 65 (2011) 919-921.
[63] N. Stanford, G. Sha, A. La Fontaine, M.R. Barnett, S.P. Ringer, Metall. Mater. Trans. A, 40 (2009) 2480-2487.
[64] J.D. Robson, Metall. Mater. Trans. A, 45 (2014) 3205-3212.
[65] J. Hadorn, K. Hantzsche, S. Yi, J. Bohlen, D. Letzig, J. Wollmershauser, S. Agnew, Metall. Mater. Trans. A, 43 (2012) 1347-1362.
[66] H. Kawamura, S. Yoshimoto, In: Proc. CAPLUS AN 2005:311159(Conference), 2005. pp. 499-502.
[67] S. Huang, J. Wang, F. Hou, Y. Li, F. Pan, Mater. Lett., 137 (2014) 143-146.
[68] J. Kim, Y. Kawamura, In: Proc. CAPLUS AN 2011:848096(Conference), 2011. pp. 229-232.
[69] M. Yamasaki, Y. Kawamura, Scr. Mater., 60 (2008) 264-267.
[70] Y. Kawamura, M. Yamasaki, Mater. Trans., 48 (2007) 2986-2992.
[71] F. Lu, A. Ma, J. Jiang, D. Yang, Q. Zhou, Rare Met. (Beijing, China), 31 (2012) 303-310.
[72] A. Inoue, Y. Kawamura, M. Matsushita, K. Hayashi, J. Koike, J. Mater. Res., 16 (2001) 1894-1900.
[73] H. Yokobayashi, K. Kishida, H. Inui, M. Yamasaki, Y. Kawamura, MRS Online Proc. Libr., 1295 (2011) No pp. given.
[74] K. Kishida, A. Inoue, H. Yokobayashi, H. Inui, Scr. Mater., 89 (2014) 25-28.
[75] K. Kishida, H. Yokobayashi, H. Inui, M. Yamasaki, Y. Kawamura, Intermetallics, 31 (2012) 55-64.
[76] J.-O. Andersson, T. Helander, L. Höglund, P. Shi, B. Sundman, Calphad, 26 (2002) 273-312.
[77] J.-H. Park, T.-H. Ahn, H.-S. Choi, J.-M. Chung, D.-I. Kim, K.H. Oh, H.N. Han, Microsc. Microanal., 19 (2013) 21-24.
[78] X. Huang, K. Suzuki, Y. Chino, Mat. Sci. Eng. A, 560 (2013) 232-240.
[79] NIST, 2002. www.nist.gov, Gaithersburg., in.
[80] J.-Y. Lee, Y.-S. Yun, B.-C. Suh, N.-J. Kim, W.-T. Kim, D.-H. Kim, J. Alloy. Compd., 589 (2014) 240-246.
[81] T. Wang, L. Jiang, R.K. Mishra, J.J. Jonas, Metall. Mater. Trans. A, 45 (2014) 4698-4709.
[82] R.H. Davies, A.T. Dinsdale, J.A. Gisby, J.A.J. Robinson, S.M. Martin, CALPHAD: Comput. Coupling Phase Diagrams Thermochem., 26 (2002) 229-271.
[83] K. Shobu, CALPHAD: Comput. Coupling Phase Diagrams Thermochem., 33 (2009) 279-287.
[84] S.L. Chen, S. Daniel, F. Zhang, Y.A. Chang, X.Y. Yan, F.Y. Xie, R. Schmid-Fetzer, W.A. Oates, CALPHAD: Comput. Coupling Phase Diagrams Thermochem., 26 (2002) 175-188.

[85] D.W. Kim, B.C. Suh, M.S. Shim, J.H. Bae, D.H. Kim, N. Kim, Metall. Mater. Trans. A, 44 (2013) 2950-2961.
[86] R. Schmid, Y.A. Chang, Calphad, 9 (1985) 363-382.
[87] A.D. Pelton, S.A. Degterov, G. Eriksson, C. Robelin, Y. Dessureault, Metall. Mater. Trans. B, 31B (2000) 651-659.
[88] A.D. Pelton, P. Chartrand, Metall. Mater. Trans. A, 32A (2001) 1355-1360.
[89] I.-H. Jung, D.-H. Kang, W.-J. Park, N.J. Kim, S. Ahn, Calphad, 31 (2007) 192-200.
[90] D. Nassyrov, I.-H. Jung, Calphad, 33 (2009) 521-529.
[91] A.D. Pelton, M. Blander, Metall. Trans. B, 17B (1986) 805-815.
[92] P. Wu, G. Eriksson, A.D. Pelton, M. Blander, ISIJ Int., 33 (1993) 26-35.
[93] A.D. Pelton, M. Blander, In: Proc. 1984. pp. 281-294.
[94] A.D. Pelton, Calphad, 25 (2001) 319-328.
[95] M. Hillert, B. Jansson, B. Sundman, Z. Metallkd., 79 (1988) 81-87.
[96] A.T. Dinsdale, Calphad, 15 (1991) 317-425.
[97] J. Leitner, P. Vonka, D. Sedmidubsky, P. Svoboda, Thermochim. Acta, 497 (2010) 7-13.
[98] G. Inden, Dusseldorf, Germany, , (1976) 111.
[99] M. Hillert, M. Jarl, Calphad, 2 (1978) 227-238.
[100] R.F. Zhang, B.X. Liu, Appl. Phys. Lett., 81 (2002) 1219-1221.
[101] R.F. Zhang, B.X. Liu, Philos. Mag. Lett., 85 (2005) 283-287.
[102] R.F. Zhang, S.H. Sheng, B.X. Liu, Chem. Phys. Lett., 442 (2007) 511-514.
[103] A.R. Miedema, P.F. De Chatel, F.R. De Boer, Physica B+C (Amsterdam), 100 (1980) 1-28.
[104] H. Zhang, S. Shang, J.E. Saal, A. Saengdeejing, Y. Wang, L.-Q. Chen, Z.-K. Liu, Intermetallics, 17 (2009) 878-885.
[105] H.R. Kirchmayr, W. Lugscheider, Z. Metallkd., 58 (1967) 185-188.
[106] H.R. Kirchmayr, W. Lugscheider, Z. Metallk., 61 (1970) 22-23.
[107] M. Zydzik, M. Smids, M.-A. Van Ende, I.-H. Jung, Calphad, 46 (2014) 1-17.
[108] M. Hillert, M. Selleby, B. Sundman, Acta Mater., 57 (2009) 5237-5244.
[109] F. Weitzer, K. Hiebl, P. Rogl, J. Solid State Chem., 98 (1992) 291-300.
[110] V.N. Eremenko, M.V. Bulanova, P.S. Martsenyuk, V.E. Listovnichii, Poroshk. Metall. (Kiev), (1989) 79-90.
[111] A. Saccone, D. Maccio, R. Ferro, J. Alloys Compd., 201 (1993) L9-L11.
[112] D.A. Petrov, M.S. Mirgalovskaya, I.A. Strel'nikova, E.M. Komova, Tr. Inst. Metall., Akad. Nauk SSSR, (1957) 142-143.
[113] X. Zhang, D. Kevorkov, I.H. Jung, M. Pekguleryuz, J Alloy Compd, 482 (2009) 420-428.
[114] A. Mostafa, M. Medraj, J Alloy Compd, 608 (2014) 247-257.
[115] C. Antion, PhD Thesis, Institut National Polytechnique de Grenoble, 2003.
[116] F. Wrubl, M. Pani, P. Manfrinetti, P. Rogl, J Solid State Chem, 182 (2009) 716-724.
[117] O.F. Zmii, E.I. Gladishevskii, Visnik L'viv. un-tu. Ser. khim., (1974) 24-26.
[118] S.K. Dhar, P. Manfrinetti, A. Palenzona, J. Alloys Compd., 252 (1997) 24-27.
[119] M.E. Drits, E.M. Padezhnova, T.V. Dobatkina, Redk. Metally V Tsvet. Splavakh, (1975) 5-11.
[120] P. Manfrinetti, A. Provino, K.A. Gschneidner, J Alloy Compd, 482 (2009) 81-85.
[121] Y. Guo, PhD Thesis, Northeastern University, Shenyang, 2009.
[122] C. Ma, D. Zhang, Y. Fan, F. Qi, J. Li, J. Phase Equilib. Diffus., 34 (2013) 9-16.
[123] H.D. Zhao, G.W. Qin, Y.P. Ren, W.L. Pei, Y. Guo, J. Alloys Compd., 481 (2009) 140-143.

[124] H.-d. Zhao, Y.-p. Ren, W.-l. Pei, Y. Guo, D. Chen, G.-w. Qin, Zhongguo Youse Jinshu Xuebao, 20 (2010) 177-181.
[125] X.Y. Fang, D.Q. Yi, J.F. Nie, X.J. Zhang, B. Wang, L.R. Xiao, J. Alloys Compd., 470 (2009) 311-316.
[126] X.Y. Fang, D.Q. Yi, J.F. Nie, J. Alloys Compd., 486 (2009) 900-904.
[127] I.-H. Jung, D.H. Kang, W.-J. Park, N.J. Kim, S.H. Ahn, Int. J. Mater. Res., 98 (2007) 807-815.
[128] J.J. Kim, D.H. Kim, K.S. Shin, N.J. Kim, Scripta Mater., 41 (1999) 333-340.
[129] L.W.F. Mackenzie, M.O. Pekguleryuz, Scripta Mater., 59 (2008) 665-668.
[130] P. Dobroň, J. Balík, F. Chmelík, K. Illková, J. Bohlen, D. Letzig, P. Lukáč, J. Alloy. Compd., 588 (2014) 628-632.
[131] Y. Chino, X. Huang, K. Suzuki, K. Sassa, M. Mabuchi, Mat. Sci. Eng. A, 528 (2010) 566-572.
[132] Z.X. Cai, H.T. Jiang, D. Tang, Z. Ma, Q. Kang, Rare Metals, 32 (2013) 441-447.
[133] J. Bohlen, M.R. Nürnberg, J.W. Senn, D. Letzig, S.R. Agnew, Acta Mater., 55 (2007) 2101-2112.
[134] L. Ma, R.K. Mishra, M.P. Balogh, L. Peng, A.A. Luo, A.K. Sachdev, W. Ding, Mat. Sci. Eng. A, 543 (2012) 12-21.
[135] Y. Chino, K. Sassa, M. Mabuchi, Mat. Sci. Eng. A, 513–514 (2009) 394-400.
[136] M. Masoumi, M. Hoseini, M. Pekguleryuz, Mater. Sci. Eng., A, A528 (2011) 3122-3129.
[137] Q. Yang, B. Jiang, W. Jiang, S. Luo, F. Pan, Mater. Sci. Eng., A, 628 (2015) 143-148.

Appendix IV

Appendix IV

Critical evaluation and thermodynamic optimization of the Si-RE systems: Part I. Si-RE system (RE = La, Ce, Pr, Nd and Sm)

Junghwan Kim and In-Ho Jung

Department of Mining and Materials Engineering, McGill University, 3610 University St., Montreal, Quebec, H3A 2B2, Canada

Corresponding author: In-Ho Jung

Tel : 1-514-398-2608

Fax : 1-514-398-4492

E-mail: in-ho.jung@mcgill.ca

Published in

The Journal of Chemical Thermodynamics 81 (2015) 253-272

Abstract

A critical evaluation and optimization of all available phase diagrams and thermodynamic data of the binary Si-RE (RE = La, Ce, Pr, Nd and Sm) systems was conducted to obtain reliable thermodynamic functions of all the phases in the systems. In the thermodynamic modeling, a systematic analysis involving the similarity and periodicity observed in the lanthanide series was applied to resolve inconsistencies in the experimental data and to estimate the unknown thermodynamic properties and phase equilibria data. The phase diagram of the Si-Sm system was predicted using this approach.

Keywords

Mg-RE alloy, Si-RE system, Thermodynamic Modeling, Phase Diagrams, Thermodynamic Properties.

1. Introduction

Rare Earth (RE) metals are extensively used in many industrial applications including permanent magnets, electronic materials and structural materials [1, 2]. Even a small addition of RE elements can enhance magnetic, electronic, optical and mechanical properties of numerous materials. For example, several recent studies [3-7] show that the additions of small amounts of RE can noticeably enhance the ductility of Mg alloys. Despite the fact that Mg alloys are the subject of great industrial attention as the lightest structural materials, their inferior formability at ambient temperature due to the limited slip system make their usage restricted. Therefore, much research on Mg-RE alloys is undertaken to elucidate the role of RE on the enhanced deformation mechanism and to find out the most optimum alloy compositions. As a necessity of Mg-RE alloy development, a large thermodynamic database of Mg-RE alloys containing Al, Zn, Mn, Sn, etc. has been built by the CALPHAD type thermodynamic optimization based on a critical and systematic analysis of available thermodynamic and phase diagram data [8-20]. It is also known that the addition of Si into Mg alloys induces grain refinement [21], formation of stable intermetallic compound [22] and increased fluidity of the molten metal [23].

In the thermodynamic "optimization (modeling)" of a chemical system, all available thermodynamic and phase equilibrium data are evaluated simultaneously to obtain a set of model equations for the Gibbs energies of all phases as functions of temperature and composition. From these equations, all the thermodynamic properties and phase diagrams can be back-calculated. In this way, all the data are rendered self-consistent and consistent with thermodynamic principles. Discrepancies in available experimental data can be resolved during the thermodynamic optimization because different kind of experimental data such as thermodynamic properties data and phase diagram are interconnected in term of Gibbs energy.

The main objective of the present study is to perform a critical review and systematic optimization of thermodynamic data and phase diagrams of the binary Si-RE alloy systems. The study is divided into two parts according to the RE subgroups: Part I for the Si-light RE systems (light RE = La, Ce, Pr, Nd and Sm) and Part II for the Si-heavy RE systems (heavy RE = Gd, Tb, Dy, Ho, Er, Tm,

Lu and Y). Until now, no thermodynamic optimization of the entire series of binary Si-RE systems has been carried out; thermodynamic optimizations were only performed on only a few Si-RE systems such as Si-Ce [16, 24], Si-Gd [25] and Si-Y [16, 26]. In the present study, a systematic analysis involving the similarity and periodicity observed in the lanthanide series was applied to resolve inconsistencies in the experimental data and to estimate the unknown thermodynamic properties and phase equilibria data of the Si-RE systems. Among the RE elements, Pm, Eu and Yb were not included in the present study due to the radioactivity of Pm and the abnormal properties of Eu and Yb. The properties of Eu and Yb are clearly distinct from other RE elements due to their divalent behavior (other RE are trivalent [27]). The present study is part of the thermodynamic database development for the Mg-RE alloys containing Al, Zn, Mn, Si, Sn, etc. It will be also helpful to understand accurate thermodynamic properties of RE silicides, promising materials in semiconductor and optical engineering, microelectronics, and chemical and metallurgical engineering [28].

2. Thermodynamic models

2.1. Liquid phase

The Modified Quasichemical Model [29, 30], which accounts for short-range-ordering of nearest-neighbor atoms, was used to model the liquid solutions because it gives a more realistic thermodynamic description of the liquid phase compared to the conventional simple random-mixing Bragg Williams model [29, 30]. The Modified Quasichemical Model was successfully applied to many liquid metallic solutions [30-32] and ionic solutions [33, 34] exhibiting strong short-range-ordering behavior.

Recently, the energy of nearest-neighbor pair formation in the Modified Quasichemical Model was expanded as a polynomial in the pair fractions [29, 30] instead of the component fractions [33, 35]. In addition, coordination numbers are now allowed to vary with composition. These modifications provide greater flexibility in reproducing the binary experimental data and in combining optimized

binary liquid parameters into a large database for multicomponent solutions [29]. A short description of the model is given below; details can be found in previous studies [29, 30].

In the case of a binary A-B liquid solution, the atoms A and B are distributed over the sites of a quasi-lattice in liquid solution. The following pair exchange reaction can be considered:

$$(\mathrm{A}-\mathrm{A})+(\mathrm{B}-\mathrm{B})=2(\mathrm{A}-\mathrm{B}) \tag{1}$$

where (A-B) represents a first-nearest-neighbor pair of A and B. The non-configurational Gibbs energy change for the formation of two moles of (A-B) pairs according to reaction (1) is Δg_{AB}. Then the Gibbs energy of the solution is given by:

$$G=(n_{\mathrm{A}}G_{\mathrm{A}}^{\mathrm{o}}+n_{\mathrm{B}}G_{\mathrm{B}}^{\mathrm{o}})-T\Delta S^{\mathrm{config}}+n_{\mathrm{AB}}(\Delta g_{\mathrm{AB}}/2) \tag{2}$$

where $G_{\mathrm{A}}^{\mathrm{o}}$ and $G_{\mathrm{B}}^{\mathrm{o}}$ are the molar Gibbs energies of the pure components A and B, n_{A} and n_{B} are the numbers of moles of A and B atoms, and n_{AB} is the number of moles of (A-B) pairs. $\Delta S^{\mathrm{config}}$ is the configurational entropy of mixing given by a random distribution of the (A-A), (B-B) and (A-B) pairs in the one-dimensional Ising approximation:

$$\begin{aligned}\Delta S^{\mathrm{config}} &= -R(n_{\mathrm{A}}\ln X_{\mathrm{A}}+n_{\mathrm{B}}\ln X_{\mathrm{B}})\\ &\quad -R[n_{\mathrm{AA}}\ln(X_{\mathrm{AA}}/Y_{\mathrm{A}}^2)+n_{\mathrm{BB}}\ln(X_{\mathrm{BB}}/Y_{\mathrm{B}}^2)\\ &\quad +n_{\mathrm{AB}}\ln(X_{\mathrm{AB}}/2Y_{\mathrm{A}}Y_{\mathrm{B}})]\end{aligned} \tag{3}$$

where n_{AA}, n_{BB} and n_{AB} are the numbers of moles of each kind of pairs, and the pair fraction (X_{AA}, X_{BB} and X_{AB}) and coordination equivalent fraction (Y_{A} and Y_{B}) can be calculated as:

$$X_{\mathrm{AA}}=n_{\mathrm{AA}}/(n_{\mathrm{AA}}+n_{\mathrm{BB}}+n_{\mathrm{AB}}) \tag{4}$$

$$X_{BB} = n_{BB}/(n_{AA} + n_{BB} + n_{AB}) \quad (5)$$

$$X_{AB} = n_{AB}/(n_{AA} + n_{BB} + n_{AB}) \quad (6)$$

$$Y_A = X_{AA} + X_{AB}/2 \quad (7)$$

$$Y_B = X_{BB} + X_{AB}/2 \quad (8)$$

The Δg_{AB} is the model parameter to reproduce the Gibbs energy of liquid phase of the binary A-B system, which is expanded as a polynomial in terms of the pair fractions, as follows:

$$\Delta g_{AB} = \Delta g^{o}_{AB} + \sum_{i\geq 1} g^{i0}_{AB}(X_{AA})^i + \sum_{j\geq 1} g^{0j}_{AB}(X_{BB})^j \quad (9)$$

where Δg^{o}_{AB}, g^{i0}_{AB} and g^{0j}_{AB} are the adjustable model parameters which can be functions of temperature.

In the Modified Quasichemical Model, the coordination numbers of A and B, Z_A and Z_B, can be varied with composition to reproduce the short-range-ordering as follows:

$$\frac{1}{Z_A} = \frac{1}{Z^A_{AA}}\left(\frac{2n_{AA}}{2n_{AA}+n_{AB}}\right) + \frac{1}{Z^A_{AB}}\left(\frac{n_{AB}}{2n_{AA}+n_{AB}}\right) \quad (10)$$

$$\frac{1}{Z_B} = \frac{1}{Z^B_{BB}}\left(\frac{2n_{BB}}{2n_{BB}+n_{AB}}\right) + \frac{1}{Z^B_{BA}}\left(\frac{n_{AB}}{2n_{BB}+n_{AB}}\right) \quad (11)$$

where Z^A_{AA} is the value of Z_A when all nearest neighbors of an A atom are A atoms, and Z^A_{AB} is the value of Z_A when all nearest neighbors are B atoms. Z^B_{BB} and Z^B_{BA} are defined in an analogous manner. In the present study, Z^i_{ii} for all elements (i = Si and RE) are set to be 6. As the minimum

enthalpies of liquid Si-RE solutions were found at almost 0.5 mole fraction of RE, Z^{Si}_{SiRE} and Z^{RE}_{SiRE} are set to be all 6 to reproduce such minimum enthalpies.

2.2. Solid solutions

The solid solution phases like bcc and fcc solutions were described by the Compound Energy Formalism [36] with a one-sublattice approach (Si, RE) for substitutional site. The molar Gibbs energy of the solid solution can be expressed as:

$$G = (y_{Si} G^{o}_{Si} + y_{RE} G^{o}_{RE}) + RT(y_{Si} \ln y_{Si} + y_{RE} \ln y_{RE}) + {}^{a}L_{Si,RE}\, y_{Si}\, y_{RE}\, (y_{RE} - y_{Si})^{a} \quad (12)$$

where y_{Si} and y_{RE} are the site fractions of Si and RE elements in the sublattice, and R and T are the gas constant and temperature in Kelvin. G^{o}_{Si} and G^{o}_{RE} are the molar Gibbs energies of solid phases of Si and RE in the respective standard state of solid solution. The binary interaction parameters between Si and RE in the sublattice, ${}^{a}L_{Si,RE}$ where $a \geq 0$, are adjustable model parameters.

2.3. Stoichiometric compounds and elements

The Gibbs energies of all pure elements were taken from the SGTE database version 5.0 [37]. The Gibbs energies of the stoichiometric intermetallics were optimized based on available experimental data using the standard Gibbs energy expression based on heat capacity, enthalpy and entropy of formation at 298 K. When the heat capacities of stoichiometric compounds were not available, they were typically estimated using the Neumann-Kopp (NK) rule [38]. Certain intermetallic compounds in the Si-heavy RE systems (presented in Part II) such as Gd_5Si_4, Tb_5Si_4, etc. exhibit magnetic transitions associated with Néel or Curie temperatures. The magnetic transition below 298 K (typically antiferromagnetic transition with Néel temperature) was taken

directly into account in the calculation of S_{298}. The Curie temperature (ferromagnetic transition) occurs typically above 298 K, of which magnetic contribution to the Gibbs energy was considered by an empirical relationship suggested by Inden [39] and modified by Hillert and Jarl [40].

3. Critical evaluation and thermodynamic optimization

3.1. The Si-La system

Available experimental data of the Si-La phase diagram are presented in Fig. 1. The phase diagram was experimentally investigated in the whole composition range by Bulanova et al. [41] using differential thermal analysis (DTA), X-ray diffraction (XRD) and metallographic techniques. The authors prepared 24 alloys from La (99.84 %) and Si (99.999 %) by arc-melting with a water-cooled copper hearth and inconsumable tungsten electrode under purified argon atmosphere. According to them, the existence of six lanthanum silicides and of three eutectic reactions were verified. The stoichiometric compounds La_5Si_3, La_3Si_2, and La_5Si_4 formed by peritectic reactions at 1260, 1470 and 1570 ºC, respectively. Another stoichiometric compound, LaSi, melted congruently at 1625 ºC. In the literature, there are discrepancies in the homogeneity range and the phase transition reported between two crystal structures, α-$ThSi_2$ and α-$GdSi_2$, for the non-stoichiometric solid $LaSi_{2-a}$ (a = 0 to 0.35 [42], a = 0.33 [43], a = 0.31 (Si-rich boundary) [44]). Two studies [42, 45] propose that the α-$ThSi_2$ structure transforms continuously to the α-$GdSi_2$ structure with increasing silicon content of $LaSi_{2-a}$. Another study [46] rather proposed that $LaSi_{2-a}$ has two polymorphs: α-$GdSi_2$, at high temperature, and α-$ThSi_2$, at low temperature. Bulanova et al. [41] suggested the existence of two non-stoichiometric $LaSi_{2-a}$ phases based on lattice parameter measurements: $LaSi_{2-a1}$, which has an α-$GdSi_2$ structure with a1 = 0.3 to 0.33, and $LaSi_{2-a2}$, which has an α-$ThSi_2$ structure with a2 = 0 to 0.225. Bulanova et al. [41] also reported that $LaSi_{2-a1}$ melted congruently at 1730 ºC while $LaSi_{2-a2}$ formed by peritectic reaction at about 1600 ºC. Moreover, Bulanova et al. [41] reported the solubilities of Si in bcc-A2 La and fcc-A1 La to be about 0.02 and 0.01 mole fraction, respectively, which produces the catatectic transformation La (bcc-A2) → La (fcc-A1) + L at 815 ºC. No solubility of La in solid Si was detected. Previously, the melting

temperature of $LaSi_2$ was reported to be 1500 ºC [47], 1520 ºC [48] and 1580 ºC [49] however the experimental methods were not specified. In addition, the melting temperatures of $LaSi_2$, LaSi, La_5Si_4, La_3Si_2 and La_5Si_3 were determined by Bolgar et al. [50] from their heat content measurements using high temperature calorimetry.

The enthalpy of mixing of liquid Si-La was measured by Esin et al. [51] and Batalin et al. [52]. Esin et al. [51] determined the integral and partial enthalpies of mixing of liquid Si-La solution using high temperature vacuum calorimetry with an isothermal jacket. Measurements were performed up to 0.36 mole fraction of La using high purity starting materials (~ 99.95 % Si and 99.8 % La) at 1920 K in corundum crucibles under helium atmosphere. Then, based on a least-squares analysis, the authors calculated smoothed values for both, the partial and integral enthalpies of mixing, up to 0.35 mole fraction of La without experimental data. Using a similar experimental procedure, Batalin et al. [52] also calculated smoothed integral and partial enthalpies of La in liquid solution up to 0.14 mole fraction of La at 1821 K. The experimental enthalpy data from these two studies are shown in Figs. 2(a) and 2(b), respectively. The integral enthalpies of mixing of both studies are comparable. However in the study of Batalin et al. [52], the sudden drop of the integral enthalpy of mixing at 0.14 mole fraction of La and the large variation of the partial enthalpy of mixing of La in a small composition range seem to be little plausible.

Thermodynamic properties of intermetallic compounds were reported by several researchers. Bolgar et al. [53, 54] measured the low temperature heat capacities (C_p) of La_5Si_3, La_3Si_2, La_5Si_4, LaSi and $LaSi_2$ using adiabatic calorimetry. The corresponding standard entropy of formation (S^{o}_{298}) were reported to be 323.1 ± 2.6 J K^{-1} mol^{-1} for La_5Si_3, 199.9 ± 1.6 J K^{-1} mol^{-1} for La_3Si_2, 339.8 ± 2.7 J K^{-1} mol^{-1} for La_5Si_4, 66.6 ± 0.5 J K^{-1} mol^{-1} for LaSi, and 88.8 ± 0.7 J K^{-1} mol^{-1} for $LaSi_2$. In addition, Bolgar et al. [50] measured the heat contents ($H_T - H_{298}$) of the compounds using high temperature calorimetry. Based on the heat content data, the high temperature C_p of the corresponding compounds were calculated as a function of temperature. All experimental C_p and heat contents data are presented in Figs. 3 and 4, respectively. The ΔS^{o}_{298} of compounds at 298 K from the experimental data of Bolgar et al. [53, 54] are also presented in Fig. 5. The standard

enthalpies of formation (ΔH^{o}_{298}) of several compounds were determined by Meschel and Kleppa [55, 56]. They measured ΔH^{o}_{298} of $LaSi_2$, LaSi, La_5Si_4 and La_5Si_3 using direct synthesis calorimetry. They also determined the $H_{1273}-H_{298}$ of LaSi, La_5Si_4 and La_5Si_3 and the $H_{1473}-H_{298}$ of $LaSi_2$. However, their values were slightly larger than the heat contents of Bolgar et al. [50], as seen in Fig. 4. Gordienko and Fenochka [57] estimated ΔH^{o}_{298} of $LaSi_2$ and LaSi using Knudsen mass-spectrometry measurements performed at 1800-2000 K. All the ΔH^{o}_{298} data are presented in Fig. 6. Polotskaya [44] determined the Gibbs energy of formation (ΔG^{o}_{1000}) of La_3Si_5 by emf measurements (960-1050 K). Experimental data are shown in Fig. 7.

A brief review of the system was performed by Okamoto [58] based on the study of Bulanova et al. [41]. Unfortunately, no thermodynamic assessment of the system is reported yet. In this study, the phase diagram and thermodynamic properties of all phases of the Si-La system were thermodynamically optimized based on available experimental data. The optimized phase diagram of the Si-La system is presented in Fig. 1 along with experimental data. In the present optimization, the non-stoichiometric compound $LaSi_{2-a}$ was considered as two compounds, $LaSi_2$ and La_3Si_5, in agreement with Bulanova et al. [41]. However, their homogeneity ranges were not reproduced in this study. The liquidus and the melting points of the compounds were taken from the DTA results of Bulanova et al. [41] except for La_5Si_4 and La_3Si_2. The melting points of La_5Si_4 and La_3Si_2 proposed by Bulanova et al. [41] were considerably higher than those determined by Bolgar et al [50] using calorimetry. As the melting temperature obtained by calorimetry was close to the solidus temperature obtained with the Pirani-Altertum method used by Bulanova et al. [41], the peritectic melting point of La_3Si_2 was thus taken from the calorimetric measurements [50]. Moreover, the phase transformation determined by DTA corresponding to the peritectic melting of La_3Si_2 in the study of Bulanova et al. [41] is likely to be the peritectic reaction of La_5Si_4 according to the calorimetric data [50]. The solubility of Si in La (bcc-A2 and fcc-A1) were modeled with the assumption of large solid state miscibility gaps based on the study of Bulanova et al. [41]. Most liquidus and invariant reactions of the calculated phase diagram are in good agreement with the experimental data except for the liquidus near 0.23 mole fraction La and the eutectic temperature

between La_3Si_5 and LaSi which were not reproduced with other optimized thermodynamic properties. The calculated thermodynamic properties and optimized thermodynamic parameters are shown in Figs. 2 to 7. The enthalpy of mixing of the liquid Si-La solution, determined by Esin et al. [51] and Batalin et al. [52], were neglected because their data were largely in conflict with other thermodynamic properties such as the melting enthalpy of Bolgar et al. [50]. For example, the enthalpy of the liquid (enthalpy of mixing) at 0.333 mole fraction of La and 2226 K can be calculated from known $H_T - H_{298}$ of $LaSi_2$ at 2226 K [50] and ΔH^{o}_{298} of $LaSi_2$ [55]. Similarly, the enthalpy of liquid at 0.5 mole fraction of La and 2065 K can be calculated from the $H_T - H_{298}$ of LaSi at 2065 K [50] and ΔH^{o}_{298} of LaSi [56]. The calculated liquid enthalpies are much more negative (by about 10 kJ mol^{-1} or larger) than the solution calorimetry experimental data of Esin et al. [51] and Batalin et al. [52] as shown in Fig. 2(a). A more negative enthalpy of liquid solution is consistent with the liquidus of the phase diagram determined by Bulanova et al. [41] and also more consistent with the systematic trend of all Si-RE systems (systematic trend is discussed in Part II). The C_p data above 298 K of Bolgar et al. [50] were used for $LaSi_2$ and La_5Si_4 but the C_p of LaSi, La_3Si_2 and La_5Si_3 were slightly changed to make them consistent with the low temperature C_p data [10, 11], as shown in Fig. 3. The C_p of La_3Si_5 was approximated by the NK rule. Calorimetric data were mainly used to determine the ΔH^{o}_{298} and S^{o}_{298} of compounds. The calculated ΔS^{o}_{298} and ΔH^{o}_{298} are in good agreement with experimental data as depicted in Figs. 5 and 6. The ΔG^{o}_{1000} of La_3Si_5 measured by Polotskaya [44] apparently disagrees with other experimental data such as the ΔH^{o}_{298} and S^{o}_{298} of adjacent compounds. Therefore, the calculated ΔG^{o}_{1000} of La_3Si_5 is about 8 kJ mol^{-1} (based on one mole of Si-La) higher than the emf data [44] as seen in Fig. 7. The optimized thermodynamic parameters are listed in Table 1 and the calculated invariant reactions with the experimental data are tabulated in Table 2.

Table 1. Optimized model parameters for the Si-La system.

Phase	Thermodynamic parameters
Liquid	Coordination Numbers
	i j Z_{ij}^{i} Z_{ij}^{j}
	Si La 6 6
	Δg_{SiLa} / (J mol^{-1}) = (-57739.2 + 6.9036 T/K) + (-24267.2 + 10.8784 T/K) X_{SiSi}
	- 10041.6 X_{SiSi}^{2} + (-7531.2 + 0.8368 T/K) X_{LaLa} + 2510.4 X_{LaLa}^{2}
bcc-A2	${}^{0}L_{\mathrm{Si,\,La}}$ / (J mol^{-1}) = -152716.0 + 12.552 T/K
	${}^{1}L_{\mathrm{Si,\,La}}$ / (J mol^{-1}) = -29288.0 + 12.552 T/K
fcc-A1	${}^{0}L_{\mathrm{Si,\,La}}$ / (J mol^{-1}) = -146440.0
$LaSi_2$	ΔH_{298}^{o} = -180500 J mol^{-1}, S_{298}^{o} = 88.95 J K^{-1} mol^{-1}
	C_p / (J K^{-1} mol^{-1}) = 69.05 + 0.0138 T/K - 397616 (T/K)$^{-2}$
La_3Si_5	ΔH_{298}^{o} = -508000 J mol^{-1}, S_{298}^{o} = 255.1 J K^{-1} mol^{-1}
	C_p / (J K^{-1} mol^{-1}) = 3 × C_p / (J K^{-1} mol^{-1}) (La, dhcp)
	+ 5 × C_p / (J K^{-1} mol^{-1}) (Si, diamond-A4)
LaSi	ΔH_{298}^{o} = -146500 J mol^{-1}, S_{298}^{o} = 66.65 J K^{-1} mol^{-1}
	C_p / (J K^{-1} mol^{-1}) = 46.38 + 0.008598 T/K - 114238 (T/K)$^{-2}$
La_5Si_4	ΔH_{298}^{o} = -607000 J mol^{-1}, S_{298}^{o} = 329.0 J K^{-1} mol^{-1}
	C_p / (J K^{-1} mol^{-1}) = 235.82 + 0.013146 T/K - 1148380 (T/K)$^{-2}$
La_3Si_2	ΔH_{298}^{o} = -311500 J mol^{-1}, S_{298}^{o} = 198.0 J K^{-1} mol^{-1}
	C_p / (J K^{-1} mol^{-1}) = 121.48 + 0.0192 T/K - 438532 (T/K)$^{-2}$ - 1.035e-6 (T/K)^{2}
La_5Si_3	ΔH_{298}^{o} = -474500 J mol^{-1}, S_{298}^{o} = 321.6 J K^{-1} mol^{-1}
	C_p / (J K^{-1} mol^{-1}) = 218.14 + 0.006725 T/K - 1203391 (T/K)$^{-2}$ - 2.01e-7 (T/K)^{2}

Table 2. Calculated invariant reactions and experimental data in the Si-La system.

Type	Reaction	t (°C)	Reference
Eutectic	$L_{(X_{La}=0.148)} \rightarrow Si_{(dia.\text{-}A4,\ X_{La}=0)} + LaSi_2$	1213.2	This work
	$L_{(X_{La}=0.18)} \rightarrow Si_{(dia.\text{-}A4,\ X_{La}=0)} + LaSi_2$	1205 ± 7	[41]
Peritectic	$L_{(X_{La}=0.264)} + La_3Si_5 \rightarrow LaSi_2$	1575.4	This work
	$L_{(X_{La}=0.275)} + La_3Si_5 \rightarrow LaSi_2$	~1600.0	[41]
	T_m of $LaSi_2$	1500.0	[47]
		1520.0	[48]
		1580.0	[49]
		1635 ± 34	[50]
Congruent	$L_{(X_{La}=0.375)} \leftrightarrow La_3Si_5$	1727.5	This work
	$L_{(X_{La}=0.375)} \leftrightarrow La_3Si_5$	1730.0	[41]
Eutectic	$L_{(X_{La}=0.465)} \rightarrow La_3Si_5 + LaSi$	1600.9	This work
	$L_{(X_{La}=0.445)} \rightarrow La_3Si_5 + LaSi$	1528 ± 9	[41]
Congruent	$L_{(X_{La}=0.50)} \leftrightarrow LaSi$	1620.0	This work
	$L_{(X_{La}=0.50)} \leftrightarrow LaSi$	1620.0	[41]
	T_m of LaSi	1556 ± 34	[50]
Peritectic	$LaSi + L_{(X_{La}=0.591)} \rightarrow La_5Si_4$	1482.0	This work
	$LaSi + L_{(X_{La}=0.563)} \rightarrow La_5Si_4$	1570.0	[41]
	T_m of La_5Si_4	1443 ± 32	[50]
Peritectic	$La_5Si_4 + L_{(X_{La}=0.659)} \rightarrow La_3Si_2$	1328.4	This work
	$La_5Si_4 + L_{(X_{La}=0.626)} \rightarrow La_3Si_2$	1470.0	[41]
	T_m of La_3Si_2	1307 ± 35	[50]
Peritectic	$La_3Si_2 + L_{(X_{La}=0.686)} \rightarrow La_5Si_3$	1271.6	This work
	$La_3Si_2 + L_{(X_{La}=0.699)} \rightarrow La_5Si_3$	1260.0	[41]
	T_m of La_5Si_3	1316 ± 35	[50]
Eutectic	$L_{(X_{La}=0.885)} \rightarrow La_5Si_3 + La_{(fcc\text{-}A1,\ X_{La}=0.991)}$	711.2	This work
	$L_{(X_{La}=0.890)} \rightarrow La_5Si_3 + La_{(fcc\text{-}A1,\ X_{La}=0.985)}$	722 ± 9	[41]
Catatectic	$La_{(bcc\text{-}A2,\ X_{La}=0.986)} \rightarrow L_{(X_{La}=0.940)} + La_{(fcc\text{-}A1,\ X_{La}=0.995)}$	734.9	This work
	$La_{(bcc\text{-}A2,\ X_{La}=0.980)} \rightarrow L_{(X_{La}=0.938)} + La_{(fcc\text{-}A1,\ X_{La}=0.990)}$	815.0	[41]

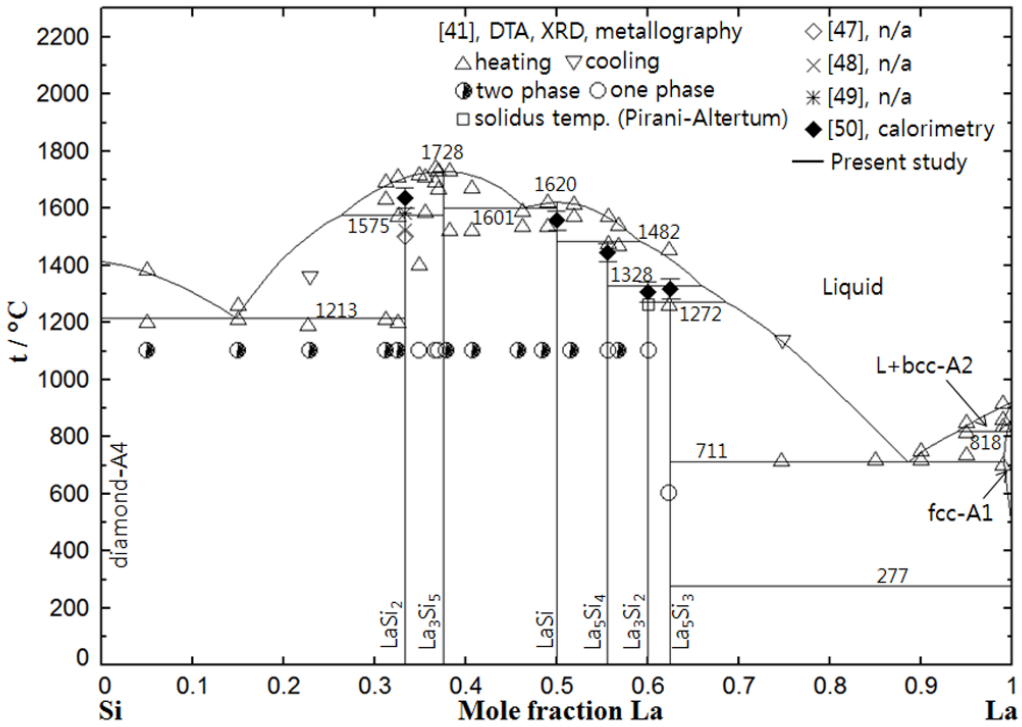


Fig. 1. The optimized Si-La phase diagram with experimental data.

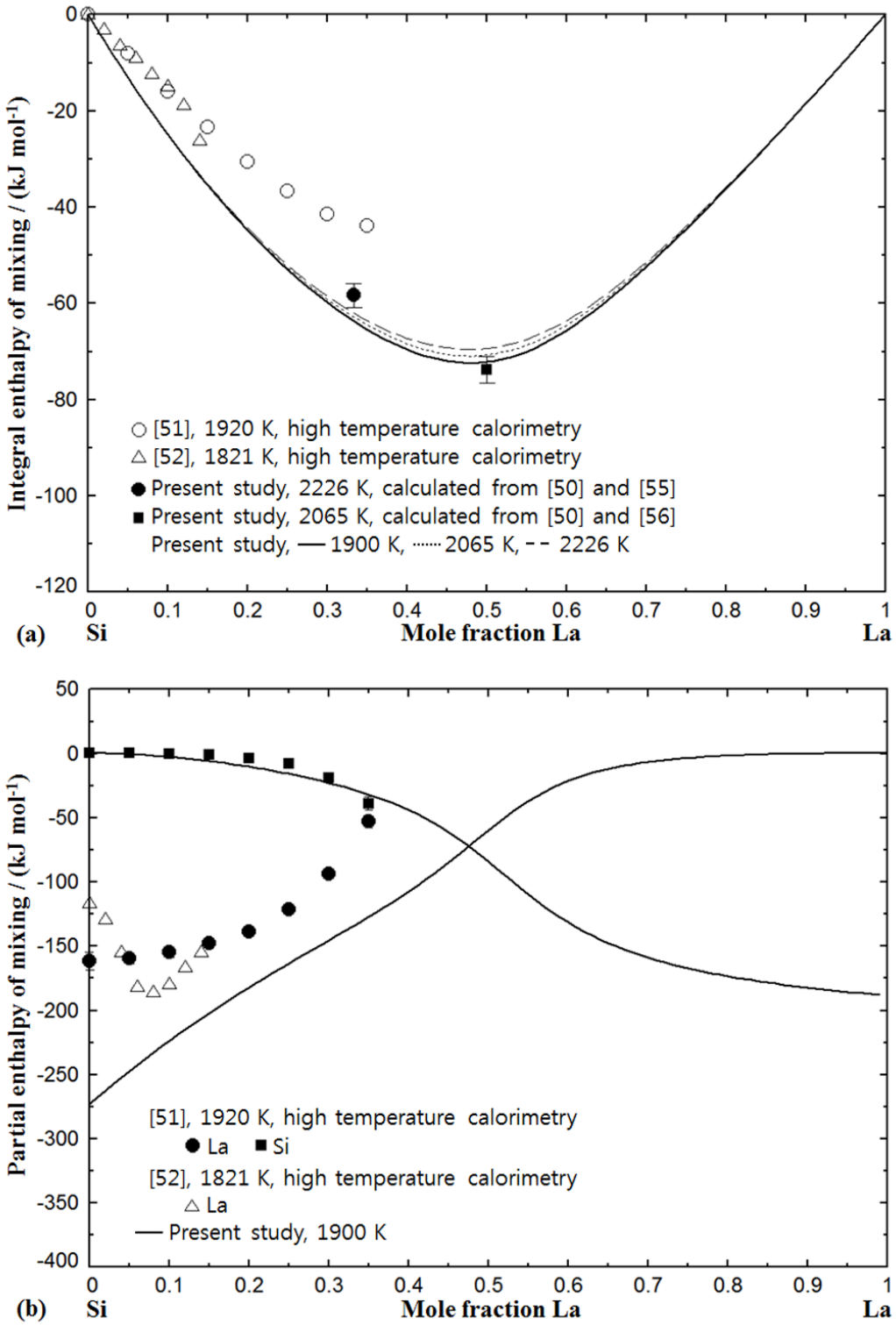


Fig. 2. (a) Integral enthalpy of mixing and (b) partial enthalpies of mixing of liquid Si-La phase at 1900 K with experimental data.

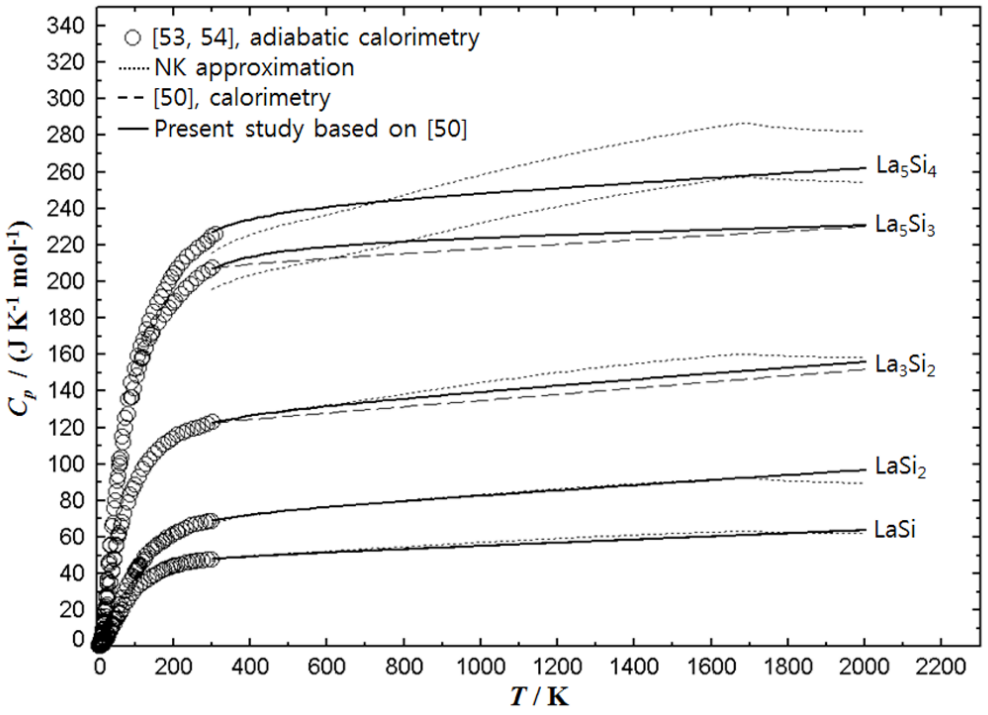


Fig. 3. Heat capacities of the compounds in the Si-La system with experimental data.

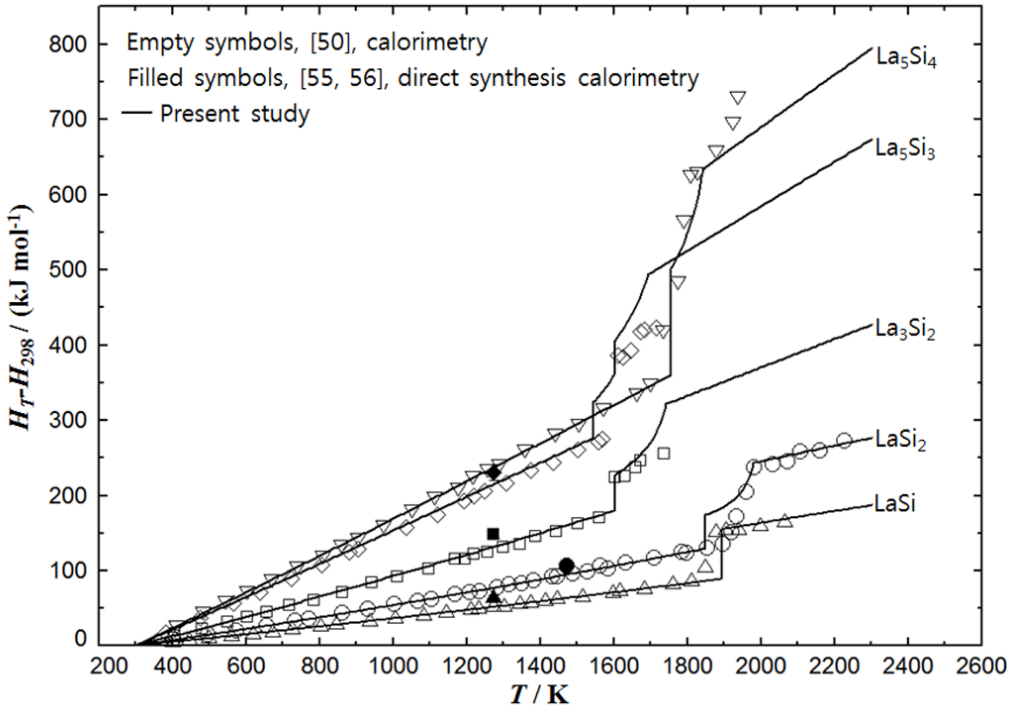


Fig. 4. Heat contents of the compounds in the Si-La system with experimental data.

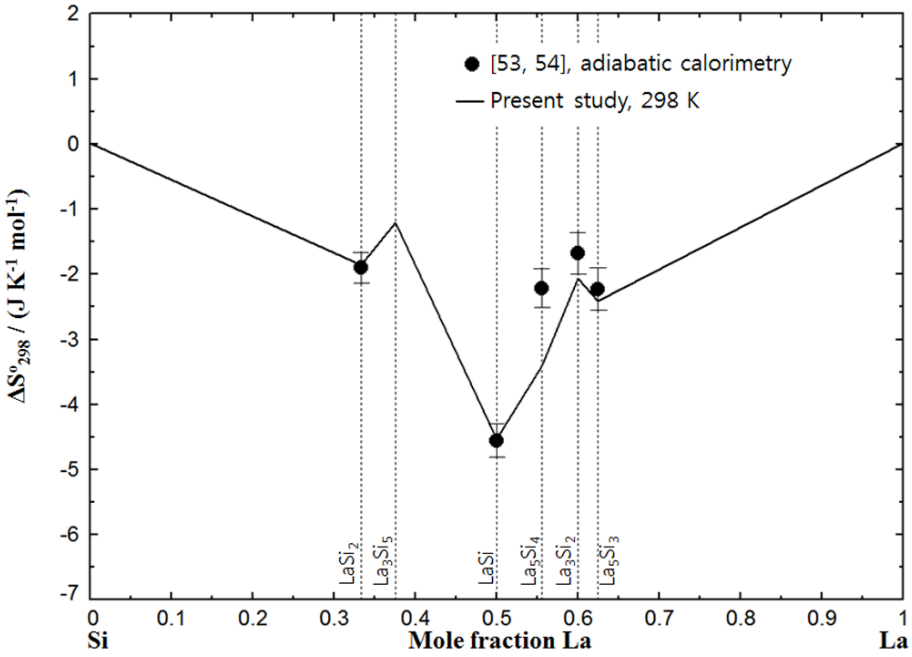


Fig. 5. Entropy of formation of the compounds in the Si-La system from elements at 298 K with experimental data.

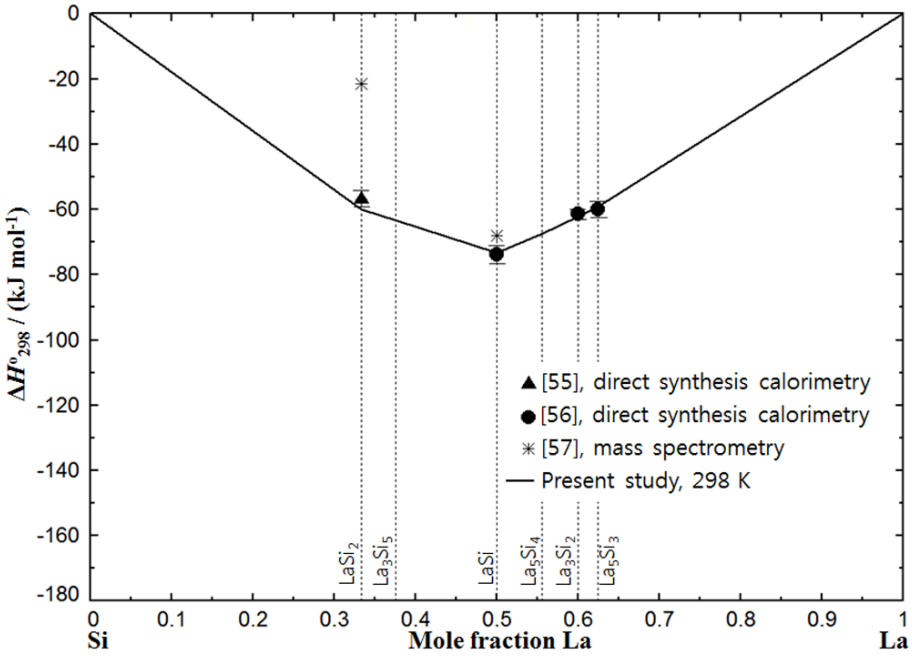


Fig. 6. Enthalpy of formation of the compounds in the Si-La system at 298 K with experimental data.

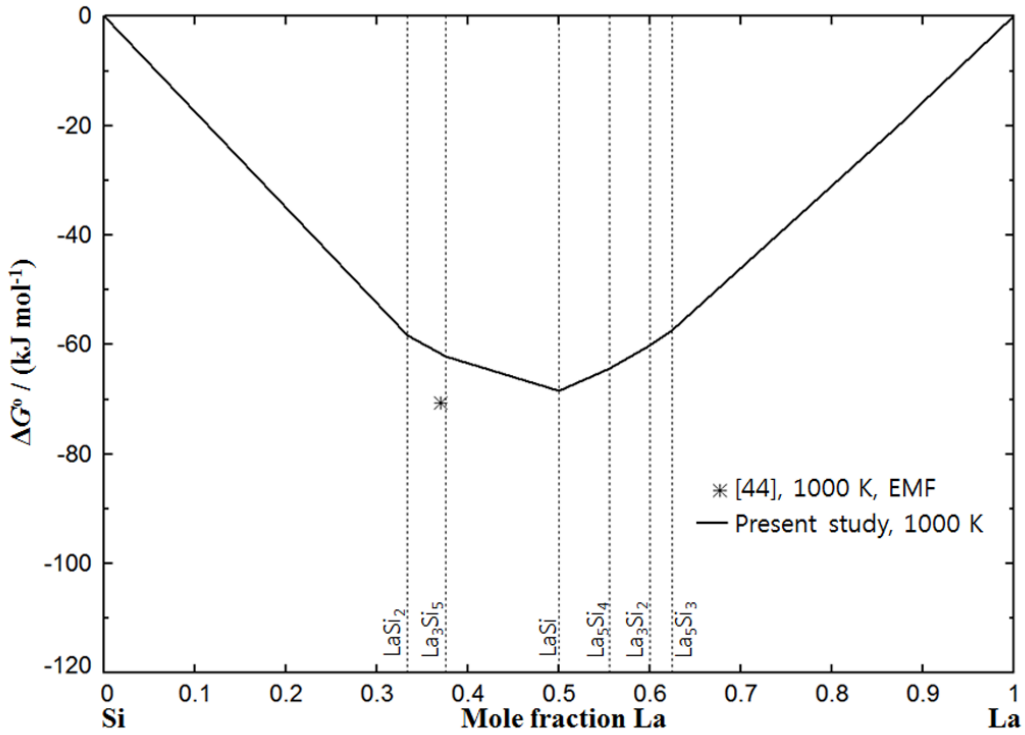


Fig. 7. Gibbs energy of formation of the compounds in the Si-La system at 1000 K with experimental data.

3.2. The Si-Ce system

Experimental data of the Si-Ce phase diagram are presented in Fig. 8. The phase diagram was investigated by Benesovsky et al. [59] using metallography. Melting points were measured by melting down Seger cones in a tungsten tube furnace under helium atmosphere. The authors found six congruent intermetallic compounds, $Ce_{\sim 2}Si$, Ce_3Si_2, $Ce_{\sim 1.2}Si$, CeSi, $CeSi_{2\text{-}a}$, and $CeSi_2$, and determined their melting points and corresponding eutectic temperatures. The exact composition of $CeSi_{2\text{-}a}$ was not established by Benesovsky et al. The stoichiometry of $Ce_{\sim 2}Si$ and $Ce_{\sim 1.2}Si$ were later amended to Ce_5Si_3 [60] and Ce_5Si_4 [61], respectively, by crystallographic studies. Like the Si-La system, there are discrepancies in the homogeneity range and the polymorphs of $CeSi_{2\text{-}a}$. Buyanov et al. [46] supposed that there are two polymorphs of $CeSi_{2\text{-}a}$ with a homogeneity range of 0.333 to 0.375 mole fraction of Ce: the high temperature α-$GdSi_2$ phase and the low temperature α-$ThSi_2$ form. Houssay et al. [45] proposed that the α-$ThSi_2$ structure transforms continuously to the α-$GdSi_2$ one with increasing silicon content of $CeSi_{2\text{-}a}$ with a homogeneity range of 0.33 to 0.385 mole fraction of Ce. Later, Bulanova et al. [62] investigated the Si-Ce system using DTA, XRD and metallography and suggested that the phase diagram was similar to the Si-La system [41]. According to Bulanova et al., CeSi and $CeSi_{2\text{-}a1}$ melt congruently and the remaining compounds form by peritectic reactions. The Si-deficient boundary of $CeSi_{2\text{-}a1}$ was located between 0.374 and 0.389 mole fraction of Ce and the Si-rich boundary of $CeSi_{2\text{-}a2}$ was positioned at 0.333 mole fraction of Ce. However, the exact composition limits of each phase were not determined. The melting temperature of $CeSi_2$ at 1620 ºC was reported by Thompson et al. [49]. Recently, the melting temperature of Ce_5Si_3 was obtained from its heat content measurement [63]. The terminal solid solubility was not investigated.

The enthalpy of mixing of the Si-Ce liquid was measured by Ryss et al. [64] and Sudavtsova et al. [65]. Ryss et al. [64] determined the integral and partial enthalpies of mixing of Si-Ce solution using high temperature vacuum calorimetry with an isothermal jacket. Measurements were performed between 0 and 0.55 and between 0.45 and 1 mole fraction of Ce at 1923 K using high purity starting materials (~ 99.99 % Si and 99.8 % Ce). The authors provided only smoothed partial and integral enthalpies of mixing in the entire composition range. Using a similar method,

Sudavtsova et al. [65] also presented smoothed integral and partial enthalpies of Ce up to 0.2 mole fraction of Ce at 1890 K. These data are presented in Figs. 9(a) and 9(b), respectively. Both studies show similar enthalpy of liquid solution within the experimental error range.

The thermodynamic properties of several intermetallic compounds were determined and available experimental data are presented in Figs 10 to 13. Low temperature C_p of Ce_5Si_3 was measured by Gorbachuk [63] using adiabatic calorimetry. The calculated S^{o}_{298} was obtained by integrating the C_p data. In the same study, the author measured the heat content ($H_T - H_{298}$) of Ce_5Si_3 from 437 to 1806 K using high temperature differential calorimetry under high-purity argon at temperatures below 1200 K, and high temperature calorimetry in vacuum at higher temperatures. The C_p above 298 K was also determined as a function of temperature as shown in Fig. 10. Heat capacities of other compounds were not reported. Meschel and Kleppa [55, 56] measured ΔH^{o}_{298} of $CeSi_2$, CeSi and Ce_5Si_3 using direct synthesis calorimetry. They also provided $H_{1273} - H_{298}$ of Ce_5Si_3 and $H_{1473} - H_{298}$ of $CeSi_2$ and CeSi.

The system was previously reviewed by Munitz et al. [66] and thermodynamically optimized by Gröbner et al. [24] and Shukla et al. [16]. In the optimization of Gröbner et al. [24], the phase diagram study of Benesovsky et al. [59] and the ΔH^{o}_{298} of $CeSi_2$, CeSi and Ce_5Si_3 measured by Meschel and Kleppa [55, 56] were taken into account. The liquid phase was modeled with the Bragg-Williams random mixing model. The calculated integral and partial enthalpies of the liquid solution were significantly far off from experimental data [64, 65]. Shukla et al. [16] considered more experimental data except for the low temperature C_p and heat content of Ce_5Si_3 measured by Gorbachuk [63]. As a result in their optimization, the S^{o}_{298} of Ce_5Si_3 was about 60 J K^{-1} mol^{-1} higher than the experimental data [63]. All the calculated thermodynamic properties in the previous optimizations are presented and compared with experimental data and the present study in Figs. 9 to 13.

Like the Si-La system, the six intermetallic compounds, Ce_5Si_3, Ce_3Si_2, Ce_5Si_4, CeSi, Ce_3Si_5 and $CeSi_2$, were modeled as line compounds in this study. The optimized phase diagram of the Si-Ce system is presented in Fig. 8 along with experimental data. Data reported by Bulanova et al. [62] were believed to be more accurate than the ones determined by Segar cones [59]. The calculated phase diagram agrees well with experimental data [62] except for the slightly higher eutectic temperature between Ce_3Si_5 and CeSi. The enthalpy term of the excess Gibbs energy of the liquid was modeled to reproduce the experimental enthalpy of mixing data [64, 65] as shown in Fig. 9. The C_p above 298 K of Ce_5Si_3 determined by Gorbachuk [63] was used as seen in Fig. 10 and the C_p of the remaining compounds were approximated with the NK rule as there is no experimental data. As seen in Fig. 11, the calculated heat content, $H_T - H_{298}$, of Ce_5Si_3 is in good agreement with experimental data [63] at low temperature (solid) but the calculated $H_T - H_{298}$ at high temperature (liquid) are slightly smaller than experimental data. The $H_T - H_{298}$ of Ce_5Si_3 for the liquid can be calculated by combining the experimental enthalpy data of the liquid (X_{Ce} = 0.625) [64, 65] and the experimental ΔH^{o}_{298} of Ce_5Si_3 [56]. However, in order to reproduce the experimental $H_T - H_{298}$ of the liquid (X_{Ce} = 0.625), a more negative ΔH^{o}_{298} of Ce_5Si_3 is required along with the liquid enthalpy [64, 65]. The previous optimization from Shukla et al. [16], which used a ΔH^{o}_{298} of Ce_5Si_3 close to experimental data, show more deviation with experimental $H_T - H_{298}$ of the liquid (X_{Ce} = 0.625) as seen in Figs. 11 and 13. A more negative ΔH^{o}_{298} of Ce_5Si_3 is also consistent with the experimental S^{o}_{298} of Gorbachuk [63] (see Fig. 12) to reproduce the melting point of Ce_5Si_3 [62, 63] along with the liquid enthalpy [64, 65]. The ΔH^{o}_{298} of $CeSi_2$ and CeSi were taken from experimental data [55] as seen in Fig. 13. Then, the temperature dependent interaction parameters of the liquid were slightly adjusted to reproduce the phase diagram accurately. The optimized thermodynamic parameters are listed in Table 3 and the calculated invariant reactions with the experimental data are tabulated in Table 4.

Table 3. Optimized model parameters of the Si-Ce system.

Phase	Thermodynamic parameters
Liquid	Coordination Numbers
	i Si; j Ce; Z_{ij}^{i} 6; Z_{ij}^{j} 6
	Δg_{SiCe} / (J mol^{-1}) = (-57739.2 + 4.184 T/K) – 21756.8 X_{SiSi} + (-15480.8 + 8.117 T/K) X_{CeCe} + 5020.8 X_{CeCe}^{2}
$CeSi_2$	ΔH_{298}^{o} = -185500 J mol^{-1}, S_{298}^{o} = 113.1 J K^{-1} mol^{-1}
	C_p / (J K^{-1} mol^{-1}) = 1 × C_p / (J K^{-1} mol^{-1}) (Ce, fcc-A1) + 2 × C_p / (J K^{-1} mol^{-1}) (Si, diamond-A4)
Ce_3Si_5	ΔH_{298}^{o} = -510000 J mol^{-1}, S_{298}^{o} = 330.0 J K^{-1} mol^{-1}
	C_p / (J K^{-1} mol^{-1}) = 3 × C_p / (J K^{-1} mol^{-1}) (Ce, fcc-A1) + 5 × C_p / (J K^{-1} mol^{-1}) (Si, diamond-A4)
CeSi	ΔH_{298}^{o} = -140000 J mol^{-1}, S_{298}^{o} = 89.0 J K^{-1} mol^{-1}
	C_p / (J K^{-1} mol^{-1}) = 1 × C_p / (J K^{-1} mol^{-1}) (Ce, fcc-A1) + 1 × C_p / (J K^{-1} mol^{-1}) (Si, diamond-A4)
Ce_5Si_4	ΔH_{298}^{o} = -610000 J mol^{-1}, S_{298}^{o} = 400.0 J K^{-1} mol^{-1}
	C_p / (J K^{-1} mol^{-1}) = 5 × C_p / (J K^{-1} mol^{-1}) (Ce, fcc-A1) + 4 × C_p / (J K^{-1} mol^{-1}) (Si, diamond-A4)
Ce_3Si_2	ΔH_{298}^{o} = -328000 J mol^{-1}, S_{298}^{o} = 226.3 J K^{-1} mol^{-1}
	C_p / (J K^{-1} mol^{-1}) = 3 × C_p / (J K^{-1} mol^{-1}) (Ce, fcc-A1) + 2 × C_p / (J K^{-1} mol^{-1}) (Si, diamond-A4)
Ce_5Si_3	ΔH_{298}^{o} = -507500 J mol^{-1}, S_{298}^{o} = 355.7 J K^{-1} mol^{-1}
	C_p / (J K^{-1} mol^{-1}) = 245.26 + 0.039868 T/K - 23583 (T/K)$^{-2}$

Table 4. Calculated invariant reactions and experimental data in the Si-Ce system.

Type	Reaction	t (°C)	Reference
Eutectic	$L_{(X_{Ce}=0.157)} \rightarrow Si_{(dia.\text{-}A4,\ X_{Ce}=0)} + CeSi_2$	1192.6	This work
	$L_{(X_{Ce}=0.130)} \rightarrow Si_{(dia.\text{-}A4,\ X_{Ce}=0)} + CeSi_2$	1200.0	[59]
	$L_{(X_{Ce}=0.180)} \rightarrow Si_{(dia.\text{-}A4,\ X_{Ce}=0)} + CeSi_2$	1198 ± 2	[62]
Peritectic	$L_{(X_{Ce}=0.290)} + Ce_3Si_5 \rightarrow CeSi_2$	1586.2	This work
	$L_{(X_{Ce}=0.297)} + Ce_3Si_5 \rightarrow CeSi_2$	1575.0	[62]
Congruent	$L_{(X_{Ce}=0.333)} \leftrightarrow CeSi_2$	1620.0	[59]
	T_m of $LaSi_2$	1620.0	[49]
Congruent	$L_{(X_{Ce}=0.375)} \leftrightarrow Ce_3Si_5$	1731.5	This work
	$L_{(X_{Ce}=0.375)} \leftrightarrow Ce_3Si_5$	1725.0	[62]
Eutectic	$L_{(X_{Ce}=0.455)} \rightarrow Ce_3Si_5 + CeSi$	1587.6	This work
	$L_{(X_{Ce}=0.470)} \rightarrow Ce_3Si_5 + CeSi$	1400.0	[59]
	$L_{(X_{Ce}=0.450)} \rightarrow Ce_3Si_5 + CeSi$	1532 ± 12	[62]
Congruent	$L_{(X_{Ce}=0.50)} \leftrightarrow CeSi$	1640.0	This work
	$L_{(X_{Ce}=0.50)} \leftrightarrow CeSi$	1470.0	[59]
	$L_{(X_{Ce}=0.50)} \leftrightarrow CeSi$	1630.0	[62]
Eutectic	$L_{(X_{Ce}=0.540)} \rightarrow Ce_5Si_4 + CeSi$	1390.0	[59]
Congruent	$L_{(X_{Ce}=0.556)} \leftrightarrow Ce_5Si_4$	1440.0	[59]
Peritectic	$CeSi + L_{(X_{Ce}=0.580)} \rightarrow Ce_5Si_4$	1498.8	This work
	$CeSi + L_{(X_{Ce}=0.602)} \rightarrow Ce_5Si_4$	1500.0	[62]
Eutectic	$L_{(X_{Ce}=0.580)} \rightarrow Ce_3Si_2 + Ce_5Si_4$	1360.0	[59]
Congruent	$L_{(X_{Ce}=0.60)} \leftrightarrow Ce_3Si_2$	1390.0	[59]
Eutectic	$L_{(X_{Ce}=0.615)} \rightarrow Ce_5Si_3 + Ce_3Si_2$	1270.0	[59]
Congruent	$L_{(X_{Ce}=0.625)} \leftrightarrow Ce_5Si_3$	1400.0	[59]
Peritectic	$Ce_5Si_4 + L_{(X_{Ce}=0.647)} \rightarrow Ce_3Si_2$	1327.6	This work
	$Ce_5Si_4 + L_{(X_{Ce}=0.667)} \rightarrow Ce_3Si_2$	1335.0	[62]
Peritectic	$Ce_3Si_2 + L_{(X_{Ce}=0.674)} \rightarrow Ce_5Si_3$	1272.6	This work
	$Ce_3Si_2 + L_{(X_{Ce}=0.687)} \rightarrow Ce_5Si_3$	1260.0	[62]
	T_m of La_5Si_3	1291 ± 30	[63]
Eutectic	$L_{(X_{Ce}=0.894)} \rightarrow Ce_5Si_3 + Ce_{(fcc\text{-}A1,\ X_{Ce}=1)}$	625.9	This work
	$L_{(X_{Ce}=0.920)} \rightarrow Ce_5Si_3 + Ce_{(fcc\text{-}A1,\ X_{Ce}=1)}$	650.0	[59]
	$L_{(X_{Ce}=0.895)} \rightarrow Ce_5Si_3 + Ce_{(fcc\text{-}A1,\ X_{Ce}=1)}$	635.0	[62]

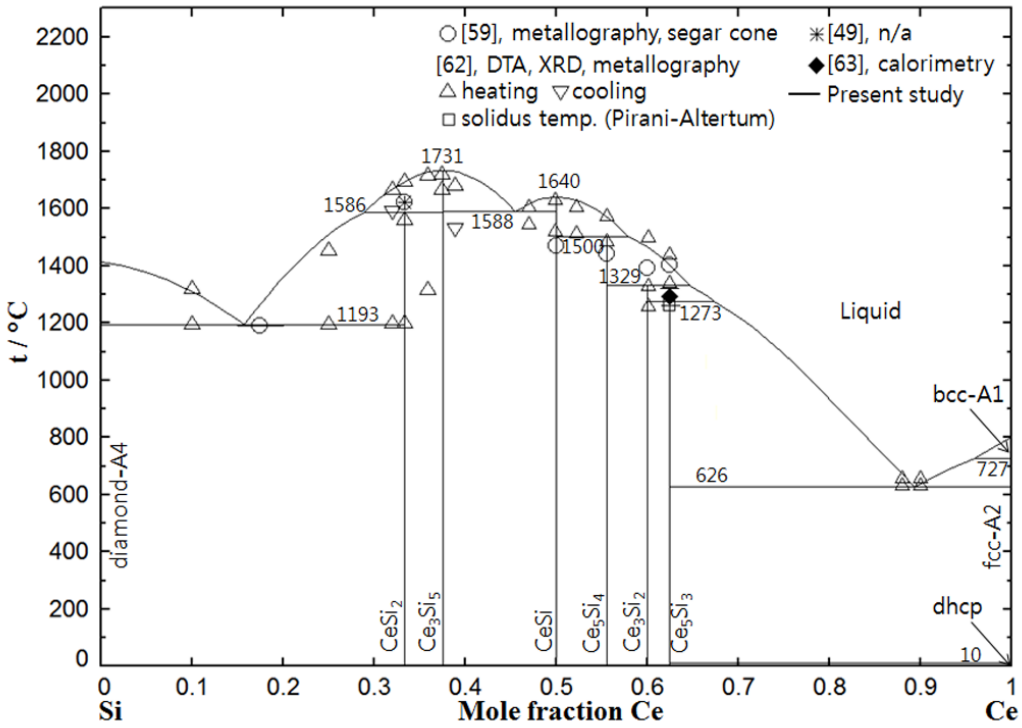


Fig. 8. The optimized Si-Ce phase diagram with experimental data.

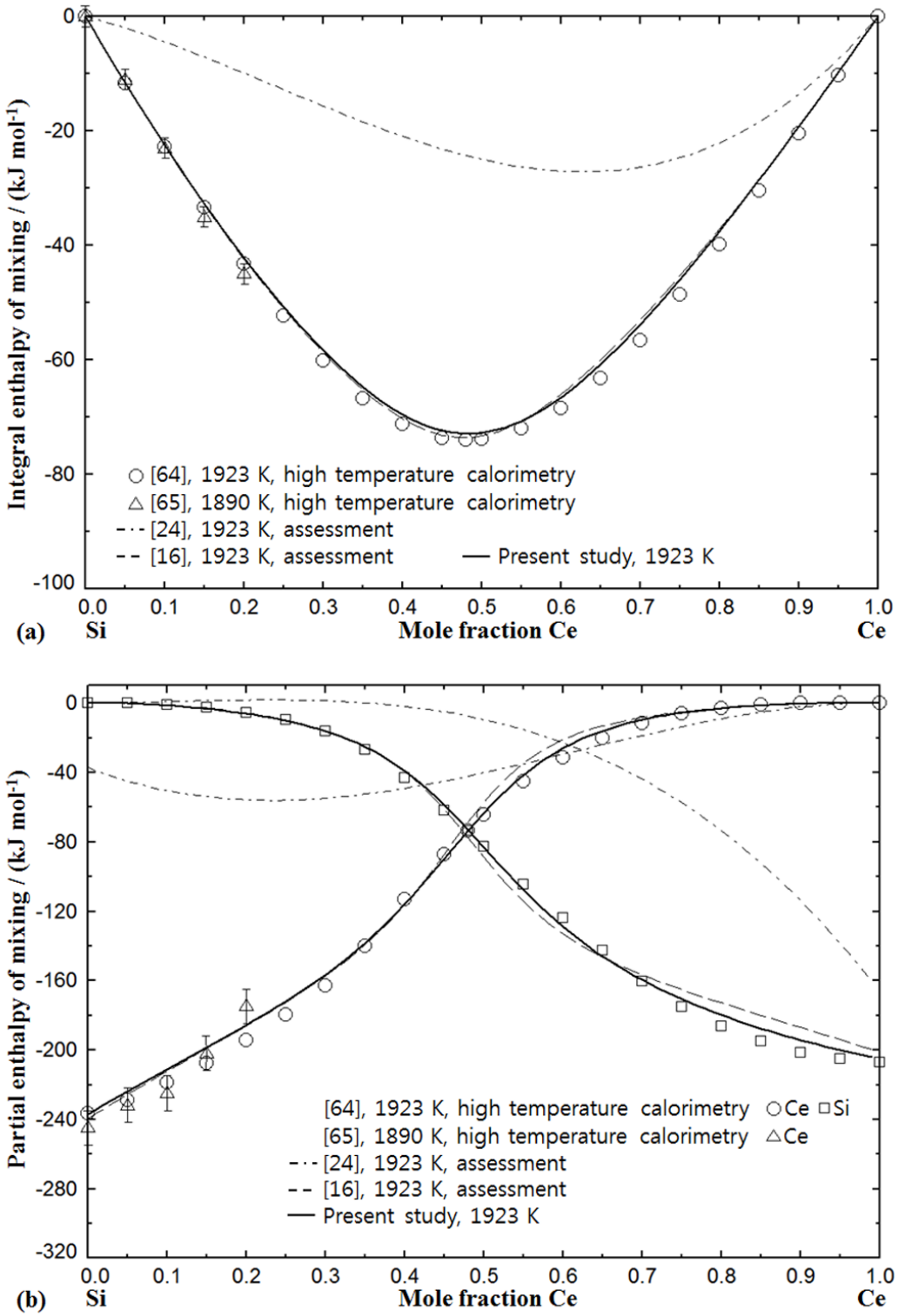


Fig. 9. (a) Integral enthalpy of mixing and (b) partial enthalpies of mixing of liquid Si-Ce phase at 1923 K with experimental data and previous thermodynamic assessments.

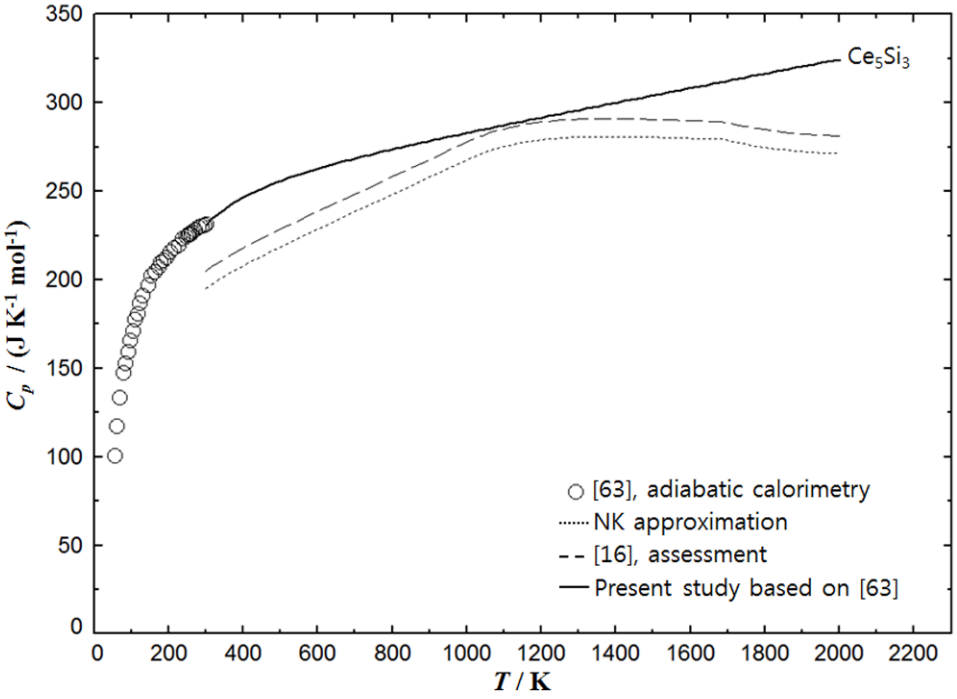


Fig. 10. Heat capacities of the Ce_5Si_3 with experimental data and previous thermodynamic assessment.

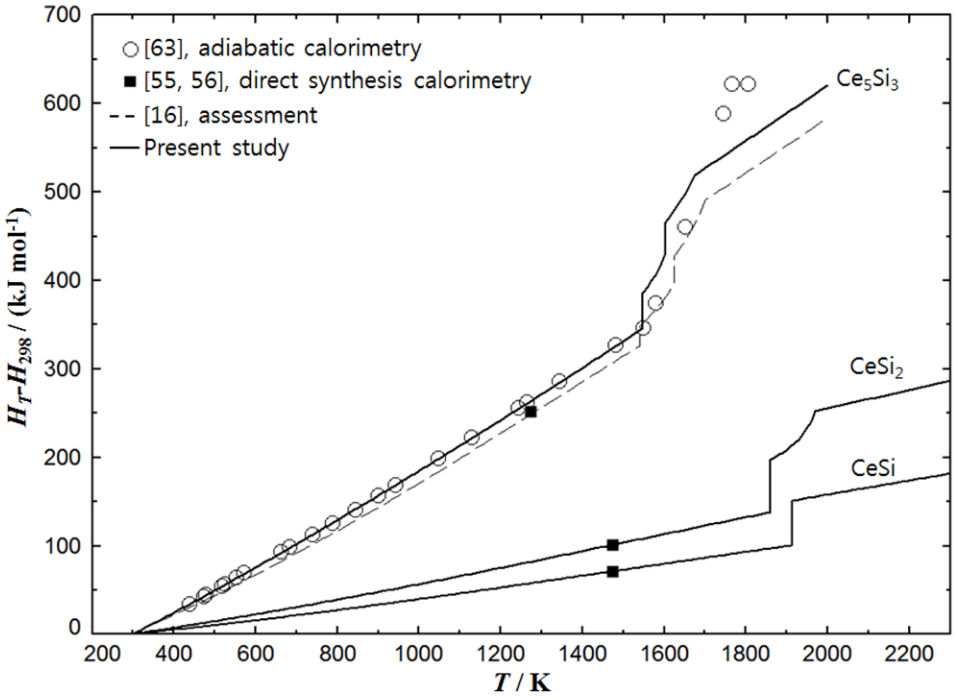


Fig. 11. Heat contents of the compounds in the Si-Ce system with experimental data and previous thermodynamic assessment.

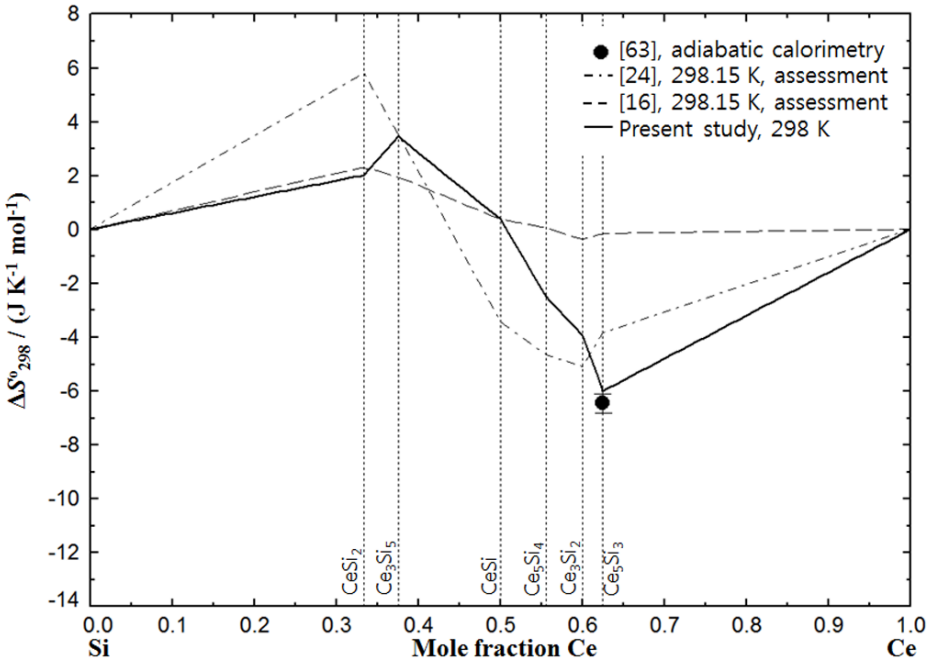


Fig. 12. Entropy of formation of the compounds in the Si-Ce system from elements at 298 K with experimental data and previous thermodynamic assessments.

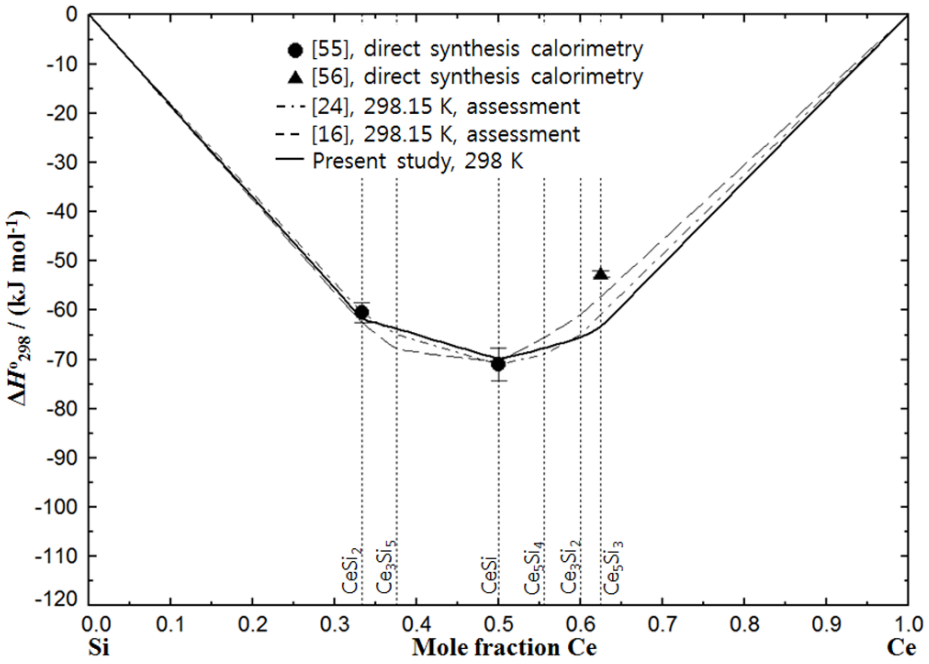


Fig. 13. Enthalpy of formation of the compounds in the Si-Ce system at 298 K with experimental data and previous thermodynamic assessments.

3.3. The Si-Pr system

Experimental data of the Si-Pr phase diagram are shown in Fig. 14. Eremenko et al. [67] investigated the phase diagram using DTA, XRD and metallography. They prepared 32 alloys by using pure (99.75 %) Pr and (99.99 %) Si by arc-melting with a water-cooled copper hearth and inconsumable tungsten electrode under purified argon atmosphere. Four stoichiometric compounds, Pr_5Si_3, Pr_5Si_4, PrSi and Pr_3Si_4, and one non-stoichiometric compound, $PrSi_{1.8}$ (Pr_5Si_9), were found in the system. Pr_5Si_3 and Pr_5Si_4 formed by peritectic reactions at 1417 and 1532 ºC, respectively. The existence of a possible polymorphic transition for Pr_5Si_3 was detected by DTA at about 1347 ºC. However, Eremenko et al. [67] failed to detect the high temperature form of Pr_5Si_3 by XRD. PrSi melted congruently at 1657 ºC and Pr_3Si_4 formed by peritectoid reaction at 1352 ºC. Pr_5Si_9 had a small homogeneity range and complex polymorphic transition. The transition between α- (orthorhombic) and β- (tetragonal) Pr_5Si_9 of the Si-deficient phase was detected at 157 ºC, while the transition of Si-rich Pr_5Si_9 was not detected due to the limitation of their apparatus. According to Perri et al. [68, 69] , the transition temperature of Si-rich Pr_5Si_9 is -123 ± 15 ºC. For Eremenko et al. [67], the transition temperature at 0.353 mole fraction Pr is 57 ºC. Results also suggest a continuous increase in the transition temperature with increasing Pr content. Regarding the homogeneity range of Pr_5Si_9, Boutarek et al. [70] reported three individual compounds between 0.333 and 0.385 mole fraction of Pr by using metallography and XRD. The homogeneity range proposed are 0.337-0.346, 0.348-0.357, and 0.37-0.382 mole fraction of Pr. The melting temperatures of Pr_5Si_3, Pr_5Si_4, PrSi and Pr_5Si_9 were taken from the study of Gorbachuk et al. [71] who measured the heat content with high temperature calorimetry. Their results were very similar to those reported by Eremenko et al. [67].

No thermodynamic properties were found in the literature for the Si-Pr liquid. Fortunately, numerous thermodynamic data were reported for intermetallics. The low temperature C_p of Pr_5Si_3, Pr_5Si_4, PrSi and Pr_5Si_9 were measured by Bolgar et al. [72, 73] using adiabatic calorimetry and their S^{o}_{298} were derived from the C_p data presented. The heat contents ($H_T - H_{298}$) of Pr_5Si_3, Pr_5Si_4, PrSi and Pr_5Si_9 were measured by Gorbachuk et al. [71] using high temperature differential calorimetry (DSC) under high purity argon between 300 and 1300 K, and high temperature

calorimetry in vacuum above 1200 K. Corresponding C_p above 298 K were also obtained as a function of temperature. Gorbachuk et al. [71] found inconsistencies in their C_p, which were derived from heat content data and low temperature C_p data [72]. Therefore, they assumed that Pr_5Si_9 undergoes a polymorphic transition between the temperature limits of two experiments, which was 308 ± 8 K. The C_p of the low temperature stable phase was estimated by extrapolating the low temperature data up to 400 K. The enthalpy of the polymorphic transformation of Pr_5Si_9 was proposed to be about 260 J mol^{-1} based on the extrapolation of the temperature dependences of the enthalpies. Experimental data for the heat capacities, heat contents and ΔS^{o}_{298} of Pr_5Si_3, Pr_5Si_4, PrSi and Pr_5Si_9 are presented in Figs. 15 to 17, respectively. In addition, Meschel and Kleppa [55, 56] measured the ΔH^{o}_{298} of $PrSi_2$, PrSi and Pr_5Si_3 using direct synthesis calorimetry. They also determined the $H_{1273}-H_{298}$ of Pr_5Si_3 and the $H_{1473}-H_{298}$ of PrSi and $PrSi_2$, which are shown in Fig. 16. Gordienko and Fenochka [57] estimated ΔH^{o}_{298} of La_5Si_9 and LaSi uising Knudsen mass-spectrometry at 1800-2000 K. However, their results were considerably more positive than the calorimetric data of Meschel and Kleppa [55, 56], as shown in Fig. 18.

No thermodynamic optimization was previously performed on the Si-Pr system. In the present optimization, the five intermetallic compounds, Pr_5Si_9, Pr_3Si_4, PrSi, Pr_5Si_4 and Pr_5Si_3 were modeled from the work of Eremenko et al. [67]. The non-stoichiometric phase Pr_5Si_9 was considered as a line compound because its homogeneity range was not significant. The optimized phase diagram is presented in Fig. 14 along with experimental data [67, 71]. The calculated phase diagram agrees well with the experimental data [67, 71] except for the abnormal liquidus shape at about 0.2 to 0.3 mole fraction Pr. Moreover, the eutectic between Pr_5Si_9 and PrSi was difficult to be reproduced. A small solubility of Si in Pr (bcc-A2) was modeled using one small temperature independent parameter to reproduce the transition temperature between Pr (dhcp) and Pr (bcc-A2) [67]. Since no experimental data were available for the thermodynamic properties of the liquid phase, the enthalpy of mixing of the liquid solution was assumed to be similar to the previous two systems. Then, the C_p above 298 K of α-Pr_5Si_9, β-Pr_5Si_9, Pr_5Si_4, Pr_5Si_3 and PrSi determined by Gorbachuk et al. [71] were modified to correspond well with low temperature data [72, 73], as shown in Fig. 15. The corresponding heat contents of Pr_5Si_9, PrSi, Pr_5Si_4 and Pr_5Si_3 were also in

good agreement with experimental data as shown in Fig. 16. The C_p of Pr_3Si_4 was approximated using the NK rule as there is no experimental data. The polymorphic transition temperature between α-Pr_5Si_9 and β-Pr_5Si_9 was fixed at 308 K (35 ºC), in agreement with Gorbachuk et al. [71]. The optimized enthalpy of transformation is 475 J mol^{-1}, which was slightly increased from that reported by Gorbachuk et al. [71]. The experimental S^{o}_{298} of Pr_5Si_4 [72] was much larger than for the adjacent compounds PrSi and Pr_5Si_3. When the experimental S^{o}_{298} of Pr_5Si_4 was used, it was very difficult to make it stable against adjacent compounds. Although the peritectic melting temperature of Pr_5Si_4 could be reproduced, it became unstable at room temperature. Therefore, the S^{o}_{298} of Pr_5Si_4 was adjusted by about -60 J K^{-1} mol^{-1} (Fig. 17) to reproduce the phase diagram more accurately. All S^{o}_{298} and ΔH^{o}_{298} of the compounds were reasonably determined to reproduce available experimental (mostly calorimetric) data, as shown in Figs. 17 and 18. The optimized thermodynamic parameters are listed in Table 5 and the calculated invariant reactions with the experimental data are tabulated in Table 6.

Table 5. Optimized model parameters of the Si-Pr system.

Phase	Thermodynamic parameters
Liquid	Coordination Numbers
	i j Z_{ij}^{i} Z_{ij}^{j}
	Si Pr 6 6
	Δg_{SiPr} / (J mol^{-1}) = (-57739.2 + 10.46 T/K) + (-21756.8 + 2.092 T/K) X_{SiSi} + 2092.0 X_{SiSi}^{2} – (15480.8 + 3.473 T/K) X_{PrPr} + (6276.0 + 8.368 T/K) X_{PrPr}^{2}
bcc-A2	${}^{0}L_{\mathrm{Si,Pr}}$ / (J mol^{-1}) = -136398.4
α-Pr_5Si_9	ΔH_{298}° = -840000 J mol^{-1}, S_{298}° = 495.0 J K^{-1} mol^{-1}
	C_p / (J K^{-1} mol^{-1}) = 296.85 + 0.1714 T/K - 1095565 (T/K)$^{-2}$
β-Pr_5Si_9	$\Delta_{\mathrm{trs}}H^{\alpha\rightarrow\beta}$ = 475 J mol^{-1}, $T_{\mathrm{trs}}^{\alpha\rightarrow\beta}$ = 308.0 K
	C_p / (J K^{-1} mol^{-1}) = 335.95 + 0.08784 T/K - 60595 (T/K)$^{-2}$
Pr_3Si_4	ΔH_{298}° = -501790 J mol^{-1}, S_{298}° = 245.0 J K^{-1} mol^{-1}
	C_p / (J K^{-1} mol^{-1}) = 3 × C_p / (J K^{-1} mol^{-1}) (Pr, dhcp) + 4 × C_p / (J K^{-1} mol^{-1}) (Si, diamond-A4)
PrSi	ΔH_{298}° = -159000 J mol^{-1}, S_{298}° = 74.0 J K^{-1} mol^{-1}
	C_p / (J K^{-1} mol^{-1}) = 47.76 + 0.011884 T/K -305781 (T/K)$^{-2}$
Pr_5Si_4	ΔH_{298}° = -646000 J mol^{-1}, S_{298}° = 374.5 J K^{-1} mol^{-1}
	C_p / (J K^{-1} mol^{-1}) = 242.91+ 0.03648 T/K- 1745640 (T/K)$^{-2}$
Pr_5Si_3	ΔH_{298}° = -483000 J mol^{-1}, S_{298}° = 393.0 J K^{-1} mol^{-1}
	C_p / (J K^{-1} mol^{-1}) = 213.63 + 0.037796 T/K - 728873 (T/K)$^{-2}$

Table 6. Calculated invariant reactions and experimental data in the Si-Pr system.

Type	Reaction	t (°C)	Reference
Eutectic	$L_{(X_{Pr}= 0.164)} \rightarrow Si_{(dia.\text{-}A4,\ X_{Pr}= 0)} + Pr_5Si_9$	1207.1	This work
	$L_{(X_{Pr}= 0.170)} \rightarrow Si_{(dia.\text{-}A4,\ X_{Pr}= 0)} + Pr_5Si_9$	1212.0	[67]
Congruent	$L_{(X_{Pr}= 0.357)} \leftrightarrow Pr_5Si_9$	1694.2	This work
	$L_{(X_{Pr}= 0.357)} \leftrightarrow Pr_5Si_9$	1712.0	[67]
	T_m of Pr_5Si_9	1698 ± 40	[71]
Allotropic	$\alpha\text{-}Pr_5Si_9 \leftrightarrow \beta\text{-}Pr_5Si_9$	35.0	This work
	$\alpha\text{-}Pr_5Si_9 \leftrightarrow \beta\text{-}Pr_5Si_9$ (Si-rich composition)	-123.0	[67]
	$\alpha\text{-}Pr_5Si_9 \leftrightarrow \beta\text{-}Pr_5Si_9$ (Pr-rich composition)	157.0	[67]
	$\alpha\text{-}Pr_5Si_9 \leftrightarrow \beta\text{-}Pr_5Si_9$	35.0	[71]
Peritectoid	$Pr_5Si_9 + PrSi \rightarrow Pr_3Si_4$	1346.5	This work
	$Pr_5Si_9 + PrSi \rightarrow Pr_3Si_4$	1352.0	[67]
Eutectic	$L_{(X_{Pr}= 0.439)} \rightarrow Pr_5Si_9 + PrSi$	1613.7	This work
	$L_{(X_{Pr}= 0.42)} \rightarrow Pr_5Si_9 + PrSi$	1542.0	[67]
Congruent	$L_{(X_{Pr}= 0.50)} \leftrightarrow PrSi$	1647.2	This work
	$L_{(X_{Pr}= 0.50)} \leftrightarrow PrSi$	1657.0	[67]
	T_m of PrSi	1661 ± 28	[71]
Peritectic	$PrSi + L_{(X_{Pr}= 0.609)} \rightarrow Pr_5Si_4$	1521.5	This work
	$PrSi + L_{(X_{Pr}= 0.597)} \rightarrow Pr_5Si_4$	1532.0	[67]
	T_m of Pr_5Si_4	1511 ± 40	[71]
Peritectic	$Pr_5Si_4 + L_{(X_{Pr}= 0.657)} \rightarrow Pr_5Si_3$	1416.7	This work
	$Pr_5Si_4 + L_{(X_{Pr}= 0.653)} \rightarrow Pr_5Si_3$	1417.0	[67]
	T_m of Pr_5Si_3	1412 ± 37	[71]
Allotropic	$\alpha\text{-}Pr_5Si_3 \leftrightarrow \beta\text{-}Pr_5Si_3$	1347.0	[67]
Eutectic	$L_{(X_{Pr}= 0.878)} \rightarrow Pr_5Si_3 + Pr_{(dhcp,\ X_{Pr}= 1)}$	727.4	This work
	$L_{(X_{Pr}= 0.89)} \rightarrow Pr_5Si_3 + Pr_{(dhcp,\ X_{Pr}= 1)}$	732.0	[67]
Catatectic	$Pr_{(bcc\text{-}A2,\ X_{Pr}= 0.994)} \rightarrow L_{(X_{Pr}= 0.903)} + Pr_{(dhcp,\ X_{Pr}= 1)}$	774.8	This work

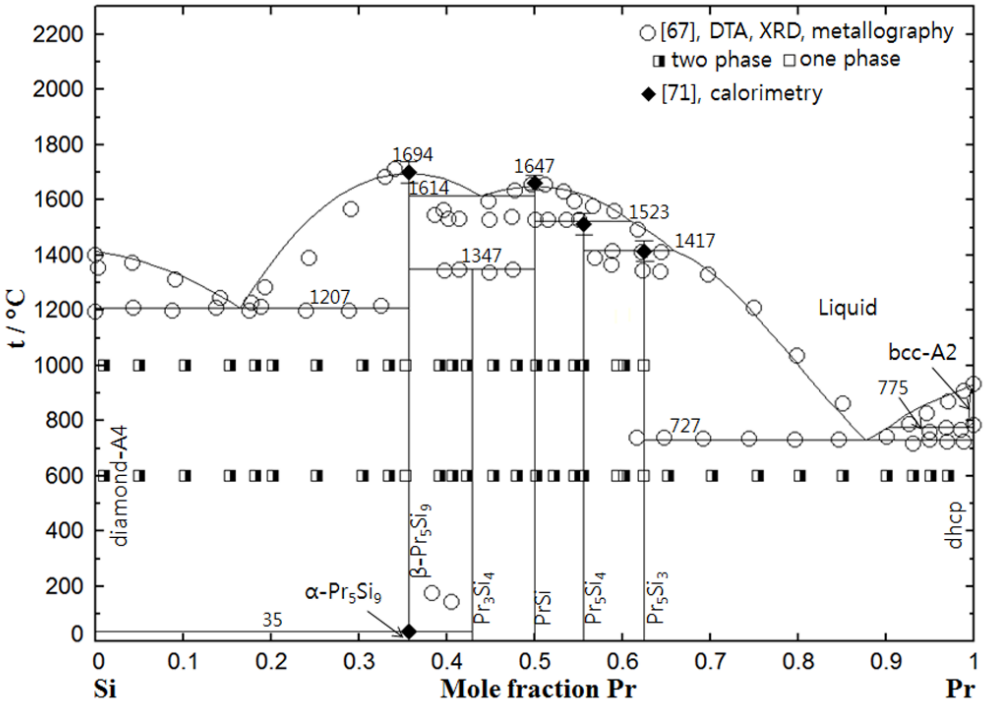


Fig. 14. The optimized Si-Pr phase diagram with experimental data.

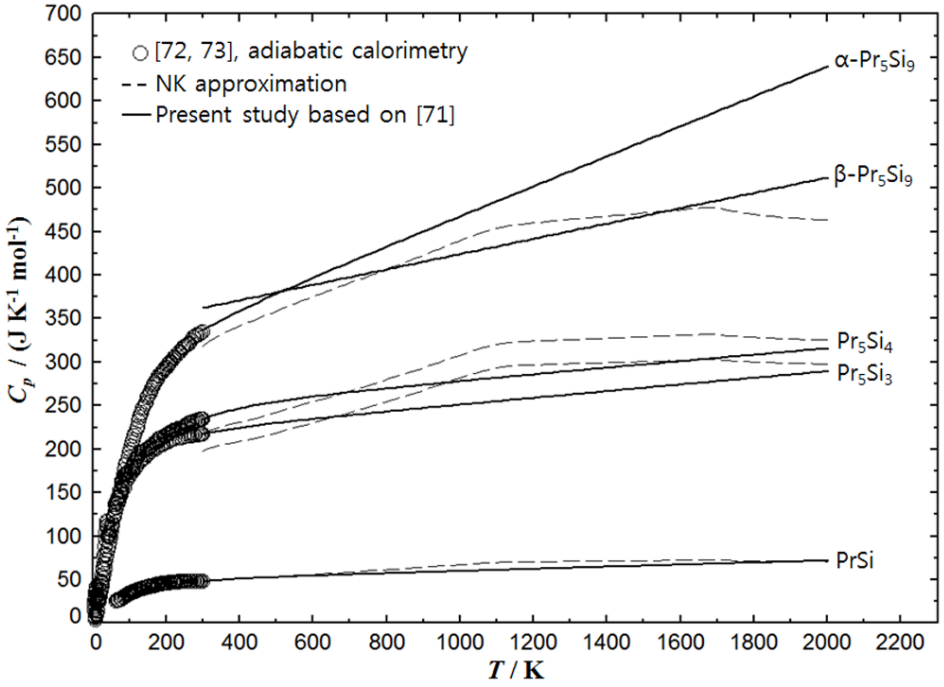


Fig. 15. Heat capacities of the compounds in the Si-Pr system with experimental data.

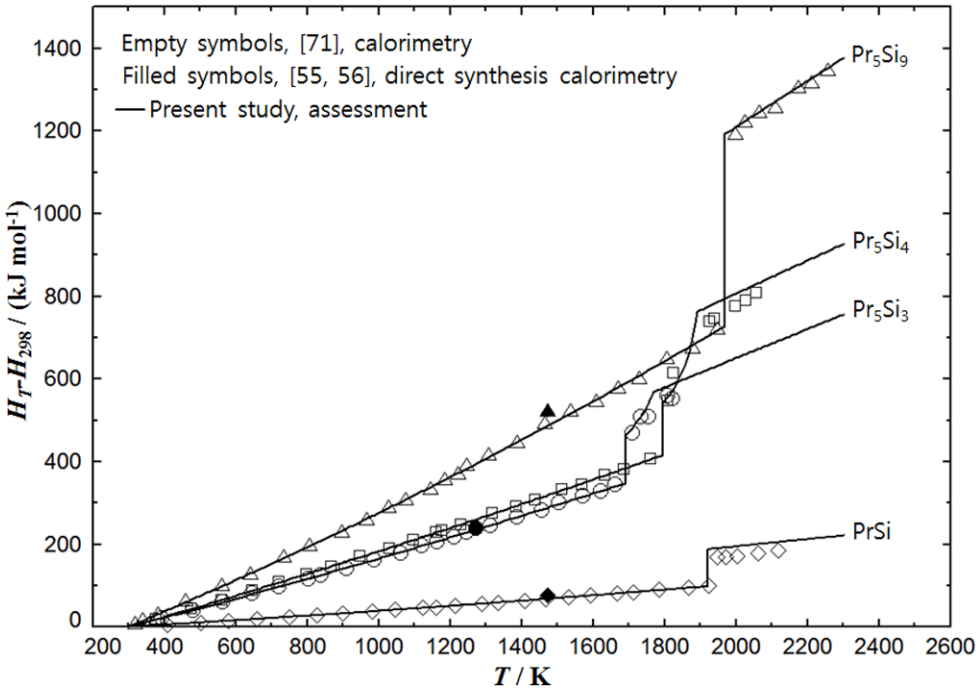


Fig. 16. Heat contents of the compounds in the Si-Pr system with experimental data.

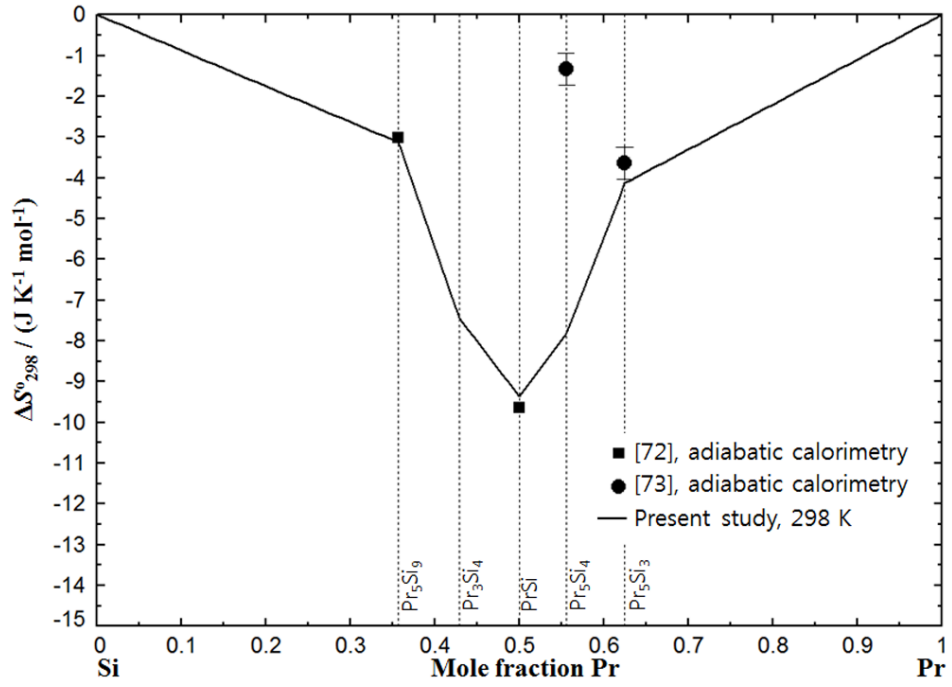


Fig. 17. Entropy of formation of the compounds in the Si-Pr system from elements at 298 K with experimental data.

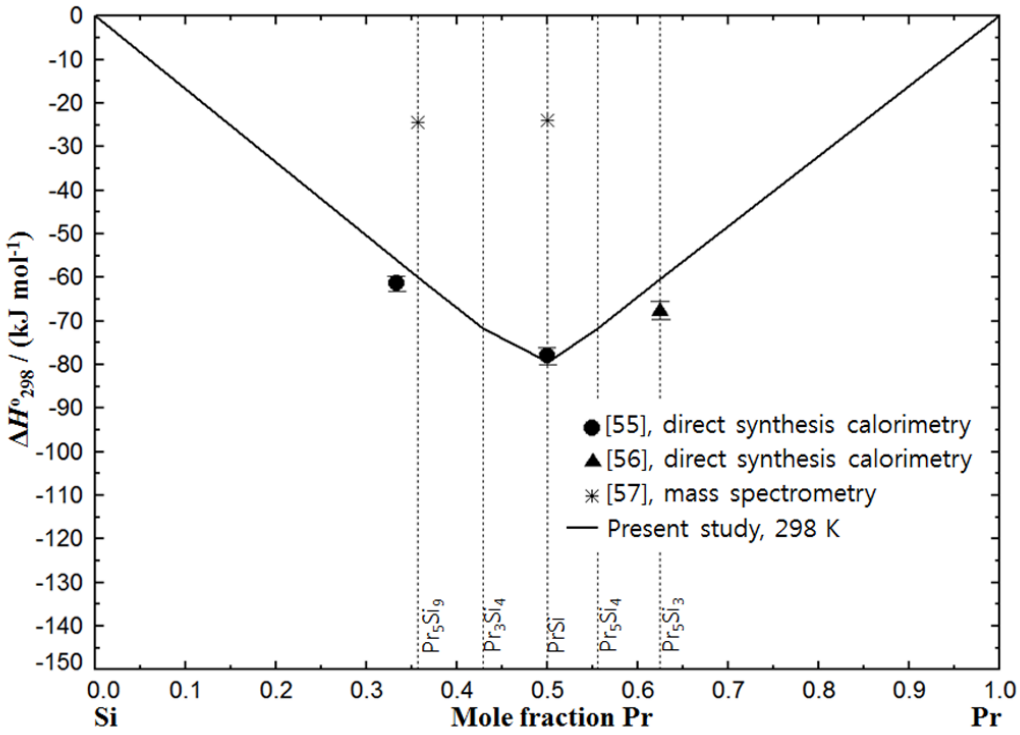


Fig. 18. Enthalpy of formation of the compounds in the Si-Pr system at 298 K with experimental data.

3.4. The Si-Nd system

Experimental data of the Si-Nd phase diagram are shown in Fig. 19. Eremenko et al. [74] investigated the system by employing DTA, XRD and metallography. The phase diagram of this system is similar to that of the Si-Pr system. The biggest difference between the two systems is the existence of Nd_2Si_3 in the Si-Nd system which forms peritectoidally at 1507 ºC and undergo an allotropic transition at 527 ºC. The homogeneity range of Nd_5Si_9 was found to be 0.35-0.36 mole fraction of Nd, which is similar to Pr_5Si_9. The transition between α-Nd_5Si_9 and β-Nd_5Si_9 was located at 147 ºC on the Si-deficient side and at 97 ºC on the Si-rich side. Gorbachuk and Bolgar [75] reported the melting and the allotropic transition temperatures and enthalpy of transition of Nd_5Si_9 to be about 1728 ºC, 125 ºC and 4.5 J mol^{-1}, respectively, from their heat content measurements. Later, the same authors modified the allotropic transition temperature and enthalpy of transition of Nd_5Si_9 to be 154 ºC and 4.0 J mol^{-1} by using DTA [76]. Previously, Binder [48] reported the melting temperature of $NdSi_2$ to be 1525 ºC and the allotropic transition of $NdSi_2$ was determined to occur between room temperature and 150 ºC by means of high temperature XRD [69].

No thermodynamic data are available for the liquid solution. For the intermetallic compounds, the low temperature C_p of Nd_5Si_9 was measured by Gorbachuk and Bolgar [75] using adiabatic calorimetry and the S^{o}_{298} was derived from the experimental data. In the same study, the authors measured the heat content ($H_T - H_{298}$) of Nd_5Si_9 using high temperature differential calorimetry (DSC) under high-purity argon between 300 and 1200 K, and high temperature calorimetry in vacuum at temperature above 1200 K. From the heat content data, the corresponding C_p above 298 K, of α-Nd_5Si_9 and β-Nd_5Si_9 were calculated as a function of temperature. The experimental C_p, $H_T - H_{298}$ and corresponding ΔS^{o}_{298} are presented in Figs. 20 to 22, respectively. Meschel and Kleppa [56, 77] measured the ΔH^{o}_{298} of $NdSi_2$, NdSi and Nd_5Si_3 using direct synthesis calorimetry; the experimental ΔH^{o}_{298} are presented in Fig. 23. In addition, the $H_{1273} - H_{298}$ of Nd_5Si_3 and the $H_{1473} - H_{298}$ of NdSi and $NdSi_2$ are shown in Fig. 21. The Gibbs energy of formation of the

$NdSi_{1.78}$ at 1000 K was determined by Polotskaya and Buyanov [78] by measuring the emf; their data are presented in Fig. 24.

An extensive literature review (up to 1989) of the Si-Nd system was performed by Gokhale et al. [79]. No previous thermodynamic optimization was performed. The six intermetallic compounds, Nd_5Si_9, Nd_2Si_3, Nd_3Si_4, NdSi, Nd_5Si_4 and Nd_5Si_3 were modeled according to the work of Eremenko et al. [74]. The non-stoichiometric phase Nd_5Si_9 was treated as a line compound, as for the previous Si-Pr system. The optimized phase diagram is presented in Fig. 19 along with experimental data [74-76]. The calculated phase diagram agrees reasonably well with the experimental data but the liquidus between about 0.2 and 0.3 and near 0.6 mole fraction Nd, and the eutectic between Nd_5Si_9 and NdSi, are not well reproduced. Like the Si-Pr system, a small solubility of Si in Nd (bcc-A2) was modeled using one small temperature independent parameter to reproduce the transition temperature between Nd (dhcp) and Nd (bcc-A2) [74]. As there were no thermodynamic data for the liquid phase, the interaction parameters for the liquid phase were first set to be similar to the values found for the Si-Pr liquid. Then, the interaction parameters were slightly changed to reproduce the phase diagram and other thermodynamic data, simultaneously. The C_p above 298 K of α-Nd_5Si_9 and β-Pr_5Si_9 reported by Gorbachuk and Bolgar [75] were applied as shown in Fig. 20 and the C_p of the remaining compounds were approximated by the NK rule. The corresponding heat contents of Nd_5Si_9, Nd_5Si_3 and NdSi are also presented in Fig. 21. The allotropic transition temperature between α-Pr_5Si_9 and β-Pr_5Si_9 was considered as 154 ºC after Gorbachuk [76]. The enthalpy of transition was increased by 200 J mol^{-1} from that reported by Gorbachuk [76] to make the low temperature stable phase, α-Nd_5Si_9, appear. For the compounds, all the experimental ΔH^{o}_{298} [56, 77] and S^{o}_{298} [75] were accepted as is and the compounds without any experimental ΔH^{o}_{298} and S^{o}_{298} were determined by considering them as adjustable parameters to reproduce the phase diagram and other available thermodynamic data as seen in Figs. 22 and 23. However, the calculated ΔG^{o}_{1000} of Nd_5Si_9 was about 9 kJ mol^{-1} (based on one mole of Si-Nd) higher than the emf data of Polotskaya and Buyanov [78] as seen in Fig. 24. Since ΔH^{o}_{298}, S^{o}_{298} and C_p of Nd_5Si_9 are known, the Gibbs energy of formation of Nd_5Si_9 can be calculated from these values. In other words, the Gibbs energy of formation determined by Polotskaya and Buyanov [78]

(using emf measurements) is inconsistent with the other data. All obtained thermodynamic parameters are listed in Table 7 and the calculated invariant reactions with the experimental data are tabulated in Table 8.

Table 7. Optimized model parameters of the Si-Nd system.

Phase	Thermodynamic parameters
Liquid	Coordination Numbers
	i j Z_{ij}^{i} Z_{ij}^{j}
	Si Nd 6 6
	Δg_{SiNd} / (J mol^{-1}) = (-57739.2 + 8.368 T/K) + (-27196.0 + 10.46 T/K) X_{SiSi} + (2092.0 – 5.0208 T/K) X_{SiSi}^{2} + (-12552.0 + 6.276 T/K) X_{NdNd} + 3138.0 X_{NdNd}^{2}
α-Nd_5Si_9	ΔH_{298}° = -887500 J mol^{-1}, S_{298}° = 457.0 J K^{-1} mol^{-1}
	C_p / (J K^{-1} mol^{-1}) = 354.25 + 0.00019 T/K - 2177220 (T/K)$^{-2}$
β- Nd_5Si_9	$\Delta_{\mathrm{trs}}H^{\alpha\rightarrow\beta}$ = 4200 J mol^{-1}, $T_{\mathrm{trs}}^{\alpha\rightarrow\beta}$ = 427.0 K
	C_p / (J K^{-1} mol^{-1}) = 401.95 + 0.046 T/K - 4504355 (T/K)$^{-2}$
α-Nd_2Si_3	ΔH_{298}° = -350000 J mol^{-1}, S_{298}° = 163.25 J K^{-1} mol^{-1}
	C_p / (J K^{-1} mol^{-1}) = 2 × C_p / (J K^{-1} mol^{-1}) (Nd, dhcp) + 3 × C_p / (J K^{-1} mol^{-1}) (Si, diamond-A4)
β-Nd_2Si_3	$\Delta_{\mathrm{trs}}H^{\alpha\rightarrow\beta}$ = 5000 J mol^{-1}, $T_{\mathrm{trs}}^{\alpha\rightarrow\beta}$ = 803.0 K
	C_p / (J K^{-1} mol^{-1}) = 2 × C_p / (J K^{-1} mol^{-1}) (Nd, dhcp) + 3 × C_p / (J K^{-1} mol^{-1}) (Si, diamond-A4)
Nd_3Si_4	ΔH_{298}° = -508000 J mol^{-1}, S_{298}° = 236.02 J K^{-1} mol^{-1}
	C_p / (J K^{-1} mol^{-1}) = 3 × C_p / (J K^{-1} mol^{-1}) (Nd, dhcp) + 4 × C_p / (J K^{-1} mol^{-1}) (Si, diamond-A4)
NdSi	ΔH_{298}° = -157400 J mol^{-1}, S_{298}° = 69.9 J K^{-1} mol^{-1}
	C_p / (J K^{-1} mol^{-1}) = 1 × C_p / (J K^{-1} mol^{-1}) (Nd, dhcp) + 1 × C_p / (J K^{-1} mol^{-1}) (Si, diamond-A4)
Nd_5Si_4	ΔH_{298}° = -668000 J mol^{-1}, S_{298}° = 347.2 J K^{-1} mol^{-1}
	C_p / (J K^{-1} mol^{-1}) = 5 × C_p / (J K^{-1} mol^{-1}) (Nd, dhcp) + 4 × C_p / (J K^{-1} mol^{-1}) (Si, diamond-A4)
Nd_5Si_3	ΔH_{298}° = -498400 J mol^{-1}, S_{298}° = 366.0 J K^{-1} mol^{-1}
	C_p / (J K^{-1} mol^{-1}) = 5 × C_p / (J K^{-1} mol^{-1}) (Nd, dhcp) + 3 × C_p / (J K^{-1} mol^{-1}) (Si, diamond-A4)

Table 8. Calculated invariant reactions and experimental data in the Si-Nd system.

Type	Reaction	t (°C)	Reference
Eutectic	$L_{(X_{Nd}=0.156)} \rightarrow Si_{(dia.\text{-}A4,\ X_{Nd}=0)} + Nd_5Si_9$	1207.1	This work
	$L_{(X_{Nd}=0.17)} \rightarrow Si_{(dia.\text{-}A4,\ X_{Nd}=0)} + Nd_5Si_9$	1197.0	[74]
	T_m of $NdSi_2$	1525.0	[48]
Congruent	$L_{(X_{Nd}=0.357)} \leftrightarrow Nd_5Si_9$	1739.7	This work
	$L_{(X_{Nd}=0.357)} \leftrightarrow Nd_5Si_9$	1757.0	[74]
	T_m of Nd_5Si_9	1728 ± 35	[75]
Allotropic	$\alpha\text{-}Nd_5Si_9 \leftrightarrow \beta\text{-}Nd_5Si_9$	154.0	This work
	$\alpha\text{-}Nd_5Si_9 \leftrightarrow \beta\text{-}Nd_5Si_9$ (Si-rich composition)	97.0	[74]
	$\alpha\text{-}Nd_5Si_9 \leftrightarrow \beta\text{-}Nd_5Si_9$ (Nd-rich composition)	147.0	[74]
	$\alpha\text{-}Nd_5Si_9 \leftrightarrow \beta\text{-}Nd_5Si_9$	125.0	[75]
	$\alpha\text{-}Nd_5Si_9 \leftrightarrow \beta\text{-}Nd_5Si_9$	154.0	[76]
Peritectoid	$Nd_5Si_9 + NdSi \rightarrow Nd_2Si_3$	1505.9	This work
	$Nd_5Si_9 + NdSi \rightarrow Nd_2Si_3$	1507.0	[74]
Allotropic	$\alpha\text{-}Nd_2Si_3 \leftrightarrow \beta\text{-}Nd_2Si_3$	530.0	This work
	$\alpha\text{-}Nd_2Si_3 \leftrightarrow \beta\text{-}Nd_2Si_3$	527.0	[74]
Peritectoid	$Nd_2Si_3 + NdSi \rightarrow Nd_3Si_4$	1395.8	This work
	$Nd_2Si_3 + NdSi \rightarrow Nd_3Si_4$	1397.0	[74]
Eutectic	$L_{(X_{Nd}=0.444)} \rightarrow Nd_5Si_9 + NdSi$	1631.6	This work
	$L_{(X_{Nd}=0.444)} \rightarrow Nd_5Si_9 + NdSi$	1577.0	[74]
Congruent	$L_{(X_{Nd}=0.50)} \leftrightarrow NdSi$	1674.5	This work
	$L_{(X_{Nd}=0.50)} \leftrightarrow NdSi$	1677.0	[74]
Peritectic	$NdSi + L_{(X_{Nd}=0.591)} \rightarrow Nd_5Si_4$	1564.5	This work
	$NdSi + L_{(X_{Nd}=0.640)} \rightarrow Nd_5Si_4$	1567.0	[74]
Peritectic	$Nd_5Si_4 + L_{(X_{Nd}=0.654)} \rightarrow Nd_5Si_3$	1459.2	This work
	$Nd_5Si_4 + L_{(X_{Nd}=0.685)} \rightarrow Nd_5Si_3$	1447.0	[74]
Eutectic	$L_{(X_{Nd}=0.90)} \rightarrow Nd_5Si_3 + Nd_{(dhcp,\ X_{Nd}=1)}$	792.2	This work
	$L_{(X_{Nd}=0.875)} \rightarrow Nd_5Si_3 + Nd_{(dhcp,\ X_{Nd}=1)}$	792.0	[74]
Catatectic	$Nd_{(bcc\text{-}A2,\ X_{Nd}=0.996)} \rightarrow L_{(X_{Nd}=0.923)} + Nd_{(dhcp,\ X_{Nd}=1)}$	841.2	This work

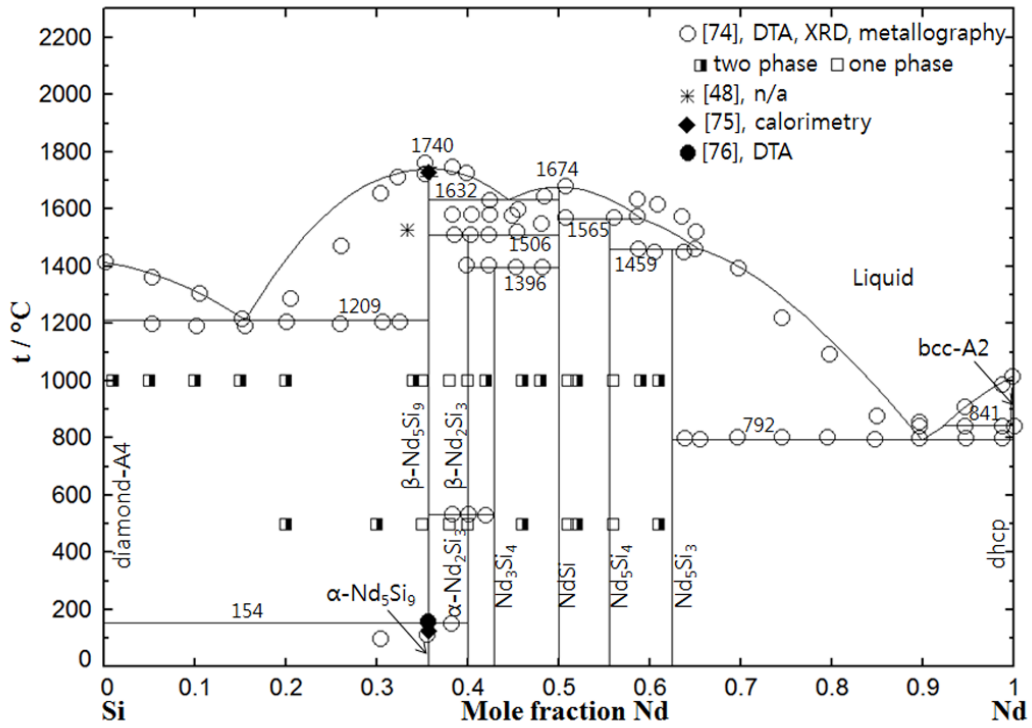


Fig. 19. The optimized Si-Nd phase diagram with experimental data.

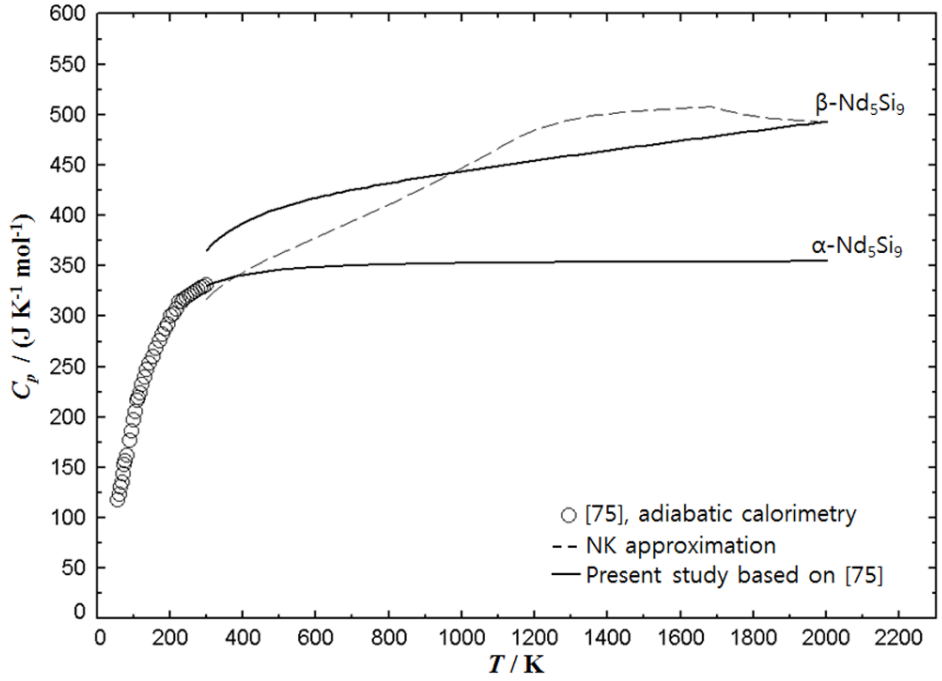


Fig. 20. Heat capacities of the Nd_5Si_9 phases with experimental data.

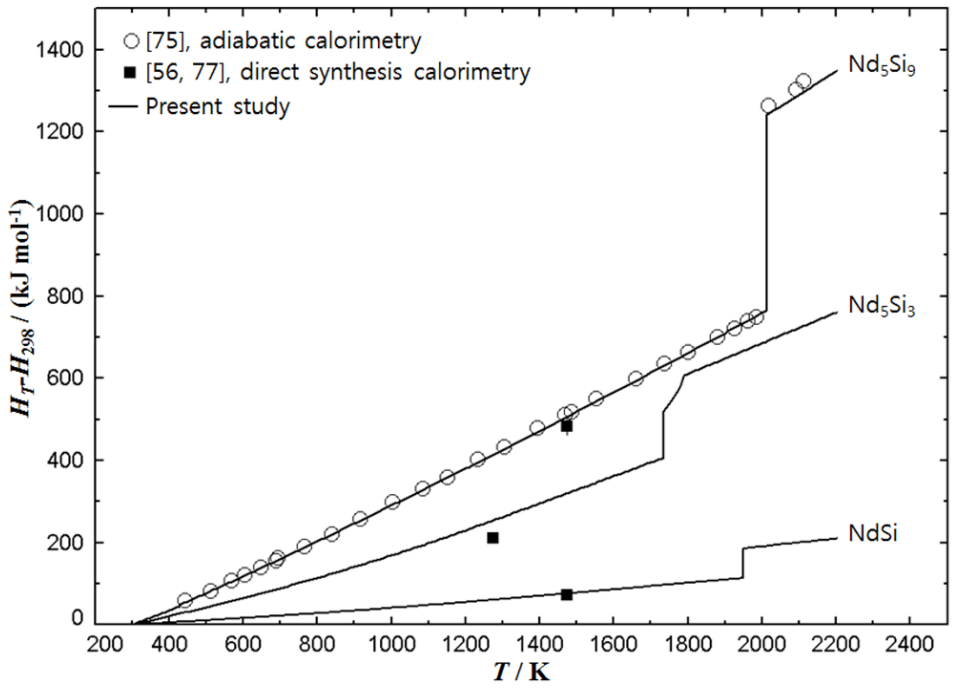


Fig. 21. Heat contents of the compounds in the Si-Nd system with experimental data.

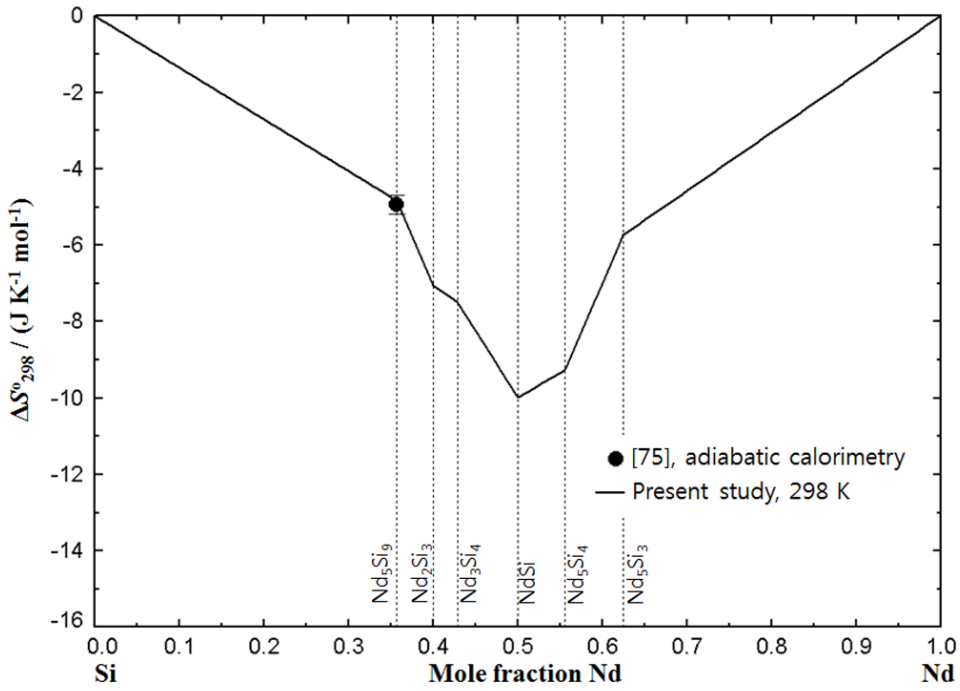


Fig. 22. Entropy of formation of the compounds in the Si-Nd system from elements at 298 K with experimental data.

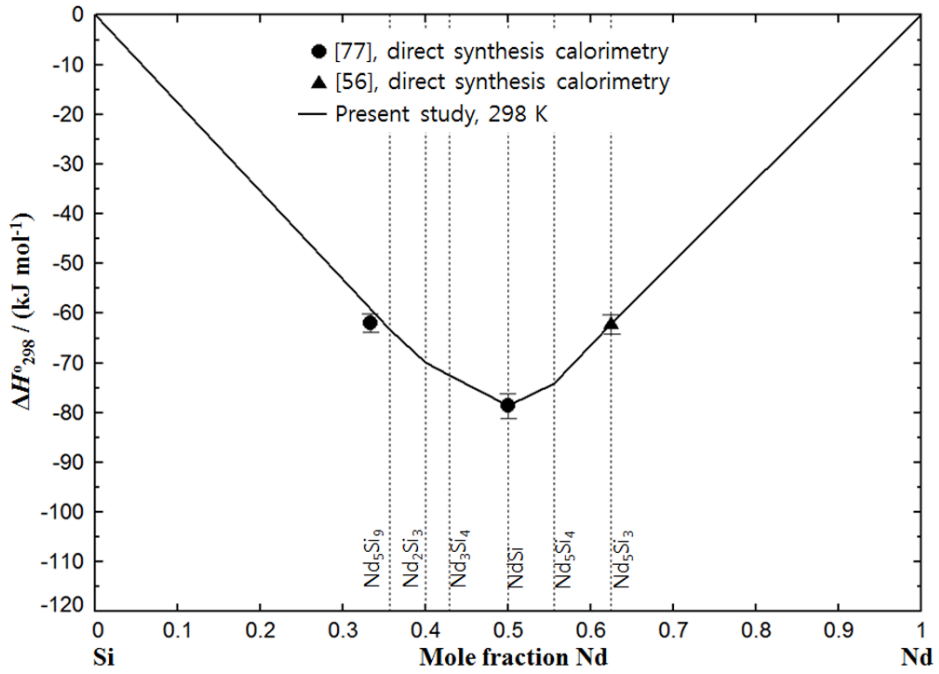


Fig. 23. Enthalpy of formation of the compounds in the Si-Nd system at 298 K with experimental data.

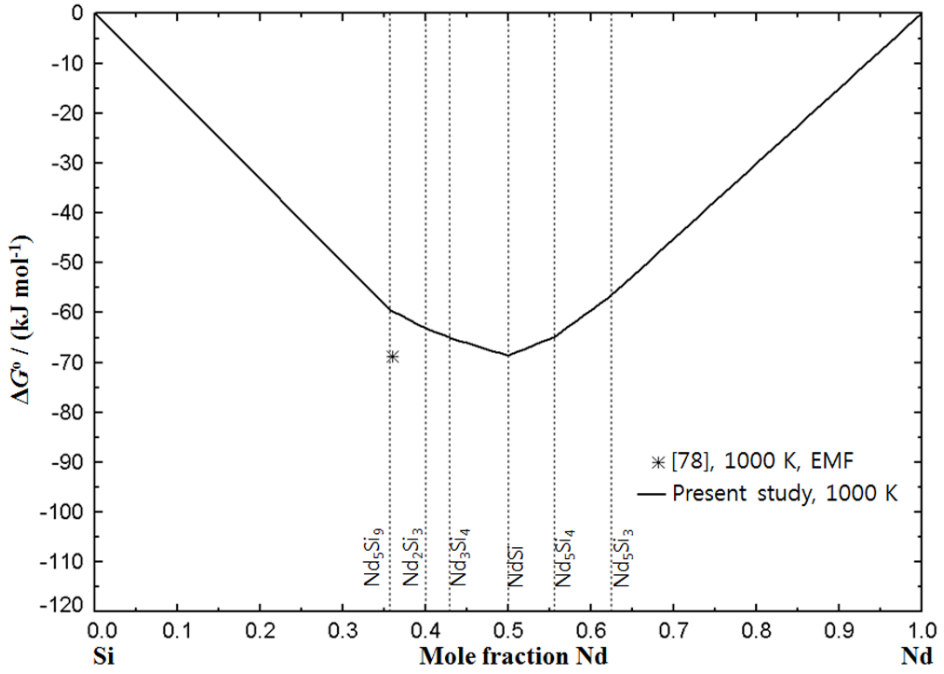


Fig. 24. Gibbs energy of formation of the compounds in the Si-Nd system at 1000 K with experimental data.

3.5. The Si-Sm system

The phase diagram of the Si-Sm system is not well investigated yet. A literature review of this system was performed by Gokhale and Abbaschian [80]. Five intermetallic compounds, Sm_5Si_3, Sm_5Si_4, SmSi, Sm_3Si_5 and $SmSi_2$ were reported from crystallographic studies. Regarding phase equilibria, very few experimental data are available in the literature. The eutectic in the Sm and Si-rich corners were found to lie at about 880 ºC and 0.85 mol fraction Sm [81] and at about 1213 ºC and 0.11 mole fraction Sm [82], respectively, by means of DTA, XRD and metallography. The polymorphic transition of $SmSi_2$ was determined to be 380 ± 40 ºC by using high temperature XRD [69]. Later, the melting temperature and polymorphic transition of $SmSi_2$ were reported to be 1627 ± 30 ºC and 415 ± 10 ºC, respectively, by Gorbachuk and Bolgar [75] using heat content measurements. Gorbachuk and Kirienko [83] reinvestigated the polymorphic transformation of $SmSi_2$ using a quantitative DTA and corrected the transformation temperature as 385 ºC. Available experimental data for the phase diagram of Si-Sm system are shown in Fig. 25.

There are no available thermodynamic data for the liquid solution. For the intermetallic compounds, the low temperature C_p of $SmSi_2$ was measured by Gorbachuk and Bolgar [75] using adiabatic calorimetry and the S^o_{298} was derived from these data. In addition, the authors measured the heat content ($H_T - H_{298}$) of $SmSi_2$ using the same techniques which were employed to measure the heat content of Nd_5Si_9. The corresponding C_p above 298 K of α-$SmSi_2$ and β-$SmSi_2$ were provided as functions of temperature. The experimental C_p, $H_T - H_{298}$, and corresponding ΔS^o_{298} are presented in Figs. 26 to 28, respectively. Meschel and Kleppa [56] measured the ΔH^o_{298} of $SmSi_2$, SmSi and Sm_5Si_3 using direct synthesis calorimetry. The $H_{1273} - H_{298}$ of Sm_5Si_3, SmSi and $SmSi_2$ were also reported as shown in Fig. 27.

No thermodynamic optimization was performed previously. In the present study, the phase diagram of the Si-Sm system was built by using the systematic changes observed in the phase diagrams of all Si-RE (RE = light rare earth) systems. As it is well known, there is a systematic

trend in the phase diagram and thermodynamic properties of RE alloy systems. In this study, the melting temperatures of Sm silicides were assumed to be slightly higher than the melting temperatures of other light RE silicides. The melting temperatures of RE silicides (La to Sm: light RE; Gd and Tb: heavy RE) are shown in Fig. 30. Due to the abnormal properties of Eu among the light RE series, Sm is considered as the last light RE element. As seen in the figure, the melting temperatures of light RE silicides increase gradually along the RE series. In addition, $RESi_x$ (0.625-0.67 mole fraction Si) have the highest melting temperature in the Si-light RE systems. It was also found that the compound which has the highest melting temperature shifts from the lowest RE-containing compound to the highest RE-containing compound in the Si-heavy RE systems. In other words, the stability of intermediate solid phases is gradually increasing from the Si-rich side to RE-rich side along the RE series. Even in the light RE systems, this trend can be captured. Therefore, the melting temperature of Sm_3Si_5 and SmSi were assumed to be similar in this study. The enthalpy of mixing of the liquid solution was assumed to be similar to the previous four light RE systems. The interaction parameters were slightly changed to reproduce the experimental eutectic temperatures [81, 82]. However, the eutectic compositions [81, 82] were too far from those seen in other Si-RE systems and as a result, these were neglected in this study. The C_p above 298 K of α- and β-$SmSi_2$ reported by Gorbachuk and Bolgar [75] were employed and the C_p of the remaining compounds were approximated by the NK rule. The polymorphic transformation temperature and enthalpy of transformation of α- and β-$SmSi_2$ were fixed at 385 ºC and 1384 J mol^{-1}, respectively, accepting the works of Gorbachuk and Kirienko [83]. The calculated phase diagram and thermodynamic properties are presented in Figs. 25 to 29 along with experimental data. The optimized thermodynamic parameters are listed in Table 9 and the calculated invariant reactions with the experimental data are tabulated in Table 10.

Table 9. Optimized model parameters of the Si-Sm system.

Phase	Thermodynamic parameters
Liquid	Coordination Numbers
	i j Z_{ij}^{i} Z_{ij}^{j}
	Si Sm 6 6
	Δg_{SiSm} / (J mol^{-1}) = (-57739.2 + 8.368 T/K) + (-48116.0 + 8.368 T/K) X_{SiSi}
	+ 17572.8 X_{SiSi}^{2} + (-12552.0 + 6.276 T/K) X_{SmSm}
	+ 1255.2 X_{SmSm}^{2}
α-$SmSi_2$	ΔH_{298}° = -198000 J mol^{-1}, S_{298}° = 93.4 J K^{-1} mol^{-1}
	C_p / (J K^{-1} mol^{-1}) = 79.72 + 0.020746 T/K - 1309740 (T/K)$^{-2}$
β-$SmSi_2$	$\Delta_{\mathrm{trs}}H^{\alpha\rightarrow\beta}$ = 1384 J mol^{-1}, $T_{\mathrm{trs}}^{\alpha\rightarrow\beta}$ = 658.0 K
	C_p / (J K^{-1} mol^{-1}) = 82.95 + 0.016934 T/K - 414251 (T/K)$^{-2}$
Sm_3Si_5	ΔH_{298}° = -551000 J mol^{-1}, S_{298}° = 276.0 J K^{-1} mol^{-1}
	C_p / (J K^{-1} mol^{-1}) = 3 × C_p / (J K^{-1} mol^{-1}) (Sm, rhombohedral)
	+ 5 × C_p / (J K^{-1} mol^{-1}) (Si, diamond-A4)
SmSi	ΔH_{298}° = -159400 J mol^{-1}, S_{298}° = 70.7 J K^{-1} mol^{-1}
	C_p / (J K^{-1} mol^{-1}) = 1 × C_p / (J K^{-1} mol^{-1}) (Sm, rhombohedral)
	+ 1 × C_p / (J K^{-1} mol^{-1}) (Si, diamond-A4)
Sm_5Si_4	ΔH_{298}° = -670000 J mol^{-1}, S_{298}° = 350.0 J K^{-1} mol^{-1}
	C_p / (J K^{-1} mol^{-1}) = 5 × C_p / (J K^{-1} mol^{-1}) (Sm, rhombohedral)
	+ 4 × C_p / (J K^{-1} mol^{-1}) (Si, diamond-A4)
Sm_5Si_3	ΔH_{298}° = -536800 J mol^{-1}, S_{298}° = 344.0 J K^{-1} mol^{-1}
	C_p / (J K^{-1} mol^{-1}) = 5 × C_p / (J K^{-1} mol^{-1}) (Sm, rhombohedral)
	+ 3 × C_p / (J K^{-1} mol^{-1}) (Si, diamond-A4)

Table 10. Calculated invariant reactions and experimental data in the Si-Sm system.

Type	Reaction	t (°C)	Reference
Eutectic	$L_{(X_{Sm}= 0.170)} \rightarrow Si_{(dia.\text{-}A4,\ X_{Sm}= 0)} + SmSi_2$	1211.0	This work
	$L_{(X_{Sm}= 0.110)} \rightarrow Si_{(dia.\text{-}A4,\ X_{Sm}= 0)} + SmSi_2$	1213.0	[82]
Peritectoid	$L_{(X_{Sm}= 0.313)} + Sm_3Si_5 \rightarrow SmSi_2$	1611.5	This work
Allotropic	T_m of $SmSi_2$	1617 ± 30	[75]
	$\alpha\text{-}SmSi_2 \leftrightarrow \beta\text{-}SmSi_2$	385.0	This work
	$\alpha\text{-}SmSi_2 \leftrightarrow \beta\text{-}SmSi_2$	380 ± 40	[69]
	$\alpha\text{-}SmSi_2 \leftrightarrow \beta\text{-}SmSi_2$	415 ± 10	[75]
	$\alpha\text{-}SmSi_2 \leftrightarrow \beta\text{-}SmSi_2$	385.0	[83]
Congruent	$L_{(X_{Sm}= 0.375)} \leftrightarrow Sm_3Si_5$	1688.9	This work
Eutectic	$L_{(X_{Sm}= 0.434)} \rightarrow Sm_3Si_5 + SmSi$	1620.7	This work
Congruent	$L_{(X_{Sm}= 0.50)} \leftrightarrow SmSi$	1684.5	This work
Peritectic	$SmSi + L_{(X_{Sm}= 0.595)} \rightarrow Sm_5Si_4$	1593.7	This work
Peritectic	$Sm_5Si_4 + L_{(X_{Sm}= 0.660)} \rightarrow Sm_5Si_3$	1510.0	This work
Eutectic	$L_{(X_{Sm}= 0.915)} \rightarrow Sm_5Si_3 + Sm_{(rhom.,\ X_{Sm}= 1)}$	884.8	This work
	$L_{(X_{Sm}= 0.850)} \rightarrow Sm_5Si_3 + Sm_{(rhom.,\ X_{Sm}= 1)}$	880.0	[81]

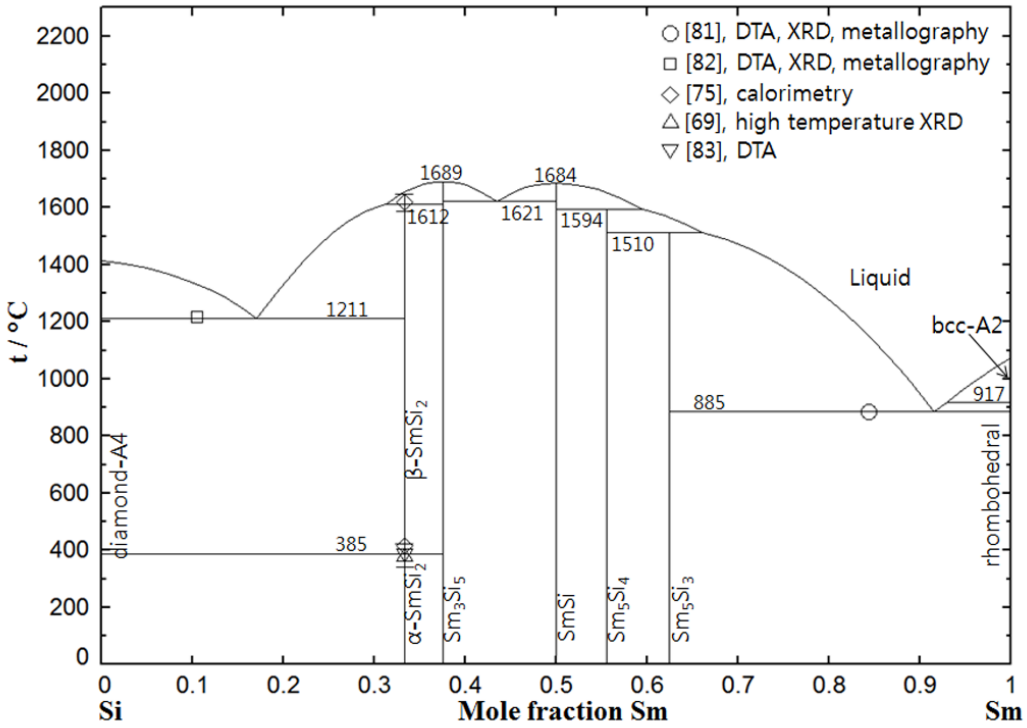


Fig. 25. The optimized Si-Sm phase diagram with experimental data.

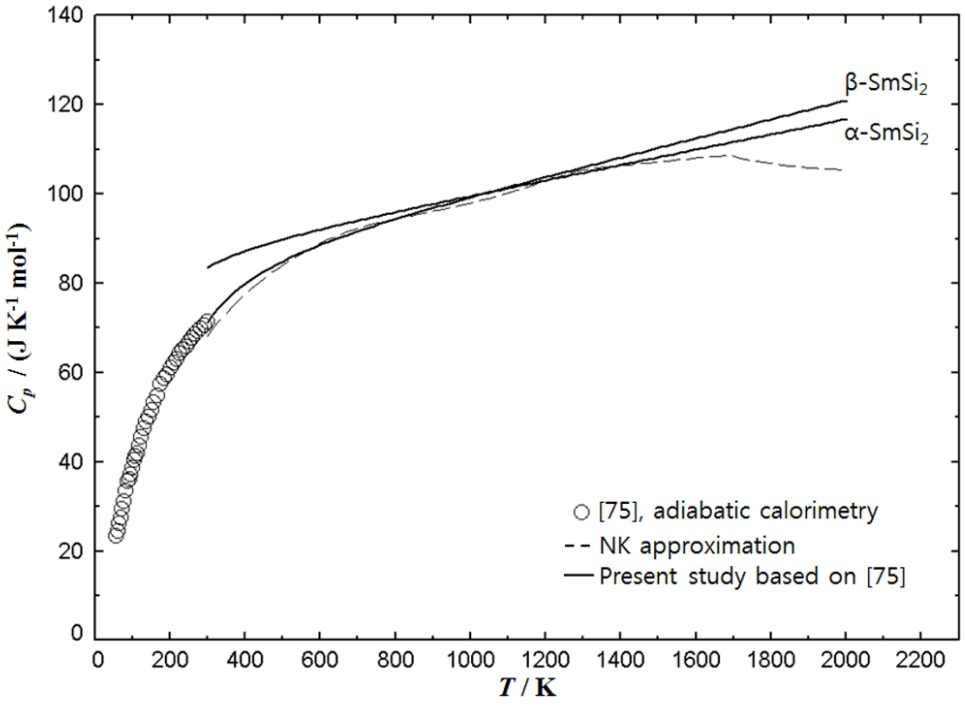


Fig. 26. Heat capacities of the $SmSi_2$ phases with experimental data.

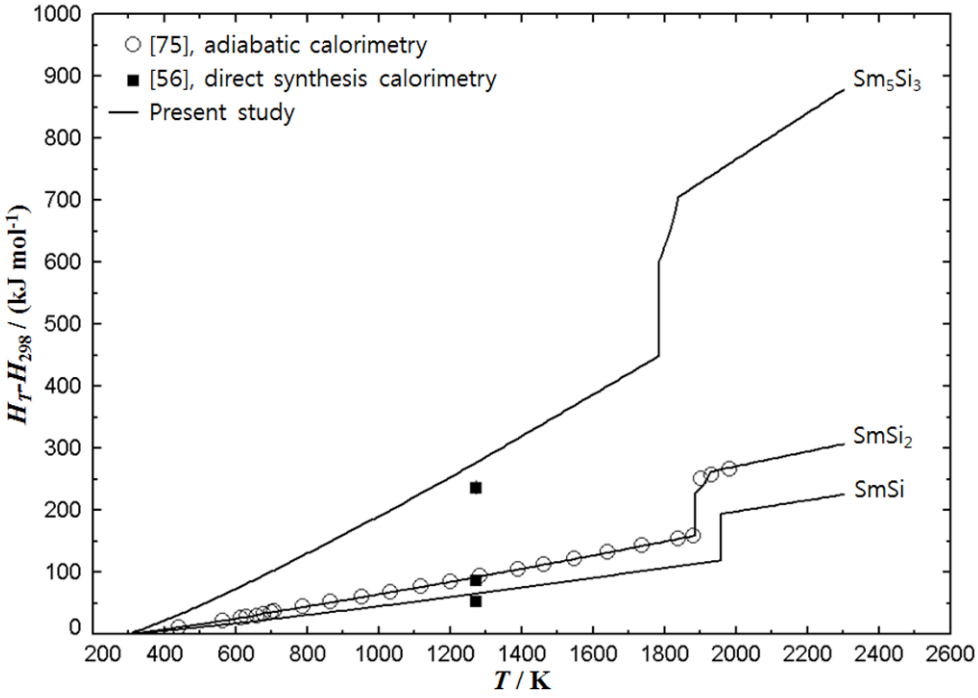


Fig. 27. Heat contents of the compounds in the Si-Sm system with experimental data.

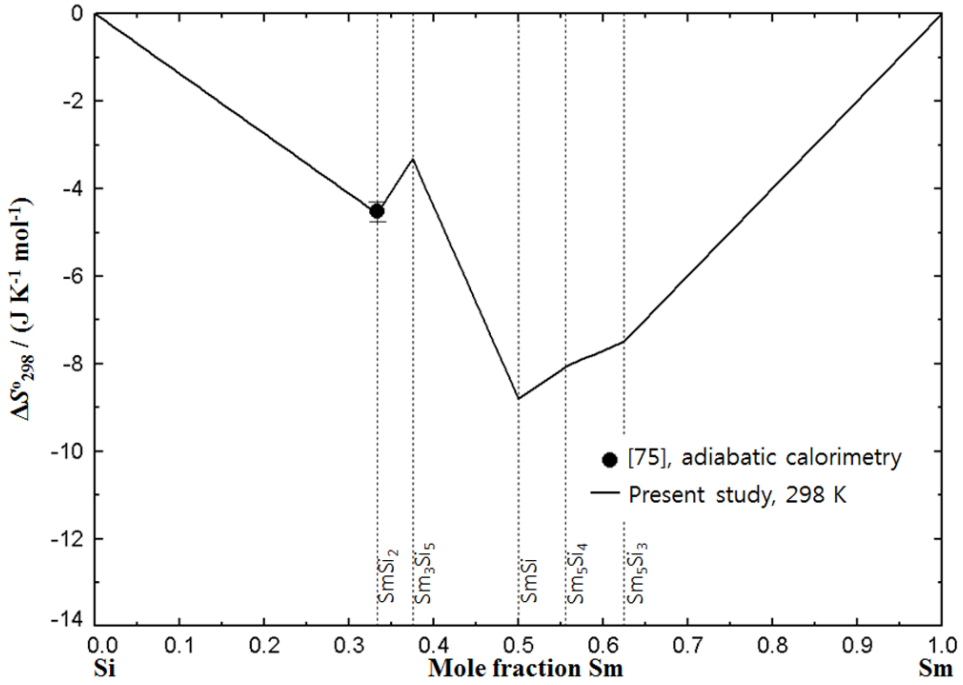


Fig. 28. Entropy of formation of the compounds in the Si-Sm system from elements at 298 K with experimental data.

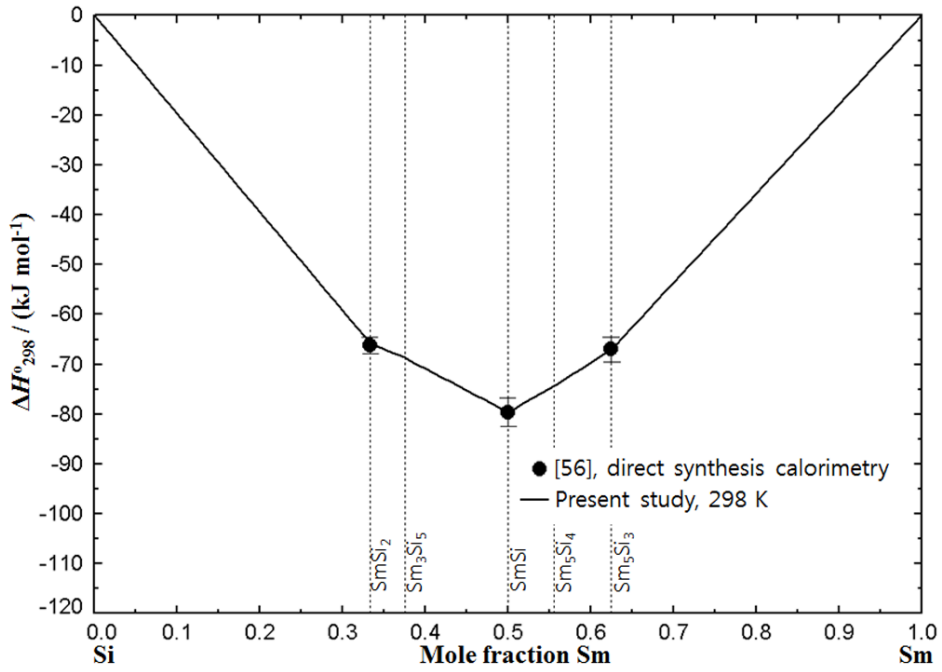


Fig. 29. Enthalpy of formation of the compounds in the Si-Sm system at 298 K with experimental data.

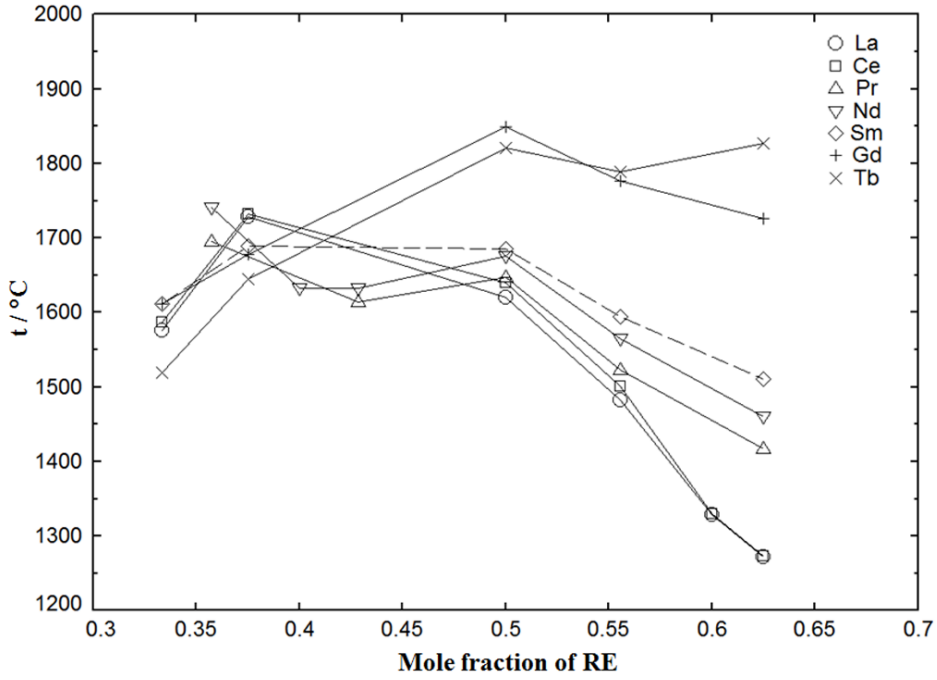


Fig. 30. The comparison of the melting temperatures of various rare earth silicides. The values are based on experimental data of each binary Si-RE system except for the Si-Sm system.

4. Discussion

4.1. Eutectic reaction between RESi and RE_3Si_5 (or RE_5Si_9)

The experimental eutectic temperatures between La_3Si_5 and LaSi, Ce_3Si_5 and CeSi, Pr_5Si_9 and PrSi, and Nd_5Si_9 and NdSi were difficult to be reproduced in this study. The calculated eutectic temperatures are higher than the experimental data by 50 to 80 ºC. Similar discrepancy in the eutectic temperature was obtained from the thermodynamic modeling by Shukla et al. [16] for the Si-Ce system. The liquidus slopes of RE_3Si_5 and RE_5Si_9 should be steeper than current calculations in order to reproduce the eutectic temperatures. The liquidus slope of a stoichiometric intermetallic compound is determined by the co-tangent line between the Gibbs energy of compound and the Gibbs energy of liquid phase. When the Gibbs energy of liquid changes smoothly with composition and temperature, the liquidus slopes of intermetallic compound at each side cannot be independent. That is, the liquidus slopes of left-side and right-side of intermetallic compound in particular near the intermetallic composition (near its melting temperature) cannot be changed independently. This was also illustrated by Okamoto [84] in his report as one of the cases of "Thermodynamically improbable phase diagrams"; he explained that a liquidus with a strongly asymmetric form is unlikely because an abrupt change in the composition dependence of the Gibbs energy of the liquid phase would be required at the composition of the compound. Of course, when the curvature of the Gibbs energy of liquid phase changes sharply at the intermetallic composition, the liquidus slope of compound in each side can be changed more independently.

Liquid phase of all Si-RE system shows the minimum Gibbs energy of mixing near RESi composition. In the present modeling, the slope of RESi compound is reasonably reproduced in all binary systems. However, it was difficult to reproduce the slopes of RE_3Si_5 and RE_5Si_9 adjacent to RESi. For example, Fig. 31 shows the calculated phase diagrams of the Ce-Si and Pr-Si systems along with the experimental liquidus of Ce_3Si_5 and Pr_5Si_9. Although the experimental slope of Ce_3Si_5 on the Si-rich side is reasonably reproduced in the present study, the experimental liquidus on the Ce-rich side is steeper than the current calculation by more than twice. The same is true for the La-Si system. In order to reproduce such a drastic change of liquidus slope, the temperature

dependence of the liquid Gibbs energy (that is, entropy) around Ce_3Si_5 composition should be changed drastically. This is very difficult to be described. In the case of Pr-Si system, the experimental liquidus of Pr_5Si_9 is straight, which is also very difficult to be reproduced. Theoretically, the liquidus slope of the intermetallic compound should be zero at its stoichiometric composition. Such a sharp liquidus slope can be happened if the enthalpy of liquid at the composition is very negative, and very strong short range ordering in liquid occurs. However, in the present evaluation, we could not find strong evidence to support this. More experiments would be required to investigate the phase diagrams of Si-RE (light RE) systems in particular at the composition range between 0.4 and 0.5 mole fraction of RE.

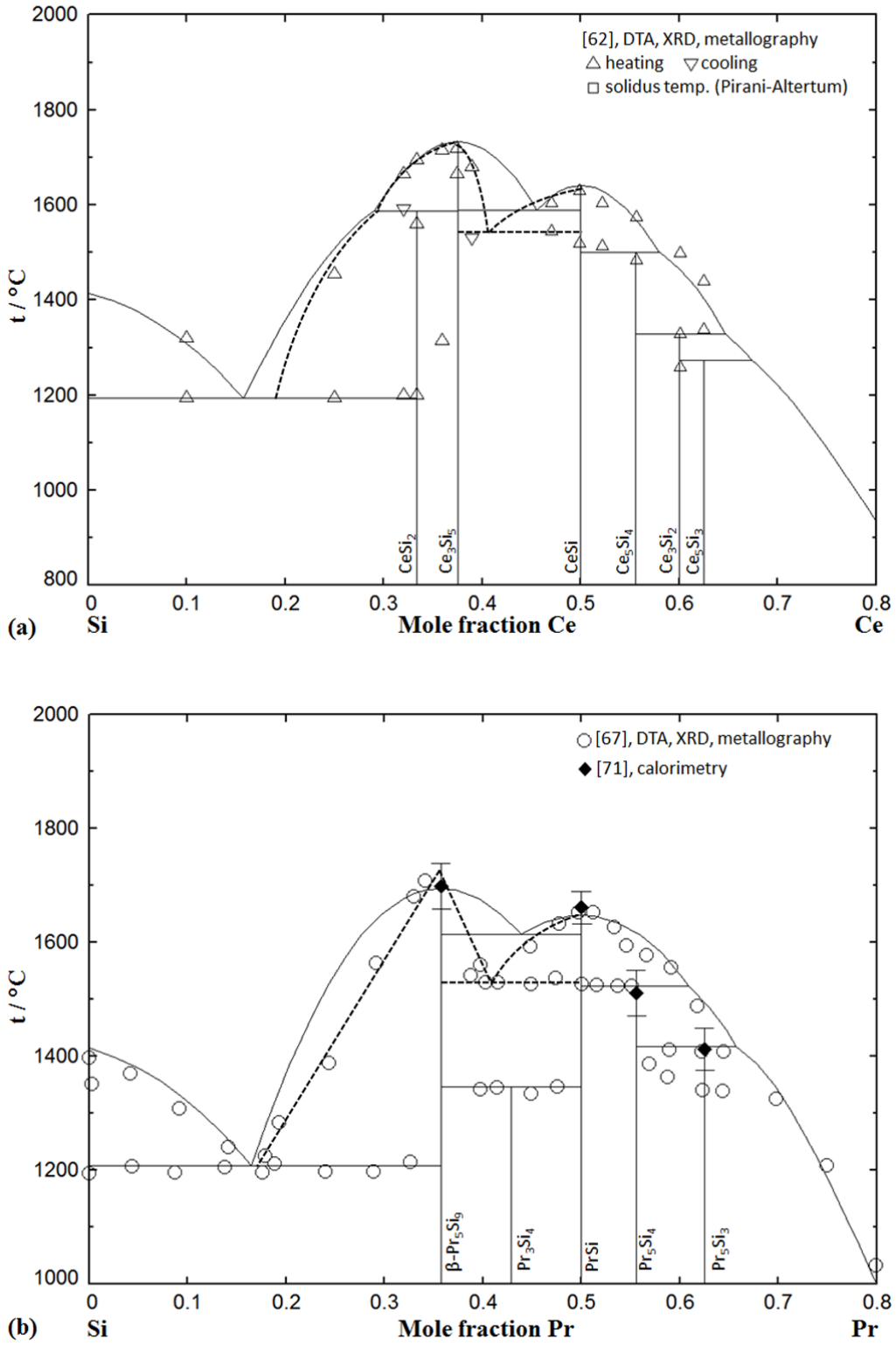


Fig. 31. Phase diagrams of (a) Si-Ce and (b) Si-Pr systems; solid lines: calculated from the present study and dotted lines: proposed by experimental studies [62, 67].

4.2. Limitation of current thermodynamic modeling

According to the present thermodynamic evaluation, the entropy of formation of solid Si-RE compounds is negative and the negative entropy of mixing of liquid Si-RE is also calculated. For example, the experimental data on the formation entropy of the Si-La system shows the negative value (see Fig. 5). Our evaluation for the entropy of mixing of liquid Si-La also shows negative entropy (see Fig. 50 in Part II of this study). Such negative entropy of mixing for liquid solution is also found in the previous assessments by Shukla et al. [16] for the Si-Ce system and Huang et al. [25] for the Si-Gd system. The entropy of mixing of a solution can be divided into configurational and non-configurational part. The configurational entropies of mixing for liquid Si-RE from the Modified Quasichemical Model (MQM) with the optimized model parameters are calculated using the Eq. (3) and presented in Fig. 32. The calculated configurational entropies of mixing for all Si-RE liquid at 2000 K are positive at the entire composition range (Fig. 32(a)). While, at 1473 K, the configurational entropy of mixing for certain liquid alloys such as Si-La, -Ce, -Nd, -Y, and -Lu are negative at 0.4 to 0.6 mole fraction of RE (Fig. 32(b)). At 873 K, the configurational entropies of mixing for all Si-RE liquids are negative at 0.35-0.65 mole fraction of RE (Fig. 32(c)). Although the negative configurational entropy can be only calculated at the composition and temperature where the liquid phase is metastable state (see all Si-RE phase diagrams), theoretically the negative configurational entropy is unrealistic. This is a drawback of the MQM when large negative model parameters are used. In the formulation of MQM model, the distribution of configurational and non-configurational entropy are not properly managed. When the solution is deviated very negatively from ideal behavior, like the present liquid Si-RE solution, the configurational entropy term is negatively overestimated from the MQM especially at low temperature, although the total entropy of solution is still correctly calculated.

Previously, Hillert et al. [85] pointed out that the MQM with coordination number other than '2' can result in negative configurational entropy when the model parameter becomes too negative. They proposed the correction of configurational entropy of MQM, which makes the configurational entropy positive even when interaction parameters are very negative. Pelton and Kang [86] also proposed the correction of configurational entropy of MQM by distributing the

negative interaction parameters (excess parameters) to both Bragg-Williams random mixing model (BWRMM) and MQM parameters. That is, this correction can help the configurational entropy of solution to be in between the BWRMM and classical MQM entropy (using only MQM interaction parameter) depending on the contribution of each interaction parameter terms. In the present study, these corrections were not used.

Several studies [16, 24-26] with description of liquid solution by the BWRMM have been made to access the Si-RE systems. For example, Gröbner et al. [24] and Huang et al. [25] performed the thermodynamic assessments of Si-Ce and Si-Gd system, respectively. In the study of Gröbner et al., both phase diagram and enthalpy data of liquid solution were not well reproduced. In Huang et al.'s work on the Si-Gd system, they used a large temperature dependent term in BWRMM to reproduce the phase diagram and enthalpy of liquid phase reasonably. According to their model parameters, the entropy of mixing at 2000 K for liquid Si-Gd solution becomes about -10 J K^{-1} mol^{-1} at 0.6 mole fraction of Gd, which is similar to our evaluation, about -8 J K^{-1} mol^{-1} (see part II of this work). As mentioned above, in order to describe the Si-RE system, negative entropy of mixing of liquid solution is required. However, in the case of BWRMM, the configurational entropy is always ideal entropy regardless of negative interaction between atoms, which is unrealistic. As a result, a large negative excess entropy term is required to describe the liquid phase. This large excess entropy term can easily produce so-called inverse miscibility gap in liquid phase at high temperature. For example, although Huang et al. [25] did not discuss this problem, the liquid inverse miscibility gap is calculated above 4700 K from their model parameters (BWRMM). This is the main drawback of BWRMM for the solution deviated highly negative from ideal behavior. This inverse miscibility gap can be prevented if the liquid is described by the MQM.

Associate model is also frequently used for the solution deviated strongly negative from ideal behavior. The assumption of associate may give a reasonable description of the Gibbs energy of binary system. However, the assumption of real associate formation in solution can create another problem in configurational entropy. When associate formation energy becomes zero, the entropy cannot become that of ideal binary solution. Very positive formation energy is needed to nearly prevent the formation of associate and then ideal mixing entropy can be achieved. It was also

proven that the prediction ability of associate model for the Gibbs energy of ternary solution (with one binary is very negatively deviated from ideal solution and two others are close to ideal solutions) is less than the MQM [87].

In summary, the configurational entropy calculated from both the BWRMM and the MQM are not good enough to accurately describe the solution deviated strongly negative from ideal solution like Si-RE. The BWRMM assumes it is ideal regardless of negative interaction energy between Si and RE. The MQM overestimates the decrease of configurational entropy with decreasing of interaction energy at low temperature. In particular, the configurational entropy from the current MQM description can be calculated negative at low temperature and increases with increasing temperature to approach random mixing entropy. However, the MQM can more easily reproduce total Gibbs energy (entropy and enthalpy) of highly ordered solution (highly negative interactions between species). The MQM can also prevent liquid inverse miscibility gap in such solution which is often induced by the BWRMM with a large negative excess entropy term. Therefore, in spite of the drawback of configurational entropy description of MQM at low temperature, we have used MQM for liquid phase.

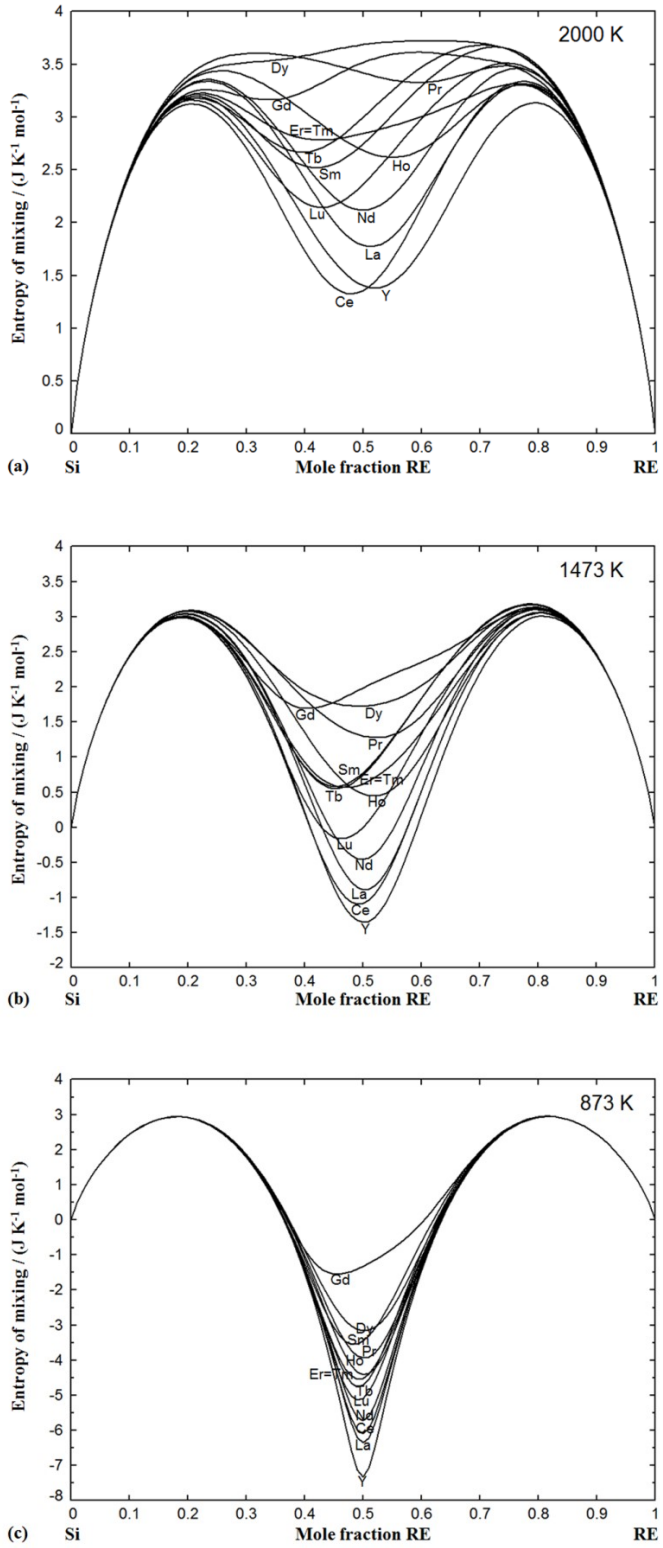


Fig. 32. Configurational entropy of mixing for Si-RE liquid at different temperatures: (a) 2000 K, (b) 1473 K, and (c) 873 K.

4.3. Model parameters for liquid Si-RE

The model parameters are determined to reproduce all available and reliable thermodynamic data and phase diagram data as close as possible. In the case of liquid, the excess Gibbs energy model parameters in Eq (9) can be determined to reproduce typically enthalpy (total and partial) of liquid phase and phase diagram once the Gibbs energy of solids are fixed. Typically, the enthalpy of liquid is less sensitive to the model parameters than the phase diagram. The error range of enthalpy data is easily about several kJ mol^{-1}, but the liquidus temperature can be changed largely (frequently more than 100 degree) by changing several kJ mol^{-1} of Gibbs energy.

In the all Si-RE system, the liquidus temperature changes from 800 ºC to 1800 ºC. In many Si-RE systems, the phase diagram data (liquidus) are available entire range of binary system. In order to accurately reproduce the phase diagram data over large temperature and composition ranges, and thermodynamic data related to liquid, many model parameters were used; typically 6 to 9 parameters including several temperature dependent terms are used for each binary liquid Si-RE solution, which is rather larger than our usual optimization. Many of these model parameters were optimized especially to reproduce the phase diagram accurately. The following two examples can show the effect of model parameters in phase diagram and Gibbs energy.

In the description of the Si-Ce liquid, 6 excess model parameters are used:

$$\Delta g_{\mathrm{SiCe}} / (\mathrm{J\ mol^{-1}}) = (-57739.2 + 4.184\ T/\mathrm{K}) - 21756.8\, X_{\mathrm{SiSi}} + (-15480.8 + 8.117\ T/\mathrm{K})\, X_{\mathrm{CeCe}} + 5020.8\, X_{\mathrm{CeCe}}^2 \quad (13)$$

The last parameter of X_{CeCe}^2 can change the thermodynamic property of liquid only at high Ce region. The changes of the enthalpy of liquid Si-Ce and the phase diagram of the Si-Ce system with and without this last parameter are presented in Fig. 33. Although the change in the enthalpy (and also Gibbs energy) is negligible (Fig. 33(a)), the eutectic temperature in Ce rich region can be changed by 100 ºC (Fig. 33(b)). Most of the Si-RE systems, the optimized parameters of X_{RERE}^2

and X_{SiSi}^2 are required to reproduce the phase diagram data more accurately in RE- and Si-rich region, respectively. If the accuracy of the phase diagram is scarified, each bianry system could reproduced even with only three major terms, $\Delta g_{\mathrm{SiRE}}^{\mathrm{o}}$, X_{SiSi} and X_{RERE} with one or two temperature dependent parameters.

The temperature dependent parameter of $\Delta g_{\mathrm{SiRE}}^{\mathrm{o}}$ in liquid Si-RE solution is necessary to simultaneously reproduce the phase diagram and enthalpy data of liquid. As mentioned above in section 4.2, the Si-RE liquid shows the negative excess entropy. This cannot be described without using temperature dependent parameters. Compared to the parameter of $\Delta g_{\mathrm{SiRE}}^{\mathrm{o}}$, other temperature dependent parameters associated to X_{SiSi} and X_{RERE} give minor effect to the thermodynamic properties of liquid phase, but again important to reproduce the phase diagram more accurately. For example, the influence of temperature dependent parameters in liquid Si-Pr to its Gibbs energy at 2000 K are calculated in Fig. 34.

$$\Delta g_{\mathrm{SiPr}} / (\mathrm{J\ mol^{-1}}) = (-57739.2 + 10.46\ T/\mathrm{K}) + (-21756.8 + 2.092\ T/\mathrm{K})\ X_{\mathrm{SiSi}} + 2092.0\ X_{\mathrm{SiSi}}^2 - (15480.8 + 3.473\ T/\mathrm{K})\ X_{\mathrm{PrPr}} + (6276.0 + 8.368\ T/\mathrm{K})\ X_{\mathrm{PrPr}}^2 \quad (14)$$

$$\Delta g_{\mathrm{SiPr}} / (\mathrm{J\ mol^{-1}}) = (-57739.2 + 10.46\ T/\mathrm{K}) - 21756.8\ X_{\mathrm{SiSi}} + 2092.0\ X_{\mathrm{SiSi}}^2 - 15480.8\ X_{\mathrm{PrPr}} + 6276.0\ X_{\mathrm{PrPr}}^2 \quad (15)$$

$$\Delta g_{\mathrm{SiPr}} / (\mathrm{J\ mol^{-1}}) = -57739.2 - 21756.8\ X_{\mathrm{SiSi}} + 2092.0\ X_{\mathrm{SiSi}}^2 - 15480.8\ X_{\mathrm{PrPr}} + 6276.0\ X_{\mathrm{PrPr}}^2 \quad (16)$$

The parameters in Eq. (14) are the optimized model parameters for liquid Si-Pr in this study. As can be seen in Fig. 34, the elimination of temperature dependent terms other than $\Delta g_{\mathrm{SiPr}}^{\mathrm{o}}$ (Eq. (15)) give insignificant change to the Gibbs energy of liquid Si-Pr. However, the removal of temperature

dependent parameter associate to Δg^{o}_{SiPr} (Eq. (16)) can largely change the Gibbs energy. The same trend can be calculated in all other Si-RE systems.

It is hard to find the physical meaning of each excess parameter for liquid Si-RE system obtained in this study. It can be said that the positive temperature dependent parameter of Δg^{o}_{SiRE} is required to reproduce negative excess entropy of liquid phase. As mentioned above, many other excess parameters were simply used to reproduce the phase diagram data as accurately as possible. No direct physical meaning can be assigned to these parameters. Because the phase diagram (liquidus) of each binary system were investigated only in one or two studies, it is hard to evaluate the accuracy of their data. So, we tried to reproduce them as close as possible using even relatively large number of model parameters.

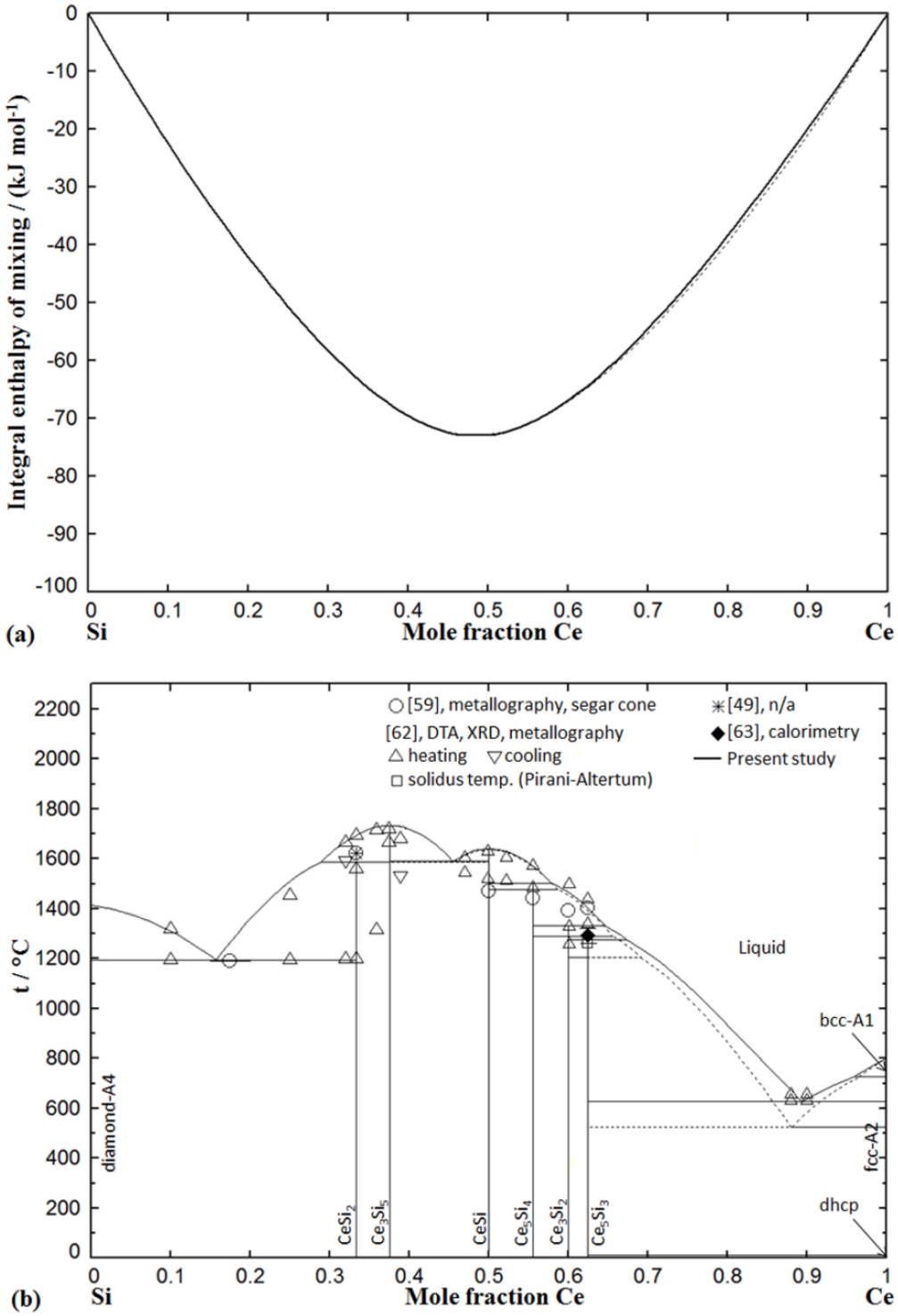


Fig. 33. (a) Enthalpy of mixing of Si-Ce liquid and (b) calculated phase diagrams of the Si-Ce system with optimized model parameters (solid lines) and modified parameters without X^2_{CeCe} term (dotted lines).

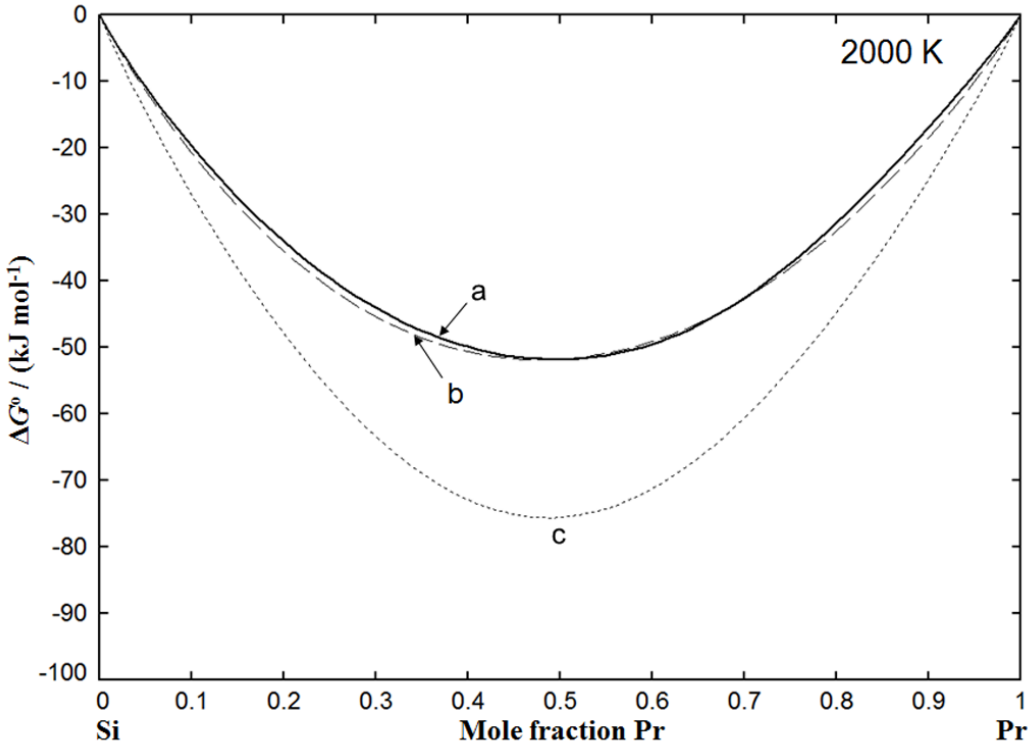


Fig. 34. Calculated Gibbs energy of mixing at 2000 K for liquid Si-Pr; line-a: calculated with Eq. (14), line-b: with Eq. (15), and line-c: with Eq. (16).

5. Conclusions

A critical evaluation and optimization of all available phase diagram and thermodynamic data of the Si-RE (RE = La, Ce, Pr, Nd and Sm) systems was conducted to obtain reliable thermodynamic functions for all the phases in the systems. The thermodynamic properties of the liquid phase were described using the Modified Quasichemical Model and the solid solution phases such as bcc and fcc were described using the one-sublattice Compound Energy Formalism.

In the thermodynamic modeling, it is found that the Si-RE systems follow a systematic trend and certain similarities in the phase diagrams and thermodynamic properties such as the enthalpy of formation of the compounds. This systematic analysis was applied to resolve inconsistencies in the experimental data in the present Si-RE systems and to predict the phase diagram of the Si-Sm system.

Acknowledgement

This project was supported by the National Sciences and Engineering Research Council of Canada (NSERC) Collaborative Research and Development grant and General Motors of Canada.

6. References

[1] Y. Liu, Mater. Chem. Phys., 31 (1992) 85-88.
[2] R.W. McCallum, In: Proc. Rare Earth Magnets and Their Applications, Newark, DE, US, Aug. 18-22, 2002. pp. 1-12.
[3] N. Stanford, D. Atwell, A. Beer, C. Davies, M.R. Barnett, Scripta Mater., 59 (2008) 772-775.
[4] N. Stanford, Mater. Sci. Eng., A, A527 (2010) 2669-2677.
[5] S. Sandloebes, S. Zaefferer, I. Schestakow, S. Yi, R. Gonzalez-Martinez, Acta Mater., 59 (2010) 429-439.
[6] H. Yan, S.W. Xu, R.S. Chen, S. Kamado, T. Honma, E.H. Han, Scripta Mater., 64 (2010) 141-144.
[7] S.A. Farzadfar, M. Sanjari, I.H. Jung, E. Essadiqi, S. Yue, Mater. Sci. Eng., A, 528 (2011) 6742-6753.
[8] Y.-B. Kang, A.D. Pelton, P. Chartrand, C.D. Fuerst, Calphad, 32 (2008) 413-422.
[9] P.J. Spencer, A.D. Pelton, Y.-B. Kang, P. Chartrand, C.D. Fuerst, Calphad, 32 (2008) 423-431.
[10] A. Shukla, Y.-B. Kang, A.D. Pelton, Calphad, 32 (2008) 470-477.
[11] Y.-B. Kang, C. Aliravci, P.J. Spencer, G. Eriksson, C.D. Fuerst, P. Chartrand, A.D. Pelton, JOM, 61 (2009) 75-82.
[12] L. Jin, Y.-B. Kang, P. Chartrand, C.D. Fuerst, Calphad, 34 (2010) 456-466.
[13] L.-L. Jin, Y.-B. Kang, P. Chartrand, C.D. Fuerst, Calphad, 35 (2011) 30-41.
[14] Y.-B. Kang, L. Jin, P. Chartrand, A.E. Gheribi, K. Bai, P. Wu, Calphad, 38 (2012) 100-116.
[15] L. Jin, D. Kevorkov, M. Medraj, P. Chartrand, J. Chem. Thermodyn., 58 (2013) 166-195.
[16] A. Shukla, Y.-B. Kang, A.D. Pelton, Int. J. Mater. Res., 100 (2009) 208-217.
[17] J. Kim, I.-H. Jung, J. Alloys Compd., 525 (2012) 191-201.
[18] J. Kim, I.H. Jung, Can. Metall. Q., 52 (2013) 311-320.
[19] A. Hussain, M.-A. Van Ende, J. Kim, I.-H. Jung, Calphad, 41 (2013) 26-41.
[20] M. Zydzik, M. Smids, M.-A. Van Ende, I.-H. Jung, Calphad, 46 (2014) 1-17.
[21] Y.C. Lee, A.K. Dahle, D.H. StJohn, Metall. Mater. Trans. A, 31A (2000) 2895-2906.
[22] G.H. Li, H.S. Gill, R.A. Varin, Metall. Trans. A, 24A (1993) 2383-2391.
[23] B. Bronfin, M. Katsir, E. Aghion, Mater. Sci. Eng. A, 302 (2001) 46-50.
[24] J. Gröbner, D. Mirkovic, R. Schmid-Fetzer, Metall. Mater. Trans. A, 35A (2004) 3349-3362.
[25] M. Huang, D.L. Schlagel, F.A. Schmidt, T.A. Lograsso, J. Alloys Compd., 441 (2007) 94-100.
[26] Q. Ran, H.L. Lukas, G. Effenberg, G. Petzow, Z. Metallkd., 80 (1989) 402-405.
[27] B.J. Beaudry, K.A. Gschneidner Jr, Chapter 2 Preparation and basic properties of the rare earth metals, in: Karl A. Gschneidner, Jr., E. LeRoy (Eds.) Handbook on the Physics and Chemistry of Rare Earths, Elsevier, 1978, pp. 173-232.
[28] L. Miglio, F. d'Heurle, (Eds.), In: Proc. CAPLUS AN 2001:170985(Book), June 5-16, 1999. pp. 377.
[29] A.D. Pelton, S.A. Degterov, G. Eriksson, C. Robelin, Y. Dessureault, Metall. Mater. Trans. B, 31B (2000) 651-659.
[30] A.D. Pelton, P. Chartrand, Metall. Mater. Trans. A, 32A (2001) 1355-1360.
[31] I.-H. Jung, D.-H. Kang, W.-J. Park, N.J. Kim, S. Ahn, Calphad, 31 (2007) 192-200.
[32] D. Nassyrov, I.-H. Jung, Calphad, 33 (2009) 521-529.

[33] A.D. Pelton, M. Blander, Metall. Trans. B, 17B (1986) 805-815.
[34] P. Wu, G. Eriksson, A.D. Pelton, M. Blander, ISIJ Int., 33 (1993) 26-35.
[35] A.D. Pelton, M. Blander, In: Proc. 1984. pp. 281-294.
[36] M. Hillert, B. Jansson, B. Sundman, Z. Metallkd., 79 (1988) 81-87.
[37] A.T. Dinsdale, Calphad, 15 (1991) 317-425.
[38] J. Leitner, P. Vonka, D. Sedmidubsky, P. Svoboda, Thermochim. Acta, 497 (2010) 7-13.
[39] G. Inden, Dusseldorf, Germany, , (1976) 111.
[40] M. Hillert, M. Jarl, Calphad, 2 (1978) 227-238.
[41] M.V. Bulanova, P.N. Zheltov, K.A. Meleshevich, P.A. Saltykov, G. Effenberg, J.C. Tedenac, J. Alloys Compd., 329 (2001) 214-223.
[42] E.I. Gladyshevskii, A.A. Kulikova, Dopov. Akad. Nauk Ukr. RSR, (1965) 1472-1474.
[43] A. Raman, Trans. Indian Inst. Metals, 21 (1968) 5-8.
[44] R.I. Polotskaya, Poroshk. Metall. (Kiev), (1988) 73-74.
[45] E. Houssay, A. Rouault, O. Thomas, R. Madar, J.P. Senateur, Appl. Surf. Sci., 38 (1989) 156-161.
[46] Y.I. Buyanov, T.Y. Velikanova, S.P. Luzan, P.S. Martsenyuk, R.I. Polotskaya, V.R. Sidorko, Preprint FIPM, Kiev, (1997).
[47] R.D. Grinthal, Journal of the Electrochemical Society, 107 (1960) 59-61.
[48] I. Binder, J. Am. Ceram. Soc., 43 (1960) 287-292.
[49] R.D. Thompson, B.Y. Tsaur, K.N. Tu, Appl. Phys. Lett., 38 (1981) 535-537.
[50] A.S. Bolgar, N.P. Gorbachuk, A.V. Blinder, Poroshk. Metall. (Kiev), (1994) 48-53.
[51] Y.O. Esin, S.P. Kolesnikov, V.M. Baev, M.S. Petrushevskii, P.V. Gel'd, Zh. Fiz. Khim., 54 (1980) 485-486.
[52] G.I. Batalin, V.S. Sudavtsova, N.V. Stroganova, Ukr. Khim. Zh. (Russ. Ed.), 51 (1985) 775-777.
[53] A.S. Bolgar, N.P. Gorbachuk, A.V. Blinder, N.V. Moiseev, Zh. Fiz. Khim., 70 (1996) 492-495.
[54] A.S. Bolgar, N.P. Gorbachuk, A.V. Blinder, N.V. Moiseev, Zh. Fiz. Khim., 70 (1996) 1185-1189.
[55] S.V. Meschel, O.J. Kleppa, J. Alloys Compd., 220 (1995) 88-93.
[56] S.V. Meschel, O.J. Kleppa, J. Alloys Compd., 243 (1996) 186-193.
[57] S.P. Gordienko, B.V. Fenochka, Poroshk. Metall. (Kiev), (1996) 58-60.
[58] H. Okamoto, J. Phase Equilib. Diffus., 28 (2007) 585.
[59] F. Benesovsky, H. Nowotny, W. Rieger, H. Rassaerts, Monatsh. Chem., 97 (1966) 221-229.
[60] I. Mayer, I. Felner, J. Less-Common Metals, 29 (1972) 25-31.
[61] G.S. Smith, A.G. Tharp, Q. Johnson, Acta Crystallogr., 22 (1967) 940-943.
[62] M.V. Bulanova, P.N. Zheltov, K.A. Meleshevich, P.A. Saltykov, G. Effenberg, J. Alloys Compd., 345 (2002) 110-115.
[63] N.P. Gorbachuk, Powder Metall. Met. Ceram., 47 (2008) 707-711.
[64] G.M. Ryss, Y.O. Esin, A.I. Stroganov, P.V. Gel'd, Zh. Fiz. Khim., 51 (1977) 232-233.
[65] V.S. Sudavtsova, Y.G. Gorobets, G.I. Batalin, Rasplavy, 2 (1988) 79-81.
[66] A. Munitz, A.B. Gokhale, G.J. Abbaschian, Bull. Alloy Phase Diagrams, 10 (1989) 73-78.
[67] V.N. Eremenko, K.A. Meleshevich, Y.I. Buyanov, Izv. Vyssh. Uchebn. Zaved., Tsvetn. Metall., (1986) 82-87.
[68] J.A. Perri, I. Binder, B. Post, J. Phys. Chem., 63 (1959) 616-619.
[69] J.A. Perri, E. Banks, B. Post, J. Phys. Chem., 63 (1959) 203-204.

[70] N. Boutarek, J. Pierre, B. Lambert-Andron, P. L'Heritier, R. Madar, J. Alloys Compd., 204 (1994) 251-260.
[71] N.P. Gorbachuk, A.S. Bolgar, A.V. Blinder, Powder Metall. Met. Ceram., 36 (1998) 498-501.
[72] A.S. Bolgar, N.P. Gorbachuk, A.V. Blinder, T.V. Egorov, A.I. Kriklya, Modern Problems in Physical Materials Science, 2 (1993) 37-46.
[73] A.S. Bolgar, N.P. Gorbachuk, A.V. Blinder, N.V. Moiseev, Zh. Fiz. Khim., 68 (1994) 2124-2127.
[74] V.N. Eremenko, K.A. Meleshevich, Y.I. Buyanov, I.M. Obushenko, Dopov. Akad. Nauk Ukr. RSR, Ser. A: Fiz.-Mat. Tekh. Nauki, (1984) 77-82.
[75] N.P. Gorbachuk, A.S. Bolgar, Powder Metall. Met. Ceram., 39 (2001) 567-571.
[76] N.P. Gorbachuk, Ukr. Khim. Zh. (Russ. Ed.), 74 (2008) 8-12.
[77] S.V. Meschel, O.J. Kleppa, J. Alloys Compd., 217 (1995) 235-239.
[78] R.I. Polotskaya, Y.I. Buyanov, Poroshk. Metall. (Kiev), (1986) 31-33.
[79] A.B. Gokhale, A. Munitz, G.J. Abbaschian, Bull. Alloy Phase Diagrams, 10 (1989) 246-251, 303-244.
[80] A.B. Gokhale, R. Abbaschian, Bull. Alloy Phase Diagrams, 9 (1988) 582-585.
[81] M.I. Copeland, H. Kato, Proc. Symp. Phys. Mater. Probl. Reactor Control Rods, Vienna, (1964) 295-316.
[82] B. Markoli, S. Spaic, F. Zupanic, Metall (Isernhagen, Ger.), 53 (1999) 604-606.
[83] N.P. Gorbachuk, S.N. Kirienko, Powder Metall. Met. Ceram., 46 (2007) 163-168.
[84] H. Okamoto, T.B. Massalski, J. Phase Equilib., 12 (1991) 148-168.
[85] M. Hillert, M. Selleby, B. Sundman, Acta Mater., 57 (2009) 5237-5244.
[86] A.D. Pelton, Y.-B. Kang, Int. J. Mater. Res., 98 (2007) 907-917.
[87] Y.-B. Kang, A.D. Pelton, Calphad, 34 (2010) 180-188.

Appendix V

Appendix V

Critical evaluation and thermodynamic optimization of the Si-RE systems: Part II. Si-RE system (RE = Gd, Tb, Dy, Ho, Er, Tm, Lu and Y)

Junghwan Kim and In-Ho Jung

Department of Mining and Materials Engineering, McGill University, 3610 University St., Montreal, Quebec, H3A 2B2, Canada

Corresponding author: In-Ho Jung

Tel : 1-514-398-2608

Fax : 1-514-398-4492

E-mail: in-ho.jung@mcgill.ca

Published in

The Journal of Chemical Thermodynamics 81 (2015) 273-297

Abstract

A critical evaluation and optimization of all available phase diagrams and thermodynamic data of the Si-RE (RE = Gd, Tb, Dy, Ho, Er, Tm, Lu and Y) systems was conducted to obtain reliable thermodynamic functions of all the phases in the system. In the thermodynamic modeling, a systematic analysis involving the similarity and periodicity observed in the lanthanide series was applied to resolve inconsistencies in the experimental data and to estimate the unknown thermodynamic properties and phase equilibria data. In particular, the phase diagrams and thermodynamic properties of Si-Tm and Si-Lu systems which are rarely investigated can be predicted from this approach. Systematic trends in thermodynamic properties of solid and liquid phases and phase diagram of the entire Si-RE systems were summarized.

Keywords

Mg-RE alloy, Si-RE system, Thermodynamic Modeling, Phase Diagrams, Thermodynamic Properties.

1. Introduction

As part of large thermodynamic database of Mg-RE alloys [1-8], the thermodynamic modeling of the Si-RE systems has been carried out. Continuing the modeling of the Si-RE systems, a critical evaluation and systematic optimization of all available thermodynamic data and phase diagrams of binary Si-RE systems (RE (heavy rare earth) = Gd, Tb, Dy, Ho, Er, Tm, Lu and Y) has been conducted in the present study. As mentioned previously, among many Si-RE systems, only three binary Si-RE systems, Si-Ce [9, 10], Si-Gd [11] and Si-Y [10, 12], were thermodynamically accessed so far. The thermodynamic models which were used in the present study are described in detail in the part I of this series of the study. As summary of this work, systematic trends in the thermodynamic properties and the phase diagrams of the overall Si-RE systems will be discussed in the end.

2. Critical evaluation and thermodynamic optimization

2.1. The Si-Gd system

Available experimental data for the Si-Gd phase diagram are presented in Fig. 1. A literature review for the phase diagram of this system was performed by Gokhale and Abbaschian in 1988 [13]. In the review, the phase equilibria of this system were incomplete due to lack of experimental data until that time. Three stoichiometric compounds, GdSi, Gd_5Si_4 and Gd_5Si_3, and two non-stoichiometric compounds, $GdSi_{2-a}$ (0.375 to 0.4 mole fraction of Gd) and $GdSi_2$ (33.2 to 36 mole fraction of Gd) were reported in several crystallographic studies [14-18]. Two eutectic reactions, between Gd and Gd_5Si_3 at 1070 ºC and 0.848 mole fraction of Gd [19] and between Gd_5Si_3 and Gd_5Si_4 at 1060 ± 20 ºC and undetermined composition [20], determined by metallographic analysis, X-ray diffraction, and thermal analysis. Lozovskii and Kolesnichenko [21] determined the liquidus of Si-rich side of the phase diagram by gravimetrical methods and also reported the eutectic reaction at 1140 ºC and 0.19 mole fraction of Gd. However, their liquidus and eutectic point are inconsistent with other data and they seem to be less reliable. The melting temperature of Gd_5Si_3

was determined as 1650 ± 20 ºC using an optical pyrometer [20]. There were discrepancies in the melting point of $GdSi_2$ in literature. It was reported as 1540 ºC [22], 1500 ºC [23] and 2100 ºC [15, 24]. The polymorphic transformation of $GdSi_2$ was also reported to be 400 ± 25 ºC (high-temperature XRD) [25]. Recently, Eremenko et al. [26] investigated the phase diagram of this system in the entire composition range using differential thermal analysis (DTA), XRD and metallography techniques. The existence of five compounds ($GdSi_a$ (a = 1.72-1.89), $GdSi_{1.5}$, GdSi, Gd_5Si_4 and Gd_5Si_3) were established. However, the invariant reactions of relevant phases were obviously different from the previously reported ones [13]. The $GdSi_a$, $GdSi_{1.5}$, Gd_5Si_4 and Gd_5Si_3 compounds melted by peritectic reactions at 1590 ºC, 1625 ºC, 1725 ºC and 1700 ºC, respectively, while the GdSi congruently melted at 1830 ºC. Two eutectic reactions were found at about 1080 ºC and 0.865 mole fraction Gd for Gd-rich side and at 1230 ºC and 0.17 mole fraction Gd for Si-rich side. It was also suggested that the polymorphic transformation temperature of $GdSi_a$ continuously decreased with increasing Gd concentration. The polymorphic transformation temperature of $GdSi_a$ (a = 1.72-1.89) was about 500 ºC at a = 1.89 and about 425 ºC at a = 1.72. The polymorphic transformation temperature of $GdSi_{1.5}$ was determined to be about 700 ºC. However, the liquidus curve between $GdSi_{1.5}$ and GdSi in the suggested phase diagram [26] showed a very unusual inflection at the liquidus. More recently, the phase diagram of the system was reinvestigated by Huang et al. [11] in order to examine the liquidus and melting features of compounds in a composition range from 0.175 to 0.7 mole fraction Gd by employing DTA, XRD and metallography. Most of the invariant reaction temperatures were similar to the reported data [26] except for the liquidus near 0.4 mole fraction of Gd. The dubious liquidus inflection near that composition [26] was not found in Huang et al.'s study [11]. In addition, the compound near 0.4 mole fraction of Gd was identified to be Gd_3Si_5 instead of Gd_2Si_3 ($GdSi_{1.5}$) [26] by XRD. The polymorphic transformation temperatures of $GdSi_2$ and Gd_3Si_5 were found, by applying differential scanning calorimetry (DSC), to be 435 ºC and 637 ºC which are slightly lower than the reported values (500 ºC and 700 ºC) by Eremenko et al. [26] while no peak in their DSC results was found at 425 ºC which was the polymorphic transformation temperatures of $GdSi_2$ at the Si-deficient boundary [26]. Heat contents of several compounds were determined by Bolgar et al. [27] using high temperature calorimetry. In the calorimetric measurement, the melting temperatures of $GdSi_{1.88}$, GdSi, Gd_5Si_4 and Gd_5Si_3 were also determined to be 1578 ºC, 1826 ºC, 1713 ºC and 1716 ºC, respectively. The polymorphic transformation temperature and enthalpy of $GdSi_{1.88}$ were also

reported to be 505 ± 8 ºC and 3.7 ± 0.5 kJ mol^{-1}, respectively. Later, Gorbachuk [28] reinvestigated polymorphic transformation temperature and enthalpy of $GdSi_{1.88}$ to be 475 ºC and 2.7 kJ mol^{-1} using a quantitative DTA. The solubility of Si in Gd was reported by Copeland and Kato [19] to be less than 0.2 wt. % Si (0.011 mole fraction of Si), but the exact amount was not determined. No other experimental data on the terminal solubility of Si and Gd are available in literature.

The thermodynamic properties of the Si-Gd liquid were reported by Batalin et al. [29], Beloborodova et al. [30] and Kanibolotsky et al. [31, 32] and their experimental data are presented in Fig. 2. Batalin et al. [29] measured the integral and partial enthalpies of mixing of liquid Si-Gd solution using high temperature calorimetry. The smoothed data of integral enthalpy and partial enthalpy of Gd of liquid solution up to 0.06 mole fraction of Gd at 1813 K were presented. Partial enthalpies of mixing for Gd and Si in the system were measured by Beloborodova et al. [30] using high temperature isoperibolic calorimetry in a high purity argon atmosphere in the composition range of 0 to 0.2 and 0.8 to 1 mole fraction of Gd at 1760 K. The integral enthalpy of mixing was also derived from the partial enthalpies. Kanibolotsky et al. [31, 32] performed the same experiments at 1760 K and presented the partial enthalpies of mixing for Gd and Si and integral enthalpies of mixing of Gd-Si solution. All liquid enthalpy experimental data are consistent with each other and the minimum in the integral enthalpy of mixing was about -80 kJ mol^{-1} at 0.4 mole fraction of Gd.

Thermodynamic properties of the intermetallic compounds were investigated by several research groups. Heat capacities (C_p) of $GdSi_2$, GdSi, Gd_5Si_4 and Gd_5Si_3 are shown in Fig. 3. The low temperature C_p of Gd_5Si_4 up to 350 K was measured by Serdyuk et al. [33] using adiabatic calorimetry. The magnetic transition of Gd_5Si_4 from ferromagnetic to paramagnetic was also reported to occur at 330 K. Several other magnetic transition temperatures (T_C) and magnetic moment (B_0) of the Gd_5Si_4 were reviewed by Spichkin et al. [34] (T_C = 336 K [35, 36], 338 K [37] and B_0 = 7.21 μ_B [35], 7.32 μ_B [38]). Spichkin et al. [34] also reported the T_C and B_0 to be 345.7 K and 7.52 μ_B from the measurement of the ac magnetic susceptibility and dc magnetization behaviors of the Gd_5Si_4. The low temperature C_p of Gd_5Si_3 was determined by Safonov et al. [39] using adiabatic calorimetry at the temperature range of 14 to 300 K. The magnetic transition

temperature (T_N) of Gd_5Si_3 from antiferromagnetic to paramagnetic was reported to be about 75 K. Similarly, the low temperature C_p of $GdSi_{1.88}$ ($GdSi_2$) [40], GdSi [40], Gd_5Si_4 [41] and Gd_5Si_3 [41] up to about 300 K were measured by Bolgar et al. [40, 41] and the calculated standard entropy (S^o_{298}) of those compounds were reported to be 101.65, 66.75, 362.8 and 384.91 J K^{-1} mol^{-1}, respectively. The T_N of Gd_5Si_3 and $GdSi_{1.88}$ were also reported to be 73.78 K and 24.71 K, respectively. The S^o_{298} of Gd_5Si_4 and Gd_5Si_3 were calculated from the experimental C_p of Serdyuk et al. [33] and Safonov et al. [39] and they were 368.24 and 400.39 J K^{-1} mol^{-1}, respectively. All the experimental S^o_{298} are presented as ΔS^o_{298} in Fig. 4. The standard enthalpies of formation (ΔH^o_{298}) of compounds were determined by several researchers. Usenko et al. [42] measured the ΔH^o_{298} of $GdSi_{1.89}$, $GdSi_{1.5}$, GdSi, Gd_5Si_4 and Gd_5Si_3 using solution drop calorimetry. Gordienko and Druzheruchenko [43] estimated ΔH^o_{298} of GdSi, Gd_5Si_4 and Gd_5Si_3 from Knudsen cell mass-spectrometry measurement at 1600 to 1950 K. Meschel and Kleppa [44, 45] measured ΔH^o_{298} of $GdSi_2$ [29], GdSi [30] and Gd_5Si_3 [29] using direct synthesis calorimetry and also reported the heat content ($H_{1473} - H_{298}$) of those compounds. All the experimental ΔH^o_{298} are presented in Fig. 5. Bolgar et al. [27] measured the heat contents ($H_T - H_{298}$) of $GdSi_{1.88}$ ($GdSi_2$), GdSi, Gd_5Si_4 and Gd_5Si_3 using high temperature calorimetry. The temperature dependent C_p for both α-$GdSi_{1.88}$ (α-$GdSi_2$) and β-$GdSi_{1.88}$ (β-$GdSi_2$), GdSi, Gd_5Si_4 and Gd_5Si_3 were derived from the experimental data. The experimental heat contents of Bolgar et al. [27] and Meschel and Kleppa [44, 45] are shown in Fig. 6. The Gibbs energies of $GdSi_2$ [46], $GdSi_{1.89}$ [47], $GdSi_{1.5}$ [47], GdSi [47], Gd_5Si_4 [48] and Gd_5Si_3 [48] were measured by Lukashenko and Polotskaya [46, 47] and Sidorko and Polotsokaya [48] by measuring the emf of high temperature galvanic cells in the temperature range of 600 to 960 K. All the experimental data on the Gibbs energies of formation (ΔG^o_{800}) are presented in Fig. 7.

The thermodynamic optimization of the Si-Gd system was previously performed by Huang et al. [11] based on their phase diagram investigation and other available experimental data. The phase diagram and thermodynamic properties calculated from the thermodynamic parameters optimized by Huang et al. [11] are compared with experimental data in Figs. 1, 2, 4, 5 and 7. The calculated

liquidus lines are off from experimental data, especially in the Si-rich and Gd-rich side as shown in Fig. 1. The excess Gibbs energy of liquid phase was expressed in the Redlich-Kister random mixing model which are known to be rather difficult to reproduce a short range ordering phenomenon in liquid phase, i.e. their calculated enthalpy of mixing of liquid at 1760 K was about 15 kJ mol^{-1} higher than the experimental data at about 0.4 mole fraction of Gd as shown in Fig. 2(a). Moreover, it should be noted that the C_p of all intermetallic compounds were estimated by the NK rule which means the experimental data of the low temperature C_p and high temperature heat contents were not considered in their thermodynamic optimization. Therefore, their estimated S^{o}_{298} of intermetallic compounds were considerably less than the experimental data as shown in Fig. 4.

The optimized phase diagram of the Si-Gd system in the present study is shown in Fig. 1 and the calculated thermodynamic properties with the optimized thermodynamic parameters are shown in Figs. 2 to 7. In the optimization, the experimental data of Eremenko et al. [26] and Huang et al. [11] were preferred in the phase diagram evaluation except for the unusual liquidus inflection of Eremenko et al. [26] between 0.35 to 0.65 mole fraction Gd. The $GdSi_{1.5}$ and the non-stoichiometric compound $GdSi_a$ (a = 1.72-1.89) reported by Eremenko et al. [26] were considered as stoichiometric compounds Gd_3Si_5 and $GdSi_2$, respectively, in agreement with Huang et al. [11]. The experimental data for the thermodynamic properties of liquid [29-32] were taken into account to obtain the temperature independent parameters of excess Gibbs energy of liquid phase. The calculated integral and partial enthalpies of mixing of liquid at 1760 K are in good agreement with experimental data as shown in Figs 2(a) and 2(b), respectively. The C_p of α-$GdSi_2$ and β-$GdSi_2$ and GdSi, Gd_5Si_4 and Gd_5Si_3 derived from the experimental heat content data [27] in Fig. 4 were used and those C_p are consistent well with the experimental low temperature C_p measured by Bolgar et al. [40, 41] as shown in Fig. 3. Therefore, the S^{o}_{298} of Gd_5Si_4 and Gd_5Si_3 from the data of Bolgar et al. [41] were preferred to the data of Serdyuk et al. [33] and Safonov et al. [39], shown in Fig. 5. The polymorphic transformation temperature and enthalpy of the $GdSi_2$ were also taken from the data of Gorbachuk [28]. The magnetic properties of Gd_5Si_4 were taken from the experimental data; T_C = 336 K [35, 36], B_0 = 7.52 μ_B [34], which are coherent with the experimental C_p data as shown in Fig. 3. The same C_p for both α-Gd_3Si_5 and β-Gd_3Si_5 were applied

using the NK rule because no experimental data were available. The polymorphic transformation temperature of Gd_3Si_5 was taken from the data of Eremenko et al. [26] and the enthalpy of polymorphic transformation was approximated to be 8.1 kJ mol^{-1} which is three times bigger than that of α-$GdSi_2$ and β-$GdSi_2$. Then, the temperature dependent parameters for liquid phase and the ΔH^{o}_{298} and S^{o}_{298} of all intermetallic compounds were determined to reproduce the experimental data on the phase diagram and thermodynamic properties, simultaneously. The calculated S^{o}_{298} of all compounds are presented along with experimental data [33, 39-41] and the optimization of Huang et al. [11] in Fig. 5. The calculated values are in accord with the experimental data [40, 41] except for the GdSi. The Gibbs energy of GdSi could be determined from the experimental data on the phase diagram and thermodynamic properties of solid and liquid at 0.5 mole fraction Gd. If the experimental S^{o}_{298} of GdSi [40] was applied, the ΔH^{o}_{298} of GdSi should be much more negative than the experimental data to reproduce the melting temperature of GdSi. However, it would result in unstable Gd_5Si_4 phase at lower temperature. Therefore, the S^{o}_{298} of GdSi was increased by 6.25 J K^{-1} mol^{-1} from the experimental data [40]. The calculated ΔH^{o}_{298} of all compounds are compared with experimental data [42-45] and the optimization of Huang et al. [11] in Fig. 6. The values are in good agreement with the calorimetric data [42, 44]. The calculated heat contents ($H_T - H_{298}$) of $GdSi_2$, GdSi, Gd_5Si_4 and Gd_5Si_3 are compared to the experimental data [27, 44, 45] in Fig. 6. The calculated heat contents of those compounds are in good agreement with the experimental data. The calculated ΔG^{o}_{800} of all compounds are presented along with experimental data [46-48] and the optimization of Huang et al. [11] in Fig. 7. The calculated ΔG^{o}_{800} in the present study are in good agreement with the experimental data except for that of Gd_5Si_4 and Gd_5Si_3. The decreasing trend in the Gibbs energies of formation along with increasing Gd content is inconsistent with other experimental data, in particular, the enthalpy of formation data in Fig. 5. Moreover, the Gibbs energies of Gd_5Si_4 and Gd_5Si_3 in the present study are based on the experimental ΔH^{o}_{298}, S^{o}_{298} and C_p of Gd_5Si_4 and Gd_5Si_3 [27, 41, 42, 44]. That is, the Gibbs energies of formation determined by Sidorko and Polotskaya [48] using the emf technique are inconsistent with the other set of data. It is worth mentioning that the Gd_3Si_5 melts congruently in the present optimization, unlike the phase diagram suggested by Huang et al. [11]. The optimized thermodynamic parameters are listed in Table 1 and the calculated invariant reactions with the experimental data are tabulated in Table 2.

Table 1. Optimized model parameters of the Si-Gd system.

Phase	Thermodynamic parameters
Liquid	Coordination Numbers
	i j Z_{ij}^{i} Z_{ij}^{j}
	Si Gd 6 6
	Δg_{SiGd} / (J mol^{-1}) = (-59412.8 + 9.2048 T/K) + (-62760.0 + 8.368 T/K) X_{SiSi}
	+ (38492.8 – 2.092 T/K) X_{SiSi}^{2} – (20920.0 + 4.184 T/K) X_{GdGd}
	+ (27196.0 – 4.184 T/K) X_{GdGd}^{2}
α-$GdSi_2$	ΔH_{298}° = -191000 J mol^{-1}, S_{298}° = 105.5 J K^{-1} mol^{-1}
	C_p / (J K^{-1} mol^{-1}) = 66.29 + 0.012818 T/K - 331314 (T/K)$^{-2}$
β-$GdSi_2$	$\Delta_{\mathrm{trs}}H^{\alpha\rightarrow\beta}$ = 2700 J mol^{-1}, $T_{\mathrm{trs}}^{\alpha\rightarrow\beta}$ = 748.0 K
	C_p / (J K^{-1} mol^{-1}) = 78.04 + 0.004096 T/K - 200769 (T/K)$^{-2}$
α-Gd_3Si_5	ΔH_{298}° = -567000 J mol^{-1}, S_{298}° = 276.0 J K^{-1} mol^{-1}
	C_p / (J K^{-1} mol^{-1}) = 3 × C_p / (J K^{-1} mol^{-1}) (Gd, hcp-A3)
	+ 5 × C_p / (J K^{-1} mol^{-1}) (Si, diamond-A4)
β-Gd_3Si_5	$\Delta_{\mathrm{trs}}H^{\alpha\rightarrow\beta}$ = 8100 J mol^{-1}, $T_{\mathrm{trs}}^{\alpha\rightarrow\beta}$ = 973.0 K
	C_p / (J K^{-1} mol^{-1}) = 3 × C_p / (J K^{-1} mol^{-1}) (Gd, hcp-A3)
	+ 5 × C_p / (J K^{-1} mol^{-1}) (Si, diamond-A4)
GdSi	ΔH_{298}° = -177400 J mol^{-1}, S_{298}° = 73.0 J K^{-1} mol^{-1}
	C_p / (J K^{-1} mol^{-1}) = 44.27 + 0.010654 T/K - 45660 (T/K)$^{-2}$
Gd_5Si_4	ΔH_{298}° = -716000 J mol^{-1}, S_{298}° = 357.0 J K^{-1} mol^{-1}
	C_p / (J K^{-1} mol^{-1}) = 236.61 + 0.02402 T/K - 975737 (T/K)$^{-2}$
	T_{C} = 336.0 K, B_0 = 7.52 μ_{B}
Gd_5Si_3	ΔH_{298}° = -529000 J mol^{-1}, S_{298}° = 384.91 J K^{-1} mol^{-1}
	C_p / (J K^{-1} mol^{-1}) = 209.98 + 0.02364 T/K - 460627 (T/K)$^{-2}$

Table 2. Calculated invariant reactions and experimental data in the Si-Gd system.

Type	Reaction	t (°C)	Reference
Eutectic	$L_{(X_{Gd}=0.186)} \rightarrow Si_{(dia.\text{-}A4,\ X_{Gd}=0)} + GdSi_2$	1221.2	This work
	$L_{(X_{Gd}=0.130)} \rightarrow Si_{(dia.\text{-}A4,\ X_{Gd}=0)} + GdSi_{2\text{-}a}$	1227.0	[11]
	$L_{(X_{Gd}=0.190)} \rightarrow Si_{(dia.\text{-}A4,\ X_{Gd}=0)} + GdSi_{2\text{-}a}$	1140.0	[21]
	$L_{(X_{Gd}=0.170)} \rightarrow Si_{(dia.\text{-}A4,\ X_{Gd}=0)} + GdSi_{2\text{-}a}$	1230.0	[26]
Peritectic	$L_{(X_{Gd}=0.319)} + Gd_3Si_5 \rightarrow GdSi_2$	1610.5	This work
	$L_{(X_{Gd}=0.283)} + Gd_3Si_5 \rightarrow GdSi_{2\text{-}a}$	1600.0	[11]
	$L_{(X_{Gd}=0.324)} + Gd_2Si_3 \rightarrow GdSi_{2\text{-}a}$	1590.0	[26]
	T_m of $GdSi_{1.88}$	1578.0	[27]
	T_m of $GdSi_2$	1540.0	[22]
		1500.0	[23]
		2100.0	[15, 24]
Allotropic	$\alpha\text{-}GdSi_2 \leftrightarrow \beta\text{-}GdSi_2$	475.0	This work
	$\alpha\text{-}GdSi_2 \leftrightarrow \beta\text{-}GdSi_2$	400 ± 25	[25]
	$\alpha\text{-}GdSi_a \leftrightarrow \beta\text{-}GdSi_a$ (Si-rich composition)	500.0	[26]
	$\alpha\text{-}GdSi_a \leftrightarrow \beta\text{-}GdSi_a$ (Gd-rich composition)	425.0	[26]
	$\alpha\text{-}GdSi_{1.88} \leftrightarrow \beta\text{-}GdSi_{1.88}$	475.0	[13]
	$\alpha\text{-}GdSi_{1.88} \leftrightarrow \beta\text{-}GdSi_{1.88}$	505 ± 8	[27]
Peritectic	$L_{(X_{Gd}=0.351)} + GdSi \rightarrow Gd_3Si_5$	1665.0	[11]
	$L_{(X_{Gd}=0.352)} + GdSi \rightarrow Gd_2Si_3$	1625.0	[26]
Congruent	$L_{(X_{Gd}=0.375)} \leftrightarrow Gd_3Si_5$	1677.9	This work
Allotropic	$\alpha\text{-}Gd_3Si_5 \leftrightarrow \beta\text{-}Gd_3Si_5$	700.0	This work
	$\alpha\text{-}Gd_2Si_3 \leftrightarrow \beta\text{-}Gd_2Si_3$	700.0	[26]
Eutectic	$L_{(X_{Gd}=0.381)} \rightarrow Gd_3Si_5 + GdSi$	1677.3	This work
Congruent	$L_{(X_{Gd}=0.50)} \leftrightarrow GdSi$	1849.2	This work
	$L_{(X_{Gd}=0.50)} \leftrightarrow GdSi$	1835.0	[11]
	$L_{(X_{Gd}=0.50)} \leftrightarrow GdSi$	1830.0	[26]
	T_m of GdSi	1826.0	[27]

Peritectic	GdSi + L(X_{Gd}= 0.589) → Gd_5Si_4	1776.0	This work
	GdSi + L(X_{Gd}*= 0.593) → Gd_5Si_4	1770.0	[11]
	GdSi + L(X_{Gd}= 0.633) → Gd_5Si_4	1725.0	[26]
	T_m of Gd_5Si_4	1713.0	[27]
Peritectic	Gd_5Si_4 + L(X_{Gd}= 0.630) → Gd_5Si_3	1726.1	This work
	Gd_5Si_4 + L(X_{Gd}*= 0.625) → Gd_5Si_3	1750.0	[11]
	Gd_5Si_4 + L(X_{Gd}= 0.655) → Gd_5Si_3	1700.0	[26]
	T_m of Gd_5Si_3	1650 ± 20	[20]
		1716.0	[27]
Eutectic	L(X_{Gd}= 0.866) → Gd_5Si_3 + Gd(hcp-A3, X_{Gd}= 1)	1070.6	This work
	L(X_{Gd}*= 0.915) → Gd_5Si_3 + Gd(hcp-A3, X_{Gd}= 1)	1088.0	[11]
	L(X_{Gd}= 0.848) → Gd_5Si_3 + Gd(hcp-A3, X_{Gd}= 1)	1070.0	[19]
	L(X_{Gd}= 0.865) → Gd_5Si_3 + Gd(hcp-A3, X_{Gd}= 1)	1080.0	[26]

* The compositions are taken from their thermodynamic optimization.

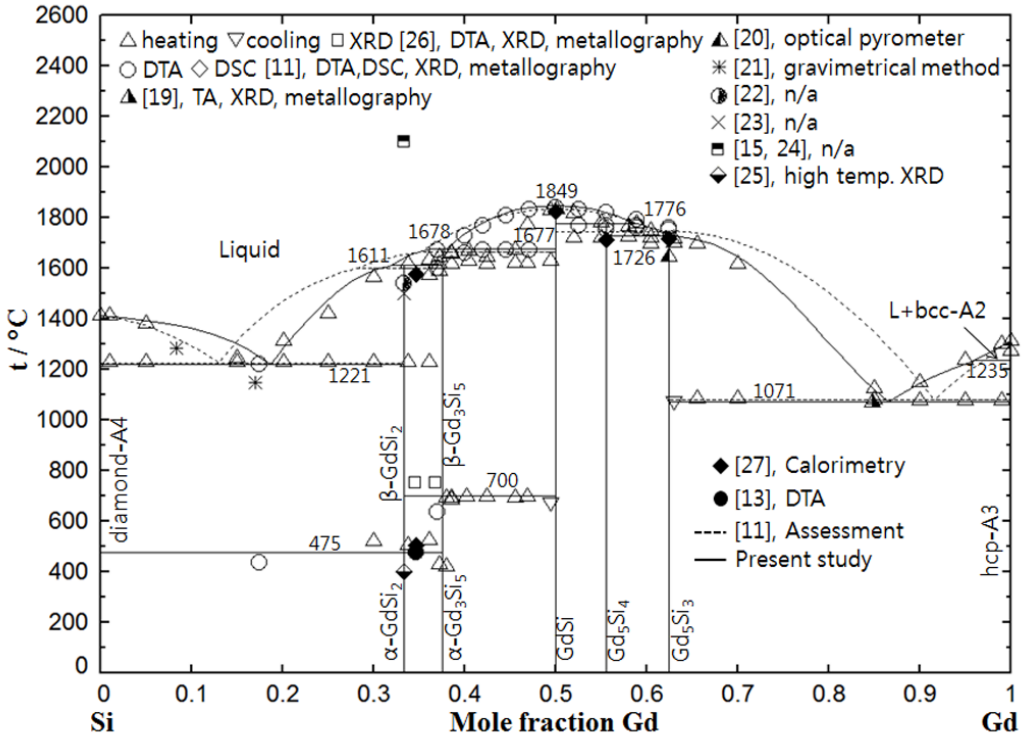


Fig. 1. The optimized Si-Gd phase diagram with experimental data and previous thermodynamic assessment.

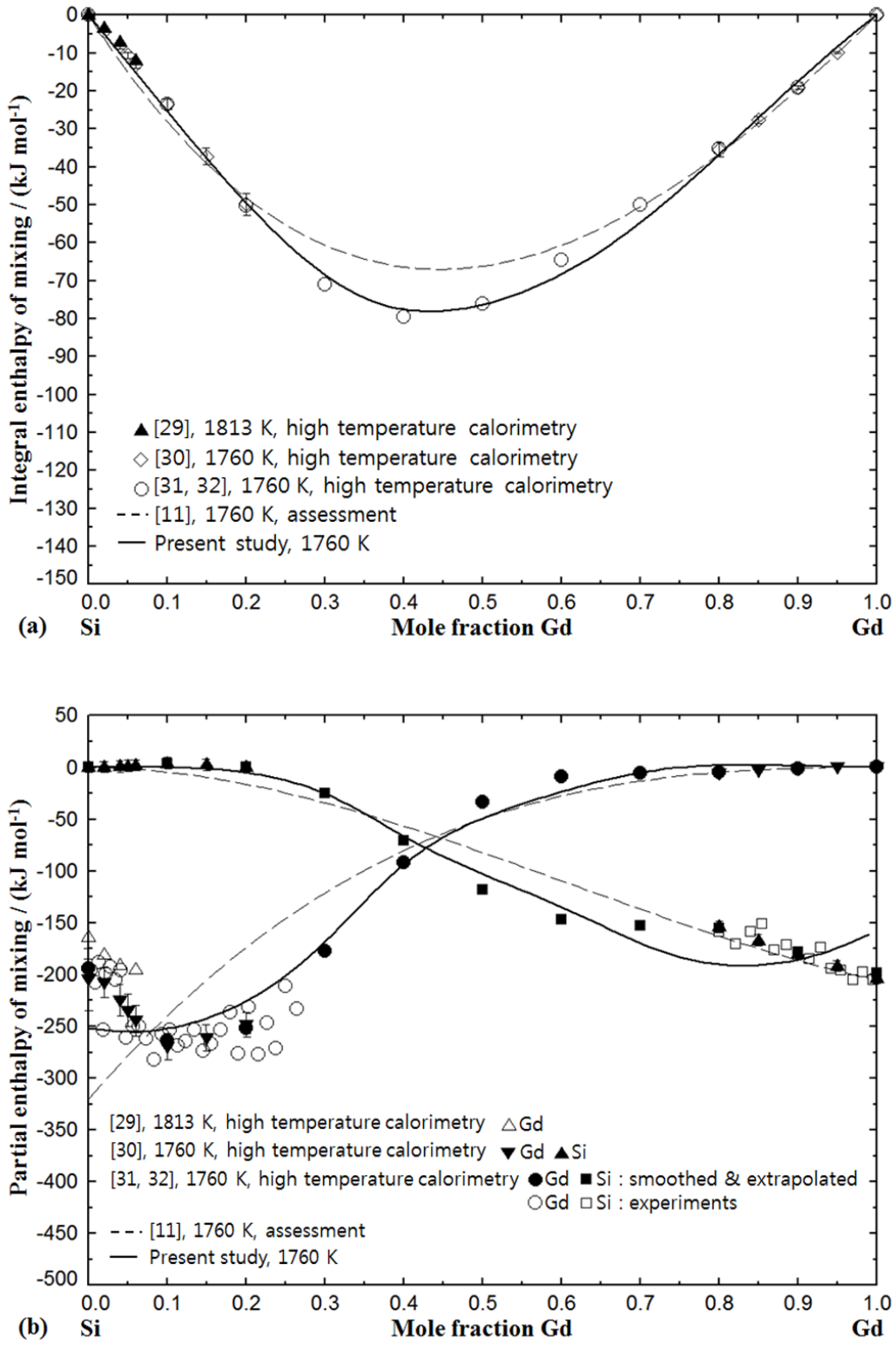


Fig. 2. (a) Integral enthalpy of mixing and (b) partial enthalpies of mixing of liquid Si-Gd phase at 1760 K with experimental data and previous thermodynamic assessment.

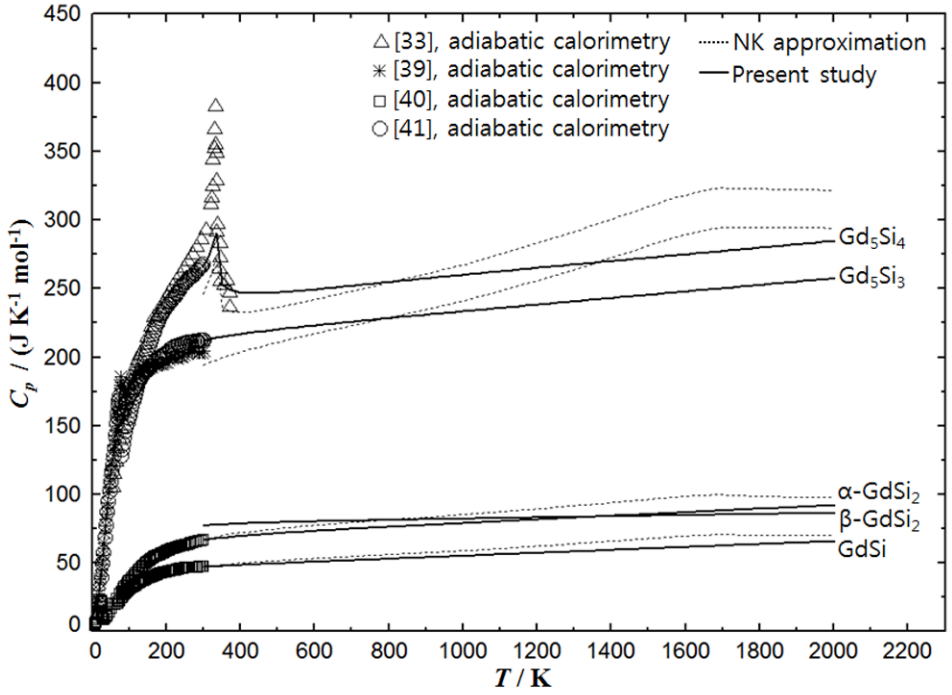


Fig. 3. Heat capacities of the compounds in the Si-Gd system with experimental data.

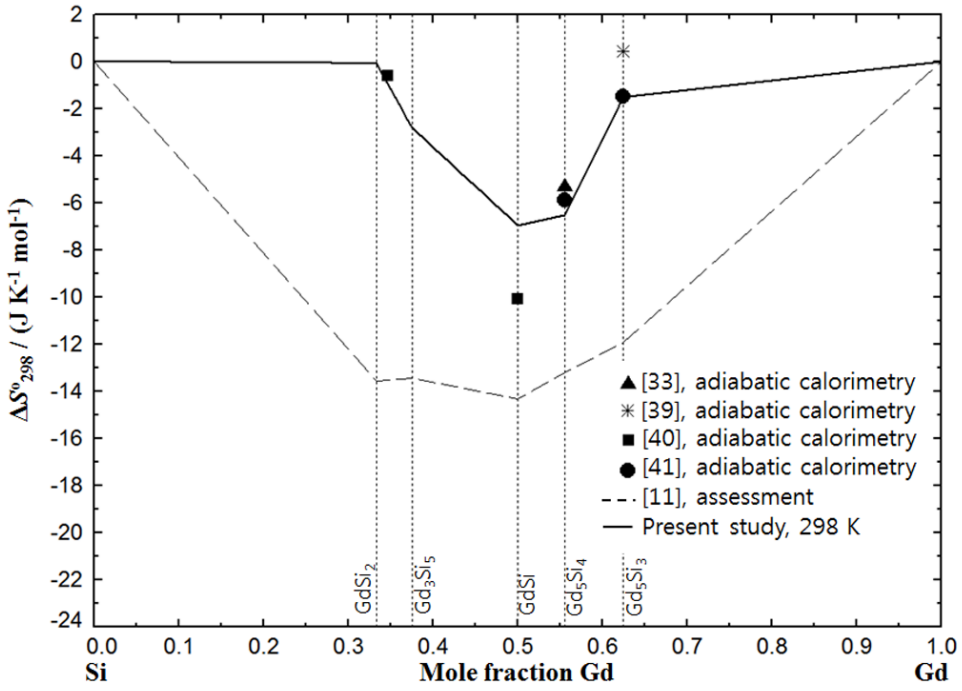


Fig. 4. Entropy of formation of the compounds in the Si-Gd system from elements at 298 K with experimental data and previous thermodynamic assessment.

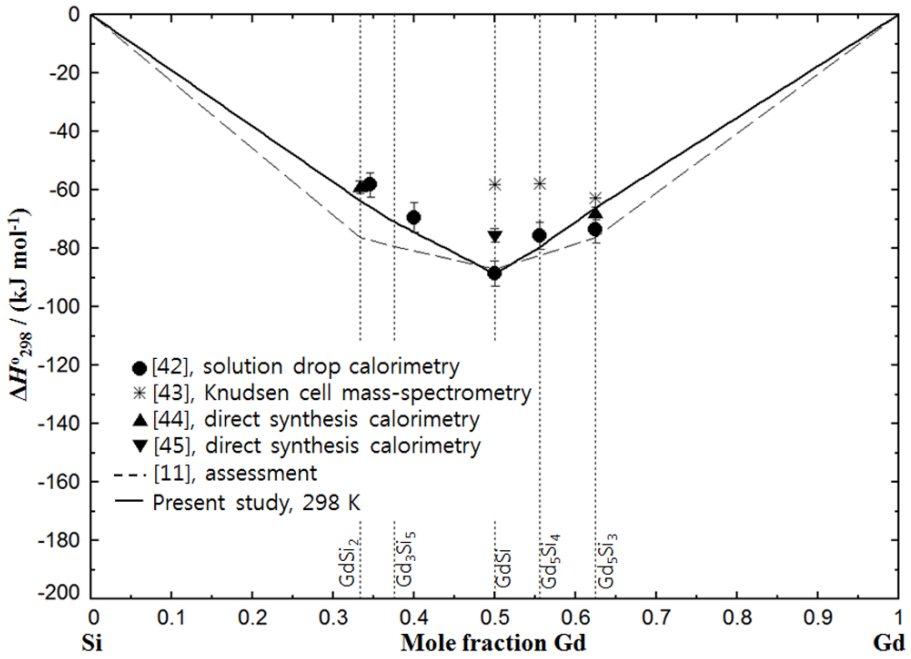


Fig. 5. Enthalpy of formation of the compounds in the Si-Gd system at 298 K with experimental data and previous thermodynamic assessment.

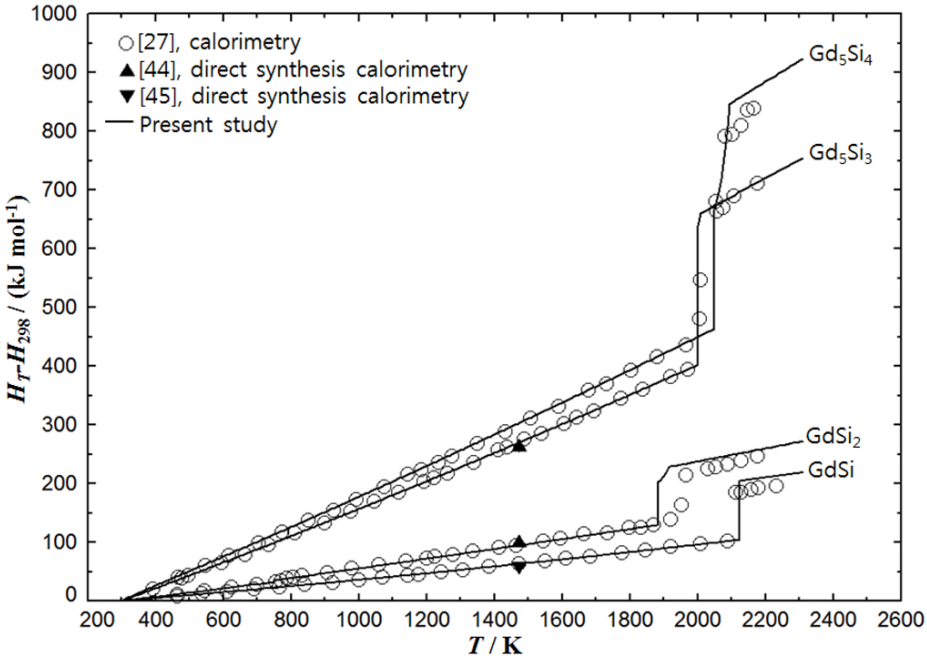


Fig. 6. Heat contents of the compounds in the Si-Gd system with experimental data and previous thermodynamic assessment.

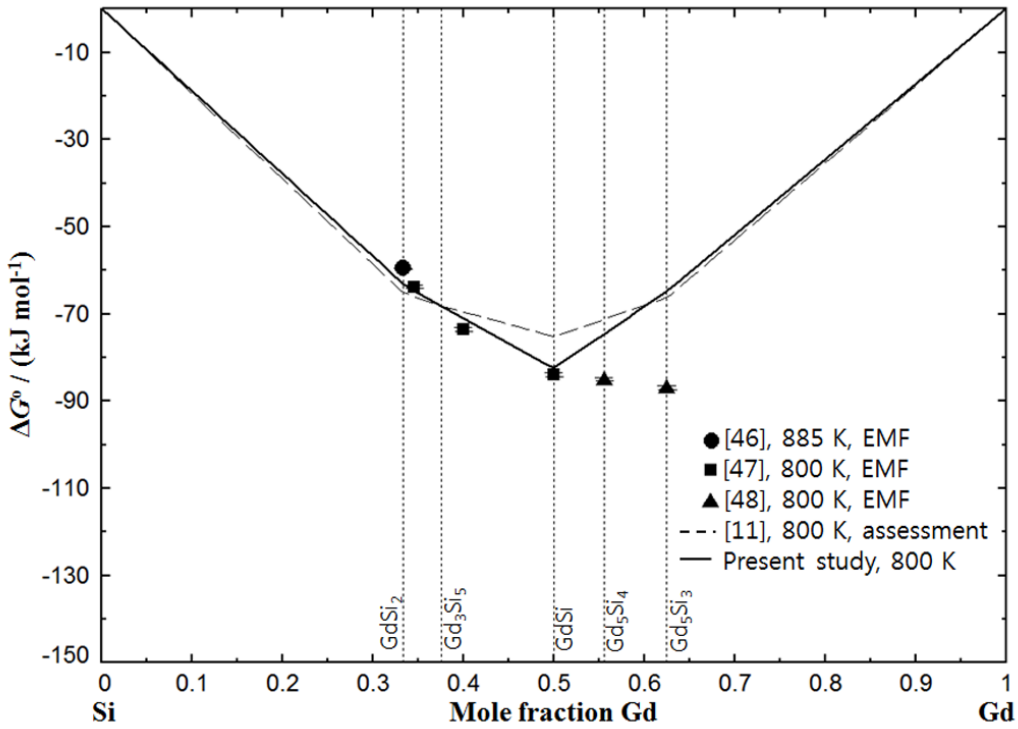


Fig. 7. Gibbs energy of formation of the compounds in the Si-Gd system at 800 K with experimental data and previous thermodynamic assessment.

2.2. The Si-Tb system

Experimental data for the phase diagram of the Si-Tb system are shown in Fig. 8. Bulanova et al. [49] investigated the phase diagram of the system by analyzing alloys of 13 compositions using DTA, XRD and metallography. The alloys were prepared from 99.83 wt. % Tb and 99.999 wt. % Si by means of arc-melting under purified argon atmosphere. Five intermetallic phases ($TbSi_{2-a}$, $TbSi_{2-b}$, TbSi, Tb_5Si_4 and Tb_5Si_3) and corresponding invariant reactions were reported. The homogeneity range of $TbSi_{2-b}$ was determined to be about 0.37 to 0.38 mole fraction Tb, which agreed with the data [50] where the Si-rich boundary of the homogeneity range was shown to have 0.374 mole fraction Tb. On the other hand, the homogeneity range of $TbSi_{2-a}$, which was previously known to be 0.351 to 0.364 mole fraction Tb [51], was not concluded in their study. It was also found that the TbSi and Tb_5Si_3 congruently melt at 1820 ºC and 1830 ºC, respectively, and the $TbSi_{2-a}$, $TbSi_{2-b}$ and Tb_5Si_4 form by peritectic reactions at 1517 ± 3 ºC, 1638 ± 4 ºC and 1775 ºC, respectively. Both eutectic reactions $L \rightarrow TbSi_{2-a} + Si$ and $L \rightarrow Tb_5Si_3 + Si$ were determined to be 1222 ± 6 ºC and 1110 ºC, respectively. The compositions of these reactions, however, were not confirmed. No experimental data on the terminal solubility of Si and Tb were previously reported. Prior to the study of Bulanova et al. [49], the eutectic reaction $L \rightarrow TbSi_2 + Si$ was estimated to occur at 1170 ºC and 0.25 mole fraction Tb [21] from gravimetrical liquidus measurement of other Si-RE system.

The thermodynamic properties of Si-Tb liquid were not available in literature. However, the thermodynamic properties of several intermetallic phases were investigated. The C_p of Tb_5Si_4 and Tb_5Si_3 are shown in Fig. 9. The low temperature C_p of Tb_5Si_3 was measured by Safonov et al. [39] between 14 and 300 K using adiabatic calorimetry and by Jammalamadaka et al. [52] between 1.8 and 250 K employing the relaxation method by means of physical property measurements system (PPMS). However, the data of Jammalamadaka et al. [52] were only reported up to 150 K and were about 20 J K^{-1} mol^{-1} less than that of Safonov et al. [39]. Safonov et al. [39] reported the multiple magnetic ordering transition temperature T_N' = 52 K and T_N = 76 K, while Jammalamadaka et al. [52] reported the transition temperature T_N = 67 K. The low temperature

C_p of Tb_5Si_4 were measured by Serdyuk et al. [53] and Spichkin et al. [34] using adiabatic calorimetry and reported the magnetic transformation at 221.5 K and 223.2 K, respectively. The S^{o}_{298} calculated from the experimental C_p data are 403.37 (Tb_5Si_3) [39], 446.11 (Tb_5Si_4) [53] and 446.27 (Tb_5Si_4) [34] J K^{-1} mol^{-1}, respectively, and the ΔS^{o}_{298} from the elements are presented in Fig. 10. Meschel and Kleppa [54] measured the ΔH^{o}_{298} of $TbSi_2$, TbSi and Tb_5Si_3 using direct synthesis calorimetry and also reported the heat content ($H_{1473} - H_{298}$) of those compounds. The experimental data reported by Meschel and Kleppa [54] are shown in Figs. 11 and 12.

A brief literature review of the Si-Tb system was carried out by Okamoto [55] based on the phase diagram study of Bulanova et al. [49]. No former study on the thermodynamic optimization of this system has been reported. The optimized phase diagram of the Si-Tb system in the present study is shown in Fig. 8. The phase diagram was constructed mostly based on the work of Bulanova et al. [49] and the phase diagram analogous to that of Si-Gd system. The non-stoichiometric compound $TbSi_{2-a}$ and $TbSi_{2-b}$ were considered as stoichiometric $TbSi_2$ and Tb_3Si_5 since the homogeneity ranges of these compounds were very small. The estimated eutectic point [21] was evidently less feasible, it was abandoned in the present study. In addition, the eutectic reaction between Tb_5Si_4 and TbSi suggested by Bulanova et al. [49] was difficult to be reproduced due to the different liquidus slopes on the left and right side of TbSi, which are less likely. Instead, the eutectic reaction was found between Tb_5Si_4 and Tb_5Si_3. The peritectic melting of Tb_3Si_5 suggested by Bulanova et al. [49] was also amended as congruent melting like Gd_3Si_5. The calculated thermodynamic properties with optimized thermodynamic parameters are shown in Figs. 9 to 12. In the optimization, the thermodynamic properties of liquid was first assumed to be similar to those of the Si-Gd system because no experimental data were available and were slightly adjusted to reproduce other experimental data. The C_p above 298 K of all compounds were estimated by NK rule. As shown in Fig. 9, the estimated C_p of Tb_5Si_3 agreed with the experimental data of Safonov et al. [39] at 298 K, while the estimated C_p of Tb_5Si_4 at 298 K was about 20 J K^{-1} mol^{-1} less than the experimental data of Serdyuk et al. [53] and Spichkin et al. [34]. The calculated S^{o}_{298} of Tb_5Si_4 from experimental data [34, 53] are comparatively much larger than those of adjacent compounds, TbSi and Tb_5Si_3. When these experimental S^{o}_{298} of Tb_5Si_4 were applied in the present optimization,

it was very difficult to reproduce the stability of this compound at room temperature against adjacent compounds. Therefore, the S^{o}_{298} of Tb_5Si_4 was set lower than the experimental data by -52 J K^{-1} mol^{-1}, as seen in Fig. 10. The experimental data of ΔH^{o}_{298} of Meschel and Kleppa [54] were well reproduced in the optimization as seen in Fig. 11. For the compounds having no available experimental data, the ΔH^{o}_{298} and S^{o}_{298} of those compounds were reasonably estimated to reproduce other thermodynamic data and the phase diagram. It should be noted that the optimized ΔH^{o}_{298} and S^{o}_{298} of the compounds in the present system are similar to those of Si-Gd system. The calculated heat content ($H_T - H_{298}$) of $TbSi_2$, TbSi and Tb_5Si_3 are compared to the experimental data of Meschel and Kleppa [54] in Fig. 12. The heat contents of $TbSi_2$ and TbSi calculated from the estimated C_p agree well with the experimental data although the calculated value of Tb_5Si_3 is about 60 kJ mol^{-1} higher than the experimental data. The optimized thermodynamic parameters are listed in Table 3 and the calculated invariant reactions with the experimental data are tabulated in Table 4.

Table 3. Optimized model parameters of the Si-Tb system.

Phase	Thermodynamic parameters
Liquid	Coordination Numbers
	i j Z_{ij}^{i} Z_{ij}^{j}
	Si Tb 6 6
	Δg_{SiTb} / (J mol^{-1}) = (-56484.0 + 7.448 T/K) – (25940.8 + 5.858 T/K) X_{SiSi} + 16736.0 X_{SiSi}^{2} – 3347.2 X_{TbTb} – 2510.4 X_{TbTb}^{2}
$TbSi_2$	ΔH_{298}° = -184500 J mol^{-1}, S_{298}° = 107.0 J K^{-1} mol^{-1}
	C_p / (J K^{-1} mol^{-1}) = 1 × C_p / (J K^{-1} mol^{-1}) (Tb, hcp-A3) + 2 × C_p / (J K^{-1} mol^{-1}) (Si, diamond-A4)
Tb_3Si_5	ΔH_{298}° = -549500 J mol^{-1}, S_{298}° = 290.0 J K^{-1} mol^{-1}
	C_p / (J K^{-1} mol^{-1}) = 3 × C_p / (J K^{-1} mol^{-1}) (Tb, hcp-A3) + 5 × C_p / (J K^{-1} mol^{-1}) (Si, diamond-A4)
TbSi	ΔH_{298}° = -161800 J mol^{-1}, S_{298}° = 77.0 J K^{-1} mol^{-1}
	C_p / (J K^{-1} mol^{-1}) = 1 × C_p / (J K^{-1} mol^{-1}) (Tb, hcp-A3) + 1 × C_p / (J K^{-1} mol^{-1}) (Si, diamond-A4)
Tb_5Si_4	ΔH_{298}° = -654500 J mol^{-1}, S_{298}° = 394.2 J K^{-1} mol^{-1}
	C_p / (J K^{-1} mol^{-1}) = 5 × C_p / (J K^{-1} mol^{-1}) (Tb, hcp-A3) + 4 × C_p / (J K^{-1} mol^{-1}) (Si, diamond-A4)
Tb_5Si_3	ΔH_{298}° = -500000 J mol^{-1}, S_{298}° = 403.37 J K^{-1} mol^{-1}
	C_p / (J K^{-1} mol^{-1}) = 5 × C_p / (J K^{-1} mol^{-1}) (Tb, hcp-A3) + 3 × C_p / (J K^{-1} mol^{-1}) (Si, diamond-A4)

Table 4. Calculated invariant reactions and experimental data in the Si-Tb system.

Type	Reaction	t (°C)	Reference
Eutectic	$L_{(X_{Tb}=0.168)} \rightarrow Si_{(dia.\text{-}A4,\ X_{Tb}=0)} + TbSi_2$	1216.1	This work
	$L_{(X_{Tb}*)} \rightarrow Si_{(dia.\text{-}A4,\ X_{Tb}=0)} + TbSi_{2\text{-}a}$	1222 ± 6	[49]
Peritectic	$L_{(X_{Tb}=0.287)} + Tb_3Si_5 \rightarrow TbSi_2$	1519.1	This work
	$L_{(X_{Tb}*)} + TbSi_{2\text{-}b} \rightarrow TbSi_{2\text{-}a}$	1517 ± 3	[49]
Congruent	$L_{(X_{Tb}=0.375)} \leftrightarrow Tb_3Si_5$	1643.9	This work
Eutectic	$L_{(X_{Tb}=0.384)} \rightarrow Tb_3Si_5 + TbSi$	1642.5	This work
Peritectic	$L_{(X_{Tb}*)} + TbSi \rightarrow TbSi_{2\text{-}b}$	1638 ± 4	[49]
Congruent	$L_{(X_{Tb}=0.50)} \leftrightarrow TbSi$	1820.4	This work
	$L_{(X_{Tb}=0.50)} \leftrightarrow TbSi$	1820.0	[49]
Peritectic	$TbSi + L_{(X_{Tb}=0.564)} \rightarrow Tb_5Si_4$	1787.9	This work
Eutectic	$L_{(X_{Tb}=0.564)} \rightarrow Tb_5Si_4 + Tb_5Si_3$	1787.8	This work
Eutectic	$L_{(X_{Tb}=\sim 0.51\text{ to }0.52)} \rightarrow TbSi + Tb_5Si_4$	1752 ± 2	[49]
Peritectic	$L_{(X_{Tb}*)} + Tb_5Si_3 \rightarrow Tb_5Si_4$	1775.0	[49]
Congruent	$L_{(X_{Tb}=0.625)} \leftrightarrow Tb_5Si_3$	1826.0	This work
	$L_{(X_{Tb}=0.625)} \leftrightarrow Tb_5Si_3$	1830.0	[49]
Eutectic	$L_{(X_{Tb}=0.866)} \rightarrow Tb_5Si_3 + Tb_{(hcp\text{-}A3,\ X_{Tb}=1)}$	1070.6	This work
	$L_{(X_{Tb}*)} \rightarrow Tb_5Si_3 + Tb_{(hcp\text{-}A3,\ X_{Tb}=1)}$	1110.0	[49]

* The exact compositions are not specified in the reference.

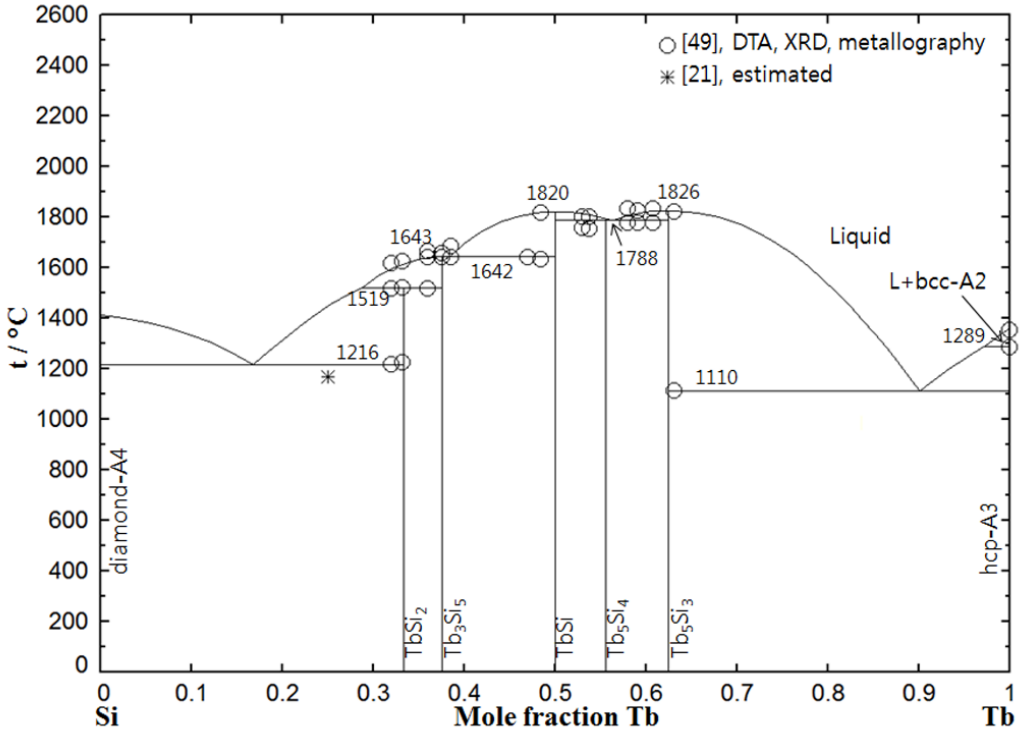


Fig. 8. The optimized Si-Tb phase diagram with experimental data.

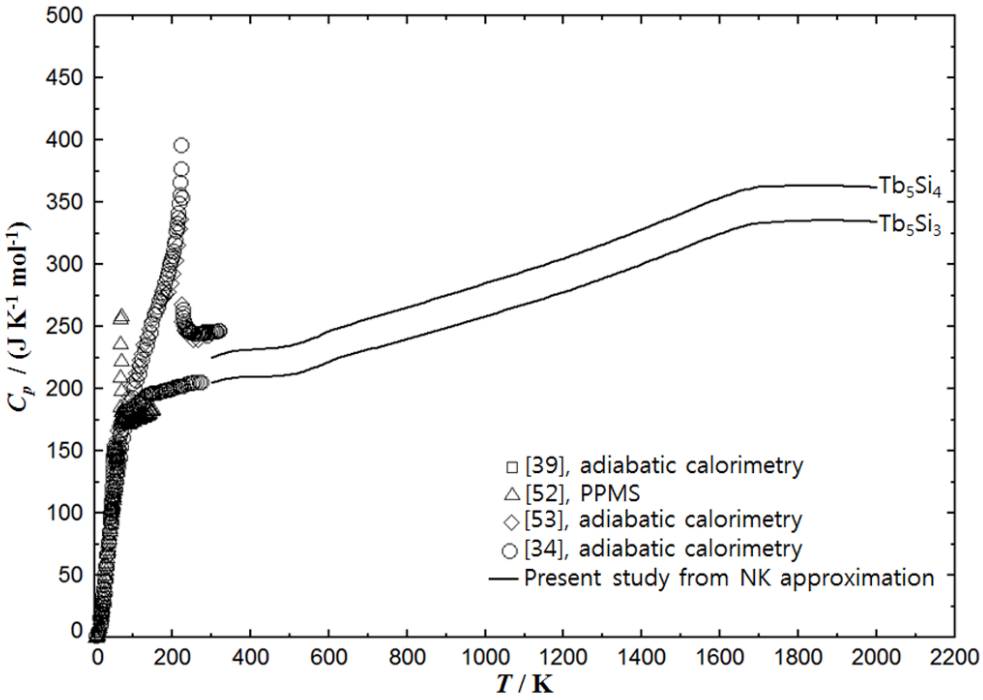


Fig. 9. Heat capacities of the compounds in the Si-Tb system with experimental data.

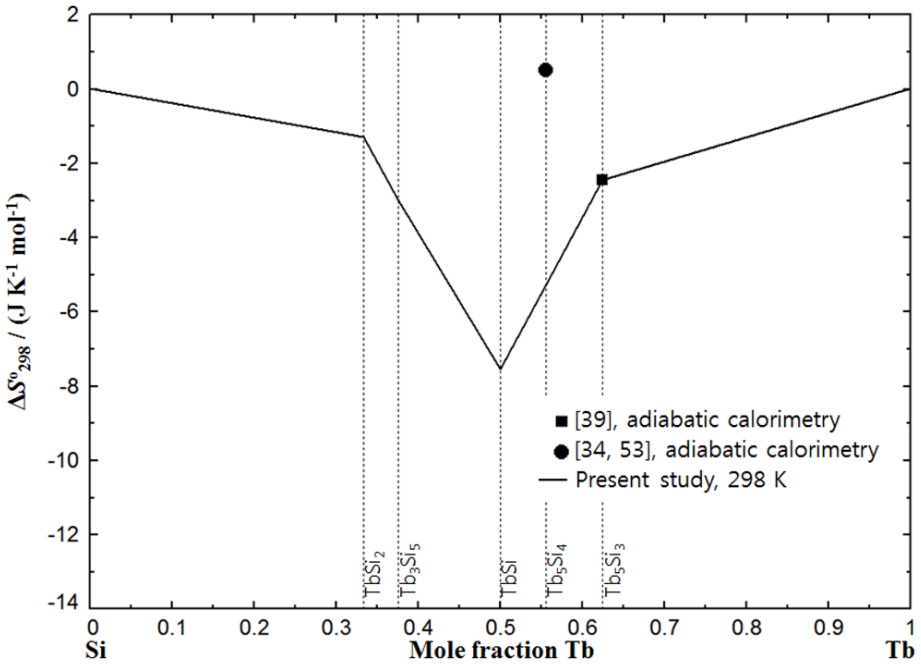


Fig. 10. Entropy of formation of the compounds in the Si-Tb system from elements at 298 K with experimental data.

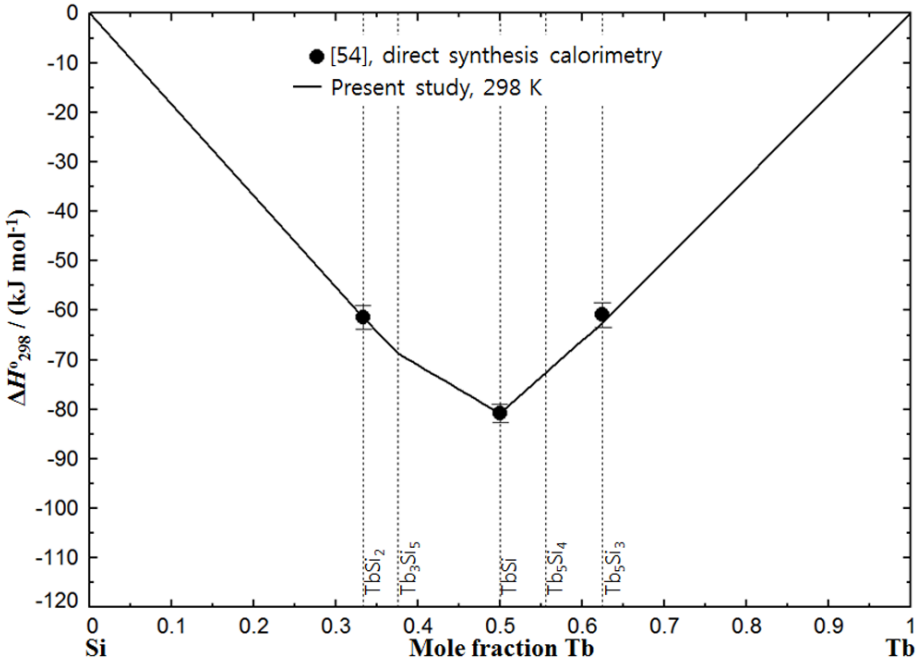


Fig. 11. Enthalpy of formation of the compounds in the Si-Tb system at 298 K with experimental data.

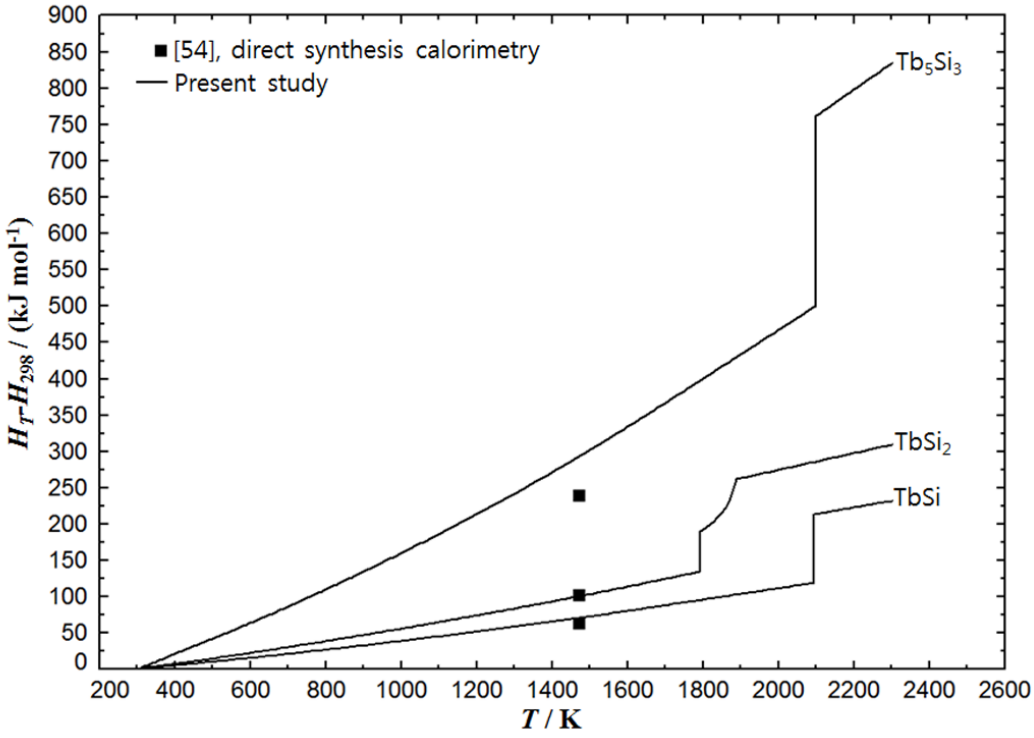


Fig. 12. Heat contents of the compounds in the Si-Tb system with experimental data.

2.3. The Si-Dy system

Experimental data of the Si-Dy phase diagram are shown in Fig. 13. Eremenko et al. [56] investigated the phase diagram of this system in the whole composition range using DTA, XRD and metallography techniques. The alloys were prepared from 99.91 wt. % Dy and 99.999 wt. % Si by arc melting under purified argon and homogenized for 200 h at 1000 ^{o}C in tantalum crucibles under purified argon. The existence of seven compounds ($DySi_{2-a}$ ($a \approx 0.18$), $DySi_{2-b}$ ($b \approx 0.33$), Dy_4Si_5, DySi, $DySi_{1-x}$ ($x \approx 0.02$), Dy_5Si_4 and Dy_5Si_3) and corresponding invariant reactions were established. The DySi and Dy_5Si_3 congruently melted at 1890 ^{o}C and 1880 ^{o}C, respectively, and the $DySi_{2-a}$, $DySi_{2-b}$, $DySi_{1-x}$ and Db_5Si_4 formed by peritectic reactions at 1430 ± 5 ^{o}C, 1635 ^{o}C, 1780 ^{o}C and 1830 ^{o}C, respectively. The Dy_4Si_5 was decomposed by a eutectoid reaction at 1350 ^{o}C. It was also suggested that the $DySi_{1-x}$ were decomposed by a peritectoid reaction between 1400 ^{o}C and 600 ^{o}C (the phase was found in the alloys annealed at 1400 ^{o}C, but it was not observed in the alloys annealed at 600 ^{o}C). The polymorphic transformation of $DySi_{2-b}$ was determined to occur at 760 ^{o}C. Three eutectic reactions were found: $L \rightarrow DySi_{2-a} + Si$ at 1215 ^{o}C and 0.17 mole fraction Dy, $L \rightarrow Dy_5Si_4 + DySi_{1-x}$ at 1780 ^{o}C and 0.55 mole fraction Dy and $L \rightarrow Dy + Dy_5Si_3$ at 1180 ^{o}C and 0.875 mole fraction Dy. Prior to the study of Eremenko et al. [56], it was reported that $DySi_2$ melted at about 1550 ^{o}C [22, 24] and 1500 ^{o}C [23], and the polymorphic transformation of $DySi_2$ occurred at about 540 ± 40 ^{o}C (high-temperature XRD) [25]. Copeland and Kato [19] suggested that the eutectic reaction between Dy and Dy_5Si_3 occurred at 1165 ^{o}C and 0.89 mole fraction of Dy and the Si solubility in Dy was less than 0.2 wt. % Si (0.011 mole fraction of Dy). The eutectic reaction between Si and $DySi_2$ was estimated to occur at 1195 ^{o}C and 0.17 mole fraction of Dy [21]. Gorbachuk and Bolgar [57] reported from their heat content measurement, the melting and the polymorphic transformation temperatures and enthalpy of transition of $DySi_2$ to be about 1455 ± 40 ^{o}C, 464 ± 19 ^{o}C and 2 ± 0.8 kJ mol^{-1}, respectively. Later, Gorbachuk [28] modified polymorphic transformation temperature and enthalpy of $DySi_2$ to be 490 ^{o}C and 2.3 kJ mol^{-1} using a quantitative DTA. Furthermore, Roger et al. [58] refined the compound Dy_4Si_5 [56] from X-ray single crystal data to be Dy_3Si_4.

The enthalpy of liquid Si-Dy solution were reported by Batalin et al. [29] and the experimental data are presented in Fig. 14. The authors measured the integral enthalpy of mixing and partial enthalpy of mixing of Dy for the Si-Dy liquid at 1785 K and a limited composition range ($0 < X_{Dy} < 0.04$) using high temperature calorimetry with isothermal jacket. The thermodynamic properties of several intermetallic phases were determined. Low temperature C_p of $DySi_2$ (see Fig. 15) was measured by Gorbachuk et al. [59] between 55 and 300 K using adiabatic calorimetry. The calculated S^{o}_{298} of $DySi_2$ was reported to be 99.6 ± 0.8 J K^{-1} mol^{-1} and the ΔS^{o}_{298} is presented in Fig. 16. Meschel and Kleppa [60] measured the ΔH^{o}_{298} of $DySi_2$, DySi and Dy_5Si_3 using direct synthesis calorimetry and also reported the heat content ($H_{1473} - H_{298}$) of those compounds. The experimental ΔH^{o}_{298} of Meschel and Kleppa [60] are presented in Fig. 17. Gorbachuk and Bolgar [57] measured the heat content ($H_T - H_{298}$) of $DySi_2$ by means of high temperature differential calorimetry between 300 and 1200 K and high temperature vacuum calorimetry at the temperature above 1200 K. The temperature dependent C_p for both α-$DySi_2$ and β-$DySi_2$ phases were derived from the experimental data. The experimental data of Gorbachuk and Bolgar [57] and Meschel and Kleppa [60] are shown in Fig. 18.

No previous study on the thermodynamic optimization of this system has been reported. The optimized phase diagram of the Si-Dy system in the present study is compared with the experimental data in Fig. 13 and the calculated thermodynamic properties by the optimized thermodynamic parameters are shown and compared to the experimental data in Figs. 14 to 18. In the optimization, the thermodynamic properties of liquid was assumed to be similar to those of the Si-Gd and Si-Tb systems and the experimental data of Batalin et al. [29] were taken to evaluate partial enthalpy of Dy. The minimum integral enthalpy of mixing was approximately estimated about -70 kJ mol^{-1} at 0.5 mole fraction of Dy to reproduce the phase diagram and thermodynamic properties of compounds. As seen in Figs. 14(a) and 14(b), the calculated integral enthalpy of mixing at 1785 K are in good agreement with the experimental data [29] although the abrupt variation of partial enthalpy of mixing of Dy shown in the experimental data [29] was difficult to be reproduced. The experimental data of Eremenko et al. [56] were preferred in the phase diagram evaluation for the most part. The intermetallic compound $DySi_{2-b}$ ($b \approx 0.33$) was considered as

stoichiometric Dy_3Si_5. On the other hand, the $DySi_{2-a}$ ($a \approx 0.18$) [56] was considered as $DySi_2$ after accepting the results of Gorbachuk and Bolgar [57] and Meschel and Kleppa [60], and Dy_3Si_4 [58] was accepted instead of Dy_4Si_5 [56]. The $DySi_{1-x}$ ($x \approx 0.02$) was neglected in the present study because it is unlikely that two compounds with similar compositions coexist in a wide temperature range [61]. The C_p of α-$DySi_2$ and β-$DySi_2$ derived from the experimental heat content data [57] were used without any modification as shown in Fig. 15. The C_p of other compounds were estimated by NK rule and the C_p of both α-Dy_3Si_5 and β-Dy_3Si_5 were assumed to be same because no experimental data were available. The polymorphic transformation temperature and enthalpy of the $DySi_2$ were taken from the data of Gorbachuk and Bolgar [57]. The polymorphic transformation temperature of Dy_3Si_5 was taken from the data of Eremenko et al. [56] and the enthalpy of polymorphic transformation was approximated to be 8 kJ mol^{-1} assuming that the value is similar to that of Gd_3Si_5. The S°_{298} of $DySi_2$ calculated from the experimental low temperature C_p up to 298 K [59] was used in the present optimization, and the S°_{298} of other compounds were estimated to reproduce the phase diagram with other thermodynamic properties simultaneously, as shown in Fig. 16. The experimental ΔH°_{298} of $DySi_2$, DySi and Dy_5Si_3 [60] were reproduced in the optimization and the ΔH°_{298} of other compounds were estimated to reproduce the phase diagram, as seen in Fig. 17. The calculated heat content ($H_T - H_{298}$) of Dy_5Si_3, $DySi_2$ and DySi are compared with the experimental data [57, 60] in Fig. 18. The calculated heat content of $DySi_2$ are in good agreement with the experimental data [57] and the heat contents of the other two compounds calculated from the estimated C_p reasonably agree with the experimental data [60]. The optimized thermodynamic parameters are listed in Table 5 and the calculated invariant reactions with the experimental data are tabulated in Table 6.

Table 5. Optimized model parameters of the Si-Dy system.

Phase	Thermodynamic parameters
Liquid	Coordination Numbers
	i j Z_{ij}^{i} Z_{ij}^{j}
	Si Dy 6 6
	Δg_{SiDy} / (J mol^{-1}) = (-56484.0 + 10.46 T/K) – (16736.0 + 5.858 T/K) X_{SiSi} + 12552.0 X_{SiSi}^{2} + (-24685.6 + 2.720 T/K) X_{DyDy} + 16736.0 X_{DyDy}^{2}
α-$DySi_2$	ΔH_{298}° = -163500 J mol^{-1}, S_{298}° = 99.6 J K^{-1} mol^{-1}
	C_p / (J K^{-1} mol^{-1}) = 74.71 + 0.018582 T/K - 900119 (T/K)$^{-2}$
β-$DySi_2$	$\Delta_{\mathrm{trs}}H^{\alpha\rightarrow\beta}$ = 2300 J mol^{-1}, $T_{\mathrm{trs}}^{\alpha\rightarrow\beta}$ = 763.0 K
	C_p / (J K^{-1} mol^{-1}) = 83.56 + 0.00933 T/K - 805432 (T/K)$^{-2}$
α-Dy_3Si_5	ΔH_{298}° = -480000 J mol^{-1}, S_{298}° = 295.5 J K^{-1} mol^{-1}
	C_p / (J K^{-1} mol^{-1}) = 3 × C_p / (J K^{-1} mol^{-1}) (Dy, hcp-A3) + 5 × C_p / (J K^{-1} mol^{-1}) (Si, diamond-A4)
β-Dy_3Si_5	$\Delta_{\mathrm{trs}}H^{\alpha\rightarrow\beta}$ = 8000 J mol^{-1}, $T_{\mathrm{trs}}^{\alpha\rightarrow\beta}$ = 1033.0 K
	C_p / (J K^{-1} mol^{-1}) = 3 × C_p / (J K^{-1} mol^{-1}) (Dy, hcp-A3) + 5 × C_p / (J K^{-1} mol^{-1}) (Si, diamond-A4)
Dy_3Si_4	ΔH_{298}° = -458000 J mol^{-1}, S_{298}° = 270.45 J K^{-1} mol^{-1}
	C_p / (J K^{-1} mol^{-1}) = 3 × C_p / (J K^{-1} mol^{-1}) (Dy, hcp-A3) + 4 × C_p / (J K^{-1} mol^{-1}) (Si, diamond-A4)
DySi	ΔH_{298}° = -137800 J mol^{-1}, S_{298}° = 85.5 J K^{-1} mol^{-1}
	C_p / (J K^{-1} mol^{-1}) = 1 × C_p / (J K^{-1} mol^{-1}) (Dy, hcp-A3) + 1 × C_p / (J K^{-1} mol^{-1}) (Si, diamond-A4)
Dy_5Si_4	ΔH_{298}° = -611900 J mol^{-1}, S_{298}° = 406.0 J K^{-1} mol^{-1}
	C_p / (J K^{-1} mol^{-1}) = 5 × C_p / (J K^{-1} mol^{-1}) (Dy, hcp-A3) + 4 × C_p / (J K^{-1} mol^{-1}) (Si, diamond-A4)

Dy_5Si_3	ΔH^{o}_{298} = -512000 J mol^{-1}, S^{o}_{298} = 395.0 J K^{-1} mol^{-1}
	C_p / (J K^{-1} mol^{-1}) = 5 × C_p / (J K^{-1} mol^{-1}) (Dy, hcp-A3)
	+ 3 × C_p / (J K^{-1} mol^{-1}) (Si, diamond-A4)

Table 6. Calculated invariant reactions and experimental data in the Si-Dy system.

Type	Reaction	t (°C)	Reference
Eutectic	$L_{(X_{Dy}= 0.174)} \rightarrow Si_{(dia.-A4,\ X_{Dy}= 0)} + DySi_2$	1224.5	This work
	$L_{(X_{Dy}= 0.240)} \rightarrow Si_{(dia.-A4,\ X_{Dy}= 0)} + DySi_2$	1215.0	[56]
Peritectic	$L_{(X_{Dy}= 0.253)} + Dy_3Si_5 \rightarrow DySi_2$	1436.7	This work
	$L_{(X_{Dy}= 0.270)} + Dy_3Si_5 \rightarrow DySi_{2-a}$	1430 ± 5	[56]
	T_m for $DySi_2$	1550.0	[22, 24]
		1500.0	[23]
		1455 ± 40	[57]
Allotropic	α-$DySi_2$ ↔ β-$DySi_2$	490.0	This work
	α-$DySi_2$ ↔ β-$DySi_2$	540 ± 40	[25]
	α-$DySi_2$ ↔ β-$DySi_2$	464 ± 19	[57]
	α-$DySi_2$ ↔ β-$DySi_2$	490.0	[28]
Peritectic	$L_{(X_{Dy}= 0.362)} + DySi \rightarrow Dy_3Si_5$	1634.7	This work
	$L_{(X_{Dy}= 0.343)} + DySi \rightarrow Dy_3Si_5$	1635.0	[56]
Allotropic	α-Dy_3Si_5 ↔ β-Dy_3Si_5	760.0	This work
	α-Dy_3Si_5 ↔ β-Dy_3Si_5	760.0	[56]
Peritectoid	$Dy_3Si_5 + DySi \rightarrow Dy_3Si_4$	1350.8	This work
	$Dy_3Si_5 + DySi \rightarrow Dy_4Si_5$	1350.0	[56]
Congruent	$L_{(X_{Dy}= 0.50)}$ ↔ DySi	1885.0	This work
	$L_{(X_{Dy}= 0.50)}$ ↔ DySi	1890.0	[56]
Peritectic	$DySi + L_{(X_{Dy}= \sim 0.52\ to\ 0.54)} \rightarrow DySi_{0.98}$	1805.0	[56]
Peritectic	$DySi + L_{(X_{Dy}= 0.567)} \rightarrow Dy_5Si_4$	1836.9	This work
Eutectic	$L_{(X_{Dy}= \sim 0.550)} \rightarrow DySi_{0.98} + Dy_5Si_4$	1780.0	[56]

Eutectic	$L(X_{Dy}= 0.570) \rightarrow Dy_5Si_4 + Dy_5Si_3$	1836.0	This work
Peritectic	$L(X_{Dy}*) + Dy_5Si_3 \rightarrow Dy_5Si_4$	1830.0	[56]
Congruent	$L(X_{Dy}= 0.625) \leftrightarrow Dy_5Si_3$	1873.6	This work
	$L(X_{Dy}= 0.625) \leftrightarrow Dy_5Si_3$	1880.0	[56]
Eutectic	$L(X_{Dy}= 0.873) \rightarrow Dy_5Si_3 + Dy(\text{hcp-A3}, X_{Dy}= 1)$	1186.5	This work
	$L(X_{Dy}= 0.890) \rightarrow Dy_5Si_3 + Dy(\text{hcp-A3}, X_{Dy}= 1)$	1165.0	[19]
	$L(X_{Dy}= 0.875) \rightarrow Dy_5Si_3 + Dy(\text{hcp-A3}, X_{Dy}= 1)$	1180.0	[56]

* The exact compositions are not specified in the reference.

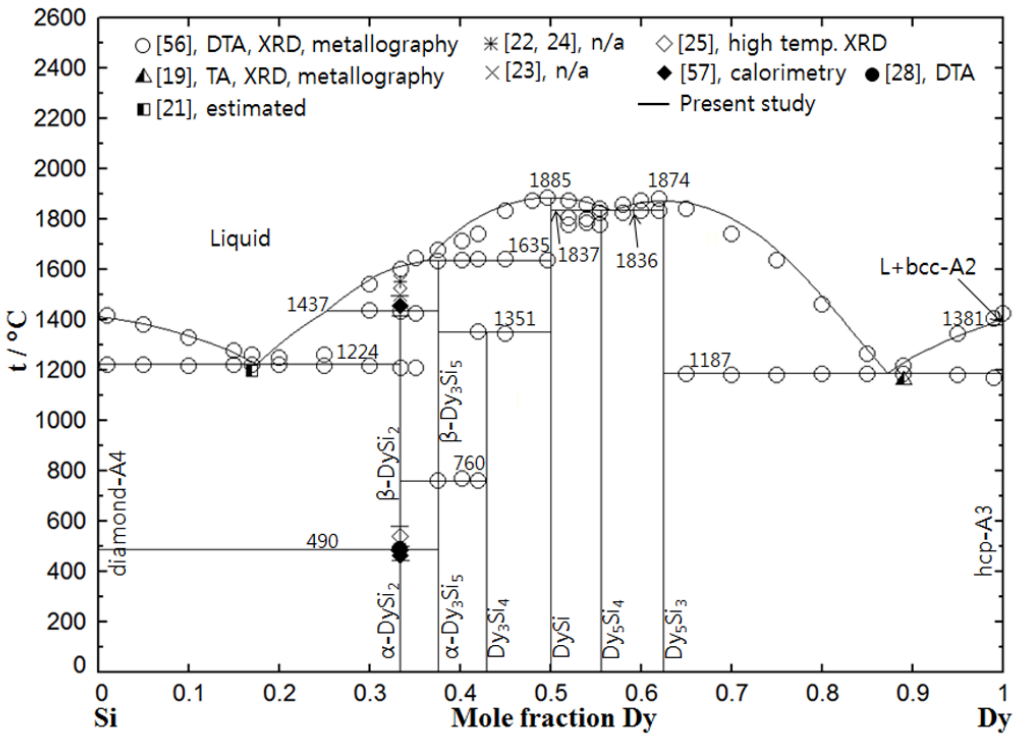


Fig. 13. The optimized Si-Dy phase diagram with experimental data.

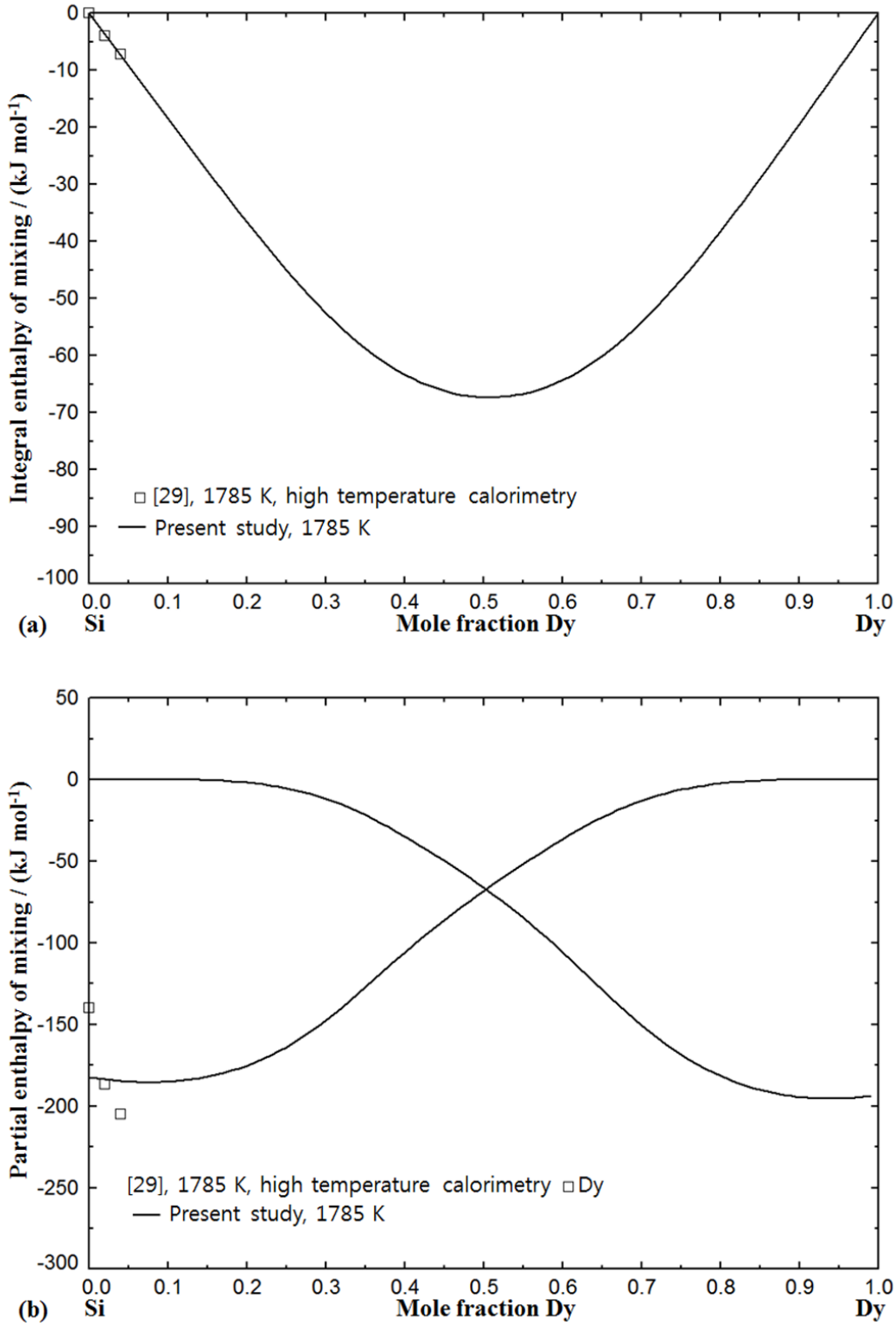


Fig. 14. (a) Integral enthalpy of mixing and (b) partial enthalpies of mixing of liquid Si-Dy phase at 1785 K with experimental data.

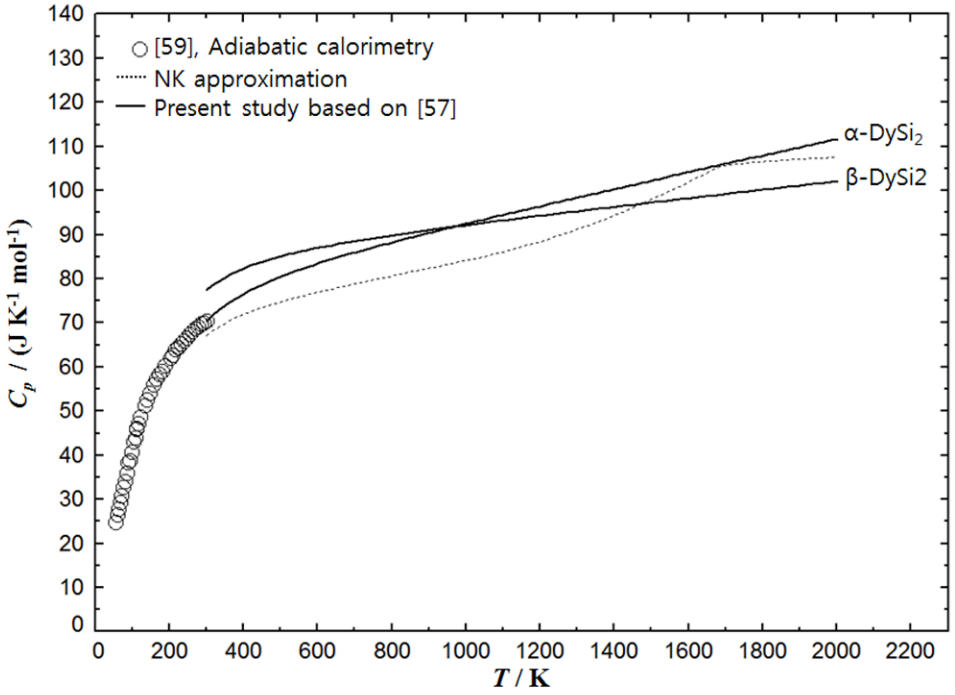


Fig. 15. Heat capacities of the $DySi_2$ phases with experimental data.

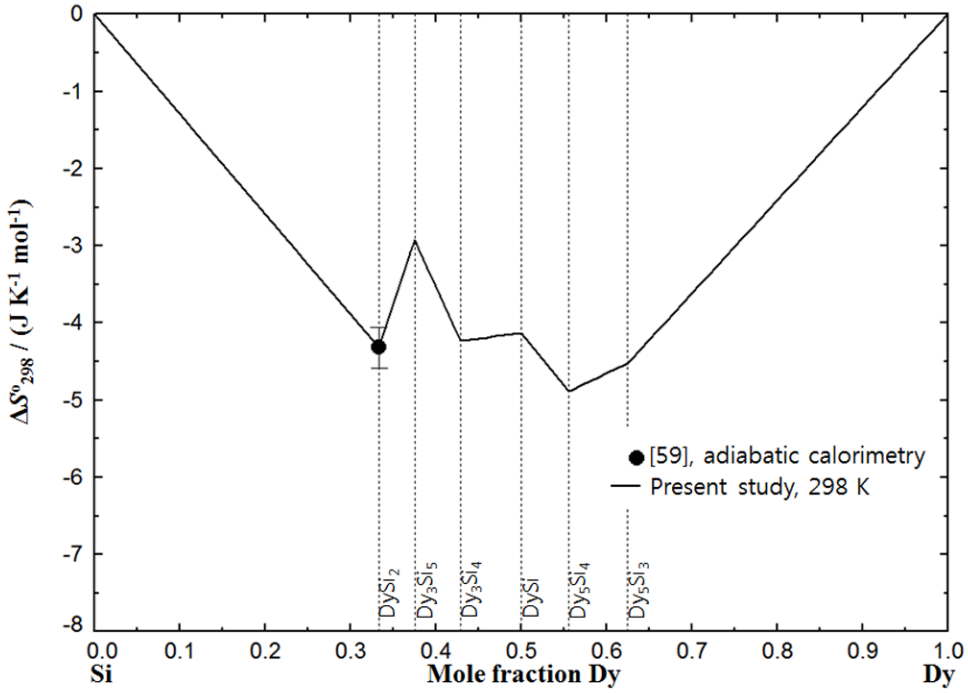


Fig. 16. Entropy of formation of the compounds in the Si-Dy system from elements at 298 K with experimental data.

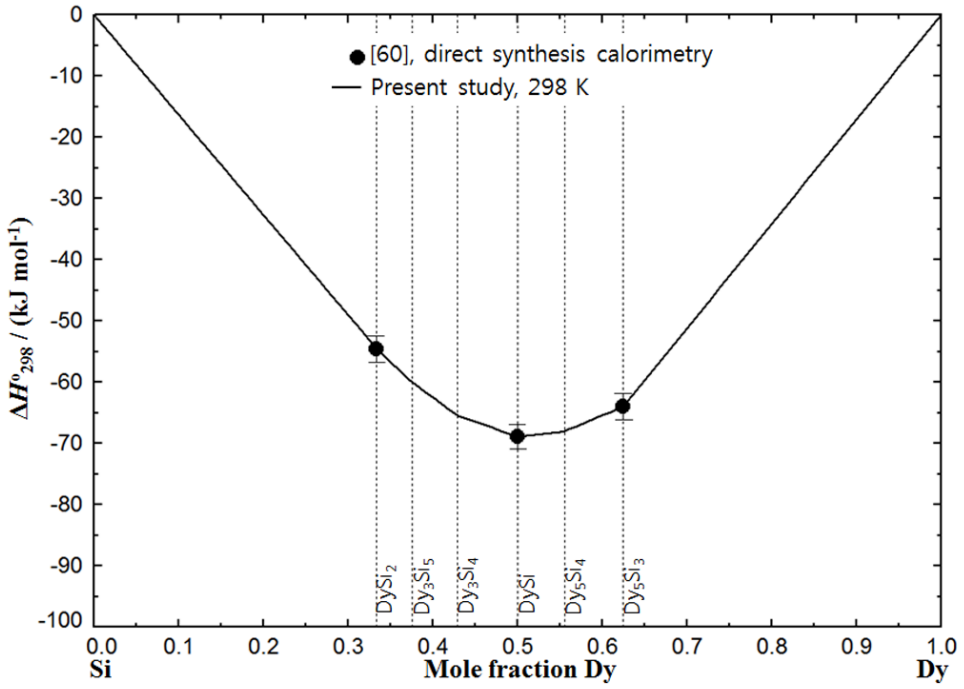


Fig. 17. Enthalpy of formation of the compounds in the Si-Dy system at 298 K with experimental data.

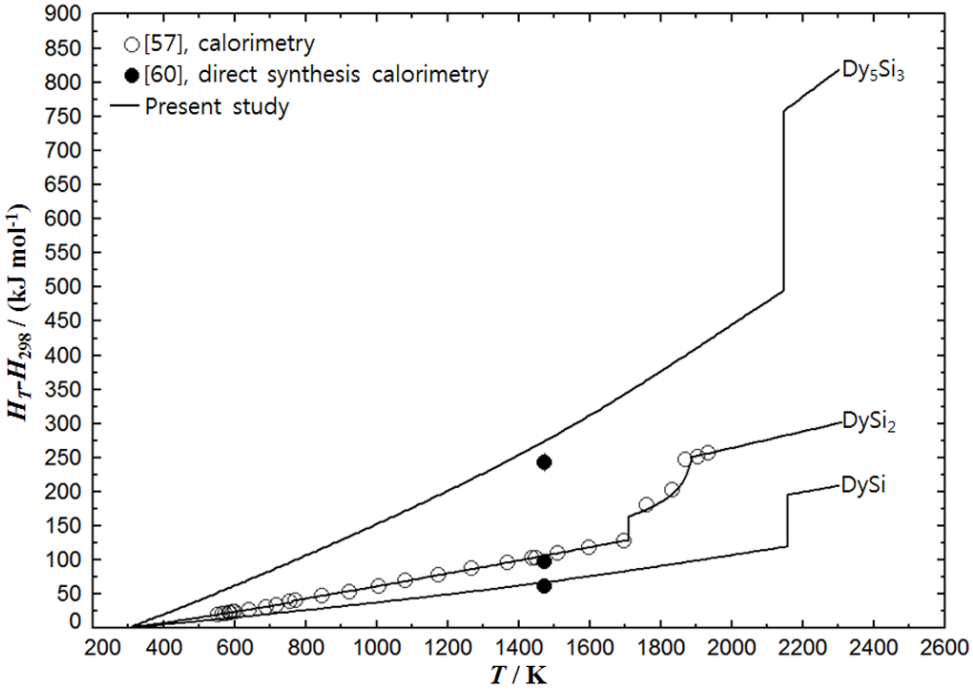


Fig. 18. Heat contents of the compounds in the Si-Dy system with experimental data.

2.4. The Si-Ho system

Experimental data of the Si-Ho phase diagram are shown in Fig. 19. Eremenko et al. [62] investigated the phase diagram of this system in the entire composition range using DTA, XRD and metallography techniques. The alloys were prepared from 99.84 wt. % Ho and 99.999 wt. % Si by arc melting under purified argon gas and homogenized for 200 h at a temperature of 1100 ºC in tantalum crucibles under purified argon gas. The existence of seven compounds ($HoSi_{2-a}$ ($a \approx 0.18$), $HoSi_{2-b}$ ($b \approx 0.33$), Ho_4Si_5, HoSi, $HoSi_{1-x}$ ($x \approx 0.02$), Ho_5Si_4 and Ho_5Si_3) and corresponding invariant reactions were established. The HoSi and Ho_5Si_3 congruently melted at 1860 ºC and 1920 ºC, respectively, and the $HoSi_{2-a}$, $HoSi_{2-b}$, $HoSi_{1-x}$ and Ho_5Si_4 formed by peritectic reactions at 1290 ºC, 1620 ºC, 1820 ºC and 1850 ºC, respectively. The Ho_4Si_5 formed by a peritectoid reaction at 1305 ºC. The polymorphic transformation of $HoSi_{2-a}$ and $HoSi_{2-b}$ were determined to be 520 ± 10 ºC and 790 ± 5 ºC, respectively. Three eutectic reactions were found: $L \rightarrow Si + HoSi_{2-a}$ at 1210 ºC and 0.18 mole fraction Ho, $L \rightarrow Ho_5Si_4 + HoSi_{1-x}$ at 1795 ºC and 0.53 mole fraction Ho and $L \rightarrow Ho_5Si_3 + Ho$ at 1255 ºC and 0.875 mole fraction Ho. It was also reported the solid solubility of Ho in Si and that of Si in Ho were both negligible (less than 0.01 mole fraction). Later, the compound Ho_4Si_5 was further investigated and corrected to be Ho_3Si_4 using single crystal X-ray structural refinement [63]. Lozovskii and Kolesnichenko [21], previously, determined the liquidus in Si-rich side by gravimetrical method and reported the eutectic reaction at 1185 ºC and 0.27 mole fraction of Ho. However, their eutectic point is very different with that of Eremenko et al. [62]. Recently, Gorbachuk and Bolgar [57] determined the melting and the polymorphic transformation temperatures and enthalpy of transition of Ho_3Si_5 to be about 1602 ± 40 ºC, 834 ± 25 ºC and 12.6 ± 4.8 kJ mol^{-1}, respectively, from the heat content measurement. Some ambiguities in the composition and homogeneity range of Si-richest compound $HoSi_{2-a}$ were reviewed by Eremenko et al. [62] and Goncharuk et al. [64]. The homogeneity range of Ho_5Si_4 and Ho_5Si_3 were accepted as $HoSi_{1.67-1.6}$ and $HoSi_{1.82-2}$, respectively.

The enthalpies of Si-Ho liquid were investigated by Batalin et al. [29]. As seen in Fig. 20, the authors measured the integral enthalpy of mixing and partial enthalpy of mixing of Ho for Si-Ho liquid ($0 < X_{Ho} < 0.04$) at 1827 K using high temperature isothermal calorimetry. The C_p of Ho_3Si_5

are shown in Fig. 21. Low temperature C_p of Ho_3Si_5 was measured by Gorbachuk et al. [59] between 55 and 300 K using adiabatic calorimetry. The calculated S^{o}_{298} of Ho_3Si_5 was reported to be 258.9 ± 2.1 J K^{-1} mol^{-1} and the ΔS^{o}_{298} is presented in Fig. 22. Meschel and Kleppa [65] measured the ΔH^{o}_{298} and heat content ($H_{1473} - H_{298}$) of $HoSi_2$, HoSi and Ho_5Si_3 using direct synthesis calorimetry, shown in Figs. 23 and 24. Gorbachuk and Bolgar [57] measured the heat content ($H_T - H_{298}$) of Ho_3Si_5 by means of high temperature differential calorimetry between 300 and 1200 K and high temperature vacuum calorimetry above 1200 K. The temperature dependent C_p for both α-Ho_3Si_5 and β-Ho_3Si_5 phases were derived from the experimental data. The experimental data of Gorbachuk and Bolgar [57] and Meschel and Kleppa [65] are shown in Fig. 24. Goncharuk et al. [66, 67] determined the Gibbs energies of formation of all intermetallic compounds using the galvanic cells in the temperatures between 610 and 970 K. The ΔG^{o}_{750} continuously decreased with increasing Ho content of the compounds as shown in Fig. 25.

Okamoto [68] presented a brief review of this system based solely on the experimental phase diagram study [62]. No previous study on the thermodynamic optimization of this system has been reported. In the present study, the Si-Ho system was thermodynamically optimized by the evaluation of Gibbs energies of all phases with all available experimental data. The optimized phase diagram agrees well with the experimental data, mostly Eremenko et al. [62], as shown in Fig. 19, and the calculated thermodynamic properties with the optimized thermodynamic parameters are compared to the experimental data in Figs. 20 to 25. As experimental data of Batalin et al. [29] is only available in the Si-rich composition range, the thermodynamic properties of liquid were assumed to be similar to those of the previous systems. The minimum integral enthalpy of mixing was estimated to be about -70 kJ mol^{-1} at 0.5 mole fraction of Ho like other Si-RE systems. As seen in Figs. 20(a) and 20(b), the calculated integral enthalpy of mixing and partial enthalpy of mixing of Ho at 1827 K agree with the experimental data [29] although the abrupt increase of the partial enthalpy of mixing of Ho shown in the experimental data was hard to be reproduced. The intermetallic compounds $HoSi_{2-b}$ ($b \approx 0.33$) and $HoSi_{2-a}$ ($a \approx 0.18$) were considered as stoichiometric Ho_3Si_5 and Ho_5Si_9. Ho_3Si_4 was accepted in the present study in agreement with the X-ray structural refinement by Ijjaali et al. [63] instead of Ho_4Si_5 [62]. The

$HoSi_{1-x}$ ($x \approx 0.02$) was neglected in the present study because two compounds with similar compositions unlikely coexist in a wide temperature range [61]. The C_p of α-Ho_3Si_5 and β-Ho_3Si_5 derived from the experimental heat content data [57] were used after a slight modification to the C_p of α-Ho_3Si_5 in order to make the low temperature C_p data consistent [59] as shown in Fig. 21. The C_p of other compounds were estimated by NK rule and the C_p of both α-Ho_5Si_9 and β-Ho_5Si_9 were assumed to be same because no experimental data were available. The polymorphic transformation temperature and enthalpy of the Ho_3Si_5 were taken from the data of Gorbachuk and Bolgar [57]. The polymorphic transformation temperature of Ho_5Si_9 was taken from the data of Eremenko et al. [62] and the enthalpy of polymorphic transformation was approximated to be 14.5 kJ mol^{-1}, assumed to be slightly higher than the $\Delta_{trs}H^{\alpha\rightarrow\beta}$ of $GdSi_2$ [28]. The S^{o}_{298} of Ho_3Si_5 calculated from the experimental low temperature C_p up to 298 K [59] was adopted and the S^{o}_{298} of other compounds were estimated to reproduce the phase diagram with other thermodynamic properties, simultaneously, as shown in Fig. 22. The experimental data of ΔH^{o}_{298} of $HoSi_2$, HoSi and Ho_5Si_3 [65] were reproduced, as seen in Fig. 23, the ΔH^{o}_{298} of other compounds were estimated to reproduce the phase diagram. The calculated heat content ($H_T - H_{298}$) of Ho_5Si_9, Ho_3Si_5, HoSi and Ho_5Si_3 are compared with the experimental data [57, 65] in Fig. 24. The heat contents of those compounds are in good agreement with the experimental data. The calculated Gibbs energies of formation of compounds at 750 K are compared with the experimental data [66, 67] in Fig. 25. The calculated ΔG^{o}_{750} are more positive than the experimental data and the minimum Gibbs energy is found at HoSi compound. In the case of Ho_3Si_5, ΔG^{o} can be calculated from the experimental ΔH^{o}_{298}, S^{o}_{298} and C_p of Ho_3Si_5 [57, 59, 65], which is higher than the data obtained by the emf measurement [66, 67]. Although the ΔH^{o}_{298} of Ho_3Si_5 was estimated in the present study, the estimated ΔH^{o}_{298} of Ho_3Si_5 are very likely to be between the experimental ΔH^{o}_{298} of $HoSi_2$ and HoSi. That is, the Gibbs energies of formation determined by Goncharuk et al. [66, 67] using the emf technique is inconsistent with the other set of data. Moreover, the decreasing trend in the Gibbs energies of formation along with increasing Ho content is inconsistent with other experimental data, in particular, the enthalpy of formation data in Fig. 23. The optimized

thermodynamic parameters are listed in Table 7 and the calculated invariant reactions with the experimental data are tabulated in Table 8.

Table 7. Optimized model parameters of the Si-Ho system.

Phase	Thermodynamic parameters
Liquid	Coordination Numbers
	i j Z_{ij}^{i} Z_{ij}^{j}
	Si Ho 6 6
	Δg_{SiHo} / (J mol^{-1}) = (-56484.0 + 7.322 T/K) + (-23012.0 + 6.485 T/K) X_{SiSi}
	+ (12552.0 – 7.531 T/K) X_{SiSi}^{2} – 20710.8 X_{HoHo}
	+ 15062.4 X_{HoHo}^{2}
α-Ho_5Si_9	ΔH_{298}° = -891500 J mol^{-1}, S_{298}° = 463.2 J K^{-1} mol^{-1}
	C_p / (J K^{-1} mol^{-1}) = 5 × C_p / (J K^{-1} mol^{-1}) (Ho, hcp-A3)
	+ 9 × C_p / (J K^{-1} mol^{-1}) (Si, diamond-A4)
β- Ho_5Si_9	$\Delta_{\mathrm{trs}}H^{\alpha\rightarrow\beta}$ = 14500 J mol^{-1}, $T_{\mathrm{trs}}^{\alpha\rightarrow\beta}$ = 793.0 K
	C_p / (J K^{-1} mol^{-1}) = 5 × C_p / (J K^{-1} mol^{-1}) (Ho, hcp-A3)
	+ 9 × C_p / (J K^{-1} mol^{-1}) (Si, diamond-A4)
α-Ho_3Si_5	ΔH_{298}° = -537800 J mol^{-1}, S_{298}° = 259.7 J K^{-1} mol^{-1}
	C_p / (J K^{-1} mol^{-1}) = 181.93 + 0.08593 T/K - 1858884 (T/K)$^{-2}$ - 2.16E-5 (T/K)^{2}
β-Ho_3Si_5	$\Delta_{\mathrm{trs}}H^{\alpha\rightarrow\beta}$ = 12600 J mol^{-1}, $T_{\mathrm{trs}}^{\alpha\rightarrow\beta}$ = 1107.0 K
	C_p / (J K^{-1} mol^{-1}) = 235.56 + 0.023574 T/K - 1736412 (T/K)$^{-2}$
Ho_3Si_4	ΔH_{298}° = -517000 J mol^{-1}, S_{298}° = 250.0 J K^{-1} mol^{-1}
	C_p / (J K^{-1} mol^{-1}) = 3 × C_p / (J K^{-1} mol^{-1}) (Ho, hcp-A3)
	+ 4 × C_p / (J K^{-1} mol^{-1}) (Si, diamond-A4)
HoSi	ΔH_{298}° = -163500 J mol^{-1}, S_{298}° = 76.8 J K^{-1} mol^{-1}
	C_p / (J K^{-1} mol^{-1}) = 1 × C_p / (J K^{-1} mol^{-1}) (Ho, hcp-A3)
	+ 1 × C_p / (J K^{-1} mol^{-1}) (Si, diamond-A4)
Ho_5Si_4	ΔH_{298}° = -708000 J mol^{-1}, S_{298}° = 381.0 J K^{-1} mol^{-1}
	C_p / (J K^{-1} mol^{-1}) = 5 × C_p / (J K^{-1} mol^{-1}) (Ho, hcp-A3)
	+ 4 × C_p / (J K^{-1} mol^{-1}) (Si, diamond-A4)
Ho_5Si_3	ΔH_{298}° = -597000 J mol^{-1}, S_{298}° = 378.0 J K^{-1} mol^{-1}
	C_p / (J K^{-1} mol^{-1}) = 5 × C_p / (J K^{-1} mol^{-1}) (Ho, hcp-A3)
	+ 3 × C_p / (J K^{-1} mol^{-1}) (Si, diamond-A4)

Table 8. Calculated invariant reactions and experimental data in the Si-Ho system.

Type	Reaction	t (°C)	Reference
Eutectic	$L_{(X_{Ho}=0.168)} \rightarrow Si_{(dia.\text{-}A4,\ X_{Ho}=0)} + Ho_5Si_9$	1221.1	This work
	$L_{(X_{Ho}=0.270)} \rightarrow Si_{(dia.\text{-}A4,\ X_{Ho}=0)} + Ho_5Si_9$	1185.0	[21]
	$L_{(X_{Ho}=0.175)} \rightarrow Si_{(dia.\text{-}A4,\ X_{Ho}=0)} + HoSi_{1.88}$	1210.0	[62]
Peritectic	$L_{(X_{Ho}=0.191)} + Ho_3Si_5 \rightarrow Ho_5Si_9$	1287.9	This work
	$L_{(X_{Ho}=0.198)} + Ho_3Si_5 \rightarrow HoSi_{1.88}$	1290.0	[62]
Allotropic	$\alpha\text{-}Ho_5Si_9 \leftrightarrow \beta\text{-}Ho_5Si_9$	520.0	This work
	$\alpha\text{-}HoSi_{1.88} \leftrightarrow \beta\text{-}HoSi_{1.88}$	520.0	[62]
Peritectic	$L_{(X_{Ho}=0.345)} + HoSi \rightarrow Ho_3Si_5$	1620.2	This work
	$L_{(X_{Ho}=0.346)} + HoSi \rightarrow HoSi_{1.88}$	1620.0	[62]
	T_m for Ho_3Si_5	1602 ± 40	[57]
Allotropic	$\alpha\text{-}Ho_3Si_5 \leftrightarrow \beta\text{-}Ho_3Si_5$	834.0	This work
	$\alpha\text{-}Ho_3Si_5 \leftrightarrow \beta\text{-}Ho_3Si_5$	834 ± 25	[57]
	$\alpha\text{-}HoSi_{1.88} \leftrightarrow \beta\text{-}HoSi_{1.88}$	795.0	[62]
Peritectoid	$Ho_3Si_5 + HoSi \rightarrow Ho_3Si_4$	1306.3	This work
	$HoSi_{1.88} + HoSi \rightarrow Ho_4Si_5$	1305.0	[62]
Congruent	$L_{(X_{Ho}=0.50)} \leftrightarrow HoSi$	1863.1	This work
	$L_{(X_{Ho}=0.50)} \leftrightarrow HoSi$	1860.0	[62]
Peritectic	$L_{(X_{Ho}=\sim0.529)} + HoSi \rightarrow HoSi_{0.98}$	1820.0	[62]
Eutectic	$L_{(X_{Ho}=0.547)} \rightarrow HoSi + Ho_5Si_4$	1838.2	This work
Eutectic	$L_{(X_{Ho}=0.530)} \rightarrow HoSi_{0.98} + Ho_5Si_4$	1795.0	[62]
Peritectic	$L_{(X_{Ho}=0.552)} + Ho_5Si_3 \rightarrow Ho_5Si_4$	1839.1	This work
	$L_{(X_{Ho}=0.552)} + Ho_5Si_3 \rightarrow Ho_5Si_4$	1850.0	[62]
Congruent	$L_{(X_{Ho}=0.625)} \leftrightarrow Ho_5Si_3$	1917.3	This work
	$L_{(X_{Ho}=0.625)} \leftrightarrow Ho_5Si_3$	1920.0	[62]
Eutectic	$L_{(X_{Ho}=0.885)} \rightarrow Ho_5Si_3 + Ho_{(hcp\text{-}A3,\ X_{Ho}=1)}$	1264.0	This work
	$L_{(X_{Ho}=0.875)} \rightarrow Ho_5Si_3 + Ho_{(hcp\text{-}A3,\ X_{Ho}=1)}$	1255.0	[62]

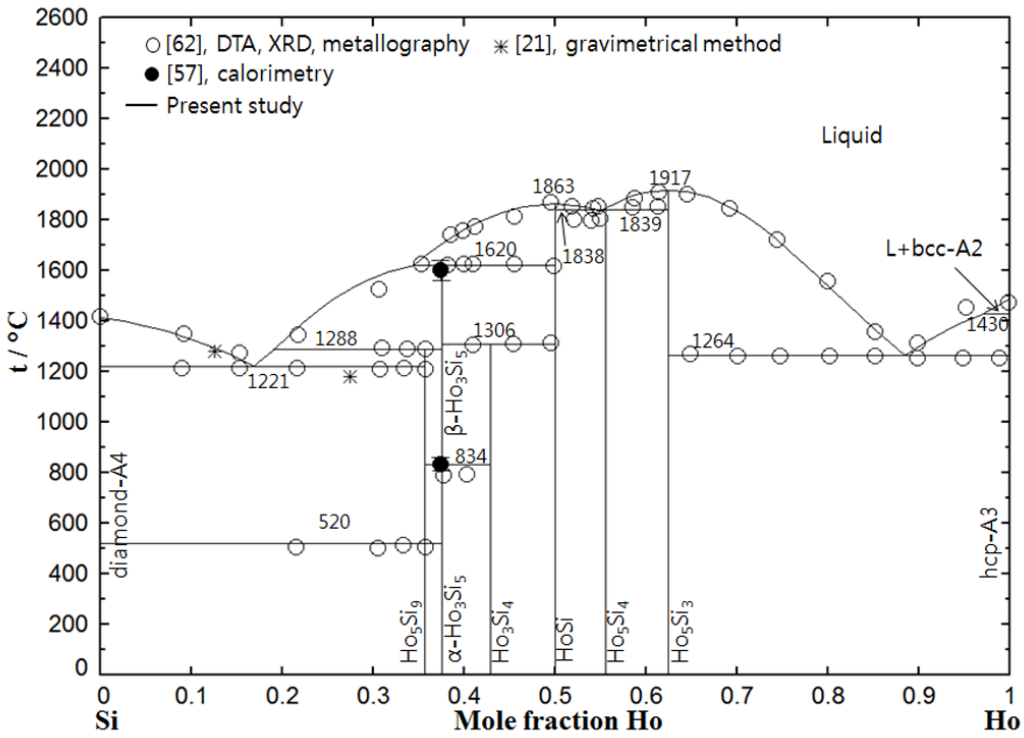


Fig. 19. The optimized Si-Ho phase diagram with experimental data.

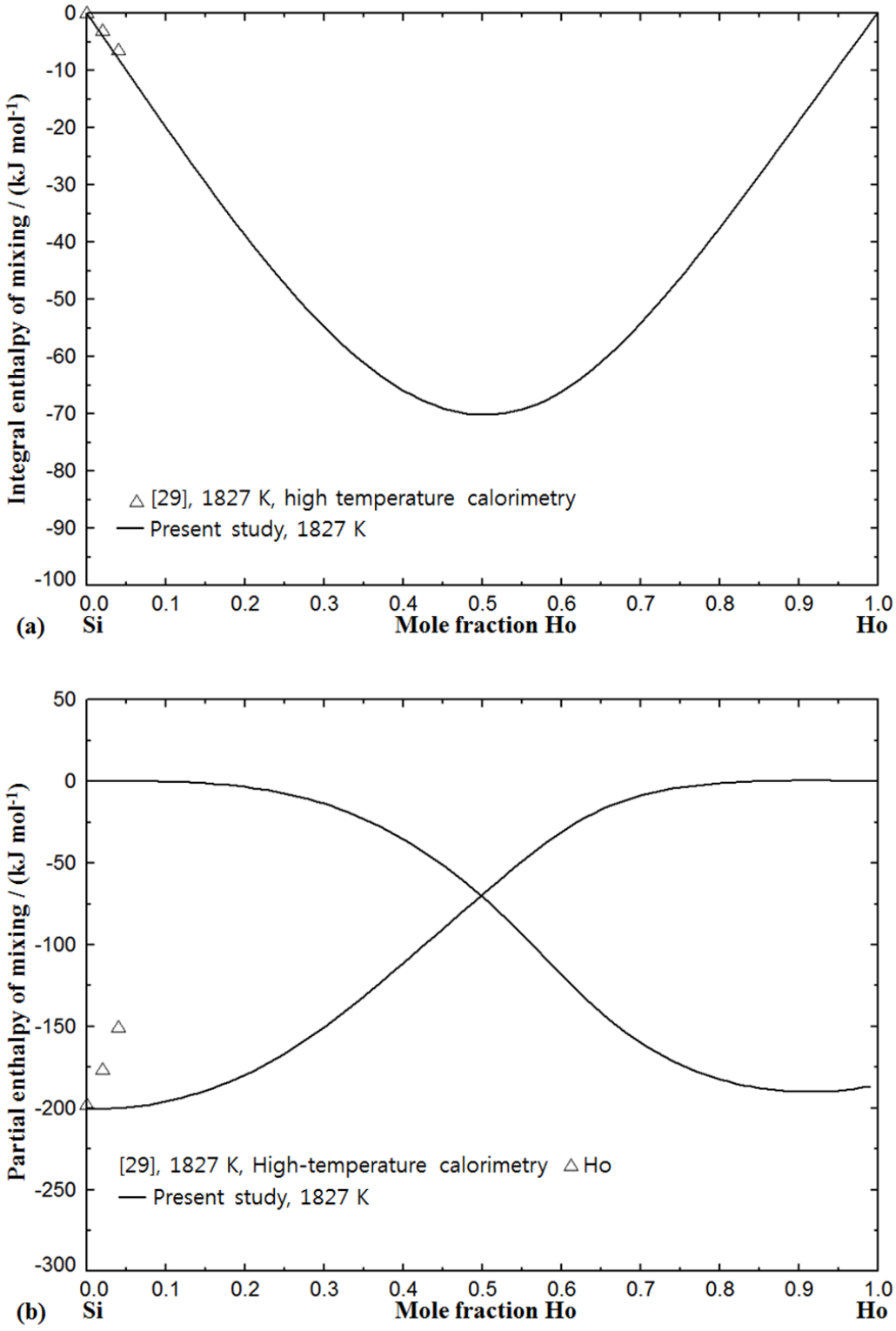


Fig. 20. (a) Integral enthalpy of mixing and (b) partial enthalpies of mixing of liquid Si-Ho phase at 1827 K with experimental data.

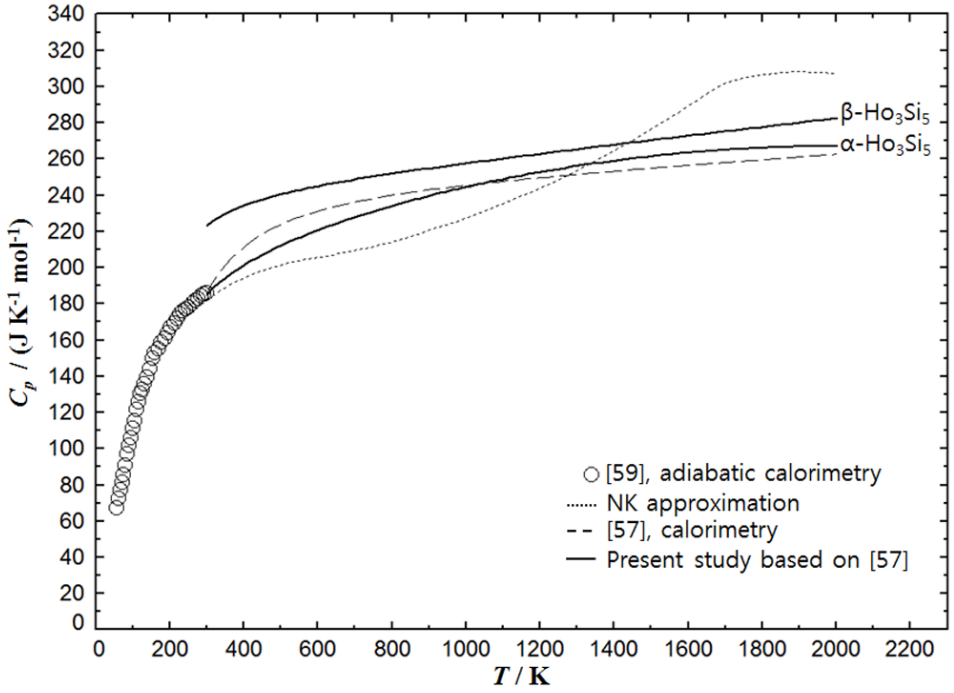


Fig. 21. Heat capacities of the Ho_3Si_5 phases with experimental data.

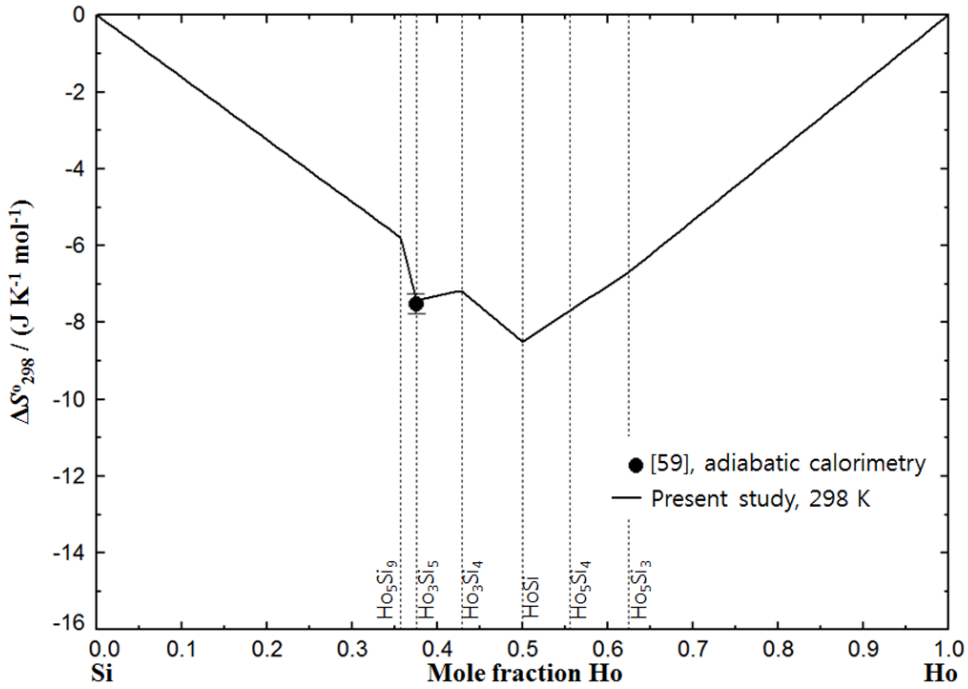


Fig. 22. Entropy of formation of the compounds in the Si-Ho system from elements at 298 K with experimental data.

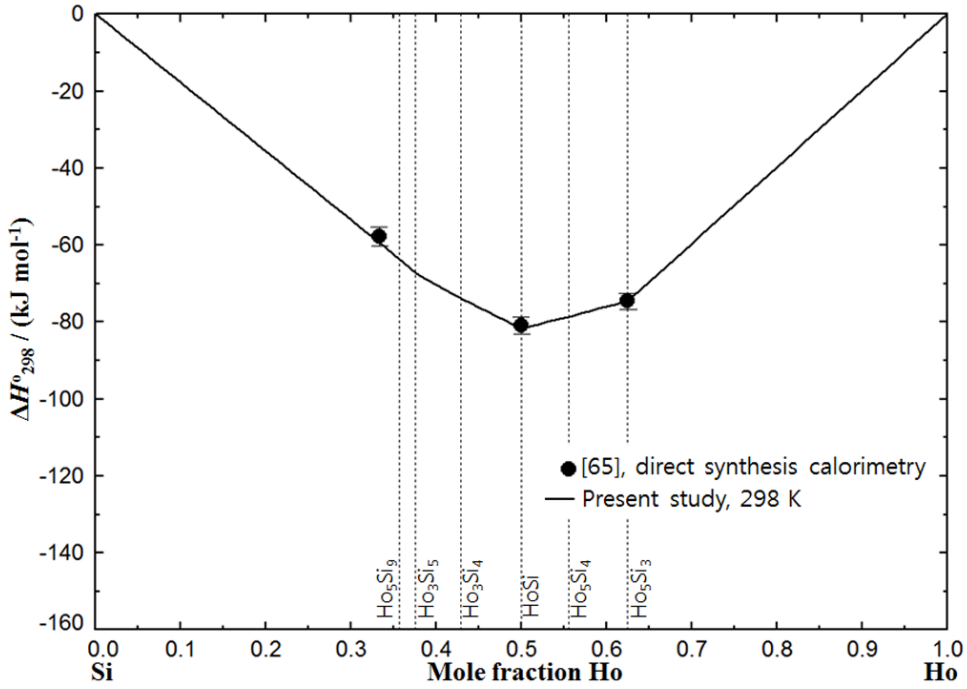


Fig. 23. Enthalpy of formation of the compounds in the Si-Ho system at 298 K with experimental data.

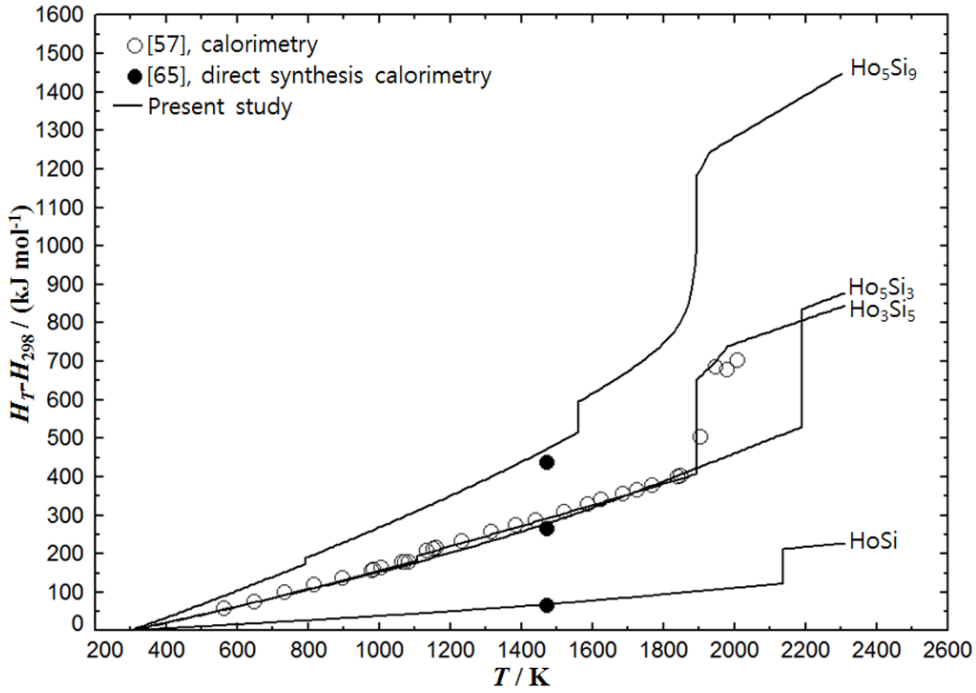


Fig. 24. Heat contents of the compounds in the Si-Ho system with experimental data.

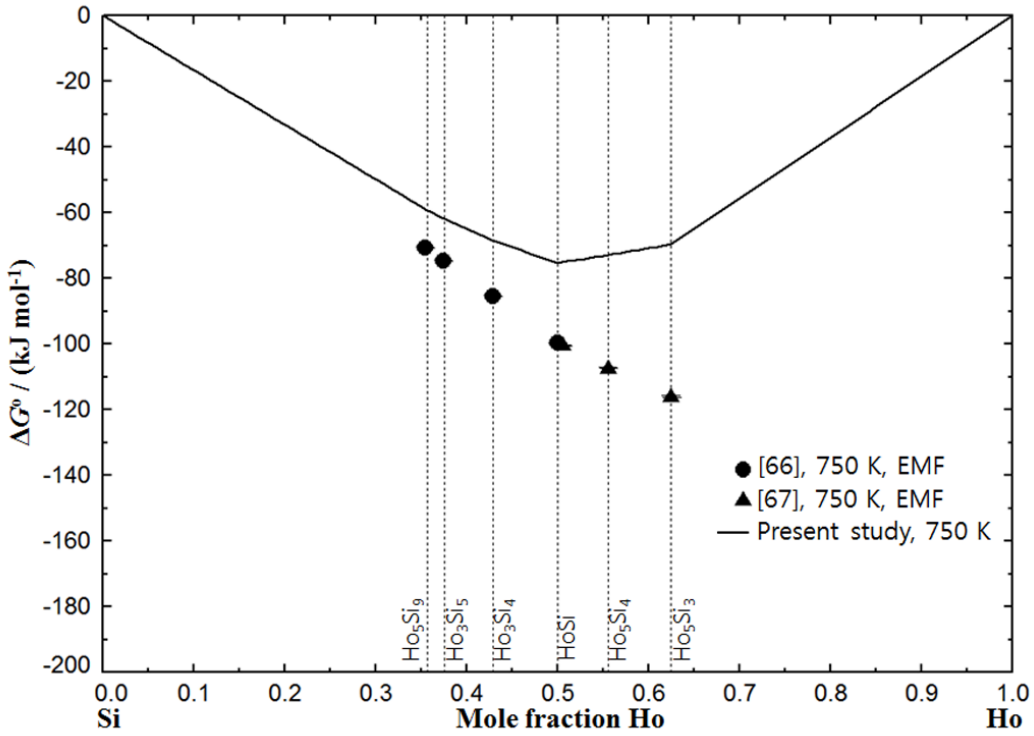


Fig. 25. Gibbs energy of formation of the compounds in the Si-Ho system at 750 K with experimental data.

2.5. The Si-Er system

Experimental phase diagram data of the Si-Er system are shown in Fig. 26. Luzan et al. [69] investigated the entire phase diagram of this system using DTA, XRD and metallography techniques. The alloys were prepared from 99.8 wt. % Er and 99.999 wt. % Si by arc melting under purified argon gas and homogenized for 250 h at a temperature of 1100 ºC in tantalum crucibles under purified argon gas. The existence of five compounds ($ErSi_{2-b}$ ($b \approx 0.33$), ErSi, $ErSi_{1-x}$ ($x \approx 0.04$), Er_5Si_4 and Er_5Si_3) were confirmed and the corresponding invariant reactions of the compounds were established. The ErSi and Er_5Si_3 congruently melted at 1910 ºC and 1948 ºC, respectively, and the peritectic reactions of $ErSi_{2-b}$, $ErSi_{1-x}$ and Er_5Si_4 occurred at 1620 ± 3 ºC, 1850 ± 3 ºC and 1875 ºC, respectively. The homogeneity range of $ErSi_{2-b}$ was reported about 0.01 mole fraction but the exact composition was not specified. The polymorphic transformation temperature of α-$ErSi_{2-b}$ to β-$ErSi_{2-b}$ was determined to be 805 ± 13 ºC at Er-rich side and 775 ± 2 ºC at Si-rich side. The weak heat effects were detected in the thermal curves at 645 ºC in the alloys corresponding to the two-phase region ($ErSi_{2-b}$ + Si), however the nature of the heat effects were undetermined. Three eutectic reactions were found: L → $ErSi_{2-b}$ + Si at 1210 ± 3ºC and 0.19 mole fraction Er, L → Er_5Si_4 + $ErSi_{1-x}$ at 1824 ºC and 0.54 mole fraction Er and L → Er + Er_5Si_3 at 1288 ± 2 ºC and 0.875 mole fraction Er. It was also reported the solid solubility of Er in Si and that of Si in Er were both negligible (less than 0.01 mole fraction). Some ambiguities in the composition of Si-richest compound $ErSi_{2-x}$ were also reviewed by Luzan et al. [69]. It was concluded that the $ErSi_{2-x}$ corresponds to the formula Er_3Si_5 with a homogeneity range of about 0.01 mole fraction. Prior to the study of Luzan et al. [69], it was reported that the eutectic reactions at 1200 ºC and 0.85 mole fraction Er were detected in Er-rich side [19] and the eutectic reaction at 1180 ºC and 0.19 mole fraction Er was suggested in Si-rich side [21]. However, both eutectic reactions were not consistent with the data of Luzan et al. [69]. Recently, Gorbachuk et al. [70, 71] reported the melting temperatures of Er_5Si_3 [70], ErSi [71] and Er_3Si_5 [71] to be about 1910 ± 30 ºC, 1642 ± 40 ºC and 1953 ± 35 ºC, respectively, from the heat content measurement. The temperature and enthalpy of polymorphic transformation of Er_3Si_5 were also reported to be 804 ± 7 ºC and 11.7 ± 3.6 kJ mol^{-1} [71].

The enthalpy of Si-Er liquid were reported by Batalin et al. [29] and the experimental data are presented in Fig. 27. The authors measured the integral enthalpy of mixing and partial enthalpy of mixing of Er for Si-Er liquid in the limited composition range ($0 < X_{Er} < 0.06$) at 1863 K using high temperature calorimetry with isothermal jacket. The thermodynamic properties of several intermetallic phases were determined. The C_p of Er_3Si_5, ErSi and Er_5Si_3 are shown in Fig. 28. Low temperature C_p of Er_3Si_5 [72], ErSi [72] and Er_5Si_3 [70] were measured by Gorbachuk et al. [70, 72] using adiabatic calorimetry. The T_N of Er_5Si_3 was about 71.9 K. The calculated S^o_{298} of Er_3Si_5, ErSi and Er_5Si_3 were reported to be 280.5 ± 2.4, 70.5 ± 0.6 and 392.9 ± 3.2 J K^{-1} mol^{-1}, respectively, and the experimental ΔS^o_{298} are presented in Fig. 29. Meschel and Kleppa [73] measured the ΔH^o_{298} and heat content ($H_{1473} - H_{298}$) of $ErSi_2$, ErSi and Er_5Si_3 and using direct synthesis calorimetry, as shown in Figs. 30 and 31. Gorbachuk et al. [70, 71] measured the heat content ($H_T - H_{298}$) of Er_3Si_5 [71], ErSi [71] and Er_5Si_3 [70] by means of high temperature differential calorimetry and high temperature vacuum calorimetry, and derived C_p for α-Er_3Si_5, β-Er_3Si_5, ErSi and Er_5Si_3 from the experimental data. The experimental data of Gorbachuk et al. [70, 71] and Meschel and Kleppa [73] are shown in Fig. 31. Sidorko and Gorbachuk [74] determined the Gibbs energies of formation of all intermetallic compounds using the emf technique, and the experimental data are presented in Fig. 32.

Okamoto [75] briefly reviewed the phase diagram of this system based solely on the experimental study by Luzan et al. [69]. No thermodynamic optimization of this system was previously performed. The Si-Er system was thermodynamically optimized by the evaluation of Gibbs energies of all phases with all available experimental data. The optimized phase diagram of the Si-Er system in the present study is compared with the experimental data in Fig. 26 and the calculated thermodynamic properties with the optimized thermodynamic parameters are shown and compared to the experimental data in Figs. 27 to 32. In the optimization, the phase diagram is mostly constructed based on the work of Luzan et al. [69]. Like other Si-RE systems, the minimum integral enthalpy of mixing was set to be about -70 kJ mol^{-1} at 0.5 mole fraction of Er, and then other experimental data such as the phase diagram and thermodynamic properties of compounds were reproduced. As seen in Figs. 27(a) and 27(b), the calculated integral enthalpy of mixing at 1863 K are in good agreement with the experimental data [29]. The abrupt variation of partial

enthalpy of mixing of Er in Fig. 27(b) is not reasonable and is difficult to be reproduced. The intermetallic compound $ErSi_{2-b}$ ($b \approx 0.33$) was considered as Er_3Si_5 accepting the observations of Luzan et al. [69] and Gorbachuk et al. [71]. The $ErSi_{1-x}$ ($x \approx 0.04$) was treated as the same compound as ErSi. The C_p of α-Er_3Si_5, β- Er_3Si_5, ErSi and Er_5Si_3 derived from the experimental heat contents [70, 71] were used without any modification, except the slight modification of C_p of α-Er_3Si_5 and ErSi to improve consistency with low temperature C_p data [72] as shown in Fig. 28. The polymorphic transformation temperature and associated enthalpy of Er_3Si_5 were taken from the data of Gorbachuk et al. [71]. The C_p of Er_5Si_4 were estimated by the NK rule. The calculated S°_{298} of Er_3Si_5, ErSi and Er_5Si_3 from the experimental low temperature C_p up to 298 K [70, 72] were applied except ErSi. When the experimental S°_{298} of ErSi [72] was used, the melting of ErSi was calculated much lower than the phase diagram, and therefore S°_{298} of ErSi was increased in the present optimization by 7.5 J K^{-1} mol^{-1}. The S°_{298} of Er_5Si_4 was similarly estimated to reproduce other data. The calculated ΔS°_{298} of all compounds are shown in Fig. 29. The experimental data of ΔH°_{298} of $ErSi_2$, ErSi and Er_5Si_3 [73] were applied and the ΔH°_{298} of Er_5Si_4 were estimated to reproduce the phase diagram as seen in Fig. 30. The calculated heat content ($H_T - H_{298}$) of Er_3Si_5, ErSi and Er_5Si_3 are compared with the experimental data [70, 71, 73] in Fig. 31. The calculated ΔG°_{950} are well in accord with the experimental data [74] as seen in Fig. 32. The optimized thermodynamic parameters are listed in Table 9 and the calculated invariant reactions with the experimental data are tabulated in Table 10.

Table 9. Optimized model parameters of the Si-Er system.

Phase	Thermodynamic parameters
Liquid	Coordination Numbers
	i j Z_{ij}^{i} Z_{ij}^{j}
	Si Er 6 6
	Δg_{SiEr} / (J mol^{-1}) = (-60249.6 + 7.531 T/K) – 32635.2 X_{SiSi}
	+ (38492.8 - 9.205 T/K) X_{SiSi}^{2} – (7531.2 + 8.368 T/K) X_{ErEr}
	+ 12552.0 X_{ErEr}^{2}
α-Er_3Si_5	ΔH_{298}° = -550000 J mol^{-1}, S_{298}° = 280.5 J K^{-1} mol^{-1}
	C_p / (J K^{-1} mol^{-1}) = 168.328 + 0.10536 T/K - 1203386 (T/K)$^{-2}$
	- 2.26E-5 (T/K)^2
β-Er_3Si_5	$\Delta_{\mathrm{trs}}H^{\alpha\rightarrow\beta}$ = 11700 J mol^{-1}, $T_{\mathrm{trs}}^{\alpha\rightarrow\beta}$ = 1077.0 K
	C_p / (J K^{-1} mol^{-1}) = 230.43 + 0.0306 T/K - 1269081 (T/K)$^{-2}$
ErSi	ΔH_{298}° = -169800 J mol^{-1}, S_{298}° = 78.0 J K^{-1} mol^{-1}
	C_p / (J K^{-1} mol^{-1}) = 46.912 + 0.0177 T/K - 388044 (T/K)$^{-2}$ - 2.405E-6 (T/K)^2
Er_5Si_4	ΔH_{298}° = -738000 J mol^{-1}, S_{298}° = 390.0 J K^{-1} mol^{-1}
	C_p / (J K^{-1} mol^{-1}) = 5 × C_p / (J K^{-1} mol^{-1}) (Er, hcp-A3)
	+ 4 × C_p / (J K^{-1} mol^{-1}) (Si, diamond-A4)
Er_5Si_3	ΔH_{298}° = -577000 J mol^{-1}, S_{298}° = 392.9 J K^{-1} mol^{-1}
	C_p / (J K^{-1} mol^{-1}) = 209.05 + 0.041916 T/K - 980753 (T/K)$^{-2}$

Table 10. Calculated invariant reactions and experimental data in the Si-Er system.

Type	Reaction	t (°C)	Reference
Eutectic	$L_{(X_{Er}= 0.206)} \rightarrow Si_{(dia.-A4,\ X_{Er}= 0)} + Er_3Si_5$	1206.7	This work
	$L_{(X_{Er}= 0.190)} \rightarrow Si_{(dia.-A4,\ X_{Er}= 0)} + Er_3Si_5$	1210 ± 3	[69]
Peritectic	$L_{(X_{Er}= 0.358)} + ErSi \rightarrow Er_3Si_5$	1619.1	This work
	$L_{(X_{Er}= 0.349)} + ErSi \rightarrow Er_3Si_5$	1620 ± 3	[69]
	T_m for Er_3Si_5	1953 ± 35	[71]
Allotropic	$\alpha\text{-}Er_3Si_5 \leftrightarrow \beta\text{-}Er_3Si_5$	804.0	This work
	$\alpha\text{-}Er_3Si_5 \leftrightarrow \beta\text{-}Er_3Si_5$ (Si-rich composition)	775 ± 2	[69]
	$\alpha\text{-}Er_3Si_5 \leftrightarrow \beta\text{-}Er_3Si_5$ (Er-rich composition)	805 ± 13	[69]
	$\alpha\text{-}Er_3Si_5 \leftrightarrow \beta\text{-}Er_3Si_5$	804 ± 7	[71]
Congruent	$L_{(X_{Er}= 0.50)} \leftrightarrow ErSi$	1898.4	This work
	$L_{(X_{Er}= 0.50)} \leftrightarrow ErSi$	1910.0	[69]
	T_m for ErSi	1642 ± 40	[71]
Peritectic	$L_{(X_{Er}= \sim 0.537)} + ErSi \rightarrow ErSi_{0.98}$	1850 ± 3	[69]
Eutectic	$L_{(X_{Er}= 0.547)} \rightarrow ErSi + Er_5Si_4$	1874.9	This work
Eutectic	$L_{(X_{Er}= 0.540)} \rightarrow ErSi_{0.98} + Er_5Si_4$	1824.0	[69]
Peritectic	$L_{(X_{Er}= 0.549)} + Er_5Si_3 \rightarrow Er_5Si_4$	1875.2	This work
	$L_{(X_{Er}= 0.545)} + Er_5Si_3 \rightarrow Er_5Si_4$	1875.0	[69]
Congruent	$L_{(X_{Er}= 0.625)} \leftrightarrow Er_5Si_3$	1951.2	This work
	$L_{(X_{Er}= 0.625)} \leftrightarrow Er_5Si_3$	1948.0	[69]
	T_m for Er_5Si_3	1910 ± 30	[70]
Eutectic	$L_{(X_{Er}= 0.875)} \rightarrow Er_5Si_3 + Er_{(hcp-A3,\ X_{Er}= 1)}$	1291.7	This work
	$L_{(X_{Er}= 0.850)} \rightarrow Er_5Si_3 + Er_{(hcp-A3,\ X_{Er}= 1)}$	1200.0	[19]
	$L_{(X_{Er}= 0.875)} \rightarrow Er_5Si_3 + Er_{(hcp-A3,\ X_{Er}= 1)}$	1288 ± 2	[69]

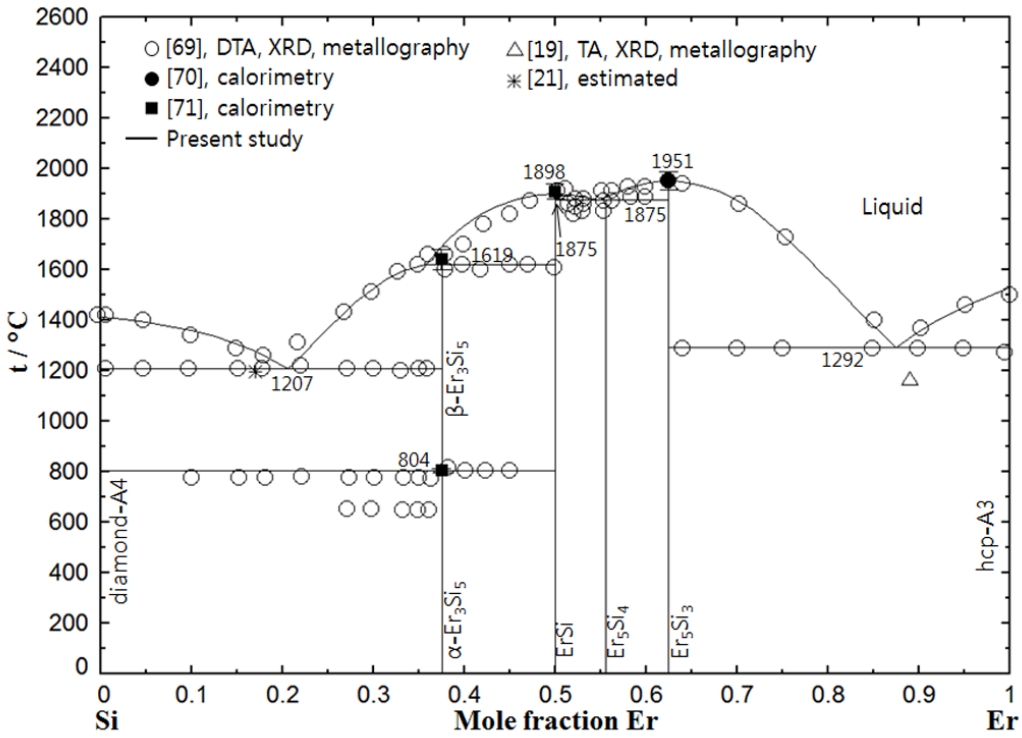


Fig. 26. The optimized Si-Er phase diagram with experimental data.

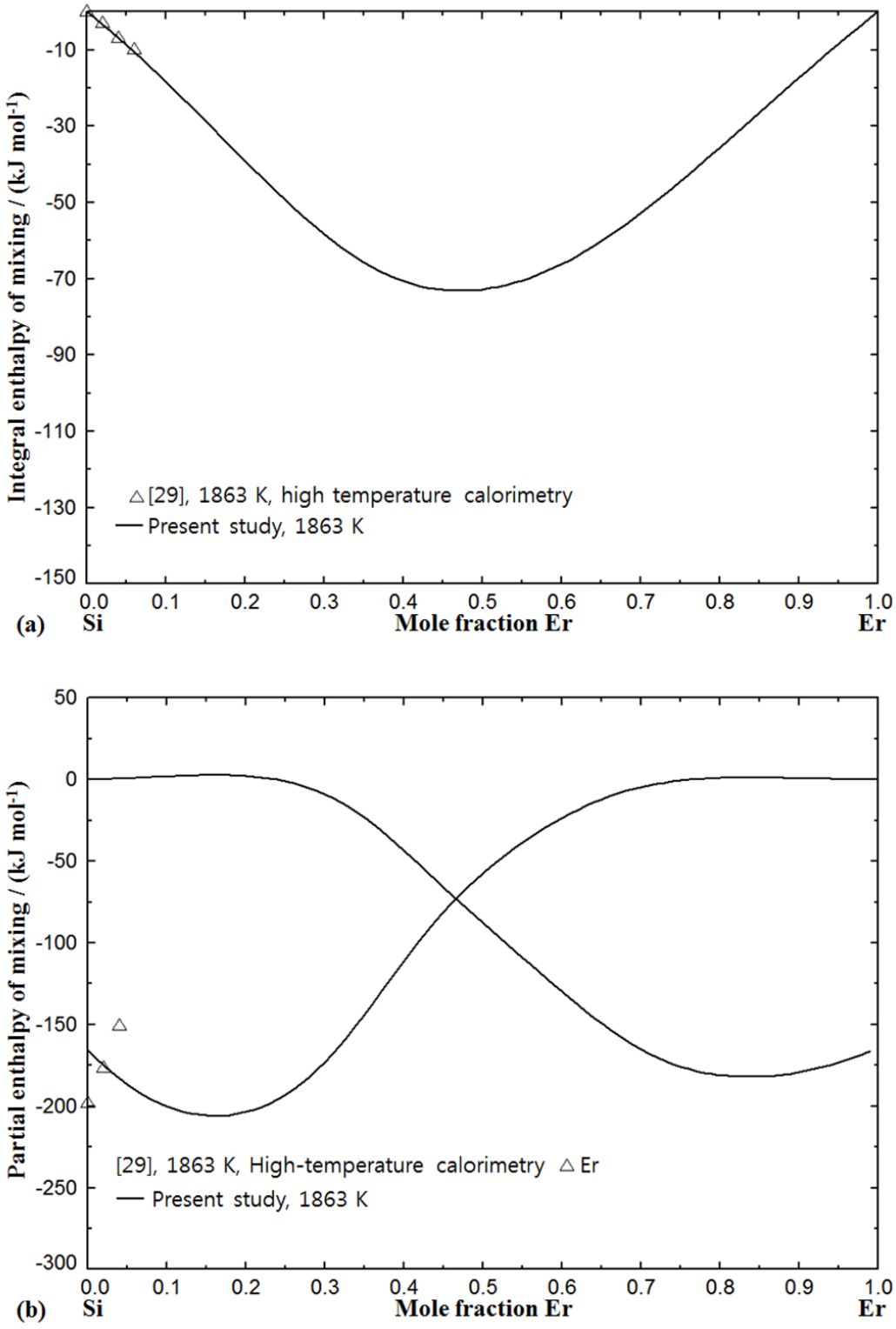


Fig. 27. (a) Integral enthalpy of mixing and (b) partial enthalpies of mixing of liquid Si-Er phase at 1863 K with experimental data.

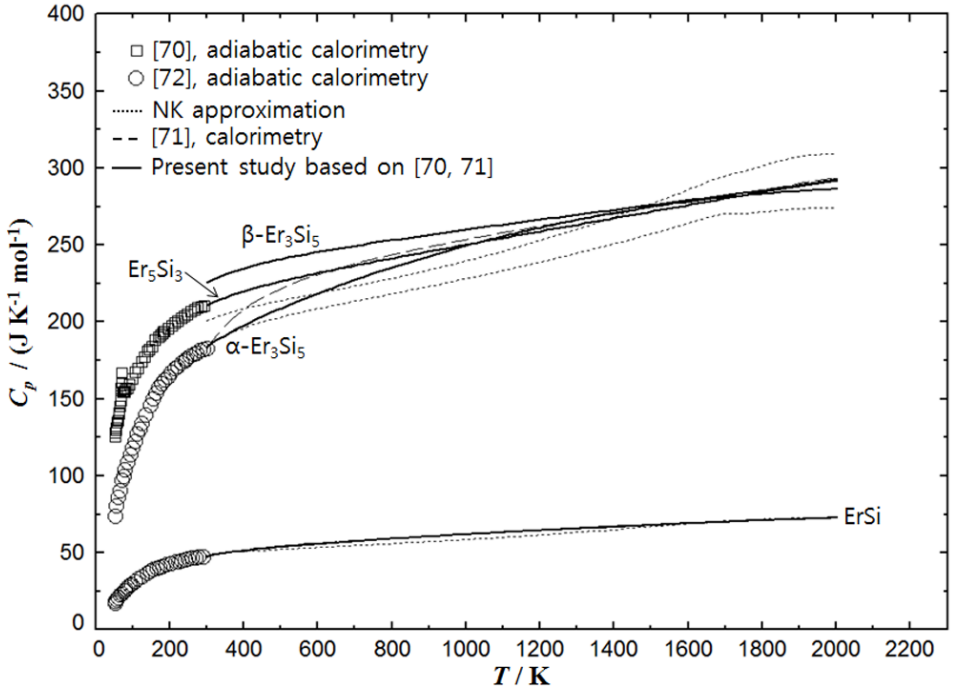


Fig. 28. Heat capacities of the compounds in the Si-Er system with experimental data.

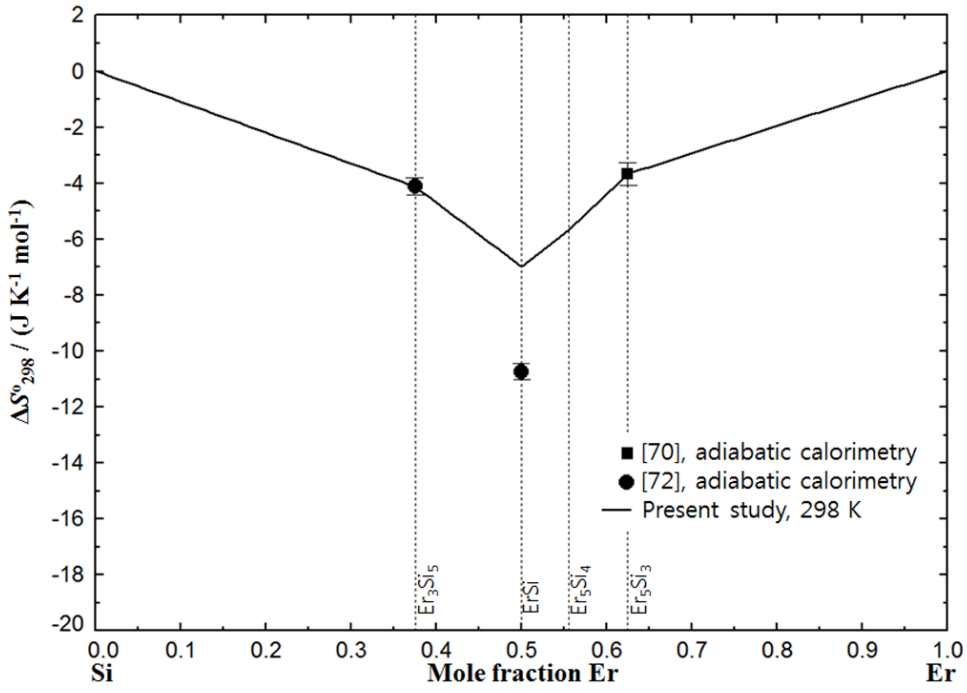


Fig. 29. Entropy of formation of the compounds in the Si-Er system from elements at 298 K with experimental data.

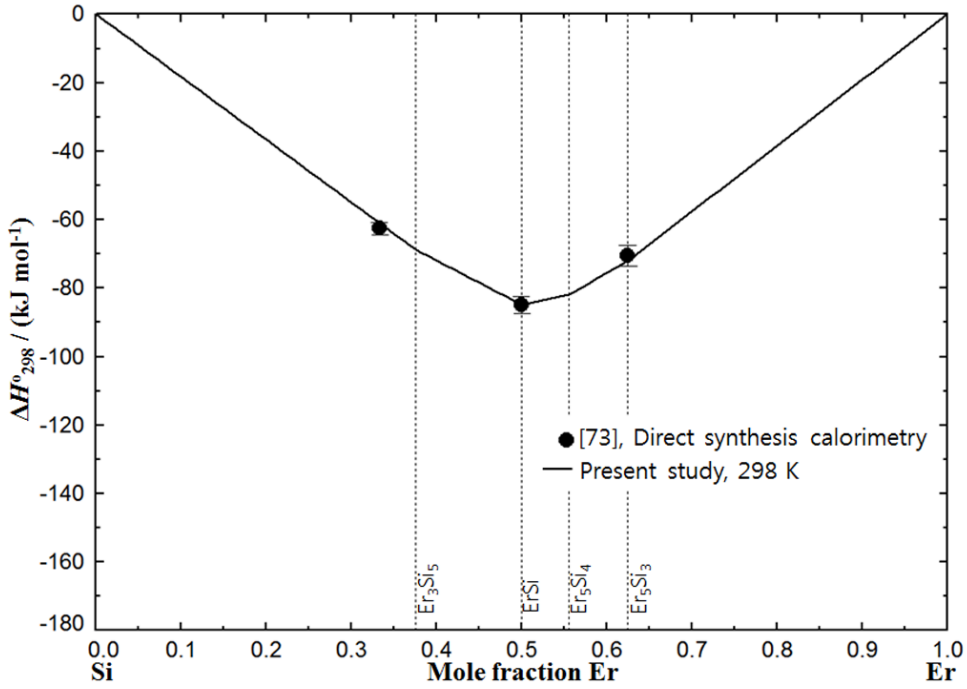


Fig. 30. Enthalpy of formation of the compounds in the Si-Er system at 298 K with experimental data.

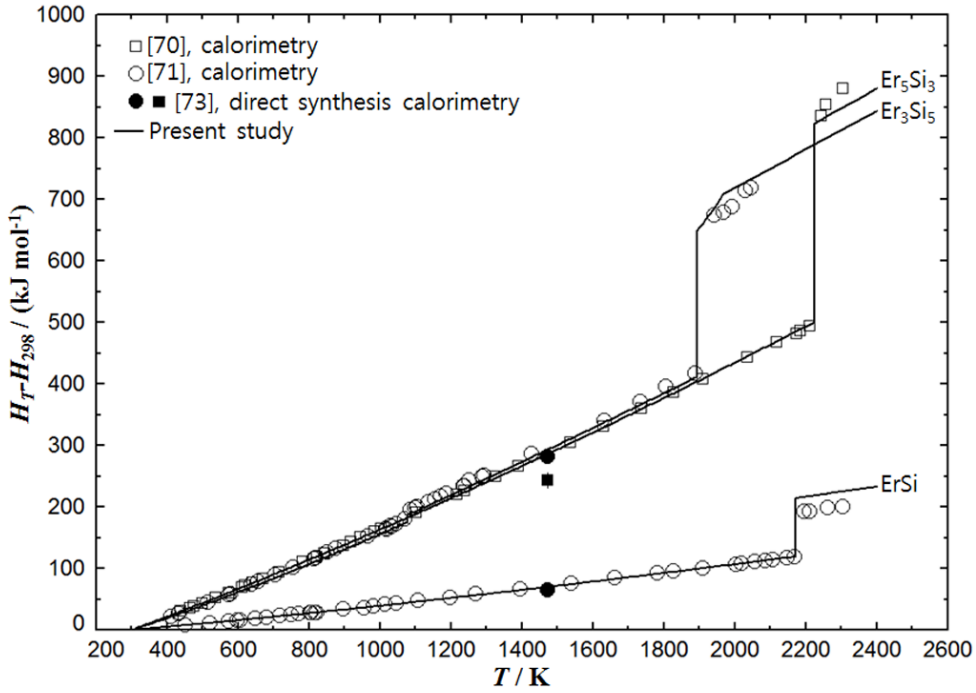


Fig. 31. Heat contents of the compounds in the Si-Er system with experimental data.

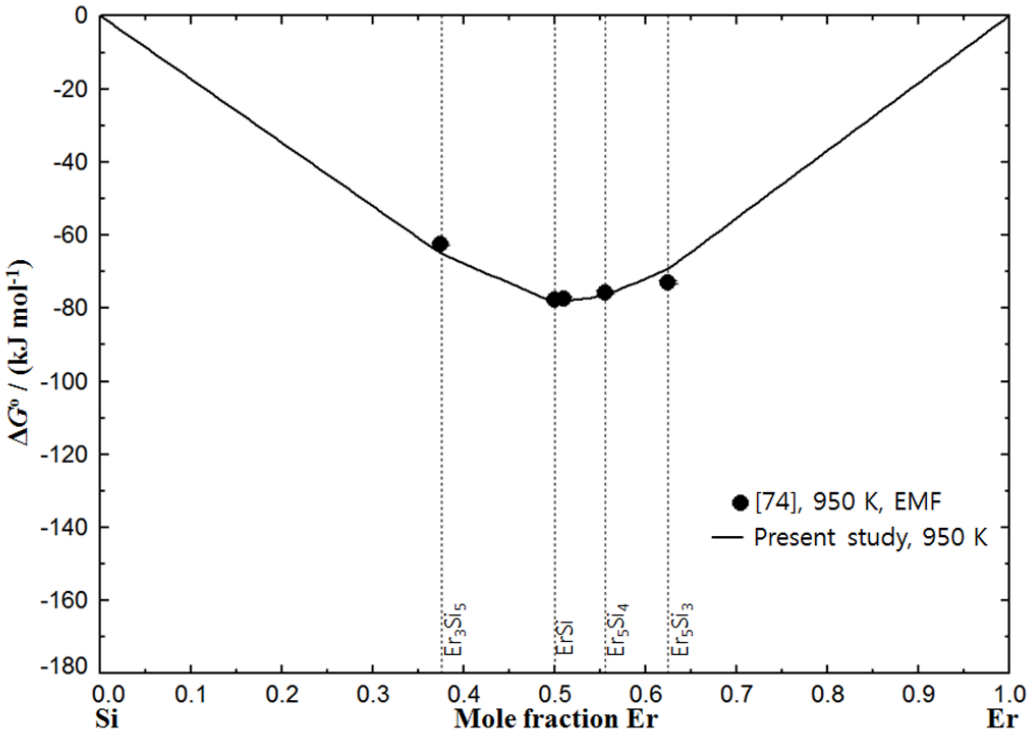


Fig. 32. Gibbs energy of formation of the compounds in the Si-Er system at 950 K with experimental data.

2.6. The Si-Tm system

The phase diagram of the Si-Tm system has not been established yet. Three intermediate phases, $TmSi_2$ [76, 77], TmSi [78, 79], Tm_5Si_3 [78-80] were found in several crystallographic studies up to now. Gorbachuk et al. [81, 82] estimated the melting temperatures of TmSi and Tm_5Si_3 compounds from the systematic analysis on the melting enthalpies of those compounds. However, no experimental data regarding the solidus and liquidus of this system were previously reported. The only available experimental data in this system are the ΔH^{o}_{298} of $TmSi_2$, TmSi, and Tm_5Si_3 measured by Meschel and Kleppa [83] using direct synthesis calorimetry. The authors also reported the heat content ($H_{1373} - H_{298}$) of those compounds. The experimental data are presented in Figs. 33 and 34. In all other RE-Si systems, $RESi_2$ compounds were not truly stoichiometric (1:2 ratio). There is always a small amount of silicon deficiency and therefore it is accepted as $RESi_{2-a}$. In the present study, we assumed that the stoichiometric Tm_3Si_5 compound exists instead of $TmSi_2$ like the Si-Er system. Although it is not reported, Tm_5Si_4 is believed to be present in the Si-Tm system based on other Si-RE systems.

Prior to the thermodynamic modeling of the system, we estimated the peritectic melting temperature of Tm_3Si_5 and Tm_5Si_4 from the regular trend in the melting temperatures of the intermetallic compounds in all other Si-RE systems. The melting temperature of RE_3Si_5 decreases with the atomic number of RE in Si-RE series, while those of RE_5Si_4 and RE_5Si_3 increase in RE series. This trend will be discussed in the section 3. By considering the systematic change in the Si-RE systems, the melting temperatures of Tm_5Si_4 and Tm_3Si_5 were estimated in the present study. In addition, the similar shape of liquidus of the Si-Tm system as the adjacent RE-Si systems was also assumed; in the lanthanide system the thermodynamic properties of adjacent rare elements are quite similar except Eu and Yb. In the present thermodynamic modeling, the thermodynamic model parameters of liquid Si-Tm were first taken from those of the adjacent Si-Er system. The C_p of all compounds were estimated by the NK rule. The experimental data of ΔH^{o}_{298} of TmSi and Tm_5Si_3 [83] were adopted, and the ΔH^{o}_{298} of Tm_3Si_5 was evaluated for the ΔH^{o}_{298} at 0.333 mole fraction of Tm to satisfy the experimental ΔH^{o}_{298} of $TmSi_2$ [83] as shown in Fig. 33. Then, the S^{o}_{298}

of Tm_3Si_5, TmSi, Tm_5Si_4 and Tm_5Si_3 were adjusted from the stoichiometric sum of Tm and Si to reproduce the estimated melting temperatures of those compounds. The predicted phase diagram and thermodynamic properties of solid phases are plotted in Figs. 33 to 35 along with experimental data. The optimized thermodynamic parameters are listed in Table 11 and the calculated invariant reactions are tabulated in Table 12.

Table 11. Optimized model parameters of the Si-Tm system.

Phase	Thermodynamic parameters
Liquid	Coordination Numbers
	i j Z_{ij}^i Z_{ij}^j
	Si Tm 6 6
	Δg_{SiTm} / (J mol^{-1}) = (-60249.6 + 7.531 T/K) – 32635.2 X_{SiSi}
	+ (38492.8 – 9.205 T/K) X_{SiSi}^2 – (7531.2 + 8.368 T/K) X_{TmTm}
	+ 12552.0 X_{TmTm}^2
Tm_3Si_5	ΔH_{298}° = -560000 J mol^{-1}, S_{298}° = 292.0 J K^{-1} mol^{-1}
	C_p / (J K^{-1} mol^{-1}) = 3 × C_p / (J K^{-1} mol^{-1}) (Tm, hcp-A3)
	+ 5 × C_p / (J K^{-1} mol^{-1}) (Si, diamond-A4)
TmSi	ΔH_{298}° = -172200 J mol^{-1}, S_{298}° = 79.0 J K^{-1} mol^{-1}
	C_p / (J K^{-1} mol^{-1}) = 1 × C_p / (J K^{-1} mol^{-1}) (Tm, hcp-A3)
	+ 1 × C_p / (J K^{-1} mol^{-1}) (Si, diamond-A4)
Tm_5Si_4	ΔH_{298}° = -755000 J mol^{-1}, S_{298}° = 388.0 J K^{-1} mol^{-1}
	C_p / (J K^{-1} mol^{-1}) = 5 × C_p / (J K^{-1} mol^{-1}) (Tm, hcp-A3)
	+ 4 × C_p / (J K^{-1} mol^{-1}) (Si, diamond-A4)
Tm_5Si_3	ΔH_{298}° = -608800 J mol^{-1}, S_{298}° = 397.0 J K^{-1} mol^{-1}
	C_p / (J K^{-1} mol^{-1}) = 5 × C_p / (J K^{-1} mol^{-1}) (Tm, hcp-A3)
	+ 3 × C_p / (J K^{-1} mol^{-1}) (Si, diamond-A4)

Table 12. Calculated invariant reactions and experimental data in the Si-Tm system.

Type	Reaction	t (°C)	Reference
Eutectic	$L(X_{Tm}= 0.20) \rightarrow Si(\text{dia.-A4}, X_{Tm}= 0) + Tm_3Si_5$	1219.1	This work
Peritectic	$L(X_{Tm}= 0.355) + TmSi \rightarrow Tm_3Si_5$	1601.1	This work
Congruent	$L(X_{Tm}= 0.50) \leftrightarrow TmSi$	1879.8	This work
Eutectic	$L(X_{Tm}= 0.505) \rightarrow TmSi + Tm_5Si_4$	1879.6	This work
Peritectic	$L(X_{Tm}= 0.525) + Tm_5Si_3 \rightarrow Tm_5Si_4$	1897.1	This work
Congruent	$L(X_{Tm}= 0.625) \leftrightarrow Tm_5Si_3$	2017.4	This work
Eutectic	$L(X_{Tm}= 0.894) \rightarrow Tm_5Si_3 + Tm(\text{hcp-A3}, X_{Tm}= 1)$	1311.0	This work

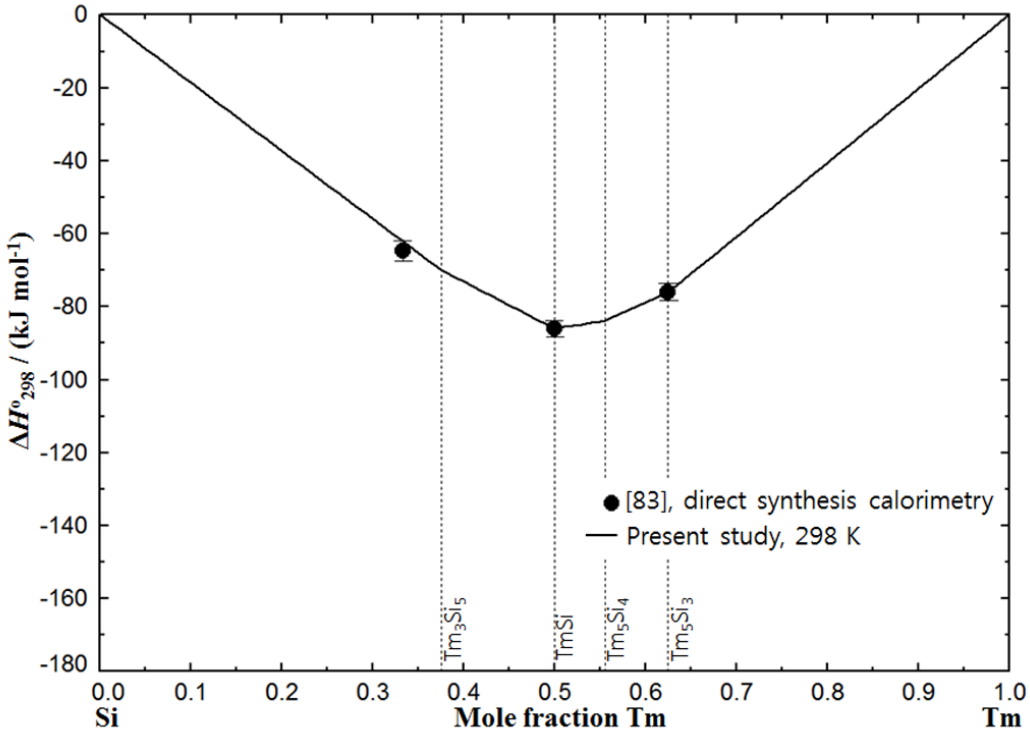


Fig. 33. Enthalpy of formation of the compounds in the Si-Tm system at 298 K with experimental data.

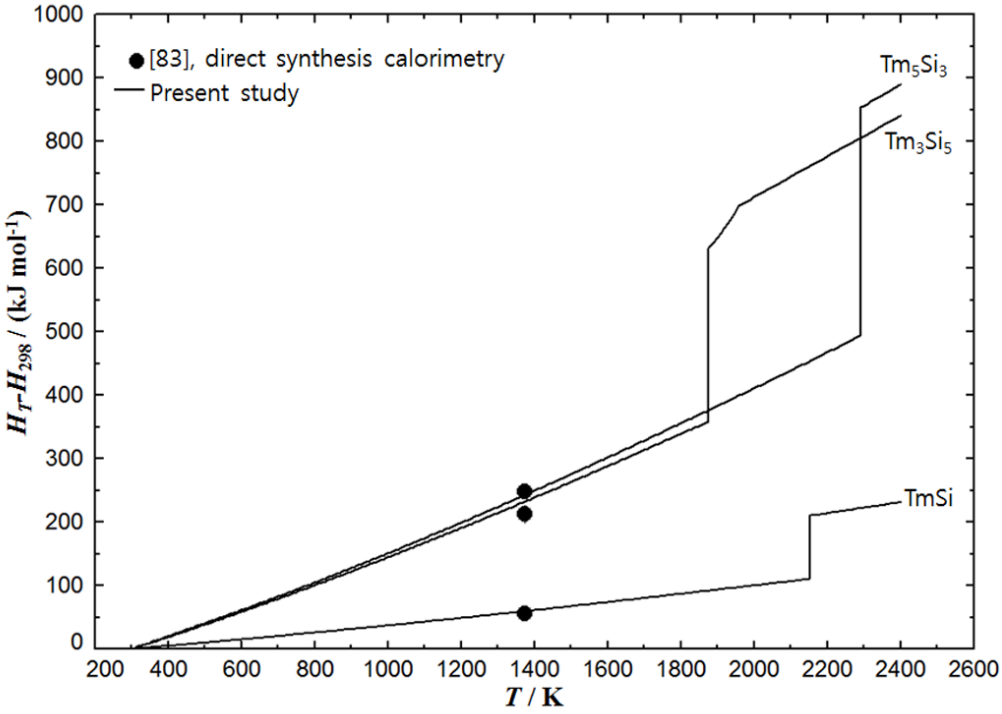


Fig. 34. Heat contents of the compounds in the Si-Tm system with experimental data.

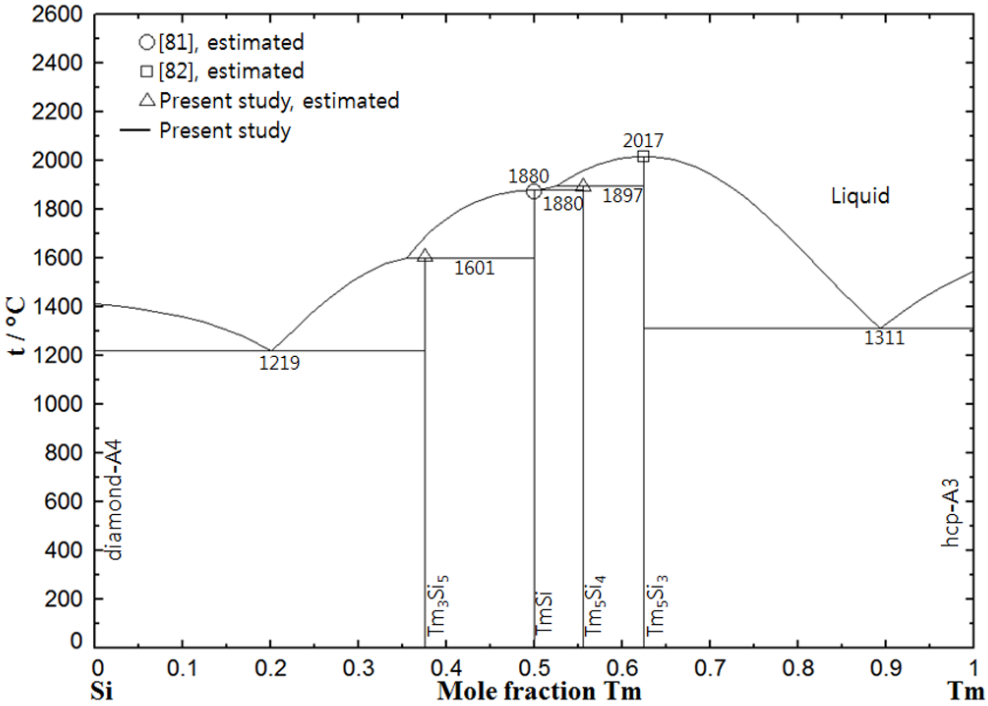


Fig. 35. The optimized Si-Tm phase diagram with experimental data.

2.7. The Si-Lu system

The phase diagram of the Si-Lu system has not been established yet. Three intermediate phases, $LuSi_2$ [76, 77], LuSi [78, 79], Lu_5Si_3 [78-80] were found in several crystallographic studies up to now. Gorbachuk et al. [84, 85] determined the melting temperatures of LuSi [84] and Lu_5Si_3 [85] to be about 1797 ± 25 ºC and 2057 ± 40 ºC, respectively, from heat content measurements. Lozovskii and Kolesnichenko [21] determined the liquidus of the Si-rich side by gravimetrical method and also reported the eutectic reaction at 1170 ºC and 0.23 mole fraction of Lu. However, no other experimental data regarding the solidus and liquidus of this system have been reported. Like the Si-Tm system, Lu_3Si_5 is assumed to be present as a stoichiometry of the $LuSi_{2-a}$ and the Lu_5Si_4 is also believed to be present in the Si-Lu system.

The thermodynamic properties of Si-Lu liquid have not been investigated. For intermetallic compounds, low temperature C_p of LuSi [84] and Lu_5Si_3 [85] were measured by Gorbachuk et al. using adiabatic calorimetry. The calculated S°_{298} of Lu_5Si_3 and LuSi from the experimental C_p data up to 298 K were also reported. The experimental C_p and the ΔS°_{298} of Lu_5Si_3 and LuSi are presented in Figs. 36 and 37. Topor and Kleppa [86] measured the ΔH°_{298} of Lu_5Si_3 using drop calorimetry. The ΔH°_{298} of LuSi was initially determined by Meschel and Kleppa as -78.3 ± 2.1 kJ mol^{-1} [45] using direct synthesis calorimetry. Later, the value was corrected as -79.1 ± 2.7 kJ mol^{-1} [87] after re-measurement using a higher grade of Lu. The experimental data [86, 87] are presented in Fig. 38. Gorbachuk et al. measured the heat content ($H_T - H_{298}$) of LuSi [84] and Lu_5Si_3 [85] by means of high temperature differential calorimetry up to 1200 K and a high temperature vacuum calorimeter above 1200 K. The experimental heat content data of Gorbachuk et al. [84, 85] and Meschel and Kleppa [87] are shown in Fig. 39.

For the thermodynamic optimization of this system, the melting temperatures of Lu_3Si_5 and Lu_5Si_4 were first estimated using the same strategy used in the Si-Tm system. The liquidus was assumed to be similar as the Si-Tm system. In the present thermodynamic modeling, the thermodynamic parameters for liquid phase were considered to be similar to those in the Si-Tm system and slightly

modified to satisfy the other available experimental data. The C_p of Lu_5Si_3 and LuSi above 298 K which were reported by Gorbachuk et al. [84, 85] were accepted as they were coherent with the low temperature C_p of LuSi [84] and Lu_5Si_3 [85] (Fig. 36). The C_p of other compounds were estimated by the NK rule. From the ΔH^{o}_{298} of LuSi [87] and Lu_5Si_3 [86] and the high temperature heat content of LuSi [84] and Lu_5Si_3 [85] (liquid), the enthalpy of mixing of liquid at 0.5 and 0.625 mole fraction of Lu can be calculated (see Fig. 40). In order to reproduce two data at the same time, it would be required to introduce positive deviations in the liquid phase on the Lu-rich side. This will bring inconsistency in the trend of enthalpy of mixing of Si-RE liquid. Consequently the high temperature heat content of Lu_5Si_3 liquid was determined to be about 80 kJ mol^{-1} smaller than the experimental data [85] as shown in Fig. 39. In addition, the experimental S^{o}_{298} of LuSi was not reproduced as seen in Fig. 37. Although it is hard to judge the accuracy of experimental data, the S^{o}_{298} of LuSi [84] is off from the trend of the ΔS^{o}_{298} of other RESi compounds in many Si-RE systems. The ΔS^{o}_{298} of RESi compound in the Si-Gd, Si-Tb, Si-Ho and Si-Er systems has the smallest (most negative) value among all intermetallic compounds in each system while the ΔS^{o}_{298} of LuSi [84] is even higher than that of Lu_5Si_3 [85]. From this point of view, the S^{o}_{298} of LuSi was reduced by 8.81 J K^{-1} mol^{-1} from the experimental data as shown in Fig. 37 to reproduce the melting temperature of the compound. The ΔH^{o}_{298} and S^{o}_{298} of Lu_5Si_4 and Lu_3Si_5 were reasonably evaluated in consideration of the enthalpies and entropies of the adjacent compounds and for reproducing the estimated melting temperatures from the general trends (see section 3), as shown in Figs. 37 and 38. The calculated heat content ($H_T - H_{298}$) of LuSi and Lu_5Si_3 are shown in Fig. 39 along with the experimental data [84, 85, 87]. The predicted phase diagram of the Si-Lu system is presented in Fig. 41. It is worth mentioning that it was thermodynamically very difficult for the Lu_3Si_5 to have peritectic melting like Tm_3Si_5 in the Si-Tm system because of the liquidus of the adjacent compound LuSi. In order to make Lu_3Si_5 be peritectically melted, the melting temperature of Lu_3Si_5 would be lower than 1500 ºC, which is too low in consideration of other Si-RE systems. Thus, the eutectic reaction between Lu_3Si_5 and LuSi is proposed in the phase diagram of the system. The optimized thermodynamic parameters are listed in Table 13 and the calculated invariant reactions with the experimental data are tabulated in Table 14.

Table 13. Optimized model parameters of the Si-Lu system.

Phase	Thermodynamic parameters
Liquid	Coordination Numbers
	i j Z_{ij}^{i} Z_{ij}^{j}
	Si Lu 6 6
	Δg_{SiLu} / (J mol^{-1}) = (-60249.6 + 7.740 T/K) – 34727.2 X_{SiSi}
	+ (38492.8 – 6.276 T/K) X_{SiSi}^2 + (-8368.0 + 2.5732 T/K) X_{LuLu}
	+ 4184.0 X_{LuLu}^2
Lu_3Si_5	ΔH_{298}^{o} = -540000 J mol^{-1}, S_{298}^{o} = 228.2 J K^{-1} mol^{-1}
	C_p / (J K^{-1} mol^{-1}) = 3 × C_p / (J K^{-1} mol^{-1}) (Lu, hcp-A3)
	+ 5 × C_p / (J K^{-1} mol^{-1}) (Si, diamond-A4)
LuSi	ΔH_{298}^{o} = -158200 J mol^{-1}, S_{298}^{o} = 54.89 J K^{-1} mol^{-1}
	C_p / (J K^{-1} mol^{-1}) = 48.57 + 0.012556 T/K - 499105 (T/K)$^{-2}$
Lu_5Si_4	ΔH_{298}^{o} = -674300 J mol^{-1}, S_{298}^{o} = 288.0 J K^{-1} mol^{-1}
	C_p / (J K^{-1} mol^{-1}) = 5 × C_p / (J K^{-1} mol^{-1}) (Lu, hcp-A3)
	+ 4 × C_p / (J K^{-1} mol^{-1}) (Si, diamond-A4)
Lu_5Si_3	ΔH_{298}^{o} = -550400 J mol^{-1}, S_{298}^{o} = 277.1 J K^{-1} mol^{-1}
	C_p / (J K^{-1} mol^{-1}) = 190.34 + 0.05511 T/K - 1507230 (T/K)$^{-2}$

Table 14. Calculated invariant reactions and experimental data in the Si-Lu system.

Type	Reaction	t (°C)	Reference
Eutectic	$L_{(X_{Lu}=0.213)} \rightarrow Si_{(dia.\text{-}A4,\ X_{Lu}=0)} + Lu_3Si_5$	1211.5	This work
	$L_{(X_{Lu}=0.230)} \rightarrow Si_{(dia.\text{-}A4,\ X_{Lu}=0)} + Lu_3Si_5$	1170.0	[21]
Congruent	$L_{(X_{Lu}=0.375)} \leftrightarrow Lu_3Si_5$	1607.4	This work
Eutectic	$L_{(X_{Lu}=0.394)} \rightarrow Lu_3Si_5 + LuSi$	1599.9	This work
Peritectic	$L_{(X_{Lu}=0.466)} + Lu_5Si_4 \rightarrow LuSi$	1796.7	This work
	T_m for LuSi	1797 ± 25	[84]
Peritectic	$L_{(X_{Lu}=0.517)} + Lu_5Si_3 \rightarrow Lu_5Si_4$	1901.9	This work
Congruent	$L_{(X_{Lu}=0.625)} \leftrightarrow Lu_5Si_3$	2058.0	This work
	T_m for Lu_5Si_3	2057 ± 40	[85]
Eutectic	$L_{(X_{Lu}=0.894)} \rightarrow Lu_5Si_3 + Lu_{(hcp\text{-}A3,\ X_{Lu}=1)}$	1453.8	This work

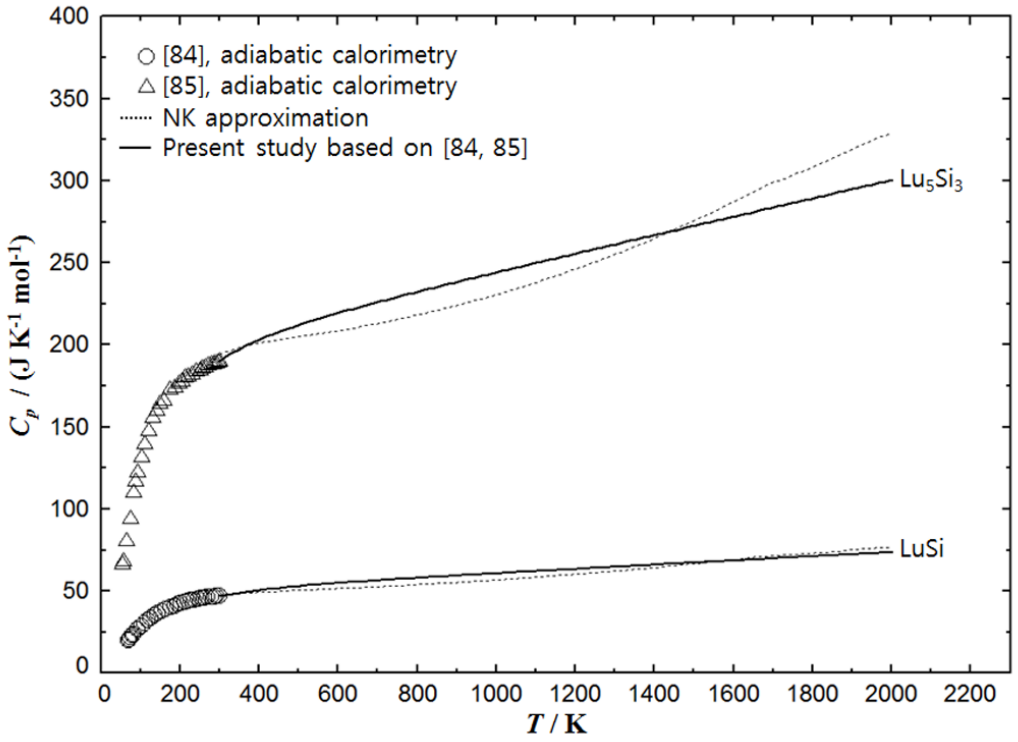


Fig. 36. Heat capacities of the compounds in the Si-Lu system with experimental data.

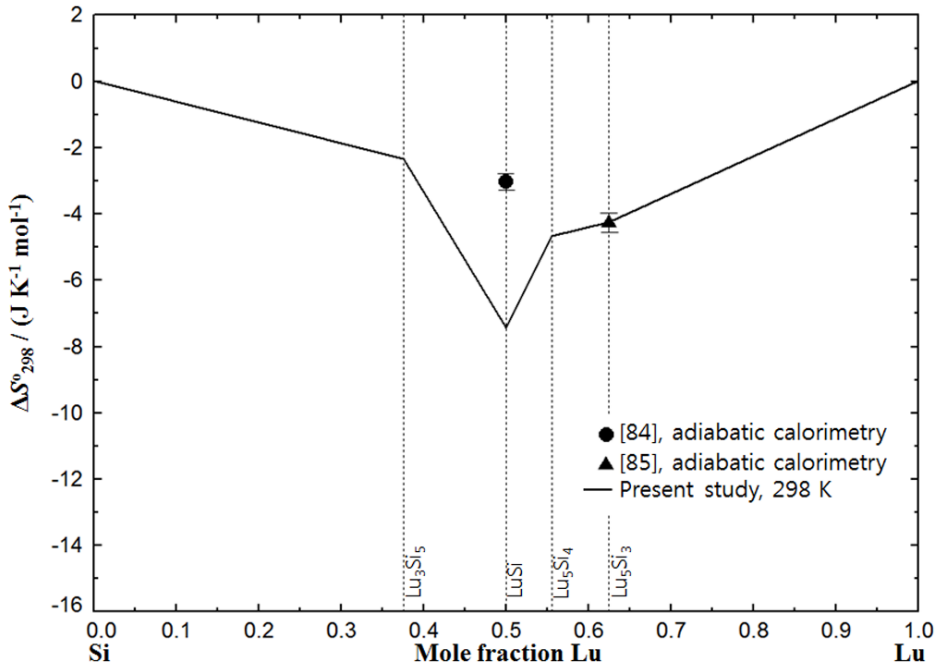


Fig. 37. Entropy of formation of the compounds in the Si-Lu system from elements at 298 K with experimental data.

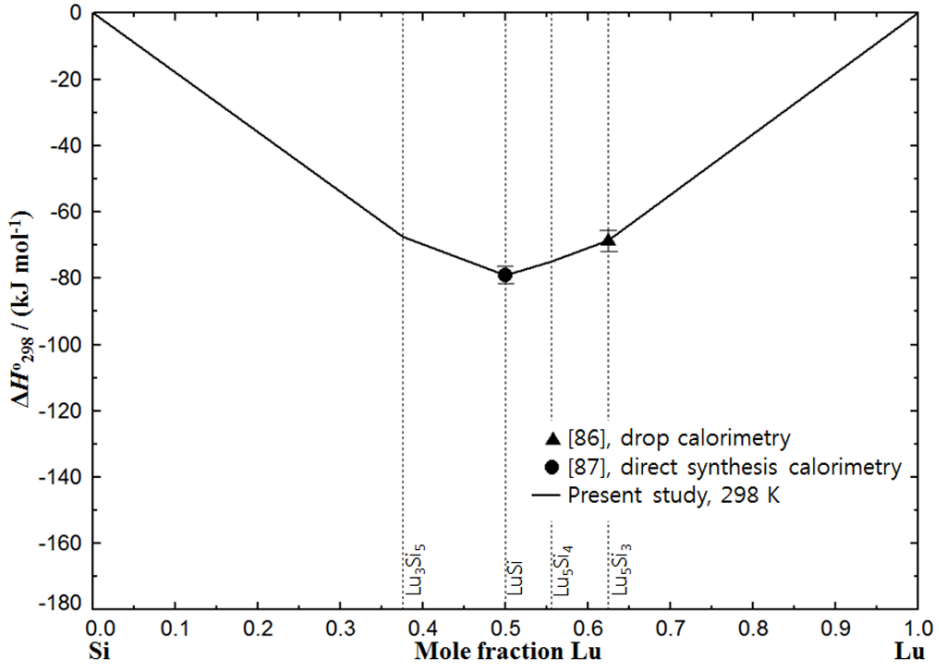


Fig. 38. Enthalpy of formation of the compounds in the Si-Lu system at 298 K with experimental data.

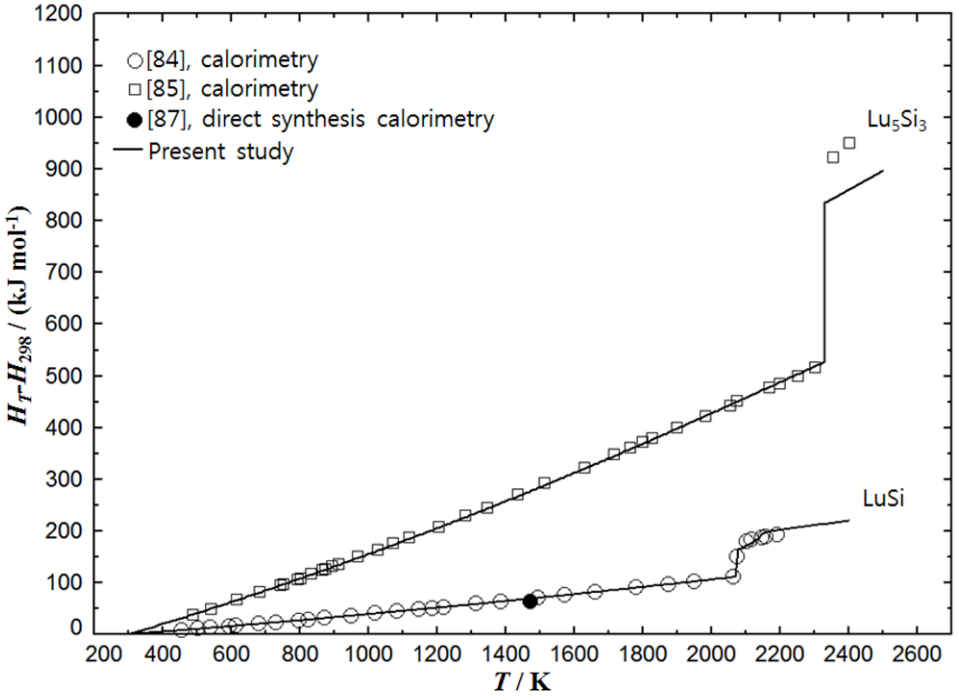


Fig. 39. Heat contents of the compounds in the Si-Lu system with experimental data.

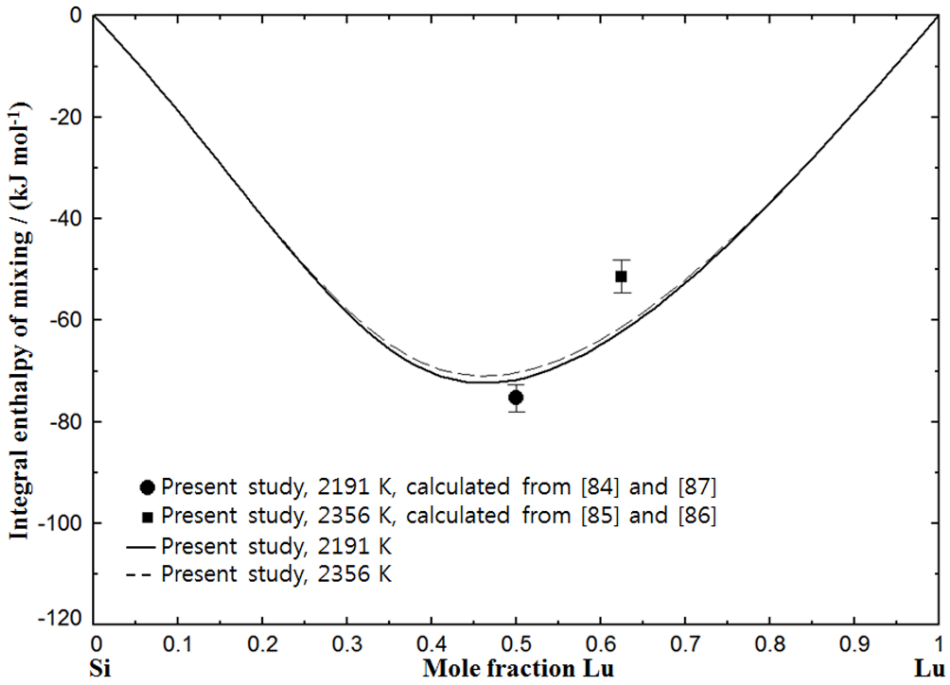


Fig. 40. Integral enthalpy of mixing of liquid Si-Lu phase at 2191 K and 2356 K with experimental data.

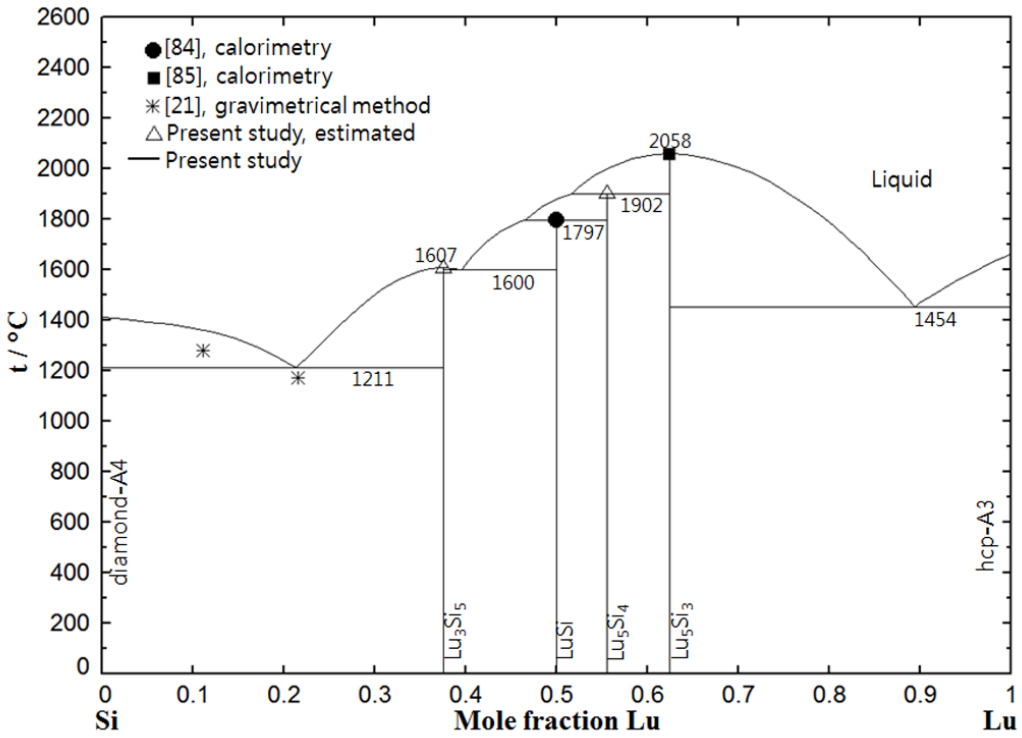


Fig. 41. The optimized Si-Lu phase diagram with experimental data.

2.8. The Si-Y system

Experimental data for the phase diagram of the Si-Y system are shown in Fig. 42. The system was first investigated by Lundin [88] using XRD and metallographic methods. The purity of the starting materials was not specified. Four intermetallic phases, Y_5Si_3, Y_5Si_4, YSi, and Y_3Si_5, and three eutectic reactions were established. The corresponding temperatures and compositions of invariant reactions are presented in Fig. 42. However, the eutectic point between Y_5Si_4 and Y_5Si_3 seems not to be reliable. Previously, the existence of YSi_2 was reported by Binder [22], Grinthal [23] and Thompson et al. [24] with its melting temperature of 1520 ºC, 1500 ºC and 1635 ºC, respectively, however the experimental methods were not specified in those studies. In addition, Mayer and Felner [89] reported the allotropic transformation from α-YSi_2 (hexagonal) to β-YSi_2 (orthorhombic) at 1250 ºC by using high temperature XRD. Perri et al. [25] also reported the allotropic transformation from α-YSi_2 (orthorhombic) to β-YSi_2 (hexagonal) at 450 ± 50 ºC by using high temperature XRD. However, Gschneidner [90] indicated that the lattice parameters for α-YSi_2 determined by Perri et al. [25] were virtually the same as those for α-Y_3Si_5 determined by Lundin [88] concluding that Y_3Si_5 is the actual stoichiometry. The eutectic reaction at 1220 ºC and 0.18 mole fraction of Y was estimated by Lozovskii and Kolesnichenko [21]. Recently, Button and McColm [91] investigated the system by using thermal analysis, metallography, XRD and hardness measurements. They established an analogous phase diagram as reported by Lundin [88] except for 25 ºC higher melting temperature of Y_5Si_3 phase and, correspondingly, for the incongruent melting of Y_5Si_4 phase. Furthermore, the solubility of Si in Y was reported to be 0.008 mole fraction and a certain homogeneity range of Y_5Si_3 phase with Y deficiency was suggested at high temperature. However, in discord with the previous studies [22-24, 89] the YSi_2 phase was not formed in their investigation.

The thermodynamic properties of the Si-Y liquid were reported by several researchers and their experimental data are presented in Fig. 43. Esin et al. [92] and Ryss et al. [93] measured the partial enthalpies of mixing for both Si and Y at 1880 K in the composition range of 0 to 0.4 mole fraction of Y and at 1870 K in the composition range of 0 to 0.35 and 0.8 to 1 mole fraction of Y, respectively, using high temperature calorimeter with an isothermal jacket. The corresponding

integral enthalpies of mixing were also reported in the respective studies. According to them, the minimum integral enthalpy was about -70 kJ mol^{-1} at near 0.5 mole fraction of Y. By using the same method, Stukalo et al. [94] determined the integral enthalpy of mixing at 2053 K in the composition range of 0 to 0.45 and 0.7 to 1 mole fraction of Y. However, their integral enthalpy was considerably less negative than the previous two studies [92, 93], especially in the composition range of 0 to 0.45 mole fraction of Y, as seen in Fig. 43.

For the intermetallic compounds, the low temperature C_p of Y_5Si_4 up to 350 K was measured by Pecharsky et al. [95] using a semi-adiabatic heat pulse calorimeter. Unfortunately, the experimental data were reported only up to 200 K. In the present study, the C_p of Y_5Si_4 was extrapolated from 200 K to 300 K where the C_p is continued to the high temperature C_p of Y_5Si_4 which was estimated by NK rule, so that the S^{o}_{298} of Y_5Si_4 was calculated by integrating the C_p from 0 to 298 K. The calculated S^{o}_{298} of Y_5Si_4 was 279.13 J K^{-1} mol^{-1}. The low temperature C_p of Y_5Si_3 up to 300 K was determined by Safonov et al. [96] using an adiabatic calorimeter. The calculated S^{o}_{298} of Y_5Si_3 was 264.94 J K^{-1} mol^{-1}. The experimental C_p data and the corresponding ΔS^{o}_{298} of Y_5Si_4 and Y_5Si_3 are presented in Figs. 44 and 45, respectively. The ΔH^{o}_{298} of Y_5Si_3 was determined by Topor and Kleppa [86] using a drop solution calorimetry. In addition, Meschel and Kleppa [97] measured the ΔH^{o}_{298} of YSi_2, YSi and Y_5Si_3 using a direct synthesis calorimetry and also reported the heat content ($H_{1473} - H_{298}$) of those compounds. The experimental ΔH^{o}_{298} of compounds and the heat contents of Meschel and Kleppa [97] are shown in Figs. 46 and 47, respectively. Recently, Polotskaya and Sidorko [98] determined ΔG^{o}_{850} of YSi_2, Y_3Si_5, YSi, Y_5Si_4 and Y_5Si_3 from an emf measurement at 820-920 K. The experimental data are shown in Fig. 48.

The system was extensively reviewed and assessed by Gokhale and Abbaschian [99] until 1986. In their work, the phase diagram was established mostly based on the work of Lundin [88] and the α-YSi_2 and β-YSi_2 were considered as stable compounds based on the works of Binder [22] and Mayer and Felner [89]. The thermodynamic optimization of the system was performed by Ran et al. [12] and Shukla et al. [10]. Ran et al. [12] described the liquid phase using a Bragg-Williams random mixing model with a Redlich-Kister polynomial. However the integral and partial

enthalpies of mixing for liquid phase presented by Ran et al. [12] could not be reproduced by using the thermodynamic parameters which were given in their study. That is, the given parameters are erroneous. Therefore, their calculated integral and partial enthalpies of mixing were extracted from the figures for comparison with experimental data. The assessed phase diagram by Ran et al. [12] was analogous to that by Gokhale and Abbaschian [99]. Recently, Shukla et al. [10] carried out the thermodynamic optimization of the system using modified quasichemical model for liquid solution. More experimental data such as the enthalpies of formation [86, 97] and the Gibbs energies of formation [98] were considered in their optimization, so that better optimization was achieved by them. The optimized phase diagram by Shukla et al. [10] is presented as dotted line in Fig. 42. The thermodynamic properties, integral and partial enthalpies of mixing, ΔS^{o}_{298}, ΔH^{o}_{298} and ΔG^{o}_{850} calculated by the thermodynamic functions in both previous optimizations are shown and compared with the experimental data in Figs. 43, 45, 46 and 48, respectively.

The optimized phase diagram of the Si-Y system in this study is presented in Fig. 42. The phase diagram is mostly constructed based on the work of Button and McColm [91]. However the liquidus in the optimized phase diagram slightly disagrees with the data of Button and McColm [91], in particular at between 0.4 and 0.5 mole fraction of Y. In addition, the peritectic melting of Y_5Si_4 and YSi in their study were less likely to be because the liquidus slope is determined by other experimental thermodynamic properties. Then, although the existence of YSi_2 phase is still controversial, α-YSi_2 and β-YSi_2 and their transformation temperature were considered in agreement with the experimental studies [22, 89]. The melting points of intermetallic compounds are more precisely reproduced the experimental data in the present optimization than those in the previous optimization by Shukla et al. [10]. The terminal solubilities of Si and Y are not considered in the present phase diagram as no precise experimental data are available. The experimental data [25] of allotropic transformation temperature of Y_3Si_5 were also reproduced. The optimization proceeded by obtaining the temperature independent parameters for the liquid phase which can reproduce the experimental enthalpy of mixing data. As seen in Fig. 43, the calculated integral and partial enthalpies of mixing are in good agreement with the experimental data, in particular, of Ryss et al. [93] which seem to be the most reasonable when considering the similarity with other Si-RE systems. Since no experimental data for the C_p of all compounds above room temperature

were available, the C_p of all compounds were estimated by NK rule and the ΔC_p of allotropic transformation of YSi_2 and Y_3Si_5 were assumed to be zero. Moreover, the enthalpy of allotropic transformations of both compounds were assumed to be 3 kJ mol^{-1} and 8 kJ mol^{-1}, respectively. After that, the C_p of Y_5Si_3 increased 4 J mol^{-1} K^{-1} to be consistent with the low temperature C_p data [96] as shown in Fig. 44. The S°_{298} of Y_5Si_4 and Y_5Si_3 calculated from the low temperature C_p data [95, 96] were used in the present optimization and the S°_{298} of remaining compounds were estimated by considering other experimental thermodynamic data and phase diagram. The calculated ΔS°_{298} in the present optimization are presented in Fig. 45 along with the experimental data [95, 96] and the previous optimizations [10, 12]. The experimental ΔH°_{298} of YSi_2 [97], YSi [97] and Y_5Si_3 [86, 97] were taken into account. The calculated ΔH°_{298} in the present optimization are compared with the experimental data [86, 97] and the previous optimizations [10, 12] in Fig. 46. In addition, the calculated heat contents of YSi_2, YSi and Y_5Si_3 are in good agreement with the experimental data [97] as shown in Fig. 47. However, like the Si-Gd and Si-Ho systems, the calculated ΔG°_{850} of compounds disagrees with the emf data [98] as shown in Fig. 48. The temperature dependent parameters for the liquid solution were finally decided according to the temperatures of invariant reactions in the phase diagram. The optimized thermodynamic parameters are listed in Table 15 and the calculated invariant reactions with the experimental data are tabulated in Table 16.

Table 15. Optimized model parameters of the Si-Y system.

Phase	Thermodynamic parameters			
Liquid	Coordination Numbers			
	i	j	Z^i_{ij}	Z^j_{ij}
	Si	Y	6	6
	Δg_{SiY} / (J mol^{-1}) = (-56484.0 + 2.092 T/K) + (-16736.0 + 2.092 T/K) X_{SiSi}			
	+ 2092.0 X^2_{SiSi} + (10460.0 – 16.318 T/K) X_{YY}			
	+ (-8368.0 + 10.46 T/K) X^2_{YY}			
α-YSi_2	ΔH°_{298} = -181000 J mol^{-1}, S°_{298} = 72.34 J K^{-1} mol^{-1}			

	C_p / (J K^{-1} mol^{-1}) = 1 × C_p / (J K^{-1} mol^{-1}) (Y, hcp-A3)
	+ 2 × C_p / (J K^{-1} mol^{-1}) (Si, diamond-A4)
β-YSi_2	$\Delta_{trs}H^{\alpha\rightarrow\beta}$ = 3000 J mol^{-1}, $T_{trs}^{\alpha\rightarrow\beta}$ = 1523.0 K
	C_p / (J K^{-1} mol^{-1}) = 1 × C_p / (J K^{-1} mol^{-1}) (Y, hcp-A3)
	+ 2 × C_p / (J K^{-1} mol^{-1}) (Si, diamond-A4)
α-Y_3Si_5	ΔH_{298}^{o} = -520000 J mol^{-1}, S_{298}^{o} = 232.1 J K^{-1} mol^{-1}
	C_p / (J K^{-1} mol^{-1}) = 3 × C_p / (J K^{-1} mol^{-1}) (Y, hcp-A3)
	+ 5 × C_p / (J K^{-1} mol^{-1}) (Si, diamond-A4)
β-Y_3Si_5	$\Delta_{trs}H^{\alpha\rightarrow\beta}$ = 8000 J mol^{-1}, $T_{trs}^{\alpha\rightarrow\beta}$ = 723.0 K
	C_p / (J K^{-1} mol^{-1}) = 3 × C_p / (J K^{-1} mol^{-1}) (Y, hcp-A3)
	+ 5 × C_p / (J K^{-1} mol^{-1}) (Si, diamond-A4)
YSi	ΔH_{298}^{o} = -165000 J mol^{-1}, S_{298}^{o} = 58.0 J K^{-1} mol^{-1}
	C_p / (J K^{-1} mol^{-1}) = 1 × C_p / (J K^{-1} mol^{-1}) (Y, hcp-A3)
	+ 1 × C_p / (J K^{-1} mol^{-1}) (Si, diamond-A4)
Y_5Si_4	ΔH_{298}^{o} = -724000 J mol^{-1}, S_{298}^{o} = 279.13 J K^{-1} mol^{-1}
	C_p / (J K^{-1} mol^{-1}) = 5 × C_p / (J K^{-1} mol^{-1}) (Y, hcp-A3)
	+ 4 × C_p / (J K^{-1} mol^{-1}) (Si, diamond-A4)
Y_5Si_3	ΔH_{298}^{o} = -600000 J mol^{-1}, S_{298}^{o} = 264.94 J K^{-1} mol^{-1}
	C_p / (J K^{-1} mol^{-1}) = 5 × C_p / (J K^{-1} mol^{-1}) (Y, hcp-A3)
	+ 3 × C_p / (J K^{-1} mol^{-1}) (Si, diamond-A4) + 4 J K^{-1} mol^{-1}

Table 16. Calculated invariant reactions and experimental data in the Si-Y system.

Type	Reaction	t (°C)	Reference
Eutectic	$L_{(X_Y=0.162)} \rightarrow Si_{(dia.-A4,\ X_Y=0)} + YSi_2$	1235.7	This work
	$L_{(X_Y=0.180)} \rightarrow Si_{(dia.-A4,\ X_Y=0)} + YSi_2$	1215.0	[88]
	$L_{(X_Y=0.180)} \rightarrow Si_{(dia.-A4,\ X_Y=0)} + YSi_2$	1230.0	[91]

Peritectic	$L_{(X_Y= 0.275)} + Y_3Si_5 \rightarrow YSi_2$	1515.7	This work
	T_m for YSi_2	1520.0	[22]
		1500.0	[23]
		1635.0	[24]
Allotropic	α-$YSi_2 \leftrightarrow \beta$-$YSi_2$	1250.0	This work
	α-$YSi_2 \leftrightarrow \beta$-$YSi_2$	1250.0	[89]
Peritectic	$L_{(X_Y= 0.373)} + YSi \rightarrow Y_3Si_5$	1636.6	This work
	$L_{(X_Y= 0.365)} + YSi \rightarrow Y_3Si_5$	1635.0	[88]
	$L_{(X_Y= 0.339)} + YSi \rightarrow Y_3Si_5$	1635.0	[91]
Allotropic	α-$Y_3Si_5 \leftrightarrow \beta$-$Y_3Si_5$	450.0	This work
	α-$Y_3Si_5 \leftrightarrow \beta$-$Y_3Si_5$	450 ± 50	[25, 90]
Peritectic	$L_{(X_Y= \sim 0.48)} + Y_5Si_4 \rightarrow YSi$	1835.0	[88]
	$L_{(X_Y= 0.487)} + Y_5Si_4 \rightarrow YSi$	1836.0	[91]
Congruent	$L_{(X_Y= 0.50)} \leftrightarrow YSi$	1837.3	This work
Eutectic	$L_{(X_Y= 0.525)} \rightarrow YSi + Y_5Si_4$	1828.1	This work
Congruent	$L_{(X_Y= 0.556)} \leftrightarrow Y_5Si_4$	1840.5	This work
	$L_{(X_Y= 0.556)} \leftrightarrow Y_5Si_4$	1840.0	[88]
Eutectic	$L_{(X_Y= 0.583)} \rightarrow Y_5Si_4 + Y_5Si_3$	1829.8	This work
	$L_{(X_Y= 0.590)} \rightarrow Y_5Si_4 + Y_5Si_3$	1710.0	[88]
Peritectic	$L_{(X_Y*)} + Y_5Si_3 \rightarrow Y_5Si_4$	+	[91]
Congruent	$L_{(X_Y= 0.625)} \leftrightarrow Y_5Si_3$	1857.5	This work
	$L_{(X_Y= 0.625)} \leftrightarrow Y_5Si_3$	1850.0	[88]
	$L_{(X_Y= 0.625)} \leftrightarrow Y_5Si_3$	1875.0	[91]
Eutectic	$L_{(X_Y= 0.894)} \rightarrow Y_5Si_3 + Y_{(hcp\text{-}A3,\ X_Y= 1)}$	1263.0	This work
	$L_{(X_Y= 0.870)} \rightarrow Y_5Si_3 + Y_{(hcp\text{-}A3,\ X_Y= 1)}$	1260.0	[88]
	$L_{(X_Y= 0.870)} \rightarrow Y_5Si_3 + Y_{(hcp\text{-}A3,\ X_Y= 1)}$	1260.0	[91]

* The exact composition is not specified in the reference.
+ The exact temperature is not specified in the reference.

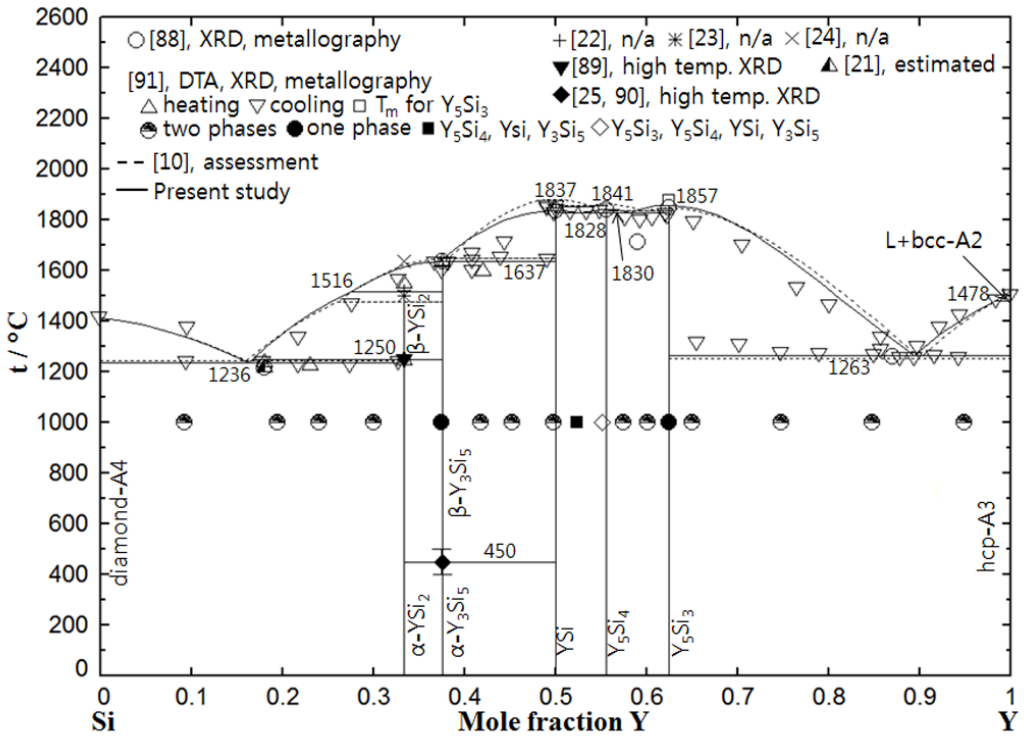


Fig. 42. The optimized Si-Y phase diagram with experimental data and previous assessment.

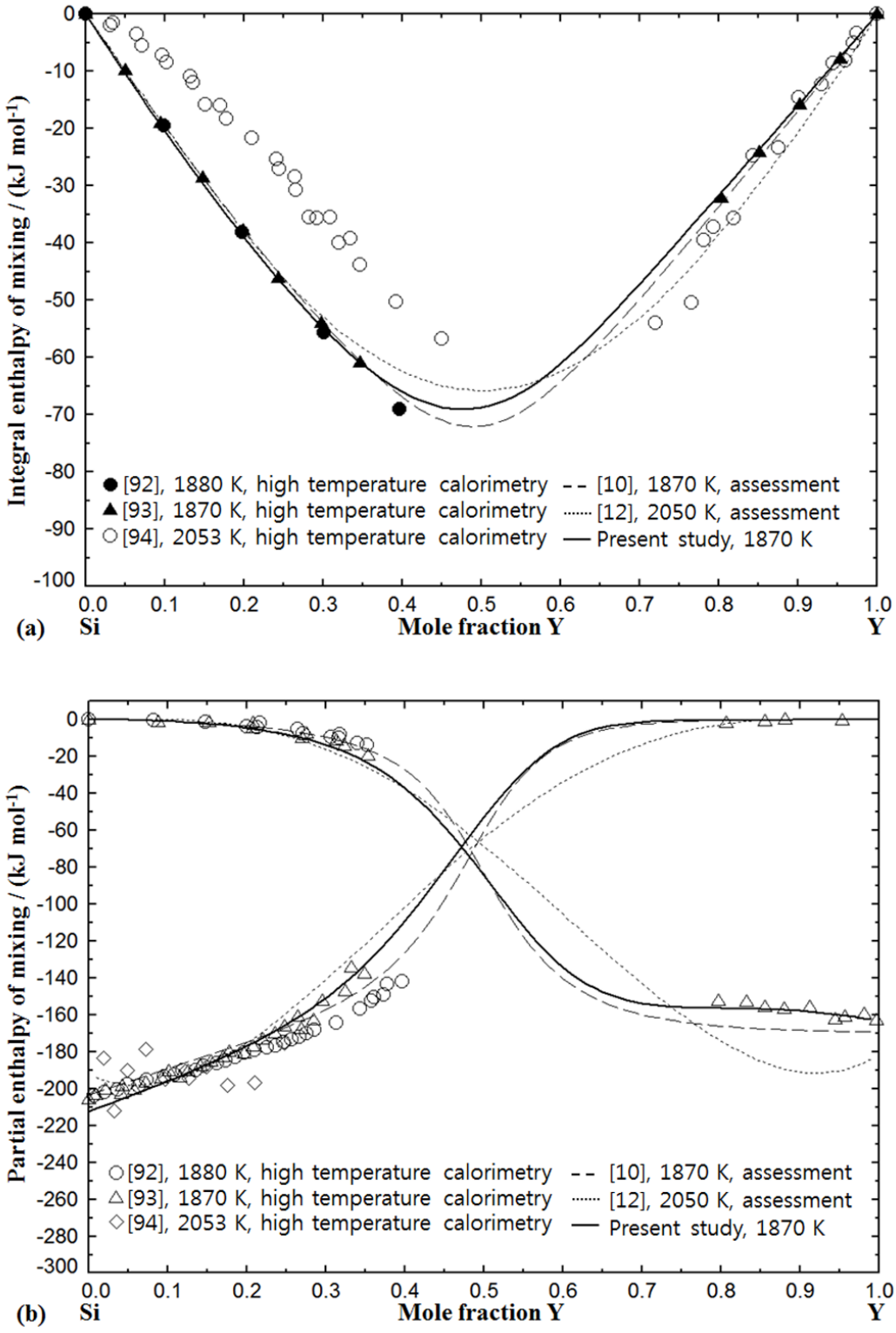


Fig. 43. (a) Integral enthalpy of mixing and (b) partial enthalpies of mixing of liquid Si-Y phase at 1870 K with experimental data and previous assessments.

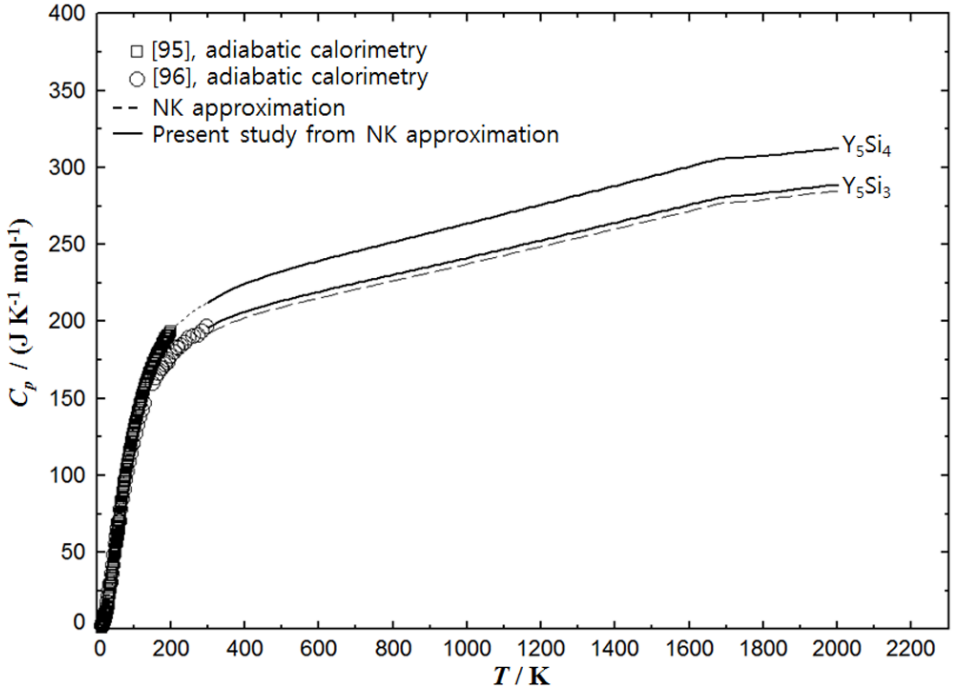


Fig. 44. Heat capacities of the compounds in the Si-Y system with experimental data.

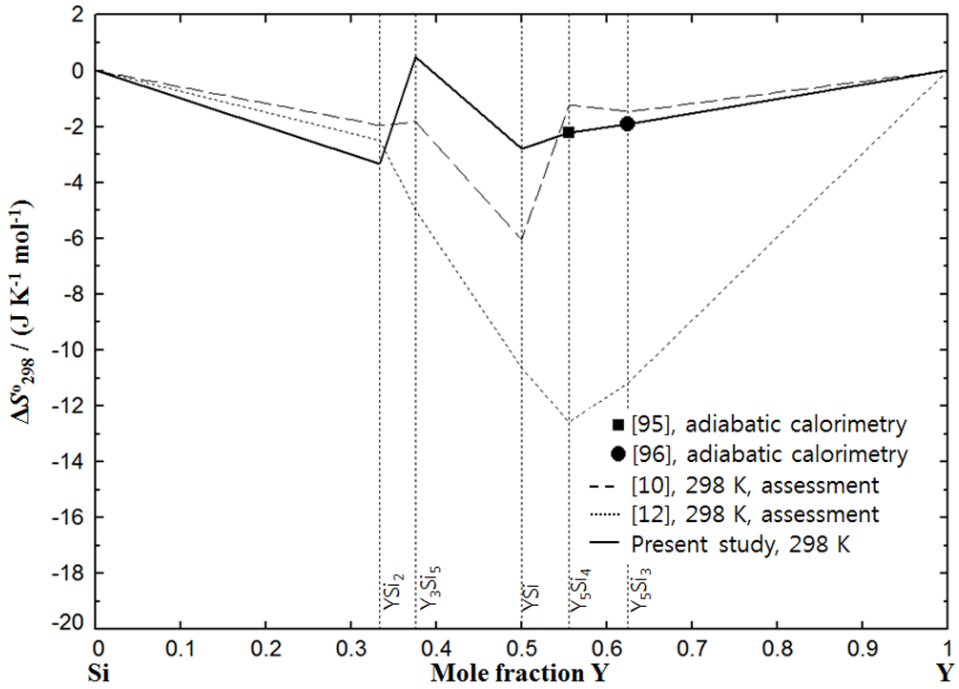


Fig. 45. Entropy of formation of the compounds in the Si-Y system from elements at 298 K with experimental data and previous assessments.

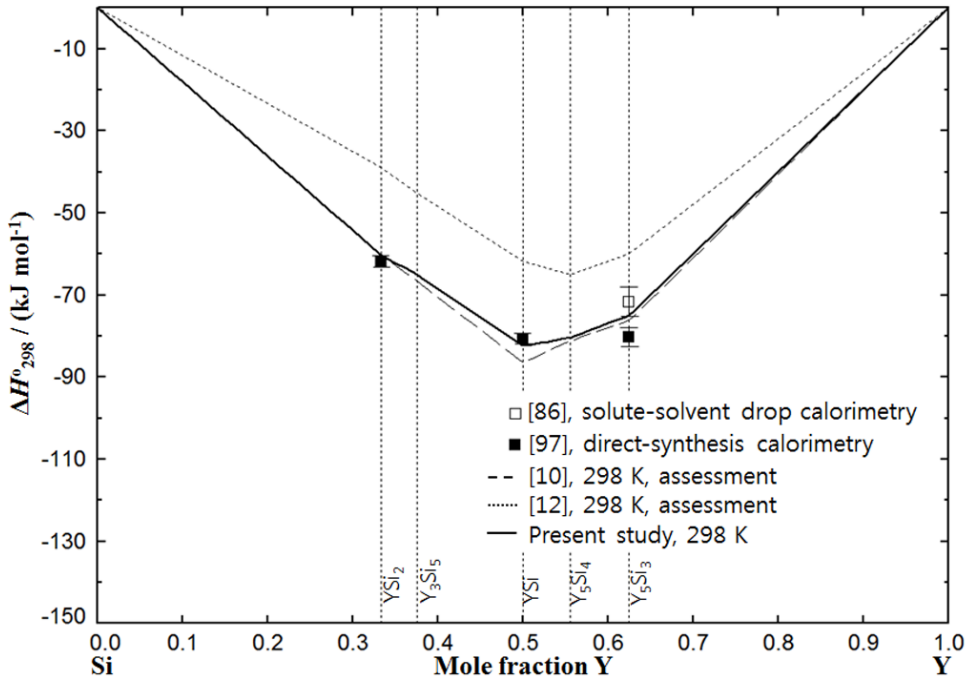


Fig. 46. Enthalpy of formation of the compounds in the Si-Y system at 298 K with experimental data and previous assessments.

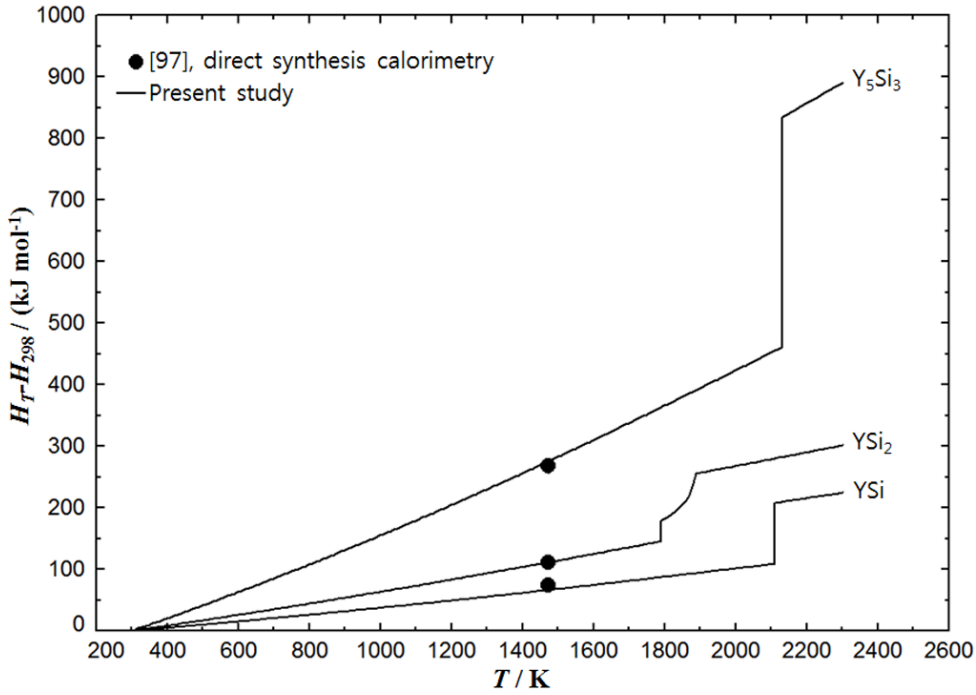


Fig. 47. Heat contents of the compounds in the Si-Y system with experimental data.

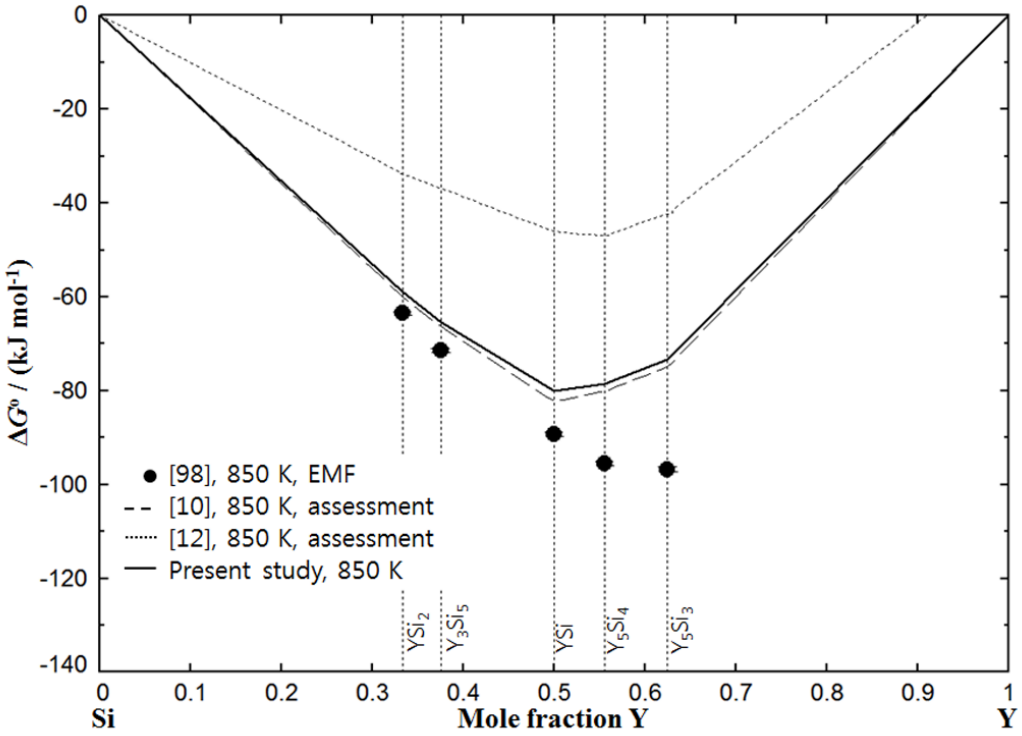


Fig. 48. Gibbs energy of formation of the compounds in the Si-Y system at 850 K with experimental data and previous assessments.

3. Systematic trends in the Si-RE systems

Recently, critical evaluations and optimizations of the binary Mn-RE systems were performed by the present authors [100, 101] using the Modified Quasichemical Model for the liquid solution. A clear systematic trend through the series of Mn-RE systems was found and discussed. For instance, the enthalpy of mixing in liquid Mn-RE was observed to gradually decrease from positive to negative values with increasing the atomic number of rare earth elements. This is most probably due to differences in thermochemical and electronic properties such as the Fermi energies, electronic density and atomic volume of the RE.

Based on the present thermodynamic optimization results, we analyzed the systematic changes in thermodynamic and phase diagram data of the Si-RE systems.

The enthalpies of mixing of all binary liquid Si-RE alloys at 2000 K are compared in Fig. 49. The enthalpies of mixing for all liquid Si-RE alloys show minimum values in the range of -65 to -75 kJ mol^{-1}. These are much larger in magnitude than those of the Mn-RE systems (8 to -8 kJ mol^{-1}) [100, 101], Al-RE systems (-30 to -40 kJ mol^{-1}) [5, 6] and Zn-RE systems (-20 to -32 kJ mol^{-1}) [unpublished], but similar to the Pb-RE systems (-40 to -50 kJ mol^{-1}) [102]. Unfortunately it is hard to find visible trend in the enthalpy of mixing changing with atomic number of RE like Mn-RE system, but still the enthalpy of mixing seems roughly decreasing with increasing atomic number of RE. The positions of minimum enthalpies of mixing are near 0.5 mole fraction of RE or slightly more rich in Si. Figure 50 shows the entropies of mixing of liquid Si-RE at 2000 K. Corresponding to the large negative enthalpies of mixing at the middle composition range, the entropies of mixing have typical “M” shape, which can be seen in the systems having short range ordering in liquid phase. In general, the entropy of mixing values are negative at 0.5, which means there could be significant non-configuration entropy can be involved in this Si-RE at liquid state possibly associated to the strong short range ordering. Like the liquid enthalpies, the enthalpies of formation of the Si-RE compounds of all Si-RE systems are similar, which show a minimum in the range of about -68 to -88 kJ mol^{-1} (based on one mole of Si-RE system) as shown in Fig. 51. The entropies of formation of the Si-RE compounds at 298 K are calculated in Fig. 52 from

corresponding elements. Most of solid RE silicides have negative entropies of formation except those in the Si-Ce system. In the overview of all the enthalpy of formation data, it is found that the Si-Dy system has distinctive difference from general trend. As seen in Fig. 51, the enthalpy of formation of Si-Dy compounds are all higher than the general trend of enthalpy data. It is hard to explain this strange behavior of Dy, which can be open area for future research.

On the other hand, a clear systematic trend in the melting temperatures of intermetallic compounds was found in the phase diagrams of the Si-RE systems. The melting temperatures of Si-RE compounds are shown in Fig. 53 in the order of atomic number of RE, and a collection of the optimized phase diagrams of the Si-RE systems is presented in Fig. 54. As seen in these figures, the compounds which have the highest melting temperature shift from the low RE-containing compounds to the high RE-containing compounds with increasing atomic number of RE. The systematic trends in the phase diagram were successfully used to assess the phase diagrams of the Si-Sm, -Tm and -Lu systems which have been rarely known. Similarly, Bulanova et al. [49, 103] tried to estimate the melting temperatures of certain RE-containing compounds (Si-RE, Ge-RE, Sn-RE and Pb-RE) by using the method which is based on the linear interpolation of the melting temperatures of the same type of the compounds versus the melting temperatures of pure RE metals. However, their method is only valid for the compounds such as RE_5Si_3 and RE_5Si_4 whose melting temperatures are increasing along with atomic number of RE. Moreover, La and Y turned out to be off from the linear relation (RE_5Si_3 and RE_5Si_4). It is still difficult to understand why such melting trend (in Figs. 53 and 54) of RE compounds can be seen in the Si-RE system. One of possible reasons can be proposed below.

As seen in the phase diagrams (Fig. 54), the melting temperature of RE is increasing with atomic number in general. Consequently, the increase in the melting temperature of RE-rich compounds can be associated to the melting temperature of RE. Therefore, the normalized melting temperatures of two series of RE compounds (RE_5Si_3 and RE_5Si_3) are shown in Fig. 55(a). The temperature was normalized based on the melting temperatures of Si and corresponding RE elements. In general, Y has physico-chemical properties similar to heavy RE elements. In order to see the trend clearly, Y is placed between Ho and Er because the melting temperature of Y is

between the melting temperature of Ho and Er. As seen in the normalized meting temperatures, the RE_5Si_3 has increasing trend with increasing atomic number of RE while the RE_3Si_5 has decreasing tendency. This clearly shows that the relative stability of RE rich silicide compounds is increasing with atomic number of RE. This trend can result from the enthalpy of formation of RE silicides. The enthalpy of formation of two series of RE compounds at 1273 K are compared in Fig. 55(b). In general, the RE_5Si_3 has decreasing tendency of the enthalpy of formation along with RE while the RE_3Si_5 shows relatively steady except for the Dy_3Si_5. Therefore, the relative stability of RE_5Si_3 is increasing from left to right as shown in Fig. 55(b). As mentioned above, this could be one of possible explanation for the phase diagram trend, but more comprehensive research using the ab initio calculations would be required to understand the physico-chemical properties of RE silicide.

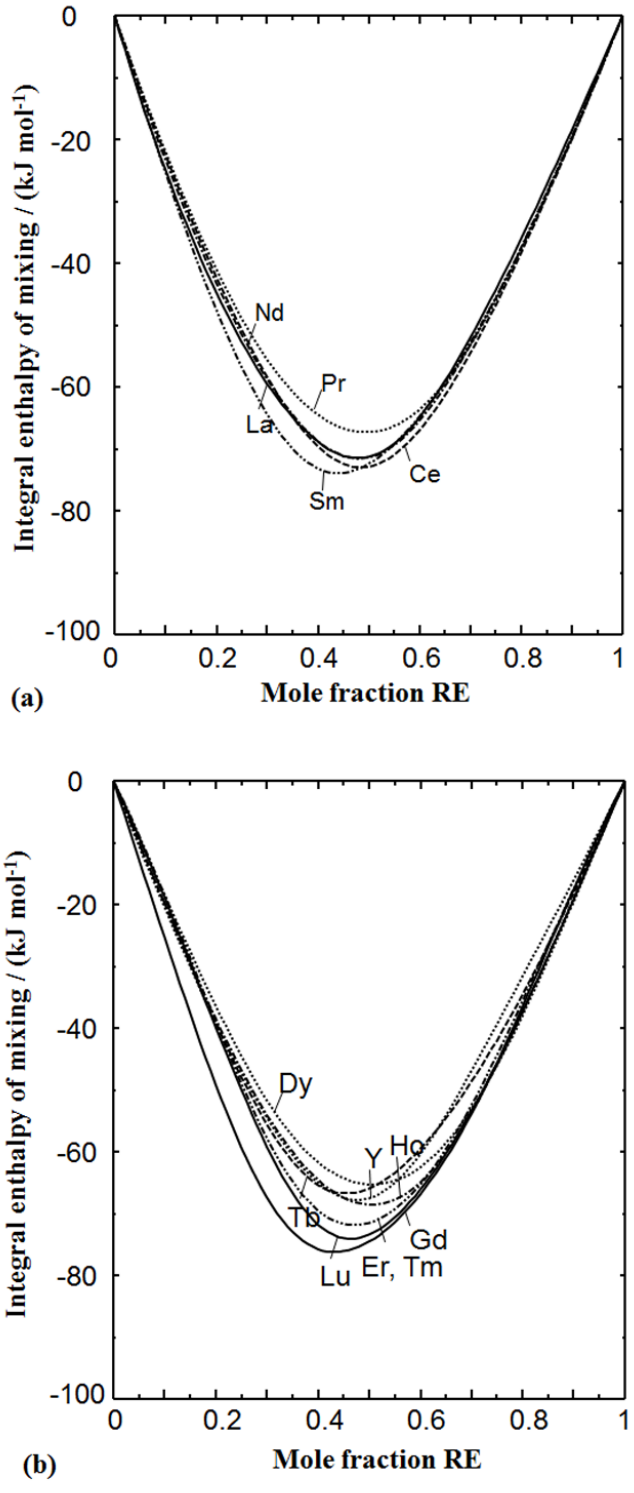
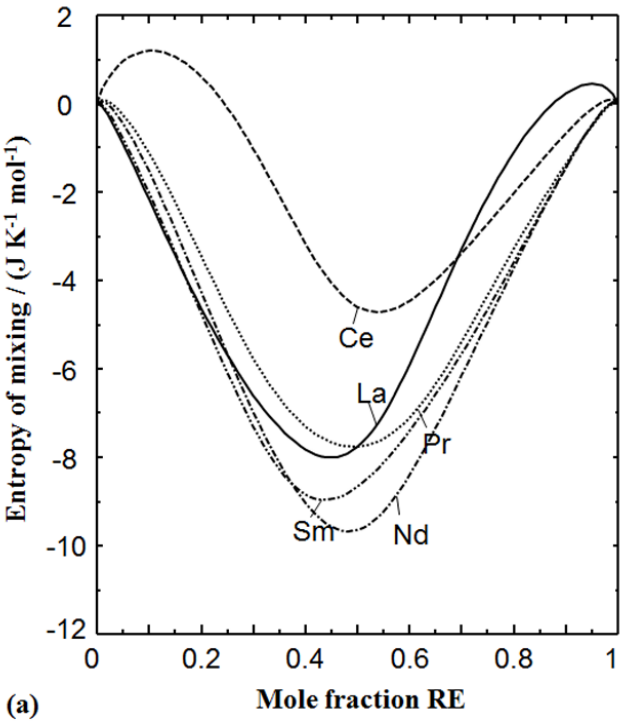


Fig. 49. Comparison of integral enthalpies of mixing of liquid Si-RE at 2000 K. ((a) Si-light RE and (b) Si-heavy RE)



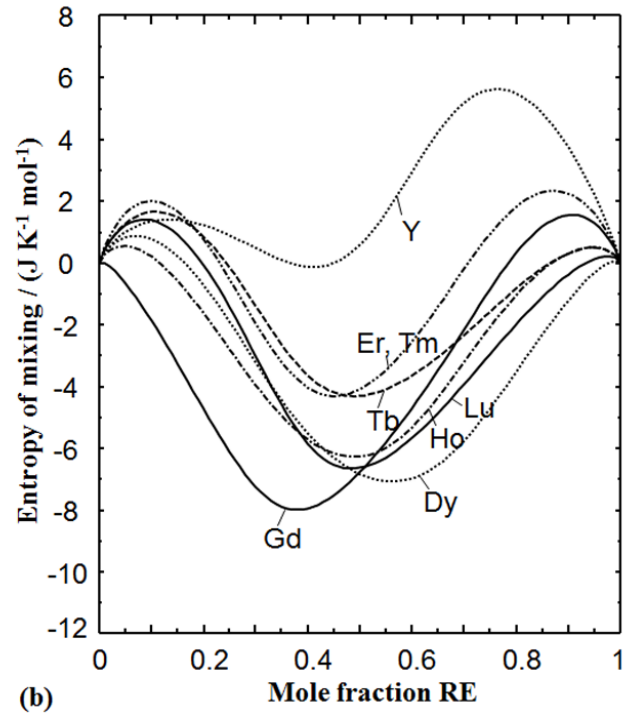


Fig. 50. Comparison of entropies of mixing of liquid Si-RE at 2000 K. ((a) Si-light RE and (b) Si-heavy RE)

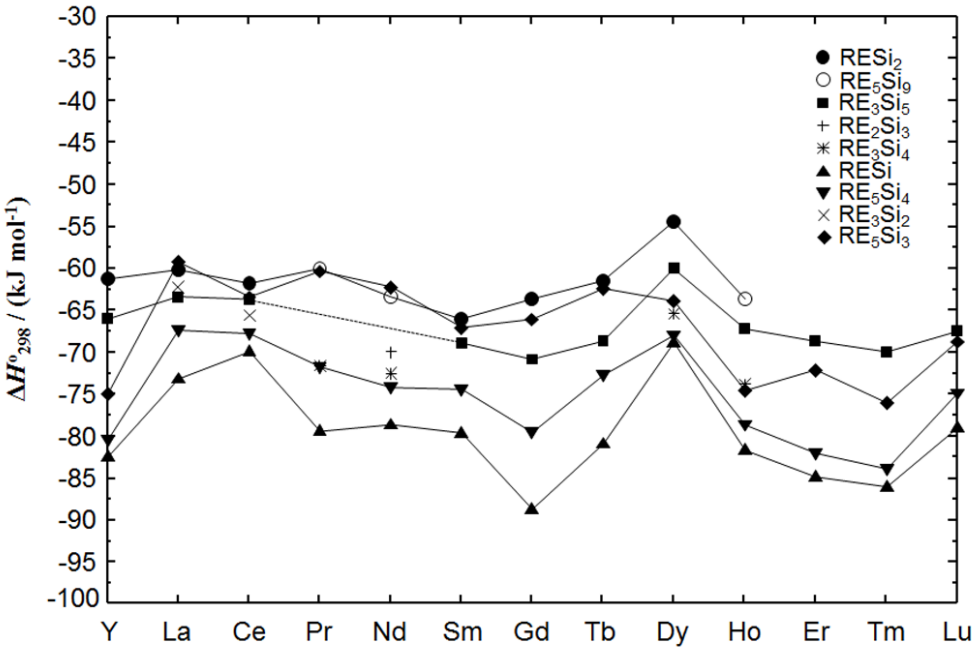


Fig. 51. Comparison of enthalpies of formation of Si-RE compounds at 298 K (based on one mole of Si-RE system).

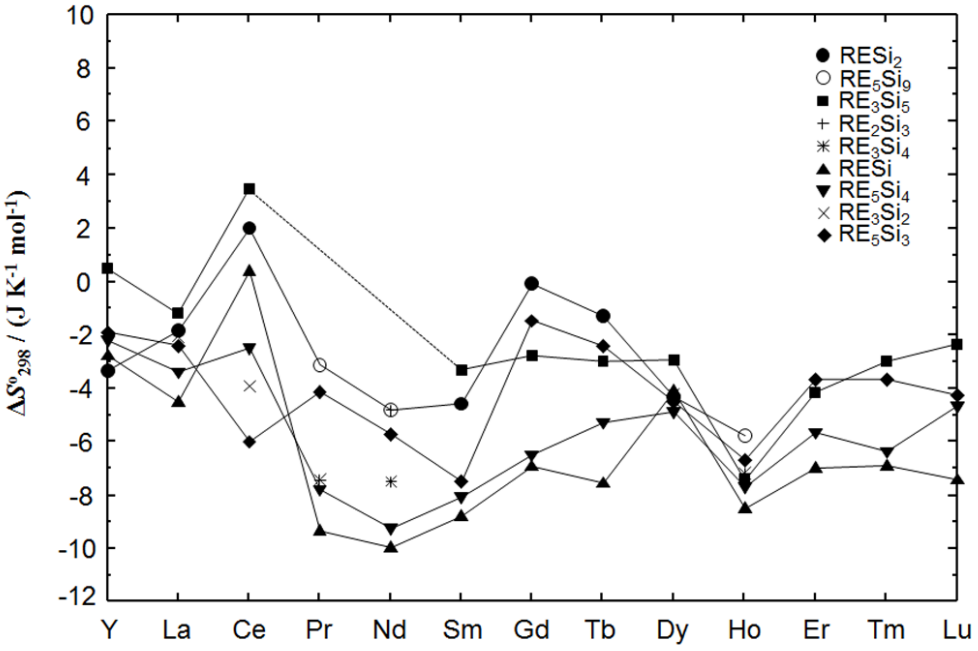


Fig. 52. Comparison of entropies of formation of Si-RE compounds at 298 K (based on one mole of Si-RE system) from elemental references.

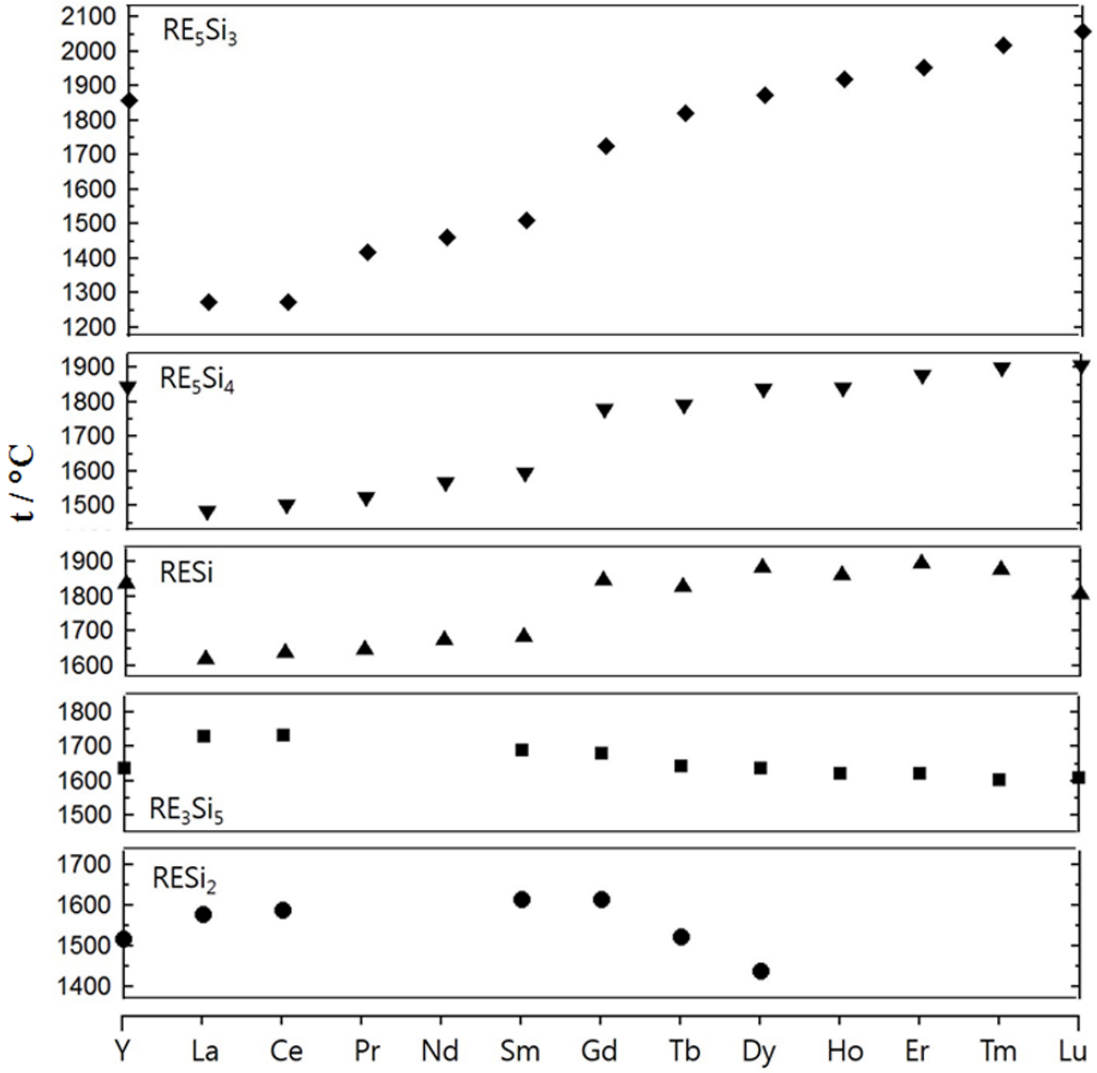


Fig. 53. Systematic changes in the melting temperatures of Si-RE compounds.

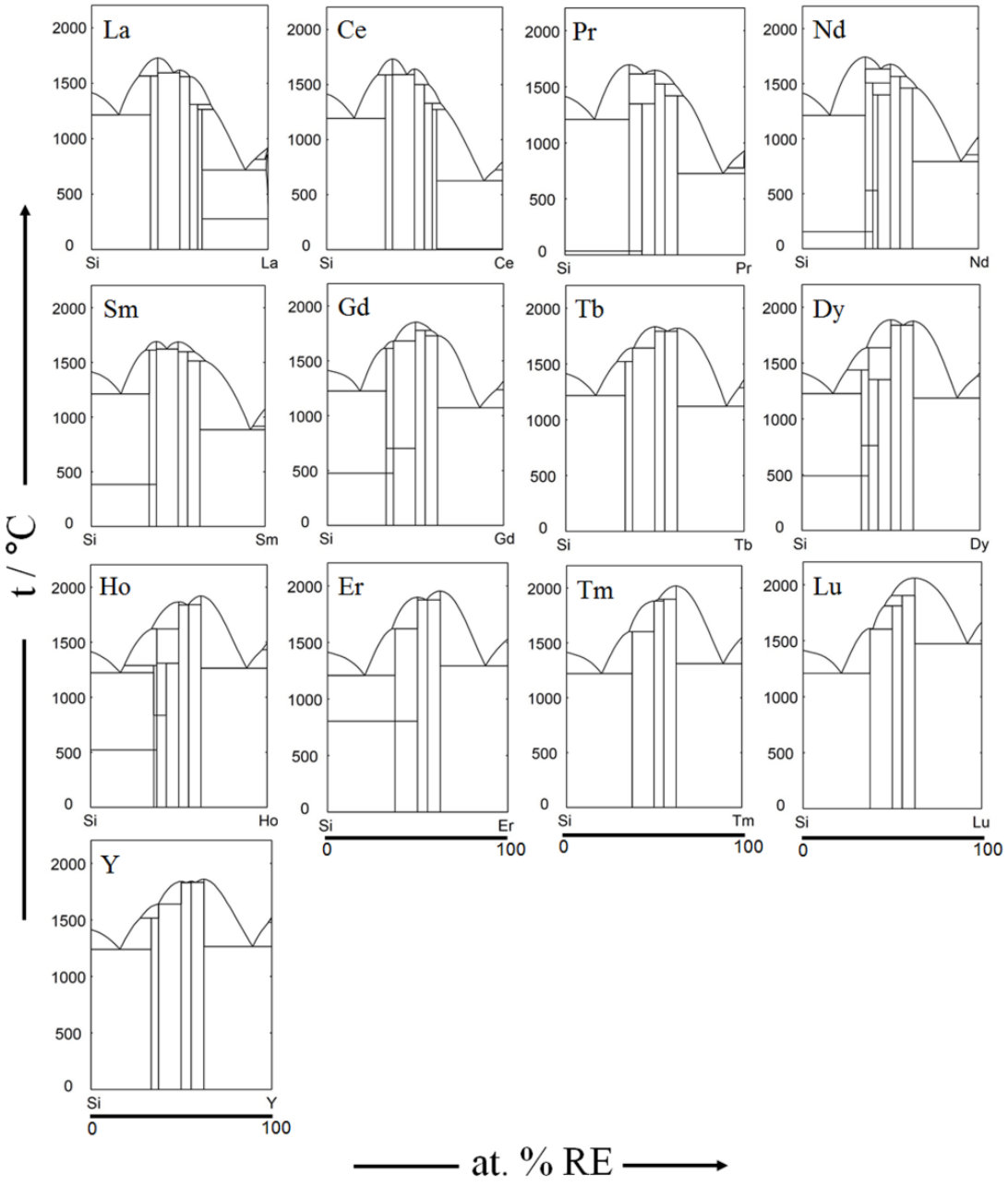


Fig. 54. Collection of the optimized phase diagrams of the Si-RE systems.

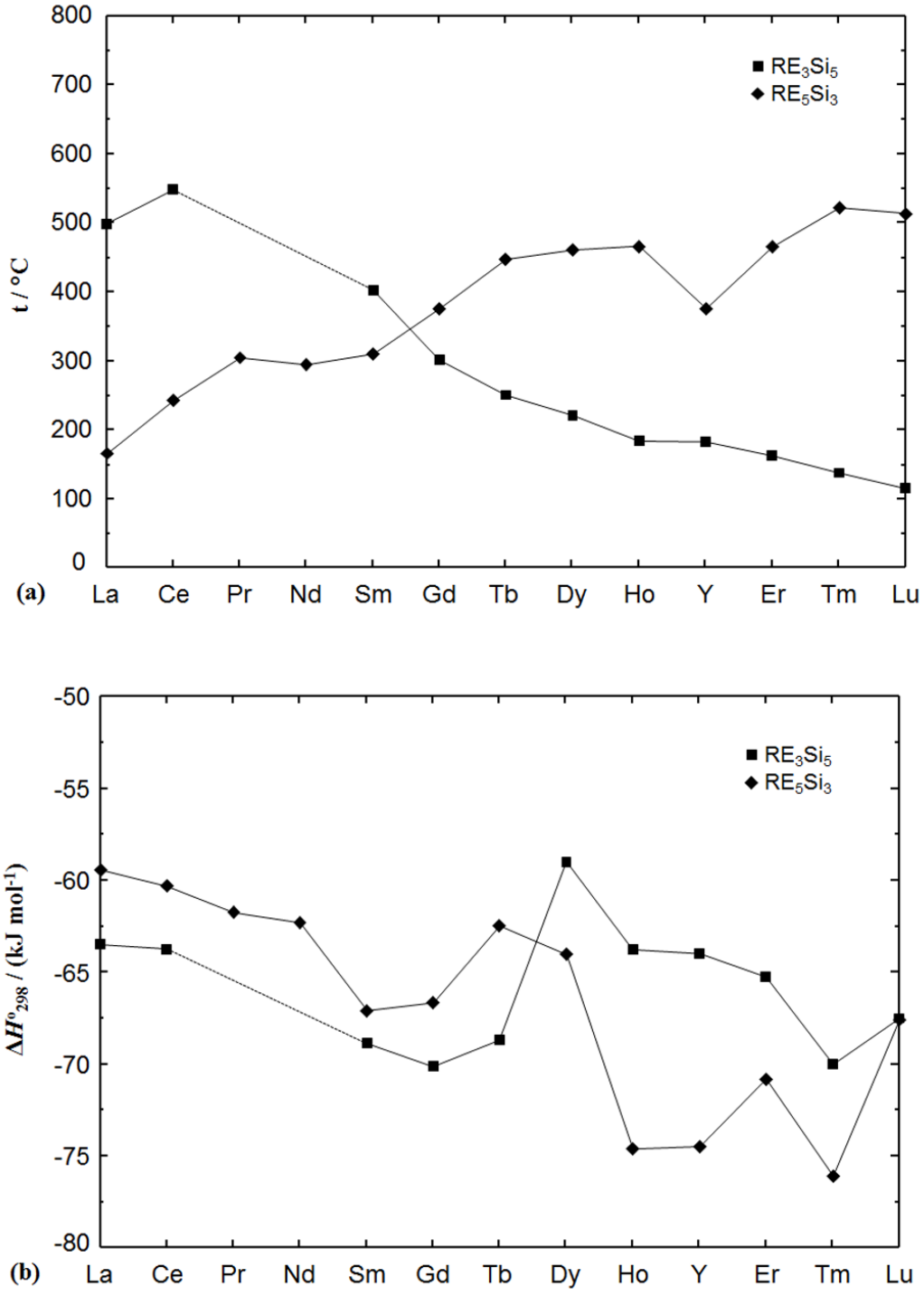


Fig. 55. (a) Normalized melting temperatures based on elemental melting temperature references and (b) enthalpies of formation of RE_3Si_5 and RE_5Si_3 compounds at 1273 K (based on one mole of Si-RE system).

4. Conclusions

A critical evaluation and optimization of all available phase diagrams and thermodynamic data of the Si-RE (RE = Gd, Tb, Dy, Ho, Er, Tm, Lu and Y) systems was conducted to obtain reliable thermodynamic functions for all the phases. The Gibbs energy functions for all stoichiometric compounds were obtained. The thermodynamic properties of the liquid phase were described using the Modified Quasichemical Model and the solid solution phases such as bcc and fcc were described using the one-sublattice Compound Energy Formalism.

In the thermodynamic modeling, it is found that the Si-RE systems follow certain similarities and a systematic trend in thermodynamic properties and phase diagrams. For example, the calculated enthalpies of mixing at 2000 K of the Si-RE liquid show similar minimum values in the range of -65 to -75 kJ mol^{-1} and the calculated enthalpies of formation at 298 K of the Si-RE compounds show a minima in the range of about -68 to -88 kJ mol^{-1} (based on one mole of Si-RE system) at the equimolar compositions. A clear systematic trend in the melting temperatures of the Si-RE compounds was found. The compounds having the highest melting temperature shift from the lower RE-containing compounds to the higher RE-containing compounds with increasing atomic number of RE. This may result from the relative stability of RE rich compound becomes more strong with increasing atomic number of RE. The systematic trends in phase diagram data and thermodynamic properties were used to assess the unexplored phase diagrams of the Si-Sm, Si-Tm and Si-Lu systems.

Acknowledgement

This project was supported by the National Sciences and Engineering Research Council of Canada (NSERC) Collaborative Research and Development grant and General Motors of Canada.

5. References

[1] Y.-B. Kang, A.D. Pelton, P. Chartrand, C.D. Fuerst, Calphad 32 (2008) 413-422.
[2] P.J. Spencer, A.D. Pelton, Y.-B. Kang, P. Chartrand, C.D. Fuerst, Calphad 32 (2008) 423-431.
[3] A. Shukla, Y.-B. Kang, A.D. Pelton, Calphad 32 (2008) 470-477.
[4] Y.-B. Kang, C. Aliravci, P.J. Spencer, G. Eriksson, C.D. Fuerst, P. Chartrand, A.D. Pelton, JOM 61 (2009) 75-82.
[5] L. Jin, Y.-B. Kang, P. Chartrand, C.D. Fuerst, CALPHAD 34 (2010) 456-466.
[6] L.-L. Jin, Y.-B. Kang, P. Chartrand, C.D. Fuerst, CALPHAD 35 (2011) 30-41.
[7] Y.-B. Kang, L. Jin, P. Chartrand, A.E. Gheribi, K. Bai, P. Wu, CALPHAD 38 (2012) 100-116.
[8] L. Jin, D. Kevorkov, M. Medraj, P. Chartrand, The Journal of Chemical Thermodynamics 58 (2013) 166-195.
[9] J. Gröbner, D. Mirkovic, R. Schmid-Fetzer, Metall. Mater. Trans. A 35A (2004) 3349-3362.
[10] A. Shukla, Y.-B. Kang, A.D. Pelton, Int. J. Mater. Res. 100 (2009) 208-217.
[11] M. Huang, D.L. Schlagel, F.A. Schmidt, T.A. Lograsso, J. Alloys Compd. 441 (2007) 94-100.
[12] Q. Ran, H.L. Lukas, G. Effenberg, G. Petzow, Z. Metallkd. 80 (1989) 402-405.
[13] A.B. Gokhale, R. Abbaschian, Bull. Alloy Phase Diagrams 9 (1988) 574-578.
[14] J.A. Perri, I. Binder, B. Post, J. Phys. Chem. 63 (1959) 616-619.
[15] G.V. Samsonov, Y.B. Paderno, T.S. Verkhoglyadova, Dopov. Akad. Nauk Ukr. RSR (1963) 224-226.
[16] I. Mayer, E. Yanir, I. Shidlovsky, Inorg. Chem. 6 (1967) 842-844.
[17] A. Raman, Trans. Indian Inst. Metals 21 (1968) 5-8.
[18] J.E. Iglesias, H. Steinfink, J. Less-Common Metals 26 (1972) 45-52.
[19] M.I. Copeland, H. Kato, Proc. Symp. Phys. Mater. Probl. Reactor Control Rods, Vienna (1964) 295-316.
[20] E.V. Ganapathy, K. Kugimiya, H. Steinfink, D.I. Tchernev, J. Less-Common Met. 44 (1976) 245-258.
[21] V.N. Lozovskii, A.I. Kolesnichenko, Izv. Akad. Nauk SSSR, Neorg. Mater. 17 (1981) 554-555.
[22] I. Binder, J. Am. Ceram. Soc. 43 (1960) 287-292.
[23] R.D. Grinthal, Journal of the Electrochemical Society 107 (1960) 59-61.
[24] R.D. Thompson, B.Y. Tsaur, K.N. Tu, Appl. Phys. Lett. 38 (1981) 535-537.
[25] J.A. Perri, E. Banks, B. Post, J. Phys. Chem. 63 (1959) 203-204.
[26] V.M. Eremenko, K.A. Meleshevich, Y.I. Buyanov, P.S. Martsenyuk, Ukr. Khim. Zh. (Russ. Ed.) 57 (1991) 1047-1054.
[27] A.S. Bolgar, N.P. Gorbachuk, A.V. Blinder, High Temp. (Transl. of Teplofiz. Vys. Temp.) 34 (1996) 535-540.
[28] N.P. Gorbachuk, Ukr. Khim. Zh. (Russ. Ed.) 74 (2008) 8-12.
[29] G.I. Batalin, V.S. Sudavtsova, N.V. Stroganova, Ukr. Khim. Zh. (Russ. Ed.) 51 (1985) 775-777.
[30] E.A. Beloborodova, N.V. Golovataya, T.N. Zinevich, N.V. Kotova, Powder Metall. Met. Ceram. 38 (2000) 603-607.

[31] D.S. Kanibolotsky, N.V. Golovataya, V.V. Lisnyak, J. Therm. Anal. Calorim. 76 (2004) 323-327.
[32] D.S. Kanibolotsky, O.A. Bieloborodova, V.V. Lisnyak, Z. Naturforsch., A: Phys. Sci. 60 (2005) 649-654.
[33] Y.V. Serdyuk, R.P. Krentsis, P.V. Gel'd, V.G. Batalin, Fiz. Tverd. Tela (Leningrad) 22 (1980) 2149-2151.
[34] Y.I. Spichkin, V.K. Pecharsky, K.A. Gschneidner, Jr., J. Appl. Phys. 89 (2001) 1738-1745.
[35] F. Holtzberg, R.J. Gambino, T.R. McGuire, J. Phys. Chem. Solids 28 (1967) 2283-2289.
[36] J. Szade, M. Neumann, J. Phys.: Condens. Matter 11 (1999) 3887-3896.
[37] S. Parviainen, Phys. Status Solidi A 60 (1980) K13-K16.
[38] J. Szade, G. Skorek, J. Magn. Magn. Mater. 196-197 (1999) 699-700.
[39] V.N. Safonov, S.M. Barmin, A.A. Sevast'yanov, P.V. Gel'd, Fiz. Tverd. Tela (Leningrad) 27 (1985) 2870-2872.
[40] A.S. Bolgar, N.P. Gorbachuk, A.V. Blinder, T.V. Egorov, A.I. Kriklya, Modern Problems in Physical Materials Science 2 (1993) 37-46.
[41] A.S. Bolgar, N.P. Gorbachuk, A.V. Blinder, K.A. Meleshevich, Modern Problems in Physical Materials Science 3 (1994) 130-138.
[42] N.I. Usenko, M.I. Ivanov, V.V. Berezutski, R.I. Polotska, J. Alloys Compd. 266 (1998) 186-190.
[43] S.P. Gordeinko, A.G. Druzheruchenko, Poroshk. Metall. (Kiev) (1996) 35-38.
[44] S.V. Meschel, O.J. Kleppa, J. Alloys Compd. 217 (1995) 235-239.
[45] S.V. Meschel, O.J. Kleppa, J. Alloys Compd. 224 (1995) 345-350.
[46] G.M. Lukashenko, R.I. Polotskaya, Poroshk. Metall. (Kiev) (1986) 70-72.
[47] G.M. Lukashenko, R.I. Polotskaya, Poroshk. Metall. (Kiev) (1992) 75-78.
[48] V.R. Sidorko, R.I. Polotsokaya, Poroshk. Metall. (Kiev) (1993) 93-95.
[49] M.V. Bulanova, A.N. Mikolenko, K.A. Meleshevich, G. Effenberg, P.A. Saltykov, Z. Metallkd. 90 (1999) 216-222.
[50] P. Schobinger-Papamantellos, M.D.B. De, K.H.J. Buschow, J. Magn. Magn. Mater. 79 (1989) 231-241.
[51] P. Schobinger-Papamantellos, T. Janssen, M.D.B. De, K.H.J. Buschow, J. Less-Common Met. 162 (1990) 197-219.
[52] S.N. Jammalamadaka, N. Mohapatra, S.D. Das, E.V. Sampathkumaran, Phys. Rev. B: Condens. Matter Mater. Phys. 79 (2009) 060403/060401-060403/060404.
[53] Y.V. Serdyuk, R.P. Krentsis, P.V. Gel'd, Fiz. Tverd. Tela (Leningrad) 23 (1981) 2716-2719.
[54] S.V. Meschel, O.J. Kleppa, J. Alloys Compd. 234 (1996) 137-142.
[55] H. Okamoto, J. Phase Equilib. 21 (2000) 500.
[56] V.N. Eremenko, K.A. Meleshevich, Y.I. Buyanov, P.S. Martsenyuk, Ukr. Khim. Zh. (Russ. Ed.) 60 (1994) 544-551.
[57] N.P. Gorbachuk, A.S. Bolgar, Powder Metall. Met. Ceram. 41 (2002) 173-176.
[58] J. Roger, T. Guizouarn, K. Hiebl, J.F. Halet, R. Guerin, J. Alloys Compd. 394 (2005) 28-34.
[59] N.P. Gorbachuk, A.S. Bolgar, V.B. Muratov, Powder Metall. Met. Ceram. 40 (2001) 183-186.
[60] S.V. Meschel, O.J. Kleppa, J. Alloys Compd. 233 (1996) 272-278.
[61] H. Okamoto, T.B. Massalski, J. Phase Equilib. 14 (1993) 316-335.
[62] V.N. Eremenko, V.E. Listovnichii, S.P. Luzan, Y.I. Buyanov, P.S. Martsenyuk, J. Alloys Compd. 219 (1995) 181-184.

[63] I. Ijjaali, G. Venturini, B. Malaman, J. Alloys Compd. 269 (1998) L6-L8.
[64] L.V. Goncharuk, V.R. Sidorko, N.P. Gorbachuk, M.V. Bulanova, Powder Metall. Met. Ceram. 50 (2011) 528-537.
[65] S.V. Meschel, O.J. Kleppa, J. Alloys Compd. 247 (1997) 52-56.
[66] L.V. Goncharuk, V.R. Sidorko, Y.I. Buyanov, Powder Metall. Met. Ceram. 48 (2009) 326-329.
[67] L.V. Goncharuk, V.R. Sidorko, Y.I. Buyanov, Powder Metall. Met. Ceram. 49 (2011) 690-694.
[68] H. Okamoto, J. Phase Equilib. 17 (1996) 370-371.
[69] S.P. Luzan, V.E. Listovnichii, Y.I. Buyanov, P.S. Martsenyuk, J. Alloys Compd. 239 (1996) 77-82.
[70] N.P. Gorbachuk, S.N. Kirienko, V.R. Sidorko, I.M. Obushenko, Ukr. Khim. Zh. (Russ. Ed.) 72 (2006) 20-24.
[71] N.P. Gorbachuk, S.N. Kirienko, V.R. Sidorko, I.M. Obushenko, High Temp. 45 (2007) 173-177.
[72] N.P. Gorbachuk, S.N. Kirienko, V.R. Sidorko, I.M. Obushenko, Powder Metall. Met. Ceram. 46 (2007) 72-76.
[73] S.V. Meschel, O.J. Kleppa, J. Chim. Phys. Phys.-Chim. Biol. 94 (1997) 928-938.
[74] V.R. Sidorko, N.P. Gorbachuk, Powder Metall. Met. Ceram. 51 (2012) 93-101.
[75] H. Okamoto, J. Phase Equilib. 18 (1997) 403.
[76] A.G. Tharp, J. Phys. Chem. 66 (1962) 758-760.
[77] I.P. Mayer, E. Banks, B. Post, J. Phys. Chem. 66 (1962) 693-696.
[78] E.I. Gladyshevskii, Vopr. Teorii i Primeneniya Redkozem. Metal., Akad. Nauk SSSR (1964) 141-143.
[79] E.I. Gladyshevskii, P.I. Kripyakevich, Zh. Strukt. Khim. 5 (1964) 853-859.
[80] E.I. Gladyshevskii, Izv. Akad. Nauk SSSR, Neorg. Mater. 1 (1965) 868-872.
[81] N.P. Gorbachuk, Powder Metall. Met. Ceram. 51 (2013) 602-607.
[82] N.P. Gorbachuk, Powder Metall. Met. Ceram. 51 (2012) 323-328.
[83] S.V. Meschel, O.J. Kleppa, J. Alloys Compd. 285 (1999) 179-184.
[84] N.P. Gorbachuk, S.N. Kirienko, V.R. Sidorko, I.M. Obushenko, Powder Metall. Met. Ceram. 51 (2012) 229-233.
[85] N.P. Gorbachuk, V.R. Sidorko, S.N. Kirienko, I.M. Obushenko, Powder Metall. Met. Ceram. 48 (2009) 449-453.
[86] L. Topor, O.J. Kleppa, J. Less-Common Met. 167 (1990) 91-99.
[87] S.V. Meschel, O.J. Kleppa, J. Alloys Compd. 245 (1996) L28-L29.
[88] C.E. Lundin, The Rare Earths, J. Wiley and Sons, Inc., New York; 1961.
[89] I. Mayer, I. Felner, J. Less-Common Metals 29 (1972) 25-31.
[90] K.A. Gschneidner Jr., Rare Earth Alloys, D. Van Nostrand Co., Inc., New York; 1961.
[91] T.W. Button, I.J. McColm, J.M. Ward, Journal of the Less Common Metals 159 (1990) 205-222.
[92] Y.O. Esin, M.G. Valishev, P.V. Gel'd, L.M. Tushkova, Russian Metallurgy (1976) 19-21.
[93] G.M. Ryss, Y.O. Esin, M.S. Petrushevskii, A.I. Stroganov, P.V. Gel'd, Russian Metallurgy (1979) 57-59.
[94] V.A. Stukalo, G.I. Batalin, N.Y. Neshchimenko, V.P. Kurach, Ukr. Khim. Zh. (Russ. Ed.) 46 (1980) 98-99.
[95] A.O. Pecharsky, V.K. Pecharsky, K.A. Gschneidner, J. Alloys Compd. 379 (2004) 127-134.

[96] V.N. Safonov, P.V. Gel'd, N.I. Sychev, G.I. Kalishevich, Zh. Fiz. Khim. 59 (1985) 2141-2144.
[97] S.V. Meschel, O.J. Kleppa, J. Alloys Compd. 274 (1998) 193-200.
[98] R.I. Polotskaya, V.R. Sidorko, Powder Metall. Met. Ceram. 36 (1997) 315-319.
[99] A.B. Gokhale, G.J. Abbaschian, Bull. Alloy Phase Diagrams 7 (1986) 485-489.
[100] J. Kim, I.-H. Jung, J. Alloys Compd. 525 (2012) 191-201.
[101] J. Kim, I.H. Jung, Can. Metall. Q. 52 (2013) 311-320.
[102] M. Zydzik, M. Smids, M.-A. Van Ende, I.-H. Jung, Calphad 46 (2014) 1-17.
[103] M.V. Bulanova, P.S. Martsenyuk, Poroshk. Metall. (Kiev) (1991) 82-85.

Appendix VI

Appendix VI

Critical evaluation and thermodynamic optimization of the Sn-RE systems: part I. Sn-RE system (RE = La, Ce, Pr, Nd and Sm)

1. Thermodynamic models

1.1. Liquid phase

The modified quasichemical model [1, 2], which accounts for short-range-ordering of nearest-neighbor atoms, was used to model the liquid solutions because it gives a more realistic thermodynamic description of the liquid phase compared to the conventional simple random-mixing Bragg Williams model [1, 2]. The modified quasichemical model was successfully applied to many liquid metallic solutions [2-4] and ionic solutions [5, 6] exhibiting strong short-range-ordering behavior.

Recently, the energy of nearest-neighbor pair formation in the modified quasichemical model was expanded as a polynomial in the pair fractions [1, 2] instead of the component fractions [5, 7]. In addition, coordination numbers are now allowed to vary with composition. These modifications provide greater flexibility in reproducing the binary experimental data and in combining optimized binary liquid parameters into a large database for multicomponent solutions [1]. A short description of the model is given below; details can be found in previous studies [1, 2].

In the case of a binary A-B liquid solution, the atoms A and B are distributed over the sites of a quasi-lattice in liquid solution. The following pair exchange reaction can be considered:

$$(A-A)+(B-B)=2(A-B) \qquad (1)$$

where (A-B) represents a first-nearest-neighbor pair of A and B. The non-configurational Gibbs energy change for the formation of two moles of (A-B) pairs according to reaction (1) is Δg_{AB}. Then the Gibbs energy of the solution is given by:

$$G = (n_A G_A^{\circ} + n_B G_B^{\circ}) - T\Delta S^{config} + n_{AB}(\Delta g_{AB}/2) \tag{2}$$

where G_A° and G_B° are the molar Gibbs energies of the pure components A and B, n_A and n_B are the numbers of moles of A and B atoms, and n_{AB} is the number of moles of (A-B) pairs. ΔS^{config} is the configurational entropy of mixing given by a random distribution of the (A-A), (B-B) and (A-B) pairs in the one-dimensional Ising approximation:

$$\begin{aligned}\Delta S^{config} &= -R(n_A \ln X_A + n_B \ln X_B) \\ &\quad - R[n_{AA} \ln(X_{AA}/Y_A^2) + n_{BB} \ln(X_{BB}/Y_B^2) \\ &\quad + n_{AB} \ln(X_{AB}/2Y_A Y_B)]\end{aligned} \tag{3}$$

where n_{AA}, n_{BB} and n_{AB} are the numbers of moles of each kind of pairs, and the pair fraction (X_{AA}, X_{BB} and X_{AB}) and coordination equivalent fraction (Y_A and Y_B) can be calculated as:

$$X_{AA} = n_{AA}/(n_{AA} + n_{BB} + n_{AB}) \tag{4}$$

$$X_{BB} = n_{BB}/(n_{AA} + n_{BB} + n_{AB}) \tag{5}$$

$$X_{AB} = n_{AB}/(n_{AA} + n_{BB} + n_{AB}) \tag{6}$$

$$Y_A = X_{AA} + X_{AB}/2 \tag{7}$$

$$Y_B = X_{BB} + X_{AB}/2 \tag{8}$$

The Δg_{AB} is the model parameter to reproduce the Gibbs energy of liquid phase of the binary A-B system, which is expanded as a polynomial in terms of the pair fractions, as follows:

$$\Delta g_{AB} = \Delta g^{\circ}_{AB} + \sum_{i\geq 1} g^{i0}_{AB}(X_{AA})^i + \sum_{j\geq 1} g^{0j}_{AB}(X_{BB})^j \quad (9)$$

where Δg°_{AB}, g^{i0}_{AB} and g^{0j}_{AB} are the adjustable model parameters which can be functions of temperature.

In the modified quasichemical model, the coordination numbers of A and B, Z_A and Z_B, can be varied with composition to reproduce the short-range-ordering as follows:

$$\frac{1}{Z_A} = \frac{1}{Z^A_{AA}}\left(\frac{2n_{AA}}{2n_{AA}+n_{AB}}\right) + \frac{1}{Z^A_{AB}}\left(\frac{n_{AB}}{2n_{AA}+n_{AB}}\right) \quad (10)$$

$$\frac{1}{Z_B} = \frac{1}{Z^B_{BB}}\left(\frac{2n_{BB}}{2n_{BB}+n_{AB}}\right) + \frac{1}{Z^B_{BA}}\left(\frac{n_{AB}}{2n_{BB}+n_{AB}}\right) \quad (11)$$

where Z^A_{AA} is the value of Z_A when all nearest neighbors of an A atom are A atoms, and Z^A_{AB} is the value of Z_A when all nearest neighbors are B atoms. Z^B_{BB} and Z^B_{BA} are defined in an analogous manner. In the present study, Z^i_{ii} for all elements (i = Sn and RE) are set to be 6. As the minimum enthalpies of liquid Sn-RE solutions were found at almost 0.5 mole fraction of RE, Z^{Sn}_{SnRE} and Z^{RE}_{SnRE} are set to be all 6 to reproduce such minimum enthalpies.

1.2. Solid solutions

The solid solution phases like bcc and fcc solutions were described by the compound energy formalism [8] with a one-sublattice approach (Sn, RE) for substitutional site. The molar Gibbs energy of the solid solution can be expressed as:

$$G = (y_{Sn} G^{\circ}_{Sn} + y_{RE} G^{\circ}_{RE}) + RT(y_{Sn} \ln y_{Sn} + y_{RE} \ln y_{RE}) + {}^{a}L_{Sn,RE} y_{Sn} y_{RE} (y_{RE} - y_{Sn})^{a} \quad (12)$$

where y_{Sn} and y_{RE} are the site fractions of Sn and RE elements in the sublattice, and R and T are the gas constant and temperature in Kelvin. G°_{Sn} and G°_{RE} are the molar Gibbs energies of solid phases of Sn and RE in the respective standard state of solid solution. The binary interaction parameters between Sn and RE in the sublattice, ${}^{a}L_{Sn,RE}$ where $a \geq 0$, are adjustable model parameters.

1.3. Stoichiometric compounds and elements

The Gibbs energies of all pure elements were taken from the SGTE database version 5.0 [9]. The Gibbs energies of the stoichiometric intermetallic compounds were optimized based on available experimental data using the standard Gibbs energy expression based on heat capacity, enthalpy and entropy of formation at 298 K. When the heat capacities of stoichiometric compounds were not available, they were typically estimated using the Neumann-Kopp (NK) rule [10]. However, the heat capacity of solid Sn was modified from its original value [11], because, as seen in Fig. 1, there is a sudden change in the shape of the heat capacity of Sn(s) above its melting temperature (505.08 K), which has no physical meaning. As this function is used to estimate the heat capacity of the RE stannides, this 'anomaly' is transferred into the heat capacity functions of the compounds. For example, the estimated heat capacities of $LaSn_3$ and $CeSn_3$ based on the original heat capacity of Sn(s) is shown as dotted line in Fig. 1. Clearly, the heat capacities of the compounds exhibit an abrupt change of slope around 500 K, which is entirely artificial. Therefore,

the modified heat capacity of Sn from 298 K to 2000 K was created to reproduce the experimental heat capacities data of $LaSn_3$ [12] using the NK rule as shown in Fig. 1. When the modified heat capacity of Sn is used to estimate the heat capacity of $CeSn_3$ using the NK rule, the estimated heat capacity of $CeSn_3$ is in good agreement with the experimental data [12] as shown in Fig. 1. As the experimental heat capacities of the rest of the RE stannides over 298 K were not available, therefore, the modified heat capacity of Sn(s) was used to estimate all the RE stannides. It should be noted that the modified heat capacity of Sn(s) was only used to estimate the heat capacity function of the compounds. The original heat capacity function of Sn was employed to calculate the phase diagram and other thermodynamic properties in order to maintain consistency with the existing FactSage database.

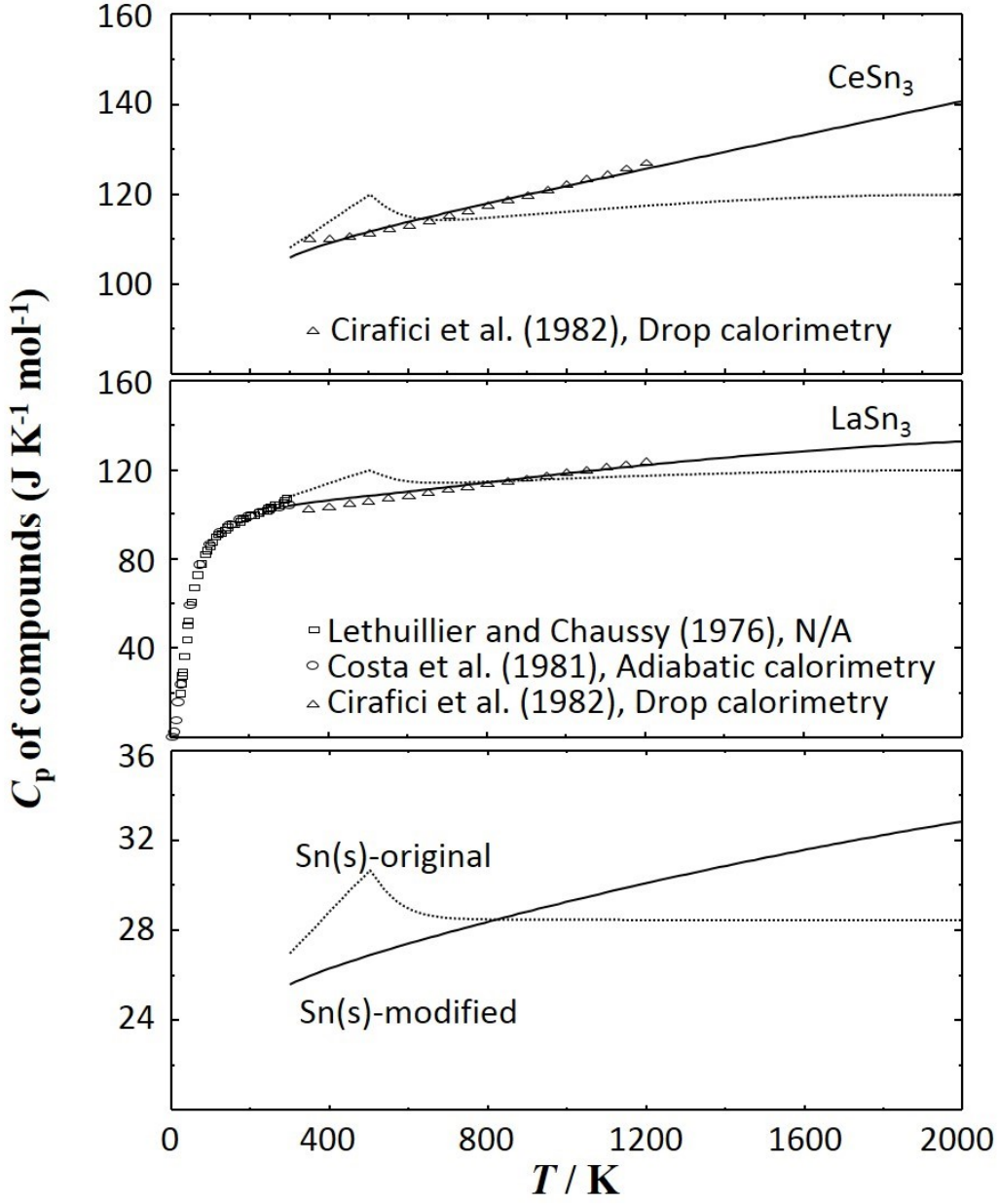


Fig. 1. Comparison between the original and modified heat capacities of pure Sn, $LaSn_3$ and $CeSn_3$. The heat capacities of $LaSn_3$ and $CeSn_3$ were obtained by the NK approximation.

2. Critical evaluation and thermodynamic optimization

2.1. The Sn-La system

Available experimental data for the Sn-La phase diagram are presented in Fig. 2. The first phase diagram investigation was performed by Canneri [13] on the basis of the thermal analysis. Three congruently melting intermediate compounds were found with four eutectic reactions: La_2Sn, La_2Sn_3, and $LaSn_2$. However, their results including the stoichiometry of the compounds and the reaction temperatures turned out to be unreliable by subsequent studies. That was mainly due to the high impurity of the starting materials (not specified), i.e., the melting temperature of La was reported as 812 ^oC much lower than the melting temperature of La: 920 ^oC, even lower than the temperature of polymorphic transition from bcc-La to fcc-La: 861 ^oC in Factsage database. Later, the existence of the $LaSn_3$ phase with the $AuCu_3$ type crystal structure was reported by Rossi [14] using powder method of X-ray diffraction. The lattice parameters of $LaSn_3$ was also reported by Harris and Raynor [15]. Vogel and Heumann [16] investigated the system in the composition range of about 0.1 to 0.5 mole fraction of La using thermal analysis. Two congruently melting compounds, La_2Sn_3 (1185 ^oC) and $LaSn_3$ (1135 ^oC) were reported with two eutectic reaction: $L \leftrightarrow La_2Sn + La_2Sn_3$ (~0.47 mole fraction of La, 1142 ^oC), $L \leftrightarrow La_2Sn_3 + LaSn_3$ (~0.35 mole fraction of La, 1108 ^oC). The $LaSn_2$ phase which was reported by Canneri [13] was withdrawn in the proposed phase diagram. The experimental data reported by Vogel and Heumann [16] are presented in Fig. 2. Again later, the crystallographic study of La_5Sn_3 was performed by Jeitschko and Parthe [17] using X-ray powder diffraction method. The $D8_8$ structure of the La_5Sn_3 was determined and the existence of a certain range of homogeneity possibly was suggested based on the similarity with the La_5Pb_3, Er_5Sn_3 and Gd_5Pb_3 in which the lattice constants of them varied with a small composition variation, but it was not specified for the La_5Sn_3, and the homogeneity range seems to be insignificant. Gambino et al. [18] re-examined the phase equilibria and reported the five intermediate compounds, La_5Sn_3, La_5Sn_4, LaSn, La_3Sn_5, and $LaSn_3$, which were different from the previous findings [13, 16] except for the $LaSn_3$. From the metallographic evidences, the La_5Sn_3, La_5Sn_4, La_3Sn_5, and $LaSn_3$ were proposed as congruently melting compounds (the melting temperatures of compounds were not provided), and the LaSn was peritectically formed because

the single phase LaSn was only obtained after a solid state annealing at 1200 ºC or less. Although the purity of initial materials (99.9% La and >99.999% Sn) and the alloy preparation process were stated, the method of phase equilibria analysis was not stated and the shape of phase diagram was not presented. The melting temperature of $LaSn_3$, 1138 ºC, was also determined by Palenzona [19] in the measurement of heat of formation of the $LaSn_3$ using dynamic differential calorimetry. The intermetallic compound, La_5Sn_4 (Sm_5Ge_4 type) was studied with lattice parameters by Fornasini and Merlo [20] using X-ray powder method. In a similar method, Franceschi [21] reported the dimorphism of La_5Sn_3 phase: α-La_5Sn_3 (W_5Si_3 type, low temperature form observed from slow cooled alloys or annealed alloys at 400ºC) and β-La_5Sn_3 (Mn_5Si_3 type, high temperature form observed from rapid cooled alloys). More recently, Borzone et al. [22] reinvestigated the system using X-ray and metallographic analyses with the alloys prepared by melting in closed Ta crucibles from high purity materials, 99.9% La and >99.99% Sn. The existence of α-La_5Sn_3 (W_5Si_3 type, low temperature form), β-La_5Sn_3 (Mn_5Si_3 type, high temperature form), La_5Sn_4 (Sm_5Ge_4 type), and $LaSn_3$ ($AuCu_3$ type) was confirmed with their respective lattice parameters. Although the existence of La_3Sn, La_3Sn_5, and La_2Sn_5 was reported in their study, the phases were not clearly identified. Kulagina et al. [23] investigated the Sn-rich region of the phase diagram (up to 0.25 mole fraction of La) using thermal analysis and microscopic examination with the alloys prepared in sealed quartz vessels. The melting temperature of $LaSn_3$ was determined to be 1132 ± 4 ºC which was close to the previous works [16, 19]. The temperature dependence of La solubility in liquid Sn was expressed by the equation, $\log(\text{at.\% La}) = 1.864 - 3648\ T^{-1}$. The experimental data points suggested by Kulagina et al. [23] are presented in Fig. 2. Later, the Sn-La phase diagram was thoroughly reinvestigated by Eremenko et al. [24] using microscopic, X-ray, and differential thermal analysis (DTA) methods. The alloys were prepared by arc melting under purified argon atmosphere from high purity materials, >99.84% La and 99.9995% Sn. The samples for DTA were placed in Ta crucible with alumina holder and the heating and cooling rate were about 30 degrees min^{-1}. However the melting temperature of pure La was determined as 910 ºC, 10 ºC lower than the known value (920 ºC) from the FactSage, and the allotropic transition temperature of bcc- and fcc-La was determined as 835 ºC, 26 ºC lower than the known value (862 ºC) possibly due to the impurities or oxidation of La. Three congruently melting compounds, La_5Sn_4 (1575 ºC), La_3Sn_5 (1240 ºC), and $LaSn_3$ (1155 ºC), and four compounds which melted peritectically, La_5Sn_3 (1500 ºC), LaSn (1295 ºC), $La_{11}Sn_{10}$ (1445 ºC), and La_2Sn_3 (1179 ºC) were found, as well as three

eutectic reactions, L ↔ La + La_5Sn_3 (0.885 mole fraction of La, 747 ± 3 ºC), L ↔ LaSn + La_3Sn_5 (0.435 mole fraction of La, 1200 ± 2 ºC), and L ↔ La_3Sn_5 + $LaSn_3$ (0.295 mole fraction of La, 1113 ± 3 ºC). Although the authors could not confirm the crystal structure of $La_{11}Sn_{10}$ and La_2Sn_3 using X-ray analysis, it was concluded that the thermal effect found near the compositions of $La_{11}Sn_{10}$ and La_2Sn_3, respectively, came from the peritectic reaction of the $La_{11}Sn_{10}$ and the peritectoid reaction of the La_2Sn_3. However, the α-La_5Sn_3 to β-La_5Sn_3 phase transformation was not detected in their thermal analysis. From the facts that the Sn-rich alloys started to melt at temperatures 2-3 ºC higher than the pure Sn, it was concluded that the peritectic type of reaction of Sn (L + $LaSn_3$ ↔ Sn). However, it is thermodynamically improbable and it requires further investigation. It was also reported that none of the intermetallic compounds contained large areas of homogeneity, and the mutual solubility of the components in the solid state was very small. Recently, the crystal structure of La_2Sn_3 with lattice parameters was identified by Fornasini et al. [25] as a triclinic structure by means of X-ray powder diffraction method. In the study of Larchev and Popova [26], it was found that the La_3Sn phase which was reported in the work of Borzone et al. [22] formed at a temperature higher than 1000 ºC and at a pressure of 7.5×10^9 Pa. Therefore, the La_3Sn phase can be considered as unstable phase at the atmospheric pressure and at a lower temperature. In later crystallographic study by Weitzer et al. [27], the existence of La_2Sn_5 (Ce_2Sn_5 type), La_3Sn_7 (Ce_3Sn_7 type), and $LaSn_2$ ($NdSn_2$ type) compounds was reported with their respective lattice parameters which were not found in the work of Eremenko et al. [24]. However, those compounds were also not found in the experimental isothermal phase diagram investigation of the ternary systems containing La and Sn [28-32].

The thermodynamic properties of the Sn-La liquid were reported by several research groups. Available experimental data as regards the integral and partial enthalpy of mixing of Sn-La liquid are presented in Fig. 3(a) to (c). The heat of solution of solid (fcc) La (>99.96%) in liquid Sn (99.999%) was measured by Pratt and Morris [33] using a liquid-metal solution calorimeter. Although a dhcp structure of La is the room-temperature modification, the fcc phase was dominant in the samples due to the sluggishness of the fcc to dhcp transformation. From the reported data of the partial heat of solution of La in liquid Sn at about 632 K referred to the fcc-La, the partial enthalpy of mixing of La was calculated in the present study by considering the heat effect between

fcc- and liquid-La which was taken from the FactSage database. Similarly, Guadagno et al. [34] measured the partial heat of solution of La (99.9%) in liquid Sn (99.9%) at 725, 750 and 775 K using a liquid-metal solution calorimeter. The reference state of solid La was not given, but it was assumed the dhcp-La to obtain the partial enthalpy of mixing of La in the present study. Later, Esin et al. [35] determined the integral and partial enthalpies of mixing of liquid Sn-La solution using a high-temperature calorimeter with an isothermal jacket. Measurements were performed up to 0.35 mole fraction of La using starting materials (99.9% Sn and 99.8% La) at 1890 K in corundum crucibles under helium atmosphere. Later again, the heat of dissolution of La into liquid Sn was measured by Castanet [36] using a direct reaction calorimeter with high purity materials (>99.9% La and Sn). The partial enthalpy of dissolution of La (bcc) in liquid Sn at 1174 K were reported up to 0.026 mole fraction of La. Based on the reported data, in the present study, the partial enthalpy of mixing of La was calculated by taking the heat effect from bcc- to liquid-La. Moreover, the integral enthalpy of mixing was calculated from the partial enthalpy values as shown in Fig. 3(a). In another studies, Colinet et al. reported the partial enthalpy of mixing of La at infinite dilution of La at 995 K [37], 930 K [38], and 1129 K [38] from the dissolution measurement using an isoperibol calorimeter (<1000 K) and a Calvet-type twin calorimeter (<1200 K) under vacuum (10^{-4} Pa) with high purity materials (99.999% Sn and 99.99% La). Sommer et al. [39] determined the integral enthalpy of mixing of La-rich solution above 0.84 mole fraction of La at 1128 and 1283 K using a high-temperature solution calorimeter with high purity materials (99.96% Sn and 99.9% La). Correspondingly, the partial enthalpies of Sn at infinite dilution of Sn were also reported as shown in Fig. 3(b). Additionally, the partial enthalpies at infinite dilution of La in liquid Sn were measured in the temperature range 1095-1478 K. The partial enthalpies of La were reported at 6 different temperatures and La-dilute compositions up to 0.1 mole fraction of La. In the present study, the reported values were used to obtain the integral enthalpy of mixing as shown in Fig. 3(a).

Thermodynamic properties of the intermetallic compounds were investigated by several research groups. Experimental data regarding the heat capacity (C_p) of $LaSn_3$ are shown in Fig. 1. Lethuillier and Chaussy [40] reported the low temperature C_p of $LaSn_3$ between 20 and 300 K without the experimental method. Costa et al. [41] determined the low temperature C_p of $LaSn_3$ using an

adiabatic calorimeter in the temperature range of 20 to 300 K. A small second order anomaly between 220 and 255 K which may correspond to lattice order-disorder was reported in both thermal expansion and heat capacity measurements. The high temperature C_p of $LaSn_3$ between 400 and 1100 K was obtained by Cirafici et al. [12] in the heat content measurements. The heat contents of $LaSn_3$ were measured over the 400-1100 K by means of a conventional drop calorimeter. The accuracy of the experimental results was estimated to be about 1-2% from a series of measurements on a sample of high purity Cu. The reported heat contents are shown in Fig. 4. Based on the heat content data, the heat capacities were reported by least squares method with a polynomial function of temperature as shown in Fig. 1. In the present study, the standard entropy of formation (S^{o}_{298}) was calculated to be 192.76 and 195.67 J K^{-1} mol^{-1} from the experimental C_p of Lethuillier and Chaussy [40] and Costa et al. [41], respectively. The experimental S^{o}_{298} values are presented as ΔS^{o}_{298} in Fig. 5. The experimental enthalpy of formation at about 298 K (ΔH^{o}_{298}) are presented in Fig. 6. Pool and Guadagno [42] calorimetrically determined the enthalpy of formation of $LaSn_3$ at 300 K. In another study, Guadagno et al. [34] determined the enthalpy of formation of $LaSn_3$ and La_2Sn_3 at 273 K using a solution calorimeter. Later, the ΔH^{o}_{298} of $LaSn_3$ was obtained by Palenzona [19] using a dynamic differential calorimetry method with a conventional DTA apparatus. The enthalpy and entropy of fusion for $LaSn_3$ were also reported to be about 48.14 kJ mol^{-1} and 34.11 J K^{-1} mol^{-1}, respectively. The enthalpy of formation of La_5Sn_3 at 300 K was reported by Borsese et al. [43] using a differential direct isoperibol calorimeter. The reported value was confirmed in the work by Borzone et al. [22], which was published later. In the work [22], the formation heats were measured in a large composition range using a direct method with an isoperibol calorimeter. The enthalpy of formation at 300 K for various composition alloys were reported. The ΔH^{o}_{298} of $LaSn_3$ was also determined by Colinet et al. [38] using a method of solution calorimetry. The experimental Gibbs energy of formation at different temperatures (ΔG^{o}) are presented in Fig. 7. Kober et al. [44] determined the Gibbs energy of formation at 0.25, 0.4 and 0.67 mole fraction of La by considering the formation of $LaSn_3$, La_2Sn_3 and La_2Sn from emf measurements at 1000 K. Similarly, Lukashenko and Polotskaya [45] determined the Gibbs energy of formation of $LaSn_3$ at 773 K based on the elemental references of La(fcc)-Sn(l) and La(fcc)-Sn(s). Matigorova and Bayanov [46] performed the emf measurements for alloys in the

composition range between 0.0049 and 0.112 mole fraction of La at 773-973 K. The activity coefficients of La in liquid at 773, 873 and 973 K at different compositions were reported (including one composition data at 673 K). Based on the reported activity coefficients of La, the activities of La at different temperatures and compositions are presented in Fig. 8. In addition, the Gibbs energy of formation of $LaSn_3$ was reported in a function of temperature, $-262.337 + 3.43 \times 10^{-2}\ T \pm 0.42$ kJ mol^{-1}, which is in good agreement with the other emf measurements [44, 45].

An extensive literature review of the Sn-La system was performed by Palenzona and Cirafici in 1992 [47]. The experimental investigations regarding the phase diagram and thermodynamic properties including crystallographic studies were widely reviewed. The thermodynamic optimization of the system was previously performed by Huang et al. [48] and Idbenali et al. [49]. The calculated thermodynamic properties from the previous optimizations are presented in Figs. 3, 5-7. In the optimization of Huang et al. [48], the excess Gibbs energy of liquid phase was expressed in the Redlich-Kister random mixing model mostly based on the experimental data of Sommer et al. [39]. However, large positive temperature-dependent parameters were applied to compensate the considerably more negative enthalpy of mixing, in particular at La-rich region, in order to reproduce the phase diagram. This resulted in an undesirable inverse miscibility gap at the temperature above 2500 ºC and at the composition about 0.75 mole fraction of La in the phase diagram. Later, Idbenali et al. [49] applied the associate solution model with a 'La_1Sn_1' associated complex to describe the liquid phase. However, their calculated enthalpy of mixing was more positive than the experimental data, in particular at both the Sn- and La-rich compositions (Fig. 3(a)). Moreover, the concave down shape of integral enthalpy of mixing induced the negative slope of partial enthalpy of mixing of La, which is inconsistent with experimental findings as shown in Fig. 3(c). The heat capacities of intermetallic compounds in both optimizations were estimated by NK approximation without the modification of heat capacity of Sn, which resulted in the abnormal kink as we explained above. Furthermore, the ΔS^{o}_{298} of $LaSn_3$ which obtained from the experimental heat capacities was not taken into account in both optimizations (Fig. 5).

The optimized phase diagram of the Sn-La system in the present study is shown in Fig. 2. In the optimization, the experimental values of Eremenko et al. [24] were preferred in the phase diagram

evaluation except for the melting temperature of $LaSn_3$ and the congruent melting behavior of La_3Sn_5. The melting temperature of $LaSn_3$ was taken from the experimental data of Palenzona [19] which agreed with Kulagina et al. [23]. If the higher melting temperature of $LaSn_3$ (1155 ^oC) from Eremenko et al. [24] was reproduced, the eutectic temperature between $LaSn_3$ and La_3Sn_5 would become higher than the present one, which is undesirable, because the liquidus slope was determined by the thermodynamic properties, i.e., the enthalpy and entropy of liquid and $LaSn_3$. In the same vein, the melting behavior of La_3Sn_5 was determined to be incongruent. The liquidus slope should be much steeper near 0.4 mole fraction of La to reproduce the congruent melting of La_3Sn_5. Although the experimental liquidus from Eremenko et al. [24] show steeper slope near 0.4 mole fraction of La, the slope is only localized at a short composition range. This is very difficult to be described because it requires a drastic change of Gibbs energy of liquid at local composition range. A similar discussion was made deeply for the Si-RE systems in our previous study [50]. On the contrary, in the two previous optimizations for the Sn-La systems [48, 49], the melting temperature of $LaSn_3$ and the congruent melting of La_3Sn_5 were reproduced closely to the experimental data of Eremenko et al. [24]. However, in order to do so, the more negative enthalpy of mixing of liquid was applied in the middle composition range in both the optimizations. For the optimization of Huang et al. [48], the more negative enthalpy of mixing at Sn-rich liquid resulted in much lower liquidus at Sn-rich composition (steep liquidus slope) in the phase diagram compared to the experimental data [16, 23, 24]. The other side (La-rich) of phase diagram have a problem as well, which discussed above (inversed miscibility gap at high temperature due to the large temperature dependent parameters). For the optimization of Idbenali et al. [49] applied the associate solution model, their enthalpy of mixing at Sn- and La-rich liquid is less negative than the data of Huang et al. [48] (Fig. 3(a)). However, in order to have a more negative enthalpy of mixing at the middle composition range (for steep liquidus slope at the middle composition range) the concave down enthalpy shape which affected the negative slope of partial enthalpies at dilute solution of both La and Sn was obtained (Fig. 3(c)). The La solubility in liquid was determined only with enthalpic effect on the excess Gibbs energy based on the experimental data presented in Fig. 3(c). The calculated liquidus at Sn-rich phase diagram agrees well with the experimental findings as seen in Fig. 2. The solid solubilities of Sn in bcc-La and fcc-La were assumed to be negligible because the allotropic transition temperature of bcc- to fcc-La did not change with the addition of Sn (0.02 mole fraction) [24]. It should be noted that even though the intermediate

phases, La_2Sn_5, La_3Sn_7, and $LaSn_2$ were not modeled in the present study, the existence of La_2Sn_5, La_3Sn_7, and $LaSn_2$, which reported by Weitzer et al. [27], should be carefully considered by further experimental investigations because the Ce_2Sn_5 and Ce_3Sn_7 exist in the Sn-Ce phase diagram. In many cases, the binary La-M and the Ce-M systems show consistent intermetallic compounds.

The calculated thermodynamic properties with the optimized thermodynamic parameters are shown in Fig. 3-8. There are discrepancies in the experimental enthalpy of mixing data as seen in Fig. 3. First of all, the data of Sommer et al. [39] in the La-rich liquid was too negative to reproduce the phase diagram as discussed above. In the middle composition range, there is no available experimental data except the data of Esin et al. [35]. However, the data of Esin et al. [35] deviate positively from other experimental data, in particular, up to 0.1 mole fraction of La. Previously, Sommer et al. [39] claimed there was a certain dependency on the temperature in the enthalpy of mixing. They showed that the temperature dependency of the enthalpy found in the experimental studies [33-37, 39] was well described with the associate solution model. However, we believe that the enthalpy of mixing modeled by Sommer et al. [39] cannot be used to describe the experimental phase diagram studies. It was revealed from the work of Idbenali et al. [49] with the associate solution model. Although they showed the temperature dependency of the enthalpy of mixing, the values were not in good agreement with the experimental data. We also tried to describe the temperature dependency of the enthalpy of mixing using the modified quasichemical model, but it was implausible when it has to be considered with the phase diagram. This may come from the limitation of solution model, but it is still unclear. Therefore, instead of considering such a drastic temperature dependency, we concentrated the temperature range that the most experimental data of the partial enthalpy of La in La-dilute solution show the values between about -160 and -180 kJ mol^{-1} with various temperature (including 1174 K [36], 1227-1472 K [39]). The temperature independent parameters (i.e., enthalpy) of the excess Gibbs energy of liquid were determined based on those experimental data [36, 39]. In this way, the experimental phase diagram studies were well reproduced with small temperature dependent parameters (i.e., entropy). The calculated heat content, $H_T - H_{298}$, of $LaSn_3$ based on the estimated heat capacities of $LaSn_3$ are in good agreement with the experimental data [12] as shown in Fig. 4. However, the calculated enthalpy of fusion of $LaSn_3$ (137 kJ mol^{-1}) is higher than the reported value, 48 kJ mol^{-1}, from the

DTA measurement [19]. Since the heat capacity of Sn(s) and the enthalpy of liquid were determined, the reported heat of fusion could not be reproduced in the present study. The calculated ΔS^{o}_{298} and ΔH^{o}_{298} of compounds are in good agreement with experimental values as depicted in Fig. 5 and 6. They are also compared with the two previous optimizations. The experimental ΔS^{o}_{298} of Costa et al. [41] was used in the present optimization because their heat capacities correspond more closely to the high temperature heat capacities [12]. The calculated Gibbs energy of formation of compounds are compared with the experimental data [44, 45] and the previous optimizations [48, 49] in Fig. 7. The present optimization is consistent with the experimental data except for the value at X_{La} = 0.67 which referred to the unstable La_2Sn phase. The calculated activities of La in liquid at the temperature range between 673 and 973 K are in good agreement with the experimental data as shown in Fig. 8. The optimized thermodynamic parameters are listed in Table 1 and the calculated invariant reactions with the experimental data are tabulated in Table 2.

Table 1. Optimized model parameters for the Sn-La system.

Phase	Thermodynamic parameters
Liquid	Coordination Numbers
	i j Z_{ij}^{i} Z_{ij}^{j}
	Sn La 6 6
	Δg_{SnLa} / (J mol^{-1}) = (-41840.0 – 5.4392 T/K) – 15480.8 X_{SnSn}
	– 1673.6 X_{SnSn}^{2} + (-29288.0 + 7.5312 T/K) X_{LaLa} + 11715.2 X_{LaLa}^{2}
$LaSn_3$	ΔH_{298}^{o} = -254200.0 J mol^{-1}, S_{298}^{o} = 195.673 J K^{-1} mol^{-1}
	C_p / (J K^{-1} mol^{-1}) = 1 × C_p / (J K^{-1} mol^{-1}) (La, dhcp)
	+ 3 × modified C_p / (J K^{-1} mol^{-1}) (Sn, bct-A5)*
La_3Sn_5	ΔH_{298}^{o} = -640000.0 J mol^{-1}, S_{298}^{o} = 379.5 J K^{-1} mol^{-1}
	C_p / (J K^{-1} mol^{-1}) = 3 × C_p / (J K^{-1} mol^{-1}) (La, dhcp)
	+ 5 × modified C_p / (J K^{-1} mol^{-1}) (Sn, bct-A5)*
La_2Sn_3	ΔH_{298}^{o} = -415030.0 J mol^{-1}, S_{298}^{o} = 233.68 J K^{-1} mol^{-1}
	C_p / (J K^{-1} mol^{-1}) = 2 × C_p / (J K^{-1} mol^{-1}) (La, dhcp)
	+ 3 × modified C_p / (J K^{-1} mol^{-1}) (Sn, bct-A5)*
LaSn	ΔH_{298}^{o} = -180000.0 J mol^{-1}, S_{298}^{o} = 94.8 J K^{-1} mol^{-1}
	C_p / (J K^{-1} mol^{-1}) = 1 × C_p / (J K^{-1} mol^{-1}) (La, dhcp)
	+ 1 × modified C_p / (J K^{-1} mol^{-1}) (Sn, bct-A5)*
$La_{11}Sn_{10}$	ΔH_{298}^{o} = -1870000.0 J mol^{-1}, S_{298}^{o} = 1027.0 J K^{-1} mol^{-1}
	C_p / (J K^{-1} mol^{-1}) = 11 × C_p / (J K^{-1} mol^{-1}) (La, dhcp)
	+ 10 × modified C_p / (J K^{-1} mol^{-1}) (Sn, bct-A5)*
La_5Sn_4	ΔH_{298}^{o} = -778000.0 J mol^{-1}, S_{298}^{o} = 457.0 J K^{-1} mol^{-1}
	C_p / (J K^{-1} mol^{-1}) = 5 × C_p / (J K^{-1} mol^{-1}) (La, dhcp)
	+ 4 × modified C_p / (J K^{-1} mol^{-1}) (Sn, bct-A5)*

La_5Sn_3 ΔH^{o}_{298} = -580000.0 J mol^{-1}, S^{o}_{298} = 441.0 J K^{-1} mol^{-1}

C_p / (J K^{-1} mol^{-1}) = 5 × C_p / (J K^{-1} mol^{-1}) (La, dhcp)
+ 3 × modified C_p / (J K^{-1} mol^{-1}) (Sn, bct-A5)*

*modified C_p / (J K^{-1} mol^{-1}) (Sn, bct-A5) = 24.477 + 5.472E-2 T/K – 40640.0 (T/K)$^{-2}$ – 6.469E-7 (T/K)^2

Table 2. Calculated invariant reactions and experimental data in the Sn-La system.

Type	Reaction	t (°C)	Reference
Eutectic	$L_{(X_{La}=<1E-5)} \rightarrow Sn_{(bct\text{-}A5,\ X_{La}=0)} + LaSn_3$	231.9	This work
	$L_{(X_{La}=*)} \rightarrow Sn_{(bct\text{-}A5,\ X_{La}=0)} + LaSn_3$	~220.0	[23]
Peritectic	$L_{(X_{La}=*)} + LaSn_3 \rightarrow Sn_{(bct\text{-}A5,\ X_{La}=0)}$	235±2	[24]
Congruent	$L_{(X_{La}=0.25)} \leftrightarrow LaSn_3$	1138.3	This work
	$L_{(X_{La}=0.25)} \leftrightarrow LaSn_3$	1135.0	[16]
	$L_{(X_{La}=0.25)} \leftrightarrow LaSn_3$	1132±4	[23]
	$L_{(X_{La}=0.25)} \leftrightarrow LaSn_3$	1155.0	[24]
	T_m of $LaSn_3$	1138.0	[19]
Eutectic	$L_{(X_{La}=0.284)} \rightarrow LaSn_3 + La_3Sn_5$	1128.1	This work
	$L_{(X_{La}=\sim0.315)} \rightarrow LaSn_3 + La_2Sn_3$	1108.0	[16]
	$L_{(X_{La}=0.295)} \rightarrow LaSn_3 + La_2Sn_3$	1113 ± 3	[24]
Peritectic	$L_{(X_{La}=0.359)} + LaSn \rightarrow La_3Sn_5$	1199.5	This work
Congruent	$L_{(X_{La}=0.375)} \leftrightarrow La_3Sn_5$	1240.0	[24]
	$L_{(X_{La}=0.4)} \leftrightarrow La_2Sn_3$	~1184.0	[16]
Eutectic	$L_{(X_{La}=\sim0.431)} \rightarrow La_2Sn_3 + La_2Sn$	1142.0	[16]
	$L_{(X_{La}=\sim0.435)} \rightarrow La_3Sn_5 + LaSn$	1200 ± 2	[24]
Peritectoid	$La_3Sn_5 + LaSn \rightarrow La_2Sn_3$	1176.4	This work
	$La_3Sn_5 + LaSn \rightarrow La_2Sn_3$	1179 ± 7	[24]
Peritectic	$L_{(X_{La}=0.397)} + La_{11}Sn_{10} \rightarrow LaSn$	1294.9	This work
	$L_{(X_{La}=\sim0.436)} + La_{11}Sn_{10} \rightarrow LaSn$	1295.0	[24]

Peritectic	$L_{(X_{La}=0.462)} + La_5Sn_4 \rightarrow La_{11}Sn_{10}$	1447.3	This work
	$L_{(X_{La}=\sim0.463)} + La_5Sn_4 \rightarrow La_{11}Sn_{10}$	1445.0	[24]
Congruent	$L_{(X_{La}=0.556)} \leftrightarrow La_5Sn_4$	1578.3	This work
	$L_{(X_{La}=0.556)} \leftrightarrow La_5Sn_4$	1575.0	[24]
Peritectic	$La_5Sn_4 + L_{(X_{La}=0.632)} \rightarrow La_5Sn_3$	1495.3	This work
	$La_5Sn_4 + L_{(X_{La}=\sim0.649)} \rightarrow La_5Sn_3$	1500.0	[24]
Eutectic	$L_{(X_{La}=0.908)} \rightarrow La_5Sn_3 + La_{(fcc\text{-}A1,\ X_{La}=1)}$	750.9	This work
	$L_{(X_{La}=0.885)} \rightarrow La_5Sn_3 + La_{(fcc\text{-}A1,\ X_{La}=1)}$	747 ± 3	[24]

* The exact compositions are not specified in the reference.

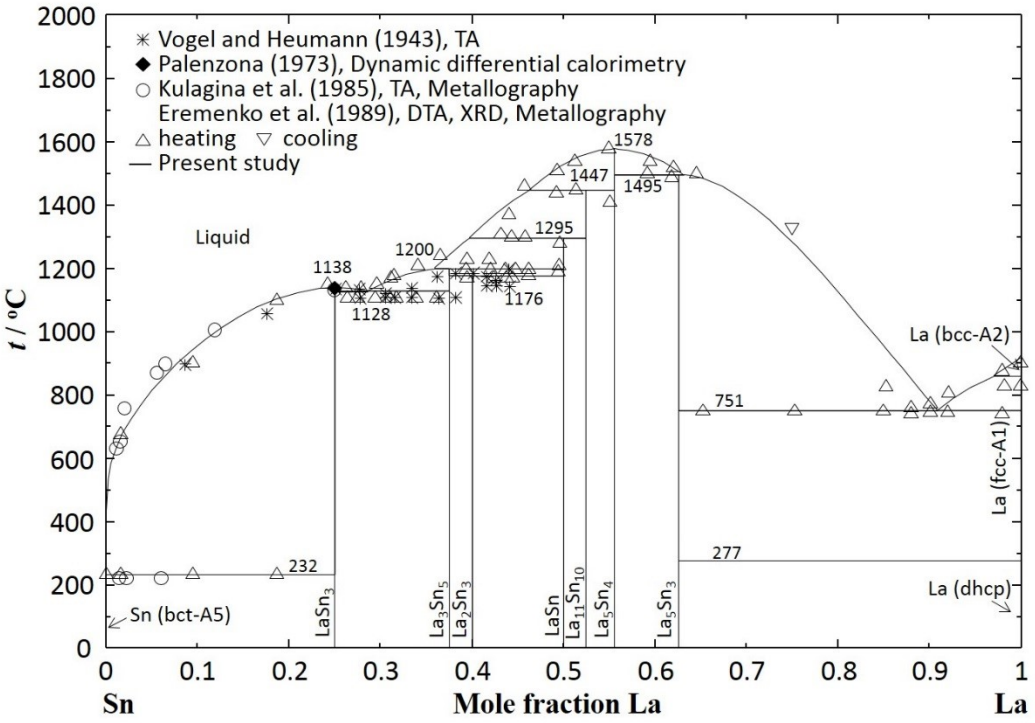
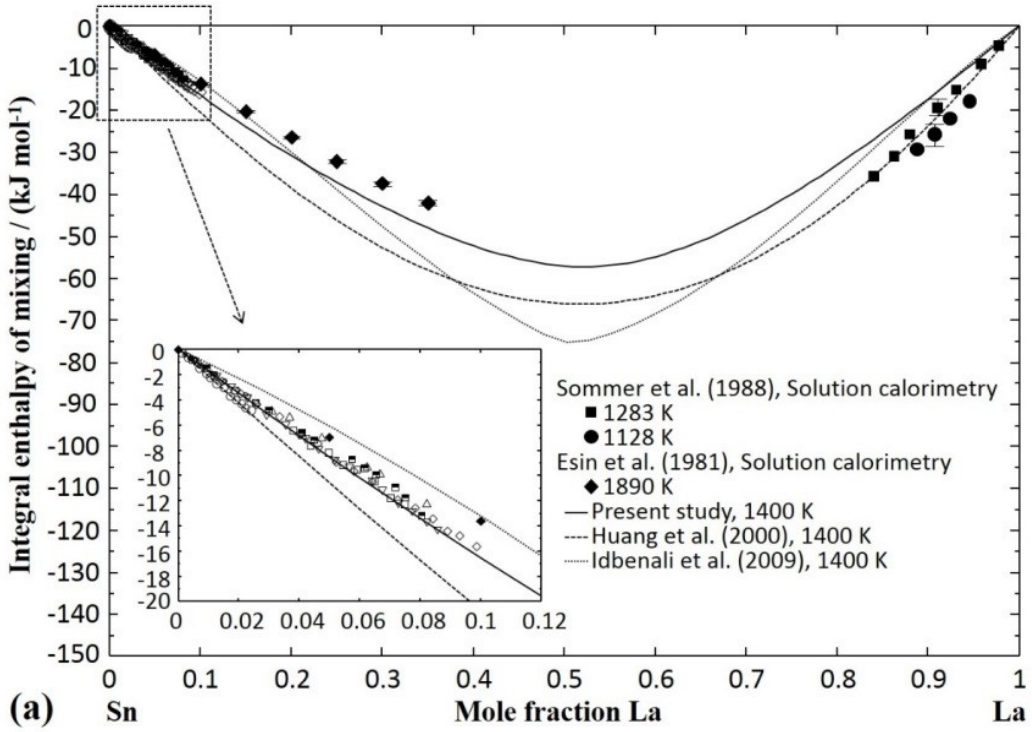
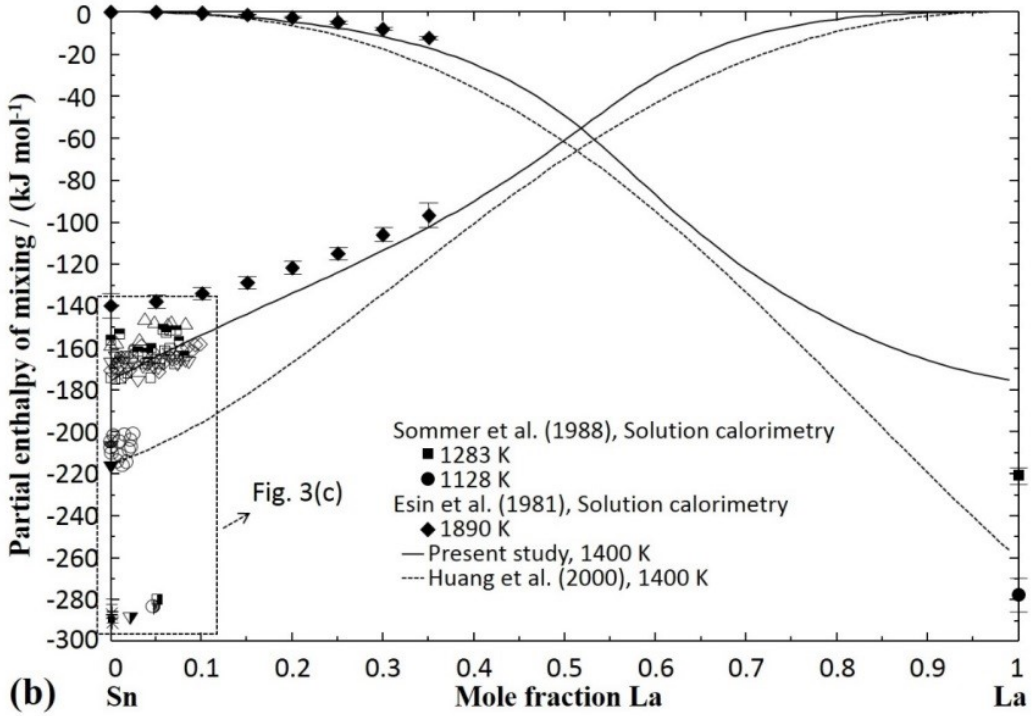


Fig. 2. The optimized Sn-La phase diagram with experimental data.


Integral enthalpy of mixing / (kJ mol-1)
Sommer et al. (1988), Solution calorimetry
1283 K
1128 K
Esin et al. (1981), Solution calorimetry
1890 K
Present study, 1400 K
Huang et al. (2000), 1400 K
Idbenali et al. (2009), 1400 K
(a)
Sn
Mole fraction La
La


Partial enthalpy of mixing / (kJ mol-1)
Fig. 3(c)
Sommer et al. (1988), Solution calorimetry
1283 K
1128 K
Esin et al. (1981), Solution calorimetry
1890 K
Present study, 1400 K
Huang et al. (2000), 1400 K
(b)
Sn
Mole fraction La
La

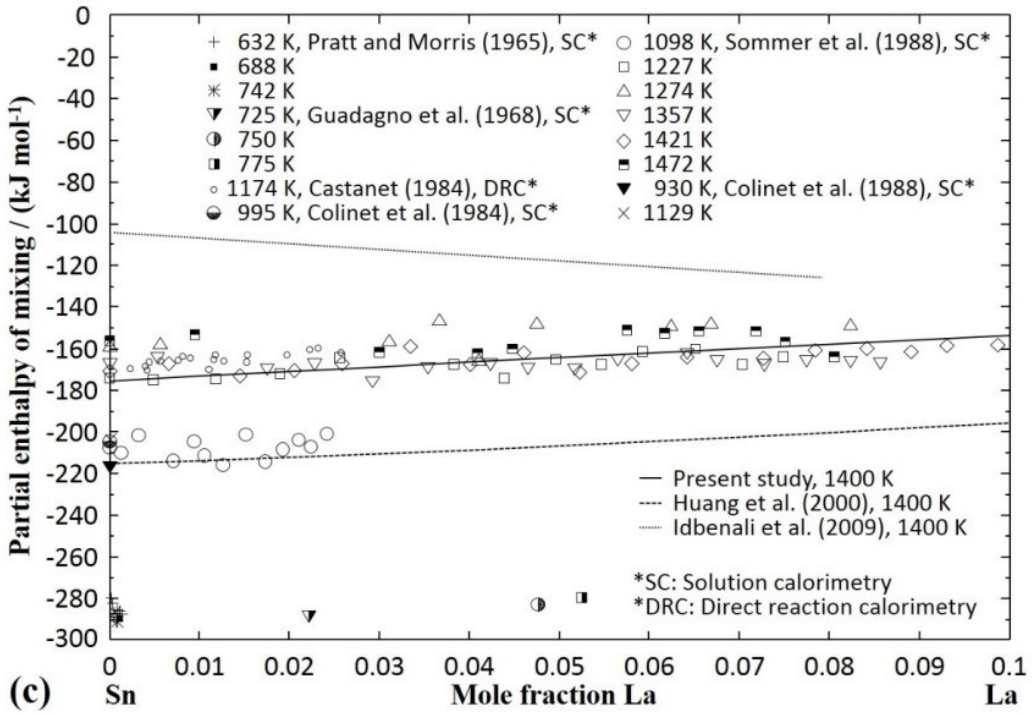


Fig. 3. (a) Integral enthalpy of mixing, (b) and (c) partial enthalpy of mixing of liquid Sn-La at 1400 K with experimental data and previous thermodynamic assessment.

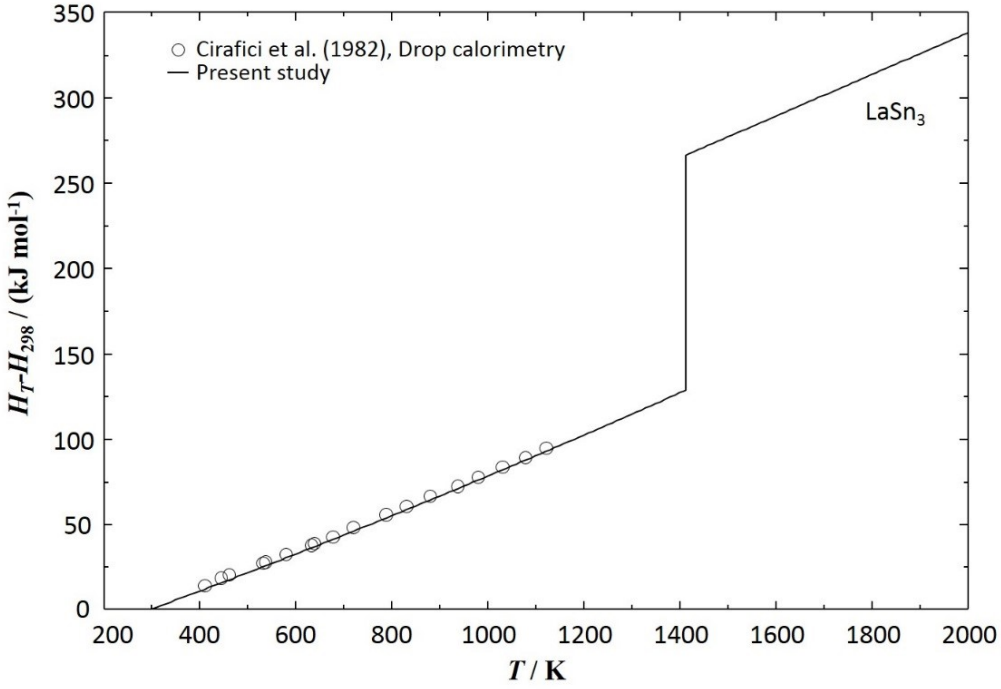


Fig. 4. Heat content of $LaSn_3$ with experimental data.

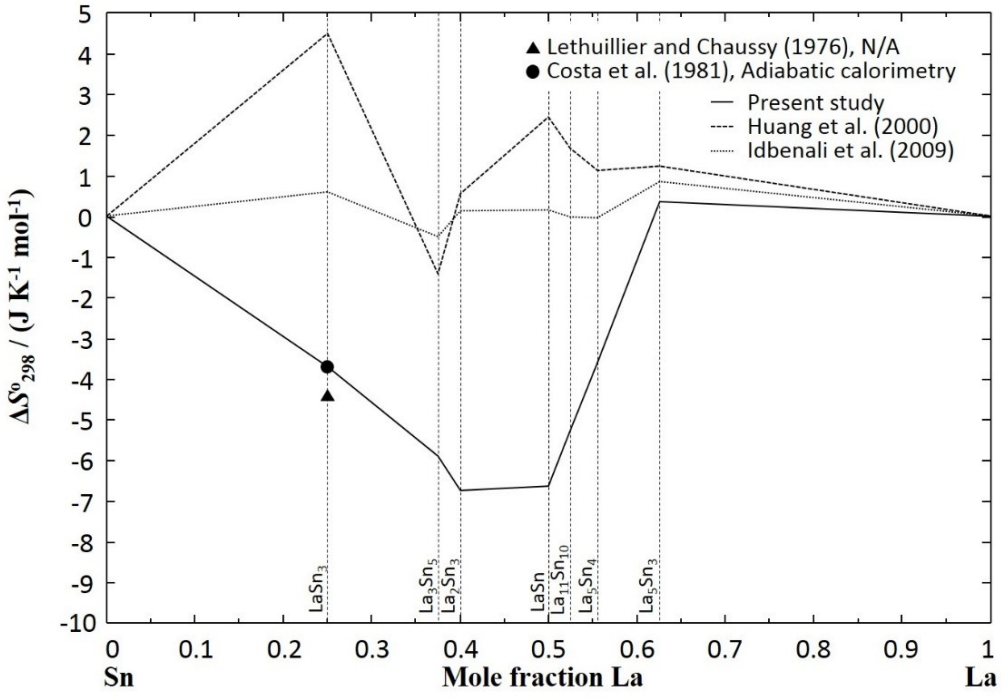


Fig. 5. Entropy of formation of the compounds in the Sn-La system from elements at 298 K with experimental data.

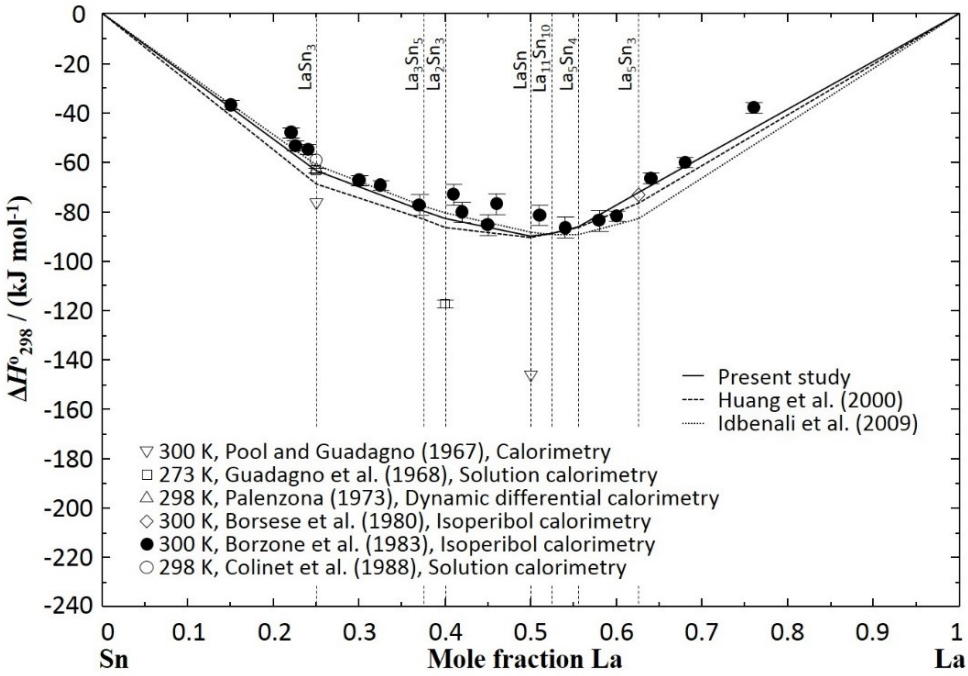


Fig. 6. Enthalpy of formation of the compounds in the Sn-La system at 298 K with experimental data.

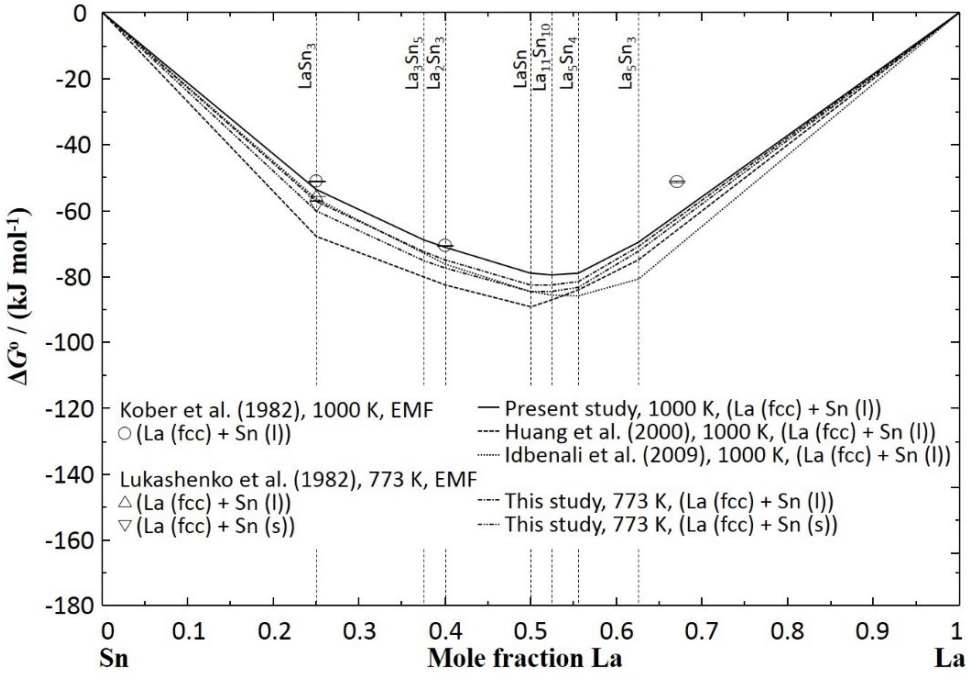


Fig. 7. Gibbs energy of formation of the compounds in the Sn-La system at 773 and 1000 K with experimental data.

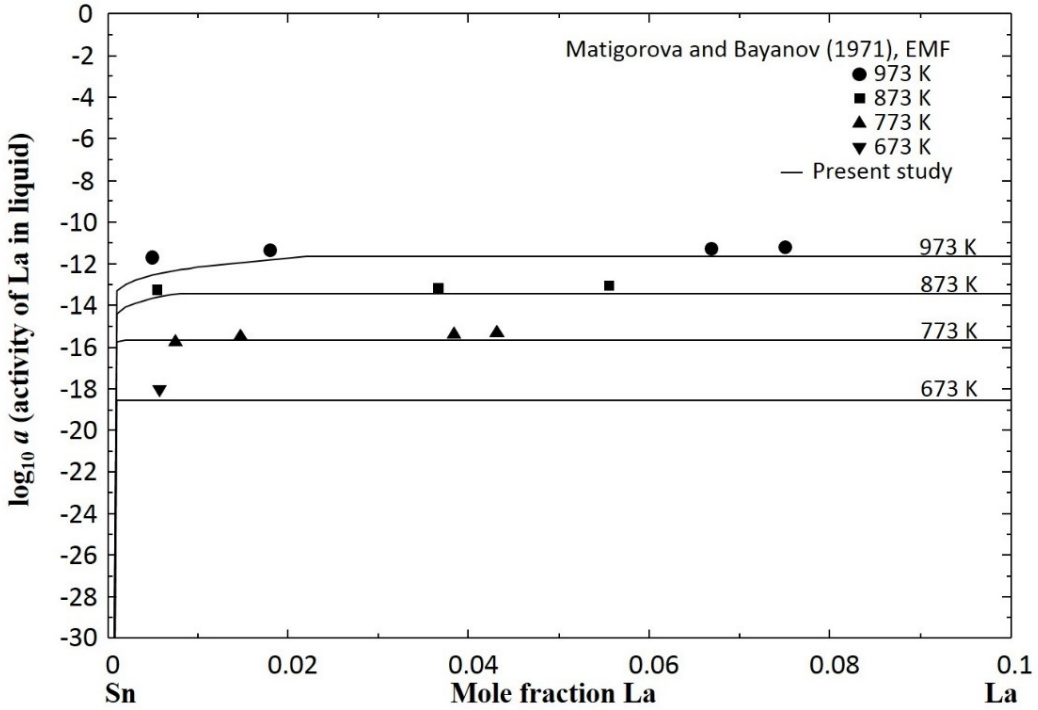


Fig. 8. The activity of La in liquid at 673-973 K (Sn-rich region).

2.2. The Sn-Ce system

Experimental data of the Sn-Ce phase diagram are presented in Fig. 9. The early investigation of the system over the whole composition range was roughly performed by Vogel [51]. The existence of intermetallic compounds, Ce_2Sn (1135 ºC), Ce_2Sn_3 (1165 ºC) and $CeSn_2$ (1400 ºC), and the liquidus points were reported. Vogel and Heumann [16] reinvestigated the system, and the existence of $CeSn_3$ was proposed with modified liquidus near the $CeSn_3$ after withdrawing the $CeSn_2$. The crystallographic studies of intermetallic compounds were performed by several research groups. The crystal structure and lattice parameters of Ce_xSn_y were reported: Ce_3Sn ($AuCu_3$ type, ordered) [52-54], Ce_3Sn (cubic, disordered) [53-55], α-Ce_5Sn_3 (W_5Si_3 type, low temperature form) [21, 53, 54], β-Ce_5Sn_3 (Mn_5Si_3 type, high temperature form) [17, 53], Ce_5Sn_4 (Sm_5Ge_4 type) [20, 54], $Ce_{11}Sn_{10}$ ($Ho_{11}Ge_{10}$ type) [53, 54], Ce_2Sn_3 (Triclinic) [25], Ce_3Sn_5 (Pu_3Pd_5 type) [53], Ce_3Sn_7 (Orthorhombic) [27, 56-58], Ce_2Sn_5 (Orthorhombic) [27, 56-58], and $CeSn_3$ ($AuCu_3$ type) [15, 27, 53, 59, 60]. The melting temperature of $CeSn_3$, 1160 ºC, was determined by Palenzona [19] in the measurement of heat of formation of the $CeSn_3$ using dynamic differential calorimetry. The solubility of Ce in liquid Sn was determined by Yamshchikov et al. [61] from the emf measurements using an electrochemical cell in the temperature range between 720 and 1140 K. The complete phase diagram of the Sn-Ce system was reported by Franceschi and Costa [54, 60] from the differential thermal and metallographic analyses. Initially, the system was investigated in the composition range of 0.5 to 1 mole fraction of Ce [54]. The samples were prepared from the initial materials, 99.95% Ce and 99.999% Sn, in Mo crucibles under argon using an induction furnace. The samples were subsequently analyzed by DTA, XRD, and metallographic methods. Four intermediate phases were found with the respective melting temperatures: Ce_3Sn (940 ºC), Ce_5Sn_3 (1505 ºC), Ce_5Sn_4 (1510 ºC), and $Ce_{11}Sn_{10}$ (~1400 ºC). The crystallographic data of the phases were consistent with the previous works [17, 20, 21, 52, 53, 55]. Although the two polymorphs of Ce_3Sn and Ce_5Sn_3 were verified by the crystallographic study, the order-disorder transition of Ce_3Sn and the α- to β-Ce_5Sn_3 transition were not detected in the thermal analysis. A small homogeneity range was suggested for the α-Ce_5Sn_3 from the X-ray powder patterns. However, the range was not specifically studied. The solid solubility of Sn in fcc-Ce was proposed to be less than 0.005 mole fraction of Sn as the lattice constant change was insignificant with

alloying Sn. The solubility of Sn in bcc-Ce was not specifically investigated, but the eutectoid reaction (bcc-Ce → fcc-Ce + Ce_3Sn) was proposed to occur at 690 ºC and at about 0.02 mole fraction of Sn. In the same manner, the system was successively investigated in the composition range of 0 to 0.5 mole fraction of Ce [60]. Four intermediate phases were additionally found with the melting temperatures: Ce_3Sn_5 (1180 ºC), Ce_3Sn_7 (1135 ºC), Ce_2Sn_5 (1145 ºC), and $CeSn_3$ (1170 ºC). The crystallographic data of the phases were also consistent with the previous studies [15, 53, 56, 57, 59]. However, the Ce_2Sn_3 phase which was previously reported [16, 25, 51] was not found in the work of Franceschi and Costa [60]. The types and number of intermediate phases in the work of Franceschi and Costa [54, 60] agree with the several experimental isothermal phase diagram investigation of the ternary systems containing Ce and Sn [62-64].

Like the Sn-La system, the thermodynamic properties of the Sn-Ce liquid were reported by several research groups. Experimental data with regard to the integral and partial enthalpy of mixing of Sn-Ce liquid are presented in Fig. 10(a) and (b), respectively. Pratt and Morris [33] measured the heat of solution of solid (fcc) Ce (>99.96%) in liquid Sn (99.999%) at 631 K and 634 K in the Ce-dilute composition range using a liquid-metal solution calorimeter. Based on the reported data, the partial enthalpy of mixing of Ce was determined to be about -290 kJ mol^{-1} by considering the heat effect between fcc- and liquid-Ce in the present study. Similarly, Yamshchikov et al. [65] determined the partial enthalpy of mixing of Ce at 1221 K using high temperature mixing calorimetry. The heat of dissolution of Ce into liquid Sn was also measured by Castanet [36] using a direct reaction calorimeter with high purity materials (>99.9% Ce and Sn). The partial enthalpy of mixing of Ce-dilute liquid solution at 1178 K were determined up to 0.037 mole fraction of Ce. In the present study, the integral enthalpy of mixing was calculated from the reported values as shown in Fig. 10(a). The partial enthalpy of mixing of Ce at infinite dilution of Ce at 999 K [37], 930 K [38], 1129 K [38], and 1133 K [38] were reported by Colinet et al. from the dissolution measurement using an isoperibol calorimeter (<1000 K) and a Calvet-type twin calorimeter (<1200 K) under vacuum (10^{-4} Pa) with high purity materials (99.999% Sn and 99.99% Ce). In the later study, Sudavtsova and Batalin [66] determined the integral and partial enthalpies of mixing of Sn-Ce liquid at 1870 K up to 0.3 mole fraction of Ce using a high temperature solution calorimetry.

Most of the experimental values mentioned above were in the range about between -195 and -215 kJ mol^{-1} except for the data of Pratt and Morris [33].

Thermodynamic properties of the intermetallic compounds were investigated by several research groups. Experimental data for the C_p of $CeSn_3$ is shown in Fig. 1. Cirafici et al. [12] determined the high temperature C_p of $CeSn_3$ between 400 and 1200 K from the heat content measurements. The heat contents of $CeSn_3$ were measured by means of the same method used for the $LaSn_3$. The obtained heat contents are shown in Fig. 11. The experimental enthalpy of formation at about 298 K (ΔH^{o}_{298}) are presented in Fig. 12. The ΔH^{o}_{298} of $CeSn_3$ was determined by Palenzona [19] using a dynamic differential calorimetry with a conventional DTA apparatus. The enthalpy and entropy of fusion for $CeSn_3$ were also reported to be about 68.83 kJ mol^{-1} and 47.91 J K^{-1} mol^{-1}, respectively. The enthalpy of formation of Ce_5Sn_3 at 300 K was reported by Borsese et al. [43] using a differential direct isoperibol calorimeter. The reported value was confirmed in the work by Borzone et al. [53], which was published later. In the work [53], the enthalpy of formation values were measured in a large composition range using a direct method with an isoperibol calorimeter. The enthalpy of formation at 300 K for various composition alloys were reported. Colinet et al. [38] reported the two values of ΔH^{o}_{298} of $CeSn_3$ based on the dissolution and precipitation methods using a solution calorimetry. Mathews et al. [67] determined the Gibbs energy of formation (ΔG^{o}) of $CeSn_3$ from solid Ce and liquid Sn by emf measurements using a high-temperature galvanic cell technique in the temperature range 723-873 K. The reported ΔG^{o} of $CeSn_3$ was -260.08 + $0.0476 \cdot T$ (±2) kJ mol^{-1}. In addition, the excess partial Gibbs energy of Ce in saturated solution as functions of temperature and composition was determined with respect to solid and liquid Ce. In the present study, the activity values of Ce in the saturated solution were calculated from the excess partial Gibbs energy of Ce as shown in Fig. 13. Previously, Yamshchikov et al. [68] reported the thermodynamic properties of the saturated solution (L+$CeSn_3$, 0.086 to 0.13 mole fraction of Ce) in the temperature range 660-1100 K from the emf measurement.

The thermodynamic optimization of the Sn-Ce system was previously performed by Dong et al. [69] in the optimization of the ternary Au-Ce-Sn system. The calculated thermodynamic properties

from the work of Dong et al. [69] are presented in Figs. 10 and 12. The excess Gibbs energy of liquid phase was expressed in the Redlich-Kister random mixing model however the calculated integral and partial enthalpy of mixing of liquid did not fit the trend of experimental data [66] as shown in Fig 10(a) and (b). For the ΔH^{o}_{298} of all compounds, the ab initio calculation at 0 K was performed by Dong et al. [69]. The values are slightly more positive than the experimental data [38, 43, 53] as seen in Fig. 12 and the ΔH^{o}_{298} of all compounds were assessed based on their ab initio calculation. In the assessed phase diagram [69], in general, the calculated liquidus did not fit accurately the experimental data [60, 61], especially at the Sn-rich side. The Ce_5Sn_3 was treated as a congruent melting compound unlike the experimental finding [54]. The assessed phase diagram [69] is not presented in this study.

The optimized phase diagram of the Sn-Ce system in the present study is shown in Fig. 9. In the optimization, the eight intermetallic compounds, $CeSn_3$, Ce_2Sn_5, Ce_3Sn_7, Ce_3Sn_5, $Ce_{11}Sn_{10}$, Ce_5Sn_4, Ce_5Sn_3 and Ce_3Sn, were modelled based on the experimental findings, in particular Franceschi and Costa [54, 60]. The disordered Ce_3Sn and β-Ce_5Sn_3 phases were not considered in the present study because the polymorphic transformation or any thermodynamic properties of them were not available. The optimized phase diagram is consistent with the experimental data [19, 54, 60, 61] except the melting behavior of Ce_5Sn_3 and Ce_2Sn_5. In the work of Franceschi and Costa [54], the Ce_5Sn_3 was suggested to form peritectically based on the micrographic analysis. However, in the optimized phase diagram, the Ce_5Sn_3 phase melts congruently in view of the liquidus slope of Ce_5Sn_4 and Ce_5Sn_3 (determined by the thermodynamic properties of liquid and compounds) and the melting temperature of them, which agrees with the previous assessment of Dong et al. [69]. Although the Ce_2Sn_5 was also reported to melt peritectically [60], the Ce_2Sn_5 melts congruently in the optimized phase diagram. The melting temperature (1140.54 ºC) is almost same to the eutectic temperature (1140.52 ºC) between $CeSn_3$ and Ce_2Sn_5. The solid solubilities of fcc-Ce and bcc-Ce phases were reproduced with one temperature independent excess Gibbs energy parameter, respectively, which can reproduce the phase transformation temperatures [54].

The calculated thermodynamic properties with the optimized thermodynamic parameters are shown in Figs. 10-13. The temperature independent parameters (i.e., enthalpy) of excess Gibbs

energy of liquid were initially determined based on the experimental enthalpy of mixing [36-38, 65, 66] (Fig. 10 (a) and (b)). The experimental values of Pratt and Morris [33] were too negative to be considered. The partial enthalpy of mixing of Ce for Ce-dilute solution was calculated about -200 kJ mol^{-1} at 1870 K. The calculated partial enthalpy of mixing of Ce starts deviating from the experimental values of Sudavtsova and Batalin [66] above 0.25 mole fraction of Ce. If the experimental data of Sudavtsova and Batalin [66] are reproduced, the minimum integral enthalpy of mixing should be slightly more positive and the minimum enthalpy composition should shift slightly to Sn side than the current one. Even though the data are available up to 0.3 mole fraction of Ce, the shape of enthalpy is predictable from the data trend. However, the composition of the minimum enthalpy of mixing of liquid generally coincides with the composition of the minimum enthalpy of formation of the compounds. Moreover, the composition is also commonly consistent with the stoichiometry of the highest melting compound. Therefore, the present enthalpy of mixing was modeled to have the minimum near equimolar composition as seen in Fig. 10 (a), which is also consistent with the enthalpy of formation of compounds as seen in Fig. 12. Then, one temperature independent parameter (i.e., entropy) at the Sn-rich side was added to reproduce the experimental phase diagram studies [54, 60, 61]. The calculated heat content, $H_T - H_{298}$, of $CeSn_3$ based on the estimated heat capacities of $CeSn_3$ are consistent with the experimental data [12] as shown in Fig. 11. The calculated enthalpy of fusion of $CeSn_3$ (77 kJ mol^{-1}) is slightly higher than the reported value, 69 kJ mol^{-1}, from the DTA measurement [19]. The calculated ΔH^{o}_{298} of compounds are in good agreement with the experimental data of Borzone et al. [53] as seen in Fig. 12. The calculated ΔG^{o}_{800} of $CeSn_3$ from liquid Sn and solid Ce was -54.36 kJ mol^{-1}, which is consistent with the experimental value, -55.5 kJ mol^{-1}, determined by Mathews et al. [67]. The activities of Ce in liquid ($X_{Ce} = 0.05$) are also calculated in the temperature range from 723 to 873 K. The calculated values (logarithmic scale) are slightly higher than the experimental data [67] as seen in Fig. 13. The calculated partial Gibbs energy of Ce in the saturated solution (L+$CeSn_3$) at 1000K, -209 kJ mol-$atom^{-1}$, is also consistent with the experimental values (-205.4 ± 0.42 kJ mol-$atom^{-1}$) determined by Yamshchikov et al. [68]. The optimized thermodynamic parameters are listed in Table 3 and the calculated invariant reactions with the experimental data are tabulated in Table 4.

Table 3. Optimized model parameters for the Sn-Ce system.

Phase	Thermodynamic parameters
Liquid	Coordination Numbers
	i j Z_{ij}^{i} Z_{ij}^{j}
	Sn Ce 6 6
	Δg_{SnCe} / (J mol^{-1}) = -50208.0 – 25104.0 X_{SnSn} + (8368.0 + 8.368 T/K) X_{SnSn}^{2}
	– 16736.0 X_{CeCe} + 10334.48 X_{CeCe}^{2}
bcc-A2	${}^{0}L_{Sn,Ce}$ / (J mol^{-1}) = -167360.0
fcc-A1	${}^{0}L_{Sn,Ce}$ / (J mol^{-1}) = -150624.0
$CeSn_3$	ΔH_{298}^{o} = -227200.0 J mol^{-1}, S_{298}^{o} = 228.0 J K^{-1} mol^{-1}
	C_p / (J K^{-1} mol^{-1}) = 1 × C_p / (J K^{-1} mol^{-1}) (Ce, fcc)
	+ 3 × modified C_p / (J K^{-1} mol^{-1}) (Sn, bct-A5)*
Ce_2Sn_5	ΔH_{298}^{o} = -430500.0 J mol^{-1}, S_{298}^{o} = 402.5 J K^{-1} mol^{-1}
	C_p / (J K^{-1} mol^{-1}) = 2 × C_p / (J K^{-1} mol^{-1}) (Ce, fcc)
	+ 5 × modified C_p / (J K^{-1} mol^{-1}) (Sn, bct-A5)*
Ce_3Sn_7	ΔH_{298}^{o} = -631784.0 J mol^{-1}, S_{298}^{o} = 577.0 J K^{-1} mol^{-1}
	C_p / (J K^{-1} mol^{-1}) = 3 × C_p / (J K^{-1} mol^{-1}) (Ce, fcc)
	+ 7 × modified C_p / (J K^{-1} mol^{-1}) (Sn, bct-A5)*
Ce_3Sn_5	ΔH_{298}^{o} = -576000.0 J mol^{-1}, S_{298}^{o} = 466.5 J K^{-1} mol^{-1}
	C_p / (J K^{-1} mol^{-1}) = 3 × C_p / (J K^{-1} mol^{-1}) (Ce, fcc)
	+ 5 × modified C_p / (J K^{-1} mol^{-1}) (Sn, bct-A5)*
$Ce_{11}Sn_{10}$	ΔH_{298}^{o} = -1795500.0 J mol^{-1}, S_{298}^{o} = 1179.0 J K^{-1} mol^{-1}
	C_p / (J K^{-1} mol^{-1}) = 11 × C_p / (J K^{-1} mol^{-1}) (Ce, fcc)
	+ 10 × modified C_p / (J K^{-1} mol^{-1}) (Sn, bct-A5)*

Ce_5Sn_4 ΔH^{o}_{298} = -738000.0 J mol^{-1}, S^{o}_{298} = 527.5 J K^{-1} mol^{-1}

C_p / (J K^{-1} mol^{-1}) = 5 × C_p / (J K^{-1} mol^{-1}) (Ce, fcc)
+ 4 × modified C_p / (J K^{-1} mol^{-1}) (Sn, bct-A5)*

Ce_5Sn_3 ΔH^{o}_{298} = -590000.0 J mol^{-1}, S^{o}_{298} = 491.7 J K^{-1} mol^{-1}

C_p / (J K^{-1} mol^{-1}) = 5 × C_p / (J K^{-1} mol^{-1}) (Ce, fcc)
+ 3 × modified C_p / (J K^{-1} mol^{-1}) (Sn, bct-A5)*

Ce_3Sn ΔH^{o}_{298} = -201000.0 J mol^{-1}, S^{o}_{298} = 258.3 J K^{-1} mol^{-1}

C_p / (J K^{-1} mol^{-1}) = 3 × C_p / (J K^{-1} mol^{-1}) (Ce, fcc)
+ 1 × modified C_p / (J K^{-1} mol^{-1}) (Sn, bct-A5)*

*modified C_p / (J K^{-1} mol^{-1}) (Sn, bct-A5) = 24.477 + 5.472E-2 T/K – 40640.0 (T/K)$^{-2}$ – 6.469E-7 (T/K)^2

Table 4. Calculated invariant reactions and experimental data in the Sn-Ce system.

Type	Reaction	t (°C)	Reference
Eutectic	$L_{(X_{Ce}= 2E\text{-}5)} \rightarrow Sn_{(bct\text{-}A5,\ X_{Ce}= 0)} + CeSn_3$	231.9	This work
	$L_{(X_{Ce}= <0.005)} \rightarrow Sn_{(bct\text{-}A5,\ X_{Ce}= 0)} + CeSn_3$	225±5	[60]
Congruent	$L_{(X_{Ce}= 0.25)} \leftrightarrow CeSn_3$	1161.5	This work
	$L_{(X_{Ce}= 0.25)} \leftrightarrow CeSn_3$	1163.0	[16]
	$L_{(X_{Ce}= 0.25)} \leftrightarrow CeSn_3$	1170±10	[60]
	T_m of $CeSn_3$	1160.0	[19]
Peritectic	$CeSn_3 + L_{(X_{Ce}= \sim 0.29)} \rightarrow Ce_2Sn_5$	1145±10	[60]
Congruent	$L_{(X_{Ce}= 0.333)} \leftrightarrow CeSn_2$	~1140	[51]
Eutectic	$L_{(X_{Ce}= 0.285)} \rightarrow CeSn_3 + Ce_2Sn_5$	1140.5	This work
	$L_{(X_{Ce}= \sim 0.34)} \rightarrow CeSn_3 + Ce_2Sn_3$	~1133	[16]
	$L_{(X_{Ce}= \sim 0.36)} \rightarrow CeSn_2 + Ce_2Sn_3$	~1133	[51]
Congruent	$L_{(X_{Ce}= 0.286)} \leftrightarrow Ce_2Sn_5$	1140.5	This work
Peritectic	$Ce_2Sn_5 + L_{(X_{Ce}= 0.309)} \rightarrow Ce_3Sn_7$	1129.6	This work
	$Ce_2Sn_5 + L_{(X_{Ce}= \sim 0.31)} \rightarrow Ce_3Sn_7$	1135±10	[60]

Eutectic	$L_{(X_{Ce}= 0.323)} \rightarrow Ce_3Sn_7 + Ce_3Sn_5$	1119.4	This work
	$L_{(X_{Ce}= \sim 0.335)} \rightarrow Ce_3Sn_7 + Ce_3Sn_5$	1130±10	[60]
Congruent	$L_{(X_{Ce}= 0.375)} \leftrightarrow Ce_3Sn_5$	1186.0	This work
	$L_{(X_{Ce}= 0.375)} \leftrightarrow Ce_3Sn_5$	1180±10	[60]
Congruent	$L_{(X_{Ce}= 0.4)} \leftrightarrow Ce_2Sn_3$	~1168	[51]
Eutectic	$L_{(X_{Ce}= 0.412)} \rightarrow Ce_3Sn_5 + Ce_{11}Sn_{10}$	1145.9	This work
	$L_{(X_{Ce}= \sim 0.418)} \rightarrow Ce_3Sn_5 + Ce_{11}Sn_{10}$	1150±10	[60]
Eutectic	$L_{(X_{Ce}= \sim 0.47)} \rightarrow Ce_2Sn_3 + ?$	~1133	[51]
Peritectic	$L_{(X_{La}= 0.485)} + Ce_5Sn_4 \rightarrow Ce_{11}Sn_{10}$	1401.4	This work
	$L_{(X_{La}= \sim 0.46)} + Ce_5Sn_4 \rightarrow Ce_{11}Sn_{10}$	~1400	[54]
Congruent	$L_{(X_{Ce}= 0.556)} \leftrightarrow Ce_5Sn_4$	1513.3	This work
	$L_{(X_{Ce}= 0.556)} \leftrightarrow Ce_5Sn_4$	1510.0	[54]
Eutectic	$L_{(X_{Ce}= 0.595)} \rightarrow Ce_5Sn_4 + Ce_5Sn_3$	1482.6	This work
Congruent	$L_{(X_{Ce}= 0.625)} \leftrightarrow Ce_5Sn_3$	1502.6	This work
Peritectic	$Ce_5Sn_4 + L_{(X_{La}= \sim 0.63)} \rightarrow Ce_5Sn_3$	1505.0	[54]
Peritectic	$Ce_5Sn_3 + L_{(X_{Ce}= 0.833)} \rightarrow Ce_3Sn$	938.0	This work
	$Ce_5Sn_3 + L_{(X_{Ce}= \sim 0.85)} \rightarrow Ce_3Sn$	940.0	[54]
Eutectic	$L_{(X_{Ce}= 0.941)} \rightarrow Ce_3Sn + Ce_{(\text{bcc-A2}, X_{Ce}= 0.985)}$	720.2	This work
	$L_{(X_{Ce}= \sim 0.96)} \rightarrow Ce_3Sn + Ce_{(\text{bcc-A2}, X_{Ce}= \sim 0.98)}$	725.0	[54]
Eutectoid	$Ce_{(\text{bcc-A2}, X_{Ce}= 0.985)} \rightarrow Ce_3Sn + Ce_{(\text{fcc-A1}, X_{Ce}= 0.997)}$	689.2	This work
	$Ce_{(\text{bcc-A2}, X_{Ce}= \sim 0.98)} \rightarrow Ce_3Sn + Ce_{(\text{fcc-A1}, X_{Ce}= >0.995)}$	690.0	[54]

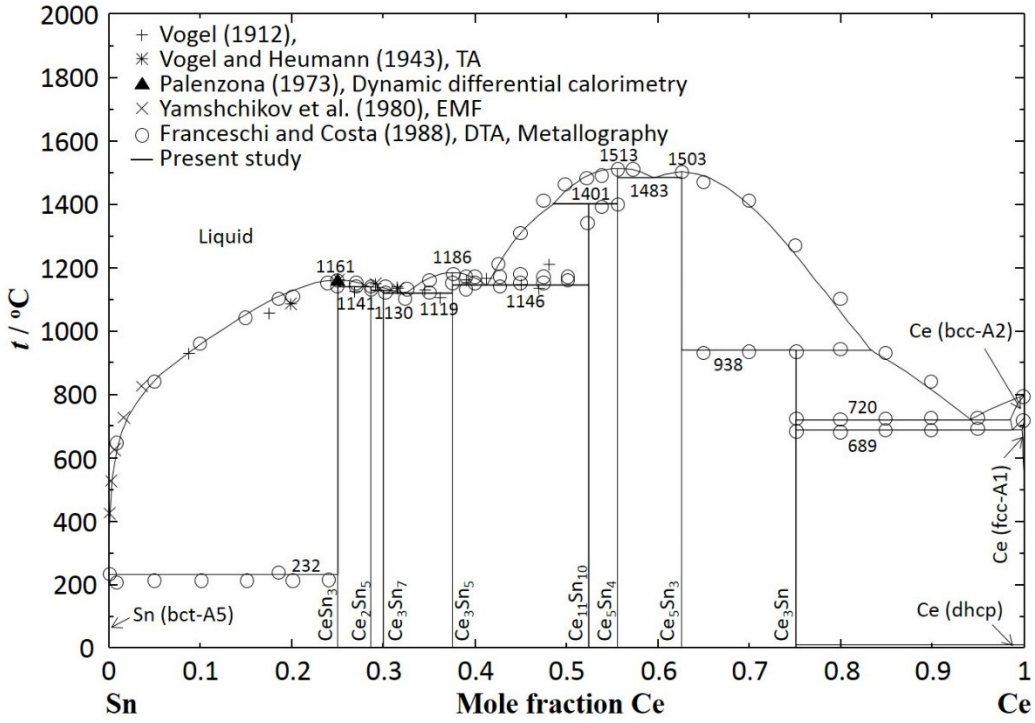


Fig. 9. The optimized Sn-Ce phase diagram with experimental data.

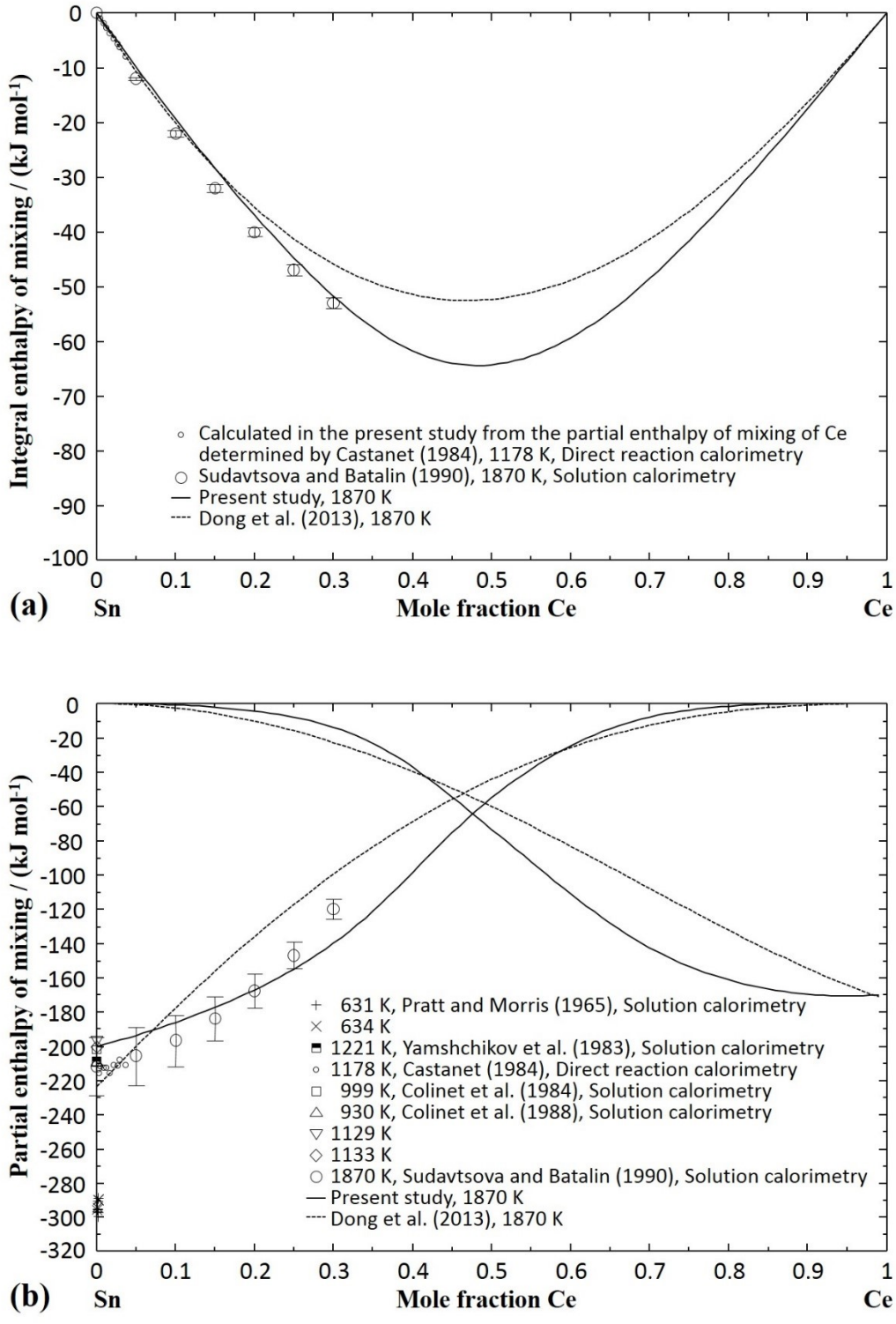


Fig. 10. (a) Integral enthalpy of mixing and (b) partial enthalpy of mixing of liquid Sn-Ce at 1870 K with experimental data and previous thermodynamic assessment.

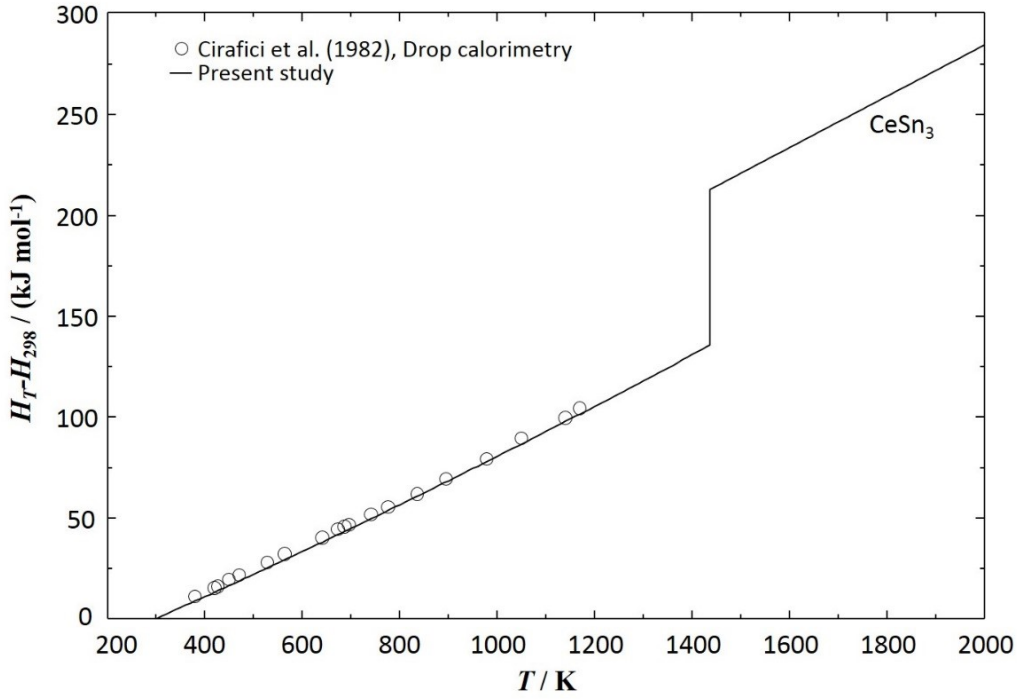


Fig. 11. Heat content of $CeSn_3$ with experimental data.

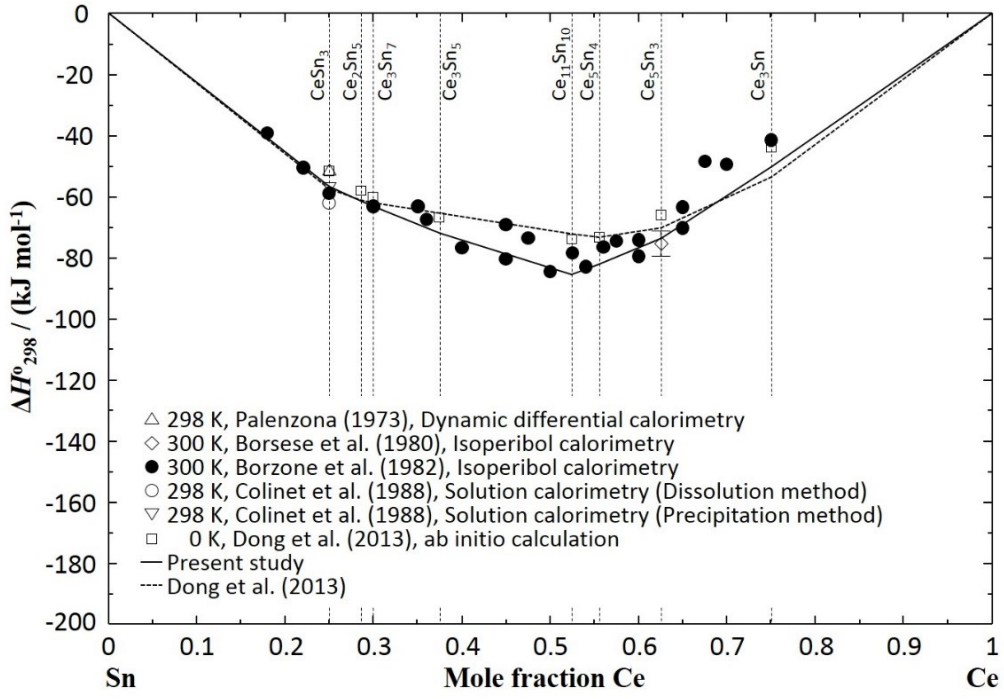


Fig. 12. Enthalpy of formation of the compounds in the Sn-Ce system at 298 K with experimental data.

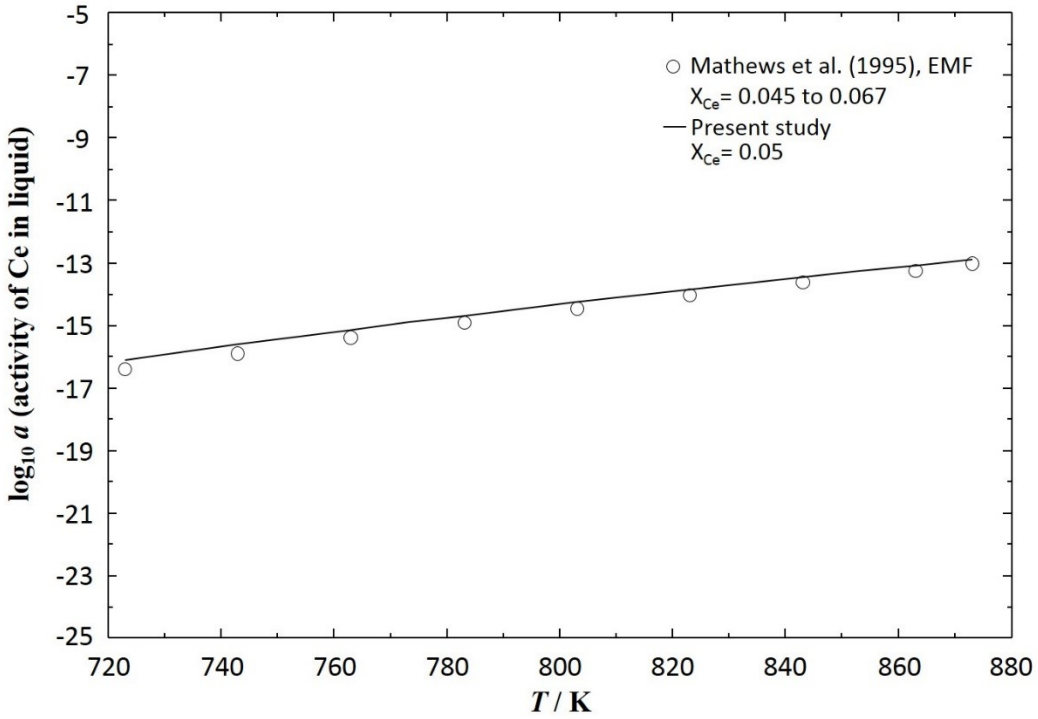


Fig. 13. The activity of Ce in liquid at 720-880 K with 0.05 mole fraction of Ce.

2.3. The Sn-Pr system

Experimental data of the Sn-Pr system are presented in Fig. 14. The early investigation was performed by Vogel and Heumann [16]. Three intermetallic compounds, $PrSn_3$, Pr_2Sn_3, and Pr_2Sn, were found to melt congruently with three eutectic temperatures. However, the investigation was rough. The Pr_2Sn_3 phase was not found in the later studies and the Pr_2Sn was refined to the Pr_5Sn_3 by the later studies. The crystallographic studies of intermetallic compounds were performed by several research groups. The crystal structure and lattice parameters of Pr_xSn_y were reported: Pr_3Sn ($AuCu_3$ type) [70, 71], Pr_3Sn (fcc) [55], α-Pr_5Sn_3 (W_5Si_3 type, low temperature form) [21, 71], β-Pr_5Sn_3 (Mn_5Si_3 type, high temperature form) [17, 71, 72], Pr_5Sn_4 (Sm_5Ge_4 type) [20, 73], Pr_2Sn_3 (Triclinic) [25], α-Pr_3Sn_5 (Pd_5Pu_3 type, low temperature form) [73], $PrSn_2$ ($NdSn_2$ type) [27], Pr_3Sn_7 (Ce_3Sn_7 type) [27], Pr_2Sn_5 (Ce_2Sn_5 type) [27], $PrSn_3$ ($AuCu_3$ type) [15, 73] and $PrSn_3$ (fcc) [55]. There were discrepancies in the existence of some intermetallic phases, i.e., non-existence of the $PrSn_2$ phase was reported by Iandelli and Palenzona [56], and the Pr_3Sn (fcc), Pr_2Sn_3, Pr_3Sn_7, Pr_2Sn_5, and Pr_3Sn (fcc) phases were not found in the study of Eremenko et al. [71, 73] who investigated the system over the whole composition range. The melting temperature of $PrSn_3$, 1155 ^oC, was determined by Palenzona [19] in the measurement of heat of formation of the $PrSn_3$ using dynamic differential calorimetry. The complete phase diagram of the Sn-Pr system was reported by Eremenko et al. [71, 73] from the DTA, XRD, and metallographic analysis. Initially, the system was investigated in the composition range of 0.6 to 1 mole fraction of Pr [71]. The samples were prepared from the initial materials, 99.75% Pr and 99.9995% Sn, using an arc furnace with tungsten electrode under purified argon gas. The samples were subsequently analyzed by DTA, XRD, and metallographic methods. Two intermetallic compounds were found: Pr_3Sn (942 ± 16 ^oC), and Pr_5Sn_3 (1610 ^oC) with eutectic reaction between Pr_3Sn and bcc-Pr at 784 ± 6 ^oC and 0.9 mole fraction of Pr. The solid solubility of Sn in fcc-Pr at 650 ^oC was reported to be less than 0.01 mole fraction of Sn. It was reported that the eutectoid reaction (bcc-Pr → fcc-Pr + Pr_3Sn) occurred at 754 ± 8 ^oC and at about 0.02 mole fraction of Sn. In the same manner, the system was successively investigated in the composition range of 0 to 0.6 mole fraction of Pr [73]. Four intermediate phases were additionally found: Pr_5Sn_4 (1440 ± 8 ^oC), PrSn (1253 ± 7 ^oC), Pr_3Sn_5 (1152 ± 8 ^oC), and $PrSn_3$ (1180 ^oC). The existence of PrSn was firstly suggested based on the

thermal effect although the crystal structure of PrSn phase was not confirmed. Similarly, the existence of the Pr_3Sn_5 phase and the polymorphic transformation from α-Pr_3Sn_5 to β-Pr_3Sn_5 were firstly suggested from the thermal effect observed at 1129 ± 6 ºC. The crystal structure of α-Pr_3Sn_5 (Pu_3Pd_5 type, low temperature form) was confirmed with the lattice parameters, but the crystal structure of β-Pr_3Sn_5 (low temperature form) was not confirmed. The solubility of Pr in liquid Sn in the temperature range of 993-1103 K was determined by Kober et al. [74] from the emf measurements. Unlike the study of Eremenko et al. [71, 73], the Pr_2Sn_5, Pr_3Sn_7, $PrSn_2$ and Pr_2Sn_3 were found in the isothermal phase diagram investigation of the ternary systems containing Pr and Sn [75, 76].

Available experimental thermodynamic properties of the Sn-Pr liquid were limited as compared to the previous two systems. Pratt and Morris [33] measured the heat of solution of solid (dhcp) Pr (>99.96%) in liquid Sn (99.999%) at about 750 K in the Pr-dilute composition range using a liquid-metal solution calorimeter. Based on the reported data, the partial enthalpy of mixing of Pr was determined to be about -265 kJ mol^{-1} by considering the heat effect between dhcp- and liquid-Pr in the present study. Previously, Peluso and Pool [77] and Lundin and Pool [78] determined the heat of solution of solid (dhcp) Pr (>99.7%) in liquid Sn (99.99%) at 750 K in the Pr-dilute composition range using a liquid-metal solution calorimeter. In the present study, the partial enthalpy of mixing of Pr at 750 K was calculated to be -284 kJ mol^{-1} and -303 kJ mol^{-1}, respectively, based on the reported data. The experimental data of partial enthalpies of mixing from literature are presented in Fig. 15 (b).

Thermodynamic properties of the intermetallic compounds were investigated by several research groups. Experimental data for the C_p of $PrSn_3$ is shown in Fig. 16. Lethuillier and Chaussy [40] reported the low temperature C_p of $PrSn_3$ between 20 and 300 K without the experimental technique. Sugiyama et al. [79] also reported the low temperature C_p of $PrSn_3$ between 1.5 and 50 K without the experimental technique. The heat capacity of $PrSn_3$ shows a very sharp peak at the Néel temperature (8.6 K) due to the magnetic transition. In the present study, the entropy of $PrSn_3$ at 298 K was determined to be about 217.5 J K^{-1} mol^{-1} by the integration of the combined experimental C_p values [40, 79] and the ΔS^{o}_{298} of $PrSn_3$ is shown in Fig. 17. The experimental

ΔH^{o}_{298} values are presented in Fig. 18. The ΔH^{o}_{298} of $PrSn_3$ was determined by Palenzona [19] using a dynamic differential calorimetry with a conventional DTA apparatus. The enthalpy and entropy of fusion for $PrSn_3$ were also reported to be about 75.35 kJ mol^{-1} and 52.76 J K^{-1} mol^{-1}, respectively. Meschel and Kleppa [80] measured the ΔH^{o}_{298} of Pr_5Sn_3 using direct synthesis calorimetry. The heat content ($H_{1473} - H_{298}$) of Pr_5Sn_3 was also reported to be 33.5 ± 1.2 kJ mol·$atom^{-1}$. Kober et al. [81] determined the thermodynamic properties of the saturated solution (L+$PrSn_3$) in the temperature range of 648-1012 K from the emf measurements and they reported the partial Gibbs energy of Pr at 1000 K. In a later study, Kober et al. [74] also determined the activity coefficient of Pr in liquid Sn in the temperature range of 993-1103 K from the emf measurements. The activity and the activity coefficient expressions as a function of temperature were derived from the emf values. The activities suggested in the two studies are presented in Fig. 19.

The thermodynamic optimization of the Sn-Pr system was performed for the first time. The optimized phase diagram of the Sn-Pr system in the present study is shown in Fig. 14. In the optimization, the ten intermetallic compounds, $PrSn_3$, Pr_2Sn_5, Pr_3Sn_7, $PrSn_2$, Pr_3Sn_5, Pr_2Sn_3, PrSn, Pr_5Sn_4, Pr_5Sn_3, and Pr_3Sn, were modelled based on the experimental findings, in particular Eremenko et al. [71, 73]. Although the Pr_2Sn_5, Pr_3Sn_7, $PrSn_2$ and Pr_2Sn_3 were not found in the study of Eremenko et al. [71, 73], they were added in the assessed phase diagram with reasonably assessed melting temperatures of them based on the isothermal phase diagram investigation of the ternary systems containing Pr and Sn [75, 76]. The complex thermal effect as well as the improbably constructed phase diagram between $PrSn_3$ and PrSn [73] also support the existence of those intermediate phases. A discussion for the thermodynamically implausible part of the phase diagram by Eremenko et al. [71, 73] is made below. The peritectic melting of Pr_5Sn_4 at 1400 °C which was reported by Erementko et al. [73], seemed to be unlikely when considering the shape of the liquidus slope. In the present study, the Pr_5Sn_4 was considered as a congruent melting compound to reproduce the liquidus. Additionally, the thermal effect at 1440 °C from the work of Eremenko et al. [71, 73] was considered as the polymorphic transformation temperature of Pr_5Sn_4, although the β-Pr_5Sn_4 (high temperature form) is arbitrary phase. Furthermore, the eutectic

reaction between $PrSn_3$ and PrSn suggested by Eremenko et al. [73] was completely unfeasible. Therefore, instead of peritectoid formation of Pr_3Sn_5 [73], the Pr_3Sn_5 was considered as a congruent melting compound to reproduce the liquidus as well as the addition of the Pr_2Sn_5 (peritectic, 1161.5 ^oC), Pr_3Sn_7 (peritectic, 1163.6 ^oC), $PrSn_2$ (congruent, 1185.2 ^oC), and Pr_2Sn_3 (peritectic, 1169.5 ^oC) between $PrSn_3$ and PrSn. However, further experimental investigation between $PrSn_3$ and PrSn would be required to verify the assessed phase diagram. The solid solubilities of Pr-dhcp and Pr-bcc phases were reproduced with one temperature independent excess Gibbs energy parameter, respectively, which can reproduce the phase transformation temperatures [71].

The calculated thermodynamic properties with the optimized thermodynamic parameters are shown in Figs. 15-19. The calculated integral and partial enthalpy of mixing of the Sn-Pr liquid at 750 K are shown in Fig. 15 (a) and (b). Similar to the two previous systems (Sn-La and -Ce), the experimental data of the partial enthalpy of mixing of Pr in the Pr-dilute solution at lower temperatures (about 750 K) [33, 77, 78] were not reproduced in the present study. Instead, the temperature independent parameters (i.e., enthalpy) for the excess Gibbs energy of liquid were estimated to be similar to the two previous systems, which corresponds to the phase diagram [71, 73] with small temperature dependent parameters (i.e., entropy). The heat capacity of $PrSn_3$ above 298 K was estimated by increasing 3 J K^{-1} mol^{-1} from the NK approximation using the modified heat capacity of Sn. The ΔH^{o}_{298} and the S^{o}_{298} of intermediate phases were determined based on the available experimental data. For instance, the S^{o}_{298} of $PrSn_3$ which was obtained from the experimental low temperature C_p data [40, 79] was used as seen in Fig. 17 (ΔS^{o}_{298}) and the experimental ΔH^{o}_{298} of $PrSn_3$ [19] and Pr_5Sn_3 [80] were reproduced as presented in Fig. 18. The rest compounds were evaluated with due consideration for the phase diagram and other thermodynamic properties. However, the calculated heat content, $H_{1473}-H_{298}$, of Pr_5Sn_3 was about 6 kJ mol·$atom^{-1}$ higher than the value reported by Meschel and Kleppa [80]. Furthermore, the calculated enthalpy of fusion of $PrSn_3$ (94.36 kJ mol^{-1}) was higher than the reported value, 75.35 kJ mol^{-1}, from the DTA measurement [19]. The activities of Pr in the solution containing up to 0.05 mole fraction of Pr were calculated at 1000 K, 1050 K, and 1100 K and they were slightly

lower than the experimental data of Kober et al. [74, 81] as seen in Fig. 19. The optimized thermodynamic parameters are listed in Table 5 and the calculated invariant reactions with the experimental data are tabulated in Table 6.

Table 5. Optimized model parameters for the Sn-Pr system.

Phase	Thermodynamic parameters
Liquid	Coordination Numbers
	i j Z_{ij}^{i} Z_{ij}^{j}
	Sn Pr 6 6
	Δg_{SnPr} / (J mol^{-1}) = -50208.0 – 25104.0 X_{SnSn} + (8368.0 + 6.276 T/K) X_{SnSn}^{2}
	+ (-25104.0 + 4.184 T/K) X_{PrPr} + 13388.8 X_{PrPr}^{2}
bcc-A2	${}^{0}L_{Sn,\mathrm{Pr}}$ / (J mol^{-1}) = -166523.2
dhcp	${}^{0}L_{Sn,\mathrm{Pr}}$ / (J mol^{-1}) = -146440.0
$PrSn_3$	ΔH_{298}^{o} = -248300.0 J mol^{-1}, S_{298}^{o} = 217.5 J K^{-1} mol^{-1}
	C_p / (J K^{-1} mol^{-1}) = 1 × C_p / (J K^{-1} mol^{-1}) (Pr, dhcp)
	+ 3 × modified C_p / (J K^{-1} mol^{-1}) (Sn, bct-A5)*
Pr_2Sn_5	ΔH_{298}^{o} = -475000.0 J mol^{-1}, S_{298}^{o} = 383.0 J K^{-1} mol^{-1}
	C_p / (J K^{-1} mol^{-1}) = 2 × C_p / (J K^{-1} mol^{-1}) (Pr, dhcp)
	+ 5 × modified C_p / (J K^{-1} mol^{-1}) (Sn, bct-A5)*
Pr_3Sn_7	ΔH_{298}^{o} = -700000.0 J mol^{-1}, S_{298}^{o} = 547.3 J K^{-1} mol^{-1}
	C_p / (J K^{-1} mol^{-1}) = 3 × C_p / (J K^{-1} mol^{-1}) (Pr, dhcp)
	+ 7 × modified C_p / (J K^{-1} mol^{-1}) (Sn, bct-A5)*
$PrSn_2$	ΔH_{298}^{o} = -225000.0 J mol^{-1}, S_{298}^{o} = 164.0 J K^{-1} mol^{-1}
	C_p / (J K^{-1} mol^{-1}) = 1 × C_p / (J K^{-1} mol^{-1}) (Pr, dhcp)
	+ 2 × modified C_p / (J K^{-1} mol^{-1}) (Sn, bct-A5)*

α-Pr_3Sn_5 ΔH^{o}_{298} = -635000.0 J mol^{-1}, S^{o}_{298} = 440.0 J K^{-1} mol^{-1}

C_p / (J K^{-1} mol^{-1}) = 3 × C_p / (J K^{-1} mol^{-1}) (Pr, dhcp)
+ 5 × modified C_p / (J K^{-1} mol^{-1}) (Sn, bct-A5)*

β-Pr_3Sn_5 $\Delta_{trs}H^{\alpha\rightarrow\beta}$ = 1000.0 J mol^{-1}, $T^{\alpha\rightarrow\beta}_{trs}$ = 1396.15 K

C_p / (J K^{-1} mol^{-1}) = 3 × C_p / (J K^{-1} mol^{-1}) (Pr, dhcp)
+ 5 × modified C_p / (J K^{-1} mol^{-1}) (Sn, bct-A5)*

Pr_2Sn_3 ΔH^{o}_{298} = -405000.0 J mol^{-1}, S^{o}_{298} = 276.0 J K^{-1} mol^{-1}

C_p / (J K^{-1} mol^{-1}) = 2 × C_p / (J K^{-1} mol^{-1}) (Pr, dhcp)
+ 3 × modified C_p / (J K^{-1} mol^{-1}) (Sn, bct-A5)*

PrSn ΔH^{o}_{298} = -171000.0 J mol^{-1}, S^{o}_{298} = 114.5 J K^{-1} mol^{-1}

C_p / (J K^{-1} mol^{-1}) = 1 × C_p / (J K^{-1} mol^{-1}) (Pr, dhcp)
+ 1 × modified C_p / (J K^{-1} mol^{-1}) (Sn, bct-A5)*

α-Pr_5Sn_4 ΔH^{o}_{298} = -760000.0 J mol^{-1}, S^{o}_{298} = 540.0 J K^{-1} mol^{-1}

C_p / (J K^{-1} mol^{-1}) = 5 × C_p / (J K^{-1} mol^{-1}) (Pr, dhcp)
+ 4 × modified C_p / (J K^{-1} mol^{-1}) (Sn, bct-A5)*

β-Pr_5Sn_4 $\Delta_{trs}H^{\alpha\rightarrow\beta}$ = 1000.0 J mol^{-1}, $T^{\alpha\rightarrow\beta}_{trs}$ = 1713.15 K

C_p / (J K^{-1} mol^{-1}) = 5 × C_p / (J K^{-1} mol^{-1}) (Pr, dhcp)
+ 4 × modified C_p / (J K^{-1} mol^{-1}) (Sn, bct-A5)*

α-Pr_5Sn_3 ΔH^{o}_{298} = -604400.0 J mol^{-1}, S^{o}_{298} = 509.8 J K^{-1} mol^{-1}

C_p / (J K^{-1} mol^{-1}) = 5 × C_p / (J K^{-1} mol^{-1}) (Pr, dhcp)
+ 3 × modified C_p / (J K^{-1} mol^{-1}) (Sn, bct-A5)*

β-Pr_5Sn_3 $\Delta_{trs}H^{\alpha\rightarrow\beta}$ = 1000.0 J mol^{-1}, $T^{\alpha\rightarrow\beta}_{trs}$ = 625.15 K

C_p / (J K^{-1} mol^{-1}) = 5 × C_p / (J K^{-1} mol^{-1}) (Pr, dhcp)
+ 3 × modified C_p / (J K^{-1} mol^{-1}) (Sn, bct-A5)*

Pr_3Sn ΔH^{o}_{298} = -208500.0 J mol^{-1}, S^{o}_{298} = 266.8 J K^{-1} mol^{-1}

C_p / (J K^{-1} mol^{-1}) = 3 × C_p / (J K^{-1} mol^{-1}) (Pr, dhcp)
+ 1 × modified C_p / (J K^{-1} mol^{-1}) (Sn, bct-A5)*

*modified C_p / (J K^{-1} mol^{-1}) (Sn, bct-A5) = 24.477 + 5.472E-2 T/K – 40640.0 $(T/K)^{-2}$ – 6.469E-7 $(T/K)^2$

Table 6. Calculated invariant reactions and experimental data in the Sn-Pr system.

Type	Reaction	t (°C)	Reference
Eutectic	$L_{(X_{Pr}=<1E-5)} \rightarrow Sn_{(bct\text{-}A5,\ X_{Pr}=0)} + PrSn_3$	231.9	This work
Peritectic	$L_{(X_{Pr}=*)} + PrSn_3 \rightarrow Sn_{(bct\text{-}A5,\ X_{Pr}=0)}$	235±5	[73]
	$L_{(X_{Pr}=0.25)} \leftrightarrow PrSn_3$	1180.9	This work
Congruent	$L_{(X_{Pr}=0.25)} \leftrightarrow PrSn_3$	~1148.0	[16]
	$L_{(X_{Pr}=0.25)} \leftrightarrow PrSn_3$	1180.0	[73]
	T_m of $PrSn_3$	1155.0	[19]
Peritectic	$L_{(X_{Pr}=0.286)} + PrSn_3 \rightarrow Pr_2Sn_5$	1161.5	This work
Eutectic	$L_{(X_{Pr}=0.287)} \rightarrow Pr_2Sn_5 + Pr_3Sn_7$	1161.5	This work
Peritectic	$L_{(X_{Pr}=0.296)} + PrSn_2 \rightarrow Pr_3Sn_7$	1163.6	This work
Congruent	$L_{(X_{Pr}=0.333)} \leftrightarrow PrSn_2$	1185.2	This work
	$L_{(X_{Pr}=0.349)} \rightarrow PrSn_2 + Pr_3Sn_5$	1180.9	This work
Eutectic	$L_{(X_{Pr}=\sim0.322)} \rightarrow PrSn_3 + Pr_3Sn_5$	~1119.0	[16]
	$L_{(X_{Pr}=\sim0.33)} \rightarrow PrSn_3 + PrSn$	1169±8	[73]
Congruent	$L_{(X_{Pr}=0.375)} \leftrightarrow Pr_3Sn_5$	1193.0	This work
Peritectoid	$PrSn_3 + PrSn \rightarrow Pr_3Sn_5$	1152±8	[73]
Allotropic	$\alpha\text{-}Pr_3Sn_5 \leftrightarrow \beta\text{-}Pr_3Sn_5$	1123.0	This work
	$\alpha\text{-}Pr_3Sn_5 \leftrightarrow \beta\text{-}Pr_3Sn_5$	1129±6	[73]
Peritectic	$L_{(X_{Pr}=0.410)} + Pr_3Sn_5 \rightarrow Pr_2Sn_3$	1169.5	This work
Congruent	$L_{(X_{Pr}=0.4)} \leftrightarrow Pr_2Sn_3$	~1169.0	[16]
Eutectic	$L_{(X_{Pr}=0.412)} \rightarrow Pr_2Sn_3 + PrSn$	1168.4	This work
Peritectic	$L_{(X_{Pr}=0.439)} + Pr_5Sn_4 \rightarrow PrSn$	1253.4	This work
	$L_{(X_{Pr}=\sim0.436)} + Pr_5Sn_4 \rightarrow PrSn$	1253±7	[73]
Eutectic	$L_{(X_{Pr}=0.463)} \rightarrow Pr_2Sn_3 + Pr_2Sn$	~1145.0	[16]
Peritectic	$L_{(X_{Pr}=\sim0.474)} + Pr_5Sn_3 \rightarrow Pr_5Sn_4$	1440±8	[73]
Congruent	$L_{(X_{Pr}=0.556)} \leftrightarrow Pr_5Sn_4$	1558.4	This work
Allotropic	$\alpha\text{-}Pr_5Sn_4 \leftrightarrow \beta\text{-}Pr_5Sn_4$	1440.0	This work
Eutectic	$L_{(X_{Pr}=0.574)} \rightarrow Pr_5Sn_4 + Pr_5Sn_3$	1551.6	This work

Congruent	$L(X_{Pr}= 0.625) \leftrightarrow Pr_5Sn_3$	1610.3	This work
	$L(X_{Pr}= 0.625) \leftrightarrow Pr_5Sn_3$	1610.0	[71]
Allotropic	$\alpha\text{-}Pr_5Sn_3 \leftrightarrow \beta\text{-}Pr_5Sn_3$	352.0	This work
	$\alpha\text{-}Pr_5Sn_3 \leftrightarrow \beta\text{-}Pr_5Sn_3$	352±7	[71]
Congruent	$L(X_{Pr}= 0.667) \leftrightarrow Pr_2Sn$	~1417.0	[16]
Peritectic	$Pr_5Sn_3 + L(X_{Dy}= 0.844) \rightarrow Pr_3Sn$	945.9	This work
	$Pr_5Sn_3 + L(X_{Dy}= \sim0.82) \rightarrow Pr_3Sn$	942±16	[71]
Eutectic	$L(X_{Pr}= 0.917) \rightarrow Pr_3Sn + Pr(\text{bcc-A2}, X_{Pr}= 0.984)$	796.2	This work
	$L(X_{Pr}= 0.9) \rightarrow Pr_3Sn + Pr(\text{bcc-A2}, X_{Pr}= \sim0.98)$	794±6	[71]
Eutectoid	$Pr(\text{bcc-A2}, X_{Pr}= 0.987) \rightarrow Pr_3Sn + Pr(\text{dhcp}, X_{Pr}= 0.998)$	753.5	This work
	$Pr(\text{bcc-A2}, X_{Pr}= \sim0.985) \rightarrow Pr_3Sn + Pr(\text{dhcp}, X_{Pr}= \text{unknown})$	754±8	[71]

* The exact compositions are not specified in the reference.

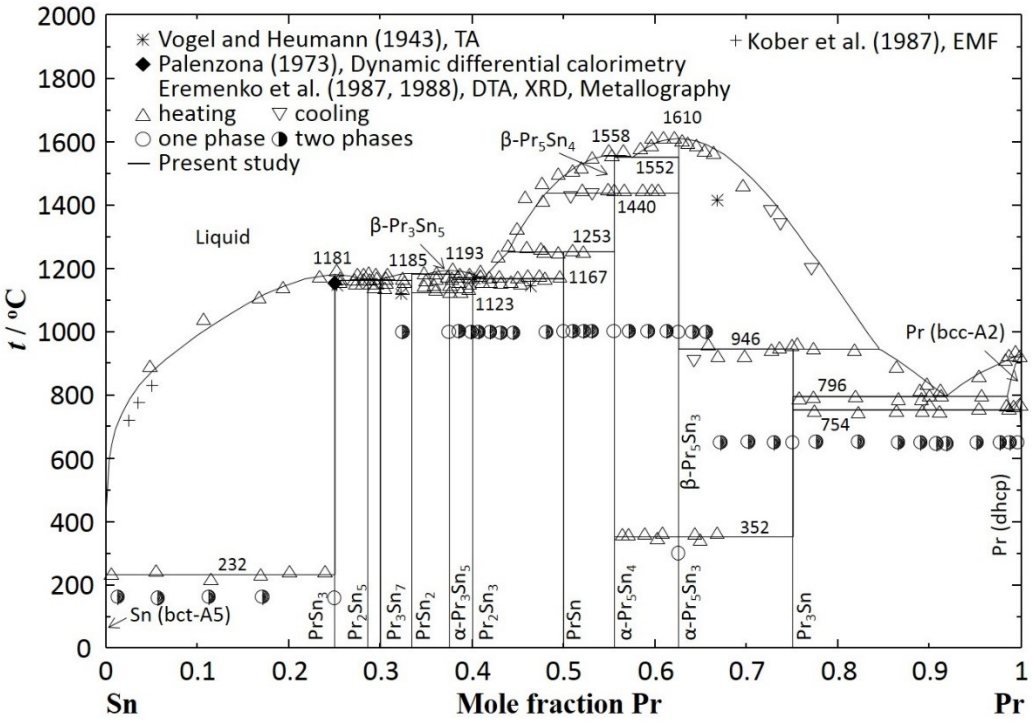


Fig. 14. The optimized Sn-Pr phase diagram with experimental data.

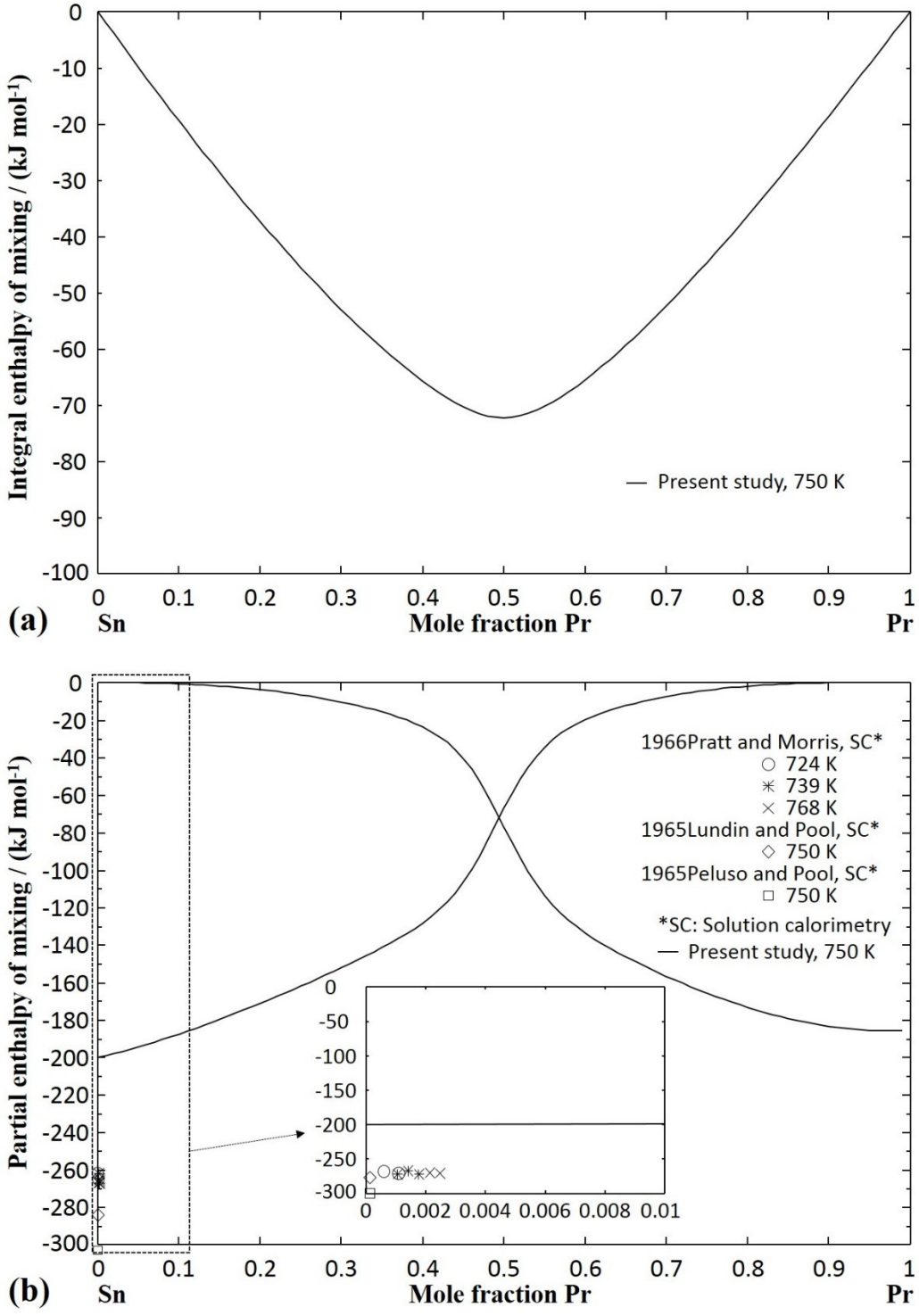


Fig. 15. (a) Integral enthalpy of mixing and (b) partial enthalpy of mixing of liquid Sn-Pr at 750 K with experimental data.

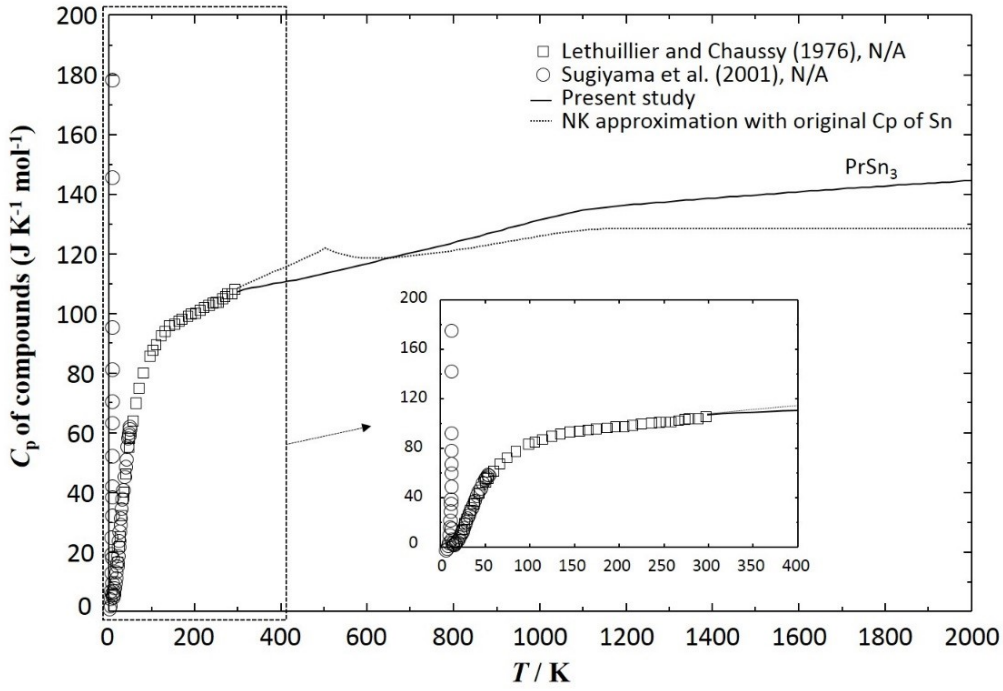


Fig. 16. Heat capacity of $PrSn_3$ with experimental data (1.5-300 K).

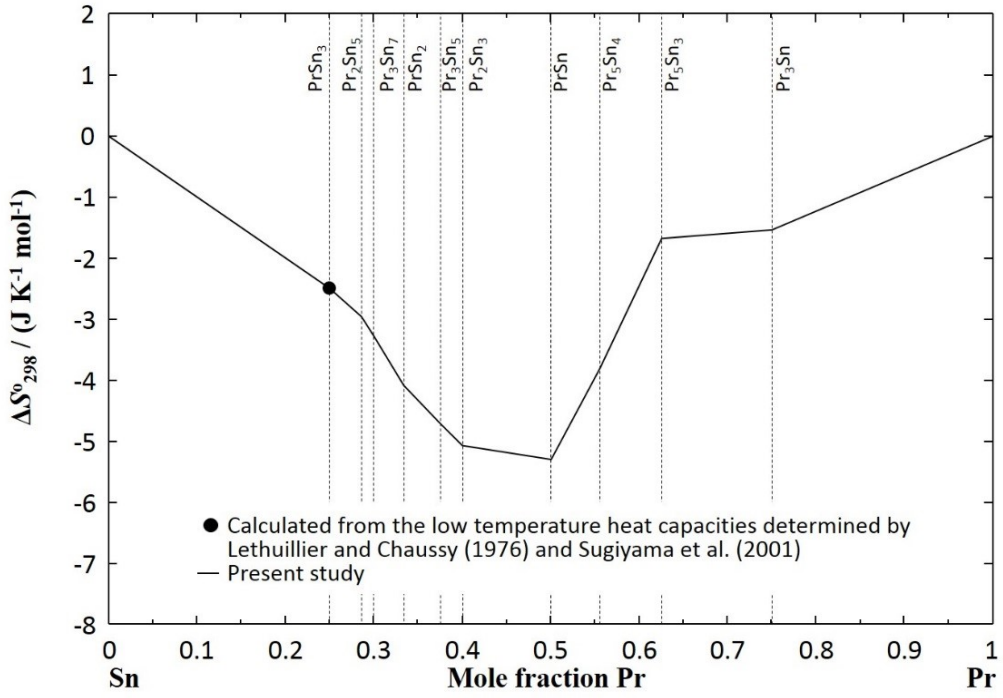


Fig. 17. Entropy of formation of the compounds in the Sn-Pr system from elements at 298 K with experimental data.

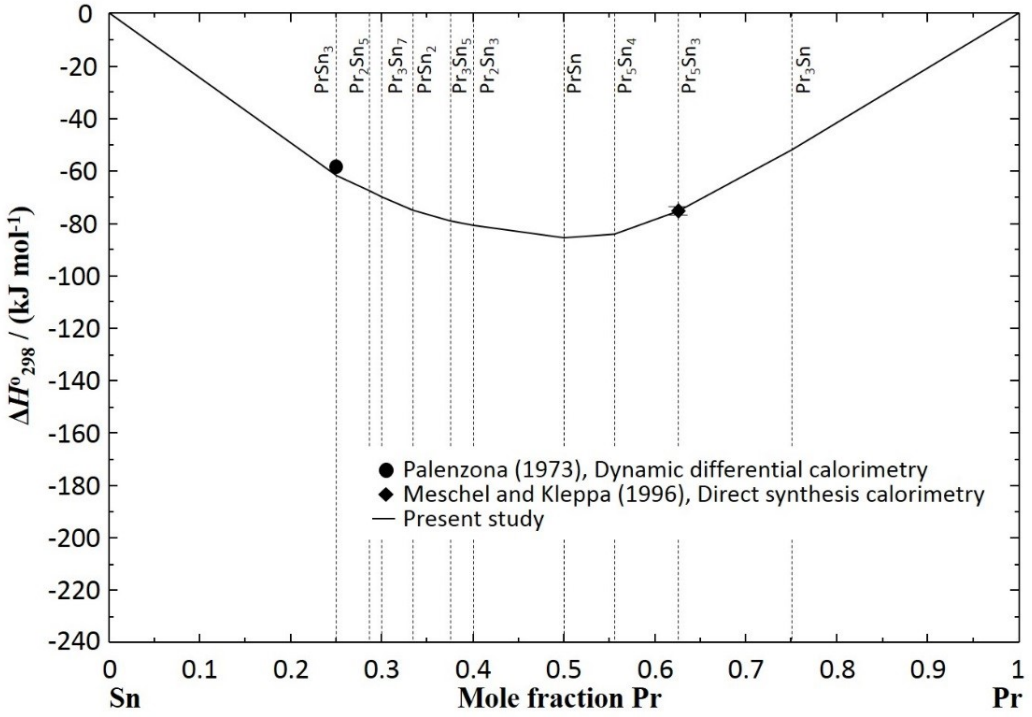


Fig. 18. Enthalpy of formation of the compounds in the Sn-Pr system at 298 K with experimental data.

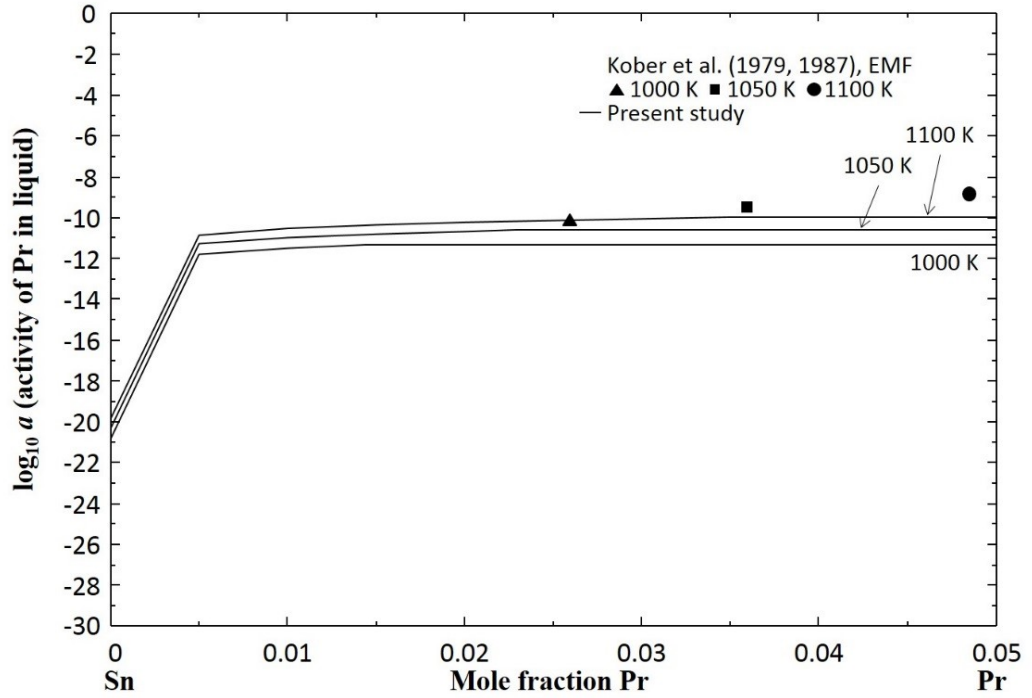


Fig. 19. The activity of Pr in liquid at 1000-1100 K (Sn-rich region).

2.4. The Sn-Nd system

Experimental data of the Sn-Nd system are presented in Fig. 20. The intermetallic compounds in this system were revealed by the crystallographic studies. The crystal structure and lattice parameters of Nd_xSn_y were reported: Nd_5Sn_3 (Mn_5Si_3 type) [17, 72, 82], Nd_5Sn_4 (Sm_5Ge_4 type) [20, 82], $Nd_{11}Sn_{10}$ ($Ho_{11}Ge_{10}$ type) [20, 83], Nd_2Sn_3 (Triclinic) [25], $NdSn_2$ ($NdSn_2$ type) [27, 84], Nd_3Sn_7 (Ce_3Sn_7 type) [27, 84], Nd_2Sn_5 (Ce_2Sn_5 type) [27, 84], $NdSn_3$ ($AuCu_3$ type) [15, 27, 84] and $NdSn_3$ (cubic) [55]. The melting temperature of $NdSn_3$, 1138 ºC, was determined by Palenzona [19] in the measurement of heat of formation of the $NdSn_3$ using dynamic differential calorimetry. Kulagina and Bayanov [85] determined the solubilities of Nd in liquid Sn at 773-973 K by the emf measurements. Later, Kulagina et al. [23] investigated the Sn-rich region of the phase diagram (up to 0.25 mole fraction of Nd) using thermal analysis and microscopic examination with the alloys prepared in sealed quartz vessels. The melting temperature of $NdSn_3$ was determined to be 1137 ± 4 ºC, which agrees with the previous work [19]. The temperature dependence of Nd solubility in liquid Sn was expressed by the equation, $\log(\text{at.\% Nd}) = 2.088 - 3826\ T^{-1}$. The solubilities were smaller than the values from the emf measurements [85]. The complete phase diagram of the Sn-Nd system was reported by Eremenko et al. [82, 83] from the DTA, XRD, and metallographic analyses. Initially, the system was investigated in the composition range of 0.5 to 1 mole fraction of Nd [82] with samples prepared from the initial materials, 99.85% Nd and 99.9999% Sn. Two intermetallic compounds were found: Nd_5Sn_3 (1640 ± 10 ºC), and Nd_5Sn_4 (1500 ºC) with eutectic reaction between Nd_5Sn_3 and bcc-Nd at 870 ± 10 ºC and 0.88 mole fraction of Nd. The solid solubility of Sn in bcc-Nd at 650 ºC was reported to be less than 0.01 mole fraction of Sn. The eutectoid reaction (bcc-Nd → dhcp-Nd + Nd_5Sn_3) occurred approximately at 820 ºC and at 0.94 mole fraction of Sn. In the same manner, the system was successively investigated in the composition range of 0 to 0.55 mole fraction of Nd [83]. The melting temperatures of Nd_5Sn_3 and Nd_5Sn_4 were slightly modified as about 1660 ºC and 1558 ± 11 ºC. Four intermediate phases were additionally found: $Nd_{11}Sn_{10}$ (1396 ± 15 ºC), NdSn (1257 ± 4 ºC), Nd_3Sn_5 (1130 ± 2 ºC), and $NdSn_3$ (1170 ºC). Like the Sn-Pr system, however, the eutectic reaction between $NdSn_3$ and NdSn reported by Eremenko et al. [83] was unfeasible. Saccone et al. [84] refined the system between 0.2 and 0.45 mole fraction of Nd by means of the DTA, XRD, and metallographic methods using

an electron probe micro-analyzer (EPMA). The samples were prepared in an induction furnace with sealed tantalum crucibles from initial materials, 99.9% Nd and 99.999% Sn. The melting temperature of $NdSn_3$ was modified to be 1150 °C. The eutectoid decomposition of Nd_3Sn_5 reported by Eremenko et al. [83] was modified as a peritectic melting (1140 °C). Three additional compounds, Nd_2Sn_5 (1135 °C), Nd_3Sn_7 (1145 °C), and $NdSn_2$ (1180 °C) were found between $NdSn_3$ and Nd_3Sn_5 with two eutectic reactions at 1130 °C and 0.395 mole fraction of Nd, and 1130 °C and 0.27 mole fraction of Nd. The existence of the Nd_2Sn_5, Nd_3Sn_7, and $NdSn_2$ were also revealed in several isothermal phase diagram investigation of the ternary systems containing Nd and Sn [86-89].

Experimental data of the thermodynamic properties of the Sn-Nd liquid were limited in literature. Peluso and Pool [77] and Lundin and Pool [78] determined the heat of solution of solid (dhcp) Nd (>99.7%) in liquid Sn (99.99%) at 750 K in the Nd-dilute composition range using a liquid-metal solution calorimeter. In the present study, the partial enthalpy of mixing of Nd at 750 K was calculated to be -251 kJ mol^{-1} and -294 kJ mol^{-1}, respectively, based on the reported data. Pratt and Morris [33] reported that the heat of solution in liquid Sn at 828 K was difficult to obtain due to the sluggish dissolution. They reported the heat of solution of solid (dhcp) Nd (>99.96%) in liquid Sn (99.999%) at 828 K in the Nd-dilute composition range were approximately -230 to -250 kJ mol^{-1}. Considering the heat effect between dhcp- and liquid-Nd, the partial enthalpy of mixing of Nd was about -238 to -258 kJ mol^{-1}. The experimental data of partial enthalpies of mixing from literature are presented in Fig. 21 (b).

Thermodynamic properties of the intermetallic compounds were investigated by several research groups. The experimental ΔH^{o}_{298} values are presented in Fig. 22. The ΔH^{o}_{298} of $NdSn_3$ was determined by Palenzona [19] using dynamic differential calorimetry with a conventional DTA apparatus. The enthalpy and entropy of fusion for $NdSn_3$ were also reported to be about 73.93 kJ mol^{-1} and 52.38 J K^{-1} mol^{-1}, respectively. Meschel and Kleppa [80] measured the ΔH^{o}_{298} of Nd_5Sn_3 using direct synthesis calorimetry. The heat content ($H_{1473} - H_{298}$) of Nd_5Sn_3 was also reported as 31.0 ± 1.3 kJ mol·$atom^{-1}$. The activities of Nd determined from the emf measurements were

presented in Fig. 23. Kulagina and Bayanov [85] reported the activities of Nd in liquid solution at 773 K, 873 K and 973 K. The Gibbs energy of formation of $NdSn_3$ was also determined to be -51.5 ± 0.1 kJ mol·atom^{-1} based on the measurements. Slightly smaller activity values for the same temperatures were again reported by Matigorova and Bayanov [90]. Kober et al. [91] determined the thermodynamic properties of the saturated solution (L+$NdSn_3$) in the temperature range of 673-973 K. The activity of Nd in the two phase (L+$NdSn_3$) at 1000 K was obtained from the reported partial Gibbs energy of Nd.

The thermodynamic optimization of the Sn-Nd system was performed for the first time. The optimized phase diagram of the Sn-Nd system in the present study is shown in Fig. 20. In the optimization, the nine intermetallic compounds, $NdSn_3$, Nd_2Sn_5, Nd_3Sn_7, $NdSn_2$, Nd_3Sn_5, NdSn, $Nd_{11}Sn_{10}$, Nd_5Sn_4, and Nd_5Sn_3 were modelled based on the experimental findings [82-84]. The refined results of Saccone et al. [84] between 0.2 and 0.45 mole fraction of Nd were reproduced in the present optimized phase diagram. The experimental data of Eremenko et al. [82, 83] were used to construct the phase diagram in the other composition range. Like the Sn-Pr system, the peritectic melting of Pr_5Sn_4 at about 1558 ºC which was reported by Erementko et al. [83] was adjusted as a congruent melting to reproduce the liquidus. However, the liquidus around 0.8 mole fraction of Nd in the optimized phase diagram is slightly lower than the experimental data [83]. The solid solubility of bcc-Nd phase was reproduced with one temperature independent excess Gibbs energy parameter and relatively large amount of excess Gibbs energy parameters including the two temperature dependent parameters were used to describe the dhcp-Nd phase in order to reproduce the solubility of Nd less than 0.01 mole fraction of Sn at 650 ºC [82].

The calculated thermodynamic properties with the optimized thermodynamic parameters are shown in Figs. 21-23. The calculated integral and partial enthalpy of mixing of the Sn-Nd liquid at 750 K are shown in Fig. 21(a) and (b). Similar to the Sn-Pr system, the experimental data of the partial enthalpy of mixing of Nd in the Nd-dilute solution at lower temperatures (about 750 K) [77, 78] were not used in the present study. The temperature independent parameters (i.e., enthalpy) for the excess Gibbs energy of liquid were estimated to be similar to the previous systems, which corresponds to the phase diagram [82-84] with small temperature dependent parameters (i.e.,

entropy). The ΔH^{o}_{298} of intermetallic compounds were determined based on the available experimental data. The experimental ΔH^{o}_{298} of $NdSn_3$ [19] and Nd_5Sn_3 [80] were reproduced as presented in Fig. 22. The ΔH^{o}_{298} of the rest compounds as well as the S^{o}_{298} of all compounds were evaluated in consideration of other thermodynamic properties and the phase diagram. The calculated heat content ($H_{1473} - H_{298}$) of Nd_5Sn_3 was about 10 kJ mol·atom^{-1} higher than the value reported by Meschel and Kleppa [80] and the calculated enthalpy of fusion of $NdSn_3$ (99.37 kJ mol^{-1}) was higher than the reported value, 73.93 kJ mol^{-1}, from the DTA measurement [19]. The activities of Nd in the solution containing up to 0.05 mole fraction of Nd were calculated at 773 K, 873 K, 973 K, and 1000 K and they were slightly lower than the experimental data [85, 90, 91] as seen in Fig. 23. The calculated Gibbs energy of formation of $NdSn_3$ was about 8 kJ mol·atom^{-1} more negative than the experimental value from the emf measurements [85]. The optimized thermodynamic parameters are listed in Table 7 and the calculated invariant reactions with the experimental data are tabulated in Table 8.

Table 7. Optimized model parameters for the Sn-Nd system.

Phase	Thermodynamic parameters
Liquid	Coordination Numbers
	i j Z_{ij}^{i} Z_{ij}^{j}
	Sn Nd 6 6
	Δg_{SnNd} / (J mol^{-1}) = -50208.0 – 25104.0 X_{SnSn} + (8368.0 + 4.184 T/K) X_{SnSn}^2
	+ (-12552.0 – 6.276 T/K) X_{NdNd} + 13388.8 X_{NdNd}^2
bcc-A2	${}^0L_{Sn,Nd}$ / (J mol^{-1}) = -175728.0
dhcp	${}^0L_{Sn,Nd}$ / (J mol^{-1}) = -54392.0 – 33.8904 T/K
	${}^1L_{Sn,Nd}$ / (J mol^{-1}) = -50208.0 – 33.8904 T/K
$NdSn_3$	ΔH_{298}^{o} = -249500 J mol^{-1}, S_{298}^{o} = 215.8 J K^{-1} mol^{-1}
	C_p / (J K^{-1} mol^{-1}) = 1 × C_p / (J K^{-1} mol^{-1}) (Nd, dhcp)
	+ 3 × modified C_p / (J K^{-1} mol^{-1}) (Sn, bct-A5)*
Nd_2Sn_5	ΔH_{298}^{o} = -469800 J mol^{-1}, S_{298}^{o} = 380.6 J K^{-1} mol^{-1}
	C_p / (J K^{-1} mol^{-1}) = 2 × C_p / (J K^{-1} mol^{-1}) (Nd, dhcp)
	+ 5 × modified C_p / (J K^{-1} mol^{-1}) (Sn, bct-A5)*
Nd_3Sn_7	ΔH_{298}^{o} = -690000 J mol^{-1}, S_{298}^{o} = 545.4 J K^{-1} mol^{-1}
	C_p / (J K^{-1} mol^{-1}) = 3 × C_p / (J K^{-1} mol^{-1}) (Nd, dhcp)
	+ 7 × modified C_p / (J K^{-1} mol^{-1}) (Sn, bct-A5)*
$NdSn_2$	ΔH_{298}^{o} = -220000 J mol^{-1}, S_{298}^{o} = 164.65 J K^{-1} mol^{-1}
	C_p / (J K^{-1} mol^{-1}) = 1 × C_p / (J K^{-1} mol^{-1}) (Nd, dhcp)
	+ 2 × modified C_p / (J K^{-1} mol^{-1}) (Sn, bct-A5)*
Nd_3Sn_5	ΔH_{298}^{o} = -610000 J mol^{-1}, S_{298}^{o} = 443.8 J K^{-1} mol^{-1}
	C_p / (J K^{-1} mol^{-1}) = 3 × C_p / (J K^{-1} mol^{-1}) (Nd, dhcp)
	+ 5 × modified C_p / (J K^{-1} mol^{-1}) (Sn, bct-A5)*

NdSn ΔH^{o}_{298} = -166900 J mol^{-1}, S^{o}_{298} = 115.485 J K^{-1} mol^{-1}

C_p / (J K^{-1} mol^{-1}) = 1 × C_p / (J K^{-1} mol^{-1}) (Nd, dhcp)
+ 1 × modified C_p / (J K^{-1} mol^{-1}) (Sn, bct-A5)*

$Nd_{11}Sn_{10}$ ΔH^{o}_{298} = -1732500 J mol^{-1}, S^{o}_{298} = 1246.8 J K^{-1} mol^{-1}

C_p / (J K^{-1} mol^{-1}) = 11 × C_p / (J K^{-1} mol^{-1}) (Nd, dhcp)
+ 10 × modified C_p / (J K^{-1} mol^{-1}) (Sn, bct-A5)*

Nd_5Sn_4 ΔH^{o}_{298} = -727000 J mol^{-1}, S^{o}_{298} = 551.0 J K^{-1} mol^{-1}

C_p / (J K^{-1} mol^{-1}) = 5 × C_p / (J K^{-1} mol^{-1}) (Nd, dhcp)
+ 4 × modified C_p / (J K^{-1} mol^{-1}) (Sn, bct-A5)*

Nd_5Sn_3 ΔH^{o}_{298} = -592800 J mol^{-1}, S^{o}_{298} = 511.95 J K^{-1} mol^{-1}

C_p / (J K^{-1} mol^{-1}) = 5 × C_p / (J K^{-1} mol^{-1}) (Nd, dhcp)
+ 3 × modified C_p / (J K^{-1} mol^{-1}) (Sn, bct-A5)*

*modified C_p / (J K^{-1} mol^{-1}) (Sn, bct-A5) = 24.477 + 5.472E-2 T/K – 40640.0 (T/K)$^{-2}$ – 6.469E-7 (T/K)^2

Table 8. Calculated invariant reactions and experimental data in the Sn-Nd system.

Type	Reaction	t (°C)	Reference
Eutectic	$L_{(X_{Nd}=<1E-5)} \rightarrow Sn_{(bct\text{-}A5,\ X_{Nd}=0)} + NdSn_3$	231.9	This work
	$L_{(X_{Nd}=*)} \rightarrow Sn_{(bct\text{-}A5,\ X_{Nd}=0)} + NdSn_3$	~230.0	[23]
Peritectic	$L_{(X_{Nd}=*)} + NdSn_3 \rightarrow Sn_{(bct\text{-}A5,\ X_{Nd}=0)}$	~240.0	[83]
Congruent	$L_{(X_{Nd}=0.25)} \leftrightarrow NdSn_3$	1150.2	This work
	$L_{(X_{Nd}=0.25)} \leftrightarrow NdSn_3$	1137.4	[23]
	$L_{(X_{Nd}=0.25)} \leftrightarrow NdSn_3$	1170.0	[83]
	$L_{(X_{Nd}=0.25)} \leftrightarrow NdSn_3$	1150.0	[84]
	T_m of $NdSn_3$	1138.0	[19]
Eutectic	$L_{(X_{Nd}=0.277)} \rightarrow NdSn_3 + Nd_2Sn_5$	1140.5	This work
	$L_{(X_{Nd}=\sim0.350)} \rightarrow NdSn_3 + PrSn$	1159±4	[83]
	$L_{(X_{Nd}=0.270)} \rightarrow NdSn_3 + Nd_2Sn_5$	1130.0	[84]

Peritectic	$L_{(X_{Nd}= 0.278)} + Nd_3Sn_7 \rightarrow Nd_2Sn_5$	1140.8	This work
	$L_{(X_{Nd}= \sim 0.270)} + Nd_3Sn_7 \rightarrow Nd_2Sn_5$	1135.0	[84]
Peritectic	$L_{(X_{Nd}= 0.286)} + NdSn_2 \rightarrow Nd_3Sn_7$	1145.1	This work
	$L_{(X_{Nd}= \sim 0.280)} + NdSn_2 \rightarrow Nd_3Sn_7$	1145.0	[84]
Congruent	$L_{(X_{Nd}= 0.333)} \leftrightarrow NdSn_2$	1180.0	This work
	$L_{(X_{Nd}= 0.333)} \leftrightarrow NdSn_2$	1180.0	[84]
Peritectoid	$NdSn_3 + NdSn \rightarrow Nd_3Sn_5$	1130±2	[83]
Peritectic	$NdSn_2 + L_{(X_{Nd}= 0.380)} \rightarrow Nd_3Sn_5$	1139.5	This work
	$NdSn_2 + L_{(X_{Nd}= \sim 0.390)} \rightarrow Nd_3Sn_5$	1140.0	[84]
Eutectic	$L_{(X_{Nd}= 0.391)} \rightarrow Nd_3Sn_5 + NdSn$	1135.1	This work
	$L_{(X_{Nd}= 0.395)} \rightarrow Nd_3Sn_5 + NdSn$	1130.0	[84]
Peritectic	$L_{(X_{Nd}= 0.420)} + Nd_{11}Sn_{10} \rightarrow NdSn$	1256.7	This work
	$L_{(X_{Nd}= \sim 0.430)} + Nd_{11}Sn_{10} \rightarrow NdSn$	1257±4	[83]
Peritectic	$L_{(X_{Nd}= 0.457)} + Nd_5Sn_4 \rightarrow Nd_{11}Sn_{10}$	1395.8	This work
	$L_{(X_{Nd}= \sim 0.450)} + Nd_5Sn_4 \rightarrow Nd_{11}Sn_{10}$	1396±15	[83]
Congruent	$L_{(X_{Nd}= 0.556)} \leftrightarrow Nd_5Sn_4$	1602.9	This work
Peritectic	$L_{(X_{Nd}= \sim 0.510)} + Nd_5Sn_3 \rightarrow Nd_5Sn_4$	1558±11	[83]
Eutectic	$L_{(X_{Nd}= 0.572)} \rightarrow Nd_5Sn_4 + Nd_5Sn_3$	1597.7	This work
Congruent	$L_{(X_{Nd}= 0.625)} \leftrightarrow Nd_5Sn_3$	1659.6	This work
	$L_{(X_{Nd}= 0.625)} \leftrightarrow Nd_5Sn_3$	1660.0	[83]
Eutectic	$L_{(X_{Nd}= 0.893)} \rightarrow Nd_5Sn_3 + Nd_{(bcc\text{-}A2,\ X_{Nd}= 0.962)}$	869.9	This work
	$L_{(X_{Nd}= 0.880)} \rightarrow Nd_5Sn_3 + Nd_{(bcc\text{-}A2,\ X_{Nd}= \sim 0.940)}$	870.0	[82]
Eutectoid	$Nd_{(bcc\text{-}A2,\ X_{Nd}= 0.966)} \rightarrow Nd_5Sn_3 + Nd_{(dhcp,\ X_{Nd}= 0.976)}$	819.5	This work
	$Nd_{(bcc\text{-}A2,\ X_{Nd}= 0.940)} \rightarrow Nd_5Sn_3 + Nd_{(dhcp,\ X_{Nd}= \sim 0.980)}$	820.0	[82]

* The exact compositions are not specified in the reference.

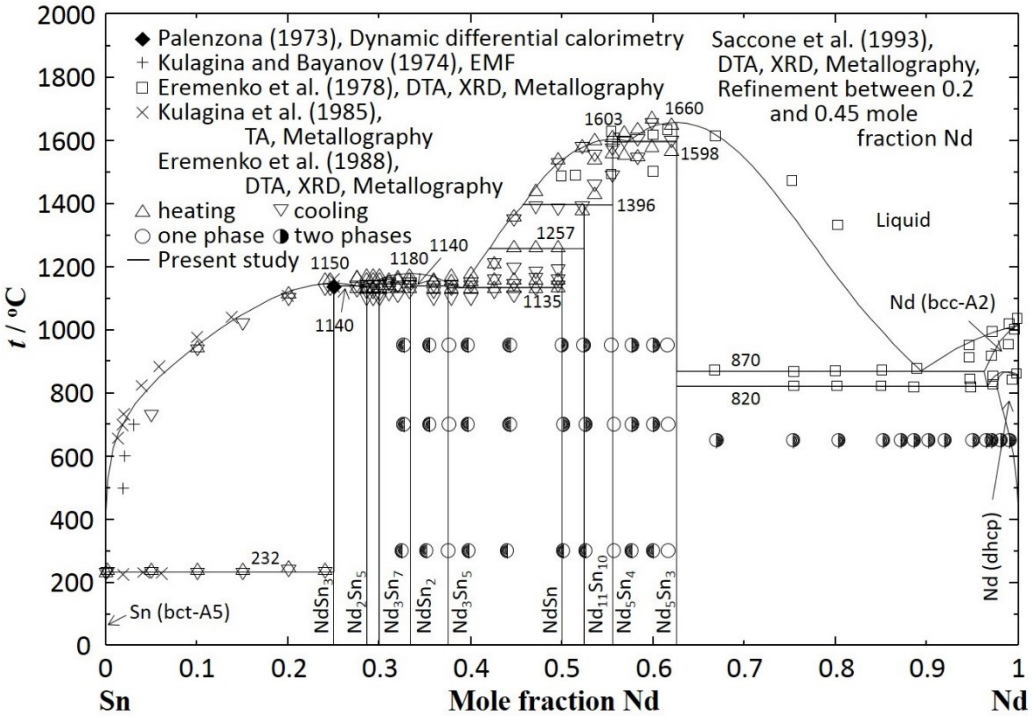


Fig. 20. The optimized Sn-Nd phase diagram with experimental data.

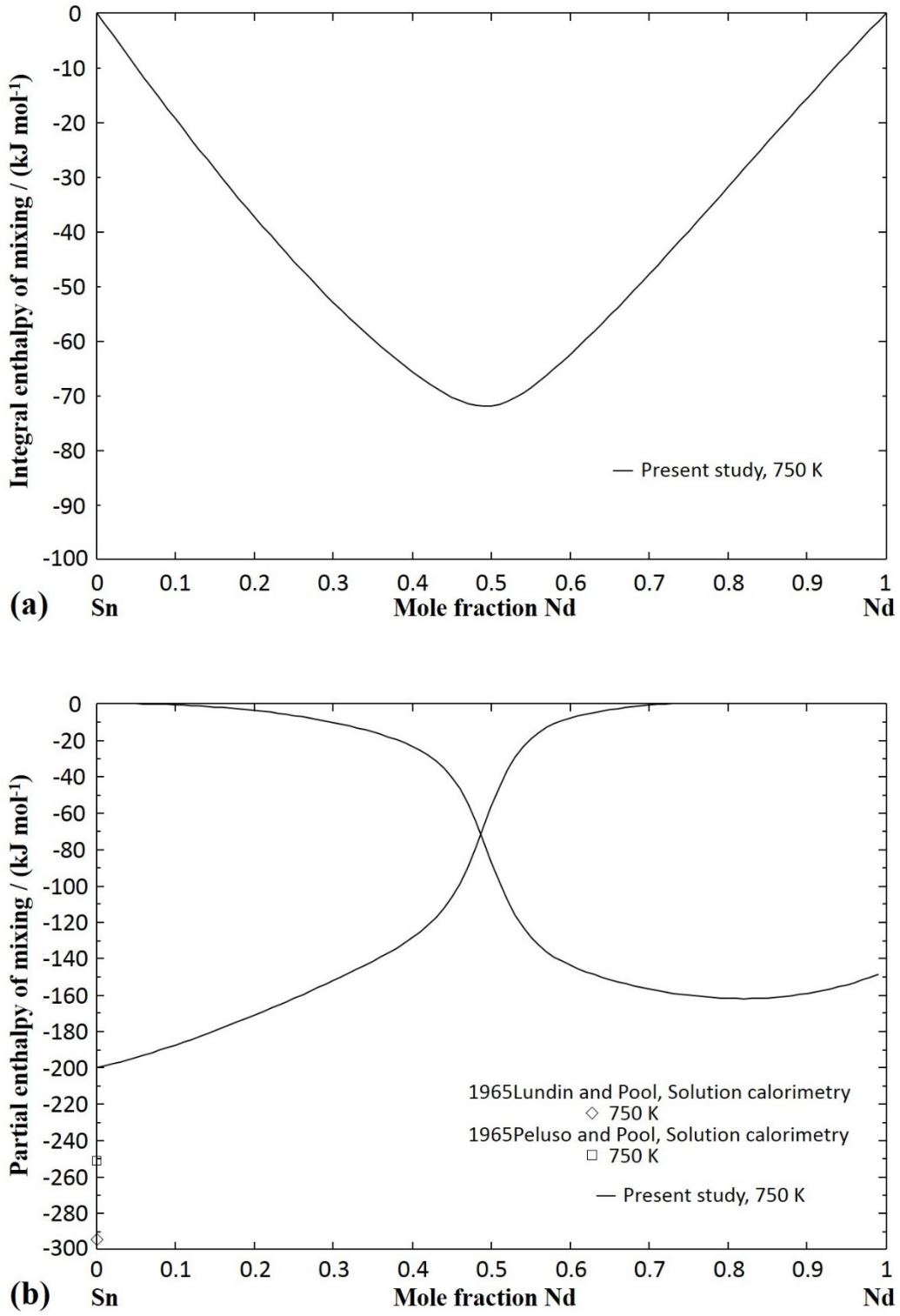


Fig. 21. (a) Integral enthalpy of mixing and (b) partial enthalpy of mixing of liquid Sn-Nd at 750 K with experimental data.

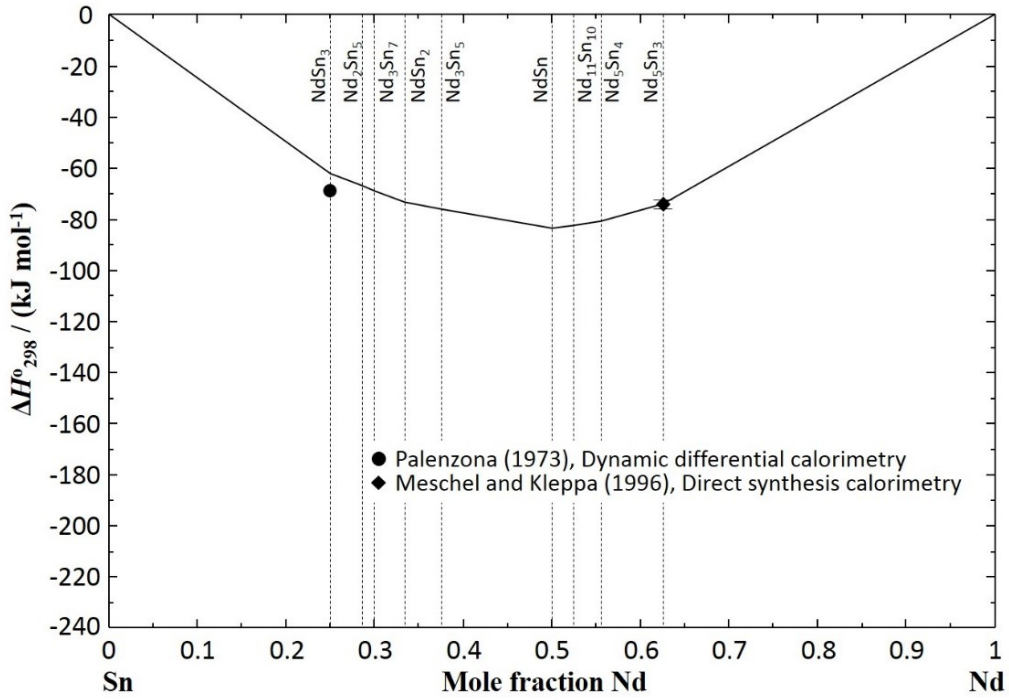


Fig. 22. Enthalpy of formation of the compounds in the Sn-Nd system at 298 K with experimental data.

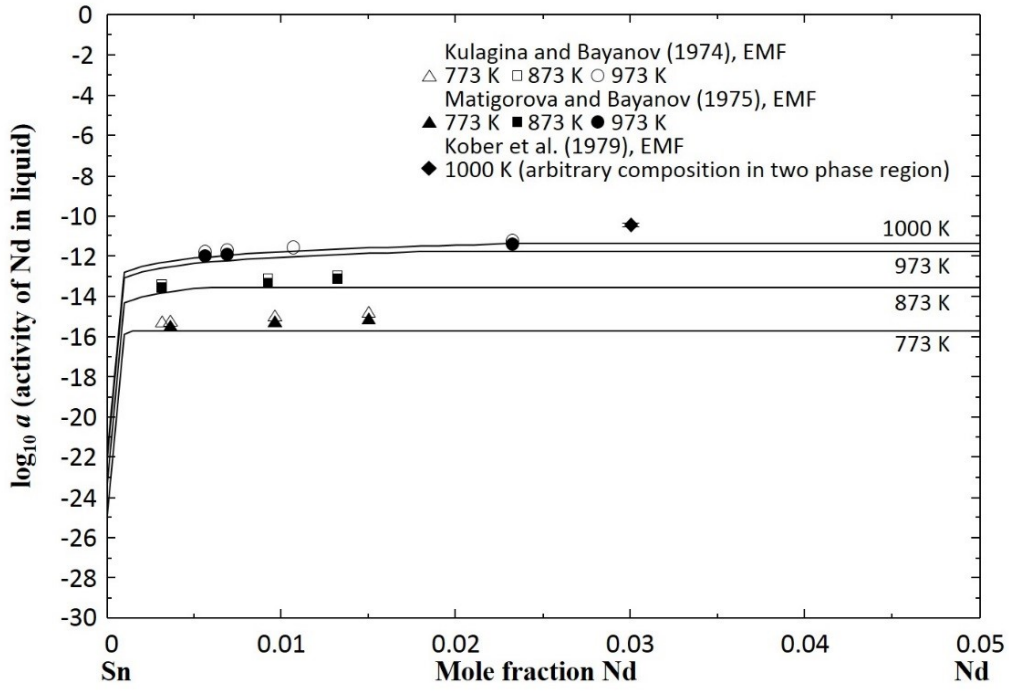


Fig. 23. The activity of Nd in liquid at 773-1000 K (Sn-rich region).

2.5. The Sn-Sm system

Experimental data of the Sn-Sm system are presented in Fig. 24. The intermetallic compounds in this system were revealed by the crystallographic studies. The crystal structure and lattice parameters of Sm_xSn_y were reported: Sm_5Sn_3 (Mn_5Si_3 type) [17, 72, 92], Sm_4Sn_3 (Th_3P_4 type) [92], Sm_5Sn_4 (Sm_5Ge_4 type) [20, 92], $Sm_{11}Sn_{10}$ ($Ho_{11}Ge_{10}$ type) [20], Sm_2Sn_3 (Triclinic) [25, 92, 93], $SmSn_2$ ($NdSn_2$ type) [27], Sm_3Sn_7 (Ce_3Sn_7 type) [27], Sm_2Sn_5 (Ce_2Sn_5 type) [27], $SmSn_3$ ($AuCu_3$ type) [15, 92] and $SmSn_3$ (cubic) [55]. The melting temperature of $SmSn_3$, 1072 ºC, was determined by Palenzona [19] in the measurement of heat of formation of the $SmSn_3$ using dynamic differential calorimetry. The phase diagram of the system in the whole composition range was investigated by Percheron [92] using DTA, XRD, and metallographic methods. The alloys were prepared in an induction furnace using tantalum crucibles with 99.8% Sm and 99.99% Sn. Six intermetallic compounds were found: Sm_5Sn_3 (1505 ºC, congruent), Sm_4Sn_3 (1440 ºC, peritectic), Sm_5Sn_4 (1420 ºC, peritectic), $Sm_{11}Sn_{10}$ (1240 ºC, peritectic, unstable below 1170 ºC), Sm_2Sn_3 (1105 ºC, peritectic), and $SmSn_3$ (1090 ºC, congruent) with two eutectic reactions at 906 ºC and 0.89 mole fraction of Sm, and 1080 ºC and 0.33 mole fraction of Sm. The solid solubility of Sn in Sm was determined to be less than 0.019 mole fraction of Sn at 900 ºC, and the solubility of Sm in Sn was less than 0.002 mole fraction of Sm at 200 ºC. However, the melting temperature of Sm_5Sn_3 (1505 ºC) (the highest melting temperature in the system) was exceptionally and significantly low compared with other RE_5Sn_3 phase. In fact, Eremenko et al. [94] predicted the melting temperature of RE_5Sn_3 by using the method which was based on the linear interpolation of the melting temperatures of RE_5Sn_3 versus the melting temperatures of pure RE metals. Similarly, the melting temperatures of $RE_{11}Sn_{10}$, RE_5Sn_4 and the eutectic temperature between RE and RE_5Sn_3 were predicted. The predicted melting temperature of Sm_5Sn_3 was 1687 ± 17 ºC. To verify their prediction, Eremenko et al. [94] prepared the alloys containing 0.61, 0.619, and 0.647 mole fraction of Sm in an arc furnace from the initial materials, 99.9995% Sn and 99.85% Sm and subsequently investigated the alloys by DTA. The melting temperature of Sm_5Sn_3 was 1605 ºC which was lower than the predicted value by about 80 ºC, but it was much higher than the one reported by Percheron [92]. The thermal effect (1520 ºC) for the alloy containing 0.61 mole fraction of Sm was corresponded to the melting temperature of Sm_5Sn_4. The Sm_4Sn_3 was not found

in the work of Eremenko et al. [94]. The thermal effect for the alloy containing 0.647 mole fraction of Sm which corresponds to the eutectic temperature between Sm_5Sn_3 and hcp-Sm occurred at 890 ºC, which were slightly lower than the value, 906 ºC, from the finding of Percheron [92]. The solubility of Sm in Sn at 727 ºC was determined to be 0.058 mole fraction of Sm by Lebedev et al. [95] from the emf measurements. Although the Sm_2Sn_5 and Sm_3Sn_7 phases were not found in the work of Percheron [92], the existence of them was revealed in the experimental isothermal phase diagram investigation of the ternary systems containing Sm and Sn [96, 97]. However, there is controversy concerning the stability of $Sm_{11}Sn_{10}$ phase. Unlike Percheron [92] who reported the decomposition of $Sm_{11}Sn_{10}$ by eutectoid reaction at 1170 ºC, the $Sm_{11}Sn_{10}$ was found in the experimental phase diagram investigation of the Sm-Fe-Sn system at 397 ºC [97]. Conversely, the $Sm_{11}Sn_{10}$ was not found in the experimental phase diagram investigation of the Sm-Cu-Sn system at 497 ºC [96].

The experimental data of the thermodynamic properties of the Sn-Sm liquid are presented in Fig. 25(a) and (b). The integral enthalpy of mixing of the Sm-Sn liquid at 1203 K up to 0.32 mole fraction of Sm was determined by Berrada et al. [98] using drop solution calorimetry as shown in Fig. 25(a). The partial enthalpy of mixing of Sm in Sn at infinite dilution was reported as -277 kJ mol^{-1} at 1203 K. Peluso and Pool [77] reported the heat of solution of solid Sm (>99.9%) in liquid Sn (99.99%) at 750 K in the Sm-dilute composition range using a liquid-metal solution calorimeter. The partial enthalpy of mixing of Sm at 750 K was calculated to be -233 kJ mol^{-1} based on the reported data. Similarly, Percheron et al. [99] determined the heat of solution of solid Sm (99.8%) in liquid Sn (99.95%) at 967 K in the Sm-dilute composition range. The partial enthalpy of mixing of Sm 967 K was calculated to be -194 kJ mol^{-1} based on the reported data. Like the Sn-Nd system, Pratt and Morris [33] reported the heat of solution of solid Sm (>99.96%) in liquid Sn (99.999%) at 828 K in the Sm-dilute composition range were approximately -230 to -250 kJ mol^{-1}. Considering the heat effect between dhcp- and liquid-Nd, the partial enthalpy of mixing of Nd was about -238 to -258 kJ mol^{-1}. The experimental partial enthalpies of mixing of Sm in the Sm-dilute solution are presented in Fig. 25(b). Very recently, Shevchenko et al. [100] determined the integral and partial enthalpies of mixing of the Sm-Sn liquid by means of an high temperature isoperibolic solution calorimeter at 1410-1670 K under purified He atmosphere with

150000 Pa. The high purity of initial materials, 99.88% Sm and 99.99% Sn, were used with the Mo crucibles. As the Sm is quite volatile, the measurements were conducted at as low temperature as possible. Therefore, the alloys, $0.87 < X_{Sm} < 1$, $0 < X_{Sm} < 0.36$, and $0.34 < X_{Sm} < 0.45$, were studied at 1450 K, 1480 K, and 1670 K, respectively. The measured enthalpy values were much less negative than the data of Berrada et al. [98], especially the partial enthalpy of mixing of Sm for Sm-dilute solution as seen in Fig. 25(b). The minimum value of the integral enthalpy of mixing at 1450 K was -67.7 ± 0.5 kJ mol^{-1} at 0.52 mole fraction of Sm.

Experimental ΔH^{o}_{298} of intermetallic compounds are presented in Fig. 26. Percheron et al. [99] determined the ΔH^{o}_{298} of $SmSn_3$, Sm_2Sn_3 and Sm_5Sn_3 using solution calorimetry. The ΔH^{o}_{298} of $SmSn_3$ was determined by Palenzona [19] using dynamic differential calorimetry with a conventional DTA apparatus. The enthalpy and entropy of fusion for $SmSn_3$ were also reported to be about 66.73 kJ mol^{-1} and 49.62 J K^{-1} mol^{-1}, respectively. Meschel and Kleppa [101] measured the ΔH^{o}_{298} of Sm_5Sn_3 using direct synthesis calorimetry. The heat content ($H_{1273} - H_{298}$) of Sm_5Sn_3 was also reported to be 27.1 ± 1.6 kJ mol·$atom^{-1}$. Lebedev et al. [95] determined the thermodynamic properties of the saturated solution (L+$SmSn_3$). The activity of Sm in the two phase (L+$SmSn_3$) at 1000 K was obtained from the emf values, which was 3.81×10^{-11}.

Along with measuring the enthalpy of mixing of liquid, Shevchenko et al. [100] performed the thermodynamic modeling of the system. The excess Gibbs energy of liquid was expressed by a random mixing model using Redlich-Kister polynomial. The integral and partial enthalpies of mixing of liquid calculated from the assessed parameters are compared with the experimental data [98, 100] in Fig. 25(a) and (b). The assessed ΔH^{o}_{298} of formation of compounds are shown in Fig. 26. The values are slightly less negative than the present study. The assessed phase diagram is not shown in the present work for simplicity. It is quite similar to the phase diagram in the present work except a few features. The Sm_4Sn_3 and $Sm_{11}Sn_{10}$ phases were not considered in their assessment. The Sn solubility in hcp-Sm was slightly underestimated than the present work. The liquidus in Sn-rich side was estimated about 80 ºC higher than the present work at 0.1 mole fraction of Sm.

The optimized phase diagram of the Sn-Sm system in the present study is shown in Fig. 24. In the optimization, the nine intermetallic compounds, $SmSn_3$, Sm_2Sn_5, Sm_3Sn_7, $SmSn_2$, Sm_2Sn_3, $Sm_{11}Sn_{10}$, Sm_5Sn_4, Sm_4Sn_3, and Sm_5Sn_3 were modelled based on the experimental findings [92, 94]. Although the Sm_2Sn_5, Sm_3Sn_7, $SmSn_2$ phases were not found in the study of Percheron [92], those phases were added in the phase diagram because the absence of the $SmSn_2$ phase caused the significantly low eutectic temperature between $SmSn_3$ and Sm_2Sn_3 which is implausible. Moreover, the existence of $SmSn_2$, Sm_3Sn_7, and Sm_2Sn_5 phases were revealed in the crystallographic study [27] and the isothermal phase diagram investigation of the ternary systems containing Sm and Sn [96, 97]. Even though there is a controversy regarding the stability of $Sm_{11}Sn_{10}$, it was believed that the phase is stable down to room temperature by considering the similarity with other $RE_{11}Sn_{10}$ phases as well as the experimental result [97]. Regarding the experimental data of Eremenko et al. [94], the melting temperatures of Sm_5Sn_3 was used as it was although it is slightly out of trend that the melting temperature of RE_5Sn_3 increases as the atomic number of RE increases. This will discussed in the Part II of the present study. Although Eremenko et al. [94] claimed the thermal effect at 1520 ºC corresponded the peritectic melting of Sm_5Sn_4, the Sm_4Sn_3 phase was experimentally found between Sm_5Sn_4 and Sm_5Sn_3 [92, 96, 97]. Therefore, the peritectic melting temperature of Sm_4Sn_3 was assumed as 1520 ºC and the peritectic melting temperature of Sm_5Sn_4 was assumed to be very similar to that of Sm_4Sn_3 which is 1516 ºC. The solid solubilities of Sn in bcc-Sm and hcp-Sm were reproduced with one temperature independent excess Gibbs energy parameter, respectively, based on the transformation temperature from bcc to hcp and the solubility at 900 ºC [92].

The calculated thermodynamic properties with the optimized thermodynamic parameters are shown in Figs. 25-26. The calculated integral and partial enthalpy of mixing of the Sn-Sm liquid at 1450 K are shown in Fig. 25(a) and (b). The temperature independent parameters (i.e., enthalpy) were determined based on the recent experimental data [100]. The calculated integral and partial enthalpies of mixing at 1450 K agrees well with the experimental findings [100]. The temperature dependent parameters (i.e., entropy) were added to reproduce the phase diagram [92, 94]. The ΔH^{o}_{298} of intermetallic compounds were determined based on the available experimental data. The experimental ΔH^{o}_{298} of $SmSn_3$ [19, 99], Sm_2Sn_3 [99], and Sm_5Sn_3 [101] were reproduced as

presented in Fig. 26. The ΔH^{o}_{298} of Sm_5Sn_3 by Percheron et al. [99] was too small to reproduce the stability of the Sm_5Sn_3 at lower temperature in the phase diagram. The ΔH^{o}_{298} of the rest compounds as well as the S^{o}_{298} of all compounds were evaluated in consideration of other thermodynamic properties and the phase diagram. The calculated heat content ($H_{1273} - H_{298}$) of Sm_5Sn_3 was about 9 kJ mol·atom^{-1} higher than the value reported by Meschel and Kleppa [101] and the calculated enthalpy of fusion of $SmSn_3$ (85.75 kJ mol^{-1}) was higher than the reported value, 66.73 kJ mol^{-1}, from the DTA measurement [19]. The optimized thermodynamic parameters are listed in Table 9 and the calculated invariant reactions with the experimental data are tabulated in Table 10.

Table 9. Optimized model parameters for the Sn-Sm system.

Phase	Thermodynamic parameters
Liquid	Coordination Numbers
	i j Z^i_{ij} Z^j_{ij}
	Sn Sm 6 6
	Δg_{SnSm} / (J mol^{-1}) = -49371.2 – (6276.0 + 5.0208 T/K) X_{SnSn}
	+ (-20920.0 + 3.3472 T/K) X_{SmSm} + 10878.4 X^2_{SmSm}
bcc-A2	${}^0L_{Sn,Sm}$ / (J mol^{-1}) = -158364.4
hcp-A3	${}^0L_{Sn,Sm}$ / (J mol^{-1}) = -158992.0
$SmSn_3$	ΔH^{o}_{298} = -234000 J mol^{-1}, S^{o}_{298} = 214.8 J K^{-1} mol^{-1}
	C_p / (J K^{-1} mol^{-1}) = 1 × C_p / (J K^{-1} mol^{-1}) (Sm, rhombohedral)
	+ 3 × modified C_p / (J K^{-1} mol^{-1}) (Sn, bct-A5)*
Sm_2Sn_5	ΔH^{o}_{298} = -440000 J mol^{-1}, S^{o}_{298} = 378.2 J K^{-1} mol^{-1}
	C_p / (J K^{-1} mol^{-1}) = 2 × C_p / (J K^{-1} mol^{-1}) (Sm, rhombohedral)
	+ 5 × modified C_p / (J K^{-1} mol^{-1}) (Sn, bct-A5)*

Sm_3Sn_7 ΔH^{o}_{298} = -645000 J mol^{-1}, S^{o}_{298} = 542.0 J K^{-1} mol^{-1}

C_p / (J K^{-1} mol^{-1}) = 3 × C_p / (J K^{-1} mol^{-1}) (Sm, rhombohedral)
+ 7 × modified C_p / (J K^{-1} mol^{-1}) (Sn, bct-A5)*

$SmSn_2$ ΔH^{o}_{298} = -205000 J mol^{-1}, S^{o}_{298} = 163.5 J K^{-1} mol^{-1}

C_p / (J K^{-1} mol^{-1}) = 1 × C_p / (J K^{-1} mol^{-1}) (Sm, rhombohedral)
+ 2 × modified C_p / (J K^{-1} mol^{-1}) (Sn, bct-A5)*

Sm_2Sn_3 ΔH^{o}_{298} = -374000 J mol^{-1}, S^{o}_{298} = 272.0 J K^{-1} mol^{-1}

C_p / (J K^{-1} mol^{-1}) = 2 × C_p / (J K^{-1} mol^{-1}) (Sm, rhombohedral)
+ 3 × modified C_p / (J K^{-1} mol^{-1}) (Sn, bct-A5)*

$Sm_{11}Sn_{10}$ ΔH^{o}_{298} = -1821000 J mol^{-1}, S^{o}_{298} = 1118.0 J K^{-1} mol^{-1}

C_p / (J K^{-1} mol^{-1}) = 11 × C_p / (J K^{-1} mol^{-1}) (Sm, rhombohedral)
+ 10 × modified C_p / (J K^{-1} mol^{-1}) (Sn, bct-A5)*

Sm_5Sn_4 ΔH^{o}_{298} = -770000 J mol^{-1}, S^{o}_{298} = 496.5 J K^{-1} mol^{-1}

C_p / (J K^{-1} mol^{-1}) = 5 × C_p / (J K^{-1} mol^{-1}) (Sm, rhombohedral)
+ 4 × modified C_p / (J K^{-1} mol^{-1}) (Sn, bct-A5)*

Sm_5Sn_3 ΔH^{o}_{298} = -623200 J mol^{-1}, S^{o}_{298} = 469.0 J K^{-1} mol^{-1}

C_p / (J K^{-1} mol^{-1}) = 5 × C_p / (J K^{-1} mol^{-1}) (Sm, rhombohedral)
+ 3 × modified C_p / (J K^{-1} mol^{-1}) (Sn, bct-A5)*

*modified C_p / (J K^{-1} mol^{-1}) (Sn, bct-A5) = 24.477 + 5.472E-2 T/K – 40640.0 (T/K)$^{-2}$ – 6.469E-7 (T/K)^2

Table 10. Calculated invariant reactions and experimental data in the Sn-Sm system.

Type	Reaction	t (°C)	Reference
Eutectic	$L_{(X_{Sm}=<1E-5)} \rightarrow Sn_{(bct\text{-}A5,\ X_{Sm}=0)} + SmSn_3$	231.9	This work
	$L_{(X_{Sm}=0.002)} \rightarrow Sn_{(bct\text{-}A5,\ X_{Sm}=0)} + SmSn_3$	229.0	[92]

Congruent	$L_{(X_{Sm}= 0.25)} \leftrightarrow SmSn_3$	1088.0	This work
	$L_{(X_{Sm}= 0.25)} \leftrightarrow SmSn_3$	1090.0	[92]
	T_m of $SmSn_3$	1072.0	[19]
Eutectic	$L_{(X_{Sm}= 0.279)} \rightarrow SmSn_3 + Sm_2Sn_5$	1079.6	This work
Congruent	$L_{(X_{Sm}= 0.286)} \leftrightarrow SmSn_3$	1080.0	This work
Eutectic	$L_{(X_{Sm}= 0.287)} \rightarrow Sm_2Sn_5 + Sm_3Sn_7$	1080.0	This work
Peritectic	$L_{(X_{Sm}= 0.297)} + SmSn_2 \rightarrow Sm_3Sn_7$	1081.5	This work
Congruent	$L_{(X_{Sm}= 0.333)} \leftrightarrow SmSn_2$	1096.2	This work
Eutectic	$L_{(X_{Sm}= 0.333)} \rightarrow SmSn_3 + Sm_2Sn_3$	1080.0	[92]
Eutectic	$L_{(X_{Sm}= 0.368)} \rightarrow SmSn_2 + Sm_2Sn_3$	1081.0	This work
Peritectic	$L_{(X_{Sm}= 0.390)} + Sm_{11}Sn_{10} \rightarrow Sm_2Sn_3$	1094.0	This work
	$L_{(X_{Sm}=0.39*)} + Sm_5Sn_4 \rightarrow Sm_2Sn_3$	1105.0	[92]
Peritectic	$L_{(X_{Sm}= 0.434)} + Sm_5Sn_4 \rightarrow Sm_{11}Sn_{10}$	1250.6	This work
	$L_{(X_{Sm}= 0.51*)} + Sm_5Sn_4 \rightarrow Sm_{11}Sn_{10}$	1240.0	[92]
Catatectic	$Sm_{11}Sn_{10} \rightarrow L_{(X_{Sm}= 0.45*)} + Sm_5Sn_4$	1170.0	[92]
Peritectic	$L_{(X_{Sm}= 0.552)} + Sm_4Sn_3 \rightarrow Sm_5Sn_4$	1516.2	This work
	$L_{(X_{Sm}= 0.55*)} + Sm_4Sn_3 \rightarrow Sm_5Sn_4$	1420.0	[92]
	$L_{(X_{Sm}= 0.53*)} + Sm_5Sn_3 \rightarrow Sm_5Sn_4$	1520.0	[94]
Peritectic	$L_{(X_{Sm}= 0.558)} + Sm_5Sn_3 \rightarrow Sm_4Sn_3$	1519.5	This work
	$L_{(X_{Sm}= 0.56*)} + Sm_5Sn_3 \rightarrow Sm_4Sn_3$	1440.0	[92]
Congruent	$L_{(X_{Sm}= 0.625)} \leftrightarrow Sm_5Sn_3$	1605.4	This work
	$L_{(X_{Sm}= 0.625)} \leftrightarrow Sm_5Sn_3$	1505.0	[92]
	$L_{(X_{Sm}= 0.625)} \leftrightarrow Sm_5Sn_3$	1605.0	[94]
Eutectic	$L_{(X_{Sm}= 0.900)} \rightarrow Sm_5Sn_3 + Sm_{(hcp\text{-}A3,\ X_{Sm}= 0.982)}$	899.6	This work
	$L_{(X_{Sm}= 0.890)} \rightarrow Sm_5Sn_3 + Sm_{(hcp\text{-}A3,\ X_{Sm}= 0.99*)}$	906.0	[92]
	$L_{(X_{Sm}= *)} \rightarrow Sm_5Sn_3 + Sm_{(hcp\text{-}A3,\ X_{Sm}= *)}$	890.0	[94]
Eutectoid	$Sm_{(bcc\text{-}A2,\ X_{Sm}= 0.982)} \rightarrow L_{(X_{Sm}= 0.909)} + Sm_{(hcp\text{-}A3,\ X_{Sm}= 0.983)}$	916.5	This work
	$Sm_{(bcc\text{-}A2,\ X_{Sm}= 0.989*)} \rightarrow L_{(X_{Sm}= 0.920*)} + Sm_{(hcp\text{-}A3,\ X_{Sm}= *)}$	916.0	[92]

* The exact compositions are not specified in the reference.

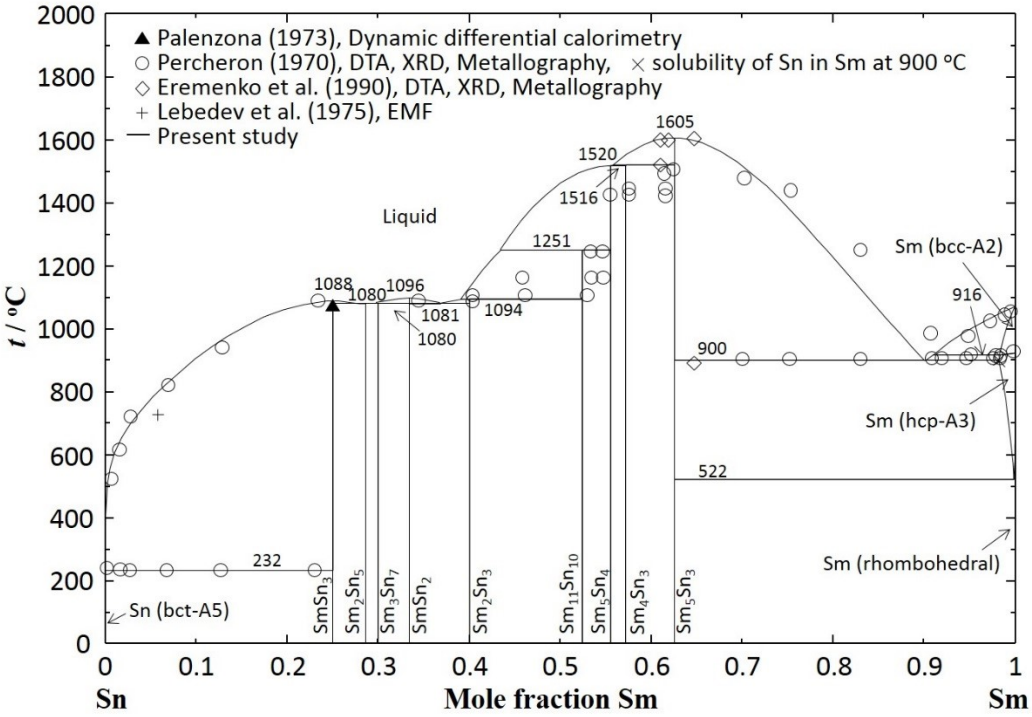


Fig. 24. The optimized Sn-Sm phase diagram with experimental data.

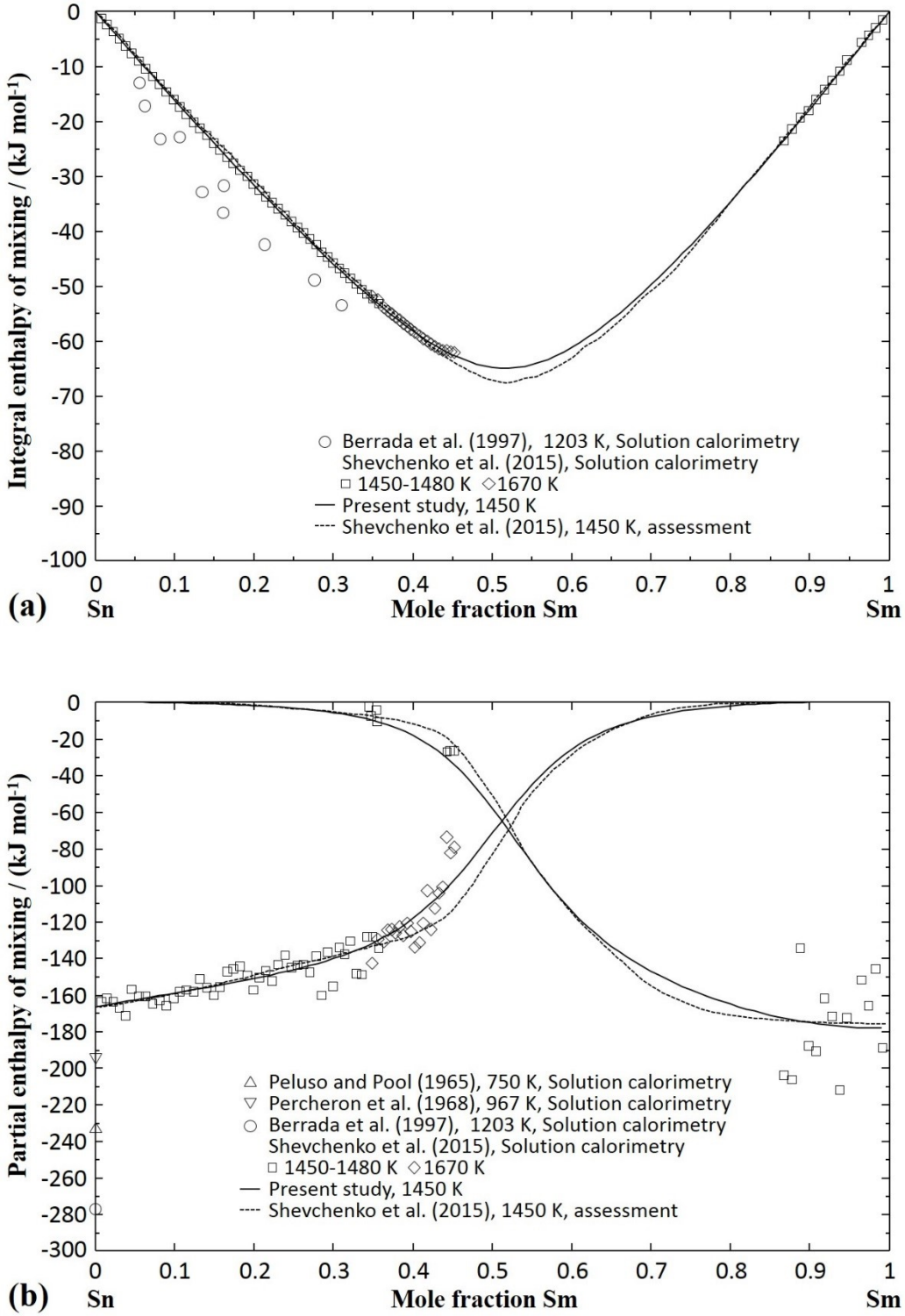


Fig. 25. (a) Integral enthalpy of mixing and (b) partial enthalpy of mixing of liquid Sn-Sm at 1450 K with experimental data and previous thermodynamic assessment.

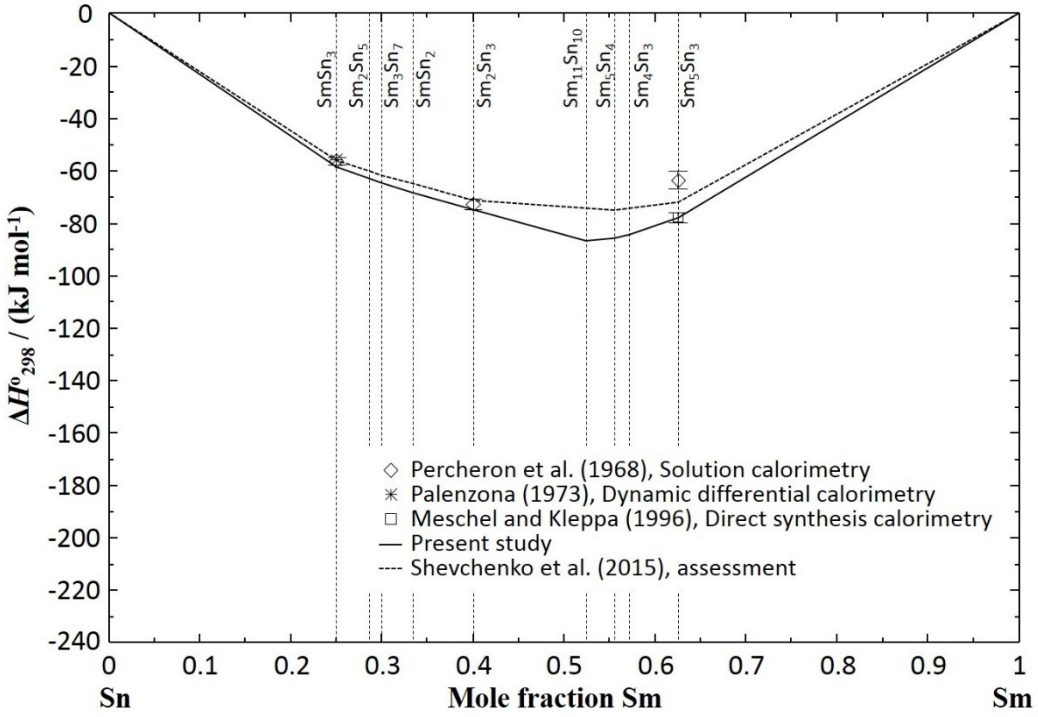


Fig. 26. Enthalpy of formation of the compounds in the Sn-Sm system at 298 K with experimental data.

3. References

[1] A.D. Pelton, S.A. Degterov, G. Eriksson, C. Robelin, Y. Dessureault, Metall. Mater. Trans. B, 31B (2000) 651-659.
[2] A.D. Pelton, P. Chartrand, Metall. Mater. Trans. A, 32A (2001) 1355-1360.
[3] I.-H. Jung, D.-H. Kang, W.-J. Park, N.J. Kim, S. Ahn, CALPHAD: Comput. Coupling Phase Diagrams Thermochem., 31 (2007) 192-200.
[4] D. Nassyrov, I.-H. Jung, CALPHAD: Comput. Coupling Phase Diagrams Thermochem., 33 (2009) 521-529.
[5] A.D. Pelton, M. Blander, Metall. Trans. B, 17B (1986) 805-815.
[6] P. Wu, G. Eriksson, A.D. Pelton, M. Blander, ISIJ Int., 33 (1993) 26-35.
[7] A.D. Pelton, M. Blander, In: Proc. 1984. pp. 281-294.
[8] M. Hillert, B. Jansson, B. Sundman, Z. Metallkd., 79 (1988) 81-87.
[9] A.T. Dinsdale, CALPHAD: Comput. Coupling Phase Diagrams Thermochem., 15 (1991) 317-425.
[10] J. Leitner, P. Vonka, D. Sedmidubsky, P. Svoboda, Thermochim. Acta, 497 (2010) 7-13.
[11] A.T. Dinsdale, Calphad, 15 (1991) 317-425.
[12] S. Cirafici, F. Canepa, G.L. Olcese, G. Costa, Solid State Commun., 44 (1982) 1507-1510.
[13] G. Canneri, Metall. Ital., 23 (1931) 803-823.
[14] A. Rossi, Atti Accad. Naz. Lincei, Cl. Sci. Fis., Mat. Nat., Rend., 17 (1933) 839-846.
[15] I.R. Harris, G.V. Raynor, J Less-Common Met, 9 (1965) 7-19.
[16] L. Rolla, A. Iandelli, G. Canneri, R. Vogel, Z. Metallkd., 35 (1943) 29-42.
[17] W. Jeitschko, E. Parthe, Acta Crystallogr., 22 (1967) 551-555.
[18] R.J. Gambino, N.R. Stemple, A.M. Toxen, J. Phys. Chem. Solids, 29 (1968) 295-302.
[19] A. Palenzona, Thermochimica Acta, 5 (1973) 473-480.
[20] M.L. Fornasini, F. Merlo, Atti Accad. Naz. Lincei, Cl. Sci. Fis., Mat. Natur., Rend., 50 (1971) 30-40.
[21] E. Franceschi, J. Less-Common Met., 66 (1979) 175-181.
[22] G. Borzone, A. Borsese, R. Ferro, Z. Anorg. Allg. Chem., 501 (1983) 199-208.
[23] N.G. Kulagina, A.P. Bayanov, N.M. Kulagin, Izv. Akad. Nauk SSSR, Met., (1985) 211-216.
[24] V.N. Eremenko, M.V. Bulanova, P.S. Martsenyuk, V.E. Listovnichii, Poroshk. Metall. (Kiev), (1989) 79-90.
[25] M.L. Fornasini, P. Manfrinetti, A. Palenzona, S.K. Dhar, Z. Naturforsch., B: Chem. Sci., 58 (2003) 521-527.
[26] V.I. Larchev, S.V. Popova, Fiz. Tverd. Tela (Leningrad), 19 (1977) 1463-1464.
[27] F. Weitzer, K. Hiebl, P. Rogl, J. Solid State Chem., 98 (1992) 291-300.
[28] Y. Zhuang, H. Deng, J. Liu, Q. Yao, J. Alloys Compd., 363 (2004) 223-226.
[29] Y. Zhan, Y. Xu, H. Xie, Z. Yu, Y. Wang, Y. Zhuang, J. Alloys Compd., 459 (2008) 174-176.
[30] Y. Zhan, H. Xie, J. Jiang, Y. Xu, Y. Wang, Y. Zhuang, J. Alloys Compd., 461 (2008) 570-573.
[31] X. Chen, Y. Zhuang, Y. Chen, Rare Met. (Beijing, China), 29 (2010) 567-571.
[32] J. Liang, C. Liao, Y. Du, Y. Tang, Y. Han, Y. He, S. Liu, J. Alloys Compd., 493 (2010) 122-127.
[33] J.N. Pratt, A.W.H. Morris, Journal of the Less Common Metals, 10 (1966) 91-97.

[34] J.R. Guadagno, M.J. Pool, S.S. Shen, P.J. Spencer, Trans. Met. Soc. AIME (Amer. Inst. Mining, Met., Petrol. Eng.), 243 (1968) 2013-2014.
[35] Y.O. Esin, S.P. Kolesnikov, V.M. Baev, M.S. Petrushevskii, P.V. Gel'd, Zh. Fiz. Khim., 55 (1981) 1587-1588.
[36] R. Castanet, C. R. Acad. Sci., Ser. 2, 298 (1984) 5-8.
[37] C. Colinet, A. Pasturel, A. Percheron-Guegan, J.C. Achard, J. Less-Common Met., 102 (1984) 167-177.
[38] C. Colinet, A. Bessoud, A. Pasturel, W. Mueller, J. Less-Common Met., 143 (1988) 265-278.
[39] F. Sommer, J. Schott, H.G. Krull, J. Less-Common Met., 144 (1988) 53-63.
[40] P. Lethuillier, J. Chaussy, Phys. Rev. B, 13 (1976) 3132-3134.
[41] G.A. Costa, F. Canepa, G.L. Olcese, Solid State Commun., 40 (1981) 169-172.
[42] M.J. Pool, J.R. Guadagno, Rep. 2410, July 1967, Denver Research Institute, (1967) 1-19.
[43] A. Borsese, G. Borzone, R. Ferro, J. Less-Common Met., 70 (1980) 213-216.
[44] V.I. Kober, I.F. Nichkov, S.P. Raspopin, P.S. Ignatchenko, Izv. Vyssh. Uchebn. Zaved., Tsvetn. Metall., (1982) 107-108.
[45] G.M. Lukashenko, R.I. Polotskaya, Ukr. Khim. Zh. (Russ. Ed.), 48 (1982) 357-358.
[46] N.G. Matigorova, A.P. Bayanov, Zh. Fiz. Khim., 45 (1971) 2440-2442.
[47] A. Palenzona, S. Cirafici, J. Phase Equilib., 13 (1992) 42-49.
[48] M. Huang, X. Su, F. Yin, P. Zhang, Z. Li, C. Chen, J. Alloys Compd., 309 (2000) 147-153.
[49] M. Idbenali, C. Servant, N. Selhaoui, L. Bouirden, CALPHAD: Comput. Coupling Phase Diagrams Thermochem., 33 (2009) 398-404.
[50] J. Kim, I.-H. Jung, The Journal of Chemical Thermodynamics, 81 (2015) 253-272.
[51] R. Vogel, Z. Anorg. Chem., 72 (1912) 319-328.
[52] W. Jeitschko, H. Nowotny, F. Benesovsky, Monatsh. Chem., 95 (1964) 1040-1043.
[53] G. Borzone, A. Borsese, R. Ferro, J. Less-Common Met., 85 (1982) 195-203.
[54] E.A. Franceschi, G.A. Costa, J. Therm. Anal., 34 (1988) 451-456.
[55] I.J. McColm, N.J. Clark, B. Mortimer, J. Inorg. Nucl. Chem., 33 (1971) 49-61.
[56] A. Iandelli, A. Palenzona, Atti Accad. Naz. Lincei, Cl. Sci. Fis., Mat. Nat., Rend., 40 (1966) 623-628.
[57] J.X. Boucherle, F. Givord, P. Lejay, J. Schweizer, A. Stunault, J. Magn. Magn. Mater., 63-64 (1987) 575-577.
[58] J.X. Boucherle, F. Givord, P. Lejay, J. Schweizer, A. Stunault, Acta Crystallogr., Sect. B: Struct. Sci., B44 (1988) 377-380.
[59] A.F. Ruggiero, G.L. Olcese, Atti Accad. Naz. Lincei, Cl. Sci. Fis., Mat. Nat., Rend., 37 (1964) 169-174.
[60] E.A. Franceschi, G.A. Costa, Lanthanide Actinide Res., 2 (1988) 407-413.
[61] L.F. Yamshchikov, V.A. Lebedev, I.F. Nichkov, S.P. Raspopin, O.K. Kokoulin, G.D. Korchinskii, Izv. Vyssh. Uchebn. Zaved., Tsvetn. Metall., (1980) 50-54.
[62] P. Riani, D. Mazzone, G. Zanicchi, R. Marazza, R. Ferro, Intermetallics, 5 (1997) 507-514.
[63] P. Riani, D. Mazzone, G. Zanicchi, R. Marazza, R. Ferro, F. Faudot, M. Harmelin, J. Phase Equilib., 19 (1998) 239-251.
[64] P. Boulet, D. Mazzone, H. Noel, P. Rogl, R. Ferro, J. Alloys Compd., 317-318 (2001) 350-356.
[65] L.F. Yamshchikov, V.A. Lebedev, I.F. Nichkov, S.P. Raspopin, V.G. Shein, Izv. Vyssh. Uchebn. Zaved., Tsvetn. Metall., (1983) 64-66.
[66] V.S. Sudavtsova, G.I. Batalin, Rasplavy, (1990) 106-109.

[67] T. Mathews, H.N. Jena, T. Subramanian, P.R. Vasudeva Rao, C.K. Mathews, J. Alloys Compd., 228 (1995) 1-5.
[68] L.F. Yamshchikov, V.A. Lebedev, V.I. Kober, I.F. Nichkov, S.P. Raspopin, Izv. Akad. Nauk SSSR, Met., (1977) 90-96.
[69] H.Q. Dong, X.M. Tao, T. Laurila, V. Vuorinen, M. Paulasto-Krockel, CALPHAD: Comput. Coupling Phase Diagrams Thermochem., 42 (2013) 38-50.
[70] H. Haschke, H. Nowotny, F. Benesovsky, Monatsh. Chem., 97 (1966) 716-717.
[71] V.N. Eremenko, M.V. Bulanova, V.G. Batalin, V.E. Listovnichii, Izv. Vyssh. Uchebn. Zaved., Tsvetn. Metall., (1987) 65-70.
[72] A. Palenzona, F. Merlo, Atti Accad. Naz. Lincei, Cl. Sci. Fis., Mat. Nat., Rend., 40 (1966) 617-622.
[73] V.N. Eremenko, M.V. Bulanova, V.E. Listovnichii, V.M. Petyukh, Ukr. Khim. Zh. (Russ. Ed.), 54 (1988) 787-795.
[74] V.I. Kober, I.F. Nichkov, C.P. Raspopin, V.V. Shvydenko, Izv. Vyssh. Uchebn. Zaved., Tsvetn. Metall., (1987) 111-112.
[75] D. Mazzone, P. Riani, G. Zanicchi, R. Marazza, R. Ferro, Intermetallics, 10 (2002) 801-809.
[76] D. Mazzone, R. Marazza, P. Riani, G. Zanicchi, G. Cacciamani, M.L. Fornasini, P. Manfrinetti, CALPHAD: Comput. Coupling Phase Diagrams Thermochem., 33 (2009) 31-43.
[77] R.F. Peluso, M.J. Pool, Proc. Conf. Rare Earth Res., 4th, Phoenix, Ariz., (1965) 269-279.
[78] C.E. Lundin, M.J. Pool, J. Less-Common Met., 9 (1965) 48-53.
[79] K. Sugiyama, A. Yamaguchi, M. Futoh, R. Settai, S. Araki, K. Miyake, T. Takeuchi, K. Kindo, Y. Ōnuki, Z. Kletowski, Journal of Magnetism and Magnetic Materials, 226–230, Part 1 (2001) 142-144.
[80] S.V. Meschel, O.J. Kleppa, Journal of Alloys and Compounds, 238 (1996) 180-186.
[81] V.I. Kober, I.F. Nichkov, S.P. Raspopin, V.M. Kuz'minykh, In: Proc. 1979. pp. 67-71.
[82] V.N. Eremenko, A.M. Khar'kova, I.M. Obushenko, Dopov. Akad. Nauk Ukr. RSR, Ser. A: Fiz.-Mat. Tekh. Nauki, (1978) 1132-1136.
[83] V.N. Eremenko, M.V. Bulanova, P.S. Martsenyuk, V.E. Listovnichii, Ukr. Khim. Zh. (Russ. Ed.), 54 (1988) 1240-1244.
[84] A. Saccone, D. Maccio, R. Ferro, J. Alloys Compd., 201 (1993) L9-L11.
[85] N.G. Kulagina, A.P. Bayanov, Zh. Fiz. Khim., 48 (1974) 466-467.
[86] F. Weitzer, P. Rogl, J. Phase Equilib., 14 (1993) 676-681.
[87] P. Salamakha, P. Demchenko, J. Stepien-Damm, J. Alloys Compd., 260 (1997) L1-L3.
[88] P. Riani, M.L. Fornasini, R. Marazza, D. Mazzone, G. Zanicchi, R. Ferro, Intermetallics, 7 (1999) 835-846.
[89] V. Babyuk, O. Bodak, L. Romaka, A. Tkachuk, Y. Gorelenko, J. Alloys Compd., 441 (2007) 107-110.
[90] N.G. Matigorova, A.P. Bayanov, v sb., Termodinam. Svoistva Metal. Splavov, (1975) 120-124.
[91] V.I. Kober, I.F. Nichkov, S.P. Raspopin, V.I. Kuz'minykh, In: Proc. 1979. pp. 72-76.
[92] A. Percheron, Colloques internationaux du Centre national de la recherche scientifique, 180 (1970) 165-172.
[93] A. Percheron, C. Henry la Blanchetais, C. R. Hebd. Seances Acad. Sci., Ser. C, 264 (1967) 2150-2152.
[94] V.N. Eremenko, M.V. Bulanova, P.S. Martsenyuk, In: Proc. 1990. pp. 70-100.

[95] V.A. Lebedev, V.V. Efremov, V.I. Kober, I.F. Nichkov, S.P. Raspopin, L.F. Yamshchikov, V.A. Kadochnikov, In: Proc. 1975. pp. 96-99.
[96] I.V. Senkovska, Y.S. Mudryk, L.P. Romaka, O.I. Bodak, J. Alloys Compd., 312 (2000) 124-129.
[97] J. Stepien-Damm, E. Galdecka, O.I. Bodak, B.D. Belan, J. Alloys Compd., 298 (2000) 26-29.
[98] A.-E.-A. Berrada, Y. Claire, M. Chafik el Idrissi, R. Castanet, J. Alloys Compd., 260 (1997) 193-195.
[99] A. Percheron, J.C. Mathieu, F. Trombe, C. R. Acad. Sci., Paris, Ser. C, 266 (1968) 848-851.
[100] M.O. Shevchenko, V.V. Berezutski, M.I. Ivanov, V.G. Kudin, V.S. Sudavtsova, J. Phase Equilib. Diffus., 36 (2015) 39-52.
[101] S.V. Meschel, O.J. Kleppa, J. Alloys Compd., 243 (1996) 186-193.

Appendix VII

Appendix VII

Critical evaluation and thermodynamic optimization of the Sn-RE systems: part II. Sn-RE system (RE = Gd, Tb, Dy, Ho, Er, Tm, Lu and Y)

Continuing the modeling of the Sn-RE systems, a critical evaluation and systematic optimization of all available thermodynamic data and phase diagrams of binary Sn-RE systems (RE (heavy rare earth) = Gd, Tb, Dy, Ho, Er, Tm, Lu and Y) has been conducted in the present study.

1. Critical evaluation and thermodynamic optimization

1.1. The Sn-Gd system

Experimental data of the Sn-Gd phase diagram are presented in Fig. 1. The intermetallic compounds in this system were revealed by the crystallographic studies. The crystal structure and lattice parameters of Gd_xSn_y were reported: Gd_5Sn_3 (Mn_5Si_3 type) [1, 2], Gd_5Sn_4 (Sm_5Ge_4 type) [3, 4], $Gd_{11}Sn_{10}$ ($Ho_{11}Ge_{10}$ type) [3], $GdSn_2$ ($ZrSi_2$ type) [5, 6], Gd_3Sn_7 (Gd_3Sn_7 type) [7, 8], $GdSn_{2.75}$ ($GdSn_{2.75}$ type) [7], α-$GdSn_3$ ($GdSn_3$ type, low temperature form) [7, 8], and β-$GdSn_3$ ($AuCu_3$ type, high temperature form) [9]. First, the melting temperature of $GdSn_3$, 915 ± 5 ºC (peritectic), was determined calorimetrically by Percheron et al. [10]. Kulagina and Bayanov [11] reported the solubility of Gd in liquid Sn to be 0.0178, 0.0209, and 0.0363 mole fraction of Gd at 500, 600, and 700 ºC, respectively, from the emf measurements. The phase diagram of the system in the whole composition range was first investigated by Liu and Zheng [12] using XRD and DTA. The alloys were prepared from 99.99% Sn and 99.9% Gd in alumina crucibles under Ar atmosphere, and were subsequently annealed under vacuum at 800 ºC for 60 days (0.5 to 1 atomic fraction of Gd), at 600 ºC for 70 days or at 800 ºC for 30 days (0.35 to 0.5 atomic fraction of Gd), and at 180 ºC for 200 days (<0.35 atomic fraction of Gd). Eight intermetallic compounds (with

melting temperature) were found: Gd_3Sn (1173 ºC, congruent), Gd_5Sn_3 (1243 ºC, congruent), Gd_5Sn_4 (1179 ºC, peritectic), Gd_8Sn_7 (1114 ºC, peritectic), $Gd_{11}Sn_{10}$ (1095 ºC, peritectic), Gd_3Sn_4 (995 ºC, peritectic), $GdSn_2$ (941 ºC, peritectic), and $GdSn_3$ (905 ºC, peritectic) with two eutectic reactions at 1141 ºC and 0.68 mole fraction of Gd, and 1103 ºC and 0.85 mole fraction of Gd. No appreciable mutual solid solubility was observed. However, the melting temperatures of Gd-rich compounds (i.e., Gd_5Sn_3, Gd_5Sn_4, and $Gd_{11}Sn_{10}$) determined by Liu and Zheng [12] were significantly low compared to the same stoichiometric other RE stannide compounds. In addition, the solubility of Gd in liquid in the Sn-rich alloys was too large compared to other experimental data [8, 13, 14]. Later, Kulagina et al. [14] investigated the Sn-rich region of the phase diagram (up to 0.25 mole fraction of Gd) using thermal analysis and microscopic examination with the alloys prepared in sealed quartz vessels. The temperature dependence of Gd solubility in liquid Sn was expressed by the equation, $\log(\text{at.\% Gd}) = 1.668 - 3166\ T^{-1}$. The solubilities were slightly smaller than the values from the previous emf measurement [13]. In addition, as for the $GdSn_3$, the melting temperature (1115 ± 4 ºC) and the type of melting (congruent) reported by Kulagina et al. [14] disagree with the other data [8, 10]. Eremenko et al. [15] predicted the melting temperature of RE_5Sn_3 by using the method which was based on the linear interpolation of the melting temperatures of RE_5Sn_3 versus the melting temperatures of pure RE metals. Similarly, the melting temperatures of $RE_{11}Sn_{10}$, RE_5Sn_4 and the eutectic temperature between RE and RE_5Sn_3 were predicted. The predicted melting temperatures of Gd_5Sn_3, Gd_5Sn_4, $Gd_{11}Sn_{10}$ and the eutectic temperature were 1819 ± 17, 1678 ± 156, 1521 ± 88, and 1097 ± 64 ºC, respectively. To verify their prediction, Eremenko et al. [15] prepared the alloys containing 0.622, 0.641, 0.662, and 0.9 mole fraction of Gd in an arc furnace from the initial materials, 99.9995% Sn and 99.85% Gd and subsequently investigated the alloys by DTA. The melting temperature of Gd_5Sn_3 was found to be 1820 ºC which was very close to the predicted value, and this is much more reasonable than the one reported by Liu and Zheng [12]. The eutectic temperature was found to be about 1120 ºC and the existence of Gd_3Sn was withdrawn from the thermal effect of the alloys. Unfortunately, the melting temperatures of Gd_5Sn_4 and $Gd_{11}Sn_{10}$ were not verified. Later again, Palenzona and Manfrinetti [8] investigated the Sn-rich side of the system up to 0.35 mole fraction of Gd using DTA, XRD, and microscopic analysis. The alloys were prepared from the initial materials, 99.99 wt.% Sn and 99.5-99.8 wt.% Gd using a sealed Mo crucible in an induction furnace. Three incongruent melting compounds were found with respective liquidus, $GdSn_2$ (1140 ºC), Gd_3Sn_7

(945 ºC), and $GdSn_3$ (920 ºC). The polymorphic transformation of $GdSn_3$ was also found at 390 ºC. However, the experimental data were unfortunately not reported. The data points in Fig. 1 were extracted from the reported graph [8]. There is controversy regarding the existence of Gd_4Sn_{11} ($GdSn_{2.75}$) and Gd_3Sn_4 in the several isothermal phase diagram investigations for the ternary systems containing Sn and Gd, with Gd_4Sn_{11} [16, 17], without Gd_4Sn_{11} [18, 19], with Gd_3Sn_4 [18], and without Gd_3Sn_4 [16, 17, 19].

The experimental data of the thermodynamic properties of the Sn-Gd liquid are presented in Fig. 2(a) and (b). Bacha et al. [20] determined the partial enthalpy of mixing of Gd in Sn at infinite dilution using solution calorimetry to be -175.3 kJ mol^{-1} at 969 K from high purity materials, 99.97% Sn and 99.9% Gd. Similarly, Sommer et al. [21] measured the enthalpy of dissolution of solid Gd in liquid Sn up to 0.1 mole fraction of Gd at 1095, 1274, and 1468 K from high purity materials, 99.96% Sn and 99.9% Gd. The partial enthalpy of mixing values of Gd were obtained by considering the heat content of Gd from room temperature to the measurement temperature based on the dissolution enthalpy, in the present study. Then, the partial enthalpy values were used to obtain the integral enthalpy of mixing as shown in Fig. 2(a) in the present study.

The standard enthalpy of formation (ΔH°_{298}) of $GdSn_3$ and Gd_5Sn_3 were experimentally determined and the experimental values are shown in Fig. 3. Bacha et al. [20] determined the ΔH°_{298} of $GdSn_3$ using solution calorimetry. The same result was reported in the work of Percheron et al. [10]. Meschel and Kleppa [22] measured the ΔH°_{298} of Gd_5Sn_3 using direct synthesis calorimetry. The heat content ($H_{1473} - H_{298}$) of Gd_5Sn_3 was also reported to be 32.2 ± 1.8 kJ mol·$atom^{-1}$. The Gibbs energy of formation (ΔG°) of $GdSn_3$ at 973 K from the references of solid Gd and liquid Sn was determined to be -44.35 ± 0.2 kJ mol·$atom^{-1}$ by Kulagina and Bayanov [13] from the emf measurement. Later, Yamshchikov [23] reported three different values of the activity of Gd in Gd saturated liquid (L + $GdSn_3$) at 800 K from the previous emf measurements. The values (logarithmic scale) were -11.85 [24] and -12.28 [13, 25].

An extensive literature review of the Sn-Gd system was performed by Palenzona and Cirafici in 1991 [26]. The experimental investigations regarding the phase diagram and thermodynamic properties including crystallographic studies were widely reviewed. A brief review of the system was also made by Okamoto [27]. However, the phase diagram of the system in the two review was constructed mostly based on the work of Liu and Zheng [12], which seems to be inaccurate in particular for the high melting temperature compounds.

The optimized phase diagram of the Sn-Gd system in the present study is shown in Fig. 1. In the optimization, the phase diagram in the composition up to 0.333 mole fraction of Gd was constructed based on the work of Palenzona and Manfrinetti [8] that studied the RE-Sn systems systematically. However, the peritectic melting of $GdSn_2$ was unlikely to be reproduced when considering the liquidus slope around between $GdSn_2$ and $Gd_{11}Sn_{10}$. Additionally, the Gd_4Sn_{11} phase was added because the existence of the Gd_4Sn_{11} was confirmed by the isothermal phase diagram investigation of the ternary systems containing Gd and Sn [16, 17]. The melting temperature of Gd_4Sn_{11} was assumed to be between the melting temperatures of Gd_3Sn_7 and $GdSn_3$. The allotropic transformation of $GdSn_3$ was reproduced by accepting the transformation temperature, 390 °C [8] with the assumption of the enthalpy of the transformation, 1 kJ mol^{-1}. The other side of the phase diagram above 0.625 mole fraction of Gd was constructed based on the work of Eremenko et al. [15] including the melting temperature of Gd_5Sn_3 and the eutectic temperature of hcp-Gd and Gd_5Sn_3. Unfortunately, the melting temperatures of Gd_5Sn_4 and $Gd_{11}Sn_{10}$ were not available because the data of Liu and Zheng [12] seemed to be very unlikely. Thus, the melting temperature of Gd_5Sn_4 and $Gd_{11}Sn_{10}$ were assumed based on the systematic analysis which will be discussed in later chapter. The terminal solid solubility was neglected.

The calculated thermodynamic properties with the optimized thermodynamic parameters are shown in Fig. 2-4. The experimental data of the integral and partial enthalpies of mixing of Sn-rich liquid [20, 21] were well reproduced by the present optimization. No temperature dependent parameters (i.e., entropy) were added. The calculated ΔH^{o}_{298} of compounds agreed with the experimental data [10, 20, 22] as seen in Fig. 3. The ΔH^{o}_{298} of the other compounds and the ΔS^{o}_{298} of all compounds were reasonably estimated by considering the stabilities and the melting

temperatures of the compounds and the liquidus in the phase diagram. The calculated heat content ($H_{1473} - H_{298}$) of Gd_5Sn_3 was 35.96 kJ mol·atom^{-1}, which is comparable with the value of Meschel and Kleppa [22]. Compared with the emf measurement [13], the calculated ΔG^{o}_{973} of $GdSn_3$ from the references of solid Gd and liquid Sn was -45.63 kJ mol·atom^{-1} corresponding to the reported value. The calculated activity of Gd in Gd saturated liquid (L + $GdSn_3$) at 800 K was -12.887 in logarithmic scale, which is still comparable with the experimental values [13, 24, 25]. The optimized thermodynamic parameters are listed in Table 1 and the calculated invariant reactions with the experimental data are tabulated in Table 2.

Table 1. Optimized model parameters for the Sn-Gd system.

Phase	Thermodynamic parameters
Liquid	Coordination Numbers
	i j Z_{ij}^{i} Z_{ij}^{j}
	Sn Gd 6 6
	Δg_{SnGd} / (J mol^{-1}) = -50208.0 – 5020.8 X_{SnSn} – 30124.8 X_{GdGd}
	+ 29288.0 X_{GdGd}^{2}
α-$GdSn_3$	ΔH^{o}_{298} = -207700 J mol^{-1}, S^{o}_{298} = 219.47 J K^{-1} mol^{-1}
	C_p / (J K^{-1} mol^{-1}) = 1 × C_p / (J K^{-1} mol^{-1}) (Gd, hcp-A3)
	+ 3 × modified C_p / (J K^{-1} mol^{-1}) (Sn, bct-A5)*
β-$GdSn_3$	$\Delta_{trs} H^{\alpha\rightarrow\beta}$ = 1000 J mol^{-1}, $T_{trs}^{\alpha\rightarrow\beta}$ = 663.15 K
	C_p / (J K^{-1} mol^{-1}) = 1 × C_p / (J K^{-1} mol^{-1}) (Tb, hcp-A3)
	+ 3 × modified C_p / (J K^{-1} mol^{-1}) (Sn, bct-A5)*
Gd_4Sn_{11}	ΔH^{o}_{298} = -828000 J mol^{-1}, S^{o}_{298} = 820.0 J K^{-1} mol^{-1}
	C_p / (J K^{-1} mol^{-1}) = 4 × C_p / (J K^{-1} mol^{-1}) (Gd, hcp-A3)
	+ 11 × modified C_p / (J K^{-1} mol^{-1}) (Sn, bct-A5)*

Gd_3Sn_7 ΔH^{o}_{298} = -610050 J mol^{-1}, S^{o}_{298} = 545.0 J K^{-1} mol^{-1}

C_p / (J K^{-1} mol^{-1}) = 3 × C_p / (J K^{-1} mol^{-1}) (Gd, hcp-A3)
+ 7 × modified C_p / (J K^{-1} mol^{-1}) (Sn, bct-A5)*

$GdSn_2$ ΔH^{o}_{298} = -198000 J mol^{-1}, S^{o}_{298} = 164. 8 J K^{-1} mol^{-1}

C_p / (J K^{-1} mol^{-1}) = 1 × C_p / (J K^{-1} mol^{-1}) (Gd, hcp-A3)
+ 2 × modified C_p / (J K^{-1} mol^{-1}) (Sn, bct-A5)*

$Gd_{11}Sn_{10}$ ΔH^{o}_{298} = -1724200 J mol^{-1}, S^{o}_{298} = 1227.0 J K^{-1} mol^{-1}

C_p / (J K^{-1} mol^{-1}) = 11 × C_p / (J K^{-1} mol^{-1}) (Gd, hcp-A3)
+ 10 × modified C_p / (J K^{-1} mol^{-1}) (Sn, bct-A5)*

Gd_5Sn_4 ΔH^{o}_{298} = -734100 J mol^{-1}, S^{o}_{298} = 536.0 J K^{-1} mol^{-1}

C_p / (J K^{-1} mol^{-1}) = 5 × C_p / (J K^{-1} mol^{-1}) (Gd, hcp-A3)
+ 4 × modified C_p / (J K^{-1} mol^{-1}) (Sn, bct-A5)*

Gd_5Sn_3 ΔH^{o}_{298} = -628000 J mol^{-1}, S^{o}_{298} = 489.15 J K^{-1} mol^{-1}

C_p / (J K^{-1} mol^{-1}) = 5 × C_p / (J K^{-1} mol^{-1}) (Gd, hcp-A3)
+ 3 × modified C_p / (J K^{-1} mol^{-1}) (Sn, bct-A5)*

*modified C_p / (J K^{-1} mol^{-1}) (Sn, bct-A5) = 24.477 + 5.472E-2 T/K – 40640.0 (T/K)$^{-2}$ – 6.469E-7 (T/K)^2

Table 2. Calculated invariant reactions and experimental data in the Sn-Gd system.

Type	Reaction	t (°C)	Reference
Eutectic	$L_{(X_{Gd}=<1E-5)} \rightarrow Sn_{(bct\text{-}A5,\ X_{Gd}=0)} + GdSn_3$	231.9	This work
	$L_{(X_{Gd}=*)} \rightarrow Sn_{(bct\text{-}A5,\ X_{Gd}=0)} + GdSn_3$	232.0	[12]
	$L_{(X_{Gd}=*)} \rightarrow Sn_{(bct\text{-}A5,\ X_{Gd}=0)} + GdSn_3$	~225.0	[14]
	$L_{(X_{Gd}=*)} \rightarrow Sn_{(bct\text{-}A5,\ X_{Gd}=0)} + GdSn_3$	230.0	[8]
Peritectic	$L_{(X_{Gd}=0.149)} + Gd_4Sn_{11} \rightarrow GdSn_3$	910.2	This work
	$L_{(X_{Gd}=\sim0.209)} + GdSn_2 \rightarrow GdSn_3$	905.0	[12]
	$L_{(X_{Gd}=\sim0.139)} + Gd_3Sn_7 \rightarrow GdSn_3$	920.0	[8]

Congruent	$L_{(X_{Gd}= 0.25)} \leftrightarrow GdSn_3$	1115±4	[14]
	T_m of $LaSn_3$	915.0	[10]
Allotropic	α-$GdSn_3 \leftrightarrow \beta$-$GdSn_3$	390.0	This work
Peritectic	$L_{(X_{Gd}= 0.160)} + Gd_3Sn_7 \rightarrow Gd_4Sn_{11}$	925.8	This work
Peritectic	$L_{(X_{Gd}= 0.171)} + GdSn_2 \rightarrow Gd_3Sn_7$	945.3	This work
	$L_{(X_{Gd}= \sim 0.158)} + GdSn_2 \rightarrow Gd_3Sn_7$	945.0	[8]
Peritectic	$L_{(X_{Gd}= \sim 0.224)} + Gd_3Sn_4 \rightarrow GdSn_2$	941.0	[12]
	$L_{(X_{Gd}= \sim 0.304)} + ** \rightarrow GdSn_2$	1140.0	[8]
Peritectic	$L_{(X_{Gd}= \sim 0.251)} + Gd_{11}Sn_{10} \rightarrow Gd_3Sn_4$	995.0	[12]
Peritectic	$L_{(X_{Gd}= \sim 0.327)} + Gd_8Sn_7 \rightarrow Gd_{11}Sn_{10}$	1095.0	[12]
Congruent	$L_{(X_{Gd}= 0.333)} \leftrightarrow GdSn_2$	1139.8	This work
Peritectic	$L_{(X_{Gd}= \sim 0.342)} + Gd_5Sn_4 \rightarrow Gd_8Sn_7$	1114.0	[12]
Eutectic	$L_{(X_{Gd}= 0.361)} \rightarrow GdSn_2 + Gd_{11}Sn_{10}$	1131.4	This work
Peritectic	$L_{(X_{Gd}= 0.485)} + Gd_5Sn_4 \rightarrow Gd_{11}Sn_{10}$	1560.3	This work
Peritectic	$L_{(X_{Gd}= \sim 0.502)} + Gd_5Sn_3 \rightarrow Gd_5Sn_4$	1179.0	[12]
Peritectic	$L_{(X_{Gd}= 0.555)} + Gd_5Sn_3 \rightarrow Gd_5Sn_4$	1680.7	This work
Congruent	$L_{(X_{Gd}= 0.625)} \leftrightarrow Gd_5Sn_3$	1820.0	This work
	$L_{(X_{Gd}= 0.625)} \leftrightarrow Gd_5Sn_3$	1820.0	[15]
Eutectic	$L_{(X_{Gd}= \sim 0.68)} \rightarrow Gd_5Sn_3 + Gd_3Sn$	1141.0	[12]
Eutectic	$L_{(X_{Gd}= 0.854)} \rightarrow Gd_5Sn_3 + Gd_{(hcp\text{-}A3,\ X_{Gd}= 1)}$	1125.8	This work
	$L_{(X_{Gd}= \sim 0.89)} \rightarrow Gd_5Sn_3 + Gd_{(hcp\text{-}A3,\ X_{Gd}= *)}$	1120.0	[15]
Eutectic	$L_{(X_{Gd}= \sim 0.85)} \rightarrow Gd_3Sn + Gd_{(hcp\text{-}A3,\ X_{Gd}= 1)}$	1103.0	[12]

* The exact compositions were not specified in the reference.
** The phase was not identified.

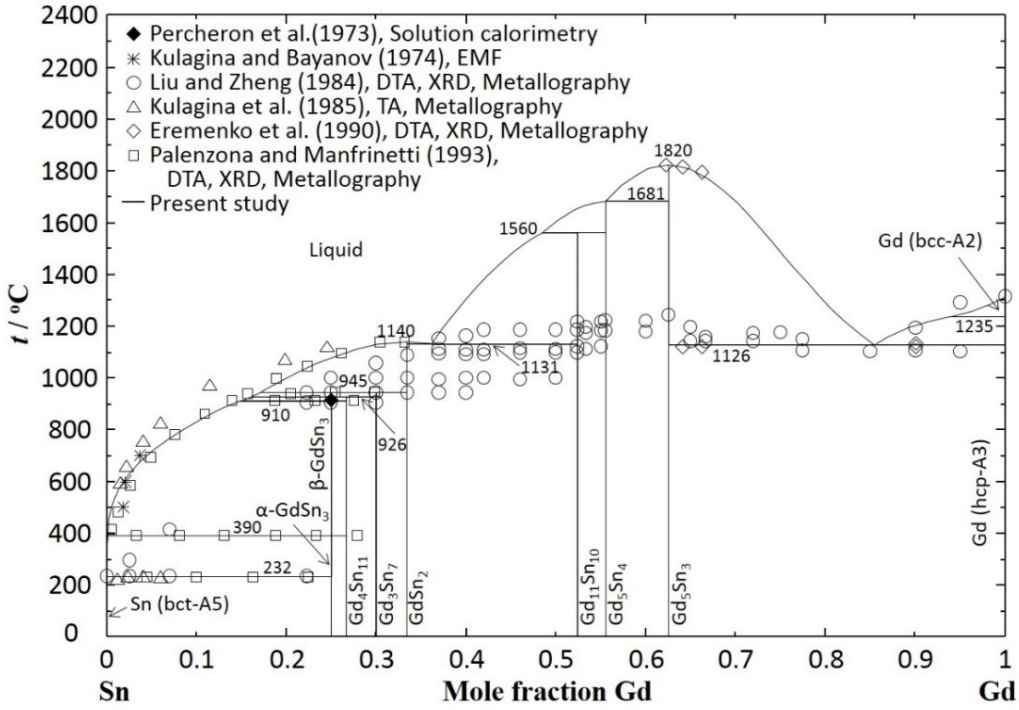
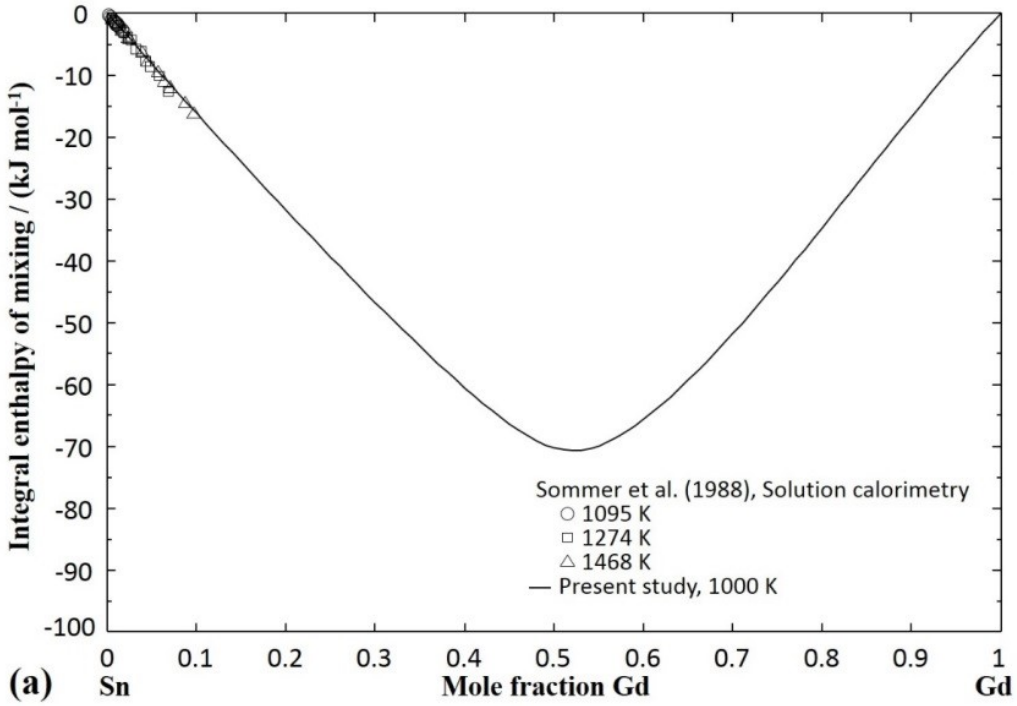
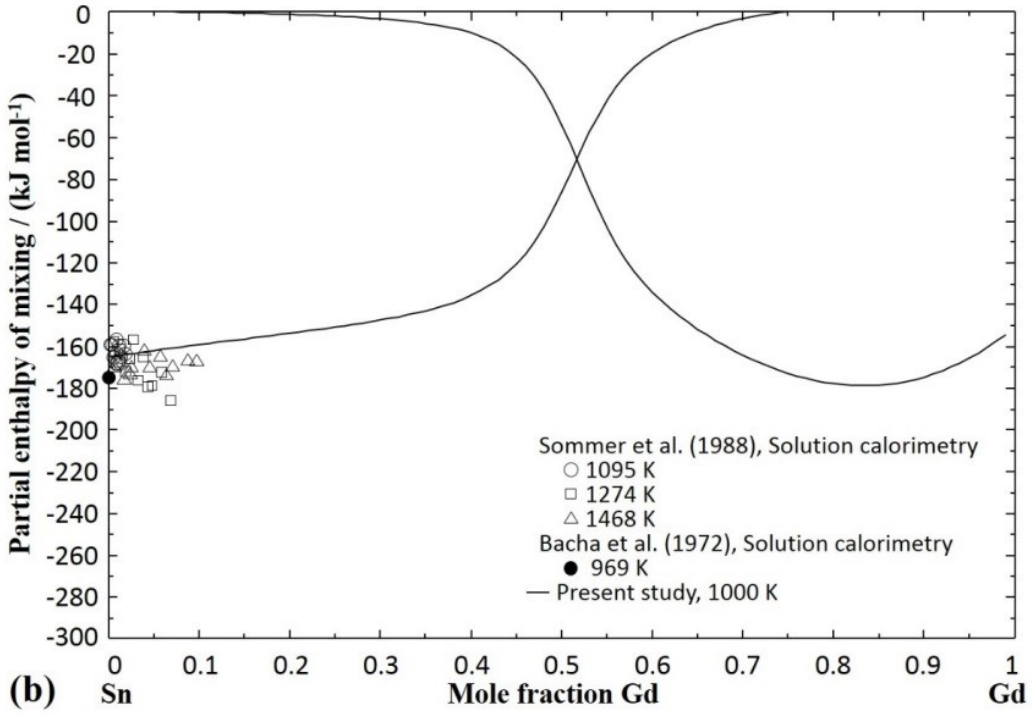


Fig. 1. The optimized Sn-Gd phase diagram with experimental data.


Integral enthalpy of mixing / (kJ mol-1)
0
-10
-20
-30
-40
-50
-60
-70
-80
-90
-100
Sommer et al. (1988), Solution calorimetry
1095 K
1274 K
1468 K
Present study, 1000 K
0
0.1
0.2
0.3
0.4
0.5
0.6
0.7
0.8
0.9
1
Sn
Mole fraction Gd
Gd

(a)


Partial enthalpy of mixing / (kJ mol-1)
0
-20
-40
-60
-80
-100
-120
-140
-160
-180
-200
-220
-240
-260
-280
-300
Sommer et al. (1988), Solution calorimetry
1095 K
1274 K
1468 K
Bacha et al. (1972), Solution calorimetry
969 K
Present study, 1000 K
0
0.1
0.2
0.3
0.4
0.5
0.6
0.7
0.8
0.9
1
Sn
Mole fraction Gd
Gd

(b)

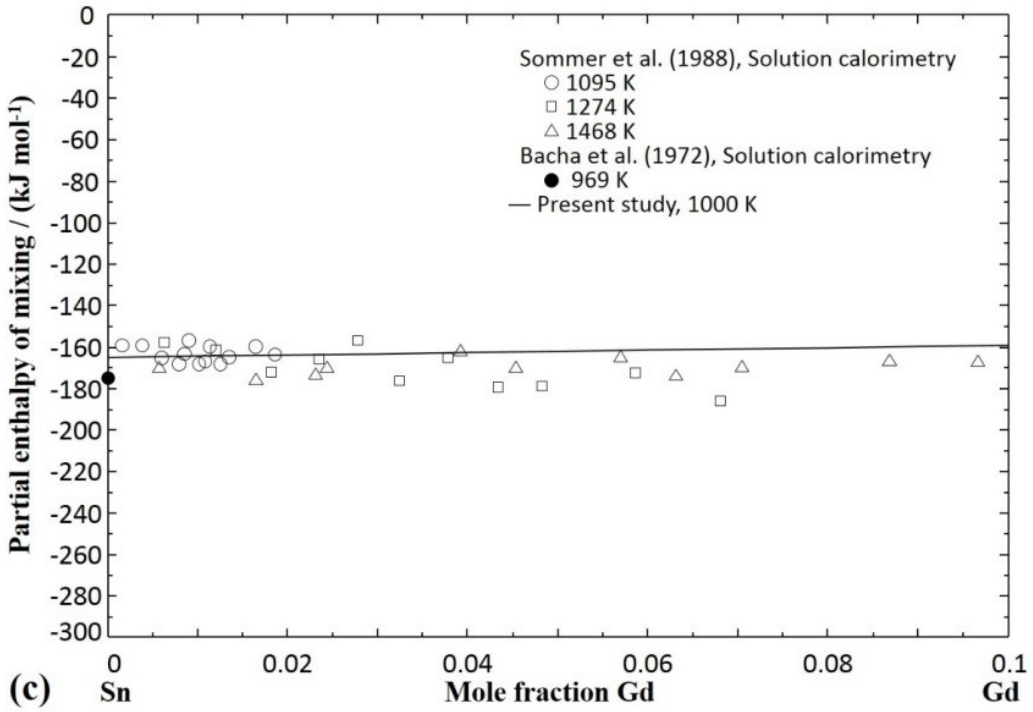


Fig. 2. (a) Integral enthalpy of mixing and (b), (c) partial enthalpy of mixing of liquid Sn-La at 1000 K with experimental data.

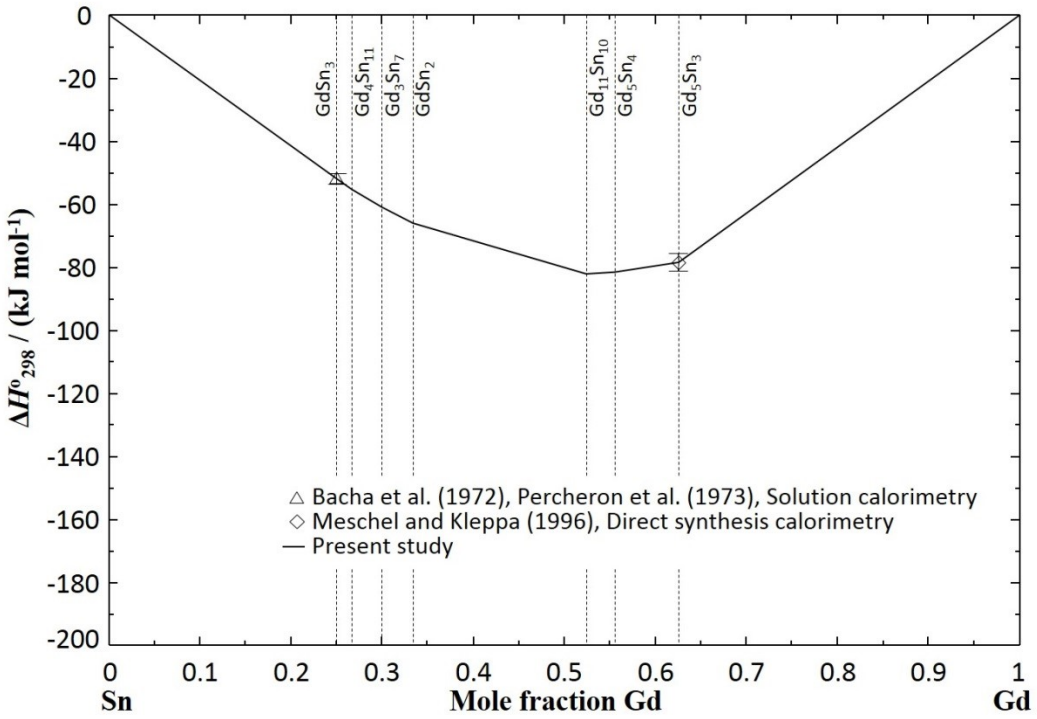


Fig. 3. Enthalpy of formation of the compounds in the Sn-Gd system at 298 K with experimental data.

1.2. The Sn-Tb system

Experimental data of the Sn-Tb phase diagram are presented in Fig. 4. The intermetallic compounds in this system were revealed by the crystallographic studies. The crystal structure and lattice parameters of Tb_xSn_y were reported: Tb_5Sn_3 (Mn_5Si_3 type) [1, 2, 28], Tb_5Sn_4 (Sm_5Ge_4 type) [3, 28, 29], $Tb_{11}Sn_{10}$ ($Ho_{11}Ge_{10}$ type) [3], $TbSn_2$ ($ZrSi_2$ type) [5, 28], α-Tb_3Sn_7 (Gd_3Sn_7 type, low temperature form) [8, 30, 31], β-Tb_3Sn_7 (Gd_3Sn_7 type, high temperature form) [8, 31], and $TbSn_3$ ($GdSn_3$ type) [8, 32]. Eremenko et al. [15] initially investigated the phase diagram of the system using DTA from the alloys containing 0.619, 0.64, and 0.908 mole fraction of Tb to verify the prediction of the melting temperature of Tb_5Sn_3 (1843 ± 17 ºC) and the eutectic temperature of Tb and Tb_5Sn_3 (1132 ± 64 ºC). The melting temperature of Tb_5Sn_3 and the eutectic temperature were found 1850 ºC and 1160 ºC, respectively, from the thermal effects of the alloys. Again, Eremenko et al. [28] investigated the phase diagram over the whole composition range by means of DTA, XRD and metallographic methods from the alloys of 26 compositions which were prepared by arc-melting under a purified Ar atmosphere from the initial materials, 99.999% Sn and 99.85% Tb. Seven intermetallic compounds (with melting temperature) were found: Tb_5Sn_3 (1850 ºC, congruent), Tb_5Sn_4 (1710 ºC, peritectic), $Tb_{11}Sn_{10}$ (1590 ºC, peritectic), TbSn (1259 ± 3 ºC, peritectic), Tb_4Sn_5 (1181 ± 6 ºC, peritectic), $TbSn_2$ (1136 ± 2 ºC, peritectic), and $TbSn_3$ (852 ± 3 ºC, peritectic) with eutectic reaction at 1158 ± 8 ºC and 0.88 mole fraction of Tb. The catatectic decomposition of $TbSn_3$ at 480 ± 9 ºC was reported and the polymorphic transformation of $TbSn_3$ was suggested at 762 ± 4 ºC. The mutual solid solubility was reported to be negligible. Later, Palenzona and Manfrinetti [8] investigated the Sn-rich side of the system up to 0.35 mole fraction of Tb using the same methods used for the Sn-Gd system. Unlike Eremenko et al. [28], the $TbSn_2$ and $TbSn_3$ melted at 1150 and 450 ºC, respectively, and the $TbSn_3$ was stable down to the room temperature. In addition, the Tb_3Sn_7 phase was found to exist in the system with the peritectic melting temperature, 745 ºC and the polymorphic transformation from α- to β-Tb_3Sn_7 at 605 ºC was reported. However, the experimental data were unfortunately not presented. The data points in Fig. 4 were extracted from the reported graph [8]. No thermodynamic properties of Sn-Tb liquid were reported.

Experimental data of the heat capacity (C_p) of $TbSn_2$ are shown in Fig. 5. Szytula et al. [33] measured the low temperature C_p of $TbSn_2$ between 1.9 and 300 K using a relaxation method implemented in a Quantum Design PPMS. The $TbSn_2$ showed the anomaly in the C_p due to the magnetic transformation at 18.7 K (Néel temperature), and two other additional anomalies in the C_p were reported at 13.1 K and 26.9 K which were likely due to small change in the magnetic structure and unknown spurious phase, respectively. In the present study, the standard entropy of formation (S^{o}_{298}) was calculated to be 159.15 J K^{-1} mol^{-1} from the experimental C_p of Szytula et al. [33]. The experimental S^{o}_{298} value is presented as ΔS^{o}_{298} in Fig. 6. The experimental standard enthalpy of formation at about 298 K (ΔH^{o}_{298}) are presented in Fig. 7. Meschel and Kleppa [34] determined the ΔH^{o}_{298} of Tb_5Sn_3 using direct synthesis calorimetry. The heat content ($H_{1473} - H_{298}$) of Tb_5Sn_3 was also reported as 35.0 ± 1.2 kJ mol·$atom^{-1}$.

A brief literature review of the Sn-Tb system was made by Okamoto [35]. The phase diagram of the system was introduced based on the work of Eremenko et al. [28] with a summary of the crystal structure of the phases and their respective lattice parameters. Later, Okamoto [36] reviewed again and constructed the phase diagram by accepting the work of Palenzona (up to 0.35 mole fraction of Tb) which were believed to be more reliable because of their systematic study along with RE series.

The optimized phase diagram of the Sn-Tb system in the present study is shown in Fig. 4. In the optimization, the phase diagram was constructed based on the work of Eremenko et al. [28] for the compositions above 0.333 mole fraction of Tb and Palenzona and Manfrinetti [8] for the compositions below. Although the existence of Tb_4Sn_5 and TbSn phases were reported in the work of Eremenko et al. [28] from the thermal effects of the alloys, the crystal structures of them were not resolved. Moreover, when considering the similarity with Sn-Dy system, the Dy_4Sn_5 and DySn phases were not found in the several isothermal phase diagram investigations of the ternary systems containing Dy and Sn [37-39] even though the two phases were similarly found in the Sn-Dy system according to Eremenko et al. [40]. It is likely that the Tb_4Sn_5 and TbSn are not stable phases in the Sn-Tb system. Therefore, the Tb_4Sn_5 and TbSn phases were excluded in the present

optimization. The mutual solid solubility was not considered by accepting Eremenko et al. [28]. The allotropic transformation of Tb_3Sn_7 was reproduced by accepting the transformation temperature, 745 °C [8] with the assumption of the enthalpy of the transformation, 2.5 kJ mol^{-1}.

The calculated thermodynamic properties with the optimized thermodynamic parameters are shown in Figs. 5-7. As the thermodynamic data of liquid phase were not available, the excess Gibbs energy parameters were estimated similarly to the Sn-Dy system with only the temperature independent parameters (i.e., enthalpy). The heat capacity of $TbSn_2$ which was estimated by NK approximation is in good agreement with the low temperature C_p data [33] as seen in Fig. 5. The experimental S^{o}_{298} of $TbSn_2$ [33] and ΔH^{o}_{298} of Tb_5Sn_3 [34] were considered as they were, and the ΔS^{o}_{298} and ΔH^{o}_{298} of the other compounds were estimated by considering the phase diagram (in Figs. 6-7). The calculated heat content ($H_{1473} - H_{298}$) of Tb_5Sn_3 was 38.09 kJ mol·$atom^{-1}$, which is comparable with the value of Meschel and Kleppa [34]. The optimized thermodynamic parameters are listed in Table 3 and the calculated invariant reactions with the experimental data are tabulated in Table 4.

Table 3. Optimized model parameters for the Sn-Tb system.

Phase	Thermodynamic parameters
Liquid	Coordination Numbers
	i = Sn, j = Tb, Z_{ij}^{i} = 6, Z_{ij}^{j} = 6
	Δg_{SnTb} / (J mol^{-1}) = -48116.0 $- 2092.0\, X_{\mathrm{SnSn}} - 2092.0\, X_{\mathrm{SnSn}}^2$ $- 20920.0\, X_{\mathrm{TbTb}} + 19790.32\, X_{\mathrm{TbTb}}^2$
$TbSn_3$	ΔH_{298}° = -205300 J mol^{-1}, S_{298}° = 214.34 J K^{-1} mol^{-1}
	C_p / (J K^{-1} mol^{-1}) = 1 × C_p / (J K^{-1} mol^{-1}) (Tb, hcp-A3) + 3 × modified C_p / (J K^{-1} mol^{-1}) (Sn, bct-A5)*
α-Tb_3Sn_7	ΔH_{298}° = -614500 J mol^{-1}, S_{298}° = 532.83 J K^{-1} mol^{-1}
	C_p / (J K^{-1} mol^{-1}) = 3 × C_p / (J K^{-1} mol^{-1}) (Tb, hcp-A3) + 7 × modified C_p / (J K^{-1} mol^{-1}) (Sn, bct-A5)*
β-Tb_3Sn_7	$\Delta_{\mathrm{trs}} H^{\alpha\rightarrow\beta}$ = 2500 J mol^{-1}, $T_{\mathrm{trs}}^{\alpha\rightarrow\beta}$ = 1018.15 K
	C_p / (J K^{-1} mol^{-1}) = 3 × C_p / (J K^{-1} mol^{-1}) (Tb, hcp-A3) + 7 × modified C_p / (J K^{-1} mol^{-1}) (Sn, bct-A5)*
$TbSn_2$	ΔH_{298}° = -202800 J mol^{-1}, S_{298}° = 159.15 J K^{-1} mol^{-1}
	C_p / (J K^{-1} mol^{-1}) = 1 × C_p / (J K^{-1} mol^{-1}) (Tb, hcp-A3) + 2 × modified C_p / (J K^{-1} mol^{-1}) (Sn, bct-A5)*
$Tb_{11}Sn_{10}$	ΔH_{298}° = -1655800 J mol^{-1}, S_{298}° = 11262.4 J K^{-1} mol^{-1}
	C_p / (J K^{-1} mol^{-1}) = 11 × C_p / (J K^{-1} mol^{-1}) (Tb, hcp-A3) + 10 × modified C_p / (J K^{-1} mol^{-1}) (Sn, bct-A5)*
Tb_5Sn_4	ΔH_{298}° = -700400 J mol^{-1}, S_{298}° = 553.65 J K^{-1} mol^{-1}
	C_p / (J K^{-1} mol^{-1}) = 5 × C_p / (J K^{-1} mol^{-1}) (Tb, hcp-A3) + 4 × modified C_p / (J K^{-1} mol^{-1}) (Sn, bct-A5)*
Tb_5Sn_3	ΔH_{298}° = -584800 J mol^{-1}, S_{298}° = 512.86 J K^{-1} mol^{-1}
	C_p / (J K^{-1} mol^{-1}) = 5 × C_p / (J K^{-1} mol^{-1}) (Tb, hcp-A3) + 3 × modified C_p / (J K^{-1} mol^{-1}) (Sn, bct-A5)*

*modified C_p / (J K^{-1} mol^{-1}) (Sn, bct-A5) = 24.477 + 5.472E-2 T/K – 40640.0 (T/K)$^{-2}$ – 6.469E-7 (T/K)^2

Table 4. Calculated invariant reactions and experimental data in the Sn-Tb system.

Type	Reaction	t (°C)	Reference
Eutectic	$L(X_{Tb}=<1E\text{-}5) \rightarrow Sn(\text{bct-A5}, X_{Tb}=0) + TbSn_3$	231.9	This work
	$L(X_{Tb}=*) \rightarrow Sn(\text{bct-A5}, X_{Tb}=0) + TbSn_3$	230.0	[8]
Peritectic	$L(X_{Tb}=*) + TbSn_2 \rightarrow Sn(\text{bct-A5}, X_{Tb}=0)$	234±2	[28]
Peritectic	$L(X_{Tb}=0.0025) + Tb_3Sn_7 \rightarrow TbSn_3$	450.3	This work
	$L(X_{Tb}=\sim0.094) + TbSn_2 \rightarrow TbSn_3$	852±3	[28]
	$L(X_{Tb}=\sim0.007) + Tb_3Sn_7 \rightarrow TbSn_3$	450.0	[8]
Peritectic	$L(X_{Tb}=0.093) + TbSn_2 \rightarrow Tb_3Sn_7$	830.4	This work
	$L(X_{Tb}=\sim0.086) + TbSn_2 \rightarrow Tb_3Sn_7$	830.0	[8]
Allotropic	α-$Tb_3Sn_7 \leftrightarrow \beta$-$Tb_3Sn_7$	745.0	This work
	α-$Tb_3Sn_7 \leftrightarrow \beta$-$Tb_3Sn_7$	762±4	[28]
	α-$Tb_3Sn_7 \leftrightarrow \beta$-$Tb_3Sn_7$	745.0	[8]
Catatectic	$TbSn_3 \rightarrow L(X_{Tb}=\sim0.005) + TbSn_2$	480±9	[28]
Congruent	$L(X_{Tb}=0.333) \leftrightarrow TbSn_2$	1150.1	This work
Peritectic	$L(X_{Tb}=\sim0.331) + Tb_4Sn_5 \rightarrow TbSn_2$	1136±2	[28]
	$L(X_{Tb}=\sim0.325) + ** \rightarrow TbSn_2$	1150.0	[8]
Peritectic	$L(X_{Tb}=\sim0.402) + TbSn \rightarrow Tb_4Sn_5$	1181±6	[28]
Peritectic	$L(X_{Tb}=\sim0.409) + Tb_{11}Sn_{10} \rightarrow TbSn$	1259±8	[28]
Eutectic	$L(X_{Tb}=0.355) \rightarrow TbSn_2 + Tb_{11}Sn_{10}$	1146.0	This work
Peritectic	$L(X_{Tb}=0.484) + Tb_5Sn_4 \rightarrow Tb_{11}Sn_{10}$	1590.4	This work
	$L(X_{Tb}=\sim0.486) + Tb_5Sn_4 \rightarrow Tb_{11}Sn_{10}$	1590.0	[28]
Peritectic	$L(X_{Tb}=0.553) + Tb_5Sn_3 \rightarrow Tb_5Sn_4$	1710.0	This work
	$L(X_{Tb}=\sim0.539) + Tb_5Sn_3 \rightarrow Tb_5Sn_4$	1710.0	[28]
Congruent	$L(X_{Tb}=0.625) \leftrightarrow Tb_5Sn_3$	1849.8	This work
	$L(X_{Tb}=0.625) \leftrightarrow Tb_5Sn_3$	1850.0	[15]
	$L(X_{Tb}=0.625) \leftrightarrow Tb_5Sn_3$	1850.0	[28]
Eutectic	$L(X_{Tb}=0.867) \rightarrow Tb_5Sn_3 + Tb(\text{hcp-A3}, X_{Tb}=1)$	1152.3	This work
	$L(X_{Tb}=\sim0.89) \rightarrow Tb_5Sn_3 + Tb(\text{hcp-A3}, X_{Tb}=*)$	1160.0	[15]
	$L(X_{Tb}=0.88) \rightarrow Tb_5Sn_3 + Tb(\text{hcp-A3}, X_{Tb}=1)$	1158±8	[28]

* The exact compositions are not specified in the reference.
** The phase was not identified.

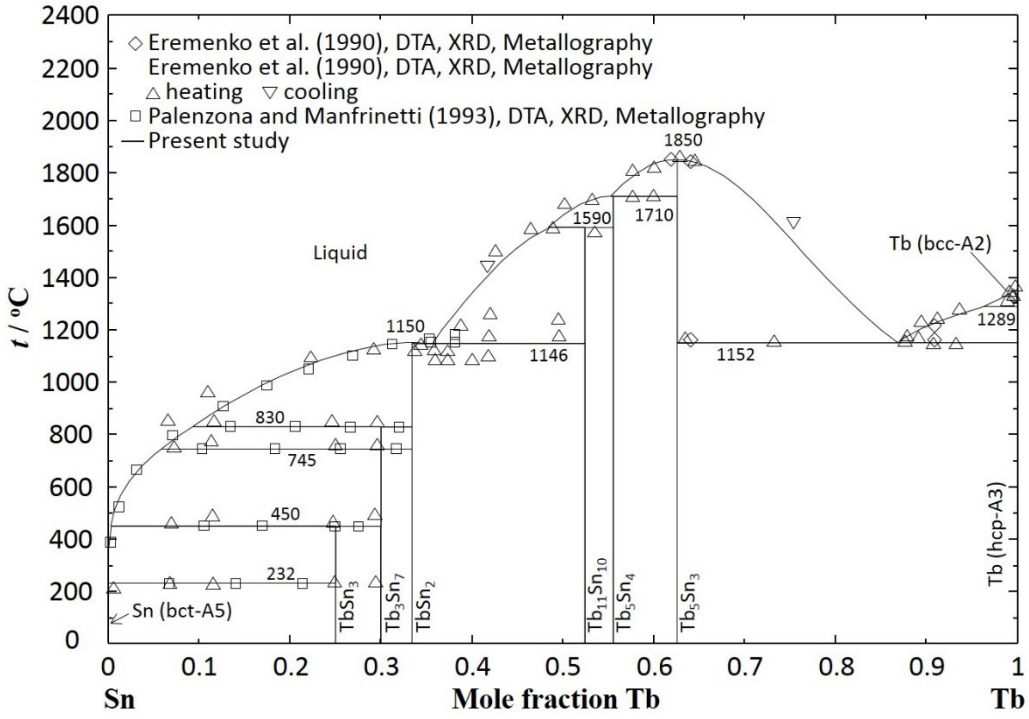


Fig. 4. The optimized Sn-Tb phase diagram with experimental data.

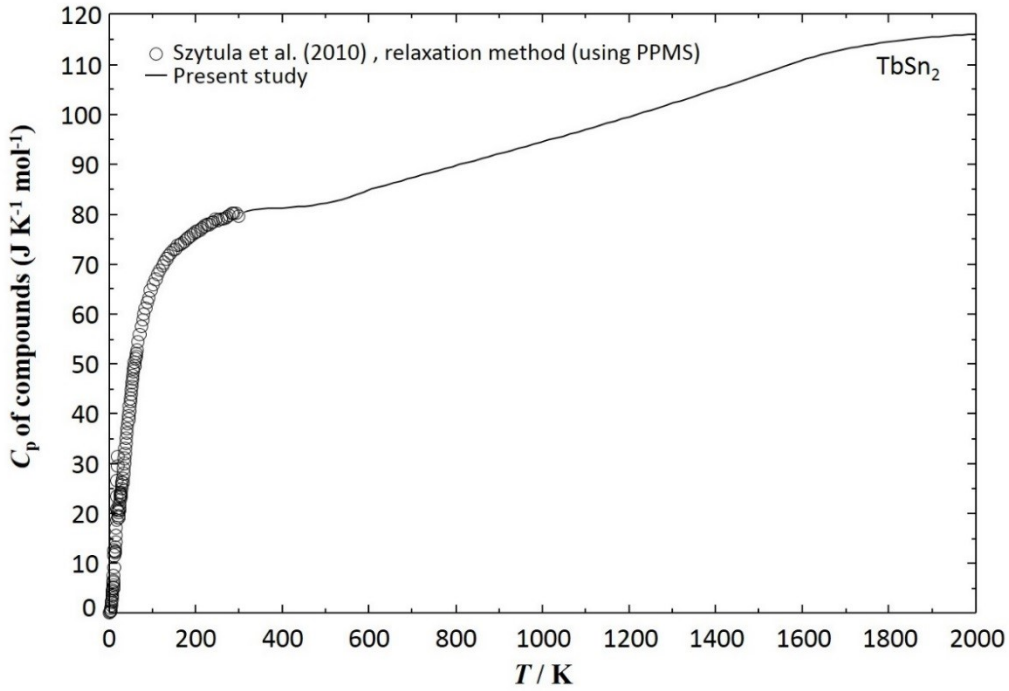


Fig. 5. Heat capacity of $TbSn_2$ with experimental data (1.9-300 K).

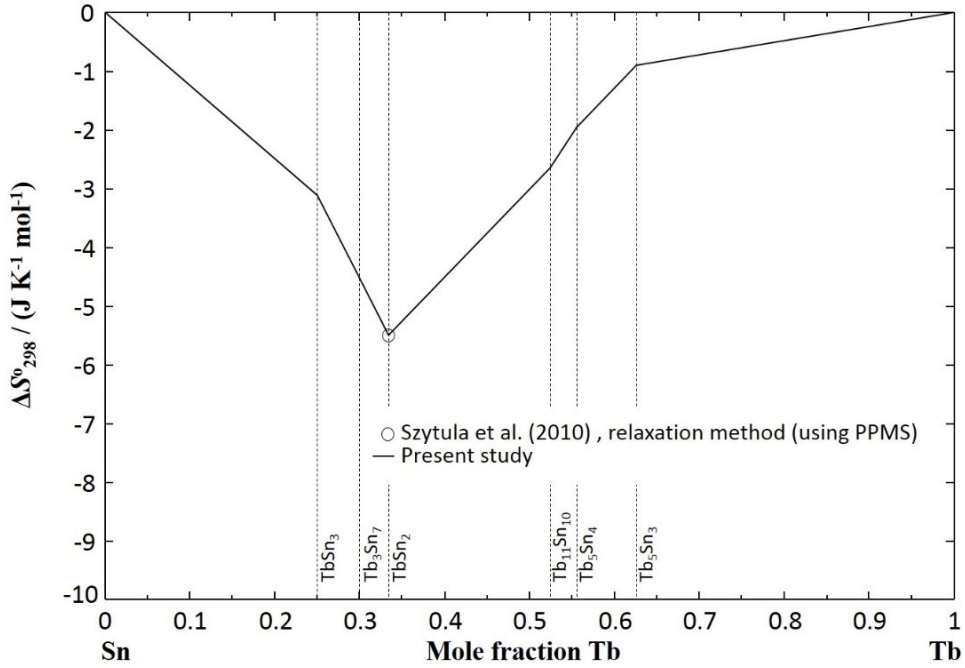


Fig. 6. Entropy of formation of the compounds in the Sn-Tb system from elements at 298 K with experimental data.

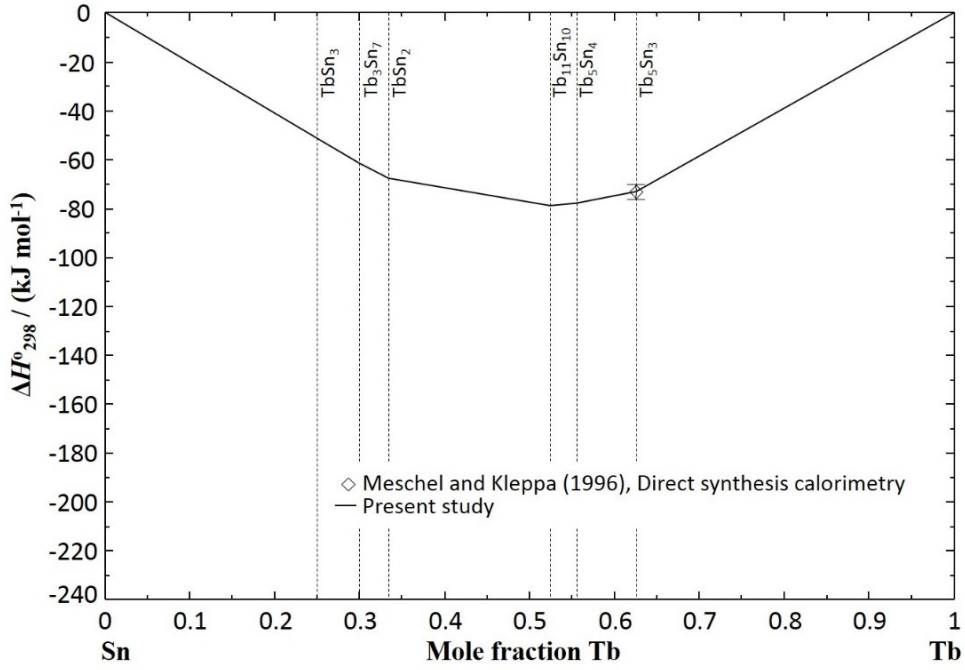


Fig. 7. Enthalpy of formation of the compounds in the Sn-Tb system at 298 K with experimental data.

1.3. The Sn-Dy system

Experimental data of the Sn-Dy phase diagram are presented in Fig. 8. The intermetallic compounds in this system were revealed by the crystallographic studies. The crystal structure and lattice parameters of Dy_xSn_y were reported: α-Dy_5Sn_3 (Mn_5Si_3 type, low temperature form) [1, 2, 40], Dy_5Sn_4 (Sm_5Ge_4 type) [3, 29, 40], $Dy_{11}Sn_{10}$ ($Ho_{11}Ge_{10}$ type) [3, 40], $DySn_2$ ($ZrSi_2$ type) [5, 40], α-Dy_3Sn_7 (Gd_3Sn_7 type, low temperature form) [8], β-Dy_3Sn_7 (Gd_3Sn_7 type, high temperature form) [8], and $DySn_3$ ($GdSn_3$ type) [8, 32]. The first phase diagram investigation was performed by Chen and Zheng [41] in the whole composition range using XRD and DTA. The alloys were prepared from (purity not specified) Sn and 99.9% Dy in high frequency induction furnace under Ar atmosphere using alumina crucibles, and were subsequently annealed at 550 ºC for 30 days (low Sn alloys, < 58 wt.% Sn), and at 150 ºC for 150 days (high Sn alloys > 58 wt.% Sn) under Ar atmosphere. Eight intermetallic compounds (with melting temperature) were found: Dy_2Sn (1237 ºC, congruent), Dy_5Sn_3 (1140 ºC, congruent), Dy_5Sn_4 (1160 ºC, peritectic), $Dy_{11}Sn_{10}$ (1175 ºC, peritectic), DySn (1222 ºC, congruent), Dy_8Sn_9 (1134 ºC, peritectic), Dy_4Sn_7 (1154 ºC, congruent), DySn3 (738 ºC, peritectic), and $DySn_4$ (442 ºC, peritectic) with four eutectic reactions. In addition, it was reported that the bcc-Dy (7 wt. %) decomposed to hcp-Dy (5 wt. %) and liquid (8 wt. %). However, the melting temperatures of Dy-rich compounds (i.e., Dy_5Sn_3, Dy_5Sn_4, and $Dy_{11}Sn_{10}$) determined by Chen and Zheng [41] were significantly low compared to the same stoichiometric other RE stannide compounds. The solubility of Dy in liquid in the Sn-rich alloys was significantly large. The results of Liu and Zheng [12] seem to be unreliable. Like for the previous systems, Eremenko et al. [15] initially investigated the phase of the system using DTA from the alloys containing 0.616 and 0.901 mole fraction of Dy to verify the prediction of the melting temperature of Dy_5Sn_3 (1872 ± 17 ºC) and the eutectic temperature of Dy and Dy_5Sn_3 (1176 ± 64 ºC). The melting temperature of Dy_5Sn_3 and the eutectic temperature were found 1870 ºC and 1210 ºC, respectively, from the thermal effects of the alloys. Again, Eremenko et al. [40] investigated the phase diagram over the whole composition range by means of DTA, XRD and metallographic methods from the alloys of 22 compositions which were prepared by arc-melting under a purified Ar atmosphere from the initial materials, 99.9995% Sn and 99.76% Dy. Seven intermetallic compounds (with melting temperature) were found: Dy_5Sn_3 (1870 ºC, congruent),

Dy_5Sn_4 (1712 ± 11 ºC, peritectic), $Dy_{11}Sn_{10}$ (1605 ± 12 ºC, peritectic), DySn (1208 ± 3 ºC, peritectic), Dy_4Sn_5 (1166 ± 7 ºC, peritectic), $DySn_2$ (1138 ± 3 ºC, peritectic), and $DySn_3$ (747 ± 6 ºC, peritectic) with eutectic reaction at 1204 ± 10 ºC and 0.87 mole fraction of Dy. The eutectoidal decomposition of $DySn_3$ at 499 ± 2 ºC was reported and the polymorphic transformation of $DySn_3$ was suggested at 608 ± 12 ºC. The solid solubility of Dy in Sn was negligible and the solubility of Sn in hcp-Dy was about 3% at eutectic temperature and none of the compounds showed noticeable homogeneity ranges. Later, Palenzona and Manfrinetti [8] investigated the Sn-rich side of the system up to 0.35 mole fraction of Dy using the same methods used for the Sn-Gd system. The phase diagram of the Sn-Dy system was similar to that of the Sn-Tb system reported in the same study [8]. The $DySn_2$ and $DySn_3$ melted at 1135 and 470 ºC, respectively, and the $DySn_3$ was stable down to the room temperature. The Dy_3Sn_7 phase was found to exist in the system with the peritectic melting temperature, 745 ºC and the polymorphic transformation from α- to β-Tb_3Sn_7 at 605 ºC was reported. However, the experimental data were unfortunately not presented. The data points in Fig. 8 were extracted from the reported graph [8]. In addition, there is controversy regarding the existence of the Dy_4Sn_5 and DySn which were found in the study of Eremenko et al. [40]. The absence of Dy_4Sn_5 [37-39] and DySn [37, 39] were reported in the isothermal phase diagram investigation of the ternary systems containing Dy and Sn.

The experimental data of the thermodynamic properties of the Sn-Dy liquid are presented in Fig. 9(a) and (b). Bacha et al. [42] reported the heat of mixing of solid Dy in liquid Sn at 955 and 960 K using solution calorimetry from high purity materials, (purity not reported) Sn and 99.9% Dy. In the present study, the enthalpy of mixing values were derived based on the dissolution enthalpy by considering the heat content of Dy from room temperature to the measurement temperature. Similarly, Sommer et al. [21] determined the heat of dissolution of solid Dy in liquid Sn up to 0.08 mole fraction of Dy at 1098, 1273, 1379 and 1478 K from high purity materials, 99.96% Sn and 99.9% Gd. The partial enthalpy of mixing values of Dy were obtained based on the dissolution enthalpy. Then, the partial enthalpy values were used to obtain the integral enthalpy of mixing as shown in Fig. 9(a) in the present study.

Experimental data of the heat capacity (C_p) of $DySn_2$ are shown in Fig. 10. Szytula et al. [33] measured the low temperature C_p of $DySn_2$ between 1.9 and 300 K using a relaxation method implemented in a Quantum Design PPMS. The $DySn_2$ showed the anomaly in the C_p due to the magnetic transformation at 12.7 K (Néel temperature). In the present study, the standard entropy of formation (S^{o}_{298}) was calculated to be 162.4 J K^{-1} mol^{-1} from the experimental C_p of Szytula et al. [33]. The experimental S^{o}_{298} values are presented as ΔS^{o}_{298} in Fig. 11. The experimental standard enthalpy of formation at about 298 K (ΔH^{o}_{298}) are presented in Fig. 12. Meschel and Kleppa [43] determined the ΔH^{o}_{298} of Dy_5Sn_3 using direct synthesis calorimetry. The heat content ($H_{1473}-H_{298}$) of Dy_5Sn_3 was also reported as 30.7 ± 1.7 kJ mol·$atom^{-1}$. The Gibbs energy of formation of $DySn_2$ from the references of Dy and liquid Sn at 800 K and 1000 K were determined to be -58.17 ± 0.08 and -55.44 ± 0.12 kJ mol·$atom^{-1}$, respectively, by Yamshchikov et al. [44] from the emf measurements. Yamshchikov et al. [23] reported the activity of Dy in Dy saturated liquid at 800 K from the previous emf measurement [44]. The value was -11.39 in logarithmic scale.

The thermodynamic optimization of the Sn-Dy system was previously performed by Wang et al. [45]. The calculated thermodynamic properties from the work of Wang et al. [45] are presented in Figs. 9, 11-12. The excess Gibbs energy of liquid phase was expressed in the Redlich-Kister random mixing model however the calculated integral and partial enthalpy of mixing of liquid did not fit the experimental data [21, 42] as seen in Fig 9(a) and (b). In addition, the enthalpy of mixing of Dy rich region was estimated so much negative that large temperature dependent parameters were required to reproduce the eutectic temperature of Dy_5Sn_3 and hcp-Dy. The heat capacities (C_p) of compounds were estimated by NK approximation, resulting in the meaningless kink from the C_p of Sn. The NK approximated C_p of $DySn_2$ using the unmodified C_p of Sn was presented in Fig. 10 as an example. The calculated the ΔS^{o}_{298} (Fig. 11) and ΔH^{o}_{298} (Fig. 12) were slightly off from the experimental values.

The optimized phase diagram of the Sn-Dy system in the present study is shown in Fig. 8. In the optimization, the phase diagram was constructed based on the work of Eremenko et al. [40] for the

compositions above 0.333 mole fraction of Dy and Palenzona and Manfrinetti [8] for the compositions below. However, the peritectic melting of $DySn_2$ [8, 40] was unlikely to be reproduced when considering the liquidus slope around between $DySn_2$ and $Dy_{11}Sn_{10}$. This was similarly found in the previous two systems. Similar to the Sn-Tb system, the Dy_4Sn_5 and DySn phases were excluded in the present optimization. Although the existence of Dy_4Sn_5 and DySn phases were reported in the work of Eremenko et al. [28] from the thermal effects of the alloys, the crystal structures of them were not resolved. The Dy_4Sn_5 and DySn phases were not found in the several isothermal phase diagram investigations of the ternary systems containing Dy and Sn [37-39]. It is likely that the Dy_4Sn_5 and DySn are not stable phases in the Sn-Dy system. The solid solubilities of Sn in hcp-Dy and bcc-Dy were modeled with one temperature independent excess Gibbs energy parameter, respectively, with reference to the work of Eremenko et al. [40]. The allotropic transformation of Dy_3Sn_7 was reproduced by accepting the transformation temperature, 605 ºC [8] with the assumption of the enthalpy of the transformation, 2.5 kJ mol^{-1}.

The calculated thermodynamic properties with the optimized thermodynamic parameters are shown in Figs. 9-12. The experimental data of the integral and partial enthalpies of mixing of Sn-rich liquid [21, 42] were well reproduced by the present optimization. No temperature dependent parameters (i.e., entropy) were added. The C_p of $DySn_2$ above 298.15 was increased by 4.357 J mol^{-1} K^{-1} from the NK approximated C_p using the modified C_p of Sn in order to be corresponded with the low temperature C_p data [33] (in Fig. 10). The experimental data of the ΔS^{o}_{298} of $DySn_2$ [33], and the ΔH^{o}_{298} of Dy_5Sn_3 [43] were considered as they were, and the ΔS^{o}_{298} and ΔH^{o}_{298} of the other compounds were estimated by considering the phase diagram (in Figs. 11-12). The calculated heat content ($H_{1473}-H_{298}$) of Dy_5Sn_3 was 35.69 kJ mol·atom^{-1}, which was slightly higher than the experimental finding [43]. The calculated ΔG^{o} values of $DySn_2$ from the references of solid Dy and liquid Sn at 800 and 1000 K were -58.15 and -55.37 kJ mol·atom^{-1}, respectively, agreeing with the experimental values [44]. The calculated activity of Dy in Dy saturated liquid at 800 K was -11.964 in logarithmic scale, which corresponds to the experimental values [44]. The optimized thermodynamic parameters are listed in Table 5 and the calculated invariant reactions with the experimental data are tabulated in Table 6.

Table 5. Optimized model parameters for the Sn-Dy system.

Phase	Thermodynamic parameters
Liquid	Coordination Numbers
	i j Z_{ij}^{i} Z_{ij}^{j}
	Sn Dy 6 6
	Δg_{SnDy} / (J mol^{-1}) = -48116.0 – 2092.0 X_{SnSn} – 2092.0 X_{SnSn}^{2}
	– 20920.0 X_{DyDy} + 17886.6 X_{DyDy}^{2}
bcc-A2	${}^{0}L_{\mathrm{Sn,\,Dy}}$ / (J mol^{-1}) = -146440.0
hcp-A3	${}^{0}L_{\mathrm{Sn,\,Dy}}$ / (J mol^{-1}) = -146440.0
$DySn_3$	ΔH_{298}° = -199600 J mol^{-1}, S_{298}° = 216.53 J K^{-1} mol^{-1}
	C_p / (J K^{-1} mol^{-1}) = 1 × C_p / (J K^{-1} mol^{-1}) (Dy, hcp-A3)
	+ 3 × modified C_p / (J K^{-1} mol^{-1}) (Sn, bct-A5)*
α-Dy_3Sn_7	ΔH_{298}° = -592000 J mol^{-1}, S_{298}° = 545.95 J K^{-1} mol^{-1}
	C_p / (J K^{-1} mol^{-1}) = 3 × C_p / (J K^{-1} mol^{-1}) (Dy, hcp-A3)
	+ 7 × modified C_p / (J K^{-1} mol^{-1}) (Sn, bct-A5)*
β-Dy_3Sn_7	$\Delta_{\mathrm{trs}} H^{\alpha\rightarrow\beta}$ = 2500 J mol^{-1}, $T_{\mathrm{trs}}^{\alpha\rightarrow\beta}$ = 878.15 K
	C_p / (J K^{-1} mol^{-1}) = 3 × C_p / (J K^{-1} mol^{-1}) (Dy, hcp-A3)
	+ 7 × modified C_p / (J K^{-1} mol^{-1}) (Sn, bct-A5)*
$DySn_2$	ΔH_{298}° = -194640 J mol^{-1}, S_{298}° = 162.4 J K^{-1} mol^{-1}
	C_p / (J K^{-1} mol^{-1}) = 1 × C_p / (J K^{-1} mol^{-1}) (Dy, hcp-A3)
	+ 2 × modified C_p / (J K^{-1} mol^{-1}) (Sn, bct-A5)*
$Dy_{11}Sn_{10}$	ΔH_{298}° = -1655000 J mol^{-1}, S_{298}° = 1282.7 J K^{-1} mol^{-1}
	C_p / (J K^{-1} mol^{-1}) = 11 × C_p / (J K^{-1} mol^{-1}) (Dy, hcp-A3)
	+ 10 × modified C_p / (J K^{-1} mol^{-1}) (Sn, bct-A5)*
Dy_5Sn_4	ΔH_{298}° = -704500 J mol^{-1}, S_{298}° = 560.4 J K^{-1} mol^{-1}
	C_p / (J K^{-1} mol^{-1}) = 5 × C_p / (J K^{-1} mol^{-1}) (Dy, hcp-A3)
	+ 4 × modified C_p / (J K^{-1} mol^{-1}) (Sn, bct-A5)*

α-Dy_5Sn_3 ΔH°_{298} = -600800 J mol^{-1}, S°_{298} = 515.65 J K^{-1} mol^{-1}

C_p / (J K^{-1} mol^{-1}) = 5 × C_p / (J K^{-1} mol^{-1}) (Dy, hcp-A3)
+ 3 × modified C_p / (J K^{-1} mol^{-1}) (Sn, bct-A5)*

β-Dy_5Sn_3 $\Delta_{trs}H^{\alpha\rightarrow\beta}$ = 2500 J mol^{-1}, $T^{\alpha\rightarrow\beta}_{trs}$ = 2096.15 K

C_p / (J K^{-1} mol^{-1}) = 5 × C_p / (J K^{-1} mol^{-1}) (Dy, hcp-A3)
+ 3 × modified C_p / (J K^{-1} mol^{-1}) (Sn, bct-A5)*

*modified C_p / (J K^{-1} mol^{-1}) (Sn, bct-A5) = 24.477 + 5.472E-2 T/K – 40640.0 (T/K)$^{-2}$ – 6.469E-7 (T/K)^2

Table 6. Calculated invariant reactions and experimental data in the Sn-Dy system.

Type	Reaction	t (°C)	Reference
Eutectic	$L_{(X_{Dy}= 2E-5)} \rightarrow Sn_{(bct-A5, X_{Dy}= 0)} + DySn_3$	231.9	This work
	$L_{(X_{Dy}= \sim0.011)} \rightarrow Sn_{(bct-A5, X_{Dy}= 0)} + DySn_4$	205.0	[41]
	$L_{(X_{Dy}= *)} \rightarrow Sn_{(bct-A5, X_{Dy}= 0)} + DySn_3$	230.0	[8]
Peritectic	$L_{(X_{Dy}= *)} + DySn_2 \rightarrow Sn_{(bct-A5, X_{Dy}= 0)}$	233±3	[40]
Peritectic	$L_{(X_{Dy}= \sim0.037)} + DySn_2 \rightarrow DySn_4$	442.0	[41]
Peritectic	$L_{(X_{Dy}= \sim0.095)} + Dy_4Sn_7 \rightarrow DySn_2$	738.0	[41]
Peritectic	$L_{(X_{Dy}= 0.007)} + Dy_3Sn_7 \rightarrow DySn_3$	470.1	This work
	$L_{(X_{Dy}= \sim0.060)} + DySn_2 \rightarrow DySn_3$	747±6	[40]
	$L_{(X_{Dy}= \sim0.016)} + Dy_3Sn_7 \rightarrow DySn_3$	470.0	[8]
Peritectic	$L_{(X_{Dy}= 0.079)} + DySn_2 \rightarrow Dy_3Sn_7$	745.1	This work
	$L_{(X_{Dy}= \sim0.075)} + DySn_2 \rightarrow Dy_3Sn_7$	745.0	[8]
Allotropic	α-$Dy_3Sn_7 \leftrightarrow \beta$-$Dy_3Sn_7$	605.0	This work
	α-$Dy_3Sn_7 \leftrightarrow \beta$-$Dy_3Sn_7$	608±12	[40]
	α-$Dy_3Sn_7 \leftrightarrow \beta$-$Dy_3Sn_7$	605.0	[8]
Catatectic	$DySn_3 \rightarrow L_{(X_{Dy}= \sim0.013)} + DySn_2$	499±2	[40]
Congruent	$L_{(X_{Dy}= 0.333)} \leftrightarrow DySn_2$	1138.3	This work
Peritectic	$L_{(X_{Dy}= \sim0.322)} + Dy_4Sn_5 \rightarrow DySn_2$	1138±3	[40]
	$L_{(X_{Dy}= \sim0.299)} + ** \rightarrow DySn_2$	1135.0	[8]

Peritectic	$L_{(X_{Tb}=\sim0.363)} + DySn \rightarrow Dy_4Sn_5$	1166±7	[40]
Peritectic	$L_{(X_{Tb}=\sim0.374)} + Dy_{11}Sn_{10} \rightarrow DySn$	1208±3	[40]
Eutectic	$L_{(X_{Dy}=0.348)} \rightarrow DySn_2 + Dy_{11}Sn_{10}$	1136.3	This work
Congruent	$L_{(X_{Dy}=0.364)} \leftrightarrow Dy_4Sn_7$	1154.0	[41]
Eutectic	$L_{(X_{Dy}=0.403)} \rightarrow Dy_4Sn_7 + Dy_8Sn_9$	1112.0	[41]
Peritectic	$L_{(X_{Dy}=\sim0.417)} + DySn \rightarrow Dy_8Sn_9$	1134.0	[41]
Congruent	$L_{(X_{Dy}=0.5)} \leftrightarrow DySn$	1222.0	[41]
Peritectic	$L_{(X_{Dy}=0.484)} + Dy_5Sn_4 \rightarrow Dy_{11}Sn_{10}$	1605.0	This work
	$L_{(X_{Dy}=\sim0.545)} + DySn \rightarrow Dy_{11}Sn_{10}$	1175.0	[41]
	$L_{(X_{Dy}=\sim0.482)} + Dy_5Sn_4 \rightarrow Dy_{11}Sn_{10}$	1605±12	[40]
Peritectic	$L_{(X_{Dy}=0.543)} + Dy_5Sn_3 \rightarrow Dy_5Sn_4$	1712.0	This work
	$L_{(X_{Dy}=\sim0.556)} + Dy_5Sn_3 \rightarrow Dy_5Sn_4$	1160.0	[41]
	$L_{(X_{Dy}=\sim0.542)} + Dy_5Sn_3 \rightarrow Dy_5Sn_4$	1712±11	[40]
Eutectic	$L_{(X_{Dy}=0.586)} \rightarrow Dy_5Sn_4 + Dy_5Sn_3$	1120.0	[41]
Peritectic	$L_{(X_{Dy}=\sim0.604)} + Dy_2Sn \rightarrow Dy_5Sn_3$	1140.0	[41]
Congruent	$L_{(X_{Dy}=0.625)} \leftrightarrow Dy_5Sn_3$	1870.3	This work
	$L_{(X_{Dy}=0.625)} \leftrightarrow Dy_5Sn_3$	1870.0	[15]
	$L_{(X_{Dy}=0.625)} \leftrightarrow Dy_5Sn_3$	1870.0	[40]
Allotropic	α-$Dy_5Sn_3 \leftrightarrow \beta$-$Dy_5Sn_3$	1823.0	This work
	α-$Dy_5Sn_3 \leftrightarrow \beta$-$Dy_5Sn_3$	1823±6	[40]
Congruent	$L_{(X_{Dy}=0.666)} \leftrightarrow Dy_2Sn$	1237.0	[41]
Eutectic	$L_{(X_{Dy}=0.863)} \rightarrow Dy_5Sn_3 + Dy_{(hcp\text{-}A3,\ X_{Dy}=0.980)}$	1204.0	This work
	$L_{(X_{Dy}=0.843)} \rightarrow Dy_5Sn_3 + Dy_{(hcp\text{-}A3,\ X_{Dy}=*)}$	1105.0	[41]
	$L_{(X_{Dy}=\sim0.89)} \rightarrow Dy_5Sn_3 + Dy_{(hcp\text{-}A3,\ X_{Dy}=*)}$	1210.0	[15]
	$L_{(X_{Dy}=0.87)} \rightarrow Dy_5Sn_3 + Dy_{(hcp\text{-}A3,\ X_{Dy}=\sim0.97)}$	1204±10	[40]
Catatectic	$Dy_{(bcc\text{-}A2,\ X_{Dy}=0.996)} \rightarrow L_{(X_{Dy}=0.982)} + Dy_{(hcp\text{-}A3,\ X_{Dy}=0.9963)}$	1385.5	This work
	$Dy_{(bcc\text{-}A2,\ X_{Dy}=0.907)} \rightarrow L_{(X_{Dy}=\sim0.894)} + Dy_{(hcp\text{-}A3,\ X_{Dy}=0.933)}$	1182.0	[41]

* The exact compositions are not specified in the reference.
** The phase was not identified.

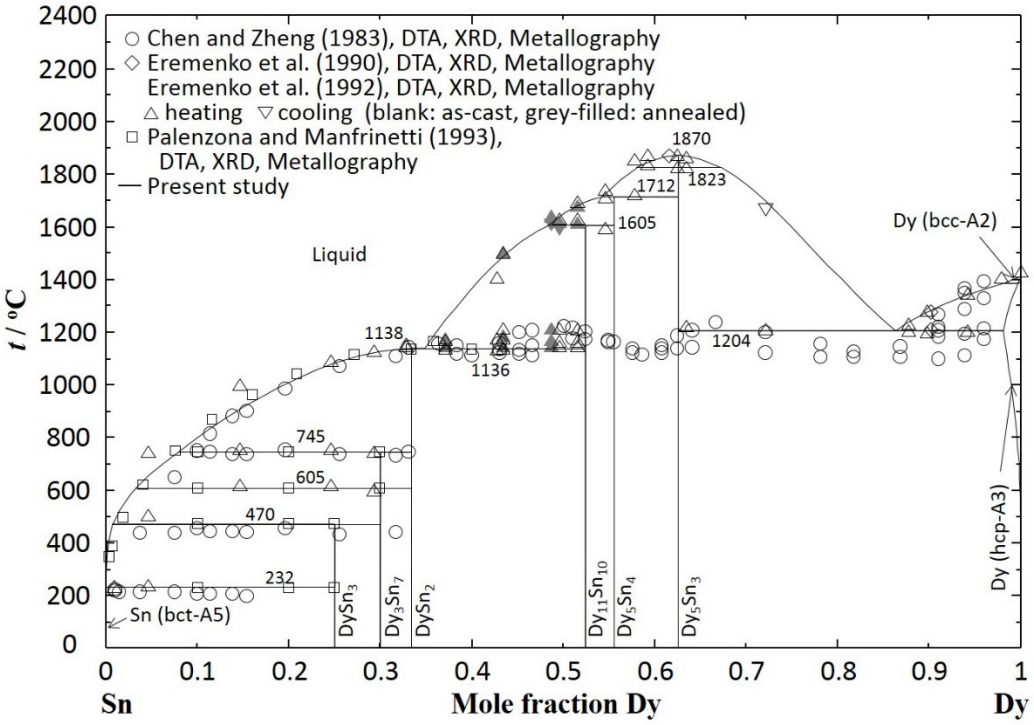
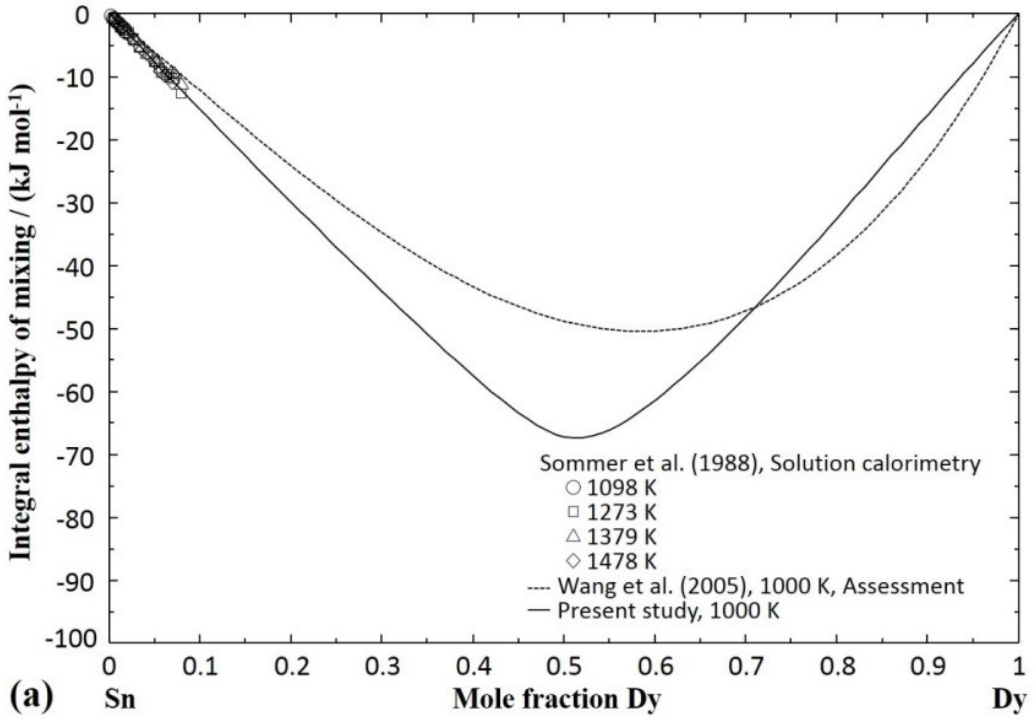
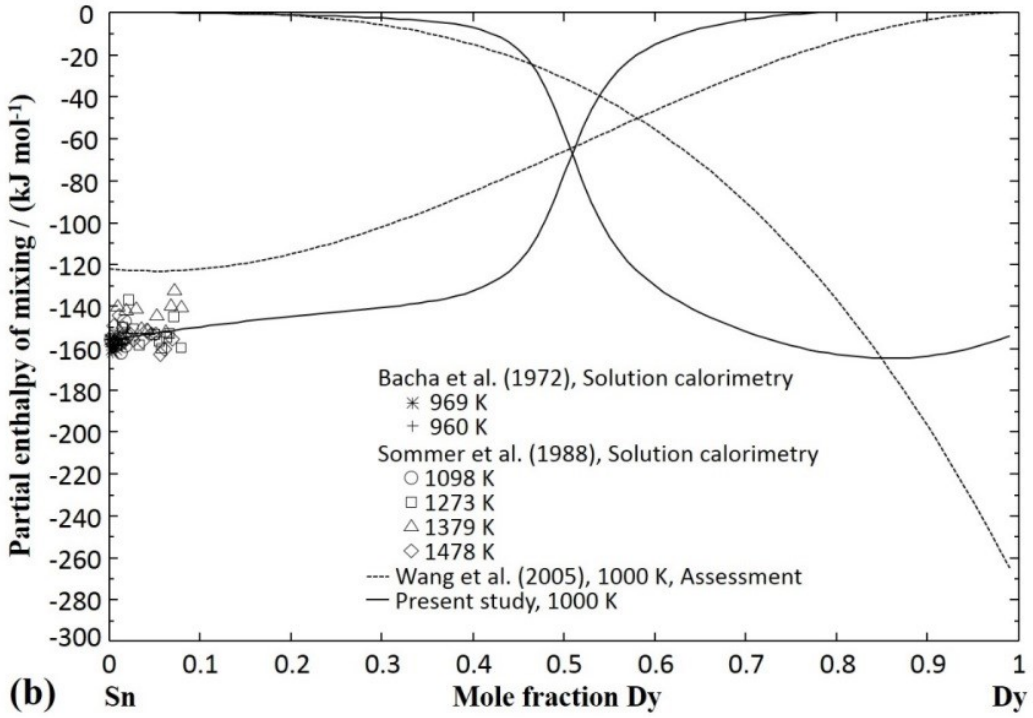


Fig. 8. The optimized Sn-Dy phase diagram with experimental data.


Integral enthalpy of mixing / (kJ mol-1)
0
-10
-20
-30
-40
-50
-60
-70
-80
-90
-100
0
0.1
0.2
0.3
0.4
0.5
0.6
0.7
0.8
0.9
1
Sn
Mole fraction Dy
Dy
Sommer et al. (1988), Solution calorimetry
1098 K
1273 K
1379 K
1478 K
Wang et al. (2005), 1000 K, Assessment
Present study, 1000 K

(a)


Partial enthalpy of mixing / (kJ mol-1)
0
-20
-40
-60
-80
-100
-120
-140
-160
-180
-200
-220
-240
-260
-280
-300
0
0.1
0.2
0.3
0.4
0.5
0.6
0.7
0.8
0.9
1
Sn
Mole fraction Dy
Dy
Bacha et al. (1972), Solution calorimetry
969 K
960 K
Sommer et al. (1988), Solution calorimetry
1098 K
1273 K
1379 K
1478 K
Wang et al. (2005), 1000 K, Assessment
Present study, 1000 K

(b)

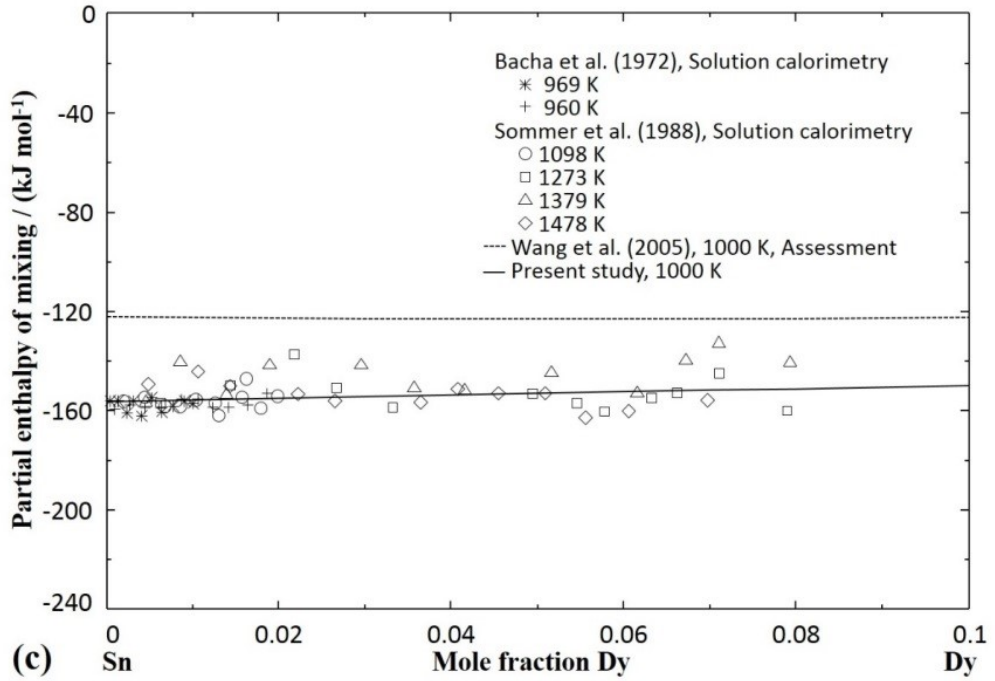


Fig. 9. (a) Integral enthalpy of mixing and (b), (c) partial enthalpy of mixing of liquid Sn-Dy at 1000 K with experimental data and previous thermodynamic assessment.

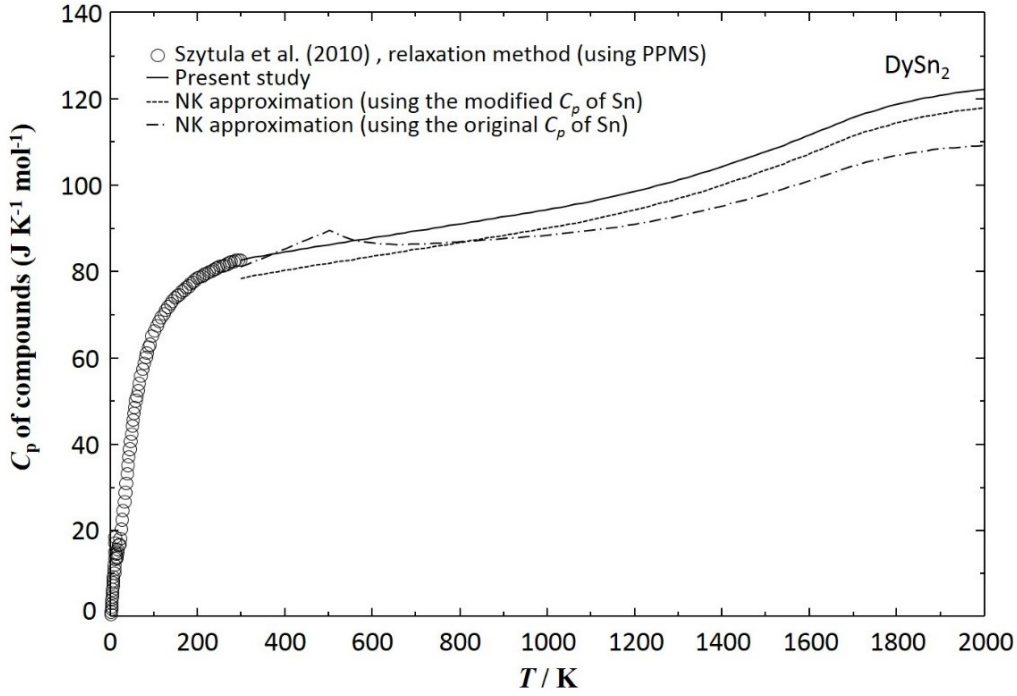


Fig. 10. Heat capacity of $DySn_2$ with experimental data (1.9-300 K).

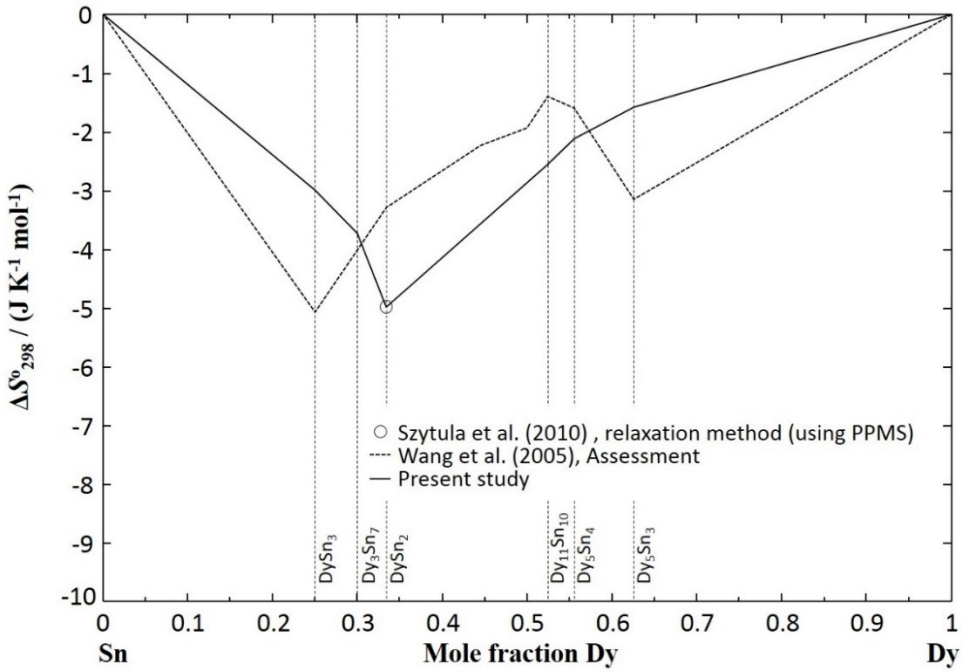


Fig. 11. Entropy of formation of the compounds in the Sn-Dy system from elements at 298 K with experimental data.

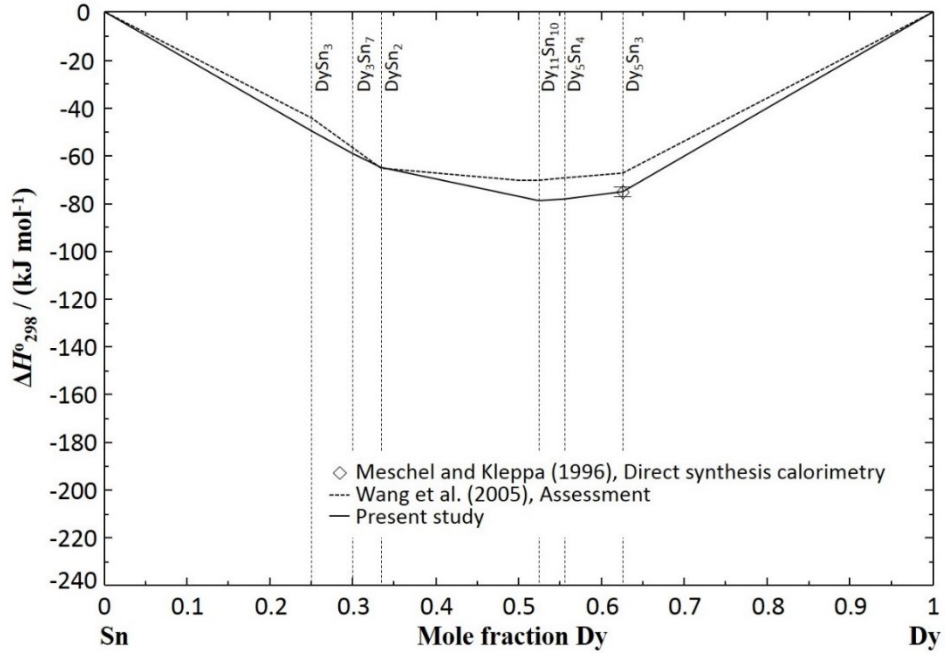


Fig. 12. Enthalpy of formation of the compounds in the Sn-Dy system at 298 K with experimental data.

1.4. The Sn-Ho system

Experimental data of the Sn-Ho phase diagram are presented in Fig. 13. The intermetallic compounds in this system were revealed by the crystallographic studies. The crystal structure and lattice parameters of Ho_xSn_y were reported: Ho_5Sn_3 (Mn_5Si_3 type, low temperature form) [1, 2, 46], Ho_5Sn_4 (Sm_5Ge_4 type) [29], $Ho_{11}Sn_{10}$ ($Ho_{11}Ge_{10}$ type) [3], $HoSn_2$ ($ZrSi_2$ type) [5, 46], Ho_2Sn_5 (Y_2Sn_5 type) [8], and $HoSn_3$ ($GdSn_3$ type) [8, 32]. Eremenko et al. [15] initially investigated the phase diagram of the system using DTA from the alloys containing 0.615 and 0.899 mole fraction of Ho to verify the prediction of the melting temperature of Ho_5Sn_3 (1906 ± 17 ºC) and the eutectic temperature of Ho and Ho_5Sn_3 (1226 ± 64 ºC). The melting temperature of Ho_5Sn_3 and the eutectic temperature were found 1915 ºC and 1265 ºC, respectively, from the thermal effects of the alloys. Later, Palenzona and Manfrinetti [8] investigated the Sn-rich side of the system up to 0.35 mole fraction of Ho using the same methods used for the Sn-Gd system. The phase diagram with three incongruent compounds, $HoSn_2$ (1130 ºC), Ho_2Sn_5 (520 ºC), and $HoSn_3$ (420 ºC) were reported. However, the experimental data were unfortunately not presented. The data points in Fig. 13 were extracted from the reported graph [8]. Later again, Bulanova et al. [46] investigated the phase diagram over the whole composition range by means of DTA, XRD and metallographic methods from the alloys of 23 compositions which were prepared by arc-melting under a purified Ar atmosphere from the initial materials, 99.9995% Sn and 99.84% Ho. Seven intermetallic compounds (with melting temperature) were reported: Ho_5Sn_3 (1915 ºC, congruent), Ho_5Sn_4 (1720 ± 13 ºC, peritectic), $Ho_{11}Sn_{10}$ (1592 ± 11 ºC, peritectic), Ho_4Sn_5 (1144 ± 11 ºC, peritectic), $HoSn_2$ (1114 ± 15 ºC, peritectic), Ho_2Sn_5 (509 ± 12 ºC, peritectic), and $HoSn_3$ (420 ºC, peritectic) with eutectic reaction at 1252 ± 11 ºC and 0.87 mole fraction of Ho. The phase diagram of the Sn-rich region agreed with the findings of Palenzona and Manfrinetti [8] except for the slightly lower melting temperatures of Ho_2Sn_5 and $HoSn_2$. However, the melting temperature of pure Ho was determined to be 510 ºC, 36 degree higher than the one in Factsage database due to the unknown reason. In addition, the peritectic reaction of $HoSn_3$ was adopted from the work of Palenzona and Manfrinetti [8] because the reaction was not found in their study. It was believed that the prolonged annealing might require to observe the reaction. The solid solubility of Ho in Sn was negligible

and the solubility of Sn in hcp-Ho was about ~2.5 at. % at eutectic temperature and none of the compounds showed noticeable homogeneity ranges.

The experimental data of the thermodynamic properties of the Sn-Ho liquid are presented in Fig. 14(a) and (b). Bulanova et al. [46] determined the partial enthalpy of mixing of Ho in liquid Sn at 1473 K up to 0.389 mole fraction of Ho using drop solution calorimetry. Along with the experimental values, the statistically treated values for the integral enthalpy of mixing and the partial enthalpies of Ho and Sn were reported.

The experimental standard enthalpy of formation at about 298 K (ΔH^{o}_{298}) are presented in Fig. 15. Meschel and Kleppa [22] determined the ΔH^{o}_{298} of Ho_5Sn_3 using direct synthesis calorimetry. The heat content ($H_{1473} - H_{298}$) of Ho_5Sn_3 was also reported as 30.9 ± 1.8 kJ mol·atom^{-1}. Yamshchikov et al. [47] determined the partial Gibbs energy of Ho from the emf measurements in the temperature range 670-945 K. The temperature dependent function was given as – (214.5±2.6) + (56.7±3.2)·10^{-3}·T kJ^{-1} mol^{-1}. Although the Gibbs energy of $HoSn_3$ was also calculated to be – (48.23±0.65) + (10.61±0.81)·10^{-3}·T kJ^{-1} mol·atom^{-1} from the partial Gibbs energy, the $HoSn_3$ is not a stable phase above 493 K according to the phase diagram. Yamshchikov et al. [23] reported the activity of Ho in Ho saturated liquid at 800 K from the previous emf measurement. The values were -11.05 [24] and -11.09 [47] in logarithmic scale.

The thermodynamic optimization of the Sn-Ho system was previously performed by Iddaoudi et al. [48]. The calculated thermodynamic properties from the work of Iddaoudi et al. [48] are presented in Figs. 14-15. The thermodynamic properties were estimated to be similar to the present assessment except the enthalpy of mixing of Sn-Ho liquid. The excess Gibbs energy of liquid phase was expressed by the random mixing model using the Redlich-Kister polynomial but the minimum integral enthalpy of mixing was rather positive (-50 kJ mol^{-1}) than the present study (-64 kJ mol^{-1}).

The optimized phase diagram of the Sn-Ho system in the present study is shown in Fig. 13. In the optimization, the phase diagram was constructed mainly based on the work of Palenzona and Manfrinetti [8] for the compositions up to 0.333 mole fraction of Ho, and Bulanova et al. [46] for the compositions above. In the work of Bulanova et al. [46], the crystal structures of Ho_4Sn_5 and Ho_5Sn_4 were not resolved. Considering the similarity with the Sn-Dy system, the Ho_4Sn_5 was excluded in the system, while the Ho_5Sn_4 was believed to exist. The peritectic melting of $HoSn_2$ [8, 46] was also unlikely to be reproduced when considering the liquidus slope around between $HoSn_2$ and $Ho_{11}Sn_{10}$. The solid solubility of Sn in hcp-Ho was modeled with one temperature independent excess Gibbs energy parameter with reference to the work of Bulanova et al. [46].

The calculated thermodynamic properties with the optimized thermodynamic parameters are shown in Figs. 14-15. In the present study, the experimental data of Bulanova et al. [46] regarding the integral and partial enthalpies of mixing of Ho-rich liquid were not considered due to the improbability of the data. Compared with the other systems, the integral enthalpy was conspicuously negative already at 0.4 mole fraction of Ho, and also the rapid variation of partial enthalpy of Ho with about -80 kJ mol^{-1} at the infinite dilution were very unlikely. Therefore, the thermodynamic parameters for the excess Gibbs energy of mixing of liquid were estimated to be similar to those for the Sn-Dy system. No temperature dependent parameters (i.e., entropy) were added. The experimental data of the ΔH^{o}_{298} of Ho_5Sn_3 [22] was adopted as it was, and the ΔH^{o}_{298} of the other compounds and the ΔS^{o}_{298} of all compounds were estimated to be similar to the values for the Sn-Dy system, which also reproduce the phase diagram. The calculated heat content ($H_{1473} - H_{298}$) of Ho_5Sn_3 was about 5 kJ mol·$atom^{-1}$ higher than the experimental finding [22]. The calculated activity of Ho in Ho saturated liquid at 800 K was -12.013 in logarithmic scale, which is slightly lower than the experimental values [24, 47]. The optimized thermodynamic parameters are listed in Table 7 and the calculated invariant reactions with the experimental data are tabulated in Table 8.

Table 7. Optimized model parameters for the Sn-Ho system.

Phase	Thermodynamic parameters
Liquid	Coordination Numbers
	i j Z_{ij}^{i} Z_{ij}^{j}
	Sn Ho 6 6
	Δg_{SnHo} / (J mol^{-1}) = -48116.0 – 2092.0 X_{SnSn} + 418.4 X_{SnSn}^2
	– 20920.0 X_{HoHo} + 18744.32 X_{HoHo}^2
hcp-A3	${}^0L_{\mathrm{Sn,Ho}}$ / (J mol^{-1}) = -146440.0
$HoSn_3$	ΔH_{298}^{o} = -196760 J mol^{-1}, S_{298}^{o} = 217.7 J K^{-1} mol^{-1}
	C_p / (J K^{-1} mol^{-1}) = 1 × C_p / (J K^{-1} mol^{-1}) (Ho, hcp-A3)
	+ 3 × modified C_p / (J K^{-1} mol^{-1}) (Sn, bct-A5)*
Ho_2Sn_5	ΔH_{298}^{o} = -391810 J mol^{-1}, S_{298}^{o} = 382.3 J K^{-1} mol^{-1}
	C_p / (J K^{-1} mol^{-1}) = 2 × C_p / (J K^{-1} mol^{-1}) (Ho, hcp-A3)
	+ 5 × modified C_p / (J K^{-1} mol^{-1}) (Sn, bct-A5)*
$HoSn_2$	ΔH_{298}^{o} = -194820 J mol^{-1}, S_{298}^{o} = 164.0 J K^{-1} mol^{-1}
	C_p / (J K^{-1} mol^{-1}) = 1 × C_p / (J K^{-1} mol^{-1}) (Ho, hcp-A3)
	+ 2 × modified C_p / (J K^{-1} mol^{-1}) (Sn, bct-A5)*
$Ho_{11}Sn_{10}$	ΔH_{298}^{o} = -1654200 J mol^{-1}, S_{298}^{o} = 1275.7 J K^{-1} mol^{-1}
	C_p / (J K^{-1} mol^{-1}) = 11 × C_p / (J K^{-1} mol^{-1}) (Ho, hcp-A3)
	+ 10 × modified C_p / (J K^{-1} mol^{-1}) (Sn, bct-A5)*
Ho_5Sn_4	ΔH_{298}^{o} = -700000 J mol^{-1}, S_{298}^{o} = 560.34 J K^{-1} mol^{-1}
	C_p / (J K^{-1} mol^{-1}) = 5 × C_p / (J K^{-1} mol^{-1}) (Ho, hcp-A3)
	+ 4 × modified C_p / (J K^{-1} mol^{-1}) (Sn, bct-A5)*
Ho_5Sn_3	ΔH_{298}^{o} = -588000 J mol^{-1}, S_{298}^{o} = 520.04 J K^{-1} mol^{-1}
	C_p / (J K^{-1} mol^{-1}) = 5 × C_p / (J K^{-1} mol^{-1}) (Ho, hcp-A3)
	+ 3 × modified C_p / (J K^{-1} mol^{-1}) (Sn, bct-A5)*

*modified C_p / (J K^{-1} mol^{-1}) (Sn, bct-A5) = 24.477 + 5.472E-2 T/K – 40640.0 (T/K)$^{-2}$ – 6.469E-7 (T/K)^2

Table 8. Calculated invariant reactions and experimental data in the Sn-Ho system.

Type	Reaction	t (°C)	Reference
Eutectic	$L(X_{Ho}=<1E\text{-}5) \rightarrow Sn(\text{bct-A5}, X_{Ho}=0) + HoSn_3$	231.9	This work
	$L(X_{Ho}=*) \rightarrow Sn(\text{bct-A5}, X_{Ho}=0) + HoSn_3$	230.0	[8]
	$L(X_{Ho}=*) \rightarrow Sn(\text{bct-A5}, X_{Ho}=0) + HoSn_3$	229±2	[46]
Peritectic	$L(X_{Ho}=0.0008) + Ho_2Sn_5 \rightarrow HoSn_3$	419.7	This work
	$L(X_{Ho}=\sim0.001) + Ho_2Sn_5 \rightarrow HoSn_3$	420.0	[8]
Peritectic	$L(X_{Ho}=0.005) + HoSn_2 \rightarrow Ho_2Sn_5$	520.0	This work
	$L(X_{Ho}=\sim0.007) + HoSn_2 \rightarrow Ho_2Sn_5$	520.0	[8]
	$L(X_{Ho}=\sim0.009) + HoSn_2 \rightarrow Ho_2Sn_5$	509±12	[46]
Congruent	$L(X_{Ho}=0.333) \leftrightarrow HoSn_2$	1130.0	This work
Peritectic	$L(X_{Ho}=\sim0.291) + ** \rightarrow HoSn_2$	1130.0	[8]
	$L(X_{Ho}=\sim0.293) + Ho_4Sn_5 \rightarrow HoSn_2$	1114±15	[46]
Peritectic	$L(X_{Ho}=\sim0.337) + Ho_{11}Sn_{10} \rightarrow Ho_4Sn_5$	1144±11	[46]
Eutectic	$L(X_{Ho}=0.349) \rightarrow HoSn_2 + Ho_{11}Sn_{10}$	1128.0	This work
Peritectic	$L(X_{Ho}=0.477) + Ho_5Sn_4 \rightarrow Ho_{11}Sn_{10}$	1582.1	This work
	$L(X_{Ho}=\sim0.511) + Ho_5Sn_4 \rightarrow Ho_{11}Sn_{10}$	1582±11	[46]
Peritectic	$L(X_{Ho}=0.541) + Ho_5Sn_3 \rightarrow Ho_5Sn_4$	1720.4	This work
	$L(X_{Ho}=\sim0.531) + Ho_5Sn_3 \rightarrow Ho_5Sn_4$	1720±13	[46]
Congruent	$L(X_{Ho}=0.625) \leftrightarrow Ho_5Sn_3$	1915.3	This work
	$L(X_{Ho}=0.625) \leftrightarrow Ho_5Sn_3$	1915.0	[15]
	$L(X_{Ho}=0.625) \leftrightarrow Ho_5Sn_3$	1915.0	[46]
Eutectic	$L(X_{Ho}=0.848) \rightarrow Ho_5Sn_3 + Ho(\text{hcp-A3}, X_{Ho}=0.975)$	1247.3	This work
	$L(X_{Ho}=\sim0.89) \rightarrow Ho_5Sn_3 + Ho(\text{hcp-A3}, X_{Ho}=*)$	1265.0	[15]
	$L(X_{Ho}=\sim0.87) \rightarrow Ho_5Sn_3 + Ho(\text{hcp-A3}, X_{Ho}=\sim0.975)$	1252±11	[46]

* The exact compositions are not specified in the reference.
** The phase was not identified.

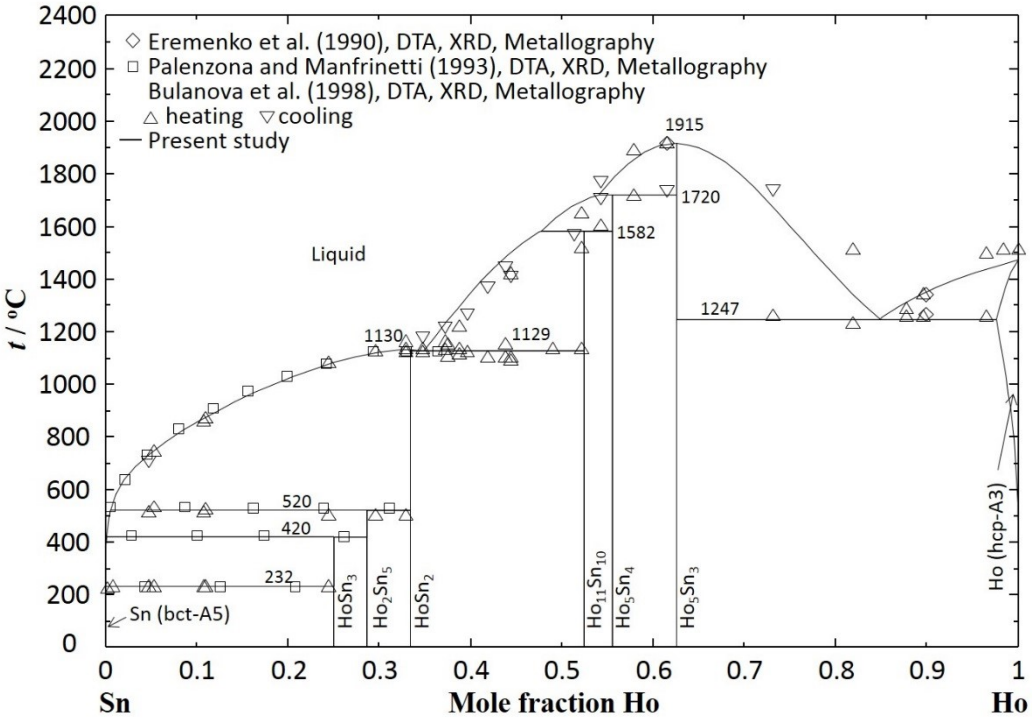


Fig. 13. The optimized Sn-Ho phase diagram with experimental data.

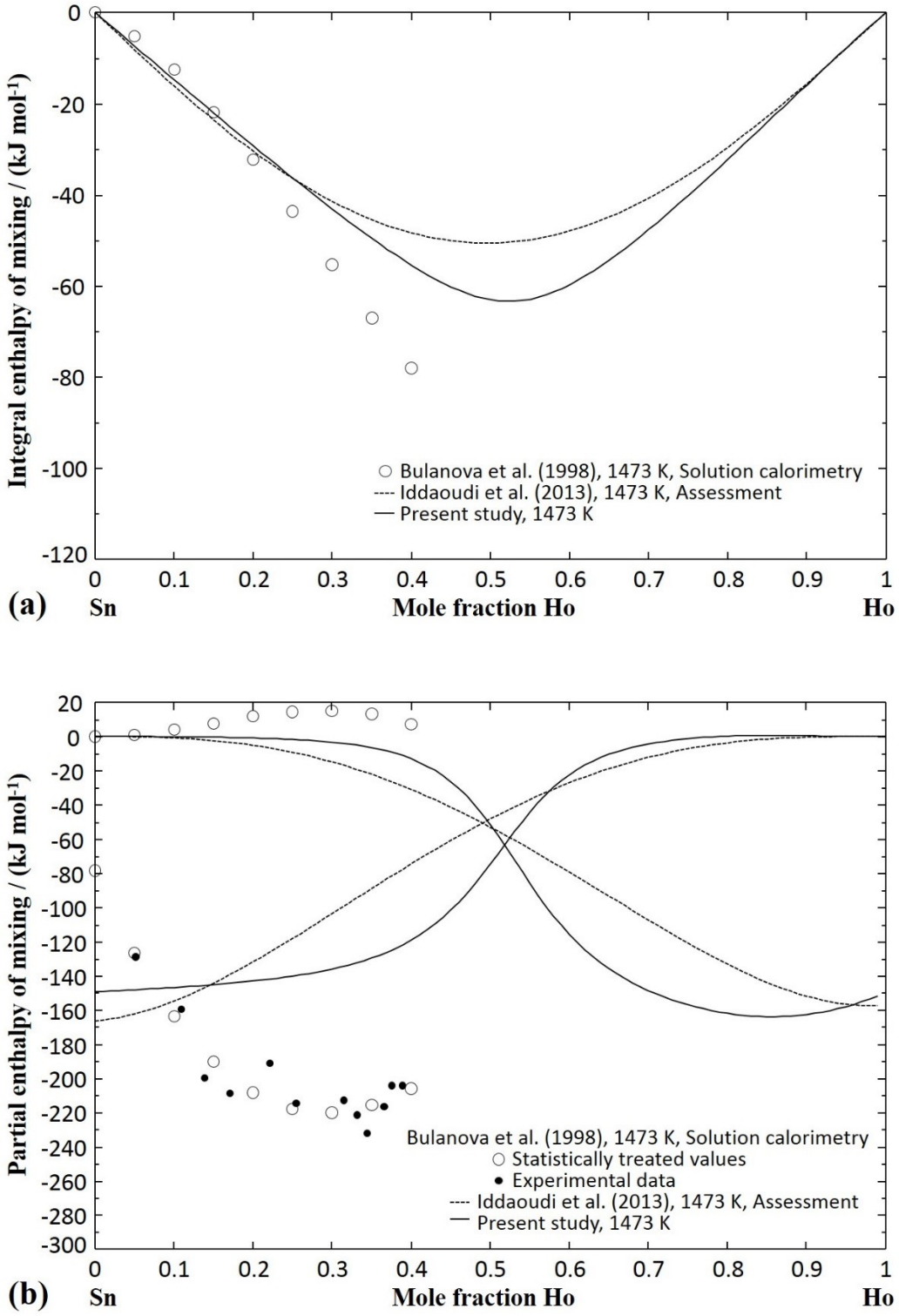


Fig. 14. (a) Integral enthalpy of mixing and (b) partial enthalpy of mixing of liquid Sn-Ho at 1473 K with experimental data and previous thermodynamic assessment.

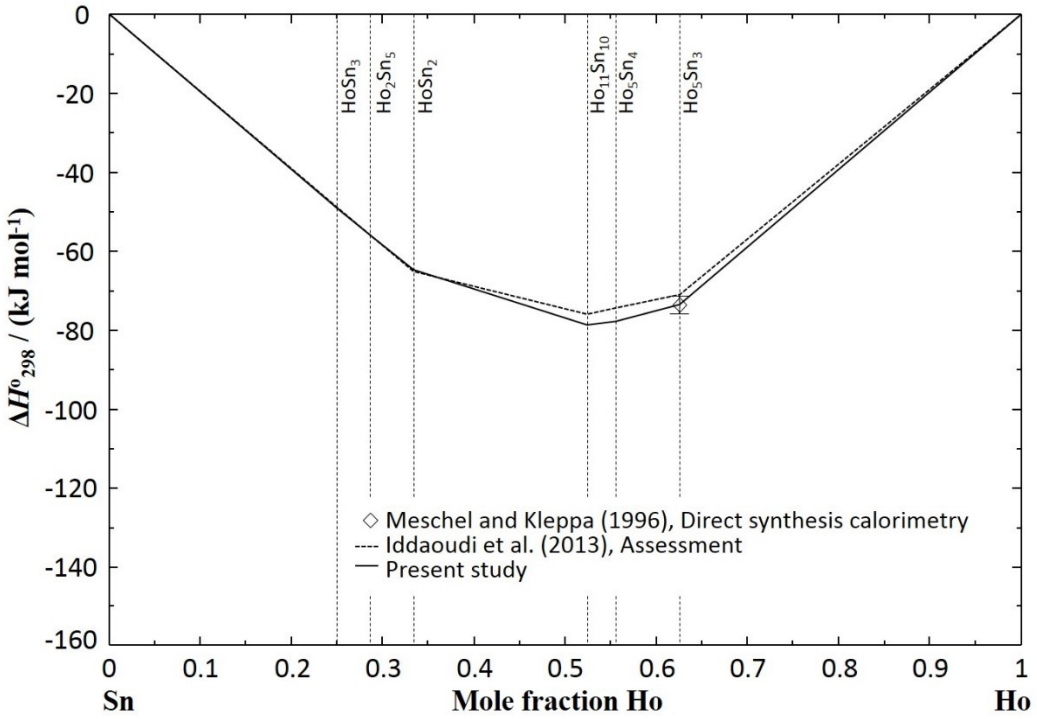


Fig. 15. Enthalpy of formation of the compounds in the Sn-Ho system at 298 K with experimental data.

1.5. The Sn-Er system

Experimental data of the Sn-Er phase diagram are presented in Fig. 16. The intermetallic compounds in this system were revealed by the crystallographic studies. The crystal structure and lattice parameters of Er_xSn_y were reported: Er_5Sn_3 (Mn_5Si_3 type, low temperature form) [1, 2], Er_5Sn_4 (Sm_5Ge_4 type) [29], $Er_{11}Sn_{10}$ ($Ho_{11}Ge_{10}$ type) [3], $ErSn_2$ ($ZrSi_2$ type) [5], Er_2Sn_5 (Y_2Sn_5 type) [8], and $ErSn_3$ ($GdSn_3$ type) [8]. The first phase diagram investigation was carried out by Love [49] in the Er-rich region up to 0.33 mole fraction of Sn. Based on the thermal analysis, XRD and metallographic analyses, the Er_2Sn compound which melted congruently at about 1550 ºC and the eutectic reaction of Er_2Sn and Er at 1230 ºC and 0.9 mole fraction of Er were reported. The maximum solid solubility of Sn in Er was also reported as approximately 0.007 mole fraction of Sn. Kulagina and Bayanov [50] studied the interaction of Er with Sn at 773-973 K and 0.4-16.1 at. % from the emf measurement and reported the solubility of Er in liquid Sn. Using the same method, Yamshchikov et al. [51] also reported the solubility of Er in liquid Sn, which is slightly lower than the values of Kulagina and Bayanov [50] in the temperature range between 720 and 1080 K. Later, Kulagina et al. [14] investigated the Sn-rich region of the phase diagram (up to 0.25 mole fraction of Er) using thermal analysis and microscopic examination with the alloys prepared in sealed quartz vessels. The temperature dependence of Er solubility in liquid Sn was expressed by the equation, $\log(\text{at.\% Er}) = 1.79 - 3207\ T^{-1}$. In addition, the melting temperature of $ErSn_3$ (congruent) was reported to be 1090 ± 4 ºC. Like the previous systems, Erementko et al. [15] investigated the phase diagram of the system using DTA from the alloys containing 0.616, 0.636, and 0.899 mole fraction of Er to verify the prediction of the melting temperature of Er_5Sn_3 (1934 ± 17 ºC) and the eutectic temperature of Er and Er_5Sn_3 (1269 ± 64 ºC). The melting temperature of Er_5Sn_3 and the eutectic temperature were found 1930 ºC and 1305 ºC, respectively, from the thermal effects of the alloys. Palenzona and Manfrinetti [8] also investigated the Sn-rich side of the system up to 0.35 mole fraction of Er using the same methods used for the Sn-Gd system. The phase diagram with three incongruent compounds, $ErSn_2$ (1125 ºC), Er_2Sn_5 (490 ºC), and $ErSn_3$ (390 ºC) were reported. However, the experimental data were unfortunately not presented. The data points in Fig. 16 were extracted from the reported graph [8]. Additionally, the existence of $Er_{11}Sn_{10}$ and Er_5Sn_3 phases were confirmed by the isothermal phase diagram investigation of the ternary systems

containing Sn and Er [52-56]. Even though the Er_5Sn_4 phase was not found in those studies [52-56], the stable Er_5Sn_4 may exist in the Sn-Er system according to the study of Zhong et al. [29]. In the work of Zhong et al. [29], the Er_5Sn_4 was found in the alloy which was prepared by arc-melting of constituent metals with the purity over 99.99 wt. %. Moreover, the amount of Er_5Sn_4 increased by annealing at 1300 °C for 24 hours as compared with the as-cast alloy. However, the experimental phase diagram investigation over the whole composition range has not been performed yet. The phase diagram of the Sn-Er system is still unclear.

The experimental data of the thermodynamic properties of the Sn-Er liquid are presented in Fig. 17(a) to (c). Bacha et al. [42] measured the heat of mixing of solid Er in liquid Sn at 959 and 967 K using solution calorimetry from high purity materials, (purity not reported) Sn and 99.9% Dy. In the present study, the enthalpy of mixing values were derived based on the dissolution enthalpy by considering the heat content of Er from the room temperature to the measurement temperature. Similarly, Sommer et al. [21] determined the heat of dissolution of solid Er in liquid Sn up to 0.1 mole fraction of Er at 1096, 1183, 1271, 1371 and 1470 K from high purity materials, 99.96% Sn and 99.9% Er. The partial enthalpy of mixing values of Er were obtained based on the dissolution enthalpy. Then, the partial enthalpy values were used to obtain the integral enthalpy of mixing as shown in Fig. 17(a) in the present study.

As for the thermodynamic properties of intermetallic compounds, the experimental standard enthalpy of formation at about 298 K (ΔH^{o}_{298}) are presented in Fig. 18. Meschel and Kleppa [57] determined the ΔH^{o}_{298} of Er_5Sn_3 using direct synthesis calorimetry. The heat content ($H_{1473} - H_{298}$) of Er_5Sn_3 was also reported as 28.1 ± 0.5 kJ mol·atom^{-1}. Yamshchikov et al. [23] reported the activity of Er in Er saturated liquid at 800 K from the previous emf measurements. The values (logarithmic scale) were -10.91 [58] and -10.63 [25].

The optimized phase diagram of the Sn-Er system in the present study is shown in Fig. 16. The phase diagram in the composition up to 0.333 mole fraction of Er reported by Palenzona and Manfrinetti [8] was well reproduced in the present optimization. As for the Er-rich region, the

eutectic reaction (L→Er_5Sn_3 + Er) and the melting temperature of Er_5Sn_3 determined by Eremenko et al. [15] were also well reproduced. However, for the mid-composition range where the experimental data were absent, the melting temperature of $Er_{11}Sn_{10}$ and Er_5Sn_4 were assumed based on the systematic analysis which will be discussed in later chapter. Although the existence of the Er_5Sn_4 phase was debatable, the Er_5Sn_4 was added by accepting Zhong et al. [29] in the present study. The maximum solid solubility of Sn in hcp-Er reported by Love [49] was adopted with one temperature independent excess Gibbs energy parameter although the investigation was very rough.

The calculated thermodynamic properties with the optimized thermodynamic parameters are shown in Figs. 17-18. The experimental data of the integral and partial enthalpies of mixing of Sn-rich liquid [21, 42] were well reproduced by the present optimization. The minimum enthalpy of mixing was assessed to be slightly less than -60 kJ mol^{-1} at about 0.5 mole fraction of Er. Owing to the less negative enthalpy of mixing compared with the previous systems, one negative temperature dependent parameters (i.e., entropy) were added to reproduce the phase diagram data. This also caused the peritectic melting of $ErSn_2$ phase with less steep liquidus in the mid-composition range in the phase diagram (in Fig. 16). The experimental data of the ΔH^{o}_{298} of Er_5Sn_3 [57] was adopted as it was, and the ΔH^{o}_{298} of the other compounds and the ΔS^{o}_{298} of all compounds were estimated by considering the systematic change from the previous systems. The calculated heat content ($H_{1473} - H_{298}$) of Er_5Sn_3 was about 8 kJ mol·$atom^{-1}$ higher than the experimental finding [57]. The calculated activity of Er in Er saturated liquid at 800 K was -11.397 in logarithmic scale, which is slightly lower than the experimental values [25, 58]. The optimized thermodynamic parameters are listed in Table 9 and the calculated invariant reactions with the experimental data are tabulated in Table 10.

Table 9. Optimized model parameters for the Sn-Er system.

Phase	Thermodynamic parameters
Liquid	Coordination Numbers
	i j Z_{ij}^{i} Z_{ij}^{j}
	Sn Er 6 6
	Δg_{SnEr} / (J mol^{-1}) = (-41840.0 – 1.841 T/K) – 2092.0 X_{SnSn} – 2092.0 X_{SnSn}^2
	– 20920.0 X_{ErEr} + 15424.2 X_{ErEr}^2
hcp-A3	${}^0L_{\mathrm{Sn,Er}}$ / (J mol^{-1}) = -120802.0
$ErSn_3$	ΔH_{298}^{o} = -185340 J mol^{-1}, S_{298}^{o} = 215.65 J K^{-1} mol^{-1}
	C_p / (J K^{-1} mol^{-1}) = 1 × C_p / (J K^{-1} mol^{-1}) (Er, hcp-A3)
	+ 3 × modified C_p / (J K^{-1} mol^{-1}) (Sn, bct-A5)*
Er_2Sn_5	ΔH_{298}^{o} = -369850 J mol^{-1}, S_{298}^{o} = 377.5 J K^{-1} mol^{-1}
	C_p / (J K^{-1} mol^{-1}) = 2 × C_p / (J K^{-1} mol^{-1}) (Er, hcp-A3)
	+ 5 × modified C_p / (J K^{-1} mol^{-1}) (Sn, bct-A5)*
$ErSn_2$	ΔH_{298}^{o} = -183000 J mol^{-1}, S_{298}^{o} = 162.95 J K^{-1} mol^{-1}
	C_p / (J K^{-1} mol^{-1}) = 1 × C_p / (J K^{-1} mol^{-1}) (Er, hcp-A3)
	+ 2 × modified C_p / (J K^{-1} mol^{-1}) (Sn, bct-A5)*
$Er_{11}Sn_{10}$	ΔH_{298}^{o} = -1600000 J mol^{-1}, S_{298}^{o} = 1251.43 J K^{-1} mol^{-1}
	C_p / (J K^{-1} mol^{-1}) = 11 × C_p / (J K^{-1} mol^{-1}) (Er, hcp-A3)
	+ 10 × modified C_p / (J K^{-1} mol^{-1}) (Sn, bct-A5)*
Er_5Sn_4	ΔH_{298}^{o} = -680000 J mol^{-1}, S_{298}^{o} = 549.95 J K^{-1} mol^{-1}
	C_p / (J K^{-1} mol^{-1}) = 5 × C_p / (J K^{-1} mol^{-1}) (Er, hcp-A3)
	+ 4 × modified C_p / (J K^{-1} mol^{-1}) (Sn, bct-A5)*
Er_5Sn_3	ΔH_{298}^{o} = -578400 J mol^{-1}, S_{298}^{o} = 510.08 J K^{-1} mol^{-1}
	C_p / (J K^{-1} mol^{-1}) = 5 × C_p / (J K^{-1} mol^{-1}) (Er, hcp-A3)
	+ 3 × modified C_p / (J K^{-1} mol^{-1}) (Sn, bct-A5)*

*modified C_p / (J K^{-1} mol^{-1}) (Sn, bct-A5) = 24.477 + 5.472E-2 T/K – 40640.0 (T/K)$^{-2}$ – 6.469E-7 (T/K)^2

Table 10. Calculated invariant reactions and experimental data in the Sn-Er system.

Type	Reaction	t (°C)	Reference
Eutectic	$L(X_{Er}=<1E\text{-}5) \rightarrow Sn(\text{bct-A5}, X_{Er}=0) + ErSn_3$	231.9	This work
	$L(X_{Er}=*) \rightarrow Sn(\text{bct-A5}, X_{Er}=0) + ErSn_3$	~225.0	[14]
	$L(X_{Er}=*) \rightarrow Sn(\text{bct-A5}, X_{Er}=0) + ErSn_3$	230.0	[8]
Peritectic	$L(X_{Er}=0.0006) + Er_2Sn_5 \rightarrow ErSn_3$	389.5	This work
	$L(X_{Er}=\sim0.0015) + Er_2Sn_5 \rightarrow ErSn_3$	390.0	[8]
Congruent	$L(X_{Er}=0.333) \leftrightarrow ErSn_3$	1090±4	[14]
Peritectic	$L(X_{Er}=0.004) + ErSn_2 \rightarrow Er_2Sn_5$	490.2	This work
	$L(X_{Er}=\sim0.012) + ErSn_2 \rightarrow Er_2Sn_5$	490.0	[8]
Peritectic	$L(X_{Er}=0.294) + Er_{11}Sn_{10} \rightarrow ErSn_2$	1124.9	This work
	$L(X_{Er}=\sim0.324) + ** \rightarrow ErSn_2$	1125.0	[8]
Peritectic	$L(X_{Er}=0.444) + Er_5Sn_4 \rightarrow Er_{11}Sn_{10}$	1561.2	This work
Peritectic	$L(X_{Er}=0.519) + Er_5Sn_3 \rightarrow Er_5Sn_4$	1723.3	This work
Congruent	$L(X_{Er}=0.625) \leftrightarrow Er_5Sn_3$	1930.2	This work
	$L(X_{Er}=0.625) \leftrightarrow Er_5Sn_3$	1930.0	[15]
Eutectic	$L(X_{Er}=0.866) \rightarrow Er_5Sn_3 + Er(\text{hcp-A3}, X_{Er}=0.992)$	1305.4	This work
	$L(X_{Er}=\sim0.89) \rightarrow Er_5Sn_3 + Er(\text{hcp-A3}, X_{Er}=*)$	1305.0	[15]

* The exact compositions are not specified in the reference.
** The phase was not identified.

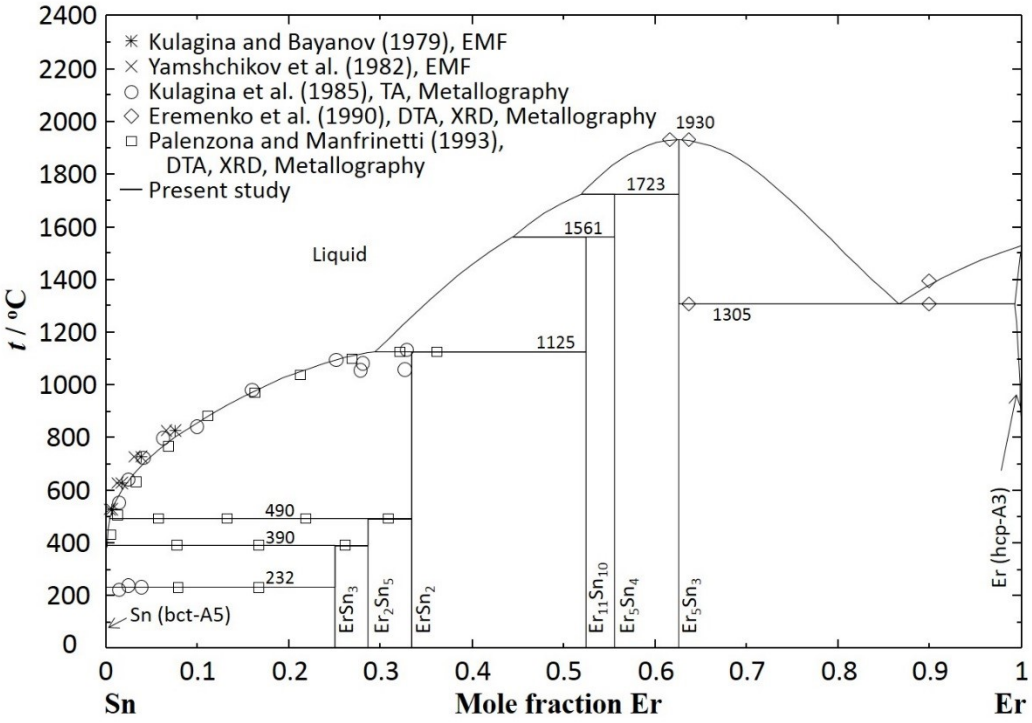
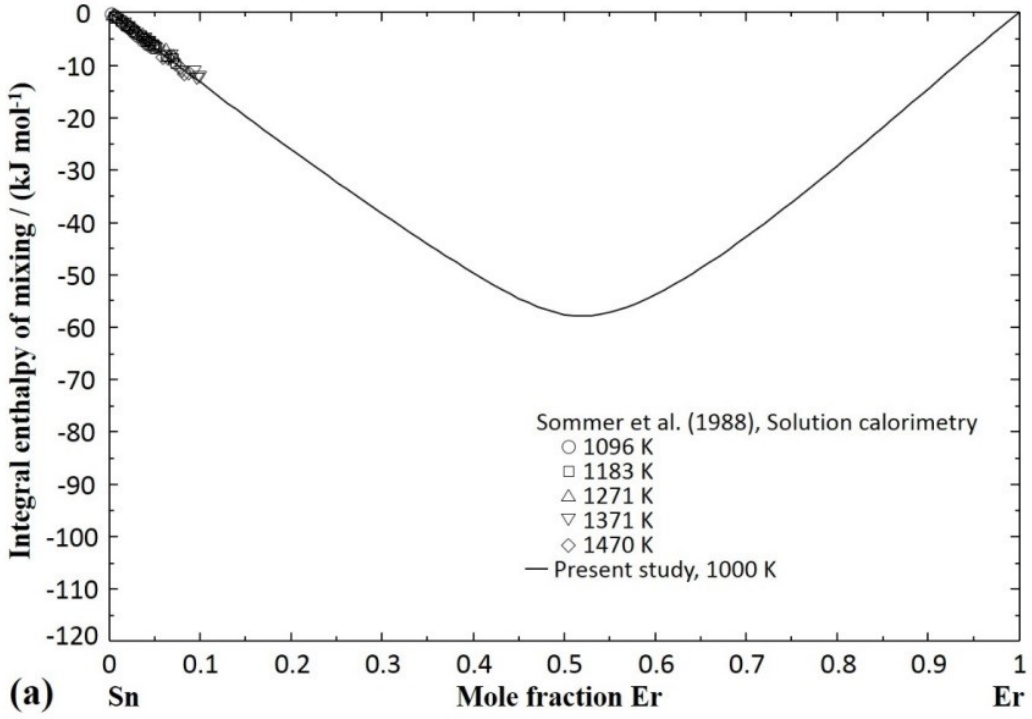
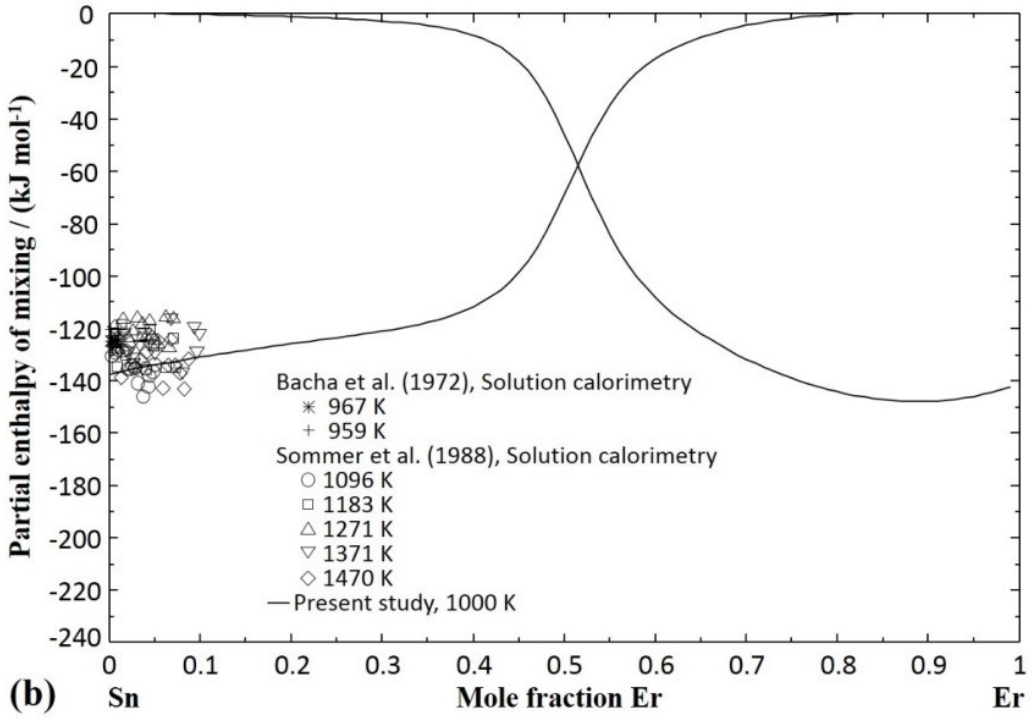


Fig. 16. The optimized Sn-Er phase diagram with experimental data.


Integral enthalpy of mixing / (kJ mol-1)
0
-10
-20
-30
-40
-50
-60
-70
-80
-90
-100
-110
-120
Sommer et al. (1988), Solution calorimetry
1096 K
1183 K
1271 K
1371 K
1470 K
Present study, 1000 K
0
0.1
0.2
0.3
0.4
0.5
0.6
0.7
0.8
0.9
1
(a)
Sn
Mole fraction Er
Er


Partial enthalpy of mixing / (kJ mol-1)
0
-20
-40
-60
-80
-100
-120
-140
-160
-180
-200
-220
-240
Bacha et al. (1972), Solution calorimetry
967 K
959 K
Sommer et al. (1988), Solution calorimetry
1096 K
1183 K
1271 K
1371 K
1470 K
Present study, 1000 K
0
0.1
0.2
0.3
0.4
0.5
0.6
0.7
0.8
0.9
1
(b)
Sn
Mole fraction Er
Er

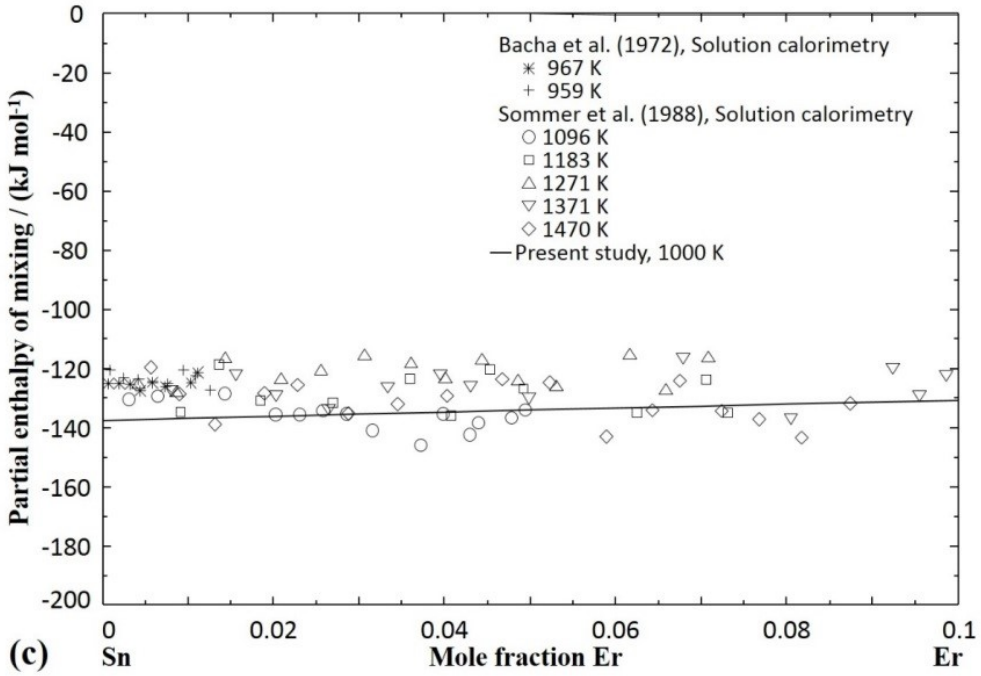


Fig. 17. (a) Integral enthalpy of mixing and (b), (c) partial enthalpy of mixing of liquid Sn-Er at 1000 K with experimental data.

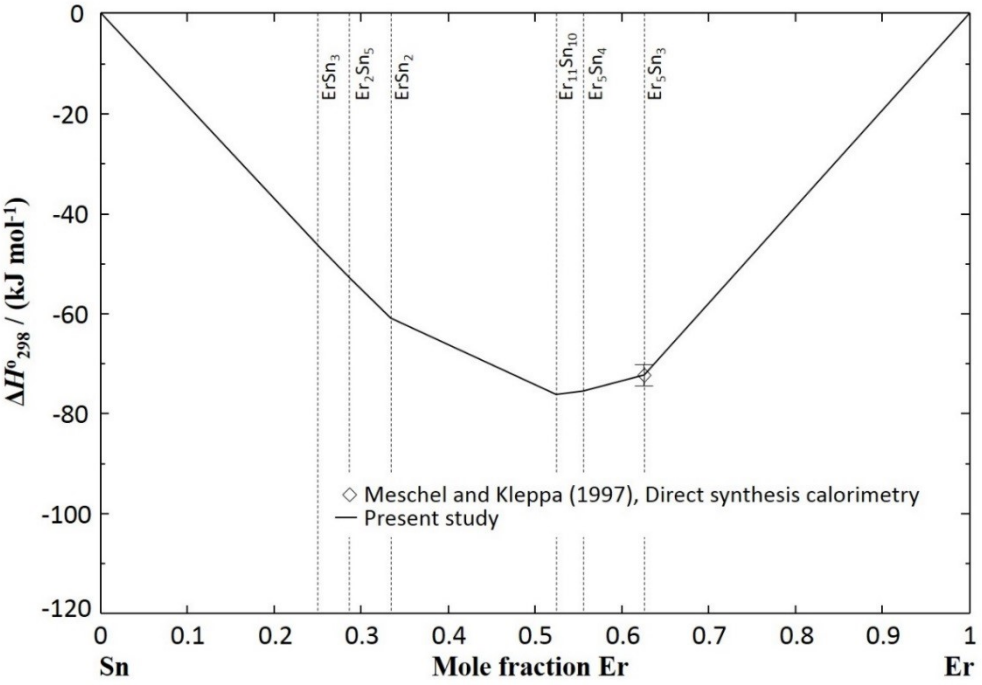


Fig. 18. Enthalpy of formation of the compounds in the Sn-Er system at 298 K with experimental data.

1.6. The Sn-Tm system

Experimental data of the Sn-Tm phase diagram are presented in Fig. 19. The intermetallic compounds in this system were revealed by the crystallographic studies. The crystal structure and lattice parameters of Tm_xSn_y were reported: Tm_5Sn_3 (Mn_5Si_3 type, low temperature form) [1, 2], $Tm_{11}Sn_{10}$ ($Ho_{11}Ge_{10}$ type) [3], $TmSn_2$ ($ZrSi_2$ type) [5], Tm_2Sn_5 (Y_2Sn_5 type) [8], and $TmSn_3$ ($GdSn_3$ type) [8]. Erementko et al. [15] investigated the phase of the system using DTA from the alloys containing 0.581, 0.593, 0.644, and 0.891 mole fraction of Tm to verify the prediction of the melting temperature of Tm_5Sn_3 (1947 ± 17 ºC) and the eutectic temperature of Tm and Tm_5Sn_3 (1288 ± 64 ºC). However, the congruent melting point of Tm_5Sn_3 was not obtained due to the limitation of equipment. The alloy with 0.644 mole fraction of Tm was still solid after heating up to 1940 ºC. Considering the liquidus for the alloys containing 0.581 and 0.593 mole fraction of Tm and the melting temperature prediction, the melting temperature of Tm_5Sn_3 phase was reported to be 1950 ºC. In addition, the thermal effect at 1685 ºC for the alloy containing 0.593 mole fraction of Tm corresponded the peritecitc melting of the $Tm_{11}Sn_{10}$, and the eutectic temperature was found 1310 ºC. Palenzona and Manfrinetti [8] also investigated the Sn-rich side of the system up to 0.35 mole fraction of Tm using the same methods used for the Sn-Gd system. The phase diagram with three incongruent compounds, $TmSn_2$ (1095 ºC), Tm_2Sn_5 (450 ºC), and $TmSn_3$ (360 ºC) were reported. However, the experimental data were unfortunately not presented. The data points in Fig. 19 were extracted from the reported graph [8]. The experimental phase diagram investigation over the whole composition range has not been performed yet. The phase diagram of the Sn-Er system is still unclear. No thermodynamic properties of Sn-Tm liquid were reported.

The experimental standard enthalpy of formation at about 298 K (ΔH^{o}_{298}) are presented in Fig. 20. Meschel and Kleppa [59] determined the ΔH^{o}_{298} of Tm_5Sn_3 using direct synthesis calorimetry. The heat content ($H_{1473} - H_{298}$) of Tm_5Sn_3 was also reported as 30.5 ± 1.6 kJ mol·atom^{-1}.

The optimized phase diagram of the Sn-Tm system in the present study is shown in Fig. 19. Similar to the Sn-Er system, the phase diagram in the composition up to 0.333 mole fraction of Er reported

by Palenzona and Manfrinetti [8] was well reproduced in the present optimization. As for the Tm-rich region, the eutectic reaction (L→Tm_5Sn_3 + Tm) and the peritectic melting temperature of $Tm_{11}Sn_{10}$ determined by Eremenko et al. [15] were also well reproduced. In addition, the predicted melting temperature of Tm_5Sn_3 [15] was believed to be reasonable considering the liquidus points from the alloys with more Sn. Although it is rather unusual that the RE_5Sn_4 phase was absent from Sn-Tm system, the phase was excluded based on the experimental finding by Eremenko et al. [15]. The solid solubility of Sn in hcp-Tm was not considered.

The excess Gibbs energy parameters were assumed to be similar to the Sn-Er system as the thermodynamic data of liquid phase were not available. The experimental data of the ΔH^{o}_{298} of Tm_5Sn_3 [59] was adopted as it was, and the ΔH^{o}_{298} of the other compounds and the ΔS^{o}_{298} of all compounds were estimated to be similar to those for the Sn-Er system. The calculated ΔH^{o}_{298} of the compounds along with experimental data [59] are shown in Fig. 20. The calculated heat content ($H_{1473} - H_{298}$) of Tm_5Sn_3 was about 4.5 kJ mol·atom^{-1} higher than the experimental finding [59]. The optimized thermodynamic parameters are listed in Table 11 and the calculated invariant reactions with the experimental data are tabulated in Table 12.

Table 11. Optimized model parameters for the Sn-Tm system.

Phase	Thermodynamic parameters
Liquid	Coordination Numbers
	i j Z_{ij}^{i} Z_{ij}^{j}
	Sn Tm 6 6
	Δg_{SnTm} / (J mol^{-1}) = (-41840.0 – 1.841 T/K) – 2092.0 X_{SnSn} – 2092.0 X_{SnSn}^{2} – 20920.0 X_{TmTm} + 17530.96 X_{TmTm}^{2}
$TmSn_3$	ΔH_{298}^{o} = -185100 J mol^{-1}, S_{298}^{o} = 215.78 J K^{-1} mol^{-1}
	C_p / (J K^{-1} mol^{-1}) = 1 × C_p / (J K^{-1} mol^{-1}) (Tm, hcp-A3) + 3 × modified C_p / (J K^{-1} mol^{-1}) (Sn, bct-A5)*
Tm_2Sn_5	ΔH_{298}^{o} = -370000 J mol^{-1}, S_{298}^{o} = 377.37 J K^{-1} mol^{-1}
	C_p / (J K^{-1} mol^{-1}) = 2 × C_p / (J K^{-1} mol^{-1}) (Tm, hcp-A3) + 5 × modified C_p / (J K^{-1} mol^{-1}) (Sn, bct-A5)*
$TmSn_2$	ΔH_{298}^{o} = -183100 J mol^{-1}, S_{298}^{o} = 163.28 J K^{-1} mol^{-1}
	C_p / (J K^{-1} mol^{-1}) = 1 × C_p / (J K^{-1} mol^{-1}) (Tm, hcp-A3) + 2 × modified C_p / (J K^{-1} mol^{-1}) (Sn, bct-A5)*
$Tm_{11}Sn_{10}$	ΔH_{298}^{o} = -1615000 J mol^{-1}, S_{298}^{o} = 1259.1 J K^{-1} mol^{-1}
	C_p / (J K^{-1} mol^{-1}) = 11 × C_p / (J K^{-1} mol^{-1}) (Tm, hcp-A3) + 10 × modified C_p / (J K^{-1} mol^{-1}) (Sn, bct-A5)*
Tm_5Sn_3	ΔH_{298}^{o} = -582400 J mol^{-1}, S_{298}^{o} = 511.9 J K^{-1} mol^{-1}
	C_p / (J K^{-1} mol^{-1}) = 5 × C_p / (J K^{-1} mol^{-1}) (Tm, hcp-A3) + 3 × modified C_p / (J K^{-1} mol^{-1}) (Sn, bct-A5)*

*modified C_p / (J K^{-1} mol^{-1}) (Sn, bct-A5) = 24.477 + 5.472E-2 T/K – 40640.0 (T/K)$^{-2}$ – 6.469E-7 (T/K)^{2}

Table 12. Calculated invariant reactions and experimental data in the Sn-Tm system.

Type	Reaction	t (°C)	Reference
Eutectic	$L_{(X_{Tm}= 1E\text{-}5)} \rightarrow Sn_{(bct\text{-}A5,\ X_{Tm}= 0)} + TmSn_3$	231.9	This work
	$L_{(X_{Tm}= *)} \rightarrow Sn_{(bct\text{-}A5,\ X_{Tm}= 0)} + TmSn_3$	~225.0	[8]
Peritectic	$L_{(X_{Tm}= 0.0006)} + Tm_2Sn_5 \rightarrow TmSn_3$	360.1	This work
	$L_{(X_{Tm}= \sim 0.0045)} + Tm_2Sn_5 \rightarrow TmSn_3$	360.0	[8]
Peritectic	$L_{(X_{Tm}= 0.004)} + TmSn_2 \rightarrow Tm_2Sn_5$	449.8	This work
	$L_{(X_{Tm}= \sim 0.009)} + TmSn_2 \rightarrow Tm_2Sn_5$	450.0	[8]
Peritectic	$L_{(X_{Tm}= 0.284)} + Tm_{11}Sn_{10} \rightarrow TmSn_2$	1094.8	This work
	$L_{(X_{Tm}= \sim 0.319)} + ** \rightarrow TmSn_2$	1095.0	[8]
Peritectic	$L_{(X_{Tm}= 0.505)} + Tm_5Sn_3 \rightarrow Tm_{11}Sn_{10}$	1685.1	This work
	$L_{(X_{Tm}= *)} + Tm_5Sn_3 \rightarrow Tm_{11}Sn_{10}$	1685.0	[15]
Congruent	$L_{(X_{Tm}= 0.625)} \leftrightarrow Tm_5Sn_3$	1950.2	This work
Eutectic	$L_{(X_{Tm}= 0.873)} \rightarrow Tm_5Sn_3 + Tm_{(hcp\text{-}A3,\ X_{Tm}= 1)}$	1310.4	This work
	$L_{(X_{Tm}= \sim 0.89)} \rightarrow Tm_5Sn_3 + Tm_{(hcp\text{-}A3,\ X_{Tm}= 1)}$	1310.0	[15]

* The exact compositions are not specified in the reference.
** The phase was not identified.

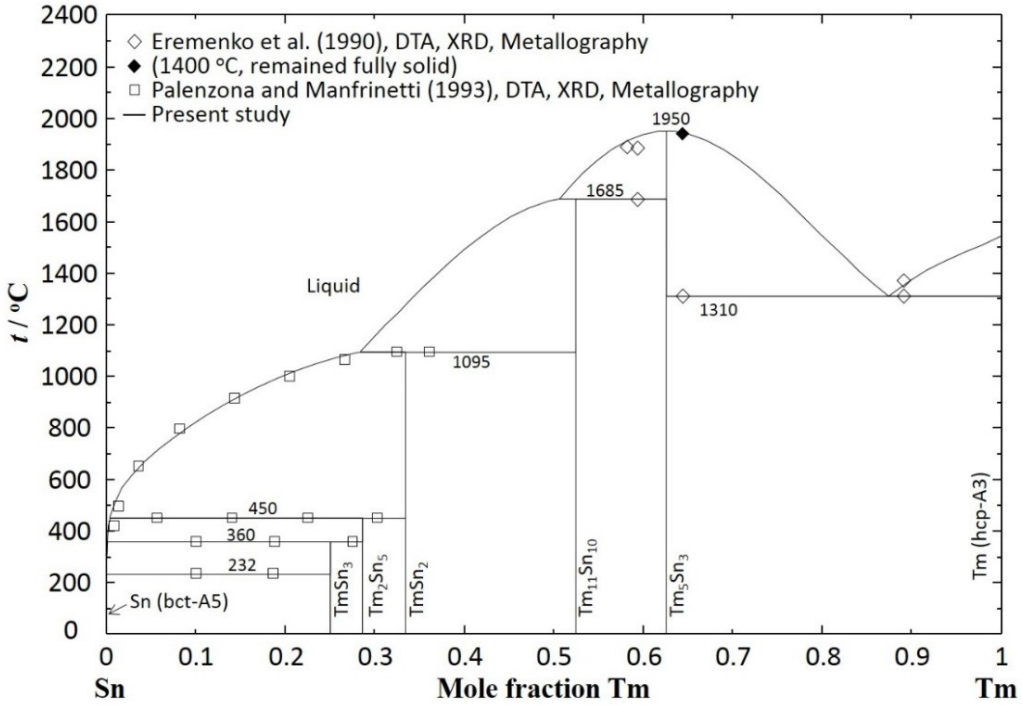


Fig. 19. The optimized Sn-Tm phase diagram with experimental data.

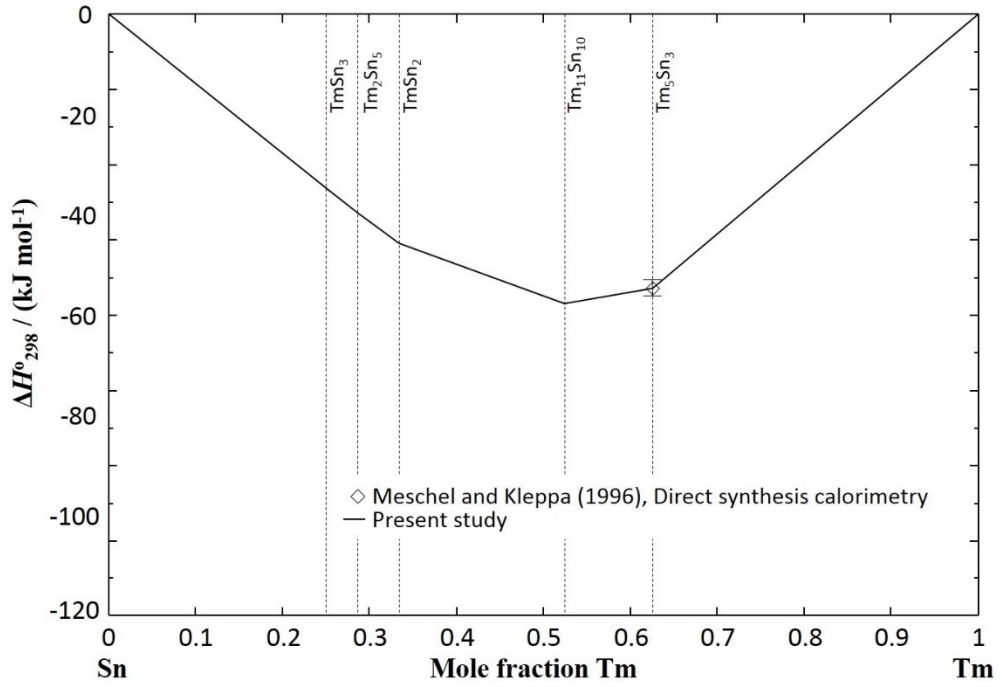


Fig. 20. Enthalpy of formation of the compounds in the Sn-Tm system at 298 K with experimental data.

1.7. The Sn-Lu system

Experimental data of the Sn-Lu phase diagram are presented in Fig. 21. The intermetallic compounds in this system were revealed by the crystallographic studies. The crystal structure and lattice parameters of Lu_xSn_y were reported: Lu_5Sn_3 (Mn_5Si_3 type, low temperature form) [1, 2], $Lu_{11}Sn_{10}$ ($Ho_{11}Ge_{10}$ type) [60], $LuSn_2$ ($ZrSi_2$ type) [5], and Lu_2Sn_5 (Y_2Sn_5 type) [8]. Kulagina et al. [14] investigated the Sn-rich region of the phase diagram (up to 0.25 mole fraction of Lu) using thermal analysis and microscopic examination with the alloys prepared in sealed quartz vessels. The temperature dependence of Lu solubility in liquid Sn was expressed by the equation, log(at.% Lu) = 1.797 – 3083 T^{-1}. In addition, the melting temperature of $LuSn_3$ (congruent) was reported to be 1017 ± 4 ºC. Palenzona and Manfrinetti [8] also investigated the Sn-rich side of the system up to 0.35 mole fraction of Lu using the same methods used for the Sn-Gd system. The phase diagram with two incongruent compounds, $LuSn_2$ (1045 ºC), and Lu_2Sn_5 (380 ºC) were reported. However, the experimental data were unfortunately not presented. The data points in Fig. 21 were extracted from the reported graph [8]. The existence of Lu_2Sn_5, $LuSn_2$ and Lu_5Sn_3 were confirmed the isothermal phase diagram investigation of the ternary Lu-Ni-Sn system [61]. The experimental phase diagram investigation over the whole composition range has not been performed yet. The phase diagram of the Sn-Er system is still unclear. No thermodynamic properties of Sn-Tm liquid were reported.

The partial thermodynamic properties of Lu-Sn alloy containing 8.9 mole fraction of Lu with respect to the pure metal in the temperature range 733-873 K were determined by Bayanov et al. [62] from the emf measurement. The partial Gibbs energy of Lu at 800 K was obtained to be – 142.34 ± 0.17 kJ mol^{-1}.

The optimized phase diagram of the Sn-Lu system in the present study is shown in Fig. 21. Similar to the Sn-Tm system, the phase diagram in the composition up to 0.333 mole fraction of Er reported by Palenzona and Manfrinetti [8] was well reproduced in the present optimization. However, the rest of compositions were not experimentally investigated. The $Lu_{11}Sn_{10}$ and Lu_5Sn_3 phases which were revealed in the crystallographic studies [1, 2, 60] were added, and the melting temperatures

of those phases and the eutectic temperature (L → Lu_5Sn_3 + Lu) were estimated by the systematic analysis. The solid solubility of Sn in hcp-Lu was not considered as no experimental data were available. The excess Gibbs energy parameters were assumed to be similar to the Sn-Tm system as the thermodynamic data of liquid phase were not available. The ΔH^{o}_{298} and the ΔS^{o}_{298} of all compounds were also estimated to be similar to those for the Sn-Tm system. The calculated activity of Lu in Lu-saturated liquid at 800 K was -8.153 in logarithmic scale, slightly more positive than the experimental value, -9.29 [62]. The optimized thermodynamic parameters are listed in Table 13 and the calculated invariant reactions with the experimental data are tabulated in Table 14.

Table 13. Optimized model parameters for the Sn-Lu system.

Phase	Thermodynamic parameters
Liquid	Coordination Numbers
	i j Z_{ij}^{i} Z_{ij}^{j}
	Sn Lu 6 6
	Δg_{SnLu} / (J mol^{-1}) = (-41840.0 – 1.841 T/K) – 2092.0 X_{SnSn}
	– 20292.4 X_{LuLu} + 17865.68 X_{LuLu}^{2}
Lu_2Sn_5	ΔH_{298}^{o} = -361310 J mol^{-1}, S_{298}^{o} = 329.2 J K^{-1} mol^{-1}
	C_p / (J K^{-1} mol^{-1}) = 2 × C_p / (J K^{-1} mol^{-1}) (Lu, hcp-A3)
	+ 5 × modified C_p / (J K^{-1} mol^{-1}) (Sn, bct-A5)*
$LuSn_2$	ΔH_{298}^{o} = -178800 J mol^{-1}, S_{298}^{o} = 140.0 J K^{-1} mol^{-1}
	C_p / (J K^{-1} mol^{-1}) = 1 × C_p / (J K^{-1} mol^{-1}) (Lu, hcp-A3)
	+ 2 × modified C_p / (J K^{-1} mol^{-1}) (Sn, bct-A5)*
$Lu_{11}Sn_{10}$	ΔH_{298}^{o} = -1592300 J mol^{-1}, S_{298}^{o} = 1012.6 J K^{-1} mol^{-1}
	C_p / (J K^{-1} mol^{-1}) = 11 × C_p / (J K^{-1} mol^{-1}) (Lu, hcp-A3)
	+ 10 × modified C_p / (J K^{-1} mol^{-1}) (Sn, bct-A5)*
Lu_5Sn_3	ΔH_{298}^{o} = -577800 J mol^{-1}, S_{298}^{o} = 396.6 J K^{-1} mol^{-1}
	C_p / (J K^{-1} mol^{-1}) = 5 × C_p / (J K^{-1} mol^{-1}) (Lu, hcp-A3)
	+ 3 × modified C_p / (J K^{-1} mol^{-1}) (Sn, bct-A5)*

*modified C_p / (J K^{-1} mol^{-1}) (Sn, bct-A5) = 24.477 + 5.472E-2 T/K – 40640.0 (T/K)$^{-2}$ – 6.469E-7 (T/K)^{2}

Table 14. Calculated invariant reactions and experimental data in the Sn-Lu system.

Type	Reaction	t (°C)	Reference
Eutectic	$L(X_{Lu}=<1E\text{-}5) \rightarrow Sn(\text{bct-A5}, X_{Lu}=0) + LuSn_3$	231.9	This work
	$L(X_{Lu}=*) \rightarrow Sn(\text{bct-A5}, X_{Lu}=0) + LuSn_3$	~225.0	[14]
	$L(X_{Lu}=*) \rightarrow Sn(\text{bct-A5}, X_{Lu}=0) + LuSn_3$	230.0	[8]
Congruent	$L(X_{Lu}=0.333) \leftrightarrow LuSn_3$	1017±4	[14]
Peritectic	$L(X_{Lu}=0.0007) + LuSn_2 \rightarrow Lu_2Sn_5$	380.0	This work
	$L(X_{Lu}=\sim0.005) + LuSn_2 \rightarrow Lu_2Sn_5$	380.0	[8]
Peritectic	$L(X_{Lu}=0.271) + Lu_{11}Sn_{10} \rightarrow LuSn_2$	1044.9	This work
	$L(X_{Lu}=\sim0.328) + ** \rightarrow LuSn_2$	1045.0	[8]
Peritectic	$L(X_{Lu}=0.505) + Lu_5Sn_3 \rightarrow Lu_{11}Sn_{10}$	1700.3	This work
Congruent	$L(X_{Lu}=0.625) \leftrightarrow Lu_5Sn_3$	1970.3	This work
Eutectic	$L(X_{Lu}=0.858) \rightarrow Lu_5Sn_3 + Lu(\text{hcp-A3}, X_{Lu}=1)$	1388.7	This work

* The exact compositions are not specified in the reference.
** The phase was not identified.

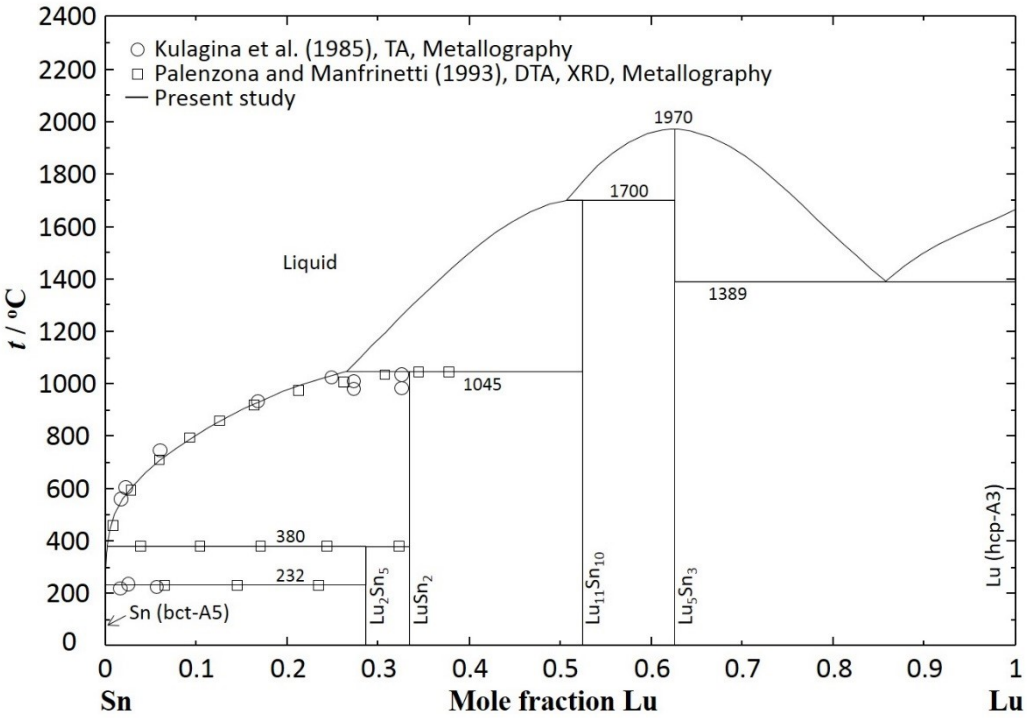


Fig. 21. The optimized Sn-Lu phase diagram with experimental data.

1.8. The Sn-Y system

Experimental data of the Sn-Y phase diagram are presented in Fig. 22. The intermetallic compounds in this system were revealed by the crystallographic studies. The crystal structure and lattice parameters of Y_xSn_y were reported: Y_5Sn_3 (Mn_5Si_3 type, low temperature form) [63-66], Y_5Sn_4 (Sm_5Ge_4 type) [65], $Y_{11}Sn_{10}$ ($Ho_{11}Ge_{10}$ type) [65, 66], YSn_2 ($ZrSi_2$ type) [5, 65, 66], Y_2Sn_5 (Y_2Sn_5 type) [8], and YSn_3 (GdSn3 type) [8]. The first phase diagram investigation was carried out by Love [49] in the Y-rich region up to 0.33 mole fraction of Sn. Based on the thermal analysis, X-ray diffraction and metallographic analysis, the partial phase diagram was tentatively suggested with the eutectic reaction of Y and Y_2Sn at 1280 ºC and 0.77 mole fraction of Y. The solid solubility of Sn in Y was reported to be very low. The phase diagram investigation over the whole composition range was performed by Schmidt and McMasters [65] using DTA, XRD and metallographic method. The alloys were prepared in arc-melting furnace under purified argon from the high purity initial metals, >99.9% Y and >99.97% Sn. Five intermetallic compounds (with melting temperature) were found: Y_5Sn_3 (1940 ºC, congruent), Y_5Sn_4 (1790 ºC, peritectic), $Y_{11}Sn_{10}$ (1600 ºC, peritectic), YSn_2 (1140 ºC, peritectic), and YSn_3 (515 ºC, peritectic) with the eutectic reaction at 1260 ± 5 ºC and 0.885 mole fraction of Y. The catatectic reaction (bcc-Y → L + hcp-Y) occurred at 1360 ± 5 ºC and approximately 4 at. % Sn. The peritectic reaction of YSn_3 was very sluggish and required heat treatment prior to DTA. The terminal solid solubility of Sn in Y was determined to be about 1.5 and 1 at. % Sn at eutectic temperature and 1150 ºC, respectively. A small homogeneity range of Y_5Sn_3 at high temperature was suggested from both the crystallographic and metallographic data however the specific data were not presented. The solubility of Y in liquid Sn was determined by Yamshchikov et al. [67] from the emf measurements using an electrochemical cell in the temperature range between 680 and 1150 K. The refined phase diagram up to 0.35 mole fraction of Y was reported by Palenzona and Manfrinetti [8] using the same methods used for the Sn-Gd system. Three incongruent melting compounds were found with respective liquidus, YSn_2 (1140 ºC), Y_2Sn_5 (525 ºC), and YSn_3 (430 ºC). The data points in Fig. 22 were extracted from the reported graph [8]. There is controversy regarding the existence of Y_2Sn_5 in the several isothermal phase diagram investigations for the ternary systems containing Sn and Y, with Y_2Sn_5 [16, 68, 69] and without Y_2Sn_5 [70, 71].

The experimental data of the thermodynamic properties of the Sn-Y liquid are presented in Fig. 23(a) to (b). Esin et al. [72] determined the enthalpy of mixing of Sn-Y liquid at 1920 K in the composition range 0-0.45 and 0.8-1.0 mole fraction of Y using solution calorimetry from the initial materials, 99.99% Sn and 99.8% Y. Nikolaenko et al. [73] also determined the enthalpy of mixing of liquid at 1523 K in the composition range up to 0.25 mole fraction of Y from the high purity materials, 99.999% Sn and 99.87% Y. However, the reported data were more negative than the values of Esin et al. [72].

Experimental data of the heat capacity (C_p) of Y_5Sn_3 are shown in Fig. 24. Gorbachuk and Bolgar [74] determined the low temperature C_p of Y_5Sn_3 in the temperature range 58-300 K using an adiabatic method in a vacuum below $2 \cdot 10^{-3}$ Pa. The samples were prepared by arc melting under Ar atmosphere from the initial materials, 99.99% Sn and 99.98% Y. The samples were subsequently annealed at 1000 ºC for 12 hours. The standard entropy of formation (S^{o}_{298}) of Y_5Sn_3 was reported to be 341.82 ± 2.73 J mole^{-1} K^{-1} based on the measured C_p values. The ΔS^{o}_{298} value from the elemental references are shown in Fig. 25. The heat content ($H_T - H_{298}$) of Y_5Sn_3 was also measured by Gorbachuk and Bolgar [74] in the range 300-1200 K using a high-temperature differential calorimeter, and above 1200 K using a high-temperature vacuum calorimeter. The experimental values are presented in Fig. 26. The C_p function of Y_5Sn_3 in the range 298.15-2300 K was derived from the measured heat content values. The proposed C_p function is shown in Fig. 26. However, there is a noticeable kink which has physically meaningless where the C_p function and the low temperature C_p data meet. The standard enthalpy of formation (ΔH^{o}_{298}) of certain compounds were determined by several researchers. The experimental ΔH^{o}_{298} values are presented in Fig. 27. Borsese et al. [75] measured the ΔH^{o}_{298} of Y_5Sn_3 at 300 K using a differential direct isoperibol calorimeter. Later, Borzone et al. [66] tried to determine the enthalpy of formation at 300 K in a large composition range using a direct method with an isoperibol calorimeter. However, only the enthalpy of formation of YSn_3 and YSn_2 phases were believed to be sufficiently accurate due to the experimental difficulties, which were not specified. Meschel and Kleppa [22] determine the ΔH^{o}_{298} of Y_5Sn_3 using direct synthesis calorimetry. The sample was prepared with a slight excess of Y corresponding to the composition $Y_{5.5}Sn_3$. Then, the ΔH^{o}_{298} and the heat content

values of Y_5Sn_3 were corrected for the contribution of the excess Y. Yamshchikov et al. [76] reported the partial Gibbs energy of Y of Y saturated liquid at 1000 K to be -145.5 ± 0.6 kJ mol^{-1} from the emf measurement.

A brief review of the phase diagram of Sn-Y was made by Okamoto [77]. The phase diagram was presented based on the work of Schmidt and McMasters [65] and the crystal structure data were summarized. The thermodynamic optimizations of the Sn-Y system were previously performed by Tang et al. [78] and Lu et al. [79]. The calculated thermodynamic properties from the previous optimizations [78, 79] are presented in Figs 23, 25, and 27. In both the optimizations, the Gibbs energy of liquid phases were described in the Redlich-Kister random mixing model. The integral enthalpies of mixing of liquid were assessed based on the data of Esin et al. [72] however the partial enthalpies of mixing of liquid which were calculated from the assessed thermodynamic parameters were slightly off from the experimental data [72] (in Fig. 23 (b)). The heat capacities (C_p) of compounds were estimated by NK approximation, resulting in the meaningless kink from the C_p of Sn. The NK approximated C_p of Y_5Sn_3 using the unmodified C_p of Sn was presented in Fig. 24 as an example. The experimental data regarding the C_p, S°_{298} and heat content of Y_5Sn_3 by Gorbachuk and Bolgar [74] were not considered in both the optimizations (in Figs. 24-26). The experimental value of Meschel and Kleppa [22] was adopted for the ΔH°_{298} of Y_5Sn_3 as seen in Fig. 27. However, if both the ΔH°_{298} of Y_5Sn_3 of Meschel and Kleppa [22] and the enthalpy of mixing data of Esin et al. [72] were considered, the heat content of Y_5Sn_3 above the melting temperature would be much lower than the experimental data of Gorbachuk and Bolgar [74] as seen in Fig. 26.

The optimized phase diagram of the Sn-Y system in the present study is shown in Fig. 22. In the optimization, the phase diagram was constructed mainly based on the work of Palenzona and Manfrinetti [8] for the compositions up to 0.333 mole fraction of Y, and Schmidt and McMasters [65] for the compositions above. The solid solubility of Sn in hcp-Y and bcc-Y was modeled with one temperature independent excess Gibbs energy parameter, respectively, with reference to the work of Schmidt and McMasters [65].

The calculated thermodynamic properties with the optimized thermodynamic parameters are shown in Figs. 23-27. As for the integral and partial enthalpies of mixing of liquid, the experimental data of Esin et al. [72] which were much less negative than the data of Nikolaenko et al. [73] were adopted. If more negative values were used, large temperature dependent parameters (i.e., entropy) would require to reproduce the phase diagram that may result in the unwanted inverse miscibility gap in the high temperature liquid region. The temperature independent parameters (i.e., enthalpy) were estimated that reproduce the experimental data of Esin et al. [72] (in Fig. 23(a) and (b)). Additionally, three temperature dependent parameters (i.e., entropy), but not too big to bring up the inverse miscibility gap, were added to reproduce the phase diagram. The heat capacity (C_p) of Y_5Sn_3 were modified from the reported one by Gorbachuk and Bolgar [74] to avoid the abrupt change of the slope at 298 K (in Fig. 24). The modified C_p should reasonably correspond to the heat content data [74] as well (in Fig. 26). The experimental data of ΔS^{o}_{298} of Y_5Sn_3 [74] was adopted as it was (in Fig. 25), and the ΔH^{o}_{298} of YSn_3 [66], YSn_2 [66], and Y_5Sn_3 [75] were used in the present optimization as seen in Fig. 27. If the ΔH^{o}_{298} of Y_5Sn_3 by Meschel and Kleppa [22] was used, it would be difficult to reproduce the heat content data for the liquid [74] as seen in Fig. 26. The calculated activity of Y in Y-saturated liquid at 1000 K was -9.37 in logarithmic scale, lower than the experimental value, -7.60 [76]. The optimized thermodynamic parameters are listed in Table 15 and the calculated invariant reactions with the experimental data are tabulated in Table 16.

Table 15. Optimized model parameters for the Sn-Y system.

Phase	Thermodynamic parameters
Liquid	Coordination Numbers
	i j Z_{ij}^{i} Z_{ij}^{j}
	Sn Y 6 6
	Δg_{SnY} / (J mol^{-1}) = (-42258.4 – 5.89944 T/K) – 8368.0 X_{SnSn}
	+ (-418.4 + 5.4392 T/K) X_{SnSn}^{2} – 25104.0 X_{YY}
	+ (8368.0 + 4.56056 T/K) X_{YY}^{2}
bcc-A2	${}^{0}L_{Sn,Y}$ / (J mol^{-1}) = -182506.08
hcp-A3	${}^{0}L_{Sn,Y}$ / (J mol^{-1}) = -163594.40
YSn_3	ΔH_{298}^{o} = -209200 J mol^{-1}, S_{298}^{o} = 179.59 J K^{-1} mol^{-1}
	C_p / (J K^{-1} mol^{-1}) = 1 × C_p / (J K^{-1} mol^{-1}) (Y, hcp-A3)
	+ 3 × modified C_p / (J K^{-1} mol^{-1}) (Sn, bct-A5)*
Y_2Sn_5	ΔH_{298}^{o} = -405000 J mol^{-1}, S_{298}^{o} = 322.49 J K^{-1} mol^{-1}
	C_p / (J K^{-1} mol^{-1}) = 2 × C_p / (J K^{-1} mol^{-1}) (Y, hcp-A3)
	+ 5 × modified C_p / (J K^{-1} mol^{-1}) (Sn, bct-A5)*
YSn_2	ΔH_{298}^{o} = -194556 J mol^{-1}, S_{298}^{o} = 142.64 J K^{-1} mol^{-1}
	C_p / (J K^{-1} mol^{-1}) = 1 × C_p / (J K^{-1} mol^{-1}) (Y, hcp-A3)
	+ 2 × modified C_p / (J K^{-1} mol^{-1}) (Sn, bct-A5)*
$Y_{11}Sn_{10}$	ΔH_{298}^{o} = -1771390 J mol^{-1}, S_{298}^{o} = 980.0 J K^{-1} mol^{-1}
	C_p / (J K^{-1} mol^{-1}) = 11 × C_p / (J K^{-1} mol^{-1}) (Y, hcp-A3)
	+ 10 × modified C_p / (J K^{-1} mol^{-1}) (Sn, bct-A5)*
Y_5Sn_4	ΔH_{298}^{o} = -784500 J mol^{-1}, S_{298}^{o} = 410.0 J K^{-1} mol^{-1}
	C_p / (J K^{-1} mol^{-1}) = 5 × C_p / (J K^{-1} mol^{-1}) (Y, hcp-A3)
	+ 4 × modified C_p / (J K^{-1} mol^{-1}) (Sn, bct-A5)*
Y_5Sn_3	ΔH_{298}^{o} = -702912.0 J mol^{-1}, S_{298}^{o} = 341.82 J K^{-1} mol^{-1}
	C_p / (J K^{-1} mol^{-1}) = 5 × C_p / (J K^{-1} mol^{-1}) (Y, hcp-A3)
	+ 3 × modified C_p / (J K^{-1} mol^{-1}) (Sn, bct-A5)*

*modified C_p / (J K^{-1} mol^{-1}) (Sn, bct-A5) = 24.477 + 5.472E-2 T/K – 40640.0 (T/K)$^{-2}$ – 6.469E-7 (T/K)^{2}

Table 16. Calculated invariant reactions and experimental data in the Sn-Y system.

Type	Reaction	t (°C)	Reference
Eutectic	$L_{(X_Y=<1E-5)} \rightarrow Sn_{(bct\text{-}A5,\ X_Y=0)} + YSn_3$	231.9	This work
	$L_{(X_Y=*)} \rightarrow Sn_{(bct\text{-}A5,\ X_Y=0)} + YSn_3$	229.0	[65]
	$L_{(X_Y=*)} \rightarrow Sn_{(bct\text{-}A5,\ X_Y=0)} + YSn_3$	230.0	[8]
Peritectic	$L_{(X_Y=0.001)} + Y_2Sn_5 \rightarrow YSn_3$	430.2	This work
	$L_{(X_Y=\sim0.25)} + YSn_2 \rightarrow YSn_3$	515.0	[65]
	$L_{(X_Y=\sim0.005)} + Y_2Sn_5 \rightarrow YSn_3$	430.0	[8]
Peritectic	$L_{(X_Y=0.006)} + YSn_2 \rightarrow Y_2Sn_5$	525.3	This work
	$L_{(X_Y=\sim0.012)} + YSn_2 \rightarrow Y_2Sn_5$	525.0	[8]
Peritectic	$L_{(X_Y=0.313)} + Y_{11}Sn_{10} \rightarrow YSn_2$	1140.0	This work
	$L_{(X_Y=\sim0.321)} + Y_{11}Sn_{10} \rightarrow YSn_2$	1140.0	[65]
	$L_{(X_Y=\sim0.323)} + ** \rightarrow YSn_2$	1140.0	[8]
Peritectic	$L_{(X_Y=0.447)} + Y_5Sn_4 \rightarrow Y_{11}Sn_{10}$	1599.9	This work
	$L_{(X_Y=\sim0.452)} + Y_5Sn_4 \rightarrow Y_{11}Sn_{10}$	1600.0	[65]
Peritectic	$L_{(X_Y=0.540)} + Y_5Sn_3 \rightarrow Y_5Sn_4$	1790.2	This work
	$L_{(X_Y=\sim0.521)} + Y_5Sn_3 \rightarrow Y_5Sn_4$	1790.0	[65]
Congruent	$L_{(X_Y=0.625)} \leftrightarrow Y_5Sn_3$	1940.0	This work
	$L_{(X_Y=0.625)} \leftrightarrow Y_5Sn_3$	1940.0	[65]
Eutectic	$L_{(X_Y=0.883)} \rightarrow Y_5Sn_3 + Y_{(hcp\text{-}A3,\ X_Y=0.985)}$	1259.8	This work
	$L_{(X_Y=\sim0.887)} \rightarrow Y_5Sn_3 + Y_{(hcp\text{-}A3,\ X_Y=\sim0.986)}$	1260.0	[65]
Catatectic	$Y_{(bcc\text{-}A2,\ X_Y=0.974)} \rightarrow L_{(X_Y=0.917)} + Y_{(hcp\text{-}A3,\ X_Y=0.991)}$	1359.8	This work
	$Y_{(bcc\text{-}A2,\ X_Y=\sim0.958)} \rightarrow L_{(X_Y=\sim0.908)} + Y_{(hcp\text{-}A3,\ X_Y=\sim0.983)}$	1360.0	[65]

* The exact compositions are not specified in the reference.
** The phase was not identified.

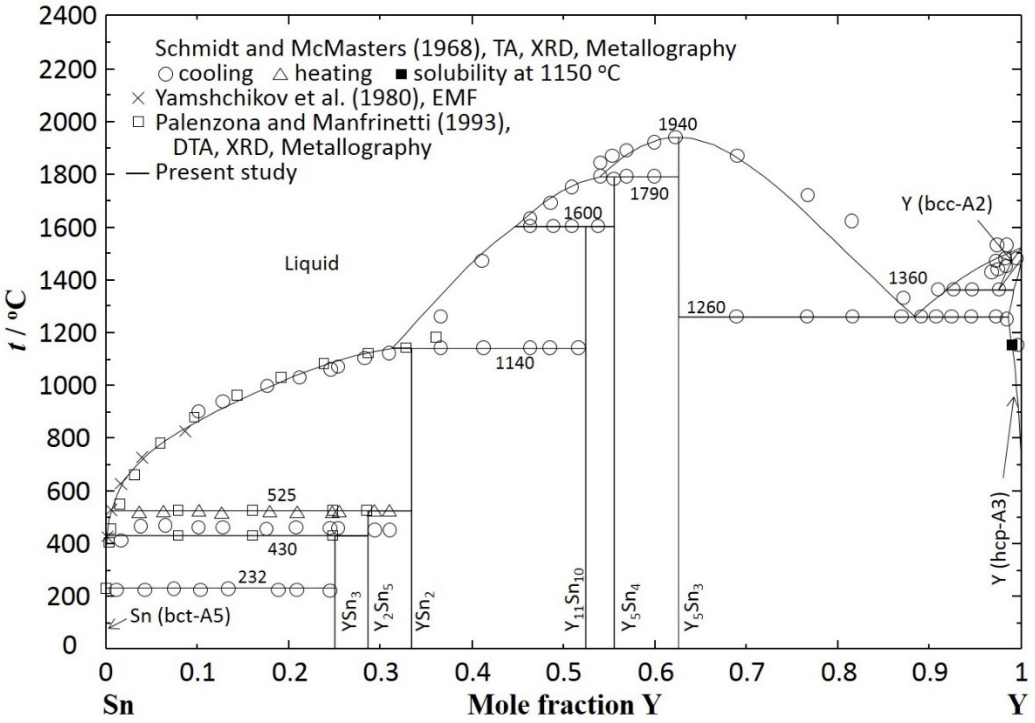


Fig. 22. The optimized Sn-Y phase diagram with experimental data.

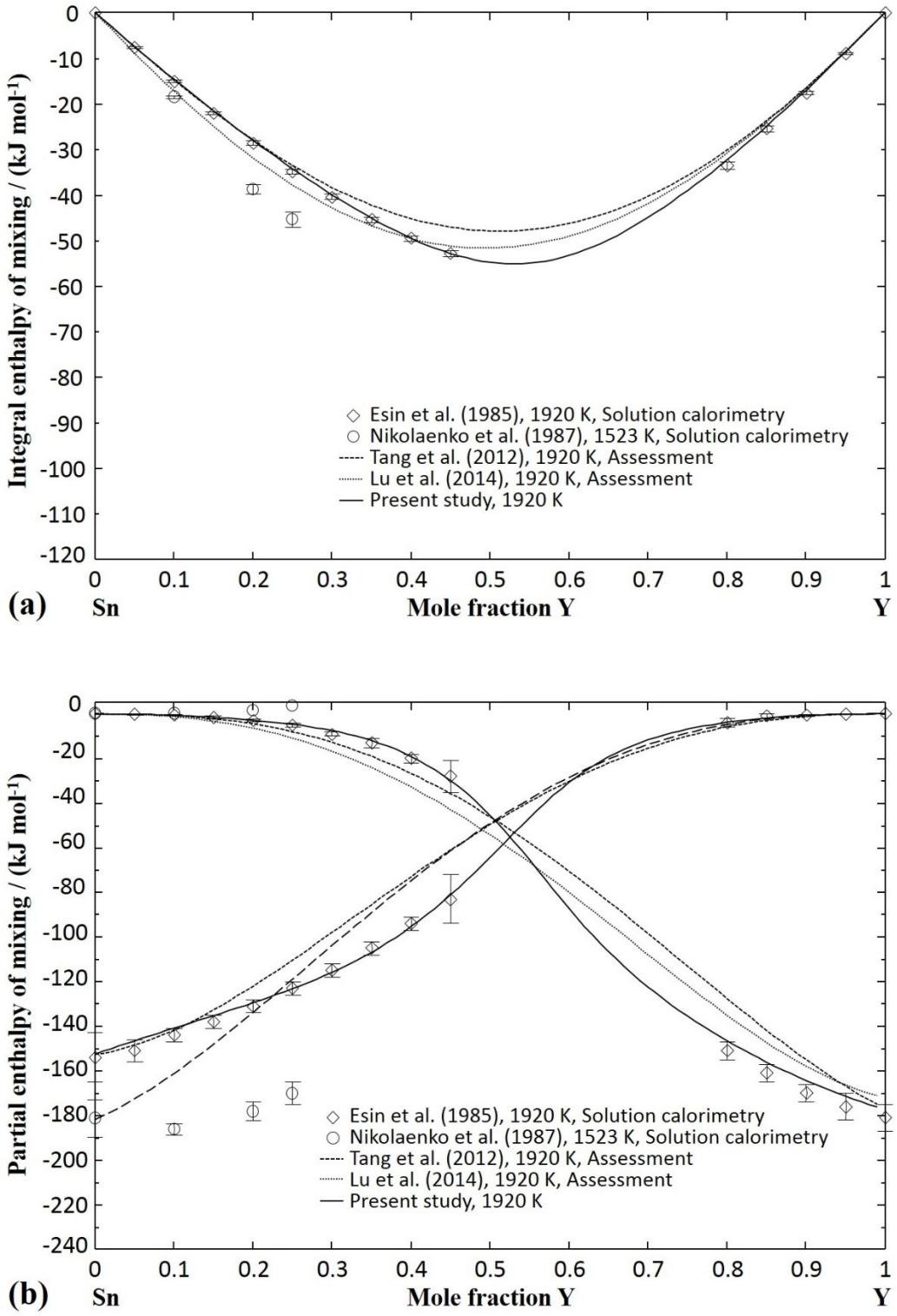


Fig. 23. (a) Integral enthalpy of mixing and (b) partial enthalpy of mixing of liquid Sn-Y at 1920 K with experimental data and previous thermodynamic assessment.

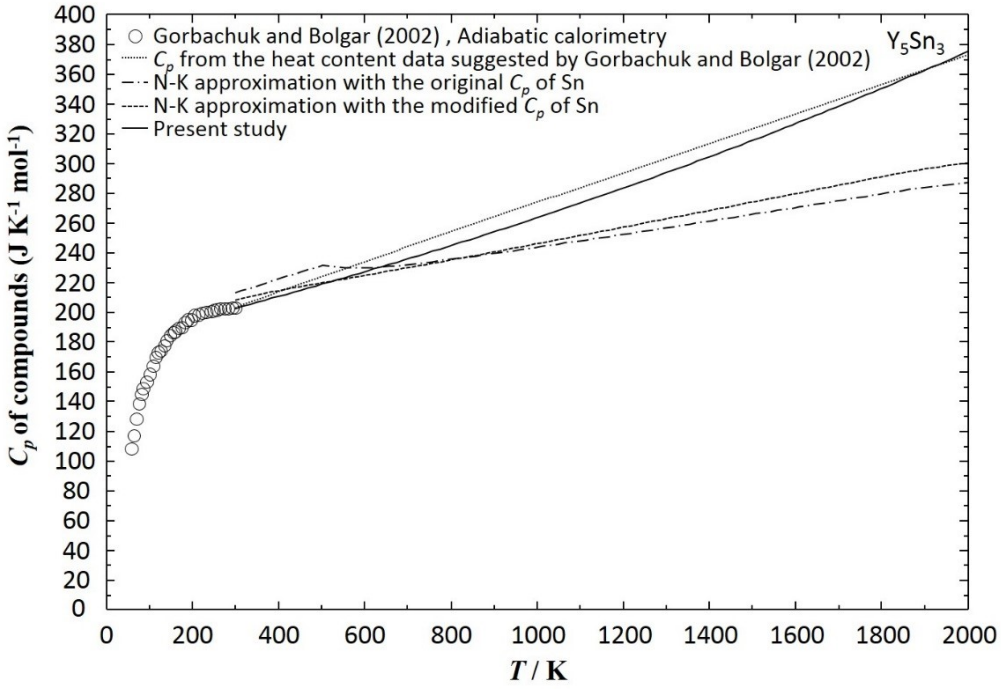


Fig. 24. Heat capacity of Y_5Sn_3 with experimental data.

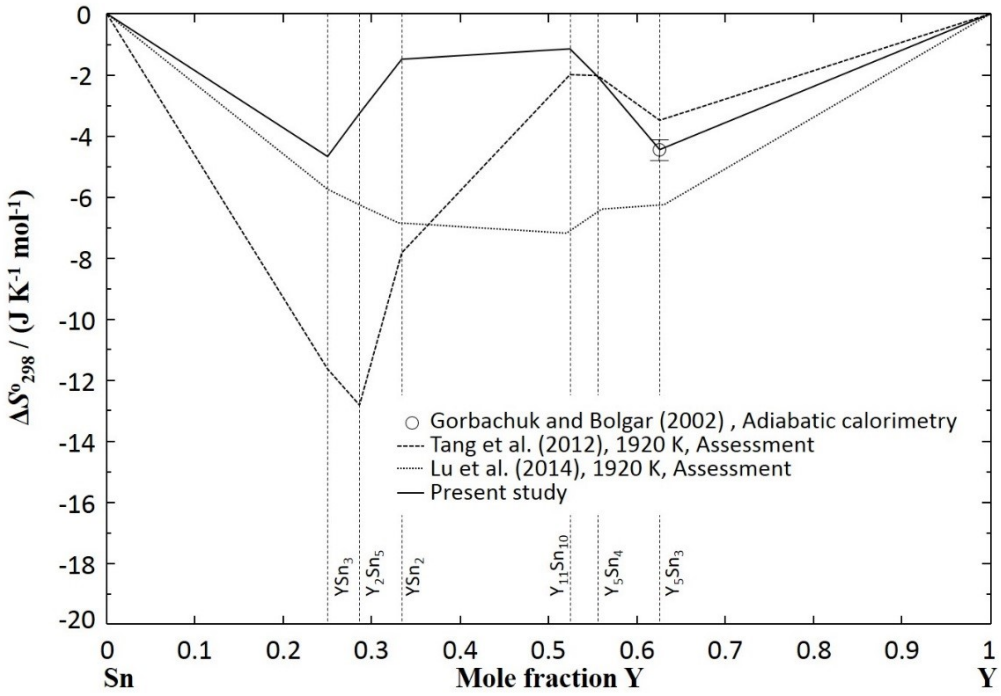


Fig. 25. Entropy of formation of the compounds in the Sn-Y system from elements at 298 K with experimental data.

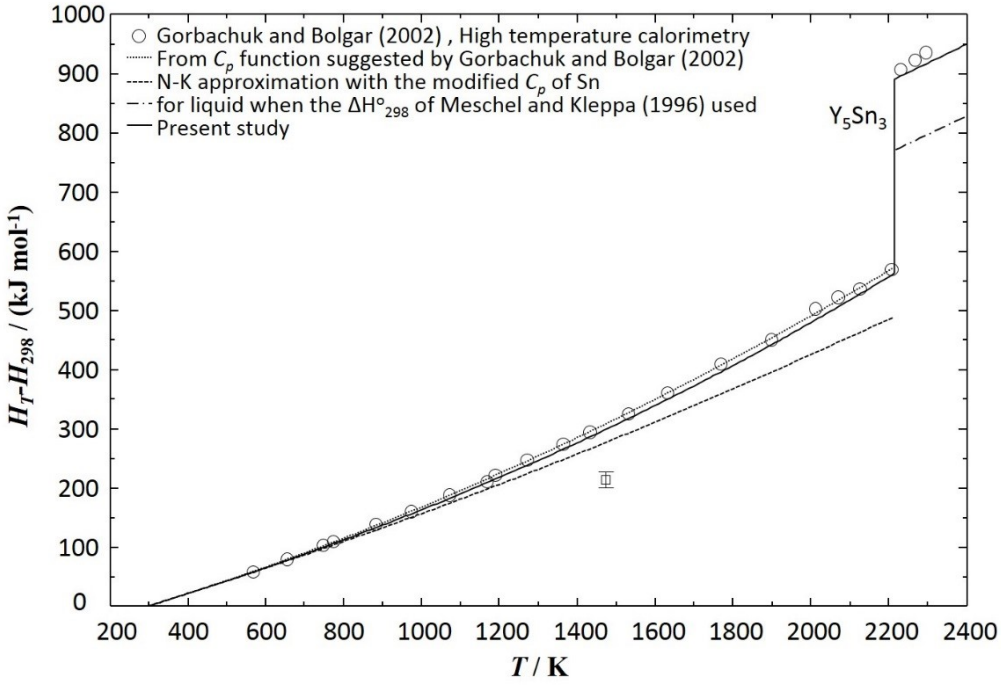


Fig. 26. Heat content of Y_5Sn_3 with experimental data.

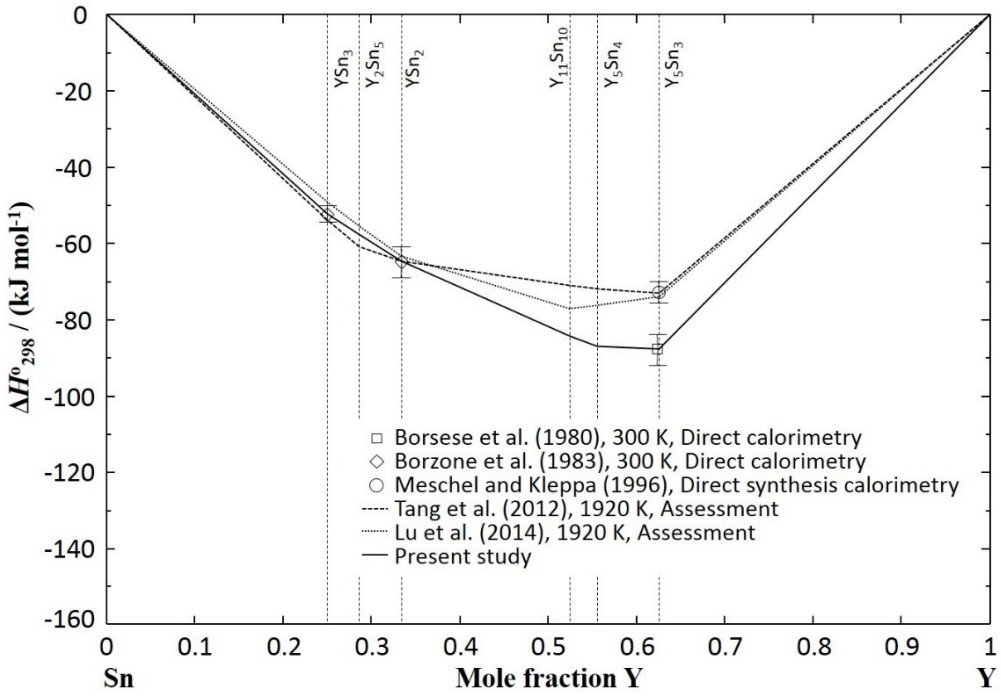


Fig. 27. Enthalpy of formation of the compounds in the Sn-Y system at 298 K with experimental data.

2. Systematic trends in the Sn-RE systems

Recently, critical evaluations and optimizations of the binary Mn-RE system [80-82] and Si-RE system [83, 84] were performed by the present authors using the Modified Quasichemical Model for the liquid solution. Regarding the similarity and regularity of RE series, a clear systematic trends through the series of Mn-RE and Si-RE systems were found and discussed. For instance, the enthalpy of mixing in liquid Mn-RE was observed to gradually decrease form positive to negative values with increasing the atomic number of RE elements. This seemed to be attributed the differences in thermochemical and electronic properties such as the Fermi energies, electronic density and atomic volume of the RE. Although, it was hard to find such a clear visible trend in the enthalpy of mixing of Sn-RE system, the minimum enthalpies were found in a similar range, about -70 ± 5 kJ mol^{-1}. Such negative enthalpy values with possible experimental errors might abolish the systematic trend. However, a clear systematic trend in the melting temperatures of intermetallic compounds was found in the phase diagram of the Si-RE system. The compounds which have the highest melting temperature shift from the low RE-containing compounds to the high RE-containing compounds with increasing atomic number of RE. The trend was used to assess the melting temperatures of compounds which did not have experimental data. The reason of the trend was not clear but the increasing stability of RE_5Si_3 and the decreasing stability of RE_3Si_5 were shown by means of the normalized melting temperatures of those compounds based on the melting temperatures of the respective elements and the enthalpy of formation.

Based on the present thermodynamic optimization results, we analyzed the systematic changes in thermodynamic and phase diagram data of the Sn-RE systems.

The enthalpies of mixing of all binary liquid Sn-RE alloys at 2000 K are compared in Fig. 28. The enthalpies of mixing of all liquid Sn-RE alloys show minimum values in the range of -50 to -65 kJ mol^{-1} near 0.5 mole fraction of RE. These are in-between the Pb-RE system (-40 to -50 kJ mol^{-1}) [85] and Si-RE system (-65 to -75 kJ mol^{-1}) [83, 84]. This seems to be very reasonable considering the fact that the Sn is in-between Si and Pb in the same group 14 of the periodic table. However, similar to the Si-RE system, it is difficult to find a trend of gradual decrease in the enthalpy of

mixing with atomic number of RE which was found in the Mn-RE system. Rather, it seems that the enthalpy of mixing increase with atomic number of RE particularly for the heavy RE as seen in Fig. 28(b). However, it is still uncertain because the experimental data for many Sn-RE systems were unavailable or partially available (Sn-rich region). The entropies of mixing of liquid Sn-RE at 2000 K are presented in Fig. 29. Corresponding to the large negative enthalpies of mixing at the middle composition range, the entropies of mixing have typical "M" shape, which can be seen in the systems having short range ordering in liquid phase. Unlike the entropies of mixing of Si-RE liquid which have negative values at 0.5 mole fraction of RE associated with significant non-configuration entropy, the entropies of mixing have positive values over the whole composition range because only small entropic parameters or none of them were used, explaining that the configuration entropies are dominant factor in total entropy. The enthalpies of formation of the Sn-RE compounds at 298 K are compiled in Fig. 30. Based on one mole of Sn-RE system, the minimum value of the enthalpy of formation is associated with the RESn or $RE_{11}Sn_{10}$ (about 0.5 mole fraction of RE) with -75 to -90 kJ mol·atom^{-1} except the Sn-Y system. Exceptionally, the Y_5Sn_3 has the most negative enthalpy of formation among the Y containing stannides. In order to reproduce the experimental data regarding the heat contents of Y_5Sn_3 [74], the ΔH°_{298} of Y_5Sn_3 was taken from Borsese et al. [75], not from Meschel and Kleppa [22]. On the other hand, most ΔH°_{298} values of RE_5Sn_3 were taken from Meschel and Kleppa [22, 34, 43, 57, 59, 86] because they were only data available from literature. The entropies of formation of the Sn-RE compounds at 298 K are compiled in Fig. 31. The variation of entropies of formation is within the range of 10 J K^{-1} mol^{-1} with mostly negative values. In general, the thermodynamic properties of the Sn-heavy RE systems vary smoothly as they were assessed similarly in the present study due to the lack of experimental data compared to the Sn-light RE systems.

A systematic trend in the melting temperatures of intermetallic compounds were found in the phase diagrams of the Sn-RE systems. The melting temperatures of Sn-RE compounds are shown in the order of atomic number of RE in Fig. 32, and a collection of the optimized phase diagrams of the Sn-RE system is presented in Fig. 33. The melting temperatures of the low RE-containing compounds are decreasing with increasing atomic number of RE, while the melting temperatures of the high RE-containing compounds are increasing with atomic number of RE. The trend is quite

similar to that found in the Si-RE systems and it was successfully used to assess the unknown melting temperatures of compounds. Although it is difficult to point out the specific reason of such trend, the relative stability of RE stannides corresponds to the relative Gibbs energies of liquid and RE stannides from the combination of enthalpies and entropies of the respective phases. However, more comprehensive research using the ab initio calculations would be required to understand the physicochemical properties of RE stannides.

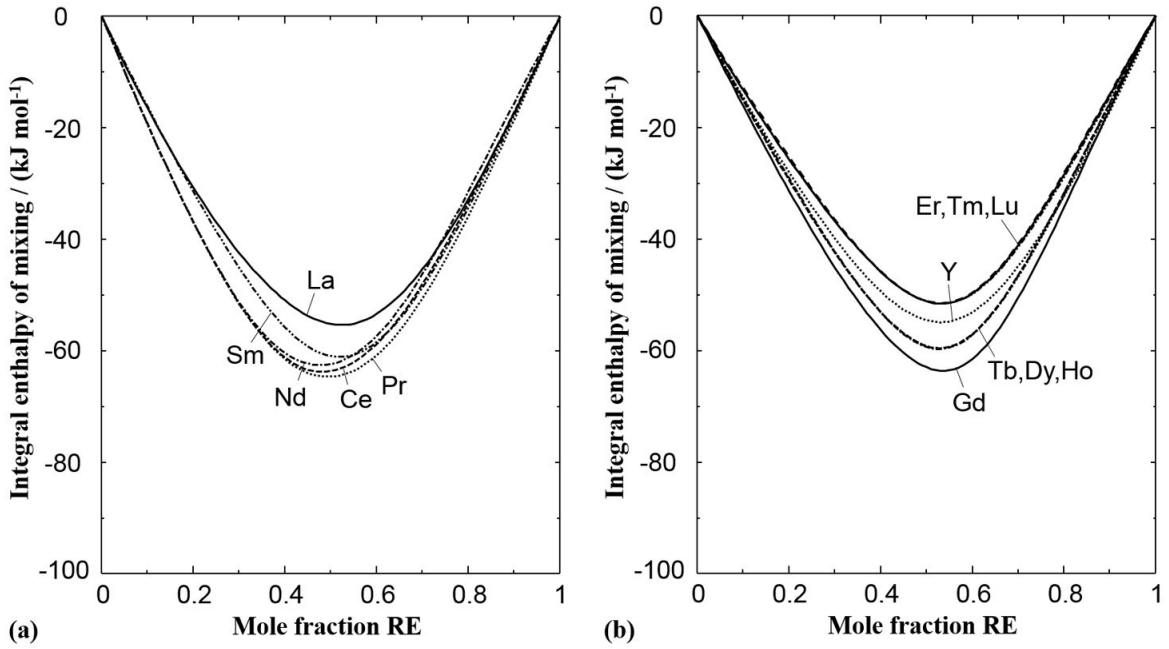


Fig. 28. Comparison of integral enthalpies of mixing of liquid Sn-RE at 2000 K ((a) Sn-light RE and (b) Sn-heavy RE).

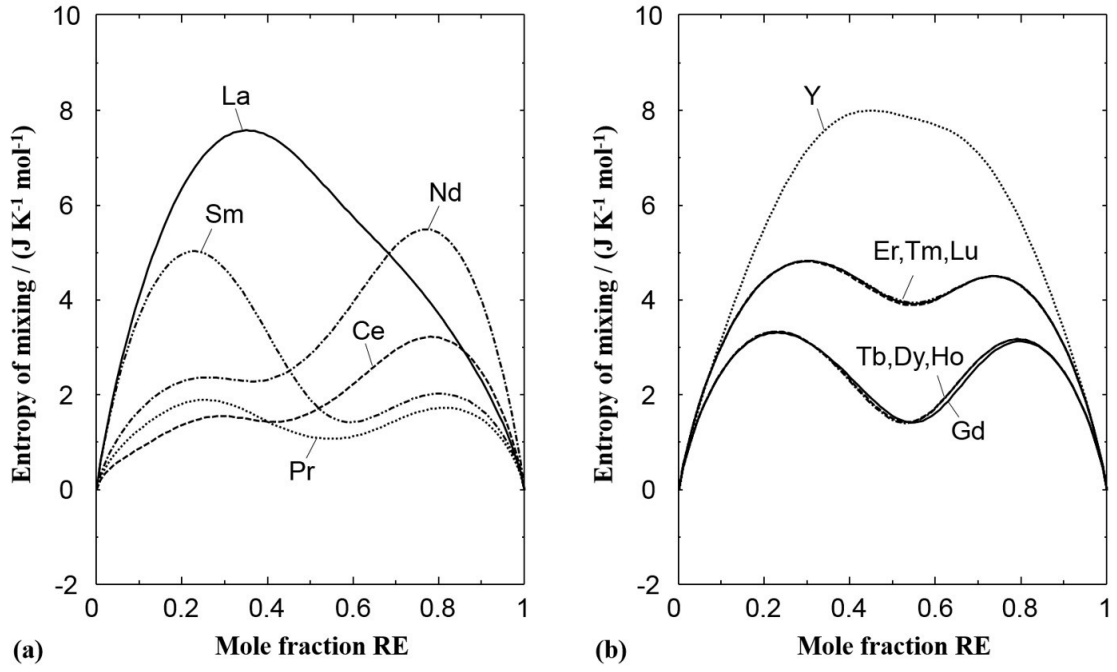


Fig. 29. Comparison of entropies of mixing of liquid Sn-RE at 2000 K ((a) Sn-light RE and (b) Sn-heavy RE).

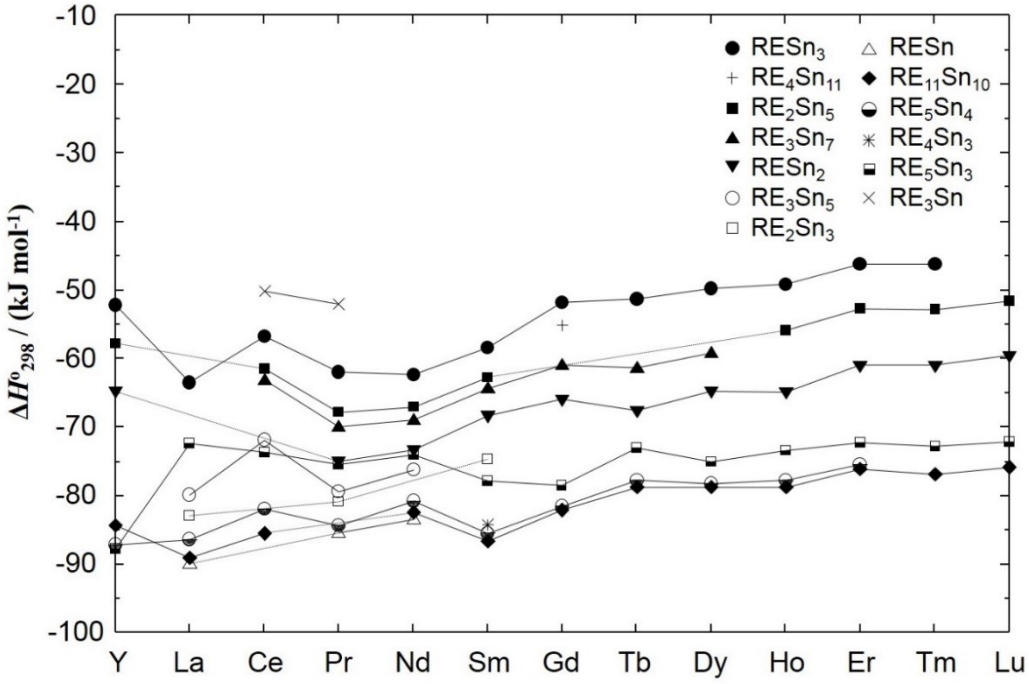


Fig. 30. Comparison of enthalpies of formation of Sn-RE compounds at 298 K (based on one mole of Sn-RE system).

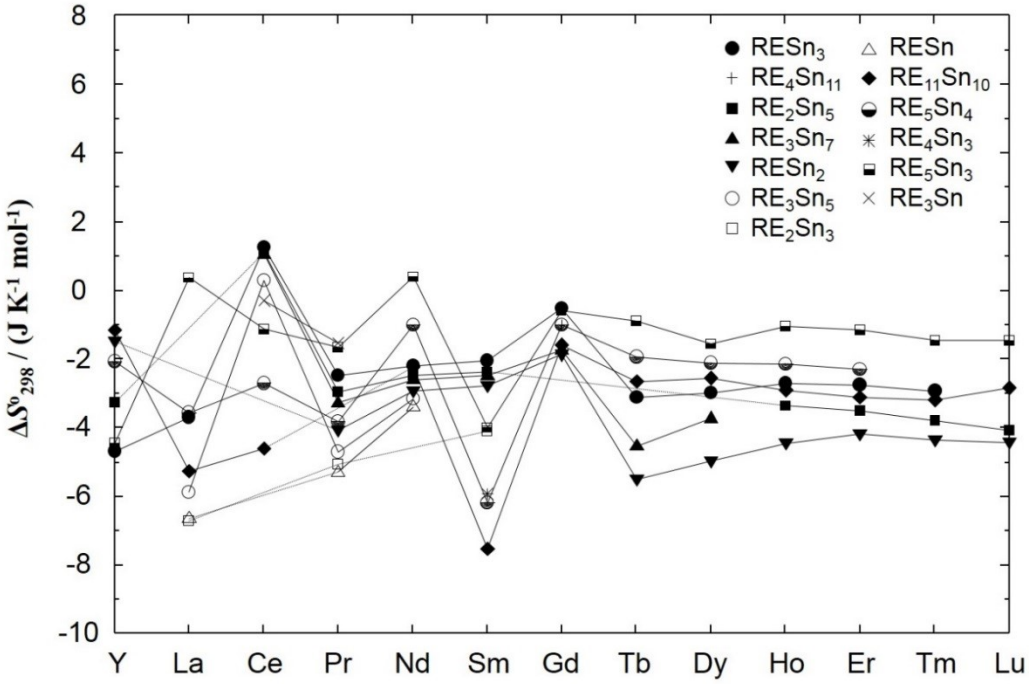


Fig. 31. Comparison of entropies of formation of Sn-RE compounds at 298 K (based on one mole of Sn-RE system) from elemental references.

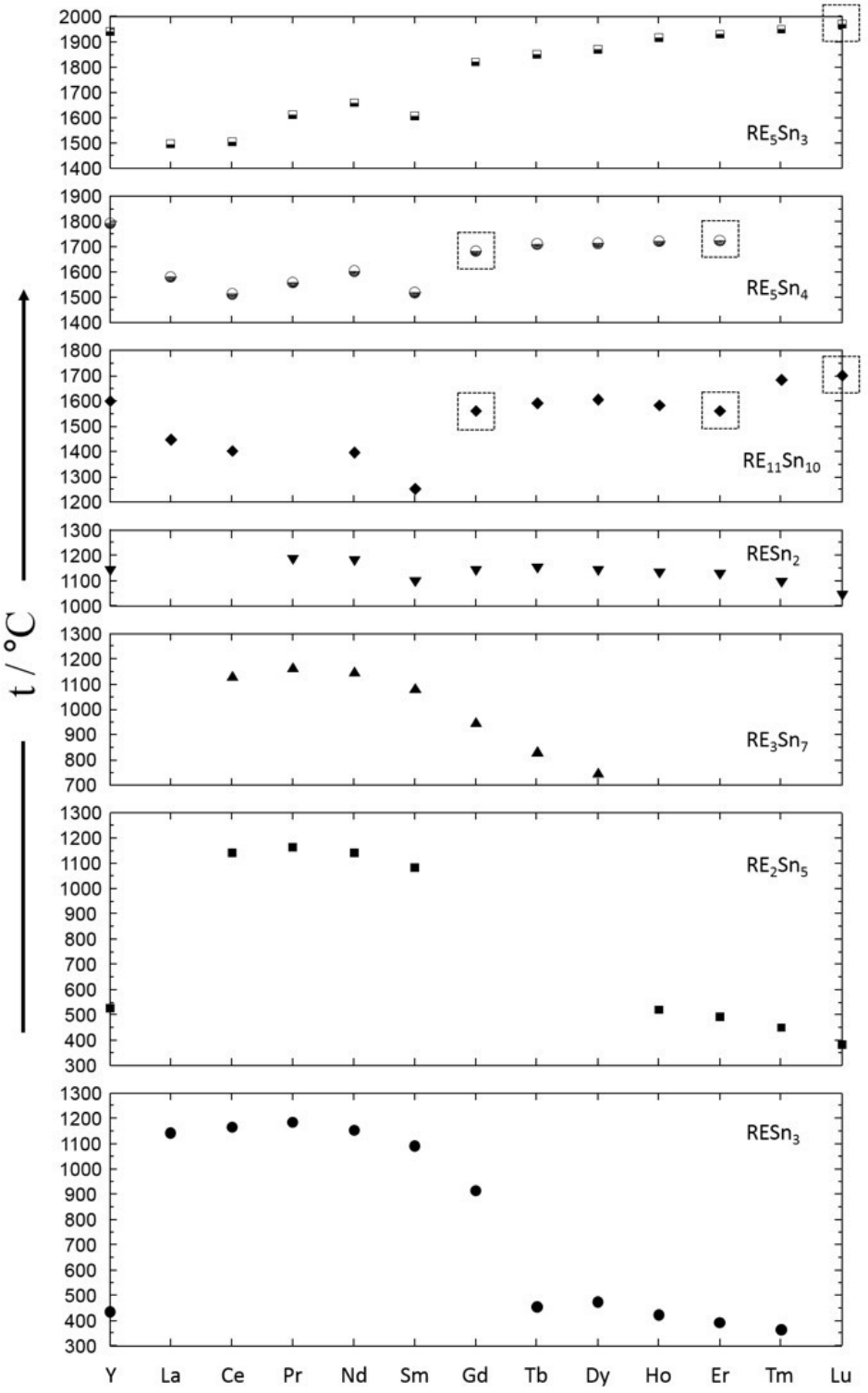


Fig. 32. Systematic changes in the melting temperatures of Sn-RE compounds. The melting temperatures estimated in the present study are indicated by the empty squares.

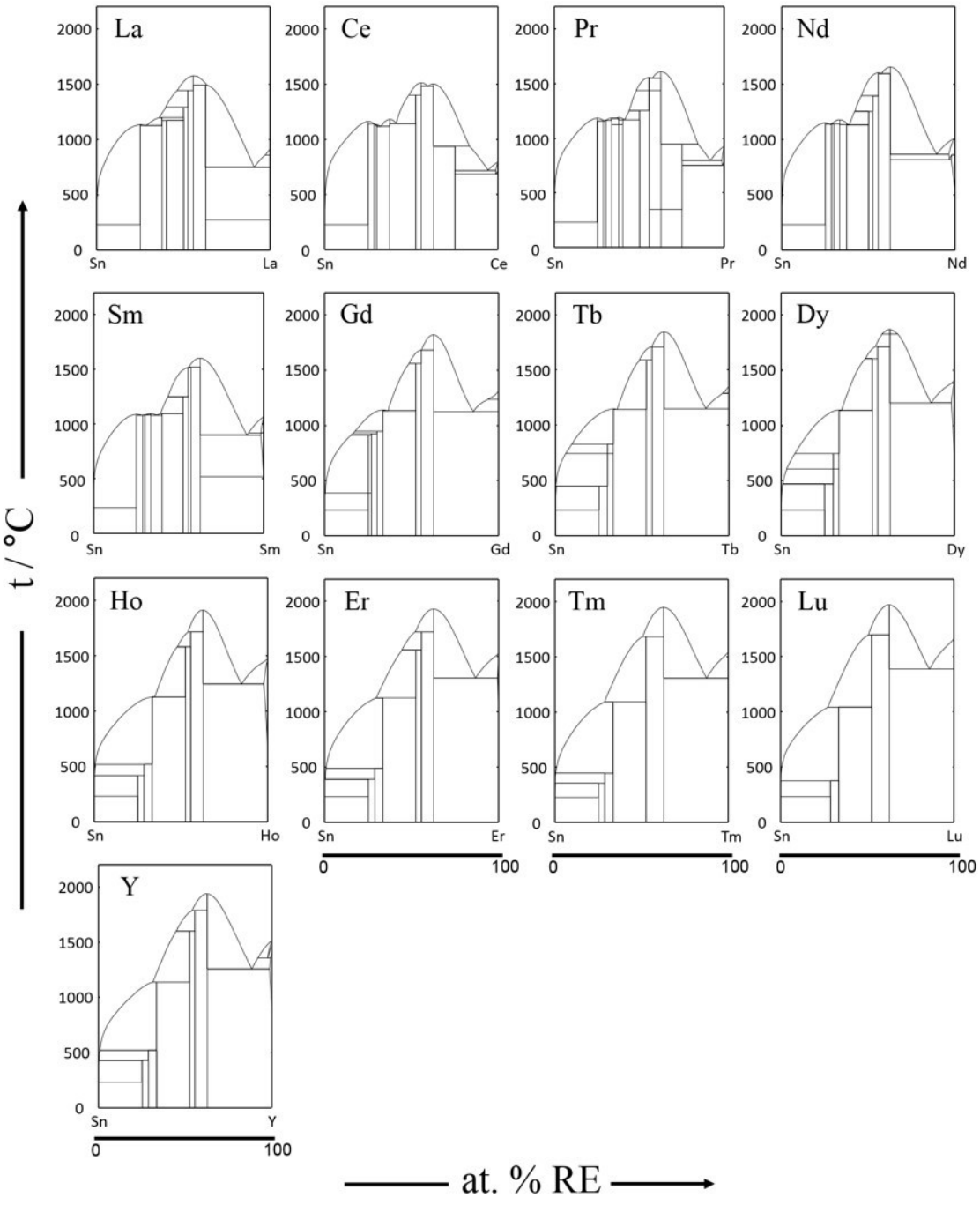


Fig. 33. Collection of the optimized phase diagrams of the Sn-RE systems.

3. References

[1] A. Palenzona, F. Merlo, Atti Accad. Naz. Lincei, Cl. Sci. Fis., Mat. Nat., Rend., 40 (1966) 617-622.
[2] W. Jeitschko, E. Parthe, Acta Crystallogr., 22 (1967) 551-555.
[3] M.L. Fornasini, F. Merlo, Atti Accad. Naz. Lincei, Cl. Sci. Fis., Mat. Natur., Rend., 50 (1971) 30-40.
[4] H.F. Yang, G.H. Rao, G.Y. Liu, Z.W. Ouyang, W.F. Liu, X.M. Feng, W.G. Chu, J.K. Liang, J. Alloys Compd., 368 (2004) 248-250.
[5] A. Iandelli, A. Palenzona, Atti Accad. Naz. Lincei, Cl. Sci. Fis., Mat. Nat., Rend., 40 (1966) 623-628.
[6] J.D. Zou, J. Liu, M. Yan, J. Magn. Magn. Mater., 385 (2015) 77-82.
[7] R.V. Skolozdra, L.G. Aksel'rud, V.K. Pecharskii, O.E. Koretskaya, Dopov. Akad. Nauk Ukr. RSR, Ser. B: Geol., Khim. Biol. Nauki, (1986) 48-52.
[8] A. Palenzona, P. Manfrinetti, J. Alloys Compd., 201 (1993) 43-47.
[9] I.R. Harris, G.V. Raynor, J Less-Common Met, 9 (1965) 7-19.
[10] A. Percheron-Guegan, J.C. Achard, A. Bacha, C. Chatillon, J.C. Mathieu, In: Proc. 1973. pp. 1046-1055.
[11] N.G. Kulagina, A.P. Bayanov, Zh. Fiz. Khim., 48 (1974) 466-467.
[12] J. Liu, J. Zheng, Wuli Xuebao, 33 (1984) 1155-1159.
[13] N.G. Kulagina, A.P. Bayanov, Zh. Fiz. Khim., 48 (1974) 233.
[14] N.G. Kulagina, A.P. Bayanov, N.M. Kulagin, Izv. Akad. Nauk SSSR, Met., (1985) 211-216.
[15] V.N. Eremenko, M.V. Bulanova, P.S. Martsenyuk, In: Proc. 1990. pp. 70-100.
[16] Y. Mudryk, L. Romaka, Y. Stadnyk, O. Bodak, D. Fruchart, J. Alloys Compd., 383 (2004) 162-165.
[17] J. Ma, Y. Zhan, J. She, Z. Yang, J. Liang, J. Alloys Compd., 489 (2009) 384-388.
[18] J.L. Liang, Y. Du, Y.Y. Tang, C.Z. Liao, J.L. Meng, H.H. Xu, J. Alloys Compd., 481 (2009) 264-269.
[19] L. Romaka, V.V. Romaka, Y. Stadnyk, P. Demchenko, J. Alloys Compd., 505 (2010) 70-75.
[20] A. Bacha, C. Chatillon-Colinet, A. Percheron, J.C. Mathieu, C. R. Acad. Sci., Ser. C, 274 (1972) 680-683.
[21] F. Sommer, J. Schott, H.G. Krull, J. Less-Common Met., 144 (1988) 53-63.
[22] S.V. Meschel, O.J. Kleppa, Journal of Alloys and Compounds, 238 (1996) 180-186.
[23] L.F. Yamshchikov, A.A. Zyapaev, Rasplavy, (2001) 43-52.
[24] V.A. Lebedev, V.I. Kober, L.F. Yamshchikov, Handbook. Chelyabinsk, Metallurgia, (1989) 336.
[25] N.G. Kulagina, Author's Abstract of Candidate's Thesis, Chemical Sciences, Sverdlovsk, (1980) 21.
[26] A. Palenzona, S. Cirafici, J. Phase Equilib., 12 (1991) 690-695.
[27] H. Okamoto, J. Phase Equilib., 16 (1995) 100-101.
[28] V.N. Eremenko, M.V. Bulanova, P.S. Martsenyuk, Dokl. Akad. Nauk Ukr. SSR, Ser. B: Geol., Khim. Biol. Nauki, (1990) 35-37.
[29] X.C. Zhong, M. Zou, H. Zhang, Z.W. Liu, D.C. Zeng, K.A. Gschneidner, V.K. Pecharsky, Journal of Applied Physics, 109 (2011) 07A917-907A917-913.

[30] K. Meier, L. Vasylechko, R. Cardoso-Gil, U. Burkhardt, W. Schnelle, M. Schmidt, Y. Grin, U. Schwarz, Z. Anorg. Allg. Chem., 636 (2010) 1695-1702.
[31] I. Oshchapovsky, V. Pavlyuk, I. Chumak, Acta Crystallogr., Sect. B: Struct. Sci., Cryst. Eng. Mater., 69 (2013) 527-533.
[32] O.E. Koretskaya, L.P. Komarovskaya, R.V. Skolozdra, Izv. Akad. Nauk SSSR, Neorg. Mater., 24 (1988) 1299-1302.
[33] A. Szytula, D. Kaczorowski, L. Gondek, J. Czub, K. Nenkov, Acta Phys. Pol., A, 117 (2010) 586-589.
[34] S.V. Meschel, O.J. Kleppa, J. Alloys Compd., 234 (1996) 137-142.
[35] H. Okamoto, Journal of Phase Equilibria, 13 (1992) 681-683.
[36] H. Okamoto, J. Phase Equilib., 16 (1995) 102-103.
[37] O.I. Bodak, V.V. Romaka, A.V. Tkachuk, L.P. Romaka, Y.V. Stadnyk, J. Alloys Compd., 395 (2005) 113-116.
[38] L.C.J. Pereira, D.P. Rojas, J.C. Waerenborgh, J. Alloys Compd., 396 (2005) 108-113.
[39] Y.H. Zhuang, J.M. Zhu, J.L. Yan, Y. Xu, J.Q. Li, J. Alloys Compd., 459 (2008) 461-465.
[40] V.N. Eremenko, M.V. Bulanova, P.S. Martsenyuk, J. Alloys Compd., 189 (1992) 229-233.
[41] R. Chen, J. Zheng, Wuli Xuebao, 32 (1983) 933-938.
[42] A. Bacha, C. Chatillon-Colinet, A. Percheron, J.C. Mathieu, C. R. Acad. Sci., Ser. C, 275 (1972) 921-923.
[43] S.V. Meschel, O.J. Kleppa, J. Alloys Compd., 233 (1996) 272-278.
[44] L.F. Yamshchikov, F.N. Sattarov, I.V. Brettser-Portnov, S.P. Raspopin, Izv. Akad. Nauk SSSR, Met., (1990) 209-211.
[45] X. Wang, X. Su, J.C. Tedenac, F. Yin, J. Wang, J. Alloys Compd., 396 (2005) 169-174.
[46] M.V. Bulanova, V.N. Eremenko, V.M. Petjukh, V.R. Sidorko, J. Phase Equilib., 19 (1998) 136-141.
[47] L.F. Yamshchikov, V.A. Lebedev, S.P. Raspopin, P.A. Arkhipov, Izv. Vyssh. Uchebn. Zaved., Tsvetn. Metall., (1984) 83-86.
[48] A. Iddaoudi, N. Selhaoui, S. Kardellass, M. Ait Amar, K. Mahdouk, H. Najih, L. Bouirden, J. Therm. Anal. Calorim., 115 (2014) 941-945.
[49] B. Love, U. S. Dep. Commer., Off. Tech. Serv., PB Rep., 171;085 (1960) 226 pp.
[50] N.G. Kulagina, A.P. Bayanov, In: Proc. 1979. pp. 191-194.
[51] L.F. Yamshchikov, V.A. Lebedev, I.F. Nichkov, A.N. Klepikov, P.A. Arkhipov, Izv. Vyssh. Uchebn. Zaved., Tsvetn. Metall., (1982) 98-99.
[52] R.V. Skolozdra, Y.S. Mudryk, L.P. Romaka, J. Alloys Compd., 296 (2000) 290-292.
[53] I.V. Senkovska, Y.S. Mudryk, L.P. Romaka, O.I. Bodak, J. Alloys Compd., 312 (2000) 124-129.
[54] J. Liang, C. Liao, Y. Tang, C. Yin, Y. Han, L. Nong, S. Xie, J. Alloys Compd., 502 (2010) 68-73.
[55] L. Romaka, V.V. Romaka, P. Demchenko, R. Serkiz, J. Alloys Compd., 507 (2010) 67-71.
[56] G. Zhang, Y. Zhan, C. Li, J. Rare Earths, 31 (2013) 800-803.
[57] S.V. Meschel, O.J. Kleppa, J. Chim. Phys. Phys.-Chim. Biol., 94 (1997) 928-938.
[58] L.F. Yamshchikov, PhD Thesis, UGTU, 1997.
[59] S.V. Meschel, O.J. Kleppa, J. Alloys Compd., 285 (1999) 179-184.
[60] C.-y. Yue, F.-x. Zhou, M.-f. Wang, H.-p. Zhang, X.-w. Lei, Chin. J. Struct. Chem., 32 (2013) 857-862.
[61] V.V. Romaka, L. Romaka, J. Alloys Compd., 509 (2011) 4530-4533.

[62] A.P. Bayanov, E.N. Ganchenko, N.G. Kulagina, Zh. Fiz. Khim., 48 (1974) 2120-2122.
[63] S. Holmen, Acta Chem. Scand., 18 (1964) 2394.
[64] W. Jeitschko, E. Parthe, Acta Crystallogr., 19 (1965) 275-277.
[65] F.A. Schmidt, O.D. McMasters, J. Less-Common Met., 15 (1968) 1-11.
[66] G. Borzone, A. Borsese, R. Ferro, Z. Anorg. Allg. Chem., 501 (1983) 199-208.
[67] L.F. Yamshchikov, V.A. Lebedev, I.F. Nichkov, S.P. Raspopin, O.K. Kokoulin, G.D. Korchinskii, Izv. Vyssh. Uchebn. Zaved., Tsvetn. Metall., (1980) 50-54.
[68] L. Romaka, Y. Dovgalyuk, V.V. Romaka, I. Lototska, Y. Stadnyk, Intermetallics, 29 (2012) 116-122.
[69] L. Romaka, I. Romaniv, Y. Stadnyk, V.V. Romaka, R. Serkiz, R. Gladyshevskii, Chemistry of Metals and Alloys, 7 (2014) 132-138.
[70] R. Chen, X. Wei, J. Liu, J. Alloys Compd., 218 (1995) 221-223.
[71] Y. Zhan, L. He, J. Ma, Z. Sun, G. Zhang, Y. Zhuang, J. Alloys Compd., 470 (2009) 173-175.
[72] Y.O. Esin, A.F. Ermakov, S.P. Kolesnikov, P.V. Gel'd, Zh. Fiz. Khim., 59 (1985) 481-482.
[73] I.V. Nikolaenko, M.A. Turchanin, G.I. Batalin, Izv. Akad. Nauk SSSR, Met., (1987) 67-71.
[74] N.P. Gorbachuk, A.S. Bolgar, Powder Metall. Met. Ceram., 41 (2002) 55-58.
[75] A. Borsese, G. Borzone, R. Ferro, J. Less-Common Met., 70 (1980) 213-216.
[76] L.F. Yamshchikov, V.A. Lebedev, I.F. Nichkov, S.P. Rasponin, O.K. Kokoulin, In: Proc. 1979. pp. 25-26.
[77] H. Okamoto, J. Phase Equilib., 16 (1995) 104.
[78] C. Tang, B. Hu, Y. Du, D. Zhao, P. Zhou, F. Zheng, Q. Gao, J. Wang, CALPHAD: Comput. Coupling Phase Diagrams Thermochem., 39 (2012) 91-96.
[79] D. Lu, C. Guo, C. Li, Z. Du, J. Rare Earths, 32 (2014) 648-654.
[80] J. Kim, I.-H. Jung, J. Alloys Compd., 525 (2012) 191-201.
[81] J. Kim, I.H. Jung, Can. Metall. Q., 52 (2013) 311-320.
[82] J. Kim, M. Paliwal, S. Zhou, H. Choi, I.-H. Jung, J. Phase Equilib. Diffus., 35 (2014) 670-694.
[83] J. Kim, I.-H. Jung, J. Chem. Thermodyn., 81 (2015) 253-272.
[84] J. Kim, I.-H. Jung, J. Chem. Thermodyn., 81 (2015) 273-297.
[85] M. Zydzik, M. Smids, M.-A. Van Ende, I.-H. Jung, Calphad, 46 (2014) 1-17.
[86] S.V. Meschel, O.J. Kleppa, J. Alloys Compd., 243 (1996) 186-193.

Appendix VIII

Appendix VIII

The thermodynamic optimizations of the ternary Mg-RE-X (X = Mn, Si, Sn) systems

1. General overview

Experimental information of the ternary Mg-RE-X (X = Mn, Si, Sn) systems was generally very limited. In the present study, the thermodynamic optimization of several systems among the Mg-RE-X systems in case that the experimental data were available. The general description of the thermodynamic model for the Gibbs energy functions of the all phases were described in Chapter 3. In addition, the Mg-Sn-Nd and Mg-Sn-Gd systems were selected for the experimental investigation to overcome the limited experimental data. The phase equilibria of the Mg-Sn-Nd and Mg-Sn-Gd systems at 500-700 ºC were determined by the equilibrated alloy method. The existence of the ternary compounds, MgNd(Gd)Sn, MgNd(Gd)Sn_2, and $Mg_4Nd_2Sn_3$ was revealed with the respective phase equilibria.

For the Mg-Mn-RE systems, the Mg-Mn-Ce, Mg-Mn-Nd, Mg-Mn-Gd, and Mg-Mn-Y systems were thermodynamically assessed with the available data [1-4]. According to the experimental studies, no ternary compounds exist in the Mg-Mn-RE systems. The reported homogeneity ranges of the certain phases such as MgRE(bcc-B2), Mg_2RE(laves-C14), etc. in the experimental studies were described with respective sublattice model depending on the crystal structure.

For the Mg-Si-RE systems, the presence of the ternary compounds, REMgSi_2 (RE = La, Ce, Pr, Nd), CeMg_2Si_2, CeMgSi, CeMg_3Si and Ce_2MgSi_2, were reported in several studies [5-7]. However, the phase equilibria or any thermodynamic properties of the compounds were not available. As the phase equilibria in the Mg-rich corner of the Mg-Si-Y was experimentally

determined [8], the comparison between the experimental data and the calculated phase diagrams from the present optimization was only made for the Mg-Si-Y system.

Based on the present experimental data regarding the phase equilibria of the Mg-Sn-Nd and Mg-Sn-Gd systems, the thermodynamic optimization of the systems was carried out with additional help of the systematic study for the melting temperature of MgRESn (RE = La-Lu and Y) determined by DTA method [9]. The thermodynamic properties of the ternary compounds, MgNd(Gd)Sn, MgNd(Gd)Sn_2, and $Mg_4Nd_2Sn_3$ were successfully estimated. Moreover, the experimental data of the phase equilibria in the Mg-Sn-Gd [10], Mg-Sn-Er [11] and Mg-Sn-Y [12, 13] at 300-500 ºC were available in the literature. The thermodynamic optimization of the Mg-Sn-Er and Mg-Sn-Y systems was similarly performed based on them.

2. The Mg-Mn-RE systems

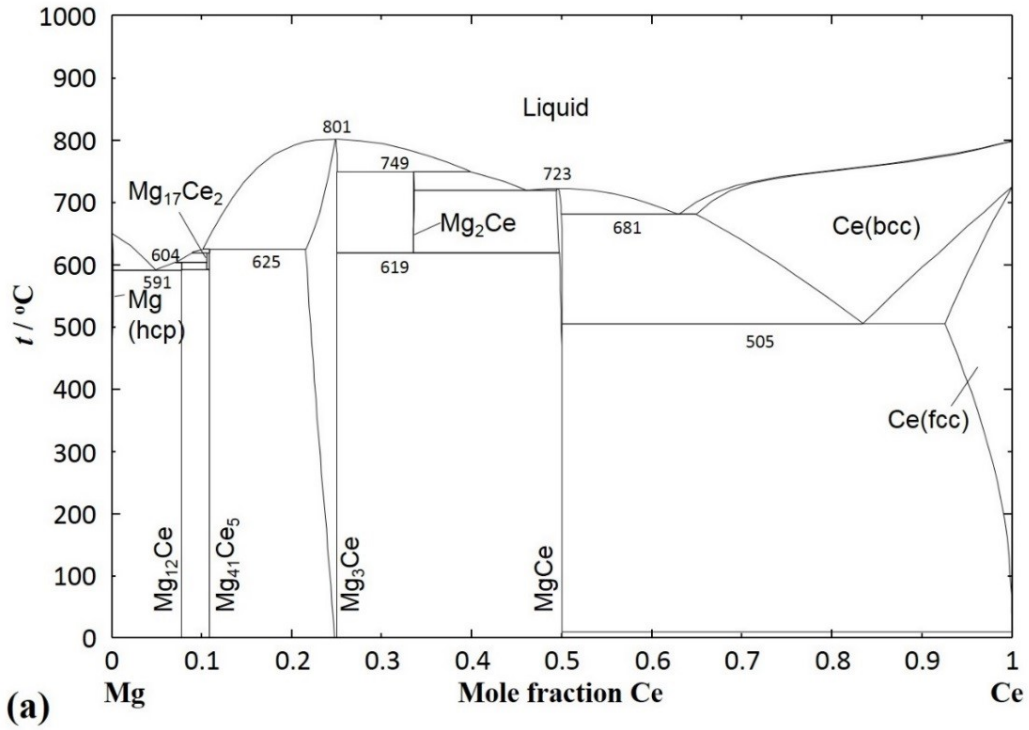
2.1. The Mg-Mn-Ce system

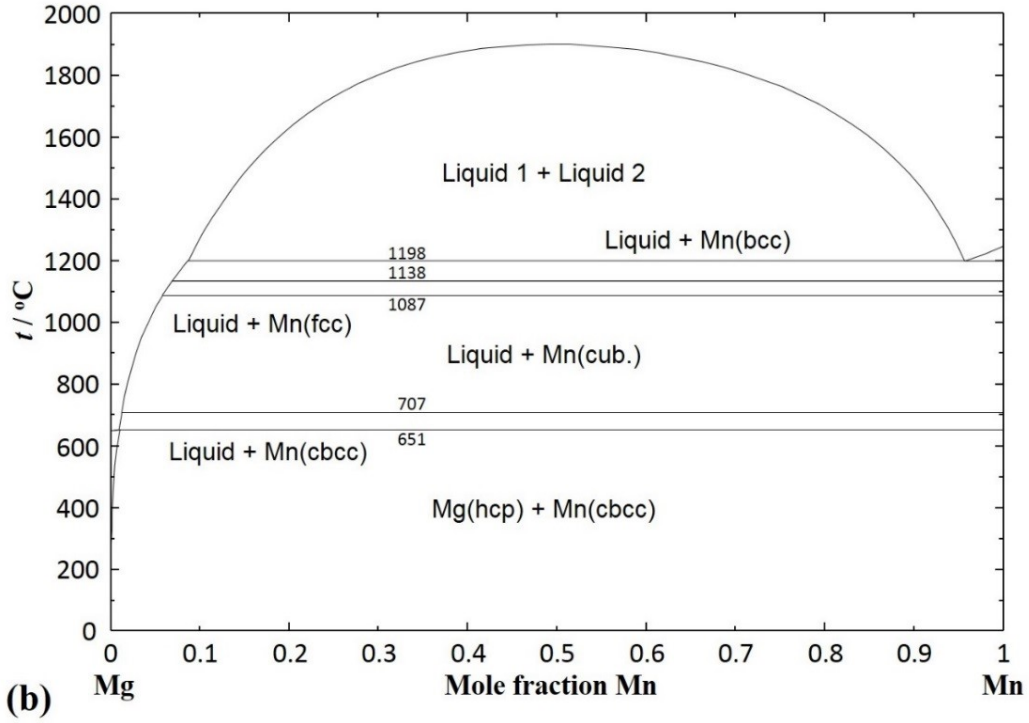
The system was previously assessed by Kang et al. [14] with the assumption of negligible ternary solid solubilities and no ternary compounds. That is, the ternary phase diagram was constructed by extrapolating the constituent binaries which were optimized by the same authors [15] without additional ternary parameters for liquid. The Kohler type of symmetric approximation was adopted as the interactions between constituent binary elements for three binary systems do not show significant difference (ΔH_{mix}: 7.5 kJ mol^{-1} (max) for Mg-Mn, 3 kJ mol^{-1} (max) for Ce-Mn, and -10 kJ mol^{-1} (min) for Mg-Ce at 2000 K). The calculated vertical sections for constant Ce, 0.3 and 1.6 wt. %, agreed with the experimental data of Petrov et al. [1] that determined two isopleths by using thermal and microscopic methods. Later, more vertical sections for constant Mn, 0.6, 1.8, and 2.5 wt. %, were investigated by Zhang et al. [2] using the two types of thermal analyses, cooling curve analysis (CCA) and differential scanning calorimetry (DSC). The experimental results compared with the thermodynamic calculations. It was found that the calculated eutectic

temperature for L → hcp-Mg + $Mg_{12}Ce$ from the assessment of Kang et al. [14] was constantly higher than the experimental data by 8 ºC. Accordingly, the Gibbs energy of $Mg_{12}Ce$ was adjusted by changing the ΔH^{o}_{298} of $Mg_{12}Ce$ from -139880 J mol^{-1} to -137580 J mol^{-1} to reproduce the experimental data. Recently, Ghosh et al. [16] made the thermodynamic assessment of the system along with the re-optimization of the constituent binaries without additional ternary parameter for liquid. No significant changes were made for the Mn-Ce system from the present author's published study (discussed in the Mn-Ce system, Appendix I), except the exclusion of the solid solubility of Ce in cubic-Mn. As no clear evidence exists for the solubility, the specific investigation is required to determine the Ce solubility in cubic-Mn. As for the Mg-Mn system, the consolute temperature for the liquid miscibility gap was believed much higher than the work of Kang et al. [14] as well as the slight increase in the solubility of Mn in hcp-Mg. As a result, the transition temperature of hcp-Mg → hcp-Mg + $Mg_{12}Ce$ was slightly increased by about 20 ºC in the vertical section for 0.3 wt. % Ce, which agreed the experimental findings at 550 ºC by Petrov et al. [1]. However, the solubility of Mn in hcp-Mg was slightly overestimated at lower temperatures (about 400~500 ºC) in their calculations for the vertical sections for 0.3 wt. % Ce and 1.6 wt. % Ce. In addition, they adopted the binary Mg-Ce system from the Kang et al. [14] with refusing the Zhang et al.'s modification for the ΔH^{o}_{298} of $Mg_{12}Ce$ [2] because the modification brought the increase the solubility of Ce in hcp-Mg. However, this brought back the problem of the higher transition temperature of L → hcp-Mg + $Mg_{12}Ce$ pointed out by Zhang et al. [2].

In the present study, the phase diagram of the Mg-Mn-Ce system was constructed in the same manner as the previous assessments without additional ternary parameter. In addition to the optimized Mn-Ce system in the present study, the data of Kang et al. [15] for the Mg-Mn were used. As for the Mg-Ce system, Kang et al. [17] reassessed the system, in particular the slight increase of Ce solubility in hcp-Mg and the ΔH^{o}_{298} of $Mg_{12}Ce$ based on the recent experimental data and the estimations including the Miedema's model and the first-principles calculations. The eutectic temperature of L → hcp-Mg + $Mg_{12}Ce$ was lowered by 10 ºC with the considerably less negative value of ΔH^{o}_{298} of $Mg_{12}Ce$. The reassessed data for the Mg-Ce system were adopted in

the present study. The phase diagrams of the three constituent binary systems are presented in the Fig. 1 and the calculated liquidus surface from the present optimization is shown in Fig. 2. The calculated vertical sections for the constant Ce and Mn are also presented with the experimental data in Figs. 2 and 3, respectively. The liquidus projection is similar to the previous optimizations. Slight differences are found in the vertical sections. For instance, as the stability of $Mg_{12}Ce$ was decreased in the Mg-Ce binary system, the transition temperature of hcp-Mg → hcp-Mg + $Mg_{12}Ce$ is lower than the experimental data of Petrov et al. [1] in the 0.3 wt. % Ce section (in Fig. 3(a)). The solubilities in hcp-Mg are in good agreement with the experimental data [1] in both 0.3 and 1.6 wt. % Ce. However, the hcp-Mg + cbcc-Mn region in the experimental data was not found in the calculated phase diagram as the previous optimizations. For the vertical sections with constant Mn, the calculated phase diagrams are in good agreement with the thermal analyses data [2] as seen in Fig. 4.





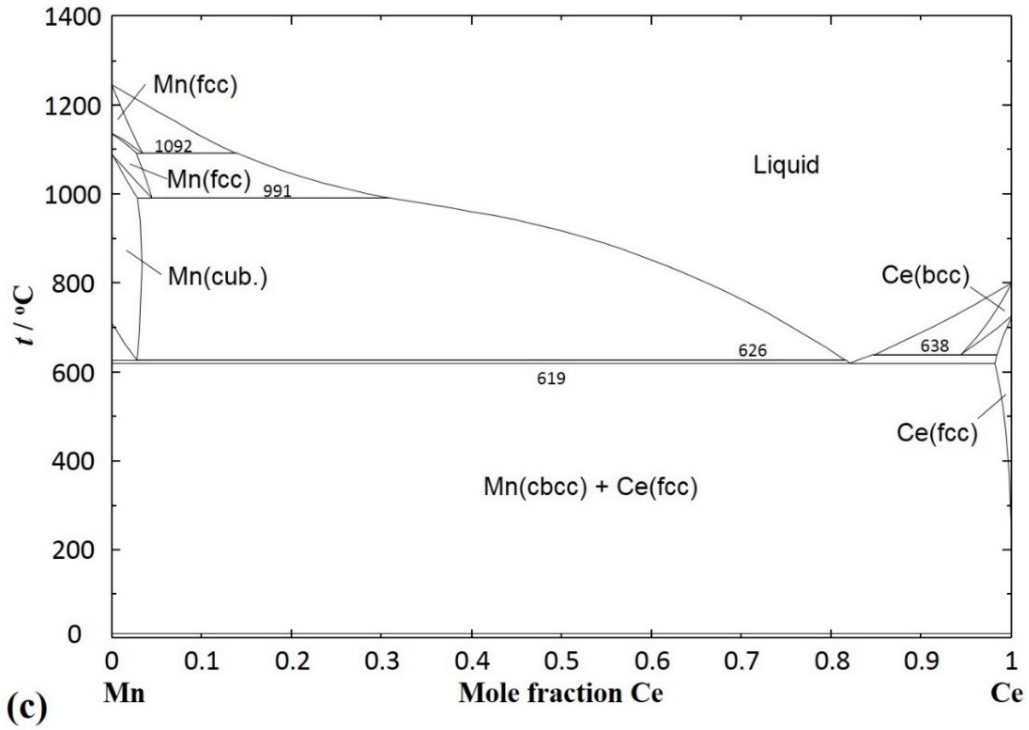


Fig. 1. Optimized phase diagrams of the (a) Mg-Ce system [17], (b) Mg-Mn system [15], and (c) Mn-Ce system (present study, Appendix I).

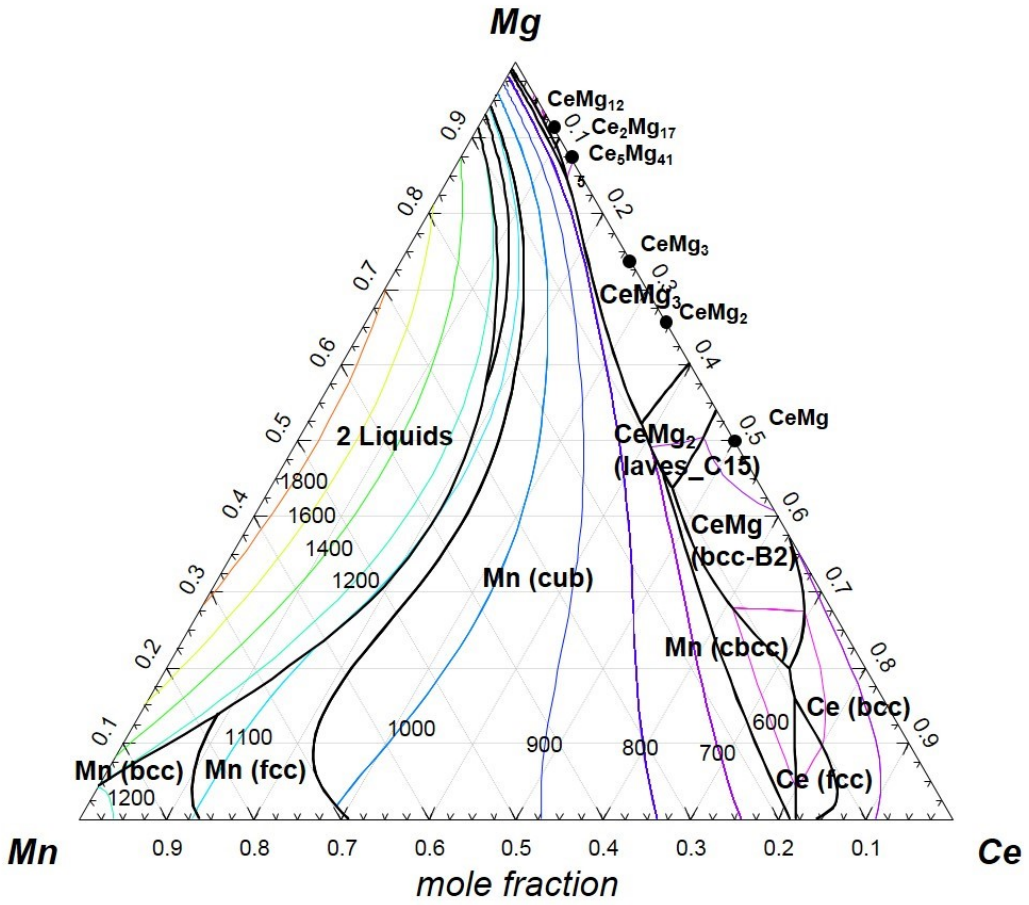


Fig. 2. Calculated liquidus projection of the Mg-Mn-Ce system.

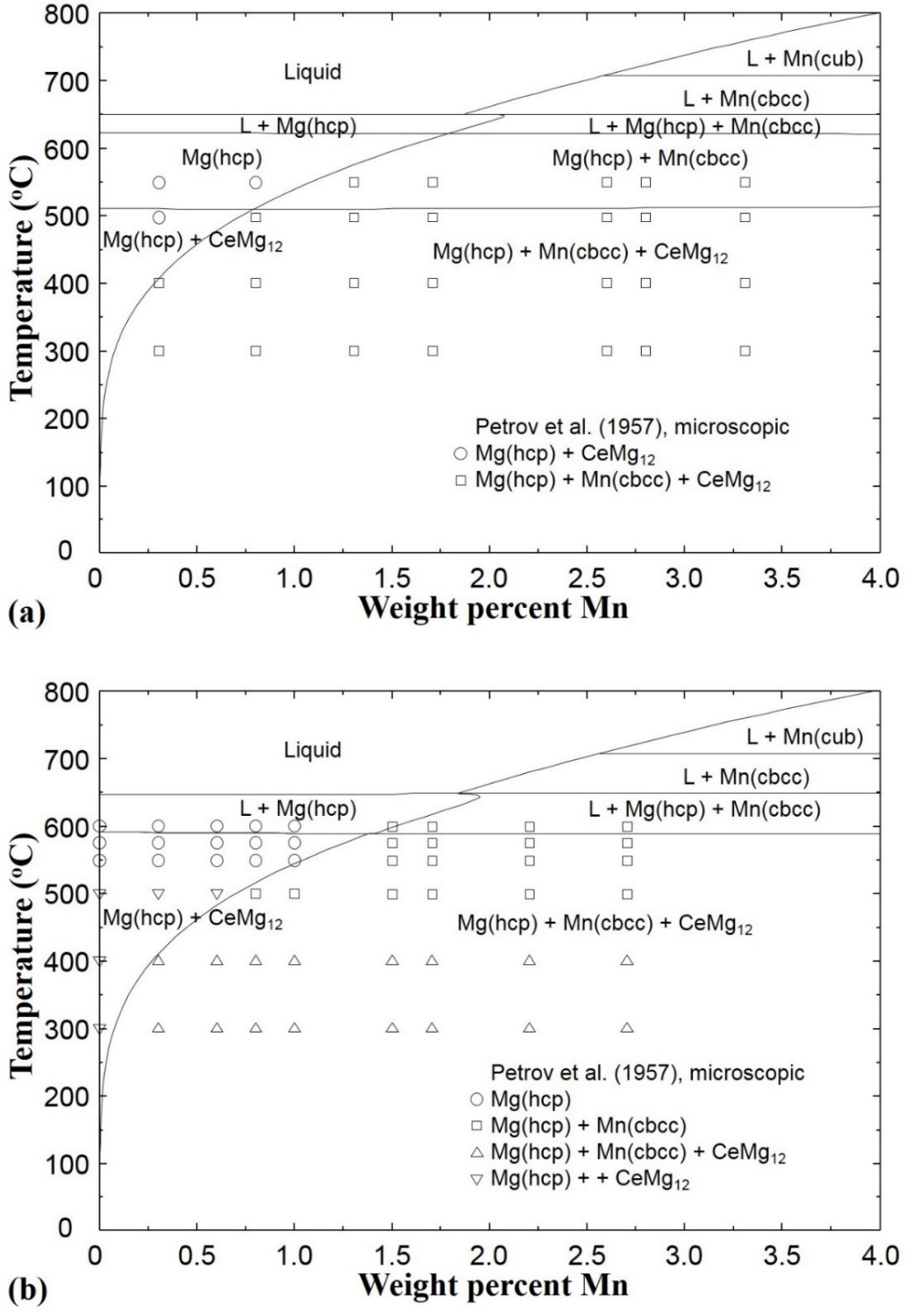
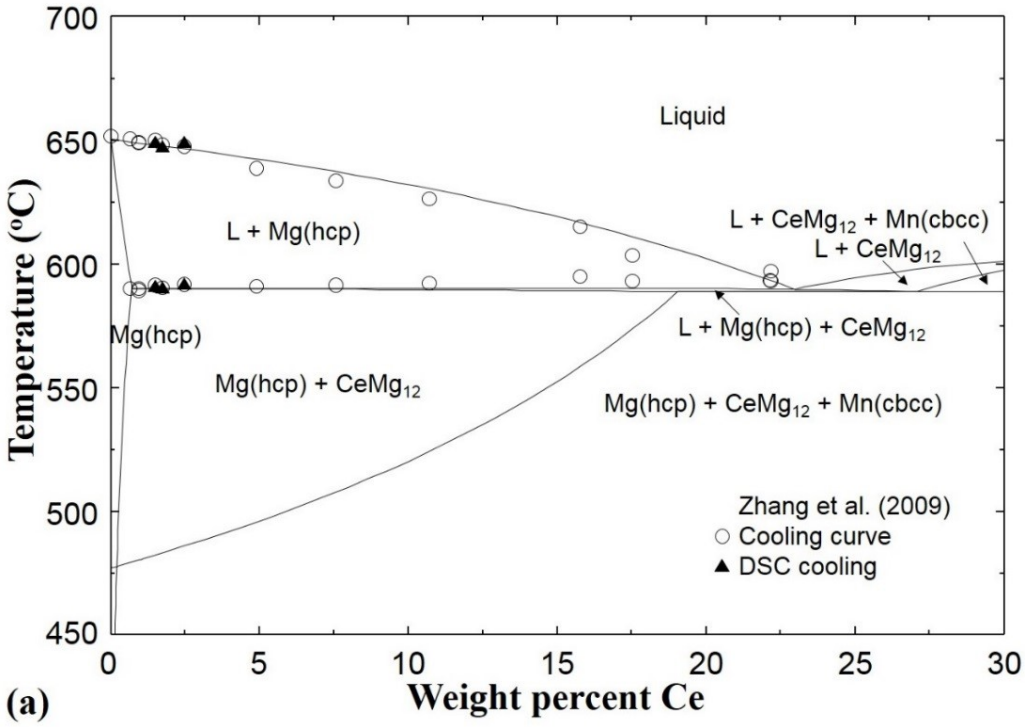
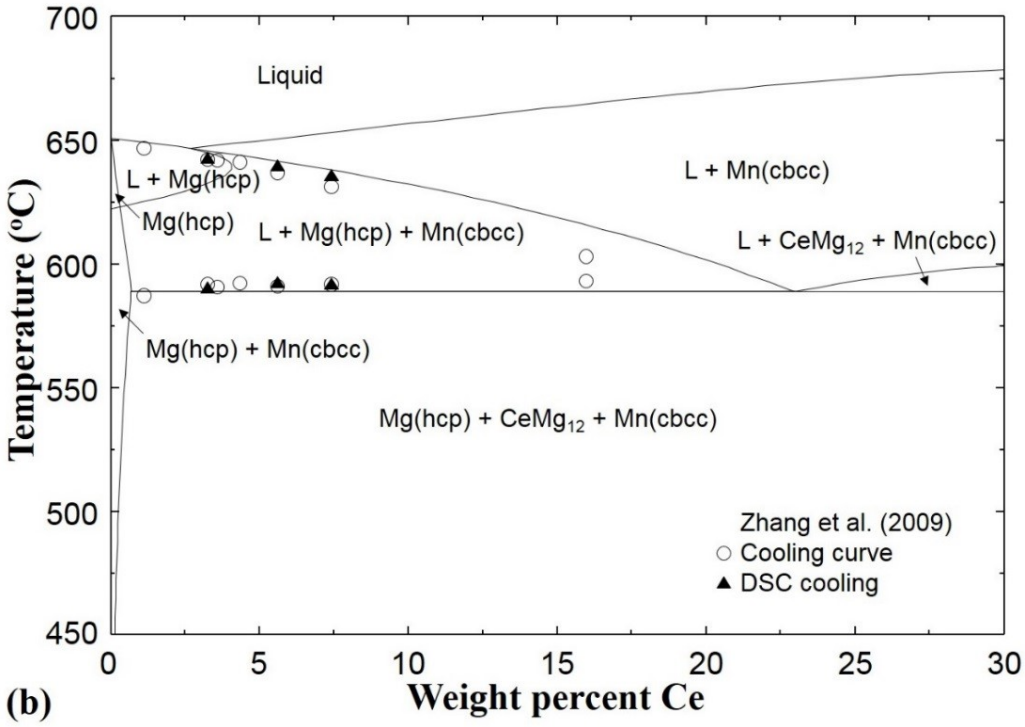


Fig. 3. Calculated vertical sections of (a) 0.3 wt. % Ce, and (b) 1.6 wt. % Ce along with experimental data [1].


Liquid
L + Mg(hcp)
L + CeMg12 + Mn(cbcc)
L + CeMg12
Mg(hcp)
L + Mg(hcp) + CeMg12
Mg(hcp) + CeMg12
Mg(hcp) + CeMg12 + Mn(cbcc)
Zhang et al. (2009)
Cooling curve
DSC cooling
Temperature (°C)
Weight percent Ce
700
650
600
550
500
450
0
5
10
15
20
25
30

(a)


Liquid
L + Mg(hcp)
L + Mn(cbcc)
Mg(hcp)
L + Mg(hcp) + Mn(cbcc)
L + CeMg12 + Mn(cbcc)
Mg(hcp) + Mn(cbcc)
Mg(hcp) + CeMg12 + Mn(cbcc)
Zhang et al. (2009)
Cooling curve
DSC cooling
Temperature (°C)
Weight percent Ce
700
650
600
550
500
450
0
5
10
15
20
25
30

(b)

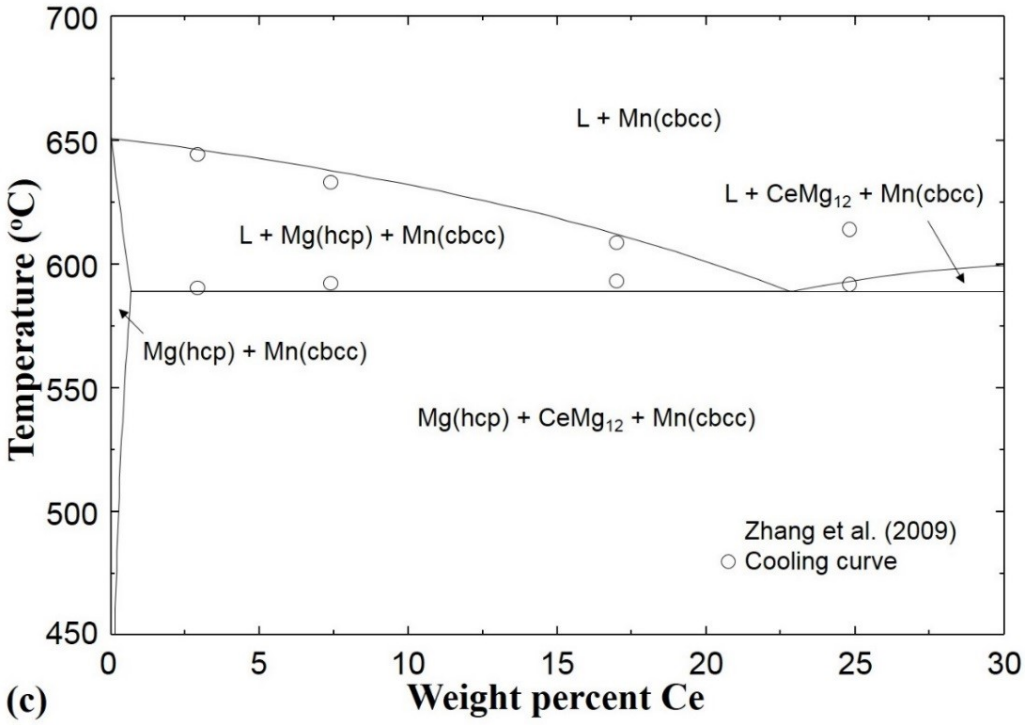


Fig. 4. Calculated vertical sections of (a) 0.6 wt. % Mn, (b) 1.8 wt. % Mn, and (c) 2.5 wt. % Mn along with experimental data [2].

2.2. The Mg-Mn-Nd system

The isothermal phase diagram of the system was experimentally investigated at 450 °C by Mostafa and Medraj [3] using solid-solid diffusion couples and key alloys. The samples were prepared in an arc-melting furnace under argon gas from the initial materials, 99.9 wt. % Mn, 99.95 wt. % Nd, and 99.8 wt. % Mg. The compositions of the sample were confirmed by inductively coupled plasma with optical emission spectrometer (ICP-OES). The diffusion couples and the key alloys were wrapped in tantalum foil, encapsulated in an argon flushed quartz tube and annealed at 450 °C for different annealing time. The quenched samples were analyzed by using the X-ray diffraction (XRD), scanning electron microscope (SEM) equipped with wavelength dispersive X-ray spectrometer (WDS) and energy dispersive X-ray spectrometer (EDS). The determined compositions of the constituent phases in the equilibrated alloys are summarized in Fig. 5.

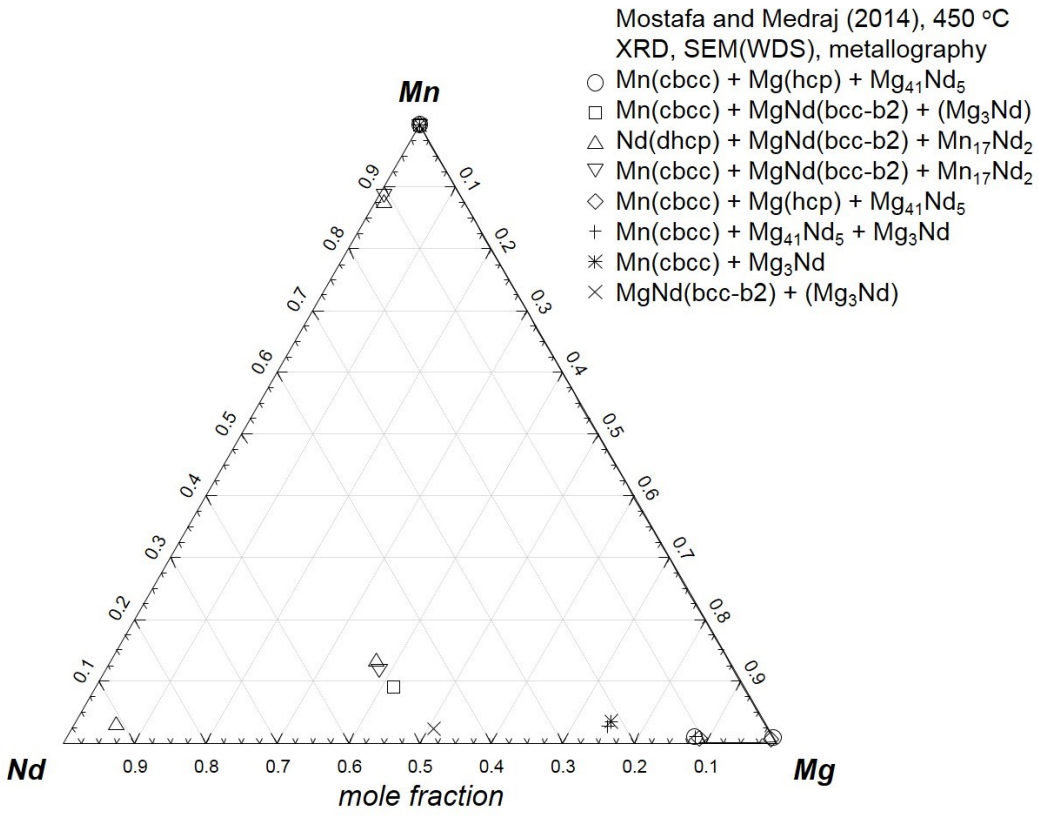


Fig. 5. The compositions of the constituent phases in the experimental investigation [3].

In the present optimization, the binary Mn-Nd system was first re-optimized from the one optimized in Appendix I as new binary phase, $Mn_{17}Nd_2$ was found to exist in the Mn-Nd system. Previously, the existence of the $Mn_{17}Nd_2$ phase was determined in the experimental investigation by Mostafa et al. [18]. The phase diagram was investigated using diffusion couples and key alloys. The equilibrated samples were analyzed by the differential scanning calorimetry (DSC), XRD, electron probe microanalysis (EPMA), and SEM. As well as the liquidus, the eutectoidal decompositions of the compounds, Mn_2Nd and $Mn_{23}N_6$ were confirmed in the temperature ranges of 650-550 and 550-400 ºC, respectively, which agreed with our previous optimization. In addition, the solubilities of Mn in dhcp- and bcc-Nd were determined to be 2.3 at. % Mn and about 5 at. % Mn at eutectic temperature (685 ºC) and 728 ºC, respectively. The existence of $Mn_{17}Nd_2$ (Th_2Ni_{17} type) was confirmed using EPMA and XRD. Based on their experimental findings, Mostafa et al. [18] carried out the thermodynamic optimization of the system using a similar

approach to the present study. The first-principles calculations were also used to determine the enthalpy of formation of the intermetallic compounds. In the present study, a modification was made from the previous one (in Appendix I). The re-optimized parameters are presented in Table 1. The re-optimized phase diagram of the Mn-Nd system is shown in Fig. 6. The $Mn_{17}Nd_2$ phase was added and the solubilities of Mn in dhcp- and bcc-Nd from the work of Mostafa et al. [18] were reproduced. The Gibbs energy parameters of liquid phase were remained unchanged except one temperature dependent parameter in the Nd side. The ΔH^{o}_{298} of compounds were estimated by considering the values from the first-principles calculations [18]. The S^{o}_{298} of compounds were adjusted from the NK approximated values to reproduce the phase transformation temperatures of the compounds.

Table 1. Re-optimized model parameters for the binary Mn-Nd system (J mol^{-1} or J mol^{-1} K^{-1}).

Phase	Thermodynamic parameters
Liquid	Coordination Numbers i j Z^i_{ij} Z^j_{ij} Mn Nd 3 6 Δg_{MnNd}= 2092 − 1.883 T + (-4184 + 6.276 T) X_{MnMn} + (4184 – 2.092 T) X_{NdNd}
BCC-A2	${}^0L_{Mn,Nd}$ = 48116 – 4.184 T ${}^1L_{Mn,Nd}$ = -33472 + 4.184 T $T^{BCC-A2}_{c,Mn}$ (Curie temperature) = 580 K, $B^{BCC-A2}_{o,Mn}$ (Magnetic moment) = 0.27 μ_B mol^{-1}
DHCP	${}^0L_{Mn,Nd}$ = 25104
Mn_2Nd	ΔH^{o}_{298} = 11566.5 (10950.0), S^{o}_{298} = 153.47 C_p = 2 × C_p (Mn, cbcc) + C_p (Nd, dhcp)
$Mn_{23}Nd_6$	ΔH^{o}_{298} = 53211.9 (62350.0), S^{o}_{298} = 1279.6 C_p = 23 × C_p (Mn, cbcc) + 6 × C_p (Nd, dhcp)
$Mn_{17}Nd_2$	ΔH^{o}_{298} = 2000 (23750.0), S^{o}_{298} = 722.93 C_p = 17 × C_p (Mn, cbcc) + 2 × C_p (Nd, dhcp)

The values in the parenthesis are the enthalpy of formation from the first-principles calculations [18].

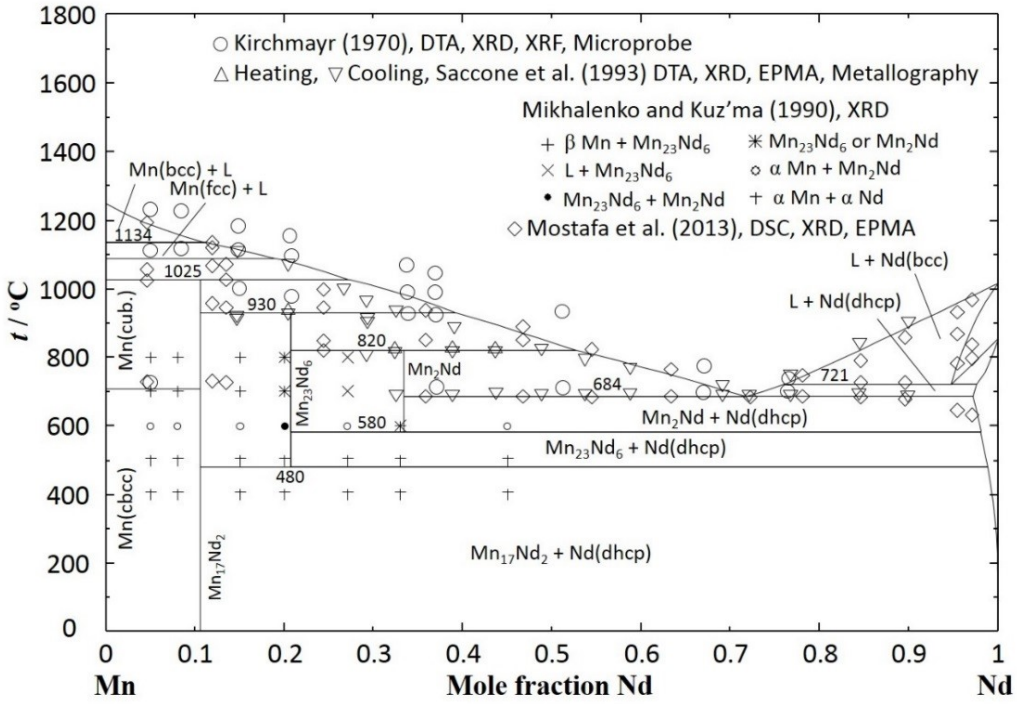


Fig. 6. Re-optimized phase diagram of the Mn-Nd system along with the recent experimental data [18].

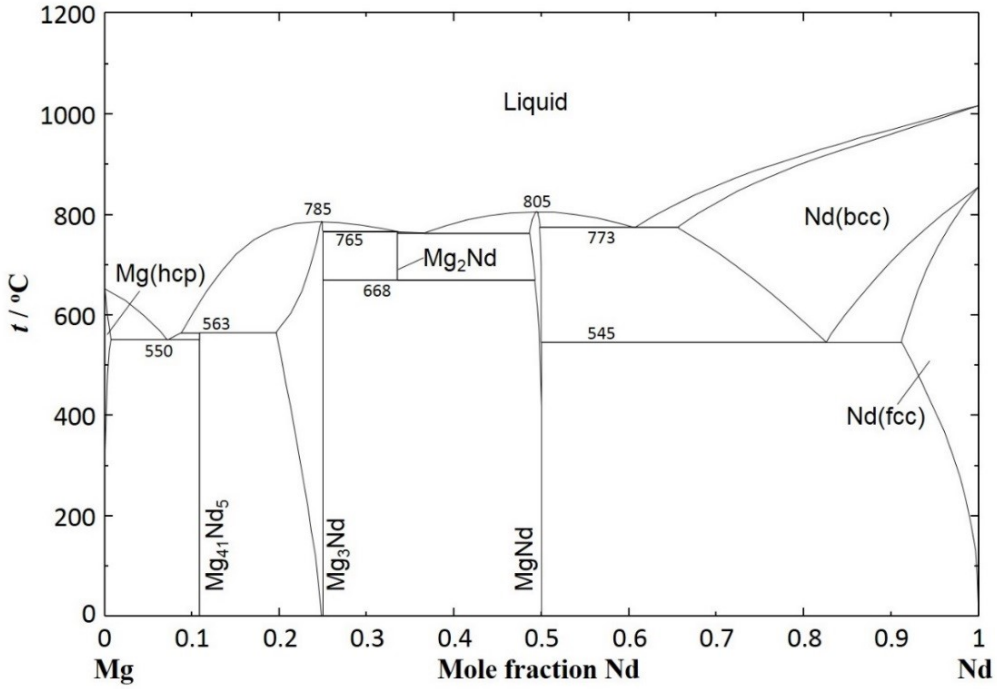


Fig. 7. Optimized phase diagram of the Mg-Nd system [17].

Based on the experimental data in the isothermal phase diagram at 450 °C [3], the ternary Mg-Mn-Nd system was thermodynamically optimized using the optimized binary systems, Mg-Mn system [15] (Fig. 1(b)), Mg-Nd system [17] (Fig. 7), and Mn-Nd system (present study) (Fig. 6). Like the Mg-Mn-Ce system, the Kohler type of symmetric approximation was adopted (ΔH_{mix}: 7.5 kJ mol^{-1} (max) for Mg-Mn, 2 kJ mol^{-1} (max) for Nd-Mn, and -10 kJ mol^{-1} (min) for Mg-Nd at 2000 K) without additional ternary parameter. Three ternary solid solutions (dhcp, bcc-B2, and Mg_3Nd) were modeled with two sublattices using the compound energy formalism (CEF). The optimized model parameters are presented in Table 2. The calculated isothermal section at 450 °C and the calculated liquidus surface are shown in Figs. 8 and 9, respectively.

For the dhcp-Nd phase with the structure (Mg,Mn,Nd)[Va], the interaction parameter of Mg-Mn was adjusted to be minimum not until appearing unwanted dhcp phase in the Mg-Mn binary system. However, the experimental solubilities of Mg and Mn in dhcp-Nd was still difficult to be reproduced in this approach. For the MgNd(bcc-B2) phase with the structure (Mg,Mn)[Mg,Nd], the negative interaction parameter of Mg-Mn in the first sublattice and the positive Gibbs energy of end member, MnNd were applied to reproduce the compositions of bcc-B2 phase for the three phase regions determined experimentally. Although the compositions of bcc-B2 phase agree well with the experimental data [3], the negative Gibbs energy of the bcc-B2 phase reduced the solubilities of Mg and Mn in dhcp-Nd to some extent. Similarly, the ternary solubility in Mg_3Nd phase was modeled with the structure $(Mg,Mn)_3$[Mg,Nd]. As the experimental solubility of Mg in Mg_3Nd seemed to be much less than that in the optimized Mg-Nd system, further investigation would be required to determine the accurate homogeneity range. At the moment, the Gibbs energies of end members, Mn_3Mg and Mn_3Nd were estimated not to overestimate the solubility in Mg_3Nd.

Table 2. Optimized model parameters for ternary solutions in the Mg-Mn-Nd system (J mol^{-1}).

Phase	Thermodynamic parameters
dhcp-Nd	G(Mg) = G(Mg, hcp) + 2188.232*
(Mg,Mn,Nd)[Va]	G(Mn) = G(Mn, cbcc) + 2000.0*
	G(Nd) = G(Nd, dhcp)*
	^{0}L(Mg,Mn) = 16736.0
	^{0}L(Mg,Nd) = -10460.0 – 2.092 *T**
	^{0}L(Mn,Nd) = 25104.0*
MgNd(bcc-B2)	G(Mg:Mg) = 2G(Mg, hcp) + 8368.0*
(Mg,Mn)[Mg,Nd]	G(Mg:Nd) = G(Mg, hcp) + G(Nd, dhcp) – 29290.8 + 5.08 *T**
	G(Mn:Mg) = G(Mn,cbcc) + G(Mg, hcp) + 41840.0*
	G(Mn:Nd) = G(Mn,cbcc) + G(Nd, dhcp) + 62760.0
	^{0}L(Mg,Mn:Nd) = -104600.0
Mg_3Nd	G(Mg:Mg) = 4G(Mg, hcp) + 8368.0*
$(Mg,Mn)_3[Mg,Nd]$	G(Mg:Nd) = 3G(Mg, hcp) + G(Nd, dhcp) − 73500.0 + 26.5 *T**
	G(Mn:Mg) = 3G(Mn, cbcc) + G(Mg, hcp) + 83680.0
	G(Mn:Nd) = 3G(Mn, cbcc) + G(Nd, dhcp) + 62760.0

* : Taken from previous studies for the binary and ternary systems [15, 17].

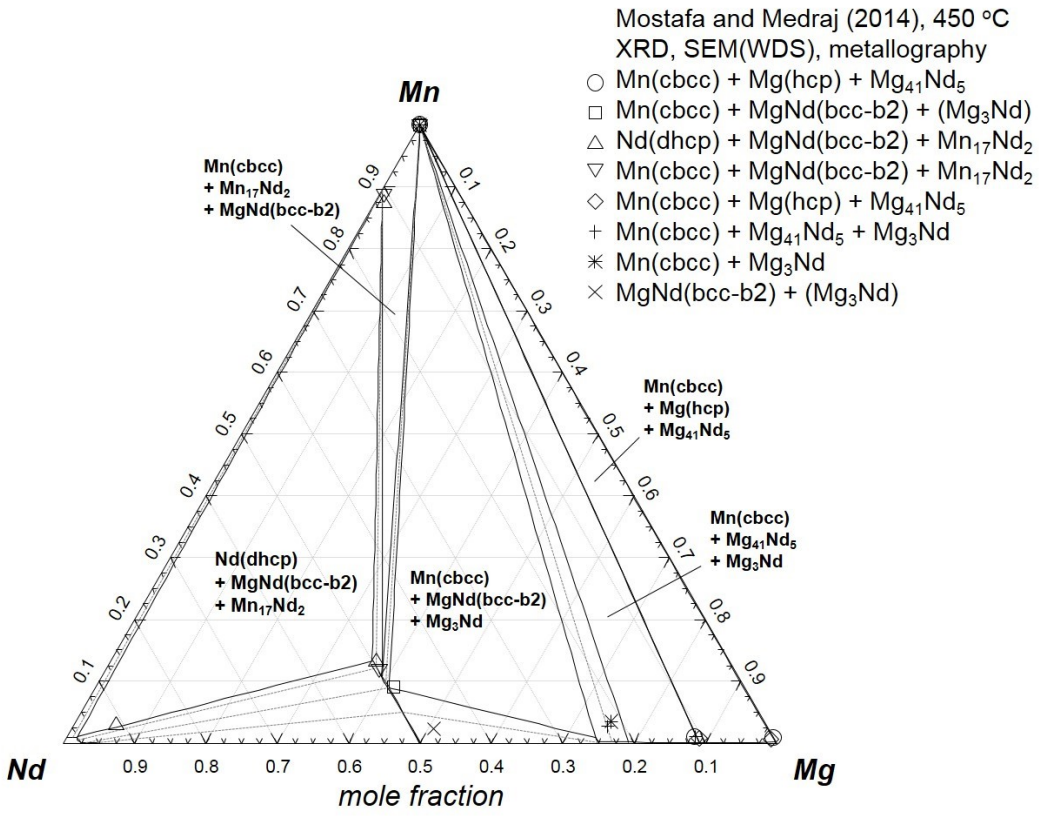


Fig. 8. Isothermal section of the Mg-Mn-Nd system at 450 ºC along with the experimental data [18].

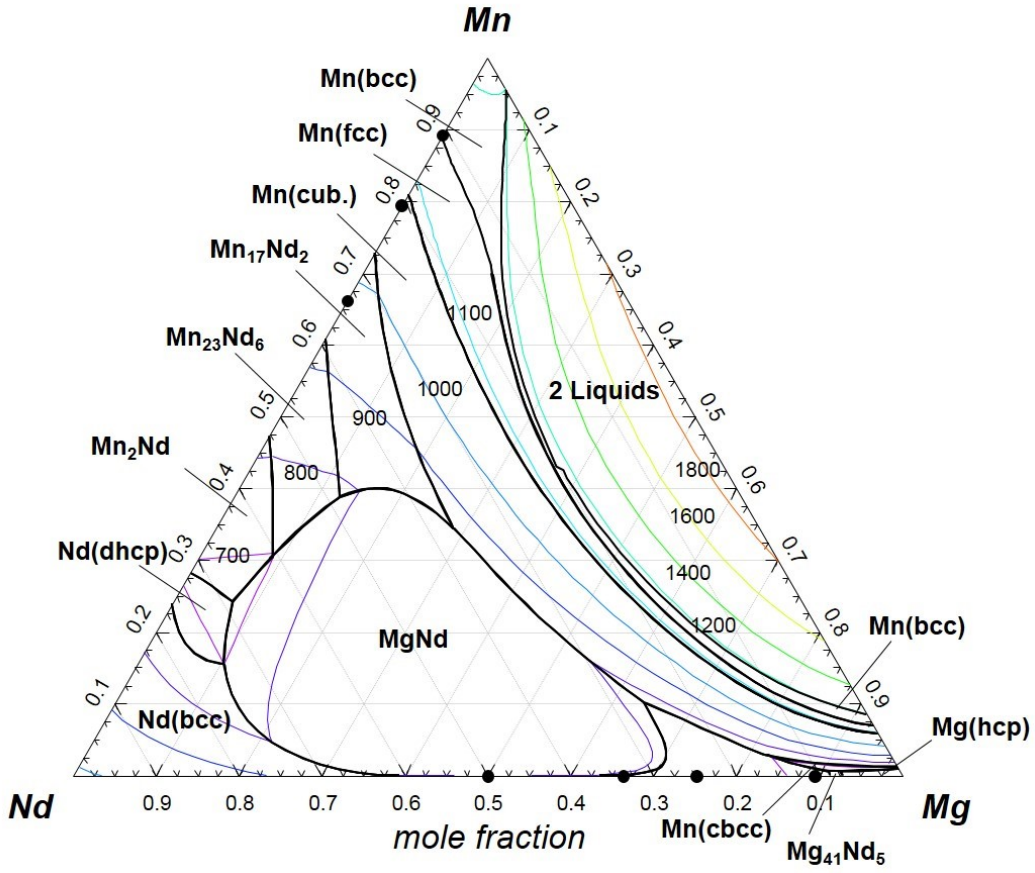


Fig. 9. Calculated liquidus projection of the Mg-Mn-Nd system.

2.3. The Mg-Mn-Gd system

A phase diagram study using DTA and EDS combined with thermodynamic assessment was carried out by Antion [4]. Since three constituent binary systems used in his thermodynamic assessment seem to be less accurate than our database, experimental data were only taken into account in the present study. Two isothermal studies were investigated using two alloys equilibrated for 1.5 month at 600 ºC and one alloy equilibrated for 1.5 month at 800 ºC. For all three alloys, three equilibrium phases were found with limited solubilities of Mn in MgGd (~15 at. %) and of Mg in Mn_2Gd (~2.6 at. %), $Mn_{23}Gd_6$ (~2.5 at. %) and $Mn_{12}Gd$ (~1 at. %). In the present study, three constituent systems, Mg-Mn [15] (Fig. 1(b)), Mg-Gd [17] (Fig. 10), and Mn-Nd (present study) (Fig. 11) were merged using the symmetric Kohler approximation (ΔH_{mix}: 7.5 kJ mol^{-1} (max) for Mg-Mn, -2 kJ mol^{-1} (min) for Gd-Mn, and -8 kJ mol^{-1} (min) for Mg-Gd at 2000 K).

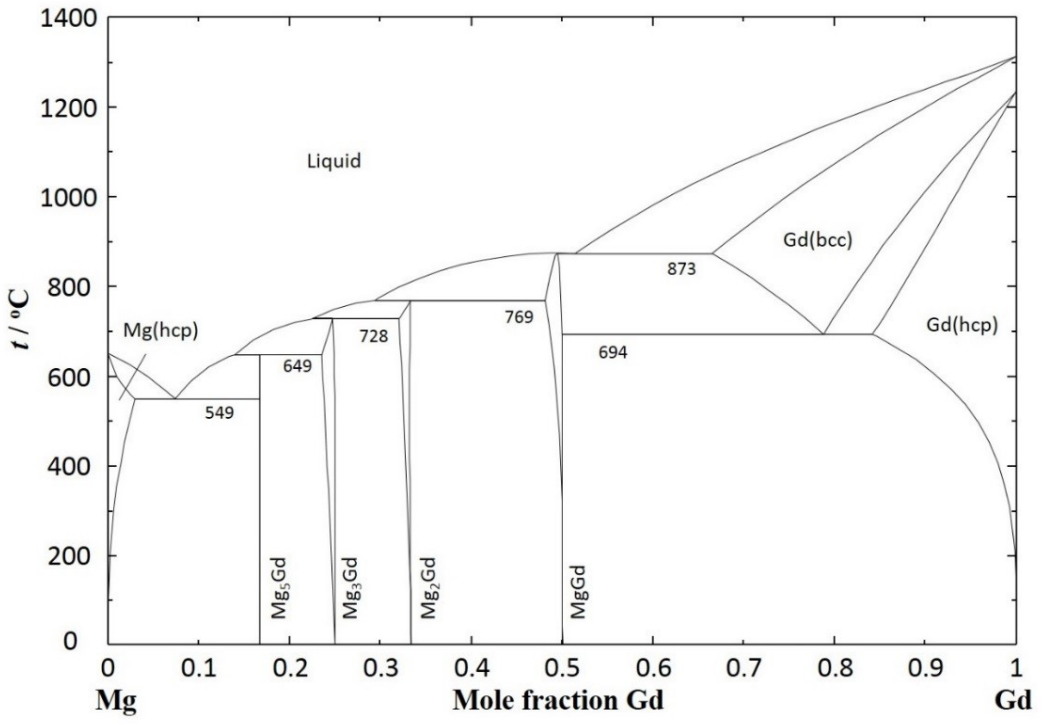


Fig. 10. Optimized phase diagram of the Mg-Gd system [17].

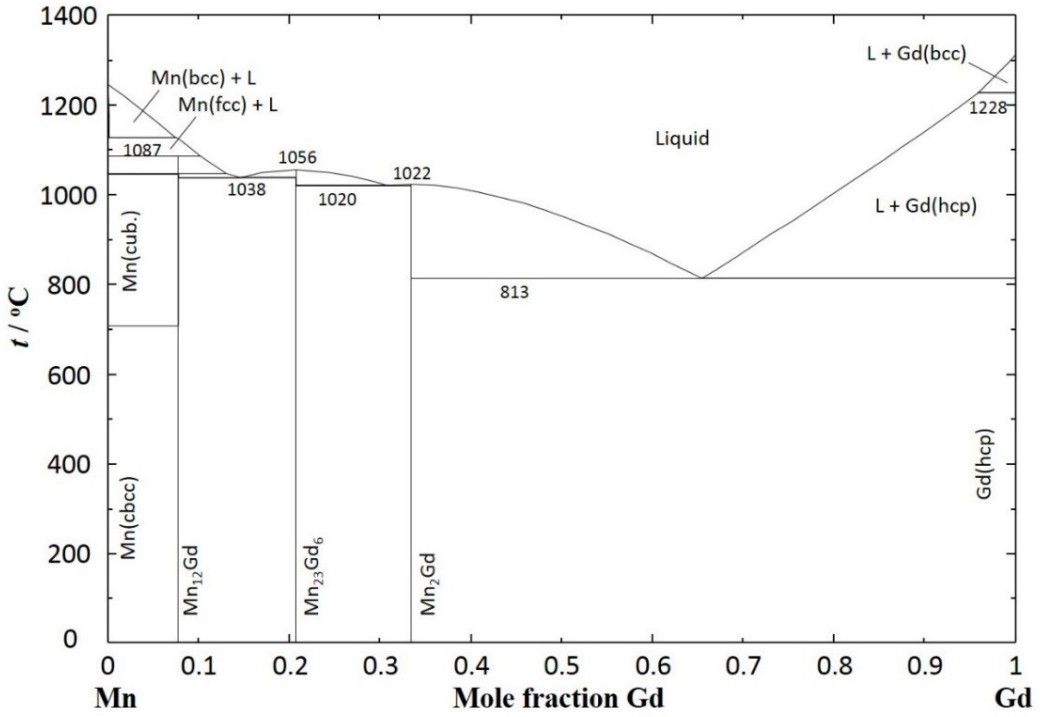


Fig. 11. Optimized phase diagram of the Mn-Gd system (Appendix II).

The experimental solubilities were modeled as four ternary solid solutions ($(Mg,Mn)_2Gd$(laves-C15), MgGd(bcc-B2), $Mn_{23}Gd_6$, and $Mn_{12}Gd$) using Compound Energy Formalism (CEF). For example, the MgGd(bcc-B2) phase was considered two sublattices: (Mg,Mn)[Mg,Gd]. It was assumed that Mg and Mn mix predominantly only on the first sublattice. The Gibbs energies of the end-members were taken from previous optimizations for other ternary systems or were set to arbitrarily large positive values which was optimized to reproduce the Mn solubility in the MgGd phase. The other solid solution phases were similarly modeled. Moreover, three equilibrium phases which were experimentally observed are in good agreement with the thermodynamic calculations in our optimization. Antion [4] also performed thermal analysis and metallographic analysis using two different alloys and found the primary phases and invariant temperatures. According to the result, the Mn_2Gd phase was transformed from liquid (19.7 at. % Mg, 31.7 at. % Mn and 48.6 at. % Gd) at 896 ºC and the $Mn_{23}Gd_6$ phase was transformed from liquid (20.5 at. % Mg, 58.5 at. % Mn and 21 at. % Gd) at 1030 ºC. In the calculation from our preliminary optimization, the former alloy

transformed from liquid to the Mn_2Gd phase at 842.28 ºC and the latter alloy transformed from liquid to the $Mn_{12}Gd$ at 1002.6 ºC. In order to reproduce the experimental data, positive ternary interaction parameter (~33 kJ) was applied in our ternary optimization. As a result, the phases and temperatures in our calculation is in reasonable agreement to the experimental data. Although two immiscible liquid is the primary phase in our calculation for the latter alloy, the $Mn_{23}Gd_6$ phase is the first solid phase transformed from liquid as the microstructure shown in the study of Antion [4]. Figs. 12 and 13 show the calculated isothermal sections of the system at 600 ºC and 800 ºC with experimental data of Antion [4]. The calculated liquid projection for the Mg-Mn-Gd system in the present study is shown in Fig. 14 with experimental data of Antion [4]. The thermodynamic parameters in the present study are listed in Table 3.

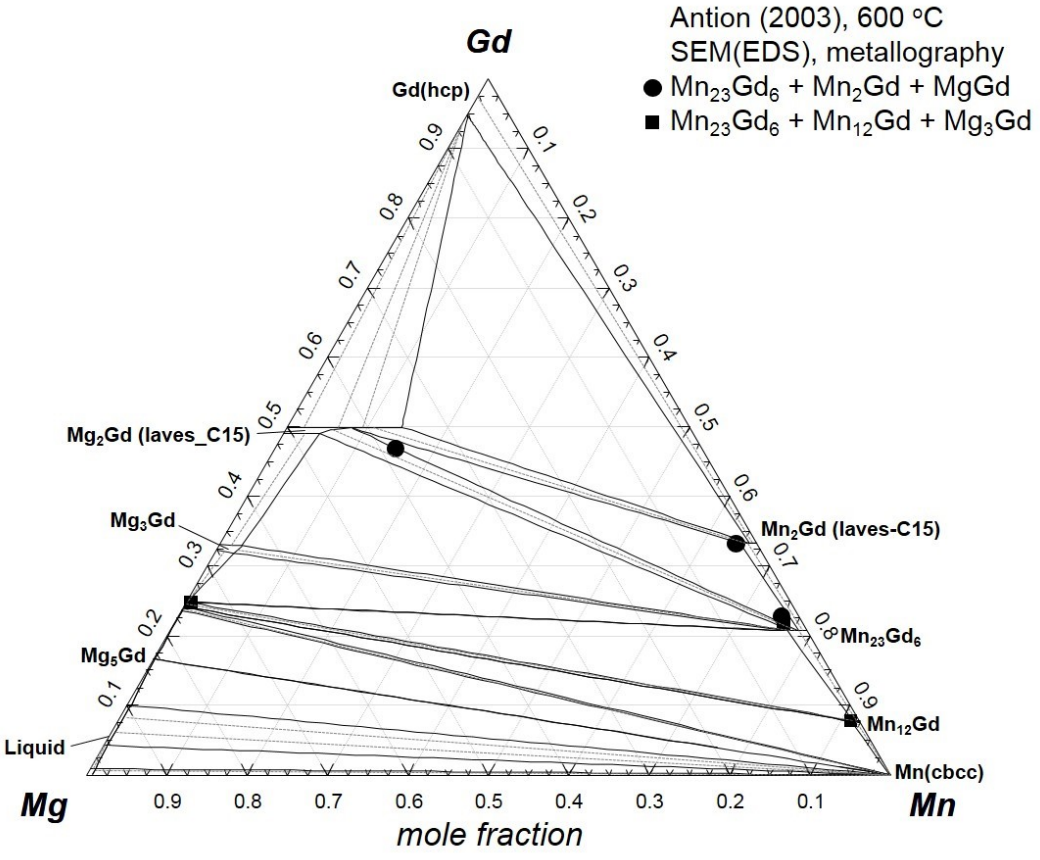


Fig. 12(cbcc). Isothermal section of the Mg-Mn-Gd system at 600 ºC along with the experimental data [4].

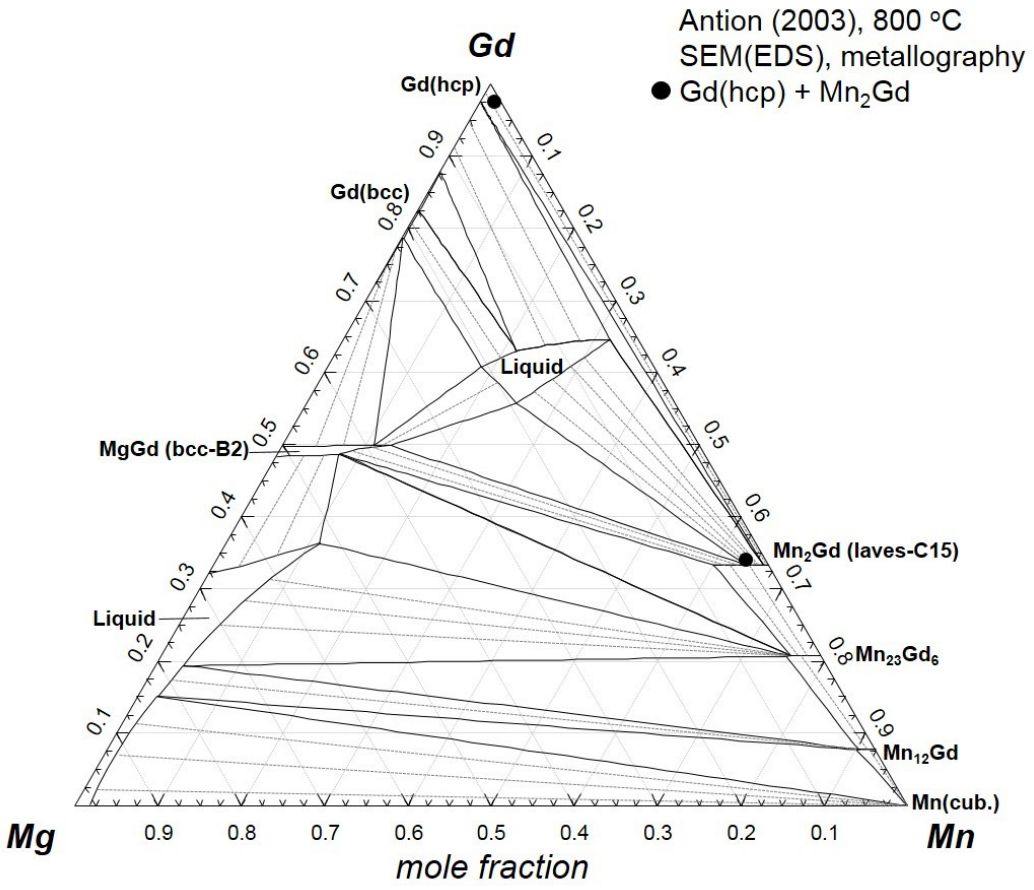


Fig. 13. Isothermal section of the Mg-Mn-Gd system at 800 ºC along with the experimental data [4].

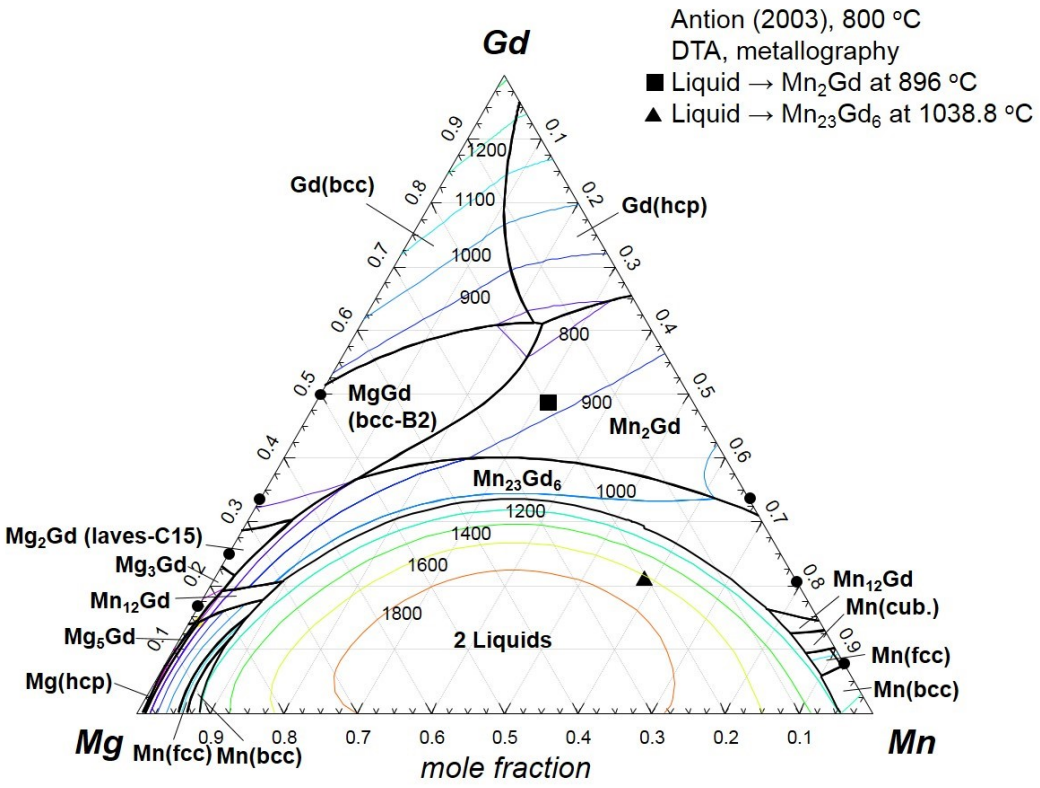


Fig. 14. Calculated liquidus projection of the Mg-Mn-Nd system along with the experimental data [4].

Table 3. Optimized model parameters for ternary solutions in the Mg-Mn-Gd system (J mol^{-1} or J $K^{-1}mol^{-1}$).

Phase	Thermodynamic parameters
Liquid	$g^{001}_{MgMn(Gd)} = 33472.0$
$(Mg,Mn)_2Gd$(laves-C15)	G(Gd:Gd) = 3G(Gd, hcp) + 75000.0*
$(Mg,Mn,Gd)_2$[Mg,Mn,Gd]	G(Gd:Mg) = 2G(Gd, hcp) + G(Mg, hcp) + 15000.0*
	G(Gd:Mn) = 2G(Gd, hcp) + G(Mn, cbcc) + 75000.0*
	G(Mg:Gd) = 2G(Mg, hcp) + G(Gd, hcp) – 43629.5 + 10.92 *T**
	G(Mg:Mg) = 3G(Mg, hcp) + 22740.0*
	G(Mg:Mn) = 2G(Mg, hcp) + G(Mn, cbcc) + 49340.0*
	G(Mn:Gd) = G(Mn_2Gd)*
	G(Mn:Mg) = 2G(Mn, cbcc) + G(Mg, hcp) + 49340.0*
	G(Mn:Mn) = 3G(Mn, cbcc) + 83680.0*
	^{0}L(Mg:Mn,Gd) = 46024.0
MgGd(bcc-B2)	G(Mg:Mg) = 2G(Mg, hcp) + 8368.0*
(Mg,Mn)[Mg,Gd]	G(Mg:Gd) = G(Mg, hcp) + G(Gd, hcp) – 30000 + 7.317 *T**
	G(Mn:Mg) = G(Mn, cbcc) + G(Mg, hcp) + 41840.0*
	G(Mn:Gd) = G(Mn, cbcc) + G(Gd, hcp) + 836.8
$Mn_{23}Gd_6$	G(Mg:Gd) = 23G(Mg, hcp) + 6G(Gd, hcp) + 292880.0
	G(Mn:Gd) = G($Mn_{23}Gd_6$)*
$Mn_{12}Gd$	G(Mg:Gd) = 12G(Mg, hcp) + G(Gd, hcp) – 32521.0 + 14.94 *T**
	G(Mn:Gd) = G($Mn_{12}Gd$)*
	^{0}L(Mg:Mn,Gd) = 334720.0

* : Taken from previous studies for the binary and ternary systems ([15, 17] and present study).

2.3. The Mg-Mn-Y system

The system was previously optimized by Kang et al. [14] based on the phase diagram investigation of Antion [4]. The experimental investigation of Antion was the same as he did for the Mg-Mn-Gd system. As well as the equilibrated phases and the compositions of the respective phases at 600 and 800 ºC, the primary solid phases were determined by using DTA, XRD and SEM(EDS). In the present study, the Gibbs energies of the stable binary phases in the binary Mn-Y system were replaced by the presently optimized values (Appendix II). The system was optimized by combining three constituent systems, Mg-Mn [15] (Fig. 1(b)), Mg-Y [17] (Fig. 15), and Mn-Y (present study) (Fig. 16) using the symmetric Kohler approximation (ΔH_{mix}: 7.5 kJ mol^{-1} (max) for Mg-Mn, -2 kJ mol^{-1} (min) for Y-Mn, and -8.4 kJ mol^{-1} (min) for Mg-Y at 2000 K). The Gibbs energies of end members and the interaction parameters for the ternary solid solutions such as MgY(bcc-B2), Mg_2Y(laves-C14), Mn_2Y(laves-C15) from the optimization of Kang et al. [14] were adopted as they were. The calculated isothermal phase diagrams at 600 and 800 ºC are shown in Figs. 17 and 18, respectively. The calculated liquidus surface is presented in Fig. 19. No significant changes from the previous optimization were observed in the calculated isothermal phase diagrams and the liquidus projection except for the $Mn_{12}Y$ phase containing region. As the stability of $Mn_{12}Y$ phase was decreased (ΔH^{o}_{298} = -32695.9 → -18000 (J mol^{-1}), S^{o}_{298} = 440.59 → 437.62 (J K^{-1} mol^{-1})), three phases field containing $Mn_{12}Y$ phase in the isothermal phase diagrams are slightly different from the previous phase diagrams. It is also seen in the liquid surface by the reduced $Mn_{12}Y$ primary phase field. However, no experimental data are available to validate the changes.

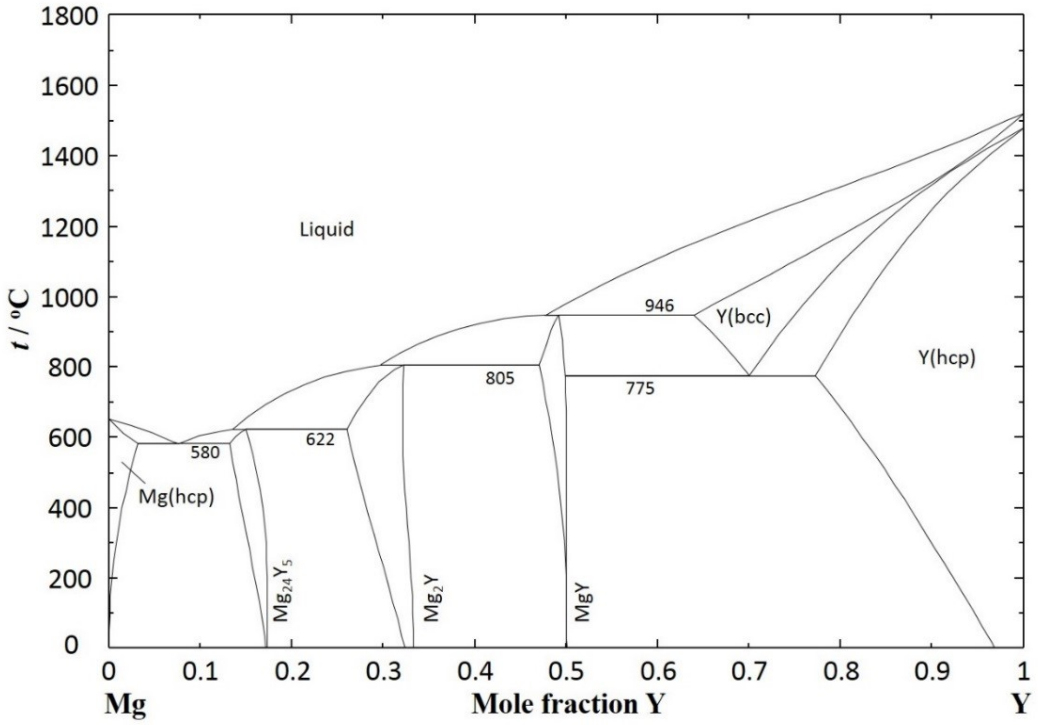


Fig. 15. Optimized phase diagram of the Mg-Y system [17].

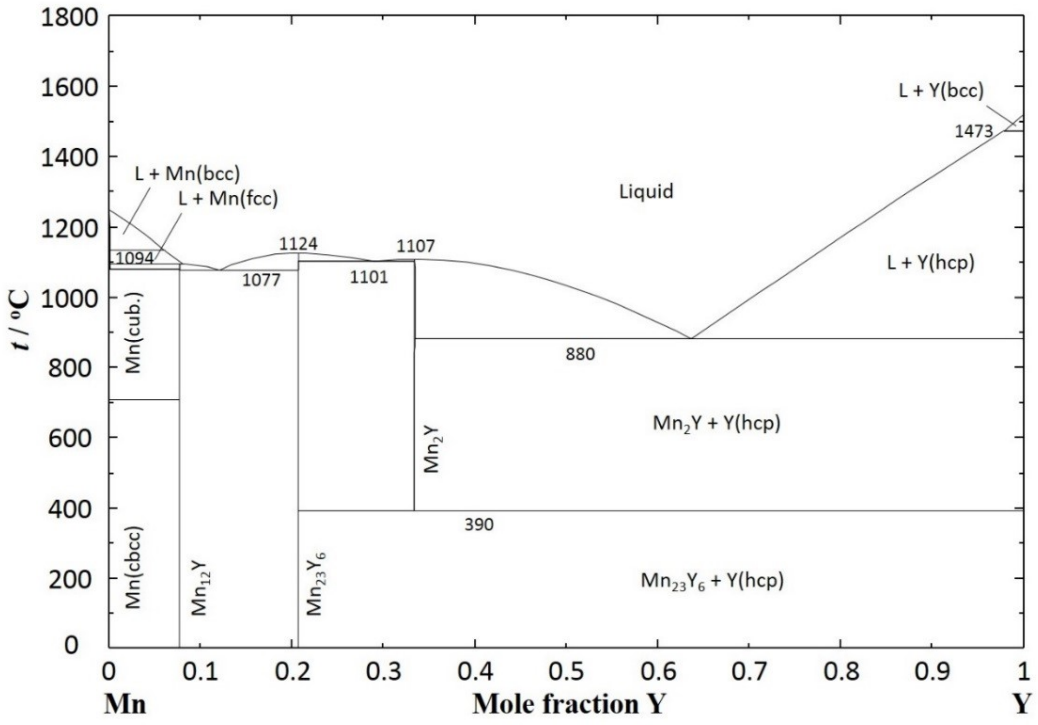


Fig. 16. Optimized phase diagram of the Mn-Y system (Appendix II).

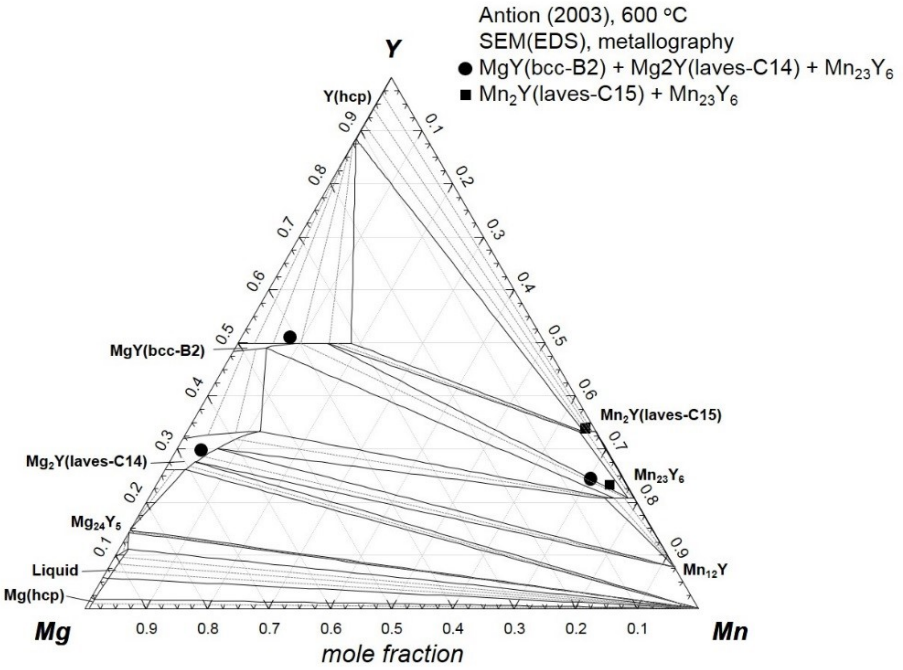


Fig. 17. Optimized isothermal section of the Mg-Mn-Y system at 600 °C along with the experimental data [4].

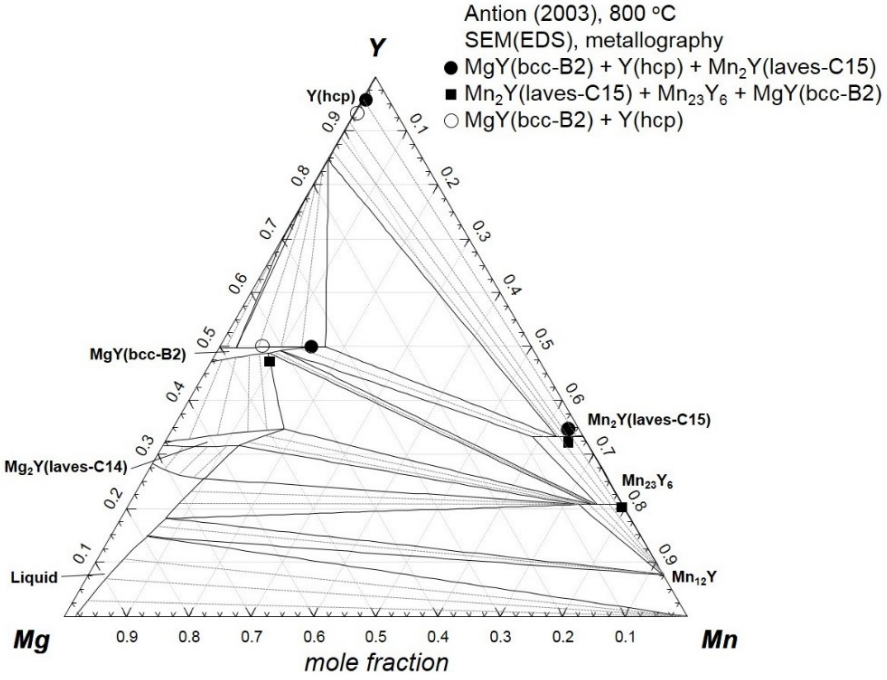


Fig. 18. Optimized isothermal section of the Mg-Mn-Y system at 600 °C along with the experimental data [4].

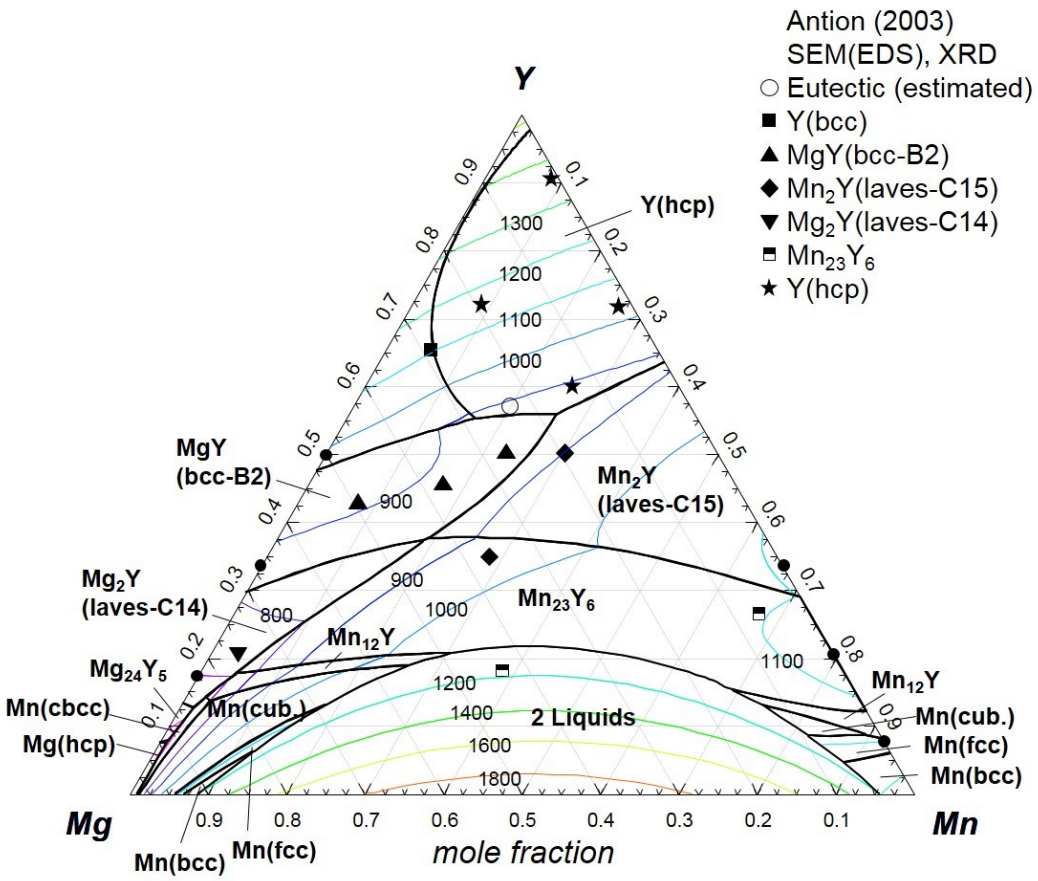


Fig. 19. Calculated liquidus surface and the primary phase fields of the Mg-Mn-Y system compared with the experimental data [4].

3. The Mg-Si-RE systems

3.1. The Mg-Si-Y system

The system was previously optimized by Shukla et al. [19] by combining the optimized three binary systems without ternary liquid parameters. The calculated phase diagrams were compared with the experimental investigation of Mg rich region by Drits et al. [8], who reported two vertical sections and one isothermal section at 400 ^{o}C by means of metallographic and thermal cooling methods. The asymmetric approximation was applied because the Y-Si liquid phase exhibits very negative deviations (ΔH_{mix}= -68 kJ mol^{-1} (min) at 2000 K) from ideal solution behavior whereas the Mg-Si (ΔH_{mix}= -16.8 kJ mol^{-1} (min) at 2000 K) and Mg-Y (ΔH_{mix}= -8.4 kJ mol^{-1} (min) at 2000 K) are closer to ideality. It was also assumed that the ternary compounds were absent as no evidence had been reported. However, in fact, the a few ternary compounds were reported for Mg-Si-RE system. For example, the existence of the $REMgSi_2$ (RE = La, Ce, Pr, Nd) and their respective lattice parameters were reported by the XRD study [5]. In addition, the presence of the compounds, $CeMg_2Si_2$ [6, 7], CeMgSi [6], $CeMg_3Si$ [6] and Ce_2MgSi_2 [7] were previously reported. Therefore it is highly possible that the ternary compounds exist in the Mg-Si-Y.

In the present study, like the work of Shukla et al. [19], the three constituent binary systems, Mg-Si [20] (Fig. 20), Mg-Y [15] (Fig. 14), and Si-Y (Appendix IV) (Fig. 21) were combined using asymmetric approximation with Mg as the asymmetric component. It was assumed that the ternary solid solubility were negligible and no ternary compounds exist. The calculated vertical sections are compared with the experimental data [8] in Figs 22-24. The calculated liquidus projection of the Mg-Si-Y system is presented in Fig. 25. The calculated vertical section from Mg-13 wt. % Y to Mg-4 wt. % Si is in good agreement with the transformation temperatures from cooling curves [8] as seen in Fig. 22. However, the calculated transformation temperatures in another vertical section with constant 15 wt. % Y are slightly off from experimental data [8] as seen in Fig. 23. For the diagram of wt. % Si vs wt. % Y, the calculated phase diagram contains more phase fields compared to the experimental data [8] as seen in Fig. 24. However, if certain stable ternary

compounds are added in the system, the unknown X phase in the experimental work [8] can be replaced by the ternary compound. Further investigation regarding the existence of ternary compounds and the solid solubilities would be required to optimize the system.

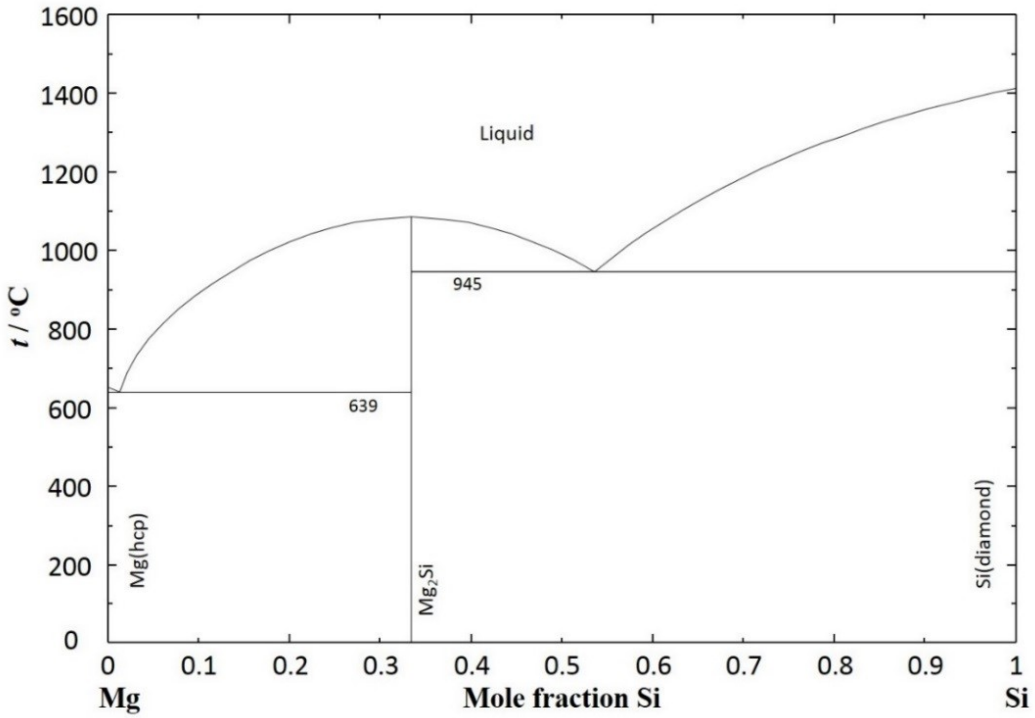


Fig. 20. Optimized phase diagram of the Mg-Si system [20].

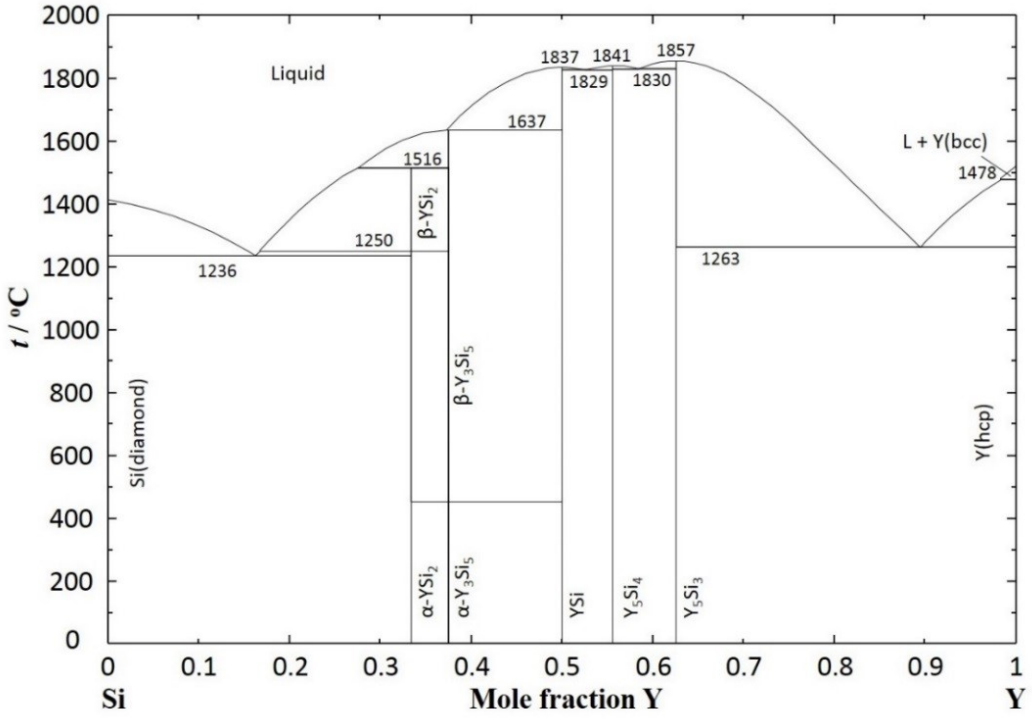


Fig. 21. Optimized phase diagram of the Si-Y system (Appendix IV).

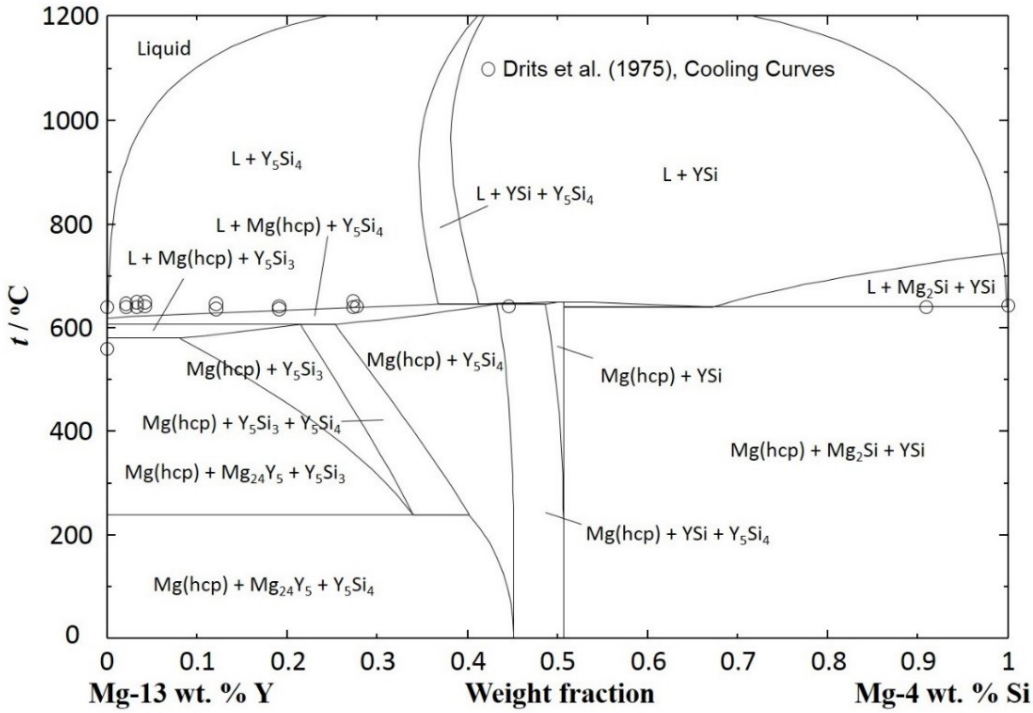


Fig. 22. Calculated vertical section of the Mg-Y-Si phase diagram with experimental data [8].

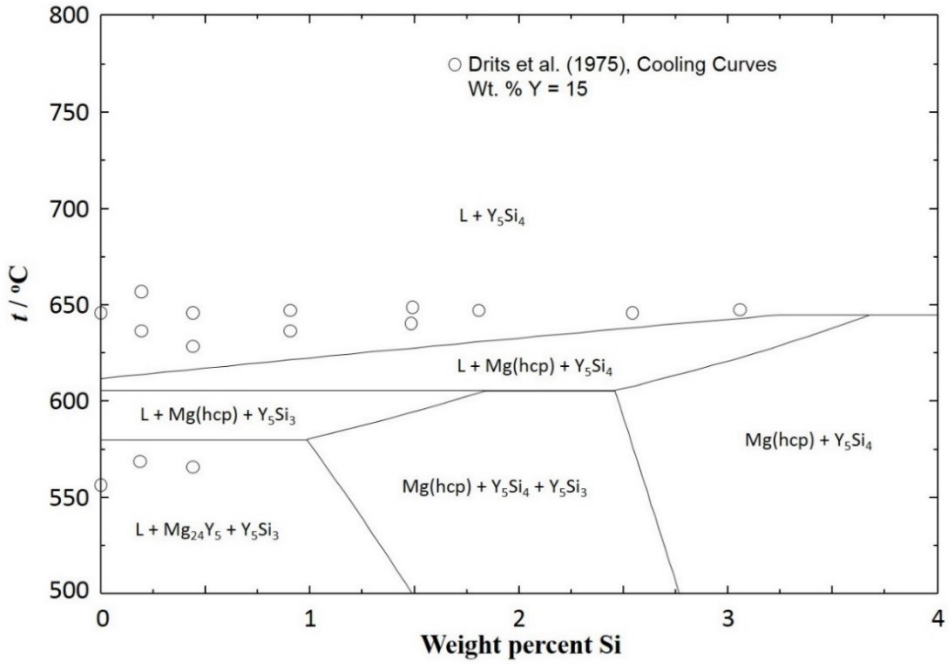


Fig. 23. Calculated vertical section of the Mg-Y-Si phase diagram at 15 wt. % Y with experimental data [8].

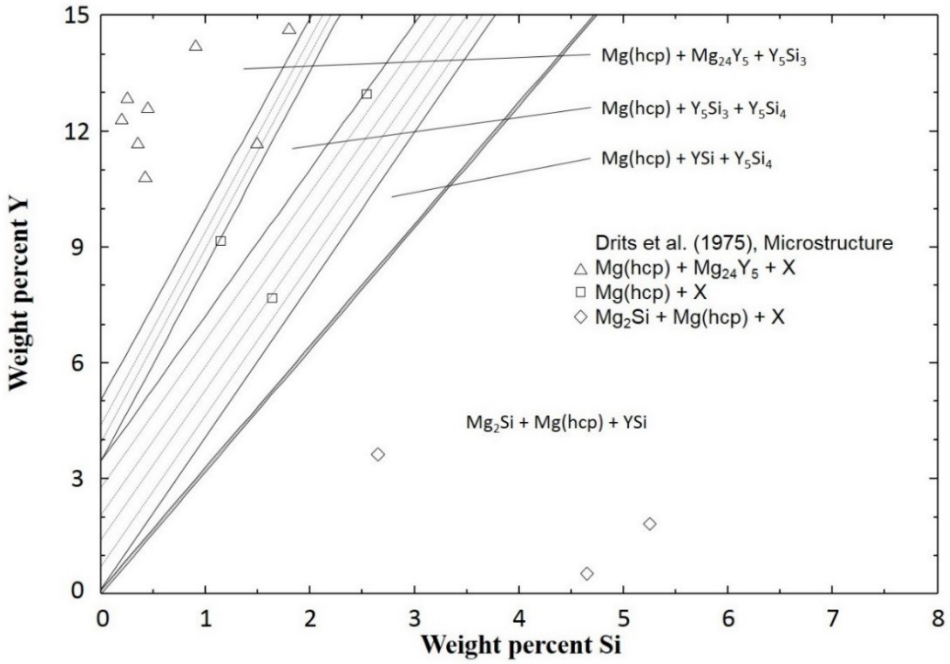


Fig. 24. Calculated isothermal section at 400 ºC of the Mg-Y-Si phase diagram with experimental data [8].

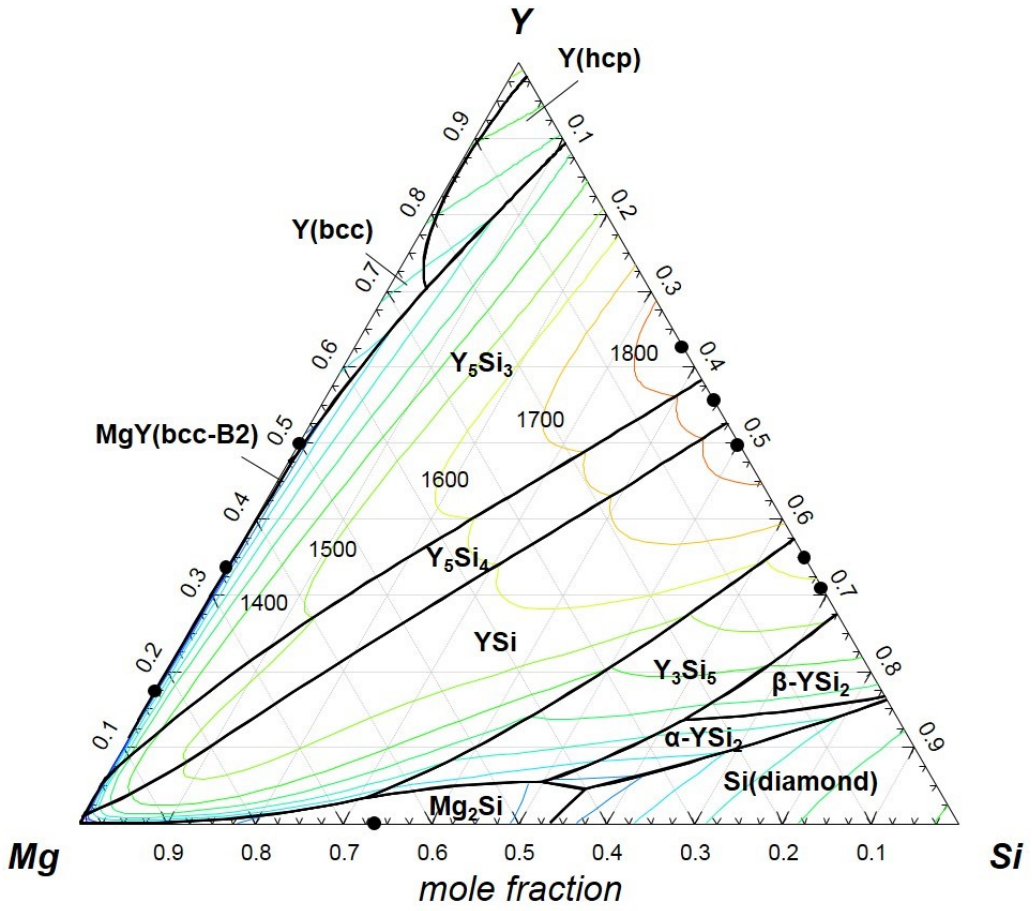


Fig. 25. Calculated liquidus surface of the Mg-Si-Y system.

4. The Mg-Sn-RE systems

4.1. Experimental procedure

In the present study, the Mg-Sn-Nd and Mg-Sn-Gd systems were investigated by equilibrated alloy method including conventional quenching and microscopic analyses. The desired ternary alloys were prepared with the high purity materials, Mg (99.99%), Sn (99.99%), and Mg-40wt.%Nd(Gd) master alloys. All starting alloys were melted homogeneously in the crucible made of Ta foil using induction melting furnace with graphite susceptor. In order to avoid the oxidation of the alloys during melting, the atmosphere inside induction furnace was controlled with continuously flowing argon gas purified by Mg turnings at 500 ^{o}C. The partial pressure of oxygen in the purified argon gas was about 1.7×10^{-8} ppm. The alloys were kept for 15-30 min. at 800-850 ^{o}C for uniform melting. About 2 wt. % of extra Mg was added to the designed ternary alloy to compensate the Mg losses during melting due to the volatilization of Mg. The compositions of initial materials and the final compositions of the alloys obtained by considering the weight change are tabulated in Table 4.

Table 4. Compositions of the initial materials and the alloys.

	Mg (wt. %) initial / in alloy	Sn (wt. %) initial / in alloy	RE (wt. %) initial / in alloy
Mg-Sn-Nd, Alloy 1	60 / 59.75	10 / 10.06	30 / 30.19
Mg-Sn-Nd, Alloy 2	80 / 81.28	10 / 9.36	10 / 9.36
Mg-Sn-Nd, Alloy 3	60 / 61.15	30 / 29.14	10 / 9.71
Mg-Sn-Nd, Alloy 4	20 / 20.18	67 / 66.74	13 / 13.08
Mg-Sn-Gd, Alloy 1	60 / 60.70	10 / 9.83	30 / 29.47
Mg-Sn-Gd, Alloy 2	80 / 80.03	10 / 9.99	10 / 9.98
Mg-Sn-Gd, Alloy 3	60 / 60.06	30 / 29.96	10 / 9.98
Mg-Sn-Gd, Alloy 4	20 / 19.37	67 / 67.42	13 / 13.21

The examples of the backscattering electron (BSE) images of the as cast alloys are shown in Fig. 26. The as cast alloys show the typical dendritic solidification microstructure with white particles distributed inhomogeneously with various sizes. The white particles turned out to be the ternary compounds, MgNdSn or MgGdSn. It was believed the melting temperatures of the ternary compounds were above 900 ºC.

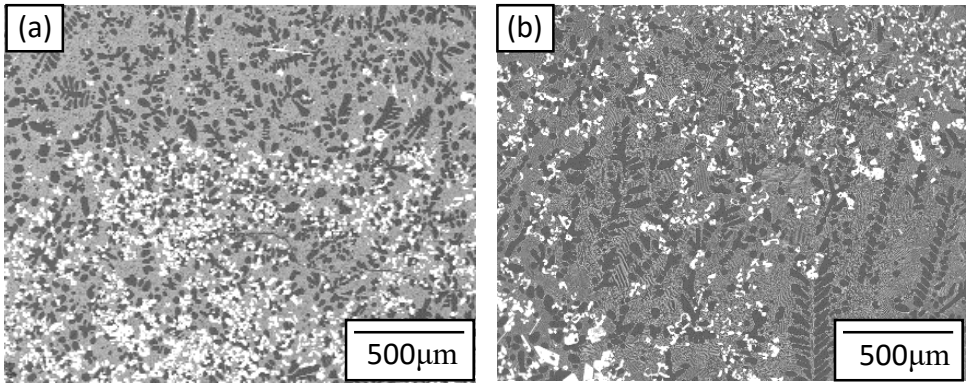


Fig. 26. The backscattering electron (BSE) images of the as cast alloys: (a) 0.6Mg-0.1Sn-0.3Nd (wt.), and (b) 0.6Mg-0.3Sn-0.1Gd (wt.)

For phase diagram study, the samples were cut into small pieces (2-3mm) and wrapped with Ta foil and sealed in Mo capsule. Then the samples were annealed in the horizontal tube furnace under high purity argon atmosphere at 500, 600, and 700 ºC for 1 month, 1 week, and 4 hours, respectively. Subsequently, all the samples were rapidly quenched by water. The chemical analysis of each sample was conducted by means of the electron probe microscopy analysis (EPMA – JEOL8600) equipped with wavelength dispersive spectroscopy (WDS). Due to the inhomogeneous distribution of the ternary compounds in the as-cast alloys, the compositions of annealed alloys, which were the small pieces of the as-cast alloys, were different from the as-cast alloys. They were determined by averaging the compositions of multiple areas. As the ternary compounds were particularly prone to oxidation, the sample preparation for the analysis required special treatment including water free alcohol lubricant for the grinding and polishing.

4.2. The Mg-Sn-Nd system

The BSE images of the annealed alloys at 700 ºC are shown in Fig. 27. The compositions of the annealed alloys and the constituent phases are presented in Table 5. The alloys 1 to 3 consisted of the ternary compound, MgNdSn and the dendritic structure which represents the liquid phase before quenching (seen in the enlarged figures in Fig. 27). In the alloy 4, two solid phases, $MgNdSn_2$ and Mg_2Sn were found. Although it was unable to analyse the small particles (< 1μm) in the enlarged figure (Fig. 27(h)), it was believed that they were the $MgNdSn_2$ according to the observation of various sizes of $MgNdSn_2$.

The BSE images of the annealed alloys at 600 ºC are shown in Fig. 28. The compositions of the annealed alloys and the constituent phases are presented in Table 6. The microstructure of alloy 1 was similar to that of alloy 1 annealed at 700 ºC. However, small grey phase was found in addition to the MgNdSn and liquid. According to the composition analysis, the phase was $Mg_{12}Nd$ which was known to be metastable, forming only as precipitates in quenched samples [17]. Therefore, it was believed that the equilibrium phases at 700 ºC were MgNdSn and liquid, and the $Mg_{12}Nd$ precipitation was formed from the liquid during quenching. The composition of liquid was determined including the $Mg_{12}Nd$ phase. On the other hand, the alloy 2 consisted of the MgNdSn and solid hcp-Mg. For the alloy 3, the ternary compound, $Mg_4Nd_2Sn_3$ was newly identified along with the dendritic structure representing the liquid. It was also believed that the hcp-Mg also coexisted with the liquid at 600 ºC. The much bigger size of the dendrite arms also supports this fact. However, it was very difficult to distinguish the primary solid hcp-Mg from the hcp-Mg phase during quenching. Instead, the composition of eutectic phase was identified, and it was identical to the eutectic composition of the binary Mg-Sn system. The microstructure of the alloy 4 was about the same as the alloy 4 annealed at 700 ºC.

The BSE images of the annealed alloys at 500 ºC are shown in Fig. 29. The compositions of the annealed alloys and the constituent phases are presented in Table 7. Due to the long term of annealing, the ternary compounds, in particular MgNdSn were oxidized partially. The alloy 1 was composed of MgNdSn, $Mg_{41}Nd_5$ and hcp-Mg. For the alloys 2 and 3, two different compositions

of hcp-Mg phases were observed in two distinct regions: compounds-rich (Fig. 29(b) and (d)) and compounds-poor (Fig. 29(c) and (e)). It is no wonder that the equilibrated hcp-Mg phase in the compounds-poor region contained higher Mg content compared to the hcp-Mg in compounds-rich region. Meanwhile, it should be noted that, for alloy 3, the hcp-Mg in the compounds-rich region equilibrated with $Mg_4Nd_2Sn_3$ and Mg_2Sn (Fig. 29(d)), whereas the hcp-Mg in the compounds-poor region equilibrated with MgNdSn (Fig. 29(e)). In general, the ternary solubilities in hcp-Mg was insignificant, which means either Gd or Sn was soluble in the hcp-Mg.. The microstructure of the alloy 4 was again analogous to the alloy 4 annealed at 600 and 700 ^{o}C.

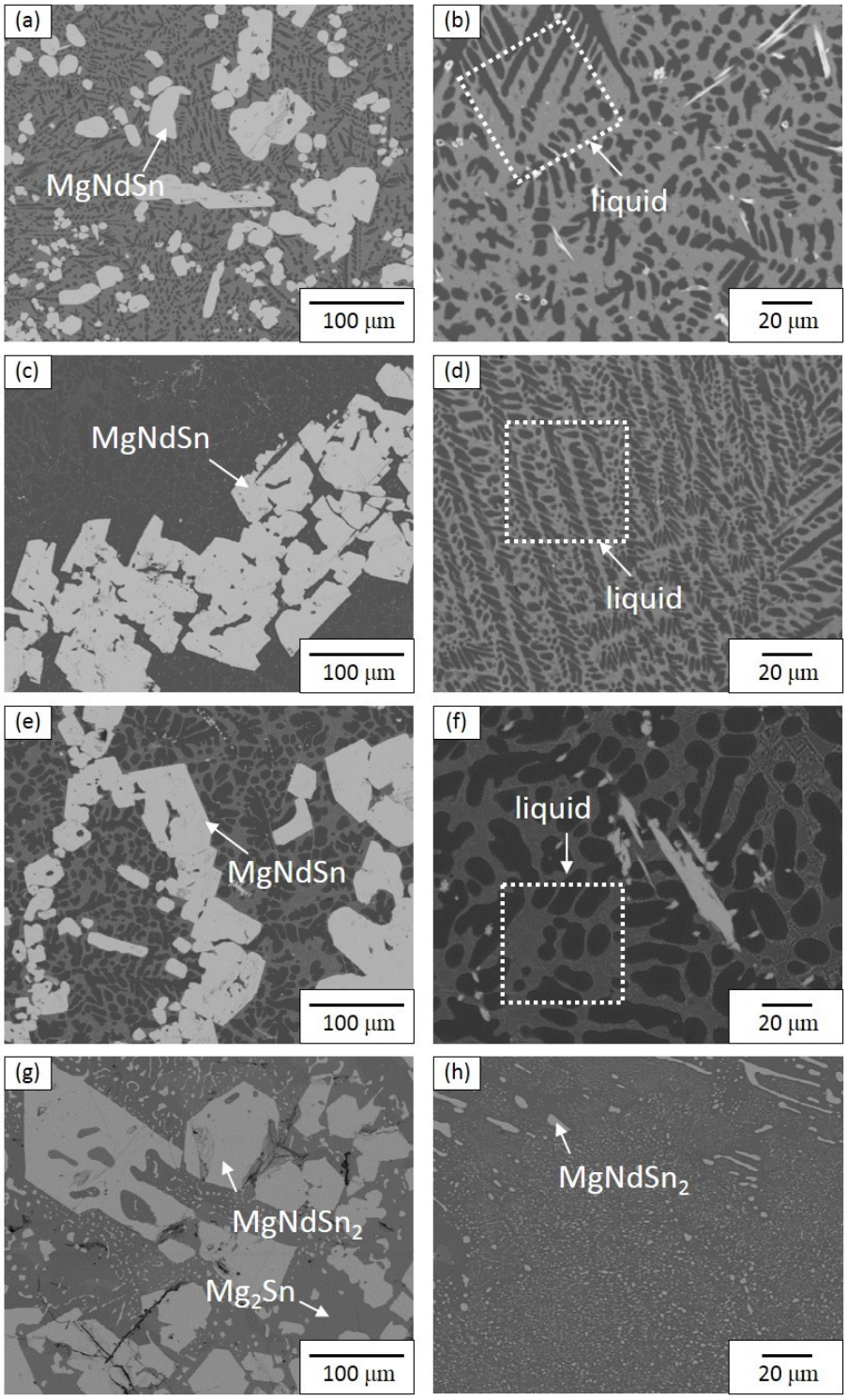


Fig. 27. The BSE images of annealed alloys at 700 ºC: (a) and (b) Alloy1, (c) and (d) Alloy2, (e) and (f) Alloy3, (g) and (h) Alloy4.

Table 5. Compositions of the constituent phases in the annealed alloys at 700 ºC.

		Mg	Sn	Nd
		wt. % / mol %	wt. % / mol %	wt. % / mol %
Alloy 1	Overall	71.20 / 93.43	4.22 / 1.13	24.58 / 5.44
	MgNdSn	8.87 / 34.50	40.89 / 32.57	50.24 / 32.93
	liquid	76.36 / 95.03	0.36 / 0.09	23.28 / 4.88
Alloy 2	Overall	91.23 / 98.22	4.71 / 1.04	4.06 / 0.74
	MgNdSn	8.90 / 34.58	40.95 / 32.58	50.15 / 32.84
	liquid	93.49 / 98.70	3.67 / 0.79	2.84 / 0.51
Alloy 3	Overall	72.35 / 92.90	24.12 / 6.34	3.53 / 0.76
	MgNdSn	8.24 / 32.72	40.89 / 33.24	50.87 / 34.04
	liquid	74.74 / 93.58	24.07 / 6.17	1.19 / 0.25
Alloy 4	Overall	22.46 / 59.19	66.73 / 36.01	10.81 / 4.80
	$MgNdSn_2$	6.36 / 26.22	58.44 / 49.33	35.20 / 24.45
	Mg_2Sn	27.56 / 65.07	71.36 / 34.50	1.08 / 0.43

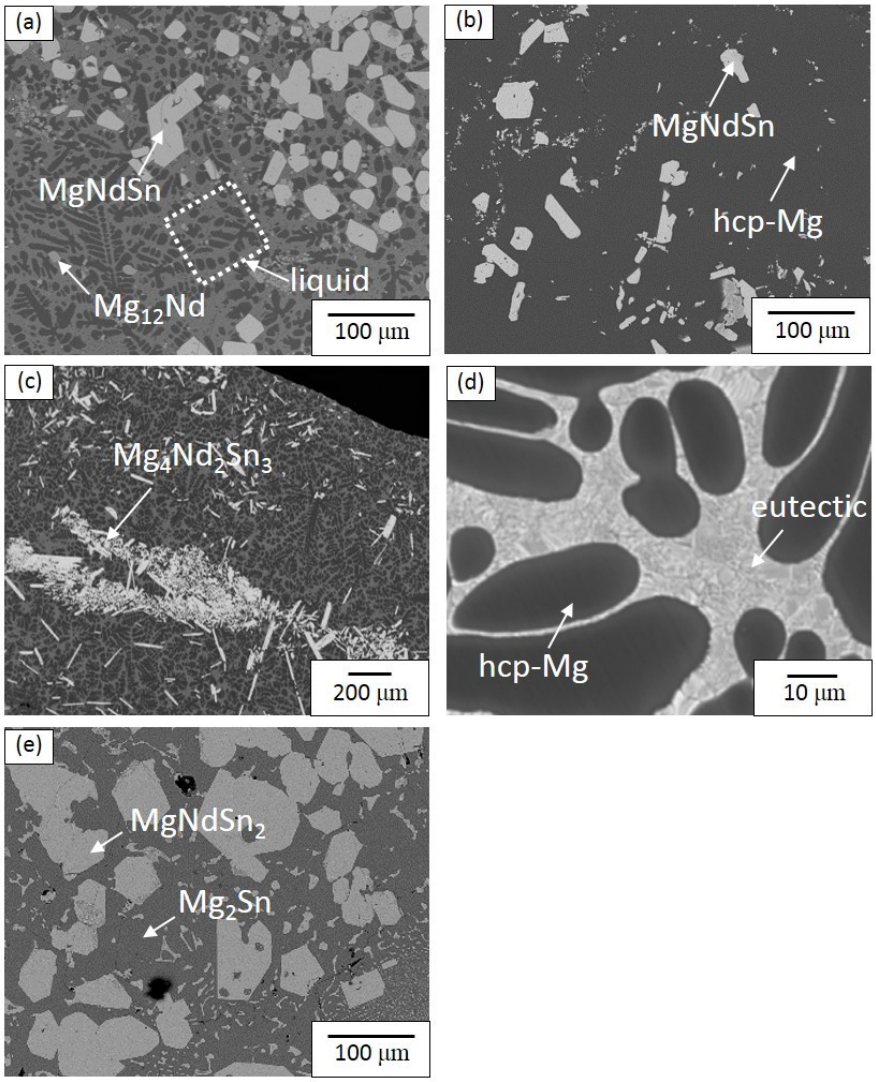


Fig. 28. The BSE images of annealed alloys at 600 °C: (a) Alloy1, (b) Alloy2, (c) and (d) Alloy3, and (e) Alloy4.

Table 6. Compositions of the constituent phases in the annealed alloys at 600 ºC.

		Mg	Sn	Nd
		wt. % / mol %	wt. % / mol %	wt. % / mol %
Alloy 1	Overall	71.91 / 93.66	3.78 / 1.01	24.31 / 5.33
	MgNdSn	8.36 / 33.06	41.00 / 33.20	50.64 / 33.74
	liquid	78.26 / 95.52	0.22 / 0.05	21.52 / 4.43
	$Mg_{12}Nd$(metastable)	67.36 / 92.45	0.11 / 0.03	32.53 / 7.52
Alloy 2	Overall	89.28 / 97.77	6.40 / 1.43	4.32 / 0.80
	MgNdSn	8.76 / 34.21	40.73 / 32.56	50.51 / 33.23
	hcp-Mg	96.67 / 99.30	3.30 / 0.69	0.03 / 0.01
Alloy 3	Overall	72.25 / 92.88	23.86 / 6.28	3.90 / 0.84
	$Mg_4Nd_2Sn_3$	13.57 / 45.43	47.97 / 32.88	38.45 / 21.69
	hcp-Mg	90.27 / 97.84	9.72 / 2.16	0.02 / 0.00
	eutectic	61.24 / 88.55	38.33 / 11.35	0.43 / 0.10
Alloy 4	Overall	22.14 / 58.77	66.59 / 36.19	11.27 / 5.04
	$MgNdSn_2$	6.14 / 25.51	58.41 / 49.68	35.45 / 24.81
	Mg_2Sn	29.22 / 66.85	70.71 / 33.12	0.07 / 0.03

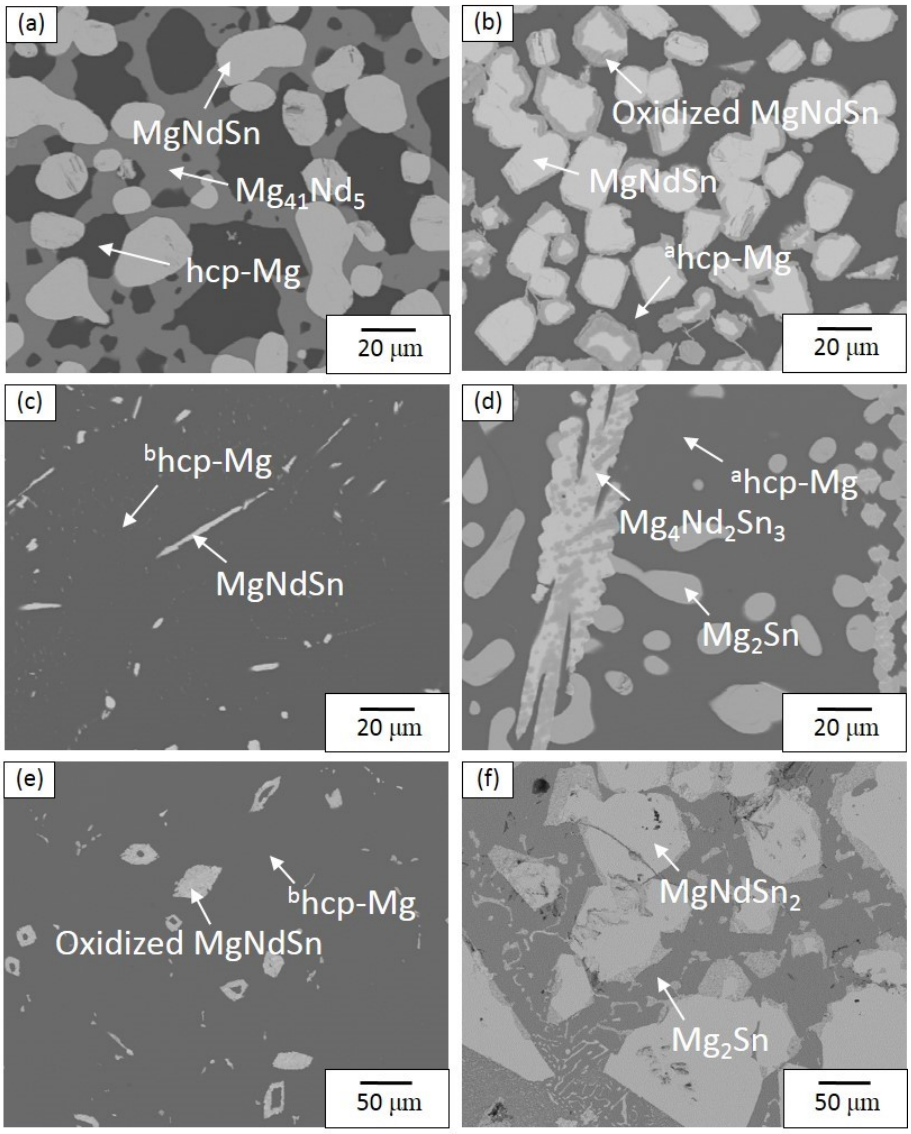


Fig. 29. The BSE images of annealed alloys at 500 ºC: (a) Alloy1, (b) and (c) Alloy2, (d) and (e) Alloy3, and (f) Alloy4.

Table 7. Compositions of the constituent phases in the annealed alloys at 500 ºC.

		Mg wt. % / mol %	Sn wt. % / mol %	Nd wt. % / mol %
Alloy 1	Overall	70.75 / 93.26	5.14 / 1.39	24.11 / 5.35
	MgNdSn	8.77 / 34.22	40.95 / 32.72	50.28 / 33.06
	$Mg_{41}Nd_5$	57.83 / 89.06	0.04 / 0.01	42.13 / 10.93
	hcp-Mg	97.04 / 99.49	0.02 / 0.00	2.94 / 0.51
Alloy 2	Overall	87.62 / 97.42	6.40 / 1.46	5.98 / 1.12
	[a]hcp-Mg	97.81 / 99.55	2.14 / 0.44	0.05 / 0.01
	[b]hcp-Mg	99.39 / 99.90	0.07 / 0.01	0.54 / 0.09
	MgNdSn	8.88 / 34.54	40.74 / 32.44	50.38 / 33.02
Alloy 3	Overall	80.30 / 95.31	17.38 / 4.22	2.32 / 0.47
	[a]hcp-Mg	89.02 / 97.54	10.97 / 2.46	0.01 / 0.00
	$Mg_4Nd_2Sn_3$	13.55 / 45.38	47.99 / 32.91	38.46 / 21.71
	Mg_2Sn	29.78 / 67.44	70.19 / 32.55	0.03 / 0.01
	[b]hcp-Mg	92.49 / 98.37	7.49 / 1.63	0.02 / 0.00
	MgNdSn	8.83 / 34.38	41.06 / 32.74	50.11 / 32.88
Alloy 4	Overall	22.48 / 59.18	67.50 / 36.38	10.02 / 4.44
	$MgNdSn_2$	6.29 / 26.00	58.31 / 49.35	35.40 / 24.65
	Mg_2Sn	29.76 / 67.42	70.20 / 32.56	0.04 / 0.02

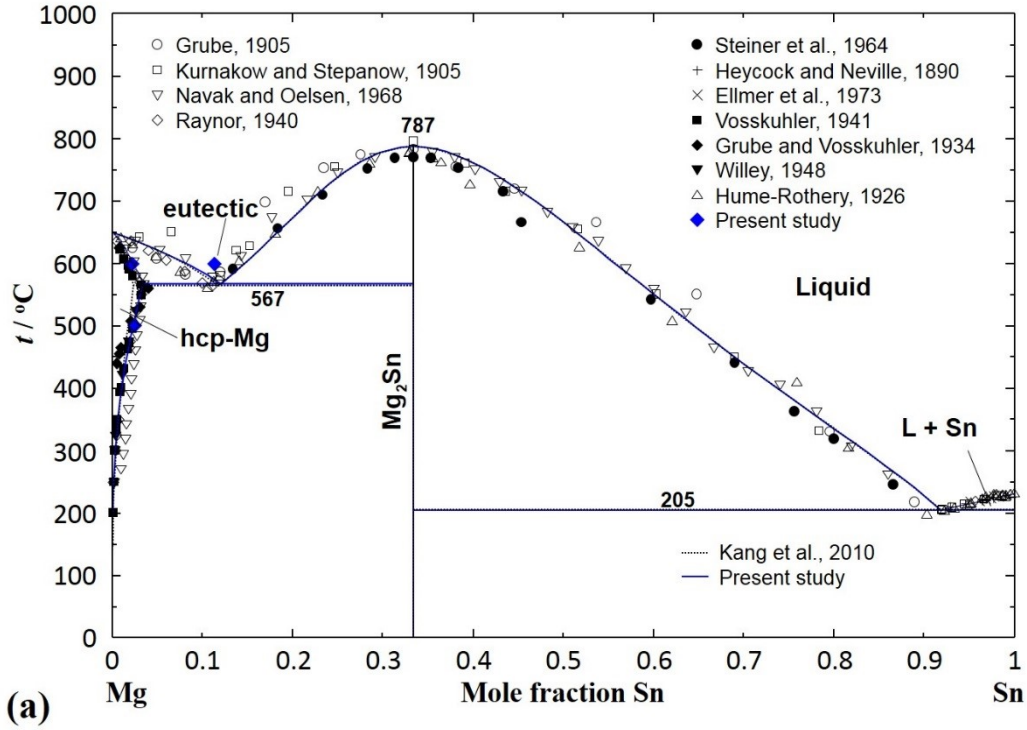
Based on the present experimental data, the ternary Mg-Sn-Nd system was thermodynamically optimized by merging the optimized binary systems and the additions of three ternary compounds, MgNdSn, $MgNdSn_2$, and $Mg_4Nd_2Sn_3$. Three constituent binary systems, Mg-Nd system [17] (Fig. 7), Mg-Sn [21] (Fig. 30), and Sn-Nd (Appendix VI) (Fig. 31) were combined by using asymmetric approximation with Mg as the asymmetric component (ΔH_{mix}: -10.2 kJ mol^{-1} (min) for Mg-Nd, -12.8 kJ mol^{-1} (min) for Mg-Sn, and -62.5 kJ mol^{-1} (min) for Sn-Nd at 2000 K).

First, the solubility of Sn in hcp-Mg in the binary Mg-Sn system was adjusted from the optimization of Kang et al. [21] based on the present experimental solubility data at 500 and 600 °C. Re-optimized Mg-Sn phase diagram is presented in Fig. 30 along with the previous diagram and experimental data. Now, the calculated solvus line is consistent with many experimental data set as seen in Fig. 30(b). The modified Gibbs energy parameters for the hcp-Mg phase are presented in Table 8. The rest of parameters are remained unchanged.

Table 8. Modified Gibbs energy parameters for the hcp-Mg in the binary Mg-Sn system and the thermodynamic properties of the ternary compounds in the Mg-Sn-Nd system (J mol^{-1} or J $K^{-1}mol^{-1}$).

Phase	Thermodynamic parameters
hcp-Mg	${}^1L_{Mg,Sn}$ = -48116 [21]
	${}^0L_{Mg,Sn}$ = -28451.2 – 23.012 T, ${}^1L_{Mg,Sn}$ = 16736.0 – 20.92 T [This work]
MgNdSn	ΔH^{O}_{298} = -206250.0, S^{O}_{298} = 133.94
	$C_p = C_p$ (Mg, hcp) + C_p (Nd, dhcp) + C_p (Sn, bct)*
$MgNdSn_2$	ΔH^{O}_{298} = -237000.0, S^{O}_{298} = 206.12
	$C_p = C_p$ (Mg, hcp) + C_p (Nd, dhcp) + 2 × C_p (Sn, bct)*
$Mg_4Nd_2Sn_3$	ΔH^{O}_{298} = -450000.0, S^{O}_{298} = 426.40
	$C_p = 4 \times C_p$ (Mg, hcp) + 2 × C_p (Nd, dhcp) + 3 × C_p (Sn, bct)*

*The modified heat capacity of Sn (in Appendix VI).



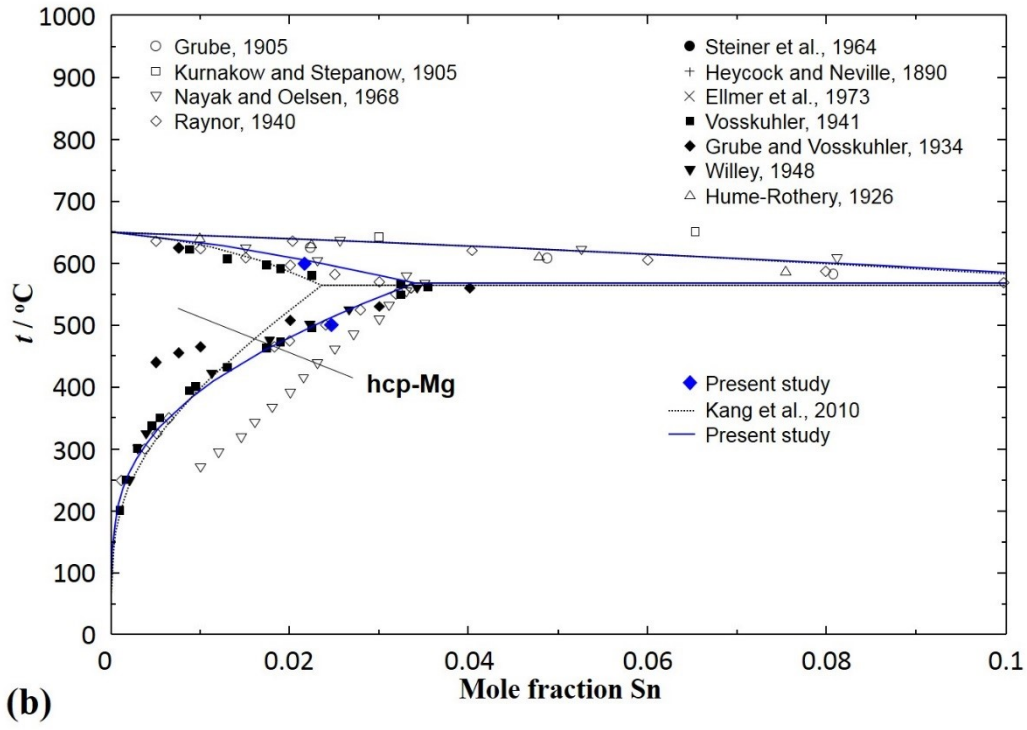


Fig. 30. (a) Re-optimized phase diagram of Mg-Sn system along with the previously optimized phase diagram and the experimental data, (b) Mg-rich side.

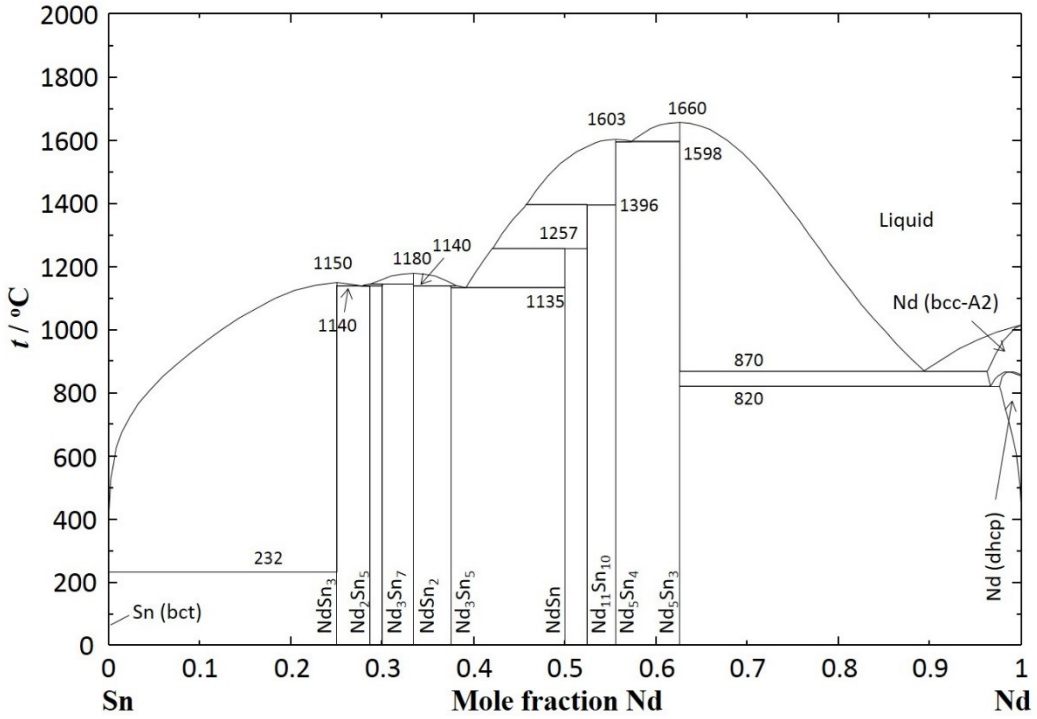


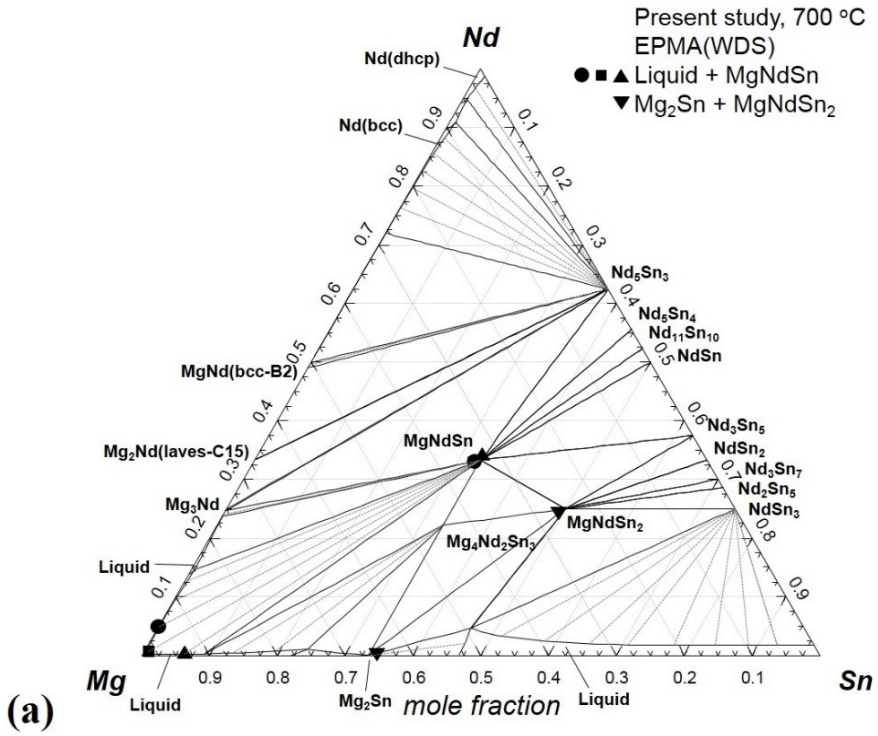
Fig. 31. Optimized phase diagram of the Sn-Nd system (Appendix VI).

For the ternary compounds, in fact, the existence of stable MgNdSn phase was previously known from the microstructure of Mg-Zn-Mn-Sn-Nd alloy [22, 23] and it was also reported that the MgNdSn phase is a high temperature phase which can enhance the age hardening response of the heat-treated alloys. In other study [9], the crystal structure of MgNdSn (CeScSi type, *tI* 12) with lattice parameters were determined by XRD, and the melting temperature of the phase was determined to be 1190 ºC (congruent) by DTA. However, the $MgNdSn_2$ and $Mg_4Nd_2Sn_3$ compounds were first discovered in the present study. No information is available for those compounds.

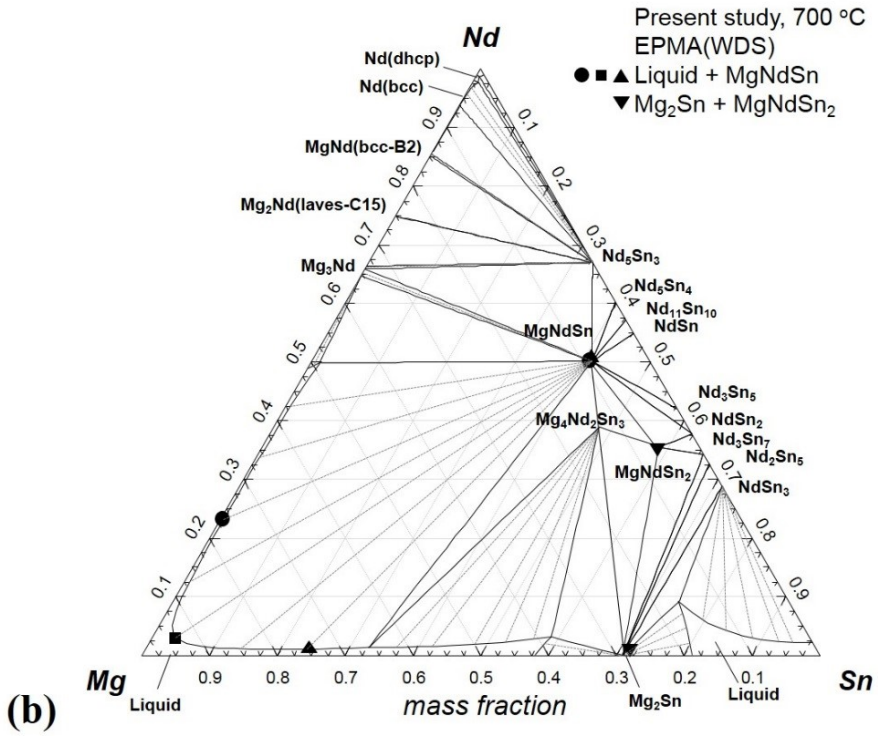
As no thermodynamic properties for all ternary compounds are known, they were estimated in the present optimization. First, the heat capacities of all compounds were estimated by NK approximation. The modified heat capacity of Sn was used (Appendix VI). Then, the ΔH°_{298} and S°_{298} of MgNdSn phase were estimated to reproduce the liquid composition for the alloys 1 to 3 at

700 ºC (see in Fig. 32) and the congruent melting temperature of the MgNdSn (1190 ºC, [9]). For the $MgNdSn_2$ phase, the ΔH^{o}_{298} was adjusted by assuming that the phase is stable down to room temperature, with keeping the S^{o}_{298} which was estimated by NK approximation. The ΔH^{o}_{298} and S^{o}_{298} of $Mg_4Nd_2Sn_3$ phase were specifically evaluated with certain criteria. At 600 ºC (Fig. 33), the stability of $Mg_4Nd_2Sn_3$ phase should be high enough to make the three phase region along with hcp-Mg and liquid phase (in the alloy 3). Otherwise, the hcp-Mg only equilibrate with the MgNdSn phase. But, it should be low enough to satisfy the equilibrium phases (Liquid + MgNdSn) for the alloy 3 at 700 ºC. In addition, at 500 ºC, the hcp-Mg with higher Mg content (grey triangle in Fig. 34) should equilibrate with MgNdSn, whereas the hcp-Mg with less Mg content (black triangle in Fig. 34) should equilibrate with $Mg_4Nd_2Sn_3$ and Mg_2Sn. The estimated thermodynamic properties of all the ternary compounds are presented in Table 8.

The optimized isothermal sections from 700 to 500 ºC are in good agreement with the present experimental data as seen in Figs. 32-34. No additional ternary parameter for the liquid phase was adopted. The calculated liquidus projection is presented in Fig. 35. The congruent melting temperature of MgNdSn, 1193.61 ºC is consistent with the experimental data (1190 ºC, [9]), and the $MgNdSn_2$ melts congruently at 1060 ºC. On the other hand, the $Mg_4Nd_2Sn_3$ peritectically melts at 1108 ºC and decompose by the eutectoid reaction at 488.9 ºC. It would be superior to investigate the vertical sections of the phase diagram, but a few trials of DSC measurements were failed due to the significant evaporation of Mg unfortunately. The decrease of the TG signal was significant and the DSC curves became ambiguous and untrustworthy.



(a)



(b)

Fig. 32. Calculated isothermal section of the Mg-Sn-Nd system at 700 °C with the present experimental data: (a) mole fraction and (b) mass fraction.

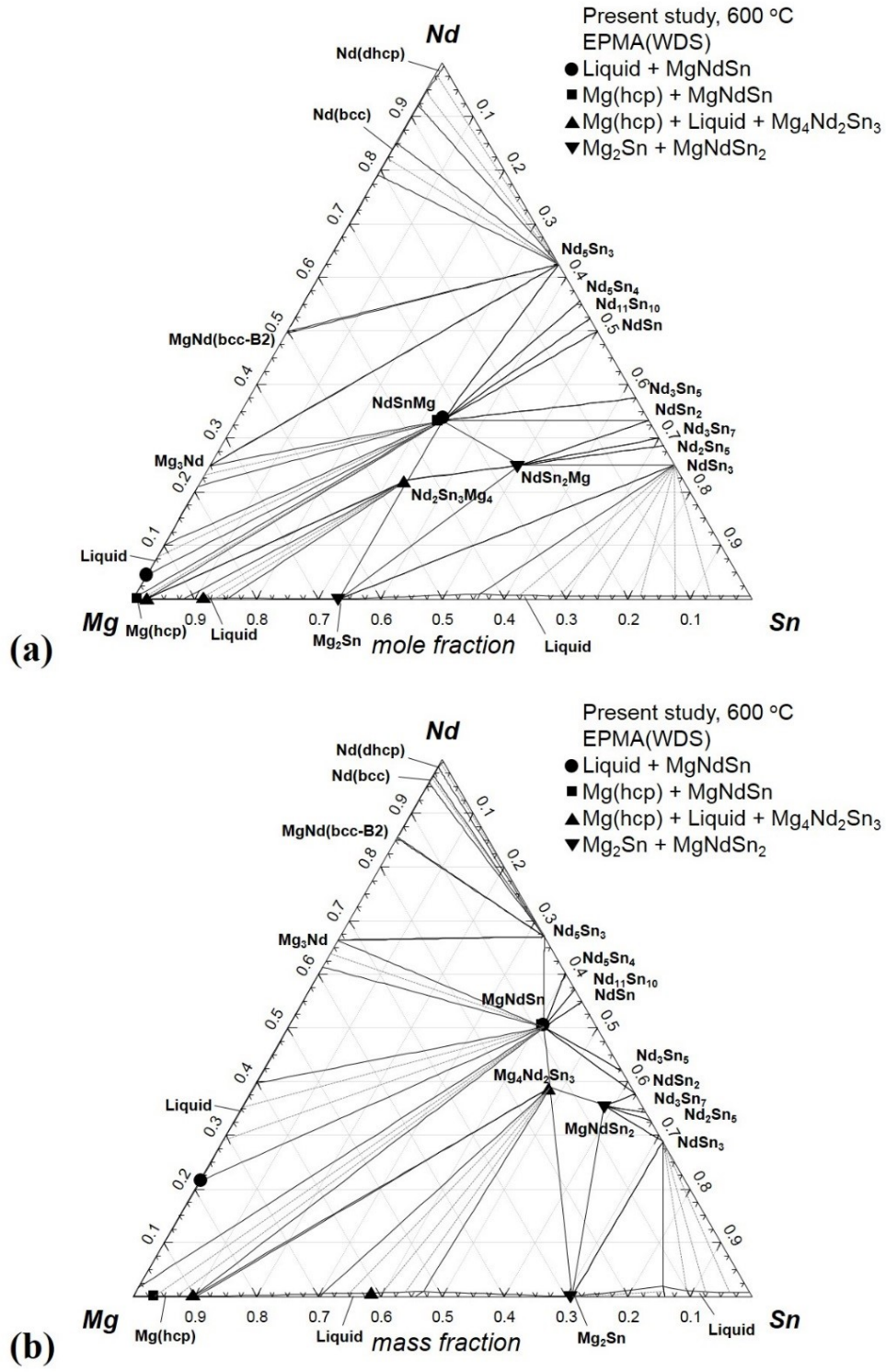


Fig. 33. Calculated isothermal section of the Mg-Sn-Nd system at 600 ºC with the present experimental data: (a) mole fraction and (b) mass fraction.

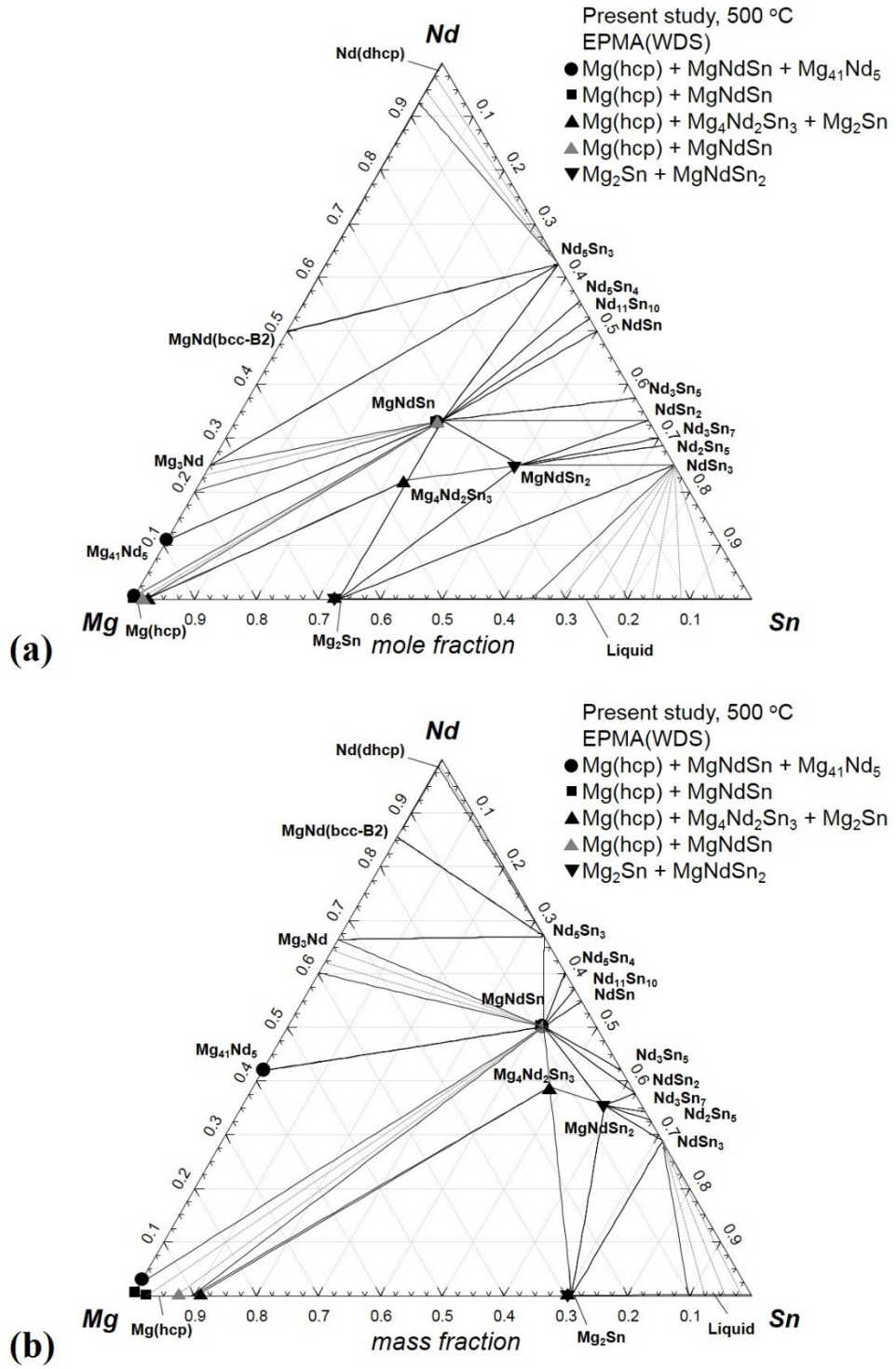


Fig. 34. Calculated isothermal section of the Mg-Sn-Nd system at 500 ºC with the present experimental data: (a) mole fraction and (b) mass fraction.

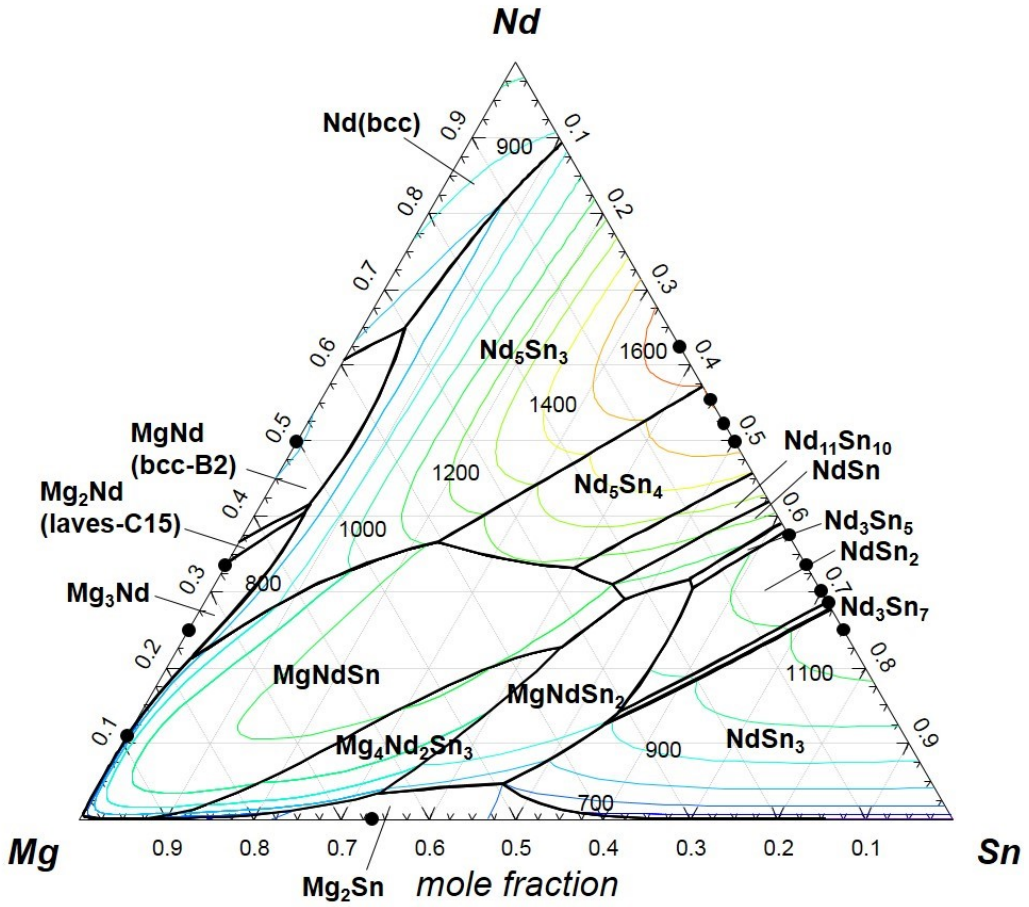


Fig. 35. Calculated liquidus projection of the Mg-Sn-Nd system.

4.2. The Mg-Sn-Gd system

The BSE images of the annealed alloys at 700 ºC are shown in Fig. 36. The compositions of the annealed alloys and the constituent phases are presented in Table 9. Similar to the Mg-Sn-Nd system, the alloys 1 to 3 consisted of two phases, MgGdSn and liquid. Two solid phases, $MgGdSn_2$ and Mg_2Sn were found in the alloy 4.

The BSE images of the annealed alloys at 600 ºC are shown in Fig. 37. The compositions of the annealed alloys and the constituent phases are presented in Table 10. Considering much bigger size of the dendrite of hcp-Mg compared to the hcp-Mg at 700 ºC, it was believed that the alloy 1 consisted of three phases, liquid, MgGdSn and hcp-Mg. As it was unable to find the composition of the liquid phase, the composition of eutectic phase in the quenched microstructure was only identified. In the microstructure of the alloy 2, two solid phase, MgGdSn and hcp-Mg were present. For the alloy 3, the $Mg_4Gd_2Sn_3$ (4:2:3) compound was not found unlike the Mg-Sn-Nd system. Instead, the MgGdSn was equilibrated with hcp-Mg and liquid phase. The composition of the eutectic phase was determined instead of the liquid. The microstructure of the alloy 4 contained the $MgGdSn_2$ and Mg_2Sn.

The BSE images of the annealed alloys at 500 ºC are shown in Fig. 38. The compositions of the annealed alloys and the constituent phases are presented in Table 11. Like the Mg-Sn-Nd system, the inhomogeneous distribution of the ternary compound, MgGdSn made the local equilibrium with different compositions of the hcp-Mg phases in the alloys 1 and 2. On the other hand, the alloy 3 consisted of the MgGdSn, Mg_2Sn and hcp-Mg. The hcp-Mg phase was approximately homogeneous in the alloy 3. The microstructure of the alloy 4 was about the same as the alloy 4 annealed at 600 and 700 ºC.

Prior to the present study, Guo [10] performed the isothermal phase diagram investigation at 300, 400, 500 ºC for the Mg-Sn-Gd system. Five alloys were prepared and annealed at 300 ºC for 3000 h, 400 ºC for 1000 h, and 500 ºC for 500 h. The alloys were examined by XRD, SEM equipped with EDS. The results were in good agreement with the present data in terms of the constituent

phases in the alloys although the compositions of the phases were slightly different. The experimental data are presented in Figs 42 to 44

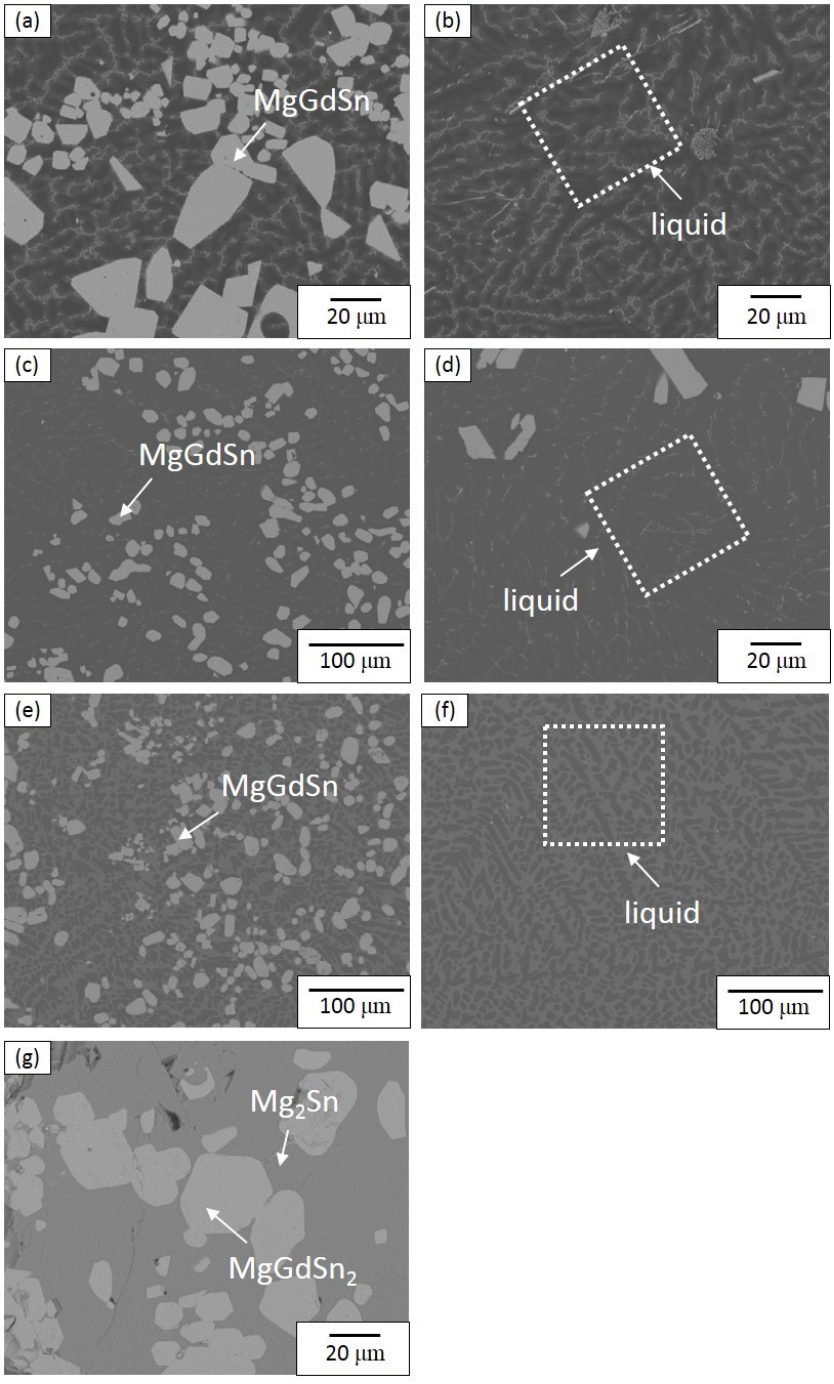


Fig. 36. The BSE images of annealed alloys at 700 ºC: (a) and (b) Alloy1, (c) and (d) Alloy2, (e) and (f) Alloy3, and (g) Alloy4.

Table 9. Compositions of the constituent phases in the annealed alloys at 700 ºC.

		Mg	Sn	Gd
		wt. % / mol %	wt. % / mol %	wt. % / mol %
Alloy 1	Overall	67.67 / 92.65	7.30 / 2.05	25.03 / 5.30
	MgGdSn	8.76 / 35.33	38.53 / 31.81	52.71 / 32.86
	liquid	78.92 / 96.02	0.30 / 0.07	20.78 / 3.91
Alloy 2	Overall	90.72 / 98.15	5.41 / 1.20	3.87 / 0.65
	MgGdSn	8.83 / 35.51	38.68 / 31.85	52.50 / 32.64
	liquid	95.22 / 99.04	3.70 / 0.79	1.08 / 0.17
Alloy 3	Overall	72.05 / 92.81	25.22 / 6.65	2.73 / 0.54
	MgGdSn	8.79 / 35.41	38.65 / 31.87	52.56 / 32.72
	liquid	72.96 / 92.98	26.43 / 6.90	0.61 / 0.12
Alloy 4	Overall	22.46 / 59.43	66.73 / 36.15	10.81 / 4.42
	$MgGdSn_2$	6.37 / 26.92	56.14 / 48.59	37.48 / 24.49
	Mg_2Sn	27.56 / 65.10	71.36 / 34.51	1.08 / 0.39

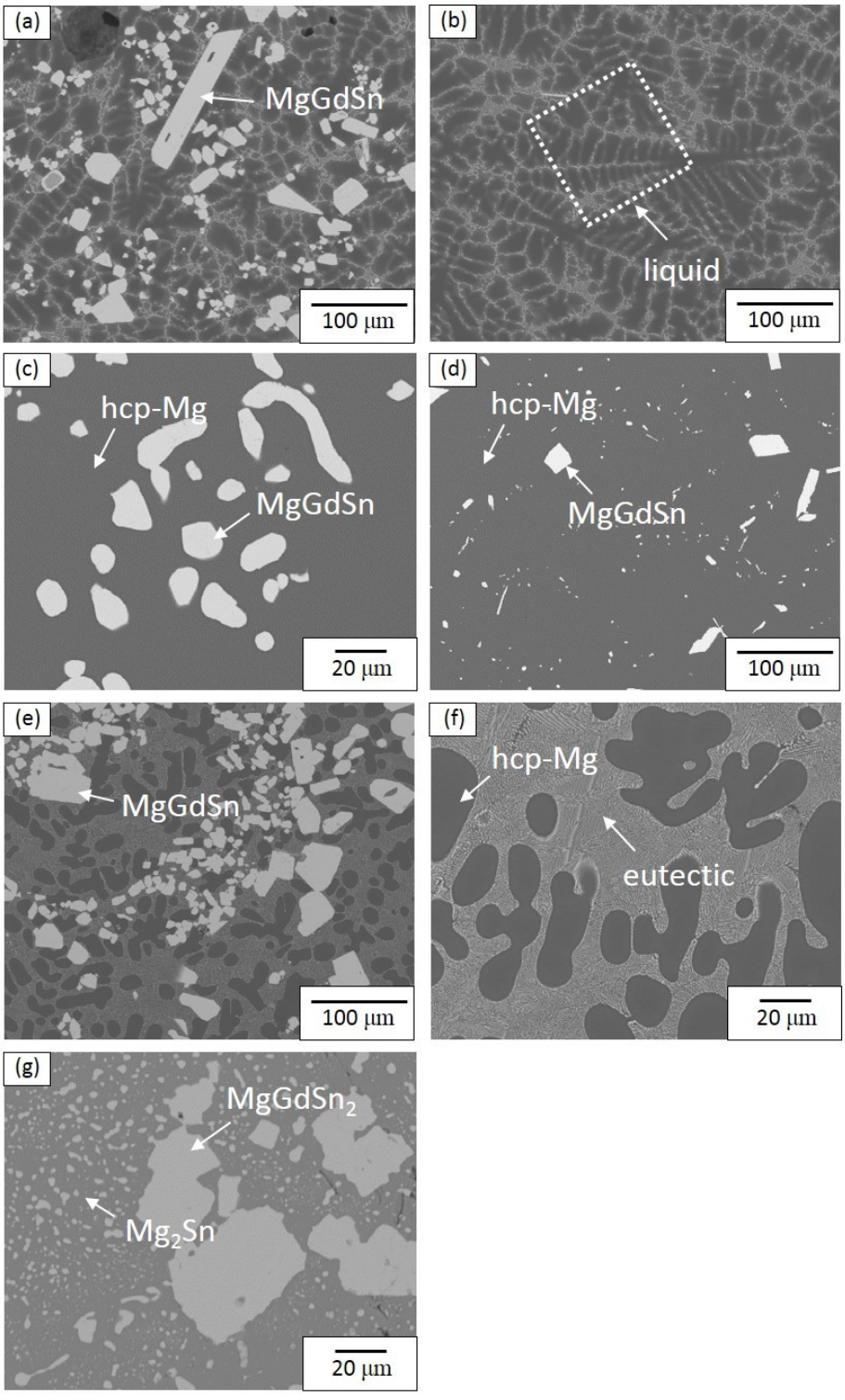


Fig. 37. The BSE images of annealed alloys at 600 °C: (a) and (b) Alloy1, (c) and (d) Alloy2, (e) and (f) Alloy3, and (g) Alloy4.

Table 10. Compositions of the constituent phases in the annealed alloys at 600 ºC.

		Mg	Sn	Gd
		wt. % / mol %	wt. % / mol %	wt. % / mol %
Alloy 1	Overall	78.11 / 95.81	0.69 / 0.17	21.20 / 4.02
	MgGdSn	8.72 / 35.21	38.60 / 31.91	52.68 / 32.88
	hcp-Mg	89.86 / 98.29	0.02 / 0.00	10.12 / 1.71
	eutectic	60.96 / 90.98	0.12 / 0.04	38.92 / 8.98
Alloy 2	Overall	90.97 / 98.17	5.96 / 1.32	3.07 / 0.51
	MgGdSn	8.89 / 35.68	38.78 / 31.86	52.33 / 32.46
	hcp-Mg	94.85 / 98.90	5.10 / 1.09	0.05 / 0.01
Alloy 3	Overall	67.26 / 91.25	27.65 / 7.68	5.09 / 1.07
	MgGdSn	8.89 / 35.67	38.87 / 31.93	52.24 / 32.40
	hcp-Mg	86.24 / 96.84	13.73 / 3.16	0.03 / 0.00
	eutectic	62.45 / 89.06	37.25 / 10.88	0.30 / 0.06
Alloy 4	Overall	26.90 / 64.63	68.21 / 33.55	4.89 / 1.82
	$MgGdSn_2$	6.37 / 26.92	56.26 / 48.67	37.37 / 24.41
	Mg_2Sn	29.47 / 67.13	70.35 / 32.81	0.17 / 0.06

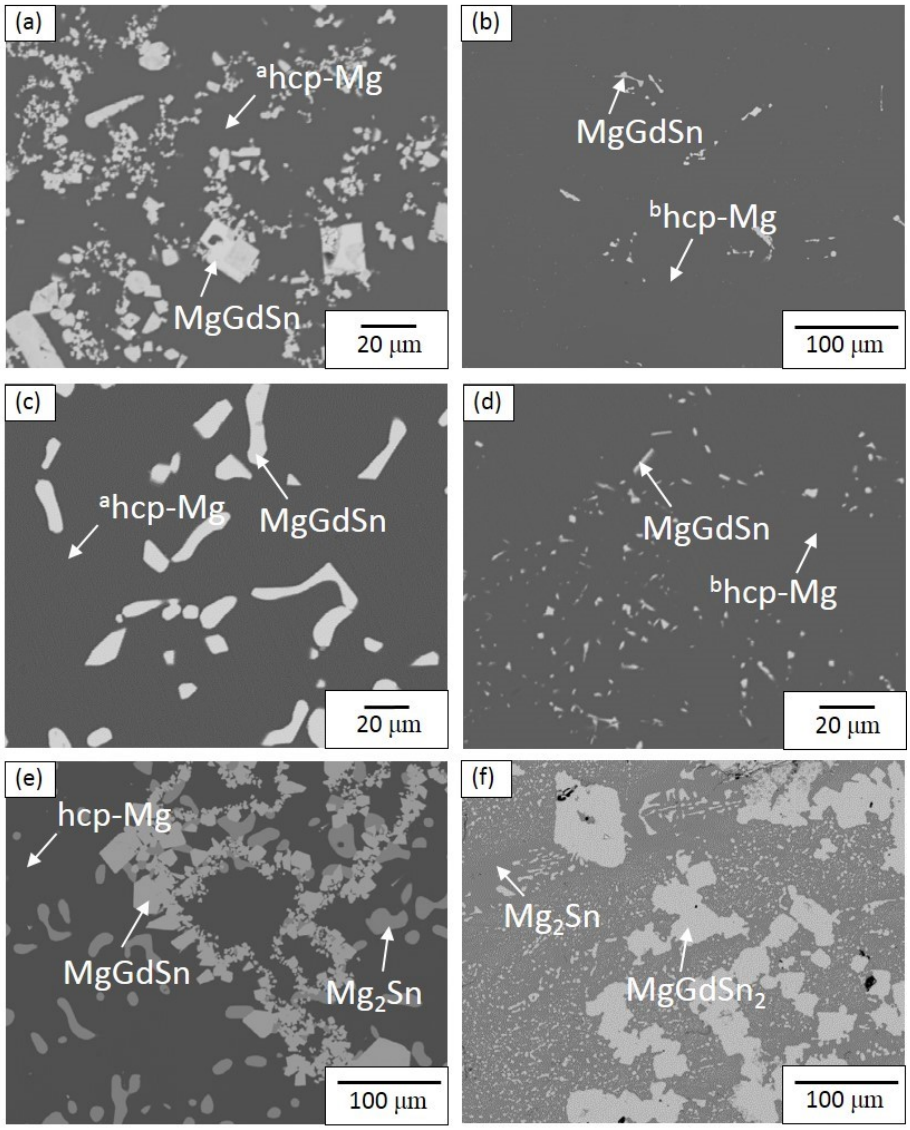


Fig. 38. The BSE images of annealed alloys at 500 ºC: (a) and (b) Alloy1, (c) and (d) Alloy2, (e) Alloy3, and (f) Alloy4.

Table 11. Compositions of the constituent phases in the annealed alloys at 500 ºC.

		Mg	Sn	Gd
		wt. % / mol %	wt. % / mol %	wt. % / mol %
Alloy 1	Overall	81.65 / 96.57	1.18 / 0.29	17.17 / 3.14
	[a]hcp-Mg	83.99 / 97.14	0.05 / 0.01	15.96 / 2.85
	[b]hcp-Mg	86.97 / 97.74	0.00 / 0.00	13.03 / 2.26
	MgGdSn	8.69 / 35.13	38.52 / 31.88	52.79 / 32.99
Alloy 2	Overall	91.52 / 98.32	5.01 / 1.10	3.47 / 0.58
	[a]hcp-Mg	91.58 / 98.16	8.28 / 1.82	0.14 / 0.02
	[b]hcp-Mg	95.74 / 99.10	4.22 / 0.89	0.04 / 0.01
	[c]hcp-Mg	99.60 / 99.92	0.34 / 0.07	0.06 / 0.01
	[d]hcp-Mg	99.67 / 99.95	0.07 / 0.01	0.26 / 0.04
	MgGdSn	8.80 / 35.42	38.77 / 31.96	52.43 / 32.62
Alloy 3	Overall	69.58 / 92.28	22.33 / 6.06	8.09 / 1.66
	hcp-Mg	88.73 / 97.47	11.24 / 2.53	0.03 / 0.00
	MgGdSn	8.74 / 35.27	38.62 / 31.90	52.64 / 32.83
	Mg_2Sn	29.58 / 67.24	70.29 / 32.71	0.14 / 0.05
Alloy 4	Overall	23.16 / 60.53	64.24 / 34.38	12.60 / 5.09
	$MgGdSn_2$	6.36 / 26.88	56.39 / 48.79	37.25 / 24.33
	Mg_2Sn	29.54 / 67.20	70.34 / 32.76	0.12 / 0.04

Based on the present experimental data and the data of Guo [10], the ternary Mg-Sn-Nd system was thermodynamically optimized by merging the optimized binary systems and the additions of two ternary compounds, MgGdSn and $MgNdSn_2$. Three constituent binary systems, Mg-Gd system [17] (Fig. 10), Mg-Sn [21] (Fig. 30), and Sn-Gd (Appendix VII) (Fig. 39) were combined by using asymmetric approximation with Mg as the asymmetric component (ΔH_{mix}: -8.3 kJ mol^{-1} (min) for Mg-Gd, -12.8 kJ mol^{-1} (min) for Mg-Sn, and -63.6 kJ mol^{-1} (min) for Sn-Gd at 2000 K).

Like the MgNdSn phase, the MgGdSn phase was previously known to form in the Mg-Sn-Gd system, it was claimed that the MgGdSn phase give a beneficial effect on the creep properties due to high thermal stability, but also the presence of the MgGdSn lead to coarsening the microstructure of the alloy by consuming the Sn, which has microstructural refining effect on Mg alloys [24, 25]. The crystal structure of MgGdSn (CeScSi type, *tI* 12) with lattice parameters were determined by XRD, and the melting temperature of the phase was determined to be 1190 ºC (congruent) by DTA [9]. The new compound, $MgGdSn_2$ was found to be formed in the system for the first time. However, no information is available for the compound.

In the present study, the thermodynamic properties for the ternary compounds, MgGdSn and $MgGdSn_2$ were estimated. The heat capacities of all compounds were estimated by NK approximation using the modified heat capacity of Sn (Appendix VI). Then, the ΔH^{o}_{298} and S^{o}_{298} of MgGdSn phase were adjusted to reproduce the liquid composition for the alloys 1 to 3 at 700 ºC (see in Fig. 40) and the congruent melting temperature of the MgGdSn (1100 ºC, [9]). However, it was unable to reproduce the congruent melting of MgGdSn. In fact, due to the strong stability of the Gd-Sn compounds (T_m of Gd_5Sn_3 = 1820 ºC), the melting behavior of the phase cannot be the congruent if the melting temperature is 1100 ºC. Therefore, the melting behavior was believed to be incongruent with the melting temperature, 1100 ºC. While keeping the melting temperature of the MgGdSn, the S^{o}_{298} was decreased (but not too low compared to the S^{o}_{298} of the MgNdSn) to increase the stability of the compound at 700 ºC to reproduce the experimental liquid

compositions at 700 ºC. However, positive ternary parameter for liquid phase was additionally required to reproduce the liquid compositions as seen in Fig. 40.

Table 12. Thermodynamic parameters for the optimization of the Mg-Gd-Sn system (J mol^{-1} or J K^{-1} mol^{-1}).

Phase	Thermodynamic parameters
Liquid	$g^{011}_{GdMg(Sn)} = 4602.4$
MgGdSn	$\Delta H^{O}_{298} = -215000.0,\ S^{O}_{298} = 118.58$ $C_p = C_p$ (Mg, hcp) + C_p (Gd, hcp) + C_p (Sn, bct)*
$MgGdSn_2$	$\Delta H^{O}_{298} = -245000.0,\ S^{O}_{298} = 205.16$ $C_p = C_p$ (Mg, hcp) + C_p (Gd, hcp) + 2 × C_p (Sn, bct)*

*The modified heat capacity of Sn (in Appendix VI).

For the $MgGdSn_2$ phase, the ΔH^{o}_{298} was estimated by assuming that the phase is stable down to room temperature, with keeping the S^{o}_{298} which was estimated by NK approximation. The ternary liquid parameter and the thermodynamic properties of all the ternary compounds are presented in Table 12. The calculated isothermal phase diagrams from 700 to 300 ºC are presented in Figs 40-44. The calculated liquidus surface of the Mg-Sn-Gd system is shown in Fig. 45. In general, the phase diagrams agreed with the present experimental data and the data of Guo [10]. However, the solubility of Gd in hcp-Mg (Alloy 1) and that of Sn in hcp-Mg (Alloy 3) at 600 and 500 ºC were slightly bigger than the optimized binary systems. In fact, the Gd solubility in hcp-Mg in the binary Mg-Gd system (in the optimized phase diagram) was not fully investigated experimentally. Therefore, it is worthwhile to consider the present experimental data with further experimental investigation to obtain the accurate solubility of Gd in hcp-Mg in future. However, for the Mg-Sn binary system, the Sn solubility in hcp-Mg was higher than that which was obtained from the Mg-Sn-Nd system. It is still unclear the reason of the difference between two alloys, but for the re-optimization of the Mg-Sn system in the present study, the experimental data for the Sn solubility in hcp-Mg from the Mg-Sn-Nd alloy were used, as it agreed with the other experimental data set

(seen in Fig. 30). At 400 and 300 ºC, among the compositions of the constituent phases determined by Guo [10], the compositions of Mg_5Gd and the Sn solubility in hcp-Mg differed from the calculated diagram. According to the optimized binary phase diagram of the Mg-Gd and Mg-Sn system, the experimental data could be considered to be less reliable. Meanwhile, the $MgGdSn_2$ phase was found to be stable up to more than 1300 ºC (seen in Fig. 45). The stability of this compound is relatively much higher than the same stoichiometric compound, $MgNdSn_2$ in the Mg-Sn-Nd system.

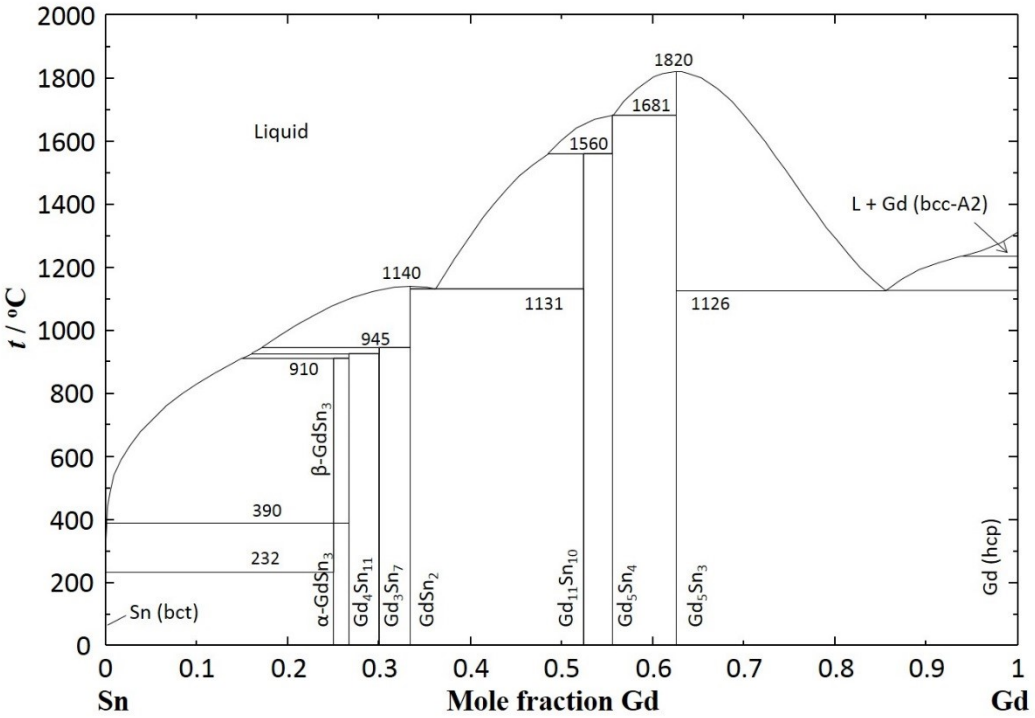


Fig. 39. Optimized phase diagram of the Sn-Gd system (Appendix VII).

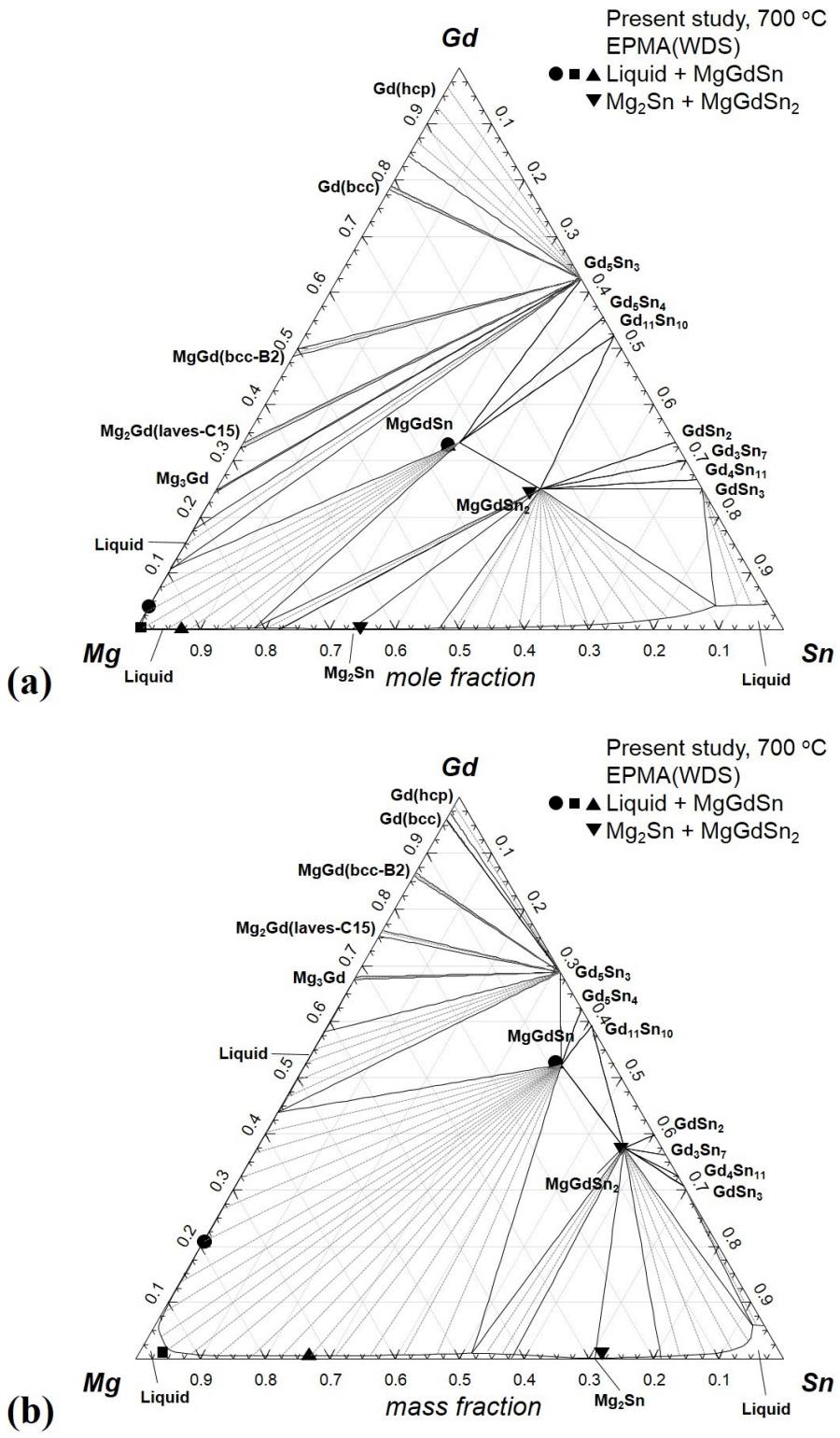


Fig. 40. Calculated isothermal section of the Mg-Sn-Gd system at 700 °C with the present experimental data: (a) mole fraction and (b) mass fraction.

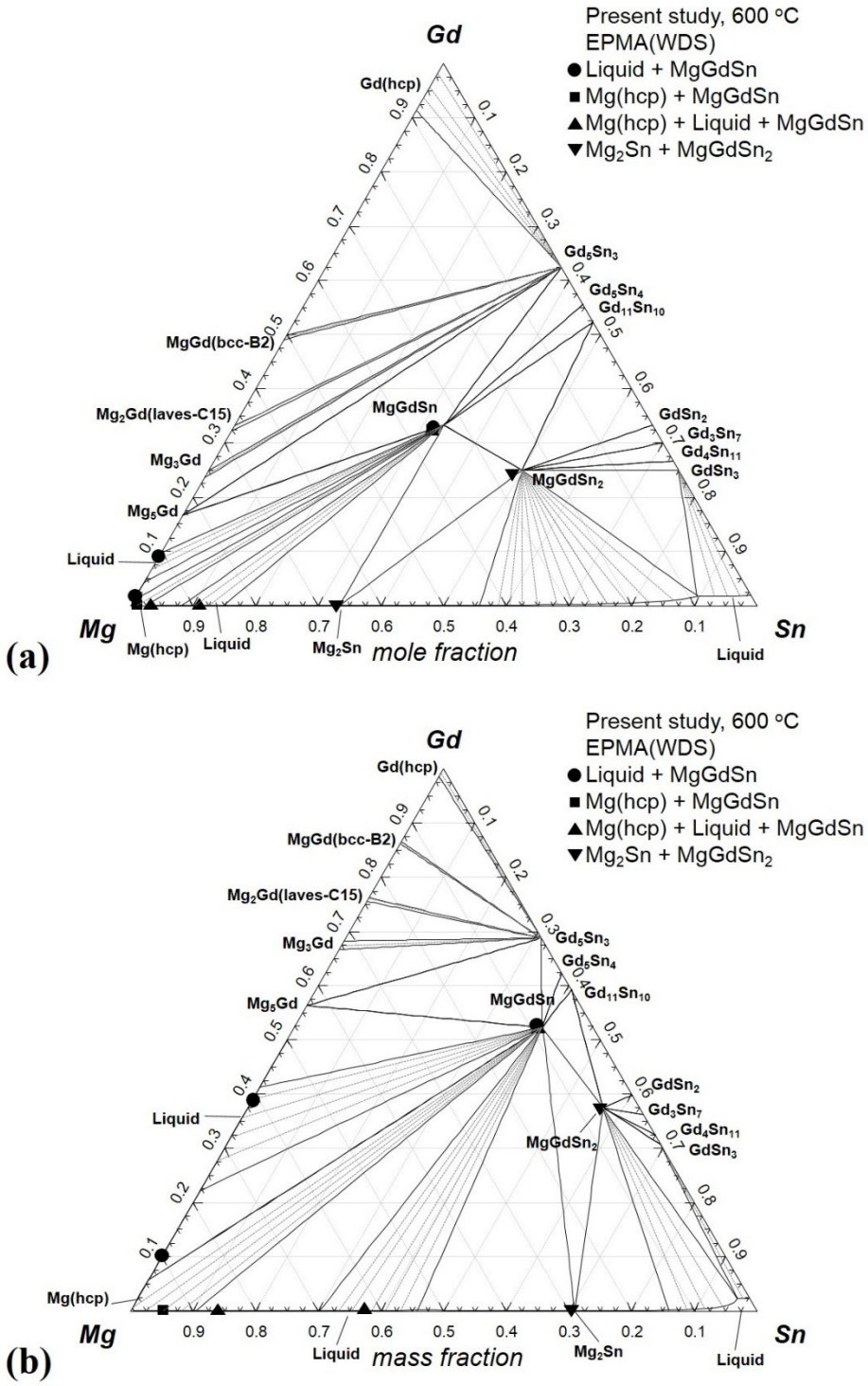


Fig. 41. Calculated isothermal section of the Mg-Sn-Gd system at 600 ºC with the present experimental data: (a) mole fraction and (b) mass fraction.

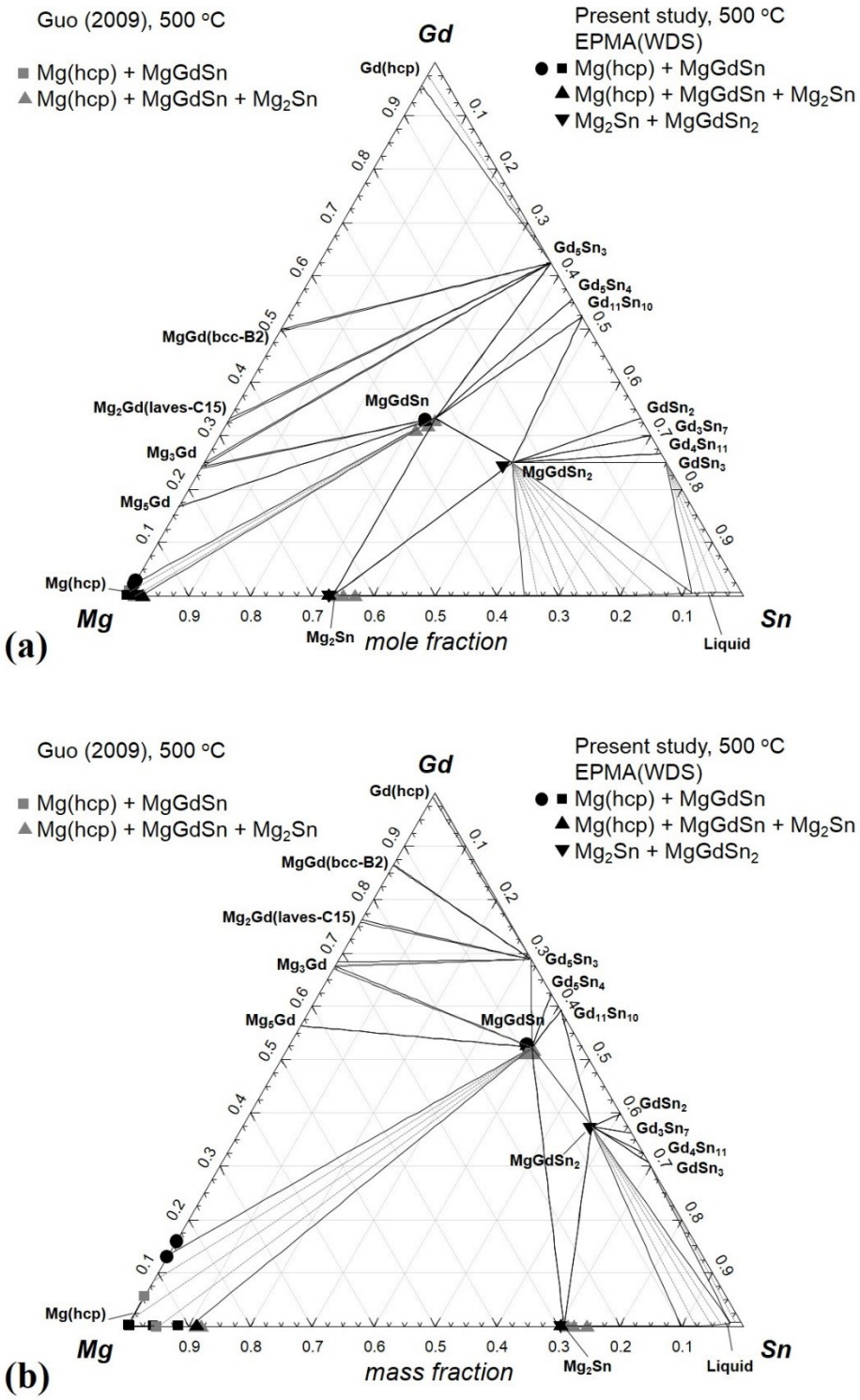


Fig. 42. Calculated isothermal section of the Mg-Sn-Gd system at 500 °C with the present experimental data and the data of Guo [10]: (a) mole fraction and (b) mass fraction.

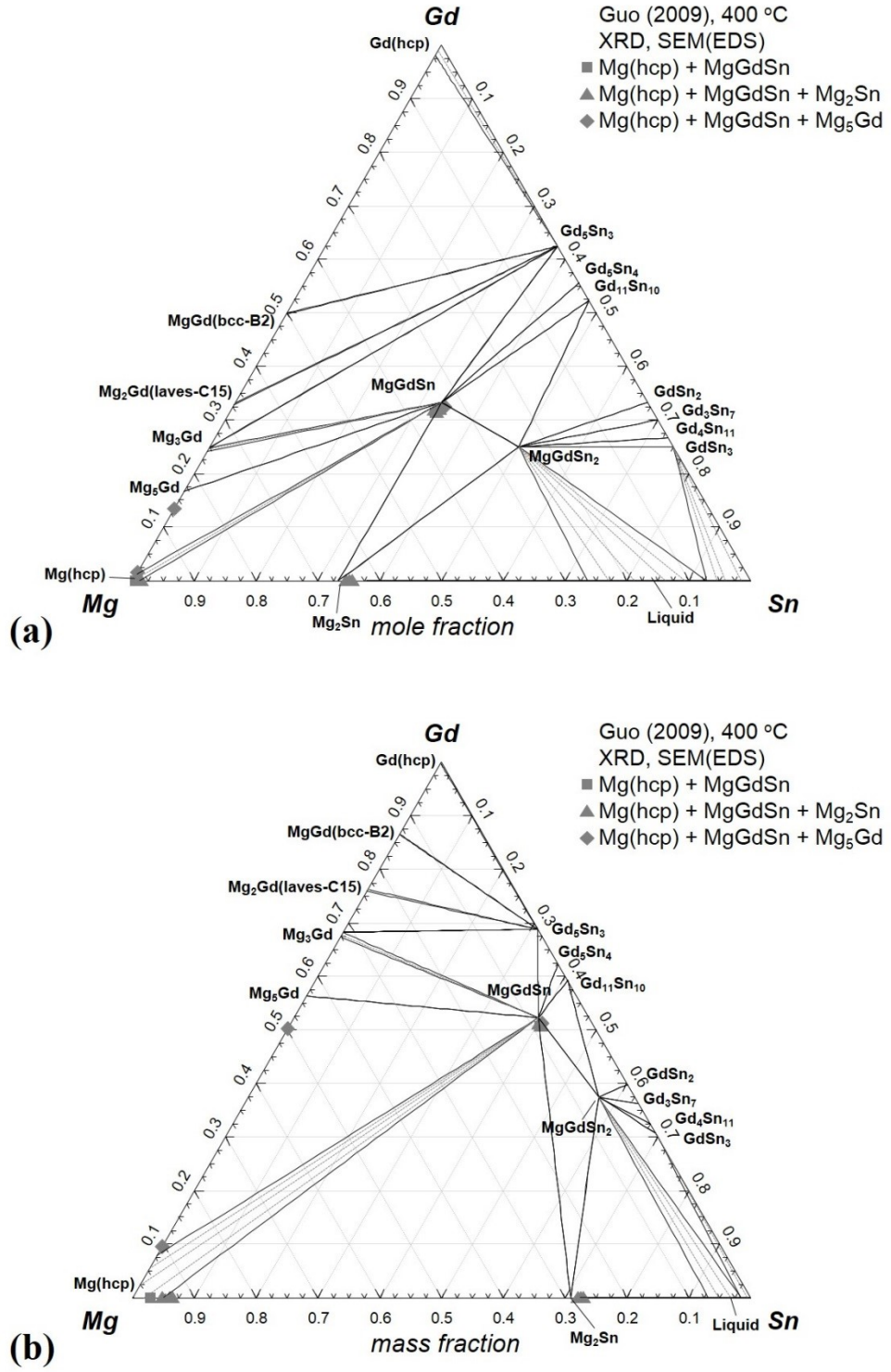


Fig. 43. Calculated isothermal section of the Mg-Sn-Gd system at 400 ºC with the experimental data of Guo [10]: (a) mole fraction and (b) mass fraction.

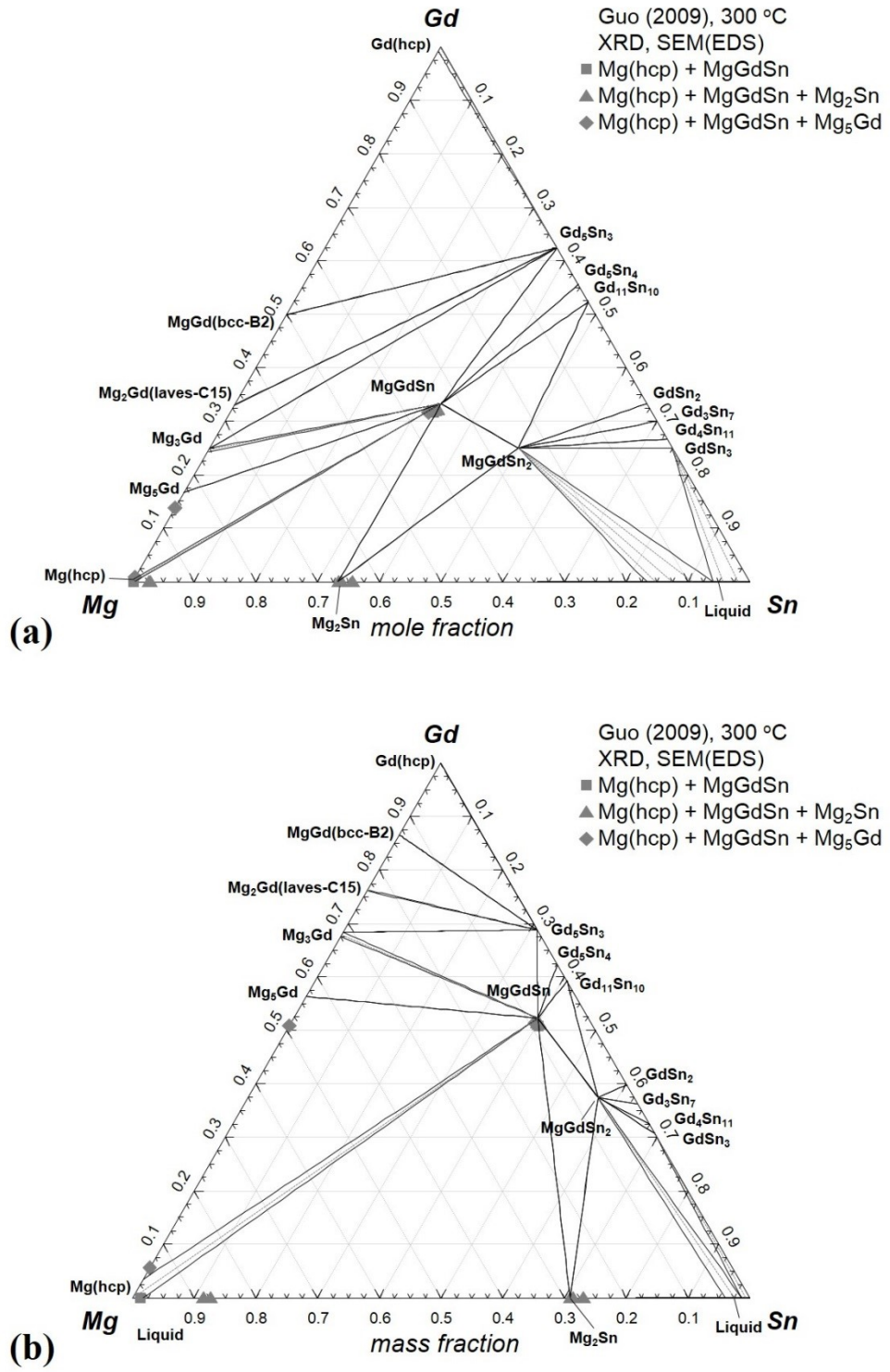


Fig. 44. Calculated isothermal section of the Mg-Sn-Gd system at 300 ºC with the experimental data of Guo [10]: (a) mole fraction and (b) mass fraction.

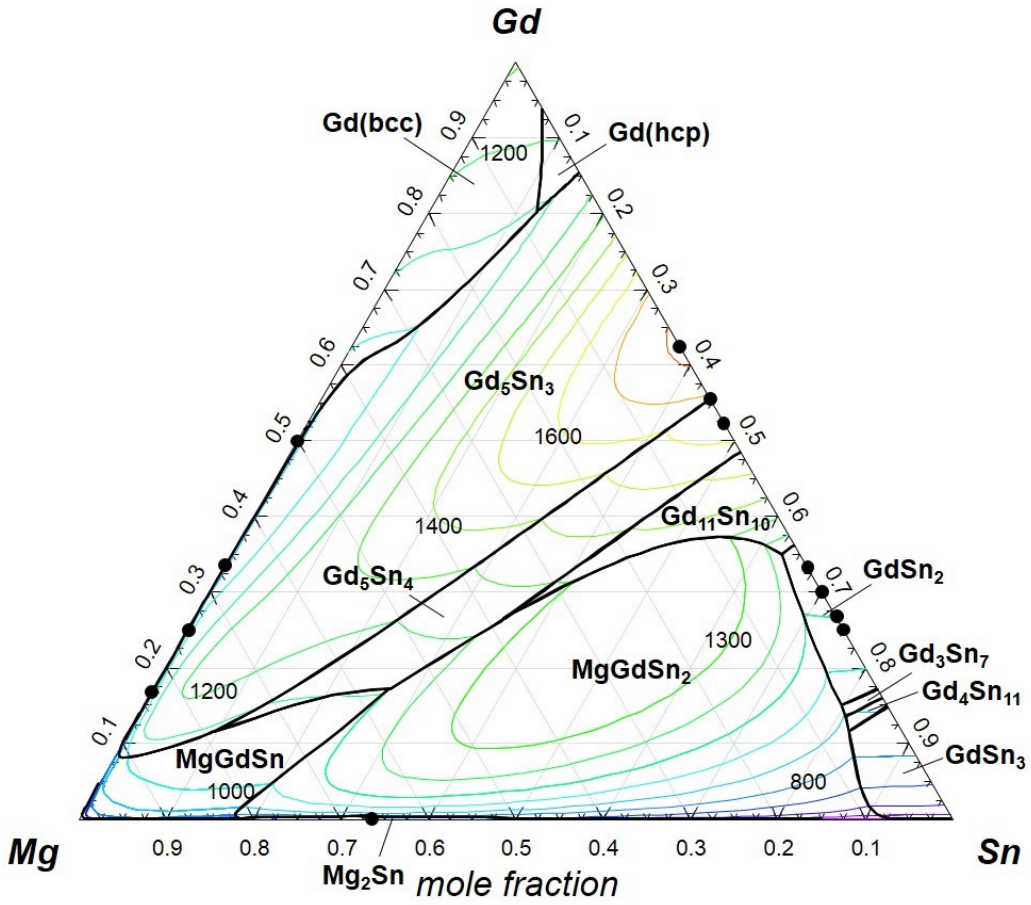


Fig. 45. Calculated liquidus projection of the Mg-Sn-Gd system.

4.3. The Mg-Sn-Er system

The phase diagram of this system was investigated by Ma et al. [11] for the isothermal sections at 500, 400 and 300 ºC. The alloys with eleven different compositions (Mg-rich only) were prepared in the induction melting furnace under argon gas from the high purity materials, 99.99 wt. % Mg, 99.99 % Sn, and Mg-30 wt.% Er. The samples were sealed into steel tube with high-purity argon atmosphere, and annealed at 300, 400, and 500 ºC for 720, 600, and 500 h, respectively. The microstructure of the quenched samples were subsequently analysed by XRD and SEM equipped with EDS. The constituent phases and the respective compositions of the phases were determined. The reported experimental data are shown in Figs 48-50. In addition, Manfrinetti et al. [9] determined the melting temperature of the ternary compound, MgErSn to be 960 ºC and, the crystal structure of MgErSn (CeScSi type, *tI* 12) with lattice parameters by using DTA and XRD, respectively. It is interesting that the hcp-Mg equilibrated with the Er-Sn compound, Er_5Sn_3 unlike the Mg-Sn-Nd and Mg-Sn-Gd systems as seen in the Figs 48-50. This fact is consistent with the lower melting temperature of the MgErSn than the MgGdSn (1100 ºC) and MgNdSn (1190 ºC). However, the congruent melting behaviour of the MgErSn reported by Manfrinetti et al. [9] is doubtful according to the phase diagram. The existence of the $MgErSn_2$ was not specifically studied in the study of Ma et al. [11].

In the present optimization, the ternary Mg-Sn-Nd system was thermodynamically optimized based on the experimental data [9, 11] by merging the optimized binary systems and the addition of MgErSn compound. Although the $MgErSn_2$ compound may be present in the system, it was assumed that the MgErSn is only ternary compound in the system. Three constituent binary systems, Mg-Er system [17] (Fig. 46), Mg-Sn [21] (Fig. 30), and Sn-Er (Appendix VII) (Fig. 47) were combined by using asymmetric approximation with Mg as the asymmetric component (ΔH_{mix}: -8.4 kJ mol^{-1} (min) for Mg-Er, -12.8 kJ mol^{-1} (min) for Mg-Sn, and -51.6 kJ mol^{-1} (min) for Sn-Er at 2000 K). The heat capacity of the MgErSn was estimated by NK approximation using the modified heat capacity of Sn (Appendix VI). Then, the ΔH^{o}_{298} and S^{o}_{298} of MgErSn phase were estimated to reproduce melting temperature [9] and the equilibrium phases in the experimental

data [11]. First, the ΔH^{o}_{298} was estimated using the NK approximated S^{o}_{298} to reproduce the peritectic melting at 960 ºC. However, by doing so, the unwanted phase equilibrium was made between hcp-Mg and Er_5Sn_4. Therefore, the S^{o}_{298} was slightly reduced not to form the equilibrium phases (hcp-Mg and Er_5Sn_4) with the same Gibbs energy at the melting temperature. The thermodynamic parameters for the MgErSn are shown in Table 13. Meanwhile, the MgErSn and the Mg_2Sn were treated as stoichiometric compounds. Although the scattered data for the compositions of those phases, which were observed from different samples, were considered the possible homogeneous range in the work of Ma et al. [11], it seems to be unlikely. In fact, the compositions of certain phases such as $Mg_{24}E_5$ and hcp-Mg (Sn solubility) were also dubious. However, the equilibrium phases in the different samples were reproduced well in the present optimization. The calculated isothermal phase diagrams at 500, 400, and 300 ºC are presented in Figs. 48-50, respectively. The calculated liquidus surface is shown in Fig. 51.

Table 13. Thermodynamic parameters for the ternary compound in the Mg-Sn-Er system (J mol^{-1} or J K^{-1} mol^{-1}).

Phase	Thermodynamic parameters
MgErSn	ΔH^{O}_{298} = -160500.0, S^{O}_{298} = 150.03 $C_p = C_p$ (Mg, hcp) + C_p (Er, hcp) + C_p (Sn, bct)*

*The modified heat capacity of Sn (in Appendix VI).

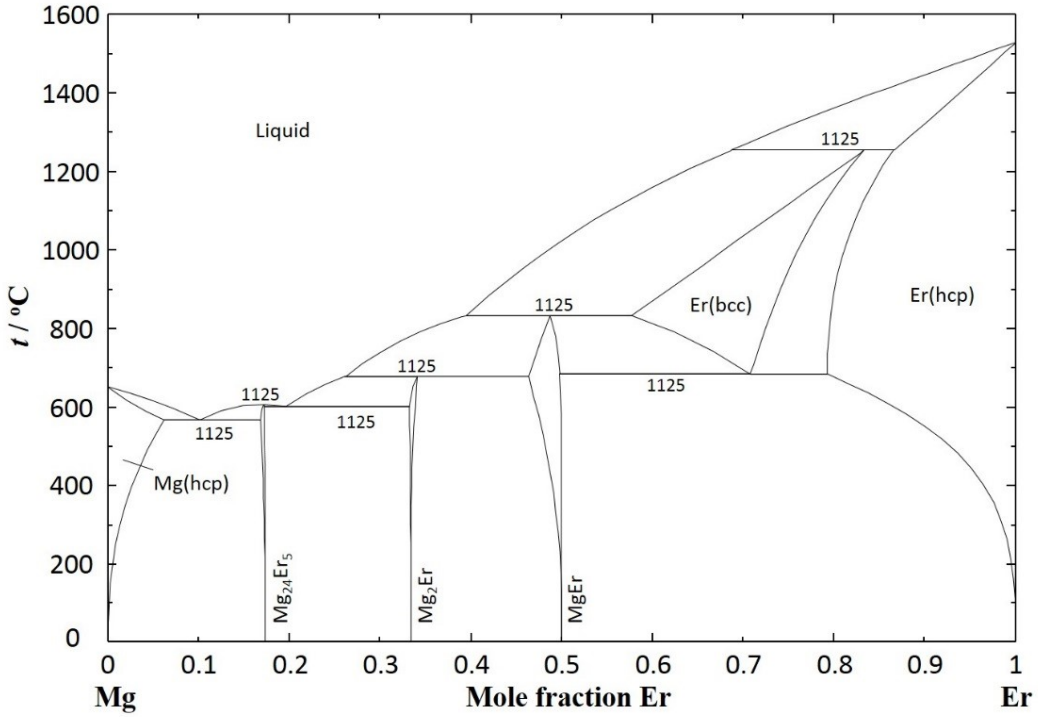


Fig. 46. Optimized phase diagram of the Mg-Er system [17].

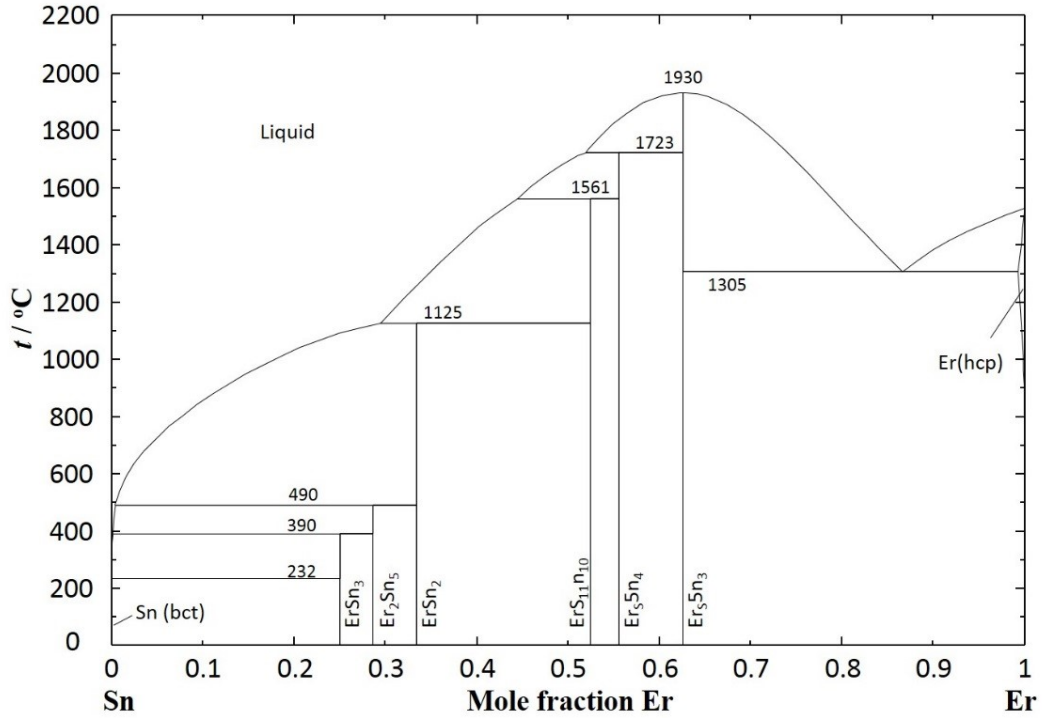


Fig. 47. Optimized phase diagram of the Sn-Er system (Appendix VII).

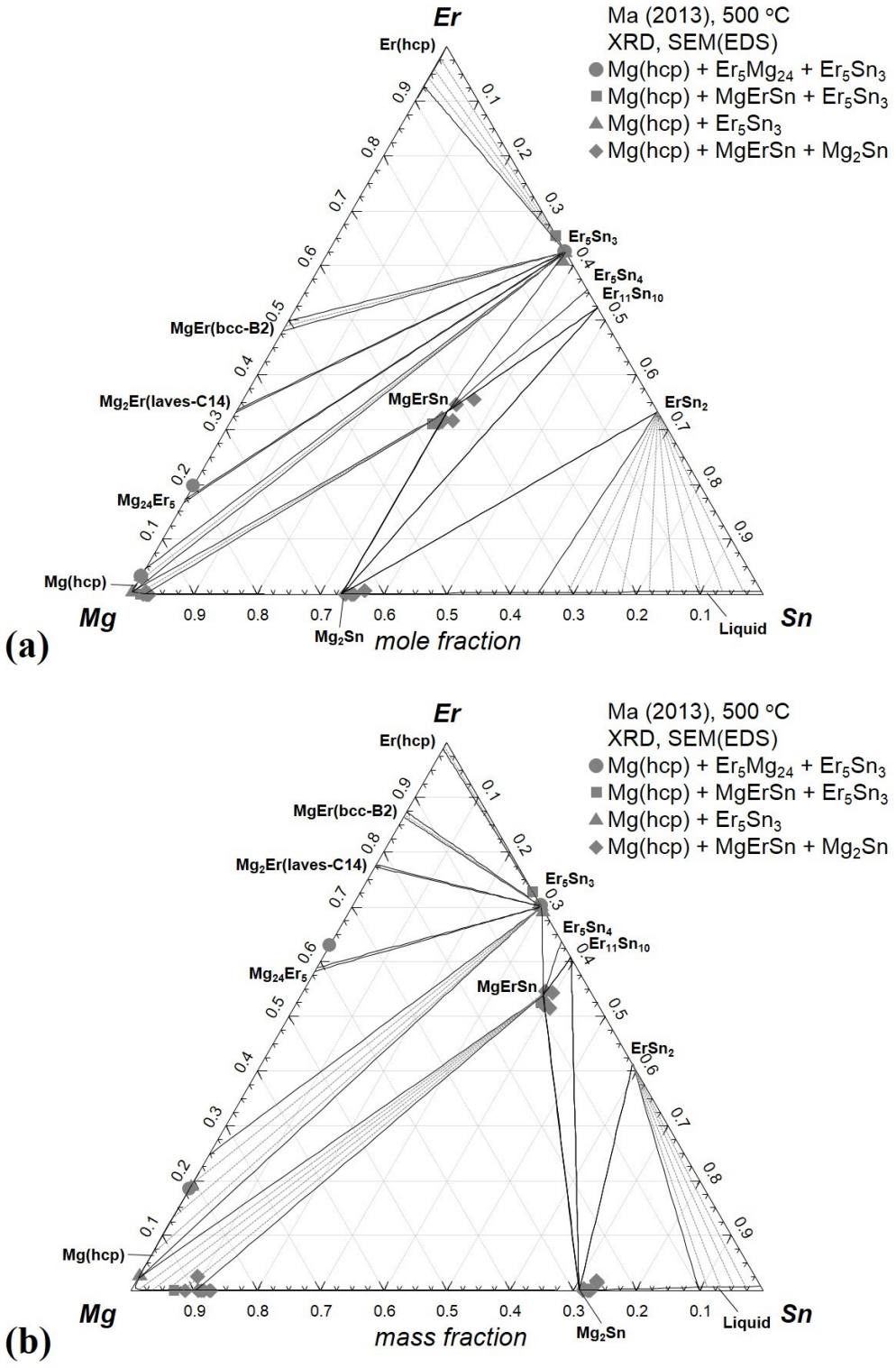


Fig. 48. Calculated isothermal section of the Mg-Sn-Er system at 500 ºC with the experimental data [11]: (a) mole fraction and (b) mass fraction.

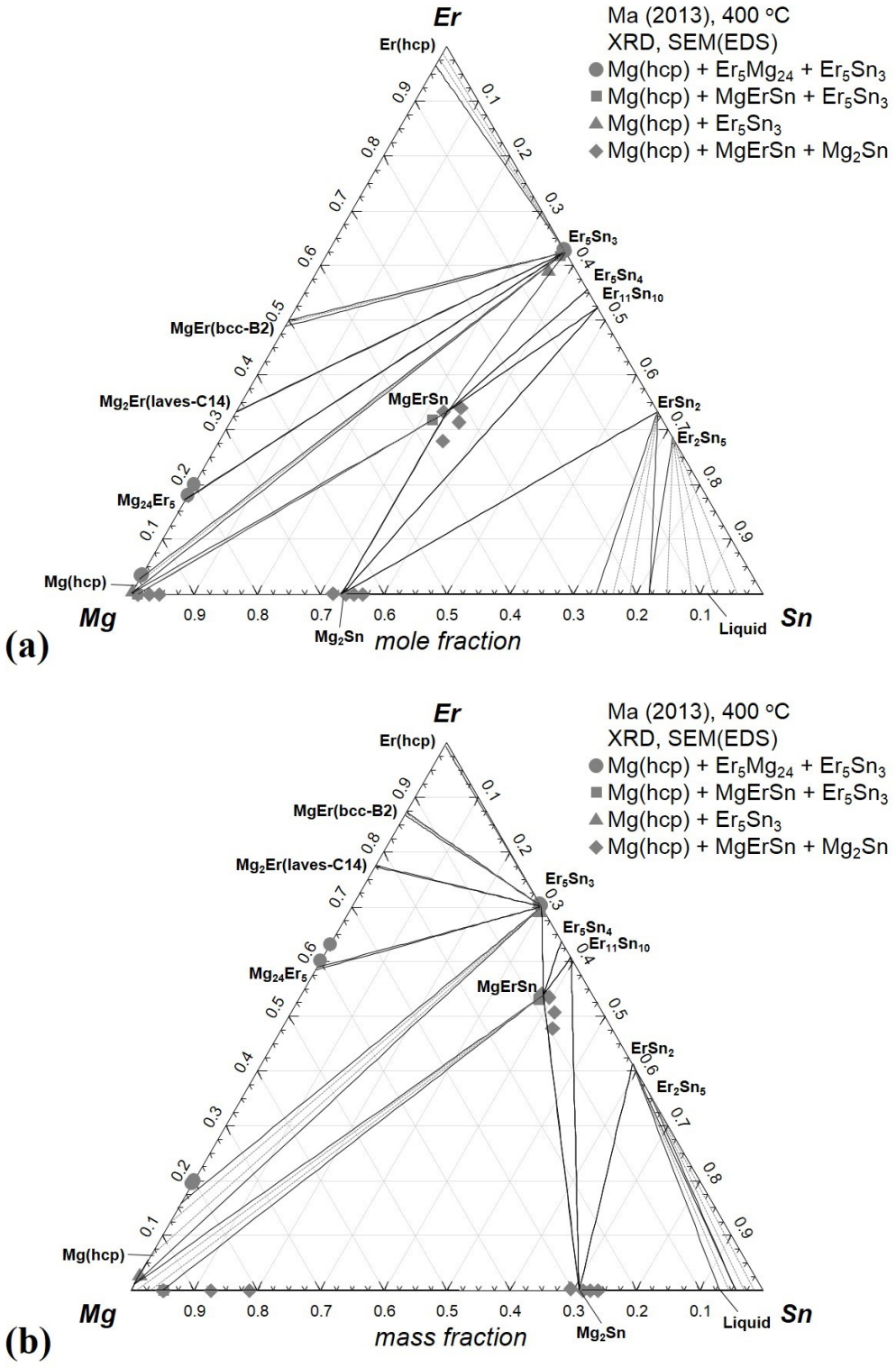


Fig. 49. Calculated isothermal section of the Mg-Sn-Er system at 400 ºC with the experimental data [11]: (a) mole fraction and (b) mass fraction.

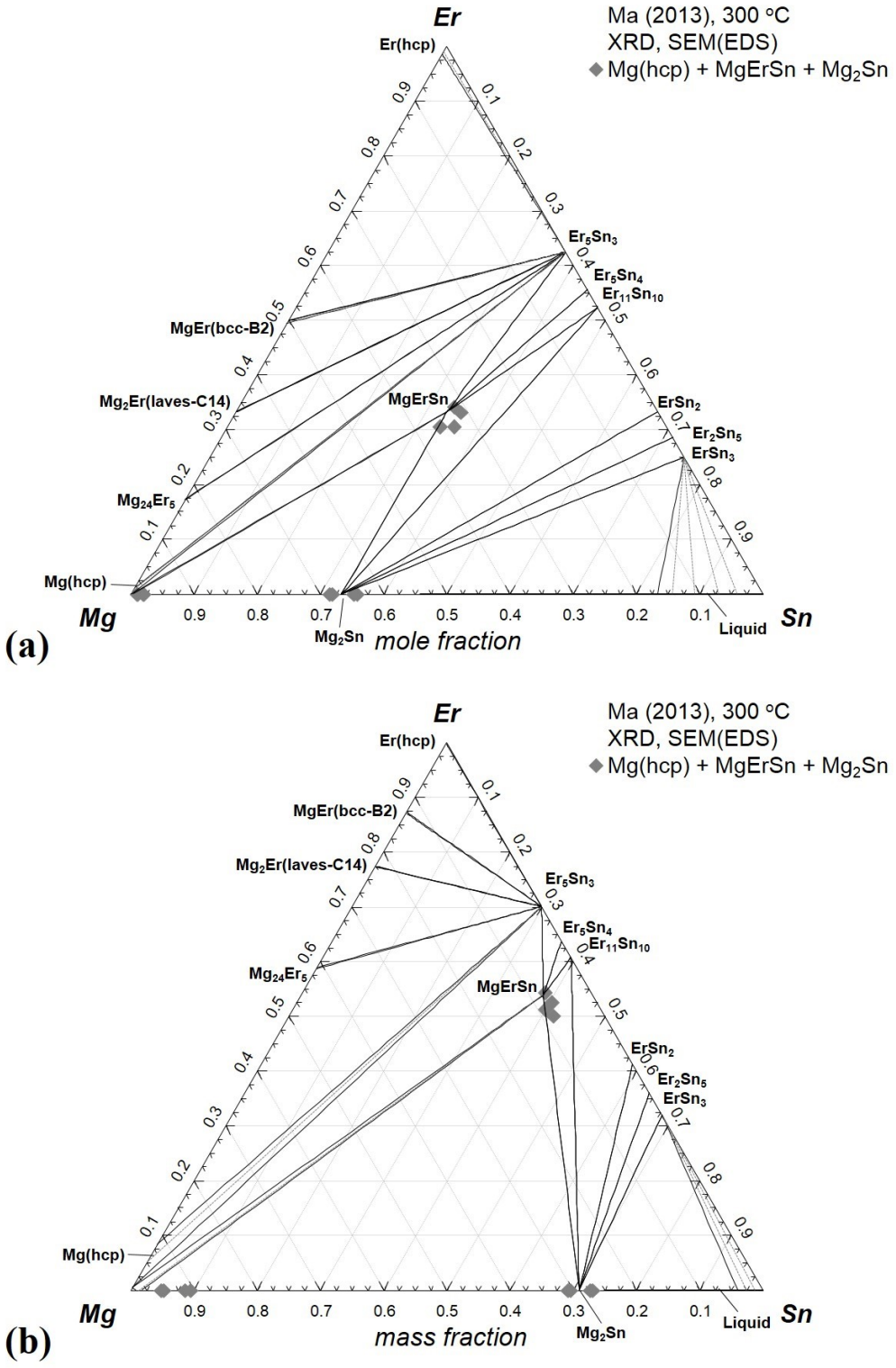


Fig. 50. Calculated isothermal section of the Mg-Sn-Er system at 300 ºC with the experimental data [11]: (a) mole fraction and (b) mass fraction.

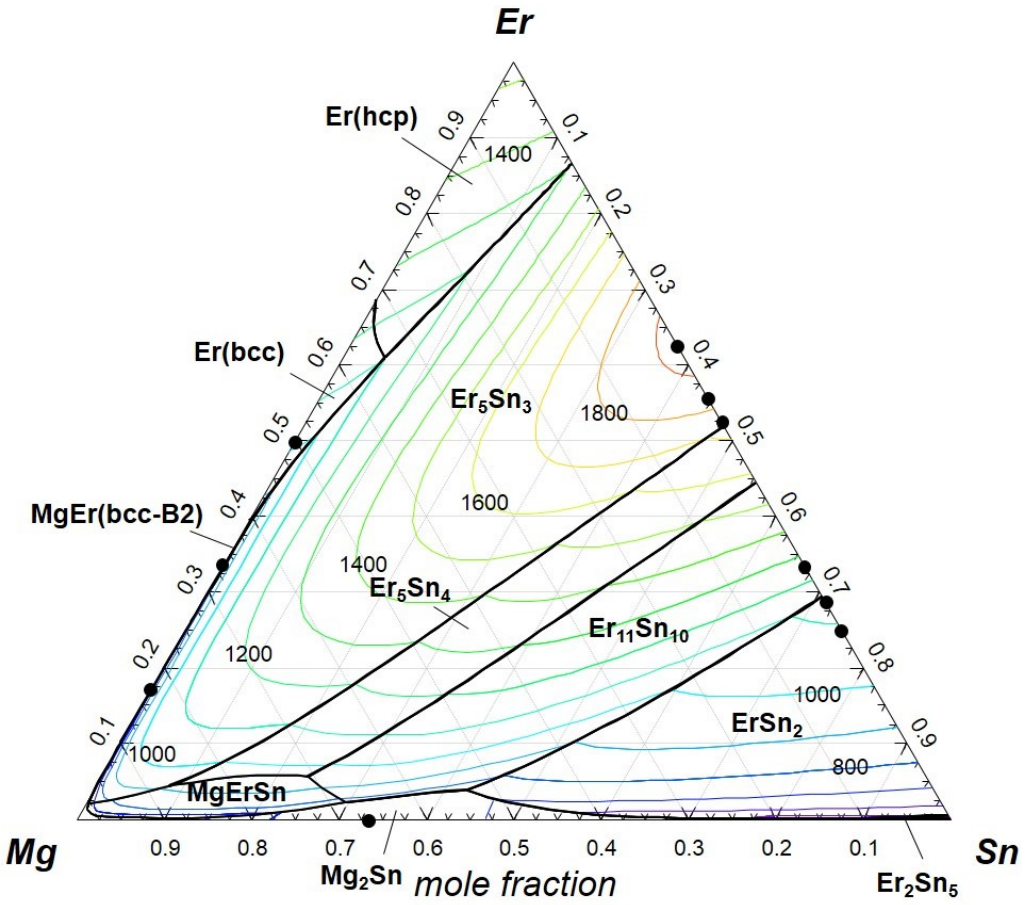


Fig. 51. Calculated liquidus projection of the Mg-Sn-Er system.

4.3. The Mg-Sn-Y system

The phase diagram of this system was investigated by Zhao et al. [12, 13] for the isothermal sections at 500 ºC [13], 400 and 300 ºC [12]. The alloys with five different compositions (Mg-rich only) were prepared in the induction melting furnace under argon gas from the high purity materials, 99.99 wt. % Mg, 99.99 % Sn, and Mg-50 wt.% Y. The samples were wrapped in tantalum sheets, and sealed in evacuated quartz tubes for equilibrium treatment at 300 ºC for 1000 h, 400 ºC for 390 or 1000 h, and 500 ºC for 120 h. The microstructure of the quenched samples were subsequently analysed by XRD and SEM equipped with EDS. The constituent phases and the respective compositions of the phases were determined. The reported experimental data are shown in Figs 53-55. For the ternary compound, MgYSn, the crystal structure (CeScSi type, *tI* 12) with lattice parameters and the melting temperature (1055 ºC) were determine by Manfrinetti et al. [9] using XRD and DTA, respectively. Like the Mg-Sn-Er system, the congruent melting behaviour of the MgErSn reported by Manfrinetti et al. [9] is doubtful according to the phase diagram. The existence of the $MgErSn_2$ was not specifically studied in the study of Zhao et al. [12, 13].

The thermodynamic optimization of the system was previously performed by Lu et al. [26] solely based on the experimental data of Zhao et al. [12, 13]. The liquid phase was describe by the associate model with additional Mg_2Sn species. The Redlich-Kister polynomial was used for the excess Gibbs energy expression. However, the asymmetry of the thermodynamic properties of the constituent binary liquid was not considered. The compound Y_5Sn_3 was treated as the formula $(Sn, Y, Mg)_3(Sn, Y, Mg)_2Y_3$ by a three-sublattice model, and the ternary solubility toward the pseudo phase Mg_5Sn_3 was reproduced based on the reported data [12, 13]. Meanwhile, the sub-binary systems, Mg-Y [27, 28], Sn-Y [26], and Mg-Sn [26, 29] which were used in their optimization were different from the present study. The evaluation and comparison with the present study for the optimization of the Sn-Y system from Zhao et al. [26] was made in the Appendix VII.

In the present optimization, the ternary Mg-Sn-Y system was thermodynamically optimized based on the experimental data [9, 12, 13] by merging the optimized binary systems and the addition of

stoichiometric compound MgYSn. Three constituent binary systems, Mg-Y system [17] (Fig. 15), Mg-Sn [21] (Fig. 30), and Sn-Y (Appendix VII) (Fig. 52) were combined by using asymmetric approximation with Mg as the asymmetric component (ΔH_{mix}: -8.4 kJ mol^{-1} (min) for Mg-Y, -12.8 kJ mol^{-1} (min) for Mg-Sn, and -55.0 kJ mol^{-1} (min) for Sn-Y at 2000 K). The heat capacity of the MgErSn was estimated by NK approximation using the modified heat capacity of Sn (Appendix VI). Then, the ΔH^{o}_{298} and S^{o}_{298} of MgYSn phase were estimated to reproduce melting temperature [9] and the equilibrium phases in the experimental data [12, 13]. The ΔH^{o}_{298} was only adjusted to reproduce the peritectic melting at 1055 ºC with the NK approximated S^{o}_{298}. The thermodynamic parameters for the MgYSn are shown in Table 14. As the accuracy of the EDS method can be rough, the reported homogeneity range of the Y_5Sn_3 was not reproduced. The reported compositions of the $Mg_{24}Y_5$ and MgYSn were also dubious. The equilibrium phases from the experimental data [12, 13] were reproduced well in the present optimization. The calculated isothermal phase diagrams at 500, 400, and 300 ºC are presented in Figs. 53-55, respectively. The calculated liquidus surface is shown in Fig. 56. The peritectic melting temperature of the MgYSn was reproduced to be 1056 ºC, which is better than the optimization by Lu et al. [26] (1079 ºC).

Table 14. Thermodynamic parameters for the ternary compound in the Mg-Sn-Y system (J mol^{-1} or J K^{-1} mol^{-1}).

Phase	Thermodynamic parameters
MgYSn	ΔH^{O}_{298} = -174250.0, S^{O}_{298} = 128.64 $C_p = C_p$ (Mg, hcp) + C_p (Y, hcp) + C_p (Sn, bct)*

*The modified heat capacity of Sn (in Appendix VI).

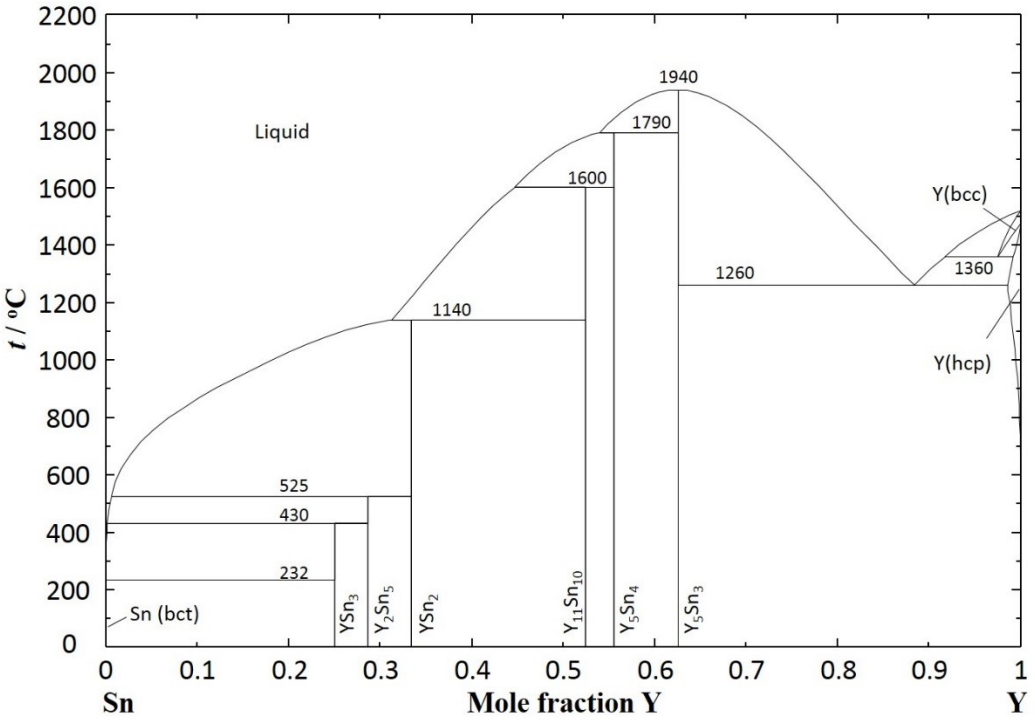


Fig. 52. Optimized phase diagram of the Sn-Y system (Appendix VII).

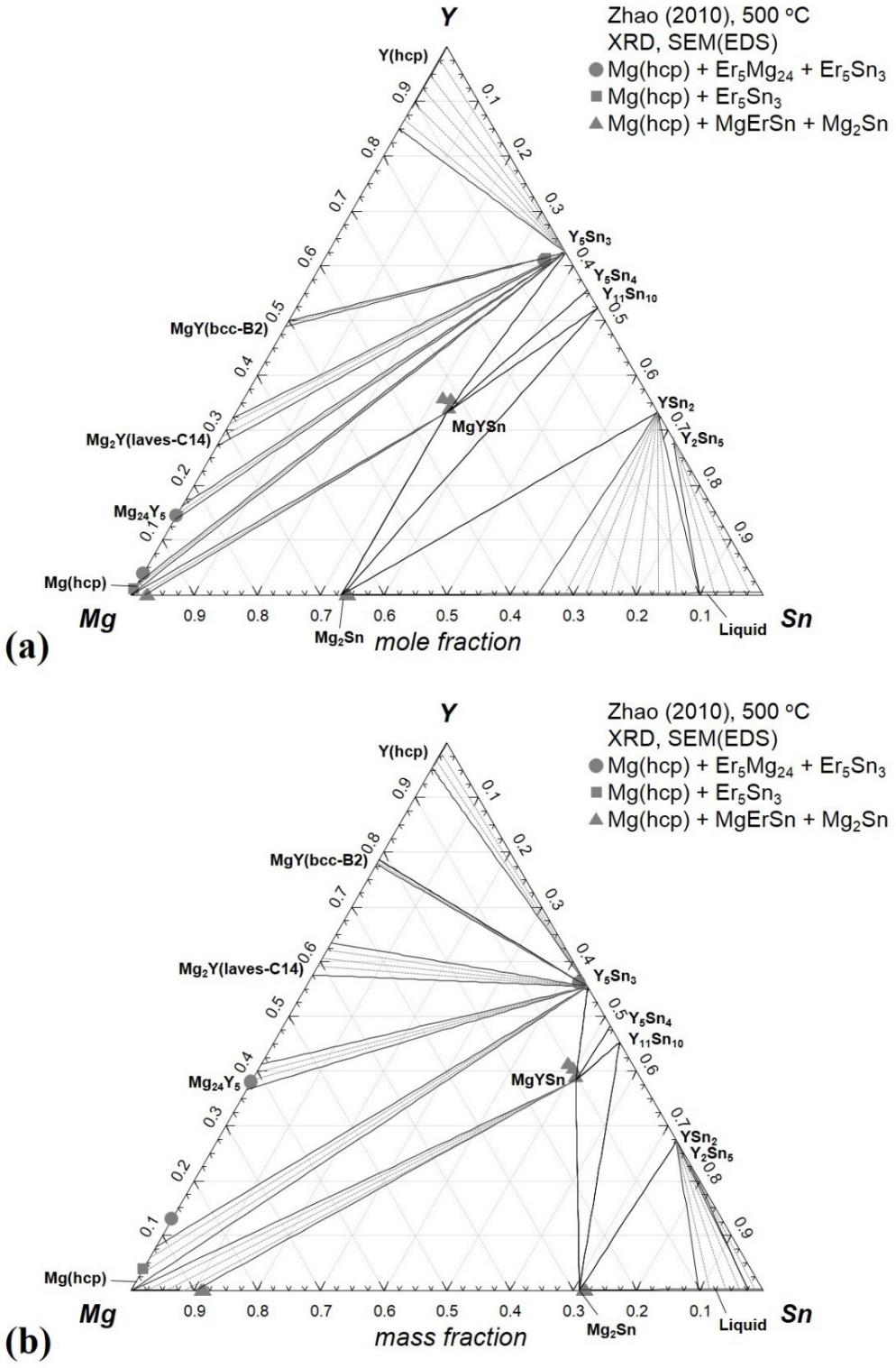


Fig. 53. Calculated isothermal section of the Mg-Sn-Y system at 500 ºC with the experimental data [13]: (a) mole fraction and (b) mass fraction.

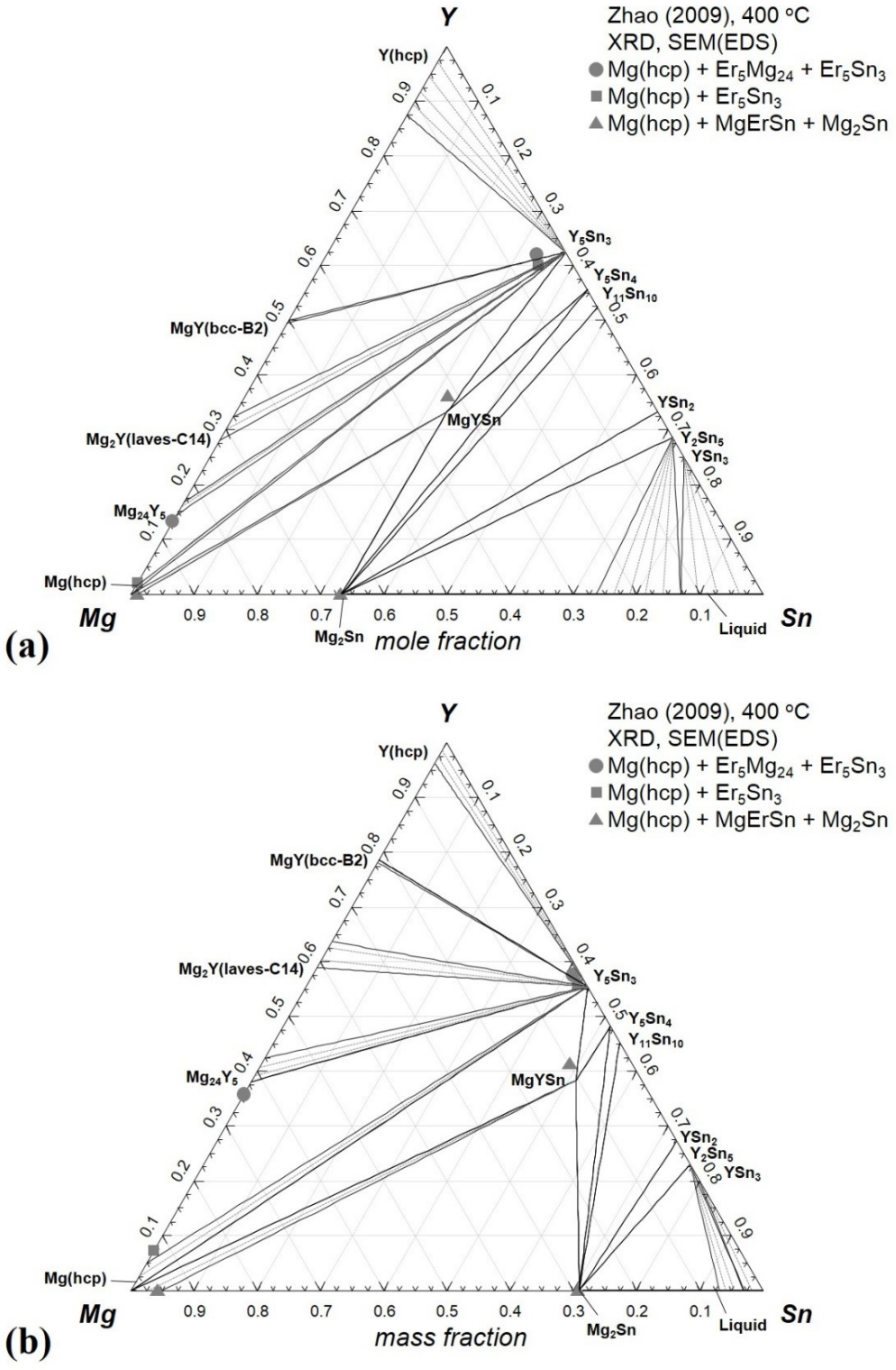


Fig. 54. Calculated isothermal section of the Mg-Sn-Y system at 400 ºC with the experimental data [12]: (a) mole fraction and (b) mass fraction.

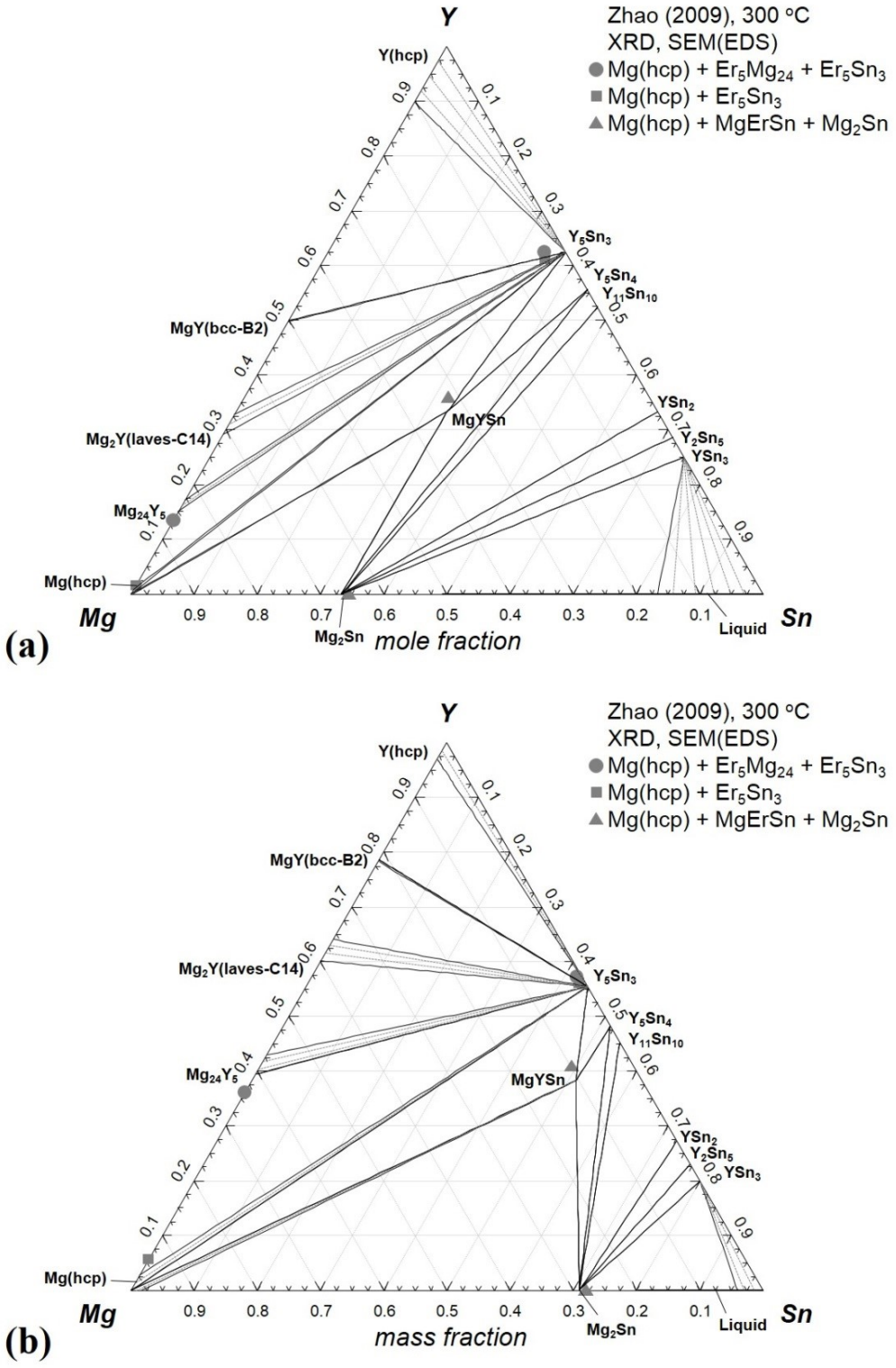


Fig. 55. Calculated isothermal section of the Mg-Sn-Y system at 300 ºC with the experimental data [12]: (a) mole fraction and (b) mass fraction.

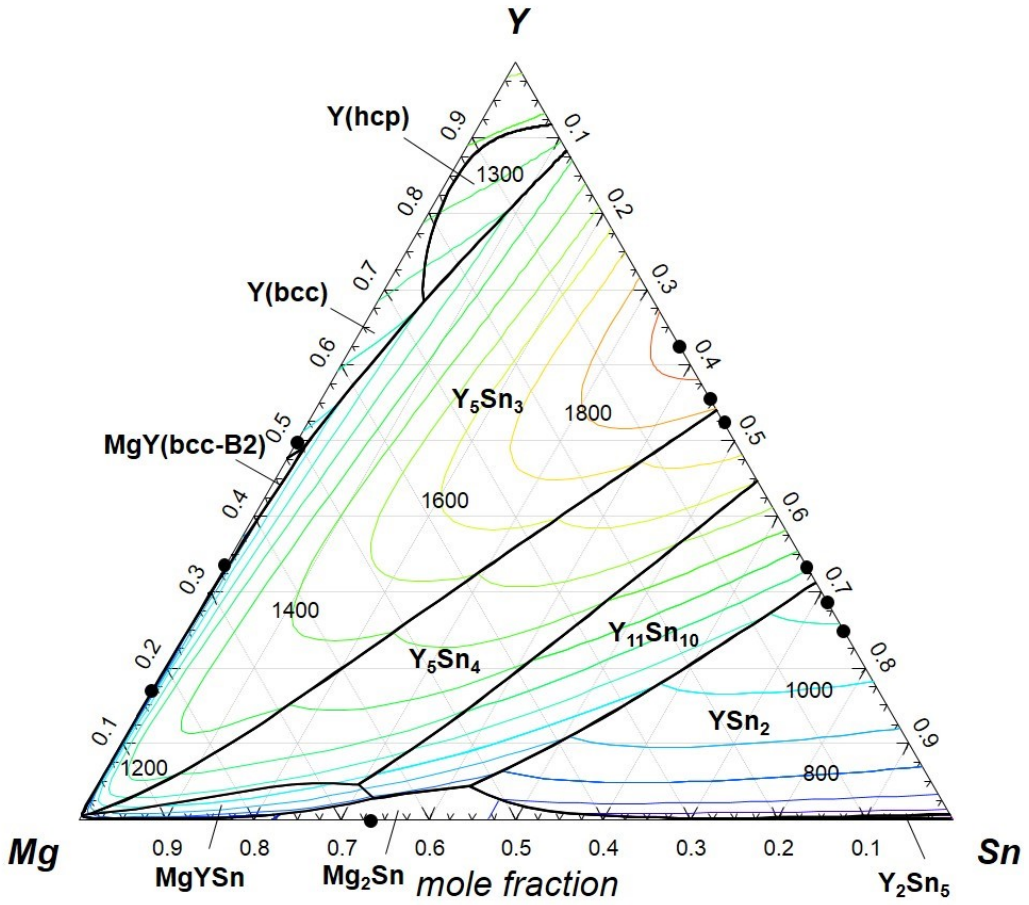


Fig. 56. Calculated liquidus projection of the Mg-Sn-Y system.

5. References

[1] D.A. Petrov, M.S. Mirgalovskaya, I.A. Strel'nikova, E.M. Komova, Tr. Inst. Metall., Akad. Nauk SSSR, (1957) 142-143.
[2] X. Zhang, D. Kevorkov, I.H. Jung, M. Pekguleryuz, J Alloy Compd, 482 (2009) 420-428.
[3] A. Mostafa, M. Medraj, J Alloy Compd, 608 (2014) 247-257.
[4] C. Antion, PhD Thesis, Institut National Polytechnique de Grenoble, 2003.
[5] F. Wrubl, M. Pani, P. Manfrinetti, P. Rogl, J Solid State Chem, 182 (2009) 716-724.
[6] O.F. Zmii, E.I. Gladishevskii, Visnik L'viv. un-tu. Ser. khim., (1974) 24-26.
[7] S.K. Dhar, P. Manfrinetti, A. Palenzona, J. Alloys Compd., 252 (1997) 24-27.
[8] M.E. Drits, E.M. Padezhnova, T.V. Dobatkina, Redk. Metally V Tsvet. Splavakh, (1975) 5-11.
[9] P. Manfrinetti, A. Provino, K.A. Gschneidner, J Alloy Compd, 482 (2009) 81-85.
[10] Y. Guo, PhD Thesis, Northeastern University, Shenyang, 2009.
[11] C. Ma, D. Zhang, Y. Fan, F. Qi, J. Li, J. Phase Equilib. Diffus., 34 (2013) 9-16.
[12] H.D. Zhao, G.W. Qin, Y.P. Ren, W.L. Pei, Y. Guo, J. Alloys Compd., 481 (2009) 140-143.
[13] H.-d. Zhao, Y.-p. Ren, W.-l. Pei, Y. Guo, D. Chen, G.-w. Qin, Zhongguo Youse Jinshu Xuebao, 20 (2010) 177-181.
[14] Y.B. Kang, A.D. Pelton, P. Chartrand, P. Spencer, C.D. Fuerst, Metall Mater Trans A, 38a (2007) 1231-1243.
[15] Y.B. Kang, A.D. Pelton, P. Chartrand, P. Spencer, C.D. Fuerst, J Phase Equilib Diff, 28 (2007) 342-354.
[16] P. Ghosh, M. Medraj, Calphad, 41 (2013) 89-107.
[17] Y.B. Kang, L.L. Jin, P. Chartrand, A.E. Gheribi, K.W. Bai, P. Wu, Calphad, 38 (2012) 100-116.
[18] A.O. Mostafa, A.E. Gheribi, D. Kevorkov, M. Mezbahul-Islam, M. Medraj, Calphad, 42 (2013) 27-37.
[19] A. Shukla, Y.-B. Kang, A.D. Pelton, Int. J. Mater. Res., 100 (2009) 208-217.
[20] J.P. Harvey, PhD Thesis, Ecole Polytechnique, Montreal, 2006.
[21] Y.B. Kang, A.D. Pelton, Calphad, 34 (2010) 180-188.
[22] G. Hu, D. Zhang, F. Guo, L. Jiang, D. Yu, F. Pan, J. Rare Earths, 32 (2014) 52-56.
[23] G. Hu, D. Zhang, T. Tang, X. Shen, L. Jiang, J. Xu, F. Pan, Mater. Sci. Eng., A, 634 (2015) 5-13.
[24] M. Yang, Y. Zhu, X. Liang, F. Pan, Materials Science and Engineering: A, 528 (2011) 1721-1726.
[25] M.-b. Yang, M.-d. Hou, J. Zhang, F.-s. Pan, Transactions of Nonferrous Metals Society of China, 24 (2014) 2497-2506.
[26] D. Lu, C. Guo, C. Li, Z. Du, J. Rare Earths, 32 (2014) 648-654.
[27] O.B. Fabrichnaya, H.L. Lukas, G. Effenberg, F. Aldinger, Intermetallics, 11 (2003) 1183-1188.
[28] C. Guo, Z. Du, C. Li, CALPHAD: Comput. Coupling Phase Diagrams Thermochem., 31 (2007) 75-88.
[29] F.G. Meng, J. Wang, L.B. Liu, Z.P. Jin, J. Alloys Compd., 508 (2010) 570-581.